

Saad Bennani · Younes Lakhrissi ·
Ghizlane Khaissidi · Anass Mansouri ·
Youness Khamlichi *Editors*

WITS 2020

Proceedings of the 6th International
Conference on Wireless Technologies,
Embedded, and Intelligent Systems

Lecture Notes in Electrical Engineering

Volume 745

Series Editors

Leopoldo Angrisani, Department of Electrical and Information Technologies Engineering, University of Napoli Federico II, Naples, Italy

Marco Arteaga, Departament de Control y Robótica, Universidad Nacional Autónoma de México, Coyoacán, Mexico

Bijaya Ketan Panigrahi, Electrical Engineering, Indian Institute of Technology Delhi, New Delhi, Delhi, India

Samarjit Chakraborty, Fakultät für Elektrotechnik und Informationstechnik, TU München, Munich, Germany

Jiming Chen, Zhejiang University, Hangzhou, Zhejiang, China

Shanben Chen, Materials Science and Engineering, Shanghai Jiao Tong University, Shanghai, China

Tan Kay Chen, Department of Electrical and Computer Engineering, National University of Singapore, Singapore, Singapore

Rüdiger Dillmann, Humanoids and Intelligent Systems Laboratory, Karlsruhe Institute for Technology, Karlsruhe, Germany

Haibin Duan, Beijing University of Aeronautics and Astronautics, Beijing, China

Gianluigi Ferrari, Università di Parma, Parma, Italy

Manuel Ferre, Centre for Automation and Robotics CAR (UPM-CSIC), Universidad Politécnica de Madrid, Madrid, Spain

Sandra Hirche, Department of Electrical Engineering and Information Science, Technische Universität München, Munich, Germany

Faryar Jabbari, Department of Mechanical and Aerospace Engineering, University of California, Irvine, CA, USA

Limin Jia, State Key Laboratory of Rail Traffic Control and Safety, Beijing Jiaotong University, Beijing, China

Janusz Kacprzyk, Systems Research Institute, Polish Academy of Sciences, Warsaw, Poland

Alaa Khamis, German University in Egypt El Tagamoa El Khames, New Cairo City, Egypt

Torsten Kroeger, Stanford University, Stanford, CA, USA

Qilian Liang, Department of Electrical Engineering, University of Texas at Arlington, Arlington, TX, USA

Ferran Martín, Departament d'Enginyeria Electrònica, Universitat Autònoma de Barcelona, Bellaterra, Barcelona, Spain

Tan Cher Ming, College of Engineering, Nanyang Technological University, Singapore, Singapore

Wolfgang Minker, Institute of Information Technology, University of Ulm, Ulm, Germany

Pradeep Misra, Department of Electrical Engineering, Wright State University, Dayton, OH, USA

Sebastian Möller, Quality and Usability Laboratory, TU Berlin, Berlin, Germany

Subhas Mukhopadhyay, School of Engineering & Advanced Technology, Massey University,

Palmerston North, Manawatu-Wanganui, New Zealand

Cun-Zheng Ning, Electrical Engineering, Arizona State University, Tempe, AZ, USA

Toyoaki Nishida, Graduate School of Informatics, Kyoto University, Kyoto, Japan

Federica Pascucci, Dipartimento di Ingegneria, Università degli Studi "Roma Tre", Rome, Italy

Yong Qin, State Key Laboratory of Rail Traffic Control and Safety, Beijing Jiaotong University, Beijing, China

Gan Woon Seng, School of Electrical & Electronic Engineering, Nanyang Technological University, Singapore, Singapore

Joachim Speidel, Institute of Telecommunications, Universität Stuttgart, Stuttgart, Germany

Germano Veiga, Campus da FEUP, INESC Porto, Porto, Portugal

Haitao Wu, Academy of Opto-electronics, Chinese Academy of Sciences, Beijing, China

Junjie James Zhang, Charlotte, NC, USA

The book series *Lecture Notes in Electrical Engineering* (LNEE) publishes the latest developments in Electrical Engineering - quickly, informally and in high quality. While original research reported in proceedings and monographs has traditionally formed the core of LNEE, we also encourage authors to submit books devoted to supporting student education and professional training in the various fields and applications areas of electrical engineering. The series cover classical and emerging topics concerning:

- Communication Engineering, Information Theory and Networks
- Electronics Engineering and Microelectronics
- Signal, Image and Speech Processing
- Wireless and Mobile Communication
- Circuits and Systems
- Energy Systems, Power Electronics and Electrical Machines
- Electro-optical Engineering
- Instrumentation Engineering
- Avionics Engineering
- Control Systems
- Internet-of-Things and Cybersecurity
- Biomedical Devices, MEMS and NEMS

For general information about this book series, comments or suggestions, please contact leontina.dicecco@springer.com.

To submit a proposal or request further information, please contact the Publishing Editor in your country:

China

Jasmine Dou, Editor (jasmine.dou@springer.com)

India, Japan, Rest of Asia

Swati Meherishi, Editorial Director (Swati.Meherishi@springer.com)

Southeast Asia, Australia, New Zealand

Ramesh Nath Premnath, Editor (ramesh.premnath@springernature.com)

USA, Canada:

Michael Luby, Senior Editor (michael.luby@springer.com)

All other Countries:

Leontina Di Cecco, Senior Editor (leontina.dicecco@springer.com)

**** This series is indexed by EI Compendex and Scopus databases. ****

More information about this series at <http://www.springer.com/series/7818>

Saad Bennani · Younes Lakhrissi ·
Ghizlane Khaissidi · Anass Mansouri ·
Youness Khamlichi
Editors

WITS 2020

Proceedings of the 6th International
Conference on Wireless Technologies,
Embedded, and Intelligent Systems

Editors

Saad Bennani
Sidi Mohamed Ben Abdellah University
Fez, Morocco

Younes Lakhri
Sidi Mohamed Ben Abdellah University
Fez, Morocco

Ghizlane Khaissidi
Sidi Mohamed Ben Abdellah University
Fez, Morocco

Anass Mansouri
Sidi Mohamed Ben Abdellah University
Fez, Morocco

Youness Khamlichi
Sidi Mohamed Ben Abdellah University
Fez, Morocco

ISSN 1876-1100

ISSN 1876-1119 (electronic)

Lecture Notes in Electrical Engineering

ISBN 978-981-33-6892-7

ISBN 978-981-33-6893-4 (eBook)

<https://doi.org/10.1007/978-981-33-6893-4>

© Springer Nature Singapore Pte Ltd. 2022

This work is subject to copyright. All rights are reserved by the Publisher, whether the whole or part of the material is concerned, specifically the rights of translation, reprinting, reuse of illustrations, recitation, broadcasting, reproduction on microfilms or in any other physical way, and transmission or information storage and retrieval, electronic adaptation, computer software, or by similar or dissimilar methodology now known or hereafter developed.

The use of general descriptive names, registered names, trademarks, service marks, etc. in this publication does not imply, even in the absence of a specific statement, that such names are exempt from the relevant protective laws and regulations and therefore free for general use.

The publisher, the authors and the editors are safe to assume that the advice and information in this book are believed to be true and accurate at the date of publication. Neither the publisher nor the authors or the editors give a warranty, expressed or implied, with respect to the material contained herein or for any errors or omissions that may have been made. The publisher remains neutral with regard to jurisdictional claims in published maps and institutional affiliations.

This Springer imprint is published by the registered company Springer Nature Singapore Pte Ltd.

The registered company address is: 152 Beach Road, #21-01/04 Gateway East, Singapore 189721, Singapore

Brief Synopsis About WITS'2020 Book

This book gathers together selected papers presented at the 6th International Conference on Wireless Technologies, Embedded and Intelligent Systems (**WITS 2020**).

WITS Conference is an event that brings together specialists from all over the world, covering multiple aspects of diverse topics such as wireless networking, embedded and intelligent systems, electronic and renewable energy to create an open space networking and exchange of information and knowledge and also to strengthen the synergy between researchers and experts from academia, research institutions and industry. During three days, presentations, discussions and side events will inspire new ideas and innovations that will support enhancing innovation.

The tremendous advances in wireless communications, embedded and intelligent systems, combined with rapid evolution in smart appliances and devices have generated new challenges and problems requiring solutions that rely on interactions between different network layers and applications in order to offer advanced mobile services. Moreover, a transformation of our energy system is already occurring due to the strong demand and acceptance of creating a carbon-free energy system, which underlines the need to develop a strategy for a renewable, sustainable and innovative energy future that enables societal, commercial and community prosperity.

This year, WITS Conference is being held from October 14 to 16, 2020. The conference received submission from many different countries all over the world.

This book results from more than 245 contributions of researchers from more than 14 countries worldwide. After a thorough peer-review process, the Program Committee has accepted 120 papers, which have undergone a selection stage to retain 104 papers for this LNEE volume. This achieves overall acceptance rate of 42.5%.

To put a conference of this magnitude together is not a small task. To that end, we would like to thank the Technical Program Chairs members, all the reviewers, Publicity and Communication Chairs and all members of the Organizing Committee for their assistance in making this conference a success. We would like to thank our distinguished speakers who have agreed to address the conference attendees.

We are very grateful to the keynote speakers who have accepted our invitation to come and share their work during the conference: **Prof. Adam. W. Skorek**, from Trois-Rivières University of Quebec (Canada); **Prof. Ruano António Eduardo De Barros** from Algarve University, Faro (Portugal); **Prof. Norma Alias** from Center for Sustainable Nanomaterials (Malaysia); **Prof. Mohamed Himdi** from the University of Rennes 1 (France); **Prof. Rachid Yazami** from KVI Holdings PTE LTD. (Singapore); **Prof. Ivashko Evgeny** from Russian Academy of Sciences, Moscow (Russia); and **Dr. Ahmed Boutejdar** from German Research Foundation DFG, Braunschweig-Bonn (Germany).

Saad Bennani
Younes Lakhrissi
Ghizlane Khaissidi
Anass Mansouri
Youness Khamlichi

Organization

Program Committee Chairs

Ruano António Eduardo De Barros, Universidade do Algarve, Faro, Portugal
Mellit Adel, University of Jijel, Algeria
Lakhssassi Ahmed, University of Quebec in Outaouais, Canada
Ruichek Yassine, UTBM, Belfort, France

General Co-chairs

Khamlichi Youness, ENSA of Fez, SMBA University, Morocco
Lakhrissi Younes, ENSA, SMBA University, Fez, Morocco
Ramdani Mohamed, ESEO Angers, France

Technical Program Committee

Aarab Abdellah, FS, SMBA University, Fez, Morocco
Abdellaoui Alaoui Larbi, E3MI, Casa, Morocco
Abdelmoumen Khalid, ENS, SMBA University, Fez, Morocco
Abou Alkalam Anas, ENSA, Cadi Ayyad University, Marrakech, Morocco
Abounaima Mohamed Chaouki, FST, SMBA University, Fez, Morocco
Aboutni Rachid, EST, Mohammed I University, Oujda, Morocco
Addaim Adnane, ENSA, Ibn Tofail University, Kenitra, Morocco
Adel Ali Abou El-Ela, Faculty of Engineering, Menoufia University, Egypt
Adib Abdellah, FST Mohammedia, Morocco
Adnane Yassine, Le Havre University, Le Havre, France
Adnani Younes, EST, Ibn Tofail University, Kenitra, Morocco

Aghoutane Badraddine, FS, Moulay Ismail University, Meknes, Morocco
 Ahaitouf Abdelaziz, FP of Taza, SMBA University, Morocco
 Ahaitouf Ali, FST, SMBA University, Fez, Morocco
 Aissaoui Karima, ENSA, SMBA University, Fez, Morocco
 Aissat Adelkader, Department of Electronics, University of Blida, Algeria
 Ait Kbir M'hamed, FST, Abdelmalek Essaadi University, Tanger, Morocco
 Ait Madi Abdessalam, ENSA, Kenitra, Morocco
 Akil Mohamed, (A2SI) Groupe ESIEE, France
 Aknin Noura, Abdelmalek Essaadi University, Tetouan, Morocco
 Aksasse Brahim, FP Errachidia, Moulay Ismail University, Morocco
 Alami Kammouri Salah Eddine, FST, SMBA University, Fez, Morocco
 Alami Marktani Malika, ENSA, SMBA, Fez, Morocco
 Alaoui Chakib, INSA, EUROMED University, Fez, Morocco
 Alaoui Chrifi Meriem, Valenciennes University, France
 Alaoui Souad, SMBA University, Fez, Morocco
 Alaoui Talibi Mohammed, FST, SMBA University, Fez, Morocco
 Alfidy Mohammed, ENSA, SMBA University, Fez, Morocco
 Allouhi Amine, EST, SMBA University, Fez, Morocco
 Almudena Suarez Rodriguez, University of Cantabria, Spain
 Amara Korba Abdelaziz, Badji Mokhtar, Annaba University, Algeria
 Amraoui Samir, FS, Mohammed I University, Oujda, Morocco
 Amroune Mohammed, University of Larbi Tebessi, Tebessa, Algeria
 Aubert Hervé, National Polytechnical Institute, Toulouse, France
 Aziz Abdelhak, EST, UMP, Oujda, Morocco
 Azouzi Salma, FS, Ibn Tofail University, Kenitra, Morocco
 Babu K. Vasu, Vasireddy Venkatadri Institute of Technology, India
 Badri Abdelmajid, FST of Mohammedia, Hassan II University, Morocco
 Baek Donghyun, Chung-Ang University, South Korea
 Baghdad Abdennaceur, FST of Mohammedia, Hassan II University, Morocco
 Bah Slimane, EMI—Mohammed V University, Rabat, Morocco
 Balboul Younes, ENSA, SMBA University, Fez, Morocco
 Bekkali Mohammed, SMBA University, Fez, Morocco
 Belkadir Jamal, EST, SMBA University, Fez, Morocco
 Belkebir Hicham, ENSA, SMBA University, Fez, Morocco
 Belkouch Said, ENSA, Cadi Ayyad University, Marrakech, Morocco
 Belmajdoub Abdelhafid, FST, SMBA University, Fez, Morocco
 Ben Abbou Rachid, FST, SMBA University, Fez, Morocco
 Ben Slima Mohamed, ENET'COM, Sfax, Tunisia
 Benaissa Ezzeddine, Le Havre University, Le Havre, France
 Benaissa Mounir, University of Sfax, Tunisia
 Benamar Nabil, EST, UMI, Meknes, Morocco
 Benbrahim Mohammed, FSDM, SMBA University, Fez, Morocco
 Benchagra Mohamed, ENSAK, Hassan I University, Khouribga, Morocco
 Bendjenna Hakim, University of Larbi Tebessi, Tebessa, Algeria
 Benelallam Imade, INSEA, Rabat, Morocco

Benhaddou Driss, University of Houston, USA
Benhala Bachir, FS, University of My Ismail, Meknes, Morocco
Bennani Saad, ENSA, SMBA University, Fez, Morocco
Bennis Hamid, EST, UMI, Meknes, Morocco
Bennis Mehdi, Centre for Wireless Communication, University of Oulu, Finland
Benslimane Anas, ENSA of Oujda, MP University, Oujda, Morocco
Benslimane Mohamed, EST USMBA, Fez, Morocco
Berrada Ismail, FSDM, SMBA University, Fez, Morocco
Berrada Mohammed, ENSA, SMBA University, Fez, Morocco
Bossoufi Badre, FSDM, SMBA University, Fez, Morocco
Bouasria Fatima, University of Saida, Algeria
Bouayad Anas, FSDM, SMBA University, Fez, Morocco
Bouchnaif Jamal, EST of Oujda, MP University, Oujda, Morocco
Boudraa Bachir, USTHB, Algeria
Bou-El-Harmel Abdelhamid, EST, SMBA University, Fez, Morocco
Bouhoute Afaf, FSDM, SMBA University, Fez, Morocco
Boufounas El-Mahjoub, FST, Moulay Ismail University, Errachidia, Morocco
Boulaalam Abdelhak, ENSA, SMBA University, Fez, Morocco
Boumhidi Jaouad, FS, SMBA University, Fez, Morocco
Bouridane Ahmed, University of Newcastle, UK
Boushaba Abdelali, FST, SMBA University, Fez, Morocco
Boutaba Raouf, University of Waterloo, Canada
Boutejdar Ahmed, DFG, Braunschweig-Bonn, Germany
Bri Seddik, EST, Moulay Ismail University, Meknes, Morocco
Cano Juan Luis, University of Cantabria, Spain
Carvalho Marcelo, University of Brasilia (UnB), Brazil
Casaneuva Alicia, University of Cantabria, Spain
Chadli Sara, Mohamed I University, Oujda, Morocco
Chaoub Abdelaali, INPT, Rabat, Morocco
Chaoui Nour El Houda, ENSA, SMBA University, Morocco
Chaoui Abdelali, FST, SMBA University, Fez, Morocco
Charaf My El Hassan, FS, Ibn Tofail University, Kenitra, Morocco
Charrel Pierre-Jean, University of Toulouse 2, France
Cheriti Ahmed, Quebec University, Trois-Rivières, Canada
Cherroud Mohamed, FST, SMBA University, Fez, Morocco
Chetoui Kaouther, ENSA, SMBA University, Fez, Morocco
Chougdali khalid, ENSA, Ibn Tofail University, Kenitra
Chougrad Hiba, ENSA, SMBA University, Fez, Morocco
Chouinard Jean-Yves, Faculty of Sciences, University of Laval, Canada
Chung Lawrence, University of Texas, USA
Conceicao Eusébio, FCT—University of Algarve, Portugal
Costen Fumie, SEEE, University of Manchester, UK
Coulette Bernard, University of Toulouse 2, France
Cyrille Bertelle, Le Havre University, Le Havre, France
Darena Frantisek, Mendel University, Czech

Das Sudipta, IMPS College of Engineering and Technology, India
 Decroze Cyril, FST Limoges, France
 Degauque Pierre, Telice, USTL-Lille, France
 Denidni Tayeb Ahmed, INRS, Canada
 Derkaoui Abdechafik, FS, Mohamed I University, Oujda, Morocco
 Despaux Gilles, IES, University of Montpellier, France
 Dhraief Amine, University of Manouba, Tunisia
 Dinh Thuc Nguyen, FIT—Hochiminh University, Vietnam
 Dousset Bernard, UPS, Toulouse, France
 Drissi M'Hamed, INSA de Rennes, France
 El Akchioui Nabil, FSTH, Morocco
 El Afou Youssef, ENSA, SMBA University, Fez, Morocco
 El Azzab Driss, FST, SMBA University, Fez, Morocco
 El Abbassi Ahmed, FST Errachidia, MI University, Morocco
 El Akkad Nabil, ENSA, SMBA University, Fez, Morocco
 El Alami Ali, FST, Moulay Ismail University, Errachidia, Morocco
 El Alami El Madani Yasser, ENSIAS, MV University, Rabat, Morocco
 El Amrani Aumeur, FST, Moulay Ismail University, Errachidia, Morocco
 El Ansari Mohamed, FS, Ibn Zohr University, Agadir, Morocco
 El Ayachi Moussa, ENSA Oujda, Morocco
 El Bachtiri Rachid, EST, SMBA University, Morocco
 El Batteoui Ismail, FSDM, SMBA University, Fez, Morocco
 El Bdouri Abdelali, ENSA, SMBA University, Fez, Morocco
 El Bekkali Moulhime, ENSA, SMBA University, Fez, Morocco
 El Beqqali Omar, FSDM, SMBA University, Fez, Morocco
 El Boushaki Abdessamad, ENSA, SMBA University, Fez, Morocco
 El Fadili Hakim, ENSA, SMBA University, Fez, Morocco
 El Fazazy Khalid, FPO, University Ibn Zohr, Morocco
 El Fergougui Abdeslam, FS, UMI Meknes, Morocco
 El Ghazi Mohammed, EST, SMBA University, Fez, Morocco
 El Ghzaoui Mohammed, EST of Fez, SMBA University, Morocco
 El Gibari Mohammed, IETR, University of Nantes, France
 El Gouri Rachid, ENSA, Ibn Tofail University, Kenitra, Morocco
 El Hafyani Mohamed Larbi, ENSA, Mohammed I University, Oujda, Morocco
 El Hassani Hind, ENSA, SMBA University, Fez, Morocco
 El Kamili Mohamed, EST, H2 University, Casa, Morocco
 El Kasri Chakir, FS, SMBA University, Fez, Morocco
 El Khamlichi Drissi Khalil, Clermont Auvergne University, Institut Pascal, France
 El Mahdaouy Abdelkader, FSDM, SMBA University, Fez, Morocco
 El Makhfi Nouredine, FST of Al Hoceima, UAE, Morocco
 El Mallahi Mostafa, FSDM, SMBA University, Fez, Morocco
 El Markhi Hassane, FST of Fez, SMBA University, Morocco
 El Mazoudi El Houssine, Cadi Ayyad University, Marrakech, Morocco
 El Mehdi Abdelmalek, ENSA, MP University, Oujda, Morocco
 El Mohajir Mohammed, FSDM, SMBA University, Fez, Morocco

El Moutaouakil Karim, ENSAH, Morocco
El Mourabit Aimad, ENSA, AE University, Tetouan, Morocco
El Moussaoui Hassan, FST of Fez, SMBA University, Morocco
El Ouaazizi Aziza, FP, SMBA University, Taza, Morocco
El Ouaazizi Mohammed, FP, SMBA University, Taza, Morocco
El Ouardi Abdelhafid, Paris-Saday University, Orsay, France
El Ouariachi Mostafa, EST, Mohammed I University, Oujda, Morocco
El Ouazzani Nabih, FST, SMBA University, Fez, Morocco
El Ougli Abdelghani, ENSA, Mohamed I University, Oujda, Morocco
Elhaj Ben Ali Safae, ENSA of Fez, SMBA University, Morocco
El Warraki El Mostafa, Cadi Ayyad University, Marrakesh, Morocco
En-Nahnahi Noureddine, FSDM, SMBA University, Fez, Morocco
Es-Sbai Najia, FST, SMBA University, Fez, Morocco
Evgeny Ivashko, IAMR KRC RAS, Russia
Ezzazi Imad, ENSA, SMBA University, Fez, Morocco
Farchi Abdelmajid, FST, Hassan I University, Settat, Morocco
Farhane Youness, ENSA, SMBA University, Fez, Morocco
Ferreira Pedro, Faculty of Sciences, University of Lisbon, Portugal
Foshi Jaouad, FST Errachidia, Moulay Ismail University, Morocco
Frant Terril, Peking University, China
Galadi Abdelghafour, Cadi Ayyad University, Marrakesh, Morocco
Garcia Jose Angel, University of Cantabria, Spain
Gargouri Faiez, University of Sfax, Tunisia
Ghfir Younes, FST, SMBA University, Fez, Morocco
Gherabi Noureddine, ENSAK, Hassan I University, Khouribga, Morocco
Ghoulmi-Zine Nacira, Badji Mokhtar, Annaba University, Algeria
Ghouili Jamel, Moncton University, Canada
Ghoumid Kamal, ENSA, UMP, Oujda, Morocco
Gilard Raphaël, IET de Rennes, France
Gonzalez Huerta Javier, University of Polytechnic-Valencia, Spain
Grande Ana, Valladolid University, Spain
Guardado Amparo Herrera, University of Cantabria, Spain
Guennoun zouhair, EMI, Mohammed V University, Rabat, Morocco
Habib Ayad, FLSH, Mohammedia, Morocco
Haffaf Hafid, University of Oran, Algeria
Hain Mustapha, Hassan II University, Mohammedia, Morocco
Hajami Abdelmajid, ENSIAS, Mohammed V University, Rabat, Morocco
Hajji Bekkay, ENSA, UMP, Oujda, Morocco
Halkhams Imane, FST of Fez, SMBA University, Morocco
Hanafi Ahmed, EST of Fez, SMBA University, Morocco
Hariri Said, Ecole des Mines de Douai, France
Harkat Houda, Institute of Telecommunications, Aveiro University, Portugal
Hassanein Hossam, Queen's University, Kingston, Ontario, Canada
Hefnawi Mostafa, Royal Military College of Canada
Herrera Amparo, University of Cantabria, Spain

Himdi Mohamed, ESIR, University of Rennes 1, France
Hinaje Said, ENSA, SMBA University, Fez, Morocco
Hraoui Said, ENSA, SMBA University, Fez, Morocco
Ibanes Tomas Fernandez, University of Cantabria, Spain
Ijaz Bilal, COMSATS Institute of Info Techno, Islamabad, Pakistan
Jafargholi Amir, Amir Kabir University of Technology, Iran
Jagdish Chand Bansal, South Asian University, New Delhi, India
James Michel, University Blaise Pascal, Clermont-Ferrand, France
Jamil Abdelmajid, EST, SMBA University, Fez, Morocco
Jararweh Yaser, University of Science and Technology, Jordan
Jarou Tariq, ENSA of Kenitra, Morocco
Jeghal Adil, ENSA, SMBA University, Fez, Morocco
João Manuel R. S. Tavares, Universidade do Porto, Portugal
Jorio Mohammed, FST, SMBA University, Fez, Morocco
Jureta Ivan, University of Namur, Namur, Belgium
Kabbaj Mohammed Nabil, FSDM, SMBA University, Fez, Morocco
Kara Ali, Atilim University, Turkey
Karli Radouane, EMI, Mohammed V University, Rabat, Morocco
Kassmi Kamal, EST, Mohammed I University, Oujda, Morocco
Kenzi Adil, ENSA, SMBA University, Fez, Morocco
Khaissidi Ghizlane, ENSA, SMBA University, Fez, Morocco
Khalil Mohammed, FST Mohammedia, Morocco
Khamjane Aziz, EST, SMBA University, Fez, Morocco
Khamlichi Youness, ENSA, SMBA University, Fez, Morocco
Kharbach Jaouad, FSDM USMBA, Fez, Morocco
Kharroubi Jamal, FST, SMBA University, Fez, Morocco
Khiredine Abdelkrim, Fac of Technology, University A/Mira Bejaia, Algeria
Khlifi Yamina, ENSA, Mohammed I University, Oujda, Morocco
Klilou Abdessamad, FST of Beni-Mellal, Morocco
Koukam Abderrafaa, UTBM, Belfort, France
Koulali Mohammed-Amine, ENSA, Mohamed I University, Oujda, Morocco
Koulali Sara, ENSA, Abdelmalek Essaadi University, Al Hoceïma, Morocco
Kulkarni Shrirang, Gogte Institute of Technology, India
Laamari Hlou, Ibn Tofail University, Kenitra, Morocco
Lachkar Abdelmonaïme, ENSA, AE University, Tangier, Morocco
Lahrech Khadija, ENSA, SMBA University, Fez, Morocco
Lahsaini Mohammed, FS, Moulay Ismail University, Meknes, Morocco
Lakhliai Zakia, EST, SMBA University, Fez, Morocco
Lakhrissi Younes, ENSA, SMBA University, Fez, Morocco
Lakhssassi Ahmed, University of Quebec in Outaouais, Canada
Lakrit Soufian, EMI, Mohammed V University, Rabat, Morocco
Lamhamdi Mohammed, ENSAK, Hassan I University, Khouribga, Morocco
Lamhamdi Tijani, FST, SMBA University, Fez, Morocco
Latrach Mohamed, ESEO Angers, France
Lebbar Hassan, FST of Mohammedia, Hassan II University, Morocco

Le Clezio Emmanuel, IES, University of Montpellier, France
Leghris Cherkaoui, FST Mohammedia, Morocco
Liu Lin, University of Tsinghua, China
M. James Stephen, Welfare Engineering College, Visakhapatnam, Andhra Pradesh, India
Maalmi Khalil, EST, SMBA University, Fez
Magdalena Salazar Palma, Universidad Carlos III de Madrid, Spain
Maher Hassan, University of Sherbrooke, Canada
Mahlous Ahmed Redha, Prince Sultan University, Riyadh, KSA
Majda Aicha, FST, SMBA University, Fez, Morocco
Malek Rachid, ENSA, Mohammed I University, Oujda, Morocco
Mansouri Anass, ENSA, SMBA University, Fez, Morocco
Mantoro Teddy, Universitas Siswa Bangsa International, Malaysia
Marzouq Manal, FST, SMBA University, Fez, Morocco
Masmoudi Nouri, Ecole Nationale De Sfax, Tunisia
Massicotte Daniel, Quebec University, Trois-Rivières, Canada
Matsuhisa Takashi, Ibaraki National College of Technology, Japan
Mazari Abdelfattah, FS, Mohammed I University, Oujda, Morocco
Mazari Bélahcène, Groupe CESI, France
Mazer Said, ENSA, SMBA University, Fez, Morocco
Mechaqrane Abdellah, FST, SMBA University, Fez, Morocco
Mellahi Mestpha, ENS, SMBA University, Fez, Morocco
Mellit Adel, University of Jijel, Algeria
Mellouli El Mehdi, ENSA, SMBA University, Fez, Morocco
Merabet Boualem, University of Mascara, Algeria
Meric Stéphane, IET de Rennes, France
Messaoudi Abdelhafid, EST, Mohammed I University, Oujda, Morocco
Motahhir Saad, ENSA, SMBA University, Fez, Morocco
Moumen Anis, ENSA of Kenitra, Ibn Tofail University, Morocco
Moumkine Nourddine, FST Mohammedia, Morocco
Mrabti Mostafa, ENSA, SMBA University, Fez, Morocco
Mylopoulos John, University of Trento, Italy
Naimi Salaeddine, ENSA, Mohammed I University, Oujda, Morocco
Najah said, FST, SMB University, Fez, Morocco
Najdawi Anas, Canadian University Dubai, United Arab Emirates
Najoui Mohamed, ENSET, Mohammed V University, Rabat, Morocco
Nasser Jamalkhan, University of Hertfordshire, UK
Naveed Bin Rais, AUST, UAE
Nfaoui El Hbib, FSDM, SMBA University, Fez, Morocco
Norma Alias, Universiti Teknologi Malaysia
Nourelidin Aboelmagd, Royal Military College of Canada
Nouvel Fabienne, INSA Rennes, France
Nurul Mahmood, Aalborg University, Denmark
Ouahabi Abdeldjalil, University of Tours, France
Ouahmane Hassan, ENSA, Chouaïb Doukkali University, El Jadida, Morocco

Ouazzani Jamil Mohammed, UPF, Fez, Morocco
 Oubenaalla Youness, FSJES, Moulay Ismail University, Meknes, Morocco
 Oughdir Lahcen, ENSA, SMBA University, Fez, Morocco
 Pathan Al-Sakib Khan, Independent University, Bangladesh
 Pescape Antonio, University of Naples, Italy
 Pruncu Catalin Iulian, University of Birmingham, UK
 Puente Antonio Tazon, University of Cantabria, Spain
 Qjidaa Hassan, FS, SMBA University, Fez, Morocco
 Raffaelli Carla, University of Bologna, Bologna, Italy
 Rahmoun Mohammed, ENSAO, Mohamed I University Oujda, Morocco
 Ramdani Mohamed, ESEO Angers, France
 Razi Mouhcine, FST, SMBA University, Fez, Morocco
 Rhallabi Ahmed, PCM IMN Nantes, France
 Ridda Mohamed, University of Larbi Tebessi, Tebessa, Algeria
 Rifi Mounir, EST, Casablanca, Morocco
 Riffi Jamal, FSDM, SMBA University, Fez, Morocco
 Roose Philippe, University of Pau, France
 Roy Avisankar, Haldia Institute of Technology, India
 Ruano António Eduardo De Barros, Universidade do Algarve, Faro, Portugal
 Ruano Maria Da Graça, Universidade do Algarve, Faro, Portugal
 Ruichek Yassine, UTBM, Belfort, France
 Saber Mohammed, ENSA of Oujda, Mohammed I University, Morocco
 Sabri Abdelouahed, FS, SMBA University, Fez, Morocco
 Sadoghi Mohammad, University of Toronto, Canada
 Saikouk Hajar, INSA, EUROMED University, Fez, Morocco
 Saleem Rashid, University of Engineering and Technology, Pakistan
 Sanchez Angel Mediavilla, University of Cantabria, Spain
 Senouci Sidi-Mohammed, University of Bourgogne, France
 Serhani Mohamed Adel, CIT, UAE University, United Arab Emirates
 Serrhini Mohammed, Mohamed I University, Oujda, Morocco
 Sheta Alaa, Electronics Research Institute, Giza, Egypt
 Sicard Etienne, INSA, Toulouse, France
 Siddiqi Imran, University of Bahria, Pakistan
 Silkan Hassan, Computer Science Department, Morocco
 Slimani Abdellatif, FST, SMBA University, Fez, Morocco
 Soumlaimani Saad, ENIM, Rabat, Morocco
 Srikanta Patnaik, SOA University and I.I.M.T., Bhubaneswar, India
 Taime Abderazzak, Sultan Moulay Slimane University
 Tairi Hamid, FS, SMBA University, Fez, Morocco
 Talbi Larbi, University of Quebec, Canada
 Tao Junwu, ENSEEIHT-LAPLACE, Toulouse University, France
 Tarbouchi Mohamed, Royal Military College, Kingston, Ontario, Canada
 Tarek M. Sobh, School of Engineering, University of Bridgeport, USA
 Tazi El Bachir, ESTK, Sultan Moulay Slimane University, Morocco
 Temcamani Farid, ENSEA, Cergy Pontois, France

Terhzaz Jaouad, CRMEF, Morocco
Tissier Jérôme, ESEO-IETR Angers, France
Tlemsani Redouane, University of Sciences and Technologies of Oran, Algeria
Vaidyanathan Sundarapandian, Vel Tech, India
Vasilakos Athanasios, University of Western Macedonia, Greece
Vegas Angel, University of Cantabria, Spain
Vizcaino Aurora, University of Castilla-La Mancha, Spain
Vladimir Mazalov, IAMR KRC RAS, Russia
Wahbi Azeddine, FS Ain Chock, University Hassan II, Casablanca, Morocco
Waldemar Skorek Adam, University of Quebec at Trois-Rivières, Canada
Whalen Michael, University of Minnesota, USA
Wiesbeck Werner, Institute of Radio Frequency Engineering and Electronics, Germany
Yahyaouy Ali, FS Fez, Morocco
Yakine Fadoua, ENSA, SMBA University, Fez, Morocco
Yamana Hayato, Waseda University, Japan
Yao Xin, School of Computer Science, University of Birmingham, UK
Yazami Rachid, Founding Director, KVI PTE LTD., Singapore
Yousfi Driss, ENSA, Mohammed I University, Oujda, Morocco
Yu-Dong Zhang, University of Leicester, England
Zahboune Hassan, EST, Mohammed I University, Oujda, Morocco
Zahi Azeddine, FST, SMBA University, Fez, Morocco
Zarghili Arsalane, FST, SMBA University, Fez, Morocco
Zaz Ghita, FST, SMBA University, Fez, Morocco
Zbitou Jamal, FST, Hassan I University, Settat, Morocco
Zenkouar Khalid, FST, SMBA University, Fez, Morocco
Zhang Qingfeng, South University of Science and Technology, China
Zouggar Smail, EST, Mohamed I University, Oujda, Morocco
Zouiten Mohammed, FP of Taza, SMBA University, Morocco
Zouhri Amal, FSDM, SMBA University, Morocco

Invited Speakers

Pr. Adam. W. Skorek

Ph.D. Eng., Trois-Rivières University, Canada

«Artificial Intelligence and Brain Biofields HPC Simulations»

Summary Artificial intelligence (AI) is present in electrical, electronics and computer engineering for years. In particular, the biofields defined as electromagnetics and thermal fields in living matter are naturally related to AI studies and applications, including brain analysis with numerical modeling and simulations. Brain functionalities inspiring all developments in AI from theoretical investigations to machine learning, humanoid robots and brains interface device implementation. The brain biofield interactions with external excitations such as 5G telecommunications devices, transcranial magnetic stimulation and even other brain biofields are currently explored more as never before. A presentation from worldwide perspective of some modern research works with their result applications is completed by lecturer's experiences and guidelines for the future. Some practical examples and instructions for researchers, engineers and students are presented, stimulating the audience to various scientific as well as R&D activities in this so promising area.

Prof. Ruano António Eduardo De Barros

Universidade do Algarve, Faro, Portugal

«Computational Intelligence Techniques for Home Energy Management Systems»

Summary The consumption of energy has increased substantially in the building sector in the past years, fueled primarily by the growth in population, households and commercial floor space. For this reason, home energy management systems (HEMS) are becoming increasingly important to invert this continuously increasing trend.

Computational intelligence (CI) techniques play an important role in existing HEMS, and its use will be much more important in the future. This talk will discuss major applications of CI methods in HEMS, with an emphasis on the use of models for forecasting energy consumption and production, on non-invasive load monitoring (NILM) of electrical appliances and on real-time predictive control of HVAC systems.

Prof. Norma Alias

Associate Professor at Center for Sustainable Nanomaterials, Malaysia

«Machine Learning System for IoT Data Stream Connected to Freeze-DIC Machine Sensor Device in Drying Pineapple»

Summary By analyzing big data generated using IoT wireless technology, synchronizing digital, physical value streams, predictive analytics, the process of control, and monitoring the manufacturing machines become more predictability and interoperability. Big data analytics of machine learning systems is proposed for optimizing the DIC-freeze-drying operation of pineapple. The IoT sensor device connected to the DIC-freeze-drying machine will generate a huge volume and high-speed velocity data signals. Machine learning helps manufacturers enhance their production, eliminate production downtime, increase the quality of processes, and reduce financial risk.

Therefore, a DIC-freeze machine with machine learning focuses on the development of artificial intelligence and a method of data analysis. The aims of complex algorithms to automate the drying process are to predict the optimum level of time duration, pressure, and temperature for drying different species of pineapple by making insightful decisions. In addition, it is easy to get fake pineapple extracts and the large quantities of data produced by DNA sequencing. DNA could be sequenced by generating fragments via the hidden scheme. The fake issue can be detected based on the DNA sequencing database integrated with the properties of phytopharmacological characteristics, physical biology, and biometric properties of pineapple species. Some analytical methods of the complex model for data generation and machine learning are useful for the visualization, observation, and monitoring process to facilitate the data decision making. Multi-processor of distributed memory architectures of high-performance computing platform supports the large sparse simulation. Parallel performance measurements and numerical analysis are the indicators to investigate the drying process. DIC-freeze-drying with this adaptive manufacturing technology preserves the sensorial quality and nutritional compounds. In the case of high water content perishable, the treatment is usually accompanied by irreversible damage of cell structures and maintains the nutrient quality and deterioration of tissue porosity.

The working principles are to identify the factors influencing the customer's choice for a new product of dry pineapple. To optimize the DIC-freeze-drying treatment and to analyze the characteristics of potential customers for the premium drying pineapple product, this paper proposed big data analytics of synchronizing digital, physical value streams and predictive analytics. The freeze-drying machine with the elements of IoT data sensor and machine learning analysis will produce the highest quality of pineapple nutrient and will affect the socioeconomic factors of local drying pineapple industry.

Prof. Mohamed Himdi

Professor of University, IETR, University of Rennes 1, France

«Technologies of Optically Transparent Antennas from VHF/UHF to the Millimeter-Wave Band»

Summary The development of wireless communications and the increase of radio applications, such as UMTS, Bluetooth, GPS and WLAN, in dense urban areas are environmental challenges requiring innovative technological solutions. To restrict the visual impact of the associated antenna networks and to improve their location in the city, an attractive possibility is to develop optically transparent antennas. In this field area of interests, thin-film materials deposited on see-through substrates provide innovative solutions.

Such transparent antennas are usually fabricated from transparent conducting oxide (TCO) films, such as indium tin oxide (ITO), fluorine tin oxide (FTO) or multilayers such as TCO/metal/TCO deposited on glass substrates. However, these solutions imply a limitation in sheet resistance R_s and/or optical transparency, T values. To circumvent these restrictions, we have developed an original approach: the fabrication of mesh metal films which exhibit very low sheet resistance value: $R_s = 0.05$ ohm/sq (to restrict the ohmic loss) combined with high thickness: $6 \mu\text{m}$ (to limit the skin depth effect) and high transparency: $T = 80\%$ in the visible light spectrum. This novel solution provides the best radiating efficiency at microwave frequency. In this communication, we report on ITO films, ITO/metal/ITO multilayers and silver/titanium films deposited on Corning glass substrates by R.F. sputtering and the fabrication of the mesh metal structures. We investigate the microwave performance of various transparent antennas made from such materials with different levels of transparency and sheet resistance values. Each transparent antenna performance is compared with that of a reference counterpart made from a continuous (opaque) metal film.

Many passive and active antenna examples will be presented and discussed during the communication.

Prof. Rachid Yazami

Founding Director KVI PTE LTD., Singapore

«The Role of Lithium-Ion Batteries in the Future Energy Transition»

Summary The main objective of the energy transition is reducing the greenhouse gas (GHG) emission due to hydrocarbon material combustion used in transportation, industry and housings and buildings so as to reduce the effects of climate change, such as global warming. Accordingly, tremendous efforts have been deployed to transit from the combustible sources of energy to clean and sustainable sources such as solar, wind, waves, hydroelectricity and geothermal, among others. As a result, the cost of solar panels both thermal and photovoltaic together with the cost of wind turbines has been dramatically reduced making clean energy economically viable as compared to fossil based one.

A serious limitation of clean energy sources is their intermittency, i.e., day/night and clouds for solar and level of wind for the turbines. Electric power companies are entitled to provide enough power to their customers 24/7. This is one area where lithium-ion batteries will play a major role in power time shifting and power peak shaving. Besides stationary energy storage, the other major applications of LIB are in mobile electronics and in electric vehicles.

Our research activity is currently focused on improving LIB performances in terms of life, safety and fast charging and will be shown in this presentation.

Prof. Ivashko Evgeny

Russian Academy of Sciences, Moscow, Russia

«Modern IT and IoT Technologies in Innovative Solutions for Aquaculture»

Summary Aquaculture (or aquafarming) is the farming cultivating freshwater and saltwater populations of fish (crustaceans, mollusks, aquatic plants, algae and other organisms) under controlled conditions.

The global aquaculture industry is an important source of fish; it recently exceeded in production world's wild fish catch and continues to grow rapidly. Such growth is met by conservatism of business processes and outdated technologies of the most of producers, which hinders further development. Therefore, it is expected that aquaculture will soon become a major consumer of innovations and modern information technologies. A number of innovative technologies are developing with the Aquaculture 4.0 (similar to Industry 4.0) and "precision aquaculture" approaches. They relate to artificial intelligence, machine learning, neural networks, pattern recognition, machine vision, big data, cloud/edge/fog computing, etc; they aimed to address the internal challenges of aquaculture in the domains of risk management, labor productivity, scalability and production growth.

The report is devoted to the most striking approaches and promising innovative solutions based on the modern IT and (I)IoT in aquaculture.

Dr. Ahmed Boutejdar

German Research Foundation DFG, Braunschweig-Bonn, Germany

«Design of Very Compact Planar Filters Using a New Hi-Lo and DGS Techniques for Radar Applications»

Summary In this work, a novel miniaturized microstrip low-pass filter using a double Hi-Lo and cross-defected ground structure resonators is presented. The Hi-Lo resonator is placed on the top layer of the structure, while the two identical cross-DGS resonators are etched in the ground plane. Each DGS shape consists of two cross-heads, which are connected with a channel slot. Both DGS resonators are electromagnetically coupled. The proposed filter has been designed simulated, optimized, and manufactured. The filter topology is simulated using HFSS simulator and measured using Agilent Field Fox NA, N9918A VNA. Both results of the proposed LPF show a sharp roll-off (ξ) of 84dB/GHz and exhibit a very low insertion loss in the pass band of 0.4 dB from DC to 0.9 GHz, and it achieves a wide rejection bandwidth with overall 20 dB attenuation from 1.2 GHz up to 3.2 GHz. The compact low-pass structure occupies an area of $(0.37\lambda_g \times 0.37\lambda_g)$ where $\lambda_g = 94$ mm is the waveguide length at the cut-off frequency 1 GHz. The carried-out results confirm the effectiveness of the proposed method.

Contents

Computer Science

A Hybrid Indoor Localization Framework in an IoT Ecosystem	3
Marc Junior Pierre Nkengue, Ivan Madjarov, Jean Luc Damoiseaux, and Rabah Iguernaissi	
Current Works on IDS Development Strategies for IoT	15
Abdelouahed Bamou, Moulay Driss EL Ouadghiri, and Badraddine Aghoutane	
New Metrics to Measure the Quality of the Ranking Results Obtained by the Multi-criteria Decision-Making Methods	25
Mohammed Chaouki Abounaima, Loubna Lamrini, Fatima Zahra EL Mazouri, Noureddine EL Makhfi, Mohammed Talibi Alaoui, and Mohamed Ouzarf	
LiteNet: A Novel Approach for Traffic Sign Classification Using a Light Architecture	37
Soufiane Naim and Noureddine Moumkine	
The Attitude of Moroccan University Students Towards an Online Assistive Application of Stress Management	49
Hakima EL Madani, Ikrame Yazghich, Maryem Baya, and Mohamed Berraho	
Detection and Prediction of Driver Drowsiness for the Prevention of Road Accidents Using Deep Neural Networks Techniques	57
Ismail Nasri, Mohammed Karrouchi, Hajar Snoussi, Kamal Kassmi, and Abdelhafid Messaoudi	
A New Framework to Secure Cloud Based e-Learning Systems	65
Karima Aissaoui, Meryem Amane, Mohammed Berrada, and Mohammed Amine Madani	

A Term Weighting Scheme Using Fuzzy Logic for Enhancing Candidate Screening Task 77
Amine Habous and El Habib Nfaoui

E-learning Recommendation System Based on Cloud Computing 89
Mounia Rahhali, Lahcen Oughdir, Youssef Jedidi,
Youssef Lahmadi, and Mohammed Zakariae El Khattabi

An Intelligent System Based on Heart Rate Variability Measures and Machine Learning Techniques for Classification of Normal and Growth Restricted Children 101
Abdulrhman Wassil Al-Jedaani, Wajid Aziz,
Abdulrahman A. Alshdadi, Mohammed Alqarni,
Malik Sajjad Ahmed Nadeem, Mike P. Wailoo, and Fernando S. Schindwein

Predicting Student’s Performance Based on Cloud Computing 113
Youssef Jedidi, Abdelali Ibriz, Mohamed Benslimane,
Mehdi Tmimi, and Mounia Rahhali

Contribution to the Optimization of Industrial Energy Efficiency by Intelligent Predictive Maintenance Tools Case of an Industrial System Unbalance 125
Ali Elkihel, Yosra Elkihel, Amar Bakdid, Hassan Gziri, and Imane Derouiche

Automobile Insurance Claims Auditing: A Comprehensive Survey on Handling Awry Datasets 135
Ezzaim Soufiane, Salah-Eddine EL Baghdadi, Aissam Berrahou,
Abderrahim Mesbah, and Hassan Berbia

Artificial Intelligence Based on the Neurons Networks at the Service Predictive Bearing 145
Ali Elkihel, Imane Derouiche, Yosra Elkihel, Amar Bakdid,
and Hassan Gziri

Intersection Management Approach based on Multi-agent System 157
Meryem Mesbah, Ali Yahyaouy, and My Abdelouahed Sabri

A Model of an Integrated Educational Management Information System to Support Educational Planning and Decision Making: A Moroccan Case 167
Mustapha Skittou, Mohamed Merrouchi, and Taoufiq Gadi

Variational Autoencoders Versus Denoising Autoencoders for Recommendations 179
Khadija Bennouna, Hiba Chougrad, Youness Khamlichi,
Abdessamad El Boushaki, and Safae El Haj Ben Ali

Toward Moroccan Virtual University: Technical Proposal 189
Ayoub Korchi, Sarah Benjelloun, Mohamed El Mehdi El Aissi,
Mohamed Karim Khachouch, Nisrine El Marzouki, and Younes Lakhrissi

Data Lake Versus Data Warehouse Architecture: A Comparative Study 201
Mohamed El Mehdi El Aissi, Sarah Benjelloun, Yassine Loukili,
Younes Lakhrissi, Abdessamad El Boushaki, Hiba Chougrad,
and Safae Elhaj Ben Ali

Machine Learning for Credit Card Fraud Detection 211
Loubna Moumeni, Mohammed Saber, Ilham Slimani,
Ilhame Elfarissi, and Zineb Bougroun

OctaNLP: A Benchmark for Evaluating Multitask Generalization of Transformer-Based Pre-trained Language Models 223
Zakaria Kaddari, Youssef Mellah, Jamal Berrich,
Mohammed G. Belkasmi, and Toumi Bouchentouf

Comparative Study of Regression and Regularization Methods: Application to Weather and Climate Data 233
El Mehdi Raouhi, Mohamed Lachgar, and Ali Kartit

Big Data Architecture for Moroccan Water Stakeholders: Proposal and Perception 241
Aniss Moumen, Badraddine Aghoutane, Younes Lakhrissi,
and Ali Essahlaoui

Towards an Integrated Platform for the Presentation and Preservation of the Scientific Heritage of Drâa-Tafilalet 247
Fouad Nafis, Badraddine Aghoutane, and Ali Yahyaouy

Keratoconus Classification Using Machine Learning 257
Aatila Mustapha, Lachgar Mohamed, and Kartit Ali

Electronics, Microelectronics, Embedded System and Control System

0.18 μm GaAs-pHEMT MMIC Frequency Doubler for Radar Area Scanning Application 265
H. El Ftouh, Moustapha El Bakkali, Naima Amar Touhami, and A. Zakriti

Fail-Safe Remote Update Method for an FPGA-Based On-Board Computer System 273
Ahmed Hanafi, Mohammed Karim, Tajjeeddine Rachidi,
and Ibtissam Latachi

Autonomous Vehicle Lateral Control for the Lane-change Maneuver	285
Lhoussain El Hajjami, El Mehdi Mellouli, and Mohammed Berrada	
Integral Sliding Mode Control of Power Transfer in a Vehicle to Grid (V2G) Charging Station	297
Hicham Ben Sassi, Chakib Alaoui, Fatima Errahimi, and Najia Es-Sbai	
Design and Analysis of an Integrated Class-D Power Output Stage in a 130 nm SOI-BCD Technology	309
Mustapha El Alaoui, Karim El khadiri, Ahmed Tahiri, and Hassan Qjidaa	
Digital Implementation of SPWM 7-Level Inverter Using Microcontroller	321
Hajar Chadli, Youssef Bikrat, Sara Chadli, Mohammed Saber, Amine Fakir, and Abdelwahed Tahani	
Embedded and Parallel Implementation of the Stereo-Vision System for the Autonomous Vehicle	333
Mohamed Sejai, Anass Mansouri, Saad Bennani Dosse, and Yassine Ruichek	
An Efficient Implementation of an Effective PFD-CP for Low Power Low-Jitter CP-PLL	341
Karim Zouaq, Abdelmalik Bouyahyaoui, Abdelhamid Aitoumeri, and Mustapha Alami	
Adaptive Fast Terminal Sliding Mode Control for Uncertain Quadrotor Based on Butterfly Optimization Algorithm (BOA)	353
Hamid Hassani, Anass Mansouri, and Ali Ahaitouf	
Localization and Navigation System for Blind Persons Using Stereo Vision and a GIS	365
Moncef Aharchi and M.'hamed Ait Kbir	
New Delay Dependent Stability Condition for a Carbon Dioxide Takagi Sugeno Model	377
Azeddine Elmajidi, Elhoussine Elmazoudi, Jamila Elalami, and Noureddine Elalami	
Simulation-Based Optimization for Automated Design of Analog/RF Circuits	389
Abdelaziz Lberni, Amin Sallem, Malika Alami Marktani, Abdelaziz Ahaitouf, Nouri Masmoudi, and Ali Ahaitouf	
Readout System of Piezoelectric Sensor Used for High Speed Weigh in Motion Application	401
Lhoussaine Oubrich, Mohammed Ouassaid, and Mohammed Maaroufi	

Towards the Implementation of Smartphone-Based Self-testing of COVID-19 Using AI 411
Hajar Saikouk, Chakib Alaoui, and Achraf Berrajaa

Design and Prototyping of an Embedded Controller Board for PV-EV Charging Station 419
Youssef Cheddadi, Fatima Cheddadi, Fatima Errahimi, and Najia Es-Sbai

New Approach for Controlling PTW Vehicle Dynamics: Characterization of Critical Scenarios 431
Fakhreddine Jalti, Bekkay Hajji, and Abderrahim Mbarki

Study of Parameters Influencing on the Performance of SiNW ISFET Sensor 445
Nabil Ayadi, Bekkay Hajji, Abdelghafour Galadi, Ahmet Lale, Jerome Launay, and Pierre Temple-Boyer

Modeling and Trajectory Tracking of an Unmanned Quadrotor Using Optimal PID Controller 457
Hamid Hassani, Anass Mansouri, and Ali Ahaitouf

Dynamic Socket Design for Transtibial Prosthesis 469
Jhon Hernández Martin, Alejandra Santos Borraez, Catalina Ríos Bustos, Fran Pérez Ortiz, and Phillip Meziath Castro

Networking

Towards an Enhanced Minimum Rank Hysteresis Objective Function for RPL IoT Routing Protocol 483
Abdelhadi Eloudrhiri Hassani, Aïcha Sahel, and Abdelmajid Badri

A Lightweight Hash Function for Cryptographic and Pseudo-Cryptographic Applications 495
Imad El Hanouti, Hakim El Fadili, Said Hraoui, and Abdellatif Jarjar

Hybrid Intrusion Detection System for Wireless Networks 507
Mohamed Amine Agalit, Ali Sadiqui, Youness Khamlichi, and El Mostapha Chakir

Implementation and QoS Evaluation of Geographical Location-Based Routing Protocols in Vehicular Ad-Hoc Networks 515
Safae Smiri, Abdelali Boushaba, Adil Ben Abbou, Azeddine Zahi, and Rachid Ben Abbou

Congestion Control Management in High Speed Networks 527
Kaoutar Bazi and Bouchaib Nassereddine

Renewable Energy

Aerodynamic Analysis of Wind Turbine Blade of NACA 0006 Using a CFD Approach 541
Mohamed Hatim Ouahabi, Houda El Khachine, and Farid Benabdelouahab

Educational Strategy Combining Technological Capacity and Ant Colony Algorithm to Improve the Ideal Dispatch Using Wind Energy 553
Neider Duan Barbosa Castro, Jhon Alexander Hernández Martin, Fabiola Sáenz Blanco, and Evy Fernanda Tapias Forero

A New Method for Photovoltaic Parameters Extraction Under Variable Weather Conditions 565
Aissa Hali and Yamina Khlifi

Applying CFD for the Optimization of the Drying Chamber of an Indirect Solar Dryer 575
Dounia Chaatouf, Mourad Salhi, Benyounes Raillani, Samir Amraoui, and Ahmed Mezrhab

Performance Comparison of Regenerative Organic Rankine Cycle Configurations 583
Rania Zhar, Amine Allouhi, Abdelmajid Jamil, and Khadija Lahrech

Performance Analysis of Combined Power and Refrigeration: ORC-VCC System 595
Rania Zhar, Amine Allouhi, Abdelmajid Jamil, and Khadija Lahrech

Fault Location Technique Using Distributed Multi Agent-Systems in Smart Grids 607
Mohamed Azeroual, Younes Boujoudar, Tijani Lamhamdi, Hassan EL Moussaoui, and Hassane EL Markhi

Hybrid Renewable Energy System Investigation Based on Power Converters Losses 615
Ilham Tyass, Omar Bouamrane, Abdelhadi Raihani, Khalifa Mansouri, and Tajeddine Khalili

Estimation of Daily Direct Normal Solar Irradiation Using Machine-Learning Methods 627
Zineb Bounoua and Abdellah Mechaqrane

Greenhouse Design Selection in Moroccan Climatic Conditions 639
Laila Ouazzani Chahidi and Abdellah Mechaqrane

Intelligent Architecture in Home Energy Management System for Smart Building, Moroccan Case Study 649
Mohammed Dhriyyef, Abdelmalek El Mehdi, and Mohammed Elhitmy

Evaluation of Adaptive Backstepping Control Applied to DFIG Wind System Used on the Real Wind Profile of the Dakhla-Morocco City 661
 Mourad Yesséf, Badre Bossoufi, Mohammed Taoussi, Ahmed Lagrioui, and Mohammed El Mahfoud

Comparative Study Between FOSMC and SMC Controllers for DFIG Under the Real Wind Profile of Asilah-Morocco City 673
 Mohamed Amine Beniss, Hassan El Moussaoui, Tijani Lamhamdi, and Hassane El Markhi

Voltage and Power Control for a Grid Tied Single Phase Single Stage Transformer-Less Photovoltaic System Using Sliding Mode Control 687
 Khalid Chigane and Mohammed Ouassaid

Automatic Extraction of Photovoltaic Panels from UAV Imagery with Object-Based Image Analysis and Machine Learning 699
 Imane Souffer, Mohamed Sghiouar, Imane Sebari, Yahya Zefri, Hicham Hajji, and Ghassane Aniba

Development of a Management Algorithm for a Compact Photovoltaic—Wind Turbine System 711
 Yahya Lahlou, Abdelghani Hajji, and Mohammed Aggour

Impact of Solar Gain on Energy Consumption and Thermal Comfort 723
 Abdelghani Hajji, Yahya Lahlou, and Ahmed Abbou

A Model-Based Predictive Control Approach for Home Energy Management Systems. First Results 735
 Antonio Ruano, Hamid Qassemi, Inoussa Habou Laouali, Manal Marzouq, Hakim El Fadili, and Saad Bennani Dosse

Comparative Study of Electricity Production by Photovoltaic Panels with Mirrors for Different Inclinations 749
 Assia Benkaddour, Hanan Boulaich, and Elhassan Aroudam

A Non Linear Autoregressive Neural Network Model for Forecasting Appliance Power Consumption 759
 Inoussa Habou Laouali, Hamid Qassemi, Manal Marzouq, Antonio Ruano, Saad Bennani Dosse, and Hakim El Fadili

Numerical Analysis of Bi-fluid PV/T Hybrid Collector Using the Finite Difference Method 769
 Oussama El Manssouri, Bekkay Hajji, Antonio Gagliano, and Giuseppe Marco Tina

Signal and Image Processing

A Novel Cryptosystem for Color Images Based on Chaotic Maps Using a Random Controller 783

Said Hraoui, Mounir Gouiouez, Faiq Gmira, Mohammed Berrada, Abdellatif Jarjar, and A. Oulidi Jarrar

New Image Encryption Scheme Based on Dynamic Substitution and Hill Cipher 797

Younes Qobbi, Abdeltif Jarjar, Mohamed Essaid, and Abdelhamid Benazzi

Touchless Palmprint Identification Based on Patch Cross Pattern Representation 809

Hakim Doghmane, Kamel Messaoudi, Mohamed Cherif Amara Korba, Zoheir Mentouri, and Hocine Bourouba

Image Segmentation Approach Based on Hybridization Between K-Means and Mask R-CNN 821

Hanae Moussaoui, Mohamed Benslimane, and Nabil El Akkad

Partial 3D Image Reconstruction by Cuboids Using Stable Computation of Hahn Polynomials 831

Mohamed Amine Tahiri, Hicham Karmouni, Ahmed Tahiri, Mhamed Sayyouri, and Hassan Qjidaa

Analysis of Online Spiral for the Early Detection of Parkinson Diseases 843

Yassir Elghzizal, Ghizlane Khaissidi, Mostafa Mrabti, Aouraghe Ibtissame, and Ammour Alae

Learning Hand-Crafted Palm-Features for a High-Performance Biometric Systems 855

Amel Bouchemha, Abdallah Meraoumia, Lakhdar Laimeche, and Lotfi Houam

CNN-Based Obstacle Avoidance Using RGB-Depth Image Fusion 867

Chaymae El Mechal, Najiba El Amrani El Idrissi, and Mostefa Mesbah

Arabic Handwriting Word Recognition Based on Convolutional Recurrent Neural Network 877

Manal Boualam, Youssef Elfakir, Ghizlane Khaissidi, and Mostafa Mrabti

Tuning Image Descriptors and Classifiers: The Case of Emotion Recognition 887

Latifa Greche, Abdelhak Taamouch, Mohamed Akil, and Najia Es-Sbai

Prediction Potential Analysis of Arabic Diacritics and Punctuation Marks in Online Handwriting: A New Marker for Parkinson’s Disease 897

Alae Ammour, Ibtissame Aouraghe, Ghizlane Khaissidi, Mostafa Mrabti, Ghita Aboulem, and Faouzi Belahsen

Telecom

Development of an Ultra Wide Band Hybrid Coupler with Adjustable Phase Shifter for 5G Applications 911
 Abdellatif Slimani, Saad Bennani Dosse, Ali El Alami, Mohammed Jorio, Abdelhafid Belmajdoub, Mohamed Amzi, Sudipta Das, and Sghir Elmahjouby

WiMAX Throughput Maximization for MIMO-OFDM Systems via Cross-Layer Design 921
 Hadj Zerrouki and Salima Azzaz-Rahmani

Equivalent Circuit Modelling of a Cantor Multifractal Slots Antenna 933
 Fatima Ez-Zaki, Hassan Belahrach, and Abdelilah Ghammaz

A Novel Two-Branch Dual-Band Rectifier for 2.45 GHz 5.8 GHz RFID Systems 943
 Sara El Mattar, Abdennaceur Baghdad, and Abdelhakim Ballouk

A Survey of NOMA for 5G: Implementation Schemes and Energy Efficiency 949
 Jamal Mestoui and Mohammed El Ghzaoui

A Modified E-Shaped Compact Printed Antenna for 28 GHz 5G Applications 961
 Yousra Ghazaoui, Ali El Alami, Sudipta Das, and Mohammed El Ghzaoui

Design of Microstrip Sierpinski Carpet Antenna Using a Circular Pattern with Improved Performance 971
 Abdelhakim Moutaouakil, Younes Jabrane, Abdelati Reha, and Abdelaziz Koumina

Load Condition for Minimum Backscattering Antennas 977
 Zaed S. A. Abdulwali and Majeed A. S. Alkanhal

LTE-M Evolution Towards Massive MTC: Performance Evaluation for 5G mMTC 989
 Adil Abou El Hassan, Abdelmalek El Mehdi, and Mohammed Saber

Communication Optimization Approach for S-Band LEO CubeSat Link Budget 1001
 Mohammed Amine El Moukalafe and Khalid Minaoui

Ground Penetrating Radar Data Acquisition to Detect Imbalances and Underground Pipes 1013
 Tahar Bachiri, Gamil Alsharahi, Abdellatif Khamlichi, Mohammed Bezzazi, and Ahmed Faize

Nash Equilibrium Based Pilot Decontamination for Multi-cell Massive MIMO Systems	1025
Abdelfettah Belhabib, Mohamed Boulouird, and Moha M'Rabet Hassani	
Channel Estimation for Massive MIMO TDD Systems and Pilot Contamination with Uniformly Distributed Users	1037
Jamal Amadid, Mohamed Boulouird, and Moha M'Rabet Hassani	
Mapping the Geothermal Potential of the Jbel Saghro Massif by Airborne Magnetism (Anti-Atlas, Morocco)	1049
Miftah Abdelhalim and El Azzab Driss	
A Compact Flexible UWB Antenna for Biomedical Applications: Especially for Breast Cancer Detection	1061
Nirmine Hammouch, Hassan Ammor, and Mohamed Himdi	
A Low Profile Frequency Reconfigurable Antenna for mmWave Applications	1073
Wahaj Abbas Awan, Niamat Hussain, Adnan Ghaffar, SyedaIffat Naqvi, Abir Zaidi, Musa Hussain, and Xue Jun Li	
On-Demand Frequency Reconfigurable Flexible Antenna for 5Gsub-6-GHz and ISM Band Applications	1085
Musa Hussain, Syed Naheel Raza Rizvi, Wahaj Abbas Awan, Niamat Husain, Halima, and Ahsan Hameed	
Dual-Band BPF Based on a Single Dual-Mode Stepped-Impedance Resonator for 4G Systems	1093
Mohamed Amzi, Jamal Zbitou, and Saad Bennani Dosse	
High Gain Cascaded GaAs-pHEMT Broadband Planar Low Noise Amplifier for WiMAX-802.16b Applications	1101
Moustapha El Bakkali, Naima Amar Touhami, and Taj-Eddin Elhamadi	
Application of Electrical Resistivity Soundings to Identify Unstable Areas, “Tghat-Oued Fez” District as a Case Study (Fez—Morocco)	1111
Jabrane Oussama, El Azzab Driss, El Mansouri Bouabid, and Charroud Mohammed	
A New Compact 1.0 GHz LPF Using Double Hi-Lo-Resonators and Cross Defected Ground Structure for Radar Applications	1123
A. Boutejdar, H. Bishoy, and Saad Bennani Dosse	
Author Index	1135

Computer Science

A Hybrid Indoor Localization Framework in an IoT Ecosystem



Marc Junior Pierre Nkengue, Ivan Madjarov, Jean Luc Damoiseaux,
and Rabah Iguernaissi

Abstract The Global Position System (GPS) does not work in the indoor environment because of the satellite signal attenuation. To overcome this lack, we propose a Hybrid Indoor Positioning and Navigation System (HIPNS), based on Li-Fi (Light-Fidelity) localization and optical camera positioning analyses deployed in an indoor environment. The localization approach is based on the fuse of two positioning strategies where the camera-based part is responsible for localizing individuals and recovering their trajectories in zones with low coverage of Li-Fi LEDs. A third-party element is planned to operate in the event of loss of contact. So, the step detection technique and heading estimation are applied in a smartphone-based indoor localization context between two referenced points. The main contribution of this paper focuses on the use of techniques, algorithms, and methods from different spheres of application that generate heterogeneous data. We apply a data integration approach based on REST Web service architecture to allow localization operations in this hybrid indoor positioning system (HIPS). In this work-in-progress paper, we also present a state-of-the-art survey of techniques and algorithms for indoor positioning with the help of smartphones, as well as the main concepts and challenges related to this emergent area.

Keywords Indoor navigation · Li-Fi-based localization · Scene analysis · Smartphone-based positioning · IoT ecosystem

M. J. P. Nkengue · I. Madjarov (✉) · J. L. Damoiseaux · R. Iguernaissi
Aix Marseille Univ, Université de Toulon, CNRS, LIS, Marseille, France
e-mail: ivan.madjarov@lis-lab.fr

M. J. P. Nkengue
e-mail: marc-junior-pierre.nkengue@etu.univ-amu.fr

J. L. Damoiseaux
e-mail: jean-luc.damoiseaux@lis-lab.fr

R. Iguernaissi
e-mail: rabah.iguernaissi@lis-lab.fr

1 Introduction

Devices providing sensing, actuation, control, and monitoring (positioning) activities are defined in [1] as the Internet of Things (IoT) ecosystem. The Indoor Positioning Systems (IPS) has been developed using a wide variety of technologies and sensors, or even combining several of them in hybrid systems. Our work is part of this approach as our indoor guidance system combines low-cost technologies that are simple to implement and operate: Li-Fi lamps and video cameras. Besides, we have chosen to process the positioning data from these sensors via a Web service platform, thus ensuring dynamic contact with the user and considering guidance constraints in real-time. Among all indoor positioning technologies, we will focus on those most often used with a mobile phone, namely Wi-Fi, low-energy Bluetooth (BLE), and inertial sensors. We will also present solutions based on the use of light and computer vision.

After a reminder of the possible technologies and the existing hybrid systems, we will then detail the architecture of our guidance system, and the tests carried out, to finally conclude with the follow-up envisaged to our work.

2 Related Work

As multiple published surveys attest [2–6], a wide variety of IPS have been proposed, for performances that are not always satisfactory in dynamic environments and often require costly investments for a significant improvement of the latter. Usually, in IPS, the position of the object or person is estimated using either the measurement of its angle of arrival (AOA), time of arrival (TOA), the difference between arrival times (TDOA), or received signal strength (RSS) [2, 4–6]. If several measurements of the same type are used to determine the position more precisely, the term lateration and angulation is used [4]. The measurement-based systems are complex to implement and expensive in terms of material.

A WLAN is a high-speed wireless network that uses high-frequency radio waves to connect and communicate between nodes and devices within the coverage area. To correctly perform indoor geolocation from a WLAN, it is necessary to densify the network infrastructure to counteract the effect of environmental and human disturbances [4, 5], and also to be able to combine several position measurements or used propagation model within the same algorithm [4, 5].

Very similar to Wi-Fi, the Bluetooth has recently seen a resurgence of interest with the development of Bluetooth Low Energy (BLE) [3, 4]. The low cost of BLE equipment and its long energy autonomy is often cited advantages as they make it easier than Wi-Fi to obtain better radio coverage also necessary for good performance [2, 4]. For geolocation systems, based on WLAN or BLE, many studies propose to improve their performance either by mapping beforehand (fingerprinting) the environment in which the object or person evolves [3–5] or by combining these technologies [2, 4, 5].

The use of the smartphone's sensors (i.e., accelerometer, gyroscope, etc.) is also a research topic tested in the context of IPS [2–4]. Most of the time, they estimate walking parameters (number of steps, length of steps, direction) or determine the nature of the movement. The performances obtained were not convincing, notably because of the difficulty of taking into account the relative position of the smartphone in motion or of integrating physiological parameters (weight, age, etc.) of the person and the nature of the surface of the movement. The current trend is, therefore, to integrate these sensors into WLAN/BLE geolocation systems [2, 3].

Other systems use LED-light for geolocation purposes [2, 4]. Because LEDs are capable of flashing very quickly without impairing human vision, they can substitute for conventional lighting while transmitting information to a smartphone. All positioning algorithms (RSS, TDOA, lateration, angulation, fingerprinting, etc.) can then be used. However, to overcome certain inherent defects of light, its short-range or its possible obscuring, couplings with other technologies have already been proposed (e.g., Li-Fi & Wi-Fi) [6].

Finally, there are IPS based on computer vision [2, 4]. In the simplest cases, the phone to determine its position identifies with its camera markers type QR-Codes. But there are also more complex solutions where the mobile device uses video scene analysis to estimate its location by comparing a snapshot of a scene generated by itself with several pre-observed simplified images of the scene taken from different positions and perspectives.

3 A Hybrid System Model for IPS

The localization methods in an IPS are classified into two groups as noted in [7]: (1) based on distance estimation; and (2) mapping-based localization. In the first group, the distance estimation process employs techniques based on the signal strength and/or the elapsed time between two signals. In our work, we opt for the second group where the mapping-based localization works with pre-stored signals (tags) values in a database.

We apply the mapping localization approach in a Li-Fi based positioning system that uses a signal emitted from a LED (light source) to determine the position of the user's device (receiving device). The user's device, which is equipped with a receptacle (e.g., photodiode-dongle), receives the signal from the LED i.e., its identifier. So, we use the ID as a positioning tag associated with a LED lamp installed in a known location, both data prior stored in a database.

We also use a vision-based positioning system to estimate the position and the orientation of a person indoor by identifying an image that is within a view. In [8] authors note that the commonly used methods for image-based indoor positioning are focused on calculating the Euclidean distance between the feature points of an image.

For smartphone-based indoor localization as a compliment, we opt for a Pedestrian Dead Reckoning (PDR) technique to give the position of a mobile user relative to a

reference, as presented in [9]. PDR approach relies on IMU (Inertial Measurements Unit) based techniques, which typically comprise an accelerometer, gyroscope, and compass. We use the step detection technique (accelerometer) and heading estimation (gyroscope) to reassure the guided person between two identified positions in case of contact losses from other technics.

In this research and development project, we opt for a hybrid IPS system based on Li-Fi technology with path positioning from optical cameras placed in shadow zones to compensate for each other's shortcomings and take advantage of each other's strengths.

3.1 Positions Data from Camera

The camera-based positioning strategies is responsible for localizing individuals and recovering their trajectories in zones with low coverage with Li-Fi LEDs. Thus, we proposed a mono-camera tracking system that is designed in three main phases. The first ones consist of the detection of individuals and the initialization of trackers which is done in two parts the motion detection and motion segmentation. Then, the second phase consists of the tracking of detected individuals from the first phase to recover their trajectories within the camera's field of view. The last part of our strategy consists of the association of image positioning of individuals with their ground plane positioning. The system design is illustrated on Fig. 1.

The first part of our positioning system is the detection of individuals within the camera's field of view. This is done in two main parts, which are motion detection and motion segmentation. We started by using a background subtraction algorithm, which is based on the use of the Gaussian mixture model as proposed in [10], to detect the foreground of the studied scene. This model is applied to all pixels gives a binary image representing the moving objects within the current frame of the video (Fig. 2).

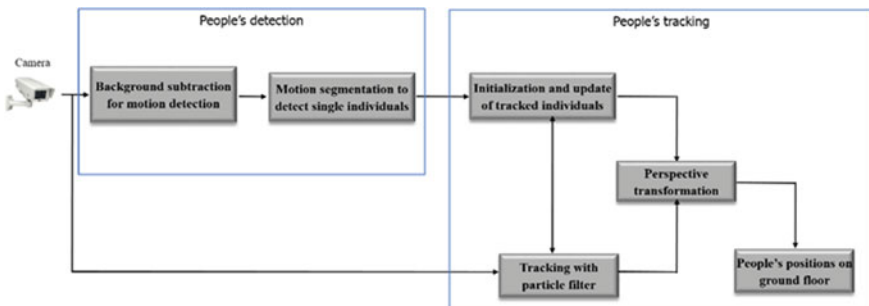


Fig. 1 Ground floor positions from a camera



Fig. 2 Motion detection: **a** original image and **b** moving parts

The used strategy for motion detection enables the detection of blobs representing the moving objects within the studied scene at a given time t . The detected blobs may represent either a single individual or a group of individuals. Thus, we used a method based on connected components analysis, which is associated with some restrictions on the width and height of blobs, to separate the detected blobs into blobs each representing a single individual. We represented each blob with a rectangle of width w and height h . The properties of this rectangle are estimated based on Eq. (1).

$$\begin{cases} (x_0, y_0) = \left(\frac{x_{min} + x_{max}}{2}, \frac{y_{min} + y_{max}}{2} \right) \\ w = x_{max} - x_{min} \\ h = y_{max} - y_{min} \end{cases} \quad (1)$$

Then, we used a restriction on the ratio between the width and the height of each blob to estimate the number of individuals within the blob. This is done by the assumption of Eq. (2).

$$N_{ind} = \begin{cases} 1 & \text{if } Th_{min} < \frac{w}{h} < Th_{max} \\ \text{round}\left(\frac{w}{h * \left(\frac{Th_{min} + Th_{max}}{2}\right)}\right) & \text{if } \frac{w}{h} > Th_{max} \\ \text{round}\left(\frac{h * \left(\frac{Th_{min} + Th_{max}}{2}\right)}{w}\right) & \text{if } \frac{w}{h} < Th_{min} \end{cases} \quad (2)$$

The estimated number of individuals is used to perform new segmentation of blobs based on Eq. (3) for an example of a blob with a ratio $\frac{w}{h} > Th_{max}$ and an estimated number of individuals $N_{ind} = 2$ (illustration of results is shown in Fig. 3).

$$\begin{cases} (x_{01}, y_{01}) = \left(\frac{x_{min} + x_{max}}{4}, \frac{y_{min} + y_{max}}{2} \right) \\ (x_{01}, y_{01}) = \left(\frac{3 * (x_{min} + x_{max})}{4}, \frac{y_{min} + y_{max}}{2} \right) \\ w = \frac{x_{max} - x_{min}}{2} \\ h = y_{max} - y_{min} \end{cases} \quad (3)$$

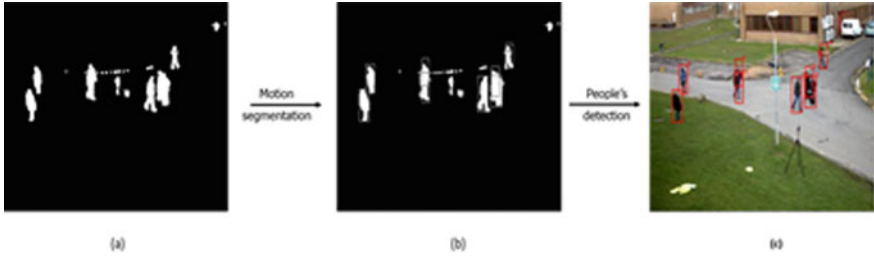


Fig. 3 Motion segmentation and people's detection: **a** moving parts, **b** segmented blobs and **c** detected individuals

The previous steps end up with the list of detected individuals at a given instant t_0 . This list is used to initialize the list of tracked individuals, which are then tracked, and their trajectories recovered. For this, we used a strategy based on the use of a particle filter similar to the one proposed in [9] to estimate the position of the tracked individual at instant t based on his position at the instant $t - 1$ (Eq. 4).

$$\begin{cases} (x, y)_t = (x, y)_{t-1} + (u, v)_{t-1} * \Delta t \\ (u, v)_t = (u, v)_{t-1} \end{cases} \quad (4)$$

With $(x, y)_t$ and $(u, v)_t$ the position and velocity of the individual at instant t .

Then a set of N particles are propagated around this position and weighted based on the difference between their color histograms and the color histogram of the individual in the HSV color space.

The positions of these weighted particles are then used to refine the position of the tracked individual at the instant t . The new position of the individual within the current frame is estimated by Eq. (5).

$$\begin{bmatrix} x \\ y \end{bmatrix} = \sum_{n=0}^N w_t^{(n)} \begin{bmatrix} x \\ y \end{bmatrix}^{(n)} \quad (5)$$

The last step of our localization algorithm consists of the association of the image positioning of individuals with their ground plane positioning. In fact, the previous steps are used to recover the trajectories of the individuals on the video. These trajectories are represented by a set of detections representing the individual while moving on the camera's field of view. These detections are then used, first, to localize the individual within the image and, second, to localize the individual on the ground plane. The first part consists of the association with the bounding box of a tracked person with a single point representing his position on the ground plane on the image (u_0, v_0) . This is done by considering the point of intersection between the central vertical axes of the detection with the bottom limit of the bounding box.

Then to get the positions of individuals on the ground plane, we use a perspective transformation, similar to the one used in [11], which maps the locations of individuals in the image with their corresponding positions in a plane representing the ground floor of the studied scene. This method is based on the use of four initial points, located by the user in both the image and the plane, that are used to calculate the transformation that will be used later on to map the points from the image to their corresponding positions on the plane. This perspective matrix is estimated using the Eq. (6) and the selected points. Then this perspective matrix is used to get the correspondence between any point on the image and its position on the viewing plane.

$$[x' \ y' \ z'] = [u \ v \ w] \begin{bmatrix} a_{11} & a_{12} & a_{13} \\ a_{21} & a_{22} & a_{23} \\ a_{31} & a_{32} & a_{33} \end{bmatrix} \quad (6)$$

With: x, y the coordinates of pixels on the viewing plane (ground floor), u, v the coordinates of pixels on the image. At the end of this part, we map the trajectories obtained previously to the estimated trajectories on the ground floor of the studied scene. These trajectories on the ground floor are then sent to the server as camera data that will be combined with the Li-Fi data to localize individuals.

3.2 Data from Li-Fi Lamp

The Li-Fi indoor data model is part of infrastructure-based positioning, non-GPS technologies, where fixed beacon nodes are used for location estimates. The positioning algorithms are associated with Proximity Based Localization (PBL) as classified in [7]. Proximity sensing techniques are used to determine when a user is near a known location. The provided location is the area in which the user is detected. In our case of using, a Li-Fi lamp emits tag to be detected by a mobile target when passes within the covered area. The most common manufacturers' technical parameters for a Li-Fi LED mounted in a standard ceiling height indicate a luminous flux dispersion in a range of 30°–40°. So, to calculate the detector's area, a simple cone-diameter equation can be used, as presented in (7).

$$D = 2 \times h \times \text{tg}(\alpha), S = \pi \times \left(\frac{D}{2}\right)^2 \quad (7)$$

where: D expresses the LED covered area, h indicates the ceiling height, α the angle of light dispersion, and S expressed the surface covered by the detector. In a general case, we can count on a detector area with 3 m of diameter i.e., approximately 7 m². This is quite reassuring for the installation of Li-Fi lamps on points of interest

in a building. So, the detection infrastructure can be developed as a mesh of Li-Fi lamps, which can be presented as nodes in a graph-path.

3.3 Data Integration and Graph Path

Hybrid System Model. Li-Fi lamps and optical cameras (OC) are two promising IPS technologies that can be implemented in all kinds of indoor environments using existing infrastructures. However, both are subjected to data heterogeneity. In this paper, we propose a hybrid IPS that integrates data from Li-Fi lamps and OC in a RESTful architecture to improve the quality-of-service (QoS) of the user’s positioning and navigation in order to provide better performance in terms of accuracy, power consumption, and reduced costs of installation.

In the proposed system model, the source of data dissemination is a Li-Fi lamp and a processed image from an OC, whereas the source data collection is a user device with a photoreceptor. The collected data are analyzed and processed, and the localization is performed via a Web service. In Fig. 4, a four layers system architecture is presented: (1) data generation and image collection, (2) communication technology, (3) data management and processing, and (4) application for data interpretation.

When the user passes under a LED his smartphone can receive the tag associated with this LED lamp. Its path is followed by an optical camera to confirm the user’s position. An alert message will be sent in case of remoteness from the prescribed

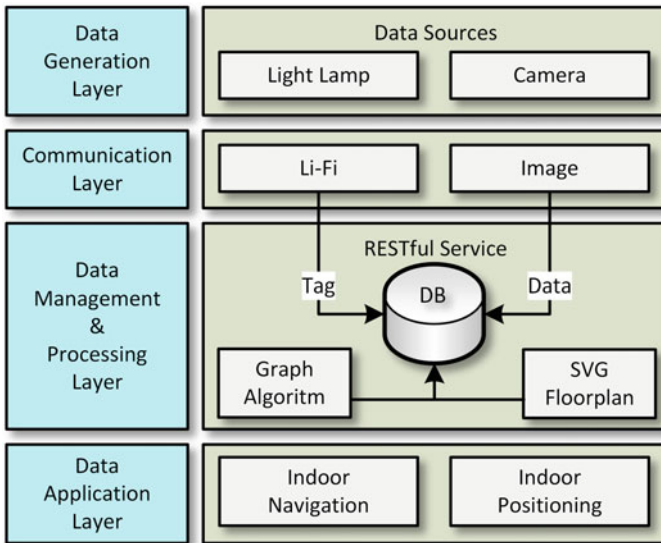


Fig. 4 System model for hybrid IPS

path or in case of unexpected barriers. A reconfigured path will be then sent to the user.

The graph-path algorithm. The BFS-based graph-path algorithm resides on the RESTful Web service side. This algorithm allows us to obtain the path to follow when a destination is defined at the beginning (e.g., the entry point of a building). With knowledge of the starting point and the endpoint, the algorithm determines all intermediary points to be followed to guide the user to the destination. These intermediary points represent the graph-vertices where the Li-Fi lamps are positioned.

The Graph algorithm is developed as a class with two methods. The first one determines the vertices in the graph corresponding to the building’s plan stored in numerical format. Once the set of vertices is retrieved, the method locates for each node the set of vertices that succeeds it in a unidirectional manner (i.e., for each vertex, the edge to follow to the next vertex throughout the part of the suggested path). The second one is essential to allow us to find the available path from the starting point to the defined endpoint. Based on the graph-paths established by the previously described method, this method allows the suggested path to be highlighted on the user’s screen.

The vector floorplan. The vector graphics format (SVG) used for the building’s plan representation allows us to manipulate the graph directly on the plan by associating it to the user’s path. Thus, the highlighting path can be displayed directly on the graph with the points of reference (i.e., graph-vertices).

4 Implementation and Evaluation

Implementation. We have focused on server-side processing as a development approach to reduce the user’s client–server interactions. So, in this IoT schema, the dedicated REST service, as shown in Fig. 4, can handle multiple requests at once with correctly achieved data integration from heterogeneous sources like Li-Fi lamp, optical camera, an accelerometer as shown in Fig. 5. On the other hand, this

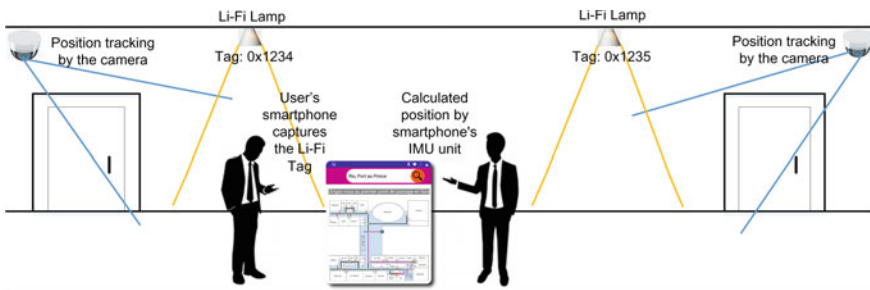


Fig. 5 Use case scenario for hybrid Li-Fi-camera-accelerometer IPS

centralization approach for indoor navigation process management allows server-side service to track simultaneously different requested paths without interferences between users.

A location-aware Android-based application for indoor navigation tracking is developed. So, when a smartphone with a light sensor, is within the range of a Li-Fi lamplight, it will compare the emitted from the lamp tag with the value recommended in the building's path-list. The graph-path is highlighted on the building's plan, already displayed on the smartphone's screen, with the highlighted intermediary point of the detected position as shown in Fig. 5. The developed Android activity is based on the Oledcomm GEOLiFi Kit [12], with GEOLiFi LED lamp, GEOLiFi Dongle to be used with a smartphone, and GEOLiFi SDK Library for Android application development.

The data integration of the camera and the Li-Fi lamps is done through the Web service installed on a Node.js server running on a Raspberry pi 4. The reference points identified by the camera for the guided person are stored in the database. When the user passes through a Li-Fi point, the retrieved coordinates are compared with those transmitted by the camera. In case of differences, the coordinates confirmed by the position of the Li-Fi lamp are considered for the user's guidance.

To improve the accuracy of the localization system, we combine different technologies. To increase the quality of the data and to reassure the user in case of failure of the main approach, an accelerometer, a gyroscope, embedded in a smartphone are employed to develop a multi-sensor fusion approach. This results in the Android application that integrates data from the IMU for the user's guidance between two reference points. However, this data is not communicated to the server and its Web service.

Evaluation. For this work-in-progress paper, the performance of each positioning approach is partially analyzed due to objective reasons. Our project started at the end of 2019. The containment imposed by the Covid-19 pandemic prevented us from deploying the entire infrastructure, namely optical cameras, and Li-Fi lamps, on a larger scale. We were planning to deploy four optical cameras and 32 Li-Fi lamps. The pretests were carried out in an enclosed space with a minimum of deployed equipment. The camera-based algorithms for localizing individuals and recovering their trajectories were tested with an extern public database. Moreover, this avoids some inconvenience in terms of image rights. The guidance activity with an accelerometer and gyroscope was tested in extern associated to the main Android application. The graph path algorithm, installed as RESTful service on Raspberry pi 4, was tested on a virtual floorplan with QR Codes in place of the Li-Fi lamps. The developed Android application for user indoor guidance gave satisfaction.

To estimate the accuracy of the IMU unit associated with the user's activity, we proceed by a test to count the number of steps over 10 m and then to compare with real values. It appears that the accuracy of the IMU unit is quite good over the tested distance. The observed error has a rate of up to 23%, which is a tolerable threshold. A real difference begins to be created between the values of the IMU unit and the real values beyond 9 m, so a distance lower than 10 m is recommended between two Li-Fi lamps.

5 Conclusion

In this article, we present a hybrid IPS system based on the integration of data from heterogeneous sources: i.e. Li-Fi tags to determine the positioning of a user on a floorplan; trajectory tracking of the user by optical cameras; step counting by a smartphone application supposed to guide the user between two reference points and in case of loss of cameras tracking due to congestion, smoke or other disruptive events.

Because it does not require any special infrastructure, the proposed solution is easy to implement and low cost, and it would be easy to install it in most indoor environments like hospitals, buildings, campuses, and malls.

References

1. ITU (2015) IoT global standards initiative. <https://handle.itu.int/11.1002/1000/11559>
2. Brena RF et al (2017) Evolution of indoor positioning technologies: a survey. *J Sens* 2017, Article ID 26304113
3. Davidson P, Piche R (2017) A survey of selected indoor positioning methods for smartphones. *IEEE Commun Surv Tutor* 19(2):1347–1370
4. Mendoza-Silva GM, Torres-Sospedra J, Huerta J (2019) A meta-review of indoor positioning systems. *Sensor* 19:4507. <https://doi.org/10.3390/s19204507>
5. Zafari F, Gkelias A, Leung KK (2019) A survey of indoor localization systems and technologies. [arXiv:1709.01015v3](https://arxiv.org/abs/1709.01015v3) [cs.NI] 16 jan 2019
6. Wu X et al (2020) Hybrid LIFI and Wifi networks: a survey. [arXiv:2001.04840v1](https://arxiv.org/abs/2001.04840v1)
7. Rahman ABMM, Li T, Wang Y (2020) Recent advances in indoor localization via visible lights: a survey. *Sensors* 20(5):1382
8. Yang S, Ma L, Jia S, Qin D (2020) An improved vision-based indoor positioning method. *IEEE Access* 8:26941–26949. <https://doi.org/10.1109/ACCESS.2020.2968958>
9. Nummiaro K, Koller-Meier E, Van Gool L (2002) Object tracking with an adaptive color-based particle filter. *Pattern Recogn*, 353–360
10. Shimada A et al (2006) Dynamic control of adaptive mixture-of-Gaussians background model. In: *Video and signal based surveillance, 2006. IEEE-AVSS'06, 2006*, pp 5–5
11. Sun M et al (2019) See-your-room: indoor localization with camera vision. In: *Proceedings of the ACM turing celebration conference-China*, pp 1–5
12. Oledcomm (2020) GEOLiFi kit. <https://www.oledcomm.net/lifimax-discovery-kit/>

Current Works on IDS Development Strategies for IoT



Abdelouahed Bamou , Moulay Driss EL Ouadghiri,
and Badraddine Aghoutane

Abstract Intrusions into the networks of the connected objects are rapidly evolving and affect its entire architecture (physical, network, application layers), as devices, networks and applications are increasingly connected and integrated. Securing these systems, which are generally constrained in resources, is becoming a necessity. Intrusion Detection Systems have proven to be an important security tool to detect attacks on the IoT network and resources. To create the IDS, Security researchers have recently used machine learning techniques because of the excellent results given by these methods (image and voice recognition, product recommendation, detection of spam and financial fraud ...). Deep learning methods known for his or her successful ability to extract high-level functionality from big data are often a resilient mechanism for detecting small variants of attacks. The target of this work is to provide a general study on IDSs implementation techniques for IoT, precisely the classical methods and also the machine learning techniques. Finally, we give some recommendations of selected works that have practiced each of the methods presented.

Keywords IoT security · Intrusion-detection system (IDS) · IDS implementation · Learning method-based IDS

1 Introduction

The explosion of the number of connected objects used in different IoT applications poses many IoT securities issues that cannot be ignored, such as: confidentiality, integrity, availability, authenticity, non-repudiation and freshness of data. To respond these threats, a permanent monitoring of IoT networks is basic, and an Intrusion

A. Bamou (✉) · M. D. EL Ouadghiri · B. Aghoutane
IA Laboratory, Science Faculty My Ismail University of Meknes, Meknes, Morocco
e-mail: abdelbamou@gmail.com

M. D. EL Ouadghiri
e-mail: dmelouad@gmail.com

B. Aghoutane
e-mail: b.aghoutane@gmail.com

Detection System (IDS) can be used, which has the mission to detect any breach of security mechanisms, as it is best suited to the IoT system that suffers from resource scarcity.

To ensure its security, the IDS monitors, records and applies algorithms on IoT system activities, in order to detect any malicious activity and inform network administrators to take the necessary precautions. Detection algorithms represent the core of IDS, and are based on classical techniques that are concerned with previously known attacks or the remoteness of previously recorded behavior; and Artificial Intelligence (AI) techniques that provide a great opportunity to automatically discover malicious behavior and prevent further without primitive knowledge. The implementation of IDS for the IoT system using AI techniques requires a learning and training module that receives a Dataset, then a classification module and finally a decision, benign or attack.

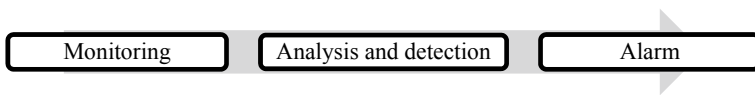
This article starts with a general review of IDS and especially intrusion detection methods; then we describe the main classical and machine learning techniques used to develop IDS in IoT. Finally, we provide some references of selected works that have experienced each of the methods studied.

2 General Study of Intrusion Detection System

2.1 Intrusion Detection Systems (IDS)

IDSs have been used since 1970 to secure computer systems [1]. They are dedicated to support the security of nodes and networks by inspecting malicious traffic in information and communication systems, thus protecting them from intruders. The mission of the IDS is to alert network administrators once attack is discovered. This attack can be launched from inside the network or from outside, it can be known by the system or unknown and the IDS can detect it.

The mechanism of the IDS is:



The IDS start by monitoring the traffic, then it analyzes it according to a suitable algorithm, if attack is detected, the alarm is launched.

2.2 *Detection Methodology*

The core of IDS is the Analysis and Detection module, which consists of specific algorithms to detect intrusions; these are developed on the basis of three approaches: signatures, anomalies, specifications.

Signature-based detection

This method starts by recording the signatures of a known attacks in a database, before compares the traffic with these signatures, and whenever there is a match, the alarm is triggered. This approach is simple, fast, and efficient for known attacks, but ineffective for unknown attacks that are not in the database; this requires regular database updates and therefore more storage space, which is not desirable for IoT [2]. We can take as an example of this approach: “if there are three successive incorrect attempts to connect to an object then it is an attack” [3].

Anomaly-based detection

This technique starts by recording normal network behavior, then the traffic is compared in real time with this normal behavior, if there is an inequality then it is an attack [4]. This method relies on statistical analysis and machine learning methods to create the normal profile and discover the anomaly. The advantage of this method is that it allows the detection of unknown attacks however, the IDS based on this method is a bit annoying for administrators because it has a high rate of False Positive (no attack but the IDS triggers the alarm); and it requires more resources for the objects containing the IDS [5]. The following paper [6] gives an example of application of this method for the detection of the DoS attack in the IoT.

Specification-based detection

It is similar to anomaly detection in that it defines the anomaly as a leaving from normal behavior; the difference is that the normal profile is determined by specifications developed manually by safety experts. The advantage of this approach is that it reduces the number of False Positives seen in the anomaly-based approach and does not require a machine learning algorithm, but the problem is the tedious development of different specifications for each platform; inadequate specifications reduce the accuracy of the IDS [7].

Hybrid-based detection

Previous methods can be combined to find a hybrid IDS with a module for each approach, which will increase accuracy, but this combination requires more resources.

This approach is the most common for current IDSs, at the beginning the detection is done using anomaly-based modules and then the IDS looks for its corresponding signature in the database [8].

3 Implementation Strategies

We specify that we are discussing here the IDSs placed in networks (NIDS), because they are the most suitable for IoT. For the implementation of NIDSs, the researchers proposed several techniques. In the following, we present the most common ones:

3.1 Classical Methods

Distributed and Collaborative

The IDS is distributed over several network points, then the collected information is shared between the nodes to make the decision, whether to attack or not, in a collaborative manner [9].

Mobile Agent

IDS moves through the network in search of possible attacks [10].

Reputation

Here again the IDS is distributed among the network nodes, except that the decision is made based on the reputation of the nodes [11]. Khardioui et al. [12] uses this method to detect the sinkhole attack in the IoT.

Game Theory

Game theory (GT) allows the realization of a mathematical model, thus, modeling the strategic interactions between the agents; with respect to the modalities of repetition, cooperation and non-cooperation between these agents [13]. For IDS, the agents are the attacker and the IDS. The role of the latter is to maximize system gains, and this comes down to solving a mark-up problem [14].

Statistical Methods

Statistical models allow us to define a stochastic model for the observed network; then the IDS compares it to the normal model; if it is exceeded, alert is launched [15].

3.2 Techniques Using Machine Learning (ML)

There are two kinds of ML procedures according to the inputs of the training data: Supervised if learning patterns are required to classify the new input and unsupervised if not.

The Fig. 1 gives the classification of the machine learning algorithms used for the IDSs in IoT:

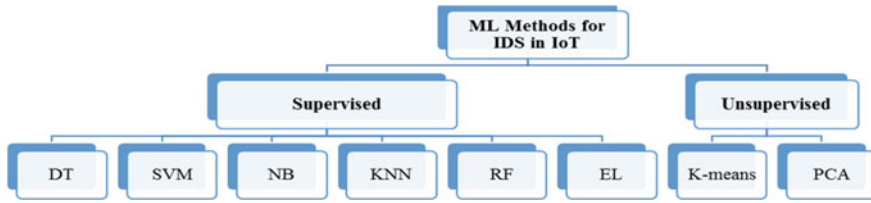


Fig. 1 Classification of machine learning methods

Support Vector Machine (SVM)

It is a ML technique that represents an extension of linear classifiers to larger spaces. It allows the discrimination and regression of data entered using a hyper-plane. This linear classifier provides significant results even with reduced training data, whereas it is less suitable for large data sets. The IDS uses this technique to classify network activities as normal or malicious, its advantage is in its ability to perform real-time detection, and training data can be updated dynamically and with fewer resources, but the challenge lies in the optimal choice of the hyper-plane [16].

Naive Bayesian (NB)

It is a linear classifier based on the conditional probability; assuming a strong independence between the features of a class. The purpose of the parameters necessary for classification is in most cases based on the maximum likelihood of probabilities.

The IDS can use the NB to detect anomalies in a network by classifying these activities as usual or not.

The NB does not require a lot of training data to find the classification variables but it is unable to find the links between the features and should not be neglected in complex cases since it assumes a strong independence between the features [17].

k-Nearest neighbour (KNN)

It is a method of classification that assumes that elements that look alike are neighbors. It consists in giving for a new entry the same group as the majority of these k neighbors. The neighbors are selected from the supervised training data (the output is known). The kNN method is the simplest among the ML methods, in addition to its efficiency, it is easy to understand, because it uses the Euclidean distance between the input features, and it accepts the updating of the training data dynamically, but it uses resources intensively, and does not manage to reduce the dimensionality, it is up to the user to choose the relevant variables; finally finding the optimal k value is decisive for the validation of the algorithm [18].

Decision Trees (DTs)

It is a prediction method using supervised learning data. It is formed by a graph (tree) that helps to make a decision. The leaves are the target class, the nodes are the conditions and the branches are therefore their answers. To classify a new entry, it is enough to respect the conditions from the beginning of the tree to the target class.

Decision trees are fasted in training, and also prediction phases, but require more resources concerning storage. IDS can use DT alone or with other classifiers [19].

Random forest (RF)

RF is a powerful model for prediction and randomization of several DTs, each tree is formed by a training sample. The classification is done on the basis of voting of the DTs of the drill; and the regression is performed according to the mean prediction of the values predicted by each DT forming RF. The advantage of this algorithm in addition to its performance, accuracy, and flexibility is that it can model missing values, it can work with few features at the input, but it takes time for training, and it is suitable for large datasets [20].

k-Means clustering

It is an unsupervised method of segmenting the input data into k groups. Each element is assigned to the nearest group according to its Euclidean distance from the group center; then a new group center is calculated using these elements. These operations are repeated iteratively until convergence to a stable state. This convergence is rapid when it exists, but the difficulty is to determine the value of K [21].

Principal component analysis (PCA)

Mainly used for feature selection; it allows to reduce the dimensionality of input data to retain only the features of interest based on their usefulness for the built model. PCA is useful for IDS to reduce system complexity and make the detection process faster, as well as to reduce resource intensity [22].

Ensemble learning (EL)

IDS can mix previous classifiers to form EL which gives better results than a single classifier. These are generally trained on diverse subsets of the dataset so as to mutually create output results with the diminished false alarms and improved accuracy [23].

3.3 Techniques Using Deep Learning (DL)

DL methods can be classified as unsupervised deep learning for unlabeled input data, as supervised if they are labeled and as hybrid if they are combined. The common DL algorithms used for IDS in IoT is shown in Table 1:

Convolutional neural networks (CNNs)

CNN's idea comes from the disposition of cells in the visual cortex of the brain; they consist of a network of neurons that is composed of a perception layer followed by convolution layers that applies filters corresponding to the features sought, then CNN applies the activation function = $\max(0, x)$ to exclude all the values of $x \leq 0$ corresponding to the features in input not interesting, this step operation is called

Table 1 Classification of deep learning methods

Supervised		Unsupervised				Hybrid
Convolutional Neural Network (CNN)	Recurrent Neural Network (RNN)	AutoEncoder (AE)	Restricted Boltzman Machine (RBM)	Deep Belief Networks (DBNs)	Generative Adversarial Network (GAN)	Ensemble of DL Networks (EDLNs)

max-pooling, it allows to decrease the dimension of the parameters of the input data. Then the flattening layer allows reducing the network to a single dimension. Finally, the classification layer gives the final result [24].

Although the CNN model is generally trained as a classification and to reduce the size of features in an artificial neural network, it is mainly oriented towards promoting image, sound, and video recognition. However, it has a high computational cost; thus, its implementation on devices with limited resources is difficult [25].

Recurrent neural networks (RNNs)

Unlike CNN which are feed-forward. RNN is a type of neural network having at least one cycle which allows it to have a kind of internal memory formed by the previous output, such that its output is a composition of contents of its memory and the input element. This structure allows it to process data sequences having temporal significance, such as voice, video and text [26]. So the main advantage of RNN is to retain the previous state of the processed data; but when their sequences become long, two problems appear, that of vanishing gradient and exploding gradient. To remedy these problems, researchers have developed a kind of RNN with so-called Long Short-Term Memory Units (LSTM), by learning just short-term dependencies through three gates (input, output and oblivion) that allow managing the holding of information in memory; Gated Recurrent Units (GRU) is a variant of LSTM with fewer gates. LSTM and GRU are often used by IDSs to classify sequential data [27].

AutoEncoder

This is an unsupervised DL algorithm in which the output aspect resembles that of the useful input for generative models. Gaussian noise can be added to AE to increase its performance in anomaly detection. IDSs use AE for dimensionality reduction, and data representation [28].

Restricted Boltzmann machines (RBMs)

RBMS is a generative neural network consisting of a visible and a hidden layer, so that information flows in both directions (visible layer to hidden and screw to screw); without having connections between neurons of the same layer. It is a DL method used for feature learning and representation, dimensionality reduction, classification and many others [29].

Deep belief networks (DBNs)

The DBN is a generative, multi-layer learning model formed by a series of RBMSs stacked on top of each other, and a direct network often composed of auto-encoders and a Bayesian network layer. The existence of RBMSs indicates that intra-layer connections do not exist. This allows it to learn layer by layer, independently of each other and therefore increase its performance. DBNs are used to initialize the classification and extract representations of the input data [30].

Generative adversarial networks (GANs)

GAN is a deep neural network architecture involved of two neural networks, setting one in opposition to the other (thus the “adversarial”), where a generator and a discriminator attempts to outmaneuver the other. The objective of the generator is to trick an IDS, the objective of the discriminator is to mirror the IDS on categorizing inputs (right or wrong) and deliver feedback to the generator [31]. The game finishes when the IDS and discriminator can’t precisely order the data made by the generator.

The advantage of GAN is that it can be formed with limited data, no approximate inferences are needed and consistency between the G and D models can be maintained after equilibrium has been reached, but it is difficult to find this equilibrium [32].

Ensemble of DL networks (EDLNs)

Several of the above techniques can be brought together to form EDLNs, giving a better result than one technique implemented alone.

4 Conclusion

IoT is constantly progressing. However, its security must be taken into account. For this reason, we propose the use of IDSs which can be a security solution adapted to the IoT.

In this work, we focused on the implementation techniques used to improve IDS, in particular classical and learning methods as well as some examples of publications for each technique.

For prospects, we plan to study the detection of “zero-day” type attacks in IoT networks; as well as the integration of IDS on fog computing platforms which could solve the problem of the scarcity of resources needed for IDS in the IoT system.

We concluded that IDS research in the field of IoT is still in its infancy. Applications of machine learning techniques can make IDS more intelligent to accompany the evolution of IoT attacks.


References

1. Ahmed M, Naser Mahmood A, Hu J (2016) A survey of network anomaly detection techniques. *J Netw Comput Appl*
2. Pacheco J, Hariri S (2016) IoT security framework for smart cyber infrastructures. In: *Proceedings—IEEE 1st international workshops on foundations and applications of self-systems, FAS-W 2016*
3. Kasinathan P, Pastrone C, Spirito MA, Vinkovits M (2013) Denial-of-service detection in 6LoWPAN based internet of things. In: *International conference wireless mobility computing and network communication*, pp 600–607
4. Scarfone K, Mell P (2007) *Guide to intrusion detection and prevention systems (IDPS)*. Natl Inst Stand Technol
5. Amaral JP, Oliveira LM, Rodrigues JJPC, Han G, Shu L (2014) Policy and network-based intrusion detection system for IPv6-enabled wireless sensor networks. In: *2014 IEEE international conference on communications, ICC 2014*
6. Bamou A, Khardioui M, El Ouadghiri MD, Aghoutane B (2020) Implementing and evaluating an intrusion detection system for denial of service attacks in IoT environments. In: *Lecture notes in networks and systems*
7. Le A, Loo J, Luo Y, Lasebae A (2011) Specification-based IDS for securing RPL from topology attacks. *IFIP Wirel Days* 1(1):4–6
8. Raza S, Wallgren L, Voigt T (2013) SVELTE: real-time intrusion detection in the internet of things. *Ad Hoc Networks*
9. Thanigaivelan NK, Nigussie E, Kanth RK, Virtanen S, Isoaho J (2016) Distributed internal anomaly detection system for internet-of-things. In: *2016 13th IEEE annual consumer communications and networking conference (CCNC)*, pp 319–320
10. Saxena AK, Sinha S, Shukla P (2017) General study of intrusion detection system and survey of agent based intrusion detection system. In: *Proceeding—IEEE international conference on computing communication and automation ICCCA 2017, vol 2017*, pp. 417–421
11. Khan ZA, Herrmann P (2017) A trust based distributed intrusion detection mechanism for internet of things. In: *Proceedings of the International Conference on Advance Information Networking and Application, AINA*, pp 1169–1176
12. Khardioui M, Bamou A, El Ouadghiri MD, Aghoutane B (2020) Implementation and evaluation of an intrusion detection system for IoT: against routing attacks. *Lect Notes Netw Syst*. 92:155–166
13. Ikram W, Petersen S, Orten P, Thornhill NF (2014) Adaptive multi-channel transmission power control for industrial wireless instrumentation. *IEEE Trans Ind Inf*
14. Sedjelmaci H, Senouci SM, Al-Bahri M (2016) A lightweight anomaly detection technique for low-resource IoT devices: a game-theoretic methodology. In: *2016 IEEE international conference on communication ICC 2016*
15. Arrington B, Barnett LE, Rufus R, Esterline A (2016) Behavioral modeling intrusion detection system (BMIDS) using internet of things (IoT) behavior-based anomaly detection via immunity-inspired algorithms. In: *2016 25th international conference on computer communications and networks, ICCCN 2016*
16. Wagner C, François J, State R, Engel T (2011) Machine learning approach for IP-flow record anomaly detection. *Lecture notes on computer science (including subseries of lecture notes artificial intelligence, lecture notes in bioinformatics)*, vol 6640 LNCS, no. PART 1, pp 28–39
17. Ng AY, Jordan MI (2002) On discriminative versus generative classifiers: a comparison of logistic regression and naive bayes. In: *Advances in neural information processing systems*
18. Gokhale DV, Box GEP, Tiao GC (1974) Bayesian inference in statistical analysis. *Biometrics*
19. Kotsiantis SB (2013) Decision trees: a recent overview. *Artif Intell Rev* 39(4):261–283
20. Buczak AL, Guven E (2016) A survey of data mining and machine learning methods for cyber security intrusion detection. In: *IEEE Communication on survey tutorials*

21. Doshi R, Aporthe N, Feamster N (2018) Machine learning DDoS detection for consumer internet of things devices. In: Proceedings—2018 IEEE symposium on security and privacy workshops, SPW 2018
22. An N, Duff A, Naik G, Faloutsos M, Weber S, Mancoridis S (2018) Behavioral anomaly detection of malware on home routers. In: Proceedings of the 2017 12th international conference on malicious and unwanted software, MALWARE 2017
23. Moustafa N, Turnbull B, Choo KKR (2019) An ensemble intrusion detection technique based on proposed statistical flow features for protecting network traffic of internet of things. *IEEE Internet Things J*
24. Bassey J, Adesina D, Li X, Qian L, Aved A, Kroecker T (2019) Intrusion detection for IoT devices based on RF fingerprinting using deep learning. In: 2019 4th international conference on fog mobile edge computing FMEC 2019, pp 98–104
25. Vrizlynn LL (2017) Thing, “IEEE 802.11 network anomaly detection and attack classification: a deep learning approach. In: IEEE wireless communications and networking conference (WCNC)
26. Staudemeyer RC (2015) Applying long short-term memory recurrent neural networks to intrusion detection. *South Afr Comput J*
27. Roy B, Cheung H (2019) A deep learning approach for intrusion detection in internet of things using bi-directional long short-term memory recurrent neural network. In: 2018 28th international telecommunication networks and applications conference, ITNAC 2018
28. Feng Q, Zhang Y, Li C, Dou Z, Wang J (2017) Anomaly detection of spectrum in wireless communication via deep auto-encoders. *J Supercomput* 73(7):3161–3178
29. Feng P, Yu M, Naqvi SM, Chambers JA (2014) Deep learning for posture analysis in fall detection. In: International conference digital signal processing DSP, vol 2014, pp 12–17
30. Chen Y, Zhang Y, Maharjan S, Alam M, Wu T (2019) Deep learning for secure mobile edge computing in cyber-physical transportation systems. *IEEE Netw* 33(4):36–41
31. Hiromoto RE, Haney M, Vakanski A (2017) A secure architecture for IoT with supply chain risk management. In: Proceedings of 2017 IEEE 9th international conference on intelligence data acquiritor advance on computing system technology applied. IDAACS 2017, vol 1, pp 431–435
32. Dimokranitou A, Tsechpenakis G, Yu Zheng J, Tuceryan M (2017) Adversarial autoencoders for anomalous event detection. Master thesis Purde University

New Metrics to Measure the Quality of the Ranking Results Obtained by the Multi-criteria Decision-Making Methods



Mohammed Chaouki Abounaima , Loubna Lamrini, Fatima Zahra EL Mazouri, Noureddine EL Makhfi, Mohammed Talibi Alaoui, and Mohamed Ouzarf

Abstract Nowadays, there is a panoply of multi-criteria decision-making methods which are proposed in the literature to solve the ranking problematic, where each method has its resolution process and has its drawbacks and advantages. These methods aim to rank from best to worst a finite set of alternatives while taking into account a set of conflictual criteria. The purpose of this article is to propose specific metrics that will be useful to measure the quality of the rankings obtained by different methods. Thus, these quality measures can help the decision-maker to choose the best ranking objectively when adopting several methods. To show and prove the importance and relevance of the metrics proposed, a set of twenty-five examples of rankings will be examined. The results of the experiment conclusively show that all the proposed metrics lead to significant and equivalent quality measures.

Keywords Multi-criteria decision making · Multi-criteria aggregation procedure · Pearson correlation coefficient · Kendall metric · Euclidian metric · Hölder metric · The measure of ranking quality

M. C. Abounaima (✉) · L. Lamrini · F. Z. EL Mazouri · M. Talibi Alaoui · M. Ouzarf
Laboratory of Intelligent Systems and Applications, Faculty of Sciences and Technologies, Sidi Mohammed Ben Abdellah University, Fez, Morocco
e-mail: medchaouki.abounaima@usmba.ac.ma

L. Lamrini
e-mail: loubna.lamrini@usmba.ac.ma

F. Z. EL Mazouri
e-mail: Fatimazahra.elmazouri@usmba.ac.ma

M. Talibi Alaoui
e-mail: mohammed.talibialaoui@usmba.ac.ma

M. Ouzarf
e-mail: mohamed.ouzarf@usmba.ac.ma

N. EL Makhfi
Faculty of Science and Technology Abdelmalek, Essaadi University, Al Hoceima, Morocco
e-mail: n.elmakhi@gmail.com

1 Introduction

In our recent work [1], we have demonstrated the usefulness of the Pearson Correlation metric to evaluate the quality of the ranking results obtained by different multi-criteria aggregation procedures (MCAP). We intend in this article to propose other possible metrics which take into account the relative importance of the criteria, which generalizes the case of an equal-weighting where all the criteria have the same importance.

The field of multi-criteria decision-making (MCDM) has reached a well advanced and remarkable maturity, which is justified by the considerable number and the abundance of the methods proposed in the literature and the great variety of real applications who have used MCDM methods [2], like industry, economy, energy, social, environmental, even military, etc. An MCDM problem can be summarized by considering, in first, a finite set of alternatives A and set of conflictual criteria F . Then, each alternative is evaluated on all the retained criteria. In the last, the decision-maker (DM) should choose the problematic to resolve and the appropriate resolution method(s). MCDM methods can mainly resolve three issues. The first allows us to rank the alternatives of set A from the best to the worst choice, known as the Ranking Problematic. The second is to sort the set A into established categories, called the Sorting Problematic. Furthermore, the third problem consists in selecting the best alternative, known as the Choice Problematic.

For the same problem, there are several resolution MCPAs, each of which gives a solution. The DM obtains such different results, which all aggregate the different criteria. Given the embarrassment of the choice of solutions obtained by the different MCPAs adopted, the DM surely will have difficulties in selecting the final solution. This work proposes many metrics to measure the quality of each solution. This quality expresses the dependence degree between the MCPA solution and the performance of the alternatives. The final solution to be retained will be that which leads to the highest dependence degree.

The rest of the article is organized as follows: the first section “Overview of multi-criteria analysis methods and comparison between MCDM methods” gives an overview of MCDM approaches and methods. Some work on the comparison of MCDM methods will also be cited in this section. The following section “The proposed approach to measure the quality of rankings” details the proposed approach to assess, on the basis of several parameters, the quality of a ranking. The different tests of the proposed approach and discussion will be presented in the last section “Numerical experimentation and discussion”. In the end, a conclusion will be given with the suggestion of some lines of research.

2 Analysis Methods and Comparison Between MCDM Methods

Undoubtedly the reality of decision has always been naturally multi-criteria, where several criteria should be taken into account to find a solution. Unless if by some artisanal transformations, the decision problem becomes mono-criterion, where a single function, called by economists, the objective function to optimize to find the best solution, called the optimal solution.

Unfortunately, it is not always possible to reduce all the functions expressing the criteria into a single function, because of the diversification of the points of view and the consequences of the problem and which can concern all planes of human life: political, military, economic, urban and interurban infrastructure, social, environment, ecology [3]. All these consequences are not expressed and measured directly by the same measurement scale, so they cannot be reduced by a single function. Furthermore, any reduction of the multi-criteria into single criteria, it will be a simplification of the problem, but surely, it will have influences and impacts on the quality and rationality of the final solution.

It is so easy to optimize a problem based on a single criterion. However, for several criteria, each criterion gives its optimal solution. The problem is to find one solution that represents all the solutions obtained by the different criteria. The main objective of MCDM methods is, therefore, to find the solution aggregating all the solutions arising from the different criteria [4].

For more than forty years, the MCDM field has known significant progress as well on the theoretical level as on the application level [5]. Several approaches have thus emerged, each with its advantages and disadvantages. There are currently two major resolution approaches [6]. The first is called the synthesis criterion approach; it consists in transforming the multi-criteria problem into a simple mono-criterion problem. As an example of methods coming under this approach: we cite the Weight Sum Method (WSM) [7], the Goal Programming method [8], the Technique for Order of Preference by Similarity to the ideal solution (TOPSIS) [9], and many other methods. The second approach is known as the outranking approach, where we build a comparison relationship between actions, called the outranking relationship. This last will be used to find the compromise solution depending on the type of problem to be solved: choice, ranking or sorting problematic. There is a panoply of methods that are based on the principle of this approach. We cite the two prevalent methods ELECTRE (Elimination and Choice Translating the REALITY) method [10, 11] and PROMETHEE (Preference Ranking Organization METHod for Enrichment of Evaluations) method [12].

The problem posed in this work is to compare MCDA methods under the same approach. Several authors have approached this question, but for the majority of them, they have tried to compare methods based on their approaches and procedures. For example, we cite the works [13, 14]. Any direct comparison between methods will be subjective and meaningless, as each method has its limitations and advantages. We propose to use metrics to measure the quality of the compromise solutions in

order to help the DM to choose the best result and not the best method because in the MCDM field, there is no best method and bad method.

3 The Proposed Approach and Metrics to Measure the Ranking Quality

For the rest of this section, we need, as the case of any MCDM method, the flowing data:

- $A = \{a_1, \dots, a_i, \dots, a_n\}$ is the set of n alternatives.
- $F = \{g_1, \dots, g_j, \dots, g_m\}$ is the family of m criteria ($m \geq 2$) to be maximized.
- $g_j(ai)$ is the performance of the alternative ai on the criterion g_j evaluated by de DM. The performance $g_j(ai)$, also called by judgment, evaluation and preference.
- $W = \{w_1, \dots, w_j, \dots, w_m\}$ is the weight vector reflecting the relative importance of each criterion.

3.1 The Proposed Approach to Measure the Ranking Quality

To measure the quality of a given ranking solution, which ranks the alternatives from best to worst, we suggest comparing this ranking to all of the rankings induced by each criterion. More precisely, each rank can be associated with a comparison matrix R of the form: if an alternative a is better classified than another alternative b , then this comparison gives $R(a,b) = 1$ and $R(b, a) = 0$. The proposed metrics are used to measure the dependencies that exist between the comparison matrix associated with the ranking solution obtained and the comparison matrices induced by the criteria. For the correlation measure, this dependence must be maximum, and for the other distance metrics, it must be minimum. The advantage of this proposal is that it does not imply any condition on the scales for measuring the performance of alternatives.

The approach proceeds in three steps: In the first step, the comparison matrices R^k induced by the different criteria g_k are calculated for all k in $\{1, \dots, m\}$, with m is the number of criteria considered. In the second step, we calculate the matrix of comparisons R^k associated with the ranking result of the MCDM method or a scenario of the robustness analysis. In the third and last step, all the matrices R^k are compared to the matrix R . We choose for this comparison one of the proposed metrics. Finally, the quality of the ranking P is calculated by the weighted average of these comparisons. The three steps are detailed and explained below.

- Step 1: Computing the comparisons matrix R^k induced by the criterion g_k
- The criterion g_k , for $k \in \{1, \dots, m\}$ induces the R^k comparison matrix.
- Let $(R_{ij}^k)_{i,j \in \{1, \dots, n\}}$ be the comparison matrix. This matrix can be calculated by the following Eq. 1.

$$R_{ij}^k = \begin{cases} 1 & \text{if } gk(i) > gk(j) \\ 0 & \text{otherwise} \end{cases} \quad (1)$$

- The matrix R^K contains only the numbers 0 and 1. The value 1 means that the alternative i is preferred to the alternative j according to the criterion gk .
- Step 2: Evaluation of the comparisons matrix R associate to the ranking P
- The comparisons matrix R , associate to the ranking P , is calculated in the same way for each criterion. The matrix R is given by the following Eq. 3.

$$R_{ij} = \begin{cases} 1 & \text{if } "i" \text{ is better ranked than } j \text{ in the ranking } P \\ 0 & \text{otherwise} \end{cases} \quad (2)$$

- The value 1 indicates that the action i is ranked before the action j for the aggregation multi-criteria method used.
- Step 3: Measure of the quality for the ranking P
- The ranking P will be a better choice if this ranking obtained sticks almost, or at least it is near, to all the criteria gk . This comes down to measuring the dependence between the matrix R and each matrix R^k . The experimentation section shows this link of dependence, which exists between the two matrices R and R^k . We propose in this article to measure this dependence by the correlation and distance metrics between the matrices. The quality $Q(P)$ of a ranking P is given by the Eqs. (3) and (4).

Correlation metric:

$$Q(P) = \frac{\sum_{k=1}^m w_k \times \text{correlation}(R^k, R)}{\sum_{k=1}^m w_k} \quad (3)$$

Distance metric:

$$Q(P) = 1 - \frac{\sum_{k=1}^m w_k \times \text{distance}(R^k, R)}{\sum_{k=1}^m w_k} \quad (4)$$

where: m is the number of criteria, and w_k is the importance of the criterion gk .

In Eqs. (3) and (4), we take into account the importance of criteria in measuring quality, both for correlation and distance. Insofar as a better correlation on an important criterion, for example, must take advantage and be taken into account in the final calculation of the measurement.

The correlation and distance metrics are explained in the following paragraphs.

Remark The quality of a ranking will be maximum when it goes in the same direction to all the criteria. In this case, the distance metric gives a result that is equal to 0, and which is the best result. That's why we chose "1-distance (R^k, R)" so that it becomes a maximization and which will have the same interpretation as the correlation measure.

3.2 The Pearson Correlation Coefficient

The correlation coefficient is a measure of the link between two variables [1]. This coefficient is used to characterize a positive or negative relationship, and it is the symmetrical measure, the closer it is to 1, in absolute value, the link and the dependence between the two variables will be better. For the measure of the correlation between two matrices X and Y , which are for our case comparison matrices translating rankings, we use the following Formula 5.

$$\text{correlation}(X, Y) = \frac{\sum_{i=1}^n \sum_{j=1}^n (X_{ij} - \bar{X}) \times (Y_{ij} - \bar{Y})}{\sqrt{\sum_{i=1}^n \sum_{j=1}^n (X_{ij} - \bar{X})^2 \times \sum_{i=1}^n \sum_{j=1}^n (Y_{ij} - \bar{Y})^2}} \quad (5)$$

where: $\bar{X} = \frac{1}{n(n-1)} \times \sum_{i, j=1}^n X_{ij}$ is the empirical average a square matrix X of order n . n is the number of alternatives of set A .

3.3 The Distance Metrics

For the evaluation of the quality, we use the matrix distance between the two matrices R^k and R . As will be demonstrated in the experimentation section, a division by $n \times (n - 1)$ is added to the distance, in order to obtain a quality result varying between 0 and 1. So for a distance that gives 0 it means that the ranking result is the same as the ranking induced by the criterion g^k , it is a better extreme result. And for a distance that gives 1 this means that the result ranking is entirely the opposite of the ranking induced by the criterion g^k , it is an extremely lousy result.

All the distances calculated between R and R^k are then aggregated using a weighted average to have the total quality, given by Eq. 4.

All possible distances are summarized in the following Table 1. For each distance, we give it a name, under which it is known in the literature, as well as the formula

Table 1 The proposed distance metrics

Metric name	distance(X,Y)
Kendall metric: d_1	$d_1(X, Y) = \frac{1}{n \times (n-1)} \times \sum_{i=1}^n \sum_{j=1}^n X_{ij} - Y_{ij} $
Euclidean metric: d_2	$d_2(X, Y) = \sqrt{\frac{1}{n \times (n-1)} \times \sum_{i=1}^n \sum_{j=1}^n (X_{ij} - Y_{ij})^2}$
Hölder metric: d_α , with $\alpha \geq 3$	$d_\alpha(X, Y) = \sqrt[\alpha]{\frac{1}{n \times (n-1)} \times \sum_{i=1}^n \sum_{j=1}^n X_{ij} - Y_{ij} ^\alpha}$

to compute the distance between any two matrices $X(X_{ij})1 \leq i, j \leq n$ and $Y(Y_{ij})1 \leq i, j \leq n$, where n is the number of alternatives.

4 Numerical Experimentation and Discussion

To verify that the metrics can correctly measure the quality of the rankings, we examine in this section an experimental example. In this last one, we suggest an MCDM ranking problem with three criteria $F = \{g1, g2, g3\}$, and a set of four alternatives $A = \{A1, A2, A3, A4\}$. In order to have a significant interpretation of the results of this experimental study, we propose three criteria that lead to the same ranking. Besides, we choose the three criteria with the same weighting $w1 = w2 = w3 = 1$. We suppose that the three criteria give the same ranking: $A1 > A2 > A3 > A4$, as shown in Table 2. This ranking means that the alternatives $A1, A2, A3$, and $A4$ are respectively ranked first, second, third, and fourth.

The comparison matrices $R1, R2$, and $R3$ deduced respectively by the three criteria $g1, g2$, and $g3$ are calculated and give the same result of the comparison between the alternatives. These matrices are given in Table 3.

4.1 Numerical Results

For the evaluation of the quality of the classifications obtained by different MCDM methods to be compared, or obtained in robustness analysis, we propose to distinguish three cases of rankings P .

Table 2 The criteria rankings $P1, P2$, and $P3$

Alternatives/Rankings	$P1(g1)$	$P2(g2)$	$P3(g3)$
A1	1	1	1
A2	2	2	2
A3	3	3	3
A4	4	4	4

Table 3 Matrices induced by the criteria R^1, R^2 , and R^3

	A1	A2	A3	A4
A1	0	1	1	1
A2	0	0	1	1
A3	0	0	0	1
A4	0	0	0	0

We distinguish two extreme cases with other intermediate cases. The first extreme case concerns a ranking coincides with all the rankings induced by the three criteria. The second extreme case concerns the case where the ranking is the opposite of all the rankings induced by the three criteria. Other intermediate cases are envisaged when the ranking obtained is slightly different from the rankings induced by the three criteria.

In this experiment, we compare 25 examples of the most representative P classifications and for which the alternatives alternate their ranks in the P classifications compared to the classifications of the three criteria $P1$, $P2$, and $P3$. Table 4 shows the calculated quality results.

The graph in Fig. 1 shows and compares the variation of the three quality measures obtained in Table 4.

Table 4 Quality measurement by the three metrics for the 25 selected rankings

Example number	Ranking P	Q_corr(P)	Q_d1(P)	Q_d2(P)
E1	A1 > A2 > A3 > A4	1.0000	1.0000	1.0000
E2	A1 > A2 > A4 > A3	0.7333	0.8333	0.9129
E3	A1 > A3 > A2 > A4	0.7333	0.8333	0.9129
E4	A1 > A3 > A4 > A2	0.4667	0.6667	0.8165
E5	A2 > A1 > A3 > A4	0.7333	0.8333	0.9129
E6	A2 > A1 > A4 > A3	0.4667	0.6667	0.8165
E7	A2 > A3 > A1 > A4	0.4667	0.6667	0.8165
E8	A2 > A3 > A4 > A1	0.2000	0.5000	0.7071
E9	A2 > A4 > A3 > A1	-0.0667	0.3333	0.5774
E10	A3 > A1 > A2 > A4	0.4667	0.6667	0.8165
E11	A3 > A2 > A1 > A4	0.2000	0.5000	0.7071
E12	A3 > A2 > A4 > A1	-0.0667	0.3333	0.5774
E13	A3 > A4 > A1 > A2	-0.0667	0.3333	0.5774
E14	A3 > A4 > A2 > A1	-0.3333	0.1667	0.4082
E15	A4 > A1 > A2 > A3	0.2000	0.5000	0.7071
E16	A4 > A1 > A3 > A2	-0.0667	0.3333	0.5774
E17	A4 > A2 > A1 > A3	-0.0667	0.3333	0.5774
E18	A4 > A2 > A3 > A1	-0.3333	0.1667	0.4082
E19	A4 > A3 > A1 > A2	-0.3333	0.1667	0.4082
E20	A4 > A3 > A2 > A1	-0.60	0.0000	0.0000
E21	A1 > A2 > A3 = A4	0.8704	0.9167	0.9574
E22	A1 > A2 = A3 = A4	0.6202	0.7500	0.8660
E23	A1 = A2 > A3 > A4	0.8704	0.9167	0.9574
E24	A1 = A2 = A3 > A4	0.6202	0.7500	0.8660
E25	A1 = A2 > A3 = A4	0.7454	0.8333	0.9129

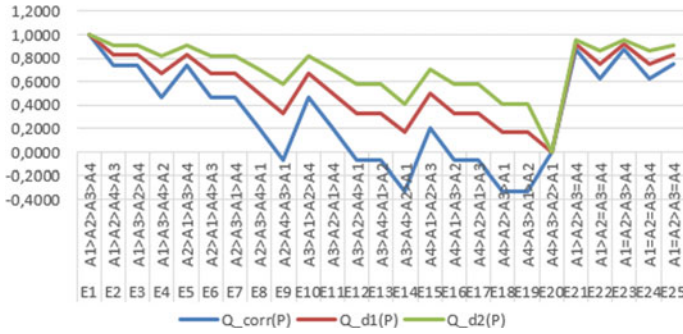


Fig. 1 Graphical representation of quality variations for the three metrics

4.2 Discussion

The graph above clearly justifies that the three metrics vary in the same direction and lead to the same interpretations and analysis of the qualities of the rankings; this allows us to conclude that the three metrics are equivalent and will give the same quality comparison result of the rankings.

Moreover, we notice that the ranking E1: $A1 > A2 > A3 > A4$, see Table 4, gives the maximum quality, which is worth 1. Indeed, this ranking coincides, by hypothesis, with the three rankings induced by the three criteria g_1, g_2 , and g_3 . However, the ranking E20: $A4 > A3 > A2 > A1$ gives the worst quality, which is 0 for the metrics d_1 and d_2 , and -0.63 for the correlation metric. That is justified by the fact that the ranking E20 is upside down from the three rankings induced by g_1, g_2 , and g_3 .

For all the other ranking cases, the quality varies between 1 and 0 for the metrics d_1 and d_2 . For the correlation metric, the quality varies between 1 and -0.6 . The negative values obtained for the quality show that there is an inverse dependence between the matrices R and R^k [1]. The quality decreases notably when the alternatives change their initial ranks for the E1 ranking.

The same results are obtained with the rankings E21–E22–E23–E24–E25, where some alternatives have equal rank.

In the conclusion of this experiment, the three metrics are equivalent and in perfect coherence. They also have significance for the measurement of the quality of the rankings.

5 Conclusions

The main objective of the paper was to suggest metrics to measure the quality of the rankings. These metrics will be beneficial to compare objectively several MCDM ranking methods.

We have proved and shown in this work that all the proposed metrics give significant results for the measurement of the ranking quality and vary correctly between 1, for the best ranking, and 0 for a bad ranking. Except for correlation, this metric can reach values less than 0, which in this case shows an inverse dependence between the matrices R and R^k . It has also been proven that all the metrics are consistent and equivalent insofar as they lead to the same results of the rankings. The proposed metrics will so serve indifferently as rational and objective tools for the comparison between the ranking results, and can thus help the decision-maker to choose the best ranking of the alternatives.

In our future research, we intend to extend the metrics for the estimation of the quality of the rankings for the case of uncertain criteria as deployed by some MCDM methods such as the famous ELECTRE III method. Other research will focus on quality measurement for sorting and selection problematics.

References

1. Abounaima MC, Mazouri FZE, Lamrini L, Nfissi N, Makhfi NE, Ouzarf M (2020) The pearson correlation coefficient applied to compare multi-criteria methods: case the ranking problematic. In: 2020 1st international conference on innovative research in applied science, engineering and technology (IRASET), pp 1–6. <https://doi.org/10.1109/IRASET48871.2020.9092242>
2. Aruldoss M, Lakshmi TM, VenkatesanVP (2013) A survey on multi criteria decision making methods and its applications. *Am J Inf Syst* 1(1). <https://doi.org/10.12691/ajis-1-1-5>
3. Govindan K, Jepsen MB (2016) Electre: a comprehensive literature review on methodologies and applications. *Eur J Oper Res* 250(1):1–29. <https://doi.org/10.1016/j.ejor.2015.07.019>
4. Roy B, Bouyssou D (1993) Aide multicritère méthodes et cas. Economica, Paris
5. Zavadskas EK, Turskis Z, Kildienė S (2014) State of art surveys of overviews on MCDM/MADM methods. *Technol Econ Dev Econ* 20(1):165–179. <https://doi.org/10.3846/20294913.2014.892037>
6. El Mazouri FZ, Abounaima MC, Zenkour K (2019) Data mining combined to the multi-criteria decision analysis for the improvement of road safety: case of France. *J Big Data* 6(1):5. <https://doi.org/10.1186/s40537-018-0165-0>
7. Kumar G, Parimala N (2019) A sensitivity analysis on weight sum method MCDM approach for product recommendation. In: Distributed computing and internet technology, pp 185–193. https://doi.org/10.1007/978-3-030-05366-6_15
8. Vivekanandan N, Viswanathan K, Gupta S (2010) Errata to: optimization of cropping pattern using goal programming approach. *Opsearch* 47(1):104–104. <https://doi.org/10.1007/s12597-010-0007-0>
9. Behzadian M, Khanmohammadi Otaghsara S, Yazdani M, Ignatius J (2012) A state-of-the-art survey of TOPSIS applications. *Exp Syst Appl* 39(17): 13051–13069. <https://doi.org/10.1016/j.eswa.2012.05.056>
10. Emovon I, Ogheniyerovwho OS (2020) Application of MCDM method in material selection for optimal design: a review. *Res Mater* 7:100115. <https://doi.org/10.1016/j.rinma.2020.100115>
11. Mazouri FZE, Abounaima MC, Zenkour K, Alaoui AEH (2018) Application of the ELECTRE III Method at the Moroccan Rural electrification program. *Int J Electr Comput Eng (IJECE)* 8(5):3285–3295. <https://doi.org/10.11591/ijece.v8i5.pp3285-3295>
12. Behzadian M, Kazemzadeh RB, Albadvi A, Aghdasi M (2010) PROMETHEE: a comprehensive literature review on methodologies and applications. *Eur J Oper Res* 200(1):198–215. <https://doi.org/10.1016/j.ejor.2009.01.021>

13. Wang M, Lin S-J, Lo Y-C (2010) The comparison between MAUT and PROMETHEE. In: 2010 IEEE international conference on industrial engineering and engineering management, pp 753–757. <https://doi.org/10.1109/IEEM.2010.5675608>
14. Sánchez-Lozano JM, García-Cascales MS, Lamata MT (2016) Comparative TOPSIS-ELECTRE TRI methods for optimal sites for photovoltaic solar farms. Case study in Spain. *J Clean Prod* 127:387–398. <https://doi.org/10.1016/j.jclepro.2016.04.005>

LiteNet: A Novel Approach for Traffic Sign Classification Using a Light Architecture



Soufiane Naim and Noureddine Moumkiné

Abstract This paper presents a deep convolutional neural network architecture to classify the traffic signs of the GTSRB dataset. Our method uses a very light architecture with a few number of parameters that achieve good results without the need of hard computation. To get at our goal, we use a filter bank. The aim of which being to extract more features, which will be used as input to a fully connected classifier. The recognition rate of our model gets an accuracy of 99.15%, overpassing the human performance being 98.81%. This way, LiteNet competes the best state of art architectures since our approach uses less memory and less computation.

Keywords Deep learning · Traffic sign · Network convolutional neural network · Classification

1 Introduction

Nowadays, traffic sign recognition and classification are challenging problems due to their critical importance in real life applications such as automated driving, road assistance, driving safety...etc. Resolving these problems will open the perspectives to build more robust cars and machines which can share decisions with drivers and avoid some traffic accidents.

Traffic signs are composed of shapes, colors, characters and symbols. They are designed to be easily noticeable for both pedestrians and drivers in order to organize road circulation and minimize accidents. Unfortunately, they sometimes lead to accidents because of real-world variabilities that make the detection and recognition an uneasy task even for humans. To deal with the traffic sign classification, many datasets have been uploaded online. The German Traffic Sign Benchmark (GTSRB) [1] is one

S. Naim (✉) · N. Moumkiné

Mathematique and Applications Laboratory, Sciences and Techniques Faculty of Mohammedia, Hassan 2 University, 146 Mohammedia, 28806 Casablanca, Morocco
e-mail: naimsoufiane@gmail.com

N. Moumkiné

e-mail: nmoumkiné@yahoo.fr

© Springer Nature Singapore Pte Ltd. 2022

S. Bennani et al. (eds.), *WITS 2020*, Lecture Notes in Electrical Engineering 745,
https://doi.org/10.1007/978-981-33-6893-4_4



Fig. 1 Overview of GTSRB dataset. It's clear that some images are suffering from picture weaknesses

of the most famous used as an entry for many articles. This dataset images show how hard it could be to do the classification task. Looking at these images (Fig. 1), we can easily observe many picture weaknesses like saturations, low-contrast, occlusions, sun glare, fading colors, etc. In addition, images don't have the same dimensions and we can even find some with a low resolution (15×15)

Indeed, some of the traffic signs have very close shapes making it hard to distinguish them when the quality of images is very low. Many deep learning techniques have been used to address these problems. We can enumerate two kinds of techniques: the convolutional neural network based and hand crafted methods.

In recent years, convolutional neural networks (CNN) [2] has been considered the pioneer in finding better solutions to the traffic sign classification problem. CNN is composed of an interconnected network of simple processing units that can learn from experience by sharing and modifying their connections. A simple CNN architecture

is composed of convolution layers responsible for capturing the image features which can be used to get a better intuition about what is inside. The layers dimensionality can be subsampled before we input the last convolution layer to a fully connected layers which will be responsible for making the predictions.

2 Related Works

Many traffic signs datasets have been uploaded online since 2011. The German Traffic Sign Benchmark Dataset (GTSRB) [1] is one of the earliest. We can also mention The Belgium Traffic Sign Dataset [3], The Russian Traffic Sign Dataset [4], and The Tsinghua-Tencent Dataset (China) [5]. This diversity has been a crucial key to encourage research comparison.

To deal with the detection and the classification tasks, many approaches have been used. Fatine and Borgan [6] have tried to address these problems using the Histogram of Oriented Gradients (HOG) [7] Their method combine the K-d trees , Random Forests and different sizes of the HOG descriptors. The HOG has been very popular before the convolution neural network era. Alefs et al. [8] and Dalal [9] combine it with machine learning methods and have obtained some accurate results. Color-based methods have been used to segment traffic signs images by thresholding them then collecting region of interest (ROI) [10] which would be the input of a classic neural network classifier. Accordingly, Shape-based methods try to distinguish the traffic signs based on their forms. Loy & Barnes [11] use the symmetric nature of triangular, square and octagonal shapes to detect the road signs. In their paper, they claim an accuracy of 95 %.

The greatest progress in the domain of traffic sign detection and classification has been done by convolution neural networks (CNN) models. If humans can detect traffic signs correctly with an accuracy of 98.84 %, CNN overpasses this value and achieves better results. Cireşan et al. [12] have won the GTSRB traffic signs competition with their Multi-column deep neural network (MCDNN) which is composed of a number of parallel CNN columns that receive preprocessed images. Then each one outputs a prediction. The MCDNN averages these predictions before taking a final decision. Sermanet, Yann [13] have used a two stages CNN structure. Both of them are made to extract features from images before feeding their outputs as entry to a classifier. Arcos-García et al. [14] use a Deep Neural Network which comprises Convolutional layers and Spatial Transformer Network. They have tried different combinations and different activation functions. Their architecture outperforms all previous state-of-the-art methods.

The rest of this paper is organized as follows: Sect. 1 is dedicated to exploring the GTSRB dataset and LiteNet architecture. Section 2 is consecrated for presenting the performed experiments in order to validate our model. The last Section is devoted to analyzing the results.

3 Methodology

3.1 Dataset

The GTSRB dataset is composed of 26,640 images belonging to 43 categories. As shown in Table 1, most of these images have triangular or circular shapes. We can also observe that the dominant traffic signs colors are red, white and blue. Looking deeper into the dataset images, we can find some challenging problems :

First, GTSRB images have got very different qualities. Many of them are suffering from blur, saturation, low-contrast and other image weaknesses.

Second, the dataset images have got 2489 different resolutions which vary from 15×15 to 250×250 . Figure 2a shows the number of images getting resolutions between the values indicated in the columns names. It demonstrates that most images have got a resolution between (20×20) and (60×60) .

Figure 2b shows the number of images by class. It is clear that we are facing an unbalanced dataset as the number of images for certain classes is 10 times less than others. This will affect the training process and the model would not correctly recognize classes with a weak representation. To handle this situation, we can use data augmentation to help them be more representative (Fig. 3).

Table 1 Different traffic signs shapes of GTSRB dataset. We can easily verify that most of them have circular or triangular shapes

Shape	Dataset percentage (%)
Circular	60
Triangular	37
Others	3

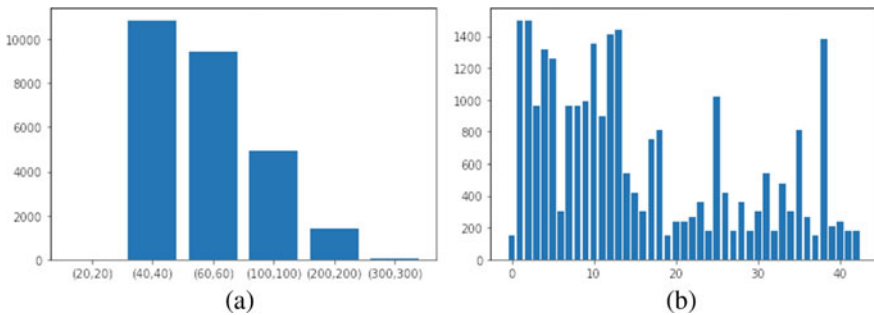


Fig. 2 a The number of images getting resolutions between the values indicated in the columns names. b Number of images by class

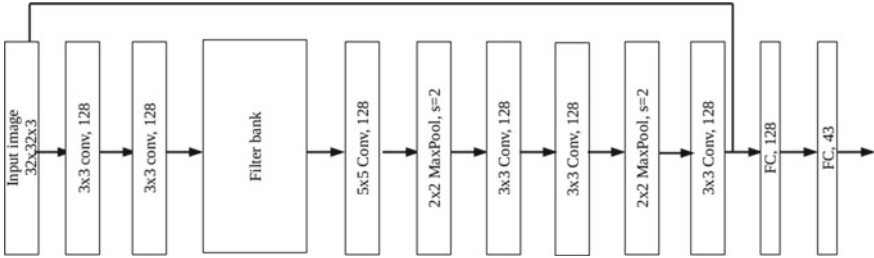
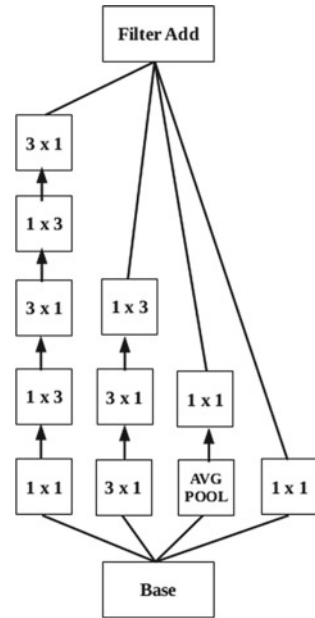


Fig. 3 LiteNet is composed from a stack of convolution neural networks layers. Each one uses a relu activation function to capture non linear features. The filter balk details are exposed in Fig.4

Fig. 4 The filter bank applies multiple convolution filters to its input tensor in order to extract features



3.2 LiteNet Architecture

LiteNet is a two stages architecture (Fig. 3). The first one keeps the size of the input image and applies a stack of filters to capture information of large features. In this stage, we also use a filter bank inspired by the inception architecture [15], the aim being to simultaneously apply multiple filters with different sizes at the same level and extract as much information as possible. Our filter bank outputs, unlike the one proposed by the Inception Architecture, are added instead of being concatenated. This allows us to reduce the spatial complexity of our block and subsequently lower the number of parameters. In the second stage, we start by downsizing the picture then using a stack of 3×3 filters to capture small details. The output of this stage is

concatenated with the input image. Then, it feeds into a classifier which is composed of some fully connected layers, the last of which uses a softmax (Eq. 1) classifier to predict the class of the image. This classifier uses a cross entropy loss function (Eq. 2) in order to measure the loss between the predicted probability distribution y' and the true distribution y represented as one-hot vector.

$$f_i(z) = \frac{e^{z_i}}{\sum_{k=1}^C e^{z_k}} \quad (1)$$

Equation 1 The softmax function takes a C-dimensional vector of arbitrary real-valued scores z then returns a vector $f(z)$ of C-values in the range $[0 \dots 1]$ representing the probability of each class. C represents the number of classes.

$$D_{y'}(y) = - \sum_{c=1}^C y_c \log(y'_c) \quad (2)$$

Equation 2 For multiclass classification, the cross entropy loss is calculated as the sum of separated loss for each class label per observation. y' is the predicted label, y the true label, and C is the number of classes.

The main goal of our work is to design an architecture that achieves quick and precise results since the traffic signs classification is a real time problem. Any proposed model must be able to do so. Our approach is about using a minimum number of learnable parameters that would give an acceptable accuracy without the need of hard computation.

To attain this, we try to use convolution operations, throughout our work, in a way to minimize calculation :

Firstly, every time we need to use a 5×5 filter, we replace it by a stack of two 3×3 filters. Szege et al. [16] shows that those operations are equivalent and this replacing operation will reduce the computation by a ratio of 28% . In fact, for an input image of 5×5 pixels, the number of operations for a 5×5 padded convolution is $25 * 25$. On the other hand, if we use two 3×3 padded convolution, each one will produce $25 * 9$ operations giving a sum of: $25 * 9 + 25 * 9 = 25 * 18$. It's clear here that we reduce the calculation by a ratio of $(1 - 18/25) = 28\%$.

Secondly, in some layers, we replace $n \times n$ filter by asymmetric ones. we can replace it by a stack of two filters $n \times 1$ and $1 \times n$. Szege et al. [16] proves that this will reduce calculations. For example, a 3×3 filter is composed of $3 * 3 = 9$ weights. When we combine 3×1 and 1×3 filters, this will have a size of $(3 * 1) + (1 * 3) = 6$ which reduces the total number of parameters by 33%.

Thirdly, our architecture uses 1×1 convolution to reduce the size of input convolution blocs before feeding them into our filter bank. This allows us to reduce the number of channels of the input and, by consequence, reduce the computation load.

This convolution also serves the function of adding more non-linearity and applying some cross channels pooling since it works on individual pixels.

4 Experiments

4.1 Data Preparation

To make our model light and fast, we limit our pre-processing operation to :

- Resizing the input images to 32×32 resolution: since most pictures have dimensions close to this value.
- Applying histogram stretching technique to adjust image contrast without losing any information. We have already tried histogram equalization but it seems that it doesn't give better results.
- Using a data generator process to produce new training data for classes with few representations. In fact the GTSRB dataset is an unbalanced one, many classes have very small representations compared to others. Our approach is to boost these classes by adding some artificial images using the data generation methods. In the same time we try to not overstrain the generation process but only raise the number of these classes to get close to the more represented ones. In our case we choose to use the zoom, rotation and (width/height) shift operations. We apply them to add some modifications to the original data in a way to avoid distortion and other image weaknesses.

4.2 Training

LiteNet is trained using TensorFlow framework. We start the training process using Adam optimization with a learning rate of 0.001 for 60 epochs with a batch size of 128. Then, we add a second stage of training using a lower learning rate of $1e-6$ then $1e-12$. To validate our model, we adopt the k-fold Cross-Validation [17] strategy by considering 20% of the data, at each step, as a test data and the rest is used to train the model. Our experiences were executed in the Kaggle environment [18] which provides a free access to NVidia K80 GPUs.

5 Results

LiteNet shows very encouraging results. Even with a light architecture of 2,107,787 trainable parameters, we have achieved an accuracy of 99.15% outstripping many other architectures. Table 2 shows how our model reacts better than human

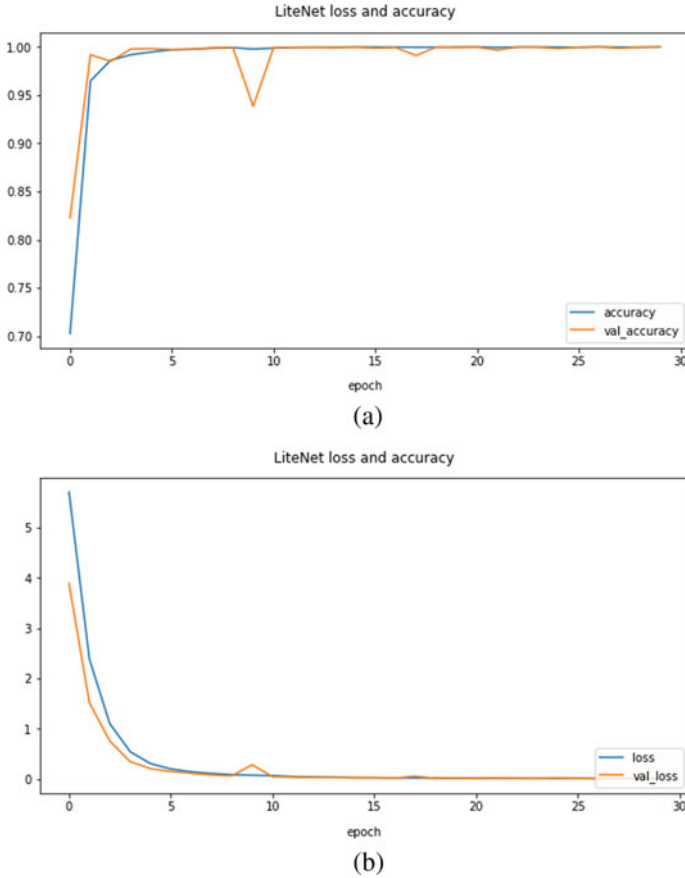


Fig. 5 Evolution of accuracy and loss during training

performance and how its precision is fairly comparable with the best models of state of art. The advantage of LiteNet is its light architecture which facilitates its implementation in real time unlike others which have a weighty architecture and require a heavier computation.

The precision and recall measurements per each class (Fig. 6) show that LiteNet works accurately for all the dataset labels. A low precision (or recall) is due to either a low representation in the dataset or a bad quality of images making the prediction hard (Fig. 5).

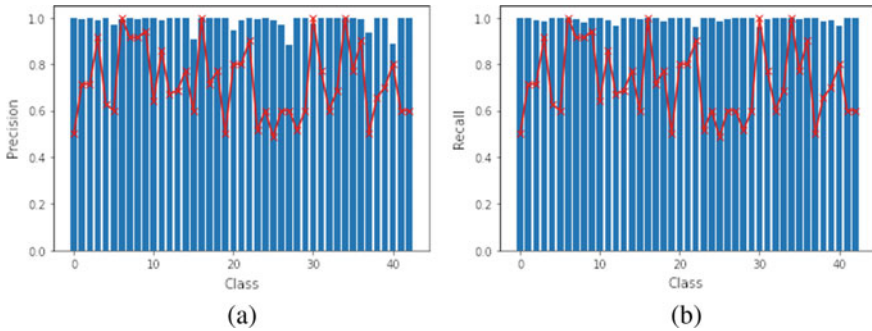


Fig. 6 The bars showing the precision and recall measurements per each class of the dataset. The curve presents the workforce for each class in the dataset divided by the largest observed value

6 Conclusions and Future Work

The most known prior works in the domain of traffic signs classification (Table 2) have managed to obtain good results due to using a deep convolutional neural network architecture. Still, their number of parameters remains high. LiteNet is designed to consume a very low amount of memory and to apply convolution operations in a faster way. It has succeeded in combining both correct predictions and fast calculations. The accuracy measurement shows how our model is promising and workable in comparison to the other works in the same domain.

Future works should be conducted with the aim being to improve our model and so get better outcomes. More emphasis is to be on boosting the filter bank with a view to taking more advantage of it. Upcoming studies can also add more filter banks at different levels of the architecture to extract more features. Moreover, they have to find ways to make this model more invariant to noisy images 90 (Table 3; Fig. 7).

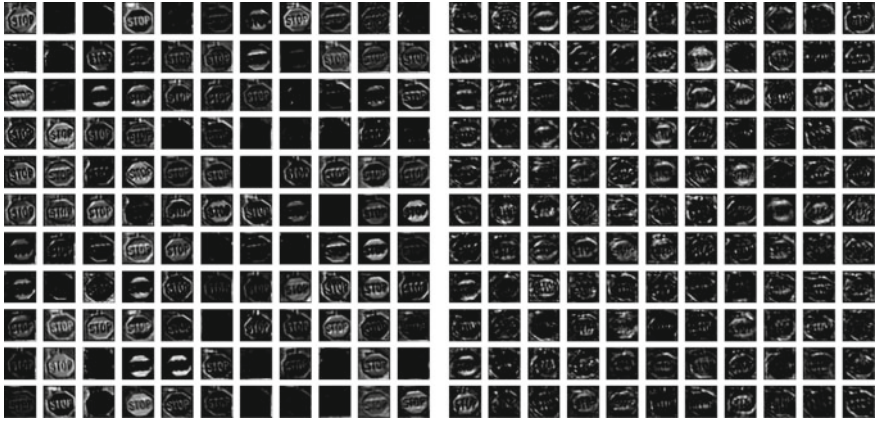
Table 2 LiteNet use less parameters then many others and its accuracy is still can be comparable to them

Model name	Number of parameters	Top-1 accuracy (GTSRB) (%)
Human [19]	–	98.8
STDNN [14]	14 M	99.7
HLSGD [20]	23.2 M	99.6
MCDNN [12]	38.5 M	99.5
LiteNet	2.10 M	99.15
CDNNy [12]	1.54 M	98.5
MicronNet [21]	0.51 M	98.9

The statistics of our LiteNet model are showed in bold, we can check that it uses less number of parameters then many state of art models and its accuracy is still can be comparable

Table 3 LiteNet accuracy, precision, recall and f1-score recognition results for the GTSRB dataset

Accuracy	Precision	Recall	F1 score
99.15 %	99.15%	99.15%	99.15%

**Fig. 7** From left to right: the outputs of the second layer and the filter bank of LiteNet

References

1. Stallkamp J, Schlipsing M, Salmen J, Igel C (2011) The German traffic sign recognition benchmark: a multi-class classification competition. In: International joint conference on neural networks
2. Schmidhuber J (2014) Deep learning in neural networks: an overview. [arXiv:1404.7828v4](https://arxiv.org/abs/1404.7828v4) [cs.NE] 8 Oct 2014
3. Mathias M, Timofte R, Benenson R, Van Gool L (2013) Traffic sign recognition how far are we from the solution? In: The 2013 international joint conference on Neural networks (IJCNN). IEEE, pp 1–8
4. Shakhuro VI, Konouchine A (2016) Russian traffic sign images dataset. *Comput Opt* 40(2):294–300
5. Zhu Z, Liang D, Zhang S, Huang X, Li B, Hu S. (2016) Traffic-sign detection and classification in the wild. In: Proceedings of the IEEE conference on computer vision and pattern recognition, pp 2110–2118
6. Zaklouta F, Stanculescu B, Hamdoun O (2011) Traffic sign classification using K-d trees and random forests. In: Proceedings of international joint conference on neural networks, San Jose, California, 31 July– 5 Aug 5 2011
7. Dalal N, Triggs B (2005) Histograms of oriented gradients for human detection. In: 2005 IEEE computer society conference on computer vision and pattern recognition (CVPR'05), vol 1, pp 886–893
8. Alefs B, Eschemann G, Ramoser H, Beleznaï C (2007) Road sign detection from edge orientation histograms. In: 2007 IEEE intelligent vehicles symposium, pp 993–998
9. Dalal N, Triggs B (2005) Histograms of oriented gradients for human detection. In: Schmid C, Soatto S, Tomasi C, (eds) International conference on computer vision & pattern recognition,

- vol 2, INRIA Rhône-Alpes, ZIRST-655, av. de l'Europe, Montbonnot-38334, June 2005, pp 886–893. (Online). Available: <http://lear.inrialpes.fr/pubs/2005/DT05>
10. De La Escalera A, Moreno L, Salichs M, Armingol J (1997) Road traffic sign detection and classification. *IEEE Trans Indus Electron* 44(6):848–859
 11. Loy G, Barnes N (2004) Fast shape-based road sign detection for a driver assistance system. In: *Proceedings of 2004 IEEE/RSJ international conference on intelligent robots and systems*, vol 1, pp 70–75
 12. Cireşan D, Meier U, Masci J, Schmidhuber J (2012) Multi-column deep neural network for traffic sign classification. *Neural Netw* 32:333–338
 13. Sermanet P, LeCun Y (2011) Traffic sign recognition with multi-scale convolutional networks. In: *The 2011 international joint conference on neural networks*, pp 2809–2813
 14. Arcos-García * A, Álvarez-García JA, Deep LM (2018) Neural network for traffic sign recognition systems: an analysis of spatial transformers and stochastic optimisation methods. Soria-Morillo, 2018 Elsevier *Neural Networks*
 15. Szegedy C, Ioffe S, Vanhoucke V, Alemi AA (2017) Inception-v4, inception-ResNet and the impact of residual connections on Learning. In: *AAAI'17: Proceedings of the thirty-first AAAI conference on artificial intelligence*, pp 4278–4284 ss
 16. Szege C, Vanhoucke V, Ioffe S, Shlens J, Wojna Z (2015) Rethinking the inception architecture for computer vision. [arXiv: 1512.00567v3](https://arxiv.org/abs/1512.00567v3) [cs.CV] 11 Dec 2015
 17. https://doi.org/10.1007/978-0-387-39940-9_565
 18. <https://www.kaggle.com/>
 19. Stallkamp J, Schlipsing M, Salmen J, Igel C (2012) Benchmarking machine learning algorithms for traffic sign recognition. *Man vs. computer. Neural Netw* 32:323–332
 20. Zhang C, Jin J, Fu K (2014) Traffic sign recognition with hinge loss trained convolutional neural networks. In: *IEEE transactions on intelligent transportation systems*, pp 1991–2000
 21. Wong A, Shafiee MJ, St. Jules M (2018) MicronNet: a highly compact deep convolutional neural network architecture for real-time embedded traffic sign classification. [arXiv:1804.00497v3](https://arxiv.org/abs/1804.00497v3) [cs.CV] 3 Oct 2018

The Attitude of Moroccan University Students Towards an Online Assistive Application of Stress Management



Hakima EL Madani, Ikrame Yazghich, Maryem Baya,
and Mohamed Berraho

Abstract Many studies show the efficacy of mental health applications to reduce several types of mental problems encountered by university students. Indeed, this type of mental treatment is not adopted at the national level. In this paper, we present the results of an online survey of acceptance of an assistive stress' management application by Moroccan university students. A total of 421 medical students were invited to complete an online survey published in the official web site of the Faculty of Medicine and Pharmacy of Fez. The mean age was 21.52 (SD = 2.05) and females represented the majority of our population (63.4%). The results of our investigation show a general acceptance of an online antistress application by a good proportion of our population (36.6%). A mobile app seems to be more accepted by our students (22.6%) than a web app (14.0%). The findings of this paper will be explored to design an evidence-based antistress app that will be designed to help our university students to access to professional online help to better manage their psychological problem.

Keywords Online antistress application · University students · Psychological stress

1 Introduction

In the modern world, mobile health applications (mHealth) are widely used thanks to the adoption of smartphones and connected devices by the general population. Those mHealth apps target many medical specialties including mental health (MHapps). MHapps offer the potential to overcome access barriers for nearly three billion people who projected to own a smartphone by 2020 [11]. Indeed, a 2015 World Health Organization (WHO) survey of 15,000 mHealth apps revealed that 29% focus on mental health [2]. These MHapps are recommended by many public health organizations like the UK's National Health Service (NHS) and the U.S. National Institute of Mental

H. EL Madani (✉) · I. Yazghich · M. Baya · M. Berraho
Faculty of Medicine and Pharmacy, Sidi Harazem Road, Post Box 1893, Fez, Morocco
e-mail: hakima.elmadani@usmba.ac.ma

Health (NIMH) as it represents cost-effective and scalable solutions to address the mental health treatment gap [4].

The general population could benefit from MHapps for many reasons ranging from guiding mental illness recovery to encouraging beneficial habits [5]. However, the majority of those apps lack scientific evidence about their efficacy [5].

Nevertheless, this new technology is also accessible by a specific population such as university students who are considered as a risky population to many psychological problems including psychological stress.

Psychological stress is defined as the way of the response of the human body to any demand [10]. Every demand or stressor—such as work, school, major life changes, or traumatic events, this mental illness could participate in the development of many psychosomatic manifestations such as depression, anxiety, and addictive behaviors [9].

At the national level, stress is one psychological problem that negatively affects the Moroccan student's wellbeing [7], with a relatively high prevalence confirmed by a recent survey among medical students reporting that among 358 students, 66.76% of them reported having psychological stress [1]. As the result, a professional and adapted online application could be a good option for this population to get access to professional online help to self-manage their psychological stress [4]. In this current study we will present the result of an online survey of acceptance of an assistive antistress online application by Moroccan university students, the findings of this study will contribute in the design of an antistress application called "Stress-free" that will be assessed by Moroccan university students to give them professional online support to better manage their psychological stress.

2 Methods

2.1 Ethics Statement

Approval of the ethics committee of the University Hospital Center of Fez-Morocco has been received for the study protocol. The aim of the study was mentioned in the heading of the online questionnaire and the student's acceptance to participate in the study was considered as consent.

2.2 Recruitment

The study took place between November 2017 and February 2018 at the Faculty of Medicine and Pharmacy of Fez (Morocco). First-year to fifth-year medical students were our target population in this study. This population was chosen to represent the Moroccan university students. Only students who fully understood the nature of the

survey given in the background of the online survey and agreed to participate were included. Receiving a psychological therapy was our criteria for exclusion.

Participants were recruited by using an advertisement on the faculty's website and through printed posters, which were placed at several designed areas around the faculty campus. The advertisements included brief information about the project, the inclusion and exclusion criteria mentioned above, the questionnaire's link published in the faculty's website and potential contact information about the project as well as the project' mailing address, and contact persons. Prospective participants who expressed interest in the survey get access to the questionnaire's link that include sociodemographic information, questions targeting their opinion about an antistress intervention by using a 5-point Likert scale, with 1 indicating "very beneficial" and 5 indicating "not at all beneficial", and a suggestion of the nature of this online intervention (mobile app or web app) and others related to the mobile devices' use.

2.3 Statistical Analysis

SPSS software for Windows version 21.0 was used for the statistical analyses. Descriptive statistics were used to characterize the data collected. Continuous variables were expressed as the means (SDs), whereas, categorical variables were expressed as percentages. Pearson's chi-square test was used to analyze the association between the categorical variables, $P < 0.05$ was considered significant.

3 Results

3.1 Sample Characteristics

A total of 421 students completed the survey. The mean age was 21.52 (SD = 2.05) and females represented 63.4% of our population (n = 267) and 39.9% (n = 164) of them reported to be stressed or very stressed. The majority of our population did not exercise any type of professional activity (n = 365), in addition, 42.2% of students did not satisfy with their faculty' organization. More details about Students' general characteristics are given in Table 1.

3.2 Stress Self-Managed by Students

Management of psychological stress seems to be difficult for 38.4% of our students. This self-management was declared to be based on using many addictive substances

Table 1 Students' general characteristics

Variable	Count	Percent (%)	Cumulative (%)
<i>Gender</i>			
Female	267	63.4	63.4
Male	154	36.6	100
<i>Parents' matrimonial statue</i>			
Married	379	91.3	91.3
Divorced	15	3.6	94.9
Widower	17	4.1	99.0
Deceased	4	1.00	100
<i>Family' income</i>			
Low	32	8.9	8.9
Medium	290	80.3	89.2
High	39	10.8	100
<i>Professional activity practice</i>			
Yes (full-time)	6	1.4	1.4
Yes (part-time)	41	10.0	11.4
No	365	88.6	100
<i>Students' satisfaction with faculty' organization</i>			
Yes	46	11.1	11.1
Between the two	164	39.7	50.8
No	203	49.2	100
<i>Student' journey time to go to the faculty</i>			
0–10 min	142	34.3	34.3
10–20 min	106	25.6	59.9
20–30 min	22	5.3	65.2
30–45 min	12	2.9	68.1
45–1 h	125	30.2	98.3
Greater than 1 h	7	1.7	100
<i>Reporting stress statue</i>			
Very stressed	94	22.9	22.9
Stressed	70	17.0	39.9
Moderately stressed	163	39.7	79.6
Rather not stressed	70	17.0	96.6
Not at all stressed	14	3.4	100

Table 2 Students' self-management of stress

Variable	Count	Percent (%)	Cumulative (%)
<i>Level of stress' self-management</i>			
Very good	17	4.3	4.3
Good	67	17.0	21.3
Rather good	159	40.4	61.7
Rather bad	96	24.4	86.1
Bad	33	8.4	94.5
Very bad	22	5.6	100
<i>Type of methods of stress' self-management</i>			
Coffee	128	31.2	31.2
Illegal drugs (alcohol, tobacco ...)	38	9.0	40.2
Physical activity	124	30.1	70.3
Informal supports	131	29.7	100

including drugs in 9% and taking coffee in 31.2% (Table 2), others tend to use informal help (parents, friends ... etc.) to manage their psychological stress.

3.3 Association Factors of Stress Self-Management'level

Univariate analysis showed that the level of self-management of stress by students was significantly associated with students' reported stress level ($p = 0.000$), gender ($p = 0.000$), and activity practice ($p = 0.000$). However, students' journey time did not show significant association with ($p = 0.240$).

3.4 Students Attitude Towards an Online Antistress App

The majority of our population declaring having access to connected devices and 94.4% of them ($N = 386$) reported having at least one mobile device with a good to a very good level of use (65.0%). 41.8% of students ($n = 176$) declaring using their mobile device for downloading applications.

Concerning the development of an online antistress application, 35.8% of students reporting their need for professional help to manage their psychological stress, and 22.6% of them suggesting a mobile antistress application as a good tool to get access to online help, therefore, 59 students (14.0%) of our population preferring a web application (Table 3).

Table 3 Students’ need for an antistress app

Variable	Count	Percent (%)	Cumulative (%)
<i>Having a connected device</i>			
Yes	386	94.4	94.4
No	35	5.6	100
<i>Reasons of use of mobile device</i>			
Downloading apps	176	43	**
<i>Reasons of use of mobile device</i>			
Playing video games	70	17.2	**
<i>Reasons of use of mobile device</i>			
Blogging	24	5.9	**
<i>Reasons of use of mobile device</i>			
Surfing in the internet	353	86.4	**
<i>Antistress intervention need</i>			
Yes	139	35.8	35.8
No	249	64.2	100
<i>Online intervention</i>			
Smartphone app	95	22.6	22.6
Web app	59	14.0	36.6
Mental health professional	267	63.4	100

**Undefined value

4 Discussion

The concept of acceptance survey could be a good option for the establishment of an efficient online psychological treatment’ apps as it may contribute to a student’s consideration when facing to stress problem. This concept could get more information about the students’ needs to consider in the design of a treatment app.

In this current study, an online survey was used to access students’ acceptance of an assistive stress-management app. Medical students were chosen to represent the general university population. The results of our investigation show that 9% of our population turning to illegal drug consumption as well as alcohol and addictive substances to manage their psychological stress these results comply with findings of a recent Chinese qualitative study [3], confirming the negative impact of psychological problems on university students.

For students’ assessment to an online antistress intervention, the results suggest an acceptance of an online psychological treatment by a good proportion of students (36.6%) and their ability for future use of an online antistress app, this result is relatively high in comparison with similar studies conducted in the USA among

college students [8], and another set up among university students [6] which could be explained by the need of our population for a new form of professional treatment based on new technology. Furthermore, the findings of our survey suggest that our students prefer a smartphone app to get their online treatment. The possible reason could be related to user's access to this type of connected device as mentioned in this study (more than 94% of students having a least one mobile device).

Limitations

The present investigation is the first study at the national level targeting university students' attitudes towards an online psychological treatment. Yet, the potential limitation must be mentioned related to students' selection bias since the target population was limited to medical students which could not reflect the special characteristics' differences between students' targets and others who enrolled in other fields of study.

5 Conclusion

The main contribution of this study was to assess university students' acceptability of an online assistive antistress app. A general positive feed-back of acceptance of the antistress app was noticed for a good proportion of university students, especially for a mobile antistress app. Further research would be important to design an adaptative antistress app that must integrate validated antistress programs to give to Moroccan university students a professional psychological tool based on the new technology and to support student resilience and wellbeing.

References

1. Abdeslam B, Hajar C, Jalal E, Amine L (2019) Mental health status among moroccan medical students at the Cadi Ayyad University. *Int J Psych Res* 2. <https://doi.org/10.33425/2641-4317.1006>
2. Anthes E (2016) Mental health: there's an app for that. *Nat News* 532:20. <https://doi.org/10.1038/532020a>
3. Bhowmik MK, Cheung RYM, Hue MT (2018) Acculturative stress and coping strategies among Mainland Chinese university students in Hong Kong: a qualitative inquiry. *Am J Orthopsych* 88:550–562. <https://doi.org/10.1037/ort0000338>
4. Chandrashekar P (2018) Do mental health mobile apps work: evidence and recommendations for designing high-efficacy mental health mobile apps. *mHealth* 4. <https://doi.org/10.21037/mhealth.2018.03.02>
5. Donker T, Petrie K, Proudfoot J, Clarke J, Birch M-R, Christensen H (2013) Smartphones for smarter delivery of mental health programs: a systematic review. *J Med Internet Res* 15:e247. <https://doi.org/10.2196/jmir.2791>
6. Kern A, Hong V, Song J, Lipson SK, Eisenberg D (2018) Mental health apps in a college setting: openness, usage, and attitudes. *Mhealth* 4. <https://doi.org/10.21037/mhealth.2018.06.01>

7. Lemtiri Chelieh M, Kadhum M, Lewis T, Molodynski A, Abouqal R, Belayachi J, Bhugra D (2019) Mental health and wellbeing among Moroccan medical students: a descriptive study. *Int Rev Psych* 31:608–612. <https://doi.org/10.1080/09540261.2019.1675276>
8. Levin ME, Stocke K, Pierce B, Levin C (2018) Do College students use online self-help? A survey of intentions and use of mental health resources. *J Col Stud Psychother* 32:181–198. <https://doi.org/10.1080/87568225.2017.1366283>
9. Shamsuddin K, Fadzil F, Ismail WSW, Shah SA, Omar K, Muhammad NA, Jaffar A, Ismail A, Mahadevan R (2013) Correlates of depression, anxiety and stress among Malaysian university students. *Asian J Psychiatr* 6:318–323. <https://doi.org/10.1016/j.ajp.2013.01.014>
10. Suzuki S, Ito D (2013) Psychological stress. In: Gellman MD, Turner JR (eds) *Encyclopedia of behavioral medicine*. Springer, New York, NY, pp 1561–1561
11. Torous J, Andersson G, Bertagnoli A, Christensen H, Cuijpers P, Firth J, Haim A, Hsin H, Hollis C, Lewis S, Mohr DC, Pratap A, Roux S, Sherrill J, Arean PA (2019) Towards a consensus around standards for smartphone apps and digital mental health. *World Psych* 18:97–98. <https://doi.org/10.1002/wps.20592>

Detection and Prediction of Driver Drowsiness for the Prevention of Road Accidents Using Deep Neural Networks Techniques



Ismail Nasri, Mohammed Karrouchi, Hajar Snoussi, Kamal Kassmi, and Abdelhafid Messaoudi

Abstract Driver drowsiness is one of the reasons for a large number of road accidents in the world. In this paper, we have proposed an approach for the detection and prediction of the driver's drowsiness based on his facial features. This approach is based on deep learning techniques using convolutional neural networks CNN, with Transfer learning and Training from Scratch, to train a CNN model. A comparison between the two methods based on model size, accuracy and training time has also been made. The proposed algorithm uses the cascade object detector (Viola-Jones algorithm) for detecting and extracting the driver's face from images, the images extracted from the videos of the Real-Life Drowsiness Dataset RLDD will act as the dataset for training and testing the CNN model. The extracted model can achieve an accuracy of more than 96% and can be saved as a file and used to classify images as driver Drowsy or Non-Drowsy with the predicted label and probabilities for each class.

Keywords Driver drowsiness detection · Deep learning · Convolutional neural networks · Transfer learning · Training from scratch

1 Introduction

Drowsiness is one of the main causes that lead to painful road accidents that take the lives of many road users in the United States. It is confirmed by statistics that 1 of 25 drivers in the age of 18 or older, had fallen asleep during the past 30 days [1, 2]. In 2013, a report was issued by the National Highway Traffic Safety Administration NHTSA, which states that drowsiness was the cause of 72,000 crashes, 44,000 injuries, and 800 deaths [3, 4]. In the most recent research conducted by the Moroccan National Highway Traffic Company [5], in 2012, on a sample consisting of about a thousand drivers, its results showed that about one out of three drivers admitted that they fell asleep while driving at least once during the month preceding the research.

I. Nasri (✉) · M. Karrouchi · H. Snoussi · K. Kassmi · A. Messaoudi
Electrical Engineering and Maintenance Laboratory, High School of Technology, Mohammed
First University, BP. 473, Oujda, Morocco
e-mail: i.nasri@ump.ac.ma

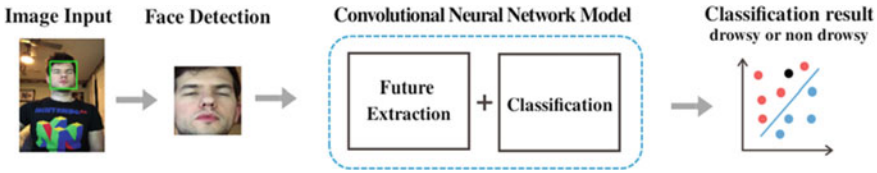


Fig. 1 Architecture of drowsiness detection system

The results also revealed that 15% of them stated that they had driven for five hours (about 500 km) without stopping, while 42% of them stated that they stopped only once during the same distance, although the normal situation is to make two stops as a minimum. This study will focus on the (UTA-RLDD) University of Texas analysis in the Arlington Real-Life Drowsiness Dataset [6]. The figure below presents the architecture of Driver Drowsiness Detection, in three phases: face detection, feature extraction and classification. If a driver's face is found, Viola-jones [7, 8] face detection algorithm is used to detect and crop the driver's face from the image and it will be given as input to CNN. The Feature Detection Layers in CNN are used to extract the deep features which will be passed to Classification Layers. Softmax layer in CNN classifies the images as drowsy or non-drowsy and gets results of predicted label and probabilities. An alert system is used when the model detects a drowsy state continuously (Fig. 1).

The rest of this paper is organized as follows. In Sect. 2, a brief description of the related work is presented. The Sect. 3 provides an overview of the proposed solution and approach to prepare a deep learning model. The results obtained from experiments are discussed in Sect. 4. Finally, we conclude in Sect. 5 with future directions.

2 Related Work

Several systems and approaches have been proposed for detecting the driver drowsiness. In this section, a review of the previous methods and approaches to detect drowsiness based on extracting facial features will be provided. Jabbar et al. [9] developed an approach based on extracting landmark coordination from images using Dlib [10] library. This approach can classify the driver's face as drowsy or non-drowsy based on his face landmark. In fact, the facial landmark detector implemented inside Dlib produces 68 (x, y) coordinates to describe specific facial structures of the face. Dlib is a general purpose platform software library written in the programming language C++ to provide a Machine Learning algorithm used in a wide range of fields and applications. Danisman et al. [11] proposed a method to detect drowsiness based on monitoring the changes in the eye blink duration. In this matter, CNN based eye detector was used to find the location of the eyes and to calculate the "no blinks" per minute. If the blink duration increases, this indicates that the driver

becomes drowsy. In this study, we take into consideration all the signs that show that the driver is drowsy (eye color and shape, yawn, and blink). All these signs are related to the face of the driver. For this purpose, we use the cascade object detector that uses the Viola-Jones algorithm for detecting and extracting the driver's face from images. These extracted images will act as the dataset for training and testing the Convolutional Neural Networks CNN proposed. The Viola-Jones [7, 8] object detection, developed by Paul Viola and Michael Jones in 2001, is the most popular object detection algorithm to provide competitive object detection rates in real-time. It can be used to solve a variety of detection problems, including the problem of face detection.

3 Proposed Solution

This section provides an overview of the proposed solution: Dataset and approach to prepare a CNN model that will be used to classify images of the driver as Drowsy or Non-drowsy.

3.1 *Dataset and Preprocessing*

About the dataset creation, this study will focus on the University of Texas analysis in the Arlington Real-Life Drowsiness Dataset (UTA-RLDD) [6]. It contains the full component of the dataset for training and testing. From this dataset, 28 subjects were selected from 60 subjects available. Subjects were instructed to take three videos from the phone or the webcam; in three different drowsiness states according to the KSS table [12]. In this work, we focus on two classes (see Fig. 3); these classes were explained to the participants in the following way:

- Non-Drowsy: In this state, subjects were told that being alert meant they were completely conscious and they can drive easily for long hours [6], as illustrated in level 1, 2 and 3 in the KSS table [12].
- Drowsy: This condition means that the subject needs to resist falling asleep, as illustrated in level 8 and 9 in Table 1.

3.2 *Proposed Approach*

In this section, an overview of the proposed approach (see Fig. 2) to prepare a CNN model will be provided. The proposed approach consists of six main steps:

Table 1 KSS table [12]

Rating	Verbal descriptions	Rating	Verbal descriptions
1	Extremely alert	6	Some signs of sleepiness
2	Very alert	7	Sleepy, but no difficulty remaining awake
3	Alert	8	Sleepy, some effort to keep alert
4	Rather alert	9	Extremely Sleepy, fighting sleep
5	Neither alert or sleepy		

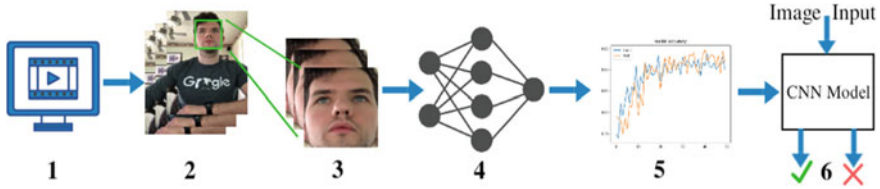


Fig. 2 Approach proposed to prepare a CNN model

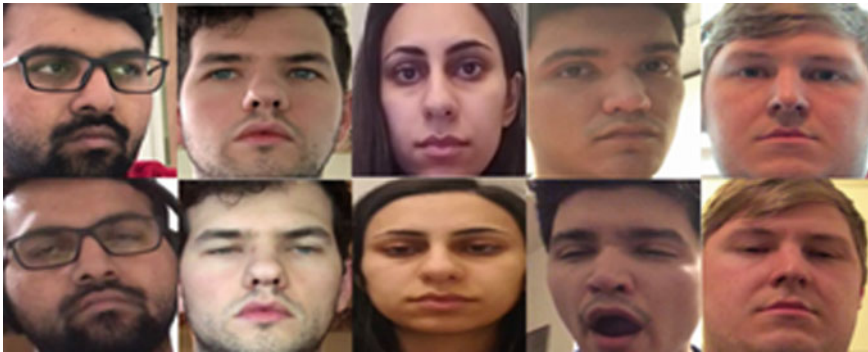


Fig. 3 Non drowsy and drowsy image samples detected by the Viola-Jones algorithm from the dataset

- Step 1: Selecting videos from RLDD Dataset: The videos were selected from the Real-Life Drowsiness Dataset RLDD based on a variety of simulated driving scenarios and conditions.
- Step 2: Extracting Images from selected videos: The frames were extracted from videos as images using VLC software.
- Step 3: Detecting and Cropping the driver’s face from images: In the third step, we use the cascade object detector that uses the Viola-Jones algorithm to detect and crop the driver’s face from images (see Fig. 3). These images will be used for training and testing the proposed models (70% for training and 30% for testing).
- Step 4: Creating and Configuring Network Layers: In this step, we define the convolutional neural networks CNN [13] architecture.

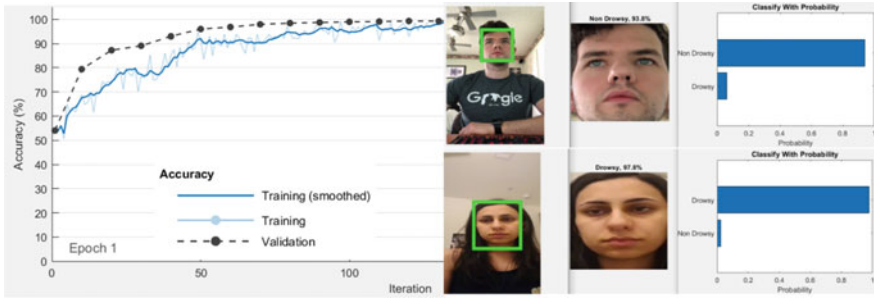


Fig. 4 The training progress plot for transfer learning and Classification images with the predicted label and the predicted probabilities %

- Step 5: Training and testing the model: The cropped driver’s face will act as the input for the algorithm detailed in (algorithm 1 and 2). The model uses Deep Neural Networks Techniques and was trained using 2 methods: Training via Transfer learning (algorithm 1) and Training from Scratch (algorithm 2).
- Step 6: Extracting the model: Finally, the CNN model can be saved as a file and used to classify images with the predicted label and probabilities (see Fig. 4).

3.3 Training via Transfer Learning

For the transfer learning, we use AlexNet [14] to classify the images by the extracted features. AlexNet is a CNN that contains eight layers and can classify images into 1000 object categories, such as a laptop, pen and many objects. In order to make the AlexNet recognize just two classes, we need to modify it. The network was trained by the following algorithm.

Algorithm 1: Training via Transfer learning

Input: Driver’s face dataset and labels
Output: Learned CNN model

1. Load and Explore Image data from My PC (Driver Face)
2. Specify Training and Testing Sets (Split data into training and test sets)
3. Load Pre-trained Network (AlexNet)
4. Modify Pre-trained Network (AlexNet): We modify final layers to recognize just 2 classes (drowsy and Non-drowsy)
5. Specify Training Options
6. Train New Network Using Training Data
7. Classify Test Images and Compute accuracy (see Fig. 4)

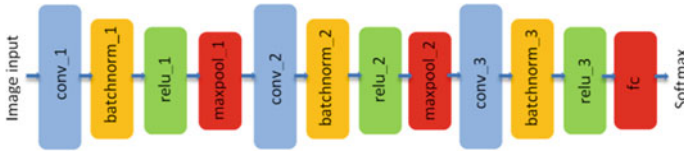


Fig. 5 Proposed deep CNN model

3.4 Training from Scratch

For the training from scratch, we are creating and configuring network layers by defining the convolutional neural network architecture and training the network by the following algorithm.

Algorithm 2: Training from Scratch

Input: Driver's face dataset and labels

Output: Learned CNN model

1. Load and Explore Image data from My PC (Driver Face)
 2. Specify Training and Testing Sets (Split data into training and test sets)
 3. Create and Configure Network Layers by defining the convolutional neural network architecture. In the proposed CNN model, we use 3 convolutional layers and one fully connected layer. Softmax classifier is used to classify images as drowsy or non-drowsy
 4. Specify Training Options
 5. Train Network Using Training Data (imdsTrain)
 6. Review Network Architecture (see Fig. 5)
 7. Classify Test Images and Compute accuracy
-

4 Experimental Results

In this section, we will present the results of the training CNN models by two commonly used approaches for deep learning: transfer learning and training from scratch. In this work, 28 subjects were selected from 60 subjects available in the Arlington Real-Life Drowsiness Dataset (UTA-RLDD) [6] to obtain training and testing data. For data processing, the frames were extracted from videos as images using VLC software. After that, the driver's face was detected and cropped from images using the Viola-Jones algorithm as it appears in the Table 2.

The processor for training and test processing platform was a 3.6 GHz Intel (R) Core (TM) i5-8350U with 8 GB memory and 256 GB SSD hard disk. The development platform for the algorithm was MATLAB R2018b.

In the rest of this section, a comparison of training the model from scratch and transfer learning is presented. In this paper, the two models were trained and evaluated by the same number of images dataset (101,793 images). Table 3 shows the network performance of these models. Training the model from scratch and achieving

Table 2 Overview of images extracted and detected by Viola-Jones algorithm

Dataset	Nbr of extracted images	Nbr of images detected by the Viola-Jones algorithm
Drowsy	55,600	52,348
Non-Drowsy	53,586	49,445
Total	109,186	101,793

Table 3 Comparison between the proposed models (CNN transfer and CNN scratch)

Model	Size (Mbit)	Accuracy (%)	Training time	Training and testing Images
CNN transfer	622	93	128 min 54 s	101,793
CNN scratch	2.38	96	159 min 11 s	101,793

reasonable results requires a lot of effort and computer time, which is due to the time needed to test the performance of the network; if it is not adequate, we should try modifying the CNN architecture and adjusting some of the training options and then retraining. The training time of the CNN Scratch model is 159 min and 11 s. Experimental results show that the accuracy rate of the developed model is almost 96% for training from scratch and 93% for transfer learning. Training the model with transfer learning is much faster and easier, and it is possible to achieve higher model accuracy in a shorter time (higher start) but with large model size. The maximum size of the developed models is equal to 622 Mbit for CNN Transfer and 2.38 Mbit for CNN Scratch.

5 Conclusion


In this work, we have proposed a method for driver drowsiness detection based on his facial features. The face is detected using the Viola-Jones algorithm. The proposed CNN with Feature Detection Layers is used to extract the deep features, and those features are passed to Classification Layers. A Softmax layer in the CNN provides the classification output as driver drowsy or non-drowsy and the probabilities for each class. The proposed model has been trained and evaluated using Real-Life Drowsiness Dataset (RLDD) by two commonly used approaches for deep learning: transfer learning and training from scratch. On the one hand, the results show that the size of the proposed model for training from scratch is small while having an accuracy rate of 96% but with a lot of effort and computer time. On the other hand, with transfer learning, we can achieve an accuracy of 93% with less computer time and effort but with large model size. Further work will focus on the implementation of the model in an embedded system and the creation of an integrated alert system into the vehicle to wake the driver up before anything undesired happens.

References

1. Drowsy driving 19 states and the District of Columbia (2009–2010). Retrieved from <https://www.cdc.gov/mmwr/pdf/wk/mm6151.pdf>
2. Drowsy driving and risk behaviors 10 states and Puerto Rico (2011–2012). Retrieved from <https://www.cdc.gov/mmwr/pdf/wk/mm6326.pdf>
3. National Highway Traffic Safety Administration. Research on Drowsy Driving external icon (October 20, 2015). Retrieved from <https://one.nhtsa.gov/Driving-Safety/Drowsy-Driving/Research-on-Drowsy-Driving>
4. The Impact of Driver Inattention on Near-Crash/Crash Risk (April 2006). Retrieved from <https://www.nhtsa.gov/>
5. lakome2. <https://lakome2.com/relation-publique/119885>, (30 May 2019)
6. Ghoddoosian R, Galib M, Athitsos V (2019) A realistic dataset and baseline temporal model for early drowsiness detection. In: The IEEE conference on computer vision and pattern recognition workshops
7. Viola P, Jones M (2001) Rapid object detection using a boosted cascade of simple features. In: The 2001 IEEE computer society conference on computer vision and pattern recognition. CVPR 2001, vol 1. IEEE
8. Viola P, Jones M (2001) Robust real-time object detection. *Int J Comput Vis* 4(34–47):4
9. Jabbar R, Al-Khalifa K, Kharbeche M, Alhajyaseen W, Jafari M, Jiang S (2018) Real-time driver drowsiness detection for android application using deep neural networks techniques. *Procedia Comput Sci* 130:400–407
10. Dlib C++ toolkit. Retrieved from <https://dlib.net/> (2018 Jan 08)
11. Danisman T, Bilasco IM, Djeraba C, Ihaddadene N (2010) Drowsy driver detection system using eye blink patterns. In: 2010 international conference on machine and web intelligence. IEEE, pp 230–233
12. Åkerstedt T, Mats G (1990) Subjective and objective sleepiness in the active individual. *Int J Neurosci* 52(1–2):29–37
13. O’Shea K, Nash R (2015) An introduction to convolutional neural networks. arXiv preprint [arXiv:1511.08458](https://arxiv.org/abs/1511.08458)
14. Krizhevsky A, Sutskever I, Hinton GE (2012) Imagenet classification with deep convolutional neural networks. In: *Advances in neural information processing systems*

A New Framework to Secure Cloud Based e-Learning Systems



Karima Aissaoui , Meryem Amane, Mohammed Berrada, and Mohammed Amine Madani

Abstract Combining cloud computing with e-learning has led to a new form of systems called: cloud-based e-learning systems. Those systems take advantages and benefits of cloud computing, and combine them with e-learning systems. This combination offers some solutions to make e-learning systems more efficient and easier for use, and contribute to deal the best conditions of using distance learning systems. However, cloud-based e-learning systems present some challenges in two principal axis: security and storage. In this paper, we propose a new architecture that aims to resolve the problems of these systems, related to security and storage. It is based on a new security layer, responsible of controlling and storing all transactions, in order to generate a security key, and to give us the ability to use generated data to offer recommended systems in the future. Also, this architecture is proposed after a study that we conducted to cover many works done related with this field.

Keywords e-learning · Cloud · Node · Architecture · Security

1 Introduction

In order to contribute on improving the quality of learning and teaching, different methods and technologies were merged, combined and used [1]. One of these technologies is cloud computing. In recent years, E-learning systems have been used with cloud computing in order to benefit from advantages of this technology [2]. Combining cloud computing with e-learning has created new form of e-learning systems supported by cloud technology, named cloud-based e-learning systems. The main objective of those systems is to facilitate the learnings task, and providing a cheaper and flexible solution that can be adopted by all academic and institutional

K. Aissaoui (✉) · M. Amane · M. Berrada
Artificial Intelligence, Data Science and Emergent Systems Laboratory, ENSAF,
Sidi Mohammed Ben Abdellah University, Fez, Morocco
e-mail: karima.aissaoui@usmba.ac.ma

M. A. Madani
Engineering Sciences Laboratory, ENSAO, Mohammed First University, Oujda, Morocco

organizations which are not able to ensure required hardware materials [3]. However, cloud-based systems present some leaks and challenges, like security and data storage. In this paper, we present our new approach based on a new architecture, where we introduce a new layer, and we define new mechanisms that should be used and applied on cloud-based e-learning systems in order to benefit from advantages of cloud technology in e-learning field.

This paper is organized as follows, in the next section we present our research methodology before presenting e-learning in its traditional form, and then we discuss benefits and limits of cloud-based e-learning systems. The fifth section is allocated for reviewing the architecture and security of cloud-based e-learning systems basing on previous researches done in this field, then, we present our methodology and all its components, and we finish with a conclusion and perspectives.

2 Research Methodology

Before proposing our approach, and since researches on cloud and e-learning fields are growing, it was necessary first to highlight all works done in this domain, especially that recently, cloud-based e-learning topic has received renewed attention from academia and practitioners. Figure 1 illustrates the remarkable resurgence of “Cloud e-learning” term research interest using Google trends from 2014 year to 2019.

Researches concerning cloud-based e-learning systems can be divided to three main categories: the first category regroups works dealing with the architecture of this type of systems, the second category regroups works related with security, while the third type of works constitutes reviews and state of the art. In this paper, a study was conducted in order to cover all of these categories of papers and we were based on many works dating from 2014 to 2019. The importance of this step resides in the fact that before proposing any solution in every field, a state of the art should be well done in order to proceed a critical study and consequently to offer best solutions for leaks and limits of previous works. Our methodology is explained as follows: the first step was to collect papers concerning all categories (review, architecture and security) using Google, Google Scholar and databases like Springer, IEEE and Scopus. Then, the second step was to organize those papers by their category. The third step was to filter articles by degree of relevance. By reading the title, and/or the abstract we were able to decide if we can name the work relevant or no. As a result of



Fig. 1 Google Trends result for research interest of “cloud e-learning” term from 2014 to 2019

this study, we summarize these works and we give to researchers a roadmap allowing them to have a recent state of the art for their future works in order to contribute on improving cloud-based e-learning systems and consequently improving the quality of learning/teaching in general.

3 E-Learning

E-learning is a way of learning based on using electronic devices and internet [4]. It allows learners and teachers to achieve the task of learning without the need of being present. Learning content is exchanged via LMS (Learning Management System) on a real time which let users being encouraged to use this form of learning due to its simplicity and efficiency. However, LMS requires several software and hardware resources [5], which let institutions think seriously about the cost and the management of these resources. Thus, it was necessary to combine e-learning systems with new technologies to simplify and make of storage and management learning content easier [2]. Starting from this, cloud computing was the key to open a new concept for e-learning and consequently giving birth to cloud-based e-learning.

4 Cloud-Based e-Learning: Benefits and Limits

Cloud Computing was defined by many researchers [3, 6–8], but the common elements that we find present in all definitions are: applications that are delivered as services using Internet, the hardware and systems software that provide these services. According to [3], cloud computing is defined a technology that could deliver elastic IT capabilities as services using Internet. Another definition was given in [7], where authors said that it can be considered as a new model allowing users to access computing resources over the network, provided as services. Some major examples of cloud computing services are: Google Drive, Amazon Cloud Drive, Apple iCloud, Microsoft's SkyDrive, Humyo, ZumoDrive. Cloud computing services are categorized into three different levels [8]. The role of cloud computing in education in general and university in particular should not be underestimated. First, it helps students and academics to have a direct access to many important resources like academic documents, educational tools and research applications [9]. Certainly, cloud computing can enable certain educational institutions to make use of global internet resources/services to improve their education system and to help students for the learning and innovation [10].

Many advantages and benefits of using cloud computing in education field could be obtained [11], we cite here some of them. The first one is the low cost: by choosing cloud-based e-learning systems, institutions could avoid the expensive investment in materials, because they should pay only for the used resources. Also, institutions have the ability to adjust the services according to their needs. Besides, cloud computing

offers unlimited data storage capacity which makes data management more efficient. In addition to this, access to e-learning systems becomes easier, everywhere and at any time. But on the other side, this combination has few limitations such as the speed or the lack of Internet, the protection of property and intellectual rights, also, risks related to security Cloud-based e-learning systems [8].

5 Architecture and Security of Cloud-Based e-Learning Systems: State of the Art

As said above, in order to study cloud-based e-learning systems, we were based on many previous articles and conference papers. The first step of this study was to filter papers by domain. We found that some researchers were interested by the architecture of this type of systems, others by security challenges and the third type of collected articles give a review and a state of the art. In this paper, we summarize many works filtered by domain of each work done. We first study the different proposed architectures, than we move to works interested by security challenges.

5.1 Architecture

Many researchers were interested by studying the architecture of cloud-based e-learning systems. We find some works where five layers were proposed [5, 11, 12]. Those five layers are: infrastructure/hardware layer, software layer, resource management layer, service layer and application layer. We find also some differences and particularities in these layers like in [13] where authors introduced the concept of Education 4.0 and presented their proposed architecture for E-learning Cloud Architecture in this new concept. Another proposition of cloud based e-learning systems is based on three layers like in [14] and [15]. Another recent proposition of architecture was based on using Eucalyptus private cloud and Openshift public cloud [16]. And we find also another work where authors propose a framework that can be implemented in case of higher education through the effective use of cloud computing service in e-learning [17].

5.2 Security Challenges

According to our study based on previous works [18–21], we can classify security challenges of cloud-based e-learning systems in two categories: those of cloud computing in general, and those of any e-learning system in particular. Besides, we find another work where authors propose encryption and decryption of message before

sending it to storage in e-learning storage system [22]. Also, in another previous work [4], the most important security challenges in such system were classified, and a solution for authentication attack was proposed.

5.3 Discussion

To conclude the state of the art, we can say that researchers were interested by either the architecture of cloud-based e-learning systems or the storage of data in those systems. However, the great majority of these proposed solutions present leaks in security. Also, they do not present a ready platform to use for a perspective goals, like behavior analysis of cloud-based e-learning systems, which makes of these solutions limited and not opened to new functionalities that should be added in order to improve the quality of such systems. Interested by attempting this goal, we propose in this paper a new architecture that offers solution for security challenges, and at the same time, helps us to analyze data concerning the learning process for students in order to apply easily big data and machine learning technologies in the future.

6 Our Proposed Solution to Secure Cloud-Based e-Learning Systems

In order to resolve the problems related to cloud-based e-learning systems, we propose a new architecture, where we offer a decentralized architecture where all actors of learning process could contribute using an efficient system.

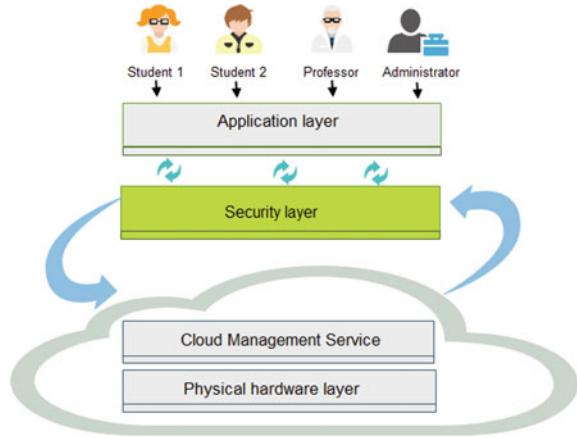
6.1 General Architecture of Proposed System

In our proposed system, we suggest to add a security layer between the application layer and cloud management service. This layer has two principal roles:

- First, it is responsible for controlling all operations and transactions done and requested by the different users by generating a key for each user. We explain with details this process in next sections.
- The second role of this layer, is to store all transactions done by users. Those transactions are stored as blocks in different nodes. We find a node for students' transactions, another node for professors' transactions, and a third one for all administrative transactions.

As it is explained, the security layer is not just responsible to verify and secure operations done before they are passed to cloud environment, but also it stores (the security layer) all transactions in nodes, which will help us to analyze those transactions and

Fig. 2 Global architecture of proposed system



propose in the future recommendation systems for different users, basing on those stored data. Figure 2 illustrates the global architecture of the proposed system.

6.2 Security Layer Composition

To request a transaction on the cloud-based e-learning system, task of authentication should be completed for all actors. This task is one of the most important parts of security and presents a security challenge for this type of systems. In our proposed architecture, we added a security layer composed of nodes. We find a node for each actor (students, professors, administrators). Those nodes are added and used for different reasons. First, they are used for verification of authentication data (login and password), then, they are responsible (the nodes) of generating key for the user. Another important role of these nodes is to store all users' transactions in blocks. This strategy will help us to build a database containing all data concerning the learning process for students in order to analyze these data and propose a smart learning process in the future, using big data and machine learning techniques. The other nodes dedicated for professors and administrators are also used to store their transactions for the same goal: building a database for each type of users in order to analyze data to improve the process of using cloud-based e-learning systems. In Fig. 3, we illustrate interactions between the user interface of e-learning platform and security layer in a chronological order.

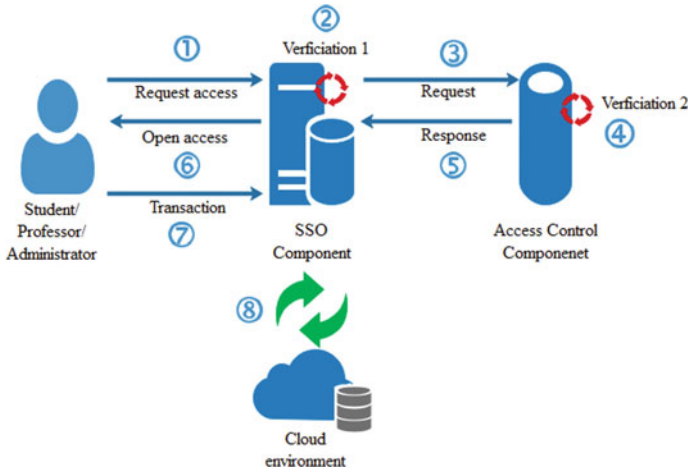
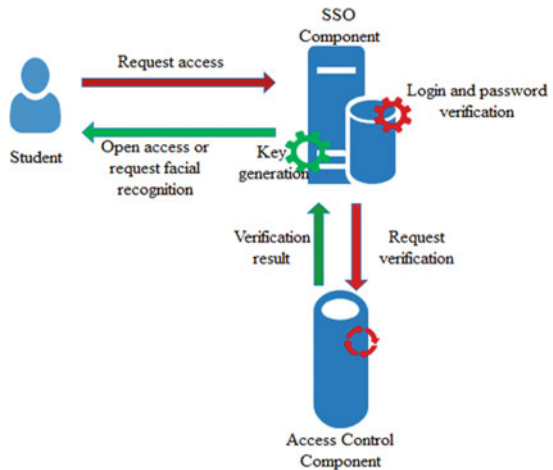


Fig. 3 Interactions between application layer and security layer

Fig. 4 Student’s case scenario



6.3 Student’s Case Scenario

Our proposed system is addressed to different users of cloud-based e-learning systems: students, professors and administrators. In a previous article [1], we have elaborated use cases for these actors. In this article, we will treat the student’s case, for the reason that in this role that we find a great number of users.

In Fig. 4, interactions of students with security layer of our proposed system are schematized. First, the student requests access to a resource. Before that this request is passed to cloud environment, it is delivered to a special node (SSO (Single Sign On) component), where the first verification is done. This verification concerns the

login and password of the student. If a positive result is returned, the request is passed to an Access Control Component (ACC), where access right is verified. Following a positive result, the node generates a key for this student. This key will identify the student and his transactions on the node. All these transactions are stored like blocks. Here, we should distinguish two cases:

- Case A: authenticated student has not changed his physical machine used the first time to authenticate on the learning system. In this case, the generated key is sufficient and he will be able to begin his transactions.
- Case B: when the student requests a transaction using another machine (not which was used for the first time), the node requests a facial recognition in order to protect access to resources. This technique is also used in exams and for all resources requiring additional security politics.

6.4 SSO Component

This component is responsible for making sure the secure authentication and identity management service. Identity management (IDM) mechanism allows authenticating the users and the services based on their credentials and/or profile/characteristics. Furthermore, this component should support the interoperability issues that could result from using different identity negotiation protocols. For this purpose, we propose to use the authentication service Single Sign-On (SSO) [23], which is a centralized session and user authentication service in which one set of login credentials can be used to access multiple applications. Using SSO Service, the users are able to utilize the diverse services which are provided through cloud based e-learning systems. Whenever a user signs to an SSO service, the service creates an authentication token to verify the identity of the user. This token is a digital resource that can be stored either in the user's browser or in the SSO service server. It is similar to a temporary identity card provided to the user. Any service provided through cloud based e-learning systems will check the user accesses with the SSO service.

6.5 Access Control Component

This component is responsible for ensuring access control service, which is a security technique that regulates who or what can view or use resources in a computing environment. During the learning process, the student needs to access and use security related information shared by the learning staffs while respecting the access control constraints. In this component, the administrator specifies the authorizations policy using an access control model. This model should support collaboration and multi-tenancy, because in cloud environment, the cloud service provider segregates the data and customers services into multiple tenants. In our system, a tenant may be a

university, school, department or classroom. Starting from this we consider that each tenant defines its policy rules. Note that at this level, this component should resolve conflicts problems detected in the security rules intra-tenants and cross-tenants). To reach this goal, in this component, we propose to use MT-ABAC [24], Multi-Tenant Attributes Based Access Control model that ensures access control in multi-tenant based e-learning system. This model is based on a decentralized approach, supports cross-tenant attribute assignment, ensures the autonomy of tenant and preserves the confidentiality of each tenant object. Finally, this component is responsible for evaluating the access request to the resources based on the collected attributes values and authorizations. When a user sends a request to access to a resource stored in the cloud, this component evaluates this request according to the policy rules in order to decide whether the user is authorized to access to this resource or not.

6.6 Discussion

As mentioned above, our goal is to contribute in improving the quality of e-learning systems. Since the last pandemic of coronavirus, it was necessary for academic institutions and universities to virtualize the maximum of physical resources in order to give to all actors in education sector the ability to continue the learning process without any obstacles. In our side, our contribution was to offer a new secured architecture for cloud-based e-learning systems. Compared to other proposed solutions, the great advantage of our proposed solution, is that it constitutes a technical solution, easy to implement, not expensive for most academic institutions and universities, and it is opened to new perspectives like using big data and machine learning algorithms to analyze the behavior of different actors and create recommendation systems for them. This perspective will be achieved in a next work. Also, we have explained in this article the steps that every institution could follow to secure its cloud-based e-learning system. It does not require advanced IT profiles, and could be implemented easily by the technic staff only, which makes our solution compared to others more efficient, cheaper, and more practical.

7 Conclusion

Using e-learning platforms was generalized and all academic institutions were looking for the best solution to offer to their students and professors during coronavirus pandemic around the world. Starting from this, we can highlight the importance of improving the quality of e-learning platforms on all levels. In this paper, we proposed a new architecture based on adding a security layer between the application layer and the cloud environment. In this security layer, we use decentralized nodes to secure authentication and store transactions done by actors. This solution offers a secured authentication by performing different types of verification: initial login

and password checking, ACL verification, key generation and facial recognition verification. The great advantages of this proposed solution is that it offers a technical method to secure authentication task, and also it will help us to apply easily big data and machine learning to offer recommendations for users. In a future work, we will conduct a comparative study between our architecture and other proposed solution, we will also implement this solution and analyze generated data using big data technologies in order to offer a recommendation system for students.

References

1. Aissaoui K, Ettifouri EH, Azizi M (2016) EXPEL protocol based architecture for cooperative E-Learning. *Int J Emerg Technol Learn (iJET)* 11(10):59–64
2. Maher AA, Najwa HMA, Roesnita I (2014) Towards an efficient privacy in cloud based e-learning. In: *Proceedings of the international conference on intelligent systems, data mining and information technology (ICIDIT'2014)*, Bangkok, Thailand
3. Siddiqui ST, Alam S, Khan ZA, Gupta A (2019) Cloud-based E-learning: using cloud computing platform for an effective E-Learning. *Smart Innov Commun Computat Sci* 335–346. Springer, Singapore
4. Aissaoui K, Azizi M (2017) El-security: E-learning systems security checker plug-in. In: *Proceedings of the 2nd international conference on big data, cloud and applications*. ACM, pp 1–6
5. Riahi G (2015) E-learning systems based on cloud computing: a review. In: *SCSE*, pp 352–359
6. Heiser J (2009) What you need to know about cloud computing security and compliance. Gartner, Research, ID, p G00168345
7. Jain A, Pandey US (2013). Role of cloud computing in higher education. *Int J Adv Res Comput Sci Softw Eng*
8. Desai MT, Patel MR, Patel P et al (2016) Cloud computing in education sector. *Int J* 2:191–194
9. Kumar BVP, Kommareddy S, Uma Rani N (2013) Effective ways cloud computing can contribute to education success. *Adv Comput* 4(4):17
10. Munjal MN (2015) An effective use of cloud computing in higher education. *Cyber Times Int J Technol Manage* 8(1):12–24
11. Maskare Poonam R, Sulke Sarika R (2014) Review paper on E-learning using cloud computing. *Int J Comput Sci Mobile Comput* 3(5):1281–1287
12. Divya P, Prakasam S (2015) Effectiveness of cloud based e-learning system (ECBELS). *Int J Comput Appl* 119(6)
13. Hendradi P, Khanapi M, Mahfuzah SN (2019) Cloud computing based e-learning system architecture in education 4.0. In: *Journal of physics: conference series*, vol 1196. No. 1. IOP Publishing
14. El Mhouthi A, Erradi M, Nasseh A (2018) Using cloud computing services in e-learning process: Benefits and challenges. *Educ Inf Technol* 23(2):893–909
15. Johnson S, Liu X, Miao H, Yuan J, Jin Y, Wei Q, Xu Z (2016) A framework of e-learning education clouds to efficiency and personalization. In: *2016 3rd international conference on information science and control engineering (ICISCE)*. IEEE
16. Chuang FC, Tsai YN, Chow YN, Chuang YC, Huang MC, Chuang TW, Chuang TH (2019) Implementation of an E-learning platform in hybrid clouds. In: *IEEE Eurasia conference on biomedical engineering*. IEEE, Healthcare and Sustainability (ECBIOS)
17. Kurian A, Peter Augustine D (2018) Next generation of e-learning through the effective usage of cloud computing services. *Int J Eng Technol* 7(4):5233–5237
18. Masud MAH, Islam MR, Abawajy J (2013) Security concerns and remedy in a cloud based e-learning system. In: *International conference on security and privacy in communication systems*. Springer, Cham

19. Durairaj M, Manimaran A (2015) A study on security issues in cloud based e-learning. *Indian J Sci Technol* 8(8):757–765
20. Rahman A, Sarfraz S, Shoaib U, Abbas G, Sattar MA (2016) Cloud based E-learning, security threats and security measures. *Indian J Sci Technol* 9(48):1–8
21. Rajesh M (2017) A systematic review of cloud security challenges in higher education. *Online J Dist Educ e-Learn* 5(1)
22. Jose GSS, Seldev Christopher C (2019) Secure cloud data storage approach in e-learning systems. *Cluster Comput* 22(5):12857–12862
23. Iadalin N, Pynbianglut H, Sarat C (2018) A survey on single sign-on. *J IJCRT* 6(2). ISSN: 2320-2882
24. Pustchi N, Sandhu R (2015) MT-ABAC: a multi-tenant attribute-based access control model with tenant trust. *International conference on network and system security*. Springer, Cham, pp 206–220

A Term Weighting Scheme Using Fuzzy Logic for Enhancing Candidate Screening Task



Amine Habous and El Habib Nfaoui

Abstract The candidate screening is an essential task in the recruitment process. It is about choosing a suitable candidate that satisfies the recruiter requirements for a given job position. The evolution of information technologies leads to an increase in the use of the recruitment web portals by the candidates that apply for the job positions published in the job boards. Thus the candidate screening process automation becomes necessary to handle the enormous volume of CVs applying for the job positions. In Information Technology (IT) domain, the technology skills are the key competencies to identify the job profile; Consequently, they have priority to the candidate screening task. In this paper, we enhance the candidate screening task in the IT field. For this purpose, we propose a fuzzy-based weighting scheme using domain ontology for Information Retrieval (IR). Experimental results on a recruiter company data show the effective results of our proposed solution.

Keywords Term weighting · Fuzzy logic · Vector space model · Candidate screening · IT recruitment

1 Introduction

Nowadays, web platforms are highly used by the candidates that apply for the job offers published by human resources (HR) managers. Consequently, those applications turn into a massive amount of textual documents known as curricula vitae (CV), which is hard to process by the human being. Thus the automation of the recruitment process becomes a vital task to facilitate the candidate screening process for the companies. The candidate screening task aims to match the job offer with the suitable candidate CVs basing on work requirements. Work requirements are criteria

A. Habous (✉) · E. H. Nfaoui
LISAC Laboratory, Faculty of Sciences Dhar EL Mehraz, Sidi Mohamed Ben
Abdellah University, Fez, Morocco
e-mail: amine.habous@usmba.ac.ma

E. H. Nfaoui
e-mail: elhabib.nfaoui@usmba.ac.ma

that should be satisfied to fill a job position, such as education degree, job tasks, and competencies. The technology skills or technology tools are the main competencies that identify the job profile in the IT domain, thereby having priority in the screening task automation. Most often, these skills are expressed imprecisely [1] and hence, necessitating the support by fuzzy logic for their processing.

In our case, we focus on enhancing the job offer and CV representation for document retrieval in the IT domain. We applied the information extraction (IE), techniques, and natural language processing (NLP) for technology skills extraction and inference using an oriented IT ontology and a fuzzy-based weighting method. To show our proposed solution performance, we apply it in information retrieval (IR) system to retrieve CVs for a given job offer (query).

The contributions of this work are summarized as follows.

- We propose a fuzzy-based method to weight the relationships in a domain ontology
- We propose a term weighting scheme for documents representation to enhance information retrieval in the IT domain.

The rest of this paper is organized as follows. Section 2 presents the related works. Section 3 describes our proposal. Section 4 presents the experiments. Finally, Sect. 5 concludes this paper.

2 Relate Works

Information extraction (IE) is the task of transformation a document collection into easier to analyze information [2], it tries to get relevant facts from documents. Whereas, Information retrieval (IR) deals with the representation, storage and organization of, and access to information items [3]. Ontology based techniques are widely used in IE from unstructured text, [4] used ontology for semantic annotation in textual documents. Therefore, [5, 6] used domain ontology for the text annotation. The use of ontologies in recruitment process is noticeable, [7] developed a human resource ontology to provide semantics in job postings and applications. Besides, [8] proposed an ER-ontology for semantic annotation basing on common parts between job offers and CVs. Fuzzy logic has been used widely as a efficient tool to deal with uncertainty and a wide range of problems. Thus many works used fuzzy logic in information extraction and human resources field. Güngör et al. [9], Balas-Timar and Ignat [10], Klosowski et al. [11] proposed a fuzzy system for candidate selection automation. In [1], the authors proposed a fuzzy method using axiomatic design principles for solving the personnel selection.

3 Methodology

As we said above, we are applying IR and IE to textual documents in the IT field. Our main contribution is presenting the key terms weighting scheme to enhance the candidate screening task using fuzzy logic to deal with data uncertainty and ontology to extract IT concepts from free text. In what follows, we explain the essential concepts to make the paper comprehension clear.

- **Technology skill:** Ability or skill developed as a result of the use of the computer and technologies; it could be a programming language, framework, and common operating system. In the IT field, these skills are considered as significant criteria for the candidate screening task. For example: 'Php', 'Eclipse IDE', 'Microstrategy', 'linux', etc.
- **Technology field:** In our vision, technology fields represent a precise context that requires a set of technology skills for achieving a job task in an IT job position. For example, 'Business intelligence', 'big data', 'Front end'.
- **Key-skill:** In our paper, we treat the relationship between the technology skill and technology field, which is a weight that represents the importance of a technology skill in regards a technology field. A key-skill is the skill that is highly required for a technology field (having a high weight according to this field). For example, 'Css' for 'Front end', 'Python' for 'machine learning'.

In Information extraction and information retrieval, The values of the weights are related to the importance of an index term in its corresponding set of knowledge [12]. The candidate screening is the task of retrieving the CV that satisfies the job requirements cited in the recruiter job offer. As we said before, technology skills are the essential competencies among job requirements that identify a job profile; hence, we consider the technology skills as index terms for the IT documents recruitment. Typically, the TF-IDF was used widely as a term weighting method for many types of research [13]. This method uses the term frequency to weight the index terms. However, in IT recruitment documents, the term frequency does not express the index terms importance. The recruiter could mention an important technology skill in a job offer without repetition. Thus we propose a weighting scheme basing on the technology skills and their relationship with technology fields since they are the key competencies in job requirements.

We mention that we used a job offer data set to weigh the relationship between the technology skill and technology fields due to the sufficient number of job offers in the corpus. Whereas, the task of filling a data set with a sufficient number of CVs to create metadata is tough; Since the companies or job boards do not publish their CV libraries.

3.1 The Overall System Architecture

In Fig. 1, we present the overall proposed architecture. Subsections below give all details for each phase. For the preprocessing step, we used the traditional document preprocessing in NLP [14]:

- Tokenization: splitting the job offer (CV resp) into tokens
- Stop words elimination (Fig. 2).

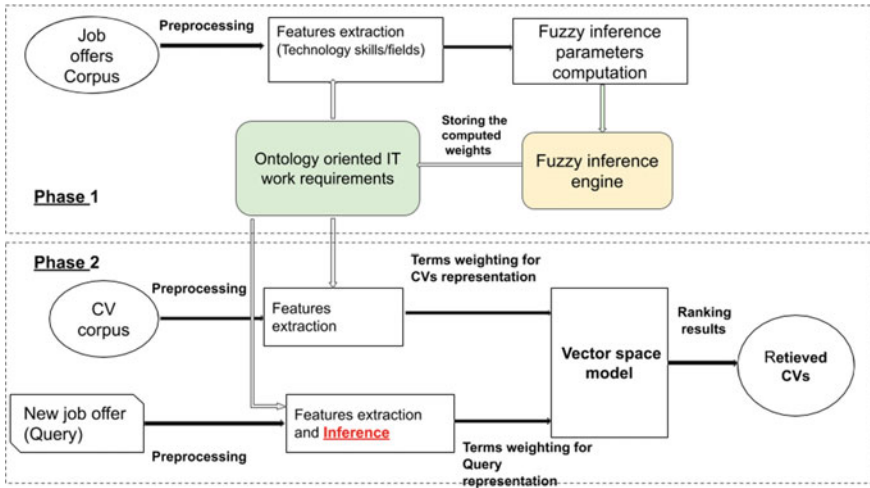


Fig. 1 The overall proposed architecture

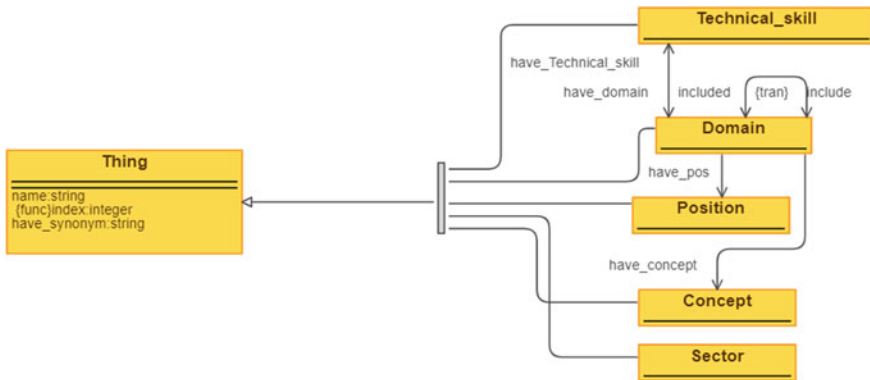


Fig. 2 Ontology-oriented ICT competencies and concepts

3.2 The Ontology-Oriented IT Work Requirements

The ontology-oriented IT work requirements gathers all the essential concepts in the IT domain. The use of this ontology is very beneficial due to the ontology mechanism to represent the knowledge related to IT recruitment and deals with the semantics through the stored concepts. It facilitates the task of extracting the technology skills and technology fields in free text from the job offers and CVs (Fig. 1).

3.3 The Fuzzy Method for Weighting the Relation Ship Between the Technology Skills and the Technology Fields

In this section, we present our proposed method for automatically weighting the relationship between the technical skills and the technology fields (Phase 1). We will use this weight for two tasks:

- Inferring new technology skills from the job offer to overcome the lack in their precision.
- In the terms weighting scheme for the CVs and job offers representation.

3.4 The Fuzzy System Inputs for Weighting the Relationship Between Technology Skills and Technology Fields

The correlation between technology fields and technology skills is an essential parameter for the task of weighting their relationship; hence we represent this correlation using the technology skill and field frequency to appear in the same job offers in the corpus. For each pair of technology skill/field 's', 'f', we compute their document frequency in the corpus using the following formula:

$$C_{\{s,f\}} = \frac{n_{\{s,f\}}}{n} \quad (1)$$

where $n_{\{s,f\}}$ is the number of job offers that contain the technology skill 's' and the technology field 'f' and n the size of the corpus. In what follows, we refer to this parameter as 'Correlation index'.

The formula above is very efficient for finding the technology skills and fields that are more likely to occur in job offers. However, this formula is not sufficient to decide if a technology skill is a key skill according to a technology field or not. For example, 'Java' has high document frequency; Consequently, it could have a high correlation with many technology fields in the job offers from the corpus even so it is not a key skill according to them. Thus we use the technology skill document frequency to solve this issue:

$$F_s = \frac{n_s}{n} \quad (2)$$

where ‘ n_s ’ is the number of the job offers in which the technology skill ‘s’ appears. We add a third parameter to enhance the weight of the relationship which is the technology field document frequency.

$$F_f = \frac{n_f}{n} \quad (3)$$

where ‘ n_f ’ is the number of the job offers in which the technology field ‘f’ appears. We obtain the assigned weight to the relationship between the technology field and skills in the ontology as the output of a fuzzy inference system, which takes the three parameters above as inputs. In what follows, we present rules that we proposed for the fuzzy inference method to compute the weight of the relationship between the technology skill and fields.

3.5 Fuzzy Logic Control System for Weighting the Relationship Between the Technology Fields/skills

Fuzzy logic proposed by by Zadeh in 1965 is an extension of the classical definition of a set [15], it is based on approximate reasoning instead of exact reasoning [16]. This model is based on the fuzzy set theory in which the membership function that maps the points in the input space to the membership values is between 1 and 0; Contrarily, in classical logic equals 1 or 0. We build a fuzzy control system that takes the three parameters: correlation index (C), technology skill, and technology field document frequency as inputs, to weight the relationship for each ‘s’ and ‘f’. The use of the fuzzy logic in our solution solves the uncertainty issues that we could have in dealing with numerical data and linguistic knowledge. We present the fuzzy sets for the inputs used in our control system in Fig. 3. Fuzzy rules have been considered as a key tool for expressing the knowledge in fuzzy logic [17]. In our case, the rules (Table 1) are set to achieve this axioms for defining the weight of the relationship between the technology skill and technology field:

- The weight is proportional to the correlation index value
- The weight value decreases as the technology skill document frequency increases.
- The weight value increases as the technology field document frequency increases.

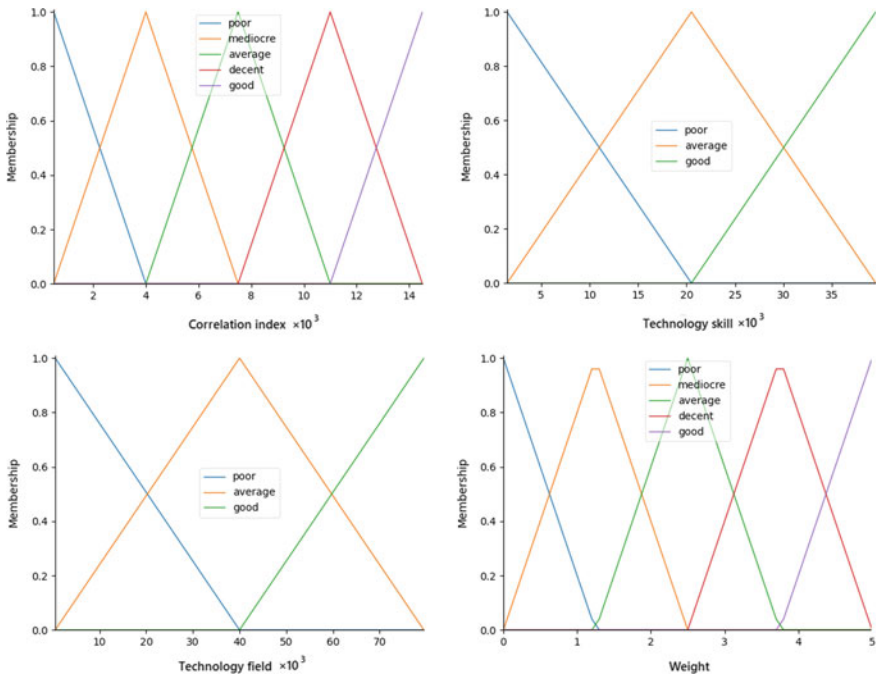


Fig. 3 The fuzzy sets inputs

3.6 Index Terms Weighting Method for CV/Job Offer Representation

The vector space model plays an essential role in information retrieval (IR), where IR concerns with methods and procedures of searching and obtaining the required information from information resource or corpus [18]. In our case, the CVs present the answers to our retrieval system where the job offers are the queries. For each CV from the CV collection, we extract the technology skills and the technology fields from the free text using the oriented IT ontology. Whereas, we extract and infer the key technology skills as we said before in order to solve the lack of precision for the job offers. After the extraction step, we use a vector representation for the CV and Job offer as follow:

$$V = [W_1, W_2, \dots W_n] \tag{4}$$

where W_i is the weight of the technology skill i .

To compute the technology skill ‘s’ weight, we use three component:

- Its weight according to the technology fields from the CV/job offer. Let’s consider that $D = \{f_1, f_2, \dots, f_n\}$ is the set of technology fields extracted from the current

Table 1 Rule definition for the weighting fuzzy control system

Rule number	Rule definition	Output (Weight)
1	C.index=GOOD & T.skill ≠ GOOD	GOOD
2	C.index=GOOD & T.skill=GOOD & T.field ≠ POOR	GOOD
3	C.index=GOOD & T.skill=GOOD & T.field=POOR	DECENT
4	C.index=DECENT & T.skill=POOR & T.field=GOOD	GOOD
5	C.index=DECENT & T.skill=AVERAGE	DECENT
6	C.index=DECENT & T.skill=GOOD & T.field=POOR	AVERAGE
7	C.index=DECENT & T.skill=GOOD & T.field ≠ POOR	DECENT
8	C.index=DECENT & T.skill=POOR & T.field ≠ GOOD	DECENT
9	C.index=AVERAGE & T.skill=POOR & T.field=GOOD	DECENT
10	C.index=AVERAGE & T.skill=AVERAGE	AVERAGE
11	C.index=AVERAGE & T.skill=GOOD & T.field=POOR	MEDIOCRE
12	C.index=AVERAGE & T.skill=GOOD & T.field ≠ POOR	AVERAGE
13	C.index=AVERAGE & T.skill=POOR & T.field ≠ GOOD	AVERAGE
14	Any other case	POOR

CV/job offer, we take the maximum weight between the technology skill ‘s’ and the technology fields from ‘D’:

$$WF_s = \max(W_{s,f_1}, W_{s,f_2}, \dots, W_{s,f_n}) \tag{5}$$

When the recruiter do not specify technology fields this factor is equal to 1.

- Technology skill/field local dependency factor:

$$WD_s = \sqrt{1 + \frac{\sum (W_{s,f_1}, W_{s,f_2}, \dots, W_{s,f_n})}{n_f}} \tag{6}$$

where $W_s, f_i > 0$ and n_d is the size of D. The technology skill/field local dependency factor is a local parameter, which means it depends on the technology skill

and the technology fields from the current job offer(CV resp). In contrast, the two other parameters that we use are global(related to the corpus).

- The technology skill inverse document frequency:

$$IDF_s = \log\left(\frac{n}{n_s}\right) \quad (7)$$

Where n is the size of the corpus and n_s the technology skill document frequency.

The technology skill weight is obtained using (5), (6) and (7):

$$W_s = WF_s \times WD_s \times IDF_s \quad (8)$$

We mention that the inferred technology skills weights in the job offers are multiplied by a penalizing factor to give priority to the extracted ones.

4 Results

In this section, we present the results performed by our retrieval system. Our data set is composed of a job offer corpus and a CV collection. As we said before, we had issues with reaching a sufficient number of CVs to weight the relationship between technical skills and fields. Thus we used a corpus of job offers (16,000) captured from different work jobs (www.apec.fr, www.meteojob.com, and www.indeed.fr) in IT French recruitment. We chose a data set of 40 CVs to test our system retrieval performance.

To compare the results, we used 20 job offers as queries and CV collection. The testing strategy that we used is based on the method presented in [19]. For each query, we continue to retrieve until a given percentage of CVs has been retrieved (for example, 25%), and then we compute the precision and recall. We used the cosine similarity to rank the retrieved CVs. Table 2 shows the details of our proposed solution results.

The results show our excellent proposed solution performance, as we only used the essential terms in the job requirements for document representation. The resulted vectors are very optimized, which is very advantageous in terms of time response compared to the traditional terms representation.

5 Conclusion

In this paper, we proposed a weighting method to enhance the candidate screening task in the IT domain. We used fuzzy logic inference to weight relationships between the IT concepts in the domain ontology. The use of these relationships solves the job requirements precision lack by inferring new technology skills according to

Table 2 The proposed system results

Query	Requested profile	Supervised results (CV id)	Precision (%)	Recall (%)
1	'Data scientist'	1,14,15,28,20,22,23,80	88.89	100
2	'BI manager'	1,3,8,20,37	40	80
3	'Test engineer'	10,19,21,23	66.67	100
4	'Test/micro-services developer'	19,21,10,25,13	40	80
5	'IA/Machine learning engineer'	14,17,20,26,30,20,1,15	60	75
6	'Symphony developer'	9,11,12,13	75	75
7	'JEE/java'	5,7,10,18,19,21,27,29,31	80	88.89
8	'Big data engineer'	1,3,14,15,17,20,26,23,27,33	80	80
9	'Data analyst'	1,3,4,6,20,37	100	100
10	'Data scientist-IA/big data'	1,14,15,17,20,26,23,30	70	87.5
11	'Front end/java script developer'	2,7,12,16,19,21,25	60	85.71
12	'Front end designer'	16,24,34,25	100	100
13	'Devops administrator'	11,18	66.67	100
14	'Data visualization engineer'	1,3,14,20,22	83.33	100
15	'Devops/production engineer'	11,26,2,12,19	71.43	100
16	'Database administrator'	3,25,20,22,21,19	60	100
17	'Back end engineer'	2,12,13,19,21,25,26	77.78	100
18	'UI designer'	16,25,2	42.86	100
19	'CMS/front end developer'	2,13,7,13,19,16	50	83.33
20	'Full stack developer'	16,26,13,12,21,25,31,2,11	80	88.89
Total			70	91

technology fields presented in the job offer. We also use them in index terms weighting scheme for building the information retrieval system that automates the candidate screening task.


The experimental results have shown that our system provides effective results in terms of information retrieval evaluation measures. In the results section, We described the results for each query used to retrieve the CVs from the corpus and compared it with the supervised ones to show the efficiency of our method.

References

1. Khandekar AV, Chakraborty S (2016) Personnel selection using fuzzy axiomatic design principles. *J Bus Theory Pract* 17:251–260
2. Ropero J, Gómez A, León C, Carrasco A (2009) Term weighting: novel fuzzy logic based method vs. classical TF-IDF method for web information extraction. iN: ICEIS 2009—11th international conference on enterprise information systems
3. Savoy J, Gaussier E (2010) *Information Retrieval*
4. Kiryakov A, Popov B, Terziev I, Manov D, Ognyanoff D (2004) Semantic annotation, indexing, and retrieval. *J Web Semant* 2:49–79. <http://www.sciencedirect.com/science/article/pii/S1570826804000162>
5. Popov B, Kiryakov A, Kirilov A, Angel M, Dimitar M, Dimitar O, Damyan G, Miroslav S, Katia M (2003) John, KIM—semantic annotation platform. *The Semantic Web-ISWC* 834–849
6. Müller, H-M, Kenny EE, Sternberg PW (2004) Expresso: an ontology-based information retrieval and extraction system for biological literature. *PLOS Biol* 2. <https://doi.org/10.1371/journal.pbio.0020309>
7. Mochol M, Oldakowski R, Heese R (2004) Ontology based recruitment process. *Informatik 2004, Informatik verbindet, Band 2, Beiträge der 34. Jahrestagung der Gesellschaft für Informatik e.V. (GI)*, pp 198–202
8. Yahiaoui L, Boufaïda Z, Prie Y (2006) Semantic annotation of documents applied to E-recruitment. *SWAP*
9. Güngör Z, Serhadlıoğlu G, Kesen SE (2009) A fuzzy AHP approach to personnel selection problem. *J Appl Soft Comput* 9:641–646. <http://www.sciencedirect.com/science/article/pii/S1568494608001282>
10. Balas-Timar D, Ignat S (2015) Conceptual applicant screening model with fuzzy logic in industrial organizational contexts. *J Procedia Soc Behav Sci* 203:257–263
11. Kłosowski G, Gola A, Świć A (2016) Application of fuzzy logic in assigning workers to production tasks. In: 13th international conference distributed computing and artificial intelligence, pp 505–513
12. Ropero J, Gómez A, Carrasco A, León C, Luque J (2012) Term weighting for information retrieval using fuzzy logic. *J Fuzzy Logic-Algorithm Techn Implement*, pp 173–192
13. Ropero J, Gómez A, León C, Carrasco A (2009) Term weighting: novel fuzzy logic based method vs. classical TF-IDF method for web information extraction. *ICEIS*
14. Kannan S, Gurusamy V (2014) Preprocessing techniques for text mining. In: *Conference paper. India*
15. Dubois D, Prade H (2005) Fuzzy elements in a fuzzy set
16. Goswami S, Shishodia MS (2013) A fuzzy based approach to text mining and document clustering. *J arXiv preprint arXiv*, pp 1306–4633
17. Didier D, Henri P (1996) What are fuzzy rules and how to use them. *J Fuzzy Sets Syst* 84:169–185
18. Kim D (2015) Group-theoretical vector space model. *J Int J Comput Math* 92:1536–1550
19. Edwards, Pottenger WA, Brian D (2005) Identification of critical values in latent semantic indexing. *J Data Min Knowl Discov—DATAMINE vol 6*, pp 333–346

E-learning Recommendation System Based on Cloud Computing



Mounia Rahhali , Lahcen Oughdir, Youssef Jedidi, Youssef Lahmadi, and Mohammed Zakariae El Khattabi

Abstract E-learning in higher education has been known as great technology to improve efficiency, augment focus and thereby, give better academic outcomes, and given its several advantages and benefits, e-learning is considered among the best strategies for instruction. Furthermore, the e-learning system can help students save time and showing further information improving student learning. However, the traditional system for conducting research work and choosing courses is a time-consuming and uninteresting activity, which not only seriously affects students' academic performance, but also affects students' learning experience, and due to information overload, it becomes more difficult to choose relevant learning resources. To resolve this problem, this paper presents a model of a recommender system for the e-learning platform that will recommend and motivate the student in selecting the courses according to their requirements; this system based on cloud computing infrastructure and particularly with the use of Google cloud services.

Keywords E-learning · Recommender system · Cloud computing

M. Rahhali (✉) · L. Oughdir · Y. Lahmadi · M. Z. El Khattabi
Engineering, Systems and Applications Laboratory, ENSA, Sidi Mohamed Ben Abdellah University, Fez, Morocco

e-mail: mounia.rahhali@usmba.ac.ma

L. Oughdir

e-mail: Lahcen.oughdir@usmba.ac.ma

Y. Lahmadi

e-mail: youssef.lahmadi@usmba.ac.ma

M. Z. El Khattabi

e-mail: z.elkhattabi@um5s.net.ma

Y. Jedidi

High School of Technology, Sidi Mohamed Ben Abdellah University, Fez, Morocco

e-mail: youssef.jedidi@usmba.ac.ma

1 Introduction

E-learning plays a significant role in helping large educational institutions meet their learning and training requirements. Today's education is increasingly associated with ICT, so educational institutions have a high demand for servers, storage, and software [1].

According to Naik and Madhavi [1], the lack of technology infrastructure can make more damage than good to teachers, students, and the learning experience. Moreover, many educational institutions cannot invest in the software and hardware required for e-learning [2]. Furthermore, due to information overload, it is difficult for learners in the e-learning environment to choose related learning resources, besides, due to the differences in the background and sequential access methods of learners, different learners have different learning needs. Therefore, how to find learning resources quickly and be expanded to mass data storage have become serious problems.

On the one hand, by incorporating the recommendation system into the learning system, there is great potential for personalization, which is beneficial to learners and other learning tools. The e-learning recommendation system targets to predict appropriate gaining knowledge of learning data according to students' preferences.

On the other hand, the system adopts the current cloud computing technology to deal with the challenges of massive data storage and computing. Cloud computing helps to access servers, storage, and databases from any location in the world and any device with an Internet connection. Cloud service providers such as (Amazon, Google, IBM ...) operate and manage underlying cloud infrastructure for these application services, providing and using the resources you need through a web application. Moreover, to these innovative technologies as Serverless computing, Artificial Intelligence, the Internet of Things, and a variety of many other resources are becoming available via cloud computing services.

The purpose of this article is to design a model of a recommender system based on cloud computing that can be integrated to improve the viability of any e-learning system, simplify information access, and personalize learners. The rest of the paper is structured as follows: Sect. 2 outlines the associated work. Section 3 introduces the online learning recommendation system. Section 4 introduces cloud computing, its features, services, and deployment models. Section 5 we describe the architecture of the proposed model. In Sect. 6, gives benefits predicted from E-learning based cloud. We will summarize our work in Sect. 7 and put forward some ideas and future work.

2 Related Works

Recently, the rapid development of information technology has brought about the problem of "data overload", and the research on recommendation systems has

attracted more and more attention. The field of use of RS has become endless. It has moved from the field of e-commerce to other fields, such as recommending movies, services, or education in recommended courses.

Dong et al. [3] introduced a personalized hybrid recommendation system. The system can be designed and implemented using Cloud technology, the system uses MapReduce for the execution procedure of proposal algorithms and is developed and deployed into SEUCloud Platform.

Jiang et al. [4] developed a new blog recommendation system based on cloud computing infrastructure. The system uses a Hadoop distributed file system to store massive blog data and adopts the user recommendation algorithm for collaborative filtering in blog search. Simultaneously, they used the cloud-computing platform to deal with the blog graph stages, which significantly enhanced network expandability and service reliability. Nevertheless, the program still has some drawbacks, such as implementing various recommendation algorithms.

Dahdouh et al. [5] proposed a new e-learning system architecture based on a new generation of big data technology implemented in a cloud computing environment.

Zhao [6] discussed several recommendation algorithms and the challenge of traditional recommender systems in big data situation, and then proposed a framework of a distributed and scalable recommender system based on Hadoop on e-commerce. In massive e-commerce, the system can bring a solution to problems of data overload and have a competitive edge for e-commerce with custom marketing.

Bourkhouk et al. [7] proposed an innovative learning method, that is, using a recommendation system to obtain a personalized learning experience by selecting and ranking the most suitable learning items. They presented a new score function to weigh teaching material by obtaining feedback from the student and also collecting preferences from current web log files. In addition, they utilized CF to select a collection of the most appropriate learning objects from the learning object repositories (LOR) focused on the student's preference collected utilizing their score function.

Though many research have indicated on recommender system, little attention has been given to recommender systems in the field of E-learning based on cloud computing.

3 Recommender System

The main functions of recommender systems permit analyzing user information and amassing valuable records for further predictions. Recommender systems (RSs) are software tools and techniques used to help users find new items or services, like books, music, transportation, or maybe people supported information about the user, or the recommended item [8, 9]. Recommendation systems are usually classified according to the idea of their rating estimation method: collaborative filtering system (rated by user), content-based system (by keyword), and hybrid system (through collaboration and content-based filtering) (Figs. 1 and 2).

Fig. 1. Collaborative filtering recommendation [9]

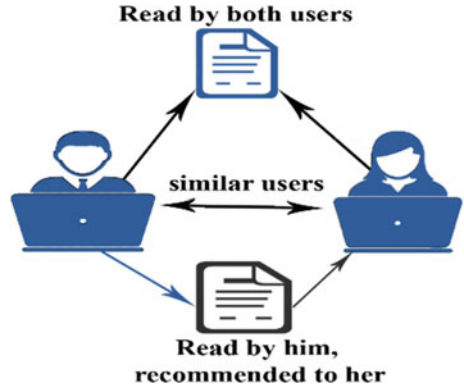
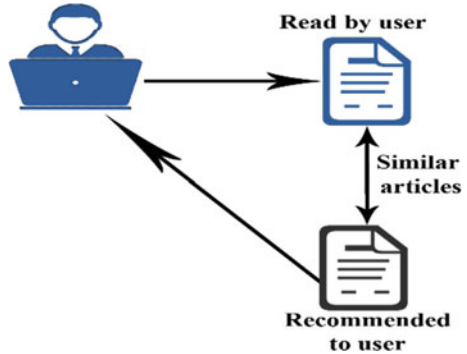


Fig. 2. Content-based recommendation [9]



Collaborative Filtering System (CF): is frequently used in e-commerce and is one of the most successful recommender systems in e-commerce [6]. Collaborative filtering is a technology (collaboration) that automatically creates automatic predictions (filters) about user interests by collecting preference or taste data from many users. For example, in an E-learning recommendation, CF system tries to find other users who share similar interests, and then recommend their favorite books.

Content-based System: recommends items, related to items that past learners liked. They make suggestions based on personal information and ignore the contributions of other learners [9].

Hybrid System: The hybrid recommendation system combines two or more recommendation techniques to achieve better performance while reducing the disadvantages of a single recommendation technique.

The recommendation system is the most important factor in the field of e-commerce and can be seen in many other fields, such as movies, E-tourism, E-business, E-library, and management science. However, several other areas posing a similar issue, such as those domains related to education and learning objects.

3.1 Recommendation System in E-learning Environment

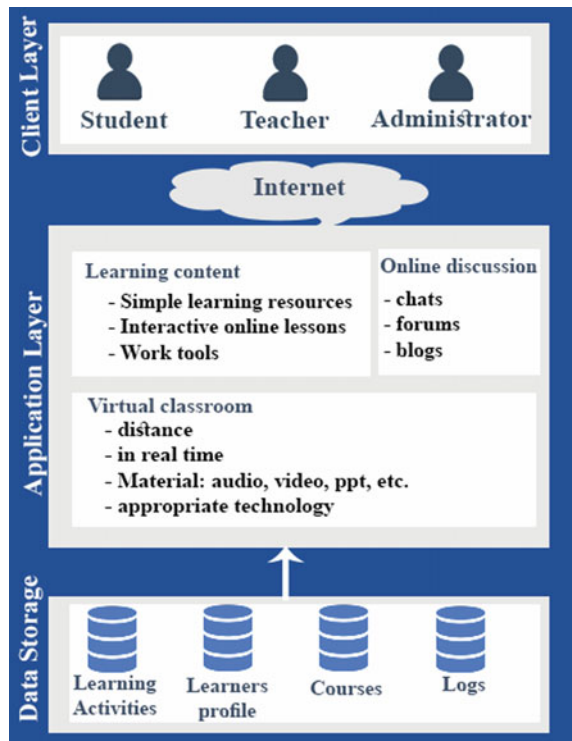
The E-learning system is a technical development aimed at reforming and adjusting the teaching and interaction of teachers and students through course materials and teaching resources [10], which will not replace traditional methods of education but significantly improve educational efficiency [11]. An e-learning system is a platform, system, or software application for pliant education. The purpose is to improve the quality of learning and teaching: organize content and resources, provide instructional courses, prepare courses, track, record, and manage tasks.

The Fig. 3 shows the components of e-learning systems. There are three layers of traditional e-learning system:

Primarily client layer: users can log in to the learning system to learn by using various enabled devices such as (iPad, laptop, desktop, and smartphones). Secondly, the Application layer has many components like (Learning content, online discussion, and virtual classroom, etc.). Finally, the data storage layer of the system enables (learning activities, learner’s profile, courses, logs, and so on).

E-learning is indeed a revolutionary way of teaching and learning in the future, compared to the normal face-to-face style [12]. Today, online learning is becoming

Fig. 3. Components of an E-learning system



more and more popular in organizational and institutional learning for its various e-learning program to learn anywhere, and anytime [7]. However, the great dissimilarity of learners on the Internet presents new defiance for the conventional "one-size-fix-all" approach, in which all learners are equipped with a common collection of learning tools [12]. Even among audiences with seemingly similar backgrounds, learners will have a variety of interests, and learners' needs and expectations and learning methods brought about by learning interventions are different, so they cannot be treated in a unified manner. It is very important to produce a customize system. In this system, the teaching environment is tailored according to the independent requires, skills and interests of each student, somewhat inverts the traditional instructor/student hierarchy. It provides students with options on how to study to support their curiosity and capacity. Besides, the recommendation in the e-learning environment may be a software agent that attempts to intelligently suggest learning resources to learners who support previous learner activities. The recommendation system in e-learning is a section of information recovery, in which learning resources are filtered and given to learners [13], by using data mining techniques and tools.

The recommendation system in online learning is different from other fields because learners have different characteristics, such as learning styles, learning goals, and changes in experience levels, which may affect learners' preferences. in addition to that materials interested by learner may not be pedagogically appropriate for them [12]. The recommendation system must also recommend learning materials without affecting the learning process, and the recommended topics must remain in the current learning environment [13].

4 Cloud Computing

Authors in [14] define cloud computing as "a paradigm for permitting everywhere, advantageous, on-demand network get entry to a shared grouping of configurable computing resources that can be immediately conveyed and released with negligible administration exertion or service supplier interaction".

The cloud architecture incorporates five principle characteristics, three service models, and four deployment models.

4.1 Characteristics

The following aspects summarize the five key characteristics that distinguish the cloud-computing paradigm from other computing methods:

On-demand self-service: Without human contact, the service provider can supply cloud-computing services. In other words, a manufacturing company can supply additional computing services where appropriate without going through the cloud

service provider. This can be a virtual machine instances, server time, network storage, and so on;

Broad network access: Cloud services are available through the Internet or private networks and by standard techniques for access.

Resource pooling: Computing resources (processing, storage, memory ...) are aggregated to provide as per the needs of multiple consumers [10].

Rapid elasticity: Can quickly and flexibly configure cloud services and computing platforms, and can be extended to various issues [10]. To the user, the provisioning capacities often seem limitless and can be borrowed in any quantity at any time.

Measured service: Tracking the resource utilization of each application and occupant, it will provide users and resource providers with used accounts.

4.2 Service Model

Although cloud computing has evolved, it is classified basically into three categories: infrastructure as a service (IaaS), platform as a service (PaaS), and software as a service (SaaS):

- In a SaaS model, a software delivery model in which a service provider manages and allows programs accessible to users over the internet to such customers.
- In PaaS, an operating system, hardware and network are given to help the application progress (design, implementation, debugging ...) [12]. For example Google App Engine and Windows Azure.
- The IaaS model refers to the computers and servers running code and storing data, and to the wires and appliances linking those devices. For example (processing, storage, networks, and other essential computing resources).

4.3 Deployment Models

Cloud deployment models demonstrate how consumers get access to cloud services. The four deployment models related to cloud computing are as follows:

Private cloud: Provides cloud infrastructure for use by a unique establishment with various consumers [14], And owned by an organization or a third party, whether it is inside or outside the enterprise [15].

Community cloud: Multiple organizations build and provide similar cloud infrastructure and strategies, requirements, values and concerns. A third party provider or one of the organizations in the network may host the cloud infrastructure [15].

Public cloud: Overall population cloud customers use this model, and cloud service providers are fully responsible for the public cloud through their strategies, values and benefits, costs and billing models [15].

Hybrid cloud: is a cloud-computing environment that uses a blend of two or more clouds (community, public or private) to coordinate between the two platforms [15].

5 Proposed Approach for Using Google Cloud in E-learning Recommender System

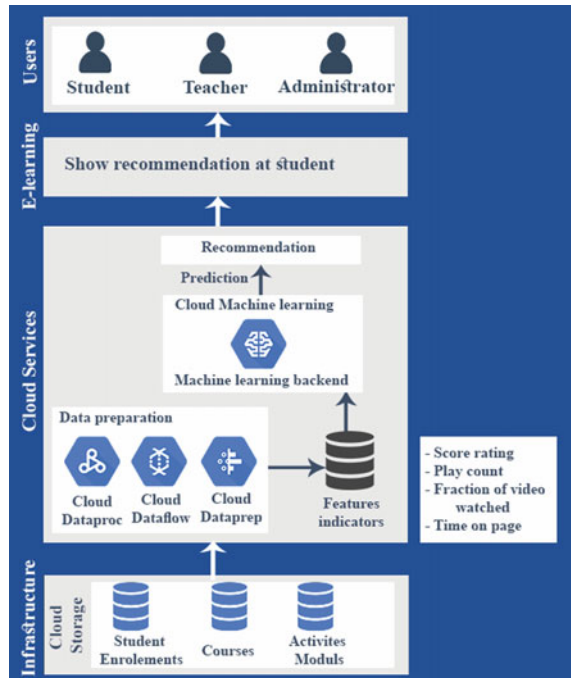
In this section, we demonstrate the overall architecture of our recommendation system using Google cloud services depicted in Fig 4, which can be divided into four layer: Infrastructure Layer, Cloud Services layer, E-learning layer and user layer.

The infrastructure is the first layer, at the lowest level of cloud service middleware. The infrastructure layer consists of virtualized computing, storage, and network resources. This allows institutions to rent these resources without having to spend money on dedicated servers and network instruments [16].

The second layer represents Cloud services: this layer introduces data preprocessing operations and stages of data readiness:

Processing Data: Raw data cannot be utilized for machine learning development purposes. It must be processed. In GCP, once we move data to Google Cloud Storage or BigQuery, data is obtainable through certain applications and tools for processing as follows: Google Cloud Dataflow: This preparation is a completely overseen administration for changing and improving information in stream and batch modes. Google Dataprep used to look at and change raw data from different as well as enormous datasets into perfect and organized information for additional analysis

Fig. 4. Approach for using Google cloud in E-learning recommender system



and processing. Cloud Dataproc enables to running Hadoop clusters on GCP and offers access to Hadoop-ecosystem tools.

Features indicators: This refers to the dataset with the tuned features expected by the model, and developing new features for the model during training and prediction. For example: Score rating, play count, Fraction of video watched and Time on-page.

Cloud machine learning: Use established machine learning techniques or define new operations and methods to develop models such as Matrix factorization and Clustering-based approach, in this section, the AI platform provides the services needed to train and evaluate models in the cloud.

The third layer show E-learning: it represents a software system designed to create a virtual learning environment through which training courses can be delivered, managed and monitored, and access to a range of facilities and arrangements.

User layer: users can log in to Cloud-based education platform like (Moodle, Chamilo, etc.) by using various enabled devices such as (iPad, laptop, desktop, and smartphones).

The pipeline contains the following phases (Fig. 5):

(a) The raw data is stored in BigQuery (or in Cloud Storage, for images, documentation, sound, and video). (b) Using Dataflow, data extraction (preparation) and features are performed on a large scale, this produces training sets, assessment and test ready for ML and stored in Cloud Storage. (c) These data sets are stored as files, which is the optimized format for Tensorflow computations. (d) On Cloud MLE, a prediction service is generated using the Model trained. (e) The external application sends data to the deployed model for inference.

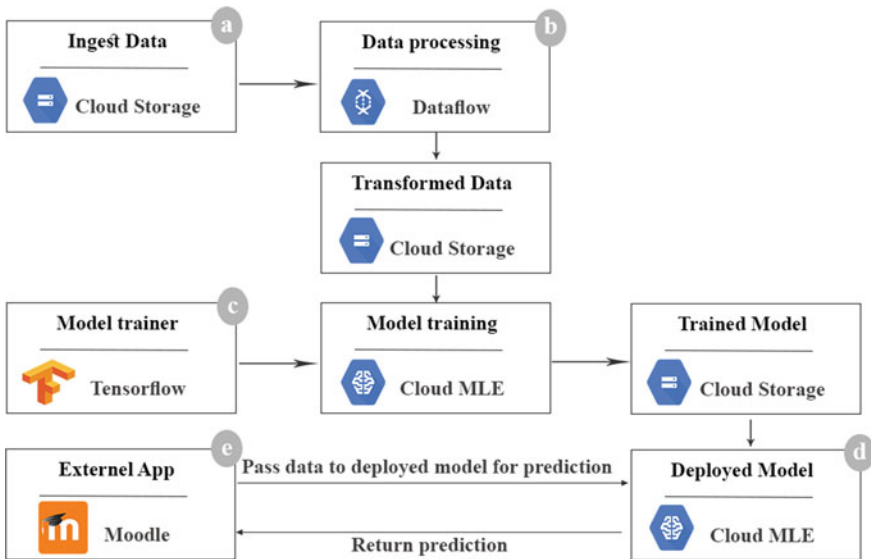


Fig. 5. The cloud ML engine prediction process [11]

6 Benefits Predicted from E-learning Based Cloud

There are plenty benefits by applying cloud-computing technology in eLearning, including:

(a) *High availability*: by combining mass storage with high-performance computing capacity, this system can provide better level of service. Cloud computing system can identify and remove the packet loss automatically, without disrupting the current functioning of the system. (b) *High security*: Data is storage intelligently in the cloud-computing model. Based on one or more data centers, administrators manage unified data, assign resources, deploy applications, and manage security. (c) *Powerful computing and storage capacity*: This requirement may resolve the characteristic of on request Self-service from cloud computing. Large-scale cloud storage offers benefits for consumers to verify the storage capacity they intend to use that is tailored to their institutions' needs and objectives as a cloud-based e-learning consumer. (d) *Stronger compatibility with file types*: as certain file types in some desktop/cell phones do not open properly, cloud-powered E-learning systems do not have to worry about these sorts of problems, as cloud based E-learning apps launch the cloud document. (e) *Students benefit* more from cloud-based eLearning, as they can improve their skills by taking online courses, attending online exams, receiving feedback from their teacher, and transferring their assessment tasks to their teachers online. (f) *Teacher benefits*: Teachers can plan for online student assessments, engagement and improved opportunities for students by content management, evaluation reviews, homework and research projects and feedback.

7 Conclusion and Future Works

The key objective of the present research was to design a model of a recommender system for finding better quality resources and reaching the learning goal. At the same time, integrated cloud computing technology can enable educational institutions to extend their services to meet their needs and promote the handling of data and educational resources. Our next work will include implementing our method and applying it to the education of our university Sidi Mohamed Ben Abdellah.

References

1. Naik NV, Madhavi K (2015) Cloud computing architecture for collaborative e-learning system. 2015 international conference on applied and theoretical computing and communication technology (iCATccT). IEEE, Davangere, Karnataka, India, pp 58–62
2. Miseviciene R, Budnikas G, Ambraziene D (2011) Application of cloud computing at KTU: MS Live@Edu Case. 12

3. Dong F, Luo J, Zhu X et al (2013) A personalized hybrid recommendation system oriented to E-commerce mass data in the cloud. 2013 IEEE international conference on systems, man, and cybernetics. IEEE, Manchester, pp 1020–1025
4. Jiang J, Pang W, Deng Y et al (2012) A blog personality recommender system based on cloud computing infrastructure. 2012 international joint conference on service sciences. IEEE, Shanghai, China, pp 1–5
5. Dahdouh K, Dakkak A, Oughdir L (2017) Integrating big data technologies in a dynamic environment EIAH dedicated to e-learning systems based on cloud infrastructure. In: Proceedings of the 2nd international conference on computing and wireless communication systems—ICWCWS'17. ACM Press, Larache, Morocco, pp 1–7
6. Zhao X (2019) A study on E-commerce recommender system based on big data. 2019 IEEE 4th international conference on cloud computing and big data analysis (ICCCBDA). IEEE, Chengdu, China, pp 222–226
7. Bourkhouk O, El Bachari E, El Adnani M (2017) A Recommender model in E-learning environment. Arab J Sci Eng 42:607–617. <https://doi.org/10.1007/s13369-016-2292-2>
8. Portugal I, Alencar P, Cowan D (2018) The use of machine learning algorithms in recommender systems: a systematic review. Exp Syst Appl 97:205–227. <https://doi.org/10.1016/j.eswa.2017.12.020>
9. Klačnja-Milićević A, Ivanović M, Nanopoulos A (2015) Recommender systems in e-learning environments: a survey of the state-of-the-art and possible extensions. Artif Intell Rev 44:571–604. <https://doi.org/10.1007/s10462-015-9440-z>
10. El Mhouthi A, Erradi M, Nasseh A (2019) Application of cloud computing in E-learning: a basic architecture of cloud-based E-learning systems for higher education. In: Ben Ahmed M, Boudhir AA, Younes A (eds) Innovations in smart cities applications edition 2. Springer International Publishing, Cham, pp 319–333
11. Laisheng X, Zhengxia W (2011) Cloud computing: a new business paradigm for E-learning. 2011 third international conference on measuring technology and mechatronics automation. IEEE, Shanghai, China, pp 716–719
12. Sikka R, Dhankhar A, Rana C (2012) A survey Paper on E-learning recommender system. IJCA 47:27–30. <https://doi.org/10.5120/7218-0024>
13. Ghauth KIB, Abdullah NA (2009) Building an E-learning recommender system using vector space model and good learners average rating. 2009 ninth IEEE international conference on advanced learning technologies. IEEE, Riga, Latvia, pp 194–196
14. Mell P, Grance T (2011) The NIST definition of cloud computing, pp 7
15. Tharam D, Chen W, Elizabeth C (2010) Cloud computing: issues and challenges. In: 2010 24th IEEE international conference on advanced information networking and applications. IEEE, Perth, WA
16. Bora UJ, Ahmed M (2013) E-learning using cloud computing. Int J Sci Mod Eng 9–12

An Intelligent System Based on Heart Rate Variability Measures and Machine Learning Techniques for Classification of Normal and Growth Restricted Children



Abdulrhman Wassil Al-Jedaani, Wajid Aziz, Abdulrahman A. Alshdadi, Mohammed Alqarni, Malik Sajjad Ahmed Nadeem, Mike P. Wailoo, and Fernando S. Schindwein

Abstract Growth restricted children have higher predisposition of developing metabolic syndrome, type-2 diabetes, hypertension and cardiovascular problems in later life. Numerous intelligence systems that have proved their effectiveness for detection of cardiac abnormalities to support medical diagnosis. Previous studies used heart rate variability (HRV) analysis techniques for distinguishing normal and growth restricted children, however those studies did not use intelligent systems for this purpose. The aim of present study is to develop an intelligent system using HRV analysis measures and machine learning (ML) techniques for early detection of cardiac abnormalities in growth restricted children. We performed two sets of experiments using interbeat interval time series data of the normal and growth restricted children and different combinations of individual characteristics of the subjects. Several ML algorithms such as linear discriminant analysis (LDA), support vector machine with linear and sigmoid kernels (SVML and SVMs), random forest (RF), and RPart are used for developing intelligent system to classify normal and growth restricted children. We evaluated the performance of the classifiers using sensitivity, specificity, area under receiver operator characteristic curve and total accuracy. The results reveal that the LDA is robust for classifying normal and LBW-IUGR children with 100% accuracy at all cross validation formulations. The SVMs and LDA revealed highest accuracy, whereas, RF and Rpart were robust for classifying LBW-IUGR and ABW_IUGR. Our findings show that the intelligent system developed using HRV analysis markers and ML techniques could be a reliable tool for identifying future risk of cardiac abnormalities in IUGR children.

A. W. Al-Jedaani (✉) · W. Aziz · A. A. Alshdadi · M. Alqarni
College of Computer Science and Engineering, University of Jeddah, Jeddah 23218, Saudi Arabia
e-mail: aaljedaani0066.stu@uj.edu.sa

W. Aziz · M. S. A. Nadeem
Department of Computer and Information Technology, University of Azad Jammu and Kashmir,
Muzaffarabad 13100, AJK, Pakistan

M. P. Wailoo · F. S. Schindwein
University of Leicester, University Road, Leicester LE1 7RH, UK

Keywords Growth restricted children · Heart rate variability · Intelligent system · Machine learning techniques

1 Introduction

Intrauterine growth restriction (IUGR) is the inability of the fetus to attain the adequate growth potential due to functional and/or anatomical disorders while in the mother's womb [1, 2]. The prevalence of IUGR is estimated to be approximately 5–7% [3]. IUGR may be connected with the risk of developing numerous later life diseases such as hypertension, type 2 diabetes and cardiovascular problems [4–6]. Studies in animals have highlighted that IUGR is related to persistent changes in a wide range of physiological, structural and metabolic parameters [7]. Low birth weight (LBW) men and women with short stature and/or stunted growth or who were small compared to the size of placenta have elevated risk of developing cardiovascular problems [4]. The growth restricted adults have statistically significant but elusive changes in structural and functional parameters of the cardiovascular system, which are not significant during childhood and are not likely to play a pathogenic role to initiate cardiovascular problems [8].

Barker et al. [4] proposed that the initiation of cardiovascular problems is due to unpropitious conditions during the life in utero and adverse environment during early childhood. Numerous epidemiological evidences have reinforced this hypothesis by elaborating the association of birth weight with risk of cardiovascular disease [9, 10]. The link of LBW with the onset of cardiovascular problems have been replicated in Europe, North America and India among both male and female [5, 11].

The autonomic nervous system (ANS) controls the regularity mechanism of heart and alterations in its controlling mechanism such as increased pulse, hypertension and HRV have been reported in LBW adults [12, 13]. HRV analysis is a non-invasive tool used to measure synergic activity of the ANS that has been extensively used in numerous studies for assessing cardiac autonomic control under both physiological and pathological conditions [14–18]. Researchers used numerous linear and nonlinear HRV analysis techniques during the last four decades for assessing malfunction of the cardiac autonomic control [14–22].

Several intelligent systems have been using information encoded in the IBI time series and ML techniques for detection of cardiac abnormalities to support medical diagnosis [20–22]. Aziz et al. [20] used normalized corrected Shannon entropy [27] for classification of normal sinus rhythm (NSR) and congestive heart failure (CHF) subjects. Awan et al. [21] proposed multiscale normalized corrected Shannon entropy used different ML classifiers for classification of NSR and CHF subjects. Choudhary et al. [22] proposed grouped horizontal visibility graph entropy for classification normal and patients suffering from CHF and atrial fibrillation. Previous studies [15–17] used HRV analysis markers for distinguishing normal and growth restricted children, however those studies did not use intelligent systems for their classification.

In this study, we have used information encoded in linear and nonlinear HRV measures as features and ML techniques such as linear discriminant analysis (LDA), support vector machine linear (SVML), SVM sigmoid (SVMS), random forest (RF) and RPart for classification. The evaluation metrics used in the study include sensitivity, specificity, total accuracy and area under ROC. The rest of paper is organized as follows: In Sect. 2, we discuss the data, HRV analysis techniques, ML techniques, statistical analysis and evaluation measures used in the study. The experimental results of different ML techniques for classification of normal and IUGR children are detailed in the Sect. 3, and Sect. 4 provides the brief conclusion of the study.

2 Materials and Methods

Figure 1 presents the schematic diagram of the procedure used for classifying normal versus LBW_IUGR, normal versus ABW_IUGR and LBW_IUGR versus ABW_IUGR children. In the first step, we extracted anthropometric and HRV features. The HRV features were extracted using linear and nonlinear HRV markers and then applied ML algorithms for classification. For training and testing of the classifiers, we used standard Jack-knife 3, 4, and fivefold cross validation techniques. Tenfold cross validation was not used due to the smaller number of subjects.

2.1 Data Set

The data used in this study was provided by the Bioengineering laboratory of the University of Leicester, UK. The data were collected from 9 to 10 year old children at Leicester Royal Infirmary, as a follow-up study for investigating the long-term effects of the IUGR and to assess the risk of cardiac abnormalities in growth restricted during adulthood [23]. Data collected include anthropometric parameters of the children and parents, clinical parameters, day and night blood pressure readings and pulse rate. A 24 h ECG of normal and IUGR children was acquired using a Lifecard CF ambulatory ECG recorder. The children were asked to perform routine daily activities and parents were asked to take notes of all activities of the children. The recording of children suffering from heart block, or recordings <23 h with more than 1% of ectopic beats were excluded. In this study we used the data of 68 children comprising of 32 normal and 36 IUGR children. Based on birth weight, we divided the IUGR children into two groups: LWB-IUGR having birth weight <2.5 kg, and ABW-IUGR having birth ≥ 2.5 kg.

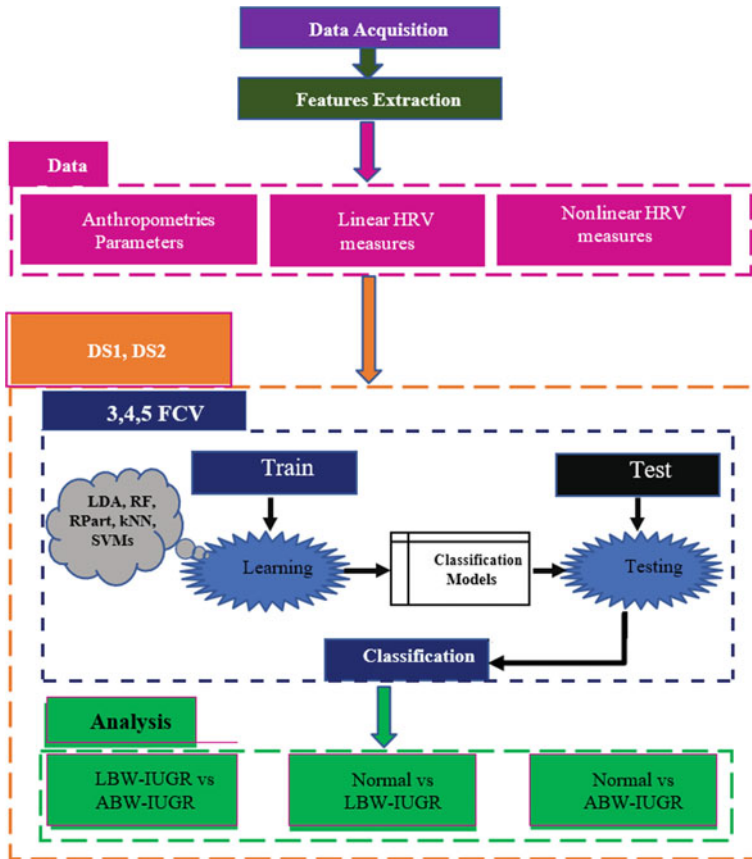


Fig. 1 Schematic diagram illustrating classification procedure

3 Feature Extraction

The feature extraction is an important step in any machine learning-based solution. In this study, we used anthropometric parameters and linear and nonlinear HRV feature sets. We used anthropometric parametric birth weight, current weight, weight gain, height and BMI as the features. The linear techniques comprise of standard time and frequency domain measures [14]. The time domain measures included mean of RR-interval (MRR), mean of heart rate (MHR), standard deviation of normal-to-normal interbeat intervals (SDNN), standard deviation of average normal-to-normal interbeat intervals calculated over 5 min segment within the entire period of recording (SDANN) and square root of mean squared differences of consecutive NN intervals (RMSSD). The frequency domain analysis was performed by estimating power spectral density using fast Fourier transform-based Welch periodogram. The ratio of high frequency to low frequency (LF/HF) is used as the frequency domain feature.

The nonlinear HRV features used in this study include approximate entropy (ApEn) [24], sample entropy (SamEn) [25], Poincaré plot descriptors SD1 and SD2 [26, 27], traditional Porta [28] and Costa indices [29] and redefined Porta and Costa indices [30].

3.1 Classification and Evaluation

In this study we used LDA, SVML, SVMs, RF and RPart supervised machine learning techniques for classification. LDA is the generalization of Fisher's linear discriminant [31], which models the distribution of predictors in each of the response classes and uses Bayes' theorem for estimating the probability of class association. The SVM is one of the most robust methods used for classification tasks and pattern recognition problems [32]. SVM is a binary classifier that maps the input vector to construct a high dimensional hyperplane or a set of hyperplanes. RF is an ensemble classifier that generates a multitude of decision trees during training and its output is the modal class (class with maximum votes) [33, 34]. RPart is the R-package that is an implementation of 'Classification And Regression Trees' (CART) algorithm. CART is an umbrella term used for predictive ML algorithms for classification and regression tree analysis [33]. We used Jack-knife k-fold cross validation technique for training/testing data formulation and parameter optimization. Due to the small sample size, three-, four- and five-fold cross validation (CV) was used to evaluate the performance of classifiers for different feature extracting strategies. Sensitivity, specificity, area under ROC (AUC) and total accuracy were used as evaluation metrics.

4 Results

Table 1 provides the comparison of the three groups based on their baseline characteristics. One-way ANOVA was used to determine the variability among group means and within the groups. One-way ANOVA is an omnibus test statistic and is unable to determine which specific groups were significantly distinguishable from each other. To determine which specific groups are significantly different we used Bonferroni post-hoc test. It is evident from the all parameters in the table that LBW-IUGR were smaller at the time of birth and remained smaller at the age of 10 years. The birthweight, current weight and BMI are significantly smaller for LBW-IUGR than normal children. To classify normal and different IUGR subjects, we designed two experimental settings. In experimental setting-1, we used features including current weight, weight gain, current height, BMI, MRR, SDNN, MHR, SDANN, RMSSD, LF/HF, SD1, SD2, ApEn, SamEn, traditional Porta index (PI), traditional Costa index (CI), redefined PI and CI, absolute deviation of traditional and redefined PI from 50 and absolute values of redefined PI and CI. Experimental setting-2 comprised of features current weight, weight gain, current height, BMI, MRR, SDNN, MHR,

Table 1 Comparison of normal, ABW-IUGR and LBW-IUGR children

Parameters	Mean \pm SD values of the parameters			Significance Level	
	Normal	ABW-IUGR	LBW-IUGR	Normal versus ABW-IUGR	Normal versus LBW-IUGR
Birth weight (kg)	3.51 \pm 0.48	2.94 \pm 0.35	2.31 \pm 0.19	<0.001	<0.001
Current weight (kg)	32.80 \pm 6.40	30.02 \pm 7.15	27.80 \pm 4.82	0.383	0.014
Weight gain (kg)	29.38 \pm 6.22	27.08 \pm 7.17	25.49 \pm 4.84	0.664	0.086
Height (m)	133.82 \pm 5.1	132.50 \pm 7.33	131.15 \pm 5.68	1	0.338
BMI (kg/m ²)	18.23 \pm 2.56	16.91 \pm 2.68	16.13 \pm 2.47	0.28	0.016
Gestational age	39.16 \pm 0.92	39.56 \pm 1.59	38.40 \pm 0.94	0.72	0.061

SDANN, RMSSD, LF/HF, SD1, SD2, ApEn, SamEn, traditional and redefined PI and CI.

In Table 2, the results of the developed classification models to classify normal and different IUGR subjects using supervised ML classifiers (setting-1) are shown. LDA outperformed all other classifiers at all the three-, fold-, and five-fold CV to classify normal and LBW-IUGR. SVMS provided best performance in distinguishing normal versus ABW-IUGR children at five-fold CV formulation. The RPart classifier was robust in distinguishing LBW-IUGR versus APW-IUGR children at three- and four-fold CV formulations whereas RF outperformed all other classifiers at fivefold CV formulation to classify LBW-IUGR versus ABW-IUGR children. In Fig. 2, the bar chart of total accuracy to distinguish different groups for setting-1 are shown. LDA achieved 100% accuracy for distinguishing normal versus LBW-IUGR children for all CV formulations, SVM provided 97.92% accuracy for classifying normal and ABW-IUGR children at fivefold cross validation, whereas RF classifier reached 100% accuracy for distinguishing LBW-IUGR and ABW-IUGR at fivefold CV.

In Table 3, results of classifiers for classification of normal and growth restricted children are detailed. In setting-2, LDA also provided highest degree of separation for classifying normal and LBW-IUGR at all the CV formulations. The LDA classifiers also revealed highest degree of separation for normal and ABW-IUGR children at three and four-fold cross validation formulations, and SVM at fivefold CV. The classifier RPart at threefold CV and RF at 4 and fivefold CV formulations provided higher degree of separation between LBW-IUG and ABW-IUGR children. Figure 3 illustrates the comparison of normal and IUGR children in terms of accuracy. The LDA classifier provided 100% accuracy for classifying normal and LBW-IUGR at all the cross validation formulations. LDA showed 97.7% accuracy at 3 and fourfold CV and SVM showed 97.7% accuracy fivefold CV for classifying normal and ABW-IUGR. The RPart revealed 97.7% accuracy at threefold CV, whereas RF provided

Table 2 Evaluation metrics to classify different groups: normal versus LBW IUGR, normal versus ABW_IUGR and ABW-IUGR versus LBW-IUGR using supervised ML classifiers (Setting 01)

Classifiers	Normal versus LBW-IUGR		Normal versus ABW-IUGR		ABW-IUGR versus LBW-IUGR	
	Sensitivity	Specificity	AUC	Sensitivity	Specificity	AUC
<i>Threefold cross validation</i>						
LDA	1.00	1.00	1.00	1.00	0.94	0.98
SVML	0.81	1.00	0.88	0.97	1.00	0.97
SVMS	0.75	1.00	0.86	0.84	1.00	0.88
RF	0.75	1.00	0.86	0.78	0.88	0.80
RPart	0.84	0.95	0.88	0.78	0.88	0.80
<i>Fourfold cross validation</i>						
LDA	1.00	1.00	1.00	1.00	0.94	0.98
SVML	0.81	1.00	0.88	0.97	1.00	1.00
SVMS	0.75	1.00	0.86	0.84	1.00	0.97
RF	0.63	1.00	0.81	0.78	1.00	0.90
RPart	0.84	1.00	0.90	0.78	1.00	0.90
<i>Fivefold cross validation</i>						
LDA	1.00	1.00	1.00	1.00	0.88	0.97
SVML	0.88	1.00	0.92	0.97	1.00	0.97
SVMS	0.75	1.00	0.86	0.97	1.00	0.97
RF	0.72	1.00	0.84	0.88	1.00	0.90
RPart	0.88	1.00	0.92	0.88	1.00	0.90

Sensitivity

Specificity

AUC

Sensitivity

Specificity

AUC

Threefold cross validation

LDA

SVML

SVMS

RF

RPart

Fourfold cross validation

LDA

SVML

SVMS

RF

RPart

Fivefold cross validation

LDA

SVML

SVMS

RF

RPart

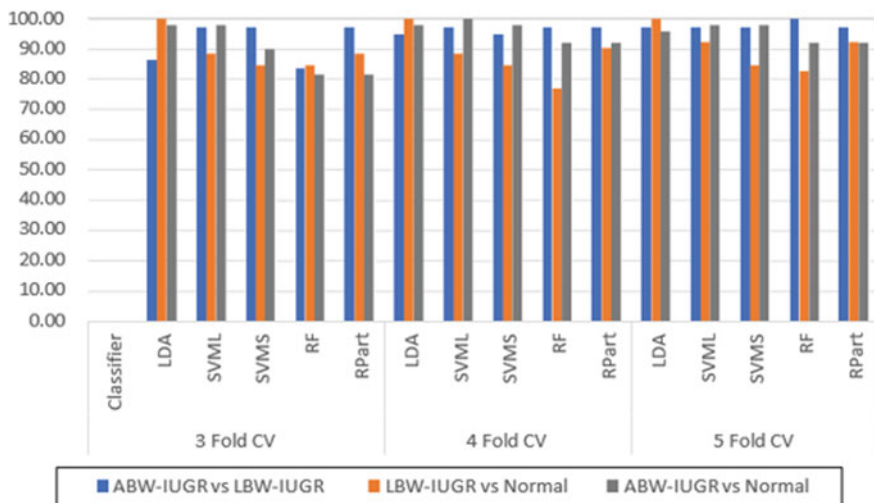


Fig. 2 Total accuracy of ML classifiers for distinguishing different groups (setting-1)

100% accuracy at 4 and fivefold CV formulations for classifying LBW-IUGR and ABW-IUGR children.

5 Conclusion

In this study, an intelligent system is developed for classification of normal and IUGR children using linear and nonlinear HRV features and ML classifiers (LDA, SVM, SVMS, RF and RPart). One of the difficulties is obtaining accurate HRV data for many children to long time. To classify normal versus LBW-IUGR, normal versus ABW-IUGR and LBW-IUGR versus ABW-IUGR, we designed two experimental settings. For all the ML classifiers and both settings the Jack-Knife three-, four-, and five-fold cross validation are used to develop intelligent systems. The results clearly demonstrate that the combination of HRV metrics and ML algorithms is useful and reliable for determining the future risks of heart anomalies in developmentally restricted children at an early stage. Moreover, our results also suggest that an intelligent system which provides a comprehensive analysis of the available HRV data using supervised ML classifiers is of benefit to the physicians for robust classification of HRV data. In this study, we have used two settings to exploit the strength of different classifiers. In future, we will explore more settings based on the combination of different HRV features to exploit the strength of different of ML classifiers effectively.

Table 3 Evaluation metrics to classify different groups: normal versus LBW IUGR, normal versus ABW_IUGR and ABW-IUGR versus LBW-IUGR using supervised ML classifiers (Setting 02)

Classifiers	Normal versus LBW-IUGR			Normal versus ABW-IUGR			ABW-IUGR versus LBW-IUGR		
	Sensitivity	Specificity	AUC	Sensitivity	Specificity	AUC	Sensitivity	Specificity	AUC
<i>Threefold cross validation</i>									
LDA	1.00	1.00	1.00	1.00	0.94	0.98	0.94	0.80	0.87
SVML	0.81	1.00	0.88	0.97	1.00	0.97	0.94	1.00	0.98
SVMS	0.75	1.00	0.86	0.84	1.00	0.88	0.94	1.00	0.98
RF	0.75	1.00	0.86	0.78	0.88	0.80	0.94	0.75	0.84
RPart	0.84	0.95	0.88	0.78	0.88	0.80	0.94	1.00	0.98
<i>Fourfold cross validation</i>									
LDA	1.00	1.00	1.00	1.00	0.94	0.98	1.00	0.90	0.94
SVML	0.81	1.00	0.88	0.97	1.00	1.00	1.00	0.95	0.97
SVMS	0.75	1.00	0.86	0.84	1.00	0.97	0.94	0.95	0.94
RF	0.63	1.00	0.81	0.78	1.00	0.90	1.00	0.95	0.97
RPart	0.84	1.00	0.90	0.78	1.00	0.90	0.94	1.00	0.98
<i>Fivefold cross validation</i>									
LDA	1.00	1.00	1.00	1.00	0.88	0.97	0.94	1.00	0.98
SVML	0.88	1.00	0.92	0.97	1.00	0.97	0.94	1.00	0.98
SVMS	0.75	1.00	0.86	0.97	1.00	0.97	0.94	1.00	0.98
RF	0.72	1.00	0.84	0.88	1.00	0.90	1.00	1.00	1.00
RPart	0.88	1.00	0.92	0.88	1.00	0.90	0.94	1.00	0.98

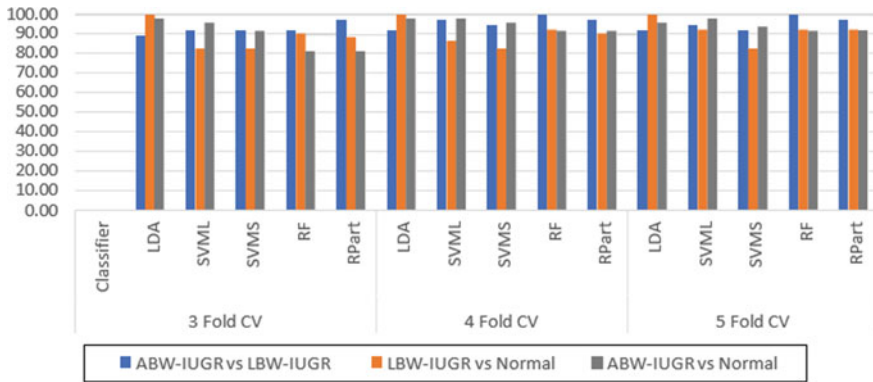


Fig. 3 Total accuracy of ML classifiers for distinguishing different groups for setting-2

References

- Ferrario M, Signorini MG, Magenes G (2009) Complexity analysis of fetal heart rate variability: early identification of severe intrauterine growth-restricted fetuses. *Med Biol Eng Comput* 47(9):911–919
- Sharma D, Shastri S, Sharma P (2016) Intrauterine growth restriction: antenatal and postnatal aspects. *Clin Med Insights Pediatr* 10:67–83
- Brodsky D, Christou D (1998) Current concepts in intrauterine growth restriction. *J Intens Care Med* 19(6):307–319
- Barker DJP, Osmond C, Golding J, Kuh D, Wadsworth MEJ (1989) Growth in utero, blood pressure in childhood and adult life, and mortality from cardiovascular disease. *Brit Med J* 298(6673):564–567
- Eriksson JG, Forsen T, Tuomilehto J, Osmond C, Barker DJP (2001) Early growth and coronary heart disease in later life; longitudinal study. *Brit Med J* 322(7292):949–953
- Kamen PW, Krum H, Tonkin AM (1996) Poincaré plot of heart rate variability allows quantitative display of parasympathetic nervous activity in humans. *Clin Sci* 91(2):201–208
- Schäffer L, Burkhardt T, Müller-Vizentini D, Rauh M, Tomaske M, Meith RA, Bauersfeld U, Beinder E (2008) Cardiac autonomic balance in small-for-gestational-age neonates. *Am J Physiol Heart Circ Physiol* 294:H884–H890
- Arnott C, Skilton MR, Ruohonen S, Juonala M, Viikari JSA, Kähönen M, Lehtimäki T, Laitinen T, Celermajer DS, Raitakari OT (2015) Subtle increases in heart size persist into adulthood in growth restricted babies: the cardiovascular risk in young finns study. *Open Heart* 2:e000265
- Huxley RR, Shiell AW, Law CM (2001) The role of size of birth and postnatal catch-up growth in determining systolic pressure: a systematic review of the literature. *J Hypertens* 18(7):815–831
- Law CM, Shiell AW (1996) Is blood pressure inversely related to birth weight? The strength of evidence from a systematic review of the literature. *J Hypertens* 14(8):935–941
- Barker DJP (2004) The developmental origin of chronic adult disease. *Acta Paediatr Suppl* 93:26–33
- Jones A, Bada A, Ward AM, Osmond C, Phillips DI, Moore VM, Simpson DM (2007) Size at birth and autonomic function during psychological stress. *Hypertension* 49(3):548–555
- Ward AM, Moore VM, Steptoe A, Cockington RA, Robinson JS, Phillips DI (2004) Size at birth and cardiovascular responses to psychological stressors: evidence for prenatal programming in women. *J Hypertens* 22(12):2295–2301
- Task force of the European society of cardiology and north American society of pacing electrophysiology: heart rate variability: standards of measurement, physiological interpretation and clinical use. *Circulation* 93(5):1043–1065 (1996)

15. Aziz W, Schlindwein FS, Wailoo MP, Biala TA, Rocha FC (2012) Heart rate variability analysis of normal and growth restricted children. *Clin Auton Res* 22(2):91–97
16. Biala T, Aziz W, Wailoo MP, Schlindwein FS (2012) Heart rate variability: linear and non-linear analysis of pre-awake period for normal and intrauterine growth restricted children at 10 year. *Measurement* 45(8):2096–2102
17. Aziz W, Biala T, Habib N, Abbasi MS, Wailoo MP, Schlindwein FS (2013) Heart rate variability in low birth weight growth restricted children during sleep and wake stages. *Measurement* 46(8):2300–2305
18. de Souza Filho LFM, de Oliveira JCM, Ribeiro MKA, Moura MC, Fernandes ND, de Sousa RD, Rebelo ACS (2019) Evaluation of the autonomic nervous system by analysis of heart rate variability in the preterm infants. *BMC Cardiovasc Disorders* 19(1):1–6
19. Arif M, Aziz W (2005) Application of threshold-based acceleration change index (TACI) in heart rate variability analysis. *Physiol Meas* 26(5):653–665
20. Aziz W, Rafique M, Ahmad I, Arif M, Habib N, Nadeem M (2014) Classification of heart rate signals of healthy and pathological subjects using threshold based symbolic entropy. *Acta Biol Hung* 65:252–264
21. Awan I, Aziz W, Shah IH, Habib N, Alowibdi JS, Saeed S, Shah SAA (2018) Studying the dynamics of interbeat interval time series of healthy and congestive heart failure subjects using scale based symbolic entropy analysis. *PLoS One* 13(5)
22. Choudhary GI, Aziz W, Khan IR, Rahardja S, Franti P (2019) Analysing the dynamics of interbeat interval time series using grouped horizontal visibility graph. *IEEE Access* 7:9926–9934
23. Jackson J, Wailoo M, Thompson J, Petersen S (2004) Early physiological development of infants with intrauterine growth retardation. *Arch Dis Childhood-Fetal Neonatal Ed* 89(1):F46–F50
24. Pincus SM (1991) Approximate entropy as a measure of system complexity. *Proc Natl Acad Sci* 88:2297–2301
25. Richman JS, Moorman JR (2000) Physiological time-series analysis using approximate entropy and sample entropy. *Am J Physiol Circ Physiol* 278:H2039–H2049
26. Marciano F, Migaux ML, Acanfora D, Furgi G, Rengo F (1994) Quantification of Poincaré maps for the evaluation of heart rate variability. *Comput Cardio* 21:577–580
27. Brennan M, Palaniswami M, Kamen P (2001) Do existing measures of Poincaré plot geometry reflect nonlinear features of heart rate variability. *IEEE Trans Biomed Eng* 48:1342–1347
28. Porta A, Guzzetti S, Montano N, Gneccchi-Ruscione T, Malliani A (2006) Time reversibility in short-term heart period variability. *Comp Cardiol* 33:77–80
29. Costa M, Goldberger AL, Peng CK (2005) Broken asymmetry of the human heartbeat: loss of time irreversibility in aging and disease. *Phys Rev Lett* 95:198102
30. Karmakar CK, Khandoker AH, Gubbi J, Palaniswami M (2009) Defining asymmetry in heart rate variability signals using a Poincaré plot. *Physiol Meas* 30(11):1227–1240
31. Fisher RA (1936) The use of multiple measurements in taxonomic problems. *Annals Eugenics* 7(2):179–188
32. Vapnik VN (1999) An overview of statistical learning theory. *IEEE Trans Neural Netw* 10(5):988–999
33. Breiman L (1984) Classification and regression trees. Chapman & Hall/CRC, Boca Raton
34. Liaw A, Wiener M (2002) Classification and regression by random forest. *R News* 2(2):18–22

Predicting Student's Performance Based on Cloud Computing



Youssef Jedidi , Abdelali Ibriz, Mohamed Benslimane, Mehdi Tmimi, and Mounia Rahhali

Abstract COVID-19 Coronavirus epidemic has created a calamitous worldwide situation. The Moroccan University Sidi Mohammed Ben Abdellah of Fez mobilized to develop platforms for distance learning. New tools for e-learning (online learning) were developed, and advanced learning management systems (LMSs) were deployed. Predicting student's performance is more difficult because of the large amount of data including the huge number of learners and the educational content variety. Currently, in the University of Fez, the lack of current mechanisms to assess and control the development and performance of the students is not discussed. In this context, Cloud computing is becoming a hot research subject when faced with large-scale data and is commonly used to solve this issue. Big Data is a leading concept because of its permanent optimization and opportunities offering data collection, analysis, storage, optimization, processing, and data representation to e-learning professionals. The objective of this paper is to develop a model of predicting student's performance based on cloud computing as part of the normal enhancement of online learning by incorporating new information and communication technologies.

Keywords Prediction student's performance · Big data · Cloud computing · Educational data mining · E-learning

Y. Jedidi (✉) · A. Ibriz · M. Benslimane · M. Tmimi
Innovative Technologies Laboratory, EST, Sidi Mohamed Ben Abdellah University, Fez, Morocco
e-mail: Youssef.jedidi@usmba.ac.ma

A. Ibriz
e-mail: a.ibriz@gmail.com

M. Benslimane
e-mail: mohamed.benslimane@usmba.ac.ma

M. Tmimi
e-mail: mehdi.tmimi@usmba.ac.ma

M. Rahhali
ENSA, Sidi Mohamed Ben Abdellah University, Fez, Morocco
e-mail: mounia.rahhali@usmba.ac.ma

1 Introduction

The novel Coronavirus disease (COVID-19) first shown in Wuhan, China on 31 December 2019. It started quickly spreading throughout the world. Universities across the world have opted for online courses in a global effort to contain the coronavirus. Countless teachers are caught off guard in the face of the challenge of transforming what is left of their normally offered course into an online course.

The Moroccan University of Fez mobilized to set up distance learning platforms. The pedagogical, administrative and technical teams of Sidi Mohammed Ben Abdellah University in Fez are hard at work preparing the distance learning platforms for students, as part of efforts to reduce the impact of the spread of Covid19.

E-learning is becoming the primary emphasis of learning modernization with the rapid development of information about education. E-learning data mining is the process of translating raw data from the software application of Sidi Mohammed Ben Abdellah University into valuable information that could be used by students, teachers, researchers, parents, educational administrators, etc. E-learning can also be comprehended as an online teaching and learning activity, and can generate systematic learning record data.

The quality of learning in academic institutions is considered to be one of all country's development keys, so it is extremely important that Sidi Mohammed Ben Abdellah University develop strategies to enhance their efficiency system. After assessing the performance of the students, these interventions can be prepared as the advanced estimate of the failure rate will help educational institutions make proactive decisions to reduce this rate [1].

Expanding beyond the at-risk students would also be desirable to predict all student's future performance to enable for a feedback mechanism to improve learning and understanding for a wide selection of students and during courses. As an automated process, prediction of student performance does have the potential to minimize the evaluation duties of teachers. The data attributes used to predict the performance of the students that include several features, such as student grades, demographic data such as age, sex, address, and social information such as cohabitation status of parents, work of father and mother, family size, etc.

Cloud computing has become a hot research subject when faced with large-scale data and is commonly used to solve this issue. Google, Amazon, IBM, and other big information technology firms have put forward their own architecture for cloud computing.

Cloud computing on the basis of parallel computing, utility computing, distributed computing and grid computing is further developed. Cloud computing is still in the primary research and implementation stage. The basic aspect of cloud computing is: cloud infrastructure has large-scale storage and processing capability, and cloud computing can provide virtualization technology services. Such cloud storage enable data to be stored, analyzed, and applied.

In this work, we are interested to design a model of predicting student's performance based on cloud computing as part of the standard improvement in online learning through the adoption of new information and communication technologies.

This paper is arranged as follows: Sect. 2 gives a literature review of related works. Section 3 describes E-learning. Prediction student's performance in educational Data Mining is presented in Sect. 4. Section 5 presents cloud computing. Section 6 describes architecture of prediction students' performance based on cloud computing. Finally, Sect. 7 presents conclusion.

2 Related Works

Education is the foundation of every country or region. It is one of the country's social, economic and political growth measures. Student success in higher learning institutions is the factor most essential to the efficiency of a university.

Sangeeta et al. [2] told That the performance of the student relies on his cognitive abilities, and is affected by several factors. Lately, a slow learner comprehends things, requires things to be understood with a lot of precise resources in order to be successful especially in comparison to a quick learner.

Shahiri et al. [3] review the data mining methods used to predict student performance, concentrates also how to use the prediction algorithm to classify a most important characteristics in the student information.

Anshari et al. [4] discussed recent challenges, issues, and developments in Internet usage, with a focus on online education and its capacity in the Big Data. Using of big data in the education guarantees better teaching and learning delivery, thereby improving the quality of services.

Ashraf et al. [5] introduced a new paradigm for Big Data Management in e-learning systems. The proposed model will determine the behavior of learners in the E-Learning system by using Hadoop and Map Reduce to manage educational big data. The article highlights the need to increase the performance of Big Data analytics in educational systems. Efficient handling of big data is needed to support learners and educational systems.

El Mhouti et al. [6] showed that cloud has enormous effects on e-learning forms, and is the central technology in higher education for the next generation of e-learning. Cloud-based e-learning platforms are evolving as an appealing way to provide versatile and accessible e-learning services that could be viewed from any laptop, anywhere, and anytime.

Though several researchers have established on prediction of student performance, very less attention has been dedicated to predicting student performance using cloud computing. This is why we are interested in proposing a new architecture of student performance prediction based on the latest generation of Big Data technologies applied in a cloud computing environment to improve e-learning systems efficiency and availability.

3 E-learning

This section presents an overview of e-learning in general including its definition and using of e-learning in education.

3.1 The Concept of E-learning

The Internet has been one of the valuable ways in which students and teachers can acquire and share information to make resources available for learning and research [7]. Technology-based e-learning involves using of the internet and other important technologies to educate learners, produce learning materials, and administer courses in an entity too though [8].

E-learning, the nature of e-learning, is learning with the “e” as the only learning method, e-learning, internet learning or online learning. Learners can find understanding any where and any time via the “e” learning method.

In certain definitions e-learning includes more than only providing courses that are completely online. For example, Hawkins and Oblinger mentioned that e-learning has changed from a full-online course to the use of new technology in order to offer portion or all of a course autonomous of place and perpetual time [9]. E-learning is also described by the European Commission as using of Internet and new technologies of multimedia to improve learning quality by enabling access to services and facilities as collaboration and exchanges.

E-learning refers using of ICT (information and communication technologies) to enable online learning/teaching resources to be accessible. Abbad et al. identified e-learning in its broadest terms to include every learning that is allowed by electronic means [10]. Nevertheless, they narrowed down this concept to mean learning driven by using of digital technologies. Some researchers further narrow this concept as any internet-activated or web-based learning [11].

3.2 The Use of E-learning in Education

The development of digital and information technology, as using of the internet as a modern learning tool, has brought about fundamental changes in the traditional teaching method. Development in information technology has created more choices for today’s education. E-learning has been recognized by school agendas and educational institutions as having the possibility of transforming people, skills, knowledge and performance. Also, universities, colleges and other higher learning institutions are also promoting the capacity of online courses in a rapidly developing market for cyber education.

E-learning, has become increasingly relevant in higher academic institutions. The expansion and introduction of a band of e-learning equipment has triggered plenty of changes in educational institutions, especially as regards their support processes and educational delivery [12].

Much like there are various forms of e- Learning, we say there are different ways to use the technique in education as well. Algahtani, In its assessment of the effectiveness, discovered three models of the use of e-learning in education, the "blended e-learning, adjunct and Wholly Online" [13].

4 Predicting Student's Performance in Educational Data Mining

Using of data mining methods in education is increasingly of interest in research. This new paradigm, Educational Data Mining, is important in developing methods of discovering knowledge from educational data environments. The data can be obtained from organizational and historical data that exist in educational institution databases. Student data can be personal or academic, and e-learning systems can collect it. Educational data mining uses numerous methods such as Naïve Bayes, Decision Trees, Neural Networks and others [14].

In the educational field, Data mining is a method of turning transforming academic institutions' collected data into useful knowledge that can be used for decision-making. It can be applied to the different data used to structure the educational domain, to model students, to communicate with the client, to predict student grade, etc.

Predicting the student's performance with high precision is more useful in recognizing beginning students with low academic achievement. Student performance is a measure of the university's enrolment management and academic performance. The capability to predict a student's performance in educational settings is very important. Student's academic performance is dependent on numerous factors such as psychological, social, physical and other variables of the environment [3]. Data Mining is Quite effective method for achieving this goal. Classification is the most important data mining techniques in e-learning. It is a technique of predictive data mining that uses known features from various data to predict values.

4.1 The Prediction Methods Used for Student Performance

Usually predictive modeling is used in the method of educational data mining in predicting student performance. There are many methods that are used to construct the predictive models, which are regression, classification, and categorization. Classification is the most famous process to predict the performance of the students. Under

classification task, several algorithms have been applied for predicting students' performance. Artificial Neural Networks, Naive Bayes, Support Vector Machine, Decision tree and K-Nearest Neighbor are amongst the algorithms used.

Decision Tree might be one of the famous predictive techniques. Most researchers have used this technique to discover large or small data structure and predict the value because of its understandability and simplicity [15]. Romero et al. said the models of the decision tree are clearly recognized by reasoning and can be converted directly into IF-THEN rules [16].

Neural Network: Another common technique used in educational data mining is the Neural network. The benefit of the neural network is that it has the ability to identify all possible variable interactions among predictors. Even in the complex nonlinear relationship between independent and dependent variables, the neural network can also do a full identification with no doubt.

Support Vector Machine: Which is a collection of supervised learning techniques developed to fix the challenges of discrimination and regression. Given a dataset with two linearly separable target classes, the SVM's aim is to find the best line dividing the two groups. This line is called a hyperplane, in higher dimensions. A hyperplane is a line or more formally called a discriminant in n -dimensional space that divides two groups. When drawn in 2-D space a hyperplane is named a line. In 3-D space, it is considered a plane, and the discriminant is named a hyperplane in dimensions greater than 3.

K-Nearest Neighbor is among the most important yet fundamental classification algorithms in machine learning it refers to the domain of supervised learning and finds strong use in pattern analysis, data mining, and intrusion detection. The KNN rule classifies every other unidentifiable example in the training set by the dominant label between many nearest k -nearest neighbors. Its success in this highly dependent on the distance measure used to define nearest neighbors. Some k NN classifiers use simple Euclidean metrics to quantify similar characteristics between examples described as vector inputs, in the absence of prior information [17].

The Naïve Bayes is a supervised classifier; these are based on Bayes theorem. The Naïve Bayes process is a good probabilistic analyzer that calculates a series of probabilities by summing the frequency and value mix of a data set [18]. The Naïve Bayes classification aims to classify the performance learners of the students for semester examination based on their marks in some topics [19].

5 Cloud Computing

This section presents an overview of cloud computing in general including its definition, Characteristics, and Services.

5.1 Definition

The term “cloud” comes from the world of telecommunications when companies started using virtual private network (VPN) services for data transmission [20].

The lack of a usual definition of cloud computing has, of course, not only generated market expectations, but also a good deal of confusion and skepticism [21].

National Institute of Standards and Technology (NIST) introduced the most acceptable definition of cloud computing.: “Cloud computing is a paradigm that enables open, secure, on-demand network access to a common set of computing customizable tools (e.g., networks, servers, storage, software, and services) that can be easily distributed and published With minimum administrative effort or interaction between service providers” [3].

5.2 Cloud Computing Characteristics

Because of their extensive requirements, cloud service providers deliver diverse models. Compared with other technologies, these requirements improve the performance and reliability of cloud-based services. Cloud computing characteristics are classified into five essential parts:

- **On-demand self-service.** Users can ask and control on demand their own computing services, and configure their computer environments later.
- **Broad network access.** Cloud services are accessible via private networks or the Internet and accessed via default mechanisms [6].
- **Resource pooling.** The company’s computing services are distributed to support multiple customers to use a multi-tenant model with dynamically distributed and reassigned specific virtual and physical resources per to the user demand [22].
- **Rapid elasticity.** Abilities can be supplied and released dynamically to quickly scale outwards and inward in line with the request in few cases directly. To the user, the supplying Abilities seem almost limitless and can be appropriated at any time in any proportion.
- **Measured service.** The use of cloud computing resources can be reported monitored, and controlled, offering accountability to both provider and the consumer [23].

5.3 Layers and Services of Cloud Computing Architecture

The architecture of the cloud environment is split into four major layers: Physical (Hardware), Virtual Infrastructure, Platform and Application. We describe each of them in detail in Fig. 1:

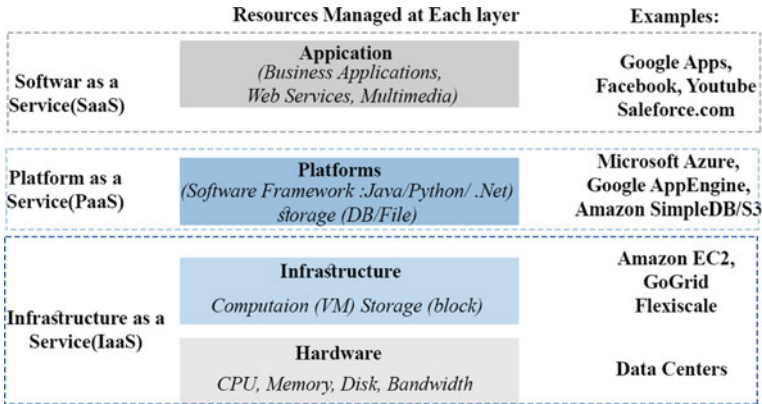


Fig. 1 Architecture of cloud computing [22]

A cloud client is a hardware computer and/or software application that focuses on cloud computing to deliver applications, or specifically designed to deliver cloud services. The cloud computing provides many services. The service models are:

Software as a Service (SaaS). The user’s ability is to use the software that the company operates on an infrastructure of the cloud. This mode requires full support for maintenance, software, and infrastructure. The provider manages the client’s servers, storage, network, databases, operating system, and applications. Examples include Google Docs and Mail.

Platform as a Service (PaaS). The capacity provided to the user is to deploy customer-generated or acquired applications on the cloud infrastructure built using libraries, programming languages, tools, and services of the provider-supported.

Example of PaaS include Google AppEngine [24].

Infrastructure as a Service (IaaS). Cloud users explicitly utilize IT infrastructures offered in the IaaS cloud (net-works, storage, processing, and other core computing resources). The user doesn’t control or manage the infrastructure of the cloud, but has monitor regarding deployed software, storage and operating systems, and limited control over specific network components.

6 Prediction student’s Performance Based on Google Cloud

In this section, we demonstrate the overall architecture for prediction student’s performance using Google cloud services depicted in Fig. 2, which can be divided into three layer: Infrastructure layer, Cloud services layer and user layer.

Infrastructure Layer. Infrastructure is the first layer that represents the lowest layer of the solution proposed. The infrastructure is composed of virtualized resources for computing, storing, and networking. The abstraction of these underlying hardware is to provide the versatility wanted by users. From within, the virtualization performs

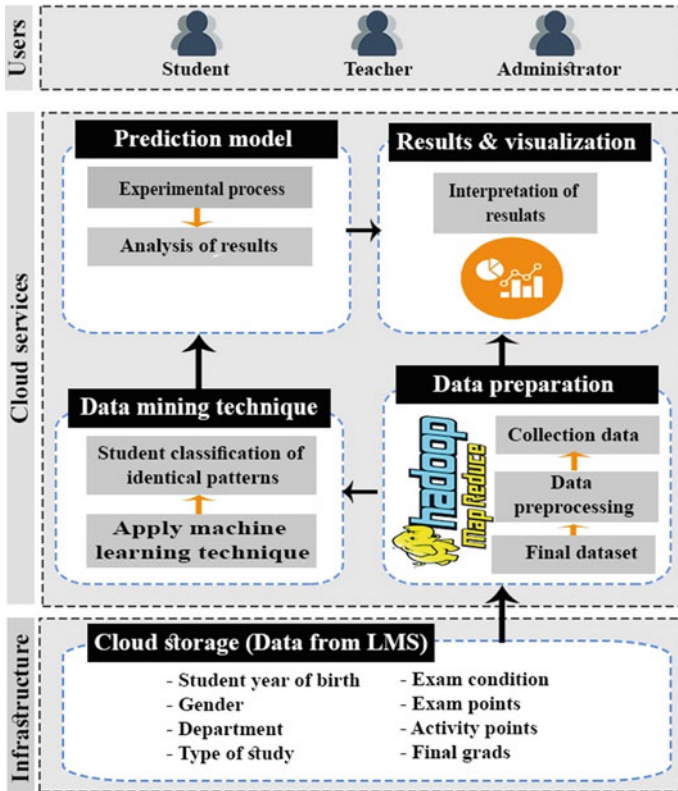


Fig. 2 Model of prediction student’s performance based on cloud computing

the automated provision of resources and optimizes the process of infrastructure management.

Cloud services Layer. This layer introduces data preparation, Data mining technique, Prediction model and Results:

Data preparation: is a work involving the reorganization, collection, and “clean-up” of data before the analysis phase. Data treatment is also essential for integrating data obtained from even more than one source, such as multiple cloud databases. Besides ordering unsorted data, non-standardized, replacing, and finding anomalies and duplicates and using Hadoop at this point is suitable for batch preparation and cleanup of large datasets.

Data mining technique: In this step, the methods of data mining and machine learning are selected such as Classification, Association, Clustering and Regression.

Prediction model: The method for predicting scores is created from data processed before hand.

Results and visualization: The results obtained are evaluated and represented.

Users' layer. Users can access to Cloud based platform by using various enabled devices such as (iPad, laptop, desktop, and smartphones) to visualize the results.

7 Conclusion and Future Work

Predicting student's performance of is more useful for recognizing the students with low academic results. Student retention is a measurement of the university's academic success and enrolment management. In educational environments, the potential to predict a student's performance is very significant. It is more difficult prediction the student's performance because of the massive quantities of data.

Cloud computing is becoming a hot research topic when faced with large-scale data and is widely used to solve this issue. The objective of the work is to design an architecture of prediction student's performance based on cloud computing as part of the normal enhancement of online learning. Our future research will be about implementing the proposed approach.

Prediction student's performance system will be proposed to predict the performance of the students with high predictive accuracy based on data including the huge number of learners and the educational content variety from Sidi Mohammed Ben Abdellah University distance learning platforms and to provide support by optimization rules for the low students.

References

1. El Aissaoui O, El Alami El Y, Madani L, Oughdir AD, El Alloui Y (2020) A Multiple linear regression-based approach to predict student performance. In: Ezziyyani M (ed) *Advanced intelligent systems for sustainable development (AI2SD'2019)*, vol 1102. Springer International Publishing, Cham, pp 9–23
2. Sangeeta K, PanduRanga Vital T (2020) Student classification based on cognitive abilities and predicting learning performances using machine learning models. *IJRTE* 8(6):3554–3569. <https://doi.org/10.35940/ijrte.F8848.038620>
3. Shahiri AM, Husain W, Rashid NA (2015) A review on predicting student's performance using data mining techniques. *Procedia Comput Sci* 72:414–422. <https://doi.org/10.1016/j.procs.2015.12.157>
4. Anshari M, Alas Y, Yunus NHM (2016) Online learning: trends, issues, and challenges in the big data era. *Online Learn* 12(1):14
5. Ashraf A, El-Bakry HM, El-razek SMA, El-Mashad Y, Mastorakis N (2015) Enhancing big data processing in educational systems, p 7
6. El Mhouti A, Erradi M, Nasseh A (2019) Application of cloud computing in e-learning: a basic architecture of cloud-based e-learning systems for higher education. In: Ben Ahmed M, Boudhir AA, Younes A (eds) *Innovations in smart cities applications*, 2 edn. Springer International Publishing, Cham, pp 319–333
7. Hartshorne R, Ajjan H (2009) Examining student decisions to adopt Web 2.0 technologies: theory and empirical tests. *J Comput High Educ* 21(3):183–198. <https://doi.org/10.1007/s12528-009-9023-6>

8. Fry K (2001) E-learning markets and providers: some issues and prospects. *Educ Train* 43(4/5):233–239. <https://doi.org/10.1108/EUM0000000005484>
9. Arkorful V, Abaidoo N (2014) The role of e-learning, the advantages and disadvantages of its adoption in higher education. 2(12):14
10. Abbad MM, Morris D, De Nahlik C (2009) Looking under the bonnet: factors affecting student adoption of e-learning systems in Jordan. *IRRODL* 10(2). <https://doi.org/10.19173/irrodl.v10i2.596>
11. Keller C, Cernerud L (2002) Students' perceptions of e-learning in university education. *J Educ Media* 27(1–2):55–67. <https://doi.org/10.1080/1358165020270105>
12. Dublin L (2003) If you only look under the street lamps ... or nine e-learning myths. <https://www.eLearningguild.com>
13. Algahtani A (2011) Evaluating the effectiveness of the e-learning experience in some universities in Saudi Arabia from male students perceptions, p 328
14. Fariba TB (2013) Academic performance of virtual students based on their personality traits, learning styles and psychological well being: a prediction. *Procedia Soc Behav Sci* 84:112–116. <https://doi.org/10.1016/j.sbspro.2013.06.519>
15. Quadri MMN Drop out feature of student data for academic performance using decision tree techniques, p 4
16. Romero C, Ventura S, Espejo PG, Hervás C (2008) Data mining algorithms to classify students, p 10
17. Sun S, Huang R (2010) An adaptive k-nearest neighbor algorithm. In: 2010 seventh international conference on fuzzy systems and knowledge discovery, Yantai, China, pp 91–94. <https://doi.org/10.1109/FSKD.2010.5569740>
18. Harahap F, Harahap AYN, Ekadiansyah E, Sari RN, Adawiyah R, Harahap CB (2018) Implementation of Naïve Bayes classification method for predicting purchase. In: 2018 6th international conference on cyber and IT service management (CITSM), Parapat, Indonesia, pp 1–5. <https://doi.org/10.1109/CITSM.2018.8674324>
19. Irfiani E, Elyana I, Indriyani F, Schaduw FE, Harmoko DD (2018) Predicting grade promotion using decision tree and Naïve Bayes classification algorithms. In: 2018 third international conference on informatics and computing (ICIC), Palembang, Indonesia, pp 1–4. <https://doi.org/10.1109/IAC.2018.8780431>
20. Kaufman LM (2009) Data security in the world of cloud computing. *IEEE Secur Privacy Mag* 7(4):61–64. <https://doi.org/10.1109/MSP.2009.87>
21. Zhang Q, Cheng L, Boutaba R (2010) Cloud computing: state-of-the-art and research challenges. *J Internet Serv Appl* 1(1):7–18. <https://doi.org/10.1007/s13174-010-0007-6>
22. Liu F et al (2011) NIST cloud computing reference architecture, p 35
23. Mell P, Grance T, (2011) The NIST definition of cloud computing, p 7
24. Tharam D, Chen W (2010) Cloud computing: issues and challenges. In: Presented at the 2010 IEEE 24th international conference on advanced information networking and applications (AINA 2010), Perth, WA

Contribution to the Optimization of Industrial Energy Efficiency by Intelligent Predictive Maintenance Tools Case of an Industrial System Unbalance



Ali Elkihel, Yosra Elkihel, Amar Bakdid, Hassan Gziri, and Imane Derouiche

Abstract Today's industry presents many challenges whose the competitiveness weighs heavily on productivity. The future industry or industry 4.0 requires a new way for organizing industrial processes and must integrate smarter maintenance tools capable of greater adaptability in production. This new organization must respond to competitiveness challenges to achieve customer expectations but with a short deadline to market and an optimized cost production in terms of energy consumed reduced breakdowns, etc. One of the failures encountered in the industry, object of our study, is the unbalance corresponds to a rotor imbalance, shaft ... due to the non-coincidence of the principal axe of inertia and the inertia center with the rotation axis. Our contribution is to develop the main components surveillance of an industrial installation continuously and follow the evolution through quantifiable and qualifiable data which allows preventing a dysfunction before stopping the production. This surveillance uses very precise predictive maintenance technologies and can tracks parameters in real time: vibration, consumed energy and the various components temperature.

Keywords The future industry · Predictive maintenance · Unbalance · Vibration analysis · Energy

A. Elkihel · H. Gziri

Laboratory of Engineering, Industrial Management and Innovation, Faculty of Science and Technology of Settat, University Hassan 1er, Casablanca, Morocco

Y. Elkihel

Laboratory of Productics Energy and Sustainable Development, EST, University Sidi Mohamed Ben Abdellah, Fez, Morocco

A. Bakdid (✉) · I. Derouiche

Laboratory of Industrial Engineering and Seismic Engineering, National School of Applied Sciences ENSA-Oujda, Mohammed Premier University, Oujda, Morocco
e-mail: a.bakdid@ump.ac.ma

1 Introduction

The industrial environment presents many challenges whose the competitiveness weighs heavily on productivity. Control costs while guaranteeing the desired quality level, constitutes the key challenge of industrial production.

The Future Industry demands a new way to organize industrial processes with the aim of implementing smarter maintenance tools capable of greater adaptability in production [1]. This new organization must respond to the competitiveness challenges to achieve customer expectations but with a short deadline to market and an optimized cost production in terms of energy consumed reduced breakdowns, etc.

In recent decades, the monitoring and diagnosis of rotating machines by vibration analysis become an effective tool to detect defaults and follow their evolution over time, which make it possible to project a predictive maintenance plan [2].

Our contribution is to develop the main components surveillance of an industrial installation (vibration, energy, temperature, etc. ...), continuously and follow the evolution through quantifiable and qualifiable data which allows preventing a dysfunction before stopping the production. Many authors have approached the industrial surveillance field; therefore, this problematic shown an increasing interest by several industrialists [3, 4].

This predictive maintenance that we will develop in the form of an industrial monitoring platform IMP [5] uses a precise instrument to anticipate the installation failures and therefore significantly increase the availability and the reliability occurring before the breakdown and increase productivity. On the other hand, we can put in evidence energy consumption according to the health state of Industrial material. Indeed, it is now common to add to the production machines, as to the mobile equipment, a sensors quantity which constantly measures the state of their functioning. It is therefore a question of monitoring and analyzing the evolution of an element to find the best time to replace it. This work based on a failure which is the system unbalance shows us how this failure manifested by vibrations will be able to generate an important energy consumption.

2 Experimental Protocol of Monitoring

2.1 *Operating Principle of the Industrial Monitoring Platform IMP*

The industrial monitoring platform IMP is an application with two components [6]:

A hardware component based on sensor networks communicating via a proprietary protocol ensuring the measurements acquisition and transferred to the platform as well as a software component.

The software component allows users to view remotely and in real time: the consumed energy by the industrial system, the temperature and vibration levels. Taking into account the predefined thresholds of each parameter, we can provide the intervention time to avoid production stoppages.

2.2 The IMP Description

The experimental device or the monitoring platform is presented in Fig. 1. It is composed of a three-phase motor group with a speed variator.

This test bench is connected by sensors to the computer in real time.

The unbalance U , thus created, is defined by:

$$U = m.r = M.e \tag{1}$$

The force created by the unbalance depends on the rotation speed and the unbalance amount:

$$F = m.r.\omega^2 = U.\omega^2 \tag{2}$$

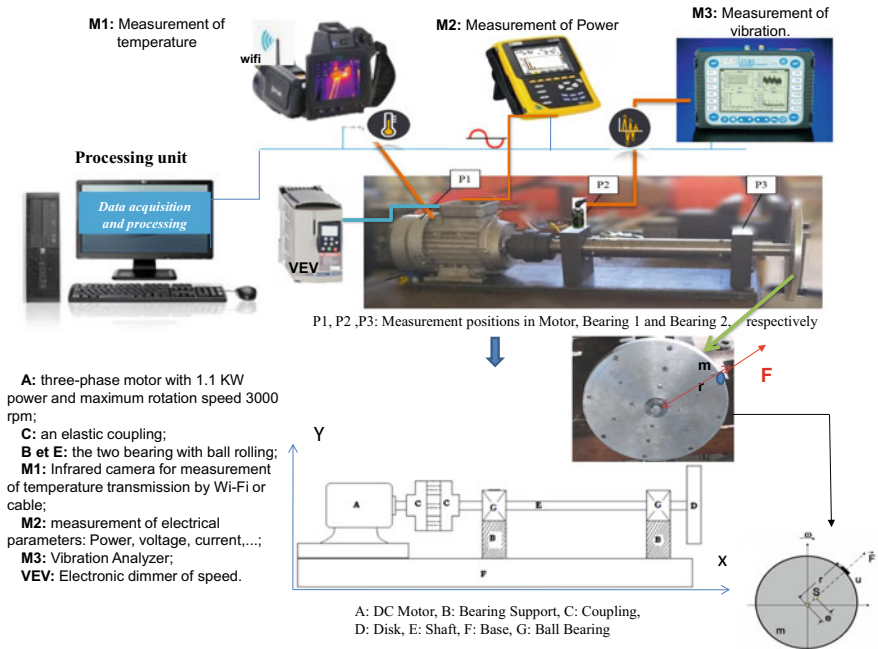


Fig. 1 Experimental device

where: F = force (N), m = mass (kg), r = radius (m), ω = speed (rad/s) and S = center of gravity.

Between unbalance and machine vibrations there is no proven relationship. However, researchers have been able to demonstrate experimentally that the vibration due to unbalance is directionally proportional to the unbalance amount.

2.3 The Operation Principle of the IMP

Three main functions of the IMP: the instruments are connected, the data is transferred and analyzed and a prediction according to the operating thresholds is summarized in Fig. 2.

2.4 Operative Method

In the first step we take measurements with mass = 0 vacuum, no unbalance, by varying the shaft rotation speed (500–3000 rpm) by recording the corresponding signals to the accelerations [7–10].

In the second step we varied the mass to create the unbalance while keeping the same measurement conditions as previously.

For the vibrations we take into consideration that the vertical component along the y axis given the system symmetry. For the electrical part, we measured the consumed power by an electrical measuring instrument and by infrared camera, we can measure the outside temperature of the electric motor.

3 Results and Discussion

In this paragraph we present the obtained results.

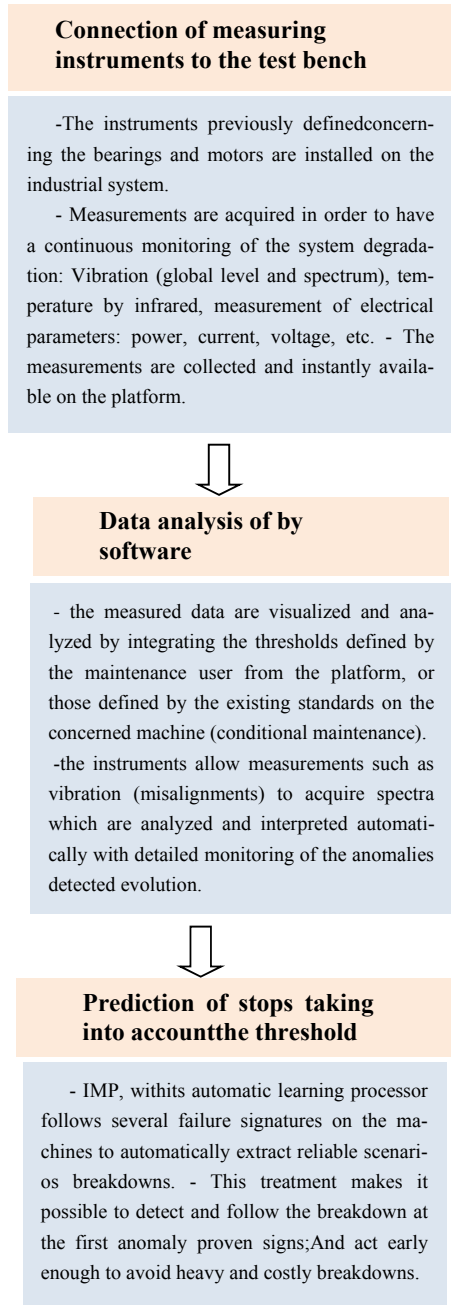
3.1 Acceleration Variation as a Function of Unbalance

Figure 3 presents the results of the different acceleration readings according to the unbalances and with different rotational speeds (500–3000 tr/min) with $r = 150$ mm.

From Fig. 3 we find that:

The acceleration increases with the unbalance and for a constant rotation speed. The acceleration increases almost linear with the unbalance whatever the drive speed.

Fig. 2 Operating principal of the IMP



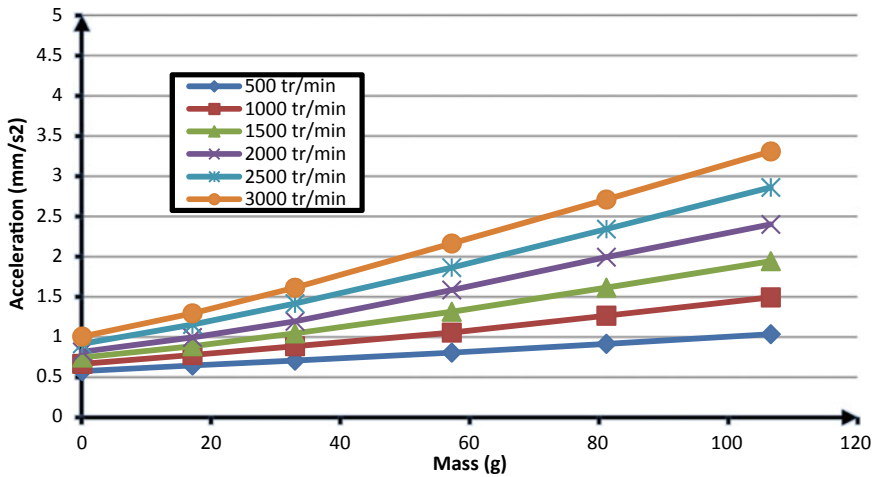


Fig. 3 Acceleration variation as a function of unbalance for the six speeds

By increasing the unbalance, the slope increases considerably with increasing speeds.

3.2 The Consumed Power by the Drive Motor as a Function of the Unbalance

Figure 4 present the consumed power by the drive motor for the different unbalances applied.

According to Fig. 4 we notice that the measured power increases in a parabolic way with the unbalance and with a constant rotation speed. Consumption increases in a considerable way for the three speeds 2000, 2500 and 3000 rpm this is explained by the introduced unbalances, hence an additional electrical consumption.

3.3 The Measured Temperature by Infrared Camera on the Engine

Figure 5 shows the measured temperature at the drive motor for the different unbalances applied.

We notice that the engine temperature increases with increasing unbalance at constant speed. It becomes more important at higher rotational speeds.

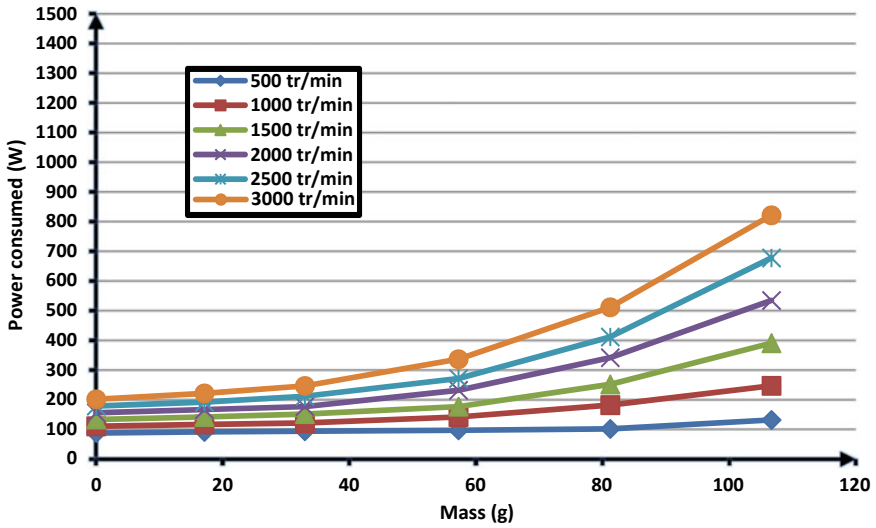


Fig. 4 The consumed power (with unbalance)

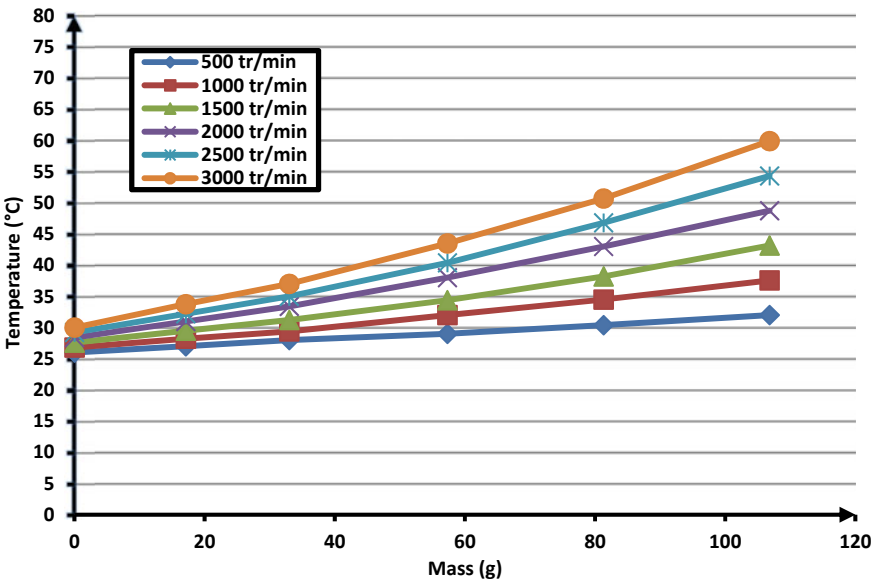


Fig. 5 Temperature to the outside the engine depending on the unbalance

4 Conclusions

Our study concerns the unbalance influence on the accelerations due to vibration, the influence on the consumed power and the engine warms up temperature. A monitoring platform is established with very precise measuring instruments and processing software. We conclude that:

- When the rotation speed increases the acceleration increases depending on the unbalance.
- Whatever the rotation speed, the acceleration increases in a linear way with the load.
 - The graphs slope (results) increases with the rotation speed.
 - The consumption energy of the electric motor increases with the unbalance and the rotation speed. We also noticed that this consumption is increasing for the last three speeds.
 - The engine temperature increases linearly with the rotation speed and the unbalance.
 - We can also predict the lifetime of each component based on the predefined thresholds.

We have implemented an intelligent monitoring of industrial equipment in operation by following several vibration, energy and temperature parameters in real time. This work allows to anticipate breakdowns in production chains, equipment reliability and reduce energy consumption by reducing failures such as the unbalance, the object of our study. Eliminating unbalance reduces energy consumption and increases the reliability of the industrial system.

References

1. Mukesh PS, Bulsara A (2016) Energy loss due to unbalance in rotor–shaft system. *J Eng Des Technol* 14(2):277–362
2. Saleem MA, Diwakar G, Satyanarayana MRS (2012) Detection of unbalance in rotating machines using shaft deflection measurement during its operation. *J Mech Civ Eng (IOSR-JMCE)* 3(3):8–20
3. Elkhatib A (2007) Energy consumption and machinery vibrations. In: International conference on sound and vibrations, ICSV14, Cairns 9–12 July, pp 1–6
4. Ahmat Fadil A (2019) Proposition d'une architecture de surveillance Holonique pour l'aide à la maintenance proactive d'une flotte de systèmes mobiles: application au domaine ferroviaire. Thèse de doctorat, Valenciennes
5. Jeffali F, Ouariach A, El Kihel A, Nougouai A (2019) Infrared thermography-based diagnosis of the impact on the kinematic chain. *Mater Today Proc* 13:949–955
6. Abouelanouar B, Elamrani M, Elkihel B, Delaunois F (2018) Application of wavelet analysis and its interpretation in rotating machines monitoring and fault diagnosis. *Int J Eng Technol (UAE)* 7:3465–3471
7. Bakdid et al (2017) Welding control using ultrasonic multi-elements method. *JMES* 8:3483–3489

8. Jeffali F, Ouariach A, El Kihel B, Nougaoui A (2019) Diagnosis of three-phase induction motor and the impact on the kinematic chain using non-destructive technique of infrared thermography. *J Infrared Phys Technol* 102:102970
9. Bakdid A, El Kihel B, Nougaoui A, Delaunois F (2019) Three-dimensional characterization of weld defects in a steel material. *J Eng Appl Sci* 14:1928–1932
10. Bouzidi Z (2018) Pronostic des systèmes industriels basé sur l'intelligence artificielle Maintenance prédictive. thèse de doctorat, Faculté des Sciences Exactes et des Sciences de la Nature et de la Vie Département d'informatique, Université Mohamed Khider—BISKRA

Automobile Insurance Claims Auditing: A Comprehensive Survey on Handling Awry Datasets



Ezzaim Soufiane , Salah-Eddine EL Baghdadi, Aissam Berrahou, Abderrahim Mesbah, and Hassan Berbia

Abstract Fraud is a very costly criminal activity. Insurance companies face the very challenging task of identifying and preventing fraudulent claims. Just like any big problem in recent years, Machine Learning has been heavily applied to fraud detection in both a supervised and non-supervised manner. But, usually supervised models do not perform well in the presence of awry, asymmetrical Datasets. This paper presents a novel approach for auditing claims in automobile insurance. Our data pipeline consists of preprocessing, feature selection, data balancing, and classification. This robust fraud detection model, built upon existing fraud detection research, gives very promising results compared to state of the art in the industry.

Keywords Insurance fraud · Imbalanced dataset · Automobile insurance · Supervised learning

1 Introduction

According to the FBI annual report [1], 1 trillion dollars was paid to clients from insurance companies in the US in 2016, in which 40 billion dollars were later found to be paid for fraudulent claims. Auto insurance does not make an exception to the rule and companies spend a tremendous amount of money for clients claiming fake accidents and illegally using auto insurance to their benefit.

This subject has gained the interest of multiple researchers. Different approaches were taken by researchers using different machine learning algorithms and techniques, trying to build a classifier capable of detecting fraudulent cases with very high precision and accuracy.

But the main problem with insurance datasets is that they are skewed. As fraud is way less probable to happen than the normal case scenario. And when training machine learning algorithms on datasets with class imbalance, that can lead to very poor classification results. The machine learning algorithms tend to learn mostly

E. Soufiane (✉) · S.-E. EL Baghdadi · A. Berrahou · A. Mesbah · H. Berbia
Mohammed V University, United Nations Avenue, Rabat 10000, Morocco
e-mail: soufiane.ezzaim@um5r.ac.ma

from the majority class samples more than the minority class samples which results in the model classifying most inputs as the majority class.

We proposed to build a data pipeline. Grid-searching a wide range of sampling methods and classifiers with all possible combinations looking for the most optimized and best-performing model.

In Sect. 2 we will go over other existing works on different insurance fraud detection methods. In Sect. 3 we will look at our approach for insurance fraud detection with the different steps and algorithms used for preprocessing the dataset, feature selection, and sampling. In Sect. 4 we will discuss the class imbalance problem in the dataset, the metrics we used to evaluate our algorithms' performances, and the results we were able to achieve with our trained models.

2 Related Works in Literature

Many methods for fraud detection and handling class imbalance have been presented over the years, we will go over some of the notable ones.

Stolfo et al. [2] studied fraudulent credit cards and combined many classifiers to improve performance. Phua et al. in [3], proposed a hybridization of two techniques stacking and bagging meta-classifiers. They introduced a fraud detection method that makes use of a single meta-classifier (stacking) to choose the best base classifiers. For detecting fraudulent claims, Pinquet et al. [4] went with a statistical model, suggested an equation approach for fraud that performed well the Spanish insurance dataset. Nian et al. [5] proposed an unsupervised method named "spectral ranking anomaly", and found their method was surpassing the existing outlier-based fraud detection models. We can also see in [6], a novel genetic-algorithm-based FCM approach, that has been presented for identifying the fraudulent claims, they proposed a comparative study between various classifiers. Furthermore, [7] presented a detailed overview of different ensemble techniques for decision-making.

And as for class imbalance, [8] proposed Synthetic Minority Oversampling Technique (SMOTE) approach, where the new synthetic minority samples are generated rather than the classic oversampling technique. Following that publication, many improved versions surfaced. He et al. [9] proposed the Adaptive Synthetic (ADASYN) over-sampling technique. MWMOTE, [10], tries to handle this situation and identifies the borderline samples by assigning a weight to the hard-to-learn minority samples based on the majority samples. Borderline-SMOTE [11] was also proven effective in handling imbalanced datasets [12]. Under-sampling also showed great promise in many cases, like in Neighborhood Cleaning Rule (NCR), which was proposed by Laurikkala [13]. It uses Wilson's Edited Nearest Rule to remove selected majority class examples. NearMiss [14], Tomek links [15], Edited Nearest-Neighbor (ENN) [16], ALLKNN [17], Instance Hardness Threshold [18], One Sided Selection [19] are all undersampling methods that proved doing very well.

3 Methodology

In this paper, we will be doing an exhaustive grid search on all known sampling methods. In order to identify the fraudulent claims, we have proposed a new data pipeline.

Initially, pre-processing is necessary for building a good classifier. Then, we'll be doing feature selection to select the features that are best suited for our problem and reduce computation power. Next, we'll be applying one of the many class imbalance solutions. After that, we'll train a classifier (MLP, KNN, SVM, Decision Tree, Random Forest, Naive Bayes) on the new dataset. We used 10-fold cross validation for training and testing these classifiers.

We will compare our result with the existing state of art method present in the literature.

This dataset is provided by Angoss Knowledge-Seeker Software, it contains 15,420 examples with 14,497 examples of non-fraud and 923 examples of fraud. It is very imbalanced, with 5.9 % fraudulent cases and 94 percent non-fraudulent cases. It comes with 6 numerical attributes, 25 categorical attributes, and a binary target label. "carclaims.txt" dataset is the only publicly available automobile insurance dataset as of now and was first studied by Phua et al. [3] (Fig. 1).

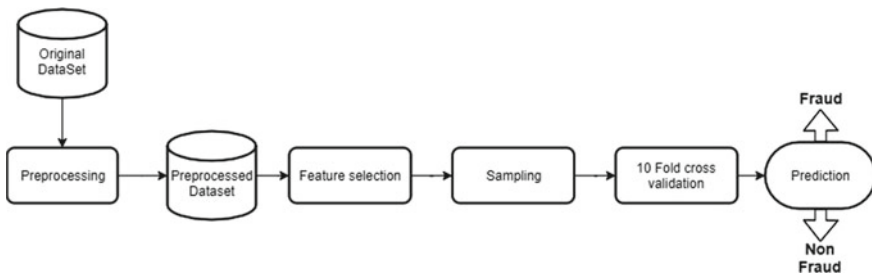


Fig. 1 Our data pipeline

3.1 Preprocessing

Dropping unnecessary data Among the original dataset attributes, three attributes appeared to be unnecessary for our training models and may even disturb the learning process leading to less accurate results.

The first attribute is 'PolicyNumber' which is an id unique to each data sample. The second attribute is 'BasePolicy', we dropped this attribute because it is already mentioned in the 'PolicyType' attribute which makes it just an unnecessary repetition. Finally, the last attribute is 'AgeOfPolicyHolder' which indicates an age range for

the policyholder, and there is already an ‘Age’ which determines the exact age of the policyholder.

Transforming categorical values to numerical Many attributes in the data set are categorical like *Sex*, *MaritalStatus*, *VehicleType*, etc. Training models won’t be able to process any data unless it is numerical. So we had to transform all categorical values by assigning them integer values.

Date features Among the data set features, there are seven features that indicate the date of the accident and the date of the accident claim (*Month*, *WeekOfMonth*, *Day-OfWeek*, *MonthClaimed*, *WeekOfMonthClaimed*, *DayOfWeekClaimed* and *Year*). We used all the seven features and merged them into one feature representing the number of days between the accident and the date of the accident claim.

3.2 Feature Selection

Feeding too much data to machine learning algorithms can cause the model to have more difficulty training and results in lower accuracy. Therefore, feature selection is an important technique that allows selecting the features which contribute the most to prediction, and also reducing the time of the training process. In our model, we used three different feature selection algorithms that are very common and that appears to be very efficient. The three algorithms used are:

1. Chi-squared method [20].
2. RFE, Recursive feature elimination [21].
3. Tree-based method [22, 23].

Chi-squared and Recursive feature elimination algorithms appear to have very similar results when selecting the features, four out of six features were selected by both algorithms. The Tree bases algorithm, on the other hand, had very different results from the previous two methods. We used SVM-RFE because it yielded the best accuracy.

3.3 Sampling Methods

The dataset we are working with is imbalanced, only 5.98% of the overall sample are samples of fraud cases. Training our models with such an imbalance won’t lead to accurate results. Therefore, we applied multiple sampling methods on the dataset trying to figure out which ones will perform best. The sampling methods that we used are:

Oversampling methods: Random oversampling, SMOTE, SVMSMOTE, Borderline-SMOTE, ADASYN, MWMOTE.

Undersampling methods: RandomUnderSampler, TomekLinks, AllKNN, NearMiss, EditedNearestNeighbors (ENN), NeighborhoodCleaningRule (NCR), OneSidedS-

election, Instance Hardness Threshold, Repeated Edited Nearest Neighbors, Cluster Centroids.

Hybrid-sampling methods: ROS + RUS, SMOTE + RUS, SMOTE + Tomek, SMOTE + ENN.

4 Experimentation and Analysis

4.1 Evaluation Metrics

The choice of metrics used when working with imbalanced datasets is extremely important. Accuracy is the most common performance metric, and is defined as the ratio of correctly predicted observation to the total number of observations. Accuracy is only meaningful when the given dataset is symmetric and balanced.

That is why we went with F1-Score, AUC, Precision, and Recall/Sensitivity.

- Precision: It is defined as the ratio of correctly predicted positive observation to the total predicted positive observations

$$\text{Precision} = \frac{TP}{TP + FP}$$

- Recall /Sensitivity: It is defined as the number of observations correctly identified as positive out of total true positives

$$\text{Recall} = \frac{TP}{TP + FN}$$

- F1-Score: It is defined as the harmonic mean of precision and recall. Therefore, this score takes both the false positive and false negative into account. It is more useful than accuracy especially if the dataset has an uneven class distribution.

$$\text{F1 Score} = 2 \times \frac{\text{Precision} \times \text{Recall}}{\text{Precision} + \text{Recall}}$$

- AUC: Measures the entire two-dimensional area underneath the entire ROC curve. AUC represents degree or measure of separability. It tells how much model is capable of distinguishing between classes

Which is why :

- high recall + high precision: the class is perfectly handled by the model
- low recall + high precision: the model can't detect the class well but is highly trustable when it does
- high recall + low precision: the class is well detected but the model also includes points of other classes in it.

4.2 *Experimental Results*

In order to find the best sampling methods suiting our dataset, we tried 21 different techniques with 6 different classifiers and compared all possible combinations, pre-feature selection, and post-feature selection, using different performance metrics, looking for the highest scores.

In the case of the Random Forest classifier, ALLKNN was the best performing method resulting in 88.35% Precision and 93.99% Recall. As for the Decision Tree classifier, MWMOTE was the best performing sampling method resulting 93.92% Precision and 93.42% Recall. For the Support Vector Machine classifier, ALLKNN was the best performing sampling method resulting 88.35% Precision and 93.99% Recall. As for the Naive Bayes classifier, Edited Nearest Neighbors was the best technique resulting 89.69% Precision and 90.96% Recall. In case of the Multi Layer Perceptron classifier, both Neighborhood Cleaning Rule and One Sided Selection sampling methods were the best performing resulting very close scores of respectively 89.96 and 88.75% Precision and 93.81 and 93.99% Recall. And finally, the KNN classifier, we found that TomekLinks was the best performing sampling method resulting 89.75% Precision and 93.60% Recall.

The overall best performing model is the combination of the MWMOTE sampling method with the Decision Tree classifier (Table 1).

4.3 *Experimental Takeaways*

We trained 252 different models and the results above are with 10-fold cross validation. On one hand, we can safely say that in general Undersampling methods yielded much better results compared to Oversampling. And on the other hand, Hybrid approaches like SMOTE + ENN are interesting to try out. Many combinations showed great results. But the best one was MWMOTE & Decision Tree. AUC is a very trustworthy performance metric when it comes to skewed data, and our model hit the 0.9796 mark. And as you can see the model performed very well compared to our peers' work. But since we are interested way more in accurately classifying the Fraudulent cases, since every miss-classification of a fraudulent case costs way more, we are interested in the Recall/Sensitivity.

Below is a comparison between the Recall of our model and state of the art in the field. We currently rank 3rd. Only behind Sundarkumar et al. [24] and Padhi and Panigrahi [25].

We also compared ours to Farquard et al. [26], Xu et al. [27], Subelj et al. [28], Tao et al. [29], Sundarkumar and ravi [30] Nian et al. [5], Subudhi and Panigrahi [6], Tian [31], Itri et al. [32] (Table 2).

Table 1 Best performing combinations, out of 21 sampling methods for each of the 6 classifiers, post feature selection

Random forest				
	F1 score (%)	AUC (%)	Precision (%)	Recall (%)
SVM SMOTE	82.96	74.26	90.99	77.73
Tomek links	91.08	77.17	88.35	93.99
AllKNN	91.08	77.52	88.35	93.99
Repeated edited nearest neighbors	91.08	77.32	88.35	93.99
SMOTE + ENN	81.65	76.83	91.63	76.04
Decision tree				
	F1 score (%)	AUC (%)	Precision (%)	Recall (%)
SVMSMOTE	86.33	73.41	90.78	83.03
BorderlineSMOTE	84.64	73	90.93	80.25
TomekLinks	91.16	73.69	89.91	93.65
AllKNN	86.64	73.17	90.49	83.68
EditedNearestNeighbors (ENN)	85.97	72.68	90.42	82.61
NeighborhoodCleaningRule (NCR)	90.74	73.71	89.74	91.96
OneSidedSelection	91.09	73.49	89.82	93.50
SMOTE + ENN	83.27	64.92	91.22	78.08
MWMOTE	93.40	97.96	93.92	93.42
SVM				
	F1 score (%)	AUC (%)	Precision (%)	Recall (%)
SVMSMOTE	83.31	76.95	91.70	78.09
TomekLinks	91.08	68.71	88.35	93.99
AllKNN	91.08	69.62	88.35	93.99
EditedNearestNeighbors (ENN)	91.08	69.59	88.35	93.99
Repeated edited nearest neighbors	91.08	73.36	88.35	93.98
Naive Bayes				
	F1 score (%)	AUC (%)	Precision (%)	Recall (%)
TomekLinks	90.92	75.67	89.43	93.06
AllKNN	90.11	76.16	89.68	90.63
EditedNearestNeighbors	90.25	75.84	89.69	90.96
NeighborhoodCleaningRule	90.44	75.83	89.69	91.33
OneSidedSelection	90.93	75.67	89.37	93.11
Multi layer perceptron				
	F1 score (%)	AUC (%)	Precision (%)	Recall (%)
SVMSMOTE	86.41	78.27	91.169	83.01
EditedNearestNeighbors	91.08	78.84	89.94	92.83
TomekLinks	91.09	79.34	88.55	93.99
AllKNN	90.95	78.84	90.00	92.43
NeighborhoodCleaningRule	91.18	79.17	89.96	93.81
OneSidedSelection	91.09	79.29	88.75	93.99
KNN				
	F1 score (%)	AUC (%)	Precision (%)	Recall (%)
TomekLinks	91.14	65.82	89.75	93.60
AllKNN	88.48	64.05	90.27	86.97
EditedNearestNeighbors	87.92	65.01	90.29	86.00
NeighborhoodCleaningRule	90.96	67.86	89.88	92.37
OneSidedSelection	91.08	58.79	89.55	93.44

Table 2 Comparison and ranking of our model with existing methods

Rank	Related research	F1 score (%)	AUC (%)	Precision (%)	Recall (%)	Accuracy (%)	Specificity (%)
9	Farquad et al. [26]	–	–	–	87.89	57.74	55.81
8	Subelj et al. [28]	–	–	–	89.13	87.2	86.67
-	Xu et al. [27]	–	–	–	–	88.7	–
5	Tao et al. [29]	–	–	–	91.31	-	–
1	Sundarkumar et al. [24]	–	–	–	95.5	58.92	56.58
7	Sundarkumar and Ravi [30]	–	–	–	90.74	60.31	58.69
6	Nian et al. [5]	–	–	–	91	–	52
10	Subudhi and Panigrahi [6]	–	–	–	83.21	87.02	88.45
-	Xiaoguang Tian [31]	–	81.7	–	–	–	–
2	Padhi and Panigrahi [25]	–	–	–	94.21	81.23	73
4	Itri et al. [32]	22.22	–	12.64	91.76	–	–
3	<i>Our final result</i>	93.4	97.96	93.92	93.42	–	–

5 Conclusion and Future Works

In this paper, we have proposed a novel data pipeline for auditing automobile insurance claims. We successfully handled the awry dataset problem. And proposed MWMOTE, as an over-sampling technique and Decision Tree to classify claims. Our final model yielded very favorable results. It adequately generates new synthetic samples and makes the dataset more symmetric.

We have also compared our results with the current state of the art in the insurance claim auditing research and found that our results rank 3rd compared to all research done before on the automobile insurance dataset.

We should note that in real life, accusing a client of fraud is a grave act that can even result in suing the insurer. The insurance company should know how to adequately use the technology at their disposal because real-life situations and people’s dignity and reputation are different from numbers and a computer screen. We strongly advise to only litigate when hard proof is available.

Our further work includes: exploring the proposed algorithm to different types of skewed datasets problems, combining deep learning into the proposed model to improve the accuracy of prediction.

References

1. FBI annual reports and publications, Insurance fraud, 2016 <https://www.fbi.gov/stats-services/publications/insurance-fraud>
2. Stolfo SJ, Prodromidis AL, Tselepis S, Lee W, Fan DW (1997a) JAM: Java agents for meta-learning over distributed databases. AAAI workshop on AI approaches to fraud detection. In: Proceedings of the 3rd international conference knowledge discovery and data mining, pp 74–81
3. Phua C, Alahakoon D, Lee V, Minority report in fraud detection: classification of skewed data. *ACMSIGKDD Explore Newslett* 6(1):50–59
4. Pinquet J, Ayuso M, Guillen M (2007) Selection bias and auditing policies for insurance claims. *J Risk Insur* 74:425–440
5. Nian K, Zhang H, Tayal A, Coleman T, Li Y (2016) Auto insurance fraud detection using unsupervised spectral ranking for anomaly. *J Finan Data Sci*, 58–75
6. Subudhi S, Panigrahi S (2017) Use of optimized fuzzy C-means clustering and supervised classifiers for automobile insurance fraud detection. *J King Saud Univ Comput Inf Sci*
7. Polikar R (2006) Ensemble based systems in decision making. *IEEE Circ Syst Mag* 6(3):21–45
8. Chawla NV, Bowyer KW, Hall LO, Kegelmeyer WP (2002) SMOTE: synthetic minority over-sampling technique. *J Artif Intell Res* 16:321–357
9. He H, Bai Y, Garcia EA, Li S (2008) ADASYN: Adaptive synthetic sampling approach for imbalanced learning. In: IEEE international joint conference on neural networks (IEEE world congress on computational intelligence), pp 1322–1328
10. Barua S, Islam MM, Yao X, Kazuyuki (2014) MWMOTE-majority weighted oversampling technique for imbalanced dataset learning. *IEEE Trans Knowl Data Eng* 26(2)
11. Han H, Wen-Yuan W, Bing-Huan M (2005) Borderline-SMOTE: a new over-sampling method in imbalanced data sets learning. *Adv Intell Comput*, 878–887
12. Nguyen HM, Cooper EW, Kamei K (2009) Borderline over-sampling for imbalanced data classification. *Int J Knowl Eng Soft Data Paradig* 3(1):4–21
13. Laurikkala J (2001) Improving identification of difficult small classes by balancing class distribution. Springer, Berlin
14. Mani I, Zhang I (2003) kNN approach to unbalanced data distributions: a case study involving information extraction. In: Proceedings of workshop on learning from imbalanced datasets
15. Tomek I (2010) Two modifications of CNN. *Syst Man Cybern IEEE Trans* 6:769–772
16. Wilson D (1972) Asymptotic Properties of nearest neighbor rules using edited data. *IEEE Trans Syst Man Cybern* 2(3):408–421
17. Tomek I (1976) An Experiment with the edited nearest-neighbor rule. *IEEE Trans Syst Man Cybern* 6(6):448–452
18. Smith D, Michael R, Martinez T, Christophe G-C (2014) An instance level analysis of data complexity. *Mach Learn* 95(2):225–256
19. Kubat M, Matwin S (1997) Addressing the curse of imbalanced training sets: one-sided selection. *ICML* 97:179–186
20. Jin X, Xu A, Bie R, Guo P (2006) Machine learning techniques and chi-square feature selection for cancer classification using SAGE gene expression profiles. In: BioDM'06: proceedings of the 2006 international conference on data mining for biomedical applications, April 2006, pp 106–115
21. Guyon I, Weston J, Barnhill S, Vapnik V (2002) Gene selection for cancer classification using support vector machines. *Mach Learn* 46(1–3):389–422
22. Baranauskas JA, Netto OP (2017) A tree-based algorithm for attribute selection, Sérgio Ricardo Nozawa & Alessandra Alaniz Macedo
23. Deng H, Runger G (2012) Feature selection via regularized trees. In: Proceedings of the 2012 international joint conference on neural networks (IJCNN). IEEE
24. Sundarkumar GG, Ravi V, Siddeshwar V (2015) One-class support vector machine based under-sampling: application to churn prediction and insurance fraud detection. In: IEEE international conference on computational intelligence and computing research (ICIC)

25. Padhi S, Panigrahi S (2019) Use of data mining techniques for data balancing and fraud detection in automobile insurance claims. In: Bhateja V et al (eds) *Intelligent computing and communication, advances in intelligent systems and computing* 1034. Springer Nature Singapore Pte Ltd., page 221
26. Farquad MAH, RaviS V, Bapi Raju (2010) Support vector regression based hybrid rule extraction methods for forecasting. <https://doi.org/10.1016/j.eswa.2010.02.055>
27. Xu W, Wang S, Zhang D, Yang B (2011) Random rough subspace based neural network ensemble for insurance fraud detection. In *Fourth international joint conference on computational science and optimization*. IEEE, pp 1276–1280
28. Subelj L, Furlan S, Bajec M, An expert system for detecting automobile insurance fraud using social network analysis
29. Tao H, Zhixin L, Xiaodong S (2012) Insurance fraud identification research based on fuzzy support vector machine with dual membership. In: *2012 international conference on information management, innovation management and industrial engineering*
30. Sundarkumar GG, Ravi V (2015) A novel hybrid undersampling method for mining unbalanced datasets in banking and insurance. In: *Engineering applications of artificial intelligence*
31. Tian X, Insurance fraud detection: an exploratory data mining approach. In: *Southwest decision sciences institute 48th annual meeting*
32. Itri B, Mohamed Y, Mohammed Q, Bouattane Q (2019) Performance comparative study of machine learning algorithms for automobile insurance fraud detection. In: *Conference: 2019 third international conference on intelligent computing in data sciences (ICDS)*

Artificial Intelligence Based on the Neurons Networks at the Service Predictive Bearing



Ali Elkihel, Imane Derouiche, Yosra Elkihel, Amar Bakdid, and Hassan Gziri

Abstract In the industrial environment, production systems are increasingly complex and cannot be free from disturbances and failures. Indeed, the following study is considered as a point of change in the service domain to effectively track disturbances and failures, by allowing the transition from old maintenance to smart maintenance. However, the following document represents a sort of passage between the old and the new maintenance by treating the operation of the bearings in the rotating mechanical systems, the study consists in studying the modes of failures of the bearings. A prediction model is developed based on neural networks.

Keywords Predictive maintenance · Bearings · Prognosis · Artificial intelligence

1 Introduction

All sectors of industry are in fact in the process of being transformed into an Industry 4.0 based in its main lines on artificial intelligence, in order to allow to optimize the industrial performances, reduce the failures, simplify simulations and automate quality controls. Artificial intelligence is also a very good tool for decision support by taking thousands of measurements of different parameters of the system monitored by plugging in intelligent sensors, to be able to predict the results instantaneously in order to avoid breakdowns, optimize maintenance costs to directly avoid high energy consumption by faulty systems [1].

A. Elkihel · H. Gziri

Laboratory of Engineering, Industrial Management and Innovation, Faculty of Science and Technology of Settat, University Hassan 1er, Casablanca, Morocco

I. Derouiche · A. Bakdid (✉)

Laboratory of Industrial Engineering and Seismic Engineering, National School of Applied Sciences ENSA-Oujda, Mohammed Premier University, Oujda, Morocco

e-mail: a.bakdid@ump.ac.ma

Y. Elkihel

Laboratory of Products Energy and Sustainable Development, EST, University Sidi Mohamed Ben Abdellah, Fez, Morocco

Knowing that bearings are essential elements in almost all rotating industrial systems, a global study of these elements is essential to understand their behaviors, and the behavior of mechanics and technicians towards these components. In the same context, this article first consists of understanding the transition from preventive maintenance to predictive maintenance. Then understand the structure, functioning and methods of building neural networks, and ultimately exploit them as an effective tool of artificial intelligence to perform accurate tracking on the state of the bearings, and use them to build a high-performance system that aims to monitor the rolling state during its operation over time and to perform predictive maintenance in rotating systems in order to optimize their failure rate and reduce energy consumed by the latter. To carry out this study, we will first carry out an experimental study on a test bench for non-destructive testing based on vibration analysis in order to take measurements of speed and acceleration for different bearing states (healthy, defective with outer ring defect, defective with inner ring defect) to be able to compare and distinguish between measurements of each operating state. The measurements will be transferred to computers for processing, in order to build the Big Data which will be used to make the network learn, test and validate which will aim to implement predictive maintenance. The main objectives of this intelligent maintenance are the monitoring of remote equipment, the prediction and detection of bearing defects, and generation of prognosis indicators that predict and resolve problems before they occur or become serious [2].

The following document contains three main axes, the first axis deals with the notion of prognosis as well as the methodology of moving from preventive maintenance to predictive maintenance. The second axis deals with the architecture of neural networks, activation functions and their operating procedure. And the last axis contains the experimental study which in turn is divided into two parts, the first part contains the measurements of the non-destructive control of the bearings, the databases recorded of the velocity and acceleration and their pretreatments. And the second part contains the results and interpretations obtained after constructing an algorithm of the neural network consisting of performing predictive maintenance of bearings.

2 Experimental from Preventive Maintenance to Predictive Maintenance

Industrial maintenance basically contains two main functions which are monitored and diagnosis, indeed the fact having correct monitoring leads to optimum diagnostic results [3, 4]. However, the development of maintenance over time had only one goal this is to arrive at an effective monitoring method that allows optimum diagnosis. For this purpose, artificial intelligence has been introduced in this area in order to build an effective, instant and very precise surveillance mode. To understand this notion, we have to first understand the notions, monitoring, diagnosis and prognosis.

2.1 *Machine Monitoring, Diagnosis and Prognosis*

The complete machine condition monitoring process consists of the following five distinct phases:

- Detection of problems: deviations from a normal state
- Diagnosis of faults and their causes: identification of the probable cause of the (or) failure(s)
- Prognosis of a future progression of the defect: the estimation of the time remaining for a failure occurrence
- Recommended actions: the action to adjust faults and maintain the components
- Damage analysis: (According to standard 13381) [5].

2.2 *Prognosis*

Indeed, the prognosis of failures corresponds to “the estimate of the time remaining for a failure and the risk for one or more components in the current state can have future failure modes”. It is the art or act of predicting future conditions on the basis of the signs and symptoms present. The implementation of the prognosis system results in an optimal maintenance program. We can also say that prognosis is a focused engineering science discipline on detecting, predicting, and managing the state of health of complex systems.

So, considerations for selecting appropriate prognosis models can be grouped into four categories, each asking a question that must be answered in order to assess the relevance of a particular model in a particular of business environment:

- The prediction requirements: “What is RUL forecasting must reach?”
- The model-process compatibility: “Can the model describe reality?”
- The resources required: “Are the resources available to undertake the modeling?”
- The availability of the approach: “Is the modeling approach sufficiently supported to be used?”

More precisely, for the rolling case, there are several types of prediction models of the service life useful remaining of bearings, in the literature we have identified the following different types of models:

- Knowledge-based models: They assess the similarity between an observed situation and a databank of previously defined failures and deduce the life expectancy from previous events
- The life expectancy models: These determine the life of the machine components in relation to the expected risk expected deterioration of known operating conditions
- Artificial neurons networks: They calculate an estimated output for the useful life of a component/machine, directly or indirectly, from a mathematical representation of the component/system that was derived from the observation data rather than from a physical understanding of the failure process

- Physical models: They calculate an estimated output for the useful life of a component/machine from a mathematical representation of the physical degradation's behavior of components [6].

3 Neurons Networks

Neurons networks are tools capable of performing operations of perception, classification, and prediction. Their functioning is based on the operating principles of biological neurons. Their main advantage over other tools is their learning ability and of generalization of their knowledge to unknown entries. One of the qualities of this type of tool is its adequacy for put in point modern surveillance systems capable of adapting to a complex system with multiple reconfigurations [7, 8].

3.1 The Parameters of an MLP-Type Neuron Network

A neuron network se built by neurons with several connections between them, neurons build 3 types of layers:

- The input layer: behaves the input neurons or the observation neurons which receive information from the outside middle to transmit it to the network, these input neurons do not make any change or processing on the incoming signal.
- The hidden layer: it can contain several layers according on the program need, it contains as well the greatest number of neurons, this layer performs a processing on the signal received by the input layer and transmits it to the last layer for the finally have the desired results.
- The output layer: contains the output neurons or the final neurons, their role is to transmit the results processed by the hidden layer, the number of neurons of this layer depends on the desired output number.

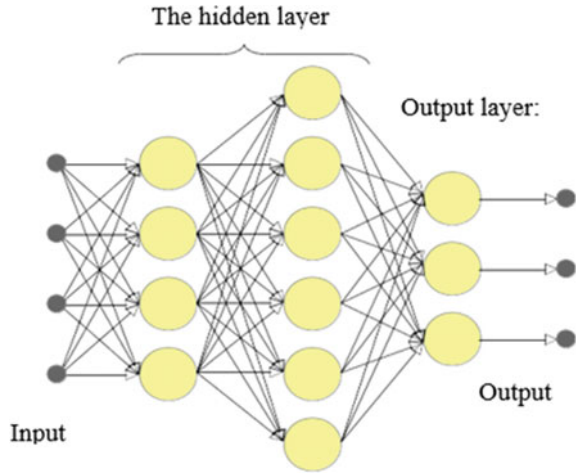
Each neuron is characterized by its bias b_i , and each link between two neurons i and j se characterized by the weight $W_{i,j}$. The connections between neurons are called Synapses; they receive information from other neurons and therefore allow neurons to communicate with each other. We distinguish two types of synapses:

- Inhibitory synapses: serve to activate neurons.
- Activators synapses: serve to stop the signal between neurons.

The total of these components builds a network (Fig. 1) characterized by:

- The number of input neurons
- The number of hidden layers
- The number of neurons in the hidden layer
- The number of output neurons

Fig. 1 Diagram of a neural network with 4 inputs and 2 hidden layers and 3 outputs



3.2 Activation Function of Neurons (Sigmoid)

At the level of each neuron, an operation is done in order to process the received signal, in networks basic the sigmoid function is applied. The signals entered are the features x multiplied by parameters $W_{i,j}$ called weight. The calculation performed by the neuron can be divided into two stages [7]:

The neuron calculates the somme of all inputs. It's a linear calculation:

$$Z(XW) = X_1W_1 + X_2W_2 + X_3W_3 + \dots + X_nW_n = \sum X_iW_i \quad (1)$$

The neuron computes the image of the z function's value by its activation function. Here the function used is sigmoid function (Fig. 2) (Logistic function). Which is considered a non-linear calculation that has the following expression (Fig. 3).

Fig. 2 The curve of the sigmoid function

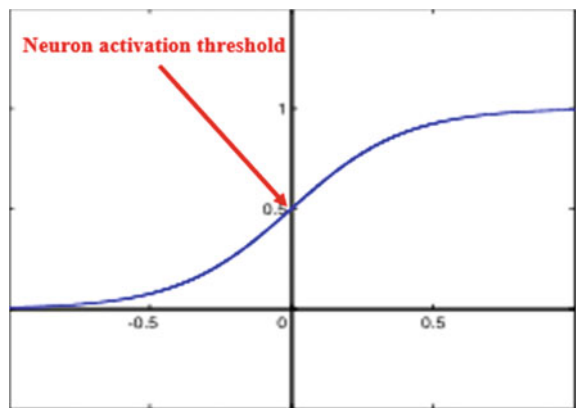
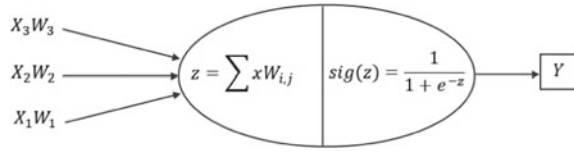


Fig. 3 Functioning of a perceptron



$$Y = \text{sig}(z) = \frac{1}{1 + e^{-z}} \quad (2)$$

Note: The advantage of the sigmoid function is to simplify the calculation of the gradient and thus obtain faster learning cycles.

Explanation: The neuron receives signals going of activating synapses and others coming of inhibitory synapses, it processes both types of signals and it adds its own bias which corresponds to putting some weight in one of the two contributions, the neuron will then activate if the signals activators plus the bias activator is greater than the inhibitor signals plus the bias inhibitor. The neuron activates between 0 and 100%, its activation is almost zero if the inhibitory contributions prevail, and close to 50% if there is quasi-equality between the contributions, and almost 100% if activating contributions prevail.

3.3 Operation of MLP-Type Neurons Networks.

Indeed, a neuron network of the MLP (Multi-Layer Perceptron) type calculates a linear combination of the inputs that is to say that the combination function returns the scalar product between the vector of the inputs and the vector of the synaptic weights.

The function to be developed will be processed by the neurons, she will be able to be in the form of a function [8]:

- Sigmoid
- Hyperbolic tangent: $\tanh(z)$
- Heaviside (z).

4 Practical Part

4.1 Test Bench Description

Experiments are carried out on a of machine failure simulator. The experimental setup is illustrated in Fig. 4. The shaft is driven by a motor and the speed of rotation is controlled by an alternating current drive. Two ER16K ball bearings are installed to

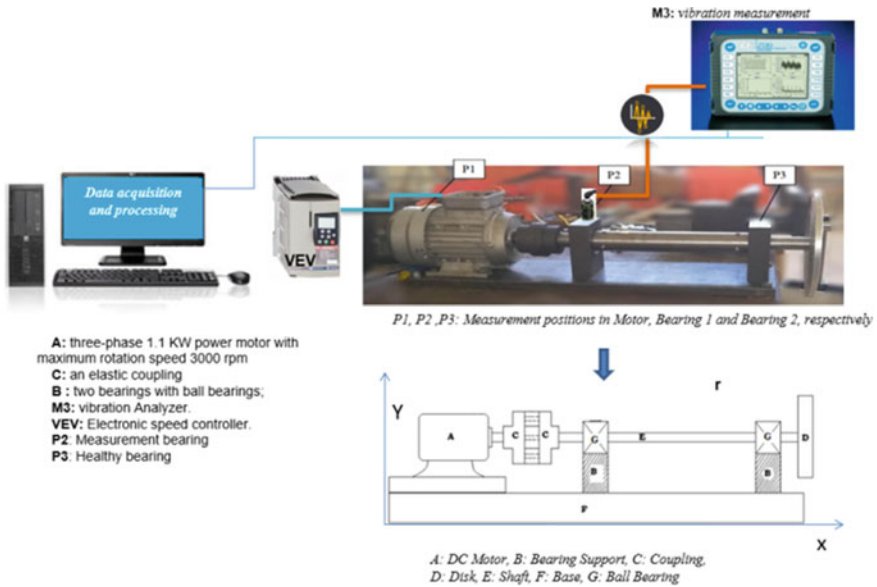


Fig. 4 Experimental device

support the shaft, the left one is a healthy bearing and the right one is the experimental bearing, which is replaced by bearings of different health conditions.

Figure 4 shows the setup of our test bench, and its schematization in 2D.

4.2 Principle of the Experience

Bearing faults can be detected and diagnosed by observing the characteristic fault frequency (FCF) in the frequency domain. For each type of fault, it has a specific FCF, which is proportional to the operating rotation frequency, and the coefficient is determined by the structural parameters of the bearing. The structural parameters of the bearings used in the experiments are given in Table 1. According to the parameters of the bearings, the coefficient FCF of the inner ring of the bearing is 5.43, that is to say the frequency of passage of the balls of the internal race (BPFI) is equal to the product of the coefficient FCF (5,43) and the frequency of rotation of the shaft f_r , Either $BPFI = 5,43 f_r$. Similarly, the FCF of the outer ring of the bearing, that is to say the frequency of passage of the balls of the outer ring (BPFO) = 3.57 f_r .

Table 1 Bearing parameters

Bearing type	Pitch diameter	Ball diameter	Number of balls	BPFI	BPFO
ER16K	38.52 mm	7.94 mm	9	5.43 f_r	3.57 f_r

4.3 Description of Data Bases

The database contains the test bench speed and acceleration measurements for three different rolling states, the first state describes measurements for healthy rolling, the second state describes measurements for rolling with failed inner ring, and the third condition is the failed outer ring bearing.

The data are all sampled at 200,000 Hz and for sampling time equal to 10 s. We will then have 2 millions data for each running state; the databases are imported into a WorkspaceMatlab. They are named

- H-A-1: for healthy turnover
- I-A-2: for inner ring bearing failure
- O-A-3: for defective outer ring bearing.

In this study, we will use only 1000 samples for each running state that are considered sufficient to build a MLP-type network.

4.4 Data Preprocessing

The obtained database contains the speed and acceleration test bench measurements for three different rolling states, the first state describes measurements of healthy bearing, the second state describes the measurements for bearing with inner ring failing, and the third state concerns the failing outer ring bearing. However, the actual data are being always incomplete, noisy or inconsistent view to the uncertainty during the exploitation of experience, for that; we opted for a pretreatment of our base to avoid noise and data imperfections.

The relation used for standardization is:

$$V_i = 0,8 \left(\max - \frac{\text{Valeur initiale}}{\max - \min} \right) + 0,1 \quad (3)$$

4.5 MLP-Type Neuron Network Algorithm for Prognosis of Bearing

In this section, we present the performance of the generated model and the prediction results in the form of graphs obtained from MATLAB.

Figure 5 represents the structure of the model thus developed, the model contains two inputs the first input represents the speed, the second input represents the acceleration, a single hidden layer at 11 neurons, the base of the outputs describes the modes of bearing operating, the value 1 describes the healthy bearing, the value 2

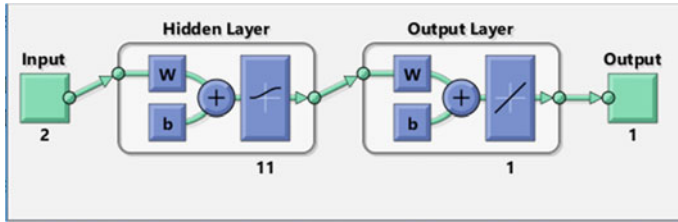


Fig. 5 Structure of the developed model

describes the failed bearing inner ring and the value 3 describes the failed bearing outer ring.

Figure 6 represents the efficiency of the network by the regression (R) of the percentage of bearing life. The 4 graphs represent the target data (Target) according to the results of our network (Output) for each matrix (of learning, testing and validation), The regression values measure the correlation between the output values and the targets. The results obtained in this study show a good correlation between the values and targets output during training ($R = 0.99933$), validation ($R = 0.99979$) and the tests ($R = 0.98692$).

Figure 7 shows the error histogram. The error is the difference between the neural network targets (Target) and the actual results (Output). The bars in blue represent training data, the bars in green represent validation data and the bars in red represent test data. We acknowledge that most of the errors are between $[-0.07595; 0.03234]$ which is close to zero, Therefore the network is performing well.

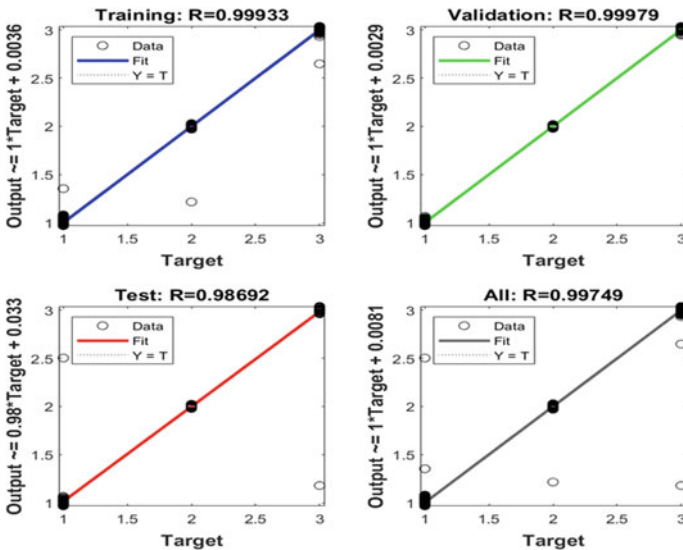
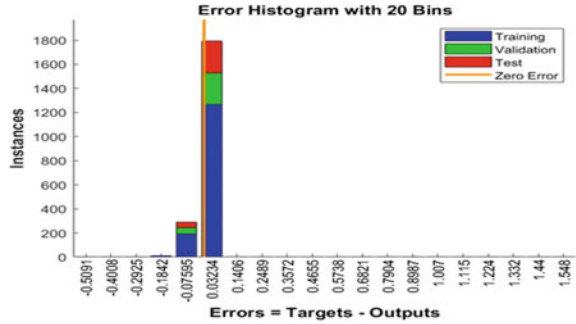


Fig. 6 Regression model performance

Fig. 7 Error histogram



The Fig. 8 represents the performance of the neurons networks MSE (Mean Squared Error) thus developed. This is the square average error depending on the number of iterations. The best validation performance equal to 0.0013925 at 5000 epochs and the test performance equal to 0.0018, The error of the “test” set and the error of the “validation” set are almost similar, The average square error final is small 0.000881.

Finally, Fig. 9 represents the speed and acceleration measurements belonging to the test base as a function of operating mode, the in red curve represents the target operating modes (Target), that is to say 1, 2 or 3, the in blue curve represents the results obtained (Finale Output) from the network.

Fig. 8 Validation performance

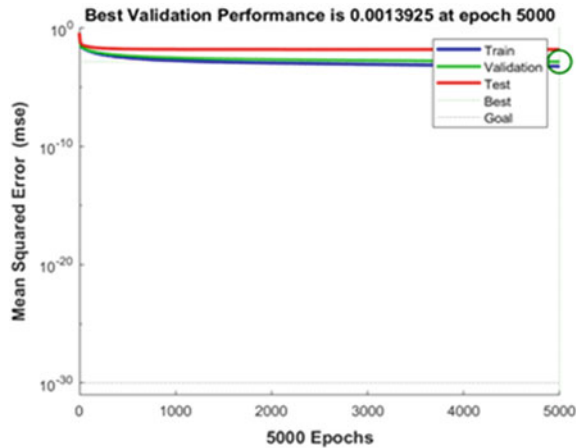
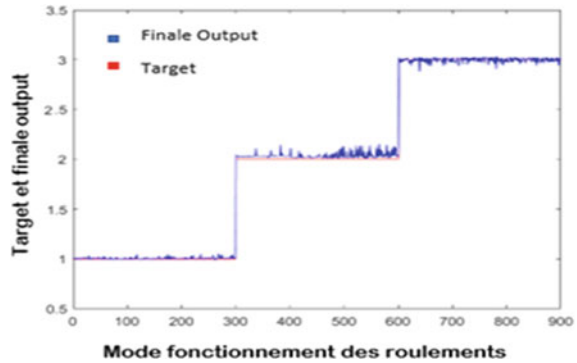


Fig. 9 Bearing operating modes



5 Conclusions

To have effective predictive maintenance based on neurons networks, it is necessary first of all know the inputs that you wish predict and in what forms, then the train of the network is considered a primordial phase during his construction, for to finally predict the state of the bearing from a measurement representing one of the network inputs.

The work done develops a prediction model from a prognosis model based on neurons networks to know the operating condition of the bearing and predict the life before failure.

For the rest of this work, it is possible to use the same model to predict the level of energy consumption of rotating machines as a result mechanical failures.

References

1. Jeffali F, El Kihel B, Nougaoui A, Delaunois F (2015) Monitoring and diagnostic misalignment of asynchronous machines by infrared thermography. *J Mater Environ Sci* 6:1192–1199
2. Mukesh PS, Bulsara A (2016) Energy loss due to unbalance in rotor–shaft system. *J Eng Des Technol* 14(2):277–362
3. Saleem MA, Diwakar G, Satyanarayana MRS (2012) Detection of unbalance in rotating machines using shaft deflection measurement during its operation. *J Mech Civ Eng (iosr-jmce)* 3(3):8–20
4. Harrouche F (2019) Etude Comparative de Deux Méthodes D’optimisation d’un Système de Classification des Défauts Mécaniques par la Logique Floue. Thèse de doctorat, Université Ferhat Abbas Sétif Algérie
5. Mattioli J, Robic P-O, Reydellet T (2018) L’intelligence artificielle au service de la maintenance prévisionnelle, 4ème conférence sur les Applications Pratiques de l’Intelligence Artificielle APIA2018, Nancy, France
6. Bouzidi Z (2018) Pronostic des systèmes industriels basé sur l’intelligence artificielle Maintenance prédictive. Thèse de doctorat, Faculté des Sciences Exactes et des Sciences de la Nature et de la Vie Département d’informatique, Université Mohamed Khider—BISKRA
7. Ayegba PO, Abdulkadir M, Hernandez-Perez V, Lowndes IS, Azzopardi BJ (2017) Applications of artificial neural network (ANN) method for performance prediction of the effect of a vertical

- 90° bend on an air–silicone oil flow. *J Taiwan Inst Chem Eng* 74:59–64. <https://doi.org/10.1016/j.jtice.2017.02.005>
8. Bouallegue K (2017) A new class of neural networks and its applications. *Neurocomputing* 249:28–47. <https://doi.org/10.1016/j.neucom.2017.03.006>

Intersection Management Approach based on Multi-agent System



Meryem Mesbah, Ali Yahyaouy, and My Abdelouahed Sabri

Abstract For several decades, urban congestion causes various problems such as pollution, road works, and congestion in intersections which deteriorates the quality of life of citizens who live in big cities. Different methods proposed to reduce urban congestion, notably traffic regulation that attract tremendous attention recently. In past years, the usage of tools from artificial intelligence, particularly distributed methods and multi-agent systems, which allow to design new methods for traffic regulation. In this context, a Multi-Agent approach for intersection management system based on the principle of trajectory reservation has been proposed to reduce the travel time average and air pollution.

Keywords Intersection management · Connected vehicle · Multi-agent system · IAS · ITS

1 Introduction

Vehicles nowadays contain many sensors for perception purposes and sometimes-complementary advantages. It has also many features such as forward collision warning (FCW), automatic emergency braking (AEB), and pedestrian detection (PD). In other words, today's vehicle has all the necessary inputs that provide a rich environment perception. Moreover, with the emergence of V2X (which includes vehicle-to-vehicle V2V and vehicle to infrastructure V2I) will play a significant role in the intelligent transportation system (ITS). It provides the accurate speed heading,

M. Mesbah (✉) · A. Yahyaouy · M. A. Sabri
Department of Computer Science, Faculty of Sciences Dhar El Mahraz, Sidi Mohamed Ben Abdellah University, Fez, Morocco
e-mail: meryem.mesbah@usmba.ac.ma

A. Yahyaouy
e-mail: ali.yahyaouy@usmba.ac.ma

M. A. Sabri
e-mail: abdelouahed.sabri@usmba.ac.ma

the status of the brake pedal, and more, which will increase the level of vehicle's surroundings.

Traffic congestion becomes a complicated problem that continues to grow day by day over the world. This phenomenon is correlated to urbanization and population growth. Especially during rush hours and in work zones, traffic congestion has important impacts on air pollution [1, 2], time loss, road fatalities, several economic consequences (such as increase in fuel consumption etc), social (such as waiting time and stress) [3], and environmental consequences [4].

According to the INRIX report in 2020, drivers in London lost the most time annually to traffic congestion with about 149 hours costing 1162 euros. For American drivers it was estimated a loss of 99 hours per year for each driver, costing \$1377 per year.

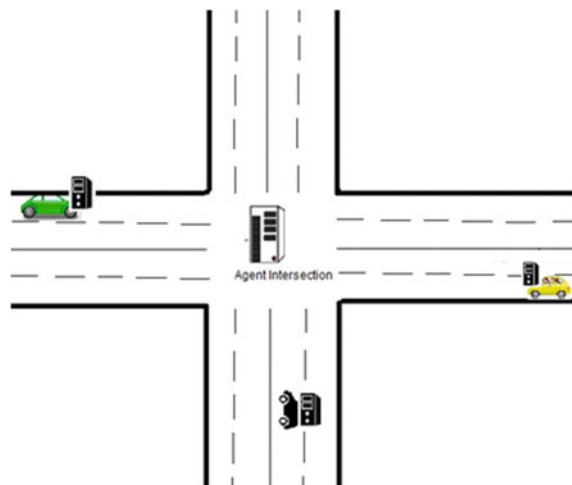
As reported by World Health Organization (WHO), more than 1.35 million people over the world died in a road accident, and about 20–50 million injured, many of them keeping a disability as a result of their injuries. According to the same organization, the death rate for the traffic accident in Africa is the highest. It stands at 26.6 deaths per 100,000 population.

Today and thanks to the rapid progress of wireless communication, vehicles can communicate with the outside world. It can now receive the traffic status [5], and traffic collisions. Agents are used recently as infrastructure support for traffic management and as a decision support system for traffic control [5, 6].

Using the capabilities of the connected vehicle, we proposed multi-agent intersection management based on the reservation approach. In other words, to cross the intersection, the vehicle agent must send a request to an intersection agent to reserve a trajectory.

This system is proposed for the classical intersection model, which is shown in Fig. 1. It is composed of four possible directions. Each direction can be decomposed

Fig. 1 An intersection management system based on multi-agent



into an inbound direction and outbound direction or both. In each incoming and outgoing direction, there are two lanes.

The rest of the paper organized as follows. Section 2 represents several research topics for intersection management including classical approaches and research based on multi-agent systems. Section 3 described the general architecture of the proposed system. The operation of components is presented in Sect. 4. Finally, Sect. 5 concludes this paper with future work.

2 Related Work

2.1 Classical Approaches

The most relevant classic approaches and algorithms, which have been proposed in order to improve the vehicle traffic flow since 1960, are below:

- TRANSYT (Traffic Network Study Tool) [7]: it is based on offline optimization that generates optimal coordination plans between the traffic lights of a network for a given period. TRANSYT requires many input parameters, such as the geometry of the intersection arteries, the vehicle flow, the rate of vehicles on each outgoing lane of each intersection (set in advance), the minimum green light time, initial fire plans, and initial values for cycle times and phase shifts. From these parameters, a mathematical model is simulated and its performance is evaluated. Finally comes the optimization stage using a Hill-Climbing optimization algorithm, which is to say gradually improving the solution by modifying the duration of the green lights and offsets between adjacent intersections.
- SCOOT: (Split Cycle and Offset Optimization Technique) [8] a fully adaptive traffic control system developed in the UK by Transport Laboratory in 1980. It is an efficient system for a signalized road, which is used in over 130 cities and towns in the UK and overseas. For this system, electromagnetic sensors are located on each section to measure vehicle flow, detect queues due to congestion and vehicles stopped for other reasons. In order to minimize the number of vehicles stops and the length of the queue at the intersection, all those information are used to define the duration of light phases for each of the intersections in the area monitored by the system.
- SCATS (Sydney Coordinated Adaptive Traffic System) [9, 10] developed in the 1980s operates on real-time data. It collects information by sensors, which are located in a traffic light. The implementation of this strategy takes the same form as the SCOOT strategy, namely change cycle times, phases, and offsets. This approach is based on a concept of subsystems that group (1–10) intersections per subsystem. It used a real-time algorithm of the light plan for intersection and predefined libraries, which store about 10 sets of offsets and 4 sets of greenlight duration. From these sets, the algorithm reconstructs light plans for every cycle.

- PRODYN [11] is a decentralized and adaptive system developed by CERT in France. It is used to optimize online traffic by using a dynamic program to minimize delays at intersections by relying on a model of traffic flow over the entire horizon. Its system allows communication with a neighbor intersection in order to anticipate the incoming flows. The strategy used by this system consists of analyzing at each time step (of 5 seconds), if changing the phase is the optimal decision.

2.2 Discussion About Classical Approaches

These systems, in particular the cyclic systems, limit actions to a certain number of possibilities, most often stemming from traditional regulation: modification of phase durations, cycles, and phase shifts between neighboring intersections. Other regulatory actions can however be considered to allow a more dynamic regulation. In addition, the connected vehicles make it possible to envisage new possibilities of action that can be used for regulation, for example, communicated on the control strategy of an intersection so that the vehicle adapts its acceleration profile. Some of these systems rely on flow models to make predictions of traffic evolution. Although it seems difficult to dispense with any predictive model in an anticipatory approach, the simplicity of the perceptions of these systems does not allow a dynamic adjustment of the predictions made. This criticism can be reinforced by the fact that the connected vehicles, by their communication and co-ordination capabilities, have different flow dynamics than conventional vehicles. The spread of this type of vehicle could make the predictions made by this type of system less and less relevant, and thus reduce the effectiveness of the regulation performed.

2.3 Approaches Based on Multi-agent

Various problems related to the regulation of urban traffic have been identified in the IT community, notably by the multi-agent community [12–14]. We describe here several works, in their diversity, that relate to the regulation or the coordination between vehicles, at the scale of an intersection or a wider zone. In the first case, the coordination and regulation at an intersection can be considered as a problem independent of the question of global regulation on a network and we speak of “isolated” intersection (the rest of the network not being taken into consideration). In the second case, coordination takes place between the intersections in order to achieve a more coherent regulation at the network level.

For an isolated intersection, different coordination problems between vehicles may be considered and different approaches are possible for each of these problems. Many of these difficulties relate to real-time traffic assignment and the right-of-way, i.e. the authorization for a vehicle to enter the intersection, is allocated to each vehicle.

Some of these approaches require a regulatory agent that applies only a regulatory policy, others involve inter-vehicular coordination.

A first approach is discussed in [15]. In this work, each vehicle communicates the information it has to others to allow vehicles to coordinate with them. The different vehicles have trajectories intersecting on points called “points of conflict”. To allocate a transit date for each vehicle, the agents’ behavior is based on a collaboration plan. In the absence of any coordination, vehicles encounter conflicts. Based on a simple method of conflict assessment, vehicles push their respective dates of entry into the intersection one by one to avoid any conflict. The collaboration plan proposed by this method allows vehicles to change the order in which their transit dates are postponed. However, the authors do not provide details of the interaction mechanism and do not indicate its properties or guarantees it provides.

Balan and Luke [16] is based on the notion of fairness for traffic regulation, proposing a control policy for intersections based on the history of vehicles. This policy reduces the variance in the total time vehicles spend waiting at traffic lights in intersections during their journey. Each intersection has a controller capable of producing different traffic lights planes. A traffic lights plan is a combination of durations of green, yellow, and red for each approach to the intersection, and avoids any conflict. The controller uses different scoring functions based on efficiency and fairness to evaluate each possible regulation plan. The efficiency and justice of each plan are evaluated, for different grid sizes and different traffic loads.

Some work on the isolated intersection concerns the coordination of vehicles, and others concern the regulation performed by the intersection [17]. AIM (Autonomous Intersection Management) seeks to coordinate autonomous vehicles on the intersection. This coordination involves the agreement of the right of way to vehicles, and the AIM, thus realizes a regulation of the intersection with the help of various information relating to the vehicles. The following works below are related to AIM:

In Dresner and Stone [18] proposed a right-of-way mechanism for autonomous vehicles based on reservation. This is based on a policy called FCFS (First Come First Served), granting the right of way to each vehicle by making the request, as soon as possible. This mechanism takes into account human drivers by using a conventional lights intersection policy for human drivers, and by providing transition dates for autonomous vehicles using the FCFS policy. Although this mechanism accommodates the presence of human drivers, its main benefits are due to the use of FCFS for autonomous vehicles.

Gregoire et al. [19] allows coordination between vehicles approaching an intersection by constructing a priority graph (oriented) determining the order of admission of the vehicles. The article proposes a characterization of a feasible priority graph.

Yan et al. [20] is based on the notion of “streams” representing the possible trajectories of vehicles at the intersection. For example, all vehicles arriving at the intersection from a lane south of the intersection to a lane east of it form a current. In this approach, groups of currents are formed so that none of the currents forming a group intersect. We talk about compatible currents between them. The currents of a group can simultaneously fire to green. The problem of assigning the right of way is then represented as a problem of scheduling tasks. From the compatible current

groups, groups of vehicles are formed. These groups are represented as groups of tasks, and thanks to this representation, the total evacuation of the intersection are minimized by using an exact resolution method (separation and evaluation, dynamic programming).

Vasirani and Ossowski [21] proposes a market-inspired approach to AIM. When choosing their routes, drivers often opt for the fastest route after estimating the travel time for each of the potential routes. In this model, drivers must purchase a reservation from managing agents in order to cross intersections. This reservation system provides drivers with incentives to explore alternate routes. In this mechanism, each intersection manager must determine his booking fees to maximize his profit. With a few vehicles, the intersection manager gets a small profit, but with a large number of vehicles, it loses profit because of congestion. It must adjust his booking fees to attract an average number of vehicles. Intersection Managers use a Q-learning to adjust these booking fees.

Kamal et al. [22] proposes an approach to building multi-agent regulation policies using unsupervised machine learning methods. On an isolated intersection, vehicles can move and avoid collisions. A traffic authority collects the information and makes case-by-case reasoning based on experience to determine the solution to be applied to resolve the current situation. Then a standards manager transforms the solutions found into standards for vehicle agents, which apply these rules using a rule engine. A reduction in the number of standards necessary to achieve the goals of the system (avoid conflicts) is also made so that the number of rules to be checked by the vehicles remains reasonable.

3 Architecture of the Proposed System

In this research, we proposed a system to manage traffic congestion in intersection based on multi-agent. It consists of two agents: Vehicle Agent (VA), and Intersection Agent (IA). Each agent is equipped with wireless communication devices (I2V/V2I).

The Vehicle Agent VA is a system installed in each vehicle. It is responsible for communicating with the Intersection agent before a distance D of the intersection to request the trajectory reservation. While the intersection agent is installed in the intersection.

The system is based on the reservation of the vehicle trajectory. In other words to pass the intersection, each vehicle agent preplans its trajectory and then send it to the Intersection agent a request for passage reservation. In addition, based on the reservation list the intersection agent will make its decision. The reservation policy is the key to reduce collision, congestion in the intersection, and waiting time.

3.1 Messages from VA to IA

There are three types of messages sent from the VA Vehicle Agent to the IA Intersection Agent:

- **Request:** a message sent by AV to reserve a trajectory. In this message, the AV specifies several parameters of the car (Direction, Vehicle ID, Priority, Vehicle Speed, Width, and Length, Position)
- **Change—Request:** message sent if the driver wants to change the direction.
- **Accident:** If the vehicle is down, at this moment an “accident” message is sent to the AI to inform it.

3.2 Messages from IA to VA

The Intersection agent can send to the vehicle agent three types of messages:

- **Confirmation:** based on the reservation request that the VA send, the IA check the reservation table to verify if there is a conflict with other reservation requests by other vehicles. This message sent to the VA to inform it that his request is approved and that he can follow the proposed path.
- **Proposition:** If the pre-planned trajectory is already occupied or a vehicle is down in the intersection. The AI sends this message to propose to the AV to accelerate, decelerate the speed, or change the way.
- **Acknowledge:** We send this message to VA if the IA receives the message “accident” (Fig. 2).

4 Agent Actions

For each agent, we specify many rules that should respect by the VA and IA to assure a good management of the traffic congestion.

Fig. 2 An abstract view of the interaction between VA and IA

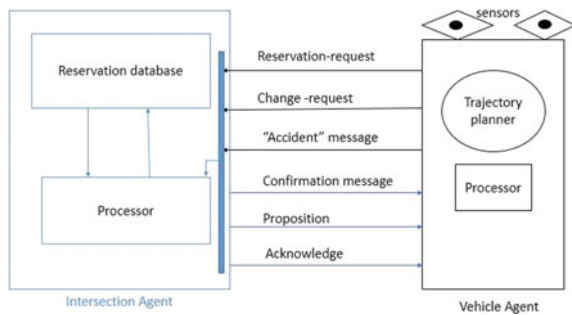
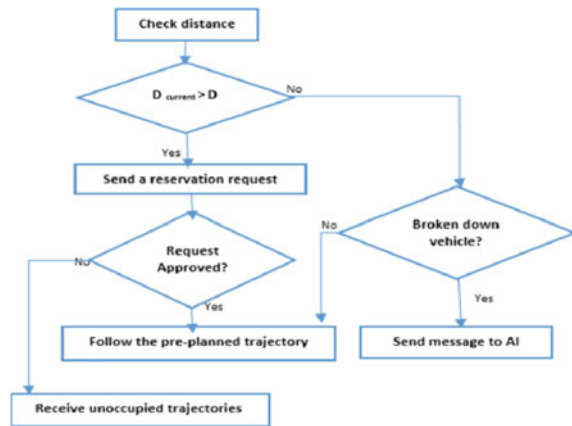


Fig. 3 Vehicle agent behavior flow chart



4.1 Rules of the Vehicle Agent

The vehicle agent must respect the following orders:

- Vehicles cannot cross the intersection without sending a passage reservation request.
- Using an embedded system, the VA gets the dynamic information of the vehicle such as: speed, position, direction ...
- Before the distance D of the intersection, the vehicle agent consists of sending a request to reserve the trajectory.
- Once the AV receives the confirmation message, it can follow the proposed path.
- If the vehicle agent has received a confirmation message (following the last request) and the driver wants to change the trajectory, the AV Vehicle Agent must send a Change-Request message request with the new parameters. In this case, the old reservation request sent by the VA will be deleted, and the reservation list will be updated.
- If the vehicle is broken down in the intersection, the VA sends the message "accident" to the IA.

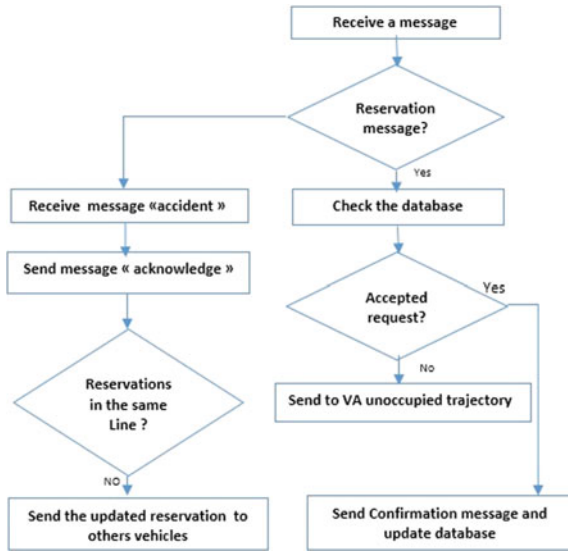
The following figure shows the flow diagram of the vehicle agent (Fig. 3).

4.2 Rules of the Intersection Agent

The following rules must be respected:

- Once the IA receives the reservation request, it verifies in its database to check if there is a possibility to accept it or not. If yes, then it sends the Confirmation message. Otherwise, it sends the message proposition that contains the unoccupied path.

Fig. 4 Intersection agent behavior flow chart



- If the VA sends the message “change-request”, the first reservation will be deleted from the database of reservation. And the IA verifies in its database to check if there is a possibility to accept the new reservation.
- If IA receives the message “accident”, it must send the message Acknowledge to the vehicle, update the reservation list and alert other vehicles that pre-planned the same trajectory by proposing to decelerate or change the track completely.

To better explain the operation of the intersection agent, we present the following diagram (Fig. 4).

5 Conclusion

In this paper, we proposed multi-agent intersection management based on the reservation approach. The main objective of this system is to reduce traffic congestion at intersections, waiting time, and fuel consumption.

We started the implementation of our system using the SUMO simulator and we want to test our system on more complicated traffic networks.

As part of future work, we would like to compare our approach with existing methods such as traffic light control and platoon-based multi-agent intersection management. Then evaluate the performance of our proposed system in different traffic conditions.

References

1. Barth M, Boriboonsomsin K (2008) RealWorld carbon dioxide impacts of traffic congestion. In: Transportation research record, pp 163–171
2. Zhang K, Batternan S (2013) Air pollution and health risks due to vehicle traffic. In: Science of the total environment, pp 307–316
3. Hennessy DA, Wiesenthal DL, Kohn PM (2000) The influence of traffic congestion, daily hassles, and trait stress susceptibility on state driver stress: an interactive perspective. *J Appl Biobehav Res* 5(2):162–179
4. Hao P, Wang C, Wu G, Boriboonsomsin K, Barth M (2017) Evaluating the environmental impact of traffic congestion based on sparse mobile crowd-sourced data. In: IEEE conference on technologies for sustainability (SusTech), Phoenix, AZ, pp 1–6. <https://doi.org/10.1109/SusTech.2017.8333528>
5. Stone P, Veloso M (2000) Multiagent systems: a survey from a machine learning perspective. *Autonom Rob* 8(3):345–383
6. Dresner K, Stone P (2008) A multiagent approach to autonomous intersection management. *J Artif Intel Res* 31:591–656
7. Robertson DI TRANSYT: a traffic network study tool. RRL report, Road Research Laboratory
8. Hunt PB, Robertson DI, Bretherton RD, Royle MC (1982) The SCOOT on-line traffic signal optimisation technique. In: Traffic engineering and control, vol 23, issue 4, pp 190–192
9. Sims AG, Dobinson KW (1980) The Sydney coordinated adaptive traffic (SCAT) system philosophy and benefits. *IEEE Trans Veh Technol* 29(2):130–137
10. Lowrie PR (1982) The Sydney coordinated adaptive traffic system-principles, methodology, algorithms. In: International conference on road traffic signalling, London, United Kingdom
11. Henry JJ, Farges JJ, Tuffal J (1983) The PRODYN real time traffic algorithm. In: Proceedings of the international federation of automatic control (IFAC) conference, IFAC, Baden-Baden
12. Zhao D, Dai Y, Zhang Z (2012) Computational intelligence in urban traffic signal control: a survey. *IEEE Trans Syst Man Cybern Part C: Appl Rev* 42(4):485–494
13. Zhao L, Li Li, Li Z (2011) A fast signal timing algorithm for individual oversaturated intersections. *IEEE Trans Intell Transp Syst* 12(1):280–286
14. Cajias R, Pardo A-G, Camacho D (2011) A multiagent simulation platform applied to the study of urban traffic lights. In: The 6th international conference on software and data technologies (ICSOFT 2011), pp 154–159
15. Zou X, Levinson D (2003) Vehicle-based intersection management with intelligent agents. In: ITS America annual meeting. Minneapolis, Minnesota, pp 15
16. Balan G, Luke S (2006) History-based traffic control. In: Proceedings of the fifth international joint conference on Autonomous agents and multiagent systems, ACM, pp 616–621
17. Jin Q, Wu G, Boriboonsomsin K, Barth M (2012) Advanced intersection management for connected vehicles using a multi-agent system approach. In: IEEE on intelligent vehicles symposium, pp 932–937
18. Desai P, Loke SW, Desai A, Singh A (2011) Multi-agent based vehicular congestion management. In: IEEE on intelligent vehicles symposium
19. Gregoire J, Bonnabel S, de La Fortelle A (2013) Optimal cooperative motion planning for vehicles at intersections. In: arXiv preprint [arXiv:1310.7729](https://arxiv.org/abs/1310.7729), pp 16
20. Yan F, Jia W, Dridi M (2014) A scheduling model and complexity proof for autonomous vehicle sequencing problem at isolated intersections. In: 2014 IEEE international conference on service operations and logistics, and informatics (SOLI). IEEE, pp 78–83
21. Vasirani M, Ossowski S (2009) A market-inspired approach to reservation based urban road traffic management. In: Proceedings of the 8th international conference on autonomous agents and multiagent systems-volume 1. International foundation for autonomous agents and multiagent systems, pp 617–624
22. Kamal MAS, Hayakawa T, Imura J-C, Ohata A, Aihara K (2015) A vehicle-intersection coordination scheme for smooth flows of traffic without using traffic lights. *IEEE Trans Intel Transp Syst* 16: 1136–1147

A Model of an Integrated Educational Management Information System to Support Educational Planning and Decision Making: A Moroccan Case



Mustapha Skittou, Mohamed Merrouchi, and Taoufiq Gadi

Abstract The planning of education in Morocco represents an essential element in the projects implementation of the educational system, on which rests the various operations of diagnostics, realization and evaluation of the educational strategic choices. The planning profession has benefited very well from technological advance, and the country has been in the process of automating information systems for a long time. But according to our analysis, the education information system will be able to be more effective if it can adopt the techniques proposed, especially with regard to the establishment of an Integrated Information System (IIS) which groups operational systems, then use a Decision Support System (DSS) to help decision makers. As well as an Early Warning System (EWS) to predict problems, and a Recommendation System (RS) to propose realistic and effective measures. The unification of such systems will improve both the quality of the educational data management and the educational administration processes.

Keywords Education planning · Integrated information system · Decision support system · Early warning system · Recommendation system · Educational management information system

1 Introduction

Planning is the driving factor for any system aimed at efficiency and performance. For a long time, the different areas of our life have taken part in this essential tool for the success of programs and projects. And with the advent of new information and communication technologies, this took on another dimension. Planning since it was introduced in education, boosted the education system, and made it possible to make in-depth diagnoses of the educational systems state, define their need on all levels and set up projects to develop their outputs. It has benefited also from technological development and the information systems automation approach. Education planners,

M. Skittou (✉) · M. Merrouchi · T. Gadi
Faculty of Sciences and Technics, Laboratory Mathematics, Computer and Engineering Sciences (MIS), Hassan First University of Serrat, Serrat, Morocco
e-mail: mustapha.skittou@gmail.com

as key players in the education system, are positioning themselves at the heart of this technological change [1]. To plan well, first of all we will need to identify all the local aspects of the system. An Integrated Information System (IIS) provides this because it brings together all the information useful for analysis and planning in a robust, consistent and reliable system. Through this information, the planners only access the interface of the integrated system once in order to collect the data useful for each level of educational planning and to interact with the various actors of the educational system.

On the other hand, to help decision makers to implement concrete and rigorous decisions, we can use a Decision Support System (DSS). The latter will allow them to fly over the education process, to maximize the benefits of learning and training projects, and promote the quality of teaching and the outputs of the system [2]. Apart from the fact that the DSS is a support tool for decision-makers, it can also be considered as a transparency element by allowing regulated access to education data by all civil society [3].

The results of educational projects and programs concern the future of a number of generations, and their repercussions can affect the whole of society. That is why it does not seem reasonable to base our plans solely on a descriptive analysis of the education system history, without carrying out a predictive analysis of how the future may be, or even a prescriptive analysis of how to be exposed to random risks. An Early Warning System (EWS) contains at its heart a prediction engine, it allows to analyze the data to extract buried models and reuse them in similar contexts to anticipate the behavior of the analyzed objects, this of course enters in the field of artificial intelligence [4]. The phenomena to predict in the educational field are numerous and diverse depending on the socio-cultural environment, whether it be: educational performance [5, 6], School Refusal [7], drop out [8, 9], or School Attendance Problems [7] etc. To finalize the image of information systems for education, and to support the outputs of the EWS, we will need what is called a Recommendation System (RS) capable of translating the scenarios developed by the EWS into active measures in the field to remedy any possible damage that may occur. The RS is similarly based on artificial intelligence techniques, and it is mainly deployed on major web platforms such as: Netflix, Google, YouTube, etc. Its advantage lies in its ability to memorize the best choices made against previous crisis situations, to learn from experience and to promise a better and quick reaction to problems.

The aim of our work is to propose a model of an integrated system for educational planning, which combine all the advantages provided by the new information systems technology: Decision Support System, Early Warning System and Recommendation System. Our architecture can be called as mixed or blended integrated architecture. It will allow to softly merge all the aspects of these systems in order to give entire control for planners and decision-makers to exploit the outputs produced sequentially and to have a continuous interaction with the whole system.

On this paper, we will first present a state of the art to describe the different contributions used for our same subject, in Sect. 2. After, we will talk about educational planning in all its aspects, in Sect. 3. And, we will present the improvements that we propose for the educational information systems in Morocco, like we think; in

Sect. 4. In Sect. 5 we will present our proposed model for the blended integrated educational information system. Lastly, the conclusion is outlined in Sect. 6.

2 Related Work

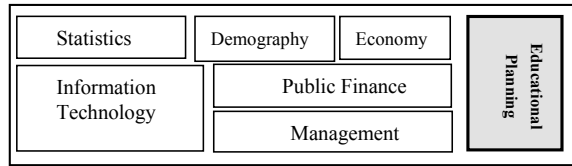
To build an integrated information system, we need to join an education management information system with other information systems. The first step in building an information system intrinsically consists of an in-depth analysis of the existing system. Especially the data flow, and it's the same with an education management information system (EMIS).

The main task of an EMIS is the education data management process. Data is divided into three types: Fundamental data, Business data and Statistical data [10]. Each of the types relates to a kind of the system basic data, the first one is not affected enormously by the change (Fundamental data) like student information, the second results from the activities implemented periodically (Business Data) like the curriculum or student performance, and the third works on the results of evaluation of the processes deployed on the system (Statistical data), like exam pass rates or results distribution ratio. One of the major challenges in the education data management process is data collection, given the diversification of data: structured/semi-structured/unstructured, formatted/unformatted. The most effective solution to date is the use of an extraction, transformation and load (ETL) tool [11].

Most information systems use the form of Web-based management information system, since the huge development of internet technologies the recent decades. the evolution also marked the level of accessibility of people to the network, which facilitated the interconnection of all education system actors. This pushed towards the adoption of this approach also in the construction of EMIS. There are two main kinds of EMIS architecture in the literature: Client/Server architecture (C/S) and Browser/Server architecture. C/S is the most used architecture to develop the technical aspect of EMIS projects. B/S architecture only differs from C/S by its no need for client software installation. Huanggang Normal University Online Educational Management Information System (HNUOEMIS) is based on B/S mode. It contains a collection of integrated systems that manages the financial level, human resources, e-learning, etc. [12]. Recently a new architecture has been proposed, called C/S and B/S combination or hybrid architecture. It brings together the two aspects of the two architecture and uses each in a field. Zhengfang is a widely used EMIS in Chinese university using service-oriented technology (REST) with hybrid architecture, university-level and school-level modules using C/S mode, teachers, students and aids staff modules using B/S mode [10]. Another implementation of EMIS was proposed adopting this hybrid mode to develop China's higher education system, especially with the application of college credit [13].

Information systems went through a stage where automated processes were combined with manual paper work, or even silo systems. But the trend has shifted to integrated systems for their numerous advantages, especially data consistency,

Fig. 1 Basic sciences to educational planning



integrity, security, time savings, etc. This is why we opt for an integrated architecture of the Moroccan EMIS, which will contain the different engines necessary for the two operational and strategic aspects of the educational information system.

3 Educational Planning

Educational planning is an intrinsic part of the education sector development, interacting with several fields of action and based on a set of techniques. Planning in its simplest definition is a succession of actions and decisions that exploit material or immaterial resources, with the aim of achieving previously established objectives. There are several varieties of planning: local/regional/national, partial/global, societal/sectoral, operational/strategic.

Educational planning is a component of sectoral planning for the education sector as a whole. Its purpose is to study the existing capacities as well as the constraints in the country on the educational side, and makes it possible to plan future actions in order to remedy the shortages recorded. Educational planning is based on several sciences (see Fig. 1).

4 Improvement Way

The profession of educational planner has evolved well since its first establishment in the administration of national education, and its impact has also been felt through the various phases of reform and development of the educational system in Morocco. Despite all the organizational and legislative constraints and the lack of resources posed to educational planning in a third world country. Lately, with the advent of new technologies, other potentials are emerging. Through our observation of education planners work, our improvement proposals presented in this paper concern the implementation of an Integrated Information System (IIS) that merges all the operational information systems of the education system, and also enter the notions of new information systems important to support decision-making for planners and all managers in the field of education, like:

- A Decision Support System (DSS) for decision makers in the education system.
- An Early Warning System (EWS) to predict failures in the education system.

- A Recommendation System (RS) to propose effective intervention measures according to the need and the case studied.

4.1 Merge of Operational Systems

The Moroccan education system is managed by several information systems, each specializing in part of the operations useful for educational planning. The following systems acting in planning are cited as follows:

GRESA: Is a system for managing the directory of educational and administrative establishments. It allows the creation of public and private establishments and fills in all fields of information on the physical and administrative structure of the establishment.

ESISE: It is an education census system, recording data from public and private establishments. Everything about schooling, human resources, social support and hosting structures.

Massar: The school management system, accessible by the various actors in the education system (Teachers, school directors, managers and decision-makers) according to predefined roles. It is a system that contains all the data of school management in real time as well as a summary dashboard of the existing gaps in the data entered.

CarteSco: The system for entering and updating the prospective school map. It is a space for writing the school map according to the cycles (Primary, Middle or High school), and according to the type of map (theoretical, prospective or adjusted). And It contains all the data of the school map for the following year: Students, classes, teachers, reception area, orientation, flow rate, etc.

The need is to adopt an architecture integrating all the latter in a single information system (see Fig. 2). Because of the different advantages that provide an Integrated Information System in this level, counted in: Ensuring the consistency and homogeneity of the data, time saving and energy, unifying the information system and optimizing its management processes, also secure data and properly control user profiles.

4.2 Decision Support System

Operational educational planning requires making effective and subtle decisions continually. This need among decision-makers in the education system requires the deployment of a Decision Support System (DSS), which will support the decision-making process by ensuring the availability of the various data analysis useful to have a panoramic view of the system. The DSS proposed in this paper mainly concerns

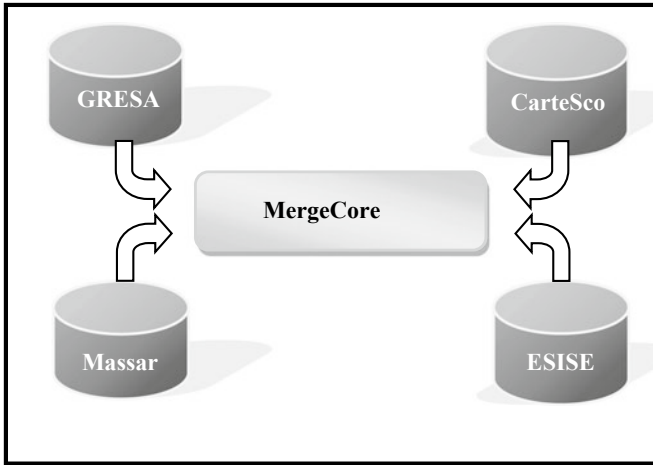


Fig. 2 Diagram of Merging the existing operational systems for the Moroccan education system

the Moroccan education system, and it is subdivided into four components (see Fig. 3). Data sources, which represent the different operational information systems of the education system, in addition to the different digital information media such as: reports from the High Commission for Planning (HCP), data births from the ministry of health, etc. Data provisioning, we will use extraction, transformation and loading (ETL) tools to automate the process of storing data in the Data warehouse. The Data

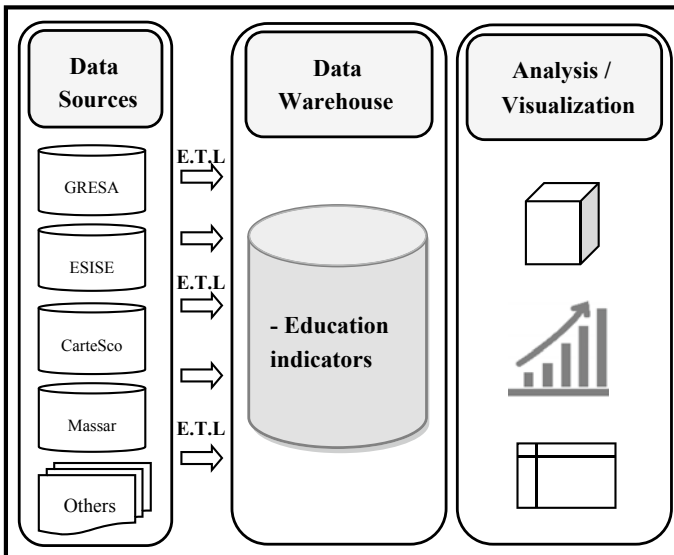


Fig. 3 Educational decision support system architecture for moroccan case

Warehouse, it Gathers all the data collected from the different heterogeneous sources in a consistent and historical manner. The idea is to add calculated columns that represent the education indicators used in educational planning. Finally, Analysis and Visualization, it analyzes the indicators already calculated and visualize the results using Business Intelligence software, in order to allow decision-makers to make an enriched and clear decision-making.

The decision-making process is a very complex managerial act. In a DSS we could have several decisions, we take $DEC = \{DEC1, DEC2, DEC3, \dots, DECn\}$ as a sequence of decisions could be taken. We can define a decision as follows:

$$dec = \{DID, Content, Nature, Level, InterventionDomain, Goal\} \quad (1)$$

where DID is the identifier of each decision, Content is the text content of the decision, Nature can be divided into operational or strategic, Level represents the intensity of decision: normal, urgent or critical; InterventionDomain identifies the precise domain subject of the decision in education. For Goal attribute, each decision has a precise goal to achieve in the field. But goal comes with constraints of time and cost, that is why we define it as:

$$Goal = \{GID, G_{Time}, G_{cost}\} \quad (2)$$

where GID identifies one goal, G_{Time} represents the time to expire, G_{cost} is the cost needed to achieve it.

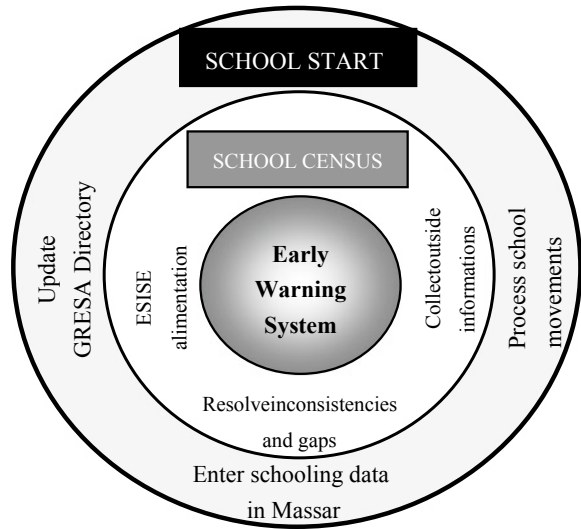
Every decision is a response to a problem or lack of something. The problem is a case to analyze and control, we can define it as: $Case = \{Indicator, DEC\}$. The indicator is a sign and quantitative rate which gives an idea on the level of the problem. The value of the indicator will determine the right decision DEC applied for each kind of problems. We denote the indicator as:

$$Indicator = \{IndID, Type, Parameters\} \quad (3)$$

The indicator is defined by an identifier IndID, Type may be: access, participation or efficiency. Parameters represents all the proportion of data required to calculate the indicator.

Finally, DSS as a decision support tool must contain a system of decisions' classification according to the most suitable to solve each specific problem; the decision is made up of several elements defining its nature as well as its purpose, and with the calculation of performance indicators we can measure the impact of the decisions taken on the resolution of the issues raised.

Fig. 4 Overview of the suggested early warning system



4.3 Early Warning System

In order to control the failures of the education system and to identify in time the gaps registered, an Early Warning System must be established to analyze the historical data of the system and makes it possible to predict the occurrence of educational phenomena.

Prediction technologies have evolved well in recent years, especially Machine Learning and Deep Learning techniques which have the capacity to process Big Data and apply the different algorithms of: Classification—Clustering—Natural Language—Text mining and others. We can observe the principle of the system (see Fig. 4).

Predictive analytics main goals reside on the production of relevant information, actionable insight, better outcomes, and smarter decisions, and to predict future events by analyzing the volume, veracity, velocity, variety, and value of large amounts of data [14].

The main contribution of an EWS for the planning and management of education is to have a proactive vision of the problems likely to arise on the ground, and give the time necessary for the decision makers to act beforehand to avoid any incident.

4.4 Recommendation System

The Early Warning System will remain incomplete if it is not accompanied by a Recommendation System (RS). This system will allow to propose intervention

measures to remedy the problems raised by the EWS. The system of recommendations will be based on the measures adopted by the competent authorities to address each case by case. So, we can summarize most of the interventions in the following points:

- Creation or extension of school hosting or accommodation spaces.
- Promote social support in a specific area: Support for families—School transport—School supplies or other.
- Evolve the pedagogical structure of the schools: Addition of attractive branches—Opening new cycles—Improving teaching and learning technics, etc.

The Recommendation System represents a memory of the measures and procedures chosen by decision-makers to counter problems that have already arisen, as well as allowing a certain speed of intervention, saves time, and ensures the effectiveness of the measures to be taken. There is a lot of types of RS, namely: content-based, collaborative, and knowledge-based [15]. Content-based approach rests on the preferences of users. And collaborative uses the interactivity between the users for studying the behavioral patterns. The new approach implementing the new technologies aspects of information is knowledge-based. It is used in the field of artificial intelligence, exploiting knowledge mined from the system to address the best recommendations.

5 A Blended Integrated Information System

Integrated information systems have proven to date their efficiency in managing education data. Our approach is based on a mixing and joining of the various operational and strategic systems using the data of the Moroccan national education (see Fig. 5).

The operational systems already exist, and are used greatly in the field of education planning. We propose to merge the outputs of these systems through ETL tools in

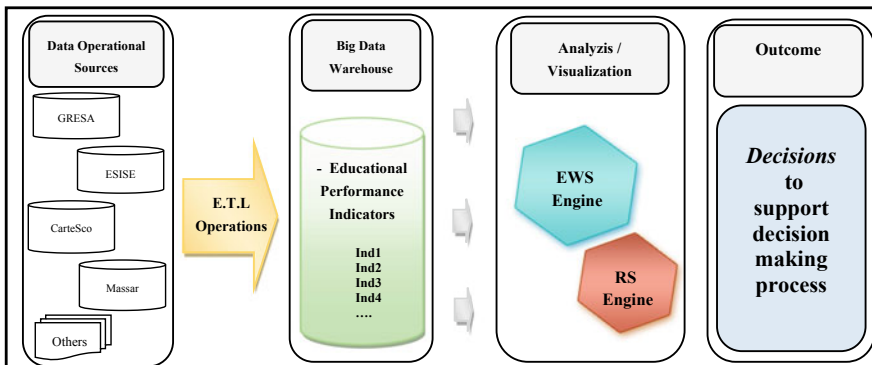


Fig. 5 A model of blended educational management information system

a single Big Data warehouse that is historically recorded and consistent, considered as a basic data center for any manipulation aimed at data relative to education. The data warehouse will contain predefined multidimensional queries in order to prepare the multidimensional cubes of the collected data and transform them as desired. At this stage enter the dynamic systems of advanced data analysis. A prediction system (EWS) which analyzes data via new techniques of Data Mining, Machine Learning and Deep Learning, and announces system anomalies and crises likely to occur. As well as a recommendation system (RS), which will handle the signals and analysis results of the EWS, and will propose measures to solve the future predicted problems. The final outcome of this architecture is the production of relevant decisions in order to help planners and managers to achieve the objectives of the education system.

6 Conclusion

Educational planning is undoubtedly one of the main pillars of success for the entire Moroccan education system. Its importance lies in carrying out educational policies effectively and efficiently. In this paper, we have proposed a vision of a blended integrated information system that can evolve the profession of educational planner and allow its performance. First, we presented a way to aggregate Decision Support System to help decision-makers in the education system to have a full vision of the situation and choose the most plausible scenarios. Third, an Early Warning System to predict system failures and report shortcomings. And fourth, a Recommendation System that offers alternative measures and quick interventions to remedy problems. Our vision claims that with the adoption of this model of information system, educational planning in Morocco can be more effective and efficient, and decision making process in the field of education will be more active, simple and targeted.

References

1. UNESCO Multi-Country Office in the Maghreb (2018) Education planner skills guide. <https://www.unesco.org/new/fileadmin/MULTIMEDIA/FIELD/Rabat/images/ED/20180511ReferentielCompetencesPlanificateur.pdf>
2. InfoDev (2006) Rethinking education management information systems: lessons from and options from less developed countries (Working paper no. 6). https://www.infodiv.org/infodiv-files/resource/InfodivDocuments_504.pdf
3. Iyengar R, Mahal AR, Liya Aklilu, Sweetland A, Karim A, Shin H, Aliyu B, Park JE, Modi V, Berg M, Pokharel P (2014) The use of technology for large-scale education planning and decision-making, information technology for development. <https://doi.org/10.1080/02681102.2014.940267>
4. Rajni J, Borah Malaya D (2015) Predictive analytics in a higher education context. IT Prof 17(4, Article number 7160892):4–33. <https://doi.org/10.1109/MITP.2015.68>
5. Anoopkumar M, Md Zubair Rahman AMJ (2016) A review on data mining techniques and factors used in educational data mining to predict student amelioration. In: Proceedings of 2016

- international conference on data mining and advanced computing, SAPIENCE 2016, art. no. 7684113, pp 122–133. <https://doi.org/10.1109/SAPIENCE.2016.7684113>
6. Shahiri AM, Husain W, Rashid NA (2015) A review on predicting student's performance using data mining techniques. *Procedia Comput Sci* 72:414–422. <https://doi.org/10.1016/j.procs.2015.12.157>
 7. Chu BC, Guarino D, Mele C, O'Connell J, Coto P (2019) Developing an online early detection system for school attendance problems: results from a research-community partnership. *Cogn Behav Pract* 26(1):35–45. <https://doi.org/10.1016/j.cbpra.2018.09.001>
 8. Márquez-Vera C, Cano A, Romero C, Noaman AYM, MousaFardoun H, Ventura S (2016) Early dropout prediction using data mining: a case study with high school students. *Expert Syst* 33(1):107–124. <https://doi.org/10.1111/exsy.12135>
 9. Gitinabard N, Khoshnevisan F, Lynch CF, Wang EY (2018) Your actions or your associates? Predicting certification and dropout in MOOCs with behavioral and social features. In: *Proceedings of the 11th international conference on educational data mining, EDM 2018*
 10. Wang Y, Zhao L (2010) Service-oriented educational management information system construction. In: *Proceedings of the international conference on computer application and system modeling (ICCASM 2010)*, vol 7, Article number 5620647, pp v7554–v7557. <https://doi.org/10.1109/ICCASM.2010.5620647>
 11. Mhon GGW, Kham NSM (2020) ETL preprocessing with multiple data sources for academic data analysis. In: *IEEE conference on computer applications, ICCA 2020*, Article number 9022824. <https://doi.org/10.1109/ICCA49400.2020.9022824>
 12. Zhu Z, Xiao F, Yang G (2011) Research on performance optimization for the web-based university educational management information system. In: *International conference on intelligence science and information engineering, ISIE 2011*, Article number 5997430, pp 261–264. <https://doi.org/10.1109/ISIE.2011.53>
 13. Hongjian T (2012) Research and implementation of educational management information system. *Adv Mater Res* 433–440:6702–6707. <https://doi.org/10.4028/www.scientific.net/AMR.433-440.6702>
 14. Rajni J, Malaya DB (2015) Predictive analytics in a higher education context. *IEEE Comput Soc* 24–33. <https://doi.org/10.1109/MITP.2015.68>
 15. Lin J, Li Y, Lian J (2020) A novel recommendation system via L0-regularized convex optimization. *J Neural Comput Appl* 32(6):1649–1663. <https://doi.org/10.1007/s00521-019-04213-w>

Variational Autoencoders Versus Denoising Autoencoders for Recommendations



Khadija Bennouna, Hiba Chougrad, Youness Khamlichi, Abdessamad El Boushaki, and Safae El Haj Ben Ali

Abstract Recommender systems help users explore new content such as music and news by showing them what they will find potentially interesting. There are many methods and algorithms that can help recommender systems create personalized recommendations. All recommendation approaches can be divided into three categories: Content-based recommendation, Collaborative filtering and Hybrid methods. In this paper, we explore and compare Variational Autoencoders and Denoising Autoencoders for Collaborative Filtering with implicit feedback. A Variational Autoencoders(VAE) is a non-linear model, so it can capture patterns that are more complex in the data and since the forward pass is sufficient to obtain the recommendation of a given user then the query time is fast. A Denoising AutoEncoder is a specific type of AutoEncoder, which is generally classed as a type of deep neural network and is trained to use a hidden layer to reconstruct a particular model based on its inputs. Comparison results between Variational Autoencoders (VAE) and Denoising Autoencoders (DAE) show that VAE has the upper hand when it comes to large datasets while DAE is better when using small datasets. We explore and evaluate both methods on three public datasets and using different metrics.

Keywords Denoising AutoEncoder (DAE) · Variational AutoEncoder (VAE) · Collaborative filtering · Recommender systems

1 Introduction

With the ease of access to the Internet, we are increasingly exposed to a huge amount of information. With all the blogs, newspapers, magazines and many others, it brings a lot of diversity to the users. However, with this multitude of information sources, information overload can become problematic and a filtering method is therefore much needed [1]. Recommender systems are tools allowing such filtering [1]. The main purpose of these systems is to provide the user with relevant resources according

K. Bennouna (✉) · H. Chougrad · Y. Khamlichi · A. El Boushaki · S. El Haj Ben Ali
Laboratory of Intelligent Systems, Georesources and Renewable Energies (SIGER), University
Sidi Mohamed Ben Abdellah, Fez, Morocco
e-mail: khadija.bennouna@usmba.ac.ma

to their preferences. The latter thus reduces his search time but also receives suggestions from the system to which he would not have spontaneously paid attention [1].

There has been a large number of research studies that tried to tackle the issue of recommendation over the years [1–4]. These works come from several fields such as Machine Learning, Statistics and Information Retrieval [2]. Recommendation techniques can be classified in different ways [2]. The mostly used are those which are Content-based (CB), Collaborative Filtering (CF) and Hybrid methods [3]. For Content-based recommendations, the task is to determine which items in the catalog best matches user preferences, so this method suggests and recommends objects and information that is comparable to objects that the user has previously liked or expressed interest in [3]. Systems based on Collaborative Filtering produce recommendations by calculating the similarity between the preferences of one user and those of other users. Such systems do not attempt to analyze or understand the content of the items to be recommended. The method involves making automatic predictions about a user’s interests by collecting reviews from many users [4]. Hybrid methods combine Content-based recommendation and collaborative filtering (CF) [1, 3].

Even though some existing recommender systems did succeed in producing decent recommendations [2], most still suffer from accuracy, scalability, cold-start and sparsity issues [2]. Recently, Deep Learning (DL) has been extensively used in recommender systems to improve their quality [2, 5, 6]. One of the most promising techniques in DL for recommendation is Variational Autoencoders (VAE) [7]. VAE is an extension of AutoEncoders (AE). In AE we use dropout in the first layer, while in the VAE instead of having a simple dense layer for the bottleneck, we have a sampling layer. This layer uses the mean and variance from the last layer of the encoder to get a Gaussian sample and use it as input for the decoder. The VAE can be seen as an AutoEncoder whose training is regularized to avoid overfitting. It also helps solve the latent space irregularity problem [7, 8]. Autoencoders are commonly used for feature selection and extraction, when there are more nodes in the hidden layer than there are inputs. The network then risks to learn the “Identity function” where the output is equal to the input, which makes the AutoEncoder useless [9]. Denoising Autoencoders (DAE) solve this problem by deliberately corrupting the data and randomly resetting some of the input values to zero [9–11].

In this paper, we compare Variational AutoEncoders and Denoising AutoEncoders for recommendations. We organized the paper as follows: Section 2 outlines the existing works on recommender systems; Section 3 formulates the problem and describes the adopted methods. Section 4 delineates the experimental results and discussion. Section 5 concludes the paper.

2 Methodology

Recommender systems suffer from a lot of problems [1, 12] among which we can cite the immense amount of data at hand while the underlying process of the data could be much simpler in a much lower dimensional space. Many techniques in machine learning have tried to compress or reduce the dimensionality of the data into a smaller space. One of the popular methods that has been widely used in recent papers is Autoencoders.

2.1 Problem Formulation

AutoEncoders are trained to reconstruct input data and reduce the dimensional representation in the learning process. The overall architecture of the AutoEncoder contains three components: Encoder, Bottleneck and Decoder. As we show in Fig. 1, the first component is what we call the encoder $h(x) = g(a(x)) = \text{sigm}(b + Wx)$.

Where $h(x)$ are hidden layers, x the input layers and we use sigmoid of linear transformation. The encoder is simply a stack of layers. They could be fully connected or convolutional. They take the input and compress it down to a smaller representation, which will have a lower dimension than the input, and this is called the bottleneck. The final component is a decoder $\hat{x} = o(\hat{a}x) = \text{sigm}(c + W^*h(x))$ where \hat{x} is the output layer. The decoder is going to take the latent representation $h(x)$ to create an output. It is going to again linear transform it and pass it through a non-linearity. So if we have input that are binary between 0 and 1. Then we use the sigmoid non-linearity to squash everything at the output between 0 and 1. It has the same range as the values

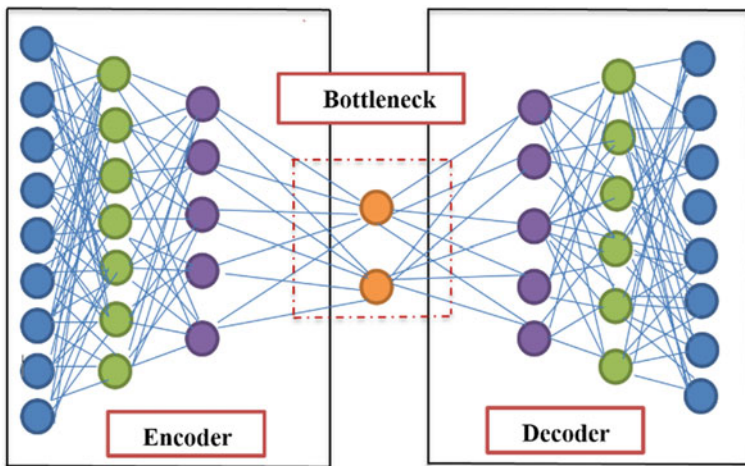


Fig. 1 Architecture of an AutoEncoder

we can have at the input. Another frequent practice is to tie the weight between W and W^* which is the weights between the hidden layers and reconstruction output layers which means that W^* will be set as the transpose W^T of the connection that goes into the hidden layers. Thus, the connections going into the hidden layers are going to be the same as the connections that go out of the hidden layer $W^* = W^T$.

The goal of the AutoEncoder is then to reconstruct the input with the lowest possible error. The Network is then trained using a loss function with hope that the bottleneck layer learns something useful related to the structure underlying the input. Formally, we can model loss function as follows: for a binary input that is the input vector x that contain elements either 0 or 1: $l(f(x)) = -\sum_k (x_k \log(\hat{x}_k) + (1 - x_k) \log(1 - \hat{x}_k))$.

Another alternative if we have real valued inputs $l(f(x)) = \frac{1}{2} \sum_k (\hat{x}_k - x_k)^2$ is to use the squared difference.

2.2 Model Variants

Variational AutoEncoders In recent years, many generative models based on deep learning have been proposed [5, 7, 12–14]. Among these deep generative models, we find Adversative Generative Networks (GAN) [13] and Variational Autoencoders (VAE) [13]. Generative Adversarial Networks (GANs) can oppose two networks, a generator and a discriminator, to push both of them into improvement iteration after iteration.

The objective of the VAE is that the encodings distribution is regularized during the training in order to ensure that its latent space has good properties allowing us to generate some new data. To train a Variational AutoEncoder the loss function in this case actually consists of two terms:

$$L_u(\theta, \varphi, x_u, z_u) = E_{q_\varphi(z_u|x_u)}[\log P_\theta(x_u|z_u)] - \beta \cdot KL(q_\varphi(z_u|x_u)||P(z_u))$$

q_φ : The approximating variational distribution

β : The additional annealing parameter.

The first term represents the reconstruction loss: $E_{q_\varphi(z_u|x_u)}[\log P_\theta(x_u|z_u)]$ this is the same as the AutoEncoder step except that here there is an expectation operator because we are sampling from a distribution. Then the second part of the loss functions is what we call the KL divergence: $KL(q_\varphi(z_u|x_u)||P(z_u))$. Here, we force the latent distribution to be relatively close to a Mean of zero and a standard deviation of one.

Before we can start training our VAE, we still have a problem, where in the middle after the bottleneck we have a sampling operation (sampled latent vector). A node there takes a sample from a distribution then feeds that sample through the decoder.

The problem is that we cannot run back propagation and cannot push gradients through a sampling node. In this case, we use the parametrization trick. We take the latent vector sample and we represent it in the following way: $z = \mu + \sigma * \epsilon$ where z is the sample latent vector, μ : mean vector, σ standard deviation and ϵ is the stochastic node and $\epsilon \sim Normal(0, 1)$.

Denoising AutoEncoders are trained to use a hidden layer to reconstruct a particular model based on its inputs as we show in Fig. 2. We can see that they start with an original input x and we also feed a noisy version x' which is the result of taking x and passing it through a noise process. The noisy x' is going to run through the encoder network and get through the bottleneck representation. Instead of reconstructing the noisy item x' , we reconstruct the original input x .

One popular way for this noise problem is to randomly assign $C(x'/x)$ certain elements of the input to 0, where we choose to assign an input to a value of 0

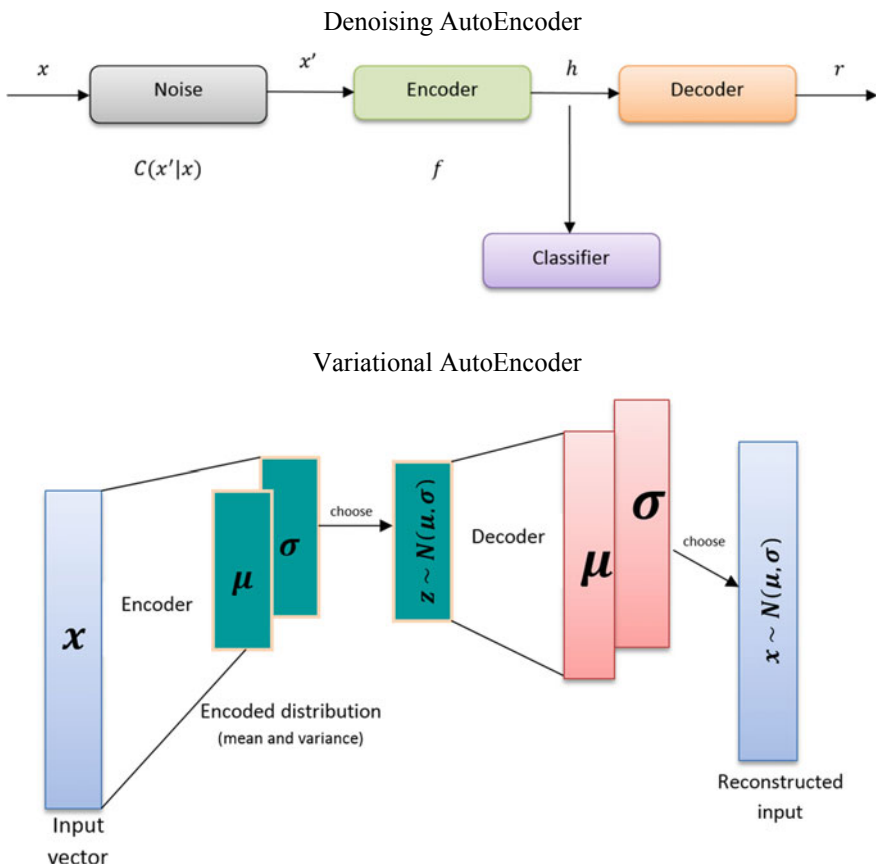


Fig. 2 Comparison of both architectures. The denoising AutoEncoder in the figure on top and the variational AutoEncoder in the bottom figure

with some probability. Using the Loss function we compare the output values with the original input x . That way, the risk of learning the identity function instead of extracting features is eliminated. To train a Denoising AutoEncoder the loss function in this case consists of:

$$L_u(\theta, \varphi) = \log P_\theta(x_u | g_\varphi(x_u))$$

where $g_\varphi(\cdot)$ is the non-linear function.

Both architectures have encoder-decoder blocks, but their function is fundamentally different. Denoising AutoEncoders are a robust variant. They have the same structure of a standard AutoEncoder but are formed using samples in which a certain amount of noise is added. Therefore, we map these noisy samples to their own version. This ensures that the network does not learn unnecessary identity mapping. Variational AutoEncoders are used when we want to model the input data into a distribution and perceive the parameters of the distribution. In short, Denoising autoencoders help us learn a more robust latent representation for a particular set of input data while Variational AutoEncoders enable us to learn the probability distribution of the input data.

2.3 Evaluation

To evaluate our models, we will be using two metrics NDCG and Recall, both metrics compare the predicted rank of the held-out items with their true rank.

NDCG [7] Measures the quality and utility of the order of the items in our recommendations. We first need to define the Discounted Cumulative Gain (DCG). The higher the DCG the better. The DCG@P is defined as:

$$\text{DCG@P} = \sum_{i=1}^P \frac{I[\text{elem}_i \in \text{test}]}{\log_2(i + 1)}$$

$I[\cdot]$ being the indicator function, elem_i the i item in the ordered list of recommendations, @P is the rank position and test the set of items that we wish to obtain in our recommendations. The NDCG is the normalized DCG, where we project the scores between 0 and 1.

Recall [7] considers all items ranked within the first P to be equally important; NDCG@P uses a monotonically increasing discount to emphasize the importance of higher ranks versus lower ones. Formally, we define $w(r)$ as the item at rank r , $I[\cdot]$ is the indicator function, and I_U is the set of held-out items that user U clicked on.

$$\text{Recall}@P(u,w) = \frac{\sum_{r=1}^R \mathbb{I}[w(r) \in I_u]}{\min(M, |I_u|)}$$

The expression in the denominator is the minimum of P and the number of items clicked on by user U . This normalizes Recall@P to have a maximum of 1, which corresponds to ranking all relevant items in the top P position.

3 Experiments and Results

In this work, we consider using implicit feedback data with multinomial likelihood. For each user $u = \{1, \dots, U\}$ and for each item $i = \{1, \dots, I\}$, we have $X \in N^{U \times I}$ the click matrix which contains user-by-item interaction. $x_u = [x_{u1}, \dots, x_{uI}]^T \in N^I$ is a bag-of-words vector with the number of clicks for each item from user u . In this section, we will investigate and compare the performance of the two models Denoising AutoEncoders (DAE) and Variational AutoEncoders as (VAE) for recommendation with implicit feedback using multinomial likelihood. We will assess the models performance on the public MovieLens datasets [15] using the evaluation metrics overviewed in the section beforehand.

3.1 Datasets

We will report the results using three datasets from the MovieLens archive: The MovieLens 20M, the MovieLens 10M and the MovieLens 1M. These datasets contains ratings of user films collected by the Group Lens research project at the University of Minnesota [15].

MovieLens 20M (ML-20M) Dataset contains 20 million ratings and 465,000 tag applications applied to 27,000 movies by 138,000 users. To split the data, we select 10,000 users as held-out users, 10,000 users as validation users and the rest was used for training.

MovieLens 10M (ML-10M) Dataset contains 10 million ratings and 100,000 tag applications applied to 10,000 movies by 72,000 users. To split the ML-10M dataset we select 3000 users as held-out users, 3000 users as validation users and the rest was used for training.

MovieLens 1M (ML-1M) Dataset contains 1 million ratings from 6000 users on 4000 movies. To split the ML-1M dataset we select 2000 users as held-out users, 2000 users as validation users and the rest was used for training.

3.2 Results and Discussion

We first load the data and split all users into training/validation and test sets. We only keep ratings \geq four to optimize the dataset. We train the models using the entire click history of users in the training set and we validate on users from the validation set to learn the necessary user-level representations for the model. We then evaluate the model by looking at how well it ranks the rest of the unseen click history from the held-out users. We train our two models the Denoising AutoEncoder (DAE) and the Variational AutoEncoder (VAE) and we evaluate them using two ranking-based metrics: Recall@P and the normalized discounted cumulative gain (NDCG@P).

Figure 3a shows the learning curve on the validation set when rank position is 100 (NDCG@100) along the epochs using the VAE model. The model was trained for 200 epochs, the validation value NDCG@100 increased from 0.300 to 0.425 between epochs 0 and 25. Then it stabilized to approximately 0.4259 starting from the 50th epoch. Figure 3b shows the learning curve of the validation set when rank position is 100 along the epochs using the DAE model. We can see that the validation of NDCG@100 is more stable in DAE than VAE. It also increased from 0.275 to 0.419 in the first 25 epochs then it stabilized to 0.41997 approximately.

In Fig. 3c on top for the VAE model, we see that when the position is equal to 0 the NDCG validation increases to the value of 0.341997 then it stabilizes starting from epoch 75 to a value of 0.35. In Fig. 3d at the bottom, for the DAE, we see that when the position is equal to 0 the NDCG validation increases to a value of 0.38 then it stabilizes starting from the 175th epoch to a value 0.38756.

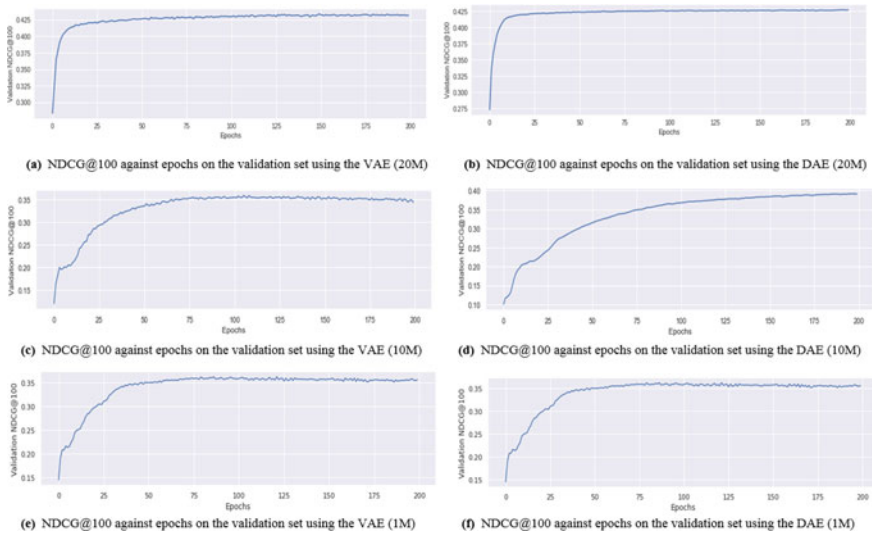


Fig. 3 NDCG@100 against epochs on the validation set using the VAE model and DAE model for all three datasets

Table 1 A comparison summary of the obtained results using the variational AutoEncoder and the denoising AutoEncoder

	ML-20M		ML-10M		ML-1M	
	DAE	VAE	DAE	VAE	DAE	VAE
NDCG@100	0.41997	0.42592	0.38756	0.35631	0.40543	0.20564
Recall@20	0.38768	0.39535	0.35766	0.33026	0.34004	0.15969
Recall@50	0.52426	0.53540	0.49772	0.47295	0.45302	0.23022

ML-20M:MovieLens 20 Million Dataset

ML-10M:MovieLens 10Million Dataset

ML-1M:MovieLens 1 Million Dataset

DAE: Denoising Autoencoder

VAE:Variational Autoencoder

In Fig. 3e, for the VAE model on top, we can see when the row position is equal to 0 the NDCG validation increases to a value of 0.35 then it stabilizes starting from the 75th epoch to a value of 0.36. In Fig. 3f, for the DAE at the bottom, we notice that when the position is equal to 0 the NDCG validation increases to the value 0.40 then it stabilizes starting from the 175th epoch also to the same value.

In Table 1 we give a comparison summary of our obtained results. We can see that VAE significantly outperforms its counterpart DAE across all datasets and using all metrics. On the ML-20M dataset we can see that the VAE achieves an NDCG@100 equal to 0.42592 superior than DAE where the NDCG@100 is equal to 0.41997. We can conclude that predictions on ML-20M are better using the Variational AutoEncoder model. However, on the ML-10M and the ML-1M datasets the best predictions were given by the Denoising AutoEncoder, where it achieved an NDCG@100 of 0.38756 and 0.40543 for ML-10M and ML-1M respectively. The assumption here is that maybe Variational AutoEncoders are more suited to large datasets while Denoising AutoEncoders will be a better fit for small datasets. In summary, VAEs favor random sampling of latent space characteristics which allows continuity. Their latent space graph for all the functionalities would be very continuous and no brutal space would be present between the representations of functionalities. DAEs compress the corrupted input into a discrete latent space, and when reconstructing, they do not allow an easy interpolation of features from latent space which results in them lacking continuity in feature space.

4 Conclusion

Recommender systems aim to provide users with content (films, music, books, news, images, web pages, etc.) which they can likely be interest in. AutoEncoders are one of many techniques that can help recommender systems create personalized recommendations. In this paper, we explored Variational AutoEncoders and Denoising AutoEncoders for building quality recommender systems. We evaluated both models

on three benchmark datasets and using different metrics. When comparing the results, we concluded that both architectures are well suited to build proper recommender systems. Furthermore, we found that Variational AutoEncoders are better when used on large datasets (i.e. 20M items and above), while Denoising AutoEncoders can be better when trained on small datasets.

In future works, we would like to try and combine a Variational AutoEncoder model with a Content-based recommendation method, which may help improve the results.

References

1. Bobadilla J, Ortega F, Hernando A, Gutiérrez A (2013) Recommender systems survey. *Knowl Based Syst* 46:109–132. <https://doi.org/10.1016/j.knosys.2013.03.012>
2. Batmaz Z, Yurekli A, Bilge A, Kaleli C (2018) A review on deep learning for recommender systems: challenges and remedies. *Artif Intell Rev*. <https://doi.org/10.1007/s10462-018-9654-y>
3. Hossein A, Rafsanjani N, Salim N, Aghdam AR (2013) Recommendation systems: a review Karamollah Bagheri Fard. *Int J Comput Eng Res* 3(5):47–52
4. Nilashi M, Bagherifard K, Ibrahim O, Alizadeh H, Nojeem LA, Roozgar N (2013) Collaborative filtering recommender systems. *Res J Appl Sci Eng Technol* 5(16):4168–4182. https://doi.org/10.1007/978-3-540-72079-9_9
5. Miao Y, Yu L, Blunsom P (2016) Neural variational inference for text processing. In: 33rd international conference on machine learning, ICML 2016, vol 4, no. Mcmc, pp 2589–2600
6. Wang H, Wang N, Yeung DY (2015) Collaborative deep learning for recommender systems. In: Proceedings of ACM SIGKDD international conference on knowledge discovery and data mining, vol 2015, pp 1235–1244. <https://doi.org/10.1145/2783258.2783273>
7. Liang D, Krishnan RG, Hoffman MD, Jebara T (2018) Variational autoencoders for collaborative filtering. In: Web conference on 2018—proceedings of world wide web conference WWW 2018, pp 689–698. <https://doi.org/10.1145/3178876.3186150>
8. Doersch C (2016) Tutorial on variational autoencoders, pp 1–23 [Online]. Available: <https://arxiv.org/abs/1606.05908>
9. Xu L, Cao M, Song B, Zhang J, Liu Y, Alsaadi FE (2018) Open-circuit fault diagnosis of power rectifier using sparse autoencoder based deep neural network. *Neurocomputing* 311:1–10. <https://doi.org/10.1016/j.neucom.2018.05.040>
10. Dolz J et al (2016) Stacking denoising auto-encoders in a deep network to segment the brainstem on MRI in brain cancer patients: a clinical study. *Comput Med Imaging Graph* 52:8–18. <https://doi.org/10.1016/j.compmedimag.2016.03.003>
11. Su X, Khoshgoftaar TM (2009) A survey of collaborative filtering techniques. *Adv Artif Intell* 2009(3):1–19. <https://doi.org/10.1155/2009/421425>
12. Kingma DP, Welling M (2014) Auto-encoding variational bayes. In: 2nd international conference on learning and representant ICLR 2014—conference track process, no. MI, pp 1–14
13. Mescheder L, Nowozin S, Geiger A (2017) Adversarial variational bayes: unifying variational autoencoders and generative adversarial networks. In: 34th international conference on machine and learning. ICML 2017, vol 5, pp 3694–3707
14. Li X, She J (2017) Collaborative variational autoencoder for recommender systems. In: Proceedings of ACM SIGKDD international conference on knowledge discovery data mining, vol. Part F1296, pp 305–314. <https://doi.org/10.1145/3097983.3098077>
15. <https://grouplens.org/datasets/movieLens/>

Toward Moroccan Virtual University: Technical Proposal



Ayoub Korchi, Sarah Benjelloun, Mohamed El Mehdi El Aissi,
Mohamed Karim Khachouch, Nisrine El Marzouki, and Younes Lakhrissi

Abstract Due to the Corona virus (COVID-19) and in order to ensure education and school continuity, universities around the world; including Moroccan ones; have moved abruptly and integrally to distance learning mode due to the confinement decision. Unfortunately, this transition occurred in an abrupt manner without the universities being sufficiently prepared for it. In this context, many countries around the world become motivated to virtual university projects, which will undoubtedly make it possible to overcome, without any difficulties, some constraints, related to the lack of qualified human resources, cost and time limitation. This concept presents the same advantages of the e-learning one but in an official form, that may target a large number of students around the world, which respects the famous slogan “Education for everyone”. In this paper, we will propose a Moroccan virtual university architecture, followed by an overview of technology proposal that could help in the implementation and data treatments steps.

Keywords E-learning · Virtual university · Functional architecture · MDA · BIG DATA

1 Introduction

According to the WHO (World Health Organization), the corona pandemic caused till now more than 7 million confirmed cases over the world with more than 400,000 deaths [1]. This pandemic causes the interruption of the commercial, economical and even the educational movement. In this article we will interest into the educational aspect by talking about the best solution to avoid school interruption due to this pandemic or any other similar dangerous situation.

A. Korchi (✉) · S. Benjelloun · M. E. M. El Aissi · M. K. Khachouch · Y. Lakhrissi
Intelligent System, Georesources and Renewable Energy Laboratory FST of Fez, Sidi Mohamed Ben Abdellah University, FeZ, Morocco
e-mail: ayoub.korchi@usmba.ac.ma

N. El Marzouki
LIMS Laboratory, Sidi Mohamed Ben Abdellah University, Fez, Morocco

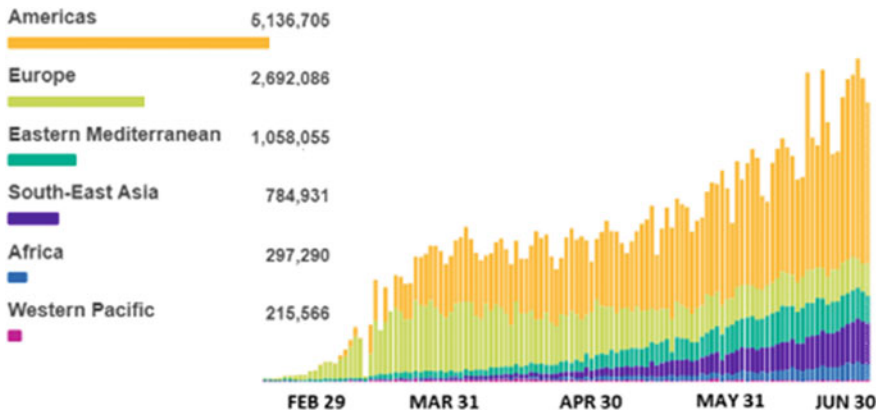


Fig. 1 Corona pandemic situation June 30 [1]

In the last 20 years ago, there has been a controversial debate over the importance of adopting distant education. Several countries around the world have decided to adopt the virtual university concept. Africa seems indifferent to this debate, and a few countries have been seriously engaged to this education topic including Morocco which has taken important steps to increase the digital rate in universities (Fig. 1).

The virtual university is a kind of distant-education which is based on the e-learning teaching methods, and benefiting from its advantages in targeting a large number of students that can use computer or mobile and internet to attend the class, regardless of the student/professor geographical position, and surpassing the time limits with the availability of data 24H/7 days.

In this paper, we will propose in a first time, an architecture of a Moroccan virtual university taking into account Moroccan society constraints in one hand and benefiting from all the advantages mentioned above in the other one. Then, we will talk about two technologies that can be used in development cycle which the MDA technology, and data process task which the BID DATA technology.

The remaining of the paper is organized as follows: An overview of the virtual university concept is found in Sect. 2, talking about its history, giving its advantages, and conclude this section with a comparison between traditional and virtual university. Section 3 and 4 will present our proposal of the functional details of the virtual university, with some technical solutions that can be used to implement the virtual university application. Finally, the conclusion is given in Sect. 5.

2 E-learning as General Concept of Virtual Universities

In this section, we talk about the virtual university as an evolution of the E-learning concept, give its advantages, and compare it with the traditional university.

2.1 *E-learning History*

In this subsection, we give an overview of the E-learning from time to time. As mentioned in [2] the E-learning concept had passed by several steps or periods such as: CBT, CBT Packages, LMS, and Web-based e-learning applications.

1990: CBT (Computer Based Training). It was the first e-learning solution using CD-ROM support to stock courses data in form of text, audio, or video. This solution is mainly used for subjects related to computer but can be also used for the other domains.

1994: CBT Packages. This one is clearly an evolved version of the first one, including 2D,3D Animations, voice comments for a best learning.

1997: LMS (Learning Management System). This one is an internet-based software solution, that took place with the connection of the world community to internet due to the development of internet technology that allows getting data in a real time or at least as quickly as possible.

1999: Web-based e-learning applications. This solution benefited from the success of LMS, its descending solution, by combining a website with an LMS to obtain a web-based-solution.

2007: Mobile-based learning application. With the appearance of the first apple mobile, mobile applications versions of the last web-based ones was launched due to the exhaustive use of the mobile in our daily-lives.

This E-learning evolution steps has led to the appearance of virtual universities concept.

2.2 *Virtual University Project*

The virtual university is a distant-education type, which is based on web/mobile technology and internet to provide a learning, evaluation and administration platform accessed by professors, students, and administrators. It has been adopted by many universities in many countries benefiting from the advantages of the different solutions mentioned in the previous subsection.

This concept allows students from different countries to attend a class in a same university and at any time suits to the learner without needing to move from a country to another due to the availability of courses in the university platforms. These courses could be in form of text, audio, video that were provided previously by professors. The virtual university will have the option of fixing a videoconference to discuss a subject in order to ensure and maintain face to face conversation. Moreover, with the current confinement situation due to the corona virus, this concept seems very useful, because it saves professors and students lives without affecting learning process.

For that, setting up virtual digital university bases turns out to be a necessity more than a choice. This virtual university project will strengthen the initiatives already taken individually by each university, in order to:

- Better value the resources developed by the contributors.
- Facilitate educational co-production and strengthening teamwork,
- Facilitate the standardization of skills and prerequisites.
- Access innovative tools and content scripting.
- Give better visibility to the departments for good decision-making.
- Participate in building a national repository of educational content.
- Participate in building an effective national digital library.
- Design and implement multinational e-Learning projects.
- Provide students with unlimited access to resources shared and co-produced by professors in different universities.
- Better manage the rules of ethics which concern the intellectual property right and educational innovation.
- Favor, through safe competition, the emergence of high-quality, and high-level content.

2.3 *Traditional/Virtual University Comparison*

In the following table we present a quick comparison between traditional and virtual university based on several criteria that were presented in paper [3] such as: the physical presence, quality of course presentation, student feedback, education cost-effective, etc (Table 1).

As it shown in the previous table the virtual university presents more advantages than the traditional one in terms of providing full access to data 24 h/7 with a low cost

Table 1 Comparison study of traditional/virtual university

Criteria	Traditional	Virtual
Attend real class	Yes	No
Course presentation quality	Normal	High
Number of course student supported	Limited	Large number
Feedback	immediate	Only in videoconference
Time and space	Limited	flexible
Cost-effective	Expensive	Very adequate
Known to professor	Yes	No
Learner privacy	Respected	Known
Professor/student-centered	Professor	Student
Access to libraries resources	Limited	Full access
Practical education	Full access	Limited

of education compared to the traditional one, targeting a larger number of students, and keeping the same learning quality.

3 Virtual University: Functional Details

Our vision of the virtual university can be realized through a web and mobile applications where their homepages will contain the following elements (see Fig. 2):

- A registration invitation on the application that will redirect the visitor to a complete registration form.
- An invitation to authenticate which opens a pop-up or a modal where the visitor will be able to enter his academic e-mail and password.

It also contains a description zone consisting of the following elements:

- An area for new announcements, which can be in the form of a carousel or other animation informing about the dates of registration sessions, exams, or other important announcements.
- List of available courses where the visitor could have an idea about the different curriculums available in the university, be it academic courses such as bachelor, master, etc.... Or other curriculums such as the multiple certifications proposed by the university in different fields.
- List of the different curriculums for each course displayed dynamically according to the chosen/clicked course.

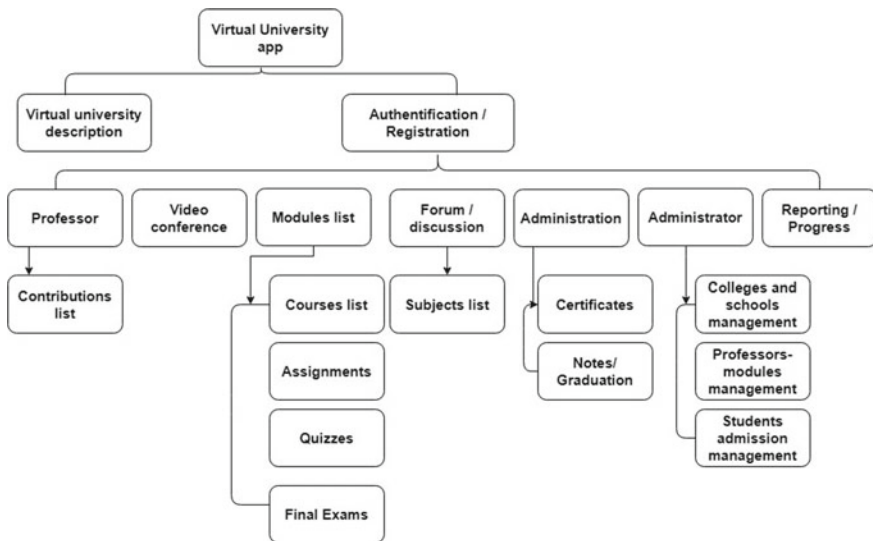


Fig. 2 Moroccan virtual university’ architecture proposal

- A tab on admission formalities redirecting the visitor to a page explaining all the acceptance modalities for different types of students, whether they are post-baccalaureate students, students wanting to join the university via gateway, students belonging to the military regime, etc...
- A tab “about the university” which will contain a word from the director and testimonials from the university alumni.

Concerning registration, a session is opened for each discipline of each curriculum. The candidate is asked to fill in the form available on the application form and then submit the necessary documents to the university. A travel is necessary in this step. After verification, the administrator can validate or reject the candidate’s registration with an explanatory reason.

Once the registration has been validated, the student can access the content offered by the university’s virtual space. This space allows navigation between modules and subjects, assignments, quizzes and exams of each module. A progress bar is implemented showing the student his or her progress for each module. The student can choose among the courses of the same subject the one that suits him or her. A subject can have several courses proposed by several professors where the program is identical. The difference remains obvious which is the pedagogy of each professor. The student can also access the grades of corrected assignments and exams communicated by his or her professors.

A forum is made available to students divided into subjects and levels for better communications.

As for the professor, once authenticated on the platform, he or she could access to a reporting page allowing him or her to obtain statistics about his or her students levels for the different subjects he or she teaches, such as the number of students who have sent their assignments, the average grade of the class for each subject, etc.

He also has the possibility to add multimedia content on the platform as long as it is properly assigned to the desired subject as a course material, assignment to be handed in, TP.

The professor can create incident tickets to notify on the status of his equipment or to make a request requiring additional fees.

In addition, the professor can also request a contribution to a subject and thus create his or her own course. A course can only be published after validation by the head of department acting as administrator.

The administrator manages user registrations and assigns the appropriate roles to each user. In the case of professors, he assigns each one to the subject he teaches. In addition, he can manage the existing disciplines as well as the modules and subjects of each one. It also has access to a reporting component like professors, with additional features such as viewing teacher statistics. In addition, he can see all the tickets submitted by the professors and manage them. Finally, the administrator can validate the request to use the videoconference space to grant the person requesting it the right to record live.

4 Technical Details Proposal

4.1 *Related Works and Discussion*

In [2], the authors started by giving an overview of the different E-learning solutions that has existed since 1990. Then, they proposed a use-case model based on user needs expressed in the same article, giving and explaining the solution proposed for each need. This use-case model can be improved by assigning some professor's exhaustive tasks to the system such as: Graduation Determination and Teaching Data Correction, in order to give more time to professors for their scientific research tasks.

In [4], the authors proposed a procedure to launch a virtual university project based on 4 steps. Firstly, the planning step which concerns the prerequisites to launch this project. Secondly, the design step that represents the architecture of the university's final application. Then, the third step concerns the performance control and observation of the content, the application tools used, and the learners. Finally, an evaluation step is set up to improve learners' performances, update content when it's necessary.

For the authors this university model will be based on writing teaching environment instead of the oral one, which can decrease teaching quality especially for scientific modules that needs more oral communication for a good comprehension. The second step which concerns the architecture needs more textual details in order to explain the architecture details.

In [3], the authors presented a model of virtual university based on traditional universities components. Then, they compared the tradition and the virtual universities and giving advantages and disadvantages of this last one, in order to propose a virtual university model mostly similar to the traditional one.

The migration from the traditional learning to e-learning requires a specific architecture, especially a data storage architecture. Accordingly, in their paper 'Big data integration for transition from e-learning to smart learning framework' [10], Prakash Kumar Udipi et.al. focused on how the integration of the big data architecture can facilitate the elaboration of a smart learning framework, as the e-learning data is complexes and has a height variety, it contains audio, video, text, animation and schematics which require immediately a huge storage. Furthermore, having a data storage architecture that allows querying data with different types very fast is a real advantage for the e-learning framework.

In Maria Dominic's. et al. paper [11], they spotted light on the Artificial intelligence and how can we use it to extract patterns from the huge amounts of data. Those patterns allow a deep understanding for the user needs, in order to offer a better user experience. It has to be noted that handling this free-from data can be done by following the big data architecture. Moreover, running deep learning/ machine learning algorithms can be possible just by adopting a dedicated storage system that allows a fast execution, and that directly push us to think about a distributed data storage system.

According to the chosen works mentioned above, we conclude that most of researches done about virtual universities were based globally on functional and

budgetary aspects neglecting the technical details that can reduce cost and time to set up this project. In the two next subsections, we will talk about two technical aspects that can help in development and data treatment processes using MDA and Bid Data.

4.2 MDA (Model Driven Architecture)

The MDA is a solution proposed by the OMG to design, develop and implement a software application. It separates the application functional aspects from its implementation details using UML and other OMG modeling standards to set up a set of models for each aspect [5]. MDA approach is base generally on three main model:

- **CIM (Computational Independent Model):** presents functional and business aspects of the application.
- **PIM (Platform Independent Model):** set up the systems architecture to satisfy needs presented in the CIM.
- **PSM (Platform Specific Model):** This one defines the application technical technologies for each platform.

The MDA process is based on multiple transformation from the CIM to PIM, then PIM to PSM, to finally generate platform-specific code from that PSM generated as it shown in Fig. 3.

During each development process the conception step is mandatory, in which we model different functional aspects in a form of diagrams, that developers will be based on to develop the result application.

Since the MDA is based globally on models, so we will define our source model using UML or other OMG modeling standard once and then generate an application for each platform web and mobile with its different most used platforms such as

Fig. 3 MDA Process [6]

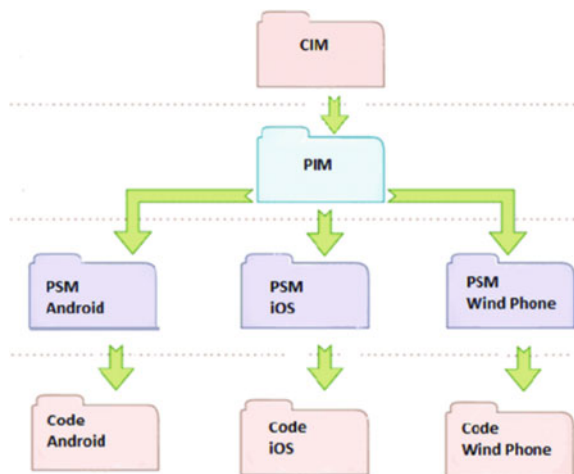
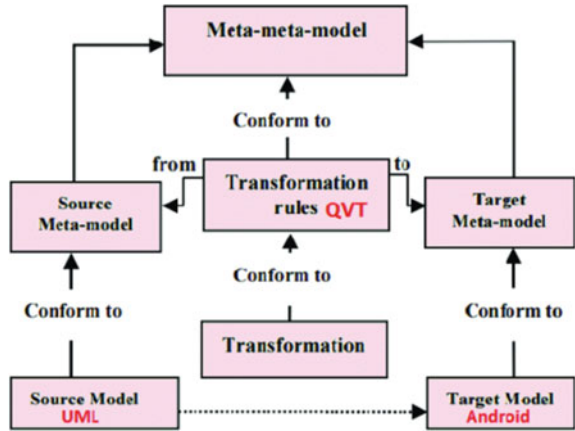


Fig. 4 MDA transformation process [7]



android, apple and windows phone as it shown in the following Fig. 4 with the case of UML as language that is used to define our source model and generate Android code after multiple transformations that were defined by a QVT language.

4.3 Big Data

There are many definitions of Big Data. However, the best way to distinguish it from the other data base management systems (DBMS), is by defining its four main characteristics [8, 9] as it shown in Fig. 5.

- **Volume** refers to the massive quantity of data generated each day.
- **Variety** is the different three category of data types, which are structured, semi-structured and unstructured.
- **Veracity** refers to the trustworthiness of data and if our data is representative.
- **Velocity** means the frequency of incoming data that needs to be processed.

Fig. 5 The four V's of BIG DATA



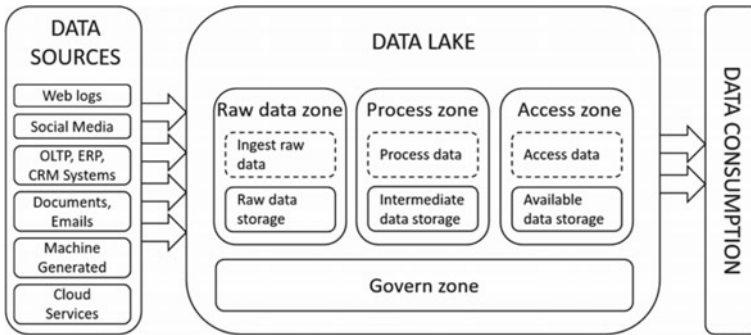


Fig. 6 Functional architecture of Data Lake [12]

As our virtual university will contain a huge amount of data with different types that increase very fast day after day, so a big data architecture is very recommended, for either storing, processing or analyzing the data.

- **Data storage** Storing a huge amount of unstructured, semi-structured and structured data can be done with a specific big data architecture, widely known as Data Lake.

In the Data Lake (DL) storing data is not the same as in Data warehouses. The DL has no specific schema/model to respect for the input data, so it is stored as it is coming from the source system. This concept allows us to store big data without spending time and energy on building models.

- **Data processing.** With Hadoop framework processing big data wouldn't take much time thanks to the MapReduce model. The MapReduce program is executed in three stages. In Map stage, the input file is passed to the mapper function line by line. The mapper processes the data and creates several small chunks of data. Then the Reduce stage which is a combination of the shuffle stage and reduce stage, where the task is to process data coming from the mappers and produce a new set of data, that will be directly stored on Hadoop Distributed File System (HDFS).
- **Data Analyzing.** Hadoop solution afford many tools for preparing data, in order to produce a data set, depending on the use case, so it can be analyzed (e.i. analysing the courses completion by each user category...).

The following figure illustrates the functional architecture of the Data Lake (Fig. 6).

5 Conclusion

Due to the world's health situation, virtual university projects seem to be the best solution to ensure school continuity, saving lives of professors, students and school

administrators. The virtual university concept presents too many advantages in terms of education quality, number of targeted students, full access to data, registration to many courses program at the same time, cost and energy reduction compared to the traditional university.

Many researches have been done in the same stream of works, but most of them focused generally on the university architecture, that satisfy the university needs and presents functional details, without interesting to the technical aspects that help in reducing cost and time of the university project, and on the other hand limiting time and energy consumed during data storage or processing.

In this paper we tried also to present some technical solutions that may help in developing the virtual university platform. We presented the MDA as a first tool that allows to model/develop once and deploy everywhere. Then we talked about the big data technology that could help in storing and processing data in terms of reducing time and energy needed. In our future works, we will focus more on the preferences of the platform's users: professors, students and administrators, using some surveys and interviews in order to enrich our platform architecture, and satisfy the platform's users by providing the maximum of functions.

References

1. <https://covid19.who.int/>
2. Batara C, Charnia I R (2020) Design and implementation of virtual university based on ICT. *Int J Res Granthaalayah* 8(4):144–152.
3. Mirzakhani M, Hossein A, Azadeh A (2010) The virtual university: advantages and disadvantages. In 2010 4th international conference on distance learning and education n. page
4. Shahtalebi S, Badri S, Fakhri S (2011) A strategic model of virtual university. *Proc Soc Behav Sci* 28:909–913
5. <https://www.omg.org/mda/>
6. Benouda H et al (2016) MDA approach to automate code generation for mobile applications. *Mobile and Wireless Technologies 2016* (2016):241–250
7. Benouda H et al (2017) Automatic code generation within MDA approach for cross-platform mobiles apps. In: 2017 first international conference on embedded & distributed systems (EDiS) (2017): n. pag
8. Rabl T, et al (2012) Solving Big Data challenges for enterprise application performance management. In: *Proceedings of the VLDB Endowment* 5.12:1724–1735
9. Megdiche I, Franck R, Yan Z (2020) A use case of data lake metadata management. *Data Lakes* (2020):97–122
10. Udupi, P.K, Puttaswamy M, Herald N (2016) Big Data integration for transition from e-Learning to smart learning framework. In: 2016 3rd MEC international conference on Big Data and smart city (ICBDSC) (2016): n. pag
11. Dominic M, Sagayaraj F, Anthony P (2014) E-Learning in Web 3.0. *Int J Modern Educ Comput Sci* 6.2 (2014): 8–14
12. Ravat F, Yan Z (2019) Data Lakes: Trends and Perspectives. *Database and Expert Systems Applications* (2019): 304–313

Data Lake Versus Data Warehouse Architecture: A Comparative Study



Mohamed El Mehdi El Aissi, Sarah Benjelloun, Yassine Loukili,
Younes Lakhri, Abdessamad El Boushaki, Hiba Chougrad,
and Safae Elhaj Ben Ali

Abstract Each day huge quantities of data are generated from digital technologies and information systems. Therefore, processing these massive data requires a specific architecture and a good knowledge on how to handle data. Traditional databases management system can no longer be used for this type of data since they were originally designed for limited and structured data. Moreover, dedicated architecture known as Data Lake has been developed in order to extract valuable information hidden in data. The main objective of this paper is to explore the two architectures, namely, data warehouse and data lake. Furthermore, it describes the main differences and exposes key factors of each one.

Keywords Data warehouse · Data lake · Big data · SQL · Hadoop · ETL/ELT · Data analysis

1 Introduction

In former times, the computer programs were focused mainly on algorithms and programming languages, so processing data as names, addresses, phone numbers... was not a priority. However, since the computers started to become commercially available and while the business people started using them for real-world cases, the data suddenly became very important.

Accordingly, researchers started proposing many databases management systems (DBMS), and as result, one of the first DBMS is the Navigational Databases by Charles Bachman [1] in the mid-1960, it was based on the CODASYL approach [2], which rely on manual navigation technics using a linked data set, forming a huge network. However, this DBMS was a very complicated system and required specific

M. E. M. El Aissi (✉) · S. Benjelloun · Y. Loukili · Y. Lakhri · A. E. Boushaki · H. Chougrad · S. Elhaj Ben Ali
SIGER Laboratory, Sidi Mohamed Ben Abdellah University, Fez, Morocco
e-mail: mohamedelmehti.elaissi@usmba.ac.ma

S. Benjelloun
e-mail: sarah.benjelloun@usmba.ac.ma

trainings and skills. As a result, in the beginning of 1970 the Navigational Databases system lost its place to a new approach called the Relational Databases Management Systems (RDBMS) by Edgar Codd [3], where data would not be stored in a form of linked records, but instead used a table with a specific structure.

The RDBMS was practical and efficient to store structured data, even the processing speed was fast thanks to the Structured Query Language (SQL). Although unstructured data as music, images, and documents... was not supported since the Relational Databases Management Systems were not planned to handle this category of data [4].

On the other hand, the incremental use of internet in the beginning of 2000 [3] has spawned a new category of DBMS called NoSQL (Not Only Structured Query Language), in order to offer speed and the ability of processing unstructured data. NoSQL is also flexible [5] since it is a distributed database system, which allows coping with high-volume data with different types.

Despite all what NoSQL DBMS offers, it requires a high CPU and RAM allocation, which is very expensive for the enterprises and not practical [6].

Nowadays, the data is omnipresent. The world generates a huge quantity of data used for extracting precise information and creating benefit. Thanks to this, a new concept appeared, which is Big Data, allowing us to manipulate massive data [7] and overcome the majority of problems encountered with the passed DBMS. First, let us give the big data a definition to distinguish it from the other types.

According to Apache Hadoop [1], big data refers to datasets, which could not be stored, managed and processed by other DBMS within an acceptable scope. Based on this definition McKinsey, a global consulting company has declared big data as the next battlefield for innovation, competition and productivity.

Although, Oracle report [8] defined big data as the voluminous datasets that traditional data processing software cannot manage them. Nevertheless, these massive volumes can be used to address business problems we would not have been able to tackle before.

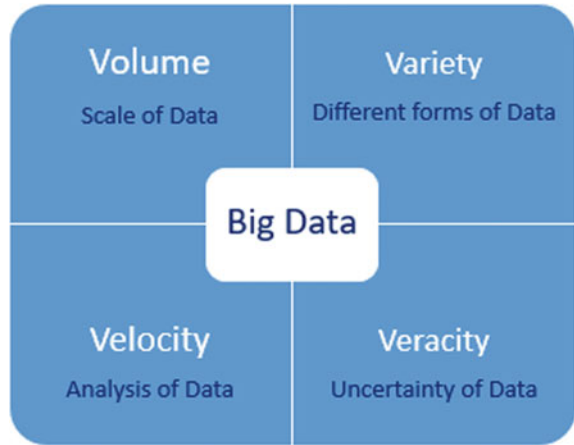
In addition, the International Data Corporation (IDC) [8] has presented big data as “big data technologies describe a new generation of technologies and architectures, designed to economically extract value from very large volumes of a wide variety of data, by enabling the high-velocity capture, discovery, and/or analysis”.

Hence, big data has four main characteristics, widely known as the four V's [9, 10]. Volume refers to the massive quantity of data generated each day; moreover, variety is the different three categories of data types, which are structured, semi-structured and unstructured. Veracity refers to the trustworthiness of data and if our data is representative, finally velocity means the frequency of incoming data that needs to be processed (Fig. 1).

With all this in mind, the challenge now is to explore the huge hidden values behind the data, either by adopting the big data approach or the relational databases approach.

In this paper, we investigate the big data architecture as well as the relational databases architecture, we take a deeper look at each one of them, compare their functionalities and understand how to choose the adequate architecture. In order to

Fig. 1 The four V's of Big Data



elaborate this, the paper is organized into five sections. Section 2 present, in details, the two approaches of data management. Then, the differences between the two architectures, Data Lake and Data Warehouse, are ranged in Sect. 3. The Sect. 4 focuses on discussing the related works. Remarks are provided in Sect. 5 to draw a conclusion.

2 Data Lake Versus Data Warehouse

Since the world started generating an interesting amount of data, a new kind of competition between the data management leaders has emerged in the market; the challenge here is to allow exploring and extracting useful information behind the collected data [11], in order to support decision-making.

For this main reason, data should be stored in a database management system following a specific architecture depending on the use case.

At this stage, we can differentiate between two concepts of databases management system.

The first concept is the data warehouse, which is simply a relational database designed especially for querying and analysing data. Usually, it contains structured historical data coming from transactional databases; furthermore, it can handle data from different sources [12]. Additionally, the organization of data in a data warehouse is subject oriented. Another key thing to remember is that before storing the data in the staging zone of a DWH it may pass through data cleansing steps to ensure high data quality in reporting.

Moreover, a data warehouse has a special data collection approach known as ETL [13] that has three main steps: Extraction, Transformation and Loading.

Data extraction refers to extracting data from homogeneous/heterogeneous sources; data transformation involves processing data in order to cleansing it and

transforming it to an adequate structure, so that querying and analysis are simple and efficient; finally, data loading means the ingestion of data into the final target [13].

The second concept is the data lake; it is defined as a powerful big data architecture for storing huge amount of structured, semi-structured and unstructured data [14]. Furthermore, it allows storing every data type [15] in its original format regardless of its size and its source.

Data Lake allows high flexibility while interacting with data [16] thanks to the absence of a strict schema/model imposed for the data coming from the sources [7].

In a data lake, we are talking about an ELT [17] (Extraction, Transformation and Loading) process rather than an ETL (Extraction, Loading and Transformation), as presented for the data warehouses. Therefore, the most important phase for a data lake architecture is to gather data as much as we can [18], then comes the transformation phase where the data consumer start building his own model, depending on the use case, by combining the different existing data [19].

Moreover, the data lake architecture provides a fast data processing, a large bandwidth for Business Intelligence as well as handling continuous data streaming.

3 Distinguish Data Lake and Data Warehouse

Whereas, the main objective of the two architectures is to provide insights by extracting added value from the data, it is primordial to set axes and measures on which we can rely for choosing the perfect architecture to be implemented.

This section, we highlight the differences between data warehouse architecture and data lake architecture.

In Data warehouse, we have a concept of schema on write, which means in order to extract data from relational database and write it in another one we need to have some information on hand [20]. First, we need to know the data structure in the database source [21], so we can adapt data by transforming it to fit the destination structure. Additionally, we have to ensure that the data being transferred meets the data types that our data warehouse is expecting, so that we avoid all types of parsing errors.

Furthermore, in a data warehouse, the data is stored in a logical form with interrelated tables and defined columns.

Additionally, the data warehouse is subject oriented [3, 21], which means business users cannot consume data from the warehouse, but they get it from data marts that contain detailed data by domain (HR, Finance, Sales, Inventory...).

One more thing to add, the data warehouses has a two-phase commit protocol (2PC) [22]. All over, it is a distributed algorithm for managing and rolling up transactions, so we are sure we get the right answer even if we don't have a complete consistency across all the process that participate in handling the transaction.

Different from data warehouses, Data Lake has a schema on write approach [20]. So when we write data into Hadoop Distributed File System (HDFS), we are directly bringing it in without any imposed rules; then when we want to retrieve data, we

implement the rules to the code that reads data rather than preconfiguring the structure of data ahead of time.

Indeed, in Hadoop, data is simply a compressed file that may be text or any other type [23]. However, the moment data enters into Hadoop, it is replicated at least four times across multiples nodes in the HDFS. It looks like wasting space, but when thinking big data, we should directly think about architecture that can handle an unlimited number of servers, and that is exactly the secret behind the scalability of Hadoop.

For instance, exploring data in the Hadoop cluster is not processed with the traditional way, instead, it relies on a java program, called Map Reduce [24], in order to define the request and distribute the calculations of that search across all the copies of data in HDFS. In addition, the java program split the workload so that each node is working on just a portion of the request [25]. As each node finishes the assigned part of the request, the outputs are delivered to the reducer program to be consolidated. The following figure illustrate data processing with HDFS [4] (Fig. 2).

It has to be noted that one more positive side of this Data Lake architecture, is when a server breaks down while processing the request, nothing affects the results since we already have copies of data in other servers [27].

Even though, the java passed query also increases the complexity of interacting with Hadoop. For the main reason, Hadoop has a lot of packaged distributions that provide some structure and focus to the Hadoop solution.

As example, in 2011, Facebook created Hive to allow team members that did not know how to write java code to write queries in standard SQL [28]. In other words, Hadoop is so flexible that Facebook was able to build a program on the top of it.

Overall, it is very important to distinguish between both databases management architectures.

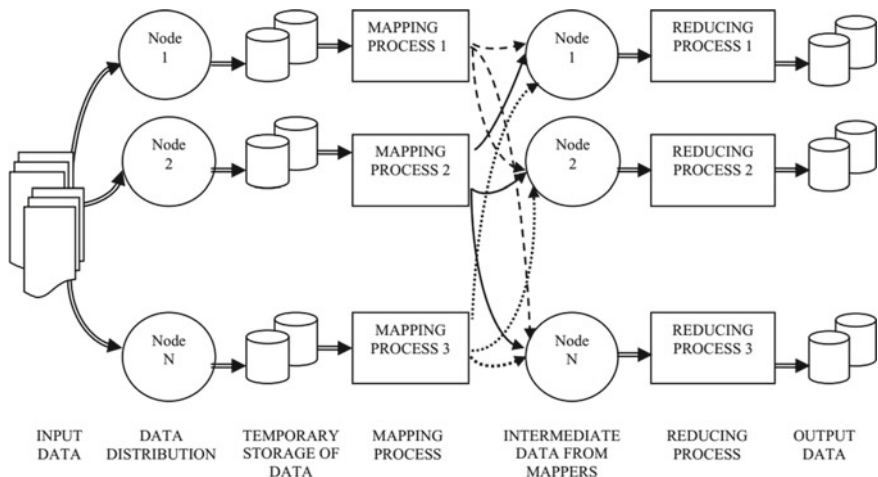


Fig. 2 Data processing in HDFS [26]

The Data Lake is mainly designed to handle a massive amount of scalable data and perform new transformations to support key business application [27]. Even if the companies spent lot of money on Data Warehouses, when the big data appeared, they started deploying Data Lakes.

The Data Warehouse is considered as highly designed system. The Data Warehouse usually has a complex data model that is carefully designed before the data is loaded in order to respond to many business questions in a specific use case [29]. Moreover, DWH supports the batch workloads and simultaneous access by many users performing analytic tasks.

In order to be able to choose wisely between the data warehouse architecture and the data lake architecture, we carried a comparison study based on specific dimensions.

In the data warehouse, the workload is heavy because it has hundreds to thousands of concurrent users and handles interactive analytics. Furthermore, the schema is built and the data is cleansed before the storage. In addition, most of BI schemas rely on complex joins. Moreover, data access is guaranteed through SQL and standardized BI tools. Finally, the data warehouse architecture provides many benefits as fast response, consistent performance, ease of use, data integration and cross-functional analysis.

Whereas, the data lake workload is still improving its capabilities to support more interactive users. Typically, the schema is defined after raw data is stored, which offers high agility and ease of data capture. Moreover, data is accessed through programs created by developers. Lastly, the data lake architecture has various benefit such as superb scalability, programming support, radically changes and low cost of storage and processing.

For a better illustration of these differences, following a table containing the key dimensions that our conducted study is based on (Table 1).

Table 1 DWH architecture versus data Lake architecture

Dimension	Data warehouse	Data Lake
Workload	- Heavy	- Medium
Schema definition	- Before data collection	- After data collection
Scale	- Large data volumes at moderate cost	- Extreme data volumes at low cost
Data access	- Standard SQL and BI tools	- Custom programs
Data stored	- Cleaned	- Raw
Limitation	- Complex joins	- Complex processing

4 Related Works

Recently, due to the advanced technology, exploring and analysing data has become highly competitive. Accordingly, many research studies have exposed the quality factors in a database management system. Moreover, studies are focused on how to implement data exploration architecture successfully. At the same time, some researchers spotted the light on the fast growth of complexity due to the huge evolution of data, as a consequence they affirmed the Data Lake as the most adequate solution, thanks to its qualities.

First, the ability to acquire data in any format and store it to the HDFS in order to be used for decision making purposes, e.g. data coming from Oracle EBS (E-Business Suite) to a Tableau dashboard. Next, it offers storing and processing data at scale, since it is continually growing [30]. Then, it allows performing complex transformations on the data with a high speed. Moreover, as the Data Lake has a schema-on-read architecture it avoid costly data modelling efforts [31]. Finally, by using this concept we can perform dedicated analytics for each specific use case.

Henceforth, the main characteristic of the Data Lake is a distributed repository across many servers [32]; it also contains dedicated tools for workflows scheduling and orchestration.

Despite all these qualities, it must be noted that some axes are not covered with this big data architecture such as data quality. Indeed, this can be explained by the inexistence of a strict schema [33] exposed while ingesting data, which gives the data lake its flexibility comparing to traditional data warehouses. However, the future research studies should focus more on data quality to ensure having a clean stored data on HDFS.

Coupled with databases management systems implementation success, we can spot the light on many aspects that directly affect the quality of databases management architecture.

According to Umar Aftab, et al. [28] following the key aspects for DBMS success.

- **Infrastructure aspects:** it measures the hardware performance by simulating the worst cases scenarios, as example the high availability of data nodes.
- **Organizational aspects:** it refers to the collaboration between all stakeholders while gathering and analysing data.
- **Project management aspects:** this aspect spotlight on project structure in general, e.g. it checks if each resource in the data management team is well chosen for its specific mission.

Even though, database management systems are still developing rapidly, especially the data lake, since it contains a huge amount of heterogeneous data that is stored in a distributed file system, so it is primordial to have experienced resources in order to handle unusual situation [34]. In a word, we need to focus more on the technical aspect.

As indicated, Data Lake implements a schema-on-read architecture. It means, the data has no specific schema/model to follow while loading it. This characteristic

allows staying away from complex data modelling tasks. This concept is called ‘Load the data and figure it out later’.

In his paper, Huang Fang [23], exposed the advantage and inconvenient of the No-Schema concept.

First, loading the data into Data Lake in raw format provides a high flexibility and this gives more power to the data engineers and data scientists to process the data in their own way.

Secondly, without a specific schema, it is very easy to support semi-structured and unstructured data types and the loading speed is much faster.

However, whether it is created on-load, on-read or on-need, there is always a schema for the data. Sooner or later, we need to define a schema for the data in order to analyse it.

No-schema refers also to ‘Late Binding’, compared to ‘Early Binding’ in the Data Warehouse architecture [23]. Whether which concept is used, there are data providers and data consumers, and data has to be collected, evaluated, defined and analysed. Nevertheless, there are some main differences between the two concepts, which make each one perfect with different use-case (Table 2).

In ‘Early Binding’, the data providers evaluates the data and create an adequate structure, then collect the data and transform it order to respect the defined data models. The data consumer use the specified data model to analyse any topics they are interested on.

In ‘Late Binding’, the data providers only collect and load it to the Data Lake, then the data consumers should achieve all the tasks by themselves to be able to extract valuable information from the data.

‘Early Binding’ is perfect for the reused data; it is usually used when data results are widely used with the same model and for a specific purpose. ‘Late Binding’ is suitable for data having an unstable schema with a variable usage.

Table 2 Difference between early binding and late binding [23]

	Early binding	Late binding
Data providers	<ul style="list-style-type: none"> - Evaluate data - Define data structure - Data collection/ingestion - Apply structure 	<ul style="list-style-type: none"> - Data collection/ingestion
Data consumers	<ul style="list-style-type: none"> - Answer questions 	<ul style="list-style-type: none"> - Evaluate data - Define data structure - Apply structure - Answer questions
Perfect For	<ul style="list-style-type: none"> - Reused and known data - Consistent results - The masses 	<ul style="list-style-type: none"> - Unfamiliar data - Infrequent usage - Unstable source schema

5 Conclusion

Recently data has become a competitive domain for companies since it offers real advantages in the decision-making process.

In this paper, we have investigated the two main data management architectures, namely, data warehouse and data lake. We started by exposing the historical of data in order to understand the source need of each architecture. Furthermore, we presented the approach of data management architecture. Then we gave a brief definition of each data management architecture. Furthermore, we presented in detail the differences between the data lake architecture and the data warehouse architecture. Finally, in the last section, we discussed the data quality issues can affect the data credibility negatively in a data lake, then how we can implement a data management solution successfully. In addition, we presented the different aspects that can affect the implementation including the technical aspect that we consider very important and the main differences between the two concepts of ‘Early Binding’ and ‘Late Binding’.

Consequently, our future works will focus more on providing details on the data lake architecture, especially the Hadoop architecture and how it provides an analytics platform with low cost for both real-time and batch data. Moreover, we will provide a detailed research paper on how to exploit raw data by integrating machine learning and deep learning and push the overall business operations to maximum efficiency.

References

1. <https://www.mckinsey.com/businessfunctions/mckinsey-digital/our-insights/big-data-the-next-frontier-for-innovation>. Accessed on May 2020
2. Haigh T (2016) How Charles Bachman invented the DBMS, a foundation of our digital world. *Commun ACM* 59(7):25–30
3. Ariyachandra T, Watson HJ (2006) Which data warehouse architecture is most successful? *Bus Intel J* 11(1):4
4. Verma K Study of HDFS architecture and services
5. Nance C et al (2013) Nosql vs rdbms-why there is room for both
6. Zafar R et al (2016) Big data: the NoSQL and RDBMS review. In: 2016 international conference on information and communication technology (ICICTM). IEEE
7. Panwar A, Bhatnagar V (2020) Data Lake architecture: a new repository for data engineer. *Int J Org Collective Intell (IJOCI)* 10(1):63–75
8. Lynch C (2008) How do your data grow? *Nature* 455(7209):28–29
9. Rabl T et al (2012) Solving big data challenges for enterprise application performance management. arXiv preprint [arXiv:1208.4167](https://arxiv.org/abs/1208.4167)
10. Megdiche I, Ravat F, Zhao Y (2020) A use case of data lake metadata management. *Data Lakes* 2:97–122
11. Llave MR (2018) Data lakes in business intelligence: reporting from the trenches. *Procedia Comput Sci* 138:516–524
12. Farnum, Michael A, et al (2019) A dimensional warehouse for integrating operational data from clinical trials. *Database* 2019
13. Vyas S, Vaishnav P (2017) A comparative study of various ETL process and their testing techniques in data warehouse. *J Stat Manage Syst* 20(4):753–763

14. Acharjya, Debi P, Ahmed K (2016) A survey on big data analytics: challenges, open research issues and tools. *Int J Adv Comput Sci Appl* 7.2:511–518. <https://doi.org/10.14569/ijacsa.2016.070267>
15. Kakhani, Manish K, Sweeti K, Biradar SR (2015) Research issues in big data analytics. *Int J Appl Innov Eng Manage* 2(8):228–232
16. Sandhu M, Purnima AS (2018) A review on Big Data analytics in business
17. Lakshmi C, Nagendra Kumar VV (2016) Survey paper on Big Data. *Int J Adv Res Comput Sci Softw Eng* 6(8)
18. Ravat F, Zhao Y (2019) *Data Lakes: trends and perspectives*. Int Conf Database Expert Syst Appl, Springer, Cham
19. Chen M, Mao S, Liu Y (2014) Big data: A survey. *Mobile Networks and Applications* 19(2):171–209
20. Campbell C (2015) Top five differences between data lakes and data warehouse, January 2015. <https://www.blue-granite.com/blog/bid/402596/top-five-differences-between-data-lakes-and-data-warehouses>
21. Anthony M, et al (2020) An evaluation of how Big-Data and data warehouses improve business intelligence decision making. In: *World conference on information systems and technologies*. Springer, Cham
22. Gore Sumit S, Ambulgekar HP (2014) MapReduce-based warehouse systems: a survey. In: *2014 International Conference on Advances in Engineering & Technology Research (ICAETR-2014)*. IEEE
23. Huang F (2015) Managing data lakes in big data era: what's a data lake and why has it become popular in data management ecosystem. In: *2015 IEEE international conference on Cyber Technology in Automation, Control, and Intelligent Systems (CYBER)*. IEEE <https://doi.org/https://doi.org/10.1109/CYBER.2015.7288049>
24. <https://hadoop.apache.org/docs/current/hadoop-project-dist/hadoop-hdfs/HdfsDesign.html>, Accessed on 21/05/2020
25. Dean J, Ghemawat S (2008) MapReduce: simplified data processing on large clusters. *Commun ACM* 51(1):107–113
26. Logica B Radulescu Magdalena, using big data in the academic environment. *Procd Econ Fin* 33:277–286. ISSN 2212–5671, 2015. [https://doi.org/10.1016/S2212-5671\(15\)01712-8](https://doi.org/10.1016/S2212-5671(15)01712-8)
27. Miloslavskaya N, Tolstoy A (2016) Big data, fast data and data lake concepts. *Procedia Computer Science* 88(300–305):63
28. Umar A, Siddiqui GF (2018) Big data augmentation with Data Warehouse: a survey. In: *2018 IEEE international conference on Big Data (Big Data)*. IEEE
29. Paulraj P (2004) *Data warehousing fundamentals: a comprehensive guide for IT professionals*. John Wiley & Sons
30. Thibaud C, et al (2013) Big data analytics on high Velocity streams: a case study. In: *2013 IEEE international conference on Big Data*. IEEE, <https://doi.org/10.1109/BigData.2013.6691653>
31. Yaqoob I (2016) Big data: from beginning to future. *Int J Inf Manage*
32. Abuqabita F (2019) A comparative study on big data analytics frameworks. *Data resources and challenges*, Canadian Center of Science and Education
33. Labrinidis A, Jagadish HV (2012) Challenges and opportunities with big data. *Proceedings of the VLDB Endowment* 5(12):2032–2033
34. Cedrine M, Laurent A (2016) The next information architecture evolution: the data lake wave. In: *Proceedings of the 8th international conference on management of digital ecosystems*

Machine Learning for Credit Card Fraud Detection



Loubna Moumeni , Mohammed Saber , Ilham Slimani, Ihame Elfarissi , and Zineb Bougroun 

Abstract E-commerce and many other online sites have increased the online payment modes, increasing the risk for online frauds. Many errors are lost due to fraudulent card transactions each year. The development of performance fraud detection methods is obligatory to minimize such losses. This article examines the usefulness of applying different learning approaches for detecting credit card fraud. Three algorithms will be applied on a database of an American bank and the data will be exploited based on supervised and unsupervised learning techniques, namely the MLP (multilayer perceptron), LR (logistic regression) and PCA (Principal Component Analysis). The main purpose of the study is comparing the classification performance of each algorithm using real dataset of fraudulent user accounts in a telecommunication network.

Keywords Credit card fraud · Machine learning · MLP (Multilayer perceptron) · LR (Logistic regression) · PCA (Principal component analysis)

1 Introduction

With the development of distance selling and e-commerce, payment methods had to evolve and adapt to the new requirements of Internet users. Worldwide, credit cards payment are still the most commonly used method for payment, this method

L. Moumeni (✉) · M. Saber · I. Slimani · I. Elfarissi · Z. Bougroun
Laboratory SmartICT, ENSAO, Université Mohammed Premier Oujda, Oujda, Morocco
e-mail: l.moumeni@ump.ac.ma

M. Saber
e-mail: m.saber@ump.ac.ma

I. Slimani
e-mail: i.slimani@ump.ac.ma

I. Elfarissi
e-mail: i.elfarissi@ump.ac.ma

Z. Bougroun
e-mail: z.bougroun@ump.ac.ma

is often preferred since the process is generally quick and easy [1]. In summary the credit card refers to a card that is given to the customer (cardholder). This card is permitting them to purchase items and offerings within credit score restriction or withdraw coins in advance. Credit card offers the cardholder a bonus of the time, it gives time for their clients to repay later in a prescribed time, by sporting it to the following billing cycle [2].

The usage of credit card as a mode of price for online, alongside with daily purchases has improved during the last few decades [3]. As the place of information is developed and still growing to be better over the time and also with the development of communication channels, attempts in a credit card for frauds, were extended worldwide, and because of that most businesses and those are facing large economic losses. “Credit card frauds are easy targets. Without any risks, a significant amount can be withdrawn without the owner’s knowledge” [4].

To resolve this problem, various techniques are used in the literature aiming to solve the fraud detection issues such as: Artificial Intelligence, Genetic Programming, Data Mining, Machine Learning, Transformed-domain-based.

In this paper, a comparative study of three different methods including Multi-layer perceptron, logistic regression learning classifiers, and PCA with the use of real data of an American bank database [5]. The database resumes transactions made in January 2017; it contains 569,614 transactions where 984 are frauds. The performance evaluation system of the studied algorithms depends on the following criteria: Precision, Recall, precision-recall curve area rate (PRC area).

This paper is structured as below: The research context and problematic are presented in the Introduction. Then, the first section is dedicated to expose the payment process and define a bank fraud including how it is detected. In the second section, a definition and explanation of the proposed algorithms are presented as well as the used dataset’s details. The third section is reserved to the interpretation of the obtained classification results.

2 Related Works

2.1 Credit Card Processing

There are several payment card systems, however, all work the same way. They all have the same functioning process. Each payment card generally goes through a series of stages and interaction between several participants. As illustrated in Fig. 1 (Fig. 1). A transaction goes through six main phases:

1. The card holder presents the card or enters the information on the internet.
2. The merchant requests authorization of the card after processing the card information.
3. The bank sends the authorization request to the card issuer.
4. The card issuer accepts or refuses the transaction.

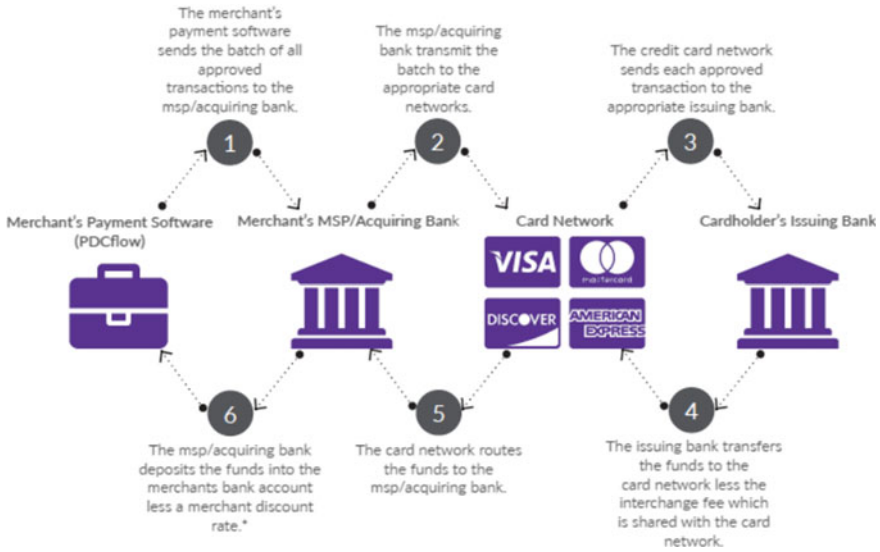


Fig. 1 Card transaction validation flow

- 5. The bank sends the response to the merchant.
- 6. The merchant receives the authorization response and completes the transaction [6].

Step 4 which is the authorization is the key step of each transaction it allows the evaluation of the transaction risk and if it is approved therefore the amount is reserved on the account.

2.2 Credit Card Fraud

According to recent studies done in article [7] we can distinguish two types of credit card fraud: Application fraud and behavioral fraud. Behavioral fraud is fraud by theft/stolen card, it is the most common categories of fraud but it is not the interest of our study we will be focused more on fraud application that describes the situations in which a credit card application is fraudulent. The credit card fraud investigated in this article occurs when a scammer requests a new credit using fake identity and the card issuer approves this request [8]. As already described, the authorization step is the gateway to fraud.

At this stage, the fraud algorithms are executed and depending on the obtained score, the authorization response can be accepted, refused, called for referral, picked up or not-adapted. Then the merchant must proceed accordingly. Even if the authorization is complete the transaction is still in progress because it must be settled [6].

Fig. 2 Credit card fraud detection systems



Depending on the settling process, this processing may take a few days, whereas when the payment approved is a fraudulent transaction, card holders cannot see this on the spot in their bank account, as they do not verify their account often. An example of system fraud detection is described in the Fig. 2

As already initialized in the introduction there are several techniques to deal with credit card fraud, such as:

- **Artificial Intelligence:** [9] uses a technique to achieve a reduction of the range of fake alarms, all through the evaluation process.
- **Genetic Programming:** the article [7], presents new calculation technique that is implemented to improve the fraud detection process, taking into account credit card transactions.
- **Data Mining:** according to the article [10], the greatest cost value effective approach for fraud detection is to determine the possible evidences of fraud from the available collected data by using mathematical algorithms, data processing techniques, that build use of advanced applied math ways, are divided in 2 main approaches: supervised and unsupervised methods.
- **Machine Learning:** as in article [8], Machine learning use the fraud detection field, directly using all of the historical group action records of every account is impractical as a result of the quantity of transactions of each account is incredibly high and is totally different.

This, group action aggregation methods are planned to get options to ameliorate the weakness of transaction-level classification. Though the selection of the amount of group action aggregation remains a drag, the idea of a group action aggregation strategy provides a reliable thanks to derive the input feature variables for fraud detection:

- Transformed-domain-based: “as in [7], where the evaluation process has been performed in a non-canonical domain (e.g., time, frequency, or frequency-time).”
- Combined Criteria: as in [7], where a multidimensional technique is exploited to improve the classification performance. One more example is given in [11], where the authors introduce several fraud indicators in the classification process.

3 Proposed Methods

In this study we will investigate the effectiveness of supervised and unsupervised algorithms of machine learning using the multilayer perceptron, regression logic algorithm and the PCA. The performance’s evaluation of each algorithm is done through recall, precision and precision-recall curve (PRC) area rates [5].

3.1 Algorithm Used in Study

1. **Multilayer perceptron:** The perceptron is a supervised learning algorithm for binary classifiers (separating two classes). It is then a type of linear classifier, and the simplest type of artificial neural network. The perceptron neural network is one of the most commonly applied Feedforward neural networks (FFNNs). MLP neurons are interconnected unidirectionally and unidirectionally fashion [12]. Figure 3 presents the architecture of a Multi Layer Perceptron Neural Network. Each MLP’s layer can be described mathematically, as illustrated in the following equation:

$$y = \varphi\left(\sum_{i=1}^n \omega_i x_i + b\right) = \varphi(w^T x + b) \quad (1)$$

where x denotes the values of inputs, w the values of weights, b is the bias and φ is the non-linear activation function.

2. **Logistic regression (sigmoid function):** It is an S-shaped curve that can take any real number and map it to a value between 0 and 1, but never exactly at these limits. Logistic regression uses an equation as a representation, just like linear regression. Input values (x) are linearly combined using weights or coefficient values (called the Greek capital letter Beta) to predict an output value (y) Fig. 4 [7]. Here is an example of a logistic regression Eq. (2):

$$y = \frac{e^{b_0 + b_1 x}}{1 + e^{b_0 + b_1 x}} \quad (2)$$

Fig. 3 Basic architecture of an MLP neural network

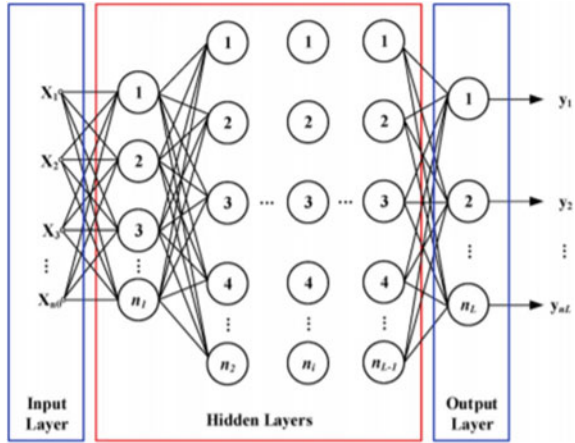
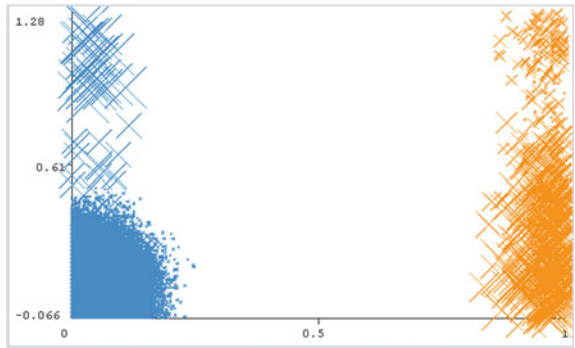


Fig. 4 Multilayer perceptron visualization



3. **Algorithm Principal Component Analysis (PCA):** is an unsupervised algorithm in machine learning. This technique is non-parametric statistical technique primarily used for dimensionality reduction in machine learning. It makes most extreme fluctuation in the dataset progressively obvious by turning the tomahawks. PCA recognizes a rundown of the main parameters to depict the underlying dataset before positioning them as per the measure of difference caught by each. The number of attribute combinations is equivalent to the number of dimensions of the dataset and in general set the maximum number of PCAs which can be constructed [6].

3.2 Credit Card Data Description

As already described in the introduction, the database used concerns data from the American bank for the month of January 2017. In Table 1 we present the main

Table 1 Fundamental characteristics for credit card transaction data

Attributes	Description
Account number	Associated account number
Credit limit	The not-to-exceed amount of credit associated to the account
Credit card identification	Credit card number
Operation date	Date of the transaction
Operation time	Time of the transaction
Transaction amount	The transaction amount validated by the merchant
Transaction type	Transaction type, for example purchase or cash withdrawal
Currency code	The currency code
Merchant category code	The merchant business type code
Merchant number	The merchant reference number
Transaction country	The country where the transaction occurs
Transaction city	The city where the transaction occurs
Entry mode	A code that indicates the way in which the cardholder account information was inserted into the terminal
Approval code	The response to the authorization request, i.e., approve or reject

features of a recorder transaction in order to expose the essential framework of the credit card. Those attributes may change slightly depending on the card issuers, it is pointed out that there are essential attributes which must be contained in the database and which will be used for fraud detection [13].

From a fraud detection modeling perspective, a credit card transaction contains the transaction detail and the status account. Most of the features related to the detail of the transaction can be considered as categorical variables. Here, the parameters of a transaction are a broader concept than the type of transaction [13].

3.3 Dataset Description

As indicated, the detection system performance depends strongly on feature engineering. Previous reviews indicate that the transaction aggregation strategies are primarily important in the functionality engineering process. The dataset [14] contains the transactions carried out by a card holder over a period of 2 days of January 2017. Where there are in total 569,614 transactions, including 984, or 0.172% of the transactions are fraudulent transactions. This dataset is very unbalanced. Since providing the transaction details of a client is considered a privacy issue, therefore most of the functionality of the dataset is transformed using principal component analysis (PCA). $V_1, V_2, V_3, \dots, V_{28}$ are functionalities applied by PCA and rest, that is to say “time”, “Amount” and “class” are functionalities not applied by the PCA, as indicated in Table 2.

Table 2 Attributes of European dataset

S. No	Feature	Description
1	Time	Time in seconds to specify the intervals between the current transaction and the first transaction
2	Amount	Transaction amount
3	Class	0—not fraud 1—fraud

3.4 Performance Measures

In this study, we will use four well-known measures to assess the methodology, namely: precision, sensitivity, specificity and precision. These measures depend entirely on the four basic metrics (alarm rate), respectively “True Positive” (TP) of the number of fraudulent transactions which have been detected as a true alarm, “False Positive” (FP) the number of authentic transactions that were detected as a false alarm, “True Negative” (TN) the number of authentic transactions that were detected as a true alarm and “False Negative” (FN) are the number of fraudulent transactions missed [14], positive (P) means that the number of “fraudulent transactions” and negative (N) represents the number of “authentic transactions” the total of P and N means all transactions. Below are the equations for each measurement:

$$Accuracy = \frac{TP + TN}{TP + FP + TN + FN} \quad (3)$$

$$Recall = \frac{TP}{TP + FN} \quad (4)$$

$$Sensitivity = \frac{TN}{FP + TN} \quad (5)$$

$$Precision = \frac{TP}{TP + FP} \quad (6)$$

“The fraud detection in the credit cards is a binary classification which means that the transactions for a credit card are divided into two sets, either (0)—genuine transactions or (1)—fraudulent transactions. Using the confusion matrix for our study the calculation of alarm rates will be different [9], where the values for each alarm rate are taken from its position in the confusion matrix such as the TP, where the value was (1, 1), TN (0, 0), FP (0, 1) and FN (1, 0)” [14].

4 Result and Discussion

4.1 Confusion Matrix

The confusion matrix summarizes the performance result of the algorithm as described on Table 3, it explains what the algorithm does correctly is what is not correct. The lines of the confusion matrix represent the predicted class, and that the lines represent the real class [14].

4.2 Experiment Result

The three algorithms are implemented in Weka [15]. All algorithms need a training dataset. Implemented algorithms gave result as an accuracy, recall, sensitivity and precision fraud transactions. For 569,614 transactions where 984 are frauds. In dataset there are 31 features where 31st is a binary variable with 0 regular transaction and 1 as fraud transaction. And Original dataset is highly imbalanced as only 0.17% of data is classified as fraud. If we predict all data inputs to be classified as class 1, we would be 99.83% accurate.

The obtained results using the performance measures are presented in Table 4 .

An illustration of the classification result are presented in Figs. (4 and 5).

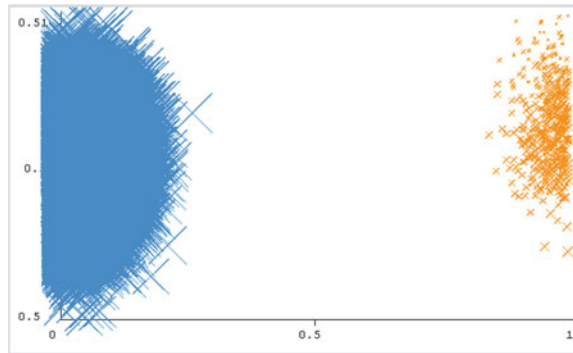
Table 3 Confusion matrix

		Predicted class	
		0	1
Actual class	0	TP	FN
	1	FP	TN

Table 4 Performance Rates

Algorithm	Accuracy (%)	Recall	Sensitivity (%)	Precision (%)	Time taken (s)
MLP	99.03	1	98.06	12.45	116.23
LR	98.25	1	97.52	7.92	48
PCA	97.18	98%	97.02	6.85	15

Fig. 5 Logistic regression visualization



4.3 Discussion

Due to the performance of machine learning algorithms, the accuracy zone rates between the three algorithms indicates that the MPL (Multilayer perceptron) has the highest rate which shows that this algorithm is very efficient in distinguishing the binary class 0 or 1 in used dataset. Also for accuracy, the rate for the class results is the highest for the MPL as well as the lowest rate is for the non-supervised algorithm the PCA to indicate to us that it is not very efficient for the detection of fraud. This is an important indicator because we are testing algorithms to predict the class of results as normal transaction or fraud.

5 Conclusion

In this article, the learning algorithms are applied to a fraud detection problem. In particular, a MLP classifier, the logistic regression and PCA technique were applied to a large data model. Data is used as a method of characterizing users, in order to detect fraudulent use in a telecommunications environment. The input data consisted of real user accounts which were defrauded. The comparative study shows that the best results for this case study are obtained using the Multilayer perceptron structure of neural networks.

References

1. Cash A, Tsai H-J (2018) Readability of the credit card agreements and financial charges. *Fin Res Lett* 24:145–150. <https://doi.org/10.1016/j.frl.2017.08.003>. ISSN 1544-6123
2. Dornadula VN, Geetha S (2019) Credit card fraud detection using machine learning algorithms. *Procedia Comput Sci* 165:631–641. <https://doi.org/10.1016/j.procs.2020.01.057>. ISSN 1877-0509

3. Kiran S, Guru J, Kumar R, Kumar N, Katariya D, Sharma M (2018) Credit card fraud detection using Naïve Bayes model based and KNN classifier. *Int J Adv Res Ideas Innov Technol* 4(3):45-65. ISSN: 2454-132X
4. Wang D, Chen B, Chen J (2019) Credit card fraud detection strategies with consumer incentives. *Omega* 88:179–195. <https://doi.org/10.1016/j.omega.2018.07.001>. ISSN 0305-0483
5. Credit Card Fraud Detection, <https://www.kaggle.com/mlg-ulb/creditcardfraud> (2019)
6. Gómez JA, Arévalo J, Paredes R, Nin J (2018) End-to-end neural network architecture for fraud scoring in card payments. *Pattern Recognit Lett* 105:175–181. <https://doi.org/10.1016/j.patrec.2017.08.024>. ISSN 0167-8655
7. Carta S, Fenu G, Recupero DR, Saia R (2019) Fraud detection for E-commerce transactions by employing a prudential multiple consensus model. *J Inf Secur Appl* 46:13–22. <https://doi.org/10.1016/j.jisa.2019.02.007>. ISSN 2214-2126
8. Zhang X, Han Y, Xu W, Wang Q (2019) HOBA: a novel feature engineering methodology for credit card fraud detection with a deep learning architecture. *Inf Sci*. <https://doi.org/10.1016/j.ins.2019.05.023>. ISSN 0020-0255
9. Ryman-Tubb NF, Krause P, Garn W (2018) How Artificial Intelligence and machine learning research impacts payment card fraud detection: a survey and industry benchmark. *Eng Appl Artif Intell* 76:130–157. <https://doi.org/10.1016/j.engappai.2018.07.008>. ISSN 0952-1976
10. Carneiro N, Figueira G, Costa M (2017) A data mining based system for credit-card fraud detection in e-tail. *Decis Support Syst* 95:91–101. <https://doi.org/10.1016/j.dss.2017.01.002>. ISSN 0167-9236
11. Suh JB, Nicolaides R, Trafford R (2019) The effects of reducing opportunity and fraud risk factors on the occurrence of occupational fraud in financial institutions. *Int J Law Crime Just* 56:79–88. <https://doi.org/10.1016/j.ijlcrj.2019.01.002>. ISSN 1756-0616
12. Ewees AA, Abd Elaziz M, Alameer Z, Ye H, Jianhua Z (2020) Improving multilayer perceptron neural network using chaotic grasshopper optimization algorithm to forecast iron ore price volatility. *Resourc Policy* 65:101555. <https://doi.org/10.1016/j.resourpol.2019.101555>. ISSN 0301-4207
13. Husejinovic A (2020) Credit card fraud detection using naive Bayesian and C4.5 decision tree classifiers 8:1–5. <https://www.researchgate.net/>, <https://doi.org/10.21533/pen.v>
14. Ata O, Hazim L (2020) Comparative analysis of different distributions dataset by using data mining techniques on credit card fraud detection. *Tehniki vjesnik* 27:618–626. <https://doi.org/10.17559/TV-20180427091048>
15. WEKA, The workbench for machine learning. <https://www.cs.waikato.ac.nz/ml/weka/>

OctaNLP: A Benchmark for Evaluating Multitask Generalization of Transformer-Based Pre-trained Language Models



Zakaria Kaddari, Youssef Mellah, Jamal Berrich, Mohammed G. Belkasmi, and Toumi Bouchentouf

Abstract In the last decade, deep learning based Natural Language Processing (NLP) models achieved remarkable performance on the majority of NLP tasks, especially, in machine translation, question answering and dialogue. NLP language models shifted from uncontextualized vector space models like word2vec and Glove in 2013, and 2014, to contextualized LSTM-based model like ELMO and ULMFit in 2018, to contextualized transformer-based models like BERT. Transformer-based language models are already trained to perform very well on individual NLP tasks. However, when applied to many tasks simultaneously, their performance drops considerably. In this paper, we overview NLP evaluation metrics, multitask benchmarks, and the recent transformer-based language models. We discuss the limitations of the current multitask benchmarks, and we propose our octaNLP benchmark for comparing the generalization capabilities of the transformer-based pre-trained language models on multiple downstream NLP tasks simultaneously.

Keywords NLP · Multitask · Benchmark · octaNLP · Metrics · Transformer

Z. Kaddari (✉) · Y. Mellah · J. Berrich · T. Bouchentouf
LaRSA Laboratory, AIRES Team, National School of Applied Sciences,
Université Mohammed Premier, Oujda, Morocco
e-mail: z.kaddari@ump.ac.ma

Y. Mellah
e-mail: y.mellah@ump.ac.ma

J. Berrich
e-mail: j.berrich@ump.ac.ma

T. Bouchentouf
e-mail: t.bouchentouf@ump.ac.ma

M. G. Belkasmi
SmartICT Laboratory, National School of Applied Sciences,
Université Mohammed Premier, Oujda, Morocco
e-mail: m.belkasmi@ump.ac.ma

1 Introduction

The rate of adoption of NLP applications by companies and customers is increasing rapidly. This is mostly due to the progress that has been made by deep learning (DL) and transformer-based pre-trained language models (LM) [21]. Some of these LM can even be used, and personalized directly without any knowledge of machine learning or coding.

The field of NLP contains many tasks, and new tasks are proposed each year by the NLP research community. In deep learning based NLP, some tasks are more studied than others. In the last couple of years, DL transformer-based LM achieved state-of-the-art performances on the majority of NLP tasks.

The field of NLP does not have a universal evaluation metric that can be used to evaluate the performance of new models on every task. But rather, a variety of metrics, like, BLEU [19], and ROUGE [15], among others. These metrics are used for specific tasks, BLEU is used in machine translation (MT) for example, and ROUGE for summarization. However, when we want to evaluate the generalization of a LM on multiple tasks at once, we confront with a major problem, which is the lack of a universal and unique metric for all or at least a subset of NLP tasks. This is one of NLP's open challenges [10] that is attracting more research in recent years. The study of this problem is the core of this paper, where we provide an overview of evaluation metrics and multitask NLP benchmarks along with our proposed octaNLP benchmarking approach for comparing the generalization capabilities of DL transformer-based language models.

This paper is organized as follows, the next section overviews the most used NLP evaluation metrics. Section 3 describes the available multitask NLP benchmarks. In Sect. 4, we overview the most important DL transformer-based pre-trained LM. In Sect. 5, we discuss the limitations of the available multitask NLP benchmarks, and we propose our octaNLP benchmark for comparing the generalization performance of transformer-based pre-trained LM on multiple downstream tasks simultaneously. Finally, we finish the paper with a conclusion.

2 Evaluation Metrics in NLP

In the field of NLP, there is no single metric that can be used to evaluate the performance of a system on all NLP tasks. But rather, a set of metrics that are used depending on the task. In the case of classification for example, the accuracy metric can be used, which indicates the percentage of correct classifications. Other metrics can also be used in the case of classification, like F1, exact match, and Matthews correlation coefficient [17] These classification metrics are not specific to NLP, but rather, used in a wide range of areas and disciplines. On the other hand, there are metrics that are specific to NLP, the most used ones are listed below:

Table 1 The most used metrics in NLP along with their associated tasks

Metric	Tasks
Accuracy	Question answering
	Sentiment analyses
	Paraphrasing
	Natural language inference
	Coreference resolution
	Word sense disambiguation
F1	Paraphrasing
	Natural language inference
	Question answering
Exact match	Question answering
Matthews correlation coefficient	Grammatical acceptability
BLEU	Machine translation
ROUGE	Summarization
Perplexity	Language modeling
Pearson correlation coefficient	Sentence similarity
Spearman correlation coefficient	Sentence similarity

BLEU: The bilingual evaluation understudy (BLEU) [19] is an automatic metric that was initially defined to evaluate systems for machine translation (MT). However, it is now also used in other Natural Language Generation (NLG) tasks like, summarization, and dialogue. The BLEU score is used to compare a candidate translation to one or more reference translations. This score can range between 0 and 1, for 1 being a perfect translation. BLEU has many strong advantages; it is an automatic metric, language independent, and proved to correlate highly with human judgment.

ROUGE: Recall-Oriented Understudy for Gisting Evaluation (ROUGE) [15] is a set of metrics that are used to evaluate the performance of automatic summarization or machine translation systems. ROUGE metrics compare a candidate summary or translation to one or more reference summarizations or translations.

In Table 1, we list the most used metrics in NLP along with their associated tasks.

3 Multitask NLP Benchmarks

decaNLP: The Natural Language Decathlon (decaNLP) [18] benchmark was introduced in 2018. The goal of this benchmark is to evaluate single models that can generalize to many different NLP tasks simultaneously. The tasks included in the benchmark are, semantic parsing, natural language inference, question answering, document summarization, machine translation, sentiment analysis, semantic role labeling, goal-oriented dialogue, pronoun resolution, and relation extraction. All

Table 2 GLUE tasks along with their associated datasets and metrics

Task	Dataset	Metric
Question answering	QNLI [23]	Accuracy
Sentiment analyses	SST-2 [25]	Accuracy
Paraphrasing	MRPC [7] and QQP ^a	F1/accuracy
Grammatical acceptability	CoLA [30]	Matthews correlation coefficient [17]
Sentence similarity	STS-B [1]	Pearson/Spearman correlation coefficients
Natural language inference	MNLI [31] and RTE [5]	F1/accuracy
Coreference resolution	WNLI [13]	Accuracy

^a <https://data.quora.com/First-Quora-Dataset-Release-Question-Pairs>

these tasks were framed as a question answering problem, and are trained jointly. All training instances are in the form of (question, context, answer) triplets. To be able to evaluate the generalization of NLP models across all tasks simultaneously, the creators of decaNLP defined their own score that they called decaScore, which is simply the sum of the scores of all tasks. The creators of decaNLP also provided and evaluated three baseline models, a pointer-generator sequence-to-sequence (S2S) model [24], an S2S model augmented with self-attentive encoder and decoder layers [26], and an S2S model augmented with a coattention mechanism [32]. In addition to the three baseline models, the creators of decaNLP also built their own model that they called the multitask question answering network (MQAN). MQAN learns all of decaNLP tasks jointly, and does not require any task-specific modules or parameters. This model achieved improved performance on the majority of decaNLP tasks.

GLUE: Similar to decaNLP, the General Language Understanding Evaluation (GLUE) [28]¹ benchmark aims to drive research in general NLP models that can generalize well to a variety of different tasks. However, the scope of GLUE is more limited than decaNLP, because GLUE is only concerned with Natural Language Understanding (NLU) tasks. These tasks along with their associated datasets and metrics are listed in Table 2. To evaluate the general performance of NLP models across all tasks, GLUE define a single score, which is simply the average score on all tasks with all tasks having the same weight. For tasks with multiple metrics, the benchmarking algorithm of GLUE first averages those metrics to get a single task score. Since its release, a large number of models have been tested on the benchmark, especially, transformer-based pre-trained language models. Recent models have surpassed the human performance on GLUE for the majority of its tasks.

SuperGLUE: Like GLUE, The SuperGLUE [27]² benchmark aims to evaluate general NLP models on a variety of tasks simultaneously. This benchmark was introduced after the surpassing of human performance on GLUE by the recent models on

¹<https://gluebenchmark.com>.

²<https://super.gluebenchmark.com>.

Table 3 Super GLUE tasks along with their associated datasets and metrics

Task	Dataset	Metric
Question answering	BoolQ [2], COPA [8], MultiRC [11], ReCoRD [33]	Accuracy/F1/EM
Natural language inference	CB [16] and RTE [5]	Accuracy/F1
Word sense disambiguation	WiC [20]	Accuracy
Coreference resolution	WSC ^a	Accuracy

^a <https://cs.nyu.edu/faculty/davise/papers/WinogradSchemas/WS.html>

the majority of GLUE tasks, which made GLUE no longer suitable for tracking the progress towards general NLU models. SuperGLUE differs from GLUE in that it contains more difficult and challenging NLU tasks with more diverse tasks formats. SuperGLUE adopts the same scoring philosophy as GLUE, by weighting each task equally and averaging all tasks score's, to provide a single general score. The tasks used in SuperGLUE along with their associated datasets and metrics are listed in Table 3.

SentEval: SentEval [4] is a benchmark and a toolkit for evaluating the quality of universal general-purpose sentence representations. The goal of this benchmark is to drive research in finding sentence representations that can yield good results when applied on a variety of different downstream NLP tasks. SentEval contains a diverse set of tasks including, binary and multi-class classification, entailment and semantic relatedness, Semantic Textual Similarity (STS), paraphrase detection, caption-Image retrieval, and sentiment analyses.

4 Transformer-Based Pre-trained Language Models

In this section, we will provide a short overview of the most important transformer-based pre-trained language models. Most of these models are based on BERT, the first transformer-based pre-trained language model released. Figure 1 shows the models that were derived from BERT, along with what was added to them.

BERT [6]: a pre-trained model based on the transformer model. BERT is designed to perform deep two-way representations from unlabeled text by jointly conditioning the left and right context in all the layers. It pre-trains a next sentence prediction task to understand sentence relationships.

SemBERT [34]: This model is capable of explicitly absorbing contextual semantics over a BERT backbone. SemBERT keeps the convenient usability of its BERT precursor with light fine-tuning and without substantial task-specific modifications. Compared with BERT, SemBERT is as simple in concept but more powerful. It obtains new state-of-the-art or substantially improves results on ten reading comprehension and language inference tasks.

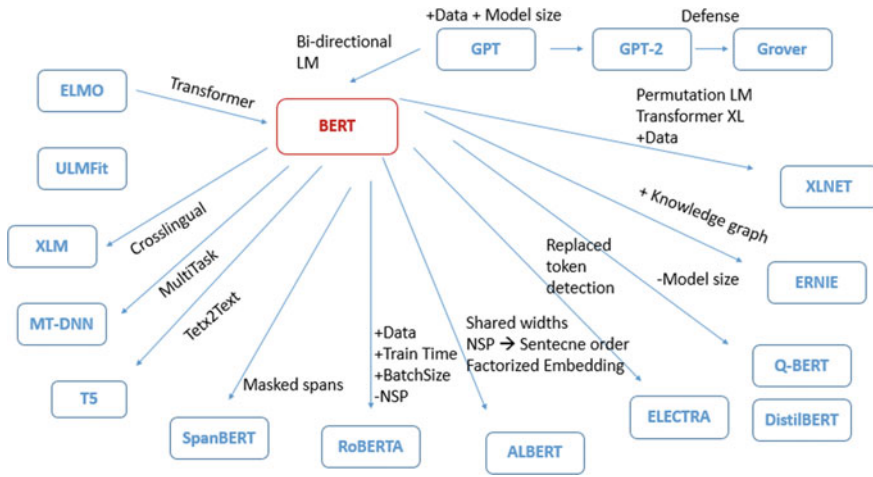


Fig. 1 Models that were derived from BERT, along with what was added to them

StructBERT [29]: This model was made by incorporating language structures into pre-training. Specifically, its trained with two auxiliary tasks to make the most of the sequential order of words and sentences, which leverage language structures at the word and sentence levels, respectively.

ALBERT [12]: This model presents two parameter-reduction techniques to lower memory consumption and increase the training speed of BERT: Splitting the embedding matrix into two smaller matrices and using repeating layers split among groups.

ELECTRA [3]: is a new pre-training approach which trains two transformer models: the generator and the discriminator. The generator’s role is to replace tokens in a sequence, and is therefore trained as a masked language model. The discriminator, which is the model we’re interested in, tries to identify which tokens were replaced by the generator in the sequence.

T5 [22]: is an encoder-decoder model pre-trained on a multi-task mixture of unsupervised and supervised tasks and for which each task is converted into a text-to-text format.

BART [14]: This model combines bidirectional and auto-regressive transformers. It is a denoising autoencoder built with a sequence-to-sequence model that can tackle a wide range of NLP tasks from NLU to NLG. Although it is particularly effective when fine-tuned for text generation tasks. BART achieved new state-of-the-art on numerous tasks such as dialogue, question answering, and summarization.

5 Our OctaNLP Benchmarking Approach

In Sect. 3, we reviewed the available multitask NLP benchmarks. We saw that decaNLP include 10 diverse tasks, with different evaluation metrics, such as F1, accuracy, BLEU and ROUGE. The variety of tasks and metrics makes decaNLP a perfect benchmark for evaluating the generalization of NLP models. However, decaNLP was released before BERT, the first transformer-based pre-trained language model. Therefore, it is not known if the benchmark is compatible with those kind of models. To the date of the writing of this paper, and to the best of our knowledge, no transformer-based pre-trained language model has been tested on decaNLP.

As for GLUE and SuperGLUE, we saw in the same section, that these two models are only concerned with evaluating the generalization on NLU tasks. The lack of any NLG task such as machine translation, summarization or dialogue, inhibits these two benchmarks from evaluating the generalization capabilities on all NLP tasks.

As for SentEval benchmark, its only goal is to evaluate the generalization of sentence representations, and same as GLUE and SuperGLUE, it is only concerned with NLU tasks.

To overcome the limitations of these multitask benchmarks, we propose a novel benchmark that we call octaNLP for evaluating the generalization capabilities of transformer-based pre-trained language models. The 8 tasks that we included in our benchmark covers the two pillars of NLP, NLU and NLG. Therefore, we think that our benchmark is more suitable for evaluating the generalization capabilities across all NLP tasks.

In Table 4, we list the datasets that we considered in our benchmark, along with their associated tasks and evaluation metrics.

We defined a single overall score, that we called octaScore, which is simply the average of the scores of all 8 tasks. We applied our benchmarking approach to two of the recent transformer-based pre-trained language models, BART and T5. Table 5 shows the results of these two models on each individual task along with the overall octaScore. We plan to apply our octaNLP benchmark to other models as a future work.

Table 4 The datasets adopted in octaNLP, along with their associated tasks and evaluation metrics

Dataset	Task	Metric
SQuAD [23]	Question answering	F1
MNLI [31]	Natural language inference	F1
QQP ^a	Semantic textual similarity	Accuracy
QNLI [23]	Question answering	Accuracy
RTE [5]	Natural language inference	Accuracy
MRPC [7]	Paraphrasing	Accuracy
CoLA [30]	Grammatical acceptability	Matthews correlation coefficient (Mcc)
CNN/DM [9]	Summarization	Rouge

^a <https://data.quora.com/First-Quora-Dataset-Release-Question-Pairs>

Table 5 Benchmarking results of BART and T5 on octaNLP benchmark

Model	SQuAD	MNLI	QQP	QNLI	RTE	MRPC	CoLA	CNN/DM	Octa score
	F1	m	Acc	Acc	Acc	Acc	Mcc	R1	
BART	94.6	89.9	92.5	94.9	87.0	90.4	62.8	44.16	82.03
T5	95.64	92.0	90.4	96.7	92.5	89.2	70.8	43.52	83.84

From this experiment, we can see that the T5 model achieved the best octaScore, which means that this model can generalize better than BART on diverse NLP tasks. This is because T5 is a text-to-text model, meaning that it approaches every NLP task in the same manner, as text input to text output.

6 Conclusion and Future Work

Transformer-based pre-trained language models have achieved remarkable results on many individual NLP tasks, but are still lacking generalization capabilities to be applied to multiple tasks simultaneously. In this paper, we provided an overview of NLP evaluation metrics, multitask benchmarks, and transformer-based pre-trained language models. We presented the limitations of the current multitask benchmarks, and proposed our octaNLP benchmark for comparing the generalization capabilities of the transformer-based pre-trained language models on multiple downstream NLP tasks simultaneously. As a future work, we plan to test the multitask generalization capabilities of other transformer-based pre-trained language models using our octaNLP benchmark.

References

1. Cer D, Diab M, Agirre E, Lopez-Gazpio I, Specia L (2017) SemEval-2017 task 1: semantic textual similarity multilingual and crosslingual focused evaluation. In: Proceedings of the 11th international workshop on semantic evaluation (SemEval-2017). Association for Computational Linguistics, Vancouver, Canada, pp 1–14
2. Clark C, Lee K, Chang MW, Kwiatkowski T, Collins M, Toutanova K (2019) BoolQ: exploring the surprising difficulty of natural yes/no questions. In: Proceedings of the 2019 conference of the North American chapter of the association for computational linguistics: human language technologies, vol 1. Association for Computational Linguistics, Minneapolis, Minnesota, pp 2924–2936
3. Clark K, Luong MT, Le QV, Manning CD (2020) ELECTRA: pre-training text encoders as discriminators rather than generators. arXiv e-prints [arXiv:2003.10555](https://arxiv.org/abs/2003.10555)
4. Conneau A, Kiela D (2018) SentEval: an evaluation toolkit for universal sentence representations. In: Proceedings of the eleventh international conference on language resources and evaluation (LREC (2018) European Language Resources Association (ELRA). Miyazaki, Japan

5. Dagan I, Glickman OMB (2006) Machine learning challenges. evaluating predictive uncertainty, visual object classification, and recognising textual entailment. *Lecture notes in computer science*, Vol 3944. Springer
6. Devlin J, Chang M, Lee K, Toutanova K (2018) BERT: pre-training of deep bidirectional transformers for language understanding. *CoRR abs/1810.04805*
7. Dolan WB, Brockett C (2005) Automatically constructing a corpus of sentential paraphrases. In: *Proceedings of the third international workshop on paraphrasing (IWP2005)*
8. Gordon A, Kozareva Z, Roemmele M (2012) SemEval-2012 task 7: choice of plausible alternatives: An evaluation of commonsense causal reasoning. In: **SEM 2012: the first joint conference on lexical and computational semantics, volume 1: Proceedings of the main conference and the shared task, and Volume 2: Proceedings of the sixth international workshop on semantic evaluation (SemEval 2012)*. Association for Computational Linguistics, Montréal, Canada, pp 394–398
9. Hermann KM, Kociský T, Grefenstette E, Espeholt L, Kay W, Suleyman M, Blunsom P (2015) Teaching machines to read and comprehend. *CoRR abs/1506.03340*
10. Kaddari Z, Mellah Y, Berrich J, Belkasmı MG, Bouchentouf T (2021) Natural language processing: Challenges and future directions. In: Masrouf T, El Hassani I, Cherrafi A (eds) *Artificial intelligence and industrial applications*. Springer International Publishing, Cham, pp 236–246
11. Khashabi D, Chaturvedi S, Roth M, Upadhyay S, Roth D (2018) Looking beyond the surface: a challenge set for reading comprehension over multiple sentences. In: *Proceedings of the 2018 conference of the North American chapter of the association for computational linguistics: human language technologies (Long Papers)*, vol 1. Association for Computational Linguistics, New Orleans, Louisiana, pp 252–262
12. Lan Z, Chen M, Goodman S, Gimpel K, Sharma P, Soricut R (2019) ALBERT: a lite bert for self-supervised learning of language representations. *arXiv e-prints arXiv:1909.11942*
13. Levesque HJ, Davis E, Morgenstern L (2011) The winograd schema challenge. In: *AAAI spring symposium: logical formalizations of commonsense reasoning, volume 46 (2011)*
14. Lewis M, Liu Y, Goyal N, Ghazvininejad M, Mohamed A, Levy O, Stoyanov V, Zettlemoyer L (2019) BART: denoising sequence-to-sequence pre-training for natural language generation, translation, and comprehension. *arXiv e-prints arXiv:1910.13461*
15. Lin CY (2004) ROUGE: A package for automatic evaluation of summaries. *Text summarization branches out*. Association for Computational Linguistics, Barcelona, Spain, pp 74–81
16. Marneffe M-C, Simmons M, Tonhauser J (2019) The commitmentbank: investigating projection in naturally occurring discourse. <https://ojs.ub.uni-konstanz.de/sub/index.php/sub/article/view/601>
17. Matthews B Comparison of the predicted and observed secondary structure of t4 phage lysozyme. *Biochimica et Biophysica Acta (BBA) - Protein Struct* 405(2) 442 – 451
18. McCann B, Keskar NS, Xiong C, Socher R (2018) The natural language decathlon: multitask learning as question answering. *CoRR abs/1806.08730*
19. Papineni K, Roukos S, Ward T, Zhu WJ (2002) Bleu: a method for automatic evaluation of machine translation. In: *Proceedings of the 40th annual meeting of the association for computational linguistics*. Association for Computational Linguistics, Philadelphia, Pennsylvania, pp 311–318
20. Pilehvar MT, Camacho-Collados J (2019) WiC: the word-in-context dataset for evaluating context-sensitive meaning representations. In: *Proceedings of the 2019 conference of the North American chapter of the association for computational linguistics: human language technologies, vol 1*. Association for computational linguistics, Minneapolis, Minnesota, pp 1267–1273
21. Qiu X, Sun T, Xu Y, Shao Y, Dai N, Huang X (2020) Pre-trained models for natural language processing: a survey. *arXiv e-prints arXiv:2003.08271*
22. Raffel C, Shazeer N, Roberts A, Lee K, Narang S, Matena M, Zhou Y, Li W, Liu PJ (2019) Exploring the limits of transfer learning with a unified text-to-text transformer. *arXiv e-prints arXiv:1910.10683*
23. Rajpurkar P, Zhang J, Lopyrev K, Liang P (2016) SQuAD: 100,000+ questions for machine comprehension of text. In: *Proceedings of the 2016 conference on empirical methods in natural language processing*. Association for computational linguistics, Austin, Texas, pp 2383–2392

24. See, A., Liu, P.J., Manning, C.D.: Get to the point: Summarization with pointer-generator networks. CoRR abs/1704.04368 (2017)
25. Socher R, Perelygin A, Wu J, Chuang J, Manning CD, Ng A, Potts C (2013) Recursive deep models for semantic compositionality over a sentiment treebank. In: Proceedings of the 2013 conference on empirical methods in natural language processing. Association for Computational Linguistics, Seattle, Washington, pp 1631–1642
26. Vaswani A, Shazeer N, Parmar N, Uszkoreit J, Jones L, Gomez AN, Kaiser LU, Polosukhin I (2017) Attention is all you need. In: Guyon I, Luxburg UV, Bengio S, Wallach H, Fergus R, Vishwanathan S, Garnett R (eds) Advances in neural information processing systems, vol 30. Curran Associates, Inc., pp 5998–6008
27. Wang A, Pruksachatkun Y, Nangia N, Singh A, Michael J, Hill F, Levy O, Bowman SR (2019) SuperGlue: a stickier benchmark for general-purpose language understanding systems
28. Wang A, Singh A, Michael J, Hill F, Levy O, Bowman SR (2019) Glue: a multi-task benchmark and analysis platform for natural language understanding
29. Wang W, Bi B, Yan M, Wu C, Bao Z, Xia J, Peng L, Si L (2019) StructBERT: incorporating language structures into pre-training for deep language understanding. arXiv e-prints [arXiv:1908.04577](https://arxiv.org/abs/1908.04577)
30. Warstadt A, Singh A, Bowman SR (2018) Neural network acceptability judgments. CoRR abs/1805.12471
31. Williams A, Nangia N, Bowman S (2018) A broad-coverage challenge corpus for sentence understanding through inference. In: Proceedings of the 2018 conference of the North American Chapter of the association for computational linguistics: human language technologies, vol 1 (Long Papers). Association for Computational Linguistics, New Orleans, Louisiana, pp 1112–1122
32. Xiong C, Zhong V, Socher R (2016) Dynamic coattention networks for question answering. CoRR abs/1611.01604
33. Zhang S, Liu X, Liu J, Gao J, Duh K, Durme BV (2018) Record: bridging the gap between human and machine commonsense reading comprehension. CoRR abs/1810.12885
34. Zhang Z, Wu Y, Zhao H, Li Z, Zhang S, Zhou X, Zhou X (2019) Semantics-aware BERT for language understanding. arXiv e-prints [arXiv:1909.02209](https://arxiv.org/abs/1909.02209)

Comparative Study of Regression and Regularization Methods: Application to Weather and Climate Data



El Mehdi Raouhi, Mohamed Lachgar, and Ali Kartit

Abstract Regression analysis is a powerful statistical method that support to inspect the relationship between two or more variables of interest. While there are many types of regression analysis, at their core they all examine the impact of one or more independent variables on a dependent variable. It is one of the most commonly used methods in many scientific fields. Satisfying the assumptions such as collinearity between variables ought to be a significant issue in data science. Advanced level tools such as Linear, Lasso, Ridge and ElasticNet regression are methods designed to overcoming a problem of overfitting a model. This study discusses comparing regression and regularization algorithms. It also deals with how the concept of model complexity unfolds for each of these models and provides an overview of how each algorithm builds a model. Moreover, it examines the strengths and weaknesses of each algorithm, as well as the type of data to which they can best be applied to irrigation water use efficiency under climate change. Finally, this work aims also to explain the meaning of the most important regularization criteria. It remains to say that the main contributions of this study are (1) Comparing linear and multilinear regression methods: case of climate change dataset using regression metrics (2) comparing regularization methods: Ridge, Lasso and ElasticNet.

Keywords Machine learning · Regression · Regularization · Irrigation · Climate change

E. M. Raouhi (✉) · M. Lachgar · A. Kartit
LTI Laboratory, ENSA, University Chouaib Doukkali, El Jadida, Morocco
e-mail: raouhi@gmail.com

M. Lachgar
e-mail: lachgar.m@gmail.com

A. Kartit
e-mail: alikartit@gmail.com

1 Introduction

The evolution of artificial intelligence and the concept of machine learning (ML) together with the Internet of Things (IoT) allowed researchers to apply these techniques to develop the agriculture [1, 2]. This helped farmers to increase their productivity, to use the maximum of available land, and to optimize the use of water resources for irrigation [3, 4], etc.

In this study we start by looking at the linear regression model, one of the simplest models there is. Next, we look at polynomial regression, a more complex model that can adapt to non-linear data sets, since this model has more parameters than linear regression. Then we look at several regularization techniques, that can reduce the risk of over-adjusting the drive assembly [5, 12].

The main contributions of this paper are: (1) Comparing linear and multilinear regression methods: case of climate change dataset using regression metrics. (2) Comparing regularization methods: Ridge, Lasso and ElasticNet. Using regression metrics to show the algorithm who fit the best result for the change climate dataset on the above comparison 1 and 2.

The remainder of this paper is structured as follows. Section 2 defines the regression algorithms. Section 3 describes the experimental set-up and methodology used on the case study, then Sect. 4 sets out a discussion of simulation results, followed by the conclusions and future work.

2 Related Works

This section presents the related work carried out in this perspective. First, the authors on [13], conclude that Lasso model showed a better performance for the prediction of ozone concentrations, compared to multiple linear regression and its other alternative methods. This feature presents a significant advantage for the daily prediction of the ozone concentration in the Grand Casablanca.

Next, in [14] the authors of the article note that before applying multiple linear regression to predict crop yields, it is necessary to know the important attributes of the database. All the attributes used in the database will not be significant or the modification of the value of these attributes will not affect anything on the dependent variables. Otherwise, the authors in [14] shows that a regularized model are best fitting models in regression analysis when we found noise exists in the usual models.

After that, in [15], the ridge algorithm penalty reduces the estimation of parameters and works well for many markers with small effects, and therefore cannot produce an interpretable model with only the appropriate markers. With the lasso penalty, the model automatically selects the variables. Otherwise the ElasticNet penalty provides a better compromise between lasso and peak penalties and has the effect of averaging the markers that are highly correlated, then entering the average marker into the model.

Finally, result present in [16] shows that the elastic net is more consistent than ridge regularization in predicting a next year rainfall.

Our contribution consists in challenging the performance of prediction model using a comparison of the most regularization methods namely: Ridge, Lasso and ElasticNet Regressions applied to temperature average prediction with the aim of optimizing the use of water resource for irrigation.

3 Regression and Regularization

3.1 Linear Regression

A linear model predicts by simply calculating a weighted sum of the input variables, adding a constant term to it, so the prediction of a linear regression model is represented with the following equation:

$$\hat{y} = \theta_0 + \theta_1 x_1 + \theta_2 x_2 + \dots + \theta_n x_n \quad (1)$$

This equation introduces notations that we will use throughout this article:

- \hat{y} is the predicted value,
- n is the number of variables,
- x_i is the value of the i^{me} variable
- θ_j is the j th parameter of the model (constant term θ_0 and coefficients of weighting of the variables $\theta_1, \theta_2, \dots, \theta_n$)

This can be written much more concisely in vector form:

$$\hat{y} = h_{\theta}(\mathbf{x}) = \boldsymbol{\theta}^T \cdot \mathbf{x} \quad (2)$$

3.2 Ridge Regression

Ridge regression (also called peak regression or Tikhonov regularization) is a regularized version of linear regression: a regularization term equal to $\alpha \sum_{i=1}^n \theta_i^2$ is added to the cost function. This forces the learning algorithm not only to adjust the data, but also to keep the model weighting coefficients as small as possible. Note that the accrual term should only be added to the cost function during training. Once the model has been trained, the performance of the model can be assessed using an unregulated performance measure.

The following equation presents the cost function of a ridge regression:

$$J(\theta) = \text{MSE}(\theta) + \alpha \frac{1}{2} \sum_{i=1}^n \theta_i \tag{3}$$

However the analytical solution of a ridge regression is given by:

$$\hat{\theta} = (X^T \cdot X + \alpha A)^{-1} \cdot X^T \cdot y \tag{4}$$

3.3 Lasso Regression

Another regularized version of linear regression is Least Absolute Shrinkage and Selection Operator (more simply lasso regression). Like ridge regression, it adds a regularization term to the cost function, but it uses the standard ℓ_1 of the weighting vector instead of half the square of the norm ℓ_2

Thus, the cost function of the lasso regression is as follows:

$$J(\theta) = \text{MSE}(\theta) + \alpha \sum_{i=1}^n |\theta_i| \tag{5}$$

The sub-gradient vector for a lasso regression is given by:

$$g(\theta, J) = \nabla_{\theta} \text{MSE}(\theta) + \alpha \begin{pmatrix} \text{signe}(\theta_1) \\ \text{signe}(\theta_2) \\ \vdots \\ \text{signe}(\theta_n) \end{pmatrix} \quad \text{where } \text{sign}(\theta_i) = \begin{cases} -1 & \text{si } \theta_i < 0 \\ 0 & \text{si } \theta_i = 0 \\ +1 & \text{si } \theta_i > 0 \end{cases} \tag{6}$$

3.4 ElasticNet Regression

The net elastic regularization (which can be translated as \propto elastic net x) is a compromise between ridge and lasso: the regularization term is a simple mixture of the regularization terms of these two regressions, this mixture is controlled by the mix ratio r : when $r = 0$, elastic net is equivalent to the ridge regression, and when $r = 1$, it is the equivalent of a lasso regression.

The net elastic cost function is as follows:

$$J(\theta) = \text{MSE}(\theta) + r\alpha \sum_{i=1}^n |\theta_i| + \frac{1-r}{2} \alpha \sum_{i=1}^n \theta_i^2 \tag{7}$$

4 Case Study

In recent years, machine learning algorithms have been widely used for weather prediction because they perform better. This helped farmers to increase their productivity and to optimize the use of water resources for irrigation. In this case study, we used the data reported by the weather station: 601550 (GMMC), which refers to climate data on casablanca between 1957 and 2020. The complete information of the annual average values including the ephemeris of the maximum and minimum values recorded.

To solve this equation, we consider Y as a value representing the species:

$$Y = \theta_0 + \theta_1 * T + \theta_2 * TM + \theta_3 * Tm + \theta_4 * PP + \theta_5 * V \tag{8}$$

- T Average annual temperature,
- TM Annual average maximum temperature,
- Tm Average annual minimum temperature,
- PP Rain or snow precipitation total annual,
- V Annual average wind speed.

All the characteristics mentioned above, were used to predict the average temperature, the required calculations and graphical displays are performed for statistical computing using Python libraries (Below the compilation results of the regression algorithms).

Table 1 gives the results for the calculation of the mean square error and the coefficient of determination RSquared for the various regression algorithms namely linear, ridge, lasso and Elasticnet, applied to data sets of training and validation.

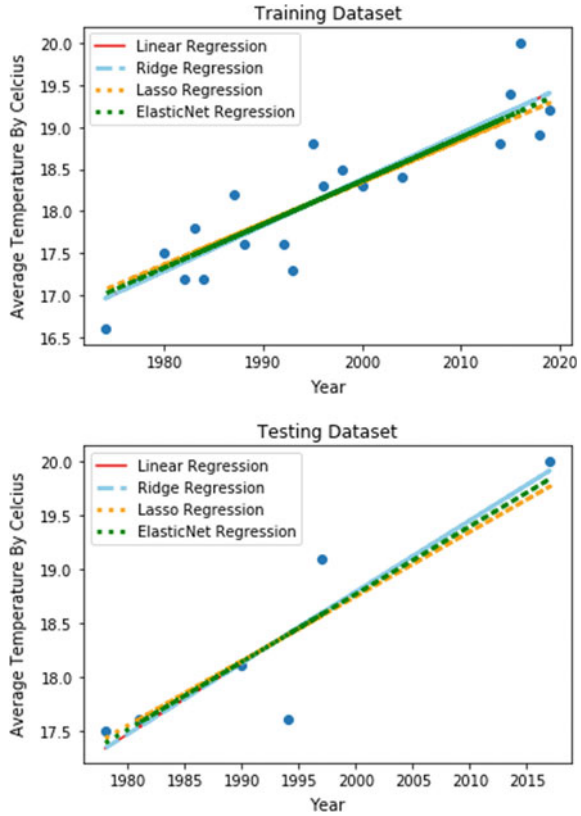
Figure 1 illustrates the graphical presentation of the average temperature predictions, based on a learning model applied to the studied regression algorithms cited previously.

The straight curve of the ridge algorithm shows a slight improvement in performance, in both training and validation case, more details will be brought on the following section.

Table 1 Comparative table of application results of MSE versus R2 regression algorithms

Algorithm	Mean square error (MSE)		Coefficient of determination (R ²)	
	Training dataset	Test dataset	Training dataset	Test dataset
Linear regression	0.372	0.810	0.393	0.821
Ridge regression	0.372	0.810	0.393	0.821
Lasso regression	0.379	0.803	0.400	0.814
ElasticNet regression	0.374	0.808	0.395	0.819

Fig. 1 Regression analysis to predict the average temperature



5 Discussion of Simulation Results

Based on the previous case study, we can conclude that: Firstly, the result obtained on training dataset for ridge regression are slightly similar to linear regression and indicate an R-squared equal to 81.05% and a mean squared error equal to 0.37, this similarity can be explained by the following: the independent variables are not collinear and the variance of the parameter estimate is not huge. The R-squared obtained on Lasso are equal to 80.37% and a mean squared error equal to 0.37. The ridge performs better because there are many large parameters of about the same value and the most predictors mentioned above i.e. precipitation and wind speed impacts the response average temperature. Elastic net is a hybrid of ridge regression and lasso regularization, fixing λ ratio called ElasticNet mixing parameter to 0.7, the penalty would be the combination of L1 and L2. we can say, lasso regression (L1) does both variable selection and parameter shrinkage, whereas ridge regression only does parameter shrinkage and end up including all the coefficients in the model. In presence of correlated variables, ridge regression might be the preferred choice. Also, ridge regression works best in our case where the least square estimates have

higher variance 0.31. Secondly, the validating scores are better than training. This means that the model has generalized fine. Otherwise it is explained by the following: training data had several arduous cases to learn or validation data containing easier cases to predict. Finally, It should be noted that our data set is limited in terms of characteristics, as well as granularity of information which prevents further development of work in the application of an intelligent irrigation system based on meteorological data, to study the correlation between weather and agricultural data.

6 Conclusion

The regression and regularization analysis shows that ridge algorithm make a compromise between the simplicity of the model (coefficients close to zero) and the non-collinearity of the independent variables like precipitation and wind speed. Instead of ridge. The main problem with lasso regression is when we have correlated variables, it retains only one variable and sets other correlated variables to zero. That lead to some loss of information resulting in lower accuracy in our model.

The perspective of this work focus on dataset, in order to enrich it with agricultural data and to compare the weather variables with others in the field of agriculture i.e. soil parameters, to help the farmer to increase their productivity and to optimize the use of water resources for irrigation.

References

1. Aurélien G (2017) Hands-on machine learning with Scikit-Learn. O'Reilly, pp 105–139
2. Balducci F, Impedovo D, Informatica D, Moro A (2018) Machine learning applications on agricultural datasets for smart farm enhancement. *Machines*:6–38
3. Chang Y, Huang T, Huang N (2019) A machine learning based smart irrigation system with LoRa P2P networks. In: Asia-Pacific network operations and management symposium (APNOMS), pp 1–4
4. Efron B, Hastie T, Johnstone I, Tibshirani (2004) Least angle regression. *Ann Stat* 32:407–499
5. Kaplan A, Haenlein M (2018) The interpretations, illustrations, and implications of artificial intelligence. *BUSHOR- 1521*:11
6. Khairnar PP, Gaikwad DV, Kale SR, Monika T (2016) Wireless sensor network application in agriculture for monitoring agriculture production process 5(5):1302–1305
7. Liakos KG, Busato P, Moshou D, Pearson S (2018) Machine learning in agriculture: a review. *Sensors* 18(2674):1–29
8. Loubna H, Bouchaib N (2018) Integration of irrigation system with wireless sensor networks: prototype and conception of intelligent irrigation system. In: World congress on engineering and computer science, vol I
9. Majumdar J, Naraseeyappa S, Ankalaki S (2017) Analysis of agriculture data using data mining techniques: application of big data. *J Big Data*
10. Musa AB (2013) Comparative study on classification performance between support vector machine and logistic regression. *Mach Learn Cyber* 13–24

11. Ogutu JO, Schulz-streeck T, Piepho H (2012) Genomic selection using regularized linear regression models: ridge regression, lasso, elastic net and their extensions. *BMC Proc* 6(Suppl 2):S10
12. Oufdou H, Bellanger L, Bergam A, El Ghaziri A, Khomsi K, Qannari EM (2018) Comparison of different regularized and shrinkage regression methods to predict daily tropospheric ozone concentration in the grand Casablanca area. *Adv Pure Math* 793–812
13. Rawal S (2019) IOT based smart irrigation system IOT based smart irrigation system. *Int J Comput Appl* 159(8):0975–8887
14. Sellam V, Poovammal E (2016) Prediction of crop yield using regression analysis. *Indian J Sci Technol* 9(38)
15. Shekhar Y, Dagur E, Mishra S, Tom RJ, Veeramanikandan M (2017) Intelligent IoT based automated irrigation system. *Int J Appl Eng Res* 12(18):7306–7320. ISSN 0973-4562
16. Thevaraja M, Nagar A, Lanka S, Gabirial M (2008) Recent developments in data science: comparing linear. Ridge and Lasso regressions techniques using wine data. *DISP '19*. United Kingdom, no. April, Oxford

Big Data Architecture for Moroccan Water Stakeholders: Proposal and Perception



Aniss Moumen, Badraddine Aghoutane, Younes Lakhri, and Ali Essahlaoui

Abstract The water data are produced from synchronous and/or asynchronous observations of water bodies. The aim of these observations is to support water resource management. The water entities and concepts give meaning to all collected data. These entities are heterogeneous, with a wealth of attributes and very varied functions. In this paper we will present the steps followed for the characterization of the entities for water resources in Morocco. From trip works, interviews with experts and observations with Moroccan stakeholders. Then in a second step, we will propose a vision on a big data architecture for water resources in Morocco, which can be used by the public administrations.

Keywords Big data architecture · Water data · Public administration

1 Introduction

The word “Big data” probably appeared from the 1990 [1, 2], used for the first time in 1989 by the American journalist and author of nonfiction books “Erik Larson”, to describe the problem he was dealing with receiving massive emails. So, “Big data” didn’t appear for the first time into computer science references, but it’s seems that was be used by the economist “Francis X. Diebold” from Pennsylvania University, on 2003 into his article titled “Big Data Dynamic Factor Models for Macroeconomic Measurement and Forecasting” [3]. Also, the big data as an idea was popularized by John Mashey [4] in a computer vision context with increasing of digital content produced by nowadays users.

A. Moumen (✉)

National School of Applied Sciences, Ibn Tofail University, Kenitra, Morocco
e-mail: amoumen@gmail.com

B. Aghoutane · A. Essahlaoui

Faculty of Sciences, Moulay Ismail University, Meknes, Morocco

Y. Lakhri

National School of Applied Sciences, Sidi Mohamed Ben Abdellah University, Fez, Morocco

We can conclude that “Big data” as a concept was introduced by non-informatics, and used to describe the massive production of unstructured data which probably contain an important economic value for the organizations. In addition, Big data environment was born because of the limitation of the classical environments which didn’t could to capture, process, analysis and storage huge data in an acceptable time. Therefore, “Big data” establish a new paradigm to deal with massive data, and redefine the IT architecture, which will upset the IT usage of the organizations.

According to Doug Laney [5], Big data can be described by the following characteristics: Volume: The quantity of generated and stored data. Variety: The type and nature of the data. Velocity: The speed at which the data is generated and processed. Veracity: refers to the data quality and the data value. Value: The utility that can be extracted from the data. Variability: It refers to data whose value or other characteristics are shifting in relation to the context in which they are being generated. Other important characteristics of Big Data are: Exhaustive, Fine-grained and uniquely lexical, Relational, Extensional, Scalability. Big data architecture [6] refers to the logical and physical structure that dictates how high volumes of data are ingested, processed, stored, managed, and accessed. This architecture is built by through the layers: Big Data Sources Layer, Management & Storage Layer, Analysis Layer, Consumption Layer.

Meteorology was the first scientific discipline to use and produce big data [7], for example The NASA Center for Climate Simulation (NCCS), Debuting in spring 2010, stores 32 petabytes of climate observations and simulations on the Discover supercomputing cluster.

In Morocco, the Climate observation is conducted by several public actors as the Royal Center for Space Remote Sensing (CRTS) which is the official distributor of the satellite images [8]. Concerning water resources, the sector is characterized by an important number of actors, which can be classed into two categories: (1) Central actors: Ministerial departments (Water, Interior, Agriculture and Fisheries, Health, Economy, HCP). (2) Regional actors: as water basin agencies, water and electricity offices, regional agricultural development offices, associations of water users, Wilaya, Regions, Municipality.

The official framework for water resources management is defined by climate and water superior council, which adopt the law 10–95 in 1995 and 36–15 in 2015, also the national strategy of water in 2001 and 2009 [9, 10]. Moroccan water stakeholders produce and use a huge dataset and a set of decision-support systems. Also, the measurement of water resources and climatic parameters require significant storage, processing and analysis resources, hence the importance of big data architectures.

2 Big Data Architectures for Water Resources

According to a systematic literature review [9–12, Zhao et al. [13], propose and implement a big data analytics architectures for Water Resources Sustainability Evaluation in the city of Zhoushan, this architecture is built with four layers: Hardware layer,

Communication layer, Middleware layer, Application layer. Yinghui Zhao architecture take into consideration multiple formats of sources: IoT, Internet, database and files. Mo et al. [14], propose an architecture based on IoT for Water Resources Monitoring and Management, the authors built this architecture around tree layers: Equipment perception layer, Information transmission layer and Data application layer. For this proposal, the authors take into consideration IoT only as an input, because the use case is to monitor and manage water resources. Ridouane Chalh et al. [15], propose a big data architecture for water resources management, it's seems that the authors have made an implementation of the support-decision module for Moroccan water resources. This architecture is built with a set of layers and components: Decision Support Tools, Knowledge-Based System, Geographic Information System (GIS), Big Data Analysis System, Simulation Models, Computation and Processing, Communication System and Search Engine Users Interfaces. the input preconized by the authors is uniquely the GIS data. Also Aghoutane et al. [16], proposed an approach to use Big Data analytics and IoT by the water stakeholders in Morocco, the architecture proposed by the authors is based on Big data layers without a specific use case.

3 Big Data Architecture for Moroccan Water Stakeholders

To propose a big data architecture for Moroccan water stakeholders, we are inspired from state of arts presented in previous section.

Our architecture is structured into 5 layers: Data Source Layer, Data Storage Layer, Data Acquisition Layer and Data Processing Layer, and finally a presentation layer for different use cases, figure summarizes the different components (Fig. 1).

4 Materials and Methods

The approach to design a Big-data architecture for water stakeholders start by an area observation to appreciate both the real objects and its components: rivers, wells, stations, dams, etc. In addition, we analyze the opinions of decision-makers, reports and measurement sheets. To observe the water entities and theirs attributes, our study area is the "Guir-Ziz-Rheris" in the South-East of Morocco. Also, in the Water Basin Agency we have conduct our observations mission to collect secondary data (Table 1).

To analyze all water management concepts and characteristics, we conducted in-depth and group interviews with stakeholders: ABH, ORMVA, ONEE, ANDZOA etc.

To complete this analysis, we made observations of different objects and their characteristics: Measuring station, Dam, drilling point, wells, water courts and springs.

In a second step, we conducted in-depth interviews (an average of 30 to 60 min), to collect the opinions on big data [17, 18].

5 Results

The content analysis of reports and measurement sheets, accompanied by in-depth interviews, allowed us to draw up a list of data on water resources that are mostly taken into consideration by decision-makers. We have noticed the diversity of both entities and attributes.

The interviews allowed us to identify the word cloud, which shows an important occurrence of the words: Data, NTIC, Citizens, Time, Services. We can conclude to a first motivation on the use of ICT by the public administration is: to improve citizens services, in particular the responsiveness. Also, the content analysis of stakeholders opinions about the perceptions and constraints, can be summarized us below:

- (1) The notion of big data is quite clear for our interviewees.
- (2) The use of big data may not used soon, but rather in the near future.
- (3) The motivation for use of Big data is to improving the users services.
- (4) There is a distinction between users: internal collaborators, external partners and citizens.
- (5) The constraints for the use of big data are: legislative, organizational, technical and human.
- (6) Data confidentiality and security are important requirements for the use of big data
- (7) Staff training actions should focus on: Training courses to raise users awareness (decision-makers and employees). Technical training for monitoring and maintenance of hardware and software platforms. Technical training for analysis.

6 Conclusion

In this works, we have focused on approach to propose a big data architecture for water resources in Morocco, from trip works, interviews with experts and observations with Moroccan stakeholders, to characterize water entities and to summarize all comments about the use of big data technologies.

Fig. 1 Proposed Big data architecture for Moroccan water stakeholders

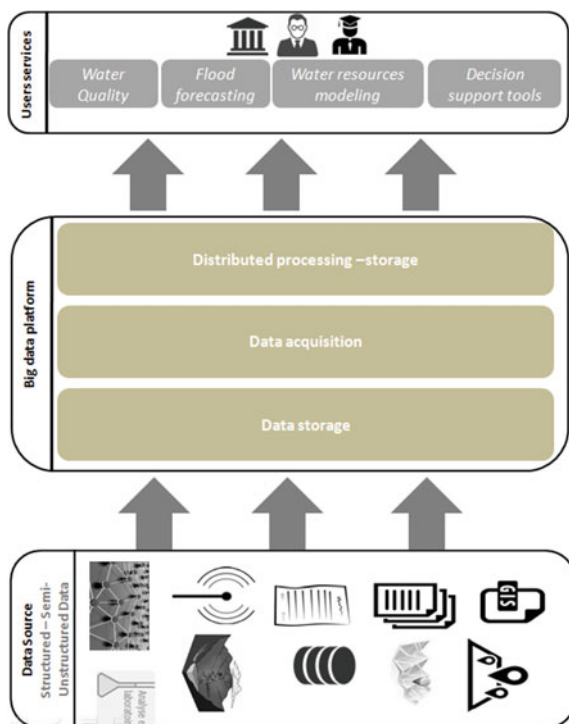


Table 1 Data collection procedure “Collection of reports and sheets” [9]

Document	Category	Format
Drill Point Sheet (Pink Sheet)	Sheet	Structured
Sheet of hydraulic stations		
Dam sheet, Measurement campaigns, Study Report and CSP	Report	Unstructured

References

1. Diebold FX (2020) On the origin(s) of the term “Big Data”. [arXiv:2008.05835\[cs, econ\]](https://arxiv.org/abs/2008.05835), août 2020, Consulté le: août 31
2. Lohr S (2013) The origins of “Big Data”: an etymological detective story. Bits Blog, févr. 01
3. Diebold F (2003) Big Data dynamic factor models for macroeconomic measurement and forecasting
4. Mashey J (1998) Big Data and the Next Wave of InfraStress, présenté à Computer Systems Laboratory Colloquium, NEC Auditorium, Gates Computer Science Building B03
5. Laney D (2001) 3D data management: controlling data volume, velocity, and variety
6. Cravero A, Saldaña O, Espinosa R, Antileo C (2018) Big Data architecture for water resources management: A systematic mapping study. In: IEEE Latin America Transactions, vol 16, no 3, pp 902–908. Mar 2018. <https://doi.org/10.1109/TLA.2018.8358672>
7. OECD Observer (2016) Big data, satellites and climate change
8. CRTS Distribution de données satellitaires | Centre Royal de Télédétection Spatiale

9. CES (2020) La gouvernance par la gestion intégrée des ressources en eau au Maroc : Levier fondamental de développement durable », Conseil Economique, Social et Environnemental, 2014. Consulté le: août 31
10. Moumen U (2016) Contribution d'une approche participative et des infrastructures de données spatiales pour la conception d'un système régional d'information sur l'eau, étude de cas au bassin Guir-Ziz-Rheris et Maider », Université Ibn Tofail
11. Hicham J, Aniss M, Bouabid M (2020) Moroccan water information system: exploratory study system literature review. In: Proceedings of the 4th edition of international conference on Geo-IT and water resources 2020, New York, NY, USA, mars 2020, doi: <https://doi.org/10.1145/3399205.3399226>
12. Elhassan J, Aniss M, Jamal C (2020) Big Data analytic architecture for water resources management: a systematic review. In: Proceedings of the 4th edition of international conference on Geo-IT and Water Resources 2020, New York, NY, USA, Mar 2020. <https://doi.org/10.1145/3399205.3399225>
13. Zhao Y, An R (2019) Big Data analytics for water resources sustainability evaluation. In: High-performance computing applications in numerical simulation and edge computing, Singapore, pp 29–38. https://doi.org/10.1007/978-981-32-9987-0_3
14. Mo X, Qiu XJ, Shen S (2015) An IoT-based system for water resources monitoring and management. In: 2015 7th International Conference on Intelligent Human-Machine Systems and Cybernetics, août 2015, vol 2, pp 365–368. <https://doi.org/10.1109/IHMISC.2015.150>
15. Chalh R, Bakkoury Z, Ouazar D, Hasnaoui MD (2015) Big data open platform for water resources management. In: 2015 international conference on cloud Ttechnologies and applications (CloudTech), Jun 2015, pp 1–8. <https://doi.org/10.1109/CloudTech.2015.7336964>.
16. Aghoutane B, Moumen B, Essahlaoui A (2020) The use of advanced technologies Big data, IoT and Cloud computing in the Water Sector. KU Leuven
17. Hafed K, Moumen A, Fakhry Y, Sellamy K (2020) Usage of Cloud Computing for natural resource management: Perception of Moroccan public administration in oasis areas. In: Proceedings of the 4th Edition of International Conference on Geo-IT and Water Resources 2020, Geo-IT and Water Resources 2020, New York, NY, USA, mars 2020, pp 1–5. <https://doi.org/10.1145/3399205.3399218>.
18. Moumen A (2020) Adoption of Big Data, Cloud Computing & IoT in Morocco perception of public administrations collaborators. In: Proceedings of the 4th Edition of international conference on Geo-IT and water resources 2020, Geo-IT and Water Resources 2020, New York, NY, USA, mars 2020, pp 1–4. <https://doi.org/10.1145/3399205.3399228>

Towards an Integrated Platform for the Presentation and Preservation of the Scientific Heritage of Drâa-Tafilalet



Fouad Nafis, Badraddine Aghoutane, and Ali Yahyaouy

Abstract The region of Drâa-Tafilalet in the south-east of Morocco is known for its unique and varied tourist qualifications, combining the greenery of the oasis with the quietness of the desert and its deep-rooted heritage, which has made it one of the best known tourist poles at the national and international levels. The region has benefited from national programs aimed at promoting the tourism sector and restoring the rich and unique local heritage. This region has benefited from national programs aimed at promoting the tourism sector and restoring the rich and unique local heritage. The main objective of this article is to present the heritage of the Drâa Tafilalet region with emphasis on the diverse and rich scientific heritage in the region. This paper presents the latest results obtained in this field, based on applications, technologies, etc., aimed at preserving this heritage from extinction and presenting it to future generations.

Keywords Cultural heritage · Ontologies · Semantic web · Preservation · RDF

1 Introduction

The region of Tafilalet (Fig. 1), in the south-east of Morocco, is rich in a cultural and human heritage that is rare in terms of diversity, richness and antiquity, showing the magnificence, culture, consciousness and creativity of the older generations that lived in the region. This heritage, whether tangible (libraries, Ksours, Kasbahs, manuscripts, books ...) or intangible (customs, traditions, folklore, gastronomy, art objects, engineering models ...) has fallen into oblivion in recent decades. This is despite few individual efforts to make it known and preserve it for future generations and despite the great role that can play if used optimally to turn the economic cycle

F. Nafis (✉) · A. Yahyaouy
LISAC Laboratory, Computer Science Department, FSDM, Sidi Mohamed Ben Abdellah University, Fez, Morocco
e-mail: fouad.nafis@usmba.ac.ma

B. Aghoutane
Department of Computer Science, Informatics and Applications Laboratory, Science Faculty of Meknes, Moulay Ismail University, 50070 Meknes, Morocco

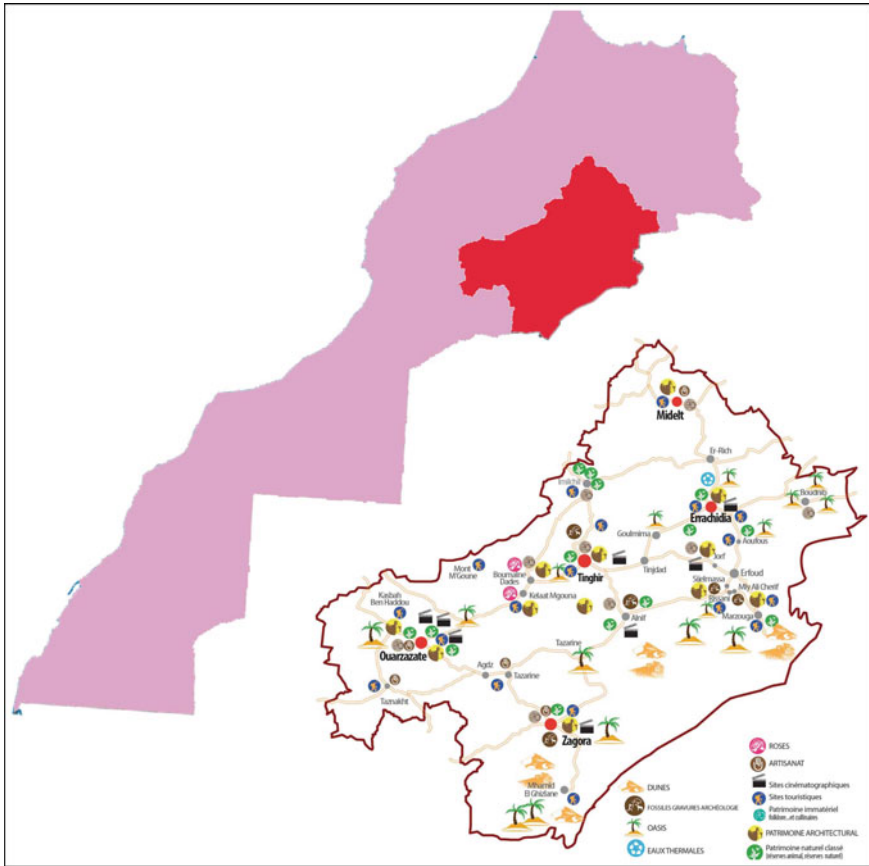


Fig. 1 The study zone: Drâa-Tafilalet

by encouraging national and foreign tourism in a region where tourism is the first and almost the only source of foreign currency.

Due to its strategic geographical location, the region is rich in a unique scientific heritage consisting of several libraries full of manuscripts, documents and books. These libraries, although most of them have been exposed to looting and extinction, the rest of them have preserved treasures in various sciences of the Qur'an and interpretation, jurisprudence and the origins of religion, Arabic language and its literature, asceticism and mysticism, biography, history, and others.

This paper is organized as follows: Section 2 presents the objects of the scientific CH of the study region on which the work has focused. Section 3 deals in detail with the basic components of the integrated system for the publication and identification of CH data of the region. Section 4 provides an overview of the results obtained and a discussion of the objectives outlined at the beginning. Section 5 gives a conclusion and a brief idea of the future work that is being developed.

2 The Scientific Cultural Heritage (CH) of Drâa-Tafilet

No one disagrees with the need to preserve the CH of the Draa-Tafilet region with all its manifestations and components. This rich and diverse heritage constitutes a collective memory, since Tafilet is a semi-desert oasis region characterized by a rich and varied cultural diversity and is characterized by a set of features that make it unique in terms of the production of its cultural systems and the values that these models hold. The Tafilet region has always been a place of collective life, tolerance, ethnic and linguistic pluralism, and perhaps its past is a symbolic capital that should be proud, preserved from extinction thanks to the documentation and motivation of researchers to work there scientifically and academically.

The CH of the region goes beyond the human and also includes the natural, as is the case with the oases which form an integral part of the identity of the Tafilet region and constitute a special environmental system that plays an important role because of its link with water and people and its proximity to the Ksours and Kasbahs, be they beach oases, desert oases or mountain oases or even hill oases.

On the other hand, and because culture plays an important role in the production of thought and the expression of the ways of life of human groups, and the highlighting of a set of values, knowledge, beliefs, languages, arts and traditions, the region is characterized by a great cultural diversity and a diversity that all actors and stakeholders must preserve, enhance and further develop in order to contribute to the promotion of the values of tolerance and coexistence. In this study, we have chosen to focus on a particular form of cultural heritage that is highly visible to visitors to the region since it is an integral part of the personality and habits of the region's population: the scientific cultural heritage (Fig. 2).

This scientific heritage consists mainly of the following three elements:

2.1 *The Zawyas*

The Zawaya are religious, scientific and social institutions whose activities and functions have crystallized and found themselves within the Islamic nation in general, and within Moroccan society in particular, which has made them contribute to various material and moral concerns, and even express them honestly and objectively, through the consolidation of the true and authentic Islamic culture and its dissemination, whether it be attached to the question of beliefs or jurisprudence and its principles or to Sufi education [1]. As an example, the region of Drâa-Tafilet abounds with a significant number of zawyas who have served and continue to serve the population of the region by fulfilling several roles such as: the famous zawya naciria of the city of Tamgroute or the zawya hamzawya. In general, the role of each zawya was not only to train the people of the region in different disciplines, but also to preserve the memory, customs and traditions of the population to pass them on to future generations. This has taken the form of one or more libraries that preserve thousands of

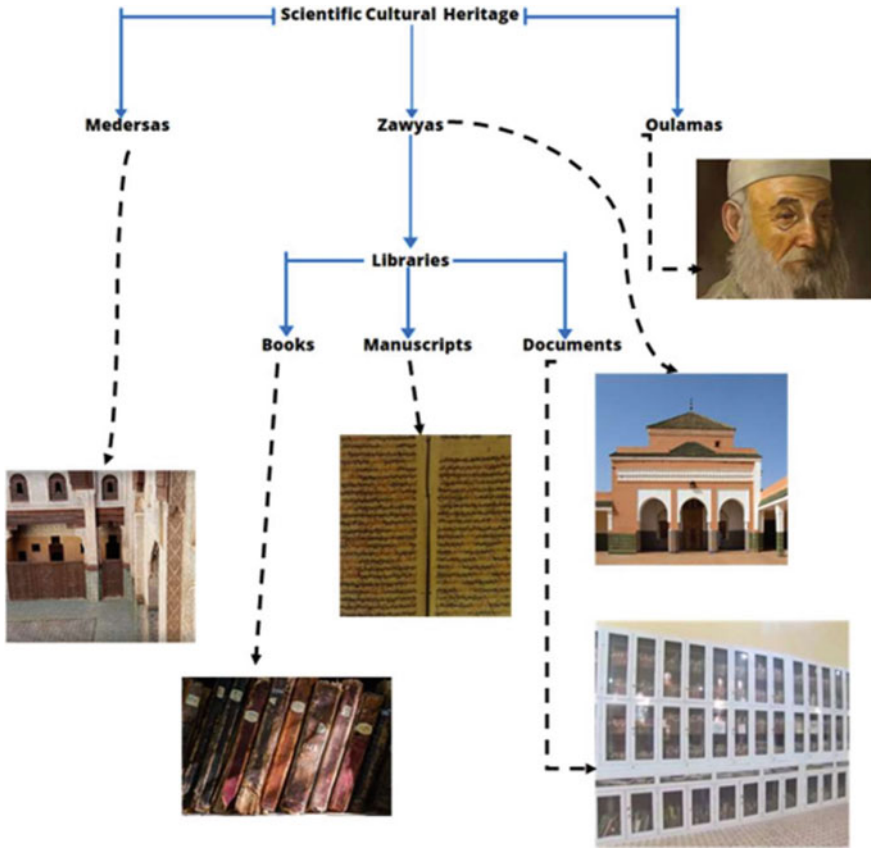


Fig. 2 Simplified structure of the data processed by the study

very old documents, such as the library of the zawya naciria, which alone holds more than 4,770 documents and manuscripts, the oldest of which dates back more than 800 years.

2.2 The Medersas

A medersa, or madrasa, is a Koranic school or a Muslim theological institution. Medersa are always administered by a pious foundation called: waqf. The name Medersa is to be related to the Hebrew Midrash, whose root means to examine, to question in depth. The main role of a Medersa was to provide higher religious education and to disseminate Sunni doctrines. The main characteristics of these places were, on the one hand, that the students were housed in the establishment,

and the services of the waqf took care of them so that they could devote themselves to their studies, and on the other hand, the teachers were appointed by the State.

2.3 The Oulamas

Between the seventh century and the end of the sixteenth century, many Islamic countries, including Morocco, were the scientific center of the world, and their universities were flourishing, their industries were elaborate and advanced, and science was in continuous development, and urbanization was increasing, so that the Arab countries were a pilgrimage for knowledge seekers and an unprecedented cultural wonder. Scientists had a great value that was respected by the public and appreciated by the leaders, and this was the period when science was established in the world.

Before that, knowledge did not reach the level of science, and there is no place in science for what we know today, other than that the Arabs established it.

3 Methodology

The work carried out in this study is part of a project aimed at the publication and semantic integration of the region’s heritage data. In [2] a study was conducted to compare the ontologies of heritage data classification and in [3] a system was proposed for the semantic integration of the data of the study region. Figure 3 provides

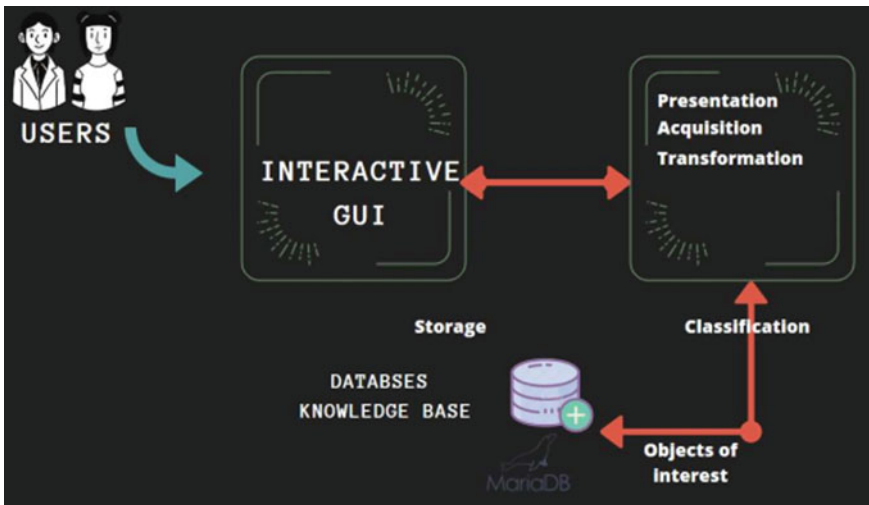


Fig. 3 Simplified structure of the data processed by the study

an overview of the various components of the proposed system.

The system offered is available in the form of a web application and another mobile application, offering the user the possibility of interacting with the data collected on the region’s heritage by exploring the different categories and benefiting from the richness they offer. The mobile application has the advantage of being available everywhere, even in the places where this heritage exists, giving visitors to the region the opportunity to get an idea of what they have come to discover. As for the web application, it offers the advantage of having a better view of the content by comparing it to the smaller screen of mobile devices and having access to a more diversified content (Fig. 4).

The preparation and submission of data is the most important step in the system and has gone through the following elements:

- Collection of raw data from the region, in relation to the study data (Fig. 5)
- Classification of the data to organize them in the different categories taken into account.

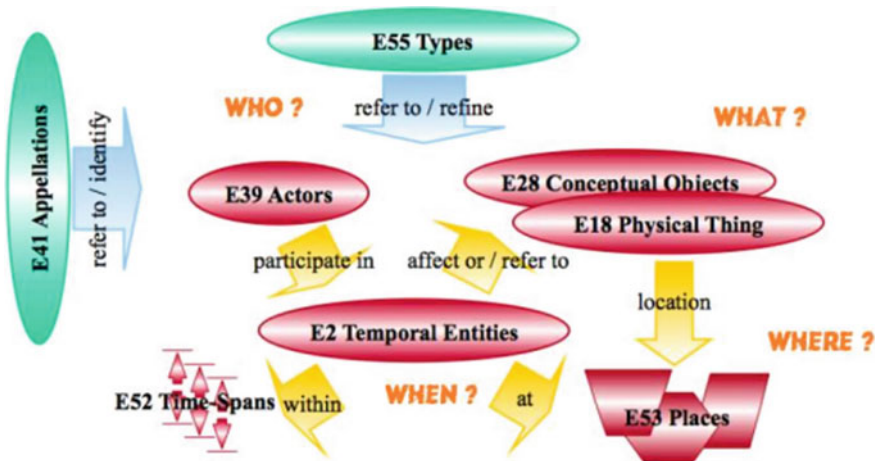


Fig. 4 CIDOC CRM top-level entities used in the study

#	الاسم	الوصف	تعديل	حذف
1	حديقة دار الكتب الناصرية بدمشق	حديقة دار الكتب الناصرية بدمشق تحتوي على كبر من الكتب		
2	حديقة الزاوية الحضرية العياشية	حديقة الزاوية الحضرية العياشية بدمشق		
3	حديقة جمعية سيدى الغازي	حديقة الزاوية العياشية هي حديقة حائطية كانت تضم العديد		
4	الحديقة الخاصة بدير الله بدير ابيحان	الصورة لمعدل قصر ابيحان		
5	الحديقة الهولندية بدمشق	تنسب الحديقة الهولندية الواقعة بمنطقة السفاليت بدمشق		
7	مكتبة التراث العربي	مكتبة ابراهيم محمد بن أحمد باعقل الخازن		
8	حديقة سيدى الهاشمي القاضي القصري	حديقة سيدى الهاشمي القاضي القصري بدمشق		
9	حديقة مولاي الشريف القاضي القصري	بقي قصر موصو بدمشق قصر أحموس التاريخي على بعد كيلومتر		

Fig. 5 Example of data collected on the libraries of the ‘zawyas’ in the study zone

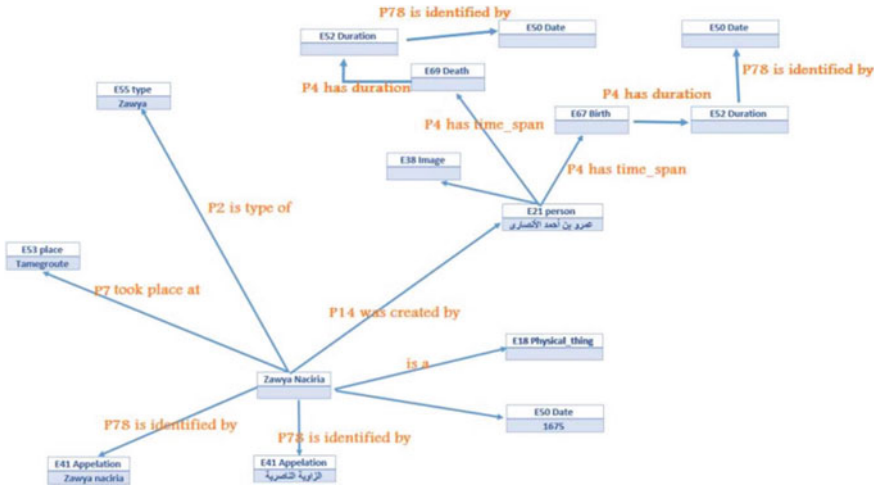


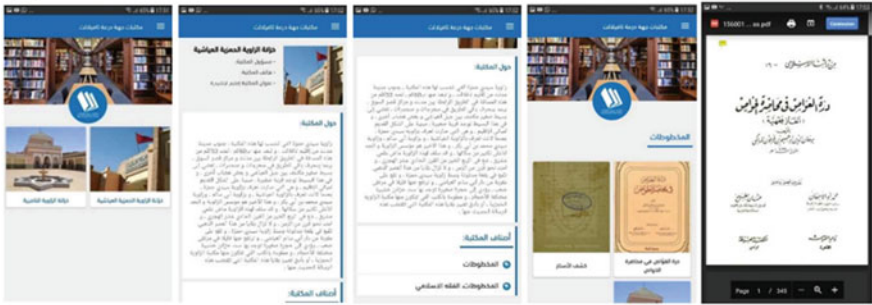
Fig. 6 Part of the model built using the CIDOC CRM ontology

- Extraction of relevant concepts
- Integration of these concepts and the relationships that link them and the properties they have using the CIDOC CRM (Fig. 6) reference.
- Publication of the ontology produced after its population with the different individuals of the different classes considered (Fig. 6).

4 Results and Discussion

Most of the work in the literature deals with the CH aspect of a specific region using the CIDOC CRM [8] ontology and other metadata models, without taking into account the scientific cultural heritage aspect or at best, pass quickly over this part [4-7]. The motivation for using a reference such as CIDOC CRM [9, 10] has been demonstrated in the literature through several case studies that have given encouraging results and this is what justifies its adoption in the case of our study. Most of the functionalities of the proposed system have been implemented and are in the testing phase for final validation but the results are already there (Fig. 7a, b).

(a)



(b)

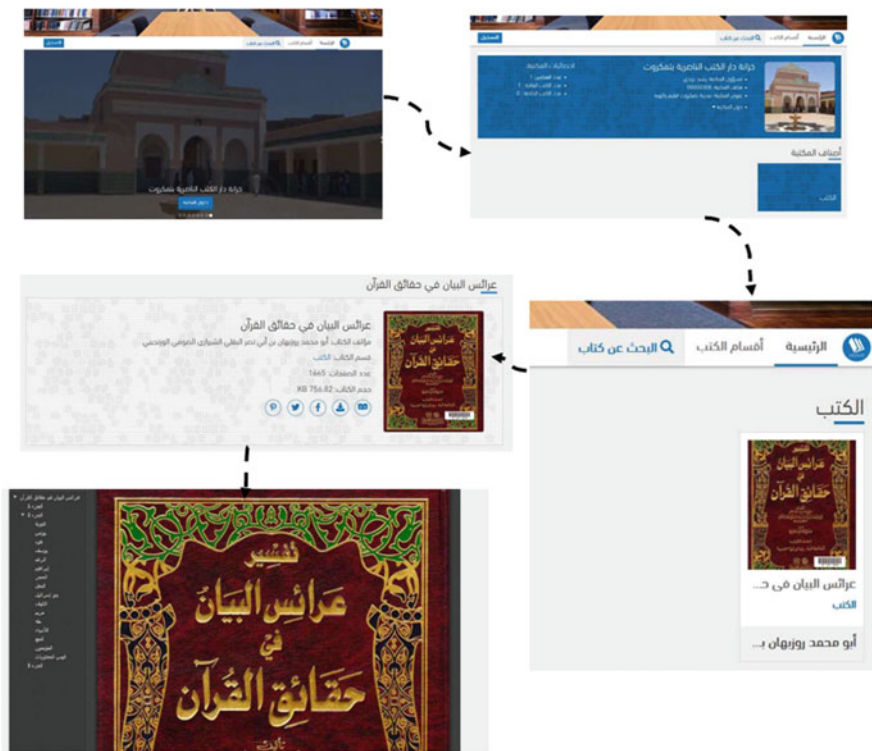


Fig. 7 a Overview of the mobile application on libraries in the study region. b Overview of the web application on libraries in the study region

5 Conclusion and Future Works

The work carried out under the project for the identification and preservation of the scientific cultural heritage of the Drâa-Tafilalet zone is motivating despite the obstacles encountered, which date back several decades and are summed up in the

difficulty of access to information, particularly that held by private actors. A first validation process has already been carried out locally but the final validation will be in the real feedback that will be collected by the users of the technologies developed and the fact of seeing the content of the web portal and the mobile application enriched with data in addition to those collected manually and which are not negligible. Some components of the system need to be improved and the final ontological model needs to be published and tested to cover all concepts and especially all properties of the entities and their relationships. This is the main task to be finished soon with the objective of having a fully operational and exploitable system.

References

1. Bouyahya D (2016) Religious tourism and sufism in Morocco. *Europ J Multidiscip Stud* 2(1): 40, août. <https://doi.org/10.26417/ejms.v2i1.p40-50>
2. Nafis F, Yahyaouy A, Aghoutane B (2019) Ontologies for the classification of cultural heritage data. p 1–7. <https://doi.org/10.1109/WITS.2019.8723850>
3. Nafis F, Aghoutane B, Yahyaouy A (2021) Semantic integration of Moroccan cultural heritage using CIDOC CRM: case of Drâa-Tafilalet zone, *IJCC ICBDSE' 19* (in press)
4. Cherny E, Haase P, Mouromtsev D, Andreev A, Pavlov D (2015) Application of CIDOC-CRM for the russian heritage cloud platform. In: Morzy T, Valduriez P, Bellatreche L (ed) *New trends in databases and information systems*, vol 539, Cham: Springer International Publishing, pp 448–457
5. Arizpe L (2015) The genealogy of intangible cultural heritage. In: *Culture, diversity and heritage: major studies*, vol 12, pp 100–117, Springer International Publishing, Cham. Basic R (2019) 'Advances in technology and cultural heritage. *Athens J Hist March*, 5(2):135–156
6. Bruseker G, Carboni N, Guillem A (2017) Cultural heritage data management: the role of formal ontology and CIDOC CRM. In: Vincent ML, López-Menchero Bendicho VM, Ioannides M, Levy TE (eds) *Heritage and Archaeology in the Digital Age*, pp 93–131, Springer International Publishing, Cham
7. Carboni N, de Luca L (2016) Towards a conceptual foundation for documenting tangible and intangible elements of a cultural object. *Digital Applications in Archaeology and Cultural Heritage* 3(4):108–116
8. Doerr M, Ore CE, Stead S (2007) The CIDOC conceptual reference model—a new standard for knowledge sharing ER2007 Tutorial, p 6
9. Hennicke S (2013) Representation of Archival User Needs Using CIDOC CRM, p 13
10. Juergen E, Tabea L (2014) Classification and indexing of complex digital objects with CIDOC CRM, p 5, Germany

Keratoconus Classification Using Machine Learning



Aatila Mustapha , Lachgar Mohamed, and Kartit Ali

Abstract The diagnosis of several ophthalmic diseases such as age-related macular degeneration, glaucoma, diabetic retinopathy and keratoconus involves the analysis of the eye topographic maps. The dependence between ophthalmology and images processing represents a point of attraction for researchers to benefit of capacity and performance of deep learning tools in image processing. These tools allow a better differentiation between a sick eye and a normal one based on the analysis of the eye topographic maps and can change potentially the practices of ophthalmologists in diagnosis and treatment of similar diseases. Among the diseases already mentioned, keratoconus, this non-inflammatory disease characterized by a progressive thinning of the cornea is often accompanied by aspens of vision. The increasing number of people diagnosed with keratoconus has made this disease the subject of several research studies. This paper represents an overview of artificial intelligence application in keratoconus classification and a proposal system of keratoconus classification based on neural networks.

Keywords Artificial intelligence · Machine learning · Deep learning · Ophthalmology · Keratoconus

1 Introduction

In recent years, Artificial Intelligence (AI) has made a remarkable change in our society lifestyle by offering intelligent systems for recommendation, automatic car driving and detection of scenes or objects in videos or pictures and many other systems based on AI. In ophthalmology, a discipline which is generally based on the

A. Mustapha (✉) · L. Mohamed · K. Ali
LTI Laboratory, ENSA, Chouaib Doukkali University, El Jadida, Morocco
e-mail: mu.aatila@gmail.com

L. Mohamed
e-mail: lachgar.m@gmail.com

K. Ali
e-mail: alikartit@gmail.com

analysis of topographic images of the eye for the detection of certain diseases, Deep Learning (DL) tools can revolutionize this field by the capacity and performance of DL in the images classification [1]. AI, Machine Learning (ML) and DL tools can improve the diagnosis and treatment of many ophthalmic diseases while reducing the time and error rate, unlike classical methods based on the expertise and professional knowledge of ophthalmologists [2]. Several research works have produced intelligent systems able to detect and classify certain ophthalmic diseases such as age-related macular degeneration [3], glaucoma [4], diabetic retinopathy [5] and keratoconus [6]. These systems, taking advantage of the capabilities and performances of ML and DL tools in image processing [7], have demonstrated a good differentiation between the normal eye and the affected eye, particularly the keratoconus one [8]. Intelligent systems are based on different AI tools, this could cause a certain confusion between AI, ML and DL. AI was defined as a set of techniques that aim to produce a machine capable to imitate some human behaviors such as task planning and especially independent learning [1]. ML is a branch of AI which consists in integrating statistics with algorithms handling large structured datasets to make them more intelligent and capable to provide generalizations (i.e. learning) [9]. In ML, the data structuring must be carried out manually. DL-based systems are made up of a multilevel suite of neural networks that perform all tasks from extraction to classification [1, 10].

Considering the increasing number of patients with ophthalmic diseases worldwide, it is important to produce intelligent systems to assist ophthalmologists in the diagnosis and treatment of the various ophthalmic diseases, while reducing time and providing a better classification precision. This paper is organized as follows: Sect. 2 represents a state of the art of AI in keratoconus classification, Sect. 3 illustrates a proposal keratoconus classification system and finally Sect. 4 represents a conclusion of this work.

2 Artificial Intelligence in Keratoconus Classification

Keratoconus is characterized by a progressive thinning of the cornea; this disease is non-inflammatory but can cause vision problems in patients. Several research teams have focused on the production of intelligent systems for keratoconus diagnosis and classification. The authors of [11] proposed a CNN-based intelligent system for keratoconus detection trained on a data set of 3000 images. This system provided a classification with an accuracy of 99.33%. In [12], the authors developed a system using Feedforward Neural Network (FNN), to identify keratoconus, of which the accuracy was 96.56% on a dataset of 851 elements. The work [13] represented a system proposal for a keratoconus detection based on the RF, the obtained system provided a classification accuracy of 76% on a dataset of 500 images. In [14], the authors proposed a keratoconus classification system based on Unsupervised Machine Learning (UnML). The authors of [15] have developed a classification system for keratoconus based on BNN, of which the classification accuracy on a dataset of 60 elements was 100%. Using a dataset of 543 images, the system proposed

Table 1 Artificial Intelligence in keratoconus classification

Authors	Year	Method	Dataset	Inputs	Accuracy
Lavric et al. [11]	2019	CNN	3000	$180 \times 240 \times 3$ (image)	99.33%
Issarti et al. [12]	2019	FNN	851	141×141 (image)	96.56%
Salem et al. [13]	2019	RF	500	N. A	76%
Luna et al. [15]	2019	BNN	60	16 parameters	100%
Kamiya et al. [6]	2019	CNN	543	$6 \times 224 \times 224$ (image)	99.1%
Yousefi et al. [14]	2018	UnML	3156	420 parameters	N. A
Hidalgo et al. [16]	2017	SVM	131	25 parameters	92.6% to 98.0%
Ali et al. [17]	2017	SVM	40	12 parameters	90%

in [6] allowed the classification of keratoconus using CNN with an accuracy of 99.1%. Based on SVM, the system proposed in [16] allowed keratoconus detection and classification with an accuracy between 92.6 and 98.0% on a dataset of 131 images. The authors of [17] set up a classification system for keratoconus with an accuracy of 90% on a dataset of 40 elements. Table 1 summarizes the works already cited.

CNN-based systems have better precision, around 99%, compared to the other methods.

3 Preliminary Proposed Classification System

3.1 System Architecture

Figure 1 below represents the architecture of the proposed system.

Features extraction. Consists generally in identifying and extracting the features of the image to be classified. This treatment is based on two principles: the extraction of all pixels from the image and the identification of points of interest of the image.

Features preprocessing. Consists in eliminating outliers, those that are either unreal and out of range. Then, data are normalized to ensure that the learning algorithms manipulate correct data and a specific range to produce a good classification.

Features selection. In this step, redundant and irrelevant features are eliminated to reduce the data size for a simplification of the calculations and a better classification.

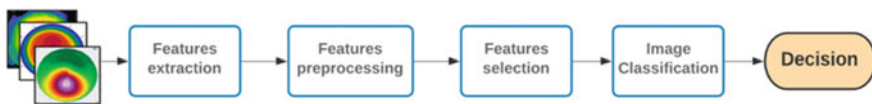


Fig. 1 Architecture of proposed classification system

Table 2 ANN details

Artificial neural networks	
Number of AN	100
Activation Function	Relu
Number of iterations	200
Optimizer	Adam

Image classification. Refers to application of classification methods on the selected features to classify the image. Given the power and good performance of systems based on CNN, this technique will be adopted for the future system.

For the following case study features are extracted and structured in a csv file.

3.2 Case Study and Simulation Results

The proposed case study is based on ANN using an extract of the keratoconus dataset of Harvard Dataverse. Using 30 parameters, the size of the used dataset is 249. The eyes in this dataset are classified in four classes: class 1 for normal eyes, class 2 for healthy eyes with form fruste keratoconus, class 3 for eyes with mild keratoconus and class 4 for eyes with advanced keratoconus stage. Table 2 bellow presents more details about the ANN implemented in the case study.

Figures 2 and 3 illustrate Receiver Operating Characteristic (ROC) curve of proposed classifier for different classes.

The obtained area under the ROC curve (AUC) is 0.85 for the average over classes. Proposed system can easily discriminate and classify the normal eye and

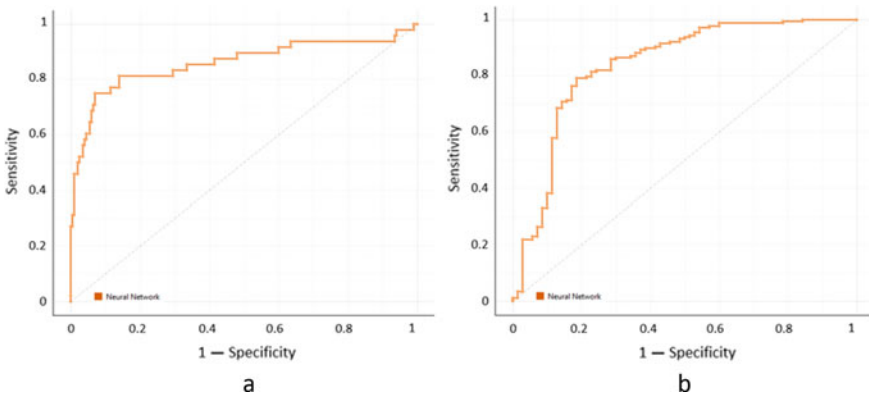


Fig. 2 ROC curve of proposed classifier for normal eyes **a** and healthy eyes with form fruste keratoconus **b**

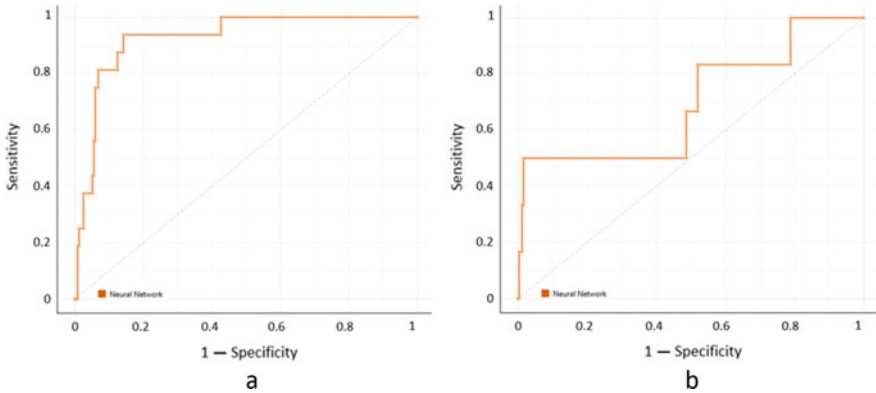


Fig. 3 ROC curve of proposed classifier for eyes with mild keratoconus **a** and eyes with advanced keratoconus stage **b**

Table 3 Performance of proposed classifiers for the average over classes

Classifier	Classification accuracy (%)	AUC (%)
ANN	80.3	85

the keratoconus one in different stages. Table 3 below presents the classifier performance.

The results reported in Table 3 are based on ten-fold cross validation test and the dataset is divided into 66% for training and 34% for testing. In the present study, proposed classification system provides an accuracy in order of 80.3%. Considering the AUC, the value provided is 85%, these results are obtained for the average over classes 1 to 4 of keratoconus stages. As a preliminary system, the obtained results could present a basis for the future keratoconus classification system.

4 Conclusion

This paper represented a study of the state of the art of AI applications in ophthalmology, particularly in the keratoconus detection and classification. The studied works allowed a classification with good precisions, in particular the systems based on CNN which produced a better classification precision, exceeding 99%. This classification method is promising, given the order of precision it offers. The obtained results of proposed classification system present good performance in terms of classification accuracy and AUC. This study was realized as part of a research project that aims to develop an intelligent system for detecting, classifying and predicting the evolution of keratoconus.

References

1. Rahimy E (2018) Deep learning applications in ophthalmology. *Curr Opin Ophthalmol* 29(3):254–260
2. Balyen L, Peto T (2019) Promising artificial intelligence–machine learning–deep learning algorithms in ophthalmology. *Asia-Pacific Journal of Ophthalmology* 8(3):264–272
3. Ting DSW, Pasquale LR et al (2019) Artificial intelligence and deep learning in ophthalmology. *Br J Ophthalmol* 103(2):167–175
4. Yousefi S et al (2018) Detection of longitudinal visual field progression in glaucoma using machine learning. *Am J Ophthalmol* 193:71–79
5. Gargeya R, Leng T (2017) Automated identification of diabetic retinopathy using deep learning. *Ophthalmology* 124(7):962–969
6. Kamiya K, Ayatsuka Y et al (2019) Keratoconus detection using deep learning of colour-coded maps with anterior segment optical coherence tomography: a diagnostic accuracy study. *BMJ Open* 9(9):1–7
7. Grewal PS, Oloumi F et al (2018) Deep learning in ophthalmology: a review. *Can J Ophthalmol* 53(4):309–313
8. Lin SR, Ladas JG et al (2019) A review of machine learning techniques for keratoconus detection and refractive surgery screening. *Seminars in Ophthalmology* 34(4):317–326
9. Deo RC (2015) Machine learning in medicine. *Circulation* 132(20):1920–1930
10. Sainath TN, Mohamed AR, et al (2013) Deep CNN for LVCSR. In: 2013 International conference on acoustics, speech and signal processing, pp 8614–8618. IEEE, Vancouver
11. Lavric A, Valentin P (2019) KeratoDetect: keratoconus detection algorithm using convolutional neural networks. *Computational Intelligence and Neuroscience* 2019:1–9
12. Issarti I, Consejo A et al (2019) Computer aided diagnosis for suspect keratoconus detection. *Comput Biol Med* 109(January):33–42
13. Salem BR, Solodovnikov VI (2019) Decision support system for an early-stage keratoconus diagnosis. *J Phys Conf Ser* 1419 (2019)
14. Yousefi E, Id HT et al (2018) Keratoconus severity identification using unsupervised machine learning. *PLoS ONE* 13(11):1–11
15. Castro-luna GM et al (2019) Contact lens and anterior eye robust keratoconus detection with bayesian network classifier for placido-based corneal indices. *Contact Lens and Anterior Eye*, Available online 20 Dec 2019
16. Hidalgo IR, Gatinel D et al (2017) Validation of an objective keratoconus detection system implemented in a Scheimpflug Tomographer and comparison with other methods. *Cornea* 36(6):689–695
17. Ali AH, Ghaeb NH, Musa ZM (2017) Support vector machine for keratoconus detection by using topographic maps with the help of image processing techniques. *IOSR-JPBS* 12(6):50–58

Electronics, Microelectronics, Embedded System and Control System

0.18 μm GaAs-pHEMT MMIC Frequency Doubler for Radar Area Scanning Application



H. El Ftouh, Moustapha El Bakkali, Naima Amar Touhami, and A. Zakriti

Abstract This paper proposes a GaAs-pHEMT MMIC frequency doubler for 60 GHz radar area scanning application using 0.18 μm GaAs technology. The aim of this study is to enter a frequency $f_0 = 30$ GHz and to recover at the output a frequency of $2 \cdot f_0$, i.e. 60 GHz. The proposed multiplier is designed and optimized thanks to OMMIC library. The latter gives to the proposed frequency doubler added values in term of circuit performances. Indeed, it has low power consumption $P_{dc} = 0.126$ mW, high spectral purity and small size; it occupies an area of $(1.35 \times 0.63\text{mm}^2)$ and achieves a conversion gain of -2.189 dB and an output power of 11.376 dBm. The results show a total efficiency of around 13.87%.

Keywords GaAs-pHEMT · Conversion gain · Frequency doubler · Multiplier

1 Introduction

Nowadays, microwave devices are the basic devices that are used in modern technology that facilitate the integration and miniaturization of components and then electronic devices, among these components are the multipliers [1, 2]. Indeed, the frequencies multipliers currently constitute the most widen frequency sources to meet the quality requirements required by applications such as: radars, satellite communications, radiometry and spectrometry. They generate an output signal whose frequency is a multiple of its input frequency [3–6].

The basic realization principle for frequency multiplication is the generation of multiple higher frequencies by distorting (amplitude or phase) a sinusoidal signal and then filtering out the desired higher frequency component [7–10].

Various techniques exist for the realization of frequency multipliers. At radio frequencies, these techniques generally use a non-linear device to generate the

H. El Ftouh (✉) · M. El Bakkali · N. A. Touhami
Faculty of Sciences, Abdelmalek Essaâdi University, Tétouan, Morocco
e-mail: elftouhhaae@hotmail.fr

A. Zakriti
Abdelmalek Essaâdi University, ENSATé, Morocco

desired multiplication of frequency. The non-linear elements such as varactor diodes, Schottky barrier diodes (SBDs), step recovery diodes (SRDs) and bipolar junction transistors (BJTs) or field effect transistors (FETs) are used as non-linear devices [7–11].

The diode multipliers constitute difficultly compatible loss devices with current MMIC integration requirements, and hence the realization of transistor multipliers providing a conversion gain and the implementation within an integrated circuit constitutes a very appreciable progress. That is why, in this work, we will study and design an MMIC multiplier based on an ED02AH pHEMT (pseudomorphic High Electron Mobility Transistor) with gate length equal to $0.18 \mu\text{m}$ [3] to provide highly stable, reliable and efficient frequency extenders for system applications.

2 Design of Studied GaAs-pHEMT MMIC Frequency Doubler

A generalized schematic circuit diagram of a pHEMT multiplier is shown in Fig. 1. Ideally, the input and output matching networks provide the required impedance to each harmonic component independently [12].

The idea behind this frequency multiplier is to generate harmonics of the input frequency. The input matching circuit consists of resonators called idler circuit, which provides short circuit to the desired output as well as other harmonic frequencies [13–15]. The output matching circuit consists of resonators which provide fundamental and other harmonic frequency components except for the desired frequency [9–12].

The idler circuits are preferably realized at input and output ports using reactive elements in order to minimize power dissipation and then maximize conversion gain.

To achieve higher conversion gain, in most of the cases the requirement of gate voltage will be smaller than the pinch-off voltage, V_{gso} , and the transistor will remain OFF during most of the signal cycle. The dimension of the pHEMT transistor is $6 \times 15 \mu\text{m}$. The C_0 capacities are used to eliminate the DC component. However, Idler f_0 is a resonator that blocks the passage of the fundamental frequency.

Fig. 1 Generalized schematic circuit diagram of pHEMT doubler

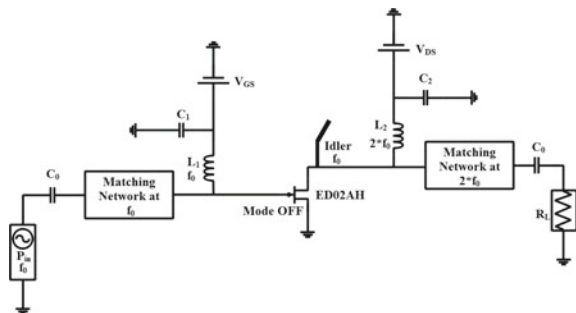


Table 1 Values of the generalized schematic components

C_0 (pF)	C_1 (pF)	C_2 (pF)	L_1 (nH)	L_2 (nH)	V_{GS} (V)	V_{DS} (V)	Idler line (μm)
1	0.5	0.09	1.33	0.91	-2.1	5.5	946

In addition, the matching networks are used to maximize the power transfer from input to output, especially that of the output whose role is to maximize the transfer of the signal with frequency equal to $2 \cdot f_0$ which is in our case 60 GHz.

The following Table 1 shows the values of the generalized schematic components.

3 Results

The following Fig. 2 shows the scattering parameters at input $f_0 = 30$ GHz and output $2 \cdot f_0 = 60$ GHz frequencies to check the working conditions of the studied GaAs-pHEMT MMIC frequency Doubler.

For the good functioning of a Doubler, it is necessary that it checks the following conditions:

- $S_{ii} < -10$ dB (i from 1 to 2) to have adaptation of the two ports.
- S_{33} tend to zero dB to have total reflection of RF signals
- S_{13} and $S_{31} < -10$ dB to have isolation between port 1 and port 3.
- S_{12} and S_{21} tend to zero dB to have total transmission of RF signal from port 1 to port 2.

So, from Fig. 2 we can observe that all the conditions are satisfied in both input and output frequencies (S_{11} & $S_{13} < -10$ dB and S_{12} tend to 0 dB).

Since the bias circuit is symmetrical, then S_{11} and S_{22} are the same.

Figure 3 shows Voltage and current response in Time domain at input frequency ($f_0 = 30$ GHz) and output frequency ($2 \cdot f_0 = 60$ GHz) in Time domain.

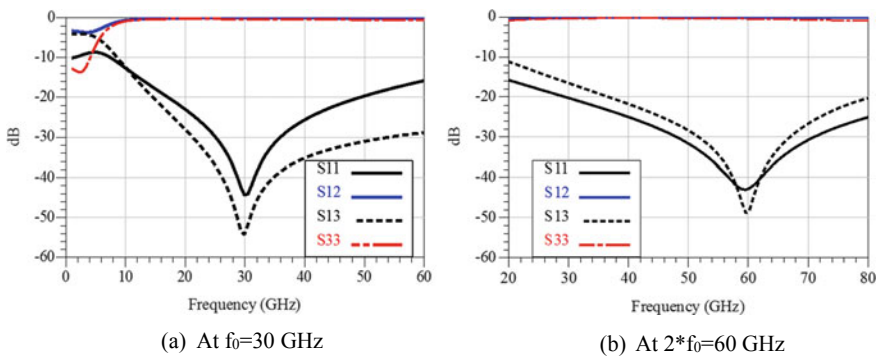


Fig. 2 Scattering parameters at **a** input frequency and **b** output frequency

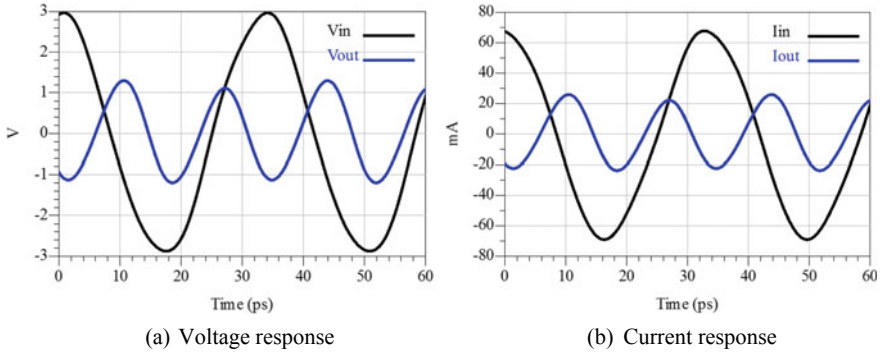


Fig. 3 Voltage and current response in Time domain

Figure 4 shows Voltage and current response in frequency domain at input frequency ($f_0 = 30$ GHz) and output frequency ($2 \cdot f_0 = 60$ GHz).

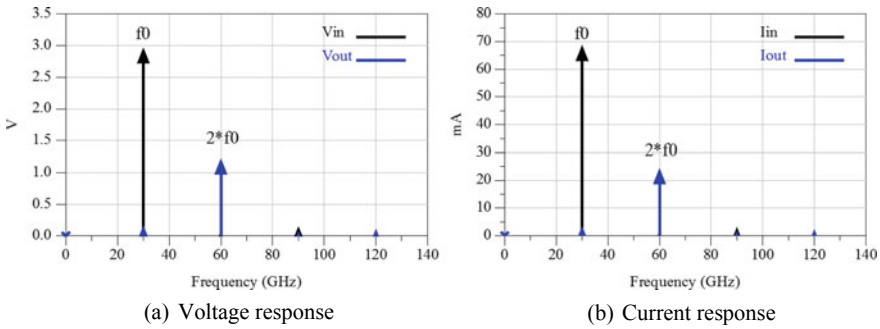


Fig. 4 Voltage and current response in frequency domain at input (f_0) and output ($2 \cdot f_0$) frequencies

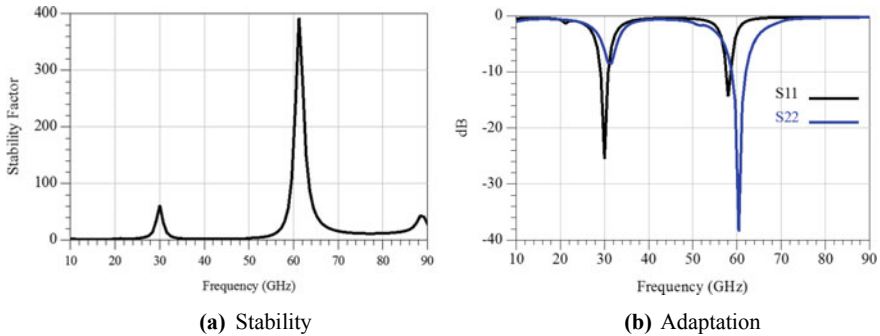


Fig. 5 Representation of a stability and b adaptation of the studied Doubler at input and output frequencies

Table 2 Voltage values at input and output frequencies

	Input signal (f_0)	Output signal ($2*f_0$)
Amplitude (V)	2.93	1.71

Table 3 Current amplitude values at input and output frequencies

	Input signal (f_0)	Output signal ($2*f_0$)
Amplitude (mA)	68	23

Tables 2 and 3 show the voltage and current amplitude values at input frequency $f_0 = 30$ GHz and output frequency $2*f_0 = 60$ GHz.

Figure 5 shows the representation of stability and adaptation of pHEMT MMIC Frequency Doubler.

For absolute stability of circuit, the condition of stability must apply. i.e., $k > 1$.

$$k = \frac{1 - |S_{11}|^2 - |S_{22}|^2 + |S_{11}S_{22} - S_{12}^*S_{21}|}{2|S_{12}S_{21}|} > 1 \quad (1)$$

$$B = 1 + |S_{11}|^2 - |S_{22}|^2 - |\Delta|^2 \quad (2)$$

where

$$\Delta = S_{22}S_{11} - S_{12}S_{21} \quad (3)$$

As shown in Fig. 5a, the circuit is stable at both of input and output frequencies (30 and 60 GHz respectively), because the stability factor is much greater than the unit ($K > > 1$).

Table 4 shows the values of circuit adaptation at input 30 GHz and output 60 GHz frequencies at shown in Fig. 5b.

Figure 6 shows the conversion Gain of pHEMT MMIC Frequency Doubler.

We observe that the conversion gain is equal to -2.189 dB and remains invariant from 22 dBm up to 33 dBm and it's a very important value if we compare it with conversion gain at [16], [17 and 18] which are respectively equal to 8 , -13 and 6 dBm.

The conversion gain is defined by:

$$\text{Conversion gain (dB)} = 10 * \log\left(\frac{P_{\text{out}}}{P_{\text{in}}}\right) \quad (4)$$

Table 4 Sii values at input and output frequencies

	S_{11} (at f_0)	S_{22} (at $2f_0$)
dB	-25.5	-38.5

Fig. 6 Conversion gain

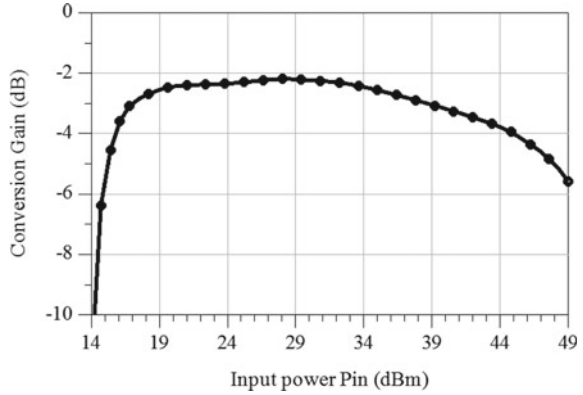
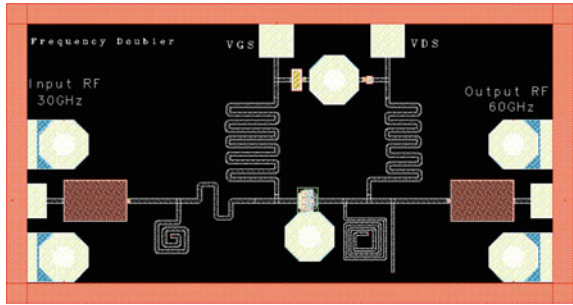


Fig. 7 Circuit Layout of a pHEMT MMIC Doubler



Also the doubler achieves a peak total power efficiency of 13.87% and it is given by:

$$\eta_{Total} = 100 * \left(\frac{P_{out}}{P_{in} + P_{dc}} \right) \tag{5}$$

Microstrip circuit layout of a microwave frequency doubler using GaAs-pHEMT is shown in Fig. 7. The proposed multiplier was designed and optimized and it’s characterized by low power consumption $P_{dc} = 0.126$ mW, high spectral purity and a small size thanks to OMMIC Library. Indeed, it occupies an area of 1.35×0.63 mm² wich is a very important value if we compare it with the study done at [18].

4 Conclusion

The GaAs- pHEMT MMIC frequency doubler for 60 GHz radar area scanning application was successfully proposed and demonstrated in this paper using 0.18 μm GaAs

technology. The simulation results show higher efficiency and lower dissipated power which value is 0.126 mW. It achieves not only a maximum output power of 11.376 dBm but also, the proposed doubler achieves a peak conversion gain of -2.198 dB and occupies an area of 1.35×0.63 mm².

References

1. Yoon H, et al (2018) A—31dBc integrated-phase-noise 29GHz fractional-N frequency synthesizer supporting multiple frequency bands for backward-compatible 5G using a frequency doubler and injection-locked frequency multipliers. In: 2018 IEEE International Solid - State Circuits Conference—(ISSCC), San Francisco, CA, pp 366–368
2. Yoo S, et al (2017) A PVT-Robust -39 dBc 1 kHz-to-100 MHz Integrated-PhaseNoise 29 GHz injection-locked frequency multiplier with a 600 μW frequency-tracking loop using the averages of phase deviations for mm-Band 5G Transceivers, ISSCC, pp 324–325, Feb 2017
3. El bakkali M, Touhami NA, Elhamadi T (2020) Microwave frequency tripler using InGaAsHEMTtransistor. *Procedia Manufacturing*, Elsevier
4. Thomas DG, Branner GR, Kumar BP (2005) Microwave and radio frequency multipliers. *Encyclopedia of RF and microwave engineering*. April 2005
5. Jeong T, Lim HM, Oh J, Sun K, Han W C, Kyeong HL, Choul YK Miniaturized Q band $\times 8$ frequency multiplier with optimized efficiency in 65 nm CMOS technology. *Microwave and optical technology letters*
6. CMOS Signal Synthesizers for Emerging RF-to-Optical Applications, thèse de Jahnavi Sharma, Columbia University 2018
7. Gilmore R (1087) Concepts in the design of frequency multipliers. *Microw J* 129–139 (1087)
8. Thomas DG, Branner GR (1996) Optimization of active microwave frequency multiplier performance utilizing harmonic terminating impedances. *IEEE Trans Microw Theory Tech* 4 (12):2617–2624.
9. JDahlback R, Drakinskiy V, Vukusic J, Stake J (2017) A Compact 128- Element Schottky Diode Grid Frequency Doubler Generating 0.25 W of Output Power at 183 GHz; *LMWC* Feb 2017, pp 162–164
10. Chou M, Chiu H, Kao H, Huang F (2017) A 60-GHz CMOS frequency tripler with broadband performance, *LMWC* March 2017, 281–283
11. Augusto JS, Rosario MJ, Vaz JC, Freire JC (1993) Optimal design of MESFET frequency multipliers. In: *Proceedings of the 23rd European microwave conference*, Madrid, pp 402–405, Sept 1993
12. Jonsson M, Zirathik H, Vhland K A new pet frequency multiplier. *Th2e-2*.
13. Rauscher C High-frequency doubler operation of GaAs field-effect transistors *IEEE Trans Microw Theory Tech* MTT-31(6):462–473
14. Siles JV et al (2011) A single-waveguide in-phase power-combined frequency doubler at 190 GHz. *IEEE Microwave Wirel Compon Lett* 21(6):332–334
15. Vera L, Long JR (2015) A DC-100 GHz active frequency doubler with a low-voltage multiplier core. *IEEE J Solid-State Circuits* 50(9):1963–1973
16. Chakraborty S, Milner LE, Mahon S, Parker A, Heimlich M (2019) A GaAs frequency doubler with 38 dB fundamental rejection from 22 to 40 GHz using a Transformer Balun. In: 2019 49th European Microwave Conference (EuMC), Paris, France, pp 848–851. <https://doi.org/10.23919/EuMC.2019.8910725>
17. RieB V, Carta C, Ellinger F (2018) A 60 GHz frequency doubler with differential output in 130 nm SiGe BiCMOS Technology. In: 2018 Asia-Pacific Microwave Conference (APMC), Kyoto, 2018, pp 279–281. <https://doi.org/10.23919/APMC.2018.8617444>

18. Fager C, Landen L, Zirath H (2000) High output power, broadband 28–56 GHz MMIC frequency doubler, 2000 IEEE MTT-S International Microwave Symposium Digest (Cat. No.00CH37017), Boston, MA, USA, 2000, vol 3, pp 1589–1591. <https://doi.org/10.1109/MWSYM.2000.862280>.

Fail-Safe Remote Update Method for an FPGA-Based On-Board Computer System



Ahmed Hanafi , Mohammed Karim, Tajjeeddine Rachidi, and Ibtissam Latachi

Abstract As part of a university project to design a Low Earth Orbit (LEO) nano-satellite payload, we investigate a System-on-Chip (SoC) solution exploiting the features of Xilinx's Spartan 6 FPGA technology to design an On-Board Computer System (OBC). Thus, the increased flexibility of the FPGA implementation will enable on-orbit updates and modifications to the software and hardware OBC architecture, in lodge to support dynamic mission requirements. Within this context, this paper introduces a method to safely remote update an FPGA-based embedded system. The proposed architecture is based on the Xilinx soft processor, i.e. the Microblaze, which controls the remote update channel (Ethernet in our case) to upload hardware and/or software application images in the system by using the Trivial File Transfer Protocol (TFTP). An on-board flash memory is used to store FPGA Hardware and firmware images. The soft processor is implemented in the Spartan-6 XC6SLX45 FPGA device and uses the fallback features and the Internal Configuration Access Port (ICAP) primitive in order to manage fail-safe FPGA reconfiguration to maintain safe and stable state after updates.

Keywords Remote update · Microblaze · TFTP · ICAP · FPGA · Nanosatellite · Fallback · Reconfiguration

1 Introduction

In recent years, the nano-satellite market is growing tremendously with the continued use of the CubeSat standard, microelectronics development, and furthering of applications. The low-cost nano/microsatellite (1–50 kg) segment is anticipated to have

A. Hanafi (✉)
EST, Sidi Mohamed Ben Abdellah University, Fes, Morocco
e-mail: ahmed.hanafi@usmba.ac.ma

M. Karim · I. Latachi
FSDM, Sidi Mohamed Ben Abdellah University, Fes, Morocco

T. Rachidi
School of Science and Engineering, Al Akhawayn University, Ifrane, Morocco

a 23.8% yearly growth over the period 2014–2020 [1]. This growing interest in the development of nano-satellite-based space missions, demands new approaches to investigate a flexible, low cost, reliable and reconfigurable alternative to the traditional processor hardware architecture used in the On-Board Computer (OBC) design.

One of the implementation devices most suited to meet these requirements are SRAM-based Commercial-Off-The Shelf (COTS) FPGAs (e.g. Spartan-6 Xilinx FPGA). This highly integrated and reconfigurable System-on-Chip (SoC) approach for designing embedded platform in space applications provide the following capabilities:

- Flexibility for reconfiguring hardware and / or software functions in orbit, e.g. to support dynamic mission requirements or to update the FPGA configuration to correct design errors.
- Decrease development time while allowing software development and hardware integration begin at the earliest phases of a project.
- An opportunity to test and evaluate, on orbit, mitigation techniques to provide good fault tolerance. Indeed, the Single Event Effects (SEE) of space radiations on the SRAM-FPGA are the main challenge to deploying reconfigurable systems in space, and they require the implementation of “Failure Detection, Isolation and Recovery” (FDIR) techniques.

This paper presents a fail-safe method for implementing remote update in a Microblaze based system, through an Ethernet port. The updates can include both the bitstream image (FPGA configuration data) and the software that the soft processor Microblaze runs, in a single remote run-time reconfiguration session.

The organization of the rest of the paper is as follows: Sect. 2 provides an overview of some related work on remote update FPGA reconfiguration, followed by the specifics of our work. A description of the adopted fail-safe remote update scheme is described in Sect. 3. Sections 4 and 5 detail the hardware and software implementation of the proposed run-time full reconfigurable embedded platform. Finally, Sect. 6 and 7 outline the main results and conclusions of this implementation.

2 Overview of Some Related Works

Within the scope of this work, two different fields of research are combined: the remote update of firmware in FPGA-based embedded system, and the managing of a fail-safe FPGA run-time full reconfiguration.

For works that focuses on the remote update, Hulme et al. [2] describe the Configurable Fault-Tolerant Processor (CFTP) project for Space Based Applications, which one of the main goals is to test and evaluate the reliability of a Triple Modular Redundant (TMR) processor, as well as getting the ability to remotely reconfigure the system to support dynamic mission requirements. They use difference-based partial

reconfiguration method that greatly reduces the bandwidth required, but is somewhat limited in its applications.

Castillo et al. [3] present a system for remote self-reconfiguration of an FPGA. The used architecture is based on an open source soft-core processor (fixed area of FPGA) which downloads a bitstream from a remote TFTP server, and partially reconfigure the FPGA in a secure way.

Du et al. [4] present a fail-safe remote FPGA upgrade method using a UDP packet switch engine to read bitstream image and program an on-board SPI flash memory through a gigabit Ethernet (GBE) communication interface. Therefore, an external MCU monitors fail-safe booting.

Fernandes et al. [5] present an alternative method for FPGA remote update in a nuclear environment. The method, based on the Xilinx Quick Boot application note, uses a dedicated Update Management Software (UMS) unit to communicate with a high-performance Xilinx Kintex 7 FPGA-based module through PCIe links.

Our synthesis work is inspired from Du et al. [4] oral presentation and proposes an FPGA-based OBC System using MicroBlaze soft processor as the core of the Hardware. Our contribution in the proposed embedded platform lies in:

- The choice of using a Real-Time Operating System (like Xilkernel) in the software implementation, which makes the proposed platform, a real-time embedded system that can be used such as OBC for nanosatellite.
- The implementation of a method to achieve more reliability in the remote run-time full reconfiguration process by using the fallback features of the FPGA.
- The software remote update can support the code executing from the internal FPGA BRAM, as well as the code executing from an external DDR SDRAM.
- Fail-Safe Remote Update Scheme.

This section presents a detailed description of the system level solution using Microblaze processor-based method for managing multiple bitstream and software application images, and safely update these images through an Ethernet interface.

The functional components of the management system are illustrated in Fig. 1.

The remote system uses the TFTP protocol to receive updated hardware and software image files via an Ethernet interface. The FPGA soft processor (Microblaze) stores the incoming file to SDRAM first, using the SDRAM controller. After the system receives and accept the valid data, the processor then uses a specific algorithm to write received data at the appropriate address of the SPI Flash memory. Once the processor finishes programming the Flash memory, it can trigger remotely the FPGA reconfiguration by rebooting the system. Communication via the UART (Universal Asynchronous Receiver Transmitter) interface allows debugging, and supervision of the system.

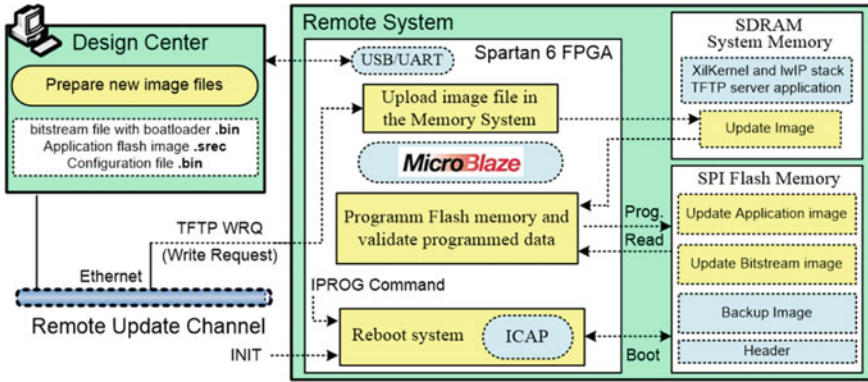


Fig. 1 Reference system hardware platform

2.1 Choice of Xilinx Spartan 6 FPGA

According to the requirements of our OBC, SRAM FPGAs are the most suitable solution in view of their price, their high degree of integration and their flexibility in the reconfiguration. Among the SRAM FPGA manufacturers, Xilinx is the most predominant in the space applications market with its development of several techniques and functionalities allowing the attenuation and recovery of SEU effects induced by the space environment [6].

Due to cost and consumption constraints, the choice fell on the Xilinx Spartan 6 FPGA even if it is not an FPGA qualified space like the Virtex-4QV and Virtex-5QV. Indeed, it's an SRAM based military grade FPGA product offering attractive performance for a low power consumption, and the work of evaluating Spartan-6 for space applications [7] has given promising results.

2.2 Preparation of the Image Files

Since the architecture adopted implements a software processor, the remote updating of the system will concern both the hardware image of the FPGA including the software processor and the software code executed by the latter.

The Fig. 2 summarizes software flow for preparing image files:

- If the software code is executed from the internal FPGA Block RAM (BRAM), we need to prepare a single configuration file in .bin format, updated with the BRAM content from the specified application executable file (.elf format).
- If the software code is executed from the system memory (external SDRAM), we need to prepare two files: a configuration file (.bin format) with a boot-loader, and a flash image of software application in S-record (.srec) format.

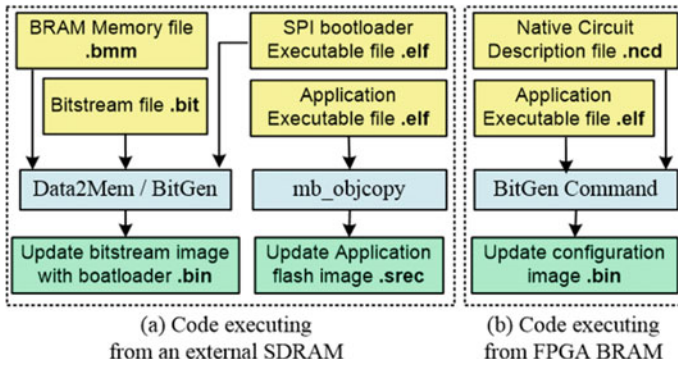


Fig. 2 Software flow for preparing image files

Note that for programming the flash memory with a bitsream image (.bit format), we must convert the file to the .bin format, which contains binary configuration data with no header information, and then can be used for custom configuration.

2.3 Uploading Image File in the System

A TFTP server working on the remote FPGA system is used to upload image file through an Ethernet interface. TFTP is a UDP-based protocol (User Datagram Protocol) for sending and receiving files, and it implements a lightweight protocol to ensure packets are not lost during file transfer.

The Design Center runs a TFTP PUT command to upload an image file. The target Microblaze remote system receives and saves incoming data into the SDRAM system memory. This part will be detailed in Sect. 5 of this paper.

2.4 Programming Image File to Flash Memory

The design uses the Xilinx SPI interface drivers in polled mode to communicate with the Serial flash memory. Software Development Kit (SDK) of Xilinx Company includes In-System Flash (LibXil Isf) library, which provides Application Programming Interfaces (APIs) to write, read, and erase the serial flash. In summary, the programming of flash memory will be managed in three steps:

- (1) Erase the flash memory blocks based on the image file size. Indeed, writing to flash memory can only change bits from 1 to 0, and erasing a flash memory block or sector sets all bits to 1, after which any value can be programmed.
- (2) Program the flash memory by reading data from SDRAM memory and writing it to the correct flash address.

- (3) Validate the programing operation by performing a read operation and comparing the data read against the data written from SDRAM memory.

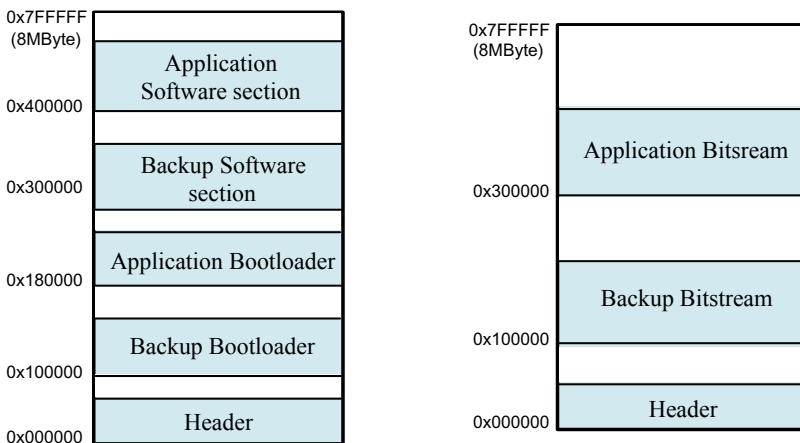
2.5 Run-Time Reconfiguration of Spartan 6 Devices

For the implementation of a complete or partial reconfiguration of FPGA Spartan-6 devices, we use the dedicated Internal Configuration Access Port (ICAP). This port allows reconfiguration autonomously at runtime with the use of ICAP_SPARTAN6 primitive as described in our previous paper [8].

2.6 Triggering Remotely the FPGA Reconfiguration

To enable the new configuration image, the system implements and triggers remotely, through an UART interface, the run-time full reconfiguration process described above. To do it safely, we use the Flash SPI memory directly connected to the Spartan 6 FPGA to exploit its fallback features which allow the management of multiple bitstream files, and the self-reconfiguration. The Flash memory organization used to store the multiple images for fallback configuration, changes depending on whether the software code is stored in the internal FPGA BRAM or the SDRAM system memory (see Fig. 3).

If the embedded software is executed from the system memory, flash memory is divided into five areas.



(a) Code executing from an external SDRAM (b) Code executing from FPGA BRAM

Fig. 3 SPI Flash memory map

Fig. 4 Header Bitstream for IPROG through ICAP

FFFF	FFFF	: Dummy word
AA99	5566	: Synchronization word
31E1	FFFF	: Enable Reset on Error
3261	0000	
3281	0318	: Set the start address of Appli Bootloader image.
32A1	0000	
32C1	0310	: Set the start address of Backup Bootloader image
3301	2100	: Set Reboot mode
3201	001F	: Do not skip initialization
30A1	000E	: Send IPROG command
2000	2000	: No Operation

- Header sector containing a set of commands sent to the FPGA configuration memory using the ICAP_SPARATN6 primitive. This small bitstream must start at address 0 to trigger a run-time full reconfiguration. The sequences of commands used in our Header file is shown in Fig. 4.
- The backup Bootloader section used to store known good data and reconfigure the FPGA if the hardware update fails. This section includes the hardware bitstream and the bootloader that will be executed by the soft processor to copy the executable software from a pre-determined location in Flash memory to SDRAM memory.
- The application Bootloader section used to run-time full reconfigure the FPGA in normal mode.
- The backup software section whose start address will be useful for the Backup Bootloader to work.
- The application software section whose start address will be useful for the Application Bootloader to work.

During FPGA reconfiguration, the system loads the application bitstream image. If an error (watchdog time-out error or CRC) is detected, the system tries to reload the previous bitsream image 3 times. If reconfiguration still fails, the backup bitstream image is reached. Note that a section write-protection can be used for the Header and Backup sections.

3 Hardware Design of the FPGA-Based Remote System

We have implemented an architecture that supports software code that the soft processor will run from an external SDRAM memory. The hardware implementation shown in Fig. 5 was made on the Xilinx Evaluation Kit Spartan-6 FPGA SP605 using Xilinx Platform Studio (XPS) Tool suite. The design is based on the AXI interconnect and it includes the main following IPs cores.

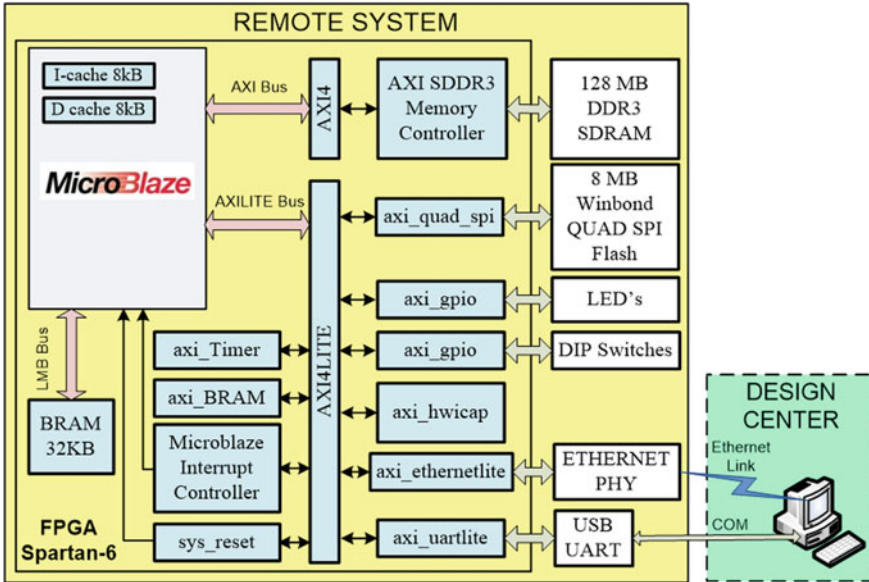


Fig. 5 Hardware architecture of the remote system

4 Software Design of the FPGA-Based Remote System

4.1 Real Time Operating System (RTOS)

Since the purpose of the proposed architecture is to be used as a nano-satellite OBC, we have adopted a real-time software platform. The key factors that motivated our choice were:

Using an RTOS for implementing tasks concerning the TFTP protocol management and especially for controlling the target-embedded system is much more intuitive, facilitates the management of shared time between applications, and increases responsiveness [9].

Ability to write application code on an abstract level using a programming language like C / C+ + .

The porting and use of free libraries as lwIP network protocols require some RTOS services (file system, time management).

The chosen Xikernel RTOS is a preemptive, small, robust, and modular kernel, and it is provided free with the Xilinx Embedded Development Kit (EDK).

Table 1 Main helper functions used

Function	Description
void lwip_init()	Provides a single initialization function for the lwIP data struct
sys_thread_t sys_thread_new()	Must be used to create Application threads that use lwIP
struct netif*xemac_add()	Provides a unified interface to add any Xilinx EMAC IP
void xemacif_input_thread()	Moves received packets from the interrupt handlers to the tcpip_thread of the lwIP

4.2 TFTP Protocol Management

We have used Lightweight IP (LwIP) TCP/IP stack to develop a TFTP server in the remote microblaze-based embedded system. This choice reduces resource utilization and makes LwIP suitable for use with tens of kilobytes of free RAM and around 40kbyte of code ROM.

The Xilinx EDK environment offers several custom versions of lwIP to run on MicroBlaze based embedded systems. The latest version provides support for the needed UDP protocol, and two APIs modes for use by applications:

- RAW API customized for high performance and lower memory overhead.
- SOCKET API provides a BSD (Berkeley Software Distribution) socket interface and is very portable. This mode requires an RTOS and it was adopted.

Since Xilkernel round-robin scheduling policy is applied, there are no particular requirements because all threads have the same time quanta. The use of lwIP APIs is simplified by helper functions provided by the Xilinx adapters. The main functions used by our application are summarized in Table 1.

To communicate and upload image file through Ethernet interface, the implemented TFTP server uses TFTP WRQ (write request) packet according to the schematic inspired from MacMahon et al. [10].

4.3 Programming the SPI Flash Memory

The proposed on-board system uses a single SPI flash memory to store both the executable kernel image and configuration data. This will reduce costs and consumption, and simplify the design of the system.

To initially program the SPI Flash memory, we must generate an MCS file (Intel MCS-86 Hexadecimal Format) from the five files that it should contain (SPI Flash Memory map already described in Fig. 3. The choice is made on the Promgen/Bitgen commands to create the MCS file whose role is to define the data file and the storage address with ASCII strings. The batch script file shown in Fig. 6 is used to generate the final file *header_remote_update_app.mcs*:


```

cd <project_path>\implementation
bitgen -w -g Binary:Yes -g spi_buswidth:1 -bd <project_path>\Appli_boot.elf system.ncd appli_boot.bit
bitgen -w -g Binary:Yes -g spi_buswidth:1 -bd <project_path>\Backup_boot.elf system.ncd backup_boot.bit
promgen -w -p mcs -r header.hex -o header.mcs
promgen -w -p mcs -spi -c FF -s 8192 -u 010000 <project_path>\backup_boot.bit -u 0180000 appli_boot.bit
-data_file up 300000 backup_apps.srec -data_file up 400000 Initial_apps.srec -o remote_update_app.mcs
type header.mcs remote_update_app.mcs > header_remote_update_app.mcs

```

Fig. 6 Batch script to generate the final MCS file

5 Implementation, Test and Results

For implementation and test, we create three software applications: Initial, update, and backup_application. For all applications, we used the same Board Support Package (BSP) after having added and configured the Xilinx RTOS, Xiliscf library and Lwip140 library. The execution of each test application includes customized messages sent via UART and addresses locations of the update image files.

In the Design Center, a serial terminal program is set to debug, monitor and remotely reboot the Remote System. The performance of each test application establishes an Ethernet connection with the remote system, then gives three options using a menu: Update bitstream bootloader file, update Application image file, or attempt a remote FPGA reconfiguration. Figure 7 shows running results of the initial application with successful transfer and programming in Flash memory of the update application image file, and successful remote reconfiguration with update application image. If a power failure occurs during the update process, or the programming of the flash memory is interrupted, the backup bitstream image is reached during the next reconfiguration.

Fig. 7 Terminal Window showing test running of the initial application

```

Tera Term - [disconnected] VT
File Edit Setup Control Window Help

Waiting choice : 3

*****Upload the update Application file*****
* Starting TFTP server at port 69
* Please run command line to upload your file :
  stftp -i 192.168.1.10 PUT <file.srec>
  TFTP WRQ (write request): Remote_update_apps.srec

Successful transfer : 561346 octets 9 Flash memory Block 2193 Flash
page
*****Initial Application*****
*****Executing Initial Image*****

Date = Aug 30 2016, Time = 20:22:49
1) Upload the update Bootloader file by TFTP protocole *
2) Program and verify the update Bootloader file *
3) Upload the update Application image file by TFTP protocole *
4) Program and verify the update Application image file *
5) Try FPGA reconfiguration *

```

6 Conclusion

The on-orbit reconfiguration concept will help contribute to improvements in the space-based computing system. In this context and as part of our ongoing research activity to develop a reconfigurable OBC as a nanosatellite payload, this work is a step that has allowed us to master the process of updating an FPGA-based system through an Ethernet link. As a future work, successful achievement of this work allows us to:

- Improve system design from a security point of view (confidentiality and integrity).
- Adapt the method for use with a radio frequency communication channel.

References

1. Buchen E, DePasquale D (2014) Nano / Microsatellite Market Assessment, SpaceWorks Enterprises, Inc. (SEI) 2014
2. Hulme CA, Loomis HH, Ross AA, Yuan R (2004) Configurable fault-tolerant processor (CFTP) for spacecraft onboard processing. In: 2004 IEEE aerospace conference proceedings (IEEE Cat. No.04TH8720), vol 4, pp 2269–2276
3. Castillo J, Huerta P, Lopez V, Martinez JI (2005) A secure self-reconfiguring architecture based on open-source hardware. Int Conf Reconfig Comput FPGAs (ReConFig'05), Puebla City, pp 7–10
4. Du Q, Olivieri J, Doolittle LR (2013) Remote FPGA Upgrades with Fail-Safe Booting, Oral presentation of the sixth Low-Level Radio Frequency Workshop, LLRF13. Lake Tahoe, USA
5. Fernandes A, Pereira RC, Sousa J (2016) FPGA remote update for nuclear environments. IEEE Trans Nucl Sci 63(3):1645–1649
6. Habinc S (2002) Suitability of reprogrammable FPGAs in space applications. Feasibility Report. Compilation from various sources, Gaisler Research
7. Wazard N, Salvaterra G, PIKE P (2016) SPARTAN 6 evaluation for space application, Airbus Defence & Space
8. Hanafi A, Karim M (2015) Run-time Fallback and Multiboot technique for embedded platform using low-cost Spartan-6 FPGA” (WSEAS) Trans Circuits Syst 14:208–215 (2015)
9. Ugurel G, Bazlamaçcı CF (2011) Context switching time and memory footprint comparison of Xilkernel and μ C/OS-II on MicroBlaze. In: 7th International conference on electrical and electronics engineering, 1–4 Dec Bursa, TURKEY. ELECO 2011
10. MacMahon S, Zang N, Sarangi A (2014) LightWeight IP (lwIP) application examples, xilinx application note XAPP1026 (v5.1) (Online)

Autonomous Vehicle Lateral Control for the Lane-change Maneuver



Lhousseain El Hajjami, El Mehdi Mellouli, and Mohammed Berrada

Abstract During the fourth industrial revolution, the automotive industry is seeking to develop a completely autonomous ground vehicle capable of adapting to all situations encountered; including the lane change maneuver during normal driving on the highway. This paper describes, at first, the planning of the lane change maneuver using a quintic mathematic function, as a second step; a law of control based on higher-order sliding mode is applied. The adopted strategy achieves good results in terms of sideslip angle and tracking error, especially with the consideration of a high longitudinal speed.

Keywords Autonomous vehicle · High-order sliding mode · Lane change maneuver · Quintic function

1 Introduction

According to the American Highway Traffic Safety Administration (NHTSA), 94% of traffic accidents caused by human factors [1], thereby the necessity of autonomous driving. Over the past few years, Autonomous Vehicle (AV) technology become increasingly mature, due to the pioneers of technology such as Tesla (Autopilot Tesla 2018), General Motors (Cruise Automation 2018), Google (Waymo 2018), and others [2]. This maturity is the mirror of different contributions of researchers in various axes, in which lateral control is an important part. Several control strategies are designed to guide the dynamic behavior of cars; these strategies are included in the Advanced Driver Assistance Systems (ADAS) systems that aim to maintain lateral and longitudinal dynamic stability. In this respect a diversity of controller structures have been proposed in the literature; while starting with classic laws such

L. El Hajjami (✉) · M. Berrada

Laboratory of Artificial Intelligence, Data Sciences and Emerging Systems (IASSE), Sidi Mohamed Ben Abdellah University, Fez, Morocco
e-mail: lhousseain.elhajjami@usmba.ac.ma

E. M. Mellouli

Laboratory of Engineering, Systems and Applications (LISA), Sidi Mohamed Ben Abdellah University, Fez, Morocco

© Springer Nature Singapore Pte Ltd. 2022

S. Bennani et al. (eds.), *WITS 2020*, Lecture Notes in Electrical Engineering 745,
https://doi.org/10.1007/978-981-33-6893-4_28

as PID, state feedback, up to the advanced non-linear controller such as sliding mode [3], backstepping [4], and others. In [5] a control mechanism based on two PID controllers, relating to lateral displacement and yaw angle plus a regulator element, a steering angle is built into the lane-keeping order. In [6] a state feedback control is used concerning the instantaneous variation of the yaw rate which is a function of the curvature related to the path traveled, the same approach was followed by [7] for the elaboration of a control law based on an optimal PID using Butterfly Optimization Algorithm (BOA). The higher order sliding mode is applied in [8] to control the lateral acceleration which allows simultaneous action on the lateral deviation and yaw angle. The direct yaw-moment control (DYC) merged with fuzzy logic is the objective of the contribution announced in [9] to ensure the stability of the car in a crosswind. However, an optimal hybrid structure between backstepping and sliding mode is proposed in [10] as an aim to satisfy lateral stability for the line change maneuver. The main contribution of this work is the employment of a control strategy based on higher-order sliding mode to execute the track change maneuver, which is planned by a mathematical function, with high lateral stability.

2 Vehicle Modeling

The four-wheel model, Fig. 1a, and the bicycle model, Fig. 1b, are the most used in the research work, the first one characterized by its complexity, while the second one known for its simplicity. Often the four-wheel used to validate the results obtained by the bicycle model. In this work, the bicycle model, which takes into consideration the lateral displacement and the yaw angle as two degrees of freedom will be used. Memorable that this model is based on several assumptions given in [6, 11].

Through various laws of mechanics, the following model represents the lateral dynamics of the vehicle [6, 8, 13]:

$$\dot{X} = AX + BU \tag{1}$$

where

$$X = \begin{pmatrix} \beta \\ \psi \\ \dot{\psi} \\ y \end{pmatrix}, A = \begin{bmatrix} -\frac{C_f+C_r}{V_x \cdot m} & 0 & -1 & -\frac{C_f l_f - C_r l_r}{m V_x^2} & 0 \\ 0 & 0 & 1 & 0 & 0 \\ \frac{C_r l_r - C_f l_f}{I_z} & 0 & -\frac{C_f l_f^2 + C_r l_r^2}{I_z V_x} & 0 & 0 \\ V_x & V_x & 0 & 0 & 0 \end{bmatrix}, B = \begin{bmatrix} \frac{C_f}{m \cdot V_x} \\ 0 \\ \frac{C_f l_f}{I_z} \\ 0 \end{bmatrix}.$$

U, is the steering wheel angle.

X, is the state vector.

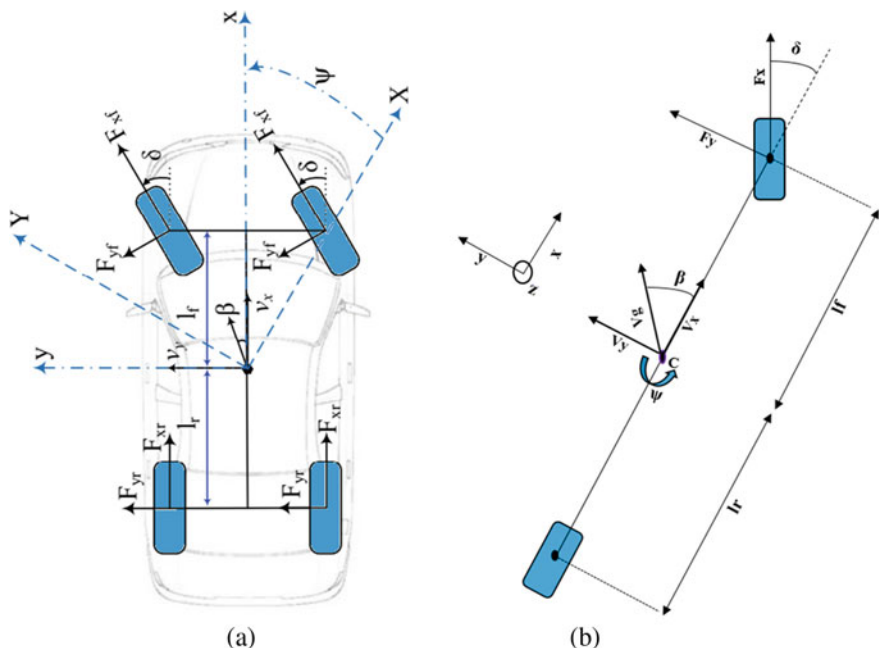


Fig. 1 Vehicle modeling. **a** Four-wheel model [12], **b** Bicycle model[7]

3 Trajectory Planning

After perception of the driving environment through the sensors installed in the car such as laser-based radar (LIDAR), ultrasonic sensor, thermal and stereo-cameras, etc [14]. The recovered data will be transmitted to other entities in charge of planning various maneuvers [15]. The lane change maneuver is one of the situations that occur during normal driving. Therefore, several models are used to design this scenario, among them the mathematical model based on the quintic function [11].

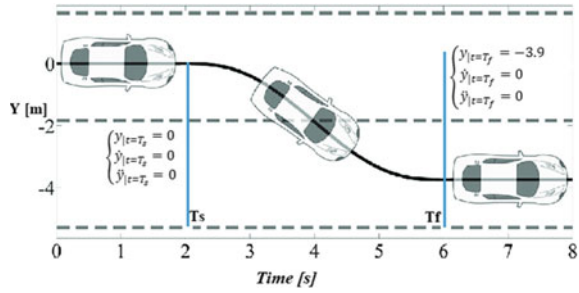
Equation 2 is a polynomial of degree five also called quintic function. The latter presents a model of the lane-switching maneuver characterized by a zero lateral velocity at the beginning of the maneuver, T_s and its end, T_f , (displayed on Fig. 2). These conditions are presented by the expressions 3 and 4 [11, 16].

$$y(t) = a_5t^5 + a_4t^4 + a_3t^3 + a_2t^2 + a_1t + a_0 \tag{2}$$

This maneuver is identified, on the one hand, by lateral displacement, y , a lateral velocity v_y and lateral acceleration, y , which are zero at the start instant, T_s , and, on the other hand, the end, T_f , of the maneuver is characterized by a lateral displacement of 3.9 m, lateral velocity and acceleration are zero.

At the beginning of the maneuver $t = T_s$

Fig. 2 Maneuver planning using a quintic function [11]



$$\begin{cases} y|_{t=T_s} = 0 \\ \dot{y}|_{t=T_s} = 0 \\ y|_{t=T_s} = 0 \end{cases} \tag{3}$$

At the end of the maneuver $t = T_f$

$$\begin{cases} y|_{t=T_f} = -3.9 \\ \dot{y}|_{t=T_f} = 0 \\ y|_{t=T_f} = 0 \end{cases} \tag{4}$$

By using equations, 2, 3 and 4 the following system is defined:

$$\begin{bmatrix} T_s^5 & T_s^4 & T_s^3 & T_s^2 & T_s & 1 \\ 5T_s^4 & 4T_s^3 & 3T_s^2 & 2T_s & 1 & 0 \\ 20T_s^3 & 12T_s^2 & 6T_s & 2 & 0 & 0 \\ T_f^5 & T_f^4 & T_f^3 & T_f^2 & T_f & 1 \\ 5T_f^4 & 4T_f^3 & 3T_f^2 & 2T_f & 1 & 0 \\ 20T_f^3 & 12T_f^2 & 6T_f & 2 & 0 & 0 \end{bmatrix} \cdot \begin{bmatrix} a_5 \\ a_4 \\ a_3 \\ a_2 \\ a_1 \\ a_0 \end{bmatrix} = \begin{bmatrix} 0 \\ 0 \\ 0 \\ -3.9 \\ 0 \\ 0 \end{bmatrix} \tag{5}$$

By resolving the matrix system (5), the lateral trajectory, y_d , concerning this maneuver is extracted, hence the desired yaw angle, ψ_d , is obtained [6, 11].

$$\psi_d = \tan^{-1} \frac{\dot{y}_d}{\dot{x}_d} \approx \frac{\dot{y}_d}{V_x} \tag{6}$$

4 Higher-Order Sliding Mode Controller Applied for Guidance on a Quintic Type Path

Being among the most refined command in control theory the Sliding Mode Controller (SMC) is the object of different contribution, in order to ensure the best

tracking, for different nonlinear systems; autonomous vehicle [17], two-link robot [18], three-tank system [3], unmanned aerial vehicle [19], and others. The SMC consists to forcing the different trajectories of the system to converge towards a sliding surface in a finite time, due to a discontinuous function this convergence is maintained [20, 21]. Higher-Order Sliding Mode Controller (HOSMC), also known by the super-twisting algorithm, was designed to overcome the major disadvantages caused by SMC of order 1, such as chattering phenomenon [8, 21, 22, 23].

The dynamics of the system are described by the form:

$$\dot{X} = f(t, x) + g(t, x)U(t) \quad (7)$$

With g, f are two continuous functions.

Consider the error e , and s the sliding variable defined as follows:

$$\begin{cases} e = \psi(t) - \psi_d(t) \\ s(t) = \dot{e}(t) + \lambda e(t) \end{cases} \quad (8)$$

The derivative of the $s(t)$ expression is written on the form [8]:

$$\dot{s}(t, s) = \xi(t, s) + \zeta(t, s)U(t) \quad (9)$$

U is the control input of the system, which is a superimposition of two terms an equivalent, U_{eq} and the switching term U_{st}

$$U(t) = U_{eq}(t) + U_{st}(t) \quad (10)$$

The equivalent command U_{eq} is calculated by resolving $\dot{s}(t, s) = 0$.

$$U_{eq}(t) = -\frac{\xi(t, s)}{\zeta(t, s)} \quad (11)$$

The system meets the requirements below [8]:

$$\begin{cases} |U(t)| \leq U_{max} \\ |s(t)| < S_0 \\ \gamma_{min} \leq |\zeta(t, s)| \leq \gamma_{max} \\ |\xi(t, s)| < M_0 \end{cases} \quad (12)$$

where $S_0, U_{max}, \gamma_{min}, \gamma_{max}$ and M_0 are positive constants.

The expression super-twisting is given in the form [8]:

$$U_{st}(t) = U_1 + U_2 \quad (13)$$

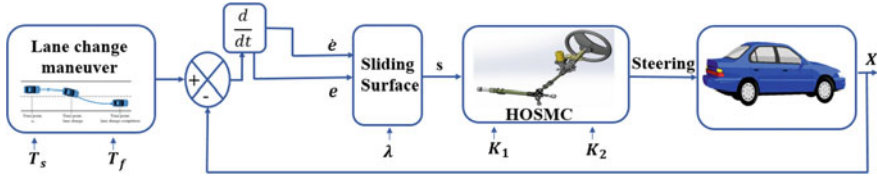


Fig. 3 The global schema

With U_1, U_2 are defined as follows [8]:

$$\begin{cases} U_1 = -K_1 |s|^\mu \text{sign}(s), \mu \in [0, \frac{1}{2}] \\ U_2 = -K_2 \text{sign}(s) \end{cases} \quad (14)$$

$$\begin{cases} K_1 \geq \left(\frac{4M_0(K_2\gamma_{max} + M_0)}{\gamma_{min}^2(\gamma_{min}K_2 - M_0)} \right)^{\frac{1}{2}} \\ K_2 > \frac{M_0}{\gamma_{min}} \end{cases} \quad (15)$$

With K_1, K_2 two positive constants ensure the conditions of inequality (15) [8, 22, 24].

According to the above, we write:

$$\begin{cases} \xi(t, s) = -\psi_d + \frac{C_{rlr} - C_{flf}}{I_z} \beta - \frac{C_{flf}l_f^2 + C_{rlr}l_r^2}{I_z V_x} \dot{\psi} + \lambda \dot{e} \\ \zeta(t, s) = \frac{I_z}{C_{flf}l_f} \end{cases} \quad (16)$$

Hence, the control law is written:

$$\delta(t) = -\frac{1}{\zeta(t, s)} \xi(t, s) - K_1 |s|^\mu \text{sign}(s) - K_2 \text{sign}(s) \quad (17)$$

The global diagram of our structure is shown in Fig. 3.

5 Results and Discussion

Simulation is performed on Matlab/Simulink using parameters (shown in table 1) related to the vehicle named DYNA which is a Peugeot 308 owned by Heudiasyc laboratory in France [21].

To evaluate the performance of the HOSMC, constructed in this paper, two simulation cases were considered. The first case is characterized by a constant vehicle speed of $V_x = 60\text{km/h}$, while the second is characterized by $V_x = 120\text{km/h}$. In both cases, we consider a maneuvers duration of 1 s ($T_s = 2\text{s}, T_f = 3\text{s}$) and 4 s ($T_s = 2\text{s}, T_f = 6\text{s}$).

Table 1 Nomenclatures and parameters of DYNA vehicle [8]

Parameter	Nomenclature	Value and unit
V_x and δ	Longitudinal speed and Steering angle	33.333 [m/s] and [rad]
ψ	Yaw angle	[rad]
β	Side slip angle	[rad]
y	Lateral displacement	[m]
C_f	Cornering stiffness of the front tire	170,550 [N/rad]
C_r	Cornering stiffness of the front tire	137,844 [N/rad]
l_f	Distance between front tire and vehicle gravity center	1.195 [m]
l_r	Distance between rear tire and vehicle gravity center	1.513 [m]
m	Mass of the DYNA vehicle	1719 [kg]
I_z	Moment of inertia	3300[kg.m ²]

It should be stressed that this simulation is made by the following values $\lambda = 20$, $\mu = \frac{1}{2}$.

In order to change lanes, for both cases. The controller is simulated for the two lengths ($T_f = 3$ s, $T_f = 6$ s). The results are presented, in Fig. 4 and Fig. 5, respectively, for the first case ($V_x = 60$ km/h) and the second ($V_x = 120$ km/h).

As shown in Fig. 4a before the start of the maneuver, the trajectory of the vehicle perfectly follows the desired path. After a distance traveled of 33.8 m, there is a slight variation from the reference path, which marks the beginning of the maneuver, for the situation with short maneuver time ($T_f = 3$), whereas in the situation with long maneuver time ($T_f = 6$), the vehicle follows the desired path completely. At the end of the maneuver, a tracking deviation for the short maneuver is noticed. However, in the long maneuver the tracking error is very small.

Figure 4b represents the tracking error for the yaw angle, which it can be seen there is a remarkable variation for the situation of $T_f = 3$, on the other hand, that of $T_f = 6$ represents a little variation not exceeding 0.025 rad, this result is confirmed in Fig. 4c which represents the yaw rate.

Being known as one of the elements that must always be kept at smaller values, the sideslip angle (shown in Fig. 4d) does not exceed 0.01 rad during the whole maneuver for $T_f = 6$ while the situation for $T_f = 3$, this angle exceeds 0.05 rad.

Figure 4e shows the lateral acceleration that reaches acceptable values for the long maneuver. Likewise for the second case with $V_x = 120$ km/h, illustrated in Fig. 5a–e it can be seen that for the short maneuver ($T_f = 3$), the yaw angle error, yaw rate, sideslip angle, and lateral acceleration are maximum with respect to the long maneuver, which is also resulted in [11].

Comparing the two cases ($V_x = 60$ km/h and $v_x = 120$ km/h), in the second case, the car has traveled a distance twice as long as that with a vehicle traveling at a speed of 60 km/h. In the situation of abrupt line change ($T_f = 3$), both cases show important variations.

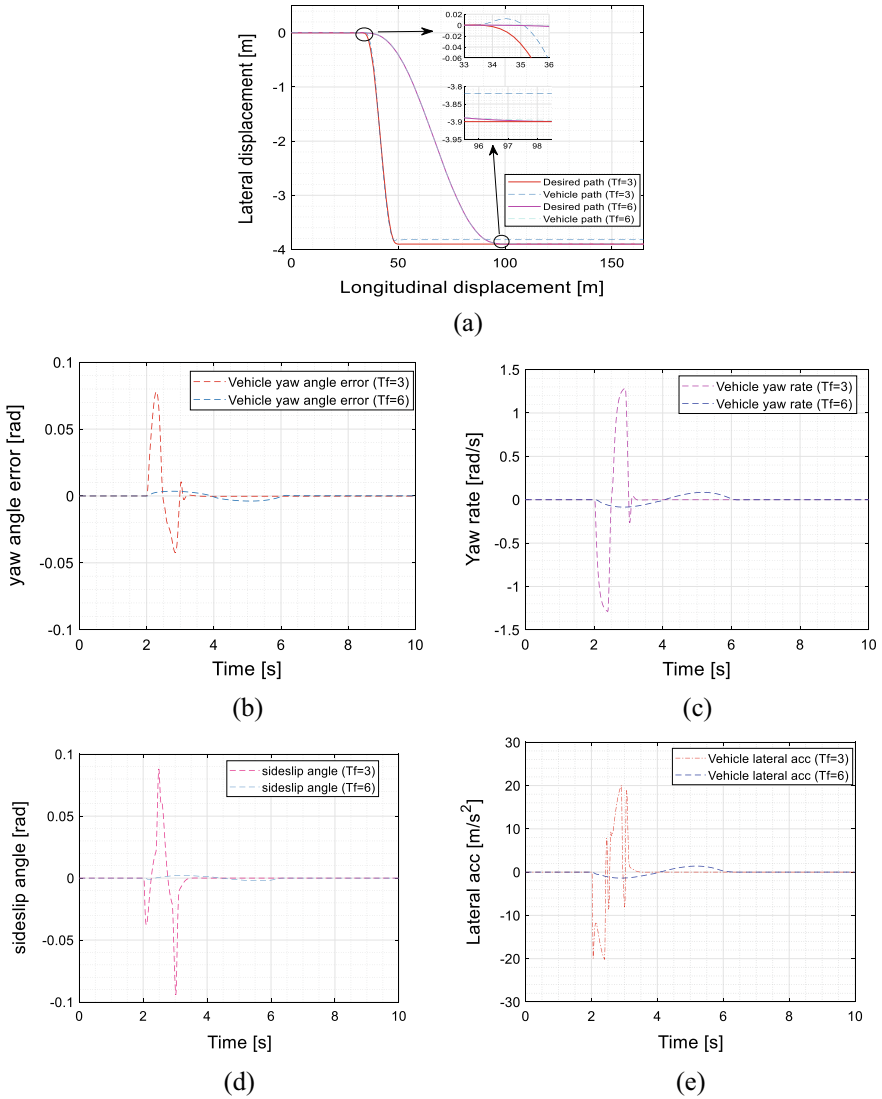


Fig. 4 The simulation results of longitudinal velocity of 60 km/h: **a** global tracking trajectory **b** yaw angle error **c** yaw rate **d** sideslip angle **e** lateral acceleration

Also, we observe in the long maneuver, Higher-order sliding mode controller ensures a better pursuit with a speed of $V_x = 120$ km / h than $V_x = 60$ km / h, the same results is obtained by [13] using a model predictive control.

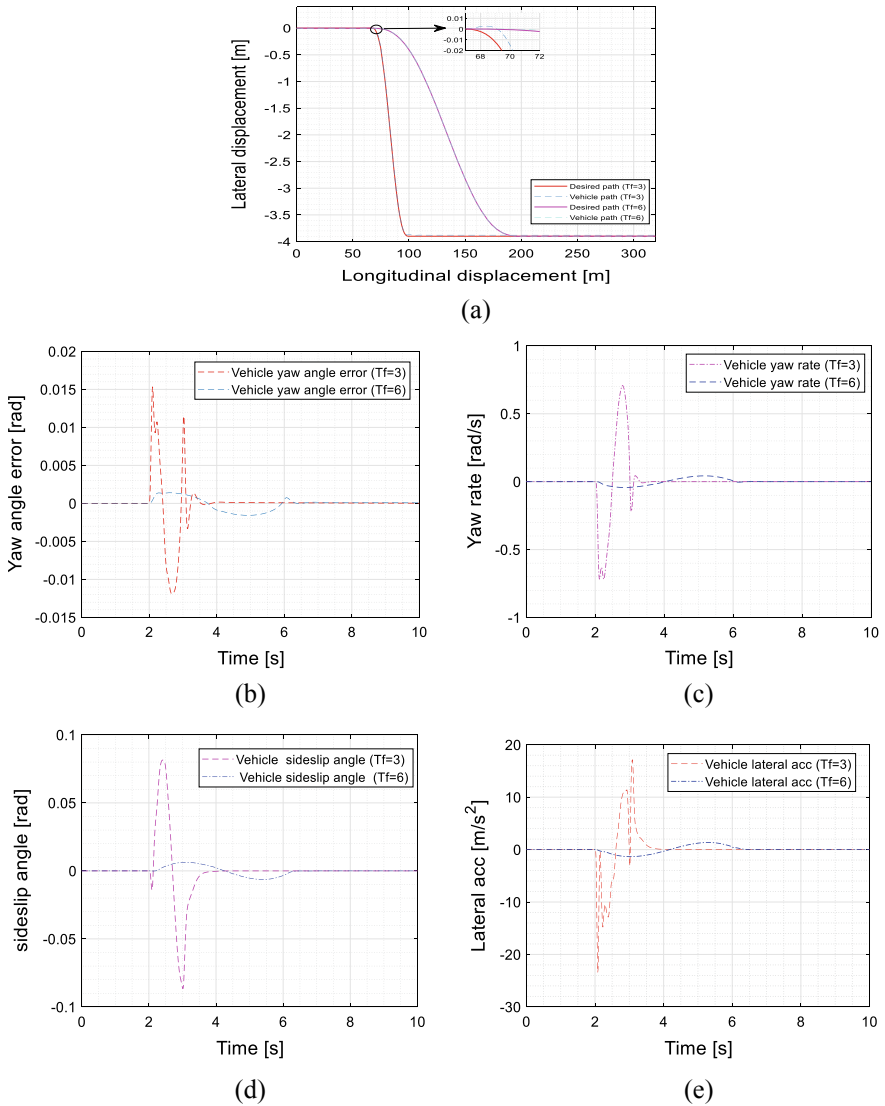


Fig. 5 The simulation results of longitudinal velocity of 120 km/h: **a** global tracking trajectory **b** yaw angle error **c** yaw rate **d** sideslip angle **e** lateral acceleration

6 Conclusion and Perspectives

Lateral stability is one of the important factors that must be ensured when driving at high speeds. In this context, this paper presented a control based on higher-order sliding mode applied to maintain the lateral stability of an autonomous vehicle.

Subsequently and as perspectives, we plan to design a control structure based on Nonsingular Fast Terminal Sliding-Mode able to stabilize the lateral dynamics of the vehicle.

References

1. Van Brummelen J, O'Brien M, Gruyer D, Najjaran H (2018) Autonomous vehicle perception: The technology of today and tomorrow. *Transportation Research Part C: Emerging Technologies* 89:384–406
2. Chehri A, Mouftah HT (2019) Autonomous vehicles in the sustainable cities, the beginning of a green adventure. *Sustainable Cities and Society*. 51:101751
3. Mellouli EM, Alfiidi M, Boumhidi I (2018) Fuzzy sliding mode control for three-tank system based on linear matrix inequality. *Int J Autom Control* 12:237–250
4. Hassani H, Mansouri A, Ahaitouf A (2019) Control system of a quadrotor UAV with an optimized backstepping controller. In: 2019 International Conference on Intelligent Systems and Advanced Computing Sciences (ISACS). pp 1–7 IEEE (2019)
5. Sharmin A, Wan R (2017) An autonomous lane-keeping ground vehicle control system for highway drive. Presented at the 9th International Conference on Robotic, Vision, Signal Processing and Power Applications
6. Rajamani R (2011) *Vehicle dynamics and control*. Springer Science & Business Media (2011)
7. Hajjami LE, Mellouli EM, Berrada M (2019) Optimal PID control of an autonomous vehicle using Butterfly Optimization Algorithm BOA. In: *Proceedings of the 4th International Conference on Big Data and Internet of Things*. p. Article 42. Association for Computing Machinery, Rabat, Morocco
8. Tagne G, Talj R, Charara A (2013) Higher-order sliding mode control for lateral dynamics of autonomous vehicles, with experimental validation. Presented at the 2013 IEEE Intelligent Vehicles Symposium (IV)
9. Haiying M, Chaopeng L (2017) Direct Yaw-Moment Control Based on Fuzzy Logic of Four Wheel Drive Vehicle under the Cross Wind. *Energy Procedia*. 105:2310–2316
10. Norouzi A, Masoumi M, Barari A, Farrokhpour Sani S (2019) Lateral control of an autonomous vehicle using integrated backstepping and sliding mode controller. *Proceedings of the Institution of Mechanical Engineers, Part K: Journal of Multi-Body Dynamics*. 233:141–151
11. Norouzi A, Kazemi R, Azadi S (2018) Vehicle lateral control in the presence of uncertainty for lane change maneuver using adaptive sliding mode control with fuzzy boundary layer. *Proceedings of the Institution of Mechanical Engineers, Part I: Journal of Systems and Control Engineering*. 232:12–28
12. Zainal Z, Rahiman W (2019) Effect of Yaw Rate and Sideslip to Lateral Vehicle Dynamic Stability. Presented at the 10th International Conference on Robotics, Vision, Signal Processing and Power Applications
13. Yoshida H, Shinohara S, Nagai M (2008) Lane change steering manoeuvre using model predictive control theory. *Vehicle System Dynamics*. 46:669–681
14. Šabanovič E, Žuraulis V, Prentkovskis O, Skrickij V (2020) Identification of road-surface type using deep neural networks for friction coefficient estimation. *Sensors* 20:612
15. Clarembaux LG, Pérez J, Gonzalez D, Nashashibi F (2016) Perception and control strategies for autonomous docking for electric freight vehicles. *Transportation Research Procedia*. 14:1516–1522
16. Samiee S, Azadi S, Kazemi R, Eichberger A (2016) Towards a decision-making algorithm for automatic lane change manoeuvre considering traffic dynamics. *PROMET-Traffic&Transportation* 28: 91–103 (2016)

17. El Hajjami L, Mellouli EM, Berrada M (2020) Neural Network Based Sliding Mode Lateral Control For Autonomous Vehicle. Presented at the 2020 1st International Conference on Innovative Research in Applied Science, Engineering and Technology (IRASET)
18. Naoual R, Mellouli EM, Sefriti S, Boumhidi I (2014) Fuzzy sliding mode control for the two-link robot. *Int J Syst Control Commun* 6:84–96
19. Hassani H, Mansouri A, Ahaitouf A (2020) Robust autonomous flight for quadrotor UAV based on adaptive nonsingular fast terminal sliding mode control. *Int J Dyn Control* 1–17
20. Utkin VI (2013) Sliding modes in control and optimization. Springer Science & Business Media
21. Tagne G, Talj R, Charara A (2015) Design and validation of a robust immersion and invariance controller for the lateral dynamics of intelligent vehicles. *Control Engineering Practice*. 40:81–92
22. Levant A (1993) Sliding order and sliding accuracy in sliding mode control. *Int J Control* 58:1247–1263
23. Hassani H, Mansouri A, Ahaitouf A (2020) A new robust adaptive sliding mode controller for quadrotor UAV flight. In: 2020 IEEE 2nd International Conference on Electronics, Control, Optimization and Computer Science (ICECOCS). IEEE, pp 1–6
24. Levant A (2010) Chattering analysis. *IEEE Trans Autom Control* 55:1380–1389

Integral Sliding Mode Control of Power Transfer in a Vehicle to Grid (V2G) Charging Station



Hicham Ben Sassi, Chakib Alaoui, Fatima Errahimi, and Najia Es-Sbai

Abstract Numerous overhauls are carried out to the electrical system in the last few years striving for more flexible and stable electric grid. Still, due to the continuous rise in demand in addition to the integration of new heavy loads such as EVs charging stations, this task is becoming more challenging. The conventional solutions include hydro storage stations and spinning reserves, be that as it may, the high cost of these solutions limits their use. As an alternative solution, vehicle to grid (V2G) offers the possibility to use the EV storage units to provide ancillary services to the grid. In this paper we propose a robust integral sliding mode (ISM) approach, to control the bidirectional power transfer in the V2G charging station. The proposed ISMC, controls the current flow in the bidirectional DC-DC converter, based on a reference signal derived from the grid power requirements. The robustness of the control scheme and its capability to respond to the desired performances were tested using different realistic scenarios. The obtained results demonstrated the effectiveness, stability, and tracking performances of the proposed controller compared to the conventional PID.

Keywords Integral sliding mode control · Vehicle to grid technology · DC fast charging station · Bidirectional power transfer

1 Introduction

The electrification of the transportation sector has gained a lot of attention in the last few years. By replacing combustion engine-based vehicles with plug-in hybrid electric vehicles (PHEV) and battery electric vehicles BEV, the greenhouse gas emission as well as fuel bells could dramatically be reduced. To help facilitate this transition, several countries offer incentives for zero- and low-emission vehicles,

H. Ben Sassi (✉) · F. Errahimi · N. Es-Sbai

Laboratory of Intelligent Systems, Georesources and Renewable Energies (LISGRE), Faculty of Sciences and Technology, Sidi Mohamed Ben Abdellah University, Fez, 2202 Fez, Box, Morocco
e-mail: hicham.bensassi@usmba.ac.ma

C. Alaoui
University EUROMED, Fez, Morocco

including exempting all EVs and hybrid EVs from taxes and customs in 2017 [1]. This approach led to an increase in the adoption of EVs and PHEVs worldwide surpassing 5.1 million units in 2018 [2]. Although this sharp increase in the numbers of EVs is beneficial and desirable from an ecological standpoint, it resulted in a continuous rise in electricity demand, thus negatively impacting the electrical grid. Furthermore, EV charging stations are considered as huge loads which, if not properly managed, could result in a voltage dip or in worst cases, disturbance to the grid [3]. In order to circumvent these issues, several strategies were proposed, and most of the authors agree that EVs must be included in the ancillary services provisions within the framework of smart grids [4]. EVs are promising candidates for this task, due to their interesting features, including significant storage capacity, and tolerance for frequent power fluctuations [5]. Initially, the integration of EVs to the grid has been investigated from different angles while considering EVs as just loads. From a control standpoint, a review on control and optimizing strategies for EV charging is presented in [6]. Striving to reduce the load on the grid during the peak demand hours, charging time scheduling is investigated in [7]. Moreover, aiming to reduce the burden of the EVs on a specific point in the grid, the correct choice of the charging station was investigated in [8], taking into consideration several criteria. Simultaneously, and as a result of the fluctuation output of many renewable energy sources (RES), The use of EVs for RES integration matching the time of production to the time of load has been explored in [9]. The idea of integrating fluctuating wind and PV sources, using hundreds of EVs with a charging power of 3.6 kW and 11 kW was also investigated in [10].

Despite the diversity of the above-mentioned solutions, they restrict the nature of ancillary services provided by the EV to the grid, by relying on unidirectional power flow. However, to better manage the production of different distributed energy sources, injecting power into the grid is often required. To achieve this, most advanced smart grids are equipped with storage systems to preserve the electricity excess and inject it back to the grid in case of a need. Nevertheless, the high cost of such storage systems limits their use. In this regard, V2G technology offers the possibility for EV to use their storage units not only as chargeable loads but also as dispatchable generators available to the grid operators if necessary. With the appropriate control strategy, a charging station can either provide or retract the power from the electrical grid depending on its status. In [11] The authors proposed five fuzzy logic controllers to integrate the V2G technology into a national electric system. The study underlines the impact of V2G on improving the grid voltage stability as well as the possibility of reactive power discharging instead of active power. The obtained results demonstrated that with the appropriate fuzzy controller the EVs were able to help with voltage stability alongside optimal charging of the EVs. The robustness characteristic of the sliding mode controllers (SMC) was explored in [12], where an adaptive sliding mode technique is adopted to control the power transfer of a bidirectional SEPIC-Zeta converter.

In this paper, we propose the integral sliding mode (ISM) approach to control the bidirectional power transfer between a V2G charging station and an EV. Unlike the conventional sliding mode control approaches [13], the ISM control eliminates

the reaching phase while benefiting from the robustness of the sliding mode, thus resulting in faster convergence time [14, 15].

The proposed ISMC approach is applied to a buck-boost two-switch converter, of a DC fast charging station. The choice of DC charger over an AC charger is due to the power limitations of level 1 and 2 AC chargers. On the other hand, the power output of DC chargers could only be limited by the ability of the batteries to accept the charging power. Therefore, making them more suitable, since the power transfer rate in the V2G charging station may vary significantly depending on the nature of ancillary services required by the grid, and on the power demand from the EV battery pack.

The layout of the rest of this paper is given as follows. Section 2 introduces the vehicle to grid technology. Followed by modeling of the bidirectional converter in Sect. 3. While in Sect. 4, the integral sliding mode controller (ISMC) and its design process are detailed. Finally, simulation results and their discussion are presented in Sect. 5, followed by a conclusion.

2 Vehicle to Grid (V2G)

Vehicle-to-grid is an emerging technology whose objective is to better integrate EVs into power systems, by their incorporation in the energy management scheme of the electrical grid. This technology relies on bidirectional power transfer instead of the classical unidirectional charge of the EV batteries [16]. When parked, an EV or an EV fleet will either consume electricity or provide the energy back to the grid. This is inspired by recent development in EVs batteries, alongside the fact that EVs are designed to operate in a frequent power fluctuation due to the nature of roadway driving.

The two-way power exchange, either from or to the vehicle, is achieved via a set of power electronic converters piloted by a robust control strategy [17]. The real-time control signals take into account the grid requirements and the EV battery state of charge (SOC) [18]. Within the framework of V2G, EVs can help balance the peak demand and peak supply, better integrate fluctuating renewable energy sources as well as provide frequency and voltage regulation. As a result, it has become the centre of interest amongst academics. In [19], different electrical and electronic components required to achieve effective implementation of V2G are presented. While [20] investigates the benefits of using the V2G as a scheme to ensure the best integration of EVs into the smart grids. Furthermore, it introduces different optimization technics deployed with the intent of benefiting the most from this technology. The ecological aspect of this technology is confirmed in [21], where the amount of greenhouse gas savings by using V2G with large scale wind power systems, were proven to be much less than the additional emissions from thermal electricity plants dedicated to electric vehicles charging.

Concerns regarding battery degradation, while using V2G, were also addressed in [22]. The authors investigated several studies in the literature about the impact of

frequent power extraction on the battery and concluded that, with the proper control scheme, this will no longer be an issue.

3 Bidirectional Buck-Boost 2sw Converter

In order to satisfy the bidirectional power transfer requirement of the V2G technology, the buck-boost 2sw converter in Fig. 1 operates in two modes, which directly depend on the grid power requirements and the EV battery SOC [18]. In case of an energy excess in the grid, coupled with the need to recharge the vehicle, the converter operates in buck mode, stepping down the voltage from the dc bus into a more suitable level to charge the EV battery. On the other hand, in case the grid is in need of ancillary services, and if sufficient energy is available in the EV's battery, the converter operates in boost mode. In this case, the converter steps up the voltage from the EV battery to match that of the DC bus, suitable to be injected into the grid using a bidirectional DC-AC inverter.

The dynamic state-space equations of the converter in Fig. 1 are obtained based on an analysis of the ON and OFF switching states.

Boost Mode:

$$V_{Sw1} = (1 - S_{w1})V_{dc} \tag{1}$$

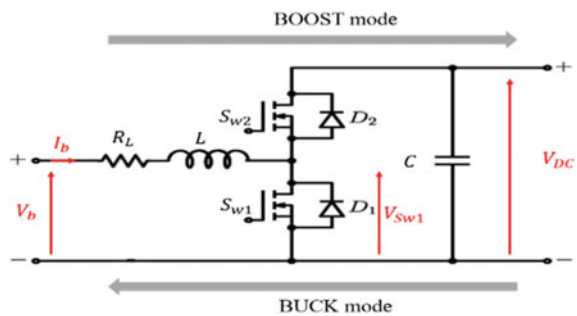
$$\frac{di_b}{dt} = -\frac{R_L i_b}{L} + \frac{V_b}{L} - \frac{V_{sw1}}{L} \tag{2}$$

$$\frac{dV_{dc}}{dt} = -(1 - S_{w1})\frac{V_{dc}}{L} - \frac{R_L i_b}{L} + \frac{V_b}{L} \tag{3}$$

$$\frac{dV_{dc}}{dt} = \frac{i_{dc}}{C} = \frac{i_b(1 - S_{w1})}{C} \tag{4}$$

Buck mode

Fig. 1 2sw buck-boost converter



$$V_{Sw1} = S_{w2} V_{dc} \quad (5)$$

$$\frac{di_b}{dt} = -S_{w2} \frac{V_{dc}}{L} - \frac{R_L i_b}{L} + \frac{V_b}{L} \quad (6)$$

$$\frac{dV_{dc}}{dt} = S_{w2} \frac{i_b}{C} \quad (7)$$

The nonlinear averaged state-space representation of the converter is obtained as follows:

$$\begin{pmatrix} \dot{x}_1 \\ \dot{x}_2 \end{pmatrix} = \begin{pmatrix} \frac{di_b}{dt} \\ \frac{dV_{dc}}{dt} \end{pmatrix} = \begin{pmatrix} \frac{-R_L}{L} & -\frac{K(1-S_{w1})+(1-K)S_{w2}}{L} \\ \frac{K(1-S_{w1})+(1-K)S_{w2}}{C} & 0 \end{pmatrix} \begin{pmatrix} i_b \\ V_{dc} \end{pmatrix} + \begin{pmatrix} \frac{1}{L} \\ 0 \end{pmatrix} V_b \quad (8)$$

$$\text{Let } S_{WG} = K(1 - S_{w1}) + (1 - K)S_{w2}$$

$$\begin{pmatrix} \dot{x}_1 \\ \dot{x}_2 \end{pmatrix} = \begin{pmatrix} \frac{di_b}{dt} \\ \frac{dV_{dc}}{dt} \end{pmatrix} = \begin{pmatrix} \frac{-R_L}{L} - \frac{S_{WG}}{L} \\ \frac{S_{WG}}{C} & 0 \end{pmatrix} \begin{pmatrix} i_b \\ V_{dc} \end{pmatrix} + \begin{pmatrix} \frac{1}{L} \\ 0 \end{pmatrix} V_b \quad (9)$$

where d represents the bounded modeling uncertainties. It is selected to account for uncertainties of 10% magnitude in the model parameters, including R_L , L and C

4 Integral Sliding Mode Control

Due to its robustness against modeling uncertainties, external disturbance, and system parameter variation, the sliding mode stands out from other control approaches such as PID. As a result, a groundswell of research activity is devoted to SMC, and it is widely adopted in several fields including electric vehicle's motion and drive control, drones and aviation, robotics, and wind turbines. Furthermore, SMC is favorable for power converters since they are generally governed by transistors which are operated as switching devices with two operating modes "ON and OFF" [23].

Similar to SMC, the ISMC generates discontinuous control signals that impose on the system to slide on a predefined sliding surface (S), in which the system stability is guaranteed. However, unlike the SMC this sliding surface contains an integral term that eliminates the reaching phase. As a result, the design process can be described in tow main steps [24]: Initially, the integral sliding path generally referred to as the switching function (S) is designed. This defines the desired dynamics and the surface on which the sliding motion will tack place. Followed by the design of a control law that makes the dynamics (S) attractive to the system state, and always ensures that the direction of motion is towards the predefined dynamics (S) [25].

Been that the goal is to control the power transfer via the charge/discharge current, the appropriate sliding surface is given in Eq. (10).

$$S = (e) + \Pi \int_0^t e dt \quad (10)$$

$$e = x_1 - I_{bref} \quad (11)$$

where x_1 represents the measured current of the battery, and e is the error between the desired and the measured current. In the sliding mode theory, the control law must always appear in the first derivative of the sliding path S , which is verified in the following equation.

$$\dot{S} = \dot{x}_1 + \Pi(x_1 - I_{bref}) \quad (12)$$

$$\dot{S} = -S_{WG} \frac{V_{dc}}{L} + x_1(\Pi - \frac{R_L}{L}) + \frac{V_b}{L} - K I_{bref} \quad (13)$$

The control law that can attract and maintain the system states on the sliding surface S is partitioned into two parts and designed as follows.

$$u = S_{WG} = u_{eq} + u_n \quad (14)$$

The objective of the equivalent control u_{eq} is to make the feedback system insensitive to disturbances once on the sliding surface. As a result, it is designed to cancel the effect of the measurable parameters on the system, hence devoting the discontinuous control u_n to robustness against uncertainties and external disturbances. The value of u_{eq} is derived using the existing condition of a sliding motion ($\dot{S} = 0$).

$$\dot{S} = 0 \Leftrightarrow \dot{S} = -u_{eq} \frac{V_{dc}}{L} + x_1 \left(\Pi - \frac{R_L}{L} \right) + \frac{V_b}{L} - \Pi I_{bref} = 0 \quad (15)$$

$$u_{eq} = \frac{L}{V_{dc}} \left(x_1 \left(\Pi - \frac{R_l}{L} \right) - \Pi I_{bref} + \frac{V_b}{L} \right) \quad (16)$$

The second part of the control law (u_n) is designed to guarantee a sliding motion on the integral sliding surface (S) regardless of the uncertainties, therefore ensuring controller stability. Based on the Lyapunov stability theory the controller is asymptotically stable if the derivative of the positive definite Lyapunov function presented in Eq. (17) is negative ($\dot{V} < 0$).

$$V = \frac{1}{2} S^2 \quad (17)$$

The time derivative of V is given as follows

$$\dot{V} = \dot{S}S = S(-u_{eq} \frac{V_{dc}}{L} - u_n \frac{V_{dc}}{L} + \left(\Pi - \frac{R_L}{L}\right)x_1 + \frac{V_b}{L} - \Pi I_{bref} + d) \quad (18)$$

In order to guarantee a finite time asymptotic convergence, the stability condition becomes $\dot{V} < -K|S|$. Henceforward, the control u_n that can fulfill this condition is designed by replacing u_{eq} with its value given in Eq. (16).

$$\dot{V} = S\left(-u_n \frac{V_{dc}}{L} + d\right) \quad (19)$$

where

$$u_n = K \text{sign}(S) \quad (20)$$

$$\dot{V} < 0 \ll \Rightarrow K > d \frac{L}{V_{dc}} \quad (21)$$

The global ISMC control law that will be fed to the PWM signal generator is obtained by adding Eq. (16) and Eq. (20).

$$u_{12} = \frac{L}{V_{dc}} \left(\left(\Pi - \frac{R_L}{L} \right) x_1 + \frac{V_b}{L} - \Pi I_{bref} \right) + K \text{sign}(S) \quad (22)$$

5 Simulation Results and Discussion

For performance validation, the 270 km autonomy Nissan leaf electric vehicle is considered. This EV model is equipped with a bidirectional charger dedicated to the V2G technology using CHAdeMO charging standard. The Nissan leaf Battery pack voltage is 360 V [26], while the DC bus voltage is set to 500 V. The values of the other parameters are presented in the Table 1. Using such configuration for the V2G charging station the power transfer can reach up to 50 KW (+100A, -100A).

Table 1 Simulation parameters

Parameter	Value
Nissan leaf battery capacity	40 kwh
Capacitor	12,000 μ F
Inductance	9e-3 H
Inductance R_L	50 m Ω
Switching frequency	25 KHz

Initially, the required power by the grid is communicated to the charging station as illustrated in Fig. 2a. The reference power profile is selected so as to mimic different possible scenarios encountered within the framework of the V2G. This includes charging the EV which is modeled with negative power demand, as well as power injecting mode which is modeled with positive power demand. Based on the required power, the charging station derives the current profile in Fig. 2 b, used as a reference for the integral sliding mode control of the bidirectional 2sw DC/DC converter.

Secondly, the EV's battery SOC is supervised in real-time by the charging station, in order to prevent any damage to the battery by an overcharging or over-discharging. Furthermore, the SOC is monitored to assure that the EV has enough charge to be driven at any time, even when delivering power to the grid. If sufficient energy is available the charging station enables the bidirectional power transfer to tack place, otherwise, the power transfer is disabled. On average, EVs are used on daily trips of 30 km [27] which in the case of the Nissan leaf corresponds to about 15% SOC. However, knowing that operating the EV at low levels of SOC is harmful to the battery, in this paper the SOC limit is set to 30%.

Based on the reference current profile above, the ISMC generates a switching control signal which is fed to the PWM signal generator. The generated switching signals Sw1 and Sw2 used to control the two transistors are presented in Fig. 3. The performances of the proposed control strategy are illustrated in Fig. 4, 5, and 6.

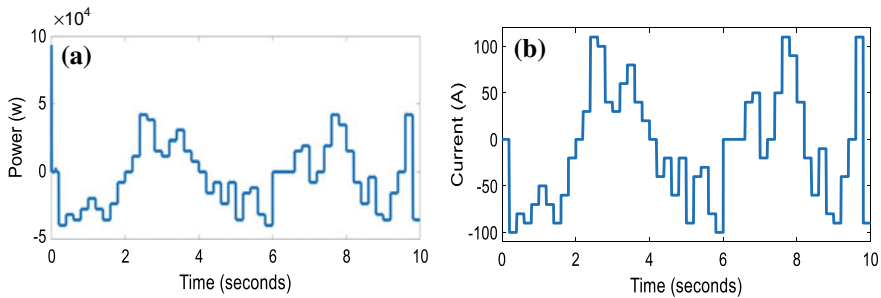


Fig. 2 a Required power by the grid. b Reference current

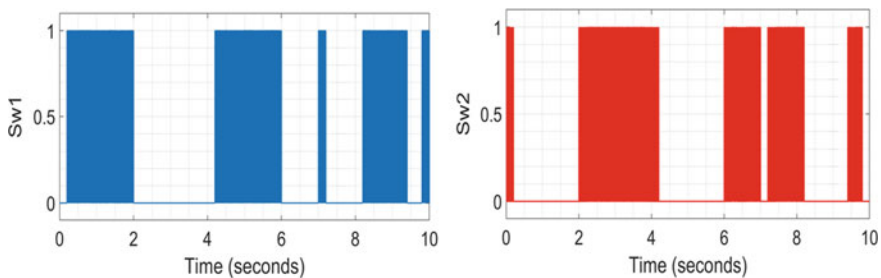


Fig. 3 PWM control signals Sw1 and Sw2

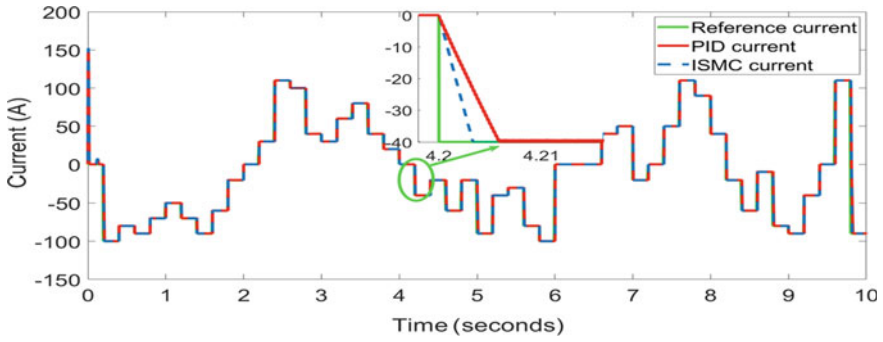


Fig. 4 Reference current and the battery charge/discharge current

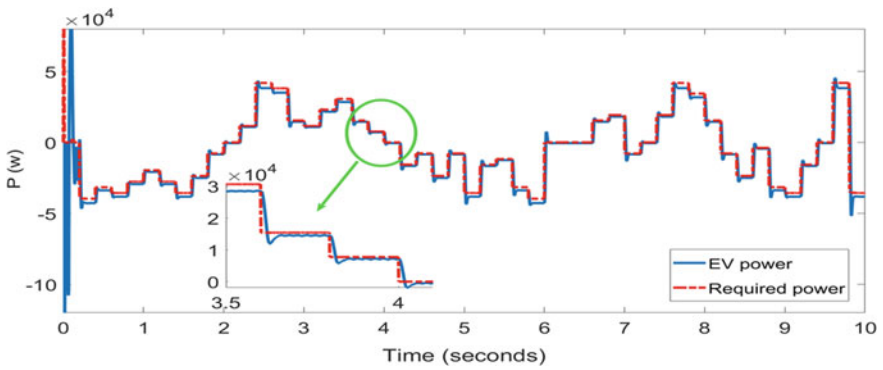


Fig. 5 Grid required power and the delivered power by the EV

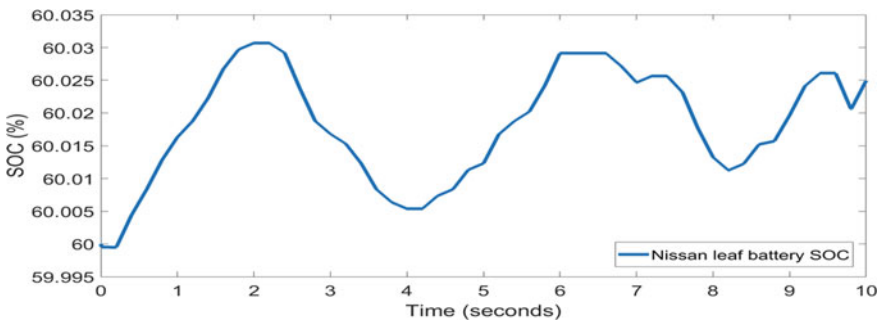


Fig. 6 Battery pack state of charge

Based on the results of Fig. 4. It is clear that the ISMC charging/discharging current tracks with great precision and zero steady-state error the reference current derived from the required power. Furthermore, the convergence speed of the ISMC is satisfactory compared to that of the conventional PID. Henceforward, the EV transferred power in Fig. 5, follows with good accuracy the reference profile provided by the grid regardless of its quick variations. This shows the robustness of the ISMC in controlling the bidirectional converter under both operation modes. The variation of the EV battery SOC during the power transfer is illustrated in Fig. 6. It is clear that the battery still operates in the safe zone generally defined between 30 and 90% state of charge.

6 Conclusion

V2G technology offers the possibility for EVs to provide ancillary services to the electric grid. In this paper, the authors proposed an integral sliding mode approach to control the bidirectional power transfer between the EV and the grid. The V2G charging station extracted the reference current profile from the required power communicated by the grid. The authors then adopted the ISMC to control the power transfer using a bidirectional DC/DC converter. The ISMC demonstrated great tracking performance, and robustness against bounded modeling uncertainties and fast-changing currents. This resulted in stable power output that matches the references provided by the grid.

References

1. “Les nouvelles technologies de la mobilité urbain” green mobility forum Marrakech 2018.: <https://www.iresen.org>. Last accessed 27 June 2020
2. IEA (2019), Global EV Outlook 2019, IEA, Paris <https://www.iea.org/reports/global-ev-outlook-2019>. last accessed 2020/06/27
3. Clement-Nyns K, Haesen E, Driesen J (2010) The Impact of Charging Plug-In Hybrid Electric Vehicles on a Residential Distribution Grid. *IEEE Trans Power Syst* 25(1):371–380
4. Dileep G (2020) A survey on smart grid technologies and applications. *Renewable Energy* 146:2589–2625
5. Tie SF, Tan CW (2013) A review of energy sources and energy management system in electric vehicles. *Renew Sustain Energy Rev* 20:82–102
6. Faddel S, Al-Awami ID AT, Mohammed OA (2018) Charge Control and Operation of Electric Vehicles in Power Grids: A Review. *Energies* 11, 701. <https://doi.org/10.3390/en11040701>
7. Khaki B, Chu C, Gadh R (2019) Hierarchical distributed framework for EV charging scheduling using exchange problem. *Appl Energy*, 241:461–471 1
8. Cao Y, Ahmad N, Kaiwartya O, Puturs G, Khalid M (2018) Intelligent transportation systems enabled ICT framework for electric vehicle charging in smart city. In: Maheswaran M, Badidi E (eds) *Handbook of Smart Cities*. Springer, Cham
9. Kempton W (2005) Vehicle-to-grid power implementation: From stabilizing the grid to supporting large-scale renewable energy. *J Power Sources* 144:280–294

10. Schuller A, Flath CM, Gottwalt S (2015) Quantifying load flexibility of electric vehicles for renewable energy Integration. *Applied Energy* 151:335–344
11. Ali mofleh ali alshogheathri.: vehicle-to-grid (V2G) integration with the power grid using a fuzzy logic controller. department of electrical engineering. college of engineering kansa state university manhattan, kansas. <https://hdl.handle.net/2097/20606>. Last accessed 27 June 2020
12. Gayen PK, Roy Chowdhury P, Dhara PK (2019) An improved dynamic performance of bidirectional SEPIC-Zeta converter-based battery energy storage system using adaptive sliding mode control technique. *Electric Power Systems Research*, vol 160, pp 348–361
13. Alsmadi YM, Utkin V, Xu L (2018) Sliding Mode Control Design Procedure for Power Electronic Converters Used in Energy Conversion Systems. In: Clempner J., Yu W. (eds) *New Perspectives and Applications of Modern Control Theory*. Springer, Cham
14. Souvik Das, Mohd Salim Qureshi, Pankaj Swarnkar.: Design of integral sliding mode control for DC-DC converters. *Materials Today: Proceedings* 5 (2018) 4290–4298
15. Vadim Utkin, Jingxin Shi.: Integral Sliding Mode in Systems Operating under Uncertainty Conditions. *Proceedings of the 35th Conference on Decision and Control Kobe, Japan December 1996*.
16. Sassi HB, Errahimi F, Essbai N, Alaoui C (2019) V2G and Wireless V2G cocepts: State of the Art and Current Challenges. In: 2019 International Conference on Wireless Technologies, Embedded and Intelligent Systems (WITS), Fez, Morocco, pp 1–5.
17. Garcés Quílez M, Abdel-Monem M, El Baghdadi M, Yang Y, Van Mierlo J, Hegazy O (2018) Modelling, Analysis and Performance Evaluation of Power Conversion Unit in G2V/V2G Application—A Review. *Energies* 11:1082
18. Sassi HB, Errahimi F, Najia Es-sbai, Alaoui C (2019) Comparative study of ANN/KF for on-board SOC estimation for vehicular applications. *J Energy Storage* 25:100822
19. Sharma A, Sharmab S (2019) Review of power electronics in vehicle-to-grid systems. *J Energy Storage* 21 (2019) 337–361
20. Tan KM, Ramachandaramurthy VK, Yong JY (2016) Integration of electric vehicles in smart grid: A review on vehicle to grid technologies and optimization techniques. *Renew Sustain Energy Rev* 53: 720–732
21. Zhao Y, Noori M, Tatari O (2017) Boosting the adoption and the reliability of renewable energy sources: Mitigating the large-scale wind power intermittency through vehicle to grid technology. *Energy* vol 120, pp 608–618
22. Uddin K, Dubarry M, Glick MB (2018) The viability of vehicle-to-grid operations from a battery technology and policy perspective. *Energy Policy* 113 (2018): 342–347
23. Mohan N, Undeland TM (2007) *Power Electronics: Converters, Applications, and Design*. Wiley, New York
24. Bessas A, Benalia A, Boudjema F (2016) Integral Sliding Mode Control for Trajectory Tracking of Wheeled Mobile Robot in Presence of Uncertainties. *Hindawi Publishing Corporation Journal of Control Science and Engineering* vol 2016, Article ID 7915375, p 10
25. Utkin VI (2008) *Sliding Mode Control: Mathematical Tools, Design and Applications*. In: Nistri P, Stefani G (eds) *Nonlinear and Optimal Control Theory. Lecture Notes in Mathematics*, vol 1932. Springer, Berlin, Heidelberg
26. <https://www.nissanusa.com/vehicles/electric-cars/leaf/features/range-charging-battery.html>. Last accessed 26 June 2020
27. Chahdi A, Rahmouni B, Aniba B (2017) Socio-economic Analysis of Electric Vehicles in Morocco. *Energy Procedia* 141:644–653

Design and Analysis of an Integrated Class-D Power Output Stage in a 130 nm SOI-BCD Technology



Mustapha El Alaoui, Karim El khadiri, Ahmed Tahiri, and Hassan Qjidaa

Abstract In this work, a design and analysis of an integrated class-D power output stage in 130 nm SOI-BCD technology is will be described. An output stage with two NMOS transistors is used for economize cost and area. A bootstrap circuit is important to affording the gate overdrive voltage of the NMOS transistor, especially in tall-current gate drivers with great transistors, it is mush large for integration. The proposed class-D power output stage utilizes an on-chip bootstrap circuit with integrated bootstrap capacitor. The class-D power output stage achieving a total root-mean-square (RMS) output power of 0.2 W, a THD + N (total harmonic distortion + noise) at the 8- Ω load less than 0.06%, and a power efficiency of 93%. The final design occupies approximately 1.25 mm².

Keywords Output stage · Class-D audio · Gate driver · Level shifter · Bootstrap circuit · SOI technology

1 Introduction

In recent years, high power class-D amplifiers get norm in lot of consumer electronic applications as home-theatre systems and television sets. Now, the class-D makes a prudent entry into the automotive field. The design defiance for automotive engineers is to sustain and ameliorate the low distortion and the tall audio amplification levels. The audio performance of the new class-D amplifiers match or higher to the conventional class-AB amplifiers. A decrease heat sink size, rise output power and

M. El Alaoui (✉) · H. Qjidaa

Laboratory of Computer Science, Signals, Automation and Cognitivism (LISAC), Department of Physics, Faculty of Sciences Dhar El Mahraz, Sidi Mohamed Ben Abdellah University, Fez, Morocco

e-mail: Mustapha.elalaoui@usmba.ac.ma

K. El khadiri · A. Tahiri

Laboratory of Computer Science and Interdisciplinary Physics, Sidi Mohamed Ben Abdellah University, ENS- Fez, Fez, Morocco

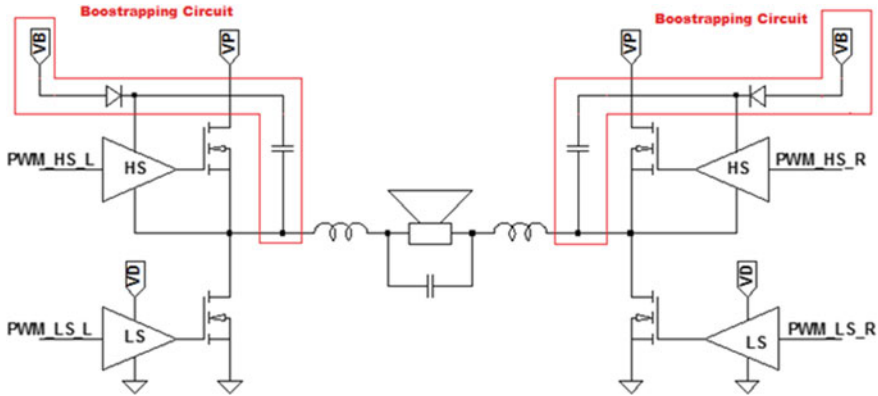


Fig. 1 A pair of NMOS totem pole output stages used for class-D audio amplifier

spread battery life can be exploited from high efficiency and nether distortion. Class-D amplifiers toward automotive applications and consumer are characteristically fabricated in high-voltage technologies [1].

Figure 1 shows the full and half decks. In smart power integrated circuits, the full and half decks are the more common switching output outlines. The output transistors are name L-S-Driver (low side driver) or H-S-Driver (high side driver), according to their position with the estimate of the power supply path, in both cases. The H-S-Driver is an N-MOS in Totem pole output stage and the L-S-Driver can be another N-MOS with its body and source to ground.

The bootstrap circuits are necessary to supply gate drive voltages greater than VP. The bootstrap capacitor (Cboot) is frequently implemented like discreet component cause of its size for delivering the tall charge amounts [2, 3]. In this paper, an output stage with two NMOS transistors is proposed using a bootstrap circuit with high voltage charge storing for economize cost and area.

The SOI technology is perfect to accomplish the electromagnetic immunity (EMI) and the problem of dead-time, this is because of the isolation of all components via an oxide. In the device substrate there is none charge accumulated when an output falls under ground that avoids crosstalk with other channels and decrease the reverse recovery time.

The first thing in the integrated design is the choice of an appropriate technology. The roughly inescapable choice for class-D audio amplifiers is an A-BCD process. The SOI technology provides advantages contrast to JI technology in the tall voltage integrated circuit of the automotive application [4, 5].

The rest of this paper will be organized as follows. Methods to optimize these power output stages will be introduced in Sect. 2. Section 3 reports and discusses the simulation results of the optimized power output stage. And finally Sect 4 concludes this paper.

2 Class-D Power Stage Design and Analysis

Figure 2 shows the structure of the Class-D whose core is made up of the power stage. The latter consists of DMOS power transistors in the formation of a totem column as high side switch and a low side switch [6–9]. The Gate driver (G-D) of the low side DMOS transistor ML uses a supply voltage VDD. The exterior bootstrap capacitor Cboot is utilized as supply for the high-side G-D, it connected among Vpwm and Vboot. When the Vpwm turns to the low side via a diode Dboot connected to VDD, the Cboot is recharged. For bootstrap supply, a linear regulator is used which equally offset the voltage drop of Dboot. The signal Vpwm_in is translated by the dead-time generator block to suitable signals for the low-side G-D and high-side G-D. The communication between the dead-time generator block and the high-side G-D and low-side G-D quires a robust level shifter (L-S).

2.1 Low-Side Gate Driver Design

The G-D is a power amplifier that from a controller IC agree a low-power input and make the suit high-current G-D for a power MOSFET. It must sink current and source to draw requested V_{gs} . A G-D is utilized when a pulse width- modulation (PWM) controller cannot furnish the output current required to conduct the gate capacitance of the MOSFET. To rise the current control of the latter stage of the driver an architecture be composed of narrow buffers was thus selected, via a row scaling of the transistor area of every stage [10]. The architecture of the L-S-Driver is show in Fig. 3, such as N is the number of stages, k is the taper factor and C_{min} is the input capacitance.

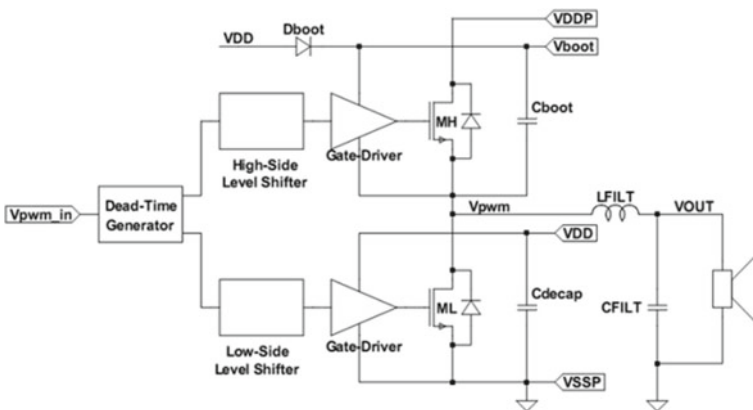


Fig. 2 Topology of the typical class-D power stage

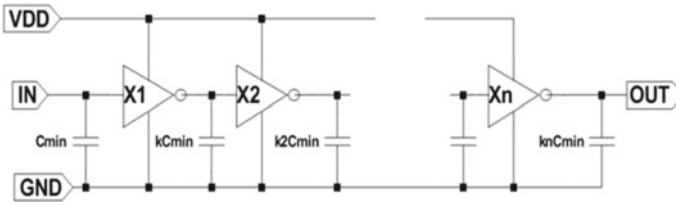


Fig. 3 The architecture of the low-side driver

Theoretically, to reduce the propagation delay of the G-D circuit, the transistors in the chain of inverters should be sized according to Eq. 1.

$$K^n = \frac{C_{out}}{C_{in}} \tag{1}$$

The power dissipation of inverter chain G-D, shown in Fig. 3, can be found from:

$$P = f_{sw} \cdot V_{dd}^2 \cdot \left(\frac{k^n - 1}{k - n} \right) \cdot (C_{in} - C_{out}) \tag{2}$$

With f_{sw} switching frequency.

The simulation results of the input and output voltage are shown in the Fig. 4.

The green curve: Input voltage of the L-S-Driver (V).

The blue curve: Output voltage of the L-S-Driver (V).

The red curve: Input voltage of the H-S-Driver (V).

The pale blue curve: Output voltage of the H-S-Driver (V).

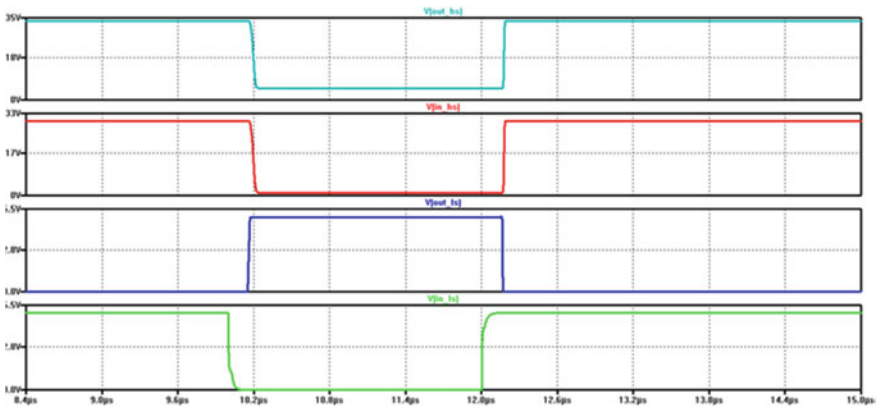


Fig. 4 Simulation results of the input and output L-S-Driver

2.2 High-Side Gate Driver Design

The H-S-Driver consists of a tapered buffer and an L-S as illustrated in Fig. 5. It's designed according to the same process used for the L-S driver. The L-S (level shifter) is utilized to keep track Vboot1, which can rock to Vsup to reaches 30 V and prove the Voutput to 5 V under Vboot1, who matches to the maximum Vgs voltage of The MH transistor (high-side DMOS transistor).

Figure 6 illustrate a schematic of L-S, which composes of a latch for rapid switching and two branches of transistors first the M2-M4-M6 transistors and second the M1-M3-M5 transistors. Also to transfer on/off input from a low level to a level maximal than hundreds of volts, a couple of level-shifting servo (M3 transistor and M4 transistor) are used.

They run by alternately working for a short period, that making a short current pulsation to flow from high side to low side, that way the suitable set and reset gates of the latch circuit are operated. In the high voltage and high frequency, the conduction damages of M3 transistor and M4 transistor can be considerable, which is determined by equation:

$$P_{\text{levelshifter}} = 2 \cdot V_{ds} \cdot I_{\text{pulse}} \cdot t_{\text{pulse}} \cdot f_{\text{sw}} \tag{3}$$

I_{pulse} : the pulse current.

t_{pulse} : the pulse current period.

V_{ds} : the drain-source voltage.

The drain-source voltage is the voltage through a drain and source of the L-S transistors. When V_{ds} reaches a value of VDDP, the superior power dissipation

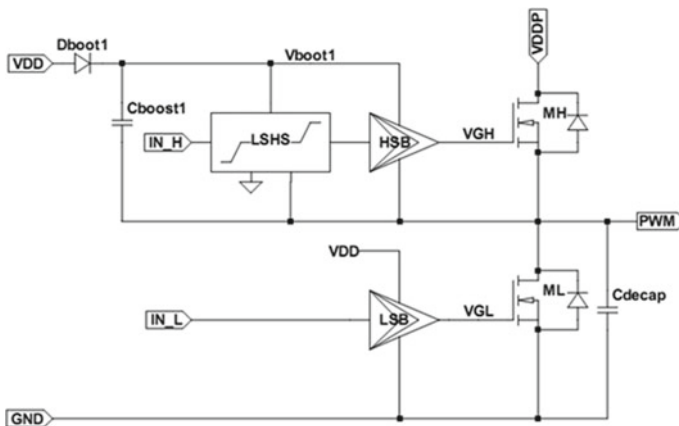


Fig. 5 The architecture of the high-side driver

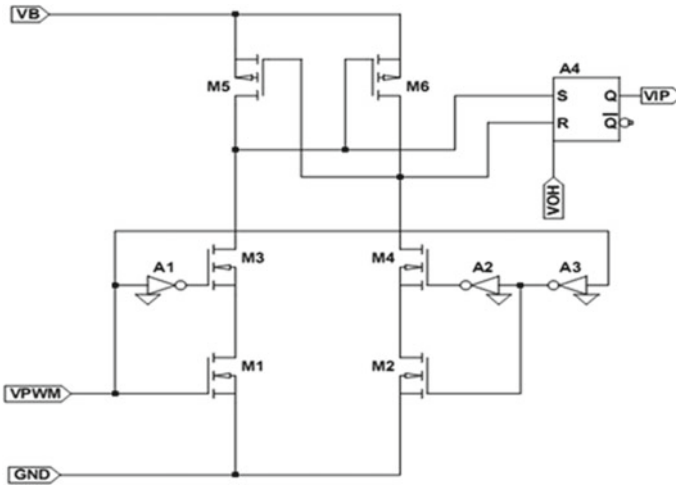


Fig. 6 Schematic of the L-S

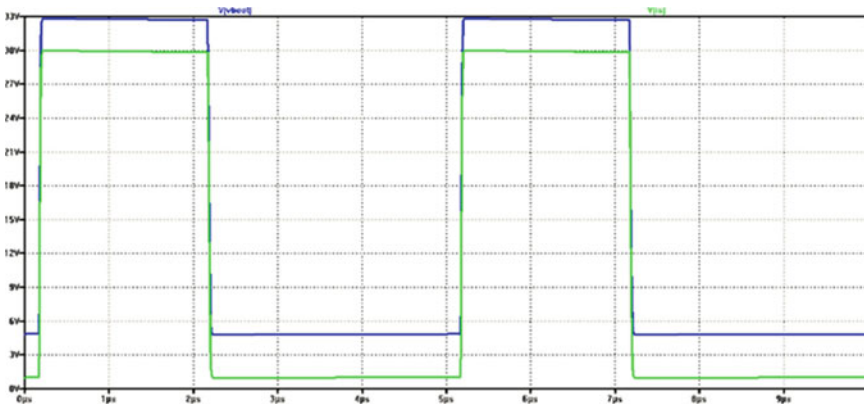


Fig. 7 The transient simulation of the H-S-Driver at 200 kHz

happens. The transient simulation of the H-S-Driver at 200 kHz for various values of the VDDH is illustrated in Fig. 7.

2.3 Proposed Bootstrap Circuit

The conventional bootstrap circuit consisting of an internal diode Dboot1 and an external capacitor Cboot1 is shown in Fig. 5. The driver is become off and the node PWM is clamp to GND by MLS transistor when INPWM is weak and $IN = 0\text{ V}$.

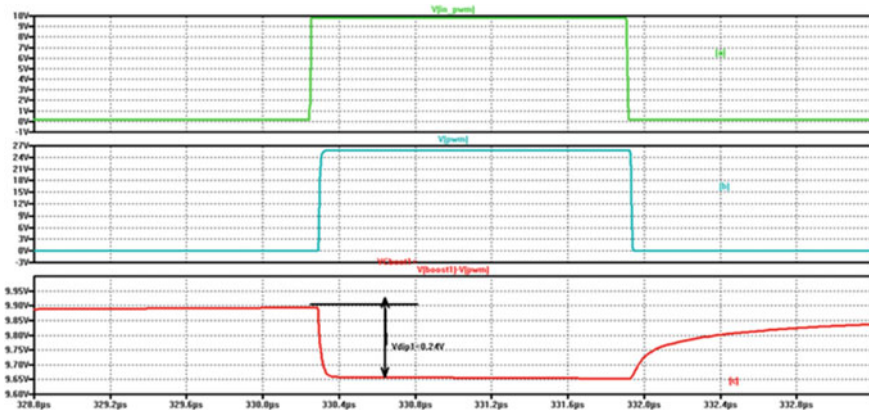


Fig. 8 The transient simulation of the conventional bootstrap circuit

Representing waveforms are illustrated in Fig. 8a, b. Cboot1 is charged by VDD to reaches 5 V less the voltage of Dboot1 that illustrated in Fig. 8c. The MH transistor is turned on and the ML transistor is turned off by the HSB (High side buffer) and the L-S signal INPWM and by tuning IN in high value, respectively. The node PWM elevates to VDDP, whilst Dboot1 arresting discharging Cboot1 to VDD. 30 V is a typical value for VDDP that provide the gate charge for the power transistor. After the discharge process a voltage drop at Cboot1 as illustrated in Fig. 8c. The available charge from Cboot1 to achieve Vdip1 voltage drop in VCboot1, Which is determined by the equation:

$$Q_{tot} = C_{boot1} \cdot V_{dip1} \tag{4}$$

The Cboot is so large for integration, for that a new bootstrap circuit is proposed to save area, which is illustrated in Fig. 9. The proposed bootstrap circuit uses a

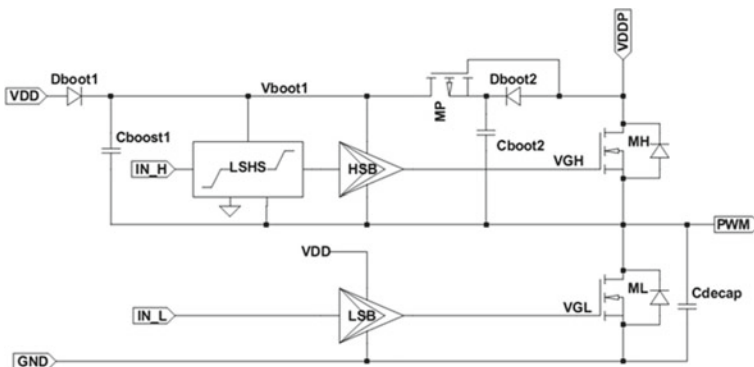


Fig. 9 Proposed bootstrap circuit

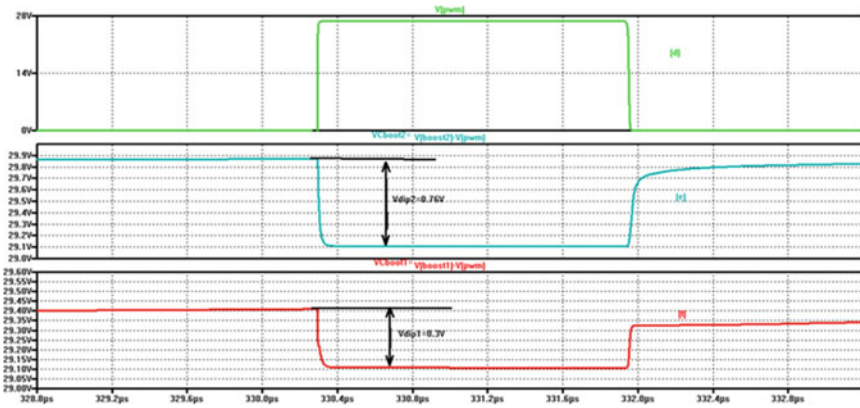


Fig. 10 The transient simulation of the proposed bootstrap circuit

Cboot2 in addendum to a conventional bootstrap circuit. As illustrated in Fig. 10d, the Cboot2 attached in parallel to the conventional Cboot1 is charged by a higher voltage than the Cboot1. When the node VPWM rises as show in Fig. 10e, Dboot2 prevents the current from Cboot2 to VDDP which leads discharged to the driving MP. In first order it discharges from values of VCboot2 to VDD (Fig. 10f). The smaller Cboot1 is used, because of high voltage swing results in a large quantity of charge. The area is saved until with the addendum of Cboot2.

The proposed bootstrap circuit is collected easily to conventional bootstrap circuit. The VDDP-VFDboot2 acquired when the Cboot2 is charged to VCboot2,o. The VFDboot2 represent the fore voltage of Dboot2. The VDD-VFDboot1 acquired when the Cboot2 is charged to VCboot1,o. Cboot2 is discharged to Cboot1 then to the gate node of MH then to the circuits provided via VCboot1. A charge equilibrium Cboot1, Cboot2 and each extra load capacitance is achieved.

For the sizing of Cboot1 and Cboot2 some, the total charge can be determined by equation:

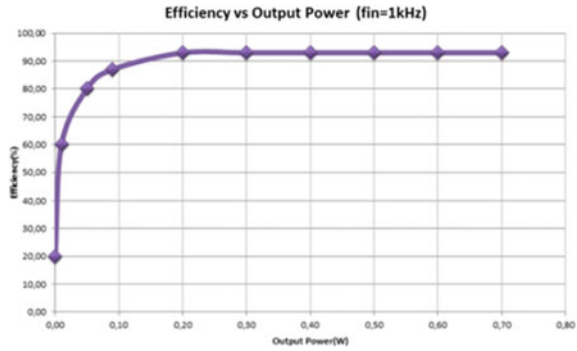
$$Q_{tot} = \alpha C_{boot1} \cdot V_{dip1} + \beta C_{boot2} \cdot V_{dip2} \tag{5}$$

The scaling operators of Cboot1 and Cboot2 are α and β . They are superior than 1 for a positive capacitance tolerance and they are lower than 1 for a negative capacitance tolerance.

2.4 Simulation Results

The main performances to achieve are efficiency, output power, THD + N and Layout.

Fig. 11 Efficiency versus power



2.5 Power Efficiency

Figure 11 illustrated the power efficiency of the proposed class-D which achieving a power efficiency equal 93% for an 8 Ω load at the output power 0.2 W.

The output stage is consists of four power transistors to drive a large load. Also a turn on resistance (Ron) will affect circuit efficiency. We minimize a CMOS Ron for reducing the conduction damages. 3.5mW is the switching loss value of the power stage. The optimizing of the power efficiency is determined via equation:

$$\rho = \frac{P_{out}}{P_{out} + P_s + P_c + P_r} \tag{6}$$

P_s, P_r, P_c, P_{out} are represent the output power at the load.

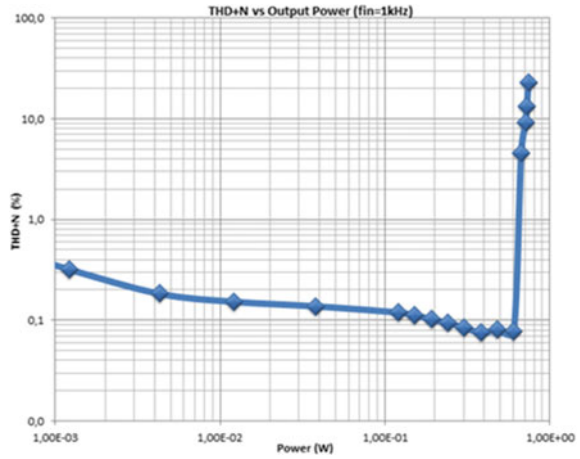
2.6 THD + N

The THD is defined as the proportion of total of all harmonics power within the audio band to the essential signal power. The THD itself is given by Eq. (7).

$$\%THD = \frac{\sqrt{(H_2^2 + H_3^2 + H_4^2 + \dots + H_i^2)}}{\sqrt{(H_1^2 + H_2^2 + H_3^2 + H_4^2 \dots + H_i^2)}} \times 100 \tag{7}$$

where H1 is the power level at the essential frequency and H2...Hi are indicate the power levels at the harmonics. The THD + N values for various values of the output power are illustrated in Fig. 12.

Fig. 12 THD + N versus output power



2.7 Layout

The design was achieved by respecting the designer constraints information (constraint straint manager, matchCat, text...) and the design rules (DRM, MRC and Density). All devices or circuits exposed to bring about electromagnetic interference are ringed with dual layer guard rings. Figure 13 illustrates the layout of the proposed class-D amplifier, the total area of our proposed Class-D is only 1.25 mm².

Table 1 shows a comparison and results of the proposed Class-D and other works.

Fig. 13 Layout of the proposed class-D

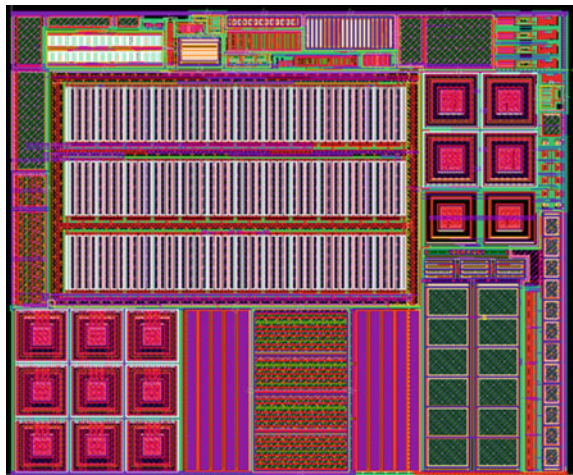


Table 1 Performance comparisons for 1 kHz Input

Design	Ref. [11]	Ref. [12]	This work
Technology	0.35 um-SOI	0.14 um-SOI	0.13 um-SOI
Supply Voltage (V)	60	80	30
THD + N (%)	0.017	0.03	0.006
Power efficiency (%)	90	94	93
Dead-time (ns)	70	90	50
Die Size (mm ²)	22	****	1.25

3 Conclusion

The proposed Class-D have been successfully designed and implemented in 130 nm SOI- BCD technology. The improvement of the performance of class-D amplifier is achieved. The bootstrap circuit was easily modified to the proposed solution by putting the new circuit parts in parallel. The general thought is the major bootstrap capacitor propped by another Cboot, which is charged to ensure high charge and high voltage when the driver is running. The proposed class-D achieving a power efficiency equal 93% for an 8 Ω load at the output power 0.2 W, high quality audio rendering with a THD + N of 0.06%. The total area of our proposed Class-D is only 1.25mm². The automotive applications is one of applications can use this proposed Class-D chip because of has excellent features.

References

1. Shi LF, Jia WG (2014) Mode-selectable high-efficiency low-quiescent-current synchronous buck DC-DC converter. *IEEE Trans Indus Electron* 61(5):2278–2285, May 2014. <https://doi.org/10.1109/TIE.2013.2267697>
2. Wessels P et al (2007) Advanced BCD technology for automotive audio and power applications. *Solid-State Electron* 51(2):195–211. <https://doi.org/10.1016/j.sse.2007.01.019>
3. van der Pol JA, et al (2000) A-BCD: An economic 100 V RESURF silicon-on-insulator BCD technology for consumer and automotive applications. In: 12th International Symposium on Power Semiconductor Devices & ICs. Proceedings (Cat. No.00CH37094), IEEE, 22–25 May 2000. <https://doi.org/10.1109/ISPSD.2000.856836>.
4. Swanenberg MJ, Ludikhuizen AW, Grakist A (2003) Applying DMOSTs, diodes and thyristors above and below substrate in thin layer SOI. In: Proceedings of ISPSD '03. 2003 IEEE 15th international symposium on power semiconductor devices and ICs, 2003, pp 14–17. <https://doi.org/10.1109/ISPSD.2003.1225271>
5. Fairchild Semiconductor Corporation (2008) Design Guide for Selection of Bootstrap Components, ser", Application Note AN-9052, October 2008
6. Huque MA, Vijayaraghavan R, Zhang M, Blalock B, Tolbert L, Islam S (2007) An soi-based high voltage, high-temperature gate-driver for sic fet. In: Power electronics specialists conference, 2007, PESC2007. IEEE, June 2007, pp 1491–1495. <https://doi.org/10.1109/PESC.2007.4342215>

7. Comer DJ (1996) A theoretical design basis for minimizing CMOS fixed taper buffer area. *IEEE J Solid-State Circuits* 31(6):865–868. <https://doi.org/10.1109/4.509876>
8. El Khadiri K, Qjidaa H (2013) Low noise, high PSR low-dropout regulator for low-cost portable electronics. In: 2013 ACS International Conference on Computer Systems and Applications (AICCSA), pp 1–5, 27–30 May 2013. <https://doi.org/10.1109/AICCSA.2013.6616415>
9. El Khadiri K, Qjidaa H (2015) design of class-d audio power amplifiers in 130nm soi-bcd technology for automotive applications. *WSEAS Trans Circuits Syst.* 14:192–200
10. El Khadiri K, Qjidaa H (2016) Design of a gate driver for a class-D audio output stage with break before-make in 130 nm SOI-BCD technology. *J Low Power Electron* 12:361–367
11. Berkhout M (2003) An integrated 200-W class-D audio amplifier. *IEEE J Solid-State Circuits* 38(7):1198–1206. <https://doi.org/10.1109/JSSC.2003.813238>
12. Ma H, Zee RVD, Nauta B (2014) Design and analysis of a high-efficiency high-voltage class-D power output stage. *IEEE J Solid-State Circuits* 49(7), July 2014. <https://doi.org/10.1109/JSSC.2014.2317780>

Digital Implementation of SPWM 7-Level Inverter Using Microcontroller



Hajar Chadli, Youssef Bikrat, Sara Chadli , Mohammed Saber ,
Amine Fakir, and Abdelwahed Tahani

Abstract Currently, green energy is knowing a massive growth in the world with the growth of newer energy sources such as wind energy, hydro energy, tidal energy geothermal energy, biomass energy and of Corse the Solar energy which is considered the second biggest source of electricity worldwide including morocco. The production of electricity via these centrals requires optimization at the different conversion levels. To obtain electricity that meets the standards of the electrical grid (sine wave of frequency 50 Hz), the inverter remains the first element to design and build. The structures based on multi-level inverters have brought an undeniable advantage to alternative continuous conversion, especially in high power applications. In this article a new 7-level inverter architecture with only six switches is presented and compared along with the other seven level inverter topologies. To improve the performance of our proposed multilevel inverter, we used a digital sinusoidal Pulse Width Modulation (SPWM) strategy using the Arduino wich leads to further reduction of THD. In this paper, the inverter was tested using Proteus software and Matlab Simulink simulator for harmonic analysis. Then real-time implementation of inverter was tested for a resistive load.

H. Chadli (✉) · Y. Bikrat · S. Chadli · A. Fakir · A. Tahani
Sciences Faculty, Laboratory LSE, Université Mohammed Premier Oujda, Oujda, Morocco
e-mail: chad.hajar@gmail.com

Y. Bikrat
e-mail: y.bikrat@ump.ac.ma

S. Chadli
e-mail: chad.saraa@gmail.com

A. Fakir
e-mail: fakir.amine@ump.ac.ma

A. Tahani
e-mail: wtahani@yahoo.fr

M. Saber
Laboratory SmartICT, ENSAO, Université Mohammed Premier Oujda, Oujda, Morocco
e-mail: m.saber@ump.ac.ma

Keywords Inverter · 7-level inverter · Sinusoidal Pulse Width Modulation (SPWM)

1 Introduction

In the last years, the use of photovoltaic energy has increased exponentially in the world. This development is boosted by international and national policies which aim to reduce the use of fossil fuels according to the objectives of the Kyoto Protocol [1]. For example, in Morocco, the government has implemented several measures to develop the photovoltaic industry. These aids are intended to make the PV (Photovoltaic) industry economically viable and competitive with fossil fuels. The recent development of the photovoltaic (PV) system has motivated researchers to improve the electrical energy conversion systems, and because of that multi-level inverter technology has become a very important alternative in the field of energy control in high power of medium voltage.

A multi-level inverter is a static converter ensuring the conversion of electrical energy from the continuous DC output of PV module to the alternative AC voltage.

The concept of using inverters with multiple voltage levels was presented by a MIT researcher some 30 years ago [2–4]. Nowadays, in the areas of medium and high power [2, 5], multi-level converters, with natural or hybrid topologies, present options which have been widely proved. Multilevel inverters offer more advantages: good quality of the output voltage with reduced harmonic distortion compared to a conventional inverter. However, this technique requires the use of a greater number of power semiconductors, this can make the general system more expensive and complex.

Three converter topologies have been considered to have commercial potential [6]: cascaded H-bridge converters with separate continuous sources, neutral clamped converters, flying capacitor converters. These three topologies use various mechanisms to generate the required output. In the first topology CMLI, we have simply series connection of several single-phase H-bridge inverters with galvanic isolated DC voltage sources, although, in flying capacitor topology, floating capacitors are used.

At [7], the author proposed a 7-level MLI uses 9 switches, minimizing 3 switches from the conventional structure of cascaded MLI [3]. It gives well results by generating desired 7-level output waveform with low THD. Afterward, a 7 level MLI using 7 switches lessening 2 more switches is presented in [8], from the precedent topology.

In order to minimize the number of switches, the number of DC sources and minimizing complexity of the multi-level inverter, the new topology is proposed using only 6 switches and 3 dc sources for 7 levels.

The main purpose of this paper is to develop, simulate and real-time implement a new 7-level converter structure with six switches, this inverter is controlled by a digital SPWM command in order to decreases the total harmonic distortion rate. In

Sect. 2 the design of the proposed inverter is presented as well as SPWM technic used. Section 3 presents the simulation of the inverter in ISIS Proteus and Matlab Simulink, a long with a comparative analysis between the proposed 7-level inverter and the existing 7-level inverter topologies. Section 4 presents a hardware results and finally conclusion is summarized in Sect. 5.

2 Proposed 7-Level Inverter

2.1 Design of Multilevel Inverter structure

The purpose of this architecture is to provide a simple structure of conception, reduce the complexity of control technique, reduce the cost of circuit building, and the total harmonic distortion. As shown in Fig. 1, the proposed 7-level inverter contains three voltage sources ($E_1, E_2 = 2E_1, E_3 = 3E_1$), six switches (K1, K2, K3, K4, K5 and K6) and two diodes D1, D2 to ensure the seven level of our system.

Table 1 indicates the value of output voltages for the different states of K1, K2, K3, K4, K5 and K6 switches.

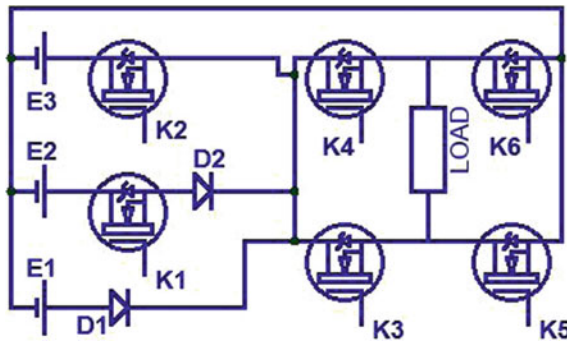


Fig. 1 Proposed 7 level inverter

Table 1 Switching sequence for simplified 7 level inverter

V_s	D1	K1	K2	K3	K4	K5	K6
+E1	Conduct	0	0	1	0	0	1
+E2	Blocked	1	0	1	0	0	1
+E3	Blocked	0	1	1	0	0	1
-E1	Conduct	0	0	0	1	1	0
-E2	Blocked	1	0	0	1	1	0
-E3	Blocked	0	1	0	1	1	0
0	X	X	X	X	X	1	1

2.2 Sinusoidal Pulse Width Modulation (SPWM)

Sinusoidal Pulse Width Modulation (SPWM) technique is used to control the output voltage of inverter by changing the duty cycles of pulses. SPWM technique is widely used in power converters because of its simplicity and strong control technique [9]. Standardly, SPWM is produced by comparing a reference sinusoidal signal of required frequency and a carrier triangular signal of high frequency (in serval KHz).

Conventionally, SPWM uses N-1 carrier signals to produce the output voltage of the N-level inverter. In our case to generate the switching pulses of the proposed 7-level inverter, we compared six carrier signals to a reference sine waveform of 50 Hz frequency, as shown in Fig. 2.

To produce the SPWM signals we chose to utilize a digital technology to escape the inconveniences of analog circuits. In our case we used the Arduino microcontroller ATmega2560 to produce the six SPWM signals by varying the duty cycles of PWM according to a sine lookup table whose frequency “ $f_r = 50 \text{ Hz}$ ” is the intended frequency of sinusoidal signal obtained at the output of the inverter.

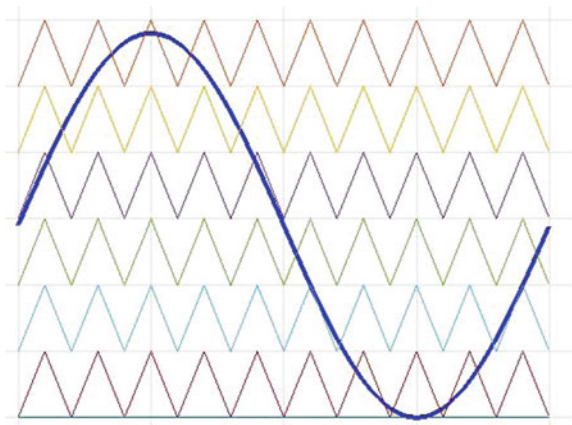
Generally, SPWM is generated for one half cycle and it can be used for both positive and negative cycle. In this case the time period desired for half cycle is 10 ms and second half cycle remain zero. For the Switching frequency we used a PWM frequency of “ $f_c = 31,250 \text{ KHz}$ ”.

To complete the half cycle time (180°) of reference signal, the number of pulses of carrier signal (N_p) needed is given by Eq. (1) and the incremental step (I_s) of sine signal in degrees is given by Eq. (2).

$$N_p = \frac{f_c}{2f_r} = 314 \text{ pulses} \tag{1}$$

$$I_s = \frac{180}{314} \tag{2}$$

Fig. 2 Proposed 7 level inverter



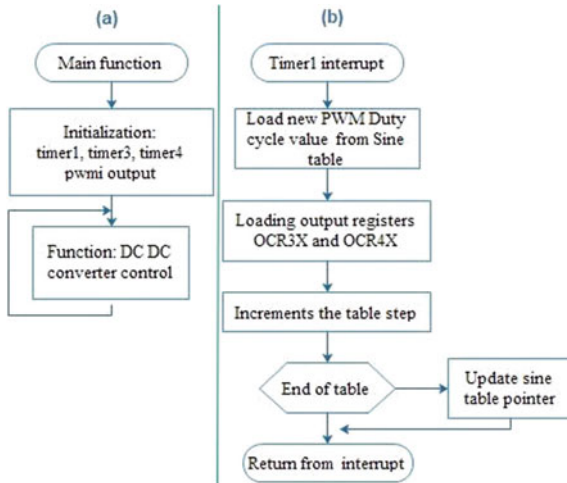


Fig. 3 SPWM flow chart

To convert the 314 values of the sine look up table into duty cycle we multiplied them with total time period of PWM.

To generated the six SPWM signals as mentioned before we used Arduino ATmega that/which has 15 PWM outputs and 6 timers which can be used to modified the frequency via its registers. We have configured timer 2 to generate interruption every 32 μs and timers 3 and 4 in way to set the frequency of PWMs outputs at 31,255 KHz. The program flowchart that has been implemented in microcontroller is presented in Fig. 3. Figure 3a presents the main function in which the PWMs outputs and the timer are initialized alongside other function. Figure 3b shows the interrupt function that is generated every 32μs by timer 1 in which the sine look up table is declared and each time the interrupt occurs a new value of duty cycle is picked up from the sine look up table. For the positive half cycle (0–10 ms) the 3 registers OCR3A, OCR3B and OCR3C will be loaded with the duty cycle values to generate SPWM1, SPWM2 and SPWM3 respectively. For the other half cycle (10–20 ms) the registers OCRA4, OCR4B and OCR4C will be loaded to generate SPWM4, SPWM5 and SPWM6 respectively.

3 Simulation and Results of Proposed Inverter

3.1 Simulation in ISIS PROTEUS and Matlab Simulink

The block diagram of the proposed inverter is illustrated in Fig. 4.

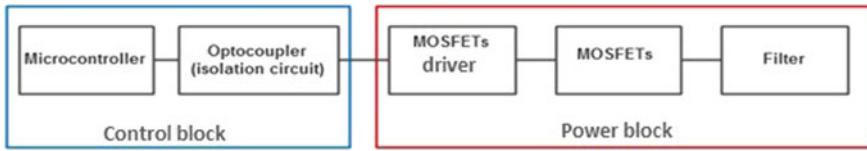


Fig. 4 Block diagram of the proposed inverter

As shown in the above figure the system consist of Arduino microcontroller ATmega2560 used to produce six SPWMs signal, then the gating signals for the six MOSFET switches of the inverter are generated using logic combination of the SPWM signals. The isolation circuit is provided by high speed optocouplers to completely isolate the low power part i-e microcontroller and the high power part that consist of six MOSFETs switches, those switches are used to convert the applied DC voltage to AC voltage. And to ensure that the MOSFETs will trigger we used MOSFET driver designed for bootstrap operation, then LC filter is used to reduce harmonic and obtain pure sine wave output at desired frequency of 50 Hz.

The simulations of 7 level inverter are developed by implementing the circuit diagram shown in Fig. 5 using ISIS PROTEUS.

3.2 Result Analysis

The simulation results at the output at every stage of inverter are shown in Figs. 6 and 7.

For harmonic analyses, the percentage of total harmonic distortion (THD) is determined using Matlab Simulink. As results, we have THD = 16.03% before filtering Fig. 8 and THD = 0.34% after filtering Fig. 9.

3.3 Comparison and Discussion

The comparison of the proposed topology with the other existing topologies based on the number of switches, total harmonic distortion (THD) and number of DC sources is presented in Table 2. As shown in the table, the new 7-level inverter architecture provides a pure sinusoidal voltage with very lower THD using few components compared to conventional and others topologies.

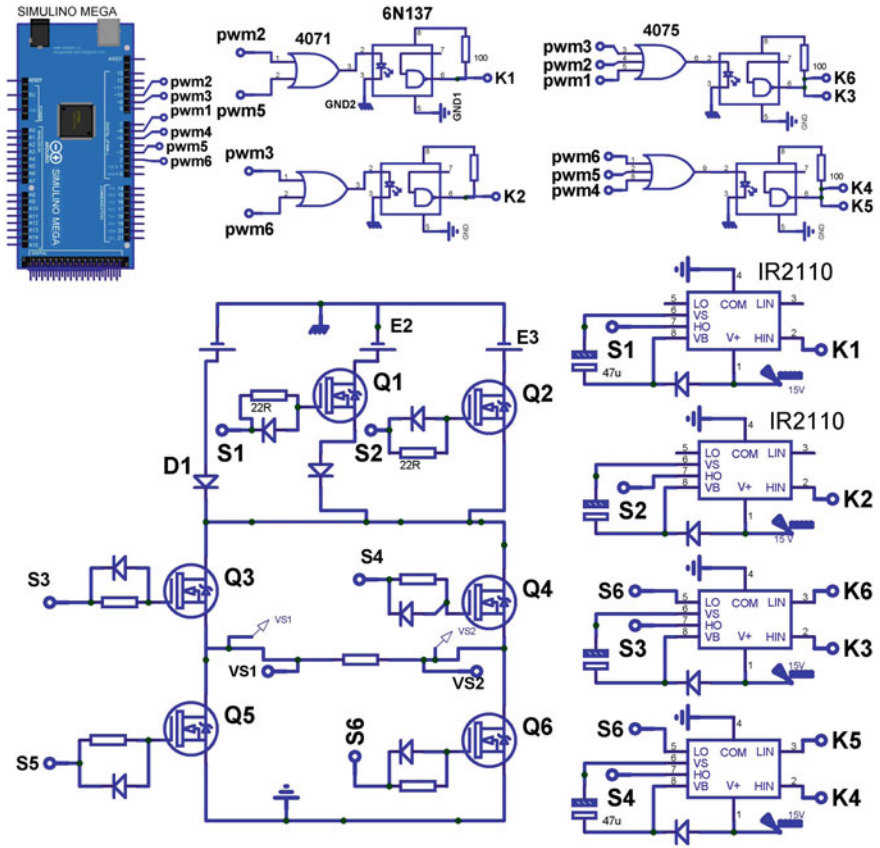
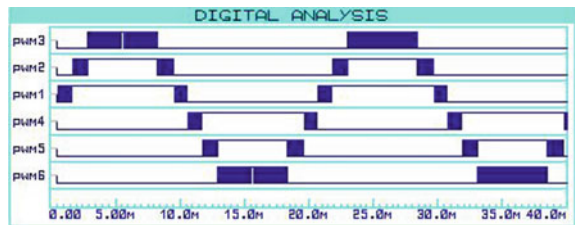


Fig. 5 Circuit diagram of proposed inverter

Fig. 6 SPWM signals generated by the microcontroller



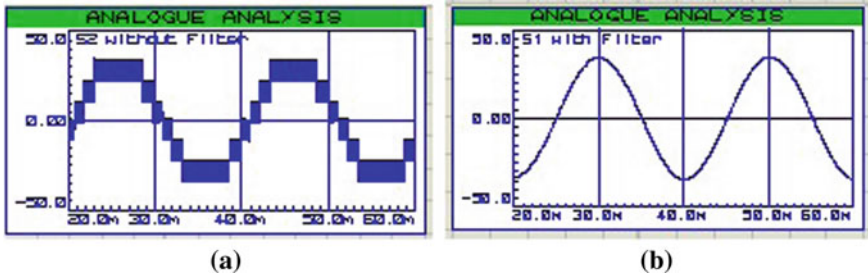


Fig. 7 a Output waveform of SPWM Inverter before filtering. b Output waveform of LC filter

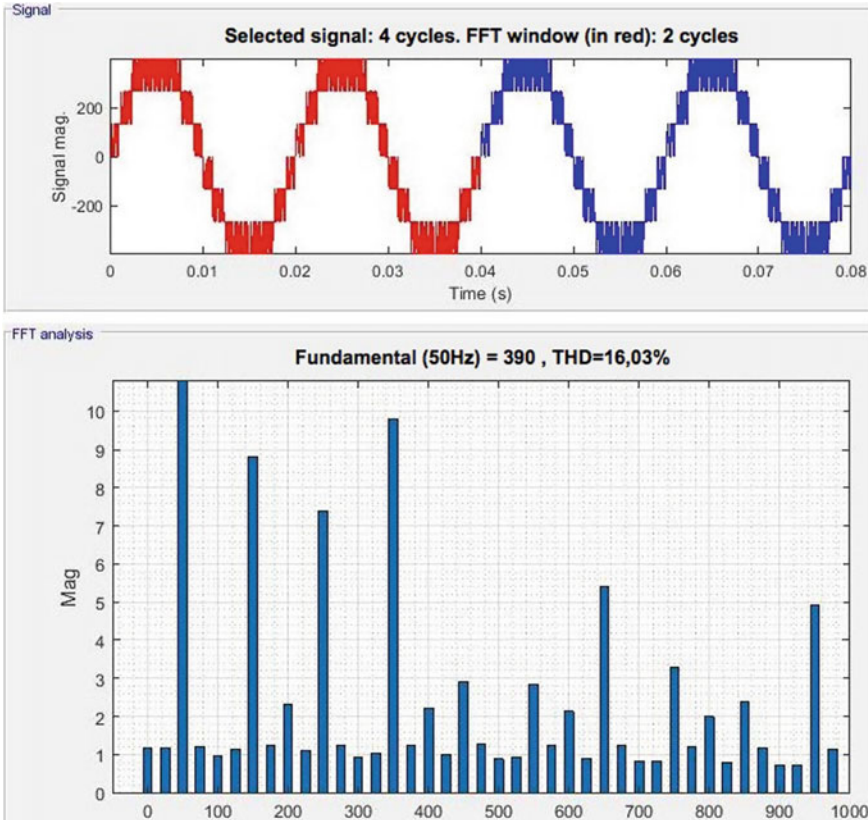


Fig. 8 Total harmonics distortion THD of the proposed inverter before filtering

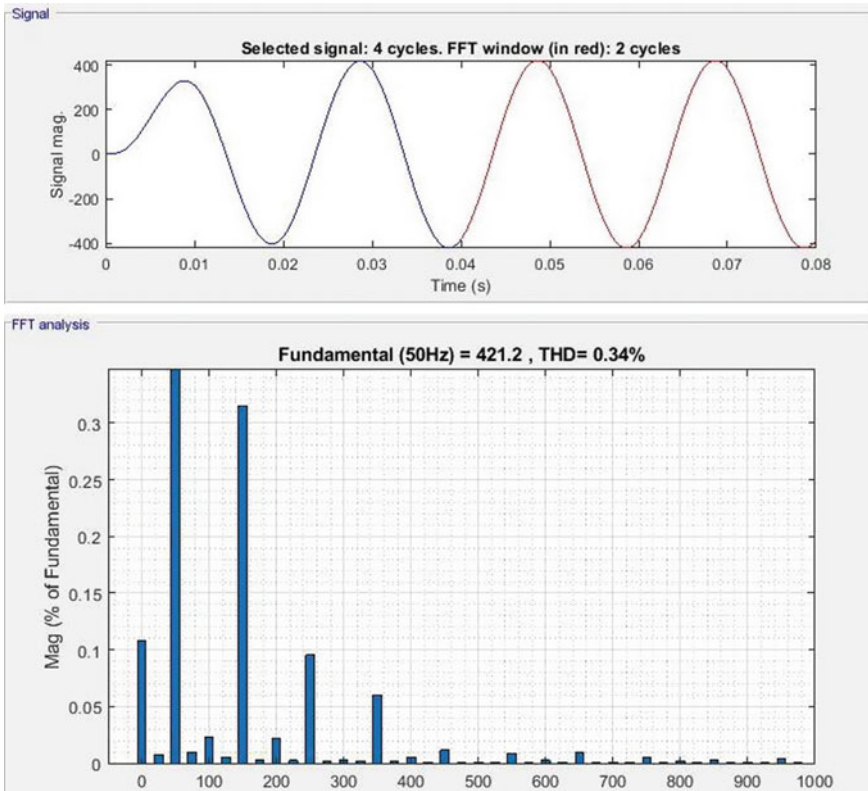


Fig. 9 Total harmonics distortion THD of the proposed inverter after filtering

Table 2 Comparison of proposed 7-level inverter with other inverters

Topologies	Number of switches	DC sources	THD (%)
Conventional cascaded 7-level inverter [6]	12	3	23.13
7-level MLI proposed in [7]	9	3	28.03
7-level MLI proposed in [8]	7	3	16.15
Proposed 7-level inverter	6	3	16.03

4 Hardware Implementation and Results

The complete hardware prototype of the 7-level inverter that have been developed as well as the output produced from this implemented hardware setup are presented in Fig. 10. And the principal required components used to implement the proposed 7-level inverter are as presented in Table 3. As shown in scope the seven levels output voltage is successfully produced and the filtered output voltage is a pure sine wave.

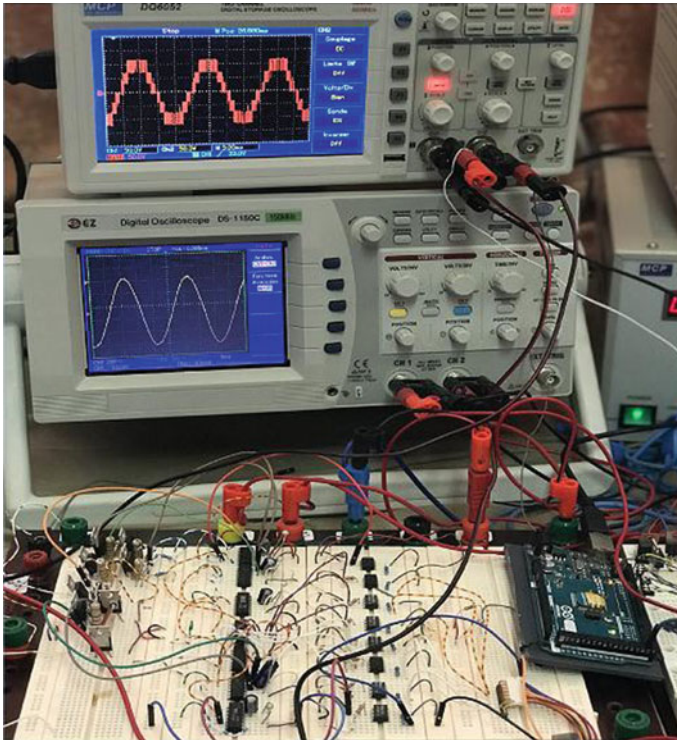


Fig. 10 Real Implementation of 7 level inverter

Table 3 Required components used to implement the proposed 7-level inverter

Name of the component	Technical specification
Microcontroller	Arduino ATmega2560
Mosfet swiches	Mosfet IRF 840: Power MOSFET (VDSS = 500 V, RDS(on) = 0.85 ohm, ID = 8.0 A)
Mosfet driver	IR 2110: high voltage, high speed driver
Optocoupler	6N137: High Speed Optocoupler, 10 Mbd
Diode	MUR 1560: Fast recovery diode, 15 A, 600 V, TO-220 A

5 Conclusion

This paper describes the design and real-time implementation of a new architecture of 7-level inverter with reduced components. This reduction has reduced the manufacturing cost, the size as well as the complexity of control strategy. Digital SPWM technique using Arduino microcontroller ATmega2560 has been used to enhance the performance of the inverter. The microcontroller can be used for other functionality in future expansion of this work. The designed seven levels inverter operation and efficiently is experimentally confirmed by the experimental results. From the result of the simulation and the real-time implementation it is clearly shown that the designed inverter total harmonics distortion (THD) is reduced as compared to the conventional structure and the filtered output is a pure sine wave with a frequency of 50 Hz.

References

1. Sean W, Keith WH, Takehiro I (2007) Strategic analysis of the Kyoto Protocol. 2007 IEEE international conference on systems, man and cybernetics, Montreal. Que, Canada, pp 1806–1811
2. Jih-Sheng L, Fang ZP (1996) Multilevel converters-a new breed of power converters. *IEEE Trans Ind Appl* 32(3):509-5-17. <https://doi.org/10.1109/28.502161>
3. Koshti AK, Rao MN (2017) A brief review on multilevel inverter topologies. In: 2017 International conference on data management, analytics and innovation (ICDMAI), Pune, 2017, pp 187–193. <https://doi.org/10.1109/ICDMAI.2017.8073508>
4. Fang ZP (2001) A generalized multilevel inverter topology with self voltage balancing. *IEEE Trans Ind Appl* 37(2):611–618. <https://doi.org/10.1109/28.913728>
5. Vijeh M, Rezanejad M, Samadaei E, Bertilsson K (2019) A general review of multi-level inverters based on main submodules: structural point of view. *IEEE Trans Power Electron* 34(10):9479–9502. <https://doi.org/10.1109/TPEL.2018.2890649>
6. Chadli H, Jebrohi Z, Chadli S, Tahani A, Aziz A (2017) Design and implementation of a novel five-level inverter topology. In: 2017 international conference on wireless technologies, embedded and intelligent systems (WITS), 2017, pp 1–6. <https://doi.org/10.1109/WITS.2017.7934641>
7. Lakshmi TVVS, George N, Umashankar Kothari SDP (2013) Cascaded seven level inverter with reduced number of switches using level shifting PWM technique. In: International conference on power, energy and control (ICPEC 2013), pp 676–680
8. Varna MS, Jose J (2014) A novel seven level inverter with reduced number of switches, In 2014 IEEE 2nd international conference on electrical energy systems (ICEES), Chennai, pp. 294–299. <https://doi.org/10.1109/ICEES.2014.6924184>
9. Ruman MR, Paul D, Barua A, Sarker AK, Iqbal A, Barua S (2019) Design and Implementation of SPWM inverter, 2019 international conference on computing, communication, and intelligent systems (ICCCIS), Greater Noida, India, pp 490–494. <https://doi.org/10.1109/ICCCIS48478.2019.8974542>

Embedded and Parallel Implementation of the Stereo-Vision System for the Autonomous Vehicle



Mohamed Sejai, Anass Mansouri, Saad Bennani Dosse, and Yassine Ruichek

Abstract Stereo-vision is the most widely used technique in the development of environmental perception systems for intelligent transportation. The main requirement for the application of stereo vision on a vehicle is the processing time which must be very fast for autonomous driving in real time, whereas the computation of the correspondence of the images in the algorithm of stereo-vision requires a more computing power. This article presents an implementation of the stereo vision system to generate a scene disparity map using the sum of absolute differences (SAD), and the triangulation method for calculating the distance between the obstacle and the stereoscopic system. A parallel treatment is used to speed data processing and this algorithm is implemented in embedded platform. Several experiments are performed from a profiling analysis to have a statistical analysis for optimization.

Keywords Stereo-vision system · Disparity map · Embedded platforms · Profiling code and optimization

1 Introduction

For several years, obstacle detection has been an active research in the field of intelligent vehicles [1, 2]. Vision systems are becoming more common in road vehicles

M. Sejai (✉) · A. Mansouri
Intelligent Systems, Georesources and Renewable Energies Laboratory, Faculty of Sciences and Technics Fez, Sidi Mohamed Ben Abdellah University, Fez, Morocco
e-mail: mohamedsejai92@gmail.com

A. Mansouri
e-mail: anas_mansouri@yahoo.fr

A. Mansouri · S. B. Dosse
Sidi Mohamed Ben Abdellah University, National School of Applied Sciences Fez, Fez, Morocco
e-mail: bennani.saad.ensaf@gmail.com

A. Mansouri · Y. Ruichek
Belfort-Montbéliard University of Technology, Belfort, France
e-mail: yassine.ruichek@utbm.fr

due to advances in technology. It is a system which is more particularly interested in the perception of the environment at the vehicle in order to extract the information necessary for an autonomous vehicle [3].

Among all the perception techniques that could be used, is stereo vision, it is the most used technique for obtaining depth information of a scene from a pair of images. Depth information is essential for the majority of the functionality of vision-system, so the matching phase is often an essential step to generate depth and to accomplish the other tasks of the system, namely the detection and localization of objects in the scene [4, 5].

The objective of this research is to reduce traffic accidents [6, 7], by avoiding collisions. This requires the detection of obstacles with precision and in real time [8]. Stereo cameras are increasingly employed in cars with advanced driver-assistance systems [9], mainly for high-level semantic reasoning and scene geometry estimation [10, 11]. Therefore, this work explores how to further exploit stereo-vision by reducing the complexity of the algorithm and by optimizing the processing time by parallel computing.

This paper is organized as follows. First section devoted to the approaches of the used algorithm. The second section presents the results of the algorithm implementation in the embedded, followed by the description of all techniques in order to optimize the implementation of this algorithm in third sections. The fourth section concludes the overall work.

2 Overview of Stereo Vision Algorithm

Multi-exposure stereoscopic is a vision technique that uses to reconstruct the third dimension that has been lost in images. This technique uses two images of the same scene taken from different points of view. The perception of the depth by stereo vision is mainly ensured by the exploitation of offset existing between the two images and can only be evaluated by establishing correspondence between the two images.

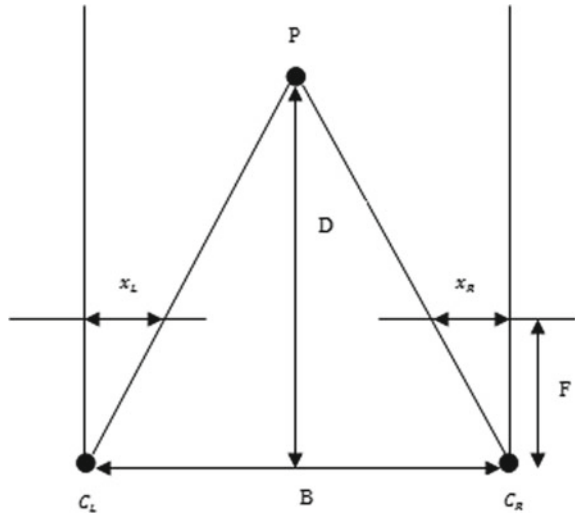
2.1 Stereo Vision System

The binocular stereo vision system consists of two cameras left and right of the same specification [12], the cameras remain the same plane, thus ensuring that the horizontal axes of the left and right camera systems are on the same line and parallel to the plane of imagery [13], the stereo vision system is illustrated in Fig. 1.

As shown in Fig. 1, if you have the disparity map, we can determine the distance D between the object P and the cameras by using the following equation:

$$D = \frac{F * B}{d} \quad (1)$$

Fig. 1 The principle of calculating the distance D of an object by stereovision



where F is the focal distance, B means the distance between the two cameras and d the disparity ($d = x_R - x_L$).

3 Stereo Matching

Stereo matching is the process of finding the corresponding points between the right and left image to generate the disparity map. Stereo matching uses a block matching algorithm based on the calculation of SAD [14]. The basic idea of the algorithm is to sum the absolute values of the differences between the corresponding values of each pixel [15, 16] in the left and the right image. The basic process is shown in Fig. 2.

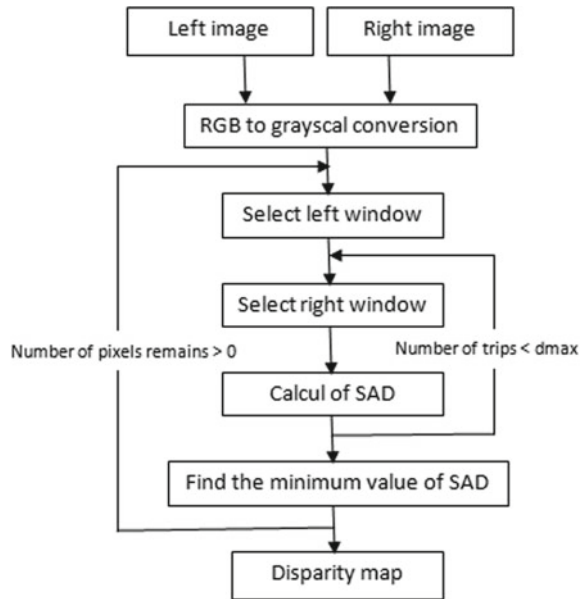
To generate the disparity map, we follow the following steps:

- (1) Choice the left image as the reference image.
- (2) Selection a rectangular left window of the pixel (x, y) to be matched.
- (3) The same window is moved by one pixel step in the right image on the same horizontal line because the images are rectified, the same point of the measured object must find on the same line in the left and right images.
- (4) For each pixel of the correlation window in the right image, we calculate a correlation index between the two windows by Eq. (2).

$$SAD(I_L(x, y), I_R(x, y')) = \sum_{(i,i) \in n} |I_L(x + i, y + j) - I_R(x + i, y' + j)| \tag{2}$$

where n corresponds to the neighborhood pixels of $I_L(x, y)$ and $I_R(x, y')$.

Fig. 2 The stereo matching algorithm.



- (1) Calculate the Minimum Value of the Correlation Index.
- (2) The disparity value retained is stored in the same coordinates as the pixel in order to construct the disparity map.

4 Experimental Results

The algorithm is implemented in two platforms using the C programming language and on the OpenCV(Open Computer Vision) 3.x library for importing, processing, and saving images. The images used are stereoscopic images with resolution of 384 * 288 pixels. Firstly, an implementation of the algorithm is done on a PC with a 2 GHz Intel Core i3 5005U processor, 4 GB of RAM, under Linux OS. Secondly, the proposed solution is implemented on a Raspberry Pi3 platform with a Quad Core 1.2GH, 1 GB RAM under Raspbian OS.

4.1 Implementation Results in the First Platform

- **Disparity map**

The inputs of the algorithm are the left images and the right image after the execution we obtain the results illustrated in Fig. 3.

- **Classification of objects by depth**

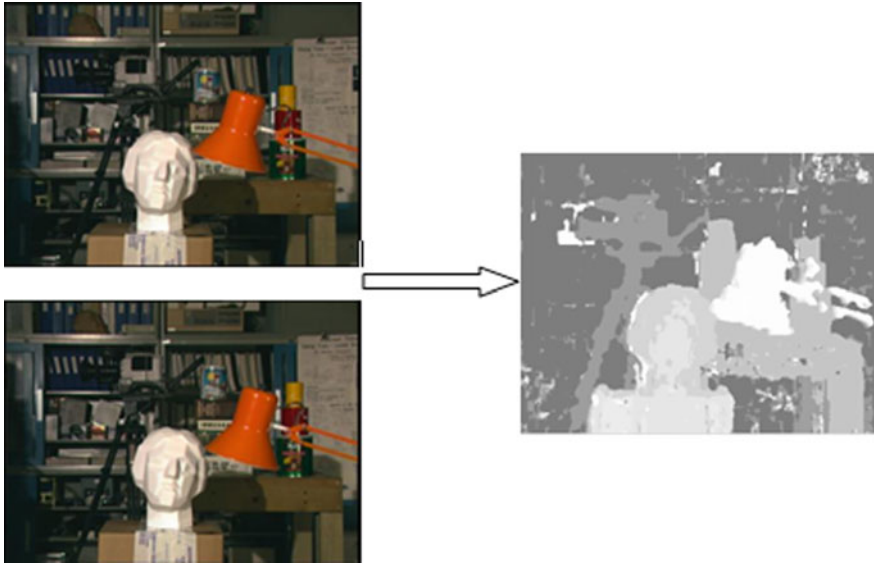


Fig. 3 Disparity map of right and left image

Stereoscopic gives the depth information of the objects in the scene. Figure 4 represents the classification of the objects extracted from the disparity map according to their depth. The object closest to the cameras represented by the number 1. The object farthest from the cameras represented by the number 4.

The results obtained show that it is perfectly possible to estimate the distance of objects in the scene from the cameras.

• **Profiling and optimization results**

The problem of generating disparity maps is the very high computation time, which makes this map unsuitable for applications which require processing in real time. This section illustrates the results of profiling with Gprof tool and the optimization results based on the OpenMP library (open Multi-processing). Profiling technical determine the functions which consume the most resources and which present a high complexity in computation time.

Table1 shows the results of the algorithm profiling before using the OpenMP library. The time consumed by the function that retrieves the window from the right image is approximately 92% of the total calculation time. This function is repeated 20 times to match each pixel, it compares with the left window to calculate the correlation index.

After using the OpenMP library and parallelizing the calculation of the algorithm, the computation time is reduced from 730 to 350 ms. The Table 2 presents the results of the optimization.

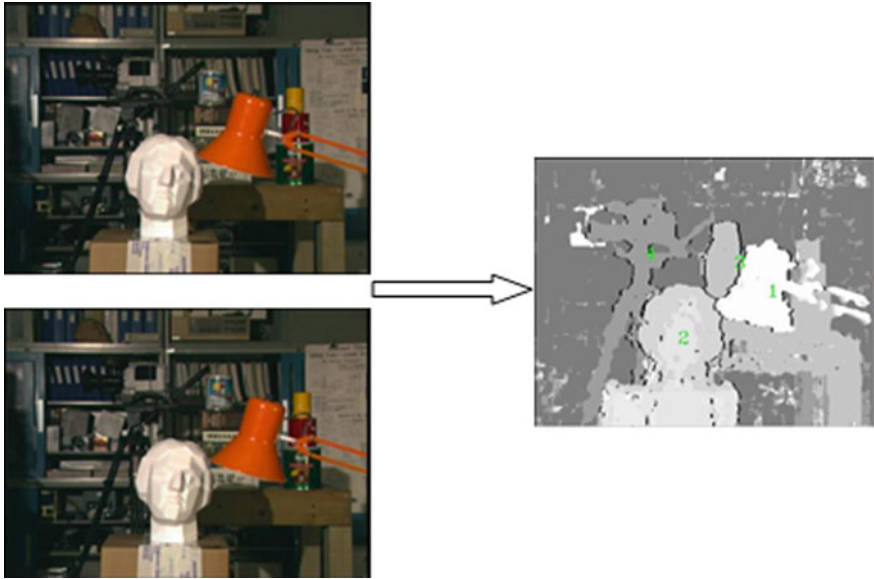


Fig. 4 Classification of objects according to their depth

Table 1 Profiling results in PC before using the OpenMP library

Functions	Consume time (s)	% time
Right window	0,67	91.43
Left window	0,03	4.28
Calcul of disparity	0,02	2.86
Min val of SAD	0,01	1.43
Total	0,73	100

Table 2 Profiling results in PC after using the OpenMP library

Functions	Consume time (s)	% time
Right window	0.20	55.56
Left window	0.07	19.44
Calcul of disparity	0.06	16.67
Min val of SAD	0.02	8.44
total	0.35	100

Table 3 Profiling results in Raspberry before using the OpenMP library

Functions	Consume time (s)	% time
Right window	4.17	79.43
Left window	0.87	16.57
Calcul of disparity	0.12	2.29
Min val of SAD	0.09	1.71
Total	5.25	100

Table 4 Profiling results in raspberry after using the OpenMP library

Function	Consume time (s)	% time
Right window	0.61	49.60
Left window	0.44	35.78
Calcul of disparity	0.10	8.12
Min val of SAD	0.08	6.51
total	1.23	100

4.2 Implementation Results in Embedded Platform

The obtained results is the same as the implementation on the PC, however the execution time is higher compared to the execution time on the PC (Table 3).

- **Profiling and optimization results**

The execution time on the Raspberry Pi 3 platform is even more important than the execution time on the PC because of the hardware constraints of the platform.

The computation time is reduced from 5.25 to 1.23 s. Table 4 presents the results of the optimization.

5 Conclusion

This paper presents the implementation results of stereovision algorithm, it presents the results of profiling and optimization. This work can be improved by: exploiting the parallelism of certain stages. Detecting mobile objects and calculate their mobility speed. Exchanging information to perform necessary actions such as speed management and inter-distance.

References

1. Gavril DM, Philomin V (1999) Real-time object detection for smart vehicles, IEEE ICCV
2. Labayrade R, Aubert D (2002) Real time obstacle detection in stereovision on non flat road geometry through v-disparity representation, IEEE IVS
3. Slimi H (2012) Système d’Assistance à la Conduite pour Véhicules à Deux-Roues Motorisés.thèse de doctorat, Université d’Evry Val d’Essonne,janvier
4. Mukhtar A, Xia L, Tang (2015) Vehicle detection techniques for collision avoidance systems : A review IEEE Transactions on Intelligent Transportation Systems
5. Nair M, Jozeph A (2019) streovision based speed estimation for autonomous driving. IEEE
6. rapport sur la sécurité routière dans le monde:// www.atlas-ag.net/article/securete-routiere-en-2017.
7. Chen L (2013) Research on navigation technology of unmanned helicopter landing based on vision. Nanjing University of Aeronautics and Astronautics

8. Marouane H (2015) Contribution à la modélisation des applications temps réel d'aide à la conduite. Université du Havre, octobre, Thèse de Doctorat
9. Huang S, Bi Y, Liu D et al (2017) Non-contact measurement of binocular stereo vision. J Yantai University (Natural Science and Engineering)
10. Li Z (2014) Research on 3D reconstruction technology based on binocular vision system. Guangxi University
11. Sun X, Jiang Y, Ji Y, Fu W, Yan S, Chen Q, Yu B, Gan X (2019) Distance Measurement System Based on Binocular Stereo Vision. 2019
12. Fakhfakh N (2012) Détection et localisation tridimensionnelle par stéréovision d'objets en mouvement dans des environnements complexes : application aux passages à niveau. Université Lille, Thèse de Doctorat
13. Wang Wei. : Research on mobile robot positioning technology based on multi-information fusion. 2015.
14. A.Bugayong.,M.Ramos.: obstacle detection using binocular stereo vision in trajectory planning for quadcopter navigation. article, 2018.
15. Quiet static.: Research on stereo matching algorithm based on binocular stereo vision. North University of China, 2012.
16. Qiao Wang.,al.:Review on Application of Binocular Vision Technology in Field Obstacle Detection. 2020.

An Efficient Implementation of an Effective PFD-CP for Low Power Low-Jitter CP-PLL



Karim Zouaq, Abdelmalik Bouyahyaoui, Abdelhamid Aitoumeri, and Mustapha Alami

Abstract A new efficient Phase-frequency Detector (PFD) paired with a new Charge-Pump (CP) is presented in this paper. This PFD-CP topology uses minimum sized devices of optimal minimum energy. The proposed PFD uses two pre-charged logic stages followed by static CMOS inverters without reset path cell or additional delay cells which leads to having a minimum blind zone, removing dead zone and occupying small chip area. Besides, the proposed design topology allows lowering power dissipation and improving speed, and can be used in high-speed CP-PLL applied in RF communication systems. Also, the paper presents an effective CP design for low-power and wide Voltage Controlled Oscillator (VCO) control voltage swing, that solely uses two CMOS inverters for charging and discharging processes, and therefore can form an effective PFD-CP topology suitable for applications where performance is needed, meanwhile minimizing energy consumption is key. Simulation results of the implemented circuit are discussed accordingly.

Keywords Phase-Frequency Detector (PFD) · Charge-Pump (CP) · Blind zone · Dead zone · Power consumption · Speed · Voltage swing

K. Zouaq (✉) · A. Bouyahyaoui · A. Aitoumeri · M. Alami
National Institute of Posts and Telecommunication, Rabat, Morocco
e-mail: karim.zouaq@ieee.org

A. Bouyahyaoui
e-mail: bouyahyaoui@inpt.ac.ma

A. Aitoumeri
e-mail: aitoumeri@ieee.org

M. Alami
e-mail: alami@inpt.ac.ma

1 Introduction

In recent years, there has been a huge demand of fully integrated and high-frequency Charge Pump-Phase Locked Loop (CP-PLL) for low power and low jitter applications. The Phase-Frequency Detector (PFD) is commonly designed to enhance either the capture range and the capture time of CP-PLL [1]. Such circuit is used by many digital systems like frequency synthesis and clock signals generation. Although it is considered as a beneficial part in CP-PLL circuit, two cases have been reported in which the PFD detects a wrong information; the dead zone occurs when the PFD is not capable to detect the phase error between the input signals around zero and the blind zone starts to be significant whenever the phase error between the two input signals approaches to $\pm 2\pi$. Recently, many researchers have given new energy and strength to the PFD design used for low-power and low-jitter applications. Currently, it is considered as an important field of research in many academic and industrial institutions, and many designers tried to enhance PFD structures for low-power and low-jitter CP-PLL [2–6]. The blind zone can be considered as a source of noise in PFD. It, therefore, adds the jitter, lead to falling-off in input detection range, abases the average PFD gain, and declines the cycle-slip effect, which hinders fast PLL acquisition [6]. In this work, the new CP-PFD structure is designed in such a manner to meet the requirement for being suitable for low-power low-jitter CP-PLL applications.

This paper is arranged as follows. Section 1 presents the main problems related to PFD-CP. Section 2 explores the basic operation of the CP-PLL and introduces the PFD as an important part. Section 3 introduces the conventional PFD and its limitations. Section 4 describes the PFD1 and shows the simulation and its results in 130-nm CMOS technology. Section 5 introduces the new topology of CP (CP1) and shows simulation and results. Section 6 presents the metrics comparisons of PFD1 and CP1 with prior works. Finally, Sect. 7 summarizes the paper.

2 CP-PLL Basis

A CP-PLL can be considered as a feedback system that use PFD for phase and frequency acquisition simultaneously, loop-pass filter and Voltage Controlled Oscillator (VCO).

The basic operation of a CP-PLL is as follows. The PFD generates two logic pulses, U_p and D_n , that control the CP. The CP produces strong currents that serve to drive the Loop Pass Filter (LPF) providing VCO control voltage to appropriately change the frequency of the clock signal. This frequency is then divided by the divider. Figure 1 presents a typical CP-PLL topology used for radio-frequency systems, from frequency synthesizers to clock generation [7].

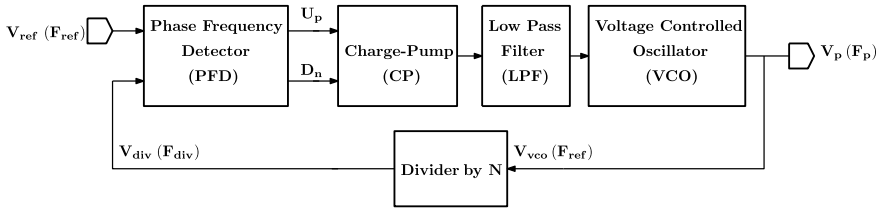


Fig. 1 Basic block diagram of a CP-PLL

3 Conventional PFD Topology

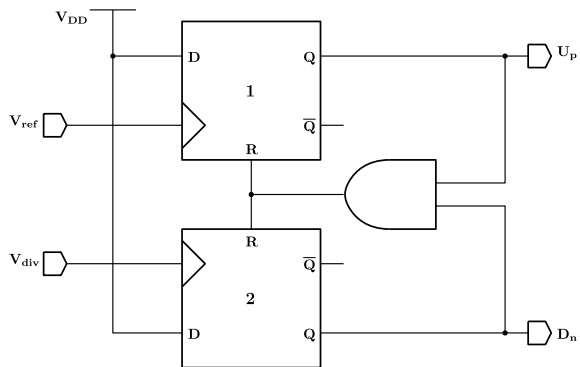
Figure 2 shows the conventional PFD architecture that uses two D-Flip Flop (DFF) and Fig. 3 shows its related Moore machine.

Both DFF detect the rising signal edges of the input signals V_{ref} and V_{div} connected to the clock inputs. The ‘D’ inputs are always held high. A rising edge of V_{ref} forces the DFF output pulse, U_p , to become high (‘1’). If $U_p = D_n = ‘1’$, the two DFF are initialized, and their outputs switch to ‘0’. In practice, two important points should be taken in consideration :

- The pulse (U_p, D_n) switches to ‘10’(‘01’) by rising edge of $V_{ref}(V_{div})$ and it will solely set to ‘00’ if $V_{div}(V_{ref})$ has a rising edge.
- If the logic gates delays are not neglected, then the state ‘11’ occurs.

The conventional PFD that uses two DFF and AND or NAND gate is commonly used in CP- PLL applications and it is considered as an useful and practical circuit that really implements the moore machine as described in Fig. 3. In the past, M. Soyuer and R.G. Meyer have presented some limitations of the conventional PFD used in CP-PLL, especially the operating frequency [1]. Therefore, They have proven that the frequency is limited due to the reset path ΔR and have given the following formula to predict the maximum operation frequency (F_{max}) of the PFD as

Fig. 2 Circuit of the conventional PFD based on DFF gates



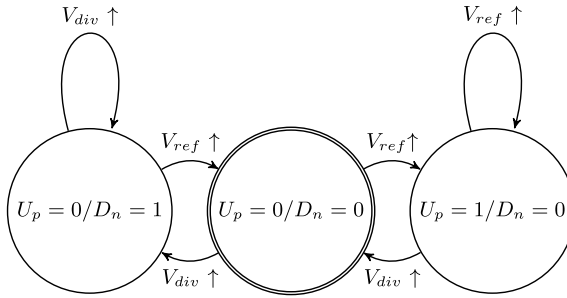


Fig. 3 Conventional PFD's moore machine

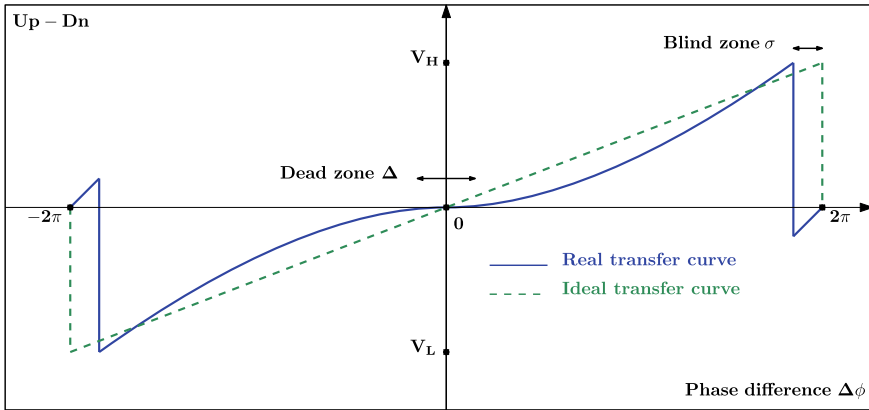


Fig. 4 Ideal and real characteristics of a three-state PFD

$$F_{max} = \frac{1}{2 x \Delta R} \tag{1}$$

Recently, Mozghan Mansuri has explained the no-ideal function of the conventional PFD and has discussed therefore the impact of the dead zone on the PLL operation [8]. The ideal and real conventional PFD's characteristics are plotted in Fig. 4. As can be seen, the dead zone appears near the origin in which the PFD fails to detect the inputs error and the blind zone occurs near $\pm 2\pi$ in which the PFD hangs up.

4 PFD1 Implementation and Optimization

4.1 Blind Zone Reducing Technique

Previously, Tak et al. [9] and Mansuri et al. [8] have believed that the reset process creates the blind zone and they have proven that the influence of the reset T_{reset} can be decreased using delay cell T_D in the PFD inputs [9]. In this context, he proposed PFD (PFD1) as can be seen in Fig. 5 is a pre-charged architecture with direct feedback from PFD outputs to inputs. Therefore, the reset path ΔR is completely removed and the reset time can be neglected. In this topology, solely the pre-charged time $T_{precharge}$ determines the blind zone. As the pre-charged process (charging and discharging nodes) depends on the bias voltage, the blind zone can be affected by the power supply V_{dd} in the circuit. Increasing V_{dd} in our PFD design decreases the pre-charged time and therefore reduces the blind zone. Thus, a value of 68 ps can be reached using 1.8 volt as power supply. Our new topology decreases the circuit complexity and removes the reset path ΔR and delay cell T_D for blind zone cancellation used in previous works [6, 9], which leads to reducing the number of transistors, power, and area. Besides, according to formula 1, the reset path limits the maximum operating frequency which makes our design suitable to high-frequency CP-PLL applications.

4.2 PFD1 Design and Optimisation

PFD1 uses symmetrical and identical connection of two pre-charged stages. Each stage consists of a CMOS cell constructed using two complementary transistors

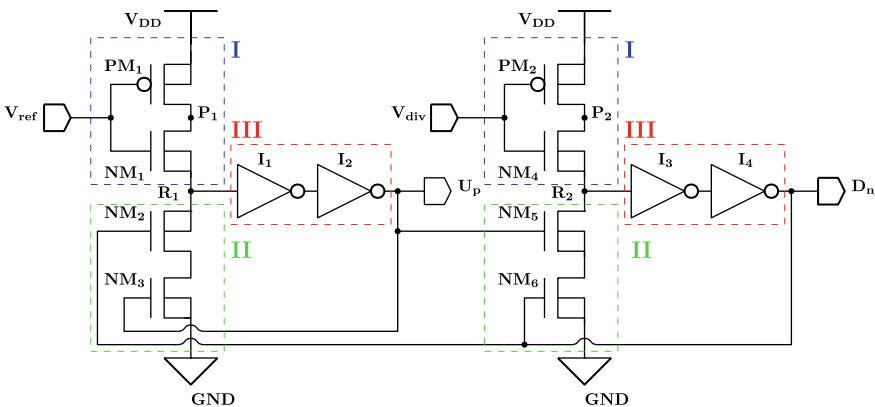


Fig. 5 Schematic of the proposed PFD

(PM1, NM1) and (PM2, PM4), respectively. Two NMOS transistors for each stage are used for rising edge operation, that results in a simple eight-transistor structure for each stage. The parts of the circuit can be split into three principal categories:

I—Pre-charged cells (PM1, NM1) and (PM2, NM4)—responsible for the behavior of the circuit. The designed cells are controlled by V_{ref} and V_{div} signals and create two charging points: P1 in the first cell and P2 in the second one. When V_{ref} and V_{div} are low, P1 and P2 are high and maintained since the NMOS transistors NM1 and NM4 close.

II—Rising edge cells (NM2, NM3) and (NM5, NM6)—responsible for rising edge operation. These cells are controlled by the signals U_p and D_n . These outputs give feedback to the NMOS transistors to open or close and they are responsible to cancel the situation where U_p and D_n are simultaneously equal to '1'.

III—Inverters (I_1 , I_2 , I_3 and I_4)—these parts buffer the internal signals R_1 and R_2 and maintain the complementary values of the internal signals as well as the circuit outputs.

This partition to categories helps to understand the circuit operation and leads to optimization. As can be seen, when $V_{ref} = '0'$ and $V_{div} = '0'$, then both PM1 and PM2 turn on and the points P1 and P2 are pre-charged to V_{DD} . NM2 and NM4 turn off and maintain the initial state until the occurrence of the rising edges of the inputs V_{ref} and V_{div} . As it is an initial state in which $U_p = D_n = '0'$, all the rising edges NMOS transistors are close. A rising edge of V_{ref} (V_{div}) signal flows '1' state through NM2 (NM4) transistor. The R1 point is buffered by the inverters I_1 and I_2 (I_3 and I_4) then the U_p (D_n) output signal goes high '1' ('1'). $U_p = '1'$ ($D_n = '1'$) turn NM6 (NM3) on. The combination $U_p = '1'$ and $D_n = '1'$ simultaneously, R1 and R2 discharge to ground, then $U_p = '0'$ and $D_n = '0'$, that leads to initialising the circuit. To optimize the performance of the proposed PFD, adjusting the transistor sizes is carefully performed (sweep parameter option in simulator) to reach the minimal power, phase noise, and reduced area. The compact structure of the proposed PFD that contains only 16 transistors, makes it an efficient solution that combines low area and high performance.

4.3 Simulation Results

Figure 6 illustrates how PFD1 behaves when V_{ref} signal and V_{div} signal operate at the same frequency (1 GHz) at 1.8 V as supply voltage, meanwhile, V_{ref} lags V_{div} by 932 ps, then this results in generation of a U_p signal. This value presents the threshold at which blind zone starts to occur.

Table 1 summarizes the important results of the proposed PFD when it is operating at 1 GHz clock frequency. Thus, the maximum operating frequency reaches the value of 7.25 GHz. The calculated phase noise is -138.78 dBc/Hz at 1 MHz. Thus, the highest value of frequency results in the absence of the reset path in our design and the good value of phase noise is given thought the sweep simulation as well as the optimization of the transistors sizes.

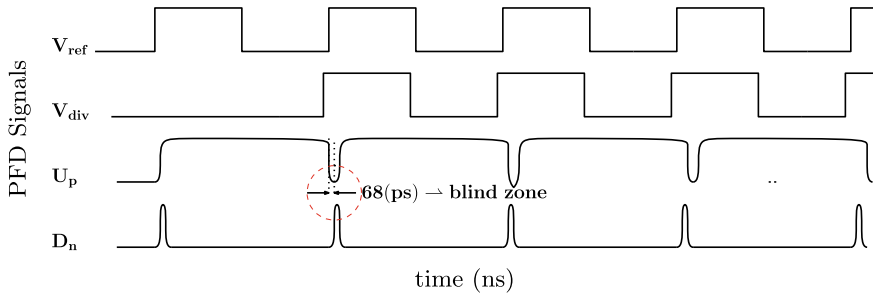


Fig. 6 Timing diagram of the proposed PFD at 1 GHz and V_{ref} lags V_{div} by 932 ps

Table 1 Simulation results of the proposed PFD

Characteristics	Proposed PFD
Technology	130 nm
Voltage (V)	1.8
Number of Transistors	16
Max. operating frequency (GHz)	7.25
Power (μ W)	27.23
Phase noise@1 Mhz (dBc/Hz)	-138.78
Blind zone (ps)	68
Area (μ m ²)	114
Dead zone (ps)	free

As can be seen, the dead zone is eliminated and the blind zone is about 68 ps. As explained before, this results in removing the reset path and optimization of transistors sizes. The power consumption is solely 44.56 μ W at the supply voltage of 1.8 V as a result of the absence of any additional delay cell for blind zone cancellation and reset path as well. Due to the minimum sized transistors approach, the proposed design chip has a die size of solely 114 μ m².

5 Charge-Pump Circuit

5.1 Proposed CP

The designed CP circuit (CP1) has the structure as shown in Fig. 7. The design uses two inverters, using two complementary CMOS transistors (PC1, NC1) and (PC3, NC3), respectively. The PMOS transistor PC2 and the NMOS transistor NC2 are used as switches. When the two signals U_p and D_n are set to '1' and '0' respectively, the transistor PC2 opens and the transistor NC2 closes. Then, the capacitance C

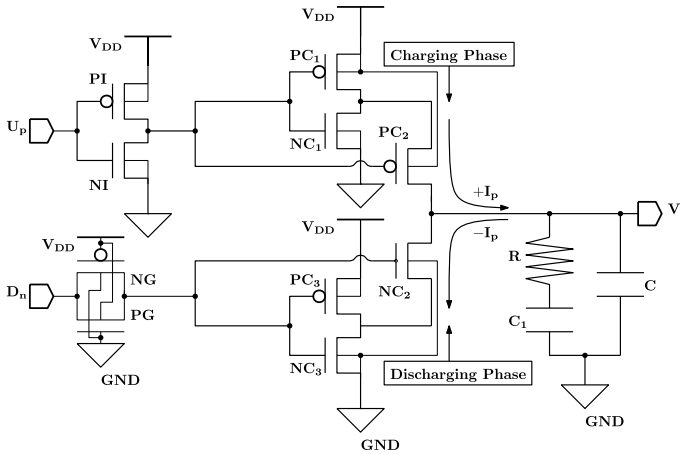


Fig. 7 Schematic of the proposed CP

charges through PC1 and PC2. When the two signals U_p and D_n are set to ‘0’ and ‘1’ respectively, the transistor PC2 closes and the transistor NC2 opens. Then, the capacitance C discharges through NC3 and NC2. When both signals U_p and D_n are set to ‘01’, both transistors PC2 and NC2 close and the output current $|I_p|$ is equal to zero. The transistor PC3 is open and V_p is set to $\frac{V_{DD}}{2}$ by sizing the transistors.

5.2 Output Swing of Proposed CP

The charging and discharging phases of the new CP, controlled by the proposed PFD, are displayed in Fig. 8. The transient analysis calculates the circuit’s response over a while equal to 5 ns. The waveform shows that the proposed CP can reach a value of 48 mV during discharging and reaches a value of 1.75 V during charging, if input signals of 1 GHz, at the supply voltage of 1.8 V, are applied, with measured output current mismatch ratio next to nothing. As can be seen, the proposed CP enables good current pumping even it has a simple structure, which makes it an effective circuit to use in combination with our proposed PFD.

Table 2 compares the new CP circuit with some recent designs in terms of swing voltage, power and number of transistors. As can be seen, the proposed CP has the better swing and consumes a small amount of energy. The results prove that the proposed CP is recommended as a PFD couple that would be a useful alternative for high performance and low-power systems.

Fig. 8 Output swing of new CP

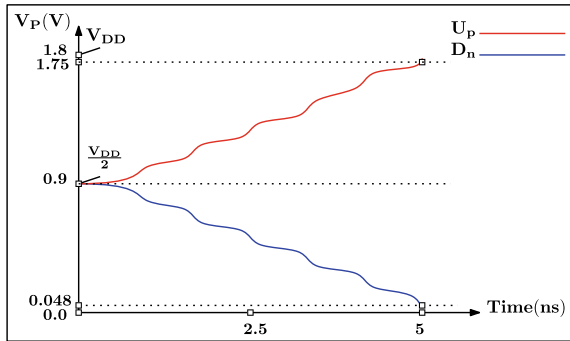


Table 2 Comparison of charge pump swing

Parameters	[10]	[11]	CP1
Tech. (nm)	180	130	130
Supply (V)	1.8	1.2	1.8
Swing (V)	0.23–1.723	0.1–1.0	0.048–1.75
Swing (%)	83		94.5
$ \pm I_p $ (μA)	100	60	100
Power (mW)	–	–	0.075
No. of transistors	–	20	10

6 Metrics Comparison with Prior Research

Table 3 compares the performance of the proposed PFD with previously given topologies. All of the architectures use same detection range ($[-2\pi, +2\pi]$). The inspected parameters are the maximum frequency, the power consumption, dead/blind zone and the number of transistors. The proposed PFD module is simple, consists of 16 transistors only, whereas the connected CP section is built with 10 transistors, and designed to have a minimum blind zone and null dead zone. The whole PFD-CP module is particularly advantageous to low power CP-PLL used in high-speed applications. In this context, Simulation results prove that all significant parameters are improved in comparison to previous works and would be a better candidate to low-power CP-PLL integrated for many applications.

Table 3 Performance comparison of PFD1 with the literature

Design	Voltage (V)	Power(μ W)	T_{α} *	Speed (Ghz)	Dead zone (ps)	Blind zone (ps)	Area (μ m ²)
[Conv.]	1.2 (130nm)	780	68	1.1	Significant	Significant	450
[PFD1]	1.8 (130nm)	27.23	16	7.25	Free	69	210
[2]	1.2 (130 nm)	76	16	4.1	25	–	250
[3]	1.8 (180 nm)	172.67	22	1	Free	–	–
[4]	1.8 (180 nm)	1360	30	1	Free	Minimal	–
[5]	1.8 (130 nm)	153	25	8	22	194	–
[6]	1.2 (130 nm)	496	26	2.94	Free	61	–

* Number of transistors

7 Conclusion

A simple and novel architecture of Phase-Frequency Detector connected to a simple and effective Charge-Pump topology was presented in this paper. The proposed PFD is designed without any reset path and additional delay circuitry that consume power and area, and therefore solely the pre-charge nodes are responsible for the blind zone which makes it easy to reduce it by increasing supply voltage. The proposed CP even has a simple structure based on CMOS inverter topology, it has a good voltage swing and offers reduced power and area. The complete module is designed to be suitable for CP-PLL used in the high-speed application including wireless and wired communications systems. In addition to the acceptable jitter (phase noise) performance, The circuit is designed to achieve low energy consumption and a small area. This topology gains its place in the literature and offers significant improvements, in simulation, compared with prior works.

References

1. Soyuer M, Meyer RG (1990) Frequency limitations of a conventional phase-frequency detector. IEEE J Solid-state Circ 25(4):1019–1022
2. Sofimowloodi S, Razaghian Farhad, Gholami Mohammad (2019) Low-power high-frequency phase frequency detector for minimal blind-zone phase-locked loops. Circ Syst Signal Process 38(2):498–511
3. Kumar N, Kumar M (2019) Design of low power and high-speed CMOS phase frequency detector for a pll. In: Advances in signal processing and communication. Springer, pp 529–540
4. Kuncham SS, Gadiyar M, Din S, Lad KK, Laxminidhi T (2018) A novel zero blind zone phase frequency detector for fast acquisition in phase locked loops. In: 2018 31st International conference on VLSI design and 2018 17th international conference on embedded systems (VLSID). IEEE, pp 167–170
5. Nikolić G, Jovanović G, Stojčev M, Nikolić T (2017) Precharged phase detector with zero dead-zone and minimal blind-zone. J Circ Syst Comput 26(11):1750179
6. Chen W-H, Inerowicz ME, Jung B (2010) Phase frequency detector with minimal blind zone for fast frequency acquisition. IEEE Trans Circ Syst II: Express Briefs 57(12):936–940

7. Zouaq K, Bouyahyaoui A, Alami M, Aitoumeri A (2018) A simple and novel scheme of LC-VCO for ultra low power low phase noise applications. *Int J Appl Eng Res* 13(9):6760–6765
8. Mansuri M, Liu D, Yang C-KK (2001) Fast frequency acquisition phase-frequency detectors for GSA/s phase-locked loops. In: *Proceedings of the 27th European solid-state circuits conference*, pp 333–336. IEEE
9. Tak G-Y, Hyun S-B, Kang TY, Choi BG, Park SS (2005) A 6.3-9-GHz CMOS fast settling PLL for MB-OFDM UWB applications. *IEEE J Solid-State Circ* 40(8):1671–1679
10. Zheng S, Li Z (2011) A novel CMOS charge pump with high performance for phase-locked loops synthesizer. In: *2011 IEEE 13th international conference on communication technology*. IEEE, pp 1062–1065
11. Zhang C, Au T, Syrzycki M (2012) A high performance NMOS-switch high swing cascode charge pump for phase-locked loops. In: *2012 IEEE 55th International Midwest Symposium on Circuits and Systems (MWSCAS)*. IEEE, pp 554–557

Adaptive Fast Terminal Sliding Mode Control for Uncertain Quadrotor Based on Butterfly Optimization Algorithm (BOA)



Hamid Hassani, Anass Mansouri, and Ali Ahaitouf

Abstract This paper proposes a robust Adaptive Fast Terminal Sliding Mode Control (AFTSMC) for the quadrotor UAV in the presence of external perturbations. First, the quadrotor position and attitude dynamics are obtained using the Newton–Euler principle, then the closed-loop stability of the suggested controller is proved by the Lyapunov theorem. The parameters of the proposed AFTSMC were automatically selected via the novel Butterfly Optimization Algorithm (BOA). Simulation experiments are conducted in Matlab/Simulink and comparison with other controllers is performed to validate the effectiveness of our new control strategy. The obtained results demonstrate that the proposed controller possesses multiple salient advantages such as fast response, high accuracy, and strong immunity to the variations across system model parameters.

Keywords Quadrotor UAV · Adaptive fast terminal sliding mode control · Butterfly optimization algorithm

1 Introduction

Quadrotors UAV have invaded civilian and military sectors and have become used for everything from monitoring and cinematography to rescue and firefighting. Hence, they have roused growing interest among researchers. It should be stated that quadrotor UAVs have several advantages over others flying robots, such as small size, simple structure, and low cost. In spite these advantages, they are under actuated, strongly coupled and highly nonlinear. Moreover, quadrotors dynamic is susceptible to some unpredictable perturbations, such as wind gust and sensors noise.

H. Hassani (✉) · A. Ahaitouf

Laboratory of Intelligent Systems, Geo-Resources and Renewable Energies, Faculty of Sciences and Technology, Sidi Mohammed Ben Abdellah University, Fez, Morocco
e-mail: Hamid.hassani@usmba.ac.ma

A. Mansouri

Laboratory of Intelligent Systems, Geo-Resources and Renewable Energies, School of Applied Sciences, Sidi Mohammed Ben Abdellah University, Fez, Morocco

In order to guarantee the closed-loop stability of the quadrotor UAV, numerous control algorithms have been developed. Involving classical approaches, nonlinear methods, adaptive and cooperative control strategies [1–4]. Among these methods, the sliding mode theory based approaches have been proved as a powerful techniques for controlling system suffering from parasitic dynamics and model uncertainties [5, 6]. Unfortunately, conventional sliding mode control (CSMC) cannot ensure the convergence in finite time, furthermore it suffers from the chattering phenomena. Integral sliding mode control (ISMC) is adopted in [7] to steer the quadrotor altitude flight, this approach has been proved to be efficient for the steady state error elimination. Similarly, the ISMC control law is used in [2] to robustly manage the six degrees-of-freedom of the quadrotor system despite the impact of external perturbations. In the same vein, Hassani et al. [8] have proposed a robust SMC based on a new adaptive reaching law for compensating the influence of unknown perturbations. In [9], an adaptive control law based on a combination of the backstepping approach with the CSMC is proposed, yielding robust tracking of the reference trajectory notwithstanding the impact of external disturbances. Recently, a sliding mode type named terminal sliding mode control has been proposed to get robustness similar to the CSMC, ensure the convergence in finite-time and improve the tracking precision. Unfortunately, the performances of this technique are not good when the system state is so far from its equilibrium. Fast terminal sliding mode control can be a good choice to deal with the aforementioned problem.

In this paper we challenge the unmodeled dynamics (wind gust and parameters uncertainties) that influence the quadrotor performances. A robust fast terminal sliding mode controller is used to regulate the quadrotor position and attitude. Different from previous works which assume that the disturbances upper limit is known in advance, herein an adaptive control law is used to estimate this limit. Using this approach the robustness against disturbances can be enhanced. In order to get optimal trajectory tracking, BOA algorithm [10, 11] is used to configure the parameters of the adopted controller. To the best of our knowledge, this is the first practical use of BOA algorithm with application to a robust nonlinear controller for the quadrotor UAV.

The rest of this work is structured as follows: the quadrotor modeling is presented in Sect. 2. The development of our new control algorithm is investigated in Sect. 3. The optimization process is described in Sect. 4. Simulation results are presented in Sect. 5. Last section concludes this paper.

2 Mathematical Model

Quadrotor is a multirotor flying robot with the ability of vertical take-off and landing. Their linear and angular movements are obtained by adjusting the angular velocity of each system propeller-rotor. Multiple researches work have presented thoroughly the entire dynamical model of the quadrotor UAV as in the following equation [12].

$$\begin{cases} \ddot{x} = \frac{U_1}{m} (\cos \varphi \sin \theta \cos \psi + \sin \varphi \sin \psi) + d_x \\ \ddot{y} = \frac{U_1}{m} (\cos \varphi \sin \theta \sin \psi - \sin \varphi \cos \psi) + d_y \\ \ddot{z} = \frac{U_1}{m} (\cos \varphi \cos \theta) - g + d_z \\ \ddot{\varphi} = \dot{\theta} \dot{\psi} \left(\frac{I_y - I_z}{I_x} \right) - \frac{J_r}{I_x} \dot{\theta} \Omega + \frac{U_\varphi}{I_x} + d_\varphi \\ \ddot{\theta} = \dot{\varphi} \dot{\psi} \left(\frac{I_z - I_x}{I_y} \right) + \frac{J_r}{I_y} \dot{\varphi} \Omega + \frac{U_\theta}{I_y} + d_\theta \\ \ddot{\psi} = \dot{\varphi} \dot{\theta} \left(\frac{I_x - I_y}{I_z} \right) + \frac{U_\psi}{I_z} + d_\psi \end{cases} \quad (1)$$

where (x, y, z) denote the position coordinates and (φ, θ, ψ) denote the Euler angles. $I(I_x, I_y, I_z)$ is the diagonal matrix of inertia, J_r is the rotor inertia, m is the quadrotor total mass, U_1, U_φ, U_θ and U_ψ are the control signals, and Ω is the quadrotor total speed.

It is well known that the quadrotor is underactuated because the number of outputs is greater than the number of inputs. To deal with this problem, two intermediate control laws are considered as:

$$\begin{aligned} U_x &= \frac{U_1}{m} (\cos \varphi \sin \theta \cos \psi + \sin \varphi \sin \psi) \\ U_y &= \frac{U_1}{m} (\cos \varphi \sin \theta \sin \psi - \sin \varphi \cos \psi) \end{aligned} \quad (2)$$

By its nature, the quadrotor translational movements are obtained through pitch and roll rotations. Therefore a nonlinear decoupling system is mandatory to transform the (x, y) position into desired roll and pitch angles as follows [8]:

$$\begin{cases} \theta_d = \arctan \left(\frac{U_x \cos(\psi_d) + U_y \sin(\psi_d)}{U_z} \right) \\ \varphi_d = \arctan \left(\cos(\theta_d) \left(\frac{U_x \sin(\psi_d) - U_y \cos(\psi_d)}{U_z} \right) \right) \\ U_z = (\cos(\varphi) \cos(\theta)) U_1 / m \end{cases} \quad (3)$$

Generally, the quadrotor dynamical model can be described by the following second order system:

$$\begin{cases} \ddot{X} = F(X) + G(X)U_X + d_X \\ |d_X| < \hat{\xi}_X \end{cases} \quad (4)$$

where $X = \{x, y, z, \varphi, \theta, \psi\} \in \mathbb{R}^6$ is the state variables, F and $G \neq 0$ are two nonlinear function, d_X is the external disturbances and $\hat{\xi}_X$ is the estimate of the disturbance upper limit.

3 Proposed Control Strategy

In this section, the proposed control algorithm is designed to achieve a controllable behavior with the attempt of tracking accurately different complex trajectories. The synoptic scheme of the proposed strategy is illustrated in Fig. 1. However, two sub-controllers are designed, a position controller that steer the quadrotor position and generates the lifting force U_1 and the virtual controls (U_x, U_y) these latter will be converted to a desired roll and pitch angle using Eq. 4. An attitude controller is used to regulate the quadrotor orientations and produces the required control torques $(U_\varphi, U_\theta, U_\psi)$. For the quadrotor position and attitude, the tracking error, its first and second time derivatives are given as:

$$\begin{cases} e_{\bar{h}, \bar{h}=(x,y,z,\varphi,\theta,\psi)} = \bar{h}_d - \bar{h} \\ \dot{e}_{\bar{h}, \bar{h}=(x,y,z,\varphi,\theta,\psi)} = \dot{\bar{h}}_d - \dot{\bar{h}} \\ \ddot{e}_{\bar{h}, \bar{h}=(x,y,z,\varphi,\theta,\psi)} = \ddot{\bar{h}}_d - \ddot{\bar{h}} = \ddot{\bar{h}}_d - F(X) - G(X).U + d_{\bar{h}} \end{cases} \quad (5)$$

The fast terminal sliding surface is defined as [5]:

$$\sigma_{\bar{h}, \bar{h}=(x,y,z,\varphi,\theta,\psi)} = \dot{e}_{\bar{h}} + a_{1\bar{h}}e_{\bar{h}} + a_{2\bar{h}}|e_{\bar{h}}|^{\left(\frac{p_{\bar{h}}}{q_{\bar{h}}}\right)} \text{sign}(e_{\bar{h}}) \quad (6)$$

$a_{1\bar{h}}$ and $a_{2\bar{h}}$ are positive constants. $p_{\bar{h}}, q_{\bar{h}}$ are odd integer's satisfying $(0 < \frac{p_{\bar{h}}}{q_{\bar{h}}} < 1)$.

The time derivative of the sliding surface is calculated as:

$$\dot{\sigma}_{\bar{h}} = \ddot{e}_{\bar{h}} + \left(a_{1\bar{h}} + a_{2\bar{h}} \frac{p_{\bar{h}}}{q_{\bar{h}}} |e_{\bar{h}}|^{\left(\frac{p_{\bar{h}}-q_{\bar{h}}}{q_{\bar{h}}}\right)} \right) \dot{e}_{\bar{h}} \quad (7)$$

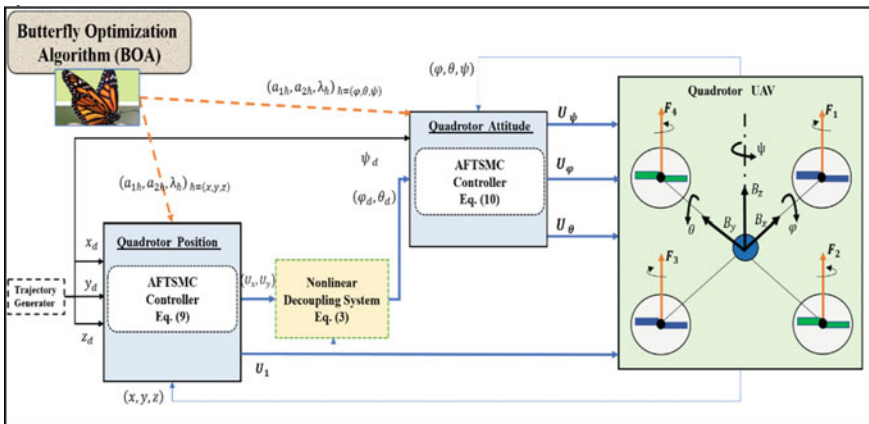


Fig. 1 Proposed control structure

In order to counter the influence of parameters uncertainties and to cancel the external perturbations influences without any previous knowledge of their upper bound, an adaptive constant plus proportional reaching law is used and designed as:

$$\begin{cases} \dot{\hat{\sigma}}_{\bar{h}, \bar{h}=(x,y,z,\varphi,\theta,\psi)} = -\lambda_{\bar{h}}\sigma_{\bar{h}} - \hat{\xi}_{\bar{h}}\tanh(\sigma_{\bar{h}}) \\ \dot{\hat{\xi}}_{\bar{h}} = \mu_{\bar{h}}|\sigma_{\bar{h}}| \end{cases} \quad (8)$$

where $\lambda_{\bar{h}}$ is a positive constant, $\hat{\xi}_{\bar{h}}$ is the estimate of the disturbance upper limit, $\mu_{\bar{h}, \bar{h}=(x,y,z,\varphi,\theta,\psi)}$ is a nonzero positive constant.

Therefore, by combining Eqs. 7 and 8, the control signals for the quadrotor position and attitude are calculated as:

$$\begin{cases} U_x = \ddot{x}_d + \left(a_{1x} + a_{2x} \frac{p_x}{q_x} |e_x|^{\left(\frac{p_x-q_x}{q_x}\right)} \right) \dot{e}_x + \lambda_x \sigma_x + \hat{\xi}_x \tanh(\sigma_x) \\ U_y = \ddot{y}_d + \left(a_{1y} + a_{2y} \frac{p_y}{q_y} |e_y|^{\left(\frac{p_y-q_y}{q_y}\right)} \right) \dot{e}_y + \lambda_y \sigma_y + \hat{\xi}_y \tanh(\sigma_y) \\ U_1 = \frac{m}{\cos\varphi\cos\theta} \left(\ddot{z}_d + g + \left(a_{1z} + a_{2z} \frac{p_z}{q_z} |e_z|^{\left(\frac{p_z-q_z}{q_z}\right)} \right) \dot{e}_z + \lambda_z \sigma_z + \hat{\xi}_z \tanh(\sigma_z) \right) \end{cases} \quad (9)$$

$$\begin{cases} U_\varphi = I_x \left(\ddot{\varphi}_d - \dot{\theta} \dot{\psi} \left(\frac{I_y - I_z}{I_x} \right) + \frac{J_r}{I_x} \dot{\theta} \Omega + \left(a_{1\varphi} + a_{2\varphi} \frac{p_\varphi}{q_\varphi} |e_\varphi|^{\left(\frac{p_\varphi-q_\varphi}{q_\varphi}\right)} \right) \dot{e}_\varphi + \lambda_\varphi \sigma_\varphi + \hat{\xi}_\varphi \tanh(\sigma_\varphi) \right) \\ U_\theta = I_y \left(\ddot{\theta}_d - \dot{\varphi} \dot{\psi} \left(\frac{I_z - I_x}{I_y} \right) - \frac{J_r}{I_y} \dot{\varphi} \Omega + \left(a_{1\theta} + a_{2\theta} \frac{p_\theta}{q_\theta} |e_\theta|^{\left(\frac{p_\theta-q_\theta}{q_\theta}\right)} \right) \dot{e}_\theta + \lambda_\theta \sigma_\theta + \hat{\xi}_\theta \tanh(\sigma_\theta) \right) \\ U_\psi = I_z \left(\ddot{\psi}_d - \dot{\varphi} \dot{\theta} \left(\frac{I_x - I_y}{I_z} \right) + \left(a_{1\psi} + a_{2\psi} \frac{p_\psi}{q_\psi} |e_\psi|^{\left(\frac{p_\psi-q_\psi}{q_\psi}\right)} \right) \dot{e}_\psi + \lambda_\psi \sigma_\psi + \hat{\xi}_\psi \tanh(\sigma_\psi) \right) \end{cases} \quad (10)$$

Theorem: For the investigated quadrotor model (Eq. 1), if the adaptive control law is conceived as (9) and (10), then the finite time convergence is guarantee.

Prove: To prove the stability of the quadrotor UAV, we propose the following generic lyapunov function designed as:

$$V = \frac{1}{2} \sum_{\bar{h}=(x,y,z,\varphi,\theta,\psi)} \left(\sigma_{\bar{h}}^2 + \frac{\tilde{\xi}_{\bar{h}}^2}{\mu_{\bar{h}}} \right) \quad (11)$$

With $\tilde{\xi} = \xi - \hat{\xi}$ is the adaption error.

The derivative of V is given by

$$\dot{V} = \sum_{\bar{h}=(x,y,z,\varphi,\theta,\psi)} \left(\sigma_{\bar{h}} \dot{\sigma}_{\bar{h}} - \frac{\tilde{\xi}_{\bar{h}} \dot{\xi}_{\bar{h}}}{\mu_{\bar{h}}} \right) \tag{12}$$

Using Eq. (7), \dot{V} becomes

$$\begin{aligned} \dot{V} &= \sum_{\bar{h}=(x,y,z,\varphi,\theta,\psi)} \left(\sigma_{\bar{h}} \left(\ddot{e}_{\bar{h}} + \left(a_{1\bar{h}} + a_{2\bar{h}} \frac{p_{\bar{h}}}{q_{\bar{h}}} |e_{\bar{h}}|^{\left(\frac{p_{\bar{h}}-q_{\bar{h}}}{q_{\bar{h}}} \right)} \right) \dot{e}_{\bar{h}} \right) - \frac{\tilde{\xi}_{\bar{h}} \dot{\xi}_{\bar{h}}}{\mu_{\bar{h}}} \right) \\ &= \sum_{\bar{h}=(x,y,z,\varphi,\theta,\psi)} \left(-\lambda_{\bar{h}} \sigma_{\bar{h}}^2 + d_{\bar{h}} \sigma_{\bar{h}} - \xi |\sigma_{\bar{h}}| + \tilde{\xi}_{\bar{h}} \left(|\sigma_{\bar{h}}| - \frac{\dot{\xi}_{\bar{h}}}{\mu_{\bar{h}}} \right) \right) \\ &\leq \sum_{\bar{h}=(x,y,z,\varphi,\theta,\psi)} \left(-\lambda_{\bar{h}} \sigma_{\bar{h}}^2 + (d_{\bar{h}} - \xi) |\sigma_{\bar{h}}| + \tilde{\xi}_{\bar{h}} \left(|\sigma_{\bar{h}}| - \frac{\dot{\xi}_{\bar{h}}}{\mu_{\bar{h}}} \right) \right) \leq 0 \end{aligned} \tag{13}$$

Using Eqs. (4) and (8) we obtain,

$$\dot{V} \leq - \sum_{\bar{h}=(x,y,z,\varphi,\theta,\psi)} \lambda_{\bar{h}} \sigma_{\bar{h}}^2 \leq 0 \tag{14}$$

According to the lyapunov criteria ($\dot{V} \leq 0$), the closed-loop stability of the quadrotor UAV is guarantee.

4 Optimal AFTSMC

The parameters of the proposed AFTSMC controller have a critical influence on the controller performances. Therefore, in order to sake high accuracy, these parameters need to be correctly adjusted. The superiority of the BOA compared to other nature inspired algorithms has been proved in [10, 13]. Therefore, the BOA is used in this work to effectively adjust the parameters of the proposed AFTSMC controller.

4.1 Overview of Butterfly Optimization Algorithm

In nature, butterflies distinguishes the shortest way to the food sources by means of smell. However, each butterfly emit a specific amount of fragrance and other nearby butterflies can sense this fragrance and move toward it. The amount of fragrance emitted by each butterfly is a function of the fitness and it can be formulated as:

$$f_i = cI^a \quad (15)$$

where f_i corresponds to the fragrance amount of butterfly i th, c symbolizes the sensory modality, I denotes the fragrance intensity which depends on the butterfly fitness and a is a constant characterizing the variation of absorption.

In their mission, butterflies move to the new position according to the following equation:

$$x_i^{t+1} = x_i^t + F_i^{t+1} \quad (16)$$

where x_i^t represents the actual solution and F_i^{t+1} denotes the moving magnitude which depends on the search type.

There exist two different search manners, respectively called local and global searches. The former corresponds to the case where the investigated butterfly can't smell the fragrance of others nearby butterflies, then it will moves randomly. In this case the moving magnitude is given by:

$$F_i^{t+1} = (r^2 \cdot x_j^t - x_k^t) \cdot f_i \quad (17)$$

where the notation $0 < r < 1$ defines a random number, x_j^t and x_k^t are respectively the i th and k th butterfly from the solution space.

If the butterfly can perceive the fragrance of other one, then it will move towards the fittest butterfly, this is called global search and can be represented by the following equation:

$$F_i^{t+1} = (r^2 \cdot g^* - x_k^t) \cdot f_i \quad (18)$$

where g^* symbolizes the best solution, i.e. the fittest butterfly.

The probability that the butterfly performs a global search is defined by a constant $p \in [0, 1]$.

4.2 Cost Function

To optimize the controller parameters is to minimize the cost function named also fitness given as function of the tracking error. In this work, the fitness is given by mean of the integral absolute error (IAE), and the best solutions are those corresponding to the minimum value of this function.

$$IAE_{\bar{h}, \bar{h}=(x,y,z,\varphi,\theta,\psi)} = \int |e_{\bar{h}}(t)| dt \quad (19)$$

5 Simulation Results

To demonstrate the effectiveness of our new control algorithm, simulation for trajectory tracking using square path is performed. Quadrotor dynamic is configured as shown in Table 1 [14].

First of all, the parameters of the adopted controller are selected using BOA algorithm, then these parameters are used to perform the required flight mission. Three parameters $(a_{1\bar{h}}, a_{2\bar{h}}, \lambda_{\bar{h}})_{\bar{h}=(x,y,z,\varphi,\theta,\psi)}$ for each movements have to be selected using the investigated algorithm, in total 18 parameters must be adjusted. The parameters of BOA algorithm are configured as:

- The population size n is fixed to 30. Sensory modality $c = 0.01$
- Power exponent $a = 0.1$. The probability of global or local search $p = 0.8$
- Total number of iteration is 100.

The parameters of the proposed AFTSMC are selected for a step input using BOA, then they will be used to perform other complicated trajectory.

The convergence of BOA algorithm is shown in Fig. 2, and clearly the algorithm achieve their minimum rapidly. The cost function minimum value obtained using BOA algorithm is 1.1588 achieved in iteration 53.

As already mentioned, the minimum value of the cost function corresponds to the controller parameters optimal values, these parameters are listed in Table 2.

To further illustrate the robustness of the proposed controller, 30% of uncertainties in the quadrotor mass and matrix of inertia, respectively, are considered. External perturbations are also added and comparison with the conventional SMC is also given.

$$\begin{cases} d_{\bar{h}=(\varphi,\theta,\psi)} = 1 \cos(0.7t) \frac{\text{rad}}{\text{s}^2}; & (10 \leq t \leq 50) \\ d_{\bar{h}=(x,y,z)} = 0.1 \cos(0.7t) \frac{\text{m}}{\text{s}^2}; & (10 \leq t \leq 50) \end{cases} \quad (20)$$

Results of trajectory tracking under external disturbances are depicted in Fig. 3. Using the proposed controller, the quadrotor can follow the given trajectory with high accuracy. As seen, conventional SMC cannot compensate effectively the influence of parameters uncertainties (30% of uncertainties), this can be seen form the vertical displacement where the quadrotor is not able to achieve the desired z position. A quantitative comparison in term of the Integral Square Error (ISE) index is given in Table 3, and the proposed controller shows better performances with reduced value

Table 1 Quadrotor configuration

Parameters	Value	Parameters	Value
m (kg)	1.1	b (N.s ²)	5
$I_x=I_y$ (Kg.m ²)	0.022	d (N.m.s ²)	2
I_z (Kg.m ²)	0.042	J_r (Kg.m ²)	0.02
ℓ	0.21	g (ms ⁻²)	9.81

of the ISE index, this means flight more precise.

$$ISE = \int e^2(t)dt \tag{21}$$

A comparison in term of 3D trajectory tracking is shown in Fig. 4. From this figure, a good tracking performance of the proposed AFTSMC controller can be observed, since the quadrotor satisfactorily tracks the planned path. The AFTSMC remains insensitive to the uncertainties, in the other hand, CSMC reduces the influence of disturbance but cannot eschew effectively the harmful impact of uncertainties and this leads to a considerable tracking error in the steady state for the z displacement.

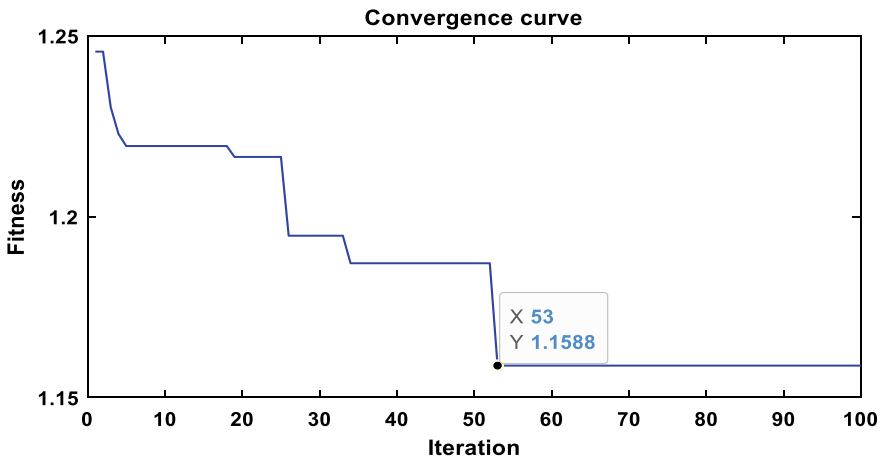


Fig. 2 Cost function versus iteration

Table 2 Controller parameters

Parameters	Value	Parameters	Value
$ph, h=(x, y, z, \psi)$	3	$pi, i=(\varphi, \theta)$	7
$qh, h=(x, y, z, \psi)$	5	$qi, i=(\varphi, \theta)$	9
a_{1x}	10.9762	$a_{1\varphi}$	15.5960
a_{2x}	0.3983	$a_{2\varphi}$	0.3139
λ_x	1.7349	λ_φ	15.6005
a_{1y}	13.7258	$a_{1\theta}$	11.4461
a_{2y}	0.4938	$a_{2\theta}$	0.6452
λ_y	1.4736	λ_θ	14.9408
a_{1z}	2.0588	$a_{1\psi}$	2.6248
a_{2z}	1.8998	$a_{2\psi}$	1.0527
λ_z	85.7428	λ_ψ	17.4962

Table 3 Quantitative comparisons of the flight test results

	CSMC	AFTSMC
x	0.4183	0.3866
y	0.4882	0.3907
z	0.2019	0.1308
ψ	0.1018	0.0768

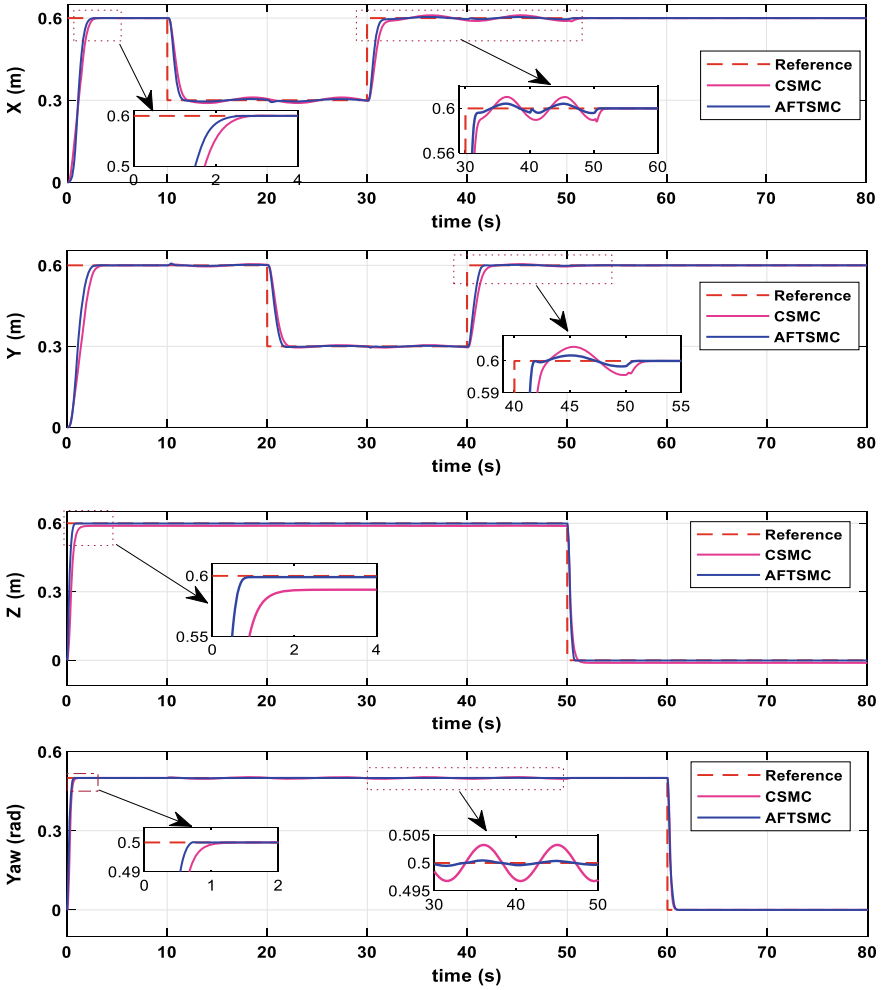


Fig. 3 Simulation results for square path tracking

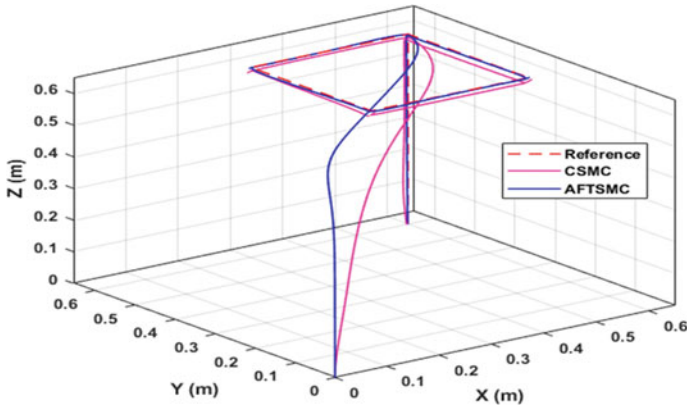


Fig. 4 3D trajectory tracking

6 Conclusion

In this paper, a finite-time adaptive nonlinear controller is proposed for the quadrotor UAV. The new Butterfly Optimization Algorithm is successfully used to optimally configure the parameters of the suggested controller. Simulation results prove that the proposed AFTSMC controller is able to drive successfully the quadrotor along the desired path with fast transient and reduced steady state error, it offer also robustness against external perturbations and parameters uncertainties.

References

1. Hassani H, Mansouri A, Ahaitouf A (2021) Mechanical modeling, control and simulation of a quadrotor UAV. In: Hajji B, Mellit A, Marco Tina G, et al (eds) proceedings of the 2nd international conference on electronic engineering and renewable energy systems. Springer Singapore, Singapore, pp 441–449
2. Yu H, Wu S, Lv Q, et al (2017) Robust integral sliding mode controller for quadrotor flight. In: 2017 Chinese Automation Congress (CAC). IEEE, pp 7352–7656
3. Dena Ruiz JA, Aouf N (2017) Real-Time Setup with PD and Backstepping Control for a Pelican Quadrotor
4. Bouabdallah S, Siegwart R (2005) Backstepping and sliding-mode techniques applied to an indoor micro quadrotor. In: Proceedings of the 2005 IEEE international conference on robotics and automation. IEEE, pp 2247–2252
5. Hassani H, Mansouri A, Ahaitouf A (2020) Robust autonomous flight for quadrotor UAV based on adaptive nonsingular fast terminal sliding mode control. *Int J Dyn Control*. <https://doi.org/10.1007/s40435-020-00666-3>
6. El Hajjami L, Mellouli EM, Berrada M (2020) Neural network based sliding mode lateral control for autonomous vehicle. In: 2020 1st International Conference on Innovative Research in Applied Science, Engineering and Technology (IRASET). IEEE, pp 1–6

7. González-Hernández I, Salazar S, Rodriguez-Mata AE et al (2017) Enhanced robust altitude controller via integral sliding modes approach for a quad-rotor aircraft: Simulations and real-time results. *J Intell Robot Syst* 88:313–327
8. Hassani H, Mansouri A, Ahaitouf A (2020) A new robust adaptive sliding mode controller for quadrotor UAV flight. In: 2020 IEEE 2nd International Conference on Electronics, Control, Optimization and Computer Science (ICECOCS). pp 1–6
9. Jiang X, Su C, Xu Y et al (2018) An adaptive backstepping sliding mode method for flight attitude of quadrotor UAVs. *J Cent South Univ* 25:616–631
10. Arora S, Singh S (2019) Butterfly optimization algorithm: a novel approach for global optimization. *Soft Comput* 23:715–734
11. El Hajjami L, Mellouli EM, Berrada M (2019) Optimal PID control of an autonomous vehicle using Butterfly Optimization Algorithm BOA. In: Proceedings of the 4th International Conference on Big Data and Internet of Things. pp 1–5
12. Hassani H, Mansouri A, Ahaitouf A (2019) Control system of a quadrotor UAV with an optimized backstepping controller. In: 2019 international conference on intelligent systems and advanced computing sciences (ISACS). pp 1–7
13. Bahgat GA, Fawzy A-A, Emara HM (2019) An unbiased butterfly optimization algorithm. In: International Conference on Bio-Inspired Computing: Theories and Applications. Springer, pp 506–516
14. Xiong J-J, Zhang G-B (2017) Global fast dynamic terminal sliding mode control for a quadrotor UAV. *ISA Trans* 66:233–240

Localization and Navigation System for Blind Persons Using Stereo Vision and a GIS



Moncef Aharchi and M.'hamed Ait Kbir

Abstract Loss of vision caused by infectious diseases has decreased significantly; however aging will increase the risk that more people acquire vision impairment. Visual information is the basis of most navigation tasks; a person is considered visually impaired when he has no appropriate information on the surrounding environment. With the latest evolution of digital technologies, the assistance provided to visually disabled people during their mobility can be improved. In this context, we propose a system to help the visually impaired move quickly and to know their environment. Indoors, the system uses a stereoscopic camera, a portable computer, and a headset to direct and help visually impaired persons navigate comfortably and securely in familiar and unfamiliar environments. Outdoors, a GPS is used as a positioning method to keep the visually impaired person on the right path; with its dynamic routing and rerouting capabilities, it provides the user with an optimized path. The system can work on an outdoor and indoor environment. A stereoscopic camera is used to detect visual indicators that are used to trace and validate user navigation, provide accurate indoor location measurements, and recognize objects in front of the user. This article is mainly focused on this system and detailed outlines description.

Keywords Blind Navigation · Autonomy · Accessibility · Computer Vision · Geographic information system

1 Introduction

According to the World Health Organization (WHO), global development since the 1990 indicates reduced rates of visual impairment and a variation in causes. Blindness and vision loss arising from infectious diseases have been significantly reduced.

M. Aharchi (✉) · M. A. Kbir (✉)

LIST Laboratory, Faculty of Sciences and Technologies, Tangier, Morocco

e-mail: maharchi@uae.ac.ma

M. A. Kbir

e-mail: m.aitkbir@fstt.ac.ma

© Springer Nature Singapore Pte Ltd. 2022

S. Bennani et al. (eds.), *WITS 2020*, Lecture Notes in Electrical Engineering 745,

https://doi.org/10.1007/978-981-33-6893-4_35

When the global population is growing, more and more people are at risk of age-related vision loss, and populations grow older, particularly in developed countries [1]. Statistically, about 314 million individuals worldwide with a visual disability, 14.3 percent of whom are fully blind (45 million).

A person is said to be visually impaired when he does not have access to information on his environment [2] because visual information is the basis of most navigation activities. There are aids widely used by the blind: the guide dog and the white cane [3]. These two supports are practical enough and have always been used. However, they only offer information on surrounding objects or obstacles and restrict the blind to traveling in familiar environments. Thanks to the latest technological advances, it has become possible to extend and improve support for visually impaired people during their travels. It has become possible to develop systems that use a digital camera and allow the visually impaired to have access to more information about the environment, such as identifying obstacles or points of interest and calculating the distance between the visually impaired and objects [4].

In this context, we suggest a description of a system that also supports outdoor and indoor navigation. The outdoor version uses the GPS to locate the user in large areas, such as streets or neighborhoods, answers different user requests and dynamically provides routing and redirecting information based on changes in the environment. It is much more challenging to move around in an indoor environment because the room is relatively small, and there are many corridors, marches, doors, and furniture.

People with visual impairment can face several obstacles. If the visually impaired person is in a new environment, (e.g., a hotel or a new street), walking alone may be dangerous. Thanks to this device, the user can have a full picture of his world. The user can also obtain distance and navigation information between the destinations and the surrounding objects. This will help him to avoid obstacles in real-time. As the GPS usually will not provide a right result inside and the measurement error criteria change, the device moves to a different location tracking technology: a stereoscopic camera would be used to construct a disparity map based on the two images taken by this camera in order to provide a high precision measurement scale and allow the user to know the layout of the indoor environment. This would also make it possible to recognize the objects in front of the user by identifying and analyzing the objects in the images captured by the stereoscopic camera. Visual indicators will be put on the scene to allow objects to be easily identified.

In the remainder of this paper, we will present a brief review of the related work in Sect. 2. The proposed approach is discussed in Sect. 3 and the device architecture is presented in Sect. 4. Section 5 describes how to create a depth map and detect obstacles. Section 6 discusses the visual indicators used to detect objects and finally an idea of future work and a conclusion and are presented in Sect. 7.

2 Related Work

Among the examples of visually impaired assistance systems that use vision sensors, there is vOICe [5]. This system captures the image using a single camera mounted on a helmet, and then a sound is produced from left to right from the scan results of this image. Tones with high frequency represent the upper part of the picture; tones represent the bottom portion of the image with low frequency. The tonal loudness depends on the pixel's brightness. Similar research was performed at NAVI [6]. In this method the image captured is resized to 32×32 and the image's gray scale is reduced to 4 levels, representing 4 categories of distance. Using image processing techniques, the image is differentiated into objects and background according to the previously established 4 distance categories, because brighter pixels represent closer objects. In this way objects are assigned with high intensity values, and low intensity values suppress the background. The processed image is then transformed into stereo sound, where the sound amplitude is directly proportional to the image pixel intensity, and the sound frequency is inversely proportional to the pixel vertical orientation.

The use of stereo vision for application of blind navigation is in the early stages and only limited research efforts have been reported. In Optophone [7], an edge detection routine is applied to images from two cameras to obtain a disparity map. Disparity is measured using edge features of both images. The disparity map is then transformed into sound using the process applied to the voice system and the sound loudness is directly proportional to the size of the pixels. The disparity map of all the edge features of the images is obtained in the optophone. With only the edge information, proper identification of the object will be difficult, since there will also be unwanted edge features.

The visual support system developed by Fumiaki Tomita and Yoshihiro Kawai [8] is another work reported in this area. A computer, three small cameras, a microphone mask, a mask and a sound processor are included in the prototype device. In order to obtain a 3D structure representing the environment in front of the user, the images captured by the small stereo cameras are analyzed and object recognition is performed. Then the results are converted and made available to the user via virtual 3D sound. Although the information that this system obtains is far more accurate than other systems, the prototype developed has big dimensions and it's not portable.

The use of haptic tools to provide the user with outputs from the machine is very useful as blind people typically rely heavily on secure navigation and environment perception in the hearing sense. A pioneering work by Zeleket. Al., involving stereo vision systems, was designed to provide tactile (haptic) feedback to the blind user on environment information [9]. In this work the cameras record the images, and from the two relative views the disparity is measured. The user is provided with the depth information by stimulating the fingers and no image processing attempts are made to highlight the object information in the output.

Although many efforts have already been made to allow visually impaired persons to navigate safely using digital cameras, there are still too many possibilities to be discovered, and there is still a lack of knowledge given to the user while traveling.

3 The Proposed Approach

When a visually impaired person is walking, he misses a lot of valuable information such as directions or obstacle locations and signage panels. He is, therefore obligated to use itineraries that are familiar to him. However, often even such routes can be subject to change: a sidewalk can be blocked for road work for example. A dog-guide or long cane can help diagnose obstacles and know the routes, but more details are needed for the visually impaired person to find alternatives to detours or new routes. To help a visually impaired person to the maximum, The navigation system must provide sufficient information to give it a full view of its surroundings and provide real-time information on its journey through voice syntheses.

The sample communication between user and system is illustrated in Table 1:

The system incorporates the indoor facilities to provide a wide image of the indoor environment for the user. While the user is walking, he can ask for the current position and request an optimal route to reach a destination. A step-by—step instruction with the orientation and angles is given with the user’s current location.

Also, the user must be assisted in his travel by vocal prompts, such as the distance that separates him from the surrounding objects or the presence of an obstacle or the new route if needed. The system must provide the route with the least risk. In case of possible obstacles, warnings are given.

The interface for the communication is user friendly. It adopts many expressions for every command that are widely used in everyday life (Fig. 1).

Table 1 An example of communication between the user and the system

User question	What is in front of me?
System response	A TV
User question	Get me to the nearest grocery store
Get me to the nearest grocery store	Keep going straight
System	Attention to the wall on your right

Fig. 1 An example of how the device would be carried by a visually impaired person

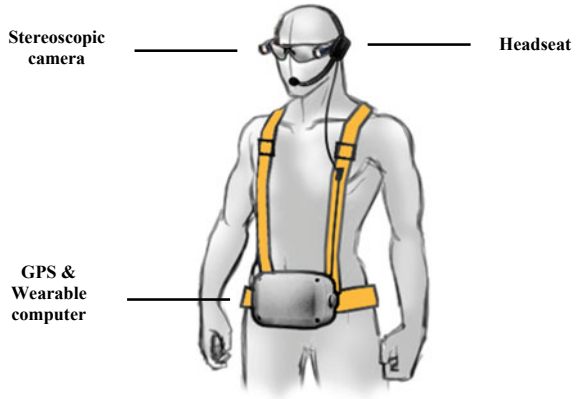
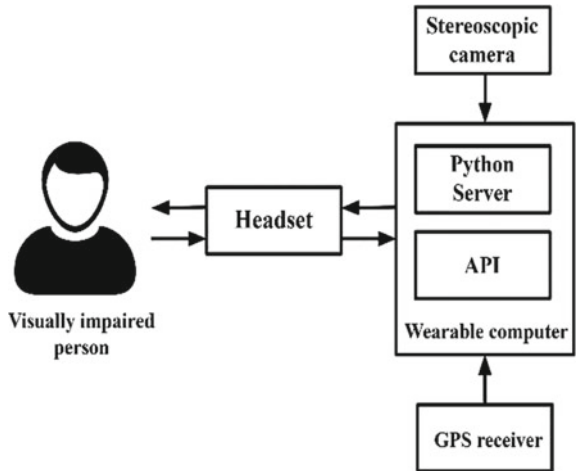


Fig. 2 System architecture



3.1 System Design

The system is composed of software and hardware, and need to be lightweight in order not to encumber and disturb the user during it navigation. Figure 2 shows how a user can carry this system:

3.2 Hardware Components

The following describes the hardware components used in the integrated in this system.

Wearable computer: As shown in Fig. 1, the wearable computer must be able to perform the necessary image processing tasks as well as the various sound / text conversion tasks in order to be able to interact correctly with the user. It represents the most important part of this system. He uses the Linux system.

GPS receiver: It is used as a positioning method to keep the user as close to the middle of the path as possible (sidewalks ...).

Headset: It is the means by which the user can hear the system response and allow him to record sound through the microphone.

Stereoscopic camera: Will take 2 images of the world in front of the user using its two cameras which will then be transformed into a depth map.

3.3 Software Components

The system software part is a python server. It receives all the data to be processed and returns the results to the user. The image processing of the stereoscopic camera images is performed using the *OpenCv* library. Audio-to-text conversion is done using the *SpeechRecognition* [10] library. Other libraries will be used as complements to these two major libraries. To help determine the correct path to take when the user is outside. This system will be based on the *Google MAPS API service* [11] and on the position of the user which will be provided by the GPS.

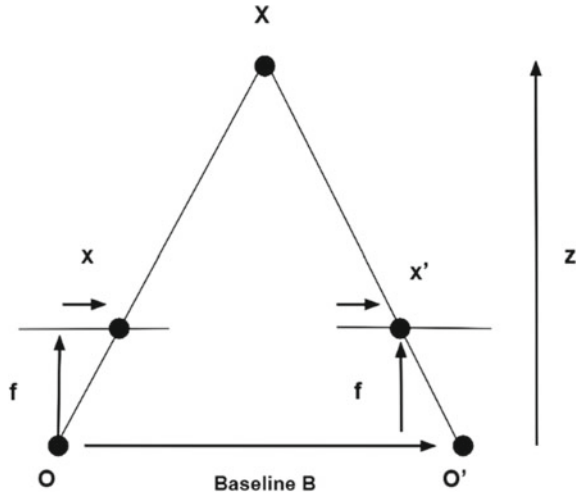
3.4 System Architecture

The architecture of this system is displayed in Fig. 3. Using the commands defined in the system grammar, the user communicates with the mobile client via the headphone and microphone, asking for route and obstacle prompts, making queries about his / her location.

The user's words are then translated to text to be evaluated and compared with the system's predefined command list at the Python server side. At the same time, the stereoscopic camera captures images of the user's environment. These 2 images are then converted to a depth map at the server side. This depth map will indicate the distance between the user and the obstacles in front of him. These two images are also used to detect the existence of visual indications that are placed on the various places in the user's environment.

If the user is indoor, then the system mainly uses the stereoscopic camera. In this situation, the GPS cannot be used as it is dedicated exclusively to outdoor situations. If the user is outdoor, the device also uses the GPS in addition to the stereoscopic camera. To find the best directions to follow, the GPS is used to determine the user's location value, this value is interpreted by the server that uses it to determine the

Fig. 3 Retrieval of the depth of a point from 2D images



route to take with the use of the Google MAPS API. The textual result of the Google MAPS API response is then converted to audio to be heard by the user. As the user moves, these operations will be repeated.

4 Converting 2D Images into a depth map

To get the distance that separates the user and the objects in front of him and allow him to avoid obstacles while moving; we use a stereoscopic camera which allows us to take 2 images. By using the two images of the same scene captured by the camera from slightly different points of view, we can manage to recover the depth of a point present on the two images.

The goal is to see the depth of objects found in a series of stereo images. Essentially we will create a grayscale heat map whereby lighter shades of gray mean objects near to the camera lens with increasingly darker shades to better differentiate objects. The depth of a point in real-world space can be calculated by using mathematical formulas and functions, which incorporate epipolar geometry principles. The image below shows a proof of those principles in practice.

Now let's break down the above diagram. First we should note the optical centers of both our O and O' cameras in addition to the point in 3D space, the depth of which we try to find; point X . Length f is the focal length of our cameras which we know from the cameras intrinsic values. Now x and x' are the points on the 2D image plane, where point X will appear respectively in each image. The concept here is that to obtain the depth Z of point X , the corresponding triangles as denoted Ofx and $O'fx'$ will be compared to each other. The equation which allows us to achieve this is shown below.

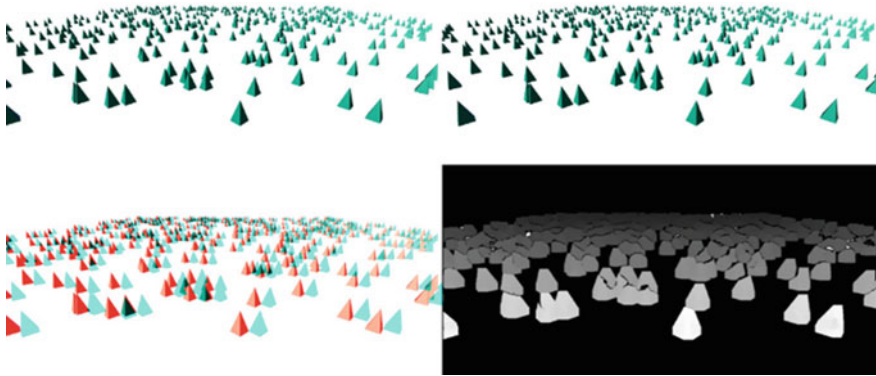


Fig. 4 Disparity map from two 2D images

$$\text{Disparity} = x - x' = \frac{Bf}{z}$$

To describe the equation as plainly as possible, it tells us that the distance Z from point X away from the optical centers of our cameras is inversely proportional to the distance difference between points x and x' (the image points of our object as they appear on the 2D plane).

In summary, OpenCV is used to find matching points in each of our images, greatly assisted by epipolar constraint principles. It then calculates the disparity between the matched points thus giving us the depth of the object in question [12].

The image below shows the result of one obtained by transforming 2D images into a disparity map using OpenCV (Fig. 4).

5 The Visual Markers

Surface recognition by itself does not allow the user to have good mobility. Therefore, it is necessary to detect the nature of these surfaces in order to allow the user a better understanding of his surrounding environment.

This system will be based on the use of visual markers that will be found throughout the route that a visually impaired person can take. They will also be placed on important places.

For example, these markers will be placed along the sidewalks and on the different access points to allow the visually impaired person to stay in the right path (Fig. 5).

In order to be observed by the stereoscopic camera from afar, these visual markers must be clear and easy to identify, this is why we decided to use ArUco markers [13].

ArUco markers are binary fiducial square markers, which can be used to estimate the camera pose. Their main benefit is that they are robust, quick and easy to detect. An ArUco marker consists of a large black border and an internal binary matrix



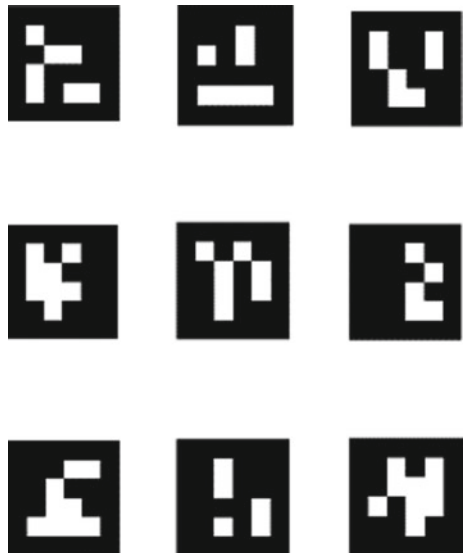
Fig. 5 Examples of acquired images, containing visual markers

determining its identifier (id). For example a 4×4 marker size is composed of 16 bits.

Some examples of ArUco markers (Fig. 6).

It should be noted that a marker can be found to be rotated in the area, but the detection mechanism must be able to establish its original orientation, so that each corner is unambiguously defined. This is also done based on the codification of the binary. A marker dictionary is a set of markers, which are considered in a

Fig. 6 Examples of ArUco markers



particular application. It is essentially the binary coding list for each of its markers. A dictionary's principal properties are the dictionary size and the size of the marker.

- The size of the dictionary is the number of markers, which compose the dictionary.
- The size of the marker is that of those markers (number of bits).

One might think the marker id is the number obtained by converting the binary coding to a decimal base number. However, this is not possible since the number of bits is too high for high marker sizes, and it is not practical to manage such huge numbers [14].

Instead, a marker id is simply the index of markers within the dictionary to which it refers. For example, in a dictionary the first 5 markers have the ids 0, 1, 2, 3, and 4.

5.1 *Detection of Visual Markers*

The detection process must return a list of detected markers, given an image that contains ArUco markers. Each marker discovered includes:

- The position of its four corners (in their original order) in the picture.
- The marker id.

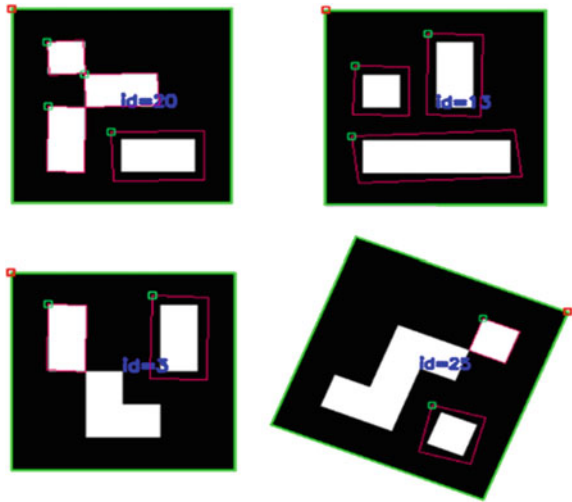
The detection process for the markers consists of two steps:

Step 1: Detection of candidate markers. In this step the image is analyzed to find square shapes that are marker candidates. It begins with an adaptive threshold to segment the markers, then it extracts contours from the threshold image and discards those that are not convex or do not correspond to a square shape. Extra filtering is also applied (Eliminating contours that are too small or too large, removing contours that are too close to each other, etc.).

Step 2: After detection of the candidate, by analyzing their inner codification, it is necessary to determine if they are really markers. This step begins with the extraction of each marker bits. For this, a transformation of perspective is first applied in order to obtain a marker in its canonical form. Then, the canonical image is thresholded using Otsu to separate white and black bits. The image is split into different cells, depending on the size of the marker and the border. The number of black or white pixels in each cell is then counted to decide if this is a white or a black bit. Finally, it analyzes the bits to decide if the marker belongs to the same dictionary. Techniques for correcting errors are used where necessary [15].

Detected visual markers are framed in green. Note that certain markers are rotated. The small red square points to the top left corner of the marker (Fig. 7).

Fig. 7 ArUco marker detection result



6 Summary and Future Work

The main objective of this work was to create a system that detects objects in the environment, provide orientation/navigation instructions and give distance information to the blind user and information about his location. Using a stereoscopic camera and using a depth map, the system provides a good idea to the blind user of the obstacles that can be found along the way. The blind user will also be able to know information about the nature of the objects in his environment and the places where he is located through the use of ArUco markers. The use of a GPS and an API would enable to know the location of blind and therefore to give him the best way to reach his destination.

Since this is a work in progress, not all has been done yet. Since this article is a description of this future system, a lot remains to be accomplished and tested. In the future we are considering creating a prototype of this system that could possibly receive modifications and improvements.

References

1. World Health Organization, Webpage, <https://www.who.int/mediacentre/factsheets/fs282/en/>. Last visited on 23 Feb 2010
2. Balakrishnan G, Sainarayanan G, Nagarajan R, Yaacob S (2007) Wearable real-time stereo vision for the visually impaired. *Eng Lett Int Assoc Eng* 6–14
3. Wong F, Nagarajan R, Yaacob S, Chekima A (2000) Electronic travel aids for visually impaired—a guided tour. In: *Proceedings of Conference in Engineering in Sarawak*, pp 377–382
4. Anderson JD, Lee DJ, Archibald JK (2007) Embedded stereo vision system providing visual guidance to the visually impaired. In: *The third iee/nih life science systems and application*

- workshop (LISSA), pp 229–232
5. Meijer P (1991) An experimental system for auditory image representations. In: IEEE Transactions on Biomedical Engineering, pp 112–121
 6. Sainarayanan G (2002) On intelligent image processing methodologies applied to navigation assistance for visually impaired, Ph.D. thesis, University Malaysia Sabah
 7. Capp M, Picton P (2000) The Optophone: an electronic blind aid. Eng Sci Educ J 137–143
 8. Kawai Y, Tomita F (2002) A support system for visually impaired persons to understand three-dimensional visual information using acoustic interface. In: IEEE 16th conference on pattern recognition, pp 974–977
 9. Zelek J, Bromley S, Aamar D, Thompson D (2003) A haptic glove as a tactile vision sensory substitution for way finding. J Vis Impairment Blindness 621–632
 10. SpeechRecognition Webpage. https://github.com/Uberi/speech_recognition
 11. Google Maps Platform Webpage. <https://cloud.google.com/maps-platform/>
 12. OpenCV documentation, Depth Map from Stereo Images. https://docs.opencv.org/master/dd/d53/tutorial_py_depthmap.html
 13. OpenCV documentation, Markers and Dictionaries. https://docs.opencv.org/trunk/d5/dae/tutorial_aruco_detection.html
 14. OpenCV documentation, Detection of ArUco Markers, Markers and Dictionaries. https://docs.opencv.org/trunk/d5/dae/tutorial_aruco_detection.html
 15. OpenCV documentation, Detection of ArUco Markers, Marker Detection. https://docs.opencv.org/trunk/d5/dae/tutorial_aruco_detection.html

New Delay Dependent Stability Condition for a Carbon Dioxide Takagi Sugeno Model



Azeddine Elmajidi, Elhoussine Elmazoudi, Jamila Elalami,
and Nouredine Elalami

Abstract The growing interest in the preservation of environment leads several researchers to investigate the causes behind the high level of CO₂ and how to decrease it. This paper, deals with continuous time delay nonlinear systems (TDNS) stability conditions using the Takagi Sugeno Fuzzy Modeling. First a Nonlinear Carbon Dioxide Model is defined and transformed to a corresponding Fuzzy Takagi Sugeno (TS) multi-model. Then, by using the Lyapunov-Krasovskii Functionals (LK-F) and extending some linear time delay systems dependent delay stability technique to TS Fuzzy Modeling, a new relaxed stability conditions involving uncommon free matrices are addressed in Linear Matrix Inequalities (LMI). Finally a numerical simulation is also carried out to support the analytic results and to compare the conservativeness of the proven condition to other existing methods.

Keywords Fuzzy · TS · Time Delay · Stability · LK-F.

1 Introduction

During these last years the greenhouse effect and air contamination have been one of the most horrendous results of the CO₂ increase due to forest and woodland

A. Elmajidi (✉) · J. Elalami
LASTIMI, High School of Technology Sale, Mohammed V University in Rabat,
Rabat, Morocco
e-mail: elmajidi@gmail.com

J. Elalami
e-mail: j.elalami@cnrst.com

E. Elmazoudi
CISIEV, FSJES, Cadi Ayyad University in Marrakech, Marrakech, Morocco
e-mail: h_mazoudi@yahoo.fr

N. Elalami
LASTIMI, Mohammadia School of Engineers, Mohammed V University in Rabat, Rabat,
Morocco
e-mail: prelalami@gmail.com

deforestation and human activities, likewise, the heightening enthusiasm for nature regard drives governments and analysts to explore the elevated level of CO_2 , in [1] a first mathematical model is represented, its stability conditions is discussed and how severe deforestation may prompt environment destabilization, additionally in [2] it is indicated that deforestation rate exceeding a critical value leads to unstableness, and using the same model in [3, 4] it is proven that controlling deforestation rate alone may not generally be a reasonable answer to the environment control, and an additional reforestation action might be an alternative. Also in [5] a variant model, exposed the impact of a delayed reforestation action on stability, and exposed that the system will become unstable if the delay transcend a maximal edge .

In the aim of studying the above model, we intend, in this paper, to analyze the stability conditions of a delayed TS fuzzy model, drown out from a CO_2 polynomial nonlinear system.

In one side, the fuzzy logic origin lies in the fuzzy set theory developed by Lotfi Zadeh in 1965 [6], which was used later to model systems based on human reasoning [7–9].

In the other side, the global stability for a delayed nonlinear system, like the delay free case, relies in most cases to sufficient conditions [9–11], in addition those conditions can be splitted to two methods, a first simplest way that resolve LMIs without involving delay terms, named delay independent conditions [9, 10, 12, 13] or a second sophisticated way that try to overcome the conservativeness by bringing out the maximum delay margin to which the nonlinear system with delay will remain stable, named delay dependent conditions [9, 10, 14] , and in most cases researchers rely on model transformation, adding slack variables, developing some cross-term bounding techniques [10, 11, 15].

The work is arranged as follows. In Sect. 2 we present the nonlinear model and its equivalent TS model. Main stability analysis results are stated in Sect. 3. In Sect. 4, numerical simulation to prove analytic results are presented. And finally, the paper is finished with some concluding remarks.

2 Takagi Sugeno Model

2.1 Carbon Dioxide Model

The model used in this document is a variant of the one proposed in [2, 3] by removing the elements representing the deforestation effects, that are replaced by reforestation measurement elements [5], also the delay introduced in the model comes from the time gap between appreciating the reforestation needs by forest biomass measurement and the reforestation program launch.

$$\dot{X} = \begin{pmatrix} \dot{C} \\ \dot{N} \\ \dot{F} \\ \dot{R} \end{pmatrix} = \begin{pmatrix} Q_0 + \lambda N - \alpha C - \lambda_1 CF \\ sN(1 - \frac{N}{L}) - \theta CN + \pi \phi NF \\ \mu F(1 - \frac{F}{M}) - \phi NF + \zeta RF \\ \gamma(M - F(t - \tau)) - \delta_0 R \end{pmatrix} \tag{1}$$

where

- $C(t)$ Atmospheric CO₂ level (ppm)
- $N(t)$ Human population (person)
- $F(t)$ Forest biomass (ton)
- $R(t)$ Reforestation Measurement (dollar)
- Q_0 Natural atmospheric CO₂ elevation rate (ppm year⁻¹)
- λ Anthropogenic atmospheric CO₂ elevation rate coefficient (ppm [person year]⁻¹)
- α Natural atmospheric CO₂ depletion rate coefficient (year⁻¹)
- λ_1 Atmospheric CO₂ depletion rate coefficient due to forest biomass ([year ton]⁻¹)
- s Intrinsic Human population growth rate (year⁻¹)
- L Human population carrying capacity (person)
- θ Human population depletion rate coefficient due to CO₂ ([ppm year]⁻¹)
- π Human population growth ratio due to forest biomass (person ton⁻¹)
- ϕ Deforestation rate coefficient (person year)⁻¹
- μ Intrinsic Forest biomass growth rate (year⁻¹)
- M Forest biomass carrying capacity (ton)
- ζ Forest biomass growth ratio due to reforestation effort (dollar year)⁻¹
- γ Reforestation efforts implementation rate coefficient dollar(ton year)⁻¹
- τ Time gap between Forest biomass measurement and reforestation efforts implementation (year)
- δ_0 Reforestation efforts declination rate coefficient (year⁻¹)

In this work, we were interested in the positive interior equilibria point E_4 due to its relevant position which meets with the actual world context where all values in E_4 are strictly positive, which is feasible if special conditions meet [5].

$$E_4 = (C^*, N^*, F^*, R^*) \tag{2}$$

All variables and parameters in Eq. (1) are positive, and more precisely $C(t) > 0$ and $F(\vartheta) \geq 0$ for $\vartheta \in [-\tau, 0]$, in addition the functional region of Eq. (1) is reduced to $[\epsilon, C_m] \times [0, N_m] \times [0, F_m] \times [0, R_m] \subset \mathbb{R}^4$ [2, 5], with ϵ is a small positive real number and where:

$$C_m = \frac{Q_0 + \lambda N_m}{\alpha} \quad N_m = L(1 + \frac{\pi \phi}{s} F_m) \quad F_m = M \quad R_m = \frac{\gamma M}{\delta_0} \tag{3}$$

2.2 Takagi Sugeno Transformation

To find a Takagi Sugeno model, the system Eq. (1) should be transformed to a zero equilibrium model by taking: $x = X - E_4$, to have the form:

$$\dot{x}(t) = Jx(t) + J_\tau x(t - \tau) + g(x) \tag{4}$$

where J and J_τ represent the linearization of Eq. (1) according to the original vector $x(t)$ and the delayed $x(t - \tau)$ near to the equilibria point E_4 , and $g(x)$ represents the nonlinear conduct of Eq. (1) away from E_4 .

Where:

$$\begin{aligned}
 J &= \begin{pmatrix} -(\alpha + \lambda_1 F^*) & \lambda & -\lambda_1 C^* & 0 \\ -\theta N^* & -\frac{sN^*}{L} & \pi \phi N^* & 0 \\ 0 & -\phi F^* & -\frac{\mu F^*}{M} & \zeta F^* \\ 0 & 0 & 0 & -\delta_0 \end{pmatrix} \\
 J_\tau &= \begin{pmatrix} 0 & 0 & 0 & 0 \\ 0 & 0 & 0 & 0 \\ 0 & 0 & 0 & 0 \\ 0 & 0 & -\gamma & 0 \end{pmatrix} \\
 g(x) &= \begin{pmatrix} -\lambda_1 x_1 x_3 \\ -\frac{s x_2^2}{L} - \theta x_1 x_2 + \pi \phi x_2 x_3 \\ -\frac{\mu x_3^2}{M} - \phi x_2 x_3 + \zeta x_3 x_4 \\ 0 \end{pmatrix}
 \end{aligned} \tag{5}$$

Next, $g(x)$ vector will be put in $\mathbf{A}(x).x$ form [9, 16–18]. For the system Eq. (4), we choose to pick up a configuration involving just two state variables which will reduce the rules number to $2^2 = 4$ rules [3]:

$$\mathbf{A} = \begin{pmatrix} -\lambda_1 x_3 & 0 & 0 & 0 \\ -\theta x_2 & -\frac{s x_2}{L} & \pi \phi x_2 & 0 \\ 0 & -\phi x_3 & -\frac{\mu x_3}{M} & \zeta x_3 \\ 0 & 0 & 0 & 0 \end{pmatrix} \tag{6}$$

The whole system will be of the form:

$$\dot{x}(t) = Ax(t) + A_\tau x_t(\tau) \tag{7}$$

where $x_t(\tau) = x(t - \tau)$, $A = J + \mathbf{A}$ and $A_\tau = J_\tau$

Next, the nonlinear system Eq. (7) will be transformed to a several LTI sub-models by using extremum values of the so called premise variables (we chose $z_1 = x_2, z_2 = x_3$), and the firing probability weighting $h_i(z(t))$ [7–9].

According to Non-linearity sector [9, 16, 19] each premise variable could be written as:

$$z_i = \text{Max}_{z_i}.M_{i1} + \text{min}_{z_i}.M_{i2} \tag{8}$$

where $z_i \in [\text{min}_{z_i}, \text{Max}_{z_i}]$ and $M_{i1} + M_{i2} = 1$ The Takagi Sugeno multi model of Eq. (7) will be then described as:

$$\dot{x}(t) = \sum_{i=1}^r h_i(A_i x(t) + A_\tau x_\tau(\tau)) \tag{9}$$

where $h_i = \frac{w_i}{\sum_{i=1}^{r=2^n} w_i}$, $w_i = \prod_{j=1}^n M_{jk_j}$, $j \in \{1..n\}$, $k_j \in \{1, 2\}$

3 Stability Analysis

The aim of this section is to extend the [20]’s work made for linear time delay systems to Takagi Sugeno Fuzzy systems, while adding a novelty by substituting common matrices in [20] by non common ones to get a more relaxed LMIs.

*In the following * denotes the off-diagonal block element’s transpose.*

Lemma 1 ([20]) *For any given vectors u, v , any positive matrices $\begin{pmatrix} X_i & Y_i \\ * & Z \end{pmatrix} \geq 0$ and any matrix N_i , we have:*

$$- 2 \int_{\Omega} u^T(s)N_i v(s)ds \leq \int_{\Omega} \begin{pmatrix} u(s) \\ v(s) \end{pmatrix}^T \begin{pmatrix} X_i & Y_i - N_i \\ * & Z \end{pmatrix} \begin{pmatrix} u(s) \\ v(s) \end{pmatrix} ds \tag{10}$$

Lemma 2 ([21]) *If there exist a matrix $Z > 0$, and a firing probability h_i then:*

$$\chi^T \sum_{i=1}^r \sum_{j=1}^r h_i h_j \begin{pmatrix} A_i^T Z A_j & A_i^T Z A_{d_j} \\ A_{d_i}^T Z A_j & A_{d_i}^T Z A_{d_j} \end{pmatrix} \chi \leq \chi^T \sum_{i=1}^r h_i \begin{pmatrix} A_i^T Z A_i & A_i^T Z A_{d_i} \\ A_{d_i}^T Z A_i & A_{d_i}^T Z A_{d_i} \end{pmatrix} \chi \tag{11}$$

where $\chi^T = [x^T \ x_\tau^T]$

3.1 Main Results

Theorem 1 *If there exist matrices $P > 0, Q > 0, Z > 0, X_i$ and Y_i such that:*

$$\begin{pmatrix} \Lambda & P A_{d_i} - Y_i & \bar{\tau} A_i^T Z \\ * & -(1 - d)Q & \bar{\tau} A_{d_i}^T Z \\ * & * & -\bar{\tau} Z \end{pmatrix} < 0, \quad \forall i \in 1 \dots r \tag{12}$$

where $\begin{pmatrix} X_i & Y_i \\ * & Z \end{pmatrix} \geq 0$ and $\Lambda = A_i^T P + P A_i^T + \bar{\tau} X_i + Y_i + Y_i^T + Q$, then the unforced TS-TDS Eq. (9) is asymptotically stable for any time-delay $\tau \in [0, \bar{\tau}]$ and $0 \leq \dot{\tau} \leq d < 1$

Proof Let's take the unforced TS-TDS $\dot{x}(t) = \sum_{i=1}^r h_i(A_i x(t) + A_{d_i} x(t - \tau))$

With: $\chi^T = [x^T(t) \ x(t - \tau)^T]$, $0 \leq \dot{\tau} \leq d < 1$, $\tau \in [0, \bar{\tau}]$

And a Lyapunov Krasovskii Functional candidate:

$$V(x(t - \tau)) = V_1 + V_2 + V_3 \tag{13}$$

where

$$\begin{aligned} V_1 &= x^T(t) P x(t) \\ V_2 &= \int_{-\bar{\tau}}^0 \int_{t+\beta}^t \dot{x}^T(\alpha) Z \dot{x}(\alpha) d\alpha d\beta \\ V_3 &= \int_{t-\tau}^t x^T(s) Q x(s) ds \end{aligned} \tag{14}$$

Which yields to:

$$\dot{V}_1 = 2x^T(t) P \dot{x}(t) = \sum_{i=1}^r h_i(2x^T(t) P A_i x(t) + 2x^T(t) P A_{d_i} x(t - \tau)) \tag{15}$$

Using the Leibniz Formula [10, 20]:

$$x(t - \tau) = x(t) - \int_{t-\tau}^t \dot{x}(s) ds \tag{16}$$

$$\dot{V}_1 = \sum_{i=1}^r h_i(x^T(t)(P(A_i + A_{d_i}) + (A_i^T + A_{d_i}^T)P)x(t) - 2x^T(t) P A_{d_i} \int_{t-\tau}^t \dot{x}(s) ds) \tag{17}$$

Using Lemma 1 with: $u(s) = x(t)$, $N_i = P A_{d_i}$ and $v(s) = \dot{x}(s)$, the Lyapunov functional's derivative \dot{V}_1 is upper bounded by:

$$\begin{aligned} \dot{V}_1 &\leq \sum_{i=1}^r h_i(x^T(t)(P A_i + A_i^T P)x(t) + \tau x^T(t) X_i x(t) + 2x^T(t) Y_i x(t) \\ &\quad - 2x^T(t)(Y_i - N_i)x(t - \tau) + \int_{t-\tau}^t \dot{x}^T(s) Z \dot{x}(s) ds) \end{aligned} \tag{18}$$

$$\begin{aligned} \dot{V}_1 \leq & \sum_{i=1}^r h_i [\chi^T \left(\begin{matrix} PA_i + A_i^T P + \bar{\tau} X_i + Y_i + Y_i^T PA_{di} - Y_i \\ * \\ 0 \end{matrix} \right) \chi] \\ & + \int_{t-\bar{\tau}}^t \dot{x}^T(s) Z \dot{x}(s) ds \end{aligned} \tag{19}$$

$$\dot{V}_2 = \bar{\tau} \dot{x}^T(s) Z \dot{x}(s) - \int_{t-\bar{\tau}}^t \dot{x}^T(s) Z \dot{x}(s) ds \tag{20}$$

Using Lemma 2 one gets:

$$\dot{V}_2 \leq \sum_{i=1}^r h_i \chi^T \bar{\tau} \begin{pmatrix} A_i^T Z A_i & A_i^T Z A_{di} \\ A_{di}^T Z A_i & A_{di}^T Z A_{di} \end{pmatrix} \chi - \int_{t-\bar{\tau}}^t \dot{x}^T(s) Z \dot{x}(s) ds \tag{21}$$

$$\dot{V}_3 \leq \chi^T \begin{pmatrix} Q & 0 \\ 0 & -(1-d)Q \end{pmatrix} \chi \tag{22}$$

Combining Eqs. (19)–(22) we get:

$$\dot{V} \leq \sum_{i=1}^r h_i \chi^T \Lambda \chi \tag{23}$$

where

$$\Lambda = \begin{pmatrix} PA_i + A_i^T P & & \\ +Y_i + Y_i^T + \bar{\tau} X & Q & PA_{di} - Y_i \\ * & & -(1-d)Q \end{pmatrix} + \begin{pmatrix} \bar{\tau} A_i^T Z \\ \bar{\tau} A_{di}^T Z \end{pmatrix} (\bar{\tau} Z)^{-1} (\bar{\tau} Z A_i \quad \bar{\tau} Z A_{di})$$

By the application of Lyapunov Krasovskii Theorem [10] and the Schur Complement to Λ [22], we got the result in Theorem 1.

This completes the Proof

□

4 Numerical Simulation

To show the reliability of the proposed method we chose to use the numerical values in Table 1, and the approaches used in [9, 17, 23, 24] on the same model and under the same conditions on Yalmip [25] and Mosek[26].

Table 1 Parameter values

Q_0	λ	α	λ_1	s	L	θ
5	5.76×10^{-4}	1.6×10^{-2}	4.8×10^{-9}	3.2×10^{-2}	10^5	10^{-6}
π	ϕ	μ	M	ζ	γ	σ_0
4×10^{-5}	7.1×10^{-7}	1.3×10^{-2}	7.5×10^5	2.6×10^{-6}	8×10^{-4}	2×10^{-4}

Table 2 Maximal delay margin in years for different methods

Method	Theorem 58 [9]	Theorem 6.1 [17]	Corollary 1 [23]	Theorem 3 [24]	Our approach
$\bar{\tau}_{\max}$	Infeasible	8.561	8.591	8.555	8.595

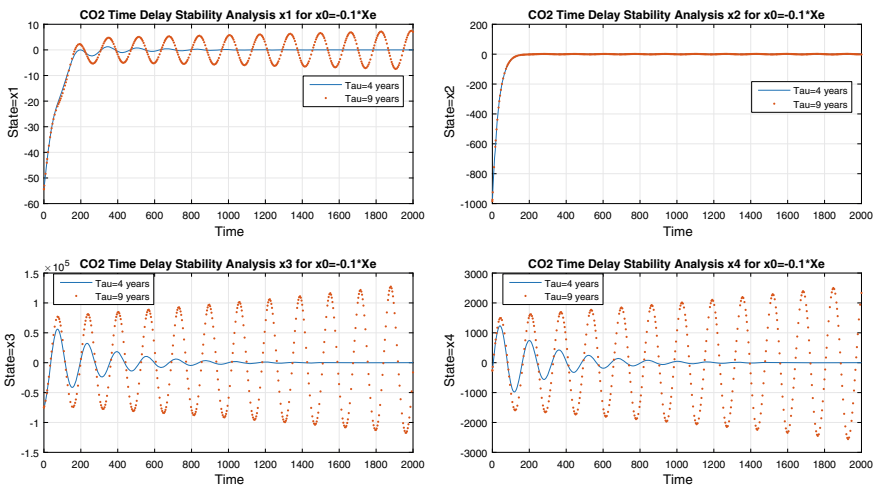


Fig. 1 CO₂ states versus time in years for $\tau = 4$ and 9 years, $x_0 = -0.1 * X_e$

First, by performing Simulation on the whole functional space (where The TS-TDS model is built assuming that $z_1 \in [N_e - N_m; N_m - N_e]$, $z_2 \in [F_e - F_m; F_m - F_e]$ and $d = 0$, we got the LMIs feasible for all the methods except the independent delay approaches, the results are stated in Table 2 showing that Theorem 1’s technique gives better result and a stability till a maximal delay $\bar{\tau}$ next to the theoretical value 8.6 [5], and in Fig. 1 we could notice that model is converging toward its equilibrium point for $\tau = 4$ years, while that of $\tau = 9$ years is diverging.

In addition, to underline the Forest Biomass Lower Boundary (FBLB) negative impact on $\bar{\tau}$, we made simulations for different ratios ϑ where $FBLB = -\vartheta F_e$ (i.e The TS-TDS model is built assuming that $z_1 \in [-N_e; N_m - N_e]$, $z_2 \in [-\vartheta * F_e; F_m - F_e]$ and $d = 0$), the results shown on Fig. 2 state that for a FBLB beyond a critical value ($-0.44 F_e$) the chosen method (Theorem 1), and eventually all the other

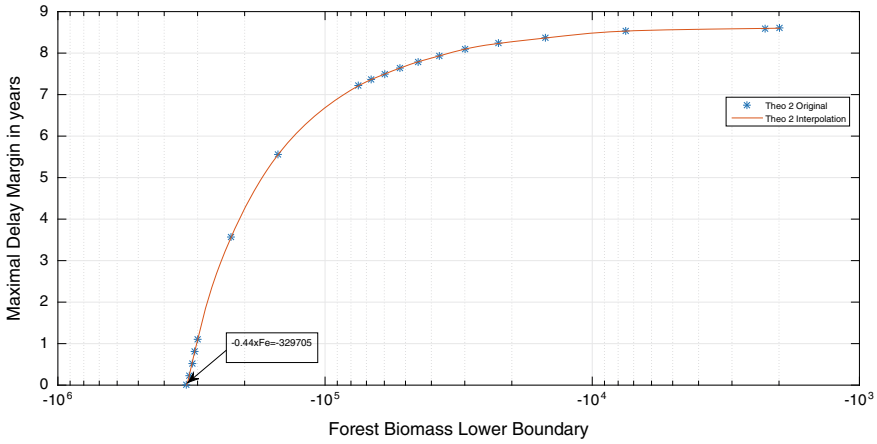
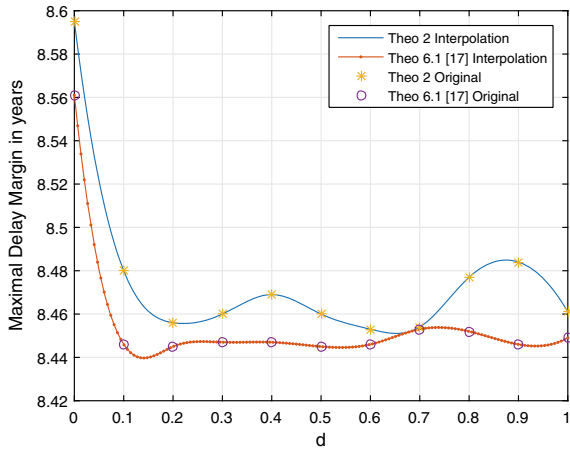


Fig. 2 Maximum feasible delay in respects to forest biomass lower boundary

Fig. 3 Derivative delay’s upper bound effect on the maximum feasible delay



methods, will become infeasible, which was expected knowing that the woodland is a basic CO₂ storage, and an initial situation x_0 where that reserve is lesser than a critical point will destabilize the system even if the delay margin is small.

Finally, we tried to pinpoint the effect of the derivative delay $\dot{\tau}$ for two chosen techniques in Fig. 3 which shows that Theorem 1 gives better results than Theorem 6.1 in [17], even if the latter gives a pseudo stable $\bar{\tau}$ for $d \in [0.1, 1]$, which is due to the presence of slack variables added to the term $-(1 - d)Q$ [27], also the effect of this LMI part is noticed to be minor when $d = 0.7$ where Theorem 1 is slightly superior.

5 Conclusion

In this paper, a new delay dependent stability condition was proved and addressed in linear matrix inequalities. By performing a numerical application we were able to show its less conservativeness in comparison to other methods, also we revealed the effect of the delayed reforestation on the carbon dioxide model and precisely forest biomass lower boundary's negative effect and the upper bound of the derivative delay on stability. Our next goal will be to construct a controller in order to stabilize the unforced system with an Output Parallel Distributed Compensation (OPDC).

Acknowledgements The authors would like to thank the reviewers for their constructive remarks and recommendations which will improve the quality of the final paper.

References

1. Tennakone K (1990) Stability of the biomass-carbon dioxide equilibrium in the atmosphere: mathematical model. *Appl Math Comput* 35:125–130
2. Misra AK, Verma M (2013) A mathematical model to study the dynamics of carbon dioxide gas in the atmosphere. *Appl Math Comput* 219:8595–8609
3. Elmajidi A, Elmazoudi E, Elalami J, Elalami N (2017) Carbon dioxide stability by a fuzzy Takagi Sugeno model. In: *Proceeding of the 4th Journée Scientifique d'Analyse des Systemes et Traitement de l'Information*, Rabat Morocco
4. Elmajidi A, Elmazoudi E, Elalami J, Elalami N (2019) A fuzzy logic control of a polynomial carbon dioxide model. *Ecol Environ Conserv* 25(2):876–887
5. Misra AK, Verma M, Venturino E (2015) Modeling the control of atmospheric carbon dioxide through reforestation: effect of time delay. *Model Earth Syst Environ* 1:24
6. Zadeh LA (1965) Fuzzy sets. *Inf Control* 8:338–353
7. Takagi T, Sugeno M (1985) Fuzzy identification of systems and its applications to modeling and control. *IEEE Trans Syst Cybern* 15(1):116–132
8. Lilly JH (2010) *Fuzzy control and identification*. Wiley (2010)
9. Tanaka K, Wang HO (2001) *Fuzzy control systems design and analysis: a linear matrix inequality approach*, 1st edn. Wiley
10. Fridman E (2014) Tutorial on Lyapunov-based methods for time-delay systems. *Eur J Control* 120:271–283
11. Seuret A, Gouaisbaut F, Baudouin L (2016) D1.1-overview of Lyapunov methods for time-delay systems. *Rapport LAAS n° 16308*, LAAS-CNRS. Hal-01369516
12. Cao YY, Frank PM (2001) Stability analysis and synthesis of nonlinear time-delay systems via linear Takagi-Sugeno fuzzy models. *Fuzzy Sets Syst.* 124:213–229
13. Kruthika HA, Mahindrakar AD, Pasumarthy R (2017) Stability analysis of nonlinear time-delayed systems with application to biological models. *Int J Appl Math Comput Sci* 27:91–103
14. Manai Y, Benrejeb M, Borne P (2011) New approach of stability for time-delay Takagi-Sugeno fuzzy system based on fuzzy weighting-dependent Lyapunov functionals. *Appl Math* 02:1339–1345
15. Seuret A, Gouaisbaut F (2012) On the use of the Wirtinger inequalities for time-delay systems. In: *Proceedings of the 10-th IFAC workshop on time delay systems*. The International Federation of Automatic Control Northeastern University Boston USA
16. Chadli M, Maquin D, Ragot J (2001) Stability and stabilisability of continuous Takagi-Sugeno systems. *Journées Doctorales d'Automatique*, Toulouse France, Sep 2001, pp. CDROM

17. Benzaouia A, El Hajjaji A (2014) Advanced Takagi-Sugeno fuzzy systems: delay and saturation, studies in systems. Decis Control 8
18. M. CHADLI, D. MAQUIN AND J. RAGOT, *Static output feedback for Takagi-Sugeno systems: an LMI approach*, Proceeding of the 10th Mediterranean conference on control and automation-MED2002, Lisbon, Portugal , (2002): pp.CDROM
19. Maria Nagy A (2010) Analyse et synthese de multimodeles pour le diagnostic: application a une station d'epuration <https://tel.archives-ouvertes.fr>
20. Moon YS, Park PG, Kwon WH, Lee YS (2001) A delay dependent robust stabilization of uncertain state-delayed systems. Int J Control 74(14):1447–1455
21. Chen B, Liu X (2005) Delay-dependent robust H control for T-S fuzzy systems with time delay. IEEE Trans Fuzzy Syst 13(4):544–556
22. Boyd S, Ghaoui L, Feron E, Balakrishnan V (1994) Linear matrix inequalities in system and control theory. Society for Industrial and Applied Mathematics SIAM, Philadelphia
23. Li C, Wang H, Liao X (2004) Delay-dependent robust stability of uncertain fuzzy systems with time-varying delays. IEEE Proc Control Theory Appl 151(4):417–421
24. Elmajidi A, Elmazoudi E, Elalami J, Elalami N (2020) Dependent delay stability characterization for a polynomial T-S carbon dioxide model. In: International conference on mathematics & data science (ICMDS 2020), pp CDROM
25. Löfberg J (2004) YALMIP : a toolbox for modeling and optimization in MATLAB. In: Proceedings of the CACSD conference, pp CDROM
26. Mosek (2020) MOSEK modeling cookbook, vol 3.2.2
27. Lin C, GuoWang Q, Lee TH, He Y (2007) LMI approach to analysis and control of Takagi-Sugeno fuzzy systems with time delay. In: Lecture notes in control and information sciences, vol 351

Simulation-Based Optimization for Automated Design of Analog/RF Circuits



Abdelaziz Lberni, Amin Sallem, Malika Alami Marktani, Abdelaziz Ahaitouf, Nouri Masmoudi, and Ali Ahaitouf

Abstract Automation tools for circuit optimization have proven their usefulness in solving design issues by considering the technological aspects of downscaling. Recent advances have proven that the optimization method based on simulation is a powerful and important solution for the optimal sizing of electronic circuits. In this paper, we propose a simulation-based methodology for automatic optimization of the multi-objective design of an analog/RF circuit. As applications, we use both analog and RF circuits, respectively the LC tank Voltage Controlled Oscillator (VCO) and the new Current-Feedback Operational Amplifier (CFOA). For the LC-VCO, we optimize the power consumption and the phase noise. For the CFOA, we optimize its important performances such as bandwidth and parasitic resistances, for low-voltage, low-power applications. All simulations are performed by HSPICE using 0.13 μm RF CMOS and 0.18 μm CMOS technologies for the LC-VCO and the CFOA, respectively.

Keywords Simulation-based method · Multi-objective optimization · Optimization algorithms · Analog circuit · IC design · Voltage controlled oscillator · CFOA · NSGA II · MOPSO-CD

1 Introduction

The progressive trend of CMOS technology towards smaller sizes has made the integration of integrated systems possible for wireless communication implementations [1]. Through the use of CMOS processes and technology development, the design

A. Lberni (✉) · M. A. Marktani · A. Ahaitouf
Laboratory of Intelligent Systems, Georesources and Renewable Energies, Sidi Mohamed Ben Abdellah University, Fez, Morocco
e-mail: abdelaziz.lberni@usmba.ac.ma

A. Sallem · N. Masmoudi
Laboratory of Electronics and Information Technologies, Sfax University, Sfax, Tunisia

A. Ahaitouf
Laboratory of Engineering Sciences, Sidi Mohamed Ben Abdellah University, Fez, Morocco

of analogue/RF circuits is imposing more stringent requirements in terms of accuracy, speed and integration [2]. Thus, the design challenge today is to design circuits meeting the required specifications with low noise and low consumption [3], despite the presence of parasitic effects in the CMOS technology. To meet the demands of low-power, low-cost wireless telecommunication technology, wireless devices must be efficiently optimized.

For instance, the most common used oscillator architecture in transceivers is the VCO. This circuit controls the oscillation frequency using a control signal. These types of oscillators always need selective circuits, usually RC circuits, LC circuits, switched capacitor, etc., which form a feedback for generating a sinusoidal output. Due to its advantages in RF applications, the LC-VCO is the most frequently used [4]. The LC resonator is made up of a spiral inductor and a CMOS variable capacitance (Varactor) which is controlled by a control signal voltage to change the oscillation frequency. However, the use of integrated inductors causes many problems, such as increased energy consumption and phase noise degradation [1].

Moreover, CFOA are among the more important integrated active elements. Compared to the operational amplifier, the CFOA are preferred in signal processing systems due to their essential advantages, namely, low power consumption, lower sensitivity, ease of performing different functionalities with few passive components and a closed-loop bandwidth that is independent of dc gain, eliminating the gain-bandwidth product constraint [5]. In addition, they provide the best performance in applications such as filters, integrators and oscillators, etc. [6].

In our previous work [7–10], we have studied the optimization of analog circuits including CMOS current conveyors, a CFOA and a Butterworth active filter using the model-based method. In this paper, we propose an efficient method based on multi-objective simulation that uses both the circuit simulation to guarantee the accuracy of the approach and the advantage of optimization algorithms to search for the optimal solutions. We focus on optimizing the important performances of the LC-VCO and the CFOA. The LC-VCO performances are evaluated by the following specifications: phase noise (PN), oscillation frequency (f_{osc}) and power consumption (P_{diss}). Thus, the purpose is to perform a multi-objective optimization while minimizing the two functions PN and P_{diss} at a fixed oscillation frequency with a given control signal. For the CFOA, the goal is to perform simultaneous optimization of four objectives such as minimizing the two parasitic input resistances, as well as maximizing the current cut-off frequency and voltage cut-off frequency.

The rest of the paper is structured as follows. In Sect. 2 presents the proposed automated design approach. In Sect. 3 shows two application examples where the automated design approach is applied to CFOA and LC-VCO. The conclusion is drawn in Sect. 4.

2 Simulation-Based Method to Analog Circuits Design

The simulation-based approach uses electrical simulations in order to evaluate the performance of the circuit. It extracts the parameters of the circuits to be optimized/sized which correspond to the results of the performed simulation. This approach is seen as very flexible in comparison to other approaches (knowledge-based, equation-based) since it adapts to any circuit topology and offers higher accuracy (depending on the simulator models) [11–13]. As long as the objective functions are adapted, the circuit design can be optimized multiple times for various specifications. As a result, almost any kind of circuits can be designed with this method and with a short set-up time. The basic diagram of the simulation-based method is shown in Fig. 1. The main part of this approach is the optimization block which is built by a meta-heuristic approach with the aim of finding the component values (transistors, inductors, resistors, etc.) that will give the best performance of the circuit. The evaluation block of this method is built with a circuit simulator.

This method works as follows: Once the Netlist file of the circuit is created, the algorithm responsible for the optimization randomly generates the input parameter vector in this netlist file, then, it calls the circuit simulator (HSPICE in this case) to check the imposed constraints and evaluate the required performances. Once the constraints are checked, the found performances are stored in an output file. After this, the optimization process returns to the first step, in which it randomly generates new values for the circuit parameters. Then, the circuit simulator is run to check the imposed constraints and evaluate the performances. Once the constraints verified, the new found performances are compared to the ones already saved in the output file, if are better, they will be saved in the output file, if not they will be rejected and the process will return to the first step. At each iteration, the best chosen solutions from the output file are saved in an external archive using the dominance sorting technique [14]. The optimization and evaluation cycle will be stopped when the stop requirement is met, and the final external archive only contains the non-dominated solutions. The proposed tool flowchart is given in Fig. 2.

Fig. 1 The simulation-based approach



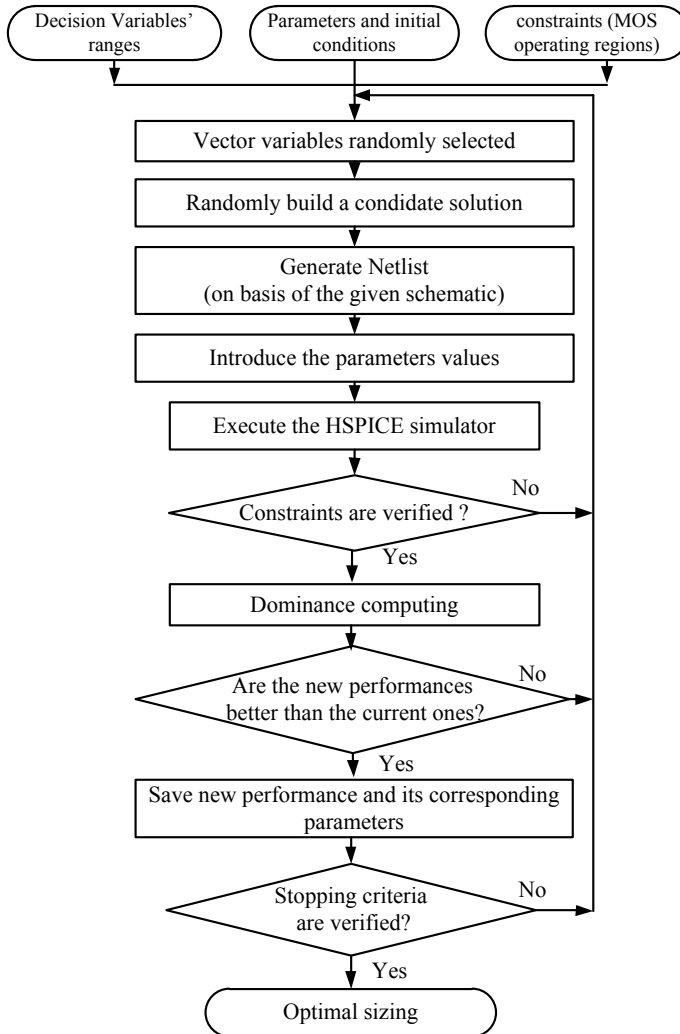


Fig. 2 The proposed tool flowchart

3 Simulation-Based Method Applications

3.1 CMOS LC-VCO

Figure 3 shows the LC-VCO circuit. The transistors M_{bias} are responsible for the polarization of the oscillator by I_{bias} . The inductor L and the capacitor C_{var} constitute the LC tank where, the variable capacitor C_{var} is designed by the transistor M_{var} as shown in Fig. 3, while the inductance L is designed by the 2π -model shown in Fig. 4.

Fig. 3 CMOS LC-VCO topology

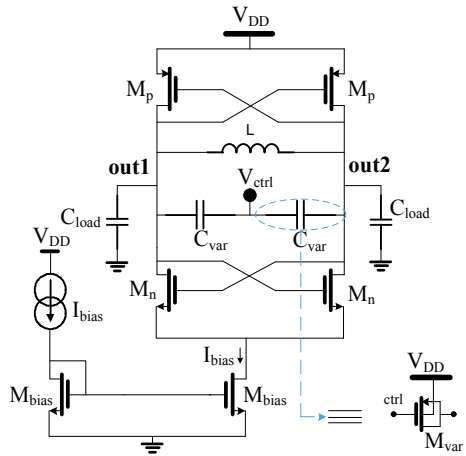
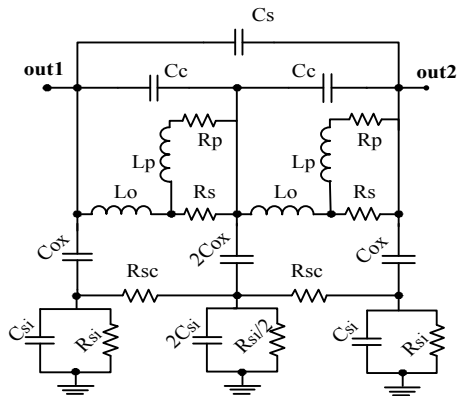


Fig. 4 Lumped inductor π -model



The oscillation frequency is controlled by varying the capacitor C_{var} by the voltage C_{ctrl} .

In an integrated spiral, the parasitic interferences occur between the metal tracks of the spiral and the layers of oxide and substrate [12], these parasites are represented by the resistances R_i , the capacitances C_i and the inductances L_i , in the inductor equivalent model given in Fig. 4.

The LC-VCO has several important performances, such as: the oscillation frequency, the Phase Margin and the Power Consumption. Most oscillator designs aim to achieve both minimum power consumption and phase noise at a given oscillation frequency. For example, if we aim for low power consumption, the bias current of the circuit must be low. However, the parasitic effects caused by the low current will have a major effect in the behaviour of the circuit, leading to the phase noise degradation. But, if we aim for low phase noise, the bias current must be high, which will lead to high power consumption. Therefore, the most appropriate objective for

Table 1 LC-VCO encoding variables and decision space

Variable	Encoding	Decision space
x ₁	f_{osc}	[1.5 GHz, 2.5 GHz]
x ₂	Mn, Mp, Mbias	[0.4 μ m, 1 μ m]
x ₃	Mvar	[0.4 μ m, 10 μ m]
x ₄	Mn	[1 μ m, 400 μ m]
x ₅	Mp	[1 μ m, 400 μ m]
x ₆	Mbias	[1 μ m, 400 μ m]
x ₇	Mvar	[1 μ m, 400 μ m]
x ₈	C_c, C_S and C_{si}	[0.1 pF, 20 pF]
x ₉	C_{ox}	[0.1 fF, 1 pF]
x ₁₀	L_o, L_p	[0.01 nH, 10 nH]
x ₁₁	R_s	[0.01 Ω , 30 Ω]
x ₁₂	R_p	[1 Ω , 1 k Ω]
x ₁₃	R_{sc}, R_{si}	[10 k Ω , 10 M Ω]

the oscillator design is to optimize simultaneously its phase noise and its power consumption. In other words, the objective is to find a set of solutions with the best trade-offs. There are thirteen design variables, their encoding and their decision space are given in Table 1.

The optimization was performed to generate a set of oscillator designs for a frequency band of 1.5–2.5 GHz using 0.13 μ m RF CMOS technology with a power supply of 1 V. Two different experiments were investigated, firstly, the inductance L is considered to be ideal, secondly, the inductance is replaced by its equivalent 2π model. The objective is to find a set of optimal parameter values of the LC-VCO that correspond to the set of trade-offs between phase noise and power consumption for an ideal and real inductance. In both experiments, the optimization results are given in Fig. 5.

As can be seen, the optimization method offers the designer the best available designs for the specific trade-off. As expected, given ideal inductors, optimization results are quite better than those with real inductors. The values of the achieved performance corresponding to the obtained Pareto front edges are shown in Table 2.

3.2 LVLP CFOA

Figure 6 shows a CMOS implementation of the CFOA, it is a current mode device with 4-ports (X, Y, Z and W). The relationships between the CFOA ports can be, in the ideal case, expressed as [15].

$$i_y = 0, \quad i_x = i_z = v_x = v_y \quad s \quad v_w = v_z \quad (1)$$

Fig. 5 The optimization results of LC-VCO

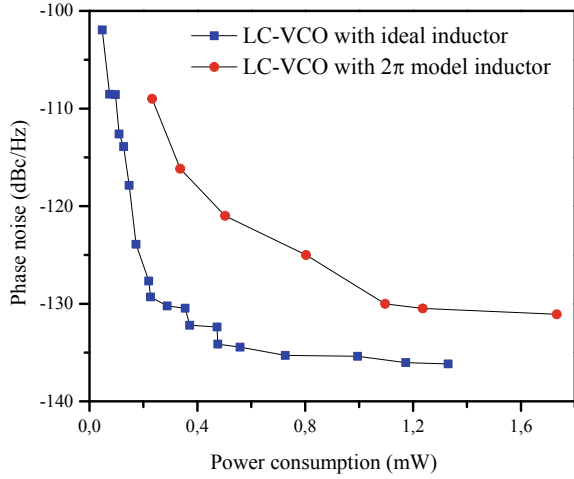


Table 2 The achieved performance values at Pareto front edges

Inductor type	Phase noise (dBc/Hz)		Power (mW)		Oscillation frequency (GHz)	
	Ideal	Real	Ideal	Real	Ideal	Real
Low Pareto front edge	-101.95	-109.23	0.0477	0.23	1.98	1.83
High Pareto front edge	-136.16	-131.08	1.33	1.73	1.57	1.52

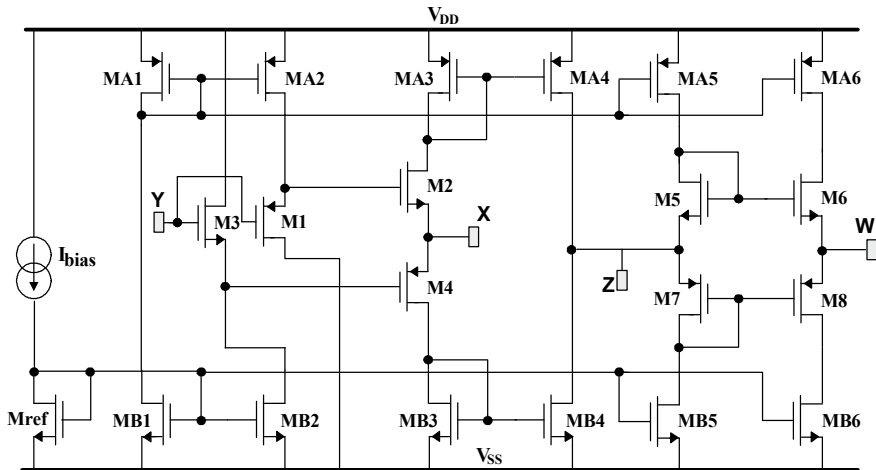


Fig. 6 CMOS CFOA circuit

Table 3 CFOA encoding variables and decision space

Variable	Encoding	Decision space
L_1	All NMOS transistors	[0.18 μm , 0.54 μm]
L_2	All PMOS transistors	[0.18 μm , 0.54 μm]
W_1	Mref,MB1-4	[1 μm , 100 μm]
W_2	M3	[1 μm , 100 μm]
W_3	M1	[1 μm , 100 μm]
W_4	M2	[1 μm , 100 μm]
W_5	M4	[1 μm , 100 μm]
W_6	MA1-4	[1 μm , 100 μm]
W_7	M5, M6, MB5, MB6	[1 μm , 100 μm]
W_8	M7, M8, MB7, MB8	[1 μm , 100 μm]
I_{bias}	Bias current	[0.1 μA , 20 μA]

where i_j and v_j are respectively the current and voltage at port j .

The CFOA is biased with ± 0.5 V and all simulations were done with the 0.18 μm CMOS process. All the CFOA transistors are encoded with W_i and L_i , i denotes a specific transistor or transistors sharing the same parameters. The variables encoding and their boundaries for this circuit are listed in Table 3.

For this circuit, we show the application of the proposed approach using two algorithms namely Multi-Objective Particle Swarm Optimization based on crowding distance (MOPSO-CD) [16] and multi-objective genetic algorithm (NSGA-II) [7, 17], to optimize the circuit performances. These algorithms have been programmed in C++ and the circuit simulations are performed by HSPICE. For all algorithms, we use a population of 100 individuals and an iteration number of 200.

The objective is to find the optimal lengths and widths of the transistors that correspond to all the trade-offs between the chosen performances. For this, three different optimization experiments were performed using the proposed approach.

- First experiment: Minimizing the X-port resistance R_X and maximizing the Z-port frequency, f_{ciZ} ,
- Second experiment: Minimizing the W-port resistance R_W and maximizing the Z-port frequency, f_{ciZ} ,
- Third experiment: Minimizing the X-port resistance R_X and maximizing the W-port frequency, f_{ciW} .

In each experiment, we aim to generate the Pareto front of the two various objectives. The optimization results are given by Figs. 7, 8 and 9 for the first, second and third experiments, respectively.

By a simple observation, it is easy to see that for a specific cut-off frequency, the parasitic resistance obtained by MOPSO-CD is better than that generated by NSGA II, which means that the obtained results with the proposed method using MOPSO-CD are more improved (more optimistic).

Fig. 7 Pareto front (R_X , - f_{ciZ})

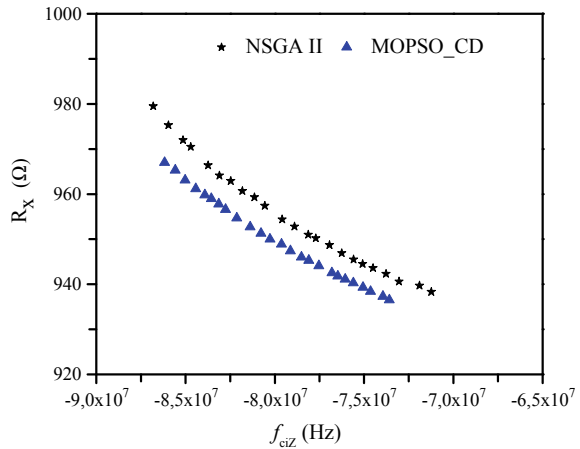
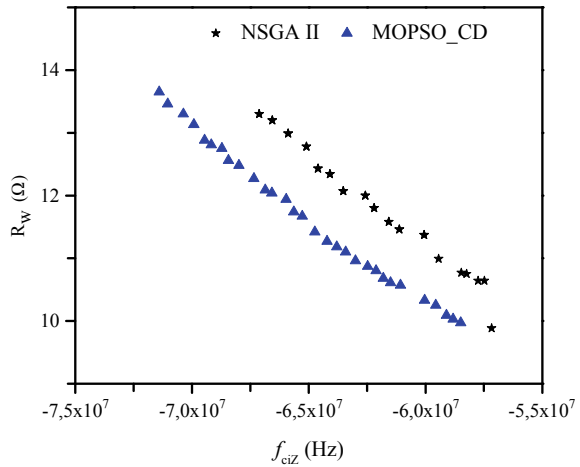


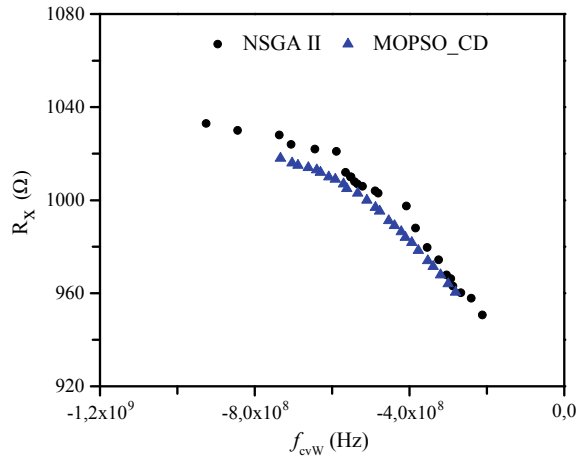
Fig. 8 Pareto front (R_W , - f_{ciZ})



4 Conclusion

A simulation-based approach was used to optimize the performances of analog and RF circuits. This approach uses meta-heuristics to search for feasible solutions and HSPICE simulator to evaluate circuits performances. As a proof of concept, our work is focused on the design of LC-VCOs and a CFOA for low-voltage, low-power applications as multi-objective optimization problems. The multi-objective optimization choice allows us to deal with the various design trade-offs, i.e., phase noise and power consumption for the oscillator and parasitic resistances and cut-off frequencies for the CFOA. Based on the obtained results, the proposed approach provides very good results. Moreover, the obtained results are more improved when using the MOPSO-CD algorithm compared to the NSGA II. Our future work focuses on the integration

Fig. 9 Pareto front (R_X , $-f_{cvW}$)



of new optimization algorithms in the proposed approach, to combine their benefits in finding optimal solutions with the accuracy of the simulation-based method.

References

- Pereira P, Fino H, Fakhfakh M, Coito F, Ventim-Neves M (2013) LC-VCO design challenges in the nano-era. in Analog/RF and mixed-signal circuit systematic design pp 363–379
- Clevenger LA, Hibbeler JD, Shao D, Wong RC (2018) Integrated circuit design layout optimizer based on process variation and failure mechanism
- Hayati M, Cheraghali S, Zarghami S (2018) Design of UWB low noise amplifier using noise-canceling and current-reused techniques. *Integration* 60:232–239
- Amin MT (2016) On the selection of passive elements for low phase noise LC tank VCO in 65 nm process. In: 2016 3rd ICEEICT, pp 1–5
- Senani R, Bhaskar DR, Singh AK, Singh VK (2013) Current feedback operational amplifiers and their applications. Springer
- Yuce E, Verma R, Pandey N, Minaei S (2019) New CFOA-based first-order all-pass filters and their applications. *AEU-International Journal of Electronics and Communications* 103:57–63
- Lberni A, Ahaitouf A, Marktani MA, Ahaitouf A (2019) Sizing of second generation current conveyor using evolutionary algorithms. In: International conference on intelligent systems and advanced computing sciences, pp 1–5 (IEEE)
- Lberni A, Ahaitouf A, Marktani MA, Ahaitouf A (2021) Application of HPSGW0 to the optimal sizing of analog active filter: In: Proceedings of the 2nd international conference on electronic engineering and renewable energy systems, Singapore, pp 309–315
- Lberni A, Marktani MA, Ahaitouf A, Ahaitouf A (2020) Adaptation of the whale optimization algorithm to the optimal sizing of analog integrated circuit: low voltage amplifier performances. In: 2020 IEEE 2nd International Conference on Electronics, Control, Optimization and Computer Science (ICECOCS), Kenitra, Morocco, 2020, pp. 1–6. <https://doi.org/10.1109/ICECOCS50124.2020.9314428>
- Lberni A, Ahaitouf A, Marktani MA, Ahaitouf A (in press) An efficient optimization-based design of current conveyor performances. *Int J Comput Aided Eng Technol*

11. Sallem A, Benhala B, Kotti M, Fakhfakh M, Ahaitouf A, Loulou M (2012) Simulation-based multi-objective optimization of current conveyors: performance evaluations. In: 7th international conference on design & technology of integrated systems in nanoscale Era pp 1–5
12. Sallem A, Pereira P, Fakhfakh M, Fino H (2013) A multi-objective simulation based tool: application to the design of high performance LC-VCOs. In: Doctoral Conference on computing, electrical and industrial systems pp 459–468 Springer
13. Lberni A, Sallem A, Marktani MA, Ahaitouf A, Masmoudi N, Ahaitouf A (2020) An efficient multi-objective simulation-based approach for low voltage low power analog ICs. In: 2020 IEEE International Conference on Design & Test of Integrated Micro & Nano-Systems (DTS), Hammamet, Tunisia, pp. 1–5. <https://doi.org/10.1109/DTS48731.2020.9196166>
14. Shahmohammadi M, Babaie M, Staszewski RB (2016) A 1/f noise upconversion reduction technique for voltage-biased RF CMOS oscillators. *IEEE J Solid-State Circuits* 51:2610–2624
15. Verma R, Pandey N, Pandey R (2019) Novel CFOA based capacitance multiplier and its application. *AEU-International Journal of Electronics and Communications* 107:192–198
16. Sheikholeslami F, Navimipour NJ (2017) Service allocation in the cloud environments using multi-objective particle swarm optimization algorithm based on crowding distance. *Swarm Evolutionary Comput* 35:53–64
17. Sallem A, Benhala B, Kotti M, Fakhfakh M, Ahaitouf A, Loulou M (2013) Application of swarm intelligence techniques to the design of analog circuits: evaluation and comparison. *Analog Integr Circ Sig Process* 75:499–516

Readout System of Piezoelectric Sensor Used for High Speed Weigh in Motion Application



Lhousseine Oubrich, Mohammed Ouassaid, and Mohammed Maaroufi

Abstract The piezoelectric sensors are the main electronic devices widely used to measure the instantaneous force that is exerted on the sensor surface by vehicle wheels moving at normal speed. This application is typically implemented in High Speed Weigh in Motion system, which has been until today under research studies. The system aims to perform an accurate and reliable axle load measurement of heavy trucks in motion. The piezoelectric sensor produces a voltage when a strain is applied on its surface. In general, the voltage signal is in a pulse form as a deterministic signal, easy to operate, but often it is not so. This problem is due to more signal noise, for the most part, because of either the modest quality of piezoelectric sensor or the inefficiency of sensor signal conditioning stage design. The present paper introduces a newly readout system allowing the processing of the piezoelectric sensor output signal in response of exerted force. The studied system consists on the charge amplifier, which is coupled with a transistor used in decoupled common emitter. This circuitry scheme cancels noise and random effect on sensor signal. The purpose of the present study focuses on the achievement of a reliable and deterministic signal, using a sensor with modest quality. The experiment results show the efficiency of the proposed readout system. Even though more noises affect the piezoelectric sensor output signal, the proposed electric interface provides a deterministic and suitable analog signal offering more possibilities to process with the standard tools of signal processing.

Keywords Weigh in motion · Axle load · Charge amplifier · Transistor · Emitter-follower · Decoupling capacitor · Piezoelectric sensor

L. Oubrich (✉) · M. Ouassaid · M. Maaroufi
Engineering for Smart and Sustainable Systems Research Center, Mohammadia School of Engineers, Mohammed V University in Rabat, Rabat, Morocco
e-mail: lhousseinoubrich@research.emi.ac.ma

M. Ouassaid
e-mail: ouassaid@emi.ac.ma

M. Maaroufi
e-mail: maaroufi@emi.ac.ma

1 Introduction

Transducer materials are component that convert one form of energy to another, either in a voltage or in a charge, and they have a large use in sensing application. The piezoelectric sensors are among the most growing transducer technologies on the research development domain using especially the quartz, ceramic and polymer materials.

For the High Speed Weigh in Motion system (HS-WIM), usually the ceramic sensors, embedded on the road pavement, are used in trucks preselection thanks to their low price, presenting however modest technical performances. On the contrary, the quartz sensors are recognized by their high accuracy of the measurement. The sensors made of polymer material are cheaper in the sensors market offering however low performances.

Besides, the literature review recommends completing a signal conditioning if the use of a piezoelectric sensor is highly desired [1]. When a sensor quality is quite good, the piezoelectric output is an aperiodic analog signal with a random impact [2], usually complex to acquire the transmitted data through this signal. The technique that has been investigated by researchers is based on the signal conditioning. The use of charge amplifier is implemented since the piezoelectric material has a capacitive nature [3, 4]. It converts the output value of the sensor into voltage, adapts the impedance of the sensor and limits the amplification in common mode [5].

The voltage generated at the charge amplifier output is defined as the ratio between the charge Q developed by the piezoelectric material and the feedback capacitance C_f of the charge amplifier as given by the Eq. (1):

$$V = -\frac{Q}{C_f} \quad (1)$$

It is indicated in state of the art that the sensing system exhibits very good signal to noise output characteristics and its sensitivity can be adjusted [1]. Obviously, following to this conclusion, the output signal of sensor should be in a pulse form as a response to the exerted strain on the sensor surface [6]. However, the output signal depends mainly on the nature and the quality of the piezoelectric material as well as the efficiency of the sensor signal conditioning design.

For the piezo-quartz sensors, the signal response shows that the sensor is very little sensitive to the vertical deflection of the pavement where the piezo-ceramic sensor is much greater sensitive to this deflection, which makes the analysis of the measurements more complex [7]. Furthermore, due to the finite time constant of a piezoelectric sensors, the developed charge following to the exerted force decays with time [8]. Hence, static and low frequency force measurements are inaccurate and unreliable.

Several algorithms are investigated by researchers, which aim to improve the response capability of piezoelectric sensors. The Incremental Readout Algorithm (IRA, equivalent to a differentiator) is developed by using repeated sampling [8].

The peak voltage of the sensor output signal is determined by detecting the change of sign of the sampled output at variance the Absolute Readout Algorithm (ARA) that is a conventional algorithm based on the measuring time.

This paper aims to assess, in laboratory, the response and performances of piezoelectric sensor, available in the sensors market for small applications, based on the polymer material. This path of study intends to create a deterministic signal suitable to perform the signal processing used in HS-WIM application. In the frame of the present study, a newly readout system is designed straightforward to process analog signal of a sensor with standard tools of signal processing. Indeed a charge amplifier is introduced that is coupled with a transistor used in decoupled common emitter. The proposed electric circuitry is designed to improve significantly the electrical output response of piezoelectric sensor [9–17].

The outcomes of this paper will contribute as a basis, for further researches, to achieve a deep analysis of the analog signal.

The rest of this paper is organized in three parts as follows: Sect. 2 is devoted to the background of signal conditioning circuitry in which different stages of the newly readout system design are described in detail; Sect. 3 is dedicated to laboratory tests; in this section the results of the studied circuitry scheme are illustrated. They are reported to the voltage measurements following an instantaneous force exerted on piezoelectric sensor surface; Sect. 4 is dedicated to the discussion of readout system results. Finally, some conclusions are withdrawn in Sect. 5.

2 Background of the Readout System Design

The charge amplifier is based on an operational amplifier using a negative feedback capacitor. A feedback current flowing in the capacitor offsets the input current that is produced by an increase in output voltage of the amplifier. Therefore, the output voltage depends on the input current as well as the inverse of the feedback capacitor value. Hence, the greater the capacitor value is, the less output voltage is produced being able to create an appropriate feedback current flow, and vice versa.

Figure 1 shows the proposed readout system described in this paper. The scheme of the studied system is mainly composed of two stages.

The first stage, depicted in Fig. 2, consists of the charge amplifier as an effective way to convert the charge generated by a piezoelectric sensor into a normal voltage signal.

A charge amplifier uses a basic integrator topology; a capacitor C_f in the feedback circuitry produces a voltage that is proportional to the integral of the input current. The resistor R_f is mounted in parallel of the capacitor C_f to prevent the amplifier to be saturated.

The output voltage of the charge amplifier is expressed, using the Kirchoff's voltage law, through the Eq. (2):

$$v_0 + v_c + \varepsilon = 0 \quad (2)$$

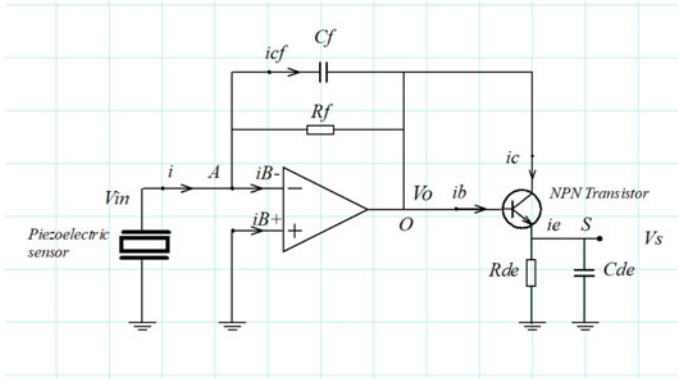
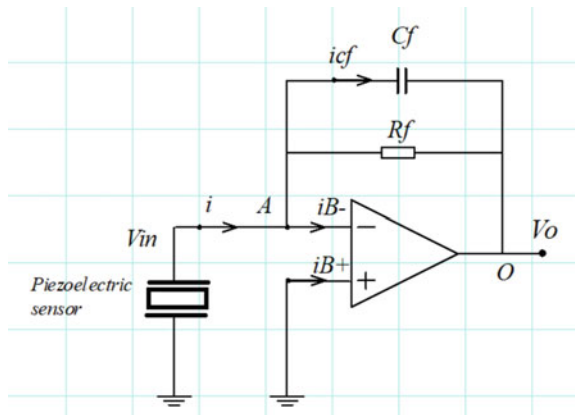


Fig. 1 Overall view of the newly readout system interface

Fig. 2 First stage: charge amplifier circuit



For an ideal operational amplifier, $\varepsilon = 0$. Equation. (2) is rewritten as follows:

$$v_0 = -v \tag{3}$$

Furthermore, the capacitor C_f has a voltage-current relationship governed by the hereafter equation:

$$i = C_f \frac{dv_c}{dt} \tag{4}$$

Besides, the relationship between electric charge produced by the piezoelectric sensor and current is given by the following equation:

$$Q = \int_0^t i(t)dt \tag{5}$$

Replacing the Eq. (4) into (5), if the initial value of v_c is assumed 0 V, the capacitor C_f voltage will be given by the Eq. (6):

$$Q = C_f \cdot v_c \tag{6}$$

Substituting v_c in the Eq. (3), the output equation of the charge amplifier is rewritten according to the Eq. (7):

$$v_0 = -\frac{Q}{C_f} \tag{7}$$

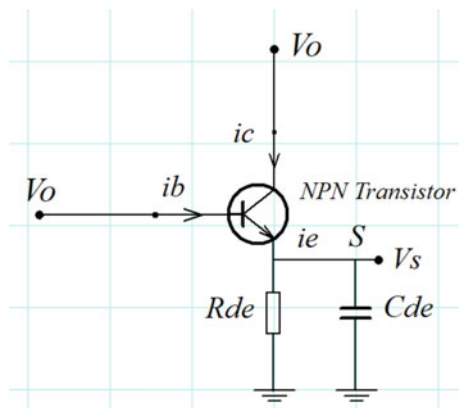
When the charge Q produced by the piezoelectric sensor varies in function of time, the voltage signal of v_0 includes a continuous and a variable components. Thereby, it could be written the following Eq. (8):

$$v_0(t) = V_0 + v_{0max} \sum_{i=0}^n \cos(w_i t + \varphi_i) \tag{8}$$

where V_0 is the continuous component and $v_{0max} \sum_{i=0}^n \cos(w_i t + \varphi_i)$ is the variable component of the charge amplifier output signal, considered as the potential signal noise. The aim of the readout system interface is to acquire precisely V_0 value in order to use it afterward for the HS-WIM application need.

The second stage, as shown in Fig. 3 is based on a bipolar transistor assembly with common collector (or emitter-follower); the emitter voltage follows the input voltage at the transistor base. The transistor emitter is connected to decoupling capacitor C_{de}

Fig. 3 Second stage: common collector circuit



that allows the separation of the polarization point of the transistor from the small signals existing in dynamic mode. Indeed, the capacitor impedance is neglected for small signals and infinite for polarization currents.

Suppose that C_{de} is disconnected (open circuit), the current of the emitter i_e varies as the collector current i_c . This variation of i_e causes a variation of the voltage across the resistor R_{de} that tends to decrease the polarization of the V_{BE} junction at the same rate of the variation of i_e .

In the case where C_{de} is connected, the decoupling capacitor eliminates the variable component of signal and then $V_{R_{de}}$ voltage. Hence, V_s is stable which is equal to V_0 voltage decreased by 0.7 V corresponding to the base-emitter junction voltage.

$$V_s = V_0 - V_{BE} \quad (9)$$

where V_{BE} is fixed around 0.7 V.

Following the theoretical analysis, it is concluded that the output voltage V_s of the readout system depends on the output voltage V_0 of the charge amplifier. This electric potential is itself a function of the charge Q produced by the piezoelectric sensor.

3 Laboratory Tests of the Readout System

3.1 Readout System Setting

For prototyping purpose, the purchase of piezoelectric sensor is intended to accomplish practical tests. An internet research has been accomplished to check the technical possibilities available in the sensors market. Thereby, for small applications, the polyvinylidene fluoride (PVDF) piezoelectric film vibration sensor has been identified which has an acceptable technical performances and price as well. The datasheet of sensor notes that is shielded permitting its use in a high electromagnetic interference environment and its feature is better for the linear applications. According to the manufacture's brochure, the PVDF sensor sensitivity is expressed in pC/N which is equal to 21 given at frequency of 1 kHz.

In the first stage, the charge amplifier is composed of an operational amplifier type LF353 using a feedback circuitry consisting of a capacitor C_f of 10 pF and a resistor R_f of 1 M Ω . The time constant of the circuitry scheme is equal to 10^{-5} s.

The second stage is carried out with a bipolar *npn* transistor type 2N2222A which requires low power and possesses a current gain of 300. The emitter of the transistor is connected to decoupling capacitor C_{de} of 150 nF, which is linked in parallel with a resistor R_{de} of 1 M Ω . The transistor collector is connected to its base.

For tests use, the Arduino card "MEGA 2560" is incorporated into the studied circuitry to acquire the output voltage of the readout system, as depicted in Fig. 4.

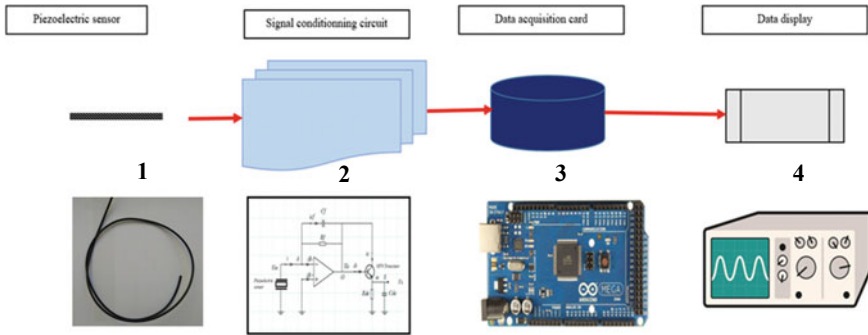


Fig. 4 Readout system process

3.2 Results of Experiment Tests

The laboratory tests are performed following the process presented in Fig. 5. According to the piezoelectric sensor performances, a linear relationship between a strain intensity and the voltage produced by a sensor is assumed. Thus, the output signal of the readout system is based on measuring the voltage V_s when a physical strain is exerted on the sample sensor surface. The tests are also focused on comparing between the output voltage V_0 of the first stage and V_s of the second stage.

Figures 6 and 7 illustrate the shapes of V_0 and V_s voltage signals displayed through Parallax Data Acquisition tool (PLX-DAQ) software synchronized with Arduino software.

Fig. 5 Interface of readout system used in experimentation tests

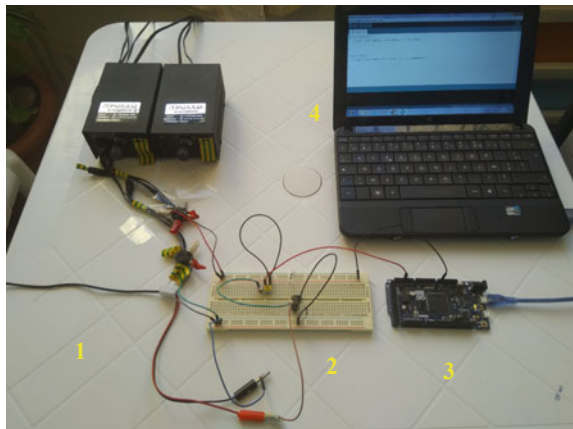


Fig. 6 V_o voltage signal in function of time (s)

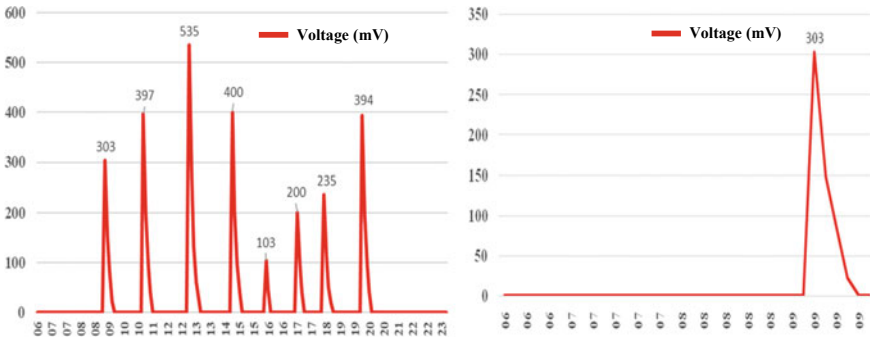
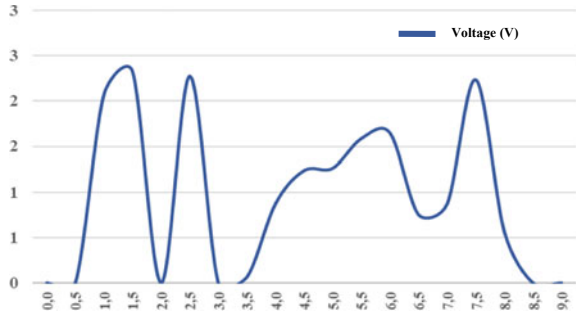


Fig. 7 V_s voltage signal in function of time (s)

4 Results Discussion

The laboratory tests show that the use of the amplifier LF353, characterized by its high input impedance the order of $10^{12} \Omega$, is very suitable achieving a large amplification gain.

Furthermore, the test results prove that the amplification gain of the first stage related to the charge amplifier is high. However, the signal is very noisier and progresses, in the time domain, in a random manner. Figure 6 illustrates a shape view of the first stage voltage signal V_o when a physical force is exerted on the piezoelectric sensor surface.

The observed noise in signal will be minimized through the improvement of the first stage above mentioned. The electronic circuitry inherent to the second stage of the signal conditioning design is mounted as shown in Fig. 1. Figure 7 highlights the encouraging improvement of the analog signal when the second stage is implemented in the overall readout system scheme. Indeed, the output signal of the readout system changes from a random to a deterministic signal in a pulses form, easy to operate with the standard tools of signal processing. Each pulse corresponds effectively to the force that is exerted on the sensor surface.

Moreover, it is proven that the amplitude peak of the voltage signal produced by the piezoelectric sensor follows in proportionally the intensity of applied strain. At the end of the process, the output voltage of the readout system is acquired thanks to the data acquisition card placed next to the signal conditioning circuitry as depicted in Fig. 4.

5 Conclusion

In this work, the authors present a newly readout system that makes the piezoelectric sensor output signal extremely readable when an external force is exerted on its surface. The system consists of a charge amplifier which is coupled with a transistor used in decoupled common collector. The aim of the studied system is to obtain a deterministic voltage signal that is produced by a sensor whose technical performances are retained modest, often subject to more noise.

The proposed readout system proves its efficiency since it allows, through experiment tests, passing from a random signal, complex to operate, to a deterministic signal, easy to process with the standard tools of signal processing. It is also verified that there is a relationship of proportionality between the signal peak and the intensity of strain.

The future action that will be carried out will focus on the measurement of vehicle axle load using the approximation algorithm. This path of research could be achieved to the encouraging results in terms of HS-WIM system accuracy and reliability.

References

1. Isarakorn D, Linder M, Briand D, de Rooij NF (2008) Detection of surface stress induced deflections in piezoelectric cantilever sensors using a charge integrator. In: International conference on control, automation and systems, pp 937–940
2. Marinov AS, Stanchev OrP, Bekov EB (2014) Application of charge amplifiers with polyvinylidene fluoride materials. Technical university of Varna, Bulgaria
3. Marinov AS, Stanchev P, Bekov B (2014) Application of charge amplifiers with Polyvinylidene Fluoride materials. In: 37th international convention on information and communication technology, electronics and microelectronics (MIPRO), Croatia
4. Ben Hassine N (2009) Etude de la fiabilité des composants à ondes acoustiques de volume (BAW) pour des applications Radio Fréquence. Université Joseph Fourier
5. Poulighet P (2006) Cours sur l'électronique de conditionnement des capteurs
6. Dyer DD, Gardner JW (1996) Interface electronics for resistive and piezoelectric polymer gas sensors. The Institution of Electrical Engineers. IEEE
7. Jacob B, Cottineau LM (2016) Weigh in motion for direct enforcement of overloaded commercial vehicles. *Transp Res Procedia* 14:1413–1422
8. Park KT, Klafter RD, Bloomfield PE (1986) A charge readout algorithm for piezoelectric force transducers. In: *Proceeding of the sixth IEEE international symposium on applications of ferroelectrics*, pp 715–717

9. Sirohi J, Chopra I (2011) Fundamental understanding of piezoelectric strain sensors. *J Intell Mater Syst Struct* 11:247–257
10. Fasoli L, Fiorini C, Bertuccio G (1996) Feedback stability of charge amplifiers with continuous reset trough forward-biased diode junctions. *IEEE Trans Nucl Sci* 43(4)
11. Chen X, Guo L, Yu J, Li J, Liu R (2008) Evaluating innovative sensors and techniques for measuring traffic loads. In: *International conference on networking, sensing and control*. IEEE
12. Lopez-Meyer P, Sazonov E (2012) Comparative sensor analysis for an electronic wearable and non-invasive respiratory signal acquisition system. In: *Sixth international conference on sensing technology (ICST)*. IEEE
13. Hopkins MB, Peter L (2015) High frequency amplifiers for piezoelectric sensors noise analysis and reduction techniques. In: *International instrumentation and measurement technology conference (I2MTC) proceedings*. IEEE
14. Gajda J, Sroka R, Stencel M, Zeglen T, Piwowar P, Burnos P, Marszalek Z (2015) Design and accuracy assessment of the multi-sensor weigh in motion system. In: *International instrumentation and measurement technology conference (I2MTC) proceedings*. IEEE
15. Xue Y, Yang B, Peng L, Sun Yq (2009) Research on WIM technology using cement-based piezoelectric sensor. In: *The 1st international conference on information science and engineering (ICISE2009)*. IEEE
16. Buxi D, Redouté J-M, Yuce M-R (2014) Frequency readout using piezoelectric sensors for sensing of physical signals. IEEE
17. Tianze L, Zhang X, Jiang C, Hou L (2009) Analysis of characteristics of piezoelectric sensor and research of its application. IEEE

Towards the Implementation of Smartphone-Based Self-testing of COVID-19 Using AI



Hajar Saikouk, Chakib Alaoui, and Achraf Berrajaa

Abstract The new type of coronavirus COVID-19 has widely spread in most of the world and causing a pandemic according to the World Health Organization (WHO). Many mechanisms to detect the coronavirus disease COVID-19 are used like clinical analysis of chest CT scan images and blood test results. Several methods can be used to detect the presence of Covid-19 such as medical detection Kits. Though, such devices require huge costs and it takes time to install and use. In addition to that, the negatively diagnosed patients consume many of the needed resources and space in hospitals that could be used by other patients having higher chance of being infected. In this paper, a new framework is proposed to detect COVID-19 using built-in smartphone sensors. The proposal provides a low-cost solution, since most of radiologists have already held smartphones for different daily purposes. Not only that but also ordinary people can use the framework on their smartphones for the virus detection purposes. Nowadays, almost every household possesses at least one smartphone with powerful processors and advanced sensors. By combining the data collected by the various sensors, such as temperature data, coughing and breathing recording with questionnaires about the background of the phone user, artificial intelligence (AI) and advanced signal processing tools may analyze the recorded data in order to produce viable diagnosis of Covid-19 infection, and hence alleviate the ongoing pressure on the health system (hospitals and stuff).

Keywords AI · Diagnostics · COVID-19 · Smartphone · Embedded sensor · Pandemic

1 Introduction

As the coronavirus pandemic brings floods of people to hospital emergency rooms around the world [1, 2], physicians are struggling to triage patients, trying to determine which ones will need intensive care. At the peak of the crisis, doctors faced

H. Saikouk (✉) · C. Alaoui · A. Berrajaa
INSA, Euromed University of Fes (UEMF), Fez, Morocco
e-mail: h.saikouk@insa.ueuromed.org

terrible decisions about who should receive help and resources. Artificial intelligence can help. AI systems that have been trained via machine learning to offer “clinical support” may play an important role in the COVID-19 crisis, helping to keep hospitals functional and patients alive. Ultimately, those predictions can improve health outcomes for both patients and hospital staff. And to minimize emergencies because every extra person that is in the hospital puts other at risk which can lead to late detection and less efficient treatment of patients [3]. Another goal of this research is to more efficiently use resources and staff time, for the good not only of the Covid-19 patients, but for the other patients in the hospital who also need care.

The model needs to accurately identify Covid-19 patients whose condition will deteriorate. COVID-19 is a tricky disease. One of the most striking aspects is the ambiguity around how and when patients’ lungs begin to fail. Everyone hopes that there won’t be future cases that max out hospitals across the world. But even if the current flood of patients slows to a steady stream, AI may be the key to keeping hospitals float.

The work proposed in the paper [4] is among the methods used for Covid-19 detection based on data obtained from different smartphone’s sensors.

An exponential rise in worldwide smartphone adoption makes smartphones a widely accessible technology to coordinate responses during large outbreaks like Covid-19 [5, 6]. A smartphone approach could open the way to a very simple diagnostic kit for Covid-19 that could be used on-site, whether in a clinic, a drive-through or pop-up testing facility, or an out-of-the way setting such as a rural location that’s far from a laboratory.

2 Description of the New Proposed Framework

This section presents a description of the general design of the proposed approach. The present framework will use smartphone’s sensors in order to predict Covid-19 specific outcomes. This method provides a low cost and practical solution that can be used by everyone having a smartphone at anytime, anywhere. Especially, in the emergency situations and critical cases.

In this context developing an application based on an algorithm using Smartphones sensors will be of great help. The framework needs to accomplish the following tasks:

- Give a location details, such as GPS coordinates, from where the user uses a phone-based web survey/ or the respondent’s usual place of stay.
- Record demographic information like gender, age, race and blood group.
- Use embedded sensor data to measure temperature, record coughing and breathing, measure heart beats.
- Ask questions that quality (and quantify) other symptoms not directly measurable like fatigue, headache, Diarrhea, sudden loss of taste or smell, among others.
- Ask questions about travel and social contacts with high risk areas in the past 14 days.

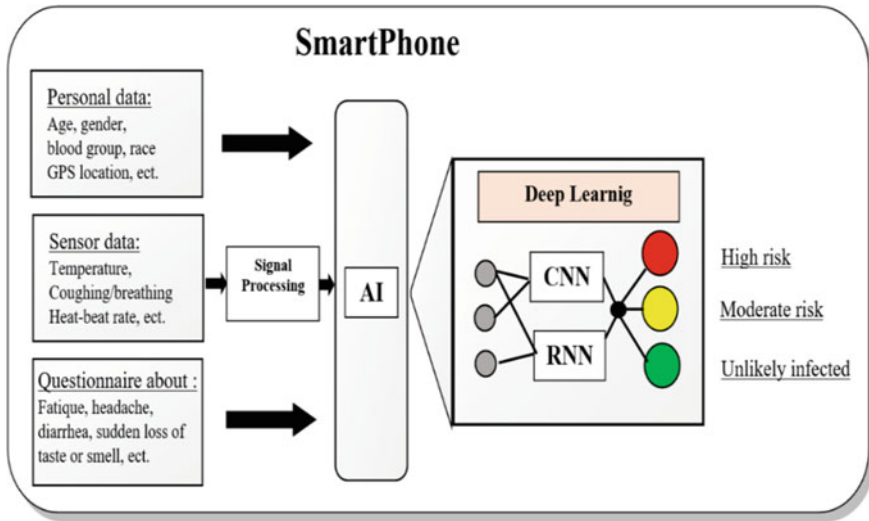


Fig. 1 Smartphone based diagnosis system

Signal processing tools would analyze the time–frequency characteristics of the recording in order to characterize the frequency components of the coughing and breathing signals. The AI tool would take the other data in order to produce ‘recommendations’ to the user by producing the likelihood of the infection in color code (red: high risk—yellow: moderate risk—green: unlikely infected). This is illustrated in Fig. 1.

3 Artificial Intelligence Design

The symptoms of the confirmed Covid-19 patient should be known in order to well understand the framework [4]. Signs and symptoms of the disease are fatigue, fever, dry-cough, sore throat, nasal congestion, headache, muscle pain, lung CT imaging features, and shortness of breath. In addition to loss of taste, loss of smell, diarrhea, and vomiting are usually observed [8].

Each of these signs has its own level of complexity. That’s why, the framework tries to discover the level of each symptoms based on the measurements taken by the sensors. Microphone, cameras, inertial and temperature sensors are embedded on the smartphones. As details in this paper [4], these sensors have been used for detecting the symptoms of Covid-19 separately. Each sensor allows to detect the level of the symptoms for the human-health purposes. We can cite for example touchscreen that is used to predict the fever level in [9]. In order to detect human fatigue, this paper [10] explains that this task is realized thanks to the camera that captured images and videos via human-gait. Inertial sensors such as accelerometers have been used in [9] and [11]

to detect the fatigue level. In [12, 13] The nasal congestion prediction can be analyzed based on smartphones observation via videos and directly observed treatments. In order to predict the level of human headache it is possible to monitor neck posture. Regarding the cough, in [14] and [15] detailed studies use smartphone-microphone to indicate the type of cough.

The present approach aims to use all the mentioned sensors in a one solution and stored all the results in a dataset as a one record. Different records from patients could be collected and used as input to an artificial intelligence (AI) system. For this purpose, there are several methods used, the most recent and accurate techniques are machine learning algorithm and deep learning.

The proposed Framework is built as a set of layers, as shown in Fig. 2. The first layer is responsible for collecting and reading data from the sensors. For example, reading the captured CT images of the lung using the smartphone camera, getting the inertial sensors (accelerometer sensor) measurements, recording microphone voice measurements during a series of cough, and finally scanning temperature sensor measurements during fingerprint touching on the smartphone screen. The second layer is structured to configure the on-board sensors of the smartphone, including image size, reading intervals, buffer size, timer resolution, etc. Additionally, the readings and configurations are then used as input to symptom algorithms that run on the smartphone app. The third layer of the framework provides the calculated symptoms level, separately, and then stored as a record input to the next layer. The last layer is to apply the machine learning techniques to predict the coronavirus disease COVID-19.

The machine learning techniques is used depending on the nature of the data recorded. For example, for the abnormal sub-image of the CT scan images, the CNN could be used [16]. This is followed by using RNN for the rest of the recorded

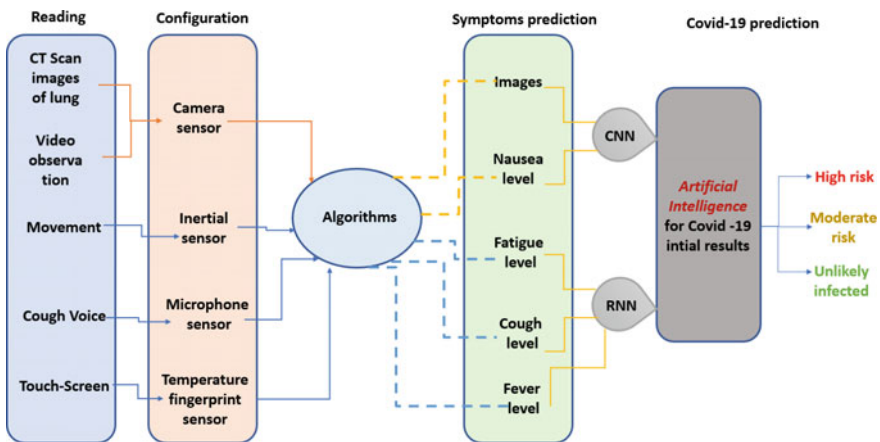


Fig. 2 Diagram of the proposed framework for predicting disease COVID-19 using AI

data [17] and [18]. Therefore, a new combined CNN and RNN machine learning technique is proposed to predict the patient category.

In the proposed framework, CT images of probable cases of pneumonia are an important input for the smartphone. Certainly, CT scans are a key method for detecting COVID-19. A CNN has been developed to diagnose a patient's lesions caused by COVID-19 and analyze its size and density. The model can compare multiple CT images of lung lesions. The most important result of the algorithm is the volume and density of the lesions. The most convincing evidence for the confirmed case of COVID-19 is an increase in lesion density and volume on CT images. This is followed by the use of RNN to process the data signals of temperature, cough, respiration, and heartbeat.

4 Data Collection and Parameters

In addition, to improve the proposed framework and to obtain a reliable prediction result. Images were collected from 5 different sources to form a dataset of more than 120 x-ray images and 400 CT images of the COVID-19 disease. Using images from different sources it is due to the diversity of the sources and countries, which is important in designing a sophisticated tool to help radiologists diagnose COVID-19 around the world. It's also because the collected images are open source to the research community. Unfortunately, the research carried out in [19] ensures that there does not have many COVID-19 images publicly available for the research community to conduct a thorough investigation and there is an immediate need to collect more radiological images.

The X-ray images of COVID-19 are of 45 patients whereas the CT images are collected from 6 patients from British Society of Thoracic Imaging (BSTI) [20] dataset and 16 patients from GitHub, in which part of the images are collected from SIRM which stands for Italian Society of Medical Radiology and Interventional [21]. Figure 3 shows an example of the images of the dataset. The proposed CNN model is trained using 120 x-ray images (60 COVID19 from github, 60 normal from Kaggle) and 400 CT images. Specifically, in the learning phase, the datasets are divided into two categories: 80% is used to train CNN while 20% is used to validate the model.

To test the proposed CNN models, 50 images are used for X-ray (25 COVID-19 X-ray images from BSTI and 25 Normal X-ray images) and 20 images for CT images. Furthermore, it is worth mentioning that the performance measures of the experiments exhibit the average of 50 simulation runs (each run is 20 epochs with batch size equal to 15). Note that the majority of images used in testing phase are from a different source which comes from a different device setting and a different country. The performance measures used in this study are accuracy, sensitivity and specificity.

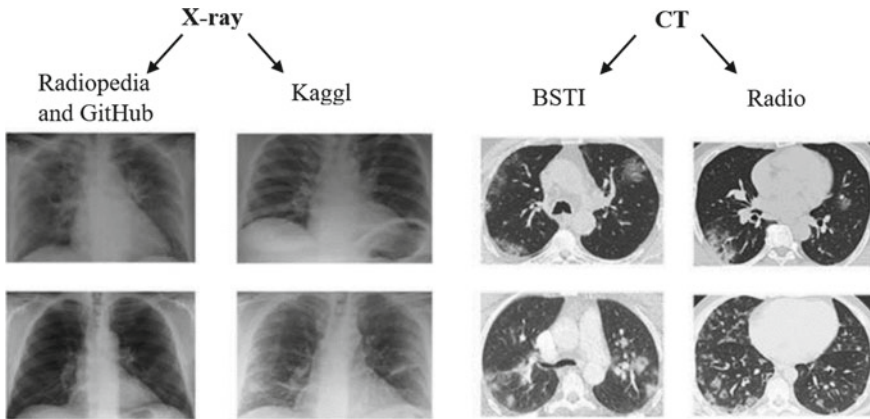


Fig. 3 X-ray and CT scan images from different sources

5 Conclusion

This research aims to contribute scientifically to research and development efforts in the field of Artificial Intelligence and its medical applications in numerous scientific and industrial communities by carrying out a medical diagnosis. It constitutes a model bridge between a real medical need and the applications of new technologies of artificial intelligence and embedded systems, which will generate an interesting scientific outcome.

This research will be developed in order to demonstrate how can an AI tools. Artificial neural networks exactly CNN that is used for CT scan images and RNN that is used to analyze signals scanned by a smartphone, such as coughing, breathing, heart-beat data along with body temperature to predict an early likelihood of COVID-19 infection. This technology will help doctors, nurses and hospital staff to better manage the influx of patients, knowing that most of them, thankfully, tested negative. However, they consume the needed resources of the hospital. Finally, the proposed framework could help regular people, from their homes, to better understand and separate regular coughing/sneezing and seasonal allergy symptoms from covid-19 virus related symptoms.

In this paper, an initial implementation of AI tool is proposed. The future work is to improve the framework used to increase the precision of the Covid-19 detection and give more results with new data depending on the evolution of Covid-19 in the world.

References

1. Chen J, Wu L, Zhang J, Zhang L, Gong D, Zhao Y, Hu S, Wang Y, Hu X, Zheng B et al (2020) Deep learning-based model for detecting 2019 novel coronavirus pneumonia on high-resolution computed tomography: a prospective study. medRxiv
2. Holshue M, DeBolt C, First LS (2019) Novel coronavirus in the united states. *N Engl J Med* 2020:31
3. National health commission of China (2020) (Online). Available: <https://www.chinadaily.com.cn/m/chinahealth/index.html>
4. Maghdid HS, Ghafoor KZ, Sadiq AS, Curran K, Rabie K (2020). A novel AI-enabled framework to diagnose coronavirus COVID-19 using smartphone embedded sensors: Design study. arXiv preprint [arXiv:2003.07434](https://arxiv.org/abs/2003.07434)
5. Udugama B, Kadhiresan P, Kozlowski HN, Malekjahani A, Osborne M, Li VYC, Chen H, Mubareka S, Gubbay JB, Chan WCW (2020) *ACS Nano* 14(4):3822–3835. <https://doi.org/10.1021/acsnano.0c02624>
6. Wood CS, Thomas MR, Budd J, Mashamba-Thompson TP, Herbst K, Pillay D, Peeling RW, Johnson AM, McKendry RA, Stevens MM (2019) Taking connected mobile-health diagnostics of infectious diseases to the field. *Nature* 566(7745):467–474. <https://doi.org/10.1038/s41586-019-0956-2>
7. Cascella M, Rajnik M, Cuomo A et al (2020) Features, evaluation and treatment coronavirus (COVID-19) (Updated 2020 Jul 4). In: StatPearls (Internet). Treasure Island (FL): StatPearls Publishing; 2020 Jan. Available from: <https://www.ncbi.nlm.nih.gov/books/NBK55477s6/>
8. Imran A, Posokhova I, Qureshi HN, Masood U, Riaz S, Ali K, ... Nabeel M (2020) AI4COVID-19: AI enabled preliminary diagnosis for COVID-19 from cough samples via an app. *Informatics in Medicine Unlocked*, 100378
9. Maddah E, Beigzadeh B (2020) Use of a smartphone thermometer to monitor thermal conductivity changes in diabetic foot ulcers: a pilot study. *J Wound Care* 29(1):61–66
10. Karvekar SB (2019) Smartphone-based human fatigue detection in an industrial environment using gait analysis
11. Rold an Jimenez C, Bennett P, Ortiz Garcia A, Cuesta Vargas AI (2019) Fatigue detection during sit-to-stand test based on surface electromyography and acceleration: a case study. *Sensors* 19(19):4202
12. Story A, Aldridge RW, Smith CM, Garber E, Hall J, Ferenando G, Possas L, Hemming S, Wurie F, Luchenski S et al (2019) Smartphone-enabled video-observed versus directly observed treatment for tuberculosis: a multicentre, analyst-blinded, randomised, controlled superiority trial. *The Lancet* 393(10177):1216–1224
13. Lawanont W, Inoue M, Mongkolnam P, Nukoolkit C (2018) Neck posture monitoring system based on image detection and smartphone sensors using the prolonged usage classification concept. *IEEJ Trans Electr Electron Eng* 13(10):1501–1510
14. Nemati E, Rahman MM, Nathan V, Vatanparvar K, Kuang J (2019) A comprehensive approach for cough type detection. In: 2019 IEEE/ACM international conference on connected health: applications, systems and engineering technologies (CHASE). IEEE, pp 15–16
15. Vhaduri S, Van Kessel T, Ko B, Wood D, Wang S, Brun-schwiler T (2019) Nocturnal cough and snore detection in noisy environments using smartphone-microphones. In: 2019 IEEE international conference on healthcare informatics (ICHI). IEEE, pp 1–7
16. Razzak MI, Naz S, Zaib A (2018) Deep learning for medical image processing: overview, challenges and the future. In: *Classification in BioApps*. Springer, pp 323–350
17. Sabir AT, Maghdid HS, Asaad SM, Ahmed MH, Asaad AT (2019) Gait-based gender classification using smartphone accelerometer sensor. In: 2019 5th international conference on frontiers of signal processing (ICFSP). IEEE, pp 12–20
18. Lin C, Ding Y, Xie B, Sun Z, Li X, Chen Z, Niu M (2020) Asymptomatic novel coronavirus pneumonia patient outside wuhan: the value of ct images in the course of the disease. *Clinical Imaging*

19. Cohen JP, Morrison P, Dao L (2020) Image data collection. arXiv 2003.11597, vol 6
20. Covid-19 BSTI Imaging database (2020) Available: <https://www.bsti.org.uk/training-and-education/covid-19-bsti-imaging-database/>
21. Hacking C, Bickle I (2020) Normal chest imaging examples. Available: Radiopaedia, <https://radiopaedia.org/articles/normal-chest-imaging-examples?lang=gb>

Design and Prototyping of an Embedded Controller Board for PV-EV Charging Station



Youssef Cheddadi, Fatima Cheddadi, Fatima Errahimi, and Najia Es-Sbai

Abstract This paper aims to present the design and realization of a fully embedded board, able to execute all the optimization, control and energy management algorithms developed in photovoltaic-electric vehicle charging stations (PVCS). It is intended to provide connectivity and interconnection between the different components of PVCS. This solution supports wired and wireless industrial and advanced computer communication protocols. It is based on the ESP32 Microcontroller, one of the most powerful microcontrollers in terms of performance, low energy consumption and cost, which makes the charging system smart, connected and simple to implement. The functions of the prototyped board are tested and a demonstration of the supervision capabilities in a small-scale PV system proved a good performance.

Keywords Embedded system · Prototyping · ESP32 · Electric vehicle · PV station

1 Introduction

Nowadays, electric vehicles and renewable energy sources presents the best alternative solution for more environmentally friendly means of transportation and power generation respectively. Electric Vehicles (EVs) are more efficient, clean and eco-friendly. However, the must question to be asking is, did the total life cycle of EV is clean with zero emission including the grid supply source, from which the EV and Plug-in Hybrid EV (PHEV) will be charged? There are three common ways to charge the battery pack inside the EV. The first method is the conductive charging, which is the most common charging method; The users have their flexibility of choosing where to charge, at home, at workplace or at a public charging station [1]. The second way is the inductive charging which has already existed but still not standardized yet, and the third method is battery swap. Both the inductive charging and the battery swap are facing challenges in standardization between car types, battery size and power level [2, 3].

Y. Cheddadi (✉) · F. Cheddadi · F. Errahimi · N. Es-Sbai
SIGER Laboratory, USMBA University, Fez, Morocco
e-mail: youssef.cheddadi@usmba.ac.ma

However, integrating renewable energy sources for charging electric vehicles is considered the most attractive within the context of future smart grid framework. Particularly, there are growing interests in employing solar photovoltaic energy (PV), among other sources of renewable energies, as the main energy source for Electric vehicle charging systems [4, 5], and this due to numerous reasons: Firstly, the PV panels are practical in the charging system, and could be installed close to the EV chargers and on the rooftop of houses and workplaces. Secondly, there is a continuous fall in prices of PV modules over the past decades. And also, electricity-generation from a solar photovoltaic system is considered as “carbon-free” because their operation does not engender any carbon dioxide [6].

In the PV charging station, numerous complex systems interact with each other's to ensure a maximum extraction of power from PV panels, an optimal control of the power converters, continuous management and quick charge of EV [7]. These include the interaction between the PV power source, energy storage unit (ESU) and power electronics for the chargers [8, 9]. For all these reasons, the embedded board that manage these kind of stations should be performant. This paper aims to present the design and implementation of a new development board, which is a connected embedded prototype that relies on the cutting edge ESP32 microcontroller. The designed board should be responsible for the digital and analog acquisition, processing, analysis, and control operations. It also permits to establish the intercommunication between the different units of the solar charging station. Further, it can ensure the communication with the external environment namely, the BMS of EV via the high speed CAN bus, and the cloud services for real time monitoring through Wi-Fi.

2 System Requirements

The lack of a standardized methodology for developing an embedded system product can result in several bugs and errors. That is why, we follow the V-cycle development process methodology, which is widely used in developing embedded automotive HW/SW and recommended in vehicle-based norms [10–12]. The typical V-cycle is a well-known methodology for products development that combines two approaches; The top-down approach for designing in successive stages of development, and the bottom-up approach for verification and validation (V&V) [13]. Moreover, V&V is considered as two essential activities in any development process of either hardware (HW) or a software (SW) product to avoid the expensive system level testing. Many papers in literature investigated this approach in aeronautical and automotive fields [14].

The purpose of this work is to design a complete embedded controller, starting from the HW design to the implementation and the testing following industrial standards. It is intended to include a connected and embedded controller that integrates all the electronic components allowing intelligent interfacing between the different entities of the PVCS or any other application. Moreover, it offers high computational

performances suitable for the computational complexity required by different algorithms of acquisition, processing and control. Finally, it should incorporate the features of the internet of things (IoT), which means the capabilities to be connected to the cloud services that ensure a real-time and remote monitoring of any system. This electronic board is recommended not only for control tasks in EV charging stations, but also for a wide range of applications such as the Internet of Things, the automotive industry, automation and robotics. It can offer a lot of flexibility and possibilities to applications thanks to the limitless features that incorporate. The intelligence layer in PVCS, which is the Central Control and Management System of the station, should be implemented and well-operated in the designed board. Additionally, the data provided by all the sensor networks of our station (current, voltage, power temperature, irradiance ...) should be monitored in real time from anywhere. Moreover, the state of charge and other parameters should be also transmitted from the Battery Management System (BMS) of the Electric vehicles via CAN bus incorporated in the designed board. The data bus required for the communication of both information captured by sensors and the control data of the power electronic systems inside the charging station (Fig. 1).

3 Hardware Design and Prototyping

The keystone hardware required for the designed ‘PVESP32’ board is the cutting-edge 32 bits and dual-core microcontroller ESP32. It is a low-cost controller with extensive functionalities. The characteristics of the device will be further described in the section below. Besides the ESP32 microcontroller itself, many other peripherals that facilitate communication with the environment, such as the graphical OLED display. A set of general purpose Inputs/Outputs (GPIO) is also included in this board to make the interaction easy with the physical environment namely sensors acquisition or actuators control. Furthermore, a DC jack for the external power supply, equipped with a double regulation system able to generate two perfectly stable voltages (respectively 5 V and 3.3 V). Moreover, a data logger system is incorporated in our board due to the micro SD card interface works with FAT16 or FAT32 formatted cards. Furthermore, wired serial communication is possible with any computer owing to the integrated RS232 protocol. Another wired communication feature is the Controller Area Network (CAN) interface, which lets a real time and reliable communication with the BMS of the EV or any other Electronic Control application. Indeed, the CAN Bus is considered as a key role component in nowadays chargers namely Chademo or Tesla charging system.

• Core controller: ESP32

The developed board (“PVESP32”) is based on the Espressif ESP32-Wroom module, which provides both Wi-Fi and BLE wireless technologies. “Espressif Systems” is a semiconductor company providing cutting-edge low power Wi-Fi System-on-Chips and wireless solutions for wireless communications and Internet of Things applications.

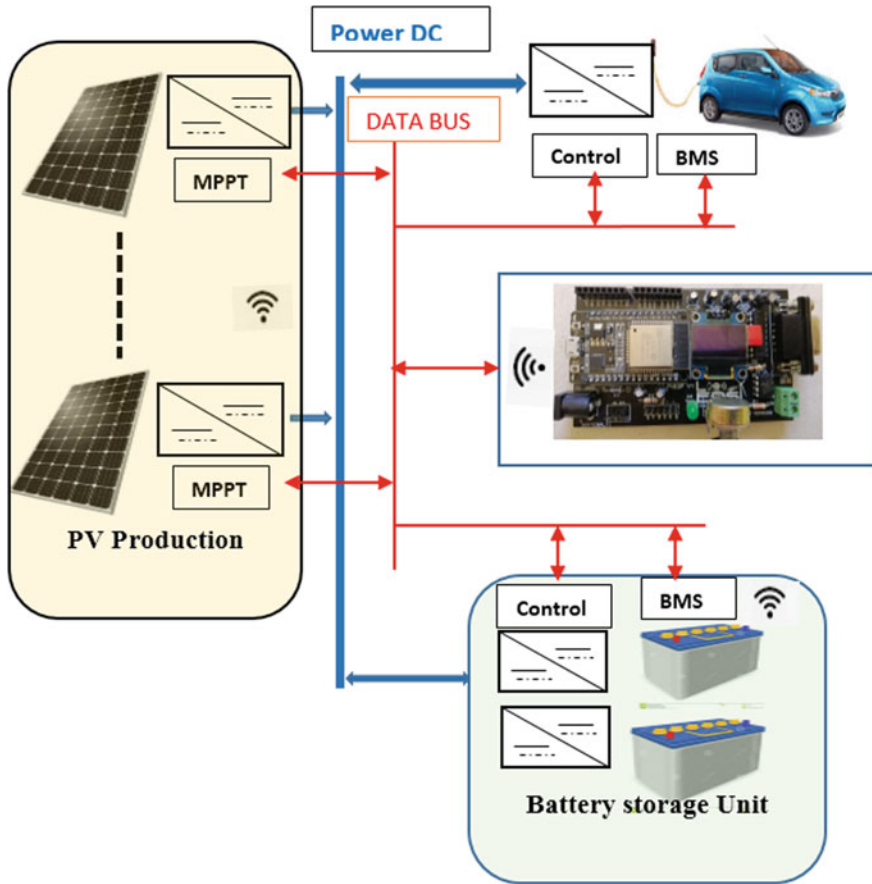


Fig. 1 The role of the controller board inside the PV charging station

This chip is highly-integrated, it requires only a few external components to operate perfectly, and is capable of operating in a wide range of temperatures, making the solution more suitable for applications requiring internet connectivity in remote and difficult operating conditions. This family of MCUs is characterized by extra-low energy consumption, reaching a maximum speed of 240 MHz [15]. With the real-time operating system (RTOS) enabled and the functional Wi-Fi stack implemented. Approximately 80% of the processing power will be available for user-side programming and application development. To summarize some of its technical specifications, Table 1 englobes some features:

- **High-speed CAN Transceiver**
- The CAN MCP2551 transceiver is a Microchip technology that serves as the interface between a CAN controller and the physical bus. The Microchip CAN transceiver provides differential signalling capability to the CAN bus via transmit

Table 1 Summary of features of ESP32 board

Feature	Value
Operating voltage	3.3 V
Digital I/O pins (GPIO)	25
Analog input pins (ADC)	6
Analog outputs pins (DAC)	2
CAN controller	1
UART	3
SPI	2
I2C	3
I2S	2
Flash memory	4 MB
SRAM	520 KB
Clock speed	240 MHz
BLE	1
Wi-Fi	IEEE 802.11 b/g/n/e/i

and receive pins of the CAN controller. The conceived board respects the ISO 11898 standard that represents the de-facto standard for all CAN communication in a vehicle and the most accepted standard by all Electronic Manufacturers.

- **OLED Screen**

The used OLED display is the 0.96 in. display with 128×64 pixels, which communicates with the microcontroller via an I2C protocol. This graphical display doesn't need a backlight, which leads to a very nice contrast in dark environments. Also, the pixels of this display consume energy only when they are activated on; therefore it consumes less power when compared to other displays.

4 Design and Implementation

Many software exist for designing Printed Circuit Boards (PCBs) such as Altium Designer, Eagle PCB, KiCAD PCB Design and Proteus, etc. In this work, we used Proteus to design our electronic circuit and make PCB layout. Proteus software is chosen because of the various advantages that integrate, it is considered as one of the best interactive simulators that are mainly used for preparing schematics and simulating their functioning. Then, used for designing PCBs. The electronic schematic of the conceived board is shown in Fig. 2.

This software incorporates many tools that are configurable, easy to use and helpful in PCB designing. We used ARES designing a suit to develop our PCB by mixing between the manual work and an integrated auto-router to obtain the best

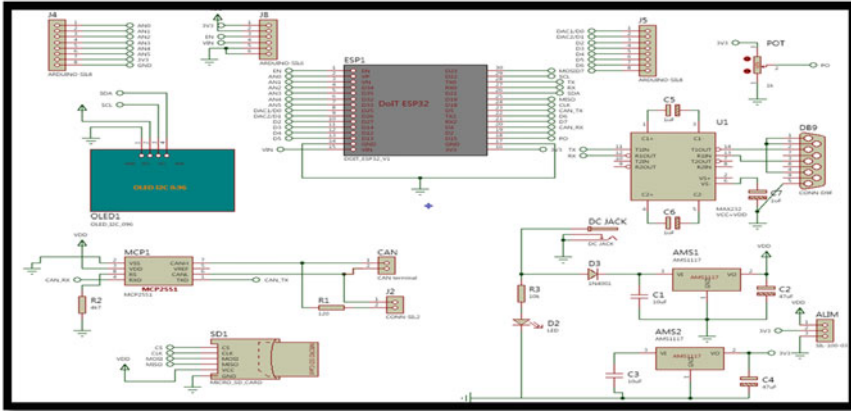


Fig. 2 The electronic schematic of the conceived board in PROTEUS software

results in routing. The routing of the designed double layer PCB board is shown in Fig. 3.

After completing the routing of the PCB layout, we can choose a 3D visualization tool to see the final product how it will appear in reality. The front view of the expected board is shown in Fig. 4. The 3D viewing of Proteus allows us to view all the angles, components and board without the components placed. Consequently, it permits to rectify any error earlier and make modification in the layout before sending Gerber files to the manufacturers. The front image of the final result of our realization is given in Fig. 5. It is crystal clear that the obtained results fit perfectly the expected board.

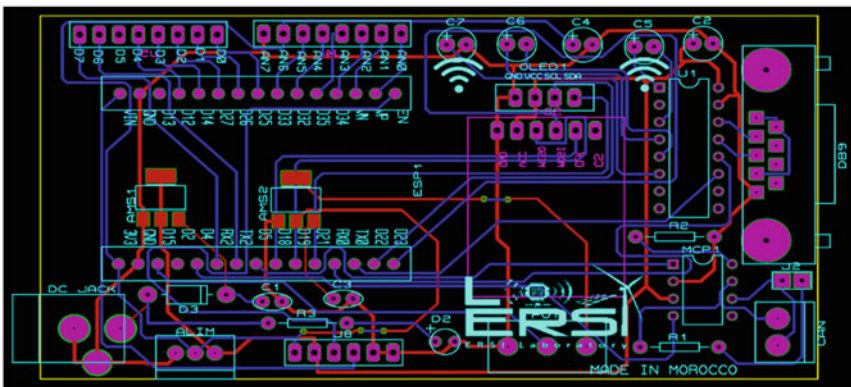


Fig. 3 The routing for the double layer PCB card

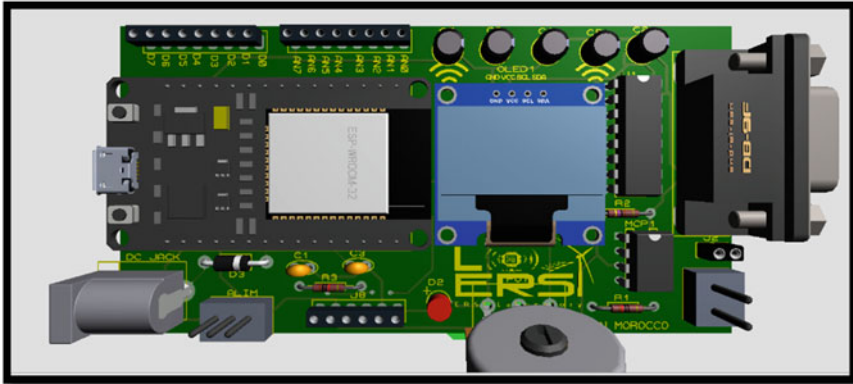


Fig. 4 The 3D model of the expected board in Proteus software

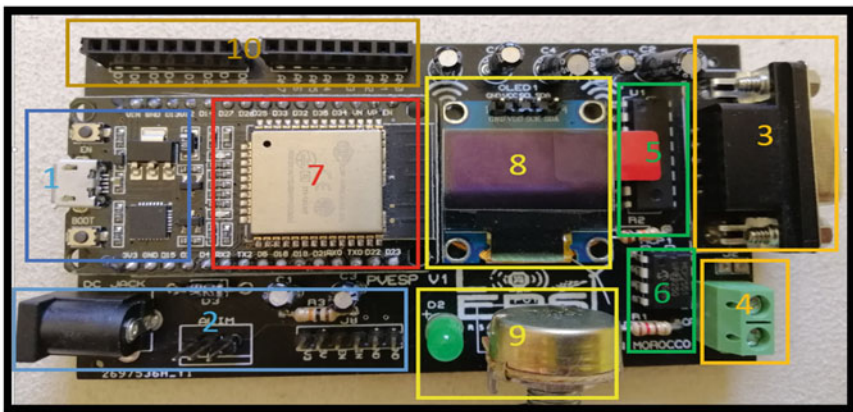


Fig. 5 Image of the front faces of the PVESP32 board

An OLED screen which represents a Graphical User interface(GUI)is added to our board to make the interaction between the user and the environment easier in any application.

The embedded memory in the ESP32 controller is very important compared to the last 32 bits microcontrollers. However, for the applications that need a big amount of data storage, we add a memory card (SD card) to the board. Hence, the device can be configured to log data either onto the micro SD card or to be uploaded via a Wi-Fi network to any open source cloud platform.

5 Application: Monitoring of the PV Charging Station

In the proposed application, the developed board acts as a central unit that acquires and processes the incoming data from electrical and environmental sensors in a small-scale photovoltaic station, then it transmits the data to the cloud and servers via built-in Wi-Fi as a demonstration of the supervision function capabilities of the board.

5.1 Hardware and Software Design

The experimental setup of the system hardware is illustrated in Fig. 6.

The sensors used in this demonstration are: the temperature sensor (DHT11), the luminosity sensor (BH1750) and the Current/Voltage sensor (INA219). Their characteristics are listed in [16]. The prototyped board is used to acquire and process the incoming data from various sensors, then transmits the data to the cloud and servers via Wi-Fi. We used the Arduino language, to develop the algorithm that will manage this monitoring operation. This latter is summarized in the flow chart illustrated in Fig. 7. Data transmitted from the prototyped board are stored in the cloud.

The open source platform “Grafana” offers tools for researchers and engineers to acquire, analyze and visualize data graphically the useful information. Grafana could be linked to various local databases and web servers. It is a free platform for data monitoring, analysis and visualization, delivered with a web server that allows access from anywhere [17]. Furthermore, it includes a real-time dashboard and could

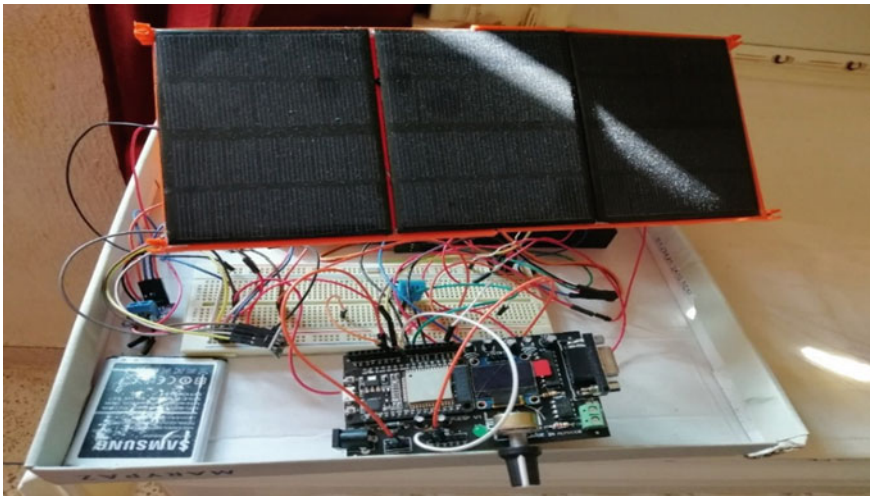
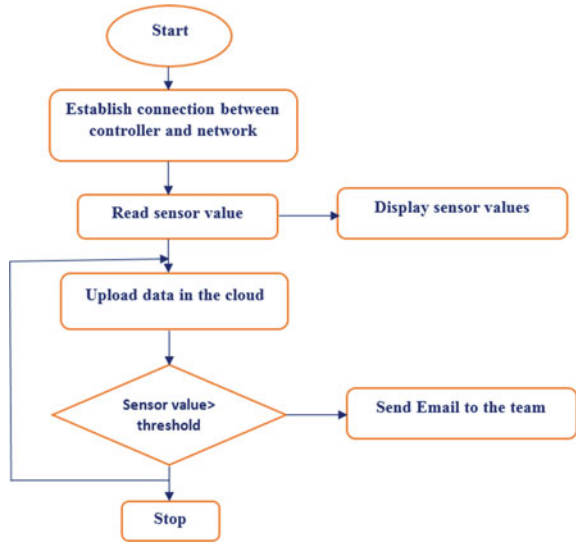


Fig. 6 Photo of the board with a small-scale PV test bench

Fig. 7 Flow chart for the proposed monitoring application



share the data through public links. Data stored in the cloud can be used for further detailed analysis.

5.2 Experimental Results

Five parameters namely power, current, voltage, temperature and luminosity level are measured using the experimental setup and visualized via the Grafana platform. Figure 8 displays the dashboard with different widgets to view the results of data collected in the cloud. This figure shows the environmental measurements namely

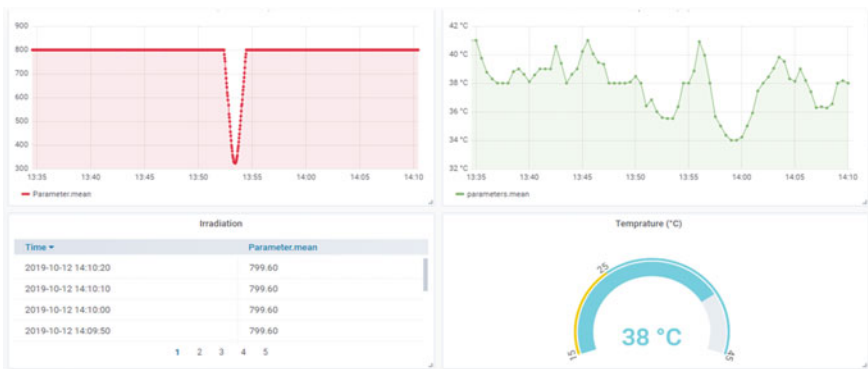


Fig. 8 A caption of the monitored illuminance and temperature



Fig. 9 A caption of the monitored PV current, voltage and power

the temperature and illuminance with the accurate time and date of sensing the data. Figure 9 shows the captured electrical measurements in the Grafana dashboard namely the current, voltage and power with the accurate time and date of collecting the data, which demonstrates the real time monitoring of station measurements. Also an alert notification displayed in the dashboard and sent it to the mail address whenever the sensor values are out of the range initially predefined.

It worth to mention that in a large scale solar PV farms, the required electrical sensors will be much powerful and expensive than those used in this prototype since the range of the power requirements will be higher but the control board will be the same. Therefore, based on the developed board, this IoT application can continuously control and monitor PV-EV charging stations and maintain it in a safe state and high operating performances.

6 Conclusion

In this work, a cutting-edge embedded electronic board was designed and prototyped to be responsible for the acquisition, processing and control tasks in the solar charging station components or any other control application. The electronic card has been designed and manufactured following international standards for the manufacturing and assembly of printed circuits boards. Finally, an IoT application was developed using this board as a demonstration to monitor the real-time production of the PV station.

References

1. Yilmaz M, Krein PT (2013) Review of battery charger topologies, charging power levels, and infrastructure for plug-in electric and hybrid vehicles. *IEEE Trans Power Electron* 28(5):2151–2169. <https://doi.org/10.1109/TPEL.2012.2212917>
2. Ahmad A, Khan ZA, SaadAlam M, Khateeb S (2018) A review of the electric vehicle charging techniques, standards, progression and evolution of EV technologies in Germany. *Smart Sci* 6(1):36–53
3. Lukic S, Pantic Z (2013) Cutting the cord: static and dynamic inductive wireless charging of electric vehicles. *IEEE Electrification Mag* 1(1):57–64
4. Richardson DB (2013) Electric vehicles and the electric grid: a review of modeling approaches, impacts, and renewable energy integration. *Renew Sustain Energy Rev* 19:247–254
5. Chandra Mouli GR (2018) Charging electric vehicles from solar energy: power converter, charging algorithm and system design. <https://doi.org/10.4233/uuid:dec62be4-d7cb-4345-a8ae-65152c78b80f>
6. Saber AY, Venayagamoorthy GK (2011) Plug-in vehicles and renewable energy sources for cost and emission reductions. *IEEE Trans Ind Electron* 58(4):1229–1238
7. Youssef C, Fatima E, Najia E, Chakib A (2018) A technological review on electric vehicle DC charging stations using photovoltaic sources. *IOP Conf Ser Mater Sci Eng* 353(1):012014. <https://doi.org/10.1088/1757-899X/353/1/012014>
8. Ashique RH, Salam Z, Aziz MJBA, Bhatti AR (2016) Integrated photovoltaic-grid dc fast charging system for electric vehicle: a review of the architecture and control. *Renew Sustain Energy Rev*
9. Cheddadi Y et al (2017) Design and simulation of an accurate neural network state-of-charge estimator for lithium ion battery pack. *Int Rev Autom Control IREACO* 10(2):186–192. <https://doi.org/10.15866/ireaco.v10i2.11957>
10. Hommes QVE (2012) Review and assessment of the ISO 26262 draft road vehicle-functional safety. SAE Technical Paper
11. Palin R, Ward D, Habli I, Rivett R (2011) ISO 26262 safety cases: compliance and assurance
12. Hillenbrand M, Heinz M, Adler N, Matheis J, Müller-Glaser KD (2010) Failure mode and effect analysis based on electric and electronic architectures of vehicles to support the safety lifecycle ISO/DIS 26262. In: 2010 21st IEEE international symposium on rapid system prototyping (RSP), pp 1–7
13. Hill D, de Beek JO, Baja M, Djemili I, Reuther P, Sutra I (2017) Use of V-cycle methodology to develop mechatronic fuel system functions. SAE International, Warrendale, PA, SAE technical paper 2017-01-1614
14. Cheddadi Y, Errahimi F, Es-sbai N (2018) Design and verification of photovoltaic MPPT algorithm as an automotive-based embedded software. *Sol Energy* 171:414–425. <https://doi.org/10.1016/j.solener.2018.06.085>
15. ‘ESP32 Overview | Espressif Systems’. <https://www.espressif.com/en/products/hardware/esp32/overview>. Accessed 19 Jan 2019
16. Cheddadi Y, Cheddadi H, Cheddadi F, Errahimi F, Es-sbai N (2020) Design and implementation of an intelligent low-cost IoT solution for energy monitoring of photovoltaic stations. *SN Appl Sci* 2(7):1165. <https://doi.org/10.1007/s42452-020-2997-4>
17. Grafana Features. Grafana Labs. <https://grafana.com/grafana/#alert>. Accessed 09 Oct 2019

New Approach for Controlling PTW Vehicle Dynamics: Characterization of Critical Scenarios



Fakhreddine Jalti, Bekkay Hajji, and Abderrahim Mbarki

Abstract At an exponential pace, the interest of ITS (intelligent transportation systems) solutions in the field of mobility has been increasing over the last two decades. However, progress in the field of driver assistance systems is unevenly distributed on the various modes of transport, with a modest development or at least not in terms of the vulnerability of users of Two Wheels. By approaching the mode of transport abbreviated in PTW (Powered Two-Wheeler), the study was devoted to bring out from the literature the different representative models as well as the different technologies known to date. In this paper, a dynamic model of a PTW vehicle based on the kinematic equations is developed and simulated using MATLAB Software. Also, a new approach based on Different scenarios of the PTW vehicle have been analyzed and discussed in both longitudinal and lateral mode. First, we have tackled the problem of collision by proposing a model of obstacle detection in longitudinal mode, then we used the NHTSA (National Highway Traffic Safety Administration) lateral dynamics model to determine the maximum cornering speed by studying the influence of road parameters. After analyzing the results, we find the developed dynamic model give a safe speed profiles suitable for two-wheeled vehicles.

Keywords PTW (powered two-wheeler) · Motorcycle · Kinematic model · NHTSA model · ARAS · ITS · Obstacle detection · Cornering speed

1 Introduction

In recent years the number of motorized two-wheeler accidents has increased considerably, although this trend is proportional to the number of users. But on the other

F. Jalti (✉) · B. Hajji

Laboratory of Renewable Energy, Embedded System and Information Processing, National School of Applied Sciences, Mohammed First University, 60000 Oujda, Morocco
e-mail: jalti.fakhreddine@ump.ac.ma

A. Mbarki

National School of Applied Sciences, Mohammed First University, 60000 Oujda, Morocco

© Springer Nature Singapore Pte Ltd. 2022

S. Bennani et al. (eds.), *WITS 2020*, Lecture Notes in Electrical Engineering 745,
https://doi.org/10.1007/978-981-33-6893-4_41

431

hand, according to WHO, studies show how vulnerable the PTW user is. In fact, the risk of mortality is 20 times greater compared to a four-wheeled vehicle [1].

Faced with this critical situation, it can be seen that the progress made in active safety systems is not keeping pace by popularizing the use of driver assistance systems for PTW, known to have had success in limiting road risks for four-wheels. Several solutions were presented, but few works have been interested in building models intended to be associated with AI.

Recently ADAS has been integrated for PTW and less than 10 years ago the literature has given us a first specific framework for driving assistance called ARAS-PTW [2]. While work on assistance systems for vehicles began to be framed for more than five decades [3]. Precisely for the last two decades, we have observed a migration towards electronic automation with an arsenal of on-board instruments. More than that, nowadays we are witnessing of a major transition characterized by digital transformation and telecommunications technologies.

In return, the evolution of models and electronic architecture allows today to catch up the delay between PTW and four-wheelers, indeed several motorcycle models have been proposed Cossalter [4], Pacejka [5] and Nehaoua et al. [6], embedded electronics is becoming common and sensors are affordable. ADAS for motorcycle might be more sensitive given the driver's exposure to the environment, So R&D in the motorcycle manufacturer focuses on the embedded architecture. Such architectures allow to facilitate the implementation of algorithms by managing the communication between algorithms and sensors [7]. It could be the best solution to make it available on a large proportion of sold motorcycles [8].

This paper proposed a solution that characterize the relationship of critical scenarios with vehicle parameters, with a view to iterating several experiments on the initially simplified model using AI. Indeed, the performance of such a system will evolve continuously.

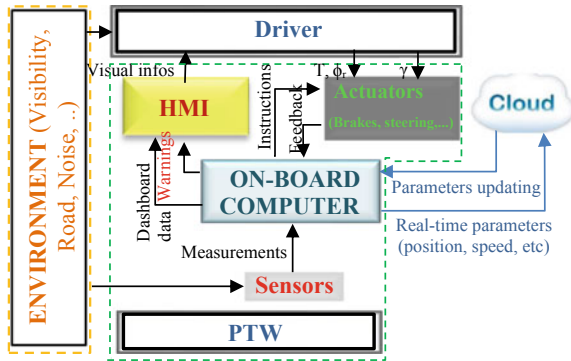
So, organization of the paper will be as follows: Sect. 2 presents the framework of the study, Sect. 3 explains the dynamic model chosen to model the vehicle according to the mode of movement, Sect. 4 presents the critical situations and the solutions proposed for each situation, Sect. 5 presents the results after simulation, and finally Sect. 6 concludes on the results and sets out the research perspectives.

2 Context and Problem Statement

The overview of our system consists of a triplet {Driver, Vehicle, Environment} where the interaction is explained in Fig. 1. Already, the studies of the interactions within this triplet concludes with several mathematical representations according to the hypotheses emitted [5, 9] and [10].

The state and parameters are generally not directly measurable and, at this stage, we accept their theoretical values. Specifically, the long-term study will aim to complete the acquisition of all parameters, in particular by using AI and connectivity.

Fig. 1 Driver assistance system architecture



So, we propose to study the two major critical scenarios: the presence of an obstacle & the turn. Taking into account charge transfer phenomenon and the influence of road characteristics, our system combines three modules, where the first assists the driver to avoid a collision and the other two helps to better control the vehicle when cornering.

3 Modeling of the Vehicle Dynamics

Our need to link the parameters of the vehicle by kinematic equations does not aim to in-depth study of the behavior of the vehicle as long as it resides in the need to have a simplified initial model in view of feeding the first experiment.

Hence, our dynamic model of the vehicle will consist of two parallel blocks activating according to the mode of movement. The longitudinal model treats longitudinal dynamics, meanwhile the lateral model treats the lateral dynamics of the PTW.

3.1 Longitudinal Model

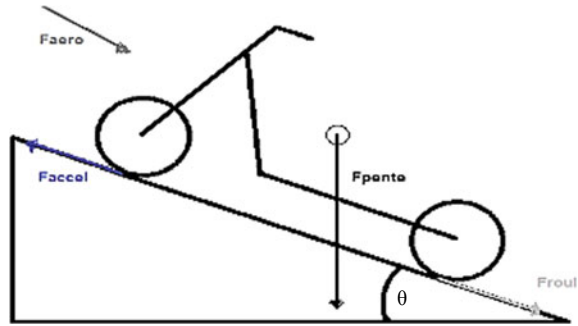
As shown in Fig. 2 in longitudinal movement the forces that govern the PTW are the gravity expressed in slope, aerodynamic forces and rolling force (traction).

So, using the fundamental principle of dynamic, the Longitudinal dynamic model of our PTW is explained by:

$$Ma_x = F_{pente} + F_{aero} + F_{roul} \tag{1}$$

With:

Fig. 2 Representation of forces on a slope



$$\begin{cases} F_{pente} = Mg\sin\theta : \text{the force related to the slope of the road} \\ F_{aero} = \frac{1}{2}\rho C_d A_f (V + V_{air})^2 : \text{the aerodynamic force} \\ F_{roul} = C_r \cdot F_z : \text{the Rolling resistance forces} \end{cases}$$

where:

$a_x, M, g, \theta, C_d, \rho, V, V_{air}, A_f, C_r, F_z$ are respectively: longitudinal acceleration, the vehicle mass, gravity, slope angle, Aerodynamic friction coefficient, Air density, Vehicle speed, Headwind speed, Vehicle frontal area, Rolling resistance coefficient of the wheels, the normal load applied to the vehicle.

3.2 Lateral Model

Referring to the assumptions and results of a previous study, we will present our dynamic study as follows [11]:

According to Figs. 3 and 4, in lateral movement the forces and moments that govern the PTW were represented in the dynamic balance to deliver our model:

$$Ma_y + Mv_x \dot{\Psi} + Mh \phi = F_{yf} + F_{yr} + F_{dev} \tag{2}$$

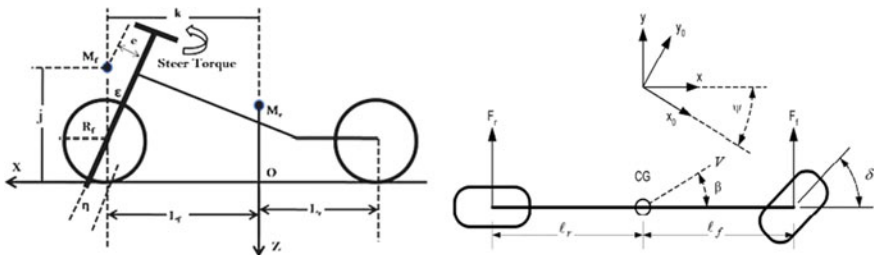
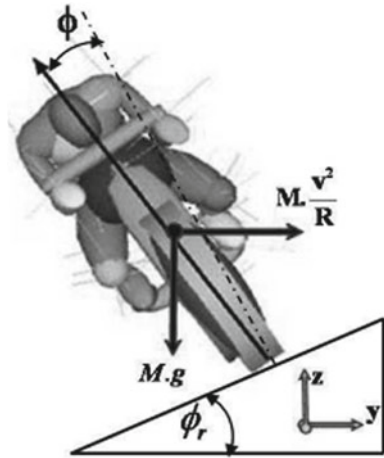


Fig. 3 Vehicle geometry—lateral and top view representation

Fig. 4 Representation of forces when cornering



With:

$$\begin{cases} F_{dev} = -mgsin\phi_r : \text{the force linked to superelevation} \\ F_{yf} = C_{f1}\alpha_f + C_{f2}\gamma_f : \text{front tire lateral force according on Pacejka model [5]} \\ F_{yr} = C_{r1}\alpha_r + C_{r2}\gamma_r : \text{rear tire lateral force according on Pacejka model [5]} \end{cases}$$

$$I_{zz} \psi = lf F_{yf} + lr F_{yr} \tag{3}$$

$$I_{xx} \phi = Mgh - (F_{yf} + F_{yr})h \tag{4}$$

where: $\dot{\phi}$, $\dot{\psi}$, v_x , ϕ_r are respectively Roll speed, Yaw speed, longitudinal speed, tilt angle of the road. I_z/I_x are respectively yaw/roll moment of inertia the vehicle and l_f/l_r , C_{f1}/C_{r1} , C_{f2}/C_{r2} , α_f/α_r , γ_f/γ_r , are respectively front/rear: longitudinal distance between the vehicle center of gravity and the tires, tire drift stiffness, camber stiffness of the tire, sliding angle of the wheel, wheel camber angle.

4 New Approach for Better PTW Control

In this section we propose handling two critical situations, collision and cornering. Our system combines three modules, where the first assists the driver to avoid a collision and the other two helps to better control the vehicle when cornering. This proposed approach treats the dangerous situations most commonly encountered by a PTW, taking into account charge transfer phenomenon and the influence of road characteristics.

4.1 Treatment of Obstacle Detection in Longitudinal Mode

The collision is one of the major dangers encountered by the driver of the PTW. Especially in front of a fixed object the risk of mortality is amplified [1].

The formula of the chosen safe distance [12]:

$$ds = dr + dc \tag{5}$$

where: dc , dr are respectively critical distance (danger zone), reaction distance which depends on speed and reaction time of the driver (generally assumed to be $h = 2$ s):

$$dr = hv \tag{6}$$

As shown in Fig. 5 the load on the rear wheel is expressed by:

$$N_r = mg \frac{l_f}{l_f + l_r} - ma \frac{h}{l_f + l_r} \tag{7}$$

where: l_f, l_r are respectively longitudinal distance between the vehicle center of gravity and the front/ rear tire and h is height center of gravity.

The loss of friction due to the load transfer phenomenon on the rear wheel to avoid lifting it (*Stoppie*) give us the condition on the acceleration:

$$a < g \frac{l_f}{h} \tag{8}$$

Our algorithm compares ds and dr and triggers deceleration as soon as $ds \leq dr$. In parallel, it evaluates the deceleration according to (8) so as not to come to loss of adhesion by load transfer.

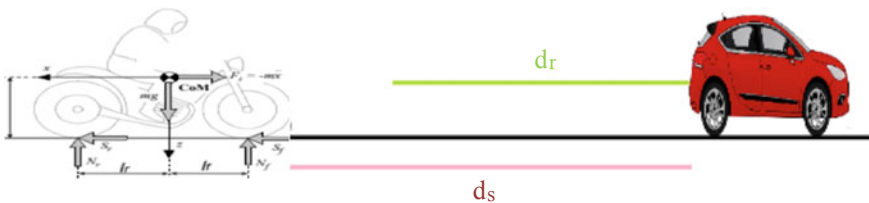
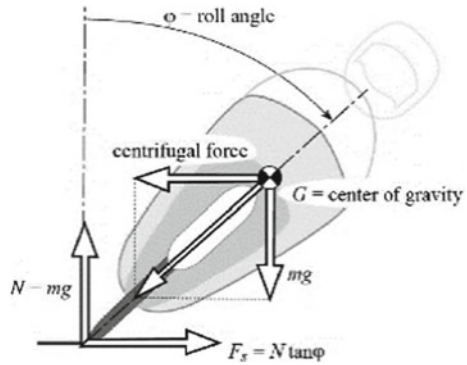


Fig. 5 Relative distance versus safety distance

Fig. 6 Equilibrium of the motorcycle in a curve



4.2 Treatment of the Speed Limit When Cornering

Referring to the dynamic study presented in Sect. 3.2, we approach here the treatment of cornering while neglecting the effect of the suspension and the aerodynamics. The formula that we are going to use is inspired by the NHTSA (National Highway Traffic Safety Administration) model where we take into account the influence of the superelevation and the friction on our PTW:

$$V_{x\max} = \sqrt{\frac{g}{\rho} \frac{\phi_r + \mu_{\text{lat}}}{1 - \phi_r \cdot \mu_{\text{lat}}}} \tag{9}$$

Also, referring to the detailed study of [4] the definition the equilibrium of the moments of the forces acting on the center of mass as represented in Fig. 6, so:

$$\phi = \tan^{-1} \left(\frac{\rho V_x^2}{g} \right) \tag{10}$$

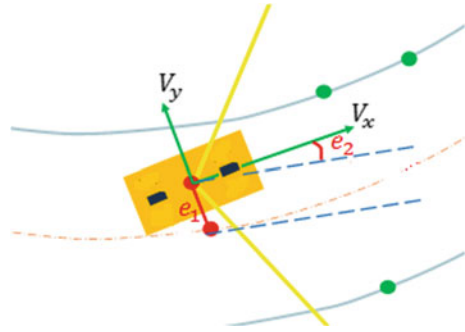
where: μ_{lat} , ρ , v_x is coefficient of static friction, is the curvature of the turn, the longitudinal speed which is assumed to be constant.

The solution we present here makes it possible to regulate the speed of the vehicle so as not to reach the calculated limit (10), Our model depends on the triplet { friction, Curvature, superelevation}, The superelevation and grip values can be estimated using the solutions proposed on [10, 13] respectively. On the other hand, our future work will consist in the estimation of these parameters by using machine learning.

4.3 Maintaining Trajectory in Lateral Mode

Considering a vehicle traveling at a longitudinal speed V_x on a road with radius R . The orientation of the vehicle is offset from the shape of the curve.

Fig. 7 Course deviation in a turn



As shown in Fig. 7, e_1 , e_2 are respectively the distance from the center line of the vehicle to the center line of the track, the orientation error of the vehicle in relation to the road.

The rate of change of the desired orientation of the vehicle is:

$$\dot{\psi}_{des} = \frac{V_x}{R} \tag{11}$$

So, the orientation error:

$$e_2 = \psi_{v2rm} - \psi_{des} \tag{12}$$

where: ψ_{v2rm} , ψ_{des} are respectively yaw angle of the PTW, yaw angle desired.

Though, the second derivative of the distance between the center of gravity of the vehicle and the center of the track given by:

$$\ddot{e}_1 = \ddot{y} + V_x * \dot{\psi}_{des} - \frac{V_x^2}{R} \tag{13}$$

As we supposed V_x constant:

$$\dot{e}_1 = \dot{y} + V_x(\dot{\psi}_{v2rm} - \dot{\psi}_{des}) \tag{14}$$

PI corrector chosen in the MATLAB/SIMULINK environment makes it possible to correct the orientation error while cornering, it is based on both Eqs. (12) and (14).

5 Simulation and Results

In order to illustrate the effectiveness of the proposed procedure, different simulation tests are conducted. For each previously proposed solution, we will analyze the results of profiles, where the vehicle has been subjected to both moderate and extreme

scenarios. Meanwhile the influence of friction and super elevation have been detailed and analyzed when the PTW is in a turning situation.

Here V2RM designate our PTW and Vlead designate the front vehicle (Obstacle).

5.1 Obstacle Detection in Longitudinal Mode

In this section, we will be interested in studying the response of the system implemented in Sect. 4.1 to two braking stimuli: **Stop-& go** and **Hard-stop** scenario.

Here we study the response of the system in terms of speed variation (Fig. 8) and inter-distance (Fig. 9).

Our Model reacted in such a way as to lower the speed of the vehicle, the tripping time is determined according to the conditions cited in Sect. 4.1.

The results that we have had shown the ability of the vehicle to adapt its speed before reaching the critical distance (8 m), the deceleration of the vehicle was however controlled, even in aggressive braking mode, and did not exceed 11.25 m/s^2 calculated using the Eq. (10).

Fig. 8 Speed profile

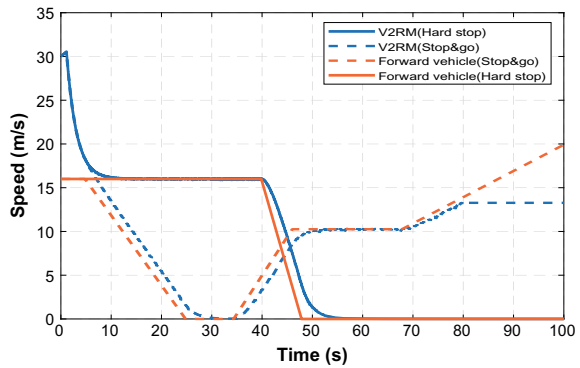
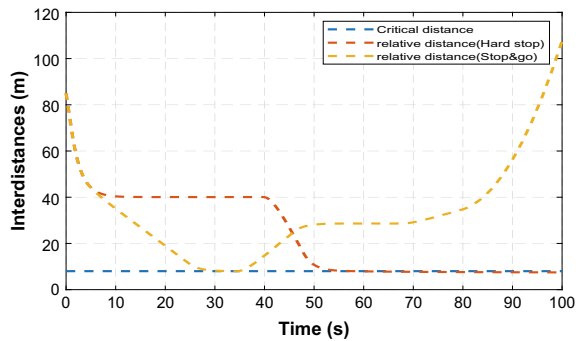


Fig. 9 Inter-distance profile



5.2 Influence of Super Elevation and Friction on Speed Limit When Cornering

In this section the simulation interested in the maximal speed in a turn, where we study the influence of the various parameters related to the road.

The influence of the superelevation is studied considering three different profiles of the road superelevation given by Fig. 10.

In the same way to study the influence of friction, we consider $\mu = \{0.4, 0.6, 0.8\}$.

We observe in the graphs below (Figs. 11 and 12) the response of the model according to each superelevation profile and each friction value.

The results show the interdependence between the cornering speed and the characteristics of the road, the correlation of the speed with the friction is clearly manifested while the influence of the superelevation is not of the same amplitude.

A study carried out previously concluded on similar comparisons using another model [11]. However, based on a standardized NHTSA formula, our model offers

Fig. 10 Superelevation profile

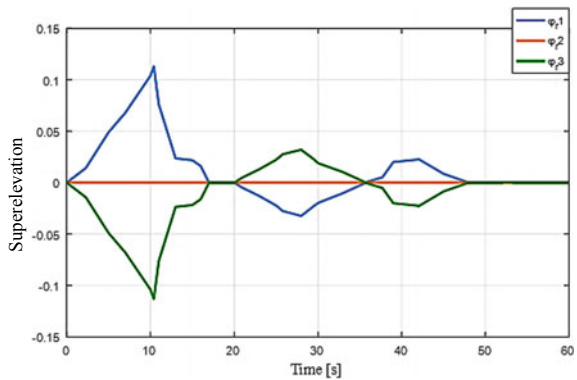


Fig. 11 Speed profiles according to different superelevation angles

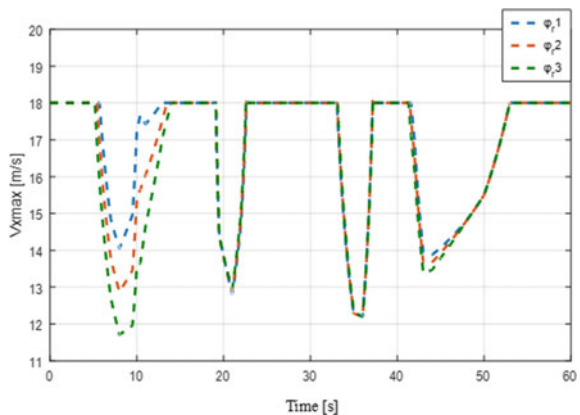
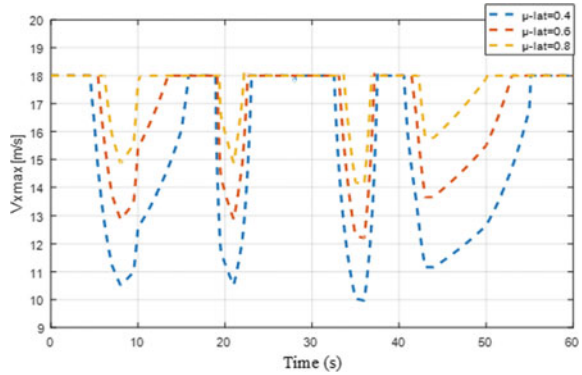


Fig. 12 Speed profiles according to different friction values



more speed margin with still vehicle stability. Also, our algorithm plans the injection of the estimated friction values, which is concluded through the successive experiments.

5.3 Correction of Position and Orientation Error

Here, we study the response of the system implemented in Sect. 4.3. Figures 13 and 14 show the curvature profiles associated with the paths traveled by our PTW, we see the superposition of the two curves which reflects the accuracy of the correction.

After that, we examine, by the two representations below (Figs. 15 and 16), the response of the system to the stimuli corresponding respectively to moderate and severe curvatures.

The results of this study give us the insurance about the capacity of the vehicle to adapt its orientation without exceeding the maximum authorized roll angle value.

The two scenarios undergone by the PTW differ in terms of difficulty. In fact, in the severe curve scenario we observe a portion where the absolute value of the roll

Fig. 13 Moderate curvature profile

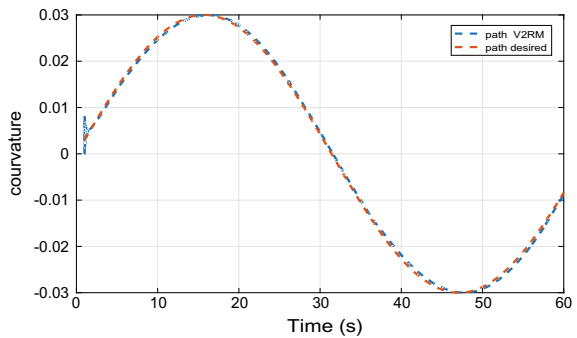


Fig. 14 Sever curvature profile

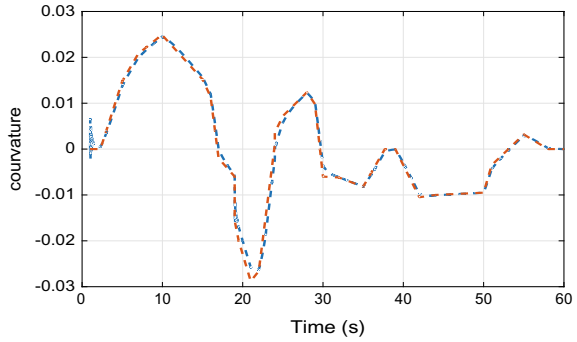


Fig. 15 Roll angle compared to ϕ_{max} value according to moderate curvature

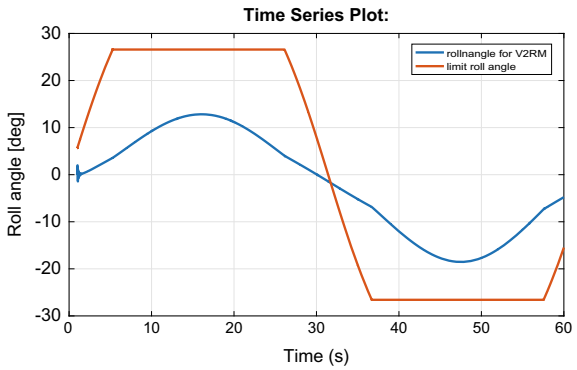
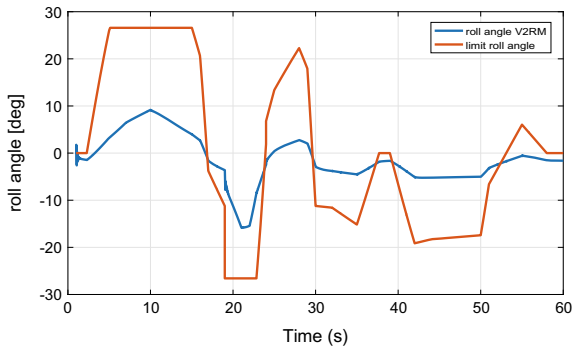


Fig. 16 Roll angle compared to ϕ_{max} value according to sever curvature



angle is slightly greater than the ϕ_{max} and where we notice an inflection (orientation change) of the curve profile. This phenomenon can be explained by the Counter steering phenomenon known to be a way of controlling the vehicle on successive bends.

6 Conclusion and Future Works

In this paper, a new approach in the treatment of the critical scenarios for the PTW was exposed. Indeed, we managed to characterize them by models implemented under the MATLAB software. These models so called longitudinal, lateral model take into account the environment characteristics using an accurate description (safe distance, radius of curvature, slope, superelevation and road roadsides). By analyzing the parameters and performing the simulations, it has been demonstrated the effectiveness of our approach. Also, the advantages of our modeling:

- Exhaustiveness since it covers both types of movement of the vehicle.
- Assists the driver without imposing on him an excessively limited speed limit (as it can be rejected by a great number of motorcycle riders [14]).

In terms of this scientific research, this step was necessary to make sure that the machine has a model sufficiently configured to collect successive experiments.

In the future, we will strengthen our PTW with a data processing system with the aim of allowing the machine to anticipate the danger and not only to control it.

Appendix

The characteristics of the PTW vehicle used for the study:

Physical characteristics				Technical characteristics	
lr (mm)	347.11	ϵ (°): Caster angle	25	Braking system	CBS
lf (mm)	949	h (mm): height center of gravity	795	Detection sensor	RADAR
η (mm): trail	89.27	M (Kg): mass of the vehicle + driver	215	Recognition technique	Image processing

The scenarios undergone during “obstacle detection”:

	Stop-&go		Hard-stop	
	PTW	Obstacle	PTW	Obstacle
Initial speed (m/s)	20	16	30	16
Initial position (m)	0	85	0	85
Critical distance (m)	8			

References

1. Etienne K, Saul B, Barry W, Jose Luis I (2017) Powered two- and three-wheelers safety: a road safety manual for decision-makers and practitioners. 3.0 IGO. ISBN 978-92-4-251192-5. World Health Organization
2. Kuschefski A, Haasper M, Vallese A (2011) Advanced rider assistance systems for powered two-wheelers (ARAS-PTW), National highway traffic safety administration. In: 22nd international technical conference on the enhanced safety of vehicles (ESV), pp 1–12, Germany Paper Number 11-0123, NHTSA
3. Bernotat R, Gärtner KP (1980) Anthropotechnische Gesichtspunkte bei der Gestaltung der Kommunikation Zwischen Mensch und Hochautomatisierten Systemen. In: Ernst D, Thoma M (eds) Meß- und Automatisierungstechnik. Fachberichte Messen • Steuern • Regeln, vol 5. Springer, Berlin, Heidelberg
4. Cossalter V (2006) Motor cycle dynamics, 2nd edn. Copyright by Vittore Cossalter
5. Pacejka H (2006) Chapter 11-Motor cycle dynamics. Butterworth-Heinemann, pp 517–585
6. Nehaoua L, Arioui H, Seguy N, Mammar S (2013) Dynamic modeling OFA two wheeled vehicle: Jourdain formalism. Veh Syst Dyn 51(5):648–670
7. Damon P-M, Ichalal D, Nehaoua L, Arioui H (2017) Lateral & steering dynamics estimation for single track vehicle: experimental tests, 2405–8963 © 2017. IFAC
8. Patrick S, Kai S, Jost G (2017) Perspectives for motorcycle stability control systems ©. 2010 Elsevier Ltd.
9. Bella F, Calvi A, D'Amico F (2012) Impact of pavement defects on motorcycles road safety. In: SIIV—5th international congress—sustainability of road infrastructures. Elsevier Ltd.
10. Ghandour R, Victorino A, Charara A, Lechner D (2011) Evaluation du risque de dérapage basée sur l'estimation du coefficient d'adhérence maximal. JDMACS, Jun 2011, France, pp 275–280 (ffhal-00697722)
11. Hamid S (2012) Système d'Assistance à la Conduite pour Véhicules à Deux-Roues Motorisés. Automatique/Robotique. Université d'Evry-Val d'Essonne
12. Fancher P, Bareket Z, Ervin R (2001) Human-centered design of an Acc-with-braking and forward-crash-warning system, 36(2–3):203–223
13. Ivo B, Savaresi SM, Tanelli M (2012) Lean angle estimation in two-wheeled vehicles with a reduced sensor configuration. IEEE /ISCAS, Seoul, South Korea
14. Füssl E (2013) Methodological development of a specific tool for assessing acceptability of assistive systems of powered two-wheeler-riders. In: 20th ITS world congress, Tokyo

Study of Parameters Influencing on the Performance of SiNW ISFET Sensor



Nabil Ayadi, Bekkay Hajji, Abdelghafour Galadi, Ahmet Lale, Jerome Launay, and Pierre Temple-Boyer

Abstract In recent years, Silicon nanowires (SiNW)-based ISFET devices have been selected as promising better sensors because of their advantages such as real-time detection and the good sensitivity caused by high surface-to-volume ratio. In this work, a mathematical model is evaluated to study the performance of the SiNW ISFET sensor. Furthermore, the effects of the parameters such as the NW width (W_{top}) and the gate insulator capacity C_{OX} on the performance of the SiNW ISFET sensor are investigated. The planar-ISFET structure and Si-nw-ISFET technology are also examined in our simulation and compared. Finally, the mathematical model of SiNW ISFET is verified with the experimental measurements and with other models indicated in the literature, gives a good accuracy at different pH values.

Keywords Silicon nanowire · Si-nw-ISFET · Parasitic resistance · Width W_{top} · Planar-ISFET

1 Introduction

The world has experienced a qualitative leap in development and innovations in the field of electronics, and particularly the advancement of small size sensors, among which we find the silicon nanowires (SiNW)-based ISFET sensor. This type of sensors is based on the ion sensitive field sensor effect transistors (ISFET) invented in 1970 by Bergveld [1] which is represented in several areas such as pH sensing, environmental monitoring, biomedical and medical diagnostics [2, 3]. One of the

N. Ayadi (✉) · B. Hajji

Laboratory of Renewable Energy, Embedded System and Information Processing, National School of Applied Sciences, Mohammed First University, Oujda, Morocco

e-mail: Nabil.ayadi.ma@gmail.com

A. Galadi

National School of Applied Sciences of Safi, Cadi Ayyad University, Marrakesh, Morocco

A. Lale · J. Launay · P. Temple-Boyer

Laboratory for Analysis and Architecture of Systems (LAAS-CNRS), University de Toulouse, 31400 Toulouse, France

challenges and innovations to consider when developing a new Si-nw-ISFET sensor is to increase its sensitivity, to reduce response times and ISFET detection limits. These characteristics making it a leader in future applications and an ideal candidate in a small industry, real-time detection, and a good sensitivity caused by high surface-to-volume ratio. In addition, the SiNWISFET can be easily integrated with CMOS reading circuits, its manufacture is reliable and at low cost [4, 5].

In this paper, a mathematical model is presented to study the performance of the SiNWISFET sensor. The influence of the parameters such as the NW width (W_{top}) and the gate insulator capacity (C_{OX}) on the performance of the SiNWISFET sensor are examined. In addition, the model developed is evaluated over a wide pH range, demonstrating good agreement between simulation, experimental data and with other models indicated in the literature.

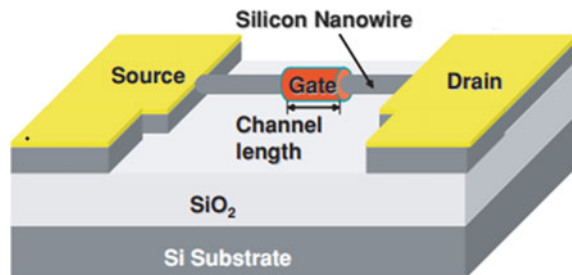
2 Modeling Approach of Silicon Nanowire ISFET Sensor

The structure of SiNWISFET sensor is shown in Fig. 1. The SiNW ISFET model that we present here is composed of three main parts: (1) Capacity of the gate insulator all-around the silicon nanowire; (2) threshold voltage shift when changing pH; and (3) equation for the drain current in all the transistor working regions.

2.1 Capacity of the Gate Insulator All-Around the Silicon Nanowire

To evaluate the performances of SiNW ISFET sensor, the modeling approach presented in this work takes into account the nanowire size effects and introduces the parameter of rectangular capacity (C_{OX}) of the gate insulator all-around the SiNW, which given by Tienda-Luna et al. [6]:

Fig. 1 Schematic view of SiNWISFET sensor



$$C_{OX} = \left(\frac{2.5\epsilon_{ox}\epsilon_0}{Ln\left(1 + \frac{5}{4} \frac{T_{ox}}{W_{nw}}\right)} + \frac{2.5\epsilon_{ox}\epsilon_0}{Ln\left(1 + \frac{5}{4} \frac{T_{ox}}{H_{nw}}\right)} \right) \frac{1}{2(H_{nw} + W_{nw})}$$

$$\text{With: } \begin{cases} \epsilon_{ox} = \frac{T_{ox}}{\epsilon_{Al_2O_3} + \epsilon_{SiO_2}} \\ T_{ox} = T_{Al_2O_3} + T_{SiO_2} \end{cases} \quad (1)$$

where: H_{nw} is the height of devices and $W_{nw} = W_{top}$ is the NW width of devices.

2.2 Threshold Voltage of Si-NW ISFET

The threshold voltage of SiNW ISFET (V_{TH}) is depends on the pH at alumina Al_2O_3 surface according to the site-binding model combined with SiNWMOSFET physics [7]:

$$V_{TH} = V_{THMOS} + V_{pH} \quad (2)$$

$$V_{pH} = E_{ref} - \psi_0 + x^{sol} - \frac{\emptyset_{Si}}{q} \quad (3)$$

$$\psi_0 = 2.303 \frac{KT}{q} \frac{\beta}{\beta + 1} (pH_{PZC} - pH) \quad (4)$$

where T is the absolute temperature, K is the Boltzmann's constant, q the electron charge, pH_{pzc} is the non-zero pH, and β [8, 9] is a parameter which reflects the chemical sensitivity of the gate insulator and is dependent on the density of surface sites N_s . The parameter β is given by:

$$\beta = \frac{2q^2 N_s \sqrt{\frac{K_b}{K_a}}}{KT C_{diff}} \quad (5)$$

where K_a , K_b are dissociation constants for the chemical reactions at the insulator interface and C_{diff} is the series combination of capacitances arising from Stern and diffuse layers is given by: Yesayan et al. [10]

$$C_{diff} = \frac{C_{stem} C_{DL}}{C_{stem} + C_{DL}} \quad (6)$$

Therefore, (6) should also be applicable to nanowire geometry, provided the Stern capacitance per unit area is also derived for the wire geometry $C_{stem} = \frac{\epsilon_1 \epsilon_0}{d_1}$, where:

$$d_1 = (2(H_{nw} + W_{nw}) + 4T_{ox}) \left(\frac{2.5}{\text{Ln}\left(1 + \frac{5}{4} \frac{d}{(W_{nw} + T_{ox})}\right)} + \frac{2.5}{\text{Ln}\left(1 + \frac{5}{4} \frac{d}{(H_{nw} + T_{ox})}\right)} \right)^{-1} \quad (7)$$

C_{DL} : defines the diffuse capacity layers per unit area [10] and is given by:

$$C_{DL} = \frac{\varepsilon_2 \varepsilon_0}{l_{d1}},$$

where:

$$l_{d1} \sim l_d \sqrt{\frac{0.5W_{nw} + T_{ox} + d + 3l_d}{0.5W_{nw} + T_{ox} + d}} \quad \text{With: } l_d = \sqrt{\frac{\varepsilon_2 V_t}{2qn_0}} \quad (8)$$

where n_0 is the concentration of ions per unit volume in the solution.

For the threshold voltage (V_{THMOS}), the BSIM3v3 based-model proposes the following expression [11]:

$$\begin{aligned} V_{THMOS} = & V_{th0} + K_1 \left(\sqrt{2\theta_f} - V_{BS} - \sqrt{2\theta_f} \right) \\ & - K_2 V_{BS} + K_1 \left(\sqrt{1 + \frac{N_{LX}}{L_{eff}}} - 1 \right) \sqrt{2\theta_f} + (K_3 + K_{3b} V_{BS}) \frac{T_{OX}}{W_{eff} + W_0} 2\theta_f \\ & - D_{VTO\omega} \left(\exp\left(-D_{VT1\omega} \frac{L_{eff}}{2l_{t\omega}}\right) + 2\exp\left(-D_{VT1\omega} \frac{L_{eff}}{l_{t\omega}}\right) \right) \\ & (V_{bi} - 2\theta_f) - D_{VT0} \left(\exp\left(-D_{VT1} \frac{L_{eff}}{2l_t}\right) + 2\exp\left(-D_{VT1} \frac{L_{eff}}{l_t}\right) \right) (V_{bi} - 2\theta_f) \\ & - \left(\exp\left(-D_{sub} \frac{L_{eff}}{2l_{t0}}\right) + 2\exp\left(-D_{sub} \frac{L_{eff}}{l_{t0}}\right) \right) (E_{1a0} + E_{1ab} V_{BS}) V_{DS} \quad (9) \end{aligned}$$

where V_{th0} is the threshold voltage for a long-channel device, T_{OX} is the thickness of gate oxide, V_{bi} is the built-in potential of drain/source-body junction, l_t and $l_{t\omega}$ are functions of T_{OX} , channel doping concentration and body bias. K_1 , K_2 , N_{LX} , K_3 , K_{3b} , W_0 , $D_{VTO\omega}$, $D_{VT1\omega}$, D_{VT0} , D_{VT1} , D_{sub} , E_{1a0} and E_{1ab} are parameters to be extracted from the measured data.

2.3 Drain Current

In the linear regime, the drain current equation is given by Beraet et al. [12, Liu et al. 13]:

$$I_{ds} = \frac{V_{DS}}{R_{nw}} = \frac{V_{DS}}{R_{S1} + R_{S2} + R_{ch}} \quad (10)$$

where R_{nw} is the resistance of nanowire. It consists of the channel resistance R_{ch} and residual parasitic resistance ($R_{S1} + R_{S2}$).

$$I_{ds} = \frac{V_{DS}}{\frac{\rho(L_{nw}-L)}{S_{nw}} + \frac{1 + \frac{V_{DS}}{E_{sat}L}}{\frac{W}{L}C_{OX}\mu_{eff}(V_{GS}-V_{TH}-0.5A_{bulk}V_{DS})}} \quad (11)$$

In the BSIM3v3 based-model, the mobility effective is presented as follows: [13]

$$\mu_{eff} = \frac{\mu_0}{1 + (U_A \left(\frac{V_{GS}+V_{TH}}{T_{OX}} \right) + U_B \left(\frac{V_{GS}+V_{TH}}{T_{OX}} \right)^2)(1 + U_C V_{BS})} \quad (12)$$

With: μ_0 , U_A , U_B and U_C are extracted parameters and R_{nw} is equal to:

$$R_{nw} = R_{S1} + R_{S2} + \frac{1 + \frac{V_{DS}}{E_{sat}L}}{\frac{W}{L}C_{OX}\mu_{eff}(V_{GS} - V_{TH} - 0.5A_{bulk}V_{DS})} \quad (13)$$

$$R_{S,nw} = R_{S1} + R_{S2} = \frac{\rho(L_{nw} - L)}{S_{nw}} \quad (14)$$

V_{DS} is the voltage applied to the drain.

where: ρ is the resistivity of the doped silicon, S_{nw} is the surface of nanowire and L_{nw} is the length of nanowire.

The conductance is defined as the derivative of the current I_{ds} per V_{DS} in the linear region, which is given by the following equation:

$$G_{ds} = \frac{\partial I_{ds}}{\partial V_{DS}} \approx \frac{1}{\frac{1 + \frac{V_{DS}}{E_{sat}L}}{\frac{W}{L}C_{OX}\mu_{eff}(V_{GS}-V_{TH}-0.5A_{bulk}V_{DS})} + \frac{\rho(L_{nw}-L)}{S_{nw}}} \quad (15)$$

In the weak-inversion, the drain current is defined as [13]:

$$I_{Dsub} = I_{s0} \left(1 - \exp\left(-\frac{V_{DS}}{V_t}\right) \right) \exp\left(\frac{V_{GS} - V_{TH} - V_{off}}{nV_t}\right) \quad (16)$$

where

$$I_{s0} = \mu_0 \frac{W}{L} \sqrt{\left(\frac{q\epsilon_s N_{ch}}{2\phi_s}\right)} V_t^2 \quad (17)$$

And:

$$n = 1 + N_{FACTOR} \frac{C_D}{C_{OX}}$$

$$\begin{aligned}
& + \frac{(C_{DSC} + C_{DSCD}V_{DS} + C_{DSCB}V_{BS})\left(\exp\left(-D_{VT1}\frac{L_{eff}}{2L_t}\right) + 2\exp\left(-D_{VT1}\frac{L_{eff}}{L_t}\right)\right)}{C_{OX}} \\
& + \frac{C_{it}}{C_{OX}}
\end{aligned} \tag{18}$$

Here, the parameter V_t is the thermal voltage and is given by $K_B T/q$, V_{off} the offset voltage, as discussed in Jeng's dissertation [13]. The parameter n is the subthreshold swing parameter, the parameters C_{DSC} , C_{DSCD} and C_{DSCB} are extracted. The parameter C_{it} is the capacitance due to interface states. The parameter N_{factor} is introduced to compensate for errors in the depletion width capacitance calculation.

3 Results and Discussion

In this part, we study the influence of the main parameters of the nanowire on the performance of the SiNW ISFET sensor such as the width NW (W_{top}) and the Capacity of the gate insulator all-around the silicon nanowire (C_{OX}). In addition, the planar-ISFET structure and SiNWISFET technology are also examined and compared.

3.1 Influence of Capacity of the Gate Insulator All-Around the Silicon Nanowire

In Fig. 2, we evaluate the influence of two capacities: C_{OX} of gate insulator all-around the silicon NW and C_{OX} of the simple gate insulator, on the response of the SiNWISFET for a nanowire of $2\ \mu\text{m}$ and a pH value of 4.

In comparison, we find that the capacity C_{OX} of gate insulator all around the silicon NW gives a better fit with the experimental measurements. This capacity is more suitable for studying the parameters of the nanowire than the capacity of a simple gate insulator and it is linked to the NW width (W_{top}) as shown in Fig. 2.

3.2 Influence of the NW Width (W_{top})

In this work, we considered the width (W_{top}) to be 150, 170 and 300 nm. As shown in Fig. 3, when NW (W_{top}) increases leads to an increase in conductance. This conductance is defined as the derivative of the current I_{ds} per V_{DS} in the linear region and it is represented by the relation (15).

Figure 4 illustrates the the $I_{ds}(V_{gs})$ curves of the SiNW ISFET sensors for 3 widths W_{top} : 150, 170 and 300 nm and at different pH values 4, 7 and 10. The sensitivity

Fig. 2 Comparison between C_{OX} of gate insulator-all-around and C_{OX} of simple gate insulator, in linear scale of the SiNWISFET I_{ds} (V_{gs}), the evolution of C_{OX} as a function of NW width W_{top}

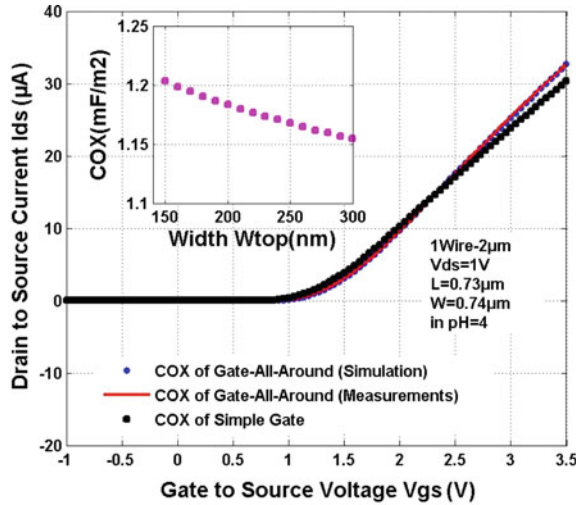
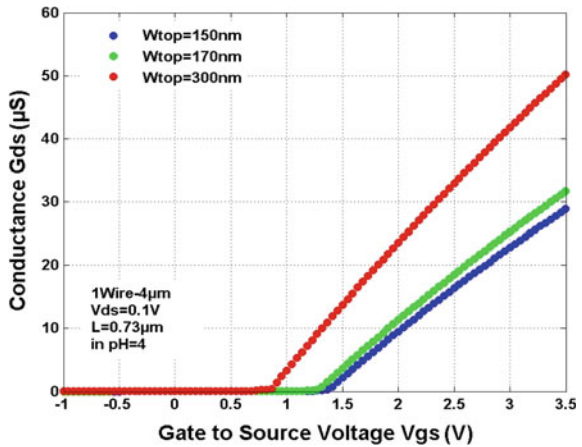


Fig. 3 Conductance G_{ds} change versus gate voltage V_{gs} of the SiNWISFET for different W_{top} (150, 170 and 300 nm)



is estimated at 56.03 mV/pH for Si-nw-ISFET and does not depend significantly on the NW width (W_{top}) of the ISFET nanowires.

3.3 Comparison Between Si-Nw-ISFET and Planar-ISFET

Figure 5a shows the evolution of the I_{ds} transfer curves (V_{gs}) as a function of the pH for the two technologies: SiNW ISFET and planar-ISFET. In the linear scale of SiNWISFET, we observe that the characteristics I_{ds} (V_{gs}) of Si-nw ISFET begin to curve to quickly enter the saturation regime while the characteristics I_{ds} (V_{gs}) of

Fig. 4 Current I_{ds} change in gate voltage V_{gs} in the semi-logarithmic of the SiNW ISFET for different W_{top} (150, 170 and 300 nm)

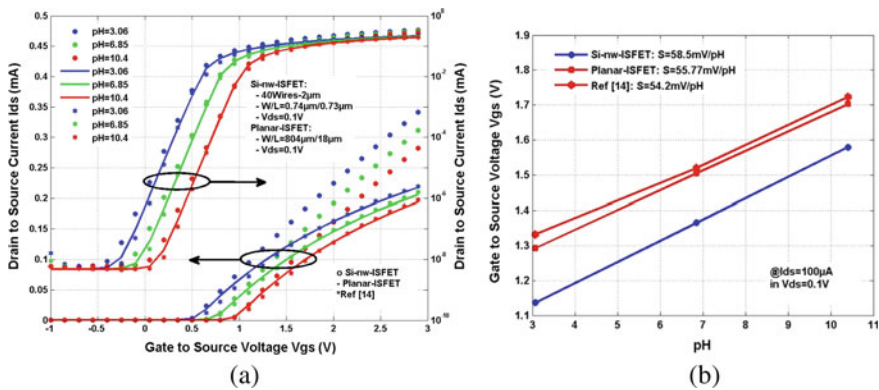
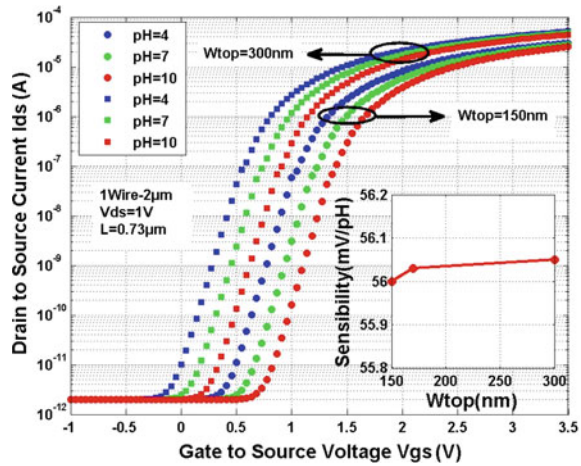


Fig. 5 I_{ds} (V_{gs}) characteristic of Si-nw-ISFET and planar-ISFET [14], with a linear and semi-logarithmic scale, for different pH. ($V_{ds} = 0.1$ V). **b.** Gate- source voltage as function of pH at $I_{ds} = 100 \mu A$ ($V_{ds} = 0.1$ V)

planar ISFETs always remain in the linear regime. This phenomena can be related to the numbers of nanowires and to the capacity C_{OX} of gate insulator all around the silicon NW. In addition, the Si-nw-ISFET sensor has an excellent I_{ds} (V_{gs}) curve with higher current values compared to planar-ISFET technology [according to Eq. (19)]. This makes the Si-nw-ISFET sensor faster in response with a good signal reliability.

$$I_{ds} = \frac{V_{DS}}{\frac{\rho(L_{nw}-L)}{NS_{nw}} + \frac{NW}{L} C_{OX} \mu_{eff} (V_{GS} - V_{TH} - 0.5 A_{bulk} V_{DS})} = \frac{NV_{DS}}{R_{nw}} \quad (19)$$

With N is number of nanowires.

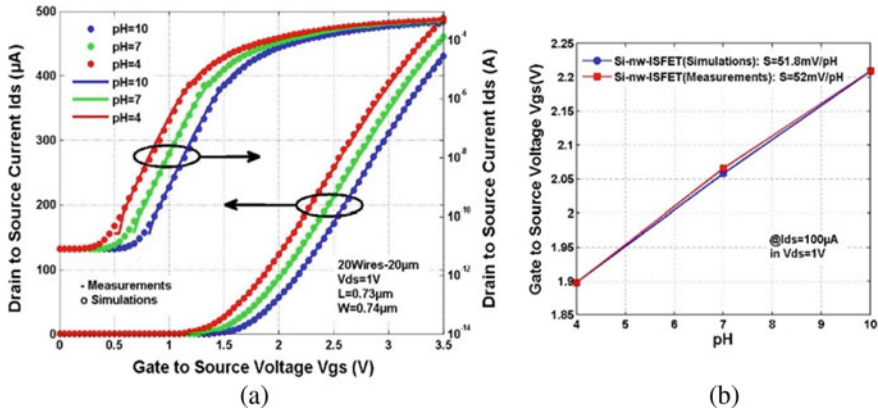


Fig. 6. a Verification between simulation results and measurement of SiNW ISFET depending on pH. b Gate-source voltage in terms of pH at $I_{ds} = 100 \mu A$ ($V_{ds} = 1 V$)

The model developed in this work was also compared with the experimental results indicated in Ref [14] and good precision was obtained for different pH values.

The influence of pH causes shift in the threshold voltage V_{TH} of the SiNWISFET and the planar-ISFET sensors. The sensitivity is estimated at 58.5 mV/pH for SiNWISFET while it is 56 mV/pH for planar-ISFET (Fig. 5b).

3.4 Model Validation

In order to demonstrate the validity of the model proposed in this work for the SiNW ISFET sensor, the simulation results were verified with the experimental results provided by the LAAS laboratory in Toulouse, France. Figure 6a show that the fit is excellent for different of pH and the main parameters of the proposed model are listed in Table 1.

As Fig. 6b shows, the measured and calculated sensitivities are practically identical and equal to 52 mV/pH and 51.8 mV/pH respectively.

Our model was also validated through the experimental results indicated in the previous literature, Ref. [15]. Figure 7 clearly confirms the effectiveness of our model for different pH values: 5, 7 and 9.

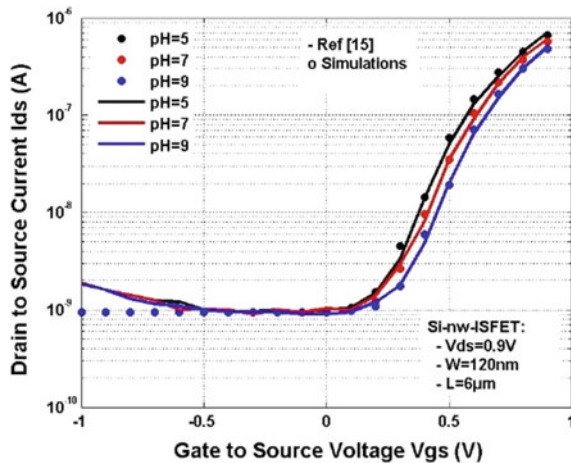
4 Conclusion

In this study, a mathematical model of the SiNWISFET sensor was developed and verified with the experimental results. The effects of different parameters such as the NW width (W_{top}) and the Capacity of the gate insulator all-around the silicon

Table 1 BSIM3v3 parameters for the SiNW ISFET sensor

Parameters	Values of BSIM3v3	Parameters	Values of BSIM3v3
Length gate (μm)	0.73	Vsat(m/s)	1.1986E6
Width channel (μm)	0.74	$W_0(\text{m})$	2.45E-7
Length of wire (μm)	20	K_3	86.3187
Number of nanowires	20	Dvt0	2.1807E-6
$\mu_0(\text{cm}^3/\text{V.s})$: mobility	213	Dsub	0.0494
Ua(m/V)	1E-18	Eta0	0.02
Ub(m/V ²)	6E-22	$C_{\text{diff}}(\text{F}/\text{cm}^2)$	3E-5
Nfactor	0.9	$N_s(\text{cm}^{-2})$	8E14
Cit(F/m ²)	8E-4	Ka (mole/l)	1.65E-7
Cdscd(F/Vm ²)	8E-4	Kb (mole/l)	8E-11
Nlx(m)	6.4233E-9	$R_s(\Omega)$	1.7E4

Fig. 7 Verification between simulation results and Ref [15] of Si-NW-ISFET depending on pH ($V_{ds} = 0.9\text{ V}$)



nanowire (C_{OX}) on the performance of the SiNWISFET sensor are investigated. Some of the most remarkable results are:

- The gate insulator capacity C_{OX} of the silicon nanowire in the form of all-around allows a better adjustment with the experimental measurements. This capacity is more suitable for studying the parameters of the nanowire than the capacity of a simple gate insulator.

- The sensitivity of Si-nw-ISFET does not significantly depend on the NWwidth (W_{top}) of the ISFET nanowires and it is estimated at 56.03 mV/ pH
- The Si-nw-ISFET sensor has an excellent I_{ds} (V_{gs}) curve with higher current values compared to planar-ISFET technology. This phenomena can be related to the numbers of nanowires and to the gate insulator capacity C_{OX} of the silicon nanowire in the form of all-around.

Finally, the developed model of SiNW ISFET has been verified with the experimental results and with others models indicated in the literature, gives good accuracy at different pH values.

References

1. Bergveld P (1970) Development of an ion-sensitive solid-state device for neurophysiological measurements. *IEEE Trans Biomed Eng BME* 17:70–71
2. Choi S et al (2020) Experimental extraction of stern-layer capacitance in biosensor detection using silicon nanowire field-effect transistors. *Curr Appl Phys* 20:828–833
3. Kim S et al (2017) Analysis of current drift on p-channel pH-Sensitive SiNW ISFET by capacitance measurement. *Curr Appl Phys*:1–7
4. Kwon DW et al (2017) Macro modeling of ion sensitive field effect transistor with current drift. *Sens Actuat B* 249:564–570
5. Laleet A et al (2017) Development of All-Around SiO₂/Al₂O₃ gate, suspended silicon nanowire chemical field effect transistors Si-nw-ChemFET[†]. In: *Proceedings* 1, 419
6. Tienda-Luna IM et al (2008) Modeling the equivalent oxide thickness of surrounding Gate SOI devices with high- κ insulators. *Solid-State Electron* 52:1854–1860
7. Hajji B et al (2000) pH, pK and pNa detection properties of SiO₂/Si₃N₄ ISFET chemical sensors. *Microelectron Reliab* 40:783–786
8. Van Den Vlekkert H et al (1988) The temperature dependence of the surface potential at the Al₂O₃ electrolyte interface. *J Co/hid Inter/rice Sci* 122(2)
9. Zarkesh-Ha P^{*‡}, Edwards J^{†‡}, Szauter P[‡] (2015) Avalanche ISFET: a highly sensitive pH sensor for genome sequencing. 978-1-4799-7234-0/15/\$31.00 ©2015 IEEE
10. Yesayan A et al (2020) Analytical modeling of double-gate and nanowire junctionless ISFETs. *IEEE Trans Electron Dev* 67(3)
11. Cheng Y et al (1997) A physical and scalable I–V model in BSIM3v3 for analog/digital circuit simulation. *IEEE Trans Electron Dev* 44(2)
12. Beraet S et al (2016) Development of a methodology for the extraction of BSIM3v3.2.2 parameters of Ge-channel MOSFETs and estimation of analog circuit performance. © Springer-Verlag Berlin Heidelberg
13. Liu W et al, BSIM3V3.2 MOSFET model, users' manual. Copyright © 1997–1998
14. Martinoia S et al (2005) Modeling ISFET microsensor and ISFET-based microsystems: a review. *Sens Actuat B* 105:14–27
15. Jang J et al (2017) Effect of liquid gate bias rising time in pH sensors based on Si nanowire ion sensitive field effect transistors. *Solid-State Electronics*

Modeling and Trajectory Tracking of an Unmanned Quadrotor Using Optimal PID Controller



Hamid Hassani, Anass Mansouri, and Ali Ahaitouf

Abstract Quadrotor Unmanned Aerial Vehicle (UAV) is a nonlinear, unstable, and coupled system which presents a great challenge in term of modeling and control design. In some cases, the nonlinear part of the quadrotor system is omitted to simplify the study and the control design, our goal is to derive the full dynamic model without neglecting the coupling influences between the translational and rotational dynamics. This paper conducted a detailed theoretical study of the dynamics and kinematics equations of the aerial vehicle based on the Newton–Euler formula. Then, a Proportional-Integral-Derivative (PID) controller is used to steer the quadrotor degrees of freedom. Ant Colony Optimization (ACO) algorithm is used to select the optimal configuration of the PID controller. Simulations for trajectory tracking are conducted to test the performance of the adopted PID controller.

Keywords Quadrotor · UAV · Nonlinear dynamic · PID controller · ACO

1 Introduction

Recently, quadrotors UAVs are becoming used in multiple application domains including photography, surveillance, investigation of the disaster, and so on ... Especially, due to their fascinating features such as vertical takeoff and landing capability, small size, and high maneuverability. Nevertheless, quadrotors are under-triggered with a nonlinear dynamic behavior and a high coupling between their movements which present a great challenge in terms of modeling and control design.

Quadrotor belongs to the class of rotary-wing vehicles, propelled by four rotors arranged in the corners of a cross-like structure. The movements in the 3D space are performed by varying the speed of the four rotors, however, the pair of rotors

H. Hassani (✉) · A. Ahaitouf

Laboratory of Intelligent Systems, Geo-Resources and Renewable Energies, Faculty of Sciences and Technology, Sidi Mohammed Ben Abdellah University, Fez, Morocco
e-mail: Hamid.hassani@usmba.ac.ma

A. Mansouri

Laboratory of Intelligent Systems, Geo-Resources and Renewable Energies, School of Applied Sciences, Sidi Mohammed Ben Abdellah University, Fez, Morocco

© Springer Nature Singapore Pte Ltd. 2022

S. Bennani et al. (eds.), *WITS 2020*, Lecture Notes in Electrical Engineering 745,
https://doi.org/10.1007/978-981-33-6893-4_43

(M_1 and M_3) rotate in the clockwise direction while the pair (M_2 and M_4) rotate in the counterclockwise direction, using this configuration the reactive moment of each pair can be eliminated. The rotation around z axis named yaw rotation is obtained by varying the speed (increasing /decreasing) of any pair of rotors. The coupling in the quadrotor movements clearly appears in the displacement in the xy plan, however, the roll rotation is coupled with the y displacement and the pitch rotation is also coupled with the x displacement.

The intricacy of modeling and controlling the quadrotors UAV has become a major challenge for the robotic community, and several research proposals have been performed to address these issues. In [1] a PID control algorithm is used to steer the quadrotor attitude and position. The reference [2] covers all the details required to success the control of the quadrotor with a classical PID controller. The references [3] presents a comparative study between the PID controller and the linear quadratic regulator (LQR). In this paper [4], the application of an optimal backstepping controller was made to regulate the quadrotor behaviors. In the same way, the quadrotor nonlinear dynamic was taken in consideration in the modeling phase and an experimental implementation of the backstepping controller was performed to steer the quadrotor flight in the 3D space [5]. In this work [6], an adaptive sliding mode controller is designed for the position and attitude tracking control of an uncertain quadrotor.

Herein, the nonlinear dynamic model of the quadrotor UAV is obtained using Newton–Euler principle. Then, based on this model, a hierarchical PID controller is used to solve the problem of underactuation and to steer the quadrotor position and attitude during the flight. The parameters of the adopted controller are automatically tuned using ACO algorithm. Simulation experiments of trajectory tracking are performed to show the performance of the PID controller.

This work starts by briefly introducing, Sect. 2 presents the full dynamic model of the quadrotor UAV. Next, Sect. 3 discusses the aims of the proposed hierarchical PID controller. Section 4 describes the optimization process. Section 5 presents the results of the simulation experiments. Finally, the last section concludes the work.

2 Quadrotor Modeling

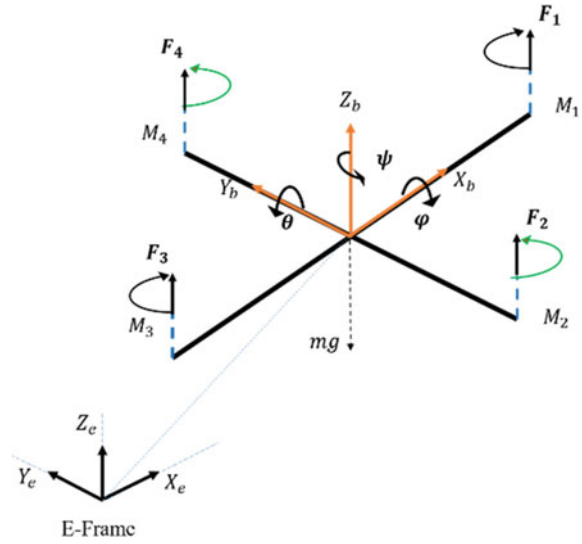
To design an accurate flight controller, quadrotor must be modeled carefully. However, quadrotor moves toward the desired path using the lifting forces generated by each rotor. These forces are function of the rotor's angular speed.

$$F_i = b.\omega_i^2 \quad (1)$$

where b is the thrust constant depends on the propulsion system (propeller-rotor) characteristics. ω_i designates the angular velocity of rotor i .

Quadrotor has six degrees of freedom including three translations represented by the Cartesian coordinates $\xi = (x, y, z)$, and three rotations symbolized by Euler

Fig. 1 Quadrotor UAV



angles $\eta = (\varphi, \theta, \psi)$. Two frame are defined as illustrated in Fig. 1, a body frame (X_b, Y_b, Z_b) and Earth frame (X_e, Y_e, Z_e) .

Kinematic studies define the relation existing between variables expressed in E-Frame and the B-Frame by respecting the following equations:

$$\dot{\xi} = \mathcal{R}.V^b \tag{2}$$

$$\Omega^b = \mathcal{J}.\dot{\eta} \tag{3}$$

where $\dot{\xi}$ and $\dot{\eta}$ are the linear and angular velocities in the E-frame, while V^b and Ω^b are the linear an angular velocities in the B-frame.

\mathcal{R} and \mathcal{J} are the rotation matrix and the transformation matrix, respectively.

$$\mathcal{R} = \begin{pmatrix} C_\theta C_\psi & S_\varphi S_\theta C_\psi - C_\varphi S_\psi & C_\varphi S_\theta C_\psi + S_\varphi S_\psi \\ C_\theta S_\psi & S_\varphi S_\theta S_\psi + C_\varphi C_\psi & C_\varphi S_\theta S_\psi - S_\varphi C_\psi \\ -S_\varphi & S_\varphi C_\theta & C_\varphi C_\theta \end{pmatrix} \tag{4}$$

$$\mathcal{J} = \begin{pmatrix} 1 & 0 & -S_\theta \\ 0 & C_\varphi & C_\theta S_\varphi \\ 0 & -S_\varphi & C_\varphi C_\theta \end{pmatrix} \tag{5}$$

where C and S designate respectively the co-sinus and sinus function.

We suppose that the quadrotor has a rigid and symmetrical structure, therefore the translational and rotational dynamics can be expressed based on Newton–Euler principle as follows [6–8]:

$$\begin{cases} m\ddot{\xi} = -mg\mathbf{e}_z + \mathcal{R}U_1 \\ \mathbf{I}\ddot{\eta} = M_p - M_G - \dot{\eta} \wedge (\mathbf{I}\dot{\eta}) \end{cases} \quad (6)$$

where $U_1 = \sum_{i=1}^4 F_i$ is the total lift force generated by the four propulsion system, $\mathbf{e}_{\ddagger} = [0, 0, 1]^T$, $\mathbf{I} = \text{diag}(\mathbb{I}_x, \mathbb{I}_y, \mathbb{I}_z)$ symbolizes the matrix of inertia, M_p and M_G are the moment produced by the propeller-rotor rotation and the gyroscopic torque, respectively.

$$M_p = \begin{pmatrix} U_\varphi \\ U_\theta \\ U_\psi \end{pmatrix} = \begin{pmatrix} bl(\omega_4^2 - \omega_2^2) \\ bl(\omega_3^2 - \omega_1^2) \\ d(\omega_4^2 + \omega_2^2 - \omega_1^2 - \omega_3^2) \end{pmatrix} \quad (7)$$

$$M_G = \begin{pmatrix} \dot{\varphi} \\ \theta \\ \dot{\psi} \end{pmatrix} \wedge J_r \begin{pmatrix} 0 \\ 0 \\ \sum_{i=1}^4 (-1)^{i+1} \omega_i \end{pmatrix} = J_r \varpi \begin{pmatrix} \dot{\theta} \\ -\dot{\varphi} \\ 0 \end{pmatrix} \quad (8)$$

With $\varpi = \omega_4 + \omega_2 - \omega_1 - \omega_3$, J_r corresponds to the rotor inertia, d is the drag factor and l is the length of the quadrotor arm.

Therefore, by expanding the previous relations, equations of motion describing the dynamics of the quadrotor can be written in the following forms:

$$\begin{pmatrix} \dot{\xi} \\ \dot{\eta} \end{pmatrix} = \begin{pmatrix} \ddot{x} \\ \ddot{y} \\ \ddot{z} \\ \ddot{\varphi} \\ \ddot{\theta} \\ \ddot{\psi} \end{pmatrix} = \begin{pmatrix} \frac{U_1}{m} (C_\varphi S_\theta C_\psi + S_\varphi S_\psi) \\ \frac{U_1}{m} (C_\varphi S_\theta S_\psi - S_\varphi C_\psi) \\ \frac{U_1}{m} (C_\varphi C_\theta) - g \\ \dot{\theta} \dot{\psi} \left(\frac{I_y - I_z}{I_x} \right) - \frac{J_r}{I_x} \dot{\theta} \varpi + \frac{U_\varphi}{I_x} \\ \dot{\varphi} \dot{\psi} \left(\frac{I_z - I_x}{I_y} \right) + \frac{J_r}{I_y} \dot{\varphi} \varpi + \frac{U_\theta}{I_y} \\ \dot{\varphi} \dot{\theta} \left(\frac{I_x - I_y}{I_z} \right) + \frac{U_\psi}{I_z} \end{pmatrix} \quad (9)$$

where U_1 , U_φ , U_θ and U_ψ are the control inputs formed by the combination of the rotor's angular speeds. However, U_1 is the lifting force which controls the quadrotor translation along z -axis, U_φ is the roll torque acting in the x -axis, U_θ is the pitch torque allowing the rotation around y -axis, while U_ψ denotes the total yawing moment acting in the z -axis.

Quadrotor can performs six movements using only four control signals U_1 , U_φ , U_θ and U_ψ . To solve the problem of underactuation it is normally to consider two virtual controls as follows [9].

$$\begin{cases} v_x = \frac{U_1}{m} (C_\varphi S_\theta C_\psi + S_\varphi S_\psi) \\ v_y = \frac{U_1}{m} (C_\varphi S_\theta S_\psi - S_\varphi C_\psi) \end{cases} \quad (10)$$

Therefore the desired roll and pitch angles required to achieve the expected translational movements are obtained as:

$$\begin{cases} \theta_d = \arctan\left(\frac{v_x \cos \psi_d + v_y \sin \psi_d}{U_z + g}\right) \\ \varphi_d = \arctan\left(C_{\theta_d} \left(\frac{v_x \sin \psi_d - v_y \cos \psi_d}{U_z + g}\right)\right) \end{cases} \quad (11)$$

With

$$U_z = C_\varphi C_\theta \frac{U_1}{m} - g \quad (12)$$

3 Controller Design

In order to eliminate the underactuation problem, a hierarchical control strategy with inner and outer loops is adopted. The inner loop controls the orientation of the quadrotor and produces the adequate control torques U_φ , U_θ and U_ψ . The outer loop steers the quadrotor position and generates the sufficient lift force required to achieve the desired vertical position and generates also the desired roll and pitch angles which serve as set-points (inputs) for the inner loop. In order to get high performance, controller parameters are selected using Ant Colony Optimization algorithm. The flowchart of the hierarchical control structure used in this work is illustrated in Fig. 2.

PID, as a control law, combines three form of the tracking error; the present, past, and future forms. Accordingly, the linear PID controller destined to the regulation of the quadrotor behaviors is given by the following equation [10]:

$$U = K_p \Delta + K_i \int \Delta dt + K_d \frac{d\Delta}{dt} \quad (13)$$

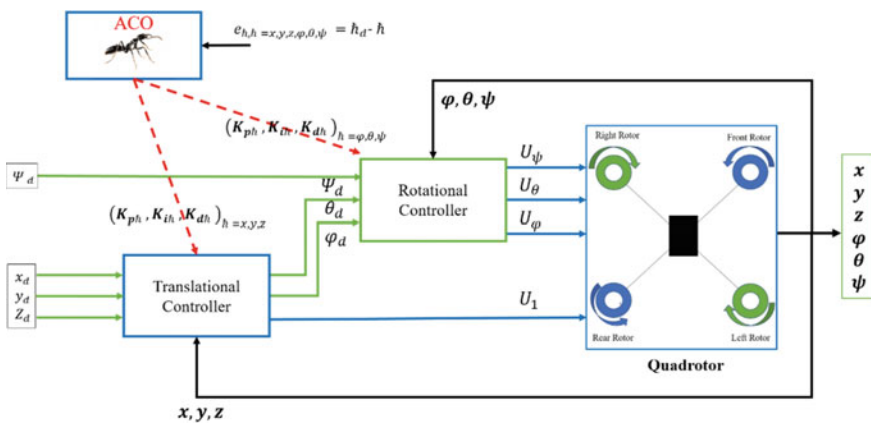


Fig. 2 Control flowchart

where K_p , K_i and K_d stand for the proportional, integral and derivative gains. $\Delta = x_d - x$ is the tracking error between the current value and the desired value.

The control equation of the quadrotor UAV are expressed as follows:

$$\begin{cases} v_x = K_{px}e_x + K_{ix} \int e_x dt + K_{dx}\dot{e}_x \\ v_y = K_{py}e_y + K_{iy} \int e_y dt + K_{dy}\dot{e}_y \\ U_1 = K_{pz}e_z + K_{iz} \int e_z dt + K_{dz}\dot{e}_z \\ U_\varphi = K_{p\varphi}e_\varphi + K_{i\varphi} \int e_\varphi dt + K_{d\varphi}\dot{e}_\varphi \\ U_\theta = K_{p\theta}e_\theta + K_{i\theta} \int e_\theta dt + K_{d\theta}\dot{e}_\theta \\ U_\psi = K_{p\psi}e_\psi + K_{i\psi} \int e_\psi dt + K_{d\psi}\dot{e}_\psi \end{cases} \quad (14)$$

The PID controller is used to reduce the deviation between the current state and the desired state, since the proportional term help to expand the phase margin (improves the system stability) and improve the transition time, the integral term reduces the steady state error, while the derivative term reduces the overshoot and improve the response time.

4 Controller Optimization

Controller performances depend on their internal parameters, an effective way to select the controller parameters is to use optimization algorithm. The idea is to design a cost function based on the tracking error, then optimization algorithm will be used to minimize the cost function and therefore this minimum will corresponds to the controller parameters optimal values. In this work the well-known Ant Colony Optimization (ACO) algorithm is adopted for the optimization purpose. The basic principle of the ACO algorithm was inspired by the social cooperative behavior of ants when searching the food source [11].

Using ACO algorithm, the controller parameters are represented by a matrix (Fig. 3), where ants choose the optimal values which give the best consistency of the controller performances.

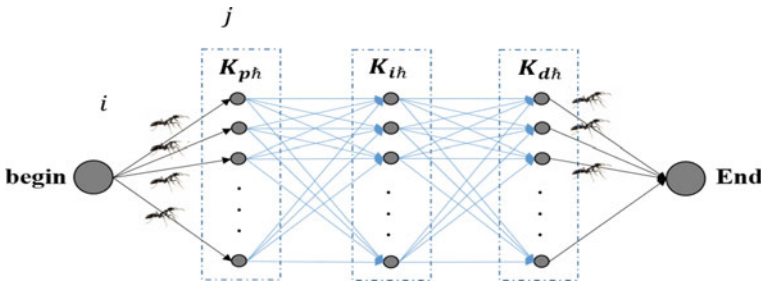


Fig. 3 Ant colony optimization graph

Through the search, each ant makes a decision on the path to be followed based on the amount of pheromone existing in this path. Therefore, the probability of choosing a node (i, j) is given by:

$$P_{i,j}^A = \frac{(\tau_{i,j})^a (\eta_{i,j})^b}{\sum_{f \in \mathcal{N}_{\Theta_i^A}} (\tau_{i,f})^a (\eta_{i,f})^b} \quad j \in \mathcal{N}_i^A \tag{15}$$

where $\tau_{i,j}$ and $\eta_{i,j}$ are the amount of pheromone and the visibility of node (i, j) , respectively. a and b are two constant defining the influence of pheromone concentration and the visibility in ant decision. \mathcal{N}_i^A corresponds to the path traced by ant A .

When traversing an arc (i, j) , ant A produces an amount of pheromone $\Delta\tau_{i,j}^A$, therefore the concentration of pheromone in an arc (i, j) is given by:

$$\tau_{i,j} = (1 - \sigma)\tau_{i,j}^{prev} + \sum_{k=1}^n \Delta\tau_{i,j}^k \tag{16}$$

Where σ is the pheromone evaporation rate.

The cost function to be minimized using ACO algorithm is defined by the integral square error (ISE) [12]:

$$ISE = \int_0^{\infty} e^2(t) dt \tag{17}$$

The process of optimizing the PID controller gains is illustrated in Fig. 4.

5 Simulation Results

This section concerns the controller performance analysis, for the purpose of scrutinizing the quadrotor response, and to test whether the controller can drive the quadrotor to their reference path and remain stable until finalizing the flight mission. The nonlinear dynamic model of the quadrotor system is implemented in Matlab/Simulink and configured as shown in Table 1 [13].

The controller parameters obtained using ACO algorithm are given in Table 2.

Remark 1 To reduce the optimization run time, we suppose that the PID controller parameters for the position subsystem are the same. Similarly for the attitude controller, the parameters for the three motions are assumed to be equal.

Remark 2 The parameters of the ACO algorithm are configured as in reference [12]. In this work only the proportional and derivative gains are selected using the adopted algorithm. Whereas the integral term is fixed to, this choice is reasonable because the integral term should have a small value in order to reduce the overshoot oscillation.

Fig. 4 ACO algorithm

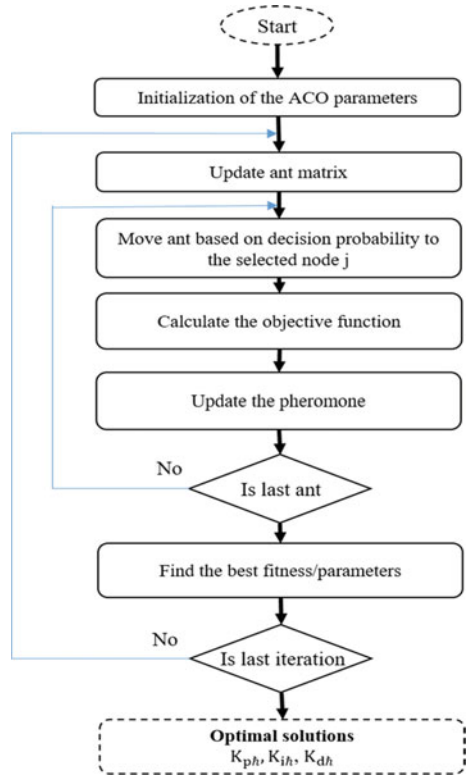


Table 1 Quadrotor configuration

Parameters	Value	Parameters	Value
m (kg)	1.1	b (N s ²)	5
$I_x=I_y$ (Kg m ²)	0.022	d (N m s ²)	2
I_z (Kg m ²)	0.042	J_r (Kg m ²)	0.02
$l(m)$	0.21	g (ms ⁻²)	9.81

Table 2 Controller parameters

Parameters	Value	Parameters	Value
$K_{px} = K_{py} = K_{pz}$	4.8564	$K_{p\varphi} = K_{p\theta} = K_{p\psi}$	16.5948
$K_{ix} = K_{iy} = K_{iz}$	0.001	$K_{i\varphi} = K_{i\theta} = K_{i\psi}$	0.001
$K_{dx} = K_{dy} = K_{dz}$	5.0542	$K_{d\varphi} = K_{d\theta} = K_{d\psi}$	13.8439

Results of trajectory tracking are illustrated in Fig. 5, as seen results are quite smooth with good accuracy tracking of the given path. Although the error in the steady state is small which reflect the efficiency of the adopted hierarchical control strategy.

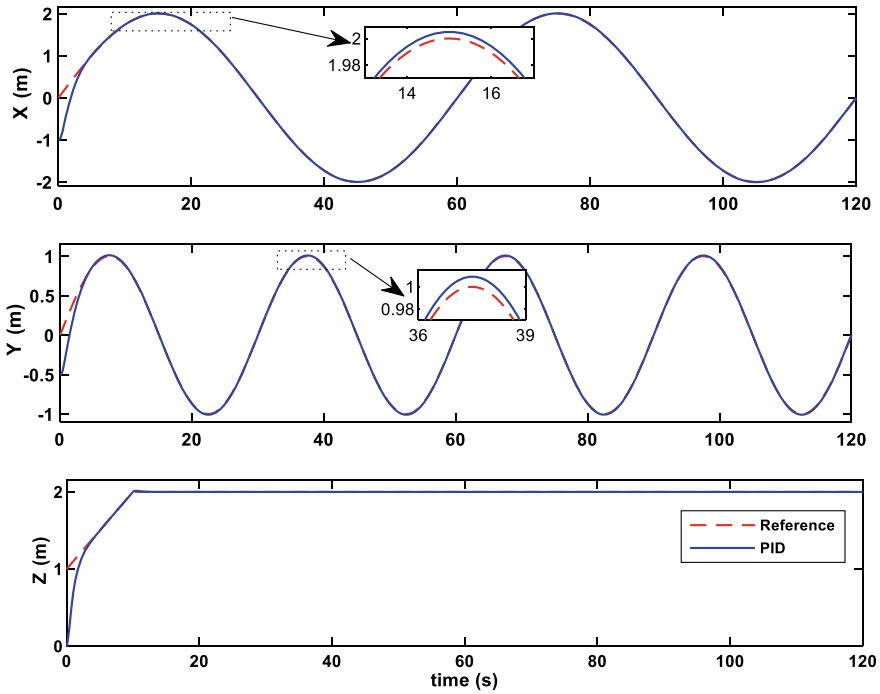


Fig. 5 Quadrotor position

Figure 6 illustrates the tracking of the quadrotor attitude, from this figure it can be observed that the magnitude of the generated Roll and Pitch angles are acceptable, furthermore the yaw rotation is effectively maintained to zero rad. The 3D representation of the tracking performance is depicted in Fig. 7, it is clear that the hierarchical PID controller has effectively controlled the quadrotor movements.

6 Conclusion

The main goal of this paper is to present the nonlinear dynamic model of the quadrotor UAV by considering several physics laws that influence the system performances. A hierarchical PID control law based Ant Colony Optimization algorithm is adopted to manage the quadrotor behavior during the flight. Simulations of trajectory tracking were performed to validate the effectiveness of the PID controller. Results of trajectory tracking were satisfactory and the controller has shown its accuracy to drive the quadrotor UAV along the programmed path successfully.

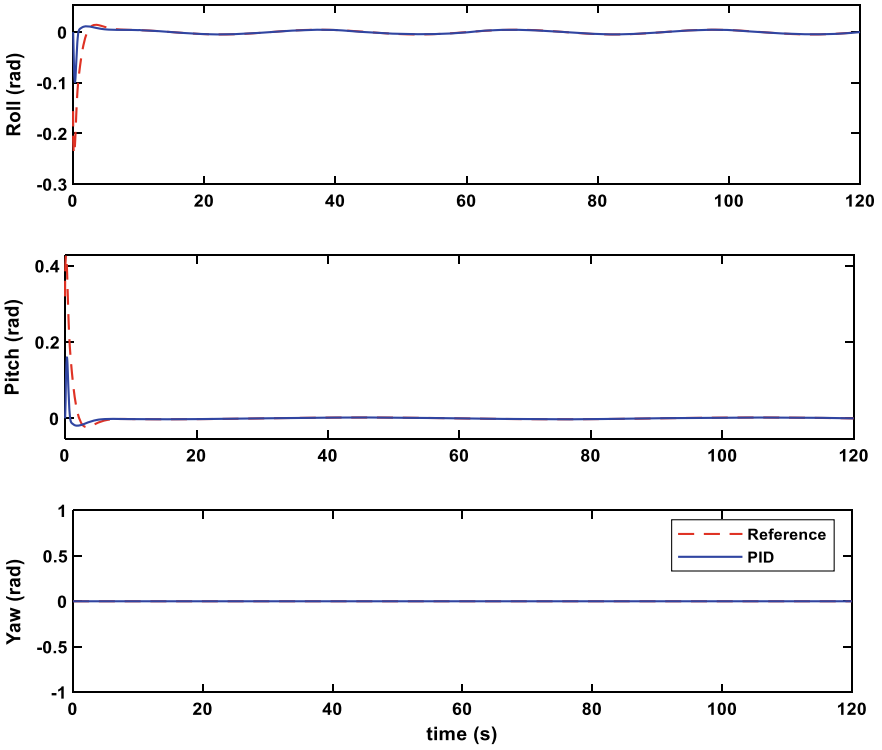


Fig. 6 Quadrotor attitude

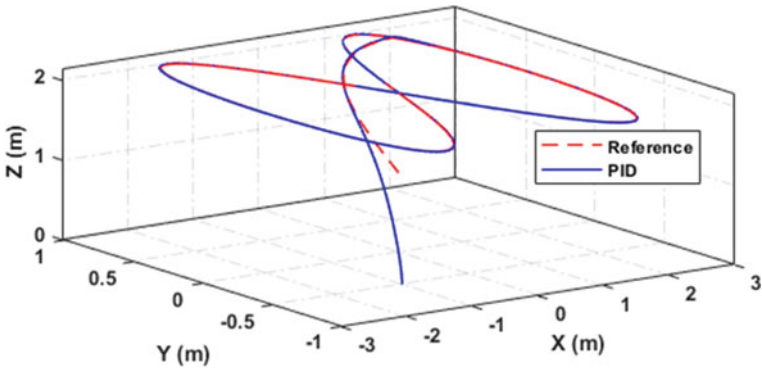


Fig. 7. 3D trajectory tracking

References

1. Hassani H, Mansouri A, Ahaitouf A (2021) Mechanical Modeling, Control and Simulation of a Quadrotor UAV. In: Hajji B, Mellit A, Marco Tina G, et al (eds) Proceedings of the 2nd International Conference on Electronic Engineering and Renewable Energy Systems. Springer Singapore, Singapore, pp 441–449
2. Luukkonen T (2011) Modelling and control of quadcopter. *Indep Res Proj Appl Math Espoo* 22
3. Argentim LM, Rezende WC, Santos PE, Aguiar RA (2013) PID, LQR and LQR-PID on a quadcopter platform. In: 2013 international conference on informatics, electronics and vision (ICIEV). IEEE, pp 1–6
4. Yacef F, Bouhali O, Hamerlain M, Rezoug A (2013) PSO optimization of integral backstepping controller for quadrotor attitude stabilization. In: 3rd international conference on systems and control. IEEE, pp 462–466
5. Dena Ruiz JA, Aouf N (2017) Real-time setup with PD and backstepping control for a Pelican quadrotor
6. Hassani H, Mansouri A, Ahaitouf A (2020) A new robust adaptive sliding mode controller for quadrotor UAV flight. In: 2020 IEEE 2nd International Conference on Electronics, Control, Optimization and Computer Science (ICECOCS). pp 1–6
7. Zhou L, Zhang J, She H, Jin H (2019) Quadrotor UAV flight control via a novel saturation integral backstepping controller. *Automatika* 60:193–206
8. Bouabdallah S, Noth A, Siegwart R (2004) PID vs LQ control techniques applied to an indoor micro quadrotor. In: 2004 IEEE/RSJ international conference on intelligent robots and systems (IROS) (IEEE Cat. No.04CH37566), vol 3, pp 2451–2456
9. Hassani H, Mansouri A, Ahaitouf A (2020) Robust autonomous flight for quadrotor UAV based on adaptive nonsingular fast terminal sliding mode control. *Int J Dyn Control*. <https://doi.org/10.1007/s40435-020-00666-3>
10. El Hajjami L, Mellouli EM, Berrada M (2019) Optimal PID control of an autonomous vehicle using Butterfly Optimization Algorithm BOA. In: Proceedings of the 4th international conference on big data and internet of things. pp 1–5
11. Dorigo M (1992) Optimization, learning and natural algorithms. PhD thesis Politec Milano
12. Hassani H, Mansouri A, Ahaitouf A (2019) Control system of a quadrotor UAV with an optimized backstepping controller. In: 2019 international conference on intelligent systems and advanced computing sciences (ISACS), pp 1–7
13. Zheng E-H, Xiong J-J, Luo J-L (2014) Second order sliding mode control for a quadrotor UAV. *ISA Trans* 53:1350–1356

Dynamic Socket Design for Transtibial Prosthesis



Jhon Hernández Martin , Alejandra Santos Borraez ,
Catalina Ríos Bustos , Fran Pérez Ortiz , and Phillip Meziath Castro 

Abstract Within the industry dedicated to build and adapt orthoses and prostheses, there has been a growing number of users or patients who require the use of prosthesis, for the replacement of one or several limbs (either lower or upper); for this reason, the innovation in devices and materials appears as a current need for the benefit of patients. Either for the manufacturing or adaptation of prosthetic components, along the experience, it has been evidenced that, in order to treat an amputee, the selection of the components to be used in the prosthesis is not the only aspect to take into account; consequently, one of the paramount factors is the proper management of adaptation. The component with the highest relevance in the adaptation of a prosthesis is the socket. This device has been specially made in accordance with the anthropometric measures of the patient, and built using rigid, lasting compounds. However, an issue arises regarding the moment when the patient, along adaptation or rehabilitation, changes his/her physical condition or stump. The previous fitting loosens and clearly depends on the suspension system to stay in position; on the other hand, if the patient's body mass increases rather than decreases, the previously manufactured socket will not allow the use of said prosthesis. Because of this, an unexplored research niche has been detected, corresponding to the design and manufacture of **dynamic** sockets, which can adapt to the user, depending on the change in morphology. Another great field of action is the use of dynamic sockets in children.

Keywords Dynamic socket · Transtibial · Stump · FEA · Socket

Within the industry dedicated to building and adapting orthoses and prostheses, the large number of users or patients that require the use of prostheses has been evidenced, either for the replacement of one or more of their extremities (lower or upper), for this reason. Innovation in devices and materials is presented as a current need that leads to the benefit of our patients; whether in the manufacture of prosthetic components or in their adaptation, throughout the experience it has been shown that for the treatment of a patient who has suffered amputation of the limb (s), not only is the selection of

J. H. Martin (✉) · A. S. Borraez · C. R. Bustos · F. P. Ortiz · P. M. Castro
Centro de Diseño y Metrología, Servicio Nacional de Aprendizaje, Bogotá, Colombia
e-mail: jhonmartin56@gmail.com

the components that are going to be implemented in the prosthesis, but one of the determining factors, is the adequate management in terms of their adaptation [1]. The component that is most relevant in fitting a prosthesis is the socket. This device has been performed in a specialized way according to the anthropometric measurements of the patient, in addition to being constructed with rigid and long-lasting compounds [2]; however, a great concern arises and it is at the moment that the patient throughout either his adaptation or his rehabilitation process changes his physical structure, or his stump (end of the body member after being amputated). The socket already made begins to loosen and clearly depend on the suspension system used so that it does not fall [3], on the other hand, if the patient, instead of decreasing his body mass, increases it substantially, since said socket already made will not allow the use of this prosthesis. Due to the above described, we have detected an unexplored research niche, and which corresponds to the design and manufacture of dynamic sockets that can be adapted to the user depending on the morphology change in which it is found [4] Another great field of action is the use of dynamic sockets used in children since the constant change in their morphology makes it impossible to fully adapt the prostheses; their growth process does not allow 100% control.

For the development of our research we will not only innovate in the element to be developed, we will use state-of-the-art equipment to acquire the three-dimensional images of the stump (3D scanner) but in the use of state-of-the-art materials that will allow us to develop high-resistance components with a very low weight [5]. We will use agile and last generation manufacturing methodologies (fourth generation 4.0) since all the analysis and modeling was determined by specialized modeling software. Throughout the research we have obtained tacit results prior to manufacturing which through the finite element analysis (FEA) methods and in whose simulations allowed the adequate selection of materials, in addition to correcting and determining the loads at which the component and the determination of stresses will be submitted, thus achieving that the structure is in equilibrium. Evidencing the previously described we have a part of tranquility and we will continue with the construction, adaptation and subsequent analysis phase in the walking laboratory.

1 Introduction

In the process of amputation of one or both lower limbs, whether transtibial or transfemoral, the implementation of a prosthesis becomes necessary to enable the restoration of the visual appearance of the missing limb(s). This replacement entails not only an aesthetic aspect, but also a functional one, which addresses the possibility of retrieving mobility of oneself; this adjustment seeks movements to be natural and similar to those prior to the amputation by a natural cadence of walking.

In the process of designing and building a prosthesis as a functional element, there are different types of components which conform what may be described as prostheses. These elements, regardless on the type of prosthesis to be built, have something in common, the socket or fitting which hosts the stump, and appears as

the main object of this research. This type of fitting usually functions as a link between the stump and the other components of the prosthesis. The socket is both primordial and critical when performing the fundamental bio-mechanic adjustment required to retrieve the function of walking [6]. Proper adjustment of this element is directly proportional to its functional and aesthetic performance, making the transference of load from the residual limb to the prosthesis to be direct and no force or stability is lost [7]. Analyzing the importance of the socket, it is evident that this component is primordial, fundamentally in the efficiency that influences the rehabilitation process of the patient.

It is important to point out that the socket, by receiving direct load from the body, will inevitably wear out, which may lead to its deformation or break [4]. On the other hand, the adjustment of this component is directly linked to the use of a suspension element, which acts directly in the adjustment of the proposed interphase.

It is well known that inappropriate adjustment can cause direct injuries to soft tissues of the residual limb, which leads to complications, such as degenerative ulcers, tissue injuries, blisters, skin rash and other pathologies [8]; on the other hand, the presence of this type of lesions prevents the patient from regularly using the prosthesis.

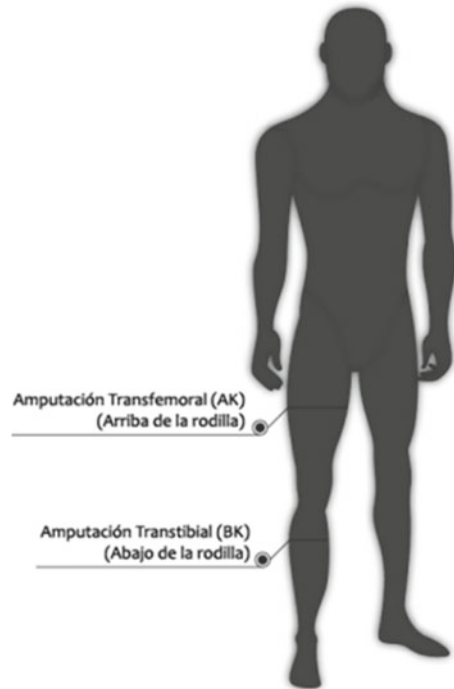
Having said that, the purpose of this research implies creating a device that easily adapts to changes in morphology of the residual limb, and that, attached to a proper suspension element, can directly prevent the appearance of lesions in soft tissues and possible skin irritation which eliminate mobility loss [9]. The proposal focuses on decreasing pressure by using a self-adjustment element, which enables the patient to easily operate and increase or decrease the volume of the socket [10], in such a manner that it can be expanded to release excessive pressure, or closed if the feeling of suspension is lost.

The direct objective of the study is founded on the voluntary elimination of a previously perceptible discomfort, which may include an increase in pressure or a decrease in suspension. The first step in the process of research is to segment and scale the displacements of the socket. Subsequently, it is necessary to narrow down the case study group (gender, age, amputation level, weight) and the specific characteristics of the residual limb of the patient.

Additionally, the analysis of prosthesis alignment will be observed using a dynamic socket, which is able to properly transfer the walking function and ideal plantar support required for comfortable and harmonic movements of the residual limb and the prosthesis, as a whole [11].

It is important to acknowledge that the socket serves a direct relationship in the alignment, as it generates different momentum and plans in the different segments of movement, depending on the instant and the load generated (flexion, extension, abduction or adduction), which exerts different levels of pressure [12]. Lastly, a different focus on the research lies in the use of this type of elements in patients whose change in morphology is rapid and prevents proper adjustment. Later work will consist on the analysis and diagnosis for the use of these components in children, as their physical change is accelerated and therefore, the variation on the residual

Fig. 1 Amputation level for socket



limb is high. The following section presents a detailed description of the procedures proposed for the design of a dynamic socket for transtibial prosthesis (Fig. 1).

In our case, we must implement a device like the one shown below and whose purpose is to be able to make the proper fit between the residual limb and the foot, joint, and ankle assembly (Fig. 2).

2 Methodology

The corpus of this article has as a methodological foundation the experimental applied research, through the design and manufacture of a dynamic socket. To do so, the project was structured in four phases, namely:

- Design parameters: This procedure is founded on the parametrization of the work niche and, consequently, in the appropriate selection of the patient for case study. For this case, a patient was selected that meets the parameters shown in Table 1.
- Reverse engineering: within the structural framework of the research, this process consisted on performing 3D scans of the residual limb of the patient and converting them into CAD format files.

Fig. 2 Transtibial socket



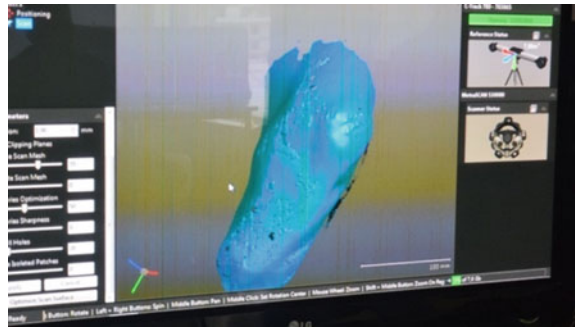
Table 1 Contralateral limb design parameters

Characteristic	Status
Gender	M/F
Age	25–35
Weight in Kilos	≤90
Height in meters	≤1.80
Level of activity	3
Length of the stump	Middle third
State of the stump	Optimal condition
Articulation status – range	Preserved
Maximum socket length	25 cm
Suggested weight of the socket in kilos	≤1.2
Contralateral limb dorsiflexion	Normal 20°
Contralateral limb plantarflexion	Normal 50°

- Design: This section corresponds to the main structure of this article, and it contemplates static, dynamic, load and material analysis for the adjustments and preparation of the prototype.
- Construction: This section corresponds to the actual construction of the element; details of this cycle will be published in a later article.

Initially, the parameters for patient selection were determined, along with the characteristics unique to the contralateral residual limb, in order to continue with the design of the prosthetic component.

Bearing in mind the parameters described, a patient was selected whose morphological and aptitude characteristics match the requirements, along with the fact of having the time and willingness required for the full development of the research.

Fig. 3 Scan of the stump**Fig. 4** Set of data obtained

Subsequently, the 3D scan was performed using MetraScan 3D, which displays a scan speed of 1.800.000 measurements per second, through 15 transversal lasers and 0.025 mm—0.064 volumetric accuracy. It was calibrated to comply with regulation VDI/VDE 2634 of ISO 17025; this element was adjusted to take signals from the residual limb. For the perfect acquisition of the image, it was necessary to apply white powder and keep the limb in inactivity over a prolonged period. Body hair removal was not necessary, as this is done using the software, during the modelling process (Fig. 3).

The process of scanning provided the digital file in *.IGS format, which was then used to proceed directly to the design of the socket (Fig. 4).

3 Modeling

The first step in the modeling consists on converting the image into a full solid, as the image obtained is shown as a “shell”; this procedure is carried out using SolidWorks version 2013, license for the Centro de Diseño y Metrología (Center for Design and Metrology). With this procedure and, making a structural approximation of the

Fig. 5 Internal structure, carbon fiber material



opposite leg, it is possible to determine the total weight of the residual and missing limb.

The structural design of the socket includes a duralumin base, which will host four carbon fiber supports, designed organically with curve lines for full adaptation and homogeneity to the opposite leg of the patient. Additionally, the duralumin base will have a system of pyramidal adapter, which contains the pipe or frame of the prosthesis; likewise, the external supports have a system of adjustment with perforations separated five millimeters from each other, that easily adapt to the physical structure of the stump. The lower part of the socket accommodates a support, specifically designed to absorb impact and direct force applied by the user. This element is composed by a flexible thermoplastic elastomer (TPE), calculated in accordance with the values of weight and force obtained from the CAD simulation (Fig. 5).

It is important to mention that after the design of the rigid structure that supports the entire weight of the patient, the coupling system was designed using external pads to smooth the contact with the stump; these pads have a precision lock with a five-millimeter leave in the upper and mid-section to fully adjust the socket. Additionally, and depending on the analysis obtained from force and material resistance tests, the viability for prototype design and resource will be determined.

4 Results and Discussion

Bearing in mind that the socket adapted to the residual limb must comply with biomechanics criteria of force control by load and unload zones in the anatomic areas of the stump, the adjustment supports must be in accordance with the dimension of the load areas in order to accomplish full control of the forces of rotation, traction, flexion and torsion that act on the socket. The suspension system, which aims at maintaining the stump inside the socket, can be anatomic, meaning that it is held in place by bone structures; or can also be held by passive vacuum, using a valve.

In either case, it is necessary to consider the interphase between the stump and the dynamic socket to accomplish full adherence and that the adjustment supports of the latter become the rigid structure that provides coupling in the regions required (load zones, soft tissue). Adjustment supports must be located at the back of the stump; in the medial section of the tibia; in the interosseous area between the tibia and fibula and in the lower region of the fibula, in order to achieve these supports by controlling mostly movements of rotation. The dynamic socket is a very functional option, as it allows the patient to self-adjust it to personal needs, whether as a first-time user or due to the volume fluctuation suffered during the day (Fig. 6).

The socket, both in design stage and later analysis is founded upon the verification of the mechanism in dynamic and static phases, which ensures that all pieces, whether internal or external, fit properly, without generating conflicts of overlapping or absence of structures for the whole model. Later, it is verified that movements and geometries are those set in the design parameters (total weight, sturdiness, movement and feeling of suspension). Before the simulation, the displacement angles were clearly defined in order to comply with suggested dorsiflexion and plantarflexion. Submission torque was set to 980 N.m. and 490 N per segment (approximate value for 100 kg), positive displacement $+15^\circ$, negative displacement -15° .

- The technical procedure is given as follows:
- Verification of restrictions.
- Verification of fastening and orientation of loads and forces influencing the model.
- Result analysis of joints.
- Force application analysis (both known and unknown).
- Trace analysis for output components.

Fig. 6 Coronal plane, design completed



- Tension analysis.
- Deformation analysis.
- Load transference analysis.

A product of the analysis will be displayed in the three most relevant images. Actual research results (Figs. 7, 8 and 9).

Fig. 7 Stress analysis

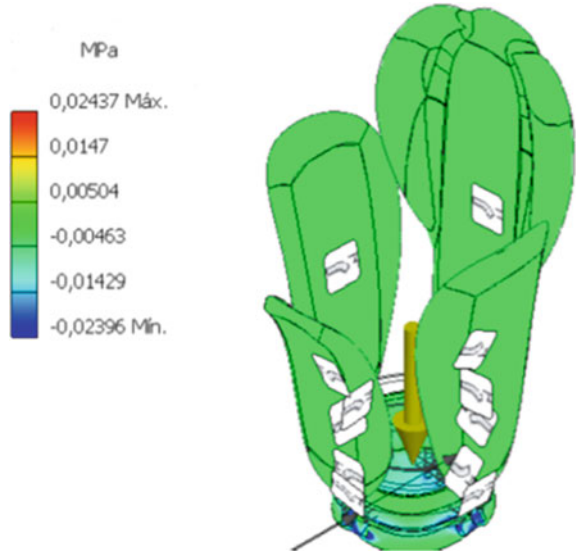


Fig. 8 Displacement analysis

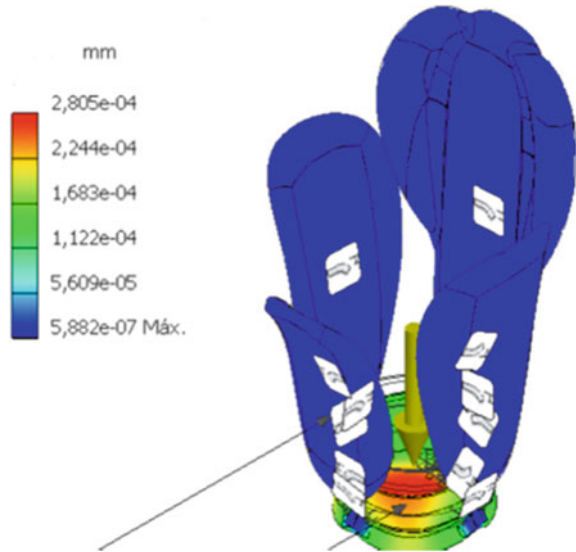
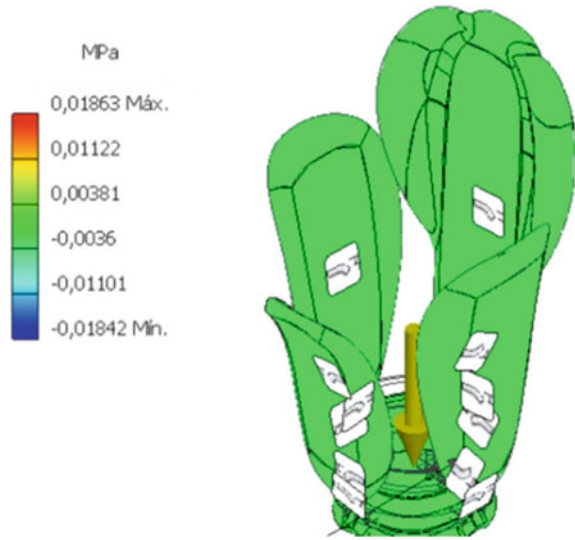


Fig. 9 Y axis, contact pressure analysis



The results of the analysis are quite satisfactory; the element built does not display interference, adjusts to design parameters. Support pads deform, due to the construction material.

5 Conclusions

- For full fastening and adaptation of the device, it is necessary to implement two adjustment systems, one at the medial section of the component and one on the condylar line for the case of transtibial amputation.
- Analyzing the results proposed, and for full development and implementation of this component, it is suggested to use an anatomic, pin suspension system and a Linner.
- For full adaptation of the component over time it is suggested to carry out a periodical alienation review, at least six months apart, as the manipulation by the user can compromise full use of the component.
- The analyzes obtained from the finite element analysis, and the suspension tests carried out previously, show a correct adaptation to the patient's stump, and the proposed suspension system will allow a solid and robust fit that allows its use.

References

1. Arnold AJ, Haworth JL, Moran VO, Abulhasan A, Steinbuch N, Kokkoni E (2020) Exploring the unmet need for technology to promote motor ability in children younger than 5 years of age: a systematic review. *Arch Rehabil Res Clin Transl* 2(2):100051
2. Swanson EC, McLean JB, Allyn KJ, Redd CB, Sanders JE (2018) Instrumented socket inserts for sensing interaction at the limb-socket interface. *Med Eng Phys* 51:111–118
3. Moradi V, Sanjari MA, Saeedi H, Hajiaghaei B (2020) Experimental study of prosthesis modifications based on passive dynamic walking model: A limit cycle stability analysis. *J Biomech* 104:109743
4. McLean JB et al (2019) Socket size adjustments in people with transtibial amputation: effects on residual limb fluid volume and limb-socket distance. *Clin Biomech* 63(September 2018):161–171
5. Waterval NFJ, Brehm, Ploeger HE, Nollet F, Harlaar J (2018) Compensations in lower limb joint work during walking in response to unilateral calf muscle weakness. *Gait Posture* 66(October 2017):38–44
6. Wolf SI, Alimusaj M, Fradet L, Siegel J, Braatz F (2009) Pressure characteristics at the stump/socket interface in transtibial amputees using an adaptive prosthetic foot. *Clin Biomech* 24(10):860–865
7. Dou P, Jia X, Suo S, Wang R, Zhang M (2006) Pressure distribution at the stump/socket interface in transtibial amputees during walking on stairs, slope and non-flat road. *Clin Biomech* 21(10):1067–1073
8. Boone DA et al (2013) Influence of malalignment on socket reaction moments during gait in amputees with transtibial prostheses. *Gait Posture* 37(4):620–626
9. Lenz AL, Bush TR (2019) Evaluating shear and normal force with the use of an instrumented transtibial socket: A case study. *Med Eng Phys* 71:102–107
10. Meng Z, Wong DWC, Zhang M, Leung AKL (2020) Analysis of compression/release stabilized transfemoral prosthetic socket by finite element modelling method. *Med Eng Phys* xxxx
11. Gholizadeh H, Osman NAA, Kamyab M, Eshraghi A, Abas WABW, Azam MN (2012) Transtibial prosthetic socket pistoning: Static evaluation of Seal-In ® X5 and Dermo® Liner using motion analysis system. *Clin Biomech* 27(1):34–39
12. Kobayashi T, Orendurff MS, Zhang M, Boone DA (2013) Effect of alignment changes on sagittal and coronal socket reaction moment interactions in transtibial prostheses. *J Biomech* 46(7):1343–1350

Networking

Towards an Enhanced Minimum Rank Hysteresis Objective Function for RPL IoT Routing Protocol



Abdelhadi Eloudhriri Hassani, Aïcha Sahel, and Abdelmajid Badri

Abstract RPL is designed as a routing protocol dedicated to Internet of Things. RPL is based on an objective function to build a Destination Oriented Directed Acyclic Graph that connects the leaf nodes in the wireless sensor network to the central node which collects all the informations. In its path selection, RPL does not offer the best network quality of service due to the unoptimized standard metrics. In this paper, we propose an improvement of Minimum Rank Hysteresis Objective function called E-MRHOF based on a new method of calculating the link metric. The simulations show that E-MRHOF can increase the number of packets delivered to the sink with low latency and power consumption, while offering a network convergence time and ICMPv6 packets inferior than the classical MRHOF based on ETX and Energy.

Keywords RPL · IoT · Objective function · MRHOF · ContikiOS · COOJA

1 Introduction

As an integration part of the physical world in Internet [1], the IoT has proven itself to be a revolutionary technology in medical [2], industrial and urban fields. Objects connected to internet have constraint resources, which is why their use in a network must be different. In this context and in order to remedy these constraint problems, several routing protocols dedicated to the Internet of Things have been standardized. Among these protocols, IPv6 protocol for low power and lossy networks called RPL was proposed by IETF working group [3]. The strength of this protocol is derived from its ability to build a network topology without pre-requisite infrastructure and react to any changes that may occur in the network [4]. RPL builds a DODAG based on an objective function which specifies the metric on which it refers for its selection of parents, thus creating closed paths oriented towards a collector node [5]. The IETF-ROLL group defined two objective functions MRHOF [6] and OF0 [7]. In this paper, we propose an improvement of minimum rank hysteresis objective function based on

A. E. Hassani (✉) · A. Sahel · A. Badri
LEEA & TI, FSTM, Hassan II University of Casablanca, Casablanca, Morocco
e-mail: eloudhriri.abdelhadi@gmail.com

© Springer Nature Singapore Pte Ltd. 2022
S. Bennani et al. (eds.), *WITS 2020*, Lecture Notes in Electrical Engineering 745,
https://doi.org/10.1007/978-981-33-6893-4_45

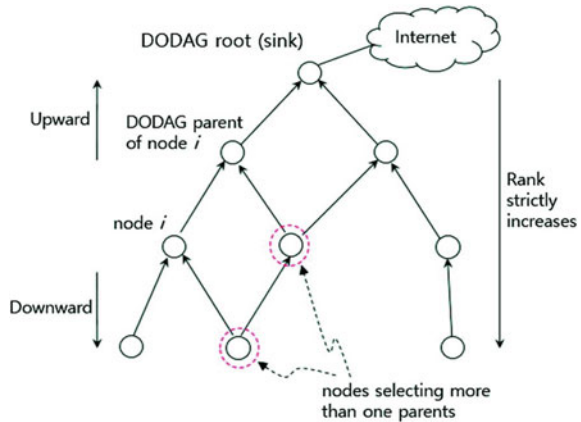
483

the average value of the link quality as a routing metric which makes possible to meet the requirements of reliability, lower power consumption, latency, convergence time too and decrease the traffic overhead packets. The rest of this paper is organized as follow. In Sect. 2 we give a brief overview of the routing protocol for low power and lossy networks RPL. In Sect. 3 we present the related works. In Sect. 4 we present the contribution and our proposal to improve the MRHOF objective function. In Sect. 5, we explain the simulation design of network and results obtained, finally a conclusion and our perspectives are given in Sect. 6.

2 RPL Overview

RPL is a routing protocol designed for IoT concept [8], to operate with up layers intended for Ipv6 and low-rate communications protocols like IEEE 802.15.4, Bluetooth low energy [9].RPL operates in Low power and Lossy Networks (LLN's), characterized by resource constraints in terms of energy, memory and processing [10], which makes routing very rigid, so RPL must cope with packet loss and energy limitation. To deal with the unpredefined topology in LLN networks and avoid cycle loop on routing [11], RPL aim to organize nodes as a Destination oriented directed acyclic graph to sink node as shown in Fig. 1, using control messages called Internet Control Messages Version 6 (ICMPv6). Four types of control messages are used: DODAG Information Object (DIO), DOGAG Information Solicitation (DIS), Destination Advertisement Object (DAO) and Destination Advertisement Object Acknowledgement (DAO-ACK). Each DODAG is related to an instance optimized by an associated objective function that makes possible to choose the best routing path based on several constraints and restrictions [12]. Its purpose is to minimize the cost of the routing path based on criteria relating to the node or the quality of links. In addition, two objective functions have been defined in the RPL specifica-

Fig. 1 Destination Oriented Directed Acyclic graph rooted to sink



tions by IETF group MRHOF and OF0 [13]. Furthermore, the construction of the DODAG whatever the metric chosen is done in two phases. The first one is to create the upward routes that initiated by the sink node which sends DIO messages to its neighbors carrying many important parameters such as rank, metric, DODAGID, and routing cost...[11]. Each node probably receives more than one DIO message from neighbor, and then makes the decision of joining the Directed Acyclic Graph (DAG) following an objective function [14]. Once a node makes a choice to join a specific DAG, it has automatically a route to the root via its parent. Then, the node processes its rank to know its position in the DODAG and multicast a new DIO message. All the nodes will repeat this process and select their parents, and join DAGs using DIO messages until the leaf nodes receipt the DIO messages, join the DAG and do not multicast DIO message. The second phase consist on creation of downward routes, a node must send a Destination Advertisement Object (DAO) to its parent containing prefix information of the nodes in its sub-DODAG, when the DAO message arrives to the root, the prefixes are aggregated and the downward routes are then built and made available to the parents, and so on [13].

Finally, to deal with new network joins, nodes send a DIS message as a request to send DIO message by the root without having to wait for the next update of the network initiated by the trickle algorithm [15]. In this context, the trickle algorithm Maintain routing stability by defining the interval time between sending DIO messages periodically in the DODAG to update the routes in the network. The flowchart presented in Fig. 2 summarizes the process of DODAG building.

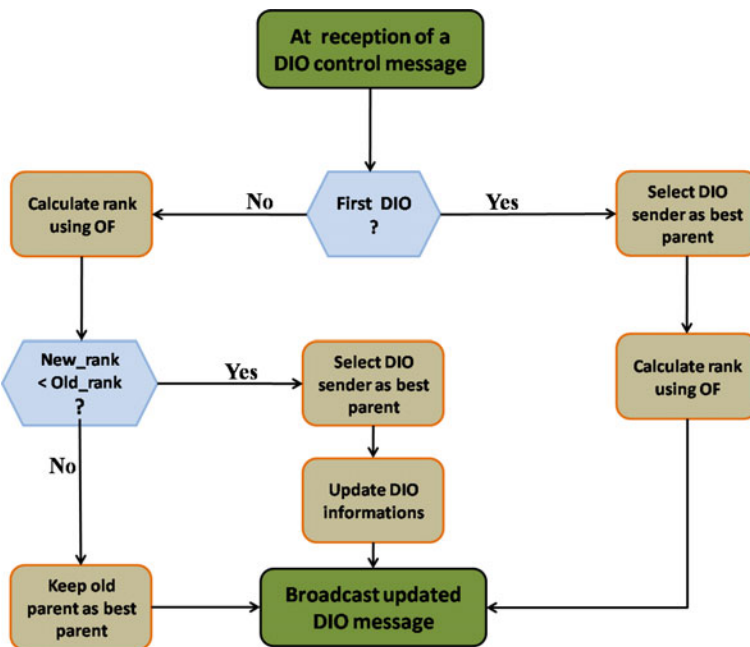


Fig. 2 Flowchart of DODAG building process

3 Related Works

Several researches are active about RPL in order to provide needed of different applications. In [16], the authors have investigated on performance of OF0 and MRHOF as objective functions especially in mobile environment in term of Hop count, packet lost, energy and control overhead. Results showed that objective function based on hop count perform better than MRHOF regardless of topology with mobile nodes. In this context, the authors in [17] present an assessment of the routing protocol in static environment taking into consideration as a metric performance the reliability, power consumption of the network, end to end delay and the radio activity. Results showed that the choice of an objective function depending on the application. Otherwise, multiple methods of enhancing RPL are proposed as in [?], where the residual energy in node battery is considered as a single metric to select the best parent, what lead to increase the network lifetime despite of a lower delivery ratio. Also, MAC based metrics were proposed in [18] to deal with traffic load balancing considering the reliability and power consumption. In [19], in order to remediate to the problems of unbalanced energy, bad data reliability and short network life time in advanced metering infrastructure (AMI) for smart grids, the authors proposed ETEN-RPL routing algorithm based on combination of ETX and remaining energy of nodes as a base selection for preferred parent. The new objective function reduces significantly the power consumption and improves the network stability. Also in [20], the congestion in paths issue is discussed due to the buffer nodes occupancy. So that, Congestion-Aware Objective Function (CAOF) were be proposed that consider ETX metric in low data rate while the buffer occupancy is considered at high data rate what leads to select a less congested paths. Other approaches are considered based on fuzzy logic as in [21] combining Hop count, energy consumption and ETX as inputs of the new objective function, what lead to an improvement of convergence time, latency, packet delivery ratio and network power consumption compared to MRHOF.

4 Proposed Work and Contribution

Most of researches are focus on improving the reliability of routing with RPL and energy consumption while being based on the combination of several metrics [22] and different approaches. The aim of our proposal work is to deal with the general quality of services that RPL can provide based on an extended single metric. The link quality metric ETX is proposed originally to choose parents with minimum of expected transmission count. Because of that, the path selection mechanism is more based on link quality than other parameters as number of nodes involved in relaying packets to the sink. In that purpose, the enhanced objective function E-MRHOF based on single metric that is average summation of ETX metric is proposed. Thus, in the structure of DIO control message, we have divided the metric container to newETX metric container and an other one for number of nodes involved on the path. After

that, we changed the process of calculating the rank in the DODAG in such a way that on reception of DIO message from a neighbor it will measure the ETX with the sender, add it the ETX forwarded in the sender DIO message, increment the path involved nodes then calculate an intermediate parameter following (1)

$$\text{IntermediateParameter} = \frac{ETX_{\text{measured}} + ETX_{\text{forwarded}}}{\text{number of involved nodes}} \quad (1)$$

where newETX is the summation of ETX_{measured} and $ETX_{\text{forwarded}}$.

Based on this Intermediate Parameter, the node select the best parent among its candidate parents with the lesser value, update the metrics container and multicast the updated DIO message. The pseudo-Algorithm 1 describe the metric processing for E-MRHOF.

Algorithm 1 Metric processing with E-MRHOF

Require: DIO message from candidate parent cp

begin:

```

1: if (cp != NULL) then
2:   number_nodes = cp.dio.nbr + 1;
3:   ETX_measured = ETX_callback();
4:   ETX_forwarded = cp.dio.newetx;
5:   IntermediateParameter = ( ETX_measured + ETX_forwarded)/ number_nodes;
6:   if (IntermediateParameter < BestParent.Inter) then
7:     Bestparent = cp;
8:     BestParent.Inter = IntermediateParameter;
9:   end if
10:  dio.nbr = number_nodes;
11:  dio.newetx = BestParent.Inter;
    Multicast updated DIO message
12: end if

end;

```

5 Performance Evaluation

In order to evaluate the performance of proposed objective functions, the simulations are done with COOJA, a wireless network sensor simulator that provide a cross approach emulation of the hardware platforms and programming the software level through applications provided by the contiki operating system API. Although, in order to experiment our proposed method, we use tree kind of density 30, 50 and 70 nodes randomly distributed on an area with 200 meters each side. The type of

Table 1 Simulation parameters

Operating system	Contiki 2.7
Hardware platform	Sky mote
Transmission/Interference ranges	70/100 m
Propagation model	UDGM-Distance loss
Number of nodes	30, 50, 70
Network protocol	RPL
Squared area	200 × 200 m
Inter-packets time	60 s

data traffic is multipoint to point (MPTP) where the nodes sent the captured data to the sink with a rate of 1 packet per minute. We set the transmitting range to 70 m, the interference range to 100 m and fix the reception success ratio to 100%. The proposed metric is injected into an objective function that has the same principle of hysteresis as MRHOF called E-MRHOF. The new objective function is compared with the classic MRHOF-ETX and MRHOF-ENERGY. The performance evaluation is done in term of several parameters as packet delivery ratio, energy consumption, convergence time of the network, latency and number of control packets. Table 1 summarizes the simulation parameters.

5.1 Evaluation of Packet Delivery Ratio

Packet Delivery Ratio (PDR) is defined as the quotient of the packets sent by all the nodes of the network during the period simulated by the number of packets received at the sink node [7].

As shown in Figure 3, when the density is light (20 nodes) the tree objective functions have the same performances, but in density is higher (50, 70 nodes) the E-MRHOF proven it ability to deliver more packets to the sink.

5.2 Evaluation of Nodes Energy Consumption

Nodes energy consumption (NEC) is defined as the summation of power used by each node. There are four kinds in measurement of power. LPM indicate the radio power consumption during sleep condition. CPU is a parameter that indicates monitore the level of node processing. RL and RT are parameters related with node communications. The formula used to calculate the energy of nodes according to the following equation.

Fig. 3 PDR vs number nodes in Random topology

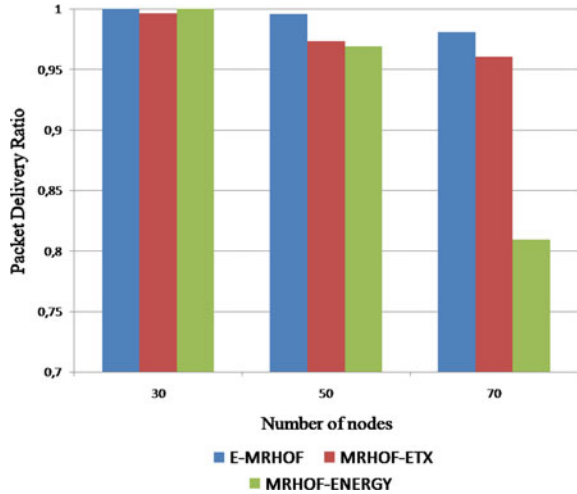
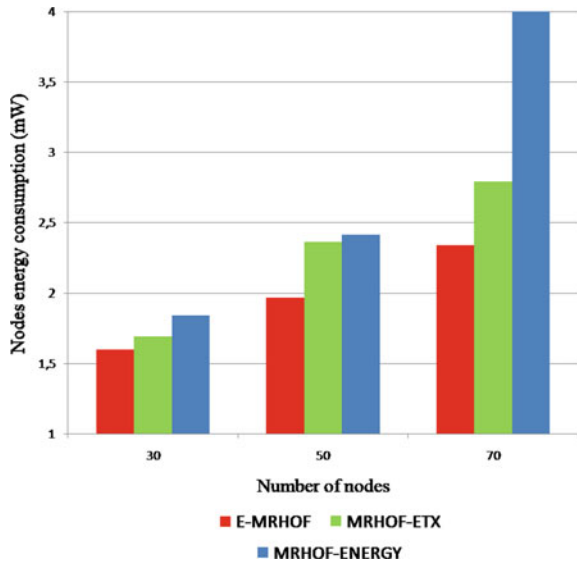


Fig. 4 Nodes energy consumption versus number nodes in Random topology



$$Energy(mJ) = (RT * 19.5 \text{ mA} + RL * 21.5 \text{ mA} + CPU * 1.8 \text{ mA} + LPM * 0.0545 \text{ mA}) * 3 \text{ V} / (32768) \tag{2}$$

To investigate on energy part, we measured the average of nodes power consumption. Figure 4 exposes the results during the simulations. Results show that the novel objective function can decrease the power consumption especially when the density is around 70 nodes, and this comes back to the fact that our routing proposal limits the overload packets and takes into account the number of nodes in the path selection which leads to less radio retransmissions.

5.3 Evaluation of Latency and Convergence Time

Latency is defined as the average period it takes for packets to be delivered by network nodes to the sink. As we can see in Fig. 5, our proposal can perform better than the two other objective function whatever the density which lead to a good delivery packets rate in less time. Otherwise, the convergence time represents the time required for all the nodes to join the network and have paths intended to sink node. Samely as the latency, the results in Fig. 6 showed that the convergence time decreased with E-MRHOF as an objective function due to the different path selection mechanism.

Fig. 5 Latency versus number nodes in Random topology

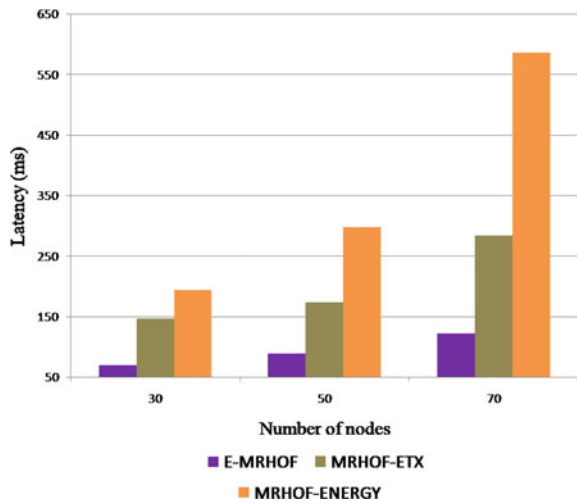


Fig. 6 Convergence time versus number nodes in Random topology

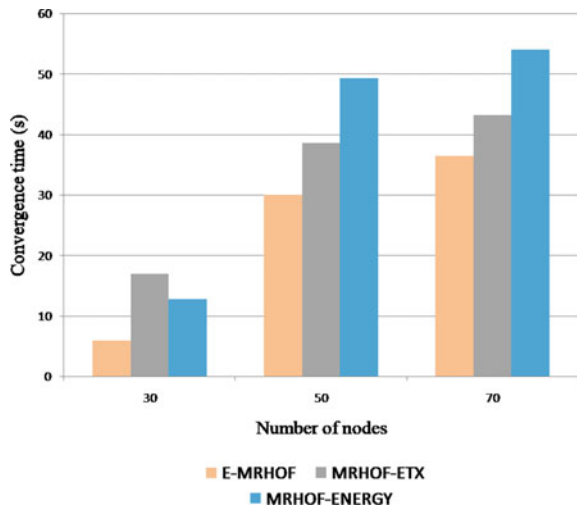
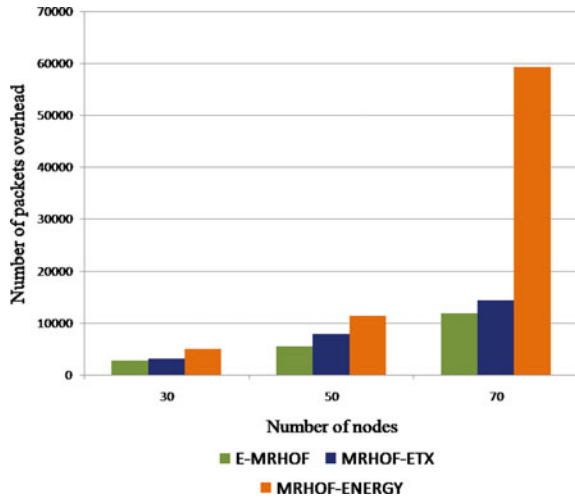


Fig. 7 Packets overhead versus number nodes in Random topology



5.4 Evaluation of Packets Overhead

The packets overhead represents the summation of ICMPv6 respectively DIO, DAO and DIS packets [23]. From Fig. 7, we showed that our objective function considerably decrease the number of control traffic overhead compared to other objective functions with lower convergence time and energy consumption.

6 Conclusion

In this paper, an enhanced objective function for minimum rank hysteresis is proposed. This new objective function is based on average link quality metric ETX in order to select the routing path to the root. Our proposal has improved the number of packets successfully routed to the sink node, reduced the number of overhead packets with a lower convergence time and also reduced the energy consumption of the nodes in the low power and lossy networks compared to the two other functions based on hysteresis namely MRHOF-ETX and MRHOF-Energy. As a future work, we will be invest on improving more the RPL routing protocol based on combination of more than one metric.

References

1. Lamaazi H, Benamar N, Jara AJ, Ladid L, El Ouadghiri D (2014) Challenges of the internet of things: IPv6 and network management. In: Proceedings—2014 8th international conference on innovative mobile and internet services in ubiquitous computing IMIS 2014, pp 328–333
2. Hssina B, Bouikhalene B, Merbouha A (2017) Europe and MENA cooperation advances in information and communication technologies, vol 520, pp 103–112
3. Oliveira LML, Rodrigues JJPC, de Sousa AF, Lloret J (2013) A network access control framework for 6LoWPAN networks. *Sensors (Switzerland)* 13:1210–1230
4. Hendrawan INR, Arsa IGNW (2017) Zolertia Z1 energy usage simulation with Cooja simulator. In: Proceedings of 1st inter conference of informatics computer science ICICoS, p 2017
5. Oliveira A, Vazão T (2016) Low-power and lossy networks under mobility: a survey. *Comput Netw* 107:339–352
6. Gnawali O, Levis P (2012) RFC 6719—The minimum rank with hysteresis objective function
7. Pradeska N, Widyanan NW, Kusumawardani SS (2017) Performance analysis of objective function MRHOF and OF0 in routing protocol RPL IPV6 over low power wireless personal area networks (6LoWPAN). In: Proceedings of 2016 8th international conference on information technology and electrical Engineering: empowering technology for better future. ICITEE 2016, pp 0–5
8. Atzori L, Iera A, Morabito G (2010) The Internet of Things: a survey. *Comput Netw* 54:2787–2805
9. Gaddour O, Koubâa A (2012) RPL in a nutshell: a survey. *Comput Netw* 56:3163–3178
10. Lim C (2019) A survey on congestion control for RPL-based wireless sensor networks. *Sensors (Switzerland)* 19
11. Kharrufa H, Al-Kashoash H, Al-Nidawi Y, Mosquera MQ, Kemp AH (2017) Dynamic RPL for multi-hop routing in IoT applications. In: 2017 13th Annual conference on wireless on-demand network systems and services WONS 2017—Proceedings, pp 100–103
12. Nassar J, Berthomé M, Dubrulle J, Gouvy N, Mitton N, Quoitin B (2018) Multiple instances QoS routing in RPL: application to smart grids. *Sensors (Switzerland)* 18:1–16
13. Khallef W, Molnar M, Benslimane A, Durand S (2017) Multiple constrained QoS routing with RPL. In: IEEE international conference communication
14. Mishra S, Singh P, Arora D, Agrawal KK (2018) Analyzing and evaluating the performance of 6LoWPAN and RPL using CONTIKI. Proceedings of international conference on intelligent sustainable systems ICISS 2017, pp 1100–1105
15. Sanmartin P, Rojas A, Fernandez L, Avila K, Jabba D, Valle S (2018) Sigma routing metric for RPL protocol. *Sensors (Switzerland)* 18
16. Lamaazi H, Benamar N, Jara AJ (2017) Study of the impact of designed objective function on the RPL-Based routing protocol. In: Advances in ubiquitous networking 2, Lecture notes in electrical engineering, vol 397
17. Elouadrhiri hassani A, Sahel A, Badri A (2019) Assessment of a proactive routing protocol RPL in Ipv6 based wireless sensor networks. In: 3th International conference on intelligence computing in data science
18. Di Marco P, Fischione C, Athanasiou G, Mekikis PV (2013) MAC-aware routing metrics for low power and lossy networks. In: 2013 IEEE conference working on computing and communication. INFOCOM WKSHPs 2013, pp 79–80
19. Gao L, Zheng Z, Huo M (2019) Improvement of RPL protocol algorithm for smart grid. In: International conference on communication technology. Proceedings, ICCT, Oct 2019, pp 927–930
20. Al-Kashoash HAA, Al-Nidawi Y, Kemp AH (2016) Congestion-aware RPL for 6LoWPAN networks. In: Wireless telecommunication symposium, May 2016
21. Lamaazi H, Benamar N (2018) OF-EC: a novel energy consumption aware objective function for RPL based on fuzzy logic. *J Netw Comput Appl* 117:42–58

22. Eloudrhiri Hassani A, Sahel A, Badri A (2020) A new objective function based on additive combination of node and link metrics as a mechanism path selection for RPL protocol. *Int J Commun Netw Inf Secur (IJCNIS)* 12:63–69
23. Kechiche I, Bousnina I, Samet A (2019) A novel opportunistic Fuzzy logic based objective function for the routing protocol for low-power and lossy networks. In: 2019 15th International wireless Communication and mobile computing conference, pp 698–703

A Lightweight Hash Function for Cryptographic and Pseudo-Cryptographic Applications



Imad El Hanouti , Hakim El Fadili, Said Hraoui, and Abdellatif Jarjar

Abstract In this paper, we design a lightweight hash function suitable for fast applications. The proposed hash function is intended to be used as a secondary component in cryptographic and pseudo-cryptographic applications (e.g., pseudorandom number generators, cryptosystems), where the required property is the fastness in addition to an acceptable security level. Based on simple logical operations used in designing primitive functions, and based on a Feistel-like network, the proposed hash function exhibits excellent performance (fastness) and good enough security properties.

Keywords Hash function · Chaotic map · Feistel network · Merkle-Damgård construction

1 Introduction

A hash function is a one-way function that takes an arbitrary input-data and produces a fixed-length hash value or *digest*. Hash functions are indispensable components in many cryptographic and pseudo-cryptographic applications (cryptosystems, pseudorandom number generators, key-generation algorithms, etc. ...) [1]. For many applications, fast processing is a mandatory requirement (e.g., real-time applications). In this case, a large variety of well-known hash functions may not be suitable for them because of their added extra load [2]. In other applications, the required property is the fastness rather than a high cryptographic level; for example, the application needs only to calculate digests with some threshold cryptographic level and in a fast fashion.

I. El Hanouti (✉) · H. El Fadili
LIPI Laboratory, Sidi Mohamed Ben Abdellah University, Fez, Morocco
e-mail: imad.elhanouti@usmba.ac.ma

S. Hraoui
LIASSE, ENSA, Sidi Mohamed Ben Abdellah University, Fez, Morocco

A. Jarjar
Moulay Rachid High School, Taza, Morocco

Motivated by this, we will propose in this paper, a fast and secure enough hash function based on simple logical operations and a Feistel-like network as main internal components in its compression function. We will adopt the Merkle-Damgård construction for digest generation, and we will introduce a new method for block padding based on the skew tent map.

The rest of this paper is organized as follows: in Sect. 2, we introduce the skew tent map and some of its properties. In Sect. 3, we describe our hash function in details. Section 4 outlines some security metrics and the fastness of our proposed hash function over some well-known hash functions. Section 5 concludes the paper.

2 The Skew Tent Map

The skew tent map [3] is a chaotic one-dimensional map (a discrete mapping) widely used in computer science applications.

Definition 1 A one-dimensional discrete dynamical system (or map) is defined by the function f that updates the state $x \in I$, (where $I \subset \mathbb{R}$ is the state space), under the control parameter $p \in M$, (where $M \subset \mathbb{R}$ is the set of parameters), according to the following rule:

$$\begin{aligned} f &: I \times M \rightarrow I \\ (x, p) &\mapsto f(x, p) \end{aligned} \quad (1)$$

For the skew tent map, the next state is determined by the previous one according to the following rule:

$$x_{n+1} = f(x_n, p) = \begin{cases} \frac{x_n}{p}, & 0 \leq x_n \leq p \\ \frac{1-x_n}{1-p}, & p < x_n \leq 1 \end{cases} \quad n \in \mathbb{N} \quad (2)$$

where $I = [0, 1]$ and $M = (0, 1)$. The skew tent map is chaotic on the entire range M of parameter.

The bifurcation diagram shows the behavior of the dynamical system according to its control parameter. Figure 1a shows the bifurcation diagram of the skew tent map. And we see that the map is chaotic on the entire interval of the parameter p .

The LE (Lyapunov exponent) is an indicator of the sensitivity to initial conditions, which is the main characteristic that leads to chaos. Figure 1b shows the LE diagram of the skew tent map. We see that the LE value is always positive, which reflects the chaotic behavior of the map, especially around the $p = 0.5$ value.

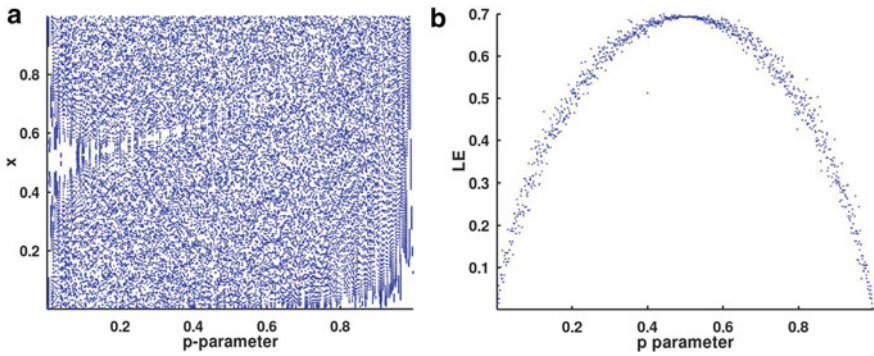


Fig. 1 The skew tent's map **a** bifurcation diagram, **b** Lyapunov exponent

3 The Proposed Hash Function

Our proposed hash function is based on *qwords* (64 bit) operations and a Feistel-like network for its compression function F with Merkle-Damgård construction. Figure 2 shows the general structure of Merkle-Damgård construction. Our proposed compression function takes a 1024-bit input to produce a 128-bit intermediate hash digest.

The main characteristic of this proposed function resides in its efficiency (fastness) and lightness, so it can be used in many fast cryptographic applications as a secondary component to enhance the security of some operations (e.g., pseudorandom number generation process, encryption process). We describe the detailed process of our hash function in the next four steps:

1. **Padding and preprocessing:** if the input message is not divisible into fixed 1024-bit blocks, then a padding process must be carried on the last block in

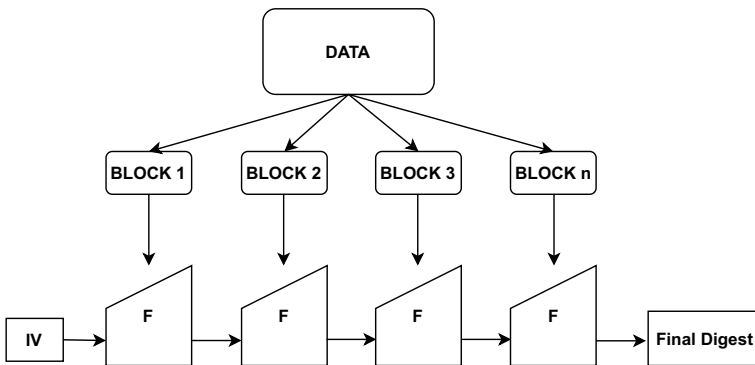


Fig. 2 Merkle-Damgård hash construction showing the diffusion property of the scheme involving both inputs and outputs of the compression function F

order to pad it to a full 1024-bit block. The padding is done by adding extra bytes extracted from the skew tent map until the desired size is reached. First, the length of the original data is calculated in bits and represented as a 64-bit number. Next, the first 52 LSB bits are XORed (with a bitwise XOR operation) with the float-value corresponding to $x_0 = 3F80000000000000$ in the hexadecimal IEEE754 double-precision format representation; this operation is used to perturb the initial value $x_0 = 0.0078125$ (chosen arbitrarily in our scheme) and make an updated initial value that depends on the size of the original data (note that all decimal point numbers in this paper are represented using the IEEE754 double-precision representation). Similarly, the remained last 12 MSB bits are XORed with the value $p_0 = 3FF8100000000000 = 1.50390625$, and the corresponding fractional part (in decimal notation) is conserved as the new parameter-value for the skew tent map. This operation perturbs the initial parameter-value at near of 0.5, which guarantees (according to the LE shown in Fig. 1b), a fast divergence between two trajectories generated from approximate initial values, and thus, an extreme chaotic properties. These operations make the generated sequence, of the skew tent map, highly dependent and sensitive to the size of the original data, which enhances the security of our hash function. Lastly, every generated state (64 bit in the IEEE754 Format) using the skew tent map is translated to 8 bytes of data, and only the four least significant bytes will be padded to the original data. We keep generating chaotic bytes until the full padding of the desired block. The overall padding process is illustrated in Fig. 3.

2. **Initialization vector:** a 128-bit buffer is used to hold intermediate, and eventually, the final hash digest. This buffer is composed of two concatenated *qwords* called *R* and *L* that are defined initially as two hexadecimal *qwords*: $L = 1707E3EF1700ADCD$ and $R = FA713A153E107EBC$.

We define a constant lookup table *I* with 64 elements, each in the range $\{1..16\}$ as depicted in Table 1. This lookup table will be used in the next processing step. The hash function is intended to be used in applications that may hash several components of data, so it can take the previous segment of plain data and construct from it a key, this key is not a cryptographic key in strict sense but it is used to enhance the diffusion property of the hash function when dealing with large input-data. So that it can be made public in many applications, but to enhance the security, we recommend making the key-elements dependent on several components of the application (e.g., the previously calculated blocks, iterations of some chaotic maps, randomly generated sequence). The key $K = \{K(i)\}_{i=1}^{64}$ is a 64-elements, each in the range $\{0..7\}$ (thus, the key space is 192-bit length), this key is used for determining the bit-shift amount in the *Feistel* function as we will see in the next step. If there are no previous data, the key could be generated from a chaotic map with secret initial conditions in the same fashion as done in the padding process, and in this case, our hash function will be extended to be a keyed hash function if the key is intended to be transmitted secretly to the receiver. In the next step, we will show how the key is get involved in our *Feistel* functions' implementation.

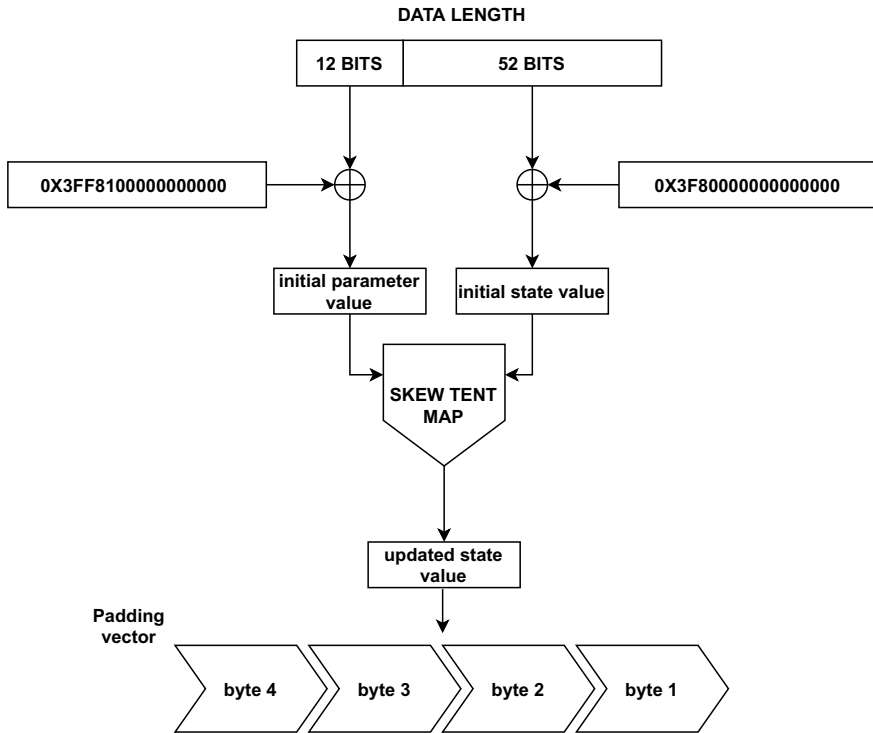


Fig. 3 General flowchart of our proposed padding process using high sensibility between data length and the padded stream

Table 1 The index lookup table *I*

1	2	3	4	5	6	7	8	9	10	11	12	13	14	15	16
4	15	14	2	6	13	7	1	5	9	12	3	16	8	10	11
6	7	11	9	14	5	10	13	16	15	2	12	1	3	4	8
16	15	14	13	12	11	10	9	8	7	6	5	4	3	2	1

- Processing:** for each data block (a 1024 bits), we divide it to 16 *qwords*, labeled as $w(i) \ i = 1, 2, \dots, 16$. And then, we iterate the following process for 64 rounds: For each round $r = 1, 2, \dots, 64$, we calculate an intermediate *qword* value T according to the primitive logical functions defined in Table 2, where $\&$ denotes bitwise AND operator, $|$ denotes bitwise OR operator, \oplus denotes bitwise XOR operator, and the $\bar{}$ symbol denotes the logical NOT operator. Then, after each round r , the 128-bit buffer (composed of L and R) is updated according to the following function:

Table 2 Primitive logical functions used in the calculation of intermediate value

From round 1..16	$T = L R$
From round 17..32	$T = L\&R$
From round 33..48	$T = L \oplus R$
From round 49..64	$T = (\bar{L} R) \oplus (\bar{R}\&L)$

$$\begin{cases} R = L \\ L = (L \ggg 7) \oplus ((R \oplus (T \oplus w(g))) \lll K(r)) \end{cases} \quad (3)$$

where \lll denotes the left bit-shift operation and \ggg denotes the right bit-shift operation and g is defined as $g = I(r)$ where $I(r)$ is the r -th element from the index table defined in Table 1 in the raster order from top-left to bottom-right. $K(r)$ is the r -th key element.

The general design of our compression function is shown in Fig. 4. We keep repeating this process for all data blocks until the processing of all blocks, where each output buffer (L and R) is the next input one, following the Merkle-Damgård construction as shown schematically in Fig. 2.

- Output:** The last 128-bit buffer value (R and L concatenated in this order) following from the last data-block processing is the final 128-bit message digest.

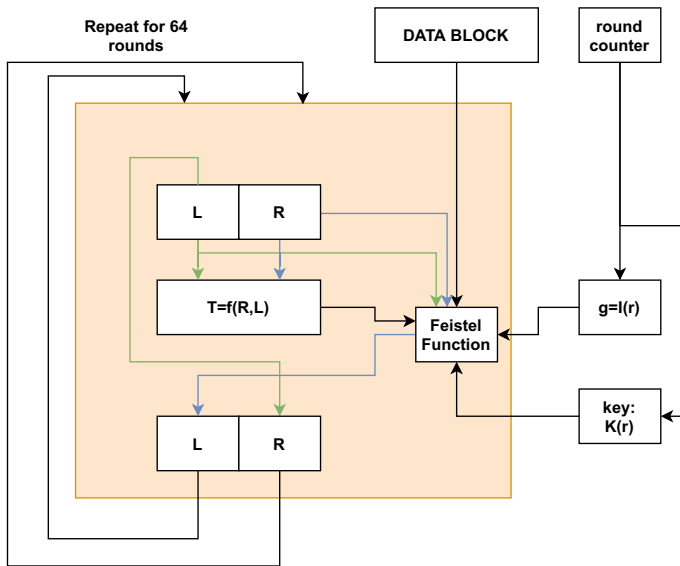


Fig. 4 General flowchart of the compression function F of our proposed hash function

Table 3 Message digests corresponding to the four different scenarios

Message	Digest
Scenario 1	024220F55FE4BB0F30C3AA87AD742EBE
Scenario 2	9F50FDA4703388AD92277545B786FB39
Scenario 3	AC30E28D9C0A89138622E59CB52DF7CA
Scenario 4	4D08A607597E2533449D4A8F403F7A3A

4 Performance Analysis

In this section, we perform some tests to evaluate our proposed hash function's results and security. Although it is not a cryptographic hash function in strict sense, we perform some cryptographic tests such as the diffusion test to evaluate its robustness. To test our hash function, we generate the key elements $K(i), i = 1, 2, \dots, 64$ from the skew tent map with arbitrary initial conditions, and we restrict values to be in the range $\{0..7\}$ by doing a binary operation (i.e., the AND operation).

4.1 Hash Results of a Slightly Changed Messages

We perform a hash simulation of different messages that are slightly changed (only one-bit change in each case), and we compare their hash values. For this purpose, we pick a random 127 bytes of data generated from the skew tent map using the initial conditions $(x, p) = (0.2345, 0.5555)$.

- The first scenario: we do not change anything in the data generated, and we calculate its hash value.
- The second scenario: we toggle the first bit of the data, and then we calculate its hash value.
- The third scenario: we toggle the last bit of data, and we calculate its hash value.
- The fourth scenario: we append one random byte to the data, and we calculate its hash value.

Table 3 shows the hash result corresponding to each scenario. Figure 5 shows the graphical plot of the digests binary-sequence corresponding to each scenario (in the order, from top to bottom). We clearly see that even a simple change in the input data leads to random changes in the hash value.

4.2 Statistical Analysis of the Diffusion Property

The diffusion concept is introduced by Shannon in [4]. Diffusion is the cryptosystem's capability to hide statistical properties of the plaintext by diffusing the effect of any

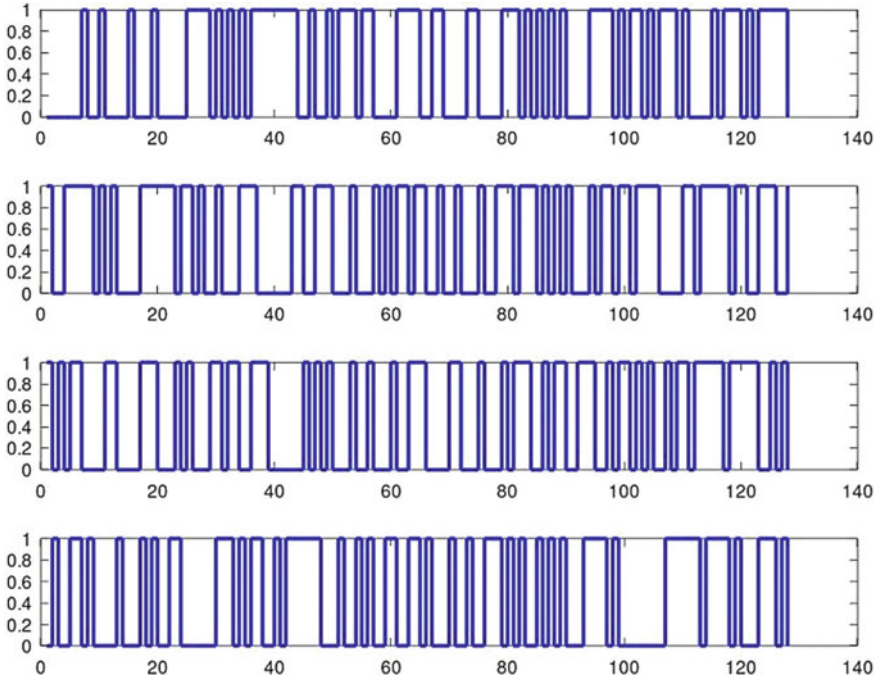


Fig. 5 Graphical representation of message-digests corresponding to the four described scenarios in the order from top to bottom

single plaintext bit over many bits in the ciphertext. The diffusion characteristic is a primordial property in cryptographic hash functions. The ideal diffusion effect should make every single bit change corresponds to changes in the digest by a probability of 50% for each bit. Although our proposed hash function is not intended to be used as a purely and solely cryptographic hash function, we perform the following test to show its overall security level against small plaintext changes. For this reason, we pick a randomly generated 1024-bits of data (extracted from the skew tent map with initial conditions $(x, p) = (0.2345, 0.5555)$). Then, we run the diffusion test for $N = \{512, 1024\}$ times, each time we toggle only one randomly-chosen bit in the data, and we calculate the new hash value, then we calculate the number D_i of bits changed compared to the original hash value.

The distribution of changed bits number D_i for every particular test is shown in Fig. 6. Moreover, In Table 4, we show four main statistical values for hash functions [5] (for $N = 512$ and 1024 respectively) that are:

Mean changed bit number defined as:

$$\bar{D} = \frac{1}{N} \sum_{i=1}^N D_i \tag{4}$$

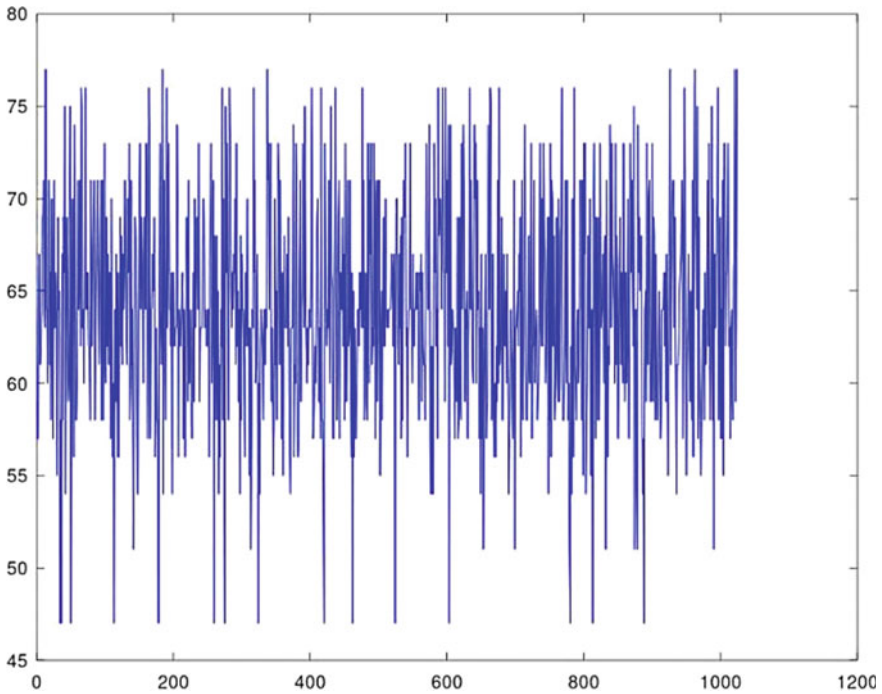


Fig. 6 Distribution of changed bits number

Table 4 Number of changed bits statistics

	$N = 512$	$N = 1024$
D	63.89	63.96
$P(\%)$	49.91	49.97
ΔD	6.02	5.85
$\Delta P(\%)$	4.71	4.57

Mean changed probability defined as:

$$P = \frac{\bar{D} \times 100}{128} \tag{5}$$

Standard deviation of the changed bit number defined as:

$$\Delta D = \sqrt{\frac{1}{N-1} \sum_{i=1}^N (D_i - \bar{D})^2} \tag{6}$$

Standard deviation probability defined as:

Table 5 Time execution of different hash functions for 1024-bit data

Hash function	Block size (bits)	Output size (bits)	Execution time (s)
Our proposed hash	1024	128	0.22
RIPEMD-160	512	160	2.62
SHA-1	512	160	17.56
SHA-2-224	512	224	19.59
SHA-2-256	512	256	22.50
MD5	512	128	2.98

$$\Delta P = \sqrt{\frac{1}{N-1} \sum_{i=1}^N \left(\frac{D_i}{128} - P \right)^2} \times 100 \quad (7)$$

We see from Fig. 6 that the distribution of changed bit number is centered on the value 64, which is exactly half the digest length 128 that is the ideal value for good diffusion property. Table 4 shows that the calculated mean and probability of changed bits are always very close to the ideal metrics 64 and 50% respectively. At the same time, ΔD and ΔP are small enough which confirms that our hash function's diffusion property approximates the ideal metrics.

4.3 Execution Time Analysis

To test the execution time of the proposed algorithm compared to other widely used hash functions, we perform the following test: we pick up randomly generated 1024-bit data, and we perform hash digest calculation using six hash functions that are implemented in Octave¹ under an Intel(R) Celeron (R) CPU N3050 @1.60 GHz PC with 4.00 GB RAM. The six functions are implemented without any optimization which are: our proposed function, RIPEMD-160 [6], SHA-1 [7], SHA-2-224 [7], SHA-2-256 [7] and MD5 [8]. The results of this implementation are shown in Table 5.

As shown in Table 5, our proposed algorithm is the fastest one, followed by the RIPEMD-160 and the MD5 algorithms. We note that all codes used in this implementation are not optimized and depends highly on the Octave environment.

¹Octave is free software licensed under the GNU General Public License (GPL): <https://www.gnu.org/software/octave/>.

5 Conclusion

In this paper, we have proposed a new fast and straightforward hash function with good enough security for use in cryptographic and pseudo-cryptographic applications (e.g., pseudorandom number generators, secondary components in cryptographic system design, cryptographic hash functions). The proposed function is based on simple logical primitive functions and a Feistel-like network to design its compression functions. We have proposed a new secure method for data padding based on the skew tent map, which can enhance further the security of the hash function. Performance and security analysis results show that the proposed function is with good enough properties for use as a secondary component in many security applications that demand fast and bulk data processing.

References

1. Paar C, Pelzl J (2013). Understanding cryptography a textbook for students and practitioners. <https://doi.org/10.1093/actrade/9780192803153.003.0002>
2. Kocarev L, Lian S (2011) Chaos-based cryptography: theory, algorithms and applications. Springer.
3. Collet P, Eckmann J-P (2009) Iterated maps on the interval as dynamical systems. Springer
4. Shannon CE (1948) A mathematical theory of communication. Bell Syst Tech J 27(3):379–423
5. Xiao Di, Liao X, Deng S (2005) One-way Hash function construction based on the chaotic map with changeable-parameter. Chaos Solitons Fractals 24(1):65–71
6. Hill D (2020) RIPEMD160 hash. <https://www.mathworks.com/matlabcentral/fileexchange/74205-ripemd160-hash>. MATLAB central file exchange. Retrieved 4 June 2020
7. Khitish (2020). SHA algorithms 160,224,256,384.512 <https://www.mathworks.com/matlabcentral/fileexchange/31795-sha-algorithms-160-224-256-384-512>. MATLAB central file exchange. Retrieved 4 June 2020
8. Stefan Stoll (2020). MD5 signature of a file. <https://www.mathworks.com/matlabcentral/fileexchange/5498-md5-signature-of-a-file>, MATLAB central file exchange. Retrieved 4 June 2020

Hybrid Intrusion Detection System for Wireless Networks



Mohamed Amine Agalit, Ali Sadiqui, Youness Khamlichi,
and El Mostapha Chakir

Abstract Local wireless networks (WLAN) are vulnerable to various types of security threats ranging from session hijacking to denial of service (DoS), and password attacks, to name a few. They are also subject to a wide range of 802.11-specific threats. The risks can become even higher and more serious when the WLAN network is made up of a number of IoT objects. As a remedy these failures, an intrusion prevention system (WIPS) has been on the network. However, the breadth of the network, the diversity of the elements to be secured and the approaches to be adopted make this integration sometimes complicated or ineffective in certain types of WLAN network. The main concern in this document is to develop, on the basis of free solutions, a flexible, easy-to-deploy and manage WIPS system that provides both intrusion detection and flow monitoring to reduce the rate of false positives, especially during home deployment or on small-scale networks.

Keywords Network security · IDS · IPS · Wireless intrusion detection · Wireless intrusion prevention · Iot

1 Introduction

An intrusion detection system (IDS) is any system, software or hardware capable of detecting suspicious activities or predefined threats to subsequently take the appropriate countermeasures [1]. These systems have become essential tools to protect a network or a computer system at an early stage. Indeed, several new intrusions are detected every day causing more and more harmful damage [2, 3] even to the point of crippling the activity of a company's information system. IDS systems scan

M. A. Agalit (✉) · Y. Khamlichi
SIGER Laboratory, FST, University of Sidi Mohamed Ben Abdellah, Fes, Morocco
e-mail: mohamedamine.agalit@usmba.ac.ma

A. Sadiqui
OFPPPT Laboratory, Meknes, Morocco

E. M. Chakir
IR2M Laboratory, FST, Hassan 1st University, Settat, Morocco

packet across the network for signs of malicious activities or unauthorized and undetected access by conventional packet filtering systems. However, computer attacks are becoming increasingly complex and have difficulty detecting intrusions correctly [4] making this concern one of the biggest challenges in the field of computer security. We distinguish three approaches to the design of an IDS system: the signature detection approach (SIDS), the anomaly detection approach (AIDS), and the hybrid detection-based approach (HyIDS) [5]. This contribution, in addition to the various work in this area, aims to achieve a HyIDS to carry out the tasks raised. We have chosen to focus on WLAN wireless networks, which are growing rapidly due to the connection comfort they provide.

We will begin by briefly presenting the different detection approaches to better situate our point. Then we will discuss wireless intrusion prevention systems (WIPS) and present the architecture of how the proposed system works. We will develop in a final part the solution adopted and we will dwell on the characteristics of the system that we proposed.

2 Background and Related Works

2.1 *The Signature Detection Approach (SIDS)*

SIDS systems rely on an attack description library (called the signature base) to detect an intrusion. A signature can refer to a single packet or group of packets. The intrusion detection system will analyze all packets transiting the network and issue an alarm immediately after a signature is detected. This approach has the advantage of almost never producing “false positive” alerts. However, detection is only effective when the signature database is updated regularly. In addition, it is vulnerable to zero-day attacks where vulnerability is exploited by an attacker even before an administrator has had the opportunity to create a fix and feed the signature library, so no alerts will be generated by the system during such attacks [6]. The size of the signature base also sees itself as a constraint in this type of system. Indeed, the higher the number of signatures is, the more significant the processing time will be, which will degrade network performance. We distinguish several implementations that perform detection by signatures, including: decision trees [7] and state transition systems [8].

2.2 *The Anomaly Detection Approach (AIDS)*

AIDS systems consider any activity which is different from the normal functioning of the system representing a threat on the network. To do this, this approach creates a “standard” behavior profile of a system by monitoring activities over a given period of time, and it defines abnormal activities based on their degree of deviation from

that standard profile [9, 10]. The standard profile is based on a statistical model and is created during the learning phase from the data received using features such as the usual devices for the connection, the number of emails sent, the number of attempts to log in in case of failure, the operating system used, etc. This detection approach is capable of detecting new attacks as any intruder who has even managed to infiltrate a system by exploiting vulnerability will have difficulty identifying the user's normal behavior, making it easy to detect. However, this approach has the disadvantage of generating a large number of false alarms especially during large networks [11].

2.3 The Hybrid Detection Approach (HyIDS)

HyIDS systems combine the advantages of the signature and anomaly detection system to detect both well-known intrusions and zero-day attacks [12]. This approach is still under development and represents a promising area of research. Many solutions have been proposed by various researchers so far and the ambition is to effectively identify any intrusion into the network as well as minimize, or even eliminate the rate of false alarms.

2.4 Introducing WIPS

Wi-Fi networks have grown strongly in recent years to offer a new range of possibilities including throughput, coverage area and number of connected hosts. As a result, a home WLAN network can now be composed, in addition to the usual elements, of a set of other elements such as TVs, surveillance cameras, detectors, actuators, etc. However, at the same time, this type of network has introduced new security threats. Whereas an attacker previously needed physical access to a cable network in order to launch an attack, a WLAN network allows anyone within their reach to passively monitor traffic or even launch an attack. As a result, multiple risks have emerged, creating an urgent need to use defense systems. Wireless intrusion prevention systems (WIPS) are part of these defense systems. Among other things, they can detect illegitimate points and have an analysis of the frames circulating on the Wi-Fi network [13]. However, the performance of these tools depends in large part on how it is used, which is, in fact, related to its configuration. Indeed, in order to protect yourself, it is essential to deploy a WIPS solution adapted, as much as possible, to its need. The goal is to succeed in a rapid and effective response to an attack, or even immediate in the best case, without degrading the quality of protected service. Personalization can involve setting up well-studied filters, adjusting coverage areas and transmission frequencies, and taking safety approaches.

3 The Proposed Architecture and System Operation

3.1 Proposed System Architecture

It is in this sense that we propose to develop a WIPS system to remedy these types of constraints and to offer such advanced personalization possibilities, especially during deployment at home or on small networks. Our WIPS system is made up of three essential parts: a radio system to listen to traffic, an analysis module to analyze frames and finally a management console, allowing a user to have an interface to manage the system (see Fig. 1).

The analysis module consists of two essential modules, namely:

- The signature detection module: The system starts by capturing and filtering packets from the WLAN network, then sending the remaining packets to preprocessors. These are essential elements for any IDS because they can thwart attacks that try to evade the detection engine by changing the structure of the packets. Once the data is processed by the preprocessors, it is then transmitted to the detection engine. The latter matches the packets to be analyzed with all the intrusion signatures contained in its database. If an intrusion has been detected, an alert will be triggered.
- The anomaly detection module: For a number of attacks, which cannot be detected by the signature database, are at the task of detecting anomalies. It receives the data stream from Step 1 and checks to see if it represents abnormal behavior. To do this, it compares the information received with the set of previously established profiles stored in the profile database. If a sign of abnormal behavior is detected,

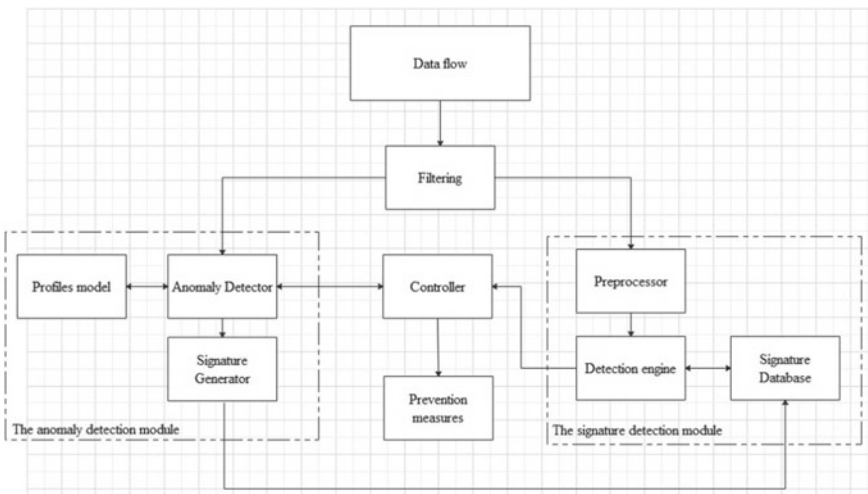


Fig. 1 The proposed system architecture

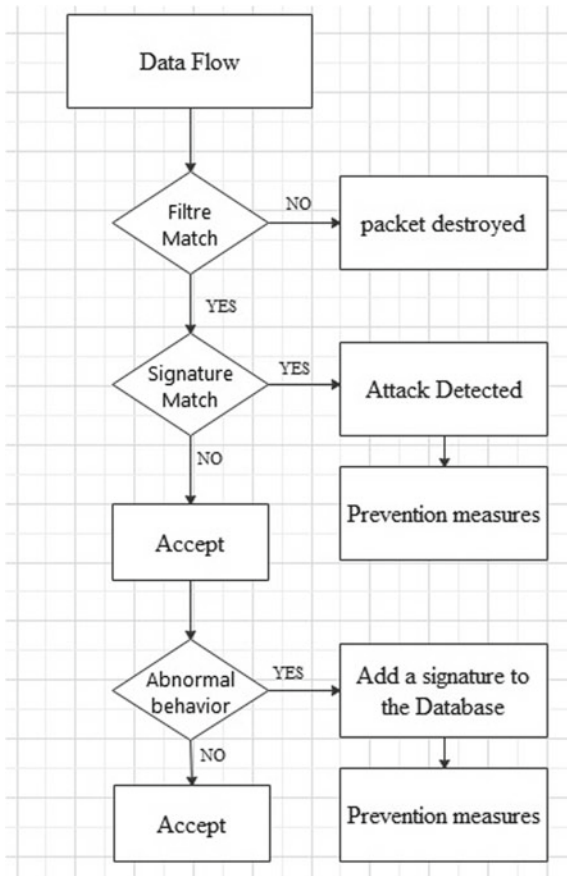
the anomaly detector activates an alert and then feeds the signature generator with the information detected as abnormal.

3.2 Proposed System Functioning:

The proposed system operation can be schematized through Fig. 2.

When a packet arrives, it will first pass through the traditional filtering system whose main purpose is to prevent unwanted traffic according to conventional methods (by IP address, MAC address, port number, etc.). Then the packet will be analyzed, via the signature detection module, for a possible predefined intrusion. If it succeeds this step, it will be processed, lastly, by the anomaly detection module. In the event of an intrusion, preventive measures will be applied. These can vary from simple logging to packet destruction.

Fig. 2 Proposed system operation



3.3 *The Features of the Proposed System*

We believe that among the major features of our system:

- It is developed based on an open system and several free tools, so it will be adaptive in nature and can adapt to different types of network and devices.
- It will offer a simple and intuitive interface of configuration and customization to adapt to the various behaviors of users.
- It will be able to operate with minimal manual supervision because any unregistered anomaly/attack will be re-signed into the system database.
- This customization capability will result in a reduction in “false positive” alerts.

For the realization of our system, we will use the Open WRT [14] and BRO [15] projects among others.

4 Conclusion and Future Works

In this contribution, we presented a study on intrusion detection techniques with the goal of proposing the implementation of a flexible and reliable hybrid WIPS system. We believe this pilot design would help administrators as well as simple users to effectively secure WLAN networks. We plan to evaluate this design both with offline testing, using standard network traffic databases [1, 16], and online testing, in a real WLAN environment.


References

1. Agalit MA, Khamlichi YI et Chakir EM (2019) A survey and taxonomy of techniques used for alerts of Intrusion Detection Systems. In: Proceedings of the 4th international conference on big data and Internet of Things. pp 1–6
2. Sun X, Dai J, Liu P, Singhal A, Yen J (2018) Using Bayesian networks for probabilistic identification of zero-day attack paths. *IEEE Trans Inf Forensics Secur.* 13:2506–2521
3. Alazab M, Tang M (2019) Deep learning applications for cyber security. Springer, Berlin/Heidelberg, Germany
4. Alazab A, Hobbs M, Abawajy J, Khraisat A (2013) Malware detection and prevention system based on multi-stage rules. *Int. J. Inf. Secur. Priv.* 7:29–43
5. Khraisat A, Gondal I, Vamplew P, Kamruzzaman J, Alazab A (2019) A Novel ensemble of hybrid intrusion detection system for detecting Internet of Things attacks. *Electronics* 8:1210
6. Alazab A, Hobbs M, Abawajy J, Khraisat A, Alazab M (2014) Using response action with intelligent intrusion detection and prevention system against web application malware. *Inf Manage Comput Secur* 22:431–449
7. Khraisat A, Gondal I, Vamplew P (2018) An anomaly intrusion detection system using C5 decision tree classifier. In Proceedings of the Pacific-Asia conference on knowledge discovery and data mining, Melbourne, Australia, 3–6 June 2018, pp 149–155
8. SumaiyaThaseen I, Aswani Kumar C (2017) Intrusion detection model using fusion of chi-square feature selection and multi class SVM. *J King Saud Univ Comput Inf Sci* 29:462–472

9. Benqdara S (2018) Anomaly intrusion detection system based on unlabeled data. *Int J Comput Appl* 181(25):18–26
10. Khraisat A et al (2019) Survey of intrusion detection systems: techniques, datasets and challenges. *Cybersecurity* 2(1):20
11. Alazab A, Abawajy J, Hobbs M, Khraisat A (2013) Crime toolkits: the current threats to web applications. *J. Inf. Priv. Secur.* 9:21–39
12. Farooq Y, Beenish H, et Fahad M (2019) Intrusion detection system in wireless sensor networks—A comprehensive survey. In: 2019 Second international conference on latest trends in electrical engineering and computing technologies (INTELLECT). IEEE, pp 1–6
13. Islam Md (2018). Comparative analysis of intrusion prevention system. Dissertation. Daffodil International University
14. WRT Homepage. <https://dd-wrt.com>. Last accessed 10 June 2020
15. BRO Homepage. <https://zeek.org>. Last accessed 07 June 2020
16. Aldwairi M, Mardini W, et Alhawaide A (2018) Anomaly payload signature generation system based on efficient tokenization methodology. *Int J Commun Antenna Propag (IRECAP)* 8(5)

Implementation and QoS Evaluation of Geographical Location-Based Routing Protocols in Vehicular Ad-Hoc Networks



Safae Smiri , Abdelali Boushaba, Adil Ben Abbou, Azeddine Zahi, and Rachid Ben Abbou

Abstract Over the last few decades, Vehicular Ad hoc Networks (VANETs) in which vehicles communicate with each other in a high dynamic topology and a high speed, have attracted considerable attention. In this type of application, routing needs to be carefully designed to handle rapid network changes and therefore geographic routing protocols have been implemented to resolve this issue. The Greedy Perimeter Stateless Routing (GPSR) protocol is one of the most promising location-based routing protocols for wireless networks. In this paper, we implement three geographical routing protocols defined as Maxduration-Minangle GPSR (MM-GPSR), Modified GPSR (MGPSR) and traditional GPSR with different approaches for node selection in VANET. We carry out an overall performance evaluation with different levels of traffics in an urban environment. The tool-set of simulation integrates NS2, Intelligent Driver Model with Lane Change (IDM_LC) based on VANETMOBISIM. The paper provides insights the choice of a geographic protocol for Quality of Service (QoS) metrics and weight value that can improve robustness in VANET.

Keywords VANET · Geographic routing · GPSR · Wireless networks · Urban environment · NS2 · VANETMOBISIM · QoS

1 Introduction

Due to increasing numbers of road accidents, it is becoming important to improve the safety and efficiency of transportation. The features of VANETs, such as their storage capability, node energy and unlimited battery power, mean that they can be used in a variety of applications [1] such as safety, road obstacle detection, congestion reduction [2], crash prevention, driver comfort and commercial services [3]. Vehicle nodes move at high speed creating highly dynamic topologies and frequent disconnections from the network, which seriously affects the overall communication performance. Routing protocols designed for Mobile Ad hoc Networks (MANETs)

S. Smiri (✉) · A. Boushaba · A. B. Abbou · A. Zahi · R. B. Abbou
Intelligent Systems and Applications Laboratory, Faculty of Sciences and Technology, Sidi Mohamed Ben Abdellah University, Fez, Morocco
e-mail: safae.smiri@usmba.ac.ma

cannot therefore be used for VANET, since a packet may be dropped or routed via a long path. Thus, new routing protocols need to be studied and developed for VANETs. In prior work [4], we showed that topology-based routing protocols are not efficient in highly dynamic networks, and that satisfactory performance is attainable with the use of location-based routing protocols. The Greedy Perimeter Stateless Routing protocol (GPSR) is considered the most suitable geographic routing for a large-scale network which combines both the greedy forwarding and the perimeter forwarding methods. In GPSR, routing tables are not used and each node periodically broadcasts information about its own position to its neighbors. However, communication with neighboring vehicles may become unstable due to the highly dynamic network, and when the packet is forwarded in the perimeter method, there may be redundancy in routing paths.

The aim of this paper is to implement and critically analyze two latest efficient geographical routing protocols for VANETs; Maxduration-Minangle GPSR (MM-GPSR) [5] and Modified GPSR (MGPSR) [6] with different weight values and compare their performance with traditional GPSR protocol. A simulation is also performed to check the Packet Delivery Ratio (PDR), end-to-end delay, jitter, routing cost and efficiency in order to help researchers to judge which one is the best for VANET applications and to open the way for improving robustness of location-based routing protocol.

The remainder of this paper is organized as follows. Section 2 describes location-based routing protocols. Section 3 discusses existing works related to position-based routing protocols. The experimental results and analysis are presented in Sect. 4. Finally, Sect. 5 concludes the paper.

2 Geographical Location-Based Routing Protocols for VANETs

Geographical routing or location-based routing has become the most efficient and promising solution for data communication in VANETs. It uses a greedy forwarding mechanism to deliver information to the destination, using only the geographic locations of the source, the destination and the neighboring vehicles. The locations of vehicles are obtained using GPS [7]. Other location-based routing protocols that exploit the geographical information of vehicles include GPSR [8], Geographic Source Routing (GSR) [9], Distance Effect Routing Algorithm for Mobility (DREAM) [10], MM-GPSR [5], Location-Aided Routing (LAR) [11], MGPSR [6] and Greedy Perimeter Coordinator Routing (GPCR) [12]. Here, we implement the latest versions of MM-GPSR and MGPSR protocol in a vehicular environment.

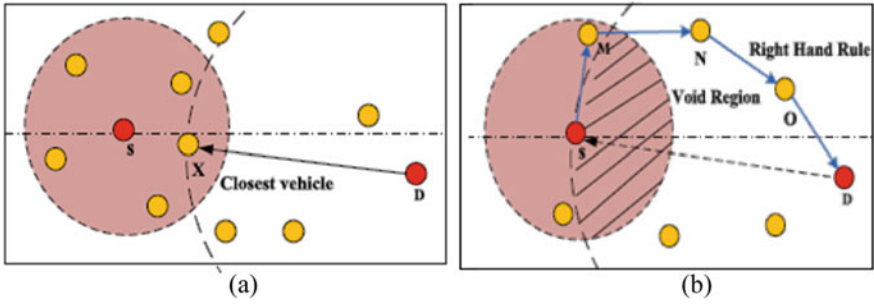


Fig. 1 GPSR protocol: a Greedy forwarding mechanism; b Perimeter forwarding

2.1 Greedy Perimeter Stateless Routing (GPSR)

In GPSR [8], each node exchanges position information with its one-hop neighbors via beacon broadcasting messages. In greedy forwarding, the current node uses the neighbor nearest to the destination node as the next hop node to forward packets. As shown in Fig. 1a, a source vehicle *S* sends a packet to its one-hop neighbor *X*, since it is closest to the destination *D*. If there is no neighbor closer to *D* than the node itself, packet is forwarded using recovery mode (perimeter forwarding) which is based on the right-hand rule, as shown in Fig. 1b. Vehicle *M* is selected as the next hop and the data packet follows the blue path. A routing loop may be generated around the nodes.

[*M*, *N*, *O*] leading to path redundancy, which can increase both end-to-end delay and packet loss.

2.2 Maxduration-Minangle GPSR (MM-GPSR)

MM-GPSR [5] aims to solve the drawbacks of GPSR by introducing a new concept to find the best next hop node in greedy forwarding based on the cumulative communication duration *T* and predefined λ parameter ($\lambda = 0.3$) that depends on the size of communication area named *Q* (Fig. 2). When transmitting packet, the source *S* finds the closest node to the destination *D* (d_{SB}) and the distance d_{BD} from *B* to *D*. In Fig. 2, the intersection of two circles (First with destination as center, d_{max} as radius and second with source as center and maximum d_{max} as radius calculated by Eq. (1)) form the allowed communication area *Q*. Where each node in *Q* is close to *D* and then is appropriate to be selected as the next hop node of the source.

$$d_{max} = d_{BD} + \lambda * d_{SB} \tag{1}$$

The neighbor node with the maximum cumulative communication duration T_i [Eq. (2)] in *Q* (Fig. 2) represents the most stable neighbor node and therefore is

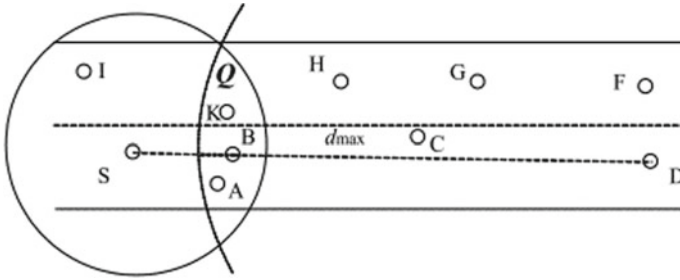


Fig. 2 Scene graph of MM-GPSR [5]

selected as the next hop node. In the following formula, T_i is calculated as the sum of the last cumulative communication and the average time to receive the hello packet.

$$T_i = T_{i-1} + t_i - t_{i-1} \tag{2}$$

When greedy forwarding fails, the improved recovery mode takes into account an improved method of minimum angle that divides the plan in two parts and the node with lowest angle value will be selected to receive data.

2.3 Modified Greedy Perimeter Stateless Routing (MGPSR)

MGPSR [6] involves a modification of the greedy forwarding strategy. If a node has several neighbors within a communication range, the possibility of choosing the node that is closest to the destination is high. To send data packets to the nearest next hop, the node with the minimum outcome will be selected as the best option. Information about the neighboring node, such as the number of neighbors and the weight entities of the nodes, are used to calculate the best next hop, as shown in the following formula:

$$\text{NextHopCriterion} = D(n, \text{end}) - (W * N_n) \tag{3}$$

where $D(n, \text{end})$ is the distance between the neighbor node (n) and the destination (end), N_n is the total number of neighbors of node n , and W is the weight entity, which is not specified in the paper [6] and also a fixed value of the weight W may not be conducive to better performance. Thus, in our work this parameter can be varied between zero and one in order to find a good path to the destination. The parameter W allows giving a degree of favoring of the parameter N_n to facilitate selection of the next hop in Eq. (3).

3 Related Works

The authors of [13] analyzed the challenges that encounters the location based routing protocol such as inaccurate positioning, local optimum problem, etc. Thereafter, they critically compare various issues of geographic routing in order to improve the reliability in VANET. In [10], the two position-based protocols DREAM and LAR are analyzed in city and highway environment using IEEE 802.11p standard. Performance metrics like packet delivery ratio, throughput, overhead and packet loss are evaluated using NS2 simulator. The authors of [14] compared different routing mechanisms from different categories and showed that position-based technique was suitable for most situations that can support Road Side Units (RSUs) in an urban network. Besides, the work of [14] provides the ability to select the most promising protocol to ensure optimal coverage and continuous connectivity by ranking the performance for QoS. The work in [13] analyzed the challenges of location-based protocols, such as the local minimum, broadcasting overhead and optimum forwarder selection problems, based on various issues of geographical protocols. Different improvements to GPSR have been suggested, such as P-GPSR [15] aims to select the optimum relay node to disseminate messages between nodes based on several parameters such as direction, speed and link stability. AGPSR [16] protocol that finds the best possible path by using additional information from the neighbor table to avoid the nodes delivering in recovery mode. MM-GPSR [5] compares the cumulative duration of communication within the allowed communication area in order to determine the stability of neighbor nodes. The authors [5] also present a new strategy of selecting the minimum angle to reduce the redundancy when building a routing path. MGPSR [6] finds a path by selecting the best relay node in order to maintain a stable connection in a highly dynamic network such as VANET, using a number of neighbors and weight entities. However, they did not specify the value of weight and they did not compare MGPSR with GPSR protocol or other position based routing protocols.

Despite the various studies proposed to analyze and evaluate performance of routing protocols. Most of them are based on the topology routing protocols. Therefore, this paper study and analyze the implementation of location based routing protocols using different weight values of MGPSR protocol and compare their performance with traditional GPSR and novel efficient MM-GPSR protocol in an urban vehicular environment.

4 Simulation and Results

Simulations were conducted using NS2.35 in an urban area. Since GPSR is not included in NS2, it was transplanted to NS2.35 at first, after MGPSR and MM-GPSR were implemented and added separately to the simulation. VANETMOBISIM was used to create realistic vehicle movements. Different numbers of CBR connections

and weight values were used for MGPSR. The performance metrics used in our simulation experiments are described as follows:

Packet Delivery Ratio (PDR) This is the ratio between the total number of received data packets and the total number sent by the source. This factor guarantees the sending of data packets.

$$\text{PDR} = \frac{\sum \text{Received Packets}}{\sum \text{Sent Packets}}$$

End-to-End Delay (E2ED) This is the average time taken by packets, measured as the ratio of the transmission packets delay to the total number of successfully received packets.

$$\text{E2ED} = \frac{\text{Time of Transmission}}{\sum \text{Received Packets}}$$

Packet Delay Variation (Jitter) This represents the average delay of two successively received packets in the same data stream.

$$\text{Jitter} = |\text{Delay of Packet } X - \text{Delay of Packet } Y|$$

Routing Cost This is the ratio between the transmitted routing packets and the number of received data packets. It also represents a measurement of the total number of control packets in the network.

$$\text{Routing Cost} = \frac{\sum \text{Transmitted Routing Packets}}{\sum \text{Received Data Packets}}$$

Efficiency This is the ratio between the total number of data packets sent and sum of the number of transmitted packets with the number of data sent in the network.

$$\text{Efficiency} = \frac{\sum \text{Sent Packets}}{\sum \text{Transmitted Routing Packets} + \sum \text{Data Sent}} \quad (4)$$

To evaluate the impact of the existing Constant Bit Rate (CBR) in the network, the number of CBR connections is varied from five to 40 for each source–destination pair. To tune the performance of the greedy forwarding method, we varied the weight factor in MGPSR from zero to one in many experiments, and found that the best performance was observed for values of 0.2 and 0.7. The results in these two cases were compared with those obtained using GPSR and MM-GPSR. The simulation parameters used in our work are summarized in Table 1.

Table 1 Simulation parameters

Description	Value	Unit
Simulation time	300	s
Simulation area size	1000 × 1000	m ²
Packets size	512	octets
Packets rate	8	pkt/s
Number of CBR connections	5, 10, 15, 20, 25, 30, 35, 40	–
Vehicles speeds	20–100	km/h
Number of vehicles	50	–
Radio range	250	M
MAC protocol	IEEE802.11p	–
Data packets type	CBR	–
Mobility model	IDM-LC	–
Propagation model	Two-Ray-Ground	–
MGPSR factor	0.2, 0.7	–
MM-GPSR factor	0.3	–

4.1 Packet Delivery Ratio

Figure 3 shows the Packet Delivery Ratio (PDR) for different numbers of connections and different values of the weight entity. In general, the PDR for MM-GPSR and MGPSR increases in two scenarios. For a weight of 0.2 (Fig. 3a), MM-GPSR and MGPSR give better performance than GPSR, and for a small number of connections, MGPSR performs better. The low PDR for MM-GPSR compared to MGPSR can be explained by the fact that MM-GPSR may make wrong decisions in recovery mode. In GPSR, a neighbor node that is moving out of communication range may

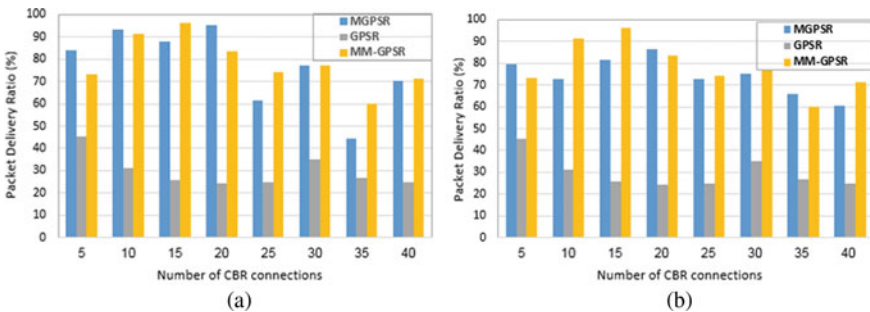


Fig. 3 Packet Delivery Ratio as function of CBR data traffic load for: **a** low weight value ($W = 0.2$); **b** high weight value ($W = 0.7$)

be selected, leading to a decrease in PDR. With a higher weight (Fig. 3b), MM-GPSR performs best for almost all numbers of connections. GPSR and GPSR have a reduced PDR. For five and 20 connections, MGPSR achieves better performance than MM-GPSR by about 6% and 3%, respectively.

4.2 End-To-End Delay

Figure 4 shows a comparison of the end-to-end delay for different numbers of connections and values of weight entity. As the number of CBR connections increases, the end-to-end delay increases for all protocols. The values for MGPSR and MM-GPSR are less than 3 ms, and GPSR achieves a higher value for a low number of CBR connections. For a low weight in Fig. 4a, MGPSR performs better than MM-GPSR in some cases, and for 40 connections, the difference is around 15%. The main reason for this is that MGPSR can maintain stable connections in a random network of vehicles. Figure 4b shows the end-to-end delay for different numbers of connections for a high value of weight entity. As the number of CBR connections increases, the end-to-end delay of MM-GPSR increases due to the use of a fixed factor to determine the maximum distance for forwarding packets, leading to incorrect path to the destination. However, the delays obtained with these two protocols (MM-GPSR and GPSR) are lower than GPSR protocol. As the vehicles move faster, the position information changes frequently, and therefore the delay increases.

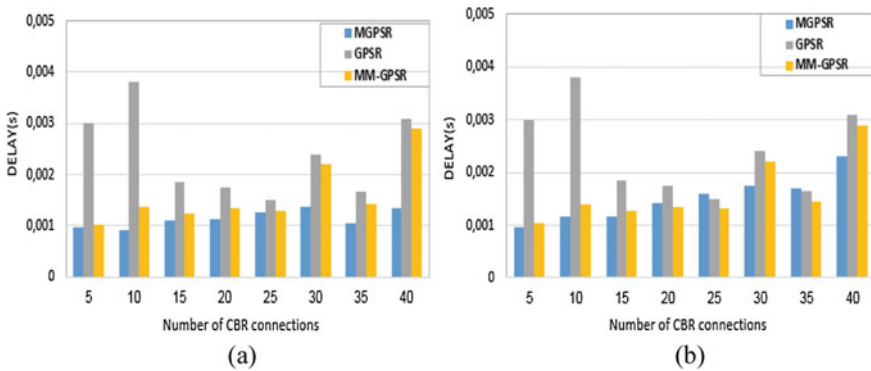


Fig. 4 End-to-end delay as function of CBR data traffic load for: **a** low weight value ($W = 0.2$); **b** high weight value ($W = 0.7$)

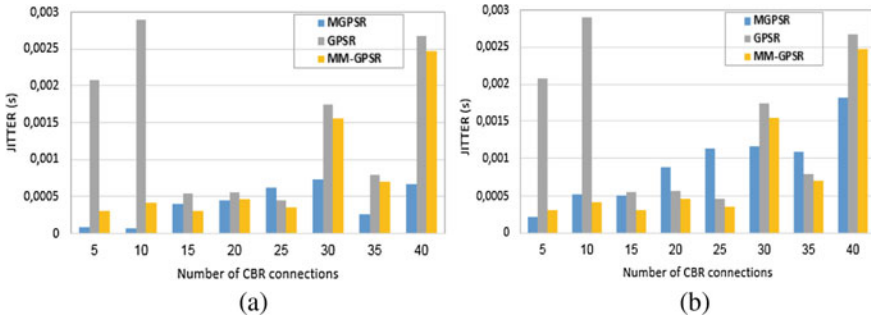


Fig. 5 Jitter as function of CBR data traffic load for: **a** low weight value ($W = 0.2$); **b** high weight value ($W = 0.7$)

4.3 Jitter

Figure 5 shows the jitter for different numbers of connections. Figure 5a illustrates that the jitter of MGPSR and MM-GPSR are lower than GPSR protocol for small numbers of CBR connections; this is because the path redundancy in GPSR resulting by the use of the right-hand-rule, leads to the worst performance. However, for 15, 20 and 25 connections, MM-GPSR achieves a lower delay than MGPSR, since it reduces the path redundancy when forwarding packets and builds stable paths. In general, Fig. 5b shows that GPSR has a higher jitter than MGPSR and MM-GPSR. The protocol MGPSR gives smaller delay for 30, 35 and 40 connections. However, for a low numbers of CBR connections, MM-GPSR performs better. The main reason for this is the use of minimum angle and left-hand rule in MM-GPSR, which allows the protocol to find the best path toward the destination.

4.4 Routing Cost

Figure 6 illustrates the routing cost for different numbers of CBR connections and weight entity. Figure 6a shows that the routing cost is highest for GPSR. One possible reason is the wrong path to the destination given in recovery mode. In Figs. 4 and 5, we show that GPSR has a lower PDR and a higher delay, respectively, and hence a lower performance in terms of routing cost. MGPSR and MM-GPSR perform better than GPSR for a small weight entity equal to 0.2 because with an increase in the network connectivity, the greedy forwarding mode reduces the number of hops to reach the destination and decreases the number of control packets. In Fig. 6b, the routing cost of MGPSR decreases with an increase of the network connectivity, and tend to be smaller than GPSR.

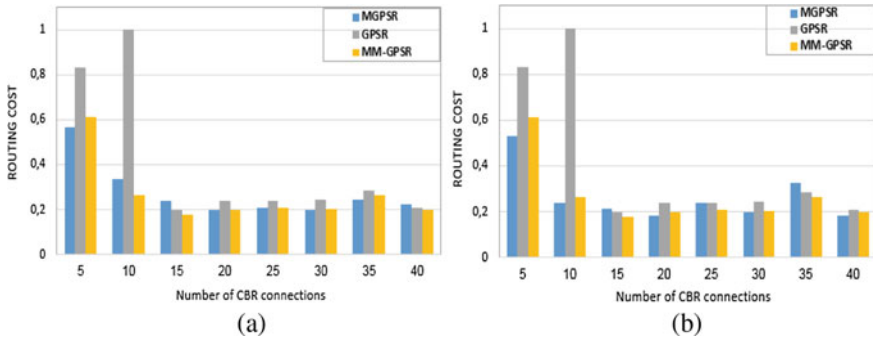


Fig. 6 Routing cost as function of CBR data traffic load for: **a** low weight value ($W = 0.2$); **b** high weight value ($W = 0.7$)

4.5 Efficiency

Figure 7 shows the efficiency for different routing protocols with small and large values of weight entity. In general, as the number of CBR connections increases, GPSR has low efficiency, especially for high levels of data traffics with 30 and 35 connections. Whereas, MGPSR (Fig. 7a) and MM-GPSR outperform GPSR in all cases. This may be because MM-GPSR uses multiple routes to attain the destination and due to the use of the minimal angle in recovery mode, since when the network is highly connected, the vehicles often switch into perimeter mode. Figure 7b shows the efficiency for different values of the weight entity. GPSR gives the same results as in Fig. 7a, while MM-GPSR and MGPSR clearly have higher efficiency than GPSR. When transmitting the packets, the protocols take into account the stability of the neighbors and selecting the minimum angle as the next hop in perimeter forwarding, which improve the efficiency.

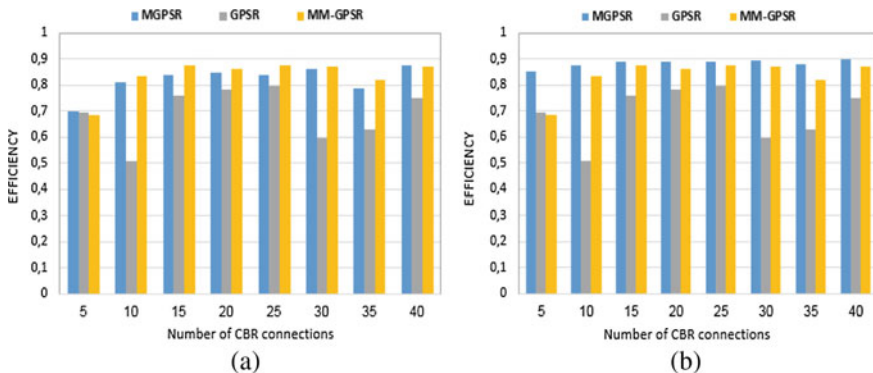


Fig. 7 Efficiency as function of CBR data traffic load for: **a** low weight value ($W = 0.2$); **b** high weight value ($W = 0.7$)

5 Conclusion and Future Work

This paper examines the performance of three GPSR-based routing protocols in a VANET, using an entity weight and several metrics in an urban scenario. There are two main contributions of this work. Firstly, we give an overview of VANETs, including the most recent research into location-based routing protocols. Secondly, we implement and analyze the MM-GPSR, MGPSR and GPSR routing protocols. Realistic vehicular traffic mobility patterns are used with IDM-LC and VANETMO-BISIM. For low weight, MM-GPSR and MGPSR perform better for most metrics, and MGPSR in particular has high PDR, low delay, low jitter and low routing cost. In future, this work will be extended to improve the stability of communication of GPSR by taking into account several routing metrics such as the link lifetime, the mobility and the density of vehicles, in order to select the optimal next hop node in a dense urban environment.

References

1. Campolo C, Molinaro A, Scopigno R (2015) Vehicular ad hoc networks: standards, solutions, and research. Springer
2. da Cunha FD, Boukerche A, Villas L, Viana AC, Loureiro AAF (2014) Data communication in VANETs: a survey, challenges and applications. INRIA Saclay ; INRIA, report
3. Ullah K, Santos LM, Ribeiro JB, Moreira EDS (2016) SADP: a Lightweight beaconing-based commercial services advertisement protocol for vehicular ad hoc network. In: Ad-hoc, Mobile, and Wireless Networks, pp 279–293
4. Smiri S, Boushaba A, Abbou RB, Zahi A (2018) Geographic and topology based routing protocols in vehicular ad-hoc networks: Performance evaluation and QoS analysis. In: 2018 International conference on intelligent systems and computer vision (ISCV), Apr 2018, pp 1–8
5. Yang X, Li M, Qian Z, Di T (2018) Improvement of GPSR protocol in vehicular ad hoc network. *IEEE Access* 6:39515–39524
6. Wang T, Anwar S, Sun H, Zhou Y (2018) Modified greedy perimeter stateless routing for vehicular ad hoc networking algorithm. *Int J Sens Netw* 27(3):163–171
7. Wischhof L, Ebner A, Rohling H (2005) Information dissemination in self-organizing intervehicle networks. *IEEE Trans Intell Transp Syst* 6(1):90–101
8. Karp B, Kung HT (2000) GPSR: greedy perimeter stateless routing for wireless networks. In: Proceedings of the 6th annual international conference on mobile computing and networking, New York, NY, USA, pp 243–254
9. Lochert C, Hartenstein H, Tian J, Fussler H, Hermann D, Mauve M (2003) A routing strategy for vehicular ad hoc networks in city environments. In: Proceedings of the IEEE IV2003 intelligent vehicles symposium. Proceedings (Cat. No. 03TH8683), Columbus, OH, USA, 9–11 June 2003, pp 156–161
10. Husain A, Sharma SC (2015) Simulated Analysis of Location and Distance Based Routing in VANET with IEEE802.11p. *Procedia Comput Sci* 57:323–331
11. Ko YB, Vaidya NH (2000) Location-Aided Routing (LAR) in mobile ad hoc networks. *Wirel Netw* 6:307–321
12. Lochert C, Mauve M, Füyler H, Hartenstein H (2005) Geographic routing in city scenarios. *ACM SIGMOBILE Mobile Comput Commun Rev* 9(1):69–72
13. Srivastava A, Prakash A, Tripathi R (2020) Location based routing protocols in VANET: issues and existing solutions. *Veh Commun* 23:100231

14. Smiri S et al (2020) Performance analysis of routing protocols with roadside unit infrastructure in a vehicular ad hoc network. *Int J Comput Netw Commun IJCNC* 12(4):19
15. Dahmane S, Lorenz P (2016) Weighted probabilistic next-hop forwarder decision-making in VANET environments. In: 2016 IEEE global communications conference (GLOBECOM). IEEE, pp 1–6
16. Silva A, Niaz Reza KM Oliveira A (2018) An adaptive GPSR routing protocol for VANETs. In: 2018 15th International symposium on wireless communication systems (ISWCS), Lisbon, Aug 2018, pp 1–6

Congestion Control Management in High Speed Networks



Kaoutar Bazi and Bouchaib Nassereddine

Abstract High-speed networks are a key technology which has brought very innovative solutions to the world of computer networks while retaining mobility, scalability, reliability... It provides a very efficient service in terms of signal speed and optimality. However, such networks with such performance needs robust systems capable of adapting to the different changes that a network connection can experience, beyond this was born the need to design congestion control algorithms capable of preserving network performance while providing high speed with low latency and good signal quality. By the way, analyzing these algorithms is the main purpose of this paper.

Keywords BIC · Congestion control · Cubic · High-speed · HSTCP · IEEE 802.11 s · Illinois · Mesh · ns2 · TCP · Westwood

1 Introduction

The various technological advances that the world has known thanks to the evolutions carried out in the computer field have made it possible to improve the standard of living of man; the interconnection of the networks has enabled the development of professional and domestic applications. Nowadays, the real capital of a company is centralized in the information stored in its IT system, such as inventory reports, customer files, product sheets, etc. Once lost, all activities will be stopped. The role of IT is not limited to the industrial field; even homes users are addicted to these services, dozens of requests are executed daily either to communicate, or to buy online, to document themselves, to distract themselves, to pay bills or even to control the security of their home from their Smartphone (manage windows, doors, lights, etc. without the need to manipulate them on the spot), even people who are

K. Bazi (✉) · B. Nassereddine
Faculty of Sciences and Technologies, Hassan First University of Settat, Settat, Morocco
e-mail: k.bazi@uhp.ac.ma

B. Nassereddine
e-mail: nassereddine_bouchaib@yahoo.com

geographically isolated from the noise of the city have the same privileges as those who live in the middle of cities. The field of medicine has also experienced qualitative leaps (the telemedicine), now it is possible to monitor patients from a distance.

In order to guarantee the continuity of its services in good conditions and to gain user satisfaction, the network must preserve its performance, the data must be transferred in order without interruption or alteration and as soon as possible. The need for such performance has given birth to a new type of network which is the wireless mesh networks (WMNs).

1.1 Wireless Mesh Networks

Wireless mesh networks [1–3] is a key technology thanks to which the transfer of information is ultra-fast, with an optimal signal and without cables, they are an optimal solution for providing a communication backbone to serve a huge number of demands while guaranteeing a response time too fast, WMNs do not require wiring and allow transmission in short time with very good signal quality. Nowadays, we can no longer imagine without IT, in the same home we find those who follow their favorite series in streaming, others who follow online video conferences, and others who have fun with their friends from a distance playing online... So, due to this demands the network finds itself unable to respond in time to all requests, and therefore it reaches saturation point; as a result some requests will be delayed or even cancelled. From this was born the need for an efficient solution capable of serving a very large number of requests by providing fast service with wide bandwidth. A Wireless Mesh Network is a network formed by the association of a certain number of network equipments connected to each other, it is thanks to this association that these wireless transmitters cover a large area and distribute the load over the entire network. These wireless transmitters (nodes) are also called Mesh stations MS, each two adjacent nodes are linked to each other by establishing a link between them, this link allows the relaying of information using a routing protocol and therefore at this stage the two nodes take the name Mesh Point MP, to ensure the continuity of the network, certain nodes must ensure the functionality of an access point then they are called Mesh Access Point MAP. Sometimes we need to link our WMN with another network with different structure such as Ethernet, 802.3,... so the Mesh Access Point must combine in this case another functionality, it is called in this case Mesh Portal Point MPP. In this way a WMN provides us with an efficient network capable of cooperating with any other type of network, ensuring broad coverage and an optimal signal.

A mesh network is an optimal solution for large areas where we cannot use the Ethernet cable; it is also very beneficial when the wifi signal is weak. The strength of this type of network lies in the fact that it is very fault tolerant; when a node is deactivated or breaks down the system very quickly switches to the most suitable neighbor node without the user of the network noticing a change in either the continuity of the signal or the speed of the response time for requests.

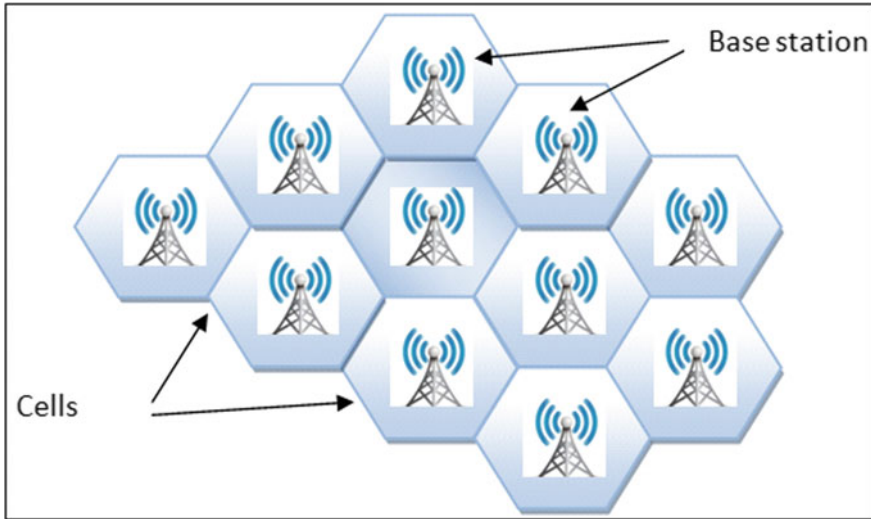


Fig. 1 Cellular mobile phone network design

1.2 Mobile Phone Networks Generations

The architecture of mobile phone networks has undergone revolutions in recent years as they have grown in a dizzying way. It all started [4] with 1G where we only transmitted voice (analog signal) then after we moved to 2G (1991) where we had the possibility to send text messages and the transmission of calls became digital in order to achieve more capacity and security (the Global System for Mobile Communications). Right after we immigrated to 3G (2001) which guaranteed us high speed services. It offers up to 14 Mbit/s downlink and nearly 6 Mbit / s uplink. To achieve higher bit rates the mobile network operators invented 4G which uses multiple antennas, so several changes and technical investments were made thanks to a new access network and a new core network which offers a reliable solution based on IP (increase the data rate, decrease latency, flexible bandwidth,...). Last but not least, we have the 5G which is the promising future. It brings very significant improvements compared to 4G (mobility management, virtualization, much reduced latency, very good quality of service, very attractive costs ...). In fact everyone knows very well that 5G is the future that aims for everyone (Fig. 1).

1.3 Wireless LAN 802.11

802.11 networks (Fig. 2) are intended for terminals [1–3] such as laptops, mobile phones ... whether for infrastructure mode or Ad hoc (computers connected without access point). 802.11 transmissions still suffer from many problems; they are sensitive

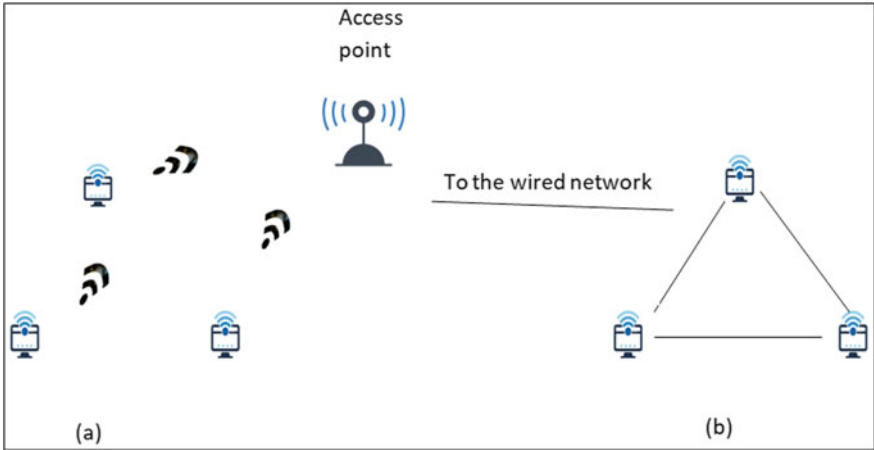


Fig. 2 a Wireless network with access point. b Ad hoc network

to the slightest change in wireless networks as propagation conditions vary. Indeed, because of the frequencies used by 802.11, the radio signals are likely to be reflected by any solid object in their path, so that for the same transmission several echoes can arrive at destination by taking different paths. These echoes will then either be canceled or reinforced which generates a remarkable fluctuation of the signal. This phenomenon is called multipath fading it is illustrated in the Fig. 3. The effective solution for this problem is the path diversity; it consists in sending information by different independent paths. In this way, the information arrives at its destination even in the case of a too strong attenuation causing the inaccessibility of one of the paths. For the implementation of this solution, the independent paths are integrated

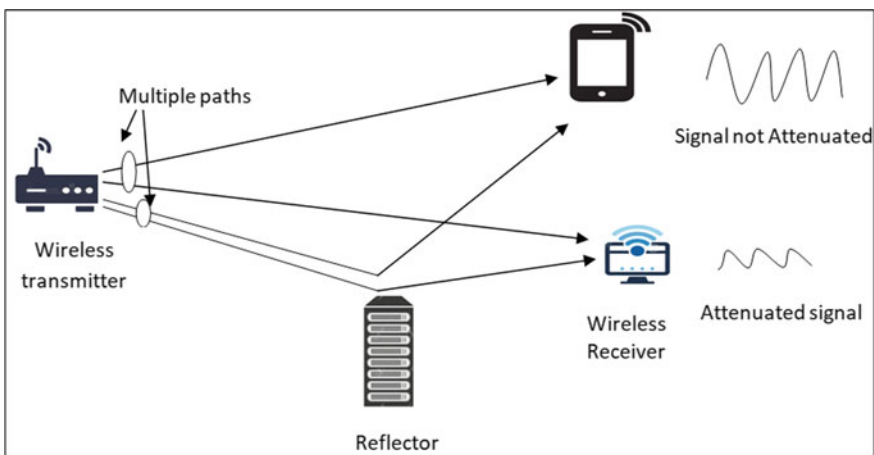


Fig. 3 Attenuation due to multipath

into the digital modulation scheme at the level of the physical layer and this using one of the different existing techniques: using spectra of different frequencies in the available band interval, follow different spatial paths between different pairs of antennas, or else re-transmit the bits for different periods.

2 Congestion Control Algorithms

2.1 High Speed TCP

As we know, networks tend more and more to have the best performances, they become more adapted for the high-speed transmissions in long-distances, with a fast and effective adaptation to the different types that exist; from networks dimensioned implementation, services, traffic... So from there was born the need for a mechanism capable of preserving the proper functioning of the network against the different challenges, especially the network congestion. TCP High-speed or HSTCP is a TCP variant designed for high-speed networks. According to [5] HSTCP is recognized as being a fair and friendly variant when it shares the same link with other types of flows, it can also quickly adapt to the different changes that the network capacity may experience in terms of bandwidth during a transmission, and therefore it allows efficient and optimal management of bandwidth. HSTCP follows an increase function which ensures an equitable allocation of the bandwidth in the presence of competing flows by adopting an approach which varies according to the time elapsed and this from the last detected packet loss. The congestion window is adjusted as follows:

$$cwnd = cwnd + \alpha(cwnd)/cwnd \quad (1)$$

Otherwise, to decrement the window:

$$cwnd = cwnd(1 - \beta(cwnd)) \quad (2)$$

When the size of the cwnd is small, the function $\alpha(cwnd)$ is assigned the value 1 and the function $\beta(cwnd)$ the value 0.5.

If the value of the cwnd exceeds a certain fixed threshold, then $\alpha(cwnd)$ and $\beta(cwnd)$ update depending on the value of the size of the current window (w). We put two variables: L1 and LP (loss probability), the formulas applied are as follows:

$$L1 = \frac{\sqrt{\frac{\alpha(cwnd)(2-\beta(cwnd))}{2\beta(cwnd)}}}{\sqrt{LP}} \quad (3)$$

For α and β :

$$\alpha(\text{cwnd}) = \frac{L1^2 * LP * 2\beta(\text{cwnd})}{2 - \beta(\text{cwnd})} \quad (4)$$

$$\beta(\text{cwnd}) = \frac{(\mu - 0.5)(\log(\text{cwnd}) - \log(w))}{\log(L1) - \log(w)} + 0.5 \quad (5)$$

With $\mu = \beta(L1)$. So in this way each increment of the cwnd implies an increment at the level of the value of the function $\alpha(\text{cwnd})$ and a decrement at the level of the value of the function $\beta(\text{cwnd})$. This implies a rapid growth of the window of the high-speed TCP protocol and a recovery as fast in case of recorded losses. HSTCP is also making changes to the Slow Start phase. In fact, we start by applying a slow start in the same usual way until the congestion window exceeds the value of certain threshold, then at this stage upon receipt of an acknowledgment,

$$\text{cwnd} = \text{cwnd} + MSS + A \quad (6)$$

with: $A = 2 * \text{cwnd}/\text{ssthresh}$, MSS is the maximum segment size and ssthresh is the slow start threshold.

Thanks to these mechanisms, high-speed TCP achieve better allocation of badwidth under conditions with a large bandwidth-delay product.

2.2 TCP BIC

TCP BIC (Binary Increase Congestion Control) [6], is also designed for high-speed networks with high-latency, the congestion management procedure implemented in TCP BIC is as follows: the process begins with a slow start phase as is the case in TCP Reno until detection of congestion (loss phenomenon), then at this time TCP BIC decreases the value of the congestion window cwnd by multiplying it by a factor less than 1. We note two variables Maxwnd and minwnd representing respectively the old value of the congestion window and the new value after reduction. We also note Midwnd defined as follows: $\text{Midwnd} = (\text{Maxwnd} + \text{minwnd})/2$. The next step is to compare the difference between the two values minwnd and Midwnd with the value of a given constant Ω , if the constant Ω is smaller, then the congestion window will be increased by the value of Ω (additive increase) of this way we guarantee rapid convergence with a RTT fairness. In the event that no loss phenomenon is detected during the cwnd takes the value of minwnd , otherwise it takes the value of Maxwnd . Just after, BIC enters a binary search increase phase where adjusting the cwnd is the problem; so this consists in calculating the Midwnd several times to adjust the value of the cwnd . When detecting a packet loss, the value of Midwnd is assigned to the variable Maxwnd , otherwise the variable Midwnd takes the value of minwnd . So by following this method the variation of the congestion window takes a linear rhythm then logarithmic. In the case where the value of the cwnd reaches that of Maxwnd , we seek another maximum. Then BIC begins a new phase is the max

probing. In this phase we adopt a symmetrical increment of the *cwnd* in the same way seen in the additive increase and the binary search. TCP BIC is very beneficial for high-speed networks; it is characterized by stability, scalability, fairness and an aggressive growth function under short RTT networks.

2.3 TCP Cubic

Designed by Rhee and Xu is an improvement of the TCP BIC congestion control protocol. In CUBIC we aim to improve the friendliness and RTT-fairness with of course an improvement of the BIC window which is characterized by aggressiveness in the presence of flow with a small RTT or a low speed environment. Improvements at the CUBIC level [7] have proposed window growth that follows a cubic function, it is defined as follow:

$$cwnd = H(t - L)^3 + windS \tag{7}$$

H is a scaling factor, t is the time that has elapsed since the last value of the window after reduction, windS is the size of the window before reduction.

For $L = \sqrt[3]{((windS * \Upsilon)/H)}$ where Υ is a window reduction factor used when detecting a loss phenomenon.

So during a reduction the size of the window increases with a very high rate even in the case of TCP BIC, and it decreases its rate of growth when it approaches the value of windS and it is thanks to this decrease as TCP CUBIC gains its stability. When the value of the congestion window is far from that of windS TCP BIC increases its window quickly which allows a good exploitation of network resources is where TCP CUBIC gains in terms of scalability.

2.4 TCP Westwood

TCP Westwood [8] is a modification of TCP on the sender side in order to achieve a good product bandwidth-delay (large pipe), with significant packet loss due to transmission or other errors, and with dynamic network load. The principle is to continuously follow the acknowledgments received from a connection, always on the transmitter side, in order to calculate the bandwidth (*bdth*), so we get an estimate on which the transmitter is based to adjust the values of the constant of threshold *ssthresh* and the congestion window *cwnd* after a congestion phase detected by the reception of three duplicate acknowledgments or by a timeout.

– In the case of congestion detected by the expiration of a timeout:

$$ssthresh = (bdth * RTT / SegmentSize), cwnd = 1 \tag{8}$$

SegmentSize is the size of the TCP segment in bits.

In the case of a congestion detected by the reception of three duplicate acknowledgments:

$$ssthresh = (bdth * RTT) / SegmentSize \quad (9)$$

$$cwnd = \min(cwnd, ssthresh) \quad (10)$$

It should be noted that TCP Westwood remains effective for wireless connections which experience sporadic losses (due to radio channel problems) which are translated as a sign of congestion which generates unnecessary reductions in the congestion window.

2.5 TCP Illinois

TCP Illinois (S. Liu et al. in) [9] is a TCP variant designed for high-speed and long-distance networks. The goal behind Illinois is to achieve good throughput with good fairness in the allocation of network resources. To determine the direction of the variation of the congestion window, we rely on the loss of packets as an initial sign of congestion detection, and on queuing delay as a second sign of congestion detection (loss-delay based algorithm). Like all other TCP variants, Illinois increases the size of the cwnd each time an acknowledgment is received. The principle is as follows:

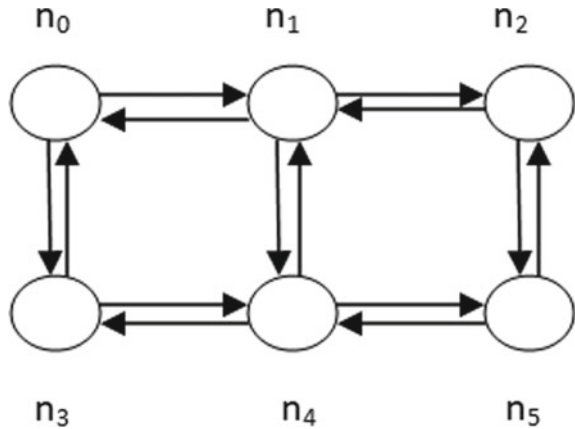
When the average waiting time μ is small, the transmitter deduces that there is no congestion then it defines a large α and a small β , otherwise if the μ is large, the transmitter presumes the risk of congestion and then defines a little α and a big β . α and β are defined in [10].

3 Proposed Work

In the previous section we shed light on certain TCP congestion management algorithms designed for high-speed networks. In this section we will try to analyze them more closely through simulations in order to practically touch on their advantages and limits in the presence of variable network conditions. For the simulation we opted for the NS2 software, we built the network topology (Fig. 4) where we applied FTP as data traffic and CBR as background traffic to congest the network. The values of the initial window and the packets size are 8000 bits and 5552 bits respectively. For the link that separates every two adjacent nodes is of 2048 MB.

We repeated the same scenario for each of the TCP variants to have the statistics relating to each. The data collected were the subject of certain calculations in order to

Fig. 4 The network topology used in ns2



have significant values reflecting the behavior of TCP flavors throughout the applied scenarios. So the simulations and calculations made allowed us to have an idea on the performance of the TCP variants in terms of variations of throughput, latency and Packet drop.

In order to facilitate the interpretation of the results obtained, and to better compare the behaviors of these algorithms, the numerical results have been transformed into significant graphs still thanks to the NS2 software using the Gnuplot tools. So the results obtained are illustrated in Figs. 5, 6 and 7

At the beginning of the simulation, for small values of CBR we notice that all the TCP variants have the same behavior; they adopt a stable rhythm with almost identical values. However in the presence of congestion (for values of CBR > 1800 Mbps) the values of the throughput experience a very significant decrease and this for all the TCP variants with a more remarkable decrease for TCP Westwood and HSTCP. Thereafter since the state of the network continues to be congested, the values of the throughput continue to decrease until the value zero.

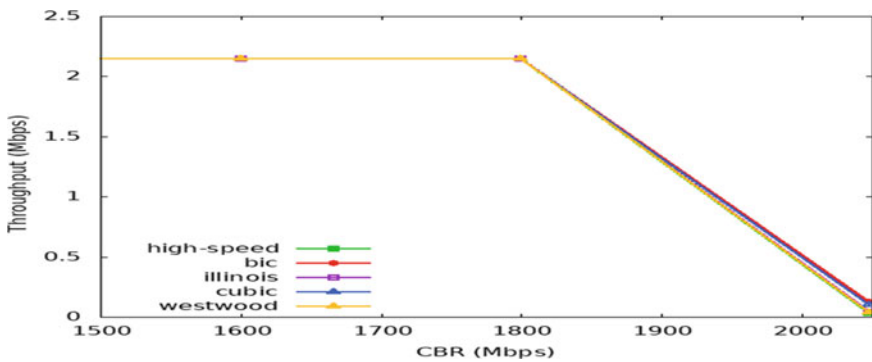


Fig. 5 Variation of the throughput according to CBR values

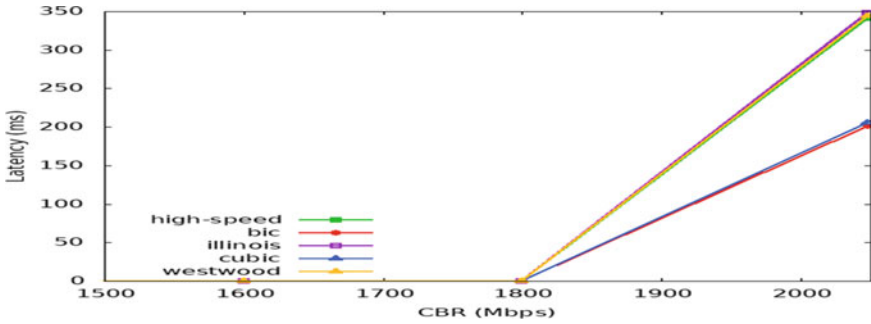


Fig. 6 Variation of the latency according to CBR values

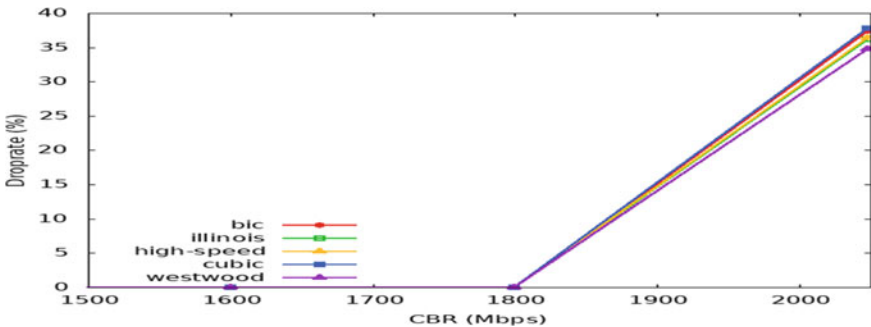


Fig. 7 Variation of the drop rate according to CBR values

At the beginning of the simulations all the TCP variants adopt a very fast rate of variations with zero latency and this is normal since we are in the presence of a congestion management algorithm designed for high-speed networks. But beyond the 1800 Mbps of CBR we have a remarkable increase in latency for all the variants with more significant increases for the three algorithms HSTCP, Illinois and Westwood.

At the start of the connection no loss is recorded and this for all TCP variants. But just after, in the presence of congestion, all the congestion management algorithms started to lose packets with almost the same loss values. We also note that the more the network congestion the more the loss rate increases. We can notice also that Westwood has the lowest loss values while Cubic has the highest loss rate.

4 Conclusion

As a conclusion we can deduce that the TCP variants have almost similar behaviors in the absence of congestion, but once the network congested each tries to solve the problem in its own way, so the choice of a variant depends on what each situation

requires since each variant is designed to meet very specific requirements. Each TCP flavor has its own behavior according to the specificities for which it was designed. From this analysis we also concluded that even within the high-speed variants we have those which are loss-based, delay-based or even other hybrids combining the two loss-delay based. Therefore the choice of one or others depend on what each application and what each type of network requires.

References

1. Akyildiz F, Wang X, Wang W (2005) Wireless mesh networks: a survey. *Comput Network Syst* 47:445–487
2. Camp JD, Knightly EW (2008) The IEEE 802.11s extended service set mesh networking standard. *IEE Commun Mag* 46:120–126
3. Hiertz GR, Max S, Zhao R, Denteneer D, Berlemann L (2007) Principles of IEEE 802.11s. In: *Proceedings of 16th international conference on computer communications and networks (ICCCN)*, Honolulu, Hawaii, USA, Aug 2007
4. Ohmori S, Yamao Y, Nakajima N (2001) The future federations of mobile communications based on broadband access methods. *Wirel Pers Commun* 17:175–190
5. Leith* D, Shorten* R (2004) NUI Maynooth. H-TCP: TCP for high-speed and long-distance networks. Hamilton Institute
6. De Cicco L, Mascolo S (2007) International conference on next generation wired/wireless networking NEW2AN 2007: next generation teletraffic and wired/wireless advanced networking, pp 73–85
7. Poojary S, Sharma V (2019) An asymptotic approximation for TCP CUBIC. *Queueing Syst* 91:171–203
8. Casetti C, Gerla M, Mascolo S et al (2002) TCP westwood: end-to-end congestion control for wired/wireless networks. *Wireless Netw* 8:467–479
9. Saedi T, El-Ocla H (2020) Improving throughput in lossy wired/wireless networks. *Wirel Pers Commun*
10. Liu S, Ba_sar T, Srikant R (2006) TCP-Illinois: a loss and delay-based congestion control algorithm for high-speed networks. In: *Proceedings of the 1st international conference on performance evaluation methodologies and tools (Valuetools'06)*. ACM, New York, p 55

Renewable Energy

Aerodynamic Analysis of Wind Turbine Blade of NACA 0006 Using a CFD Approach



Mohamed Hatim Ouahabi, Houda El Khachine, and Farid Benabdelouahab

Abstract In order to exploit wind energy and make it more and more promising and competitive with other forms of green energy, designers and researchers aim to optimize the aerodynamic performance of wind turbine blades. Our research project deals with the case of the aerodynamic profile of type NACA 0006 in order to evaluate the aerodynamic forces which act on a single blade. This article analyzes the two-dimensional model of the aerodynamic profile NACA 0006 for a specific Reynolds number as well as a range of angles of attack of $[-10.5^\circ; 10.5^\circ]$. The aerodynamic characteristics simulation is applied by the $k - \omega$ turbulence model (SST) namely; coefficient of lift, drag and pressure. That with these results it was possible to carry out the comparison of the numerical measurements with those experimental for the chosen profile of national advisory committee of aeronautics NACA in the wind tunnel. The purpose of our application is to verify the accuracy of the model and to predict the efficiency of the blade which will allow the achievement of the efficient design strategy.

Keywords NACA 0006 airfoil · Wind turbine blade · Lift and drag coefficient · Computational fluid dynamics (CFD) · Ansys fluent · Aerodynamic forces

1 Introduction

Wind power is one of the most important renewable energy sources due to its availability in many places and its sustainable characteristics, but this form of energy requires a detailed analysis of the wind characteristics of the selected region in order to optimize the production performance of wind farms [1, 2]. The maximization of the production of wind energy obtained remains the primary goal in the design

M. H. Ouahabi (✉) · F. Benabdelouahab
Department of Physics, Faculty of Sciences, Laboratory of Condensed Matter Physics,
Abdelmalek Essaadi University, 93030 Tetouan, Morocco
e-mail: ouahabitim.gc@gmail.com

H. El Khachine
Department of Physics, Laboratory of Innovative Technologies (LTI) - ENSA, Abdelmalek
Essaadi University, 90040 Tangier, Morocco

of wind turbines. For instance, in the aerodynamic profiles there are two goals are expected, firstly, the increase in lift coefficient and, in contrast, the decrease in drag coefficient following exposure to air flow [3–5]. These aerodynamic profiles allowing the conversion of kinetic energy from the wind into mechanical and then electrical energy. For this reason, several researchers are focusing on reducing the cost of wind turbines by studying the shape of the blades and optimizing their aerodynamic characteristics. There are different methods which guarantee the analysis of the flow circulating around the aerodynamic profiles. Given the necessity and the technical importance of the most precise and rapid methods in the measurement of flow fields. Computational fluid dynamics ‘CFD’ is the best tool for simulating airflow movements around a wind turbine [6–8]. Thus we note in the literature their applications in several works [9, 10]. Since the flow is turbulent in our calculations it is considered stable to solve the Navier-Stokes equations and carry out the calculations using the chosen turbulence model $k - \omega$ SST [11, 12]. The performance of the design of a new generation wind turbine requires an adequate and very precise forecast of the stall phenomenon (stall angle). Consequently, the NACA measurements in the wind tunnel experiment are compared with the numerical simulation results to validate them. Then, the velocity and pressure contours are also produced and give relevant and accurate results.

2 Materials and Methods

2.1 Navier Stokes Equations

Generally, in order to describe mathematically the flow of a fluid we use three partial differential equations namely; the conservation of mass, momentum and energy [13], with the assumption that the fluid is considered as a continuous medium. The general vision of CFD is that the variation of the variables of algebraic relationships are local with the coordinates of space at the level of cells [14]. Therefore, we can write the equation of mass conservation:

$$\frac{\partial \rho}{\partial t} + \nabla \cdot (\rho \vec{u}) = S_m \quad (1)$$

The mass conservation equation is usually presented in the form of the Eq. (1), applied for the two flows whether it is compressible or incompressible. The mass which is added to the continuous phase (the 2nd dispersion phase) is called source S_m , and this is how from any determined source. The Eq. (2) defined in an in the conservation of the momentum as follows:

$$\frac{\partial}{\partial t} (\rho \vec{u}) + \nabla \cdot (\rho \vec{u} \vec{u}) = -\nabla p + \nabla \cdot (\bar{\tau}) + \rho \vec{g} + \vec{F} \quad (2)$$

where p is the static pressure, $\bar{\tau}$ is the stress tensor, $\rho \vec{g}$ and \vec{F} are the gravitational body force and external body forces, respectively [15]. The formula of stress tensor is as follow:

$$\bar{\tau} = \mu \left[(\nabla \vec{u} + \nabla \vec{u}^T) - \frac{2}{3} \nabla \cdot \vec{u} I \right] \tag{3}$$

where μ is the molecular viscosity, I is the unit tensor. The continuity Eqs. (2) and (3) for incompressible flow are given by:

$$\frac{\partial u}{\partial x} + \frac{\partial v}{\partial y} = 0 \tag{4}$$

$$\frac{\partial u}{\partial x} + \frac{\partial v}{\partial y} + \frac{\partial w}{\partial z} = 0 \tag{5}$$

The momentum equations for viscous flow:

$$\rho \frac{Du}{Dt} = -\frac{\partial p}{\partial x} + \frac{\partial \tau_{xx}}{\partial x} + \frac{\partial \tau_{yx}}{\partial y} + \frac{\partial \tau_{zx}}{\partial z} + \rho f_x \tag{6}$$

$$\rho \frac{Dv}{Dt} = -\frac{\partial p}{\partial y} + \frac{\partial \tau_{xy}}{\partial x} + \frac{\partial \tau_{yy}}{\partial y} + \frac{\partial \tau_{zy}}{\partial z} + \rho f_y \tag{7}$$

$$\rho \frac{Dw}{Dt} = -\frac{\partial p}{\partial z} + \frac{\partial \tau_{xz}}{\partial x} + \frac{\partial \tau_{yz}}{\partial y} + \frac{\partial \tau_{zz}}{\partial z} + \rho f_z \tag{8}$$

The continuity and momentum equations are combined with the $k - \omega$ SST model.

2.2 $k - \omega$ SST Turbulence Model

The $k - \omega$ SST model is a widely used turbulence model pushing two eddy-viscosity equations [16]. This model is qualified as suitable precisely for the flow which separates the laminar from the turbulent as well as for the pressure gradients found to be unfavorable. Creating strong levels of turbulence in areas of stagnation and those with strong acceleration. Therefore, we describe the SST $k - \omega$ turbulence model as follows:

$$\frac{D\rho k}{Dt} = \tau_{ij} \frac{\partial u_i}{\partial x_j} + \beta^* \rho \omega k + \frac{\partial}{\partial x_j} \left[(\mu + \sigma_k \mu_t) \frac{\partial k}{\partial x_j} \right] \tag{9}$$

$$\frac{D\rho \omega}{Dt} = \frac{\gamma}{\nu_t} \tau_{ij} \frac{\partial u_i}{\partial x_j} - \beta \rho \omega^2 + \frac{\partial}{\partial x_j} \left[(\mu + \sigma_k \mu_t) \frac{\partial \omega}{\partial x_j} \right]$$

$$+ 2\rho(1 - F_1)\sigma_\omega \frac{1}{\omega} \frac{\partial k}{\partial x_j} \frac{\partial \omega}{\partial x_j} \quad (10)$$

where $\beta^* = \varepsilon/k\omega$ and the turbulence stress tensor is:

$$\tau_{ij} = -\overline{\rho u'_i u'_j} = \mu_t \left(\frac{\partial u_i}{\partial x_j} + \frac{\partial u_j}{\partial x_i} - \frac{2}{3} \frac{\partial u_k}{\partial x_k} \delta_{ij} \right) - \frac{2}{3} \rho k \delta_{ij} \quad (11)$$

The turbulence viscosity can be estimated by: $\nu_t = a_1 k / \max(a_1 k, \Omega F_2)$, where Ω is the absolute value of the vorticity.

2.3 Aerodynamic Characteristics

The aerodynamic profile is composed of two forces, lift and drag as well as a moment. The lift force 'FL' is the component perpendicular to the movement of air, depending on its displaced mass. On the other hand, the resistance force called drag force 'FD' is the component which is parallel to the movement of air [17]. Lift and drag coefficient (C_L and C_D) are defined as:

$$C_L = \frac{FL}{1/2 \cdot \rho \cdot C \cdot V^2} \quad (12)$$

$$C_D = \frac{FD}{1/2 \cdot \rho \cdot C \cdot V^2} \quad (13)$$

where: ρ is the density of the air, 'V' is the velocity of air and 'C' the blade length or called chord.

2.4 Geometry and Mesh Generation

Figure 1 shown the NACA 0006 airfoil profile. The coordinates of the airfoil were provided from database of NACA in order to create and simulate the wind flow around a 2-D geometry using Ansys Fluent code [15].

In this study, the applications of the lift to drag ratio coefficients (C_L/C_D) for a different attack angles were realized. Table 2 illustrates the calculation of the lift to drag ratio coefficient for predicted numerical simulation and measured data of NACA at different angles of attack.

This study simulate air flow around NACA 0006 airfoil at a range angles of attack $[-10.5^\circ; 10.5^\circ]$. Figures 2 and 3 shown respectively, the geometry of wind turbine blade and the mesh generation for the blade. The boundary conditions are addressed in the Table 1.

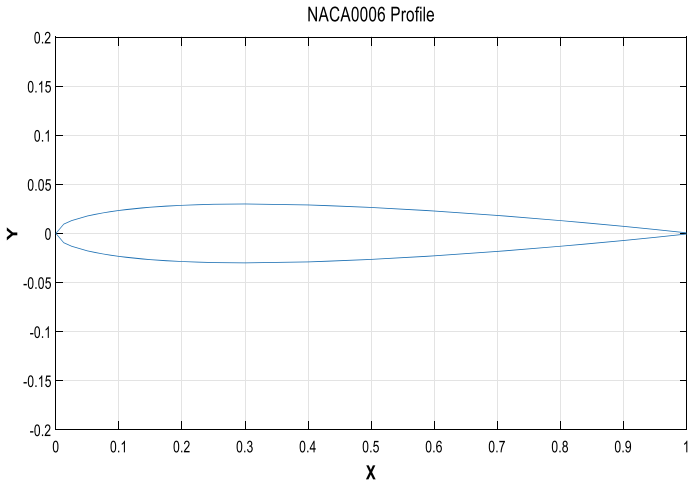


Fig. 1 NACA 0006 blade profile

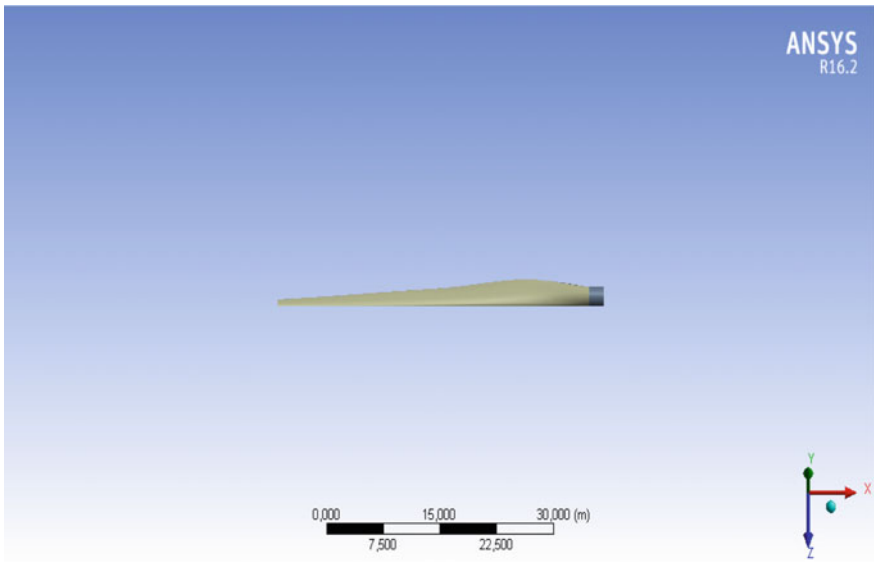


Fig. 2 Geometry of wind turbine blade

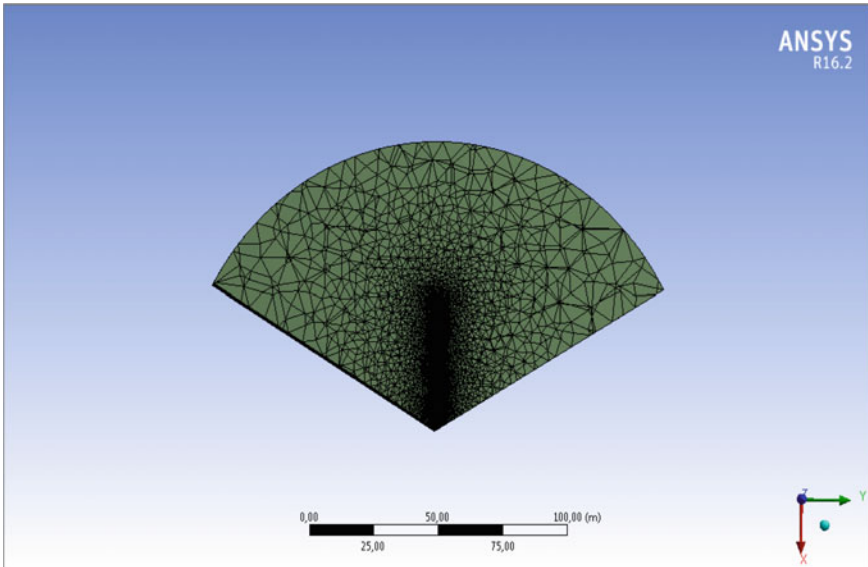


Fig. 3 Mesh generation for the blade

Table 1 Inputs and boundary conditions

Input data	Value
Fluid type	Air
Velocity	8.41 (m/s)
Pressure	101.325 (Pa)
Density of fluid	$\rho = 1.225 \text{ kg/m}^3$
Reynolds number	$Re = 50,000$
Chord length	1 (m)
Temperature	300 (K)
Angles of attack (AOA)	$[-10.5^\circ \text{ to } 10.5^\circ]$
Turbulence model	$k - \omega$ SST
Viscosity	$\mu = 1.78941 \times 10^{-4} \text{ (kg/m s)}$

3 Results and Discussion

3.1 Aerodynamic Coefficients (C_L and C_D Validation)

The distribution of aerodynamic coefficients (lift and drag) for NACA 0006 are applied at different angles of attack using both data (measured and predicted).

From Figs. 4 and 5, it can be observe that C_L and C_D values increases with increasing angles of attack until to reach at stall angle which can be noted at 10.25° .

Table 2 The lift to drag ratio C_L/C_D values with different angles of attack for NACA 0006

Angle of attack (°)	Experimental C_L	Predicted C_L	Experimental C_D	Predicted C_D	Experimental C_L/C_D	Predicted C_L/C_D
0	0	-0.0225	0.0141	0.01061	0	-2.120640
1	0.0866	0.0806	0.0143	0.01164	6.0559440	6.919642
2	0.1723	0.0923	0.0146	0.01415	11.801369	6.522968
3	0.2535	0.2694	0.0161	0.01713	15.745341	15.72679
4	0.4405	0.4130	0.0224	0.02293	19.665178	18.00976
5	0.5484	0.4816	0.0326	0.03310	16.822085	14.54668
6	0.6399	0.5296	0.0497	0.05120	12.875251	10.34294
7	0.6541	0.5691	0.0863	0.08635	7.5793742	6.590619
8	0.6770	0.6044	0.1015	0.09537	6.6699507	6.337422
9	0.6711	0.6371	0.1072	0.09679	6.2602611	6.582019
10	0.6670	0.6654	0.1095	0.09920	6.0913242	6.707600
10.5	0.6455	0.6443	0.1110	0.11292	5.8147914	5.705737

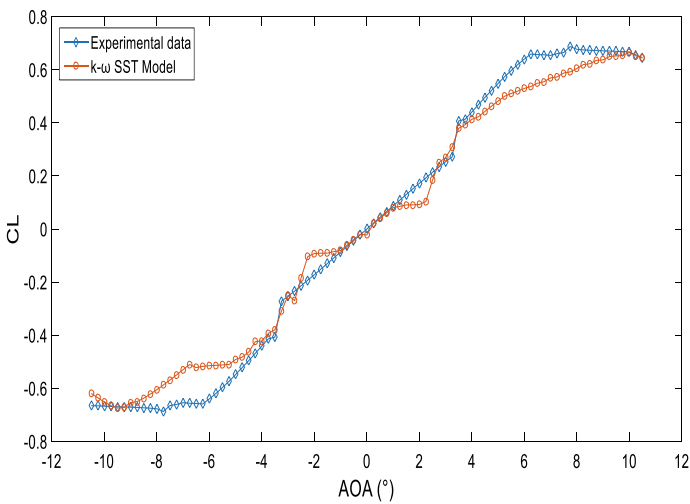


Fig. 4 C_L distribution with various angles of attack (AOA)

Because we can see it clear that lift coefficients C_L decreases and the drag coefficients C_D increases dramatically. When the lift force F_L is large enough that the drag force F_D , especially when the blade stalls, it can be said that the design of the blade is effective. In addition, the C_L/C_D values addressed in Table 2 shown that the optimum value for NACA 0006 is at the attack angle of 4°.

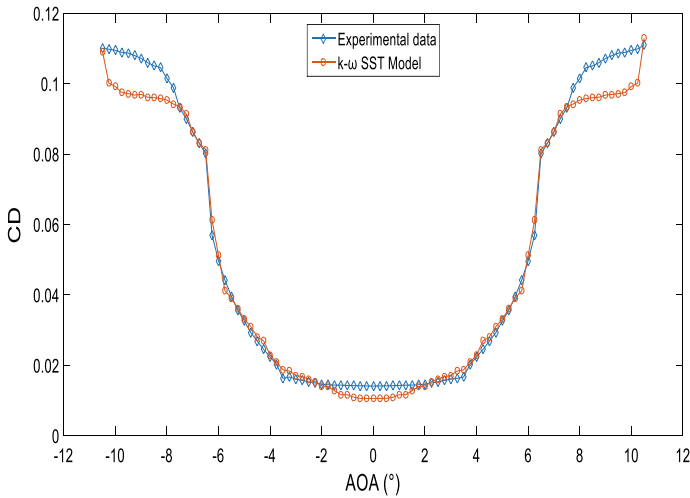


Fig. 5 C_D distribution with various angles of attack (AOA)

The comparison of the numerical simulation values of the lift coefficient vis-a-vis the experimental ones shows a difference of 4.38%, while an error of 0.37% by the comparison of the results of the drag.

3.2 *Distribution of Pressure Coefficient*

Figure 6 shown the experimental and numerical comparison of pressure coefficient distribution for NACA 0006 at $Re = 5.10^4$ at various angles of attack. Our observations are many; First the pressure coefficient which is negative on the upper side of the blade and positive on the lower side. This explains why the sense of direction of the lift force is upwards. In addition, it has been found that the increase in the pressure difference between the two surfaces is relative to the increase in the angle of attack. While, the coefficient of pressure difference is very large at the leading edge compared to the trailing edge where it is very low.

3.3 *Static Pressure and Contours of Velocity Magnitude*

After investigations of the CFD simulation of airflow around chosen blade, Fig. 7 indicates that the velocity of the air flow is very low in the leading edge, here we can see the point of stagnation. Considering that, Fig. 8 also illustrates that the pressure distribution being parallel to the flow of the incoming air tends to slow the velocity of the latter relative to the blade. Similarly, we can see in the same Fig. 8 that the

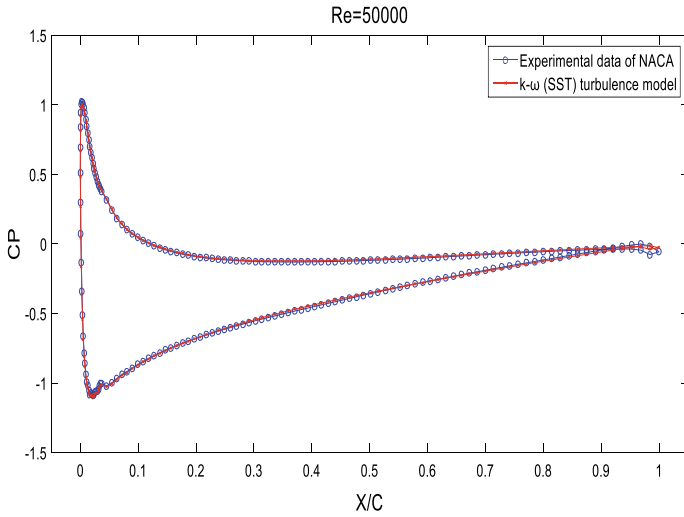


Fig. 6 Experimental and numerical comparison of pressure coefficient distribution for NACA 0006 at $Re = 5.10^4$

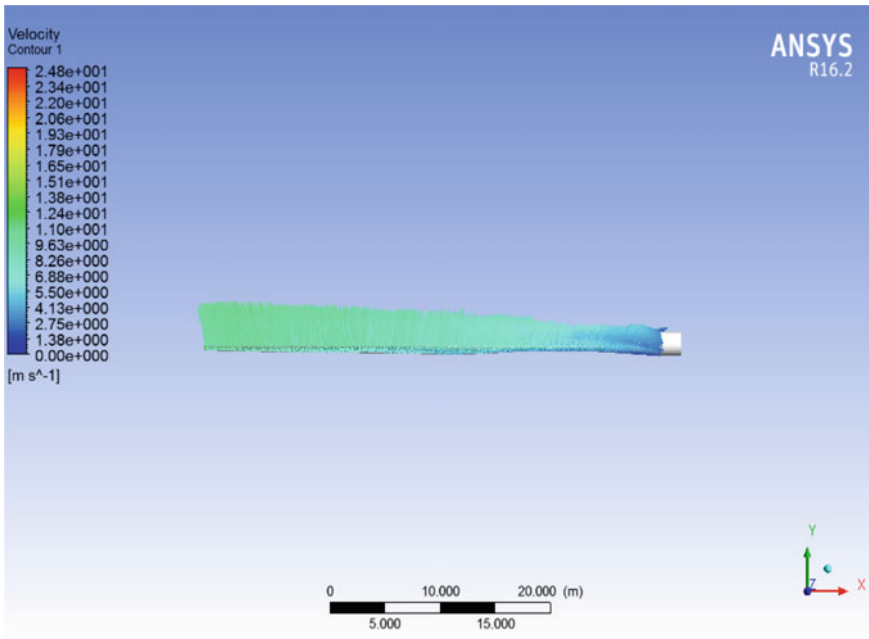


Fig. 7 Velocity contours for wind turbine run a suction outside of blade

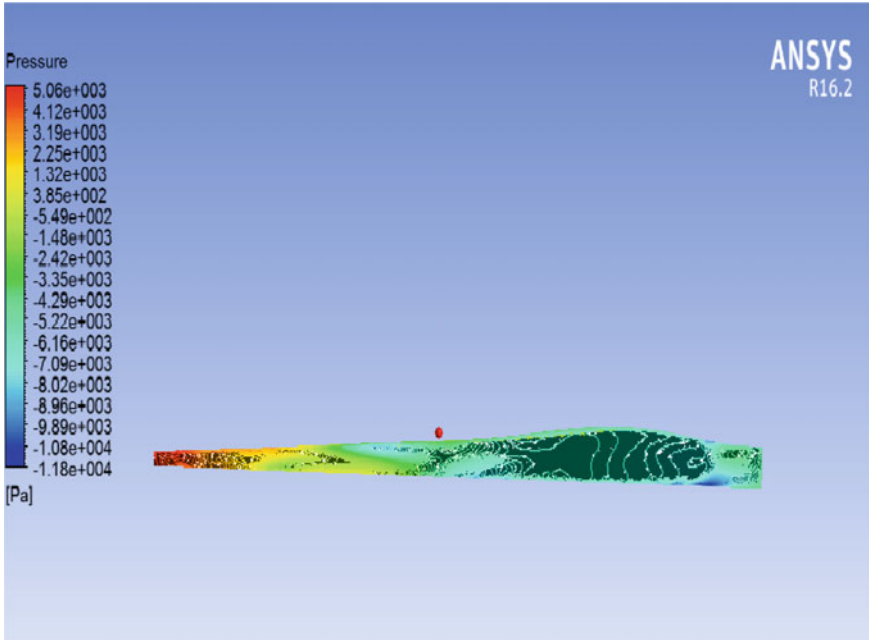


Fig. 8 Pressure contours for wind turbine run a suction outside of blade

pressure in the trailing edge is very high and that the pressure of the upper surface is very low compared to the lower surface which generates high pressures in order to lift the blade towards the high.

4 Conclusion

To extract the characteristics of the proposed NACA 0006 type wind turbine blade, the choice was made on the $k - \omega$ SST turbulence model solved using the commercial code Ansys Fluent 16.2, which proved to be the best to predict aerodynamic parameters efficiently and accurately. A preliminary study of the optimization of the shape of the blade of a low Reynolds number wind turbine is carried out. The optimization uses a straight 3D non-conical wind turbine blade with a cross section of the NACA 0006 blade as the geometry of the base blade. The CFD simulation process begins with the creation of a two- and three-dimensional domain and its appropriate discretization. The aerodynamic characteristics of the NACA 0006 for a specific Reynolds number $Re = 5 \times 10^4$ were established in order to be able to present the results of the numerical model of turbulence chosen, then to validate them with the existing experimental data of the national advisory committee of aeronautics in the wind tunnel (NACA). We used 2-D calculations to verify the results of the blade

performance simulation used on the proposed horizontal axis wind turbine HAWT. The results show a good agreement between the numerical and experimental data, furthermore we have noticed that the $k - \omega$ SST model had the same behavior with the observed data at a range angles of attack $[-10.5^\circ; 10.5^\circ]$. Therefore, we deduced that the NACA 0006 is an efficient shape at every attack angles and can be used for capturing the kinetic energy of wind and further converting it into electrical energy.

References

1. Ouahabi MH, Benabdelouahab F, Khamlichi A (2017) Analyzing wind speed data and wind power density of Tetouan city in Morocco by adjustment to Weibull and Rayleigh distribution functions. *Wind Eng* 41(3):174–184
2. Ouahabi MH, Elkhachine H, Benabdelouahab F, Khamlichi A (2020) Comparative study of five different methods of adjustment by the Weibull model to determine the most accurate method of analyzing annual variations of wind energy in Tetouan—Morocco. *Procedia Manuf.* 46c:698–707 (Elsevier)
3. Abbot H, von Doenhoff AE (1959) *Theory of wing sections*. Dover Publications, New York
4. Çetin NS, Yurdusev MA, Ata R, Özdemir A (2005) Assessment of optimum tip speed ratio of wind turbines. *Math Comput Appl* 10(1):147–154
5. Maalawi KY, Badr MA (2003) A practical approach for selecting optimum wind rotors. *Renew Energy* 803–822
6. Panagiotis-Chrysovalantis S, Kapsalis, SpyrosVoutsinas, Nicholas S. Vlachos (2016) Comparing the effect of three transition models on the CFD predictions of a NACA0012 airfoil aerodynamics. *J. Wind Eng. Ind. Aerodyn.* 157: 158–170
7. Ferreira CJ, Bijl H, van Bussel G, van Kuik G (2007) Simulating Dynamic stall in a 2D VAWT: modeling strategy, verification and validation with particle image velocimetry data. *J. Phys.* 75(1), Article ID 012023
8. Zhang T, Elsakka M, Huang W, Wang Z, Ingham DB, Ma L, Pourkashanian M (2019) Winglet design for vertical axis wind turbines based on a design of experiment and CFD approach. *Energy Convers Manage* 195:712–726
9. Spentzos A, Barakos G, Badcock K, Richards B, Wernert P, Schreck S, Raffel M (2005) Investigation of three-dimensional dynamic stall using computational fluid dynamics. *. AIAA J* 43(5):1023–1033
10. Ouahabi MH, Ichenial MM, El Hajjaji A, Benabdelouahab F (2017) Application of the turbulence models at low reynolds number for horizontal-axis wind turbine design by using computational fluid dynamics (CFD). *Int J Control Autom* 10(7):179–190
11. Niu YY (1999) Evaluation of renormalization group turbulence models for dynamic stall simulation. *AIAA Journal* 37(6):770–771
12. Denis F, Hinz , Hekmat Alighanbari, Christian Breitsamter (2013) Influence of heat transfer on the aerodynamic performance of a plunging and pitching NACA0012 airfoil at low Reynolds numbers. *Journal of Fluids and Structures* 37: 88–99
13. Wang L, Quant R, Kolios A (2016) Fluid structure interaction modelling of horizontal-axis wind turbine blades based on CFD and FEA. *J Wind Eng. Ind Aerod* 158:11–25
14. Zhu J, Cai X, Gu RR (2017) Multi-objective aerodynamic and structural optimization of horizontal-axis wind turbine blades. *Energies* 10:101
15. Walters DK, Cokljat D (2008) A three-equation eddy viscosity model for Reynolds-averaged Navier Stokes simulations of transitional flow. *J Fluids Eng* 130:121–401
16. Tiantian Zhang, Zhenguo Wang, Wei Huang, Derek Ingham, Lin Ma, Mohamed Pourkashanian (2020) A numerical study on choosing the best configuration of the blade for vertical axis wind turbines. *Journal of Wind Engineering & Industrial Aerodynamics* 201: 104162

17. Şahin İ, Acir A (2015) Numerical and experimental investigations of lift and drag performances of NACA 0015 wind turbine airfoil. *Int J Mater Mech Manuf* 3(1)

Educational Strategy Combining Technological Capacity and Ant Colony Algorithm to Improve the Ideal Dispatch Using Wind Energy



Neider Duan Barbosa Castro , Jhon Alexander Hernández Martín ,
Fabiola Sáenz Blanco , and Evy Fernanda Tapias Forero 

Abstract In this article, the reader will find an educational strategy, combining technological capacity and ant colonies to improve the ideal dispatch with plants of solid generation (hydraulic and thermal) and plants with variable generation (wind), as a case study for a Colombian electricity network. In order to achieve this process, we intend to use problem-based learning strategy as follows: posing the problem, listing the known data, dividing the main problem in analog form, looking for and implementing solutions, and consequently looking at the technological assets of all plants. This information is registered into the McKinsey matrix and finally, the solutions are analyzed.

1 Introduction

The projections of the world energy panorama for the next 20 years contemplate an energy scenario based on an intensive exploitation of resources due to the increase in energy demand throughout the world. This could have worrying consequences and impacts at the energy level, due to the reduction of reserves and at the economic level, due to the increase in fuel prices, among other aspects. Under these conditions, non-conventional renewable energies emerge as a mechanism within the energy landscape that favors environmental sustainability [1]

N. D. Barbosa Castro (✉)
Compensar University Foundation, Bogota, Colombia
e-mail: ndbarbosac@ucompensar.edu.co

J. A. Hernández Martín
National Learning Service, Medellín, Colombia
e-mail: jhonmartin56@gmail.com

F. Sáenz Blanco
University Distrital Francisco José de Caldas, Bogota, Colombia
e-mail: fsaenz@udistrital.edu.co

E. F. Tapias Forero
Colombian Technology Corporation, Bogota, Colombia
e-mail: eftapiasf@correo.udistrital.edu.co

In Colombia there are some educational strategies for the training of engineers in energy dispatch [2] but in general for the Colombian industry, adequate knowledge management loses context; therefore, in this educational strategy, it is intended to find some key factors of knowledge management that influence this process; having as a general objective to optimize resources, physical objects, processes and methods in order to improve the understanding and competence development of office and field workers of the electricity sector.

In this article, an educational strategy is applied, in order to work with technological assets and ant colony, improving the ideal dispatch with solid generation plants (hydraulic and thermal) and plants with variable generation (wind), using a problem-based learning strategy. The development of the article begins by posing the problem to work, making a list with the data that is known about the problem, dividing the main problem in an analog way, looking for and implementing solutions (in this part of the process, a strategy to dispatch energy with the anthill tool is created, by entering a wind power plant and working the technological assets with the McKinsey matrix) [3], the above is done in a case study of a Colombian electricity network.

2 Educational Strategy

The educational strategy was built from more than 60 bibliographic sources The educational strategy selected is the problem-based learning (PBL) [4], adapting it to the project as shown in the illustration [5] (Fig. 1).

3 Case Study

The system with which the strategy verification will be carried out in this method is the IEEE nine-node network. The IEEE nine-node network to be worked on has three loads, three transformers, five generators and six lines [6]; the general parameters of the system are shown in Table 1.

The voltage parameters of each network node, resistors, reactances, susceptances among other parameters of the lines, transformers and generators, can be seen in the IEEE nine-node system specifications in the bibliography [6] ((Fig. 2).

4 Strategy Application in Stages 1, 2, 3 and 4

This part of the article shows the application of the strategy designed in a case study of a IEEE electrical network.

Fig. 1 Educational strategy

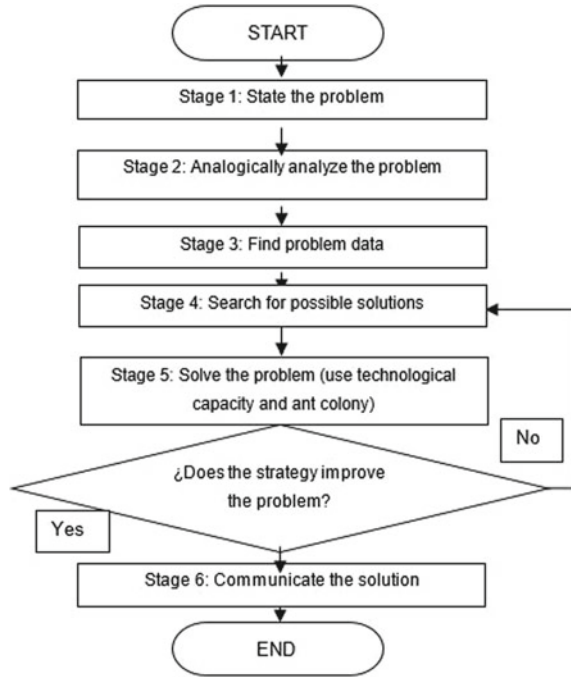


Table 1 System parameters

Parameter	Value
Base power	100 MVA
Nominal node voltage	230 kV
Maximum voltage	1.1 pu
Minimum voltage	0.9 pu
Transformer 1	16.5/230 kV
Transformer 2	18/230 kV
Transformer 3	13.8/230 kV

4.1 Stage 1: Statement of the Problem

Administrators and personnel performing the energy dispatch use complex statistical techniques to carry out this process without taking into account current learning strategies, intermittent plants, and computational tools, such as ant colony.

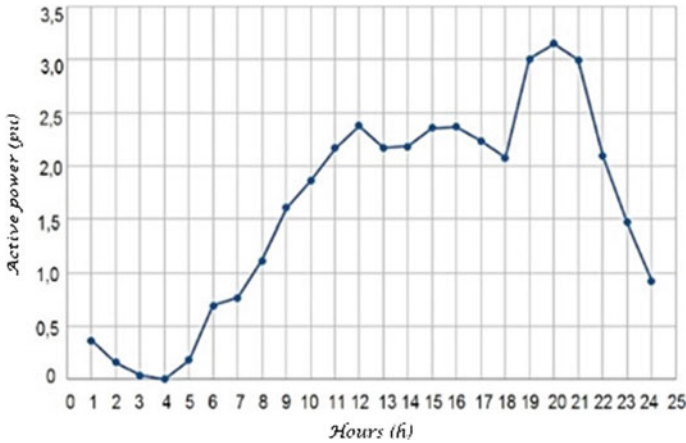


Fig. 2 Load curve for the network. *Source* Master's degree project entitled: "Method to carry out the economic dispatch of energy. Case study on a Colombian electricity grid"

4.2 Stage 2: Analogical Analysis the Problem

Based on the: "Educational strategy for economic dispatch and environmental impact in an electrical network using genetic algorithms and linear optimization" [1, 7], the following problems are proposed.

- If the dispatch continues to be carried out using current generation technologies exclusively, it will be difficult to supply the country's demand in the long term.
- The operators are unaware of the management of strategies based on metaheuristics and linear optimization methods to improve processes, such as economic dispatch and efficiency of an electrical network.
- The operators do not know the concepts of economic dispatch.
- Managers and administrative staff do not use technology management models.

Which implies the following statements:

- Problem 1: Lack of electricity market concepts, metaheuristics and linear optimization.
- Problem 2: Entrance of intermittent plants into the economic dispatch
- Problem 3: Managers and administrative staff do not use technology management models.

4.3 Stage 3: Known Data of the Problem

The known data of the problem are the following:

- Problem 1: Administrative staff's evaluations on electricity market concepts, ignorance of the concept of metaheuristics and ignorance of the concept of linear optimization.
- Problem 2: Technical variables and intermittent plant types
- Problem 3: Results of the McKinsey study.

4.4 Stage 4: Determine Possible Solutions

The possible solutions found are:

- Problem 1: Conceptual map of diagnosis, training of personnel and conceptual map of evaluation.
- Problem 2: Create strategies to assess energy dispatch.
- Problem 3: Designing models for the management of technological capabilities (An approach by Sáenz Blanco and Barbosa, 2019) [8]

5 Strategy Application in Stages 5 and 6

5.1 Solve the Problems

Next, the proposed solutions will be carried out for each of the problems.

Problem 1

The solution to this problem was proposed in three stages, taking into account the meaningful learning strategy [1]:

Stage 1: A representative sample of eight energy operator managers were asked to explain the concepts of electricity market, metaheuristics and linear optimization, graded using one (x) by those who had clear definitions, as seen in Table 2.

Stage 2: Concept training is carried out.

Stage 3: A representative sample of eight people were asked to explain the concepts of the electrical market, metaheuristics and linear optimization, after training, and then graded using one (x) by those who had clear definitions; results are displayed in Table 3.

Problem 2

In order to achieve the economic dispatch, the strategy is proposed as shown in Fig. 3, for the negotiation of the stock market price, including firm generation plants (hydraulic and thermal) and plants with variable wind generation for dispatch [1].

Each of the stages of this strategy will continue to be explained.

Table 2 Diagnostic of concepts

Person	Electricity market	Metaheuristics	Lineal optimization
Person 1	x		X
Person 2		X	
Person 3	X		
Person 4	X		
Person 5	X		X
Person 6			
Person 7	X		
Person 8			X

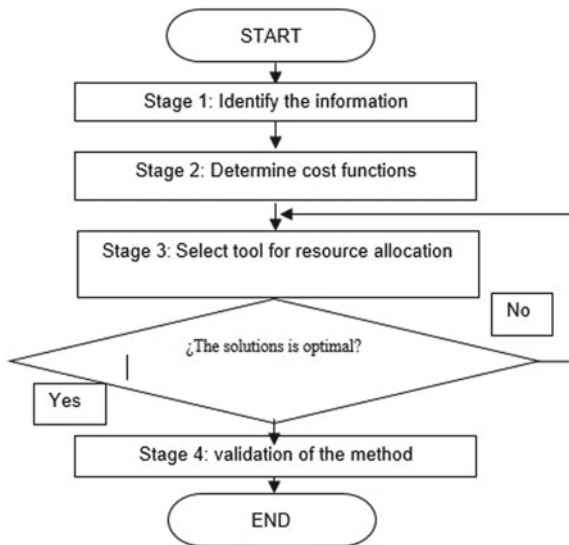
Source Own elaboration

Table 3 Concept evaluation

Person	Electricity market	Metaheuristics	Line optimization
Person 1	x	X	X
Person 2	x	X	X
Person 3	x	X	X
Person 4	x	X	X
Person 5	x	X	X
Person 6	x		X
Person 7	x	X	X
Person 8	x	X	X

Source Own elaboration

Fig. 3 Strategy for energy dispatch Source



System information

The system with which the strategy verification will be carried out in this method is the IEEE nine-node network (see information in numeral II- case study).

Cost features

For the development of this article, there are four types of generation plants: wind, solar, hydraulic and thermal; the cost of the energy injected by all plants is obtained by performing simulations in the Homer1 software [9], based on technical parameters of each plant.

Optimization tools selected for ideal dispatch

In order to determine the tool selected, it was necessary to take into account that ideal dispatch is an optimization process, which allocates resources, looking for the minimum cost. Bearing in mind that electrical networks are NP-type problems and that the functions of the parameters that will fall within the resource allocation process are not always linear functions, heuristic and metaheuristic tools are selected to perform this process [1].

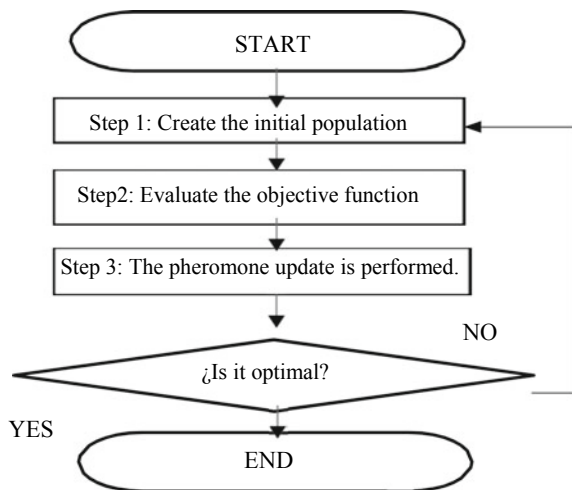
Considering the previous, the tool to be worked with is ant colony.

- Ant colony algorithm

The ACO algorithm is inspired by the actual behavior of ants. These insects find the shortest route to move from their colony to food; the above can be done taking into account a trace of pheromones that each of them leaves when moving [10]. If there are different traces of pheromones the ants are able to find which of the paths has the highest concentration; this process is performed in the following steps (See flowchart and explanation) [10].

Next, each of the steps set out in this diagram will be explained (Fig. 4).

Fig. 4 Ant colony algorithms. *Source* Master's degree project entitled: "Method to carry out the economic dispatch of energy. Case study on a Colombian electricity grid"



- Step 1: Define number of ants of the colony or initial population and define the paths that each individual will follow, bearing in mind the cost (pheromone intensity), given by the established merit function.
- Step 2: Fitness and exercise restrictions are evaluated for this problem (See Eq. 1).

$$F = CX1 + CX2 + CX3 \tag{1}$$

where:

- CX1: Cost of power injected in one hour by a wind plant.
- CX2: Cost of power injected in one hour by a thermal plant
- CX3: Cost of power injected in one hour by a hydraulic plant

The following restrictions will be met for this issue:

- The Power injected per hour must be less than the demand
- The power injected by each plant type must be less than or equal to the maximum power generated by the plant.
- Step 3: Feedback must be made by updating and checking if the selected path is the one with the highest concentration of pheromones.
- Step 4: The path is verified to be optimal.

For this process, the software is run over a 24-h period. The best dispatch obtained shows an input percentage of 80% for the hydraulic plant, 14% for the thermal plant and 6% for the wind plant (Fig. 5).

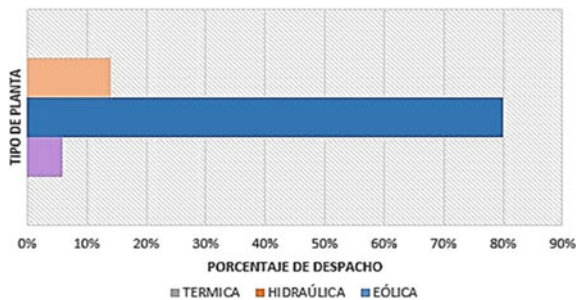
Validation of the method

The results were contrasted with those obtained by the operator and it was established that the lower dispatch price per kWh/day is obtained using the tool presented.

Problem 3

As a solution to problem 3, a technological management model is proposed, which includes the stages of:

Fig. 5 Percentage of dispatch of each plant in a day. *Source* Master’s degree project entitled: “Method to carry out the economic dispatch of energy. Case study on a Colombian electricity grid”



Technology classification

Considering technology as the input and tools that more easily allow to achieve a specific purpose, they can be classified as: [11, 12]

Humanware: these are technologies that contemplate all the efforts and strategies aimed at achieving the human element to adopt attitudes, behaviors and understanding [13, 14] of the production process; among these, we can include all those which allow the strengthening of intellectual and relational capital.

Infoware: these are technologies that allow the persistence of accumulated knowledge to save time in individual learning. Among them, we have all the manuals of processes and procedures, digitized and non-digitized databases and also document management.

Technoware: this is the technology embedded in objects, whether tangible or intangible. In particular, these technological assets refer to software and hardware [15].

Orgware: these technological assets are embedded in the organization [15] and consists of the activities of planning, organization, activation, motivation and control of operations [13] that is, the administrative aspects in the Generating Units.

Determination of the technological asset

The technological inventory of a generation plant is determined by listing all of its strategic technologies, based on the national guide to surveillance and strategic intelligence and using technological management techniques.

Evaluation of the technological asset

The evaluation of technological assets is carried out globally (by groups of technology generation and classification), according to degree of maturity, modernity, importance and strategy in the project. In this order of ideas:

- According to maturity
 - Emerging (Score 5)
 - Growth (Score 4)
 - Mature (Score 3)
 - Saturation (Score 2)
 - Obsolescence (Score 1)
- According to degree of modernity
 - Cutting edge (Score 4)
 - Modern (Score 3)
 - Outdated (Score 2)
 - Primitive (Score 1)
- According to the level of strategic importance
 - Key (Score 5)
 - Emerging (Score 3)

- Basic (Score 1)
- From The Point of View of a Project
 - Essential (Score 5)
 - Convenient (Score 3)
 - Auxiliary (Score 1)

After determining the technological assets to be evaluated with the previous scale, the McKinsey matrix is made.

The McKinsey matrix was implemented, as it allows to “position each of our assets on a Cartesian plane (X-axis importance, Y-axis evaluation), resulting in a field given by a diagonal division of the plane, thus determining that the red technological assets are not decisive for the development of the strategic unit, the yellow ones are causal, that is, they are important, as they create an effect but are not strategic and the green ones are strategic” [16], characterizing the axes as follows:

$$X = \frac{\text{Strategic Importance}(1 \text{ to } 5) * \% \text{ de Dispatch}}{5} \tag{2}$$

$$Y = \frac{\text{Cost } (1 \text{ to } 5)}{5} \tag{3}$$

The evaluation of these assets is reflected in the following figure, where the ideal energy dispatch characterized by the Ant colony algorithm is:

- Wind 6%
- Hydraulic 80%
- Thermal 14%

The results of this analysis are reflected in the graph (Fig. 6).

Analysis of results of the McKinsey matrix

Taking into account the previous figure, results are:

Fig. 6 McKinsey matrix.
Source Author based in [17, 18]

ACTIVO TECNOLÓGICO		CALIFICACION
HUMANWARE	EOLICA	0,108
INFOWARE		0,24
TECHNOWARE		0,18
ORGWARE	HIDRAULICA	0,18
HUMANWARE		1,28
INFOWARE		1,92
TECHNOWARE		2,56
ORGWARE	TERMICA	1,28
HUMANWARE		0,14
INFOWARE		0,448
TECHNOWARE		0,56
ORGWARE		0,224

- In the wind plant, work should be done to improve strategic planning and the management of manuals, instructions, protocols for the use of the plants, seeking to reduce technical costs.
- In the hydraulic plant, work must be done to improve the handling of manuals, instructions, protocols and the errors that human resources (engineers and technicians) may commit, in the management of plants, seeking to reduce resources.
- On the other hand, it is necessary to take into account that the assets to be potentiated, in order to improve dispatch, are technoware and infoware of this type of technology, since they are the ones that provide the best result to the process.
- In the thermal plant, work should be done to improve strategic planning, selection, maintenance, and purchase of resources and the management of manuals, instructions, and protocols for plant management, seeking to reduce resources.

6 Conclusions

The strategy implemented shows that through the application of problem-based learning (PBL) and meaningful learning, the energy dispatch process can be improved by finding the solution to the three problems identified; leading to concept acquisition, finding the best price on the market and selecting the technological assets that, if implemented, could improve the cost of generation.

The solution to the first problem involved using meaningful learning to see that the administrative staff and operative personnel of the energy sector understood the concepts of metaheuristics, linear optimization and the electricity market by 95.8%.

For the solution of the second problem, the ant colony tool, used to improve the ideal dispatch in an electrical network, gives us the optimal score in all simulations, thus obtaining the lowest cost on the market.

Concerning the third problem, the solution consisted on using the technological management model proposed, as it shows that the strategic technological assets of technoware and infoware in hydraulic generation require improvement in order to achieve better cost in ideal dispatch.

References

1. Tapias EF (2019) Model for economic dispatch with wind and/or photovoltaic generation plants. Case study on a Colombian electricity grid
2. Trujillo-Guajardo LA, Conde-Enr-quez A (2012) Educational tool for the training of engineers in electrical protections: distance relay. *Ing Investig Tecnol* 13:215–225
3. Solleiro JL (2004) Competitiveness and innovation systems: the challenges for the insertion of Mexico into the global context. *Ibero-America-Globalization Top Cienc Tecnol* 2:165–197
4. Educational Innovation Service of the Polytechnic University of Madrid (2008) Problem-based learning
5. Y. Fields (2000) Learning teaching strategies

6. Terzioğlu R (2013) Probabilistic load flow analysis of the 9 bus WSCC system. *Int J Sci Res Publ* 3(2250–3153):62
7. Tapias EF, Santamaría F, Alarcón A (2019) Educational study for economic office and environmental impact in an electrical network using genetic algorithms and linear optimization
8. Barbosa ND, Saenz Blanco F (2019) Design, structuring and verification of a model of management of technological capacities: applicable to categorized research groups of the University of Distrital (Document in Construction), Francisco District University Jose de Caldas
9. HOMER Pro - Microgrid software for designing optimized hybrid microgrids, HOMER Energy by UL 1790 30th St, Suite 100 Boulder, CO 80301 USA
10. Carvajal SX, López JM, Lemoine CA (2009) «Reconfiguración de sistemas de distribución de energía eléctrica usando un algoritmo de optimización basado en colonia de hormigas» *Tecnura* 12:14–22
11. Durán Pabón A, Robles Algarín C, Rodríguez Alvarez O (2019) Analysis of the management model for the development of technological innovation in the public universities of the Caribbean coast region of Colombia Analysis of the management model for the development of technological innovation in public universities. *Spaces* 40(1)
12. T. e I. P. Ministry of Science, National Guide to Surveillance and Strategic Intelligence (2015) Good practices for generating territorial VeIE management systems
13. Ojeda Gómez S (2000) Proposal for traffic pacification in the White City—National University of. *Rev Ing Investig* No, no. 46, pp 24–27
14. Restrepo González G (2000) The concept and scope of technology management
15. Toro D, Cadavid A (2014) Proposal of methodology for the transfer of technology in Colombian Locería s.a.
16. Sáenz Blanco F, Barbosa ND, Tapias Forero EF (2018) Methodological proposal to determine the strategic technological capabilities needed to assemble an electrical processing substation, with European dual bar configuration (bar main and transfer), vol 10, no 5, pp 883–1056
17. White Elders F (2016) Technological management class notes
18. Tapias A, Santamaría EF, Alarcón F (2019) Educational study for economic office and environmental impact in an electrical network using genetic algorithms and linear optimization

A New Method for Photovoltaic Parameters Extraction Under Variable Weather Conditions



Aissa Hali and Yamina Khlifi

Abstract This work suggests a new method for extracting parameters from the current-voltage characteristics of photovoltaic (PV) panel to establish translational relations that allows to predict these PV parameters in other conditions of temperature and irradiation levels. This method is based on the knowledge of few selected points which are the short-circuit point, the maximum power point, and the open circuit point. These points are extracted from the current-voltage characteristics provided by the manufacturer's datasheet. Single diode model is chosen to represent the PV panel which is known as five parameters model. It includes two parasitic resistances, diode saturation current, diode ideality factor, and photo-current. The main results of simulations in Matlab environment show that the five PV parameters varies as function of irradiance and temperature. The proposed technique is compared to other published methods applied on Kyocera KC175GHT-2 PV panel. The obtained results show that the new suggested method of predicting PV parameters presents a lower statistical error whatever the weather conditions. Therefore, the new method is validated and more precise than extraction methods reported in the literature.

Keywords Matlab · Panel · Photovoltaics parameters · Statistical errors · Trust Region Dogleg algorithm · Translational relations

1 Introduction

The overall performance of a photovoltaic (PV) panel is willing to degrade over time, due to exposure weather conditions and aging. Consequently, predicting these degradations is crucial to avoid their destructive influences on photovoltaic energy production. In this framework, the evaluation of photovoltaic panel behavior in differ-

A. Hali (✉) · Y. Khlifi
Laboratory of Renewable Energy, Embedded Systems and Data Processing,
National School of Applied Sciences Oujda, Oujda, Morocco
e-mail: haliassa11@gmail.com

Y. Khlifi
e-mail: khlifi_yamina@yahoo.fr

ent climatic conditions, mainly temperature and irradiance, is required. The current-voltage characteristics of PN junction photovoltaic cells are usually described based on a single diode circuit model [1]. As mentioned in reference [2], this simple model provides a good compromise between the accuracy and simplicity of photovoltaic modeling. The photovoltaic circuit includes five parameters, called photocurrent, reverse saturation current, diode ideality factor, series resistance and shunt resistance.

Over the years, much attention has been devoted to developing an accurate model for determining PV parameters over a wide range of irradiation and temperature conditions [3–5]. The currently disclosed PV parameter extraction methods can be divided into two categories [6]. The first type is the curve fitting method. It uses all ranges of current-voltage data, so it can produce more accurate parameter values. Therefore, this method is expensive because it requires all experimental points of current-voltage characteristics. The second category requires only the coordinates of few selected points on the current-voltage characteristics, such as short circuit, open circuit and maximum power point (MPP), which are usually provided by the manufacturer's data sheet under standard test conditions (STC). This method is very important in practical applications because it is fast and requires a small amount of data.

Most published works involve parameter extraction under STC. In addition, it is assumed that some of the determined parameters are unchanged under environmental conditions, therefore, except STC, it can be used in the case of no change in climatic conditions [4]. In fact, the experiment proves that the PV parameter value will change with the temperature and the irradiance. Therefore, the assumption that certain parameters are constant under weather changes is physically invalid [7–10]. Therefore, it is necessary to develop accurate translation equations for the unknown PV parameters.

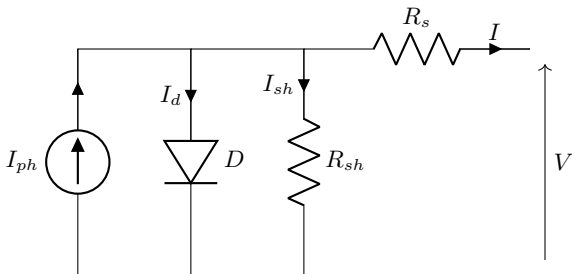
In this context, this work presents a simple, fast and accurate method of extracting PV parameters based on the use of few selected points in the current-voltage curves provided by the manufacturer's data sheet for different temperatures and irradiance. Therefore, based on the evolution of PV parameters along with temperature and irradiation, it is possible to determine translation formulas suitable for predicting these parameters in other weather conditions with high accuracy. The high precision of the proposed method is demonstrated by a comparative study, in terms of statistical errors, with the recently reported methods Celik and Acikgoz [11], Brano et al. [12], Laudani et al. [13], Femia et al. [14], Villalva et al. [5], Cubas [16] Tuyen Nguyen-Duc [5].

2 Electrical Modeling of a PV Cell

The most frequently used equivalent circuits in literature to model solar cells, are known as single diode model or five PV parameters as shown in Fig. 1.

The equation relating the current I generated by the photovoltaic cell to the voltage V is given by:

Fig. 1 Equivalent electrical photovoltaic cell model



$$I = I_{ph} - I_s \left(e^{\frac{V+R_s I}{nV_t}} - 1 \right) - \frac{V + R_s I}{R_{sh}} \tag{1}$$

where: I : output current [A], V : output voltage [V], I_{ph} : photo-current [A], I_s : diode reverse saturation current [μA], R_s, R_{sh} : are respectively series resistance associated with the cell [Ω] and the shunt resistance [Ω], n : the ideality factor, and $V_t = \frac{N_s K_B T}{q}$ is the thermal voltage of the module where N_s : photovoltaic cells are connected in series q : Electron charge [$q = 1.602 \cdot 10^{-19} \text{ } ^\circ C$], K_B : Boltzmann's constant [$K_B = 1.38 \cdot 10^{-23} \text{ J/}^\circ K$], T : Temperature [$^\circ K$].

3 Description of the New Method for Extracting PV Parameters

In the case of a single diode model, the new PV parameter extraction method described below will be used. In order to extract the physical parameters R_s, R_{sh}, n, I_s and I_{ph} , by evaluating Eq. (1) at three remarkable points: the short circuit point ($0, I_{sc}$), the open circuit point ($V_{oc}, 0$), and the maximum power point (MPP) (V_m, I_m):

$$I_{sc} - I_{ph} + I_s \left(e^{\frac{R_s I_{sc}}{nV_t}} - 1 \right) + \frac{R_s I_{sc}}{R_{sh}} = 0 \tag{2}$$

$$I_{ph} - I_s \left(e^{\frac{V_{oc}}{nV_t}} - 1 \right) - \frac{V_{oc}}{R_{sh}} = 0 \tag{3}$$

$$I_m - I_{ph} + I_s \left(e^{\frac{V_m + R_s I_m}{nV_t}} - 1 \right) + \frac{V_m + R_s I_m}{R_{sh}} = 0 \tag{4}$$

The fourth nonlinear equation is derived from the fact that the power derivative with respect to voltage in MPP is zero:

$$I_m - I_s \left(\frac{V_m - R_s I_m}{nV_t} \right) \left(e^{\frac{V_m + R_s I_m}{nV_t}} \right) - \frac{V_m - R_s I_m}{R_{sh}} = 0 \tag{5}$$

By eliminating the R_{sh} , reformulating Eqs. (2)–(5) and assuming that $I_{ph} \gg e \frac{R_s I_{sc}}{nV_t}$ [17], a fifth equation can be evaluated at MPP. Therefore, a first parameter which is the ideality factor can be determined:

$$nV_t \left(\frac{I_{sc}}{I_{sc} - I_m} + \ln \left(\frac{I_{sc} - I_m}{I_{sc}} \right) \right) - 2V_m + V_{oc} = 0 \tag{6}$$

So the system, which initially consists of five equations, can then be reduced to a system of four equations as a function of five PV. the ideality factor (n) from Eq. 6 is injected into Eqs. (2)–(5). Thus, four PV parameters (R_s , R_{sh} , I_{ph} and I_s) are extracted by solving this system of non-linear equations using Trust-Region-Dogleg Algorithm (TRDLA).

4 Results and Discussion

4.1 Parameters and Characteristics of PV Panel

The three remarkable points values for evaluating the PV parameters extraction model are extracted from the current-voltage I(V) characteristics of Kyocera KC175GHT-2 panel provided by manufacture’s datasheet [18] for various temperature and irradiation levels. The injection of the remarkable points values into Eqs. (2)–(6) allows to extract the five unknown PV parameters. The obtained values are represented in Table 1:

Taking account of these extracted parameters values, one can reproduce the theoretical I(V) characteristics as shown in Fig. 2. The comparison with experimental current-voltage curves show a good agreement whatever the irradiation and temperature values and thus the proposed TRDLA method is validated.

Table 1 Extracted PV parameters values as function of temperature and irradiance

Temperature and irradiance		Five unknown parameters					RMSE [A]
T (°C)	G (W/m ²)	R_s (Ω)	R_{sh} (K Ω)	n	I_s (μA)	I_{ph} (A)	
25	200	0.8056	1.5767	1.3963	0.2089	1.6188	0.0092
25	400	0.3499	0.8358	1.4459	0.4574	3.2374	0.0180
25	600	0.1861	0.5760	1.4838	0.8263	4.8556	0.0369
25	800	0.1357	0.4419	1.5033	1.0922	6.4740	0.0354
25	1000	0.1005	0.3597	1.5219	1.4225	8.0923	0.0476
50	1000	0.1509	0.2768	1.2955	1.8735	8.1739	0.0386
75	1000	0.1727	0.1908	1.1525	5.0109	8.2564	0.0557

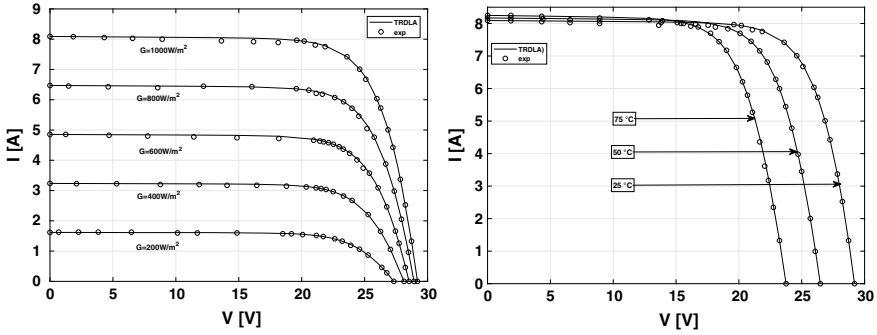


Fig. 2 Comparison between Simulated and experimental I(V) characteristics of Kyocera KC175GHT-2 panel: (left) as function of irradiation level (G) and fixed T = 25 °C; (right) as function of temperature and fixed G = 1000 (W/m²)

4.2 Extraction Method Validation

The method considered can be accurately evaluated by calculating the root mean square error (RMSE), which measures the deviation rate between the value predicted by the extraction method and the experimental value. For the m current measurements performed, RSME is defined as:

$$RMSE = \sqrt{\frac{1}{m} \sum_{i=1}^m \left(I_i - I_{cal,i}(V_i, P) \right)^2} \tag{7}$$

I_i is the measured current for each voltage V_i at i^{th} of m measured data points (I_i, V_i) . $I_{cal,i}(V_i, P)$ is the calculated current determined for each V_i , solving the nonlinear Eq. 1 with the optimized set of five parameters $P = (I_{ph}, I_s, n, R_s, R_{sh})$. Fig. 3 reports the RMSE of the eight methods in two cases. The first case is function of temperature and fixed irradiation level ($G_{ref} = 1000 \text{ W/m}^2$), and the second case is function of the irradiation level at fixed temperature T_{ref} is equal to 25 °C. In addition, the RMSE values obtained by the proposed TRDLA-based method (Table 1) are compared with the most recent methods [5, 11–16]. From the results presented in Fig. 3 it can be clearly seen that the five PV parameters identified by the proposed method exceed the generally compared methods. Its high accuracy determines the best RMSE value regardless of weather conditions.

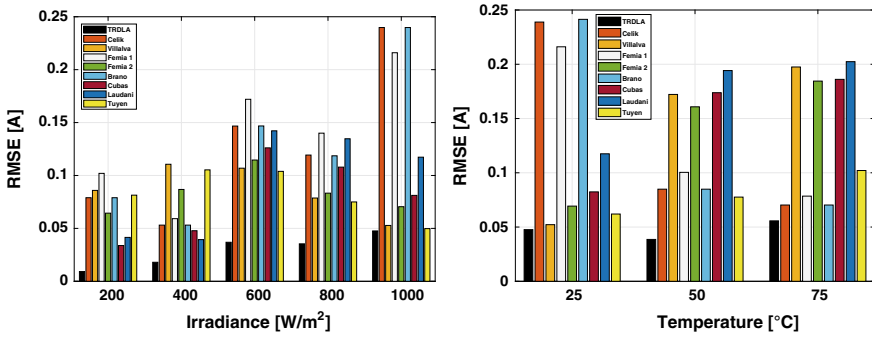


Fig. 3 Comparison of RMSE values obtained by TRDLA and published methods of parameters extraction of Kyocera KC175GHT-2 panel: (left) RMSE as function of irradiance at fixed $T_{ref} = 25 \text{ }^\circ\text{C}$; (right) RMSE as function of temperature at fixed irradiation level $G_{ref} = 1000 \text{ (W/m}^2\text{)}$

5 Effect of Temperature on Photovoltaic Parameters

The variation of the five extracted PV parameters with constant radiation level ($G_{ref} = 1000 \text{ W/m}^2$) with temperature is shown in Fig. 4, as a function of the radiation level at a fixed temperature ($T_{ref} = 25 \text{ }^\circ\text{C}$) as shown in Fig. 5. The fitting curve obtained by non-linear regression represents the change of PV parameters with temperature, and an expression describing its behavior can be derived:

$$\log[I_s(T, G_{ref})] = \log[I_s(T_{ref}, G_{ref})][1 + a_{I_s}(T - T_{ref})^2 + b_{I_s}(T - T_{ref})] \quad (8)$$

$$I_{ph}(T, G_{ref}) = I_{ph}(T_{ref}, G_{ref})[1 + a_{I_{ph}}(T - T_{ref})] \quad (9)$$

$$n(T, G_{ref}) = n(T_{ref}, G_{ref})[1 + a_n(T - T_{ref})^2 + b_n(T - T_{ref})] \quad (10)$$

$$R_s(T, G_{ref}) = R_s(T_{ref}, G_{ref})[1 + a_{R_s}(T - T_{ref})^2 + b_{R_s}(T - T_{ref})] \quad (11)$$

$$R_{sh}(T, G_{ref}) = R_{sh}(T_{ref}, G_{ref})[1 + a_{R_{sh}}(T - T_{ref})^2 + b_{R_{sh}}(T - T_{ref})] \quad (12)$$

Coefficients a_i and b_i , where i is I_{ph} , I_s , n , R_s and R_{sh} , refer to the PV parameter value $I_{ph}(T_{ref}, G_{ref})$, $\log[I_s(T_{ref}, G_{ref})]$, $n(T_{ref}, G_{ref})$, through nonlinear The $R_s(T_{ref}, G_{ref})$ and $R_{sh}(T_{ref}, G_{ref})$ obtained by regression are shown in Fig. 4.

As can be seen in Fig. 4, the temperatures affect all the extracted PV parameters. Therefore, its influence must be considered when modeling, evaluating and controlling the production of PV panels. The behavior of the obtained PV parameters with temperature changes is highly consistent with the previously published results [3], [4].

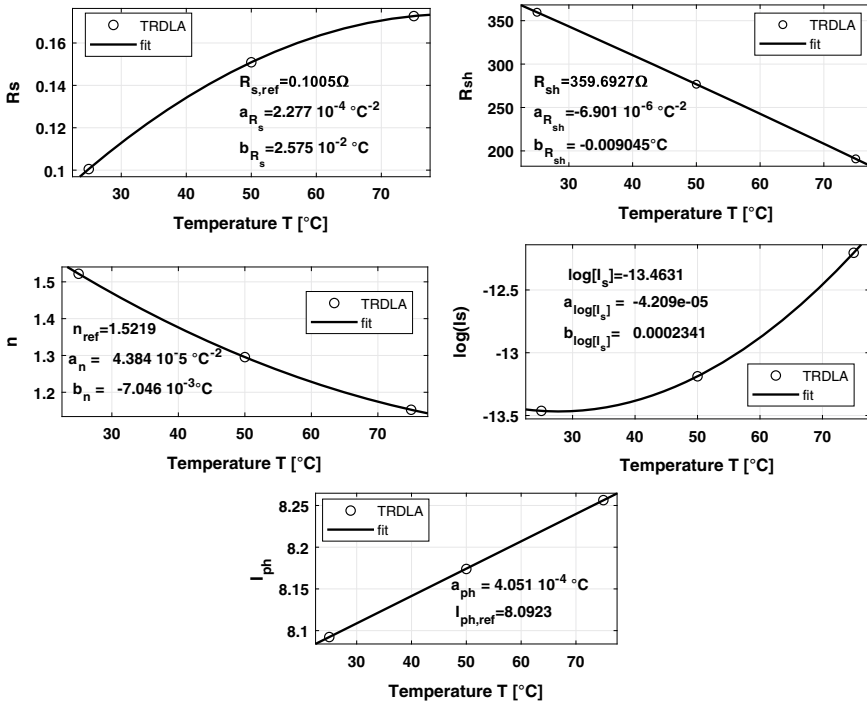


Fig. 4 Evolution of the five PV parameters of Kyocera KC175GHT-2 panel as function of temperature at fixed irradiation level $G = 1000 \text{ (W/m}^2\text{)}$

The observed behavior of R_s may be understood in terms of various contributions to the series resistance. In fact, in a junction cell, the series resistance (R_s) is mainly the sum of the contact resistance of the metal semiconductor R_C , the base resistance R_B , the emitter resistance R_E , the resistance of the busbars R_{bus} , and the resistance of the finger R_F [19].

The decrease in shunt resistance was explained by the combination of tunneling and trapping-detrapping due to the states of defects in the space charge area of the solar cell [20]. The reason why the value of n decreases with increasing temperature can be explained as: the resistance of the semiconductor active layer decreases [7], or the effect of temperature on the surface and the Shockley-Hall-Hall recombination mechanism [21].

The increase in reverse saturation current and photocurrent can be attributed to the decrease in band gap [8, 22].

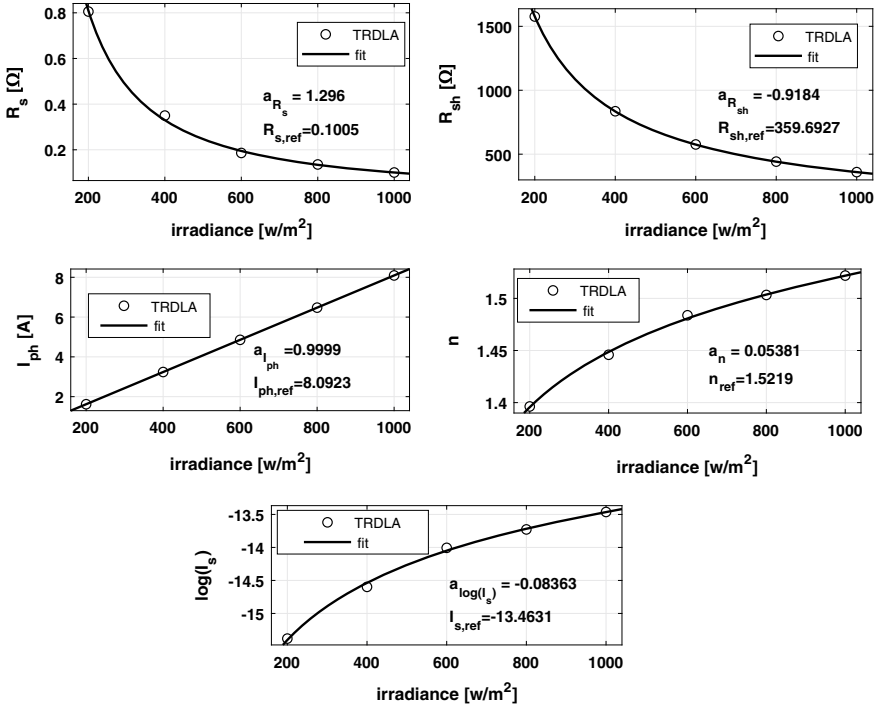


Fig. 5 Evolution of the five PV parameters of Kyocera KC175GHT-2 panel extracted using TRDLA based method as function of irradiation level at fixed temperature $T = 25\text{ }^{\circ}\text{C}$

6 Effect of Irradiance on Photovoltaic Parameters

In order to study the effect of irradiation level on the performance of photovoltaic panels, a study similar to the effect of temperature was carried out. Figure 5 shows the variation of PV extraction parameters at a solar irradiance of $T_{ref} = 25\text{ }^{\circ}\text{C}$. The non-linear regression fit curves allow us to deduce the expressions that describe these variations. Therefore, the PV parameter value at a given irradiance can be expressed by the following formula:

$$\log[I_s(T_{ref}, G)] = \log[I_s(T_{ref}, G_{ref})] \left(\frac{G}{G_{ref}} \right)^{a_{I_s}} \tag{13}$$

$$I_{ph}(T_{ref}, G) = I_{ph}(T_{ref}, G_{ref}) \left(\frac{G}{G_{ref}} \right)^{a_{I_{ph}}} \tag{14}$$

$$n(T_{ref}, G) = n(T_{ref}, G_{ref}) \left(\frac{G}{G_{ref}} \right)^{a_n} \tag{15}$$

$$R_s(T_{ref}, G) = R_s(T_{ref}, G_{ref}) \left(\frac{G}{G_{ref}} \right)^{a_{R_s}} \quad (16)$$

$$R_{sh}(T_{ref}, G) = R_{sh}(T_{ref}, G_{ref}) \left(\frac{G}{G_{ref}} \right)^{a_{R_{sh}}} \quad (17)$$

Equations 13–17 can be used to accurately predict PV parameters, and therefore I (V) characteristics at any level of irradiation and constant temperature.

An increase in the level of irradiation leads to an increase in reverse saturation current, photocurrent and ideality factors, but to a reduction in series resistance and shunt resistance. These results are consistent with the results from previous works [3, 4].

7 Conclusion

In this work, an accurate and simple method to predict the photovoltaic parameters of solar panel in different weather conditions is performed. The advantage of the new method is that very few selection points need to be understood from the current-voltage characteristics. A suitable equation is determined to express the influence of temperature and irradiance on PV parameters. Furthermore, from the comparison with reported methods in literature, one can conclude that the proposed Trust Region Dogleg Algorithm-based method gives the best value of RMSE whatever temperature and irradiation levels. So, it outperforms the overall of the compared methods.

References

1. Hall RN (1981) Silicon photovoltaic cells. *Solid State Electron* 24(7):595–616. [https://doi.org/10.1016/0038-1101\(81\)90188-X](https://doi.org/10.1016/0038-1101(81)90188-X)
2. Harrag A, Messalti S (2017) Three, five and seven PV model parameters extraction using PSO. *Energy Procedia* 119:767–774. <https://doi.org/10.1016/j.egypro.2017.07.104>
3. Yadir S et al (2020) Evolution of the physical parameters of photovoltaic generators as a function of temperature and irradiance: New method of prediction based on the manufacturer’s datasheet. *Energy Convers Manag* 203(August 2019):112141. <https://doi.org/10.1016/j.enconman.2019.112141>
4. Hejri M, Mokhtari H (2016) On the comprehensive parametrization of the photovoltaic (PV) cells and modules, pp 1–9 (2016) <https://doi.org/10.1109/JPHOTOV.2016.2617038>
5. Nguyen-Duc T, Nguyen-Duc H, Le-Viet T, Takano H (2020) Single-diode models of PV modules: a comparison of conventional approaches and proposal of a novel model. *Energies* 13(6). <https://doi.org/10.3390/en13061296>
6. Hejri M, Mokhtari H, Azizian MR, Ghandhari M, Söder L (2014) On the parameter extraction of a five-parameter double-diode model of photovoltaic cells and modules. *IEEE J Photovolt* 4(3):915–923. <https://doi.org/10.1109/JPHOTOV.2014.2307161>

7. Cuce E, Cuce PM, Bali T (2013) An experimental analysis of illumination intensity and temperature dependency of photovoltaic cell parameters. *Appl Energy* 111:374–382. <https://doi.org/10.1016/j.apenergy.2013.05.025>
8. Ghani F, Rosengarten G, Duke M, Carson JK (2015) On the influence of temperature on crystalline silicon solar cell characterisation parameters. *Sol Energy* 112:437–445. <https://doi.org/10.1016/j.solener.2014.12.018>
9. Khan F, Singh SN, Husain M (2010) Effect of illumination intensity on cell parameters of a silicon solar cell. *Sol Energy Mater Sol Cells* 94(9):1473–1476. <https://doi.org/10.1016/j.solmat.2010.03.018>
10. Chegaar M, Hamzaoui A, Namoda A, Petit P, Aillerie M, Herguth A (2013) Effect of illumination intensity on solar cells parameters. *Energy Procedia* 36:722–729. <https://doi.org/10.1016/j.egypro.2013.07.084>
11. Celik AN, Acikgoz N (2007) Modelling and experimental verification of the operating current of mono-crystalline photovoltaic modules using four- and five-parameter models. *Appl Energy* 84(1):1–15. <https://doi.org/10.1016/j.apenergy.2006.04.007>
12. Lo Brano V, Orioli A, Ciulla G, Di Gangi A (2010) An improved five-parameter model for photovoltaic modules. *Sol Energy Mater Sol Cells* 94(8):1358–1370. <https://doi.org/10.1016/j.solmat.2010.04.003>
13. Laudani A, Riganti Fulginei F, Salvini A. Identification of the one-diode model for photovoltaic modules from datasheet values. *Sol Energy* 108:432–446. <https://doi.org/10.1016/j.solener.2014.07.024>
14. Femia N, Petrone G, Spagnuolo G, Vitelli M (2017) Power electronics and control techniques for maximum energy harvesting in photovoltaic systems
15. Janzen DE, Mann KR (2015) Heteroleptic platinum(ii) isocyanide complexes: convenient synthetic access, polymorphs, and vapoluminescence. *Dalt Trans* 44(9):4223–4237. <https://doi.org/10.1039/c4dt03820g>
16. Cubas J, Pindado S, Victoria M (2014) On the analytical approach for modeling photovoltaic systems behavior. *J Power Sources* 247:467–474. <https://doi.org/10.1016/j.jpowsour.2013.09.008>
17. Ibrahim H, Anani N (2017) Evaluation of analytical methods for parameter extraction of PV modules. *Energy Procedia* 134:69–78. <https://doi.org/10.1016/j.egypro.2017.09.601>
18. http://www.testenergia.it/pdf/Kyocera_KC175GHT-2.pdf
19. Arora JD, Verma AV, Bhatnagar M (1986) Variation of series resistance with temperature and illumination level in diffused junction poly- and single-crystalline silicon solar cells. *J Mater Sci Lett*
20. Fébba DM, Rubinger RM, Oliveira AF, Bortoni EC (2018) Impacts of temperature and irradiance on polycrystalline silicon solar cells parameters. *Sol Energy* 174(September):628–639. <https://doi.org/10.1016/j.solener.2018.09.051>
21. Cotfas DT, Cotfas PA, Machidon OM (2018) Study of temperature coefficients for parameters of photovoltaic cells. *Int J Photoenergy* <https://doi.org/10.1155/2018/5945602>
22. Day J, Senthilarasu S, Mallick TK (2019) Improving spectral modification for applications in solar cells: A review. *Renew Energy* 132:186–205. <https://doi.org/10.1016/j.renene.2018.07.101>

Applying CFD for the Optimization of the Drying Chamber of an Indirect Solar Dryer



Dounia Chaatouf, Mourad Salhi, Benyounes Raillani, Samir Amraqui, and Ahmed Mezrhab

Abstract The importance of renewable energy technologies is illustrated by their dependence on inexhaustible sources, and it has a friendly relationship with the environment, because of its several advantages. This type of systems are more attractive to investors as well for researchers in terms of development. In this paper, we are particularly interested in the modern system used for drying products, more precisely the one based on solar energy, like the indirect solar dryer. It generally consists of a solar air collector that generates a flow of air that passes through it and goes up to the drying chamber. In order to make the performance of the chamber more efficient, we try in this work to improve the efficiency of the solar dryer by improving the geometry, with the aim of reducing the drying time while guaranteeing the high quality of the dried product. The geometry of the chamber is divided into two sections: the first where the trays are located and the second one is a side-mounted plenum chamber. The width of this latter as well the distance between the first tray and the rooftop of the drying chamber were studied using ANSYS FLUENT software, under the climate of the oriental region of Morocco. And the results showed that the most suitable width for the side-mounted plenum chamber is 0.4 m with an optimal distance between the first tray (the upper tray) and the top of the chamber of 0.06 m.

Keywords ANSYS FLUENT · Indirect solar dryer · Side plenum chamber

1 Introduction

The indirect solar dryer is one of the best solar dryers in terms of conserving the quality of products from the shape, color, and vitamins. Besides this, its simple structure doesn't require electricity or too much equipment, which makes it low cost [1] and the best choice for farmers. However, this type of solar dryer was not of interest to some producers due to its inherent flaw, which is the non-uniform moisture content of the end product caused by the non-uniformity of air distribution inside the

D. Chaatouf · M. Salhi · B. Raillani · S. Amraqui (✉) · A. Mezrhab
Laboratory of Mechanics and Energetics, Faculty of Sciences, Mohammed First University, 60000 Oujda, Morocco
e-mail: samir.nova@gmail.com

solar dryer. And that was one of the topics that interested the researchers that try to improve the air distribution inside the indirect solar dryer.

In general, the indirect solar dryer consists of a solar air heater and a drying chamber that contains the trays filled with the product. The hot air enters from the bottom of the chamber which makes the lower tray receive a lot of heat compared to the upper trays where the heat won't reach it because the air gets cold and moisty when it will arrive at it. To overcome this disadvantages, Kabeel and Abdelgaied [2] divided the drying chamber into two stages with reheating systems that composed with two double pass solar air heaters in a way that the outlet of the first stage is the inlet of the second solar air heater that is going to reheat the air and send it to the second stage, this method makes sure that the hot air is going to reach all the trays in the chamber non just the lower ones. In another way, a lot of researches choose to use air duct to guide the air directly to the corresponding tray, like Abubakar et al. [3] and Darabi et al. [4] who studied a drying chamber containing three independent trays and each one is connected to a pipe which makes the air distributed uniformly along the trays.

The computational fluid dynamics is a powerful tool that has been widely used to solve many problems related to fluid dynamics and it has been proved that it's an effective and efficient design and analysis tool for the food industry [5].

The aim of this study is the improvement of the air distribution inside the drying chamber of an indirect natural convection solar dryer using the ANSYS FLUENT software under the climate of the oriental region in Morocco to make the study more realistic. The studied geometry characterizes by a side plenum chamber mounted on the side of the drying chamber, in order to improve the air distribution by passing it horizontally through the trays, while the study is based on the improvement of the side-mounted plenum chamber by finding the optimal dimensions corresponding to a uniform air distribution along the trays.

2 Methodology

2.1 Solar Dryer Description

The solar dryer studied is an indirect type working under natural convection, composed of a 1.5 m² simple solar air heater, that generates the hot air and guides it to the drying chamber, which composed of 2 sections a drying chamber that contains the three trays filled with the product which is figs in our case, and a side-mounted plenum chamber as shown in Fig. 1.

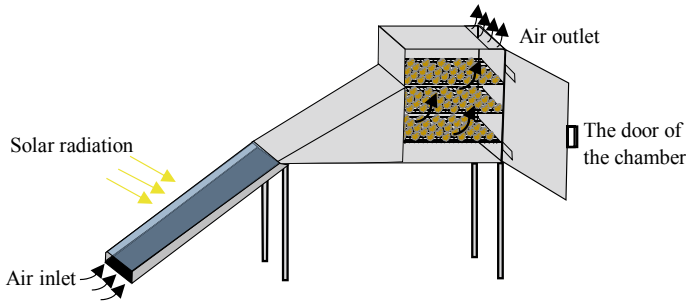


Fig. 1 Schematic diagram of the solar dryer studied

2.2 Boundary Conditions and Climate Data

To make the study more realistic, we studied the solar dryer under the climate of the oriental region in Morocco, specifically, the Oujda city. The meteorological data were collected from the meteorological station installed in the Mohammed first university in Oujda city, the data provided for our study where the ambient temperature and the solar irradiations of a sunny summer day. An Excel treatment is made to present the data in form of approximated Eqs. (1) and (2).

$$T_{amb}(t) = 25 + 6 \cos\left(\frac{\pi}{12}(t - 14)\right) \tag{1}$$

$$G_{sun}(t) = 965 \sin\left(\frac{t - 6}{14}\pi\right), \quad 6 < t < 20 \tag{2}$$

The inlet and the outlet of the solar dryer are a pressure type and the walls of the chamber are made of wood in which we have convective losses where the heat transfer coefficient is defined in (3), for the glass cover of the solar air heater we have a combination of external convection and radiation boundary conditions.

$$h_0 = 2.8 + 3V_w \tag{3}$$

where $V_w = 3 \text{ m s}^{-1}$ is the wind velocity.

To simulate the resistance to the airflow by the trays that are filled with the fruit of the fig, we modeled them as a porous medium with 50% porosity using the power-law model [6].

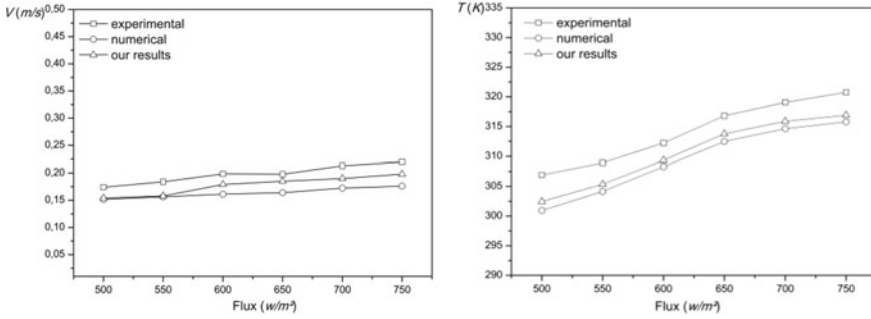


Fig. 2 Comparison of the average outlet temperature and velocity with those of [7]

3 Results

3.1 Validation of the Results

In order to validate the obtained results, we compare our results with the ones studied by Jyotirmay et al. [7] that studied experimentally and numerically a cubical wooden chamber, similar to a cabinet dryer equipped with an inclined solar chimney for natural ventilation. The results are presented in Fig. 2. In terms of average outlet velocity and temperature. The results found by ANSYS FLUENT showed a good correlation to the experimental ones, it's even better than the numerical results found by the authors.

3.2 The Optimal Size of the Plenum Chamber

In this section, we are going to study the side-mounted plenum chamber, specifically its optimum deflection angle, and to do so, there are two ways, either to change the width of the plenum chamber or the distance between the upper tray and the rooftop of the chamber. And that is exactly what we are going to do.

Before every simulation, we must first make an independency mesh test, and for that, four different grids 5532, 12,130, 16,606, and 23,820 triangular cells were studied, and the results show that a mesh grid with 12,130 cells is quite enough to study the geometry.

In order to obtain the optimal width of the plenum chamber in the studied case, we analyze nine different widths that range from 0.25 to 0.65 m. The results are presented in the Fig. 3 in terms of the average velocity of each tray in the sunshine hours of the chosen day. We can see that the velocity increase with the increase in width. However, when the width arrives at 0.4 m, the velocity starts to decrease even if the width increases. But the distribution form of the air along the trays stayed the same even if we increase in the width of the plenum chamber.

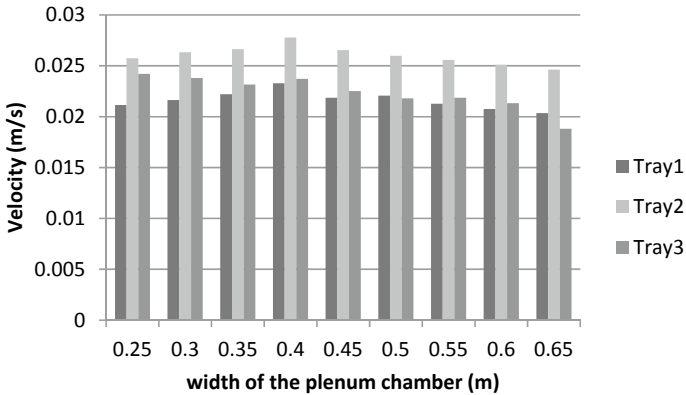


Fig. 3 The average velocity of the three trays in the sunshine hours of the chosen day for different widths at 1:00 pm

Regarding the distance between the first tray (the upper tray) and the rooftop, we analyzed six different distances and the results are presented in the Fig. 4, in terms of the average velocity of each tray in the sunshine hours of the chosen day. The results show that as the distance between the upper tray and the rooftop increase, the velocity decreases. As well the air distribution becomes more uniformed along the trays as long as we decrease that distance.

The optimal geometry is simulated and presented in four different hours along the chosen day in the Fig. 5. The side-mounted plenum chamber allows the air to crosses horizontally in the trays, and that prevents the reduction in temperature as well as the velocity of air after crossing the lower tray. The optimal geometry shows a good uniformity of air along the trays.

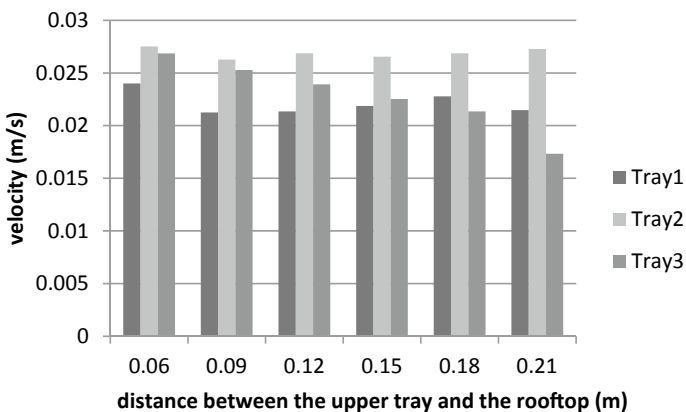


Fig. 4 The average velocity of the three trays in the sunshine hours of the chosen day for different distances between the upper tray and the rooftop at 1:00 pm

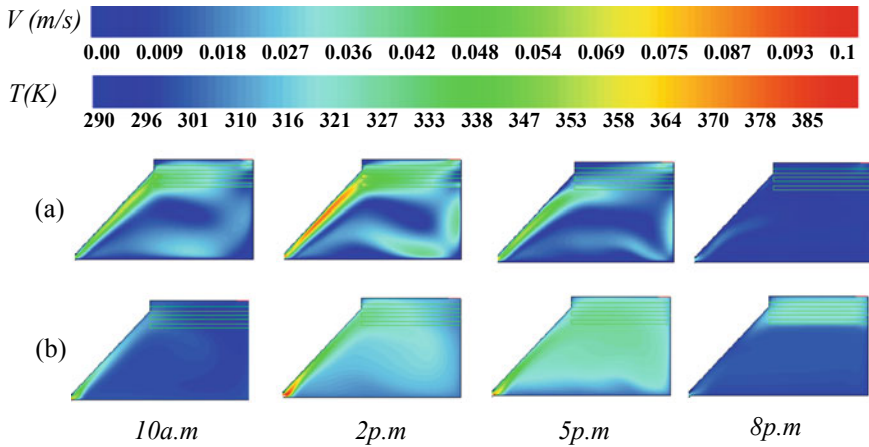


Fig. 5 Distribution of velocity (a) and temperature (b) inside the chamber at 4 different hours in the chosen day

4 Conclusion

The new technologies dedicated to the drying process are diverse, and each of them has a specific operating principle and its own source of energy to carry out this operation. In this study, we have focused mainly on indirect solar drying systems due to their importance in terms of quality and environmental cleanliness. The whole system, consisting of a solar air heater, a drying chamber equipped with a side-mounted plenum chamber. The width of this latter as well the distance between the first tray and the rooftop where studied using ANSYS FLUENT software, and the results showed that the most suitable width for the side-mounted plenum chamber is 0.4 m and the optimal distance between the first tray (the upper tray) and the top of the chamber is 0.06 m.

References

1. Purohit P, Kumar A, Kandpal TC (2006) Solar drying vs. open sun drying: a framework for financial evaluation. *Solar Energy* 80(12):1568–1579
2. Kabeel AE, Abdelgaied M (2018) Experimental evaluation of a two-stage indirect solar dryer with reheating coupled with HDH desalination system for remote areas. *Desalination* 425:22–29
3. Abubakar S, Umaru S, Kaisan MU, Umar UA, Ashok B, Nanthagopal K (2018) Development and performance comparison of mixed-mode solar crop dryers with and without thermal storage. *Renew Energy* 128:285–298
4. Darabi H, Zomorodian A, Akbari MH, Lorestani AN (2015) Design a cabinet dryer with two geometric configurations using CFD. *J Food Sci Technol* 52(1):359–366
5. Norton T, Sun DW (2006) Computational fluid dynamics (CFD)—an effective and efficient design and analysis tool for the food industry: a review. *Trends Food Sci Technol* 17(11):600–620

6. Amanlou Y, Zomorodian A (2010) Applying CFD for designing a new fruit cabinet dryer. *J Food Eng* 101(1):8–15
7. Mathur J, Mathur S (2006) Summer-performance of inclined roof solar chimney for natural ventilation. *Energy and Buildings* 38(10):1156–1163

Performance Comparison of Regenerative Organic Rankine Cycle Configurations



Rania Zhar, Amine Allouhi, Abdelmajid Jamil, and Khadija Lahrech

Abstract In order to ameliorate the ORC performances, the Regenerative Organic Rankine Cycle (RORC) is presented. This study presents a comparison of an ORC with an open feedwater heater (ORC-OFWH) an ORC with a closed feedwater heater (ORC-CFWH) and double stage regenerative ORC (DSR-ORC) using both OFWH and CFWH. The thermodynamic performances of each system are investigated adopting R123 as working fluid. Summing up the results, it can be concluded that the double stage regenerative ORC shows greater performances in term of thermal efficiency and exergy efficiency with 14% and 17% respectively higher over the ORC-OFWH and ORC-CFWH.

Keywords Regenerative Organic Rankine Cycle · Energy · Exergy · Open/closed feedwater heater · Double stage regenerative ORC

Nomenclature

h	Specific enthalpy (kJ/kg)
\dot{I}	Irreversibility rate (kW)
\dot{m}	Mass flow rate (kg/s)
P	Pressure (MPa)
\dot{Q}	Heat transfer rate (kW)
s	Specific entropy (kJ/kg K)
T	Temperature (K)
\dot{W}	Power (kW)

R. Zhar (✉) · K. Lahrech
University of Sidi Mohamed Ben Abdellah, USMBA, Imouzzer Road, BP 2626, Fez, Morocco
e-mail: rania.zhar@usmba.ac.ma

R. Zhar
IPI Laboratory, ENS, USMBA, Fez, Morocco

A. Allouhi · A. Jamil
High School of Technology, USMBA, Fez, Morocco

η	Isentropic efficiency
η_{th}	Thermal efficiency (%)
η_{EX}	Exergy efficiency (%)

Abbreviations

CFWH	Closed feedwater heater
DSR-ORC	Double stage regenerative ORC
GWP	Global warming potential
ODP	Ozone depletion potential
OFWH	Open feedwater heater
ORC	Organic Rankine Cycle
RORC	Regenerative ORC

Subscripts

0	Reference state
b	Boiler
bp	Boiling point
c	Condenser
crit	Critical
H	Heat reservoir
HPT	High pressure turbine
In	Inlet
L	Cold reservoir
LPT	Low pressure turbine
mx	Mixing chamber
net	Net power output
out	Outlet
p	Pump
t	Turbine
th	Thermal
wf	Working fluid

1 Introduction

The globe is facing an energy and environmental crisis due to the electricity generation using fossil fuels. Therefore, the use of fossil energy is increasingly depleted and

causes environmental problems [1]. On other hand, in industrial fields, the energy consumed is about 53% of the total energy, and 73% of this primary energy is wasted during various industrial processes and released to the environment directly without any further use. Low temperature waste heat is accountable to for about 60% of total waste heat. Recovering industrial waste heat presents a powerful solution to ameliorate companies' energy efficiency and energy consumption [2].

In this setting, Organic Rankine Cycle (ORC) is the most practical technology for recovering waste heat for electricity production at low temperatures (<230 °C) because of its simple structure, low cost, easy maintenance and environmental friendly [3, 4]. Many researchers have been investigated to the improvement of ORC performance. Mago et al. [5] carried out a performance analysis of two types of ORCs using dry fluids to cover low-grade waste heat to power based on both energy and exergy evaluations. The results showed that the regenerative ORC shows better performances than the basic ORC in term of first and second law efficiencies. Xi et al. [6] developed a parametric optimization of three different configurations of ORC system with six working fluids. However in their study, the ORC with double-stage regenerative configurations (DRORC) shows best thermal and exergy efficiencies, followed by ORC with single-stage regenerative system (SRORC) while the basic configuration of ORC (BORC) has the lowest efficiencies. Imran et al. [7] presented a thermodynamic and economic analysis of regenerative ORC for waste heat recovery. Results indicated that evaporation pressure has a considerable impact on thermal efficiency as well as specific investment cost. In order to improve the ORC system performances, several efforts have been devoted for selecting an appropriate working fluid. Chen et al. [8] compared the performance of 35 working fluids considering thermodynamic performances, environmental impacts, safety and cost. They concluded that isentropic and dry fluids are preferred for ORC systems. Tian et al. [9] analyzed and optimized the performance of 20 working fluids. R141b, R123 and R245fa presented the best thermal efficiency as well as the net power output in range of 16.6–13.3% and from 60 to 49 kJ/kg respectively.

This paper presents a performance analysis of three regenerative ORC (RORC) configurations for waste heat source at low grade temperature based on combined first and second law of thermodynamics. These configurations include an ORC with an open feed-water heater (ORC-OFWH), an ORC with a closed feedwater heater (ORC-CFWH) and double stage regenerative ORC (DSR-ORC) using waste heat source at low grade temperature. Energy and exergy estimation were presented based on the first and second thermodynamic laws. Thermal efficiency, net power output, exergy efficiency and exergy destruction of each system are selected.

2 System Description

In order to ameliorate the ORC performances, different modified cycles namely regenerative ORCs have to be analysed. Single and double stage regenerative ORC are two from many modifications that are used to better the system performance.

Schematics of regenerative ORC with an open feed water heater is shown in Fig. 1a. As observed, a feedwater heater is incorporated into the ORC. After being expanded at the turbine, a fraction of the stream extracted at state 3 mixes with the feedwater. The working fluid leaving the OFWH is in saturated liquid state. Figure 1b depicts the ORC with a closed feedwater heater. The heat exchange in the CFWH can be fulfilled without requiring a flow pressure at state 3 equal to state 6. At the CFWH exit, the flow at state 8 is pressurized by pump 2. The flow at states 7 and 9 are mixed in the mixing chamber. The double stage regenerative ORC is shown in Fig. 1c. A fraction of the working fluid is taken out at state 3 and at state 4. These amount of flow feed the open and closed feed water heaters, respectively.

In this study, R123 was selected as working fluid. The physical data, safety and environmental properties of R123 are listed in Table 1. R123 is a dry organic working fluid, non-flammable with a zero ozone depletion potential (ODP) and a low global warming potential (GWP) [10].

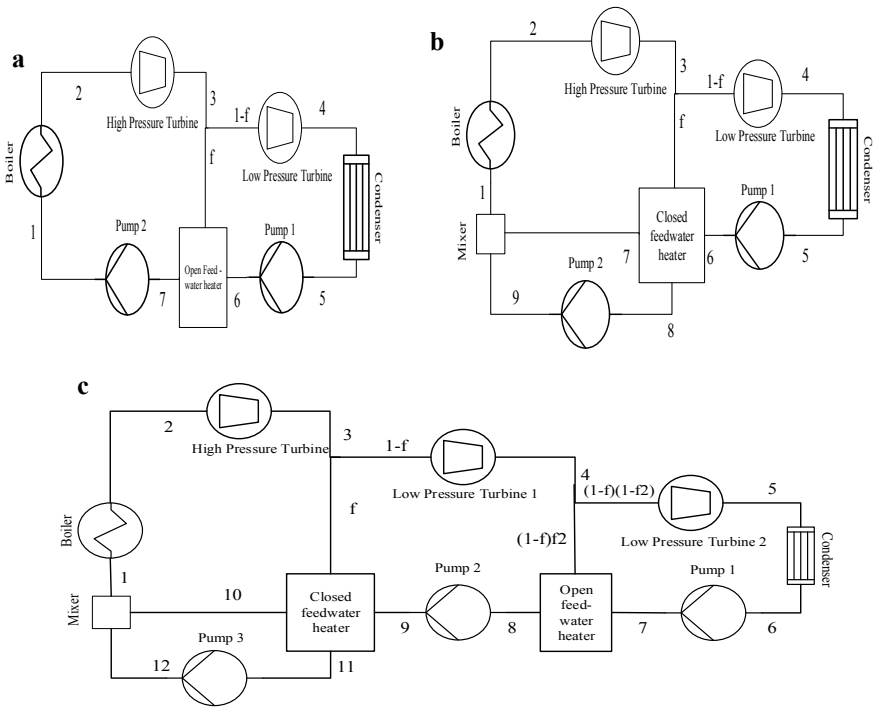


Fig. 1 a Schematic of ORC-OFWH, b ORC-CFWH, c DSR-ORC

Table 1 Physical, safety and environment data of R123

Fluid	Physical data			Safety data	Environment data		
	T _{bp} (°C)	T _{crit} (°C)	P _{crit} (MPa)	ASHRAE 34 safety group	Atm life time (year)	ODP	GWP (100 year)
R123	27.82	183.68	3.6	B1	1.3	0	77

1: No flame propagation. B: higher toxicity

3 Thermodynamic Analysis

Simulation of the different regenerative ORC configurations is developed using Engineering Equation Solver software (EES). Based on the first and second law of thermodynamics, energy and exergy destruction rate equations for each system components can be built as follow.

3.1 Regenerative ORC with OFWH/CFHWH

The heat supplied and the exergy destruction in the boiler:

$$\dot{Q}_b = \dot{m}_{wf}(h_{out} - h_{in}) \quad (1)$$

$$\dot{I}_b = T_0 \dot{m}_{wf} \left[s_{out} - s_{in} - \frac{h_{out} - h_{in}}{T_H} \right] \quad (2)$$

The high pressure turbine power and the exergy destruction are given by:

$$\dot{W}_{HPT} = [\dot{m}_{wf}(h_{in} - h_{s,out})] \cdot \eta_t \quad (3)$$

$$\dot{I}_{HPT} = T_0 \dot{m}_{wf}(s_{out} - s_{in}) \quad (4)$$

The low pressure turbine power and the exergy destruction:

$$\dot{W}_{LPT} = [\dot{m}_{wf}(h_{in} - h_{s,out})] \cdot \eta_t \cdot (1 - f) \quad (5)$$

$$\dot{I}_{LPT} = T_0 \dot{m}_{wf}(s_{out} - s_{in}) \cdot (1 - f) \quad (6)$$

The condenser transfer rate:

$$\dot{Q}_C = \dot{m}_{wf}(h_{in} - h_{out}) \cdot (1 - f) \quad (7)$$

$$\dot{I}_C = T_0 \dot{m}_{wf} \left[s_{out} - s_{in} - \frac{\dot{Q}_c}{T_L} \right] \cdot (1 - f) \quad (8)$$

The pump power and exergy destruction:

$$\dot{W}_{p1} = \left[\frac{\dot{m}_{wf}(h_{s,out} - h_{in})}{\eta_p} \right] \cdot (1 - f) \quad (9)$$

$$\dot{I}_{p1} = T_0 \dot{m}_{wf} (s_{out} - s_{in}) \cdot (1 - f) \quad (10)$$

Open feed water heater:

$$f h_3 + (1 - f) h_6 = h_7 \quad (11)$$

$$\dot{I}_{OFWH} = T_0 \dot{m}_{wf} [s_7 - f s_3 - (1 - f) s_6] \quad (12)$$

Closed feed water heater:

$$f(h_8 - h_3) = (1 - f)(h_6 - h_7) \quad (13)$$

$$\dot{I}_{CFWH} = T_0 \dot{m}_{wf} [f(s_8 - s_3) + (1 - f)(s_7 - s_6)] \quad (14)$$

The pump work and the exergy destruction for the RORC-OFWH:

$$\dot{W}_{p2} = \frac{\dot{m}_{wf}(h_{s,out} - h_{in})}{\eta_p} \quad (15)$$

$$\dot{I}_{p2} = T_0 \dot{m}_{wf} (s_{out} - s_{in}) \quad (16)$$

The pump work and the exergy destruction for the RORC-CFWH:

$$\dot{W}_{p2} = \frac{\dot{m}_{wf}(h_{s,9} - h_8)}{\eta_p} f \quad (17)$$

$$\dot{I}_{p2} = T_0 \dot{m}_{wf} (s_{out} - s_{in}) \cdot f \quad (18)$$

The system net power output:

$$\dot{W}_{net} = \dot{W}_{HPT} + \dot{W}_{LPT} - \dot{W}_{P1} - \dot{W}_{P2} \quad (19)$$

The system thermal efficiency:

$$\eta_{th} = \frac{\dot{W}_{net}}{\dot{Q}_b} \quad (20)$$

3.2 Double Stage Regenerative ORC (DSR-ORC)

The heat transferred in the boiler and the condenser are respectively:

$$\dot{Q}_b = \dot{m}_{wf}(h_2 - h_1) \quad (21)$$

$$\dot{Q}_C = \dot{m}_{wf}(h_5 - h_6) \cdot (1 - f_1) \cdot (1 - f_2) \quad (22)$$

The turbines power and pumps power consumption are given by:

$$\dot{W}_{HPT} = [\dot{m}_{wf}(h_2 - h_{s,3})] \cdot \eta_t \quad (23)$$

$$\dot{W}_{LPT1} = [\dot{m}_{wf}(h_3 - h_{s,4})] \cdot \eta_t \cdot (1 - f) \quad (24)$$

$$\dot{W}_{LPT2} = [\dot{m}_{wf}(h_4 - h_{s,5})] \cdot \eta_t \cdot (1 - f) \cdot (1 - f_2) \quad (25)$$

$$\dot{W}_{p1} = \frac{\dot{m}_{wf}(h_{s,8} - h_7)}{\eta_p} \cdot (1 - f) \cdot (1 - f_2) \quad (26)$$

$$\dot{W}_{p2} = \frac{\dot{m}_{wf}(h_{s,9} - h_8)}{\eta_p} \cdot (1 - f) \quad (27)$$

$$\dot{W}_{p3} = \frac{\dot{m}_{wf}(h_{s,12} - h_{11})}{\eta_p} \cdot f \quad (28)$$

The energy balance of the OFWH, CFWH and mixing chamber are given by Eqs. (29–31) respectively:

$$(1 - f) \cdot f_2 \cdot h_4 + (1 - f) \cdot (1 - f_2) \cdot h_7 = (1 - f) \cdot h_8 \quad (29)$$

$$f(h_{11} - h_3) = (1 - f)(1 - f_2)(h_{10} - h_9) \quad (30)$$

$$h_1 = f \cdot h_{12} + (1 - f) \cdot h_{10} \quad (31)$$

The exergy destruction of each component of the DSR-ORC system is expressed in Eqs. (32)–(42):

$$\dot{I}_b = T_0 \dot{m}_{wf} \left[s_2 - s_1 - \frac{h_2 - h_1}{T_H} \right] \quad (32)$$

$$\dot{I}_{HPT} = T_0 \dot{m}_{wf} (s_3 - s_2) \quad (33)$$

$$\dot{I}_{LPT1} = T_0 \dot{m}_{wf} (s_4 - s_3) \cdot (1 - f) \quad (34)$$

$$\dot{I}_{LPT2} = T_0 \dot{m}_{wf} (s_5 - s_4) \cdot (1 - f) \cdot (1 - f_2) \quad (35)$$

$$\dot{I}_C = T_0 \dot{m}_{wf} \left[s_6 - s_5 - \frac{\dot{Q}_c}{T_L} \right] \cdot (1 - f_1) \cdot (1 - f_2) \quad (36)$$

$$\dot{I}_{p1} = T_0 \dot{m}_{wf} (s_7 - s_6) \cdot (1 - f) \cdot (1 - f_2) \quad (37)$$

$$\dot{I}_{OFWH} = T_0 \dot{m}_{wf} [(1 - f_1)s_8 - (1 - f_1)f_2 \cdot s_4 - (1 - f_1)(1 - f_2)s_7] \quad (38)$$

$$\dot{I}_{p2} = T_0 \dot{m}_{wf} (s_9 - s_8) \cdot (1 - f) \quad (39)$$

$$\dot{I}_{CFWH} = T_0 \dot{m}_{wf} [f_1(s_{11} - s_3) + (1 - f_1)(1 - f_2)(s_{10} - s_9)] \quad (40)$$

$$\dot{I}_{p3} = T_0 \dot{m}_{wf} (s_{12} - s_{11}) \cdot f_1 \quad (41)$$

$$\dot{I}_{mx} = T_0 \dot{m}_{wf} [s_1 - f_1 \cdot s_{12} - (1 - f_1) \cdot s_{10}] \quad (42)$$

The net power output of the DSR-ORC system:

$$\dot{W}_{net} = \dot{W}_{HPT} + \dot{W}_{LPT1} + \dot{W}_{LPT2} - \dot{W}_{P1} - \dot{W}_{P2} - \dot{W}_{P3} \quad (43)$$

The system thermal and exergy efficiencies are respectively:

$$\eta_{th} = \frac{\dot{W}_{net}}{\dot{Q}_b} \quad (44)$$

$$\eta_{EX} = \frac{\dot{W}_{net}}{\dot{Q}_b \left(1 - \frac{T_C}{T_H}\right)} \quad (45)$$

4 Results and Discussion

Based on the operation conditions, the behavior of the different regenerative ORC configurations under different evaporation temperature is studied adopting R123 as a working fluid. A comparison of thermal efficiencies, in addition to the net power output are outlined in Fig. 2. As for the thermal efficiency of studied ORC configurations is illustrated in Fig. 2a.

The thermal efficiency shows an increase with the rise of the evaporation temperature. It is apparently that the ORC with DSR configuration has the largest thermal efficiency with 14% for $T_H = 423$ K, while the ORC with CFWH configuration has a thermal efficiency slightly higher than that of the OFWH-ORC. As for the change of output net power according to varying the temperature of heat source T_H , the global trend is quite similar to that of the thermal efficiency. The ORC with DSR configuration net power output is the greatest among other configurations at any T_H . The net power output continuously rises with the increment of T_H .

In order to the difference between the ORC configurations, the result for energy analysis is shown in Table 2. As follows from Table 2, the rate of heat transferred from

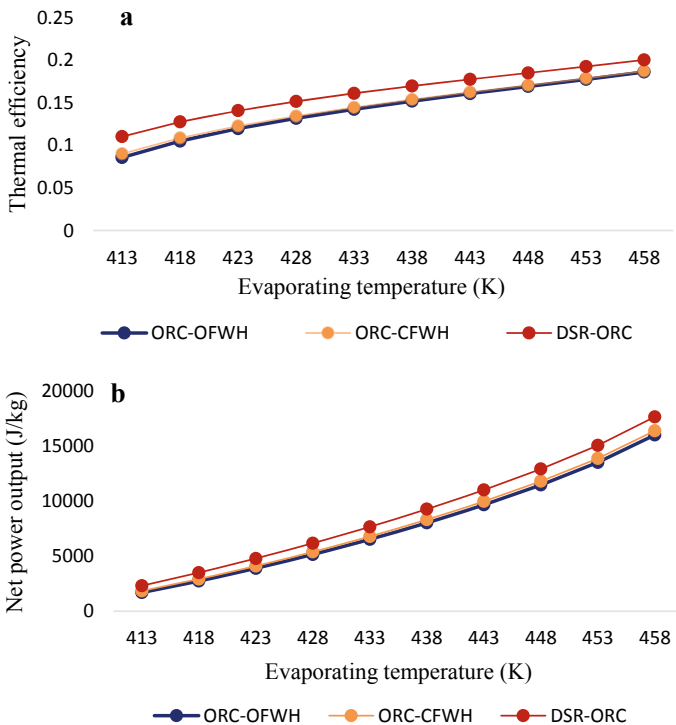


Fig. 2 The change of the thermal efficiency and net power output with the evaporation temperature for different ORC configurations

Table 2 Results for energy analysis

Parameters	ORC-OFWH	ORC-CFWH	DSR-ORC
\dot{Q}_b (kW)	835	714	710
\dot{Q}_c (kW)	735	714	610
W_{net} (J/kg)	3890	4100	4787
η_{th} (%)	11.9	12.2	14

the boiler to the working fluid of the DSR-ORC is reduced by 17.6 and 16% compared to ORC-OFWH and ORC-CFWH respectively. The ORC with DSR configuration output net power is the largest followed by the ORC-CFWH and finally ORC-OFWH.

Figure 3 depicts the variation of the system exergy efficiency with T_H . It can be clearly seen that for any kind of ORC configurations, increasing evaporating temperature T_H , contributes to an increase in exergy efficiency. A comparison between ORC configurations show that the DSR-ORC has the largest exergy efficiency 52% for $T_H = 423$ K, while the ORC with an open feed water heater has the lowest exergy efficiency (44%). The exergy efficiency of the ORC with an OFWH is very close to that of the ORC with a CFWH 14% smaller than the DSR-ORC.

Table 3 shows the result for the exergy analysis for the three different regenerative configurations of ORC. It is apparently that the DSR-ORC boiler exergy destruction

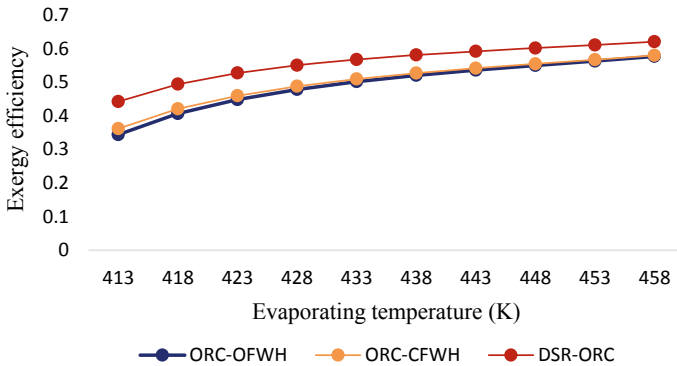


Fig. 3 Variation of the exergy efficiency with T_H

Table 3 Results for exergy analysis

Parameters	ORC-OFWH	ORC-CFWH	DSR-ORC
\dot{I}_b (kW)	29.8	29.6	26.2
\dot{I}_c (kW)	11.2	10.8	9.3
\dot{I}_{OFWH} (kW)	42.3	–	11.9
\dot{I}_{CFWH} (kW)	–	38.8	8.2
η_{ex} (%)	44.8	45.9	52.6

is the smallest compared to other configurations. It reduced by about 13% from the ORC-OFWH and 12% from the ORC-CFWH.

5 Conclusion

In this study, an energetic and exergetic performance comparison of three regenerative ORC configurations were evaluated. Based on the results of this work, we concluded the following:

The DSR-ORC determines 4.7 kJ/kg of net power output, and 14% of thermal efficiency. It resulting a higher value for 14% than the ORC with an OFWH. Moreover, the thermal efficiency of the OFWH-ORC is very close to that of the ORC with a CFWH.

The exergy efficiency for DSR-ORC obtain a higher result for 17% largest than ORC-OFWH. The amount of the exergy destruction in the boiler of DRS-ORC is the lowest, while there is not a significant difference between the ORC with an OFWH and ORC with a CFWH.

References

1. Yamamoto T, Furuhashi T, Arai N, Mori K (2001) Design and testing of the organic rankine cycle. *Energy* 26(3):239–251
2. Forman C, Muritala IK, Pardemann R, Meyer B (2016) Estimating the global waste heat potential. *Renew Sustain Energy Rev*
3. Ji C, Qin Z, Dubey S, Choo FH, Duan F (2017) Three-dimensional transient numerical study on latent heat thermal storage for waste heat recovery from a low temperature gas flow. *Appl Energy* 205:1–12
4. Song P, Wei M, Shi L, Danish SN, Ma C (2015) A review of scroll expanders for organic rankine cycle systems. *Appl Therm Eng* 75:54–64
5. Mago PJ, Chamra LM, Srinivasan K, Somayaji C (2008) An examination of regenerative organic rankine cycles using dry fluids. *Appl Therm Eng* 28:998–1007
6. Xi H, Li MJ, Xu C, He YL (2013) Parametric optimization of regenerative organic Rankine cycle (ORC) for low grade waste heat recovery using genetic algorithm. *Energy* 58:473–482
7. Imran M, Sik B, Ju H, Hyun D, Usman M, Heo M (2014) Thermo-economic optimization of regenerative organic rankine cycle for waste heat recovery applications. *Energy Convers Manag* 87:107–118
8. Chen H, Goswami DY, Stefanakos EK (2010) A review of thermodynamic cycles and working fluids for the conversion of low-grade heat. *Renew Sustain Energy Rev* 14(9):3059–3067
9. Tian H, Shu G, Wei H, Liang X, Liu L (2012) Fluids and parameters optimization for the organic Rankine cycles (ORCs) used in exhaust heat recovery of Internal Combustion Engine (ICE). *Energy* 47(1):125–136
10. Shengjun Z, Huaixin W, Tao G (2011) Performance comparison and parametric optimization of subcritical organic rankine cycle (ORC) and transcritical power cycle system for low-temperature geothermal power generation. *Appl Energy* 88(8):2740–2754

Performance Analysis of Combined Power and Refrigeration: ORC-VCC System



Rania Zhar, Amine Allouhi, Abdelmajid Jamil, and Khadija Lahrech

Abstract The paper aims to give a performance examination of a cogeneration system combining power and refrigeration, based on an Organic Rankine Cycle (ORC) as well as Vapour Compression Cycle (VCC). The following working fluids R123, R11 and R601a were assessed energetically and exergetically. The impact of different parameters including the boiler temperature and evaporator temperature are carried out on ORC thermal efficiency, also coefficient of performance (COP) as well as total system efficiency. The exergy efficiency and the amount of the exergy destroyed in each system component were detected. R123 was recommended.

Keywords Combined cycle · Organic rankine cycle · Energy · Exergy · Vapour compression cycle · Exergy destruction

Nomenclature

h	Specific enthalpy (kJ/kg)
\dot{I}	Irreversibility rate (kW)
\dot{m}	Mass flow rate (kg/s)
P	Pressure (MPa)
\dot{Q}	Heat transfer rate (kW)
s	Specific entropy (kJ/kg K)
T	Temperature (K)
\dot{W}	Power (kW)
η	Isentropic efficiency

R. Zhar (✉) · K. Lahrech
University of Sidi Mohamed Ben Abdellah, USMBA, Imouzzer Road, BP 2626, Fez, Morocco
e-mail: rania.zhar@usmba.ac.ma

R. Zhar
IPI Laboratory, ENS, USMBA, Fez, Morocco

A. Allouhi · A. Jamil
High School of Technology, USMBA, Fez, Morocco

η_{th}	Thermal efficiency (%)
η_{EX}	Exergy efficiency (%)

Abbreviation

COP	Coefficient of performance
ORC	Organic rankine cycle
VCC	Vapour compression cycle

Subscripts

0	Reference state
b	Boiler
bp	Boiling point
c	Condenser
com	Compressor
crit	Critical
eva	Evaporator
H	Heat reservoir
In	Inlet
net	Net power output
out	Outlet
p	Pump
ref	Refrigeration
t	Turbine
th	Thermal
wf	Working fluid

1 Introduction

With the strong growth of energy demand, a large part of the energy demand is provided by fossil fuels, resulting the global resource crisis and environment problems [1]. Renewable energy systems namely solar, biomass, geothermal as well as wind have progressively adopted. Among the alternative energy sources, waste heat recovery have a promising effect to find an energy efficient and sustainable society [2]. In this regard, waste heat recovery technologies combining power and refrigeration systems have attracted considerable attention in recent years, because of its

capacity to produce both cooling supply as well as electrical power from one heat source [3].

Organic Rankine Cycle (ORC) is the most common system to convert heat at low and medium temperature into power [4]. The ORC working concept is practically the same with the Steam Rankine cycle (SRC) where organic fluid is employed as working fluid instead of vapour steam [5]. The selection of an adequate working fluid plays a vital role in improving system performance, but also the organic fluid have to be chosen according to safety and environmental impact [6]. Chen et al. [7] compared the performance of 35 working fluids considering thermodynamic performances, environmental impacts, safety and cost. The T-S diagram is the best way to represent and categorize the type of organic fluids. We distinguish three types of saturation vapour curves shown on T-S diagram: A dry fluid with positive slopes, a wet fluid with negative slopes and an isentropic fluid with nearly infinitely large slopes. The results show that for ORC systems, the dry and isentropic fluids are the best choice [8].

Besides power generation, cooling is another type of energy usage. Vapour compression cycle (VCC) system is the most used refrigeration cycle for refrigeration and air conditioning. Improving vapour compression refrigeration cycle performance has been investigated in several studies [9]. Furthermore, a mechanical power is required to train the VCC compressor. Thus, the concept of an ORC integrated to VCC which aims to provide the mechanical power for the VCC compressor, and has attracted considerable attention in recent years [10]. Karellas and Braimakis [11] presented both thermodynamic examination and economic consideration of a coupled ORC-VCC system using three working fluids. R245fa shows better performance in term of thermal efficiency, exergy efficiency and COP with 5.5%, 7% and 3.88 respectively with a payback period of 7 years. Nasir and Kim [12] carried out the thermal performance comparison of a coupled ORC-VCC system utilizing seven working fluids. R134a was adopted as the most appropriate working fluid having a total system thermal efficiency in the range of 0.172–0.217.

In this paper, a thermodynamic examination using both energy as well as exergy performances of a heat powered refrigeration cycle are investigated. An organic rankine cycle is employed to generate the power from low grade waste heat that drives the compressor in the vapour compression refrigeration cycle.

2 System Description

A heat powered refrigeration cycle is shown in Fig. 1. As it shown in the figure, the ORC system is made up of four components: Boiler, turbine, condenser, pump and four different processes: Process 1–2 (isobaric evaporation), Process 2–3 (adiabatic detente in the turbine), Process 3–4 (isobaric condensation), and Process 4–1 (adiabatic compression process).

The VCC system includes an evaporator, compressor, expansion valve and condenser. The system has a condenser in common for refrigeration and ORC.

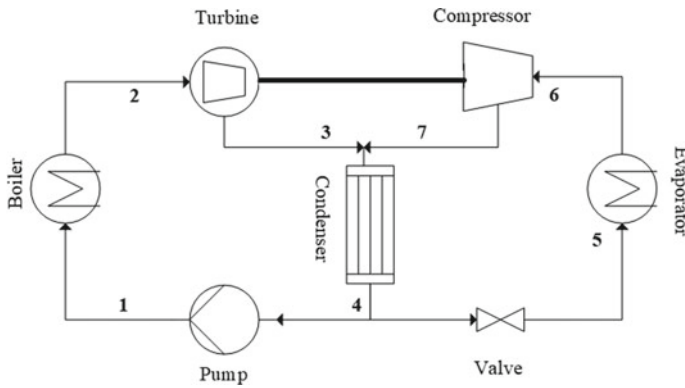


Fig. 1 Combined ORC-VCC system

The power produced by the ORC system operates the compressor in the vapour compression refrigeration cycle.

The thermodynamic, safety data based on ASHRAE 34 refrigeration group and environmental data for of the working fluids selected for this analysis are appointed in Table 1. Table 2 shows input parameters and boundary conditions.

3 Thermodynamic Modelling

3.1 Thermodynamic Analysis

The thermodynamic model is developed using Equation Engineering Solver software (EES), and based on the first and second thermodynamic laws, the mathematical model is given below.

Process 1–2: The heat transferred in the ORC boiler:

$$\dot{Q}_b = \dot{m}_{wf}(h_2 - h_1) \tag{1}$$

Process 2–3: The ORC expander power:

$$\dot{W}_t = \dot{W}_{t,s} \cdot \eta_t = [\dot{m}_{wf}(h_2 - h_{s,3})] \cdot \eta_t \tag{2}$$

Process 4–1: The power consumed by the ORC pump:

$$\dot{W}_p = \frac{\dot{W}_{p,s}}{\eta_p} = \frac{\dot{m}_{wf}(h_{1,s} - h_4)}{\eta_p} \tag{3}$$

The ORC net power output is as follow:

Table 1 Working fluids properties

Working fluid	Physical properties				Safety data ASHRAE 34 safety group	Environment data	
	Fluid type	T _{bp} (°C)	T _{crit} (°C)	P _{crit} (Mpa)		Atm life time (year)	ODP
R123	d	27.82	183.68	3.6	B1	1.3	0 77
Iso-Pentane (R601a)	d	27.8	187.4	3.37	A3	–	0 20
R11	i	23.8	198.11	4.4	A1	45	1 4600

i: No flame propagation, 2: Lower flammability, 3: Higher flammability

A: Lower toxicity, B: higher toxicity

d: Dry, i: Isentropic

Table 2 Input parameters

Parameters	Value	Ranges
Ambient temperature, T_0	293 K	–
Ambient pressure, P_0	0.1 MPa	–
Boiler temperature, T_h	373 K	383–423 K
Compressor isentropic efficiency, η_{com}	80%	–
Condenser temperature, T_c	318 K	–
Evaporator temperature, T_{eva}	273 K	265–281 K
Pump isentropic efficiency, η_p	70%	–
Turbine isentropic efficiency, η_t	90%	–

$$\dot{W}_{net} = \dot{W}_t - \dot{W}_p \tag{4}$$

The ORC thermal efficiency can be computed by:

$$\eta_{ORC} = \frac{\dot{W}_{net}}{\dot{Q}_b} \tag{5}$$

Process 5–6: The VCC evaporator heat transfer is given by:

$$\dot{Q}_{eva} = \dot{m}_{ref}(h_6 - h_5) \tag{6}$$

Process 6–7: The work required by the VCC compressor:

$$\dot{W}_{com} = \frac{\dot{W}_{com,s}}{\eta_{com}} = \frac{\dot{m}_{ref}(h_{7,s} - h_6)}{\eta_{com}} \tag{7}$$

The coefficient of performance (COP) for refrigeration cycle defined by:

$$COP_{ref} = \frac{\dot{Q}_{eva}}{\dot{W}_{com}} \tag{8}$$

The condenser heat rate can be calculated by:

$$\dot{Q}_c = (\dot{m}_{wf} + \dot{m}_{ref})(h_3 - h_4) \tag{9}$$

The total system thermal efficiency can be expressed as:

$$\eta_{sys} = \eta_{ORC} * COP_{ref} = \frac{\dot{Q}_{evap}}{\dot{Q}_b + \dot{W}_p} \tag{10}$$

3.2 Exergy Analysis

The exergy destroyed due to the thermodynamic irreversibility in each component of coupled system can be defined as:

For the ORC components, the exergy destruction are described in Eqs. (11–13).

$$\dot{I}_b = T_0 \dot{m}_{wf} \left[(s_2 - s_1) - \frac{h_2 - h_1}{T_H} \right] \quad (11)$$

$$\dot{I}_t = T_0 \dot{m}_{wf} (s_3 - s_2) \quad (12)$$

$$\dot{I}_p = T_0 \dot{m}_{wf} (s_1 - s_4) \quad (13)$$

The exergy efficiency of ORC:

$$\eta_{ex,ORC} = \frac{\eta_{th}}{\left(1 - \frac{T_0}{T_H}\right)} \quad (14)$$

For the VCC components, the exergy destruction are defined in Eqs. (15) and (16).

$$\dot{I}_{eva} = T_0 \dot{m}_{ref} \left[(s_5 - s_6) - \frac{h_6 - h_5}{T_{eva}} \right] \quad (15)$$

$$\dot{I}_{com} = T_0 \dot{m}_{ref} (s_7 - s_6) \quad (16)$$

The condenser exergy destruction:

$$\dot{I}_c = T_0 (\dot{m}_{wf} + \dot{m}_{ref}) \left[(s_4 - s_3) + \frac{h_3 - h_4}{T_c} \right] \quad (17)$$

The exergy efficiency of VCC:

$$\eta_{ex,VCC} = \frac{\dot{Q}_{eva} \left(\frac{T_0}{T_{eva}} - 1 \right)}{\dot{W}_{comp}} \quad (18)$$

The total system exergy efficiency:

$$\eta_{ex,sys} = \frac{\dot{E}_{cooling}}{\dot{E}_{in}} = \frac{\dot{m}_{ref} [h_6 - h_5 - T_0 (s_6 - s_5)]}{\dot{m}_{wf} [h_2 - h_1 - T_0 (s_2 - s_1)] + \dot{W}_p} \quad (19)$$

4 Results and Discussion

This part aims to display the effect of the boiler temperature. For that, the condenser and evaporator temperature are fixed to 318 K and 273 K, respectively. Figure 2 shows the variation of the thermal efficiency of the ORC system and total system thermal efficiency under different boiler temperature. As shown in Fig. 2a that for the three selected working fluids, the ORC thermal efficiency rises with the increment of the heat source temperature. It can be explained that with the increase of the boiler temperature, the turbine output power always equals the desired input power of the compressor, which results a diminution in the ORC mass flow rate. This causes reduction in the boiler heat transfer rate and increase in the ORC thermal efficiency. The same trend is observed for the total system efficiency, it increases with the rising of the temperature of the heat source. R123 shows the best performance among all selected working fluid with ORC and system thermal efficiencies, over 10% and 37%, respectively.

By adjusting the temperature of the condenser and boiler to 318 K and 393 K, respectively. This part aims to analyze the impact of the evaporator temperature. Figure 3 shows the variation of the COP and total system thermal efficiency under different evaporator temperatures. As can be noticed from Fig. 3a, for all the working fluids, the COP of the system shows an increase with the increment of the evaporator temperature for all selected working fluids. The same trend is observed for the total

Fig. 2 The change of the thermal efficiency of the ORC (a) and coupled system (b) according to varying boiler temperature

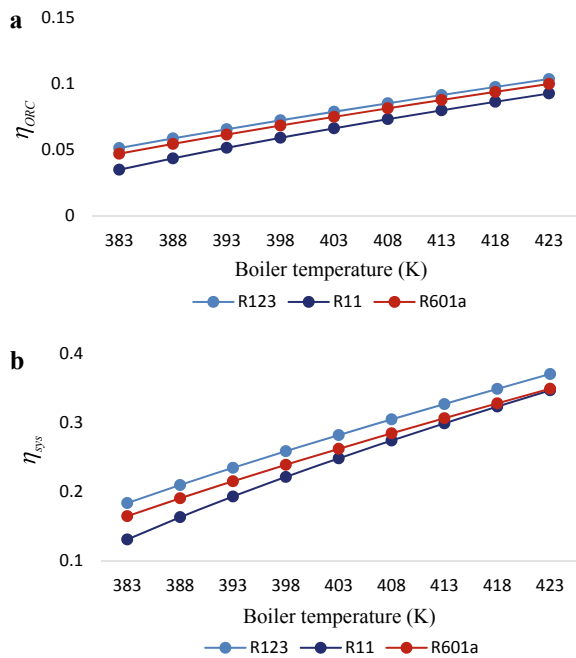
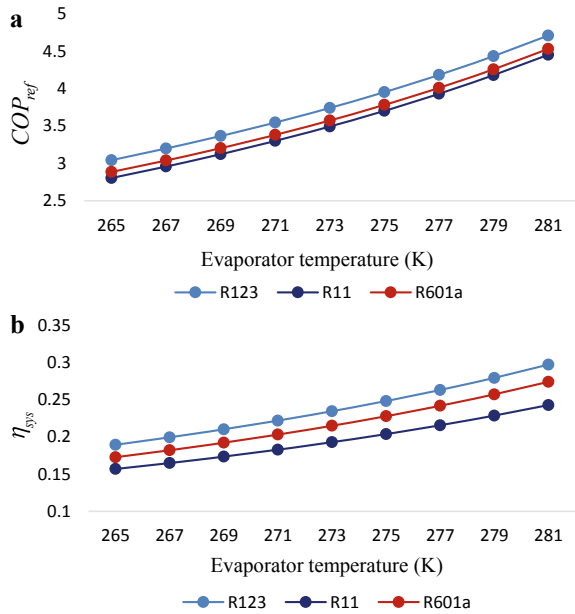


Fig. 3 The variation of the COP (a) and total system efficiency (b) under evaporator temperature



system efficiency. R123 have the largest value of COP and total system efficiency for 4.7 and 29%, respectively, where the worst performance has been shown by R11.

Figure 4 depicts the impact of the temperature of the evaporator on the combined system exergy efficiency. The increase of the evaporator temperature decreases the total system exergy efficiency. The greatest value of total system exergy efficiency, over 12%, has been obtained by R123 at the smallest evaporator temperature, while R11 has the worst performance for this parameter.

Figure 5 depicts the exergy destroyed in the different combined system components using R123 as working fluid. As can be clearly noticed, the boiler have the highest exergy destruction with 36%. It can be explained by the important amount of the entropy generated in the boiler due to its irreversibility. Regarding the refrigeration cycle, the maximum exergy destruction occurs in the compressor with 14%.

Fig. 4 The change of the system exergy efficiency according to varying evaporator temperature

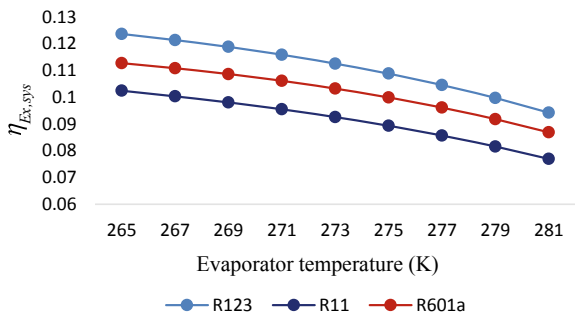
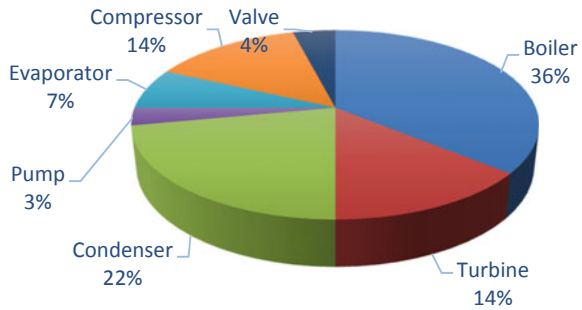


Fig. 5 The amount of the exergy destroyed of combined ORC-VCC system components



5 Conclusion

This paper aims to give a thermodynamic examination based on both energy and exergy performances of a combined ORC and VCC system. R123, R11 and R601a has been employed as working fluid. The impact of different parameters including boiler temperature and evaporator temperature on ORC thermal efficiency, COP as well as total system efficiency are investigated.

High boiler temperatures increase ORC thermal efficiency and total system efficiency. By increasing evaporator temperature, both COP and total system efficiency will be better, unlike the total system exergy efficiency which reduces with the increment of the evaporator temperature. R123 shows the best performances among the selected working fluids according to this study.

The amount of the exergy destroyed of the system components has been investigated. The results show that the maximum exergy destruction for the combined system takes place in the boiler with 36%, and the compressor for the refrigeration cycle.

References

1. Xia L et al (2019) A review of low-temperature heat recovery technologies for industry processes. *Chin J Chem Eng* 27(10):2227–2237
2. Sun W, Yue X, Wang Y (2017) Exergy efficiency analysis of ORC (Organic Rankine Cycle) and ORC-based combined cycles driven by low-temperature waste heat. *Energy Convers Manag* 135:63–73
3. Parikhani T, Ghaebi H, Rostamzadeh H (2018) A novel geothermal combined cooling and power cycle based on the absorption power cycle: energy, exergy and exergoeconomic analysis. *Energy*
4. Mahmoudi A, Fazli M, Morad MR (2018) A recent review of waste heat recovery by Organic Rankine Cycle. *Appl Therm Eng* 143(January):660–675
5. Aghahosseini S, Dincer I (2013) Comparative performance analysis of low-temperature Organic Rankine Cycle (ORC) using pure and zeotropic working fluids. *Appl Therm Eng* 54(1):35–42

6. Wang S, Liu C, Li Q, Liu L, Huo E, Zhang C (2020) Selection principle of working fluid for organic Rankine cycle based on environmental benefits and economic performance. *Appl Therm Eng* 178:115598
7. Chen H, Goswami DY, Stefanakos EK (2010) A review of thermodynamic cycles and working fluids for the conversion of low-grade heat. *Renew Sustain Energy Rev* 14(9):3059–3067
8. Bao J, Zhao L (2013) A review of working fluid and expander selections for organic rankine cycle. *Renew Sustain Energy Rev* 24:325–342
9. Maalem Y, Fedali S, Madani H, Tamene Y (2020) Performance analysis of ternary azeotropic mixtures in different vapor compression refrigeration cycles. *Int J Refrig*
10. Liang Y, Yu Z, Li W (2019) A waste heat-driven cooling system based on combined organic Rankine and vapour compression refrigeration cycles. *Appl Sci* 9(20)
11. Karellas S, Braimakis K (2016) Energy-exergy analysis and economic investigation of a cogeneration and trigeneration ORC-VCC hybrid system utilizing biomass fuel and solar power. *Energy Convers Manag* 107:103–113
12. Nasir MT, Kim KC (2016) Working fluids selection and parametric optimization of an organic rankine cycle coupled vapor compression cycle (ORC-VCC) for air conditioning using low grade heat. *Energy Build* 129:378–395

Fault Location Technique Using Distributed Multi Agent-Systems in Smart Grids



Mohamed Azeroual , Younes Boujoudar , Tijani Lamhamdi, Hassan EL Moussaoui, and Hassane EL Markhi

Abstract Efficient detection of fault and location can increase the safety and Efficiency of electrical power systems. The fault in power systems can create other faults and outages in the network. Fault analysis includes fault detection, location, isolation of the faulted section from the network, and energy restoration as soon as possible. In this study, an innovative multi-agent system approach proposed for fault location in the electrical network. The smart agents collect the power data (Voltage and current at each point) between different power components (sources, bus, relays, loads) for fault location and efficiently control of circuit breakers operations to restore service in the power systems. The simulation results show the performance of the proposed techniques for fault location in the power system.

Keywords Fault location · Smart grids · Multi-agent systems (MAS) · Phasor measurement units (PMU)

1 Introduction

The stability and safety of power systems have been a field of several studies of power generation, transmission, and distribution systems that required the utilization of intelligent distributed control techniques [1]. Several protection relays are installed at separate positions in transmission and distribution systems to keep the electrical components from several faults and accidents. The past few years have observed the fast development in several fields concerning the detection, analysis, and location of faults in power systems [2].

Recently, some methods based on knowledge of smart fault analysis and system restoration have been proposed for increasing the protection automation [3]. The intelligent electronic devices (IEDs) such as smart meters, fault passage indicators (FPI), phasor measurement units (PMU) and communication protocols are used for

M. Azeroual (✉) · Y. Boujoudar · T. Lamhamdi · H. EL Moussaoui · H. EL Markhi
Laboratory of Intelligent Systems, Georesources and Renewable Energies, FST Fez, Morocco
e-mail: Mohamed.azeroual1@usmba.ac.ma

fast fault location and isolation [4]. The intelligent methods, like the genetic algorithm (GA), artificial neural network (ANN), multiagent systems (MAS), and particle swarm optimization (PSO) have been used for power system protection [5].

The multiagent systems (MAS) extensively used in power system control to resolve many problems for fault analysis and location [6].

In [7], a co-simulation platform based on multi-agent system is proposed for fault location and power restoration in a distribution system, the data exchange operation between agents used by high-level architecture (HLA) framework.

A novel method based on MAS for fault location, faulted section elimination, calculation of fault distance, and autonomy power restoration is proposed in [8]. Eriksson et al. [9], proposed a self-healing algorithm based on MAS for fault detection and location in the power distribution network and automation energy restoration. A section agent placed in the central and at the two terminals of each distribution line for fault position and power recovery is proposed in [10]. An agent-based method for fault isolation and service restoration in smart distribution systems with renewables energy integration is proposed in [11].

In this paper, a novel intelligent technique based on the multi-agent system used for detection, location of the fault, and faulted section separation. The IEEE 9-Bus power system is used in this paper and the simulation results show the influence of the purposed technique. The agents proposed can identify the fault and control the network. The agents based on data of the system collected by (PMU) to control the system in abnormal operation.

The rest of the paper is organized as follows. Section 2 presents the Multi-agent framework for smart grid control. Case Studies and Results are described in Sect. 3. Finally, the most relevant conclusions of the paper are summarized in Sect. 4.

2 Multi-agent Framework for the Smart Microgrid

The complex systems management and control such as power systems require intelligent methods and equipment. MAS is generally classified as an artificial intelligence system composed of many smart agents used for the automation and security of electrical systems [12].

MAS is intelligent networks of smart agents operating in coordination for system control. An agent is an electronic equipment that can collect the data from power system elements, make computational processes, and also can communicate with other agents through a communication network. These agents are located in power systems and rely just on the local measurements or data exchange with other agents.

In this paper, a new multi-agent framework proposed for detection and fault location in the power system. Three types of agents proposed (Table 1): Load Agents (LDA), Line Agents (LA), Generator Agents (GA).

The principal idea of this study is the current values are measured using PLMs devices at both ends of each line. The data collected by PMUs transfer to Line Agents (LA) located in the middle of each line. LAs take corrective steps when a

Table. 1 Agents' tasks

Agents	Tasks
Load agents (LDA)	<ul style="list-style-type: none"> Collect the parameters of the load like the voltage, current value, and active power Communicated with other agents
Line agents (LA)	<ul style="list-style-type: none"> Located in the middle of each line Fault detection and location Circuit breakers control and isolation of faulted line Communicated with other agents
Generator agents (GA)	<ul style="list-style-type: none"> Parameters of the generator Communicated with other agents

fault occurs and send a command signal to circuit breakers (CBs) that are connected in both extremities of each line to remove the faulted section.

Figure 1 shows the technique proposed for fault detection and location. At normal conditions, the current flow in one direction at both extremity of the line.

The LA agent can detect the fault in the power system from the following equation between fault current status (F_s), current measurement I_M by PMUs, and the current threshold (I_T) determined by the Agent:

$$F_s = \begin{cases} 0, & 0 < I_M \leq I_T \text{ No fault} \\ 1, & I_T < I_M < \infty \text{ Fault detected} \end{cases} \quad (1)$$

After fault detection, if any PMU in the ends of the line detected that the current direction changes then the fault is located in the protected line and the LA corresponding send a control signal (z_p) to both circuit breakers.

The control signal (z_p) sends by agents to CBs can be written as:

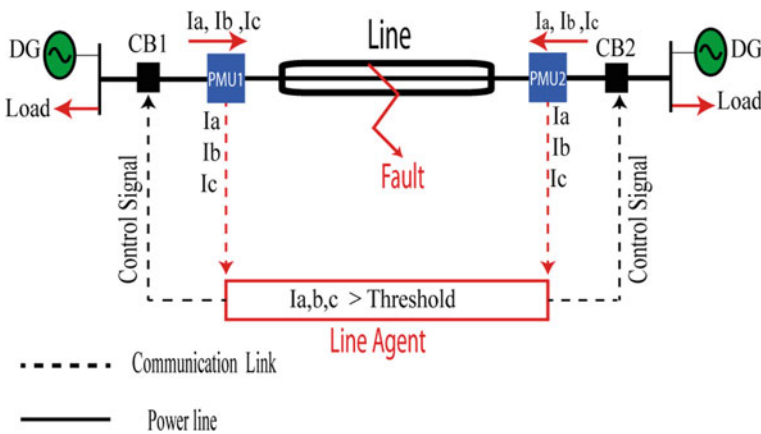


Fig. 1 The power grid and multi-agent system interaction

$$z_p = \begin{cases} 0, & F_s = 1 \text{ (Open the breaker)} \\ 1, & F_s = 0 \text{ No fault} \end{cases} \quad (2)$$

In this paper, the power systems and multi-agent systems are simulated on two different software platforms in the same machine. MATLAB/Simulink used for testing power systems and the MAS proposed is designed using the java simulator JADE (Java Agent Development Framework). The two simulators are linked together through a co-simulation MACSimJX for real-time data exchange and faster fault location to control (open/close) the circuit breakers in the power system.

3 Case Studies and Results

The IEEE 9-Bus power system used in this study shown in Fig. 2 to test the performance of the proposed distributed multi-agent systems for fault location. The system

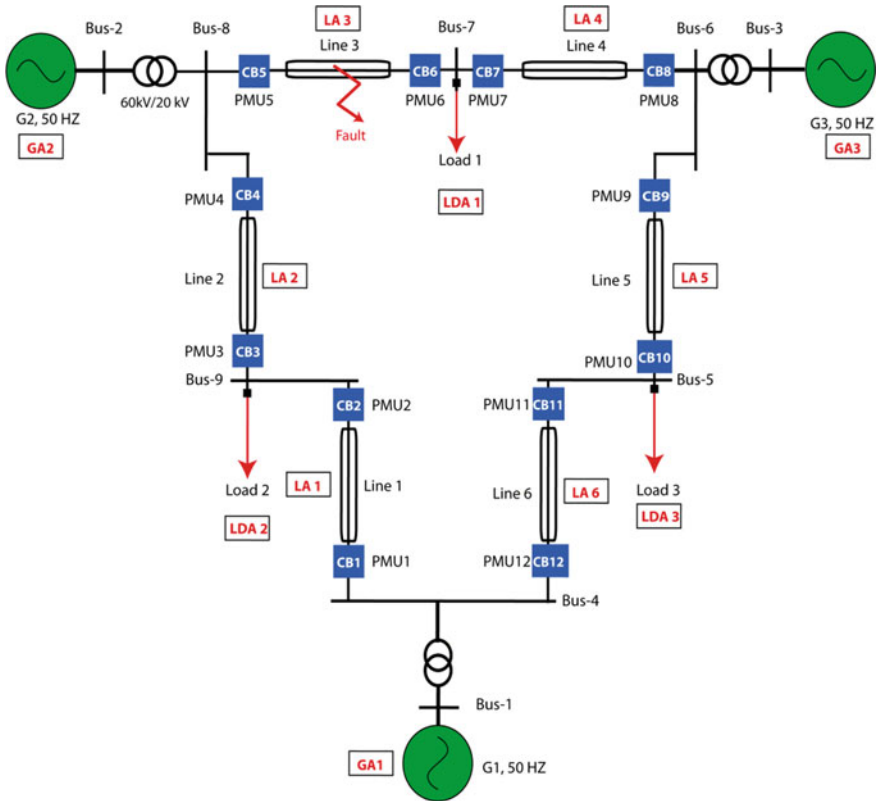


Fig. 2 IEEE 9-Bus power system

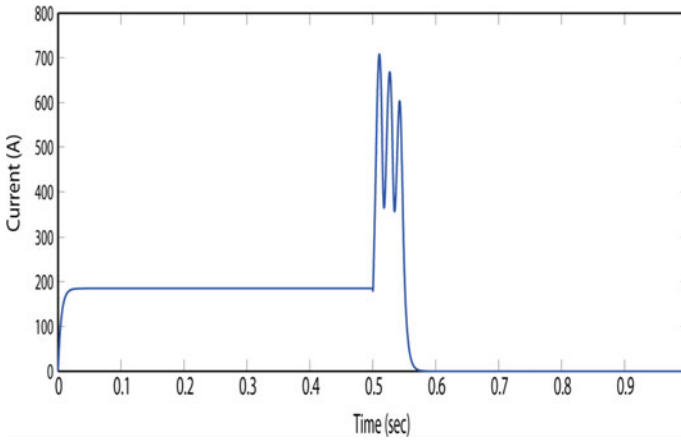


Fig. 3 Current through line 3 during fault period

consists of three power generators 50Hz to supply the total load on the system with active and reactive power $P_L = 315\text{MW}$ and $Q_L = 115\text{MVar}$. The system comprises six lines modeled as a single Π , twelve PMUs, and twelve circuit breakers (CB). Each line has one Line Agent located in the center of the line and at both extremity of the protective section there is PMU and CB. The performance of our method based on multiagent systems is evaluated using the IEEE 9-Bus power system as seen in Fig. 2. The LAs are able to detect, locate, and remove the faults from the system.

A three-phase fault is applied in the of line 3, through a 0.5Ω fault resistance at $t = 0.5$ s. The three-phase current amplitude at both ends of line 3 is measured using PMU 5 and PMU 6 and sends these values to LA3. As the fault current measured (I_M) is more than the current threshold value (I_T) as shown in Fig. 3 and the current changes its direction to satisfy the fault at line 3. This indicates that the fault is located in line 3. The LA3 sends a control signal (z_p) to both circuit breakers CB5 and CB6 ($z_p = 0$) to eliminate the faulted line from the system as shown in Fig. 4. The current flows in line 3 is zero after $t = 0.54$ second because of that fast fault clearing.

While a fault applied in line 3, removing the faulted section from the system using the data exchange between the LA3, PMU 5, and PMU 6 with fast fault detection and isolation time (0.04 s). After fault isolation, generator agent GA2 sends a message to GA3 to increase the current and feed the load 1 (100 MW).

Figures 5 and 6 shows the three-phase currents of G2 and voltages at Bus 8 respectively. It can be noted that the current after fault clearing decreased on account of the line isolation and the load1 supplied from G3 (at normal condition load 1 supplied from G2 and G3).

From the simulation results, it can be revealed that the agents take the precise action to locate the fault and to growing the stability of the power system.

Fig. 4 CB5 and CB6 status during fault

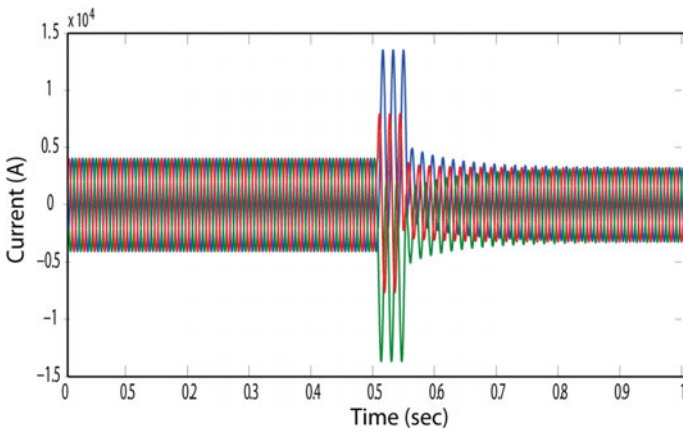
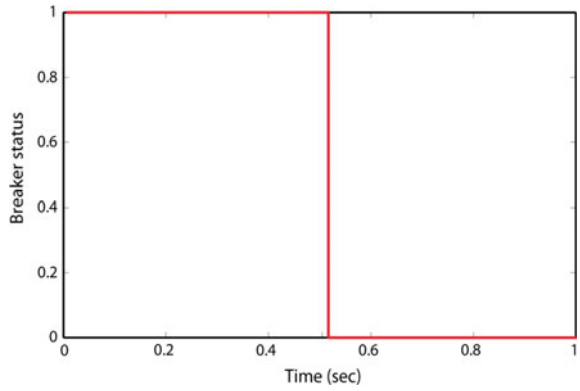


Fig. 5 The three-phase current of DG2 during a fault in line 3

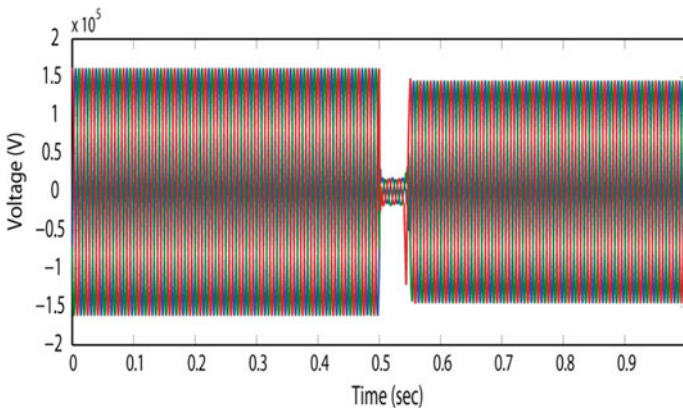


Fig. 6 The voltage at bus 8 during a fault in line 3

4 Conclusion

A new distributed method base on a multi-agent system for the location of the fault and faulted line isolation using the communication technologies between smart agents. The smart agents used the power system data collected by PMUs to coordinate with each other agents and take the logic operation used in the algorithm for solving the problem for CB control. The simulation results show the efficiency of MAS for fault location and power control proposed in this paper.

References

1. Azeroual M, El Makrini A, El Moussaoui H, El Markhi H (2018) Renewable energy potential and available capacity for wind and solar power in Morocco towards 2030. *J Eng Sci Technol Rev* 11(1)
2. Farughian A, Kumpulainen L, Kauhaniemi K (2018) Review of methodologies for earth fault indication and location in compensated and unearthed MV distribution networks. *Electric Power Syst Res* 154:373–380
3. Estebasari A, Pons E, Bompard E, Bahmanyar A, Jamali S (2016) An improved fault location method for distribution networks exploiting emerging LV smart meters. In: *IEEE Workshop on Environmental, Energy, and Structural Monitoring Systems (EESMS)*, Bari, Italy
4. Zhang Y, Jiang Y, Chen Y, Zhang Y (2020) Fault diagnosis of high voltage circuit breaker based on multi-classification relevance vector machine. *J Electr Eng Technol* 15(1):413–420
5. Trindade FC, Freitas W, Vieira J (2013) C: Fault location in distribution systems based on smart feeder meters. *IEEE Trans Power Deliv* 29(1):251–260
6. Mohamed A, Younes B, Lamhamdi T, El Moussaoui H, El Markhi H (2020) Fault location and isolation technique in smart distribution systems with distributed generation. In: *2020 1st international conference on innovative research in applied science, engineering and technology (IRASET)*, pp 1–5. IEEE, Apr 2020
7. Albagli AN, Falcão DM, de Rezende JF (2016) Smart grid framework co-simulation using HLA architecture. *Electr Power Syst Res* 130:22–33
8. Mohamed A, Lamhamdi T, El Moussaoui H, El Markhi H (2019) A multi-agent system for fault location and service restoration in power distribution systems. *Multiagent Grid Syst* 15(4):343–358
9. Eriksson M, Armendariz M, Vasilenko OO, Saleem A, Nordström L. Multiagent based distribution automation solution for self-healing grids. *IEEE Trans Ind Electr*, 62(4):2620–8, (2015)
10. Habib HF, Youssef T, Cintuglu MH, Mohammed O (2017) A multi-agent-based technique for fault location, isolation, and service restoration. *IEEE Trans Ind Appl* 53(3):1841–1851
11. Shirazi E, Jadid S (2019) A multiagent design for self-healing in electric power distribution systems. *Electr Power Syst Res* 171:230–239
12. Solanki NS (2007) A multi-agent solution to distribution systems restoration. *IEEE Trans Power Syst* 22(3):1026–1034

Hybrid Renewable Energy System Investigation Based on Power Converters Losses



Ilham Tyass, Omar Bouamrane, Abdelhadi Raihani, Khalifa Mansouri, and Tajeddine Khalili

Abstract Given the renewable sources complementarity, hybrid renewable energy systems (HRES) have been mostly used to address the limitations of single renewable source in terms of stability and reliability. In this regards many researches have been conducted to improve the hybrid efficiency. The aim of this work is to perform a comparative study of HRES architectures based on a qualitative investigation of the power converters efficiency used in each topology. Numerical application is performed based on technical features of converters in order to distinguish the best HRES configuration.

Keywords Renewable energy · Hybrid system · Power converter · Semiconductors losses · Converter efficiency

1 Introduction

The use of renewable energy sources (RES) has consistently increased in recent years [1]. The key cause of this renewed interest is the conventional energy resources depletion such as fuel, natural gas, coal, etc. Subsequently, the use of renewable energy systems considered inexhaustible has become indispensable.

Given the complementarity of some renewable energy sources, like solar and wind energies, their use in a hybrid energy system (HES) became a very attractive solution for electricity production in terms of cost, availability and flexibility.

In order to ensure the AC or DC loads demands, multiple energy sources can be hybridized into one. The composition of such system generally includes renewable energy sources, conventional energy sources, electronics power converters and often-times a storage system is used to ensure the instantaneous power balance. The HES components are interconnected using a DC, AC or DC-AC bus system. Therefore, it is essential to choose the most suitable architecture based on performance, technical installation and economic aspect.

I. Tyass (✉) · O. Bouamrane · A. Raihani · K. Mansouri · T. Khalili
ENSET—SSDIA Laboratory, Hassan II University of Casablanca, Casablanca, Morocco
e-mail: ilham.tyass-etu@etu.univh2c.ma

The purpose of this article is to conduct, through a literature review, a comparative analysis of existing HES topologies by estimating the power converters losses. This is in order to choose the most suitable configuration to a given application. In the following, different hybrid systems architectures will be presented based on extensive bibliographic review. Afterward, we explain different methods to evaluate the losses in used power converters. Indeed, estimating losses in power converters has long been a major research topic in power electronics sector and an ongoing quest for optimal methods to achieve a better converters efficiency [2]. Based on individual converter efficiency, we propose an overall evaluation of the total system efficiency related of each hybrid system configuration in order to conclude about the powerful one.

The previous work will focus on other types of power losses such as losses in bus connection point and lines losses.

2 Hybrid Renewable Energy Systems (HRES) Classification

Combining the two solar and wind renewable sources can provide better reliability than single-renewable energy system since the weakness of one system can be overcome by the strength of the other. Conventionally, a hybrid renewable energy system (HRES) consists of PV and wind power subsystems with/without conventional source acting as backup system. Frequently, it is necessary to provide an energy storage system (battery and/or super-capacitor bank) to save the energy excess from the renewable generators and supply it to cover loads demand. Likewise, some power devices are used to interface HRES components to the used bus connection and the consumer load DC-AC requirements both in stand-alone or grid-connected modes. Compared to stand-alone systems, the use of network-connected systems is widely adopted [3].

In 2014, the authors in [4] claimed through a study on hybrid energy systems that among renewable energy, solar and wind can meet the world's demand. In this work, we focus on the study of the hybrid system with two renewable energy sources, photovoltaic and wind.

3 Hybrid System Architectures

In the renewable energy field, three large system architectures are widely depicted: DC bus architecture, AC bus architecture and mixed bus architecture (AC-DC). The name of each coupling mode refers to the BUS on which the renewable source generators are connected.

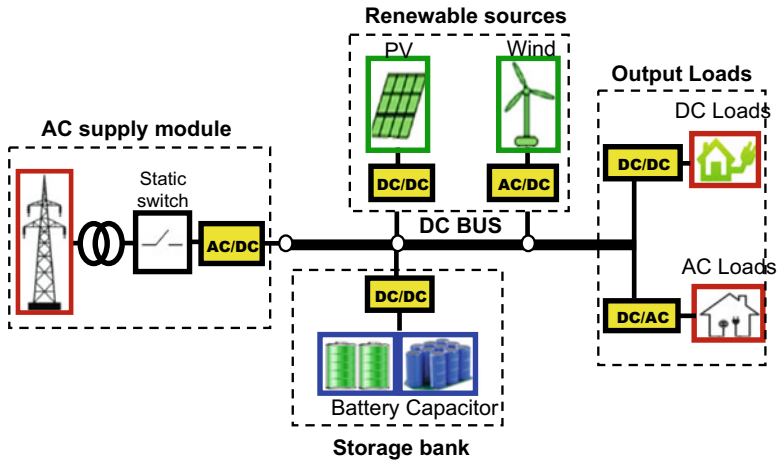


Fig. 1 Typical DC configuration of HRES system

3.1 The Bus Series Configuration (DC)

As shown in Fig. 1, power generators are connected through individual DC/DC and AC/DC devices on DC bus side and reversible AC/DC converter on the grid side [5]. Several authors have widely studied this type of coupling [6, 7].

3.2 The Parallel Bus Configuration (AC)

In this configuration, all sources are directly connected to the grid via individual DC/AC and AC/DC-DC/AC converters (Fig. 2). Also, the AC loads draw the required power from the AC bus through an AC/AC unit while the DC loads use an AC/DC converter. This coupling technique is more used in distributed generation connected to the grid and is frequently used in the case of high-power production with the required financial and logistical resources [7].

3.3 Mixed DC-AC Configuration

The hybrid DC-AC bus configuration is shown in Fig. 3. In this case, both the AC and the DC buses are combined. Thereby, the AC sources and loads are used on AC bus side while the DC ones are connected to the DC bus. The generated energy can be swapped amongst both AC and DC edges through a bidirectional converter [8, 9].

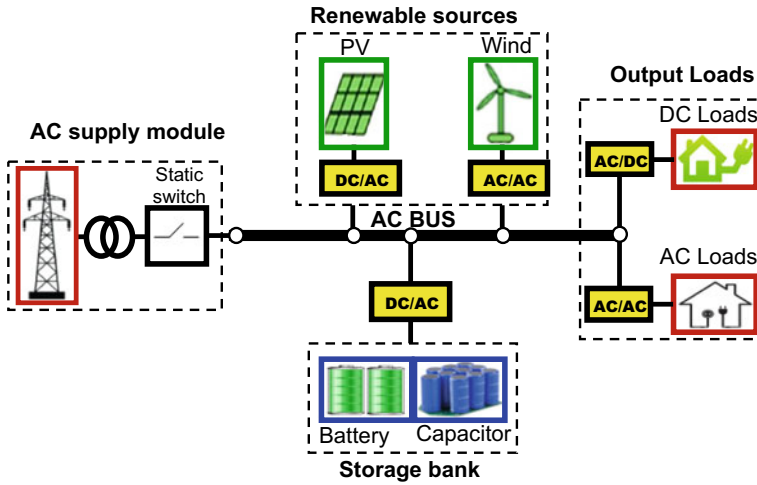


Fig. 2 Typical AC configuration of HRES system

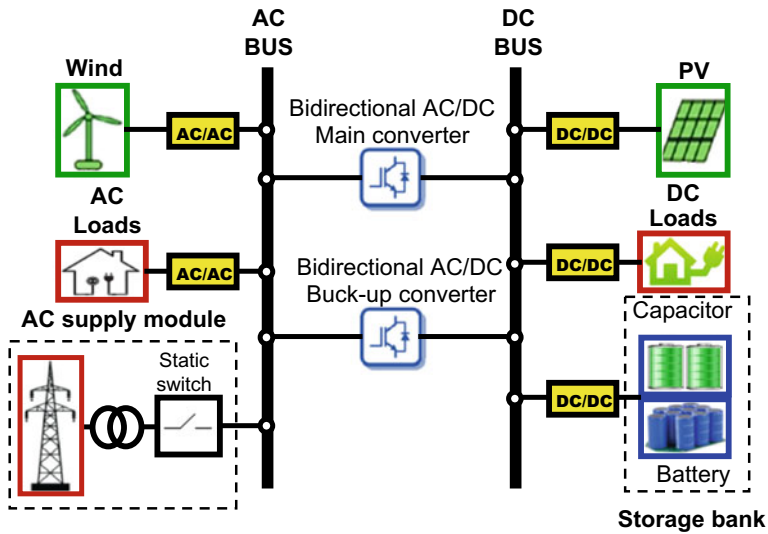


Fig. 3 Typical AC-DC configuration of HRES system

3.4 Bus Configuration Choice

Several studies have probed the optimization of the configuration of the hybrid system according to various here in criteria [10, 11].

In the following, we propose a comparative bus analysis, based on losses estimating in power devices to assess the energy efficiency of each architecture.

4 Losses Estimation in Power Converters

Taking into account losses in power electronics components is crucial for designing a hybrid solar-wind power generating system. These losses are generally depicted by converter's efficiency [12–15].

The efficiency closely depends on the instantaneous load current, input voltage, and switching frequency. Indeed, it has been proved that the Joule effect of the output circuit introduces a loss that increases quadratically with current or power. This leads to a decrease in efficiency beyond the point of maximum efficiency [16].

4.1 Estimated Losses in the DC/DC Converter

In a photovoltaic/Wind hybrid system, a DC/DC converter (chopper) is essential to raise or lower the voltage of the source. In the PV field, the Boost converter is simple but it is mainly used when the load requires a power greater than that supplied by the source.

These losses can be categorized into two main categories: Conduction losses and switching losses.

Conduction Losses in DC/DC Converter. This type of power losses is widely discussed in [17] where authors evaluated power losses in DC-DC converter based on semiconductor parameters, which are given on the manufacturer's datasheet.

Switching Losses In A DC/DC Converter. In fact, the turn-off and turn-on of the power components require a significant rise and fall time to achieve the maximum and minimum switching voltage respectively. This behavior involves turn-off and turn-on losses, which are proportional to the switching frequency [18, 19].

In [17], authors assume that switching losses are only due to transistor. So, DC-DC switching losses depend only on rise time t_r , fall time t_f and switching frequency.

In this way, others studies have proposed some approaches to evaluate DC-DC switching losses [20].

4.2 Estimated Losses in AC/DC Converter

In [21], authors assume that a diode bridge rectifier is used for synchronous machines and a Pulse With Modulation rectifier for asynchronous machines.

In the literature, switching losses are usually negligible at the frequency of operation [17]. Thus, conduction losses correspond to six times the losses by conduction in the supposedly identical diodes [22].

4.3 *Estimated Losses in a DC/AC Converter*

According to the authors of [23], the DC/AC converter's efficiency is calculated through weather data and the estimated performance of photovoltaic panels. They propose the European efficiency, which is the average efficiency subject to the irradiation conditions corresponding to the climate of Central Europe [24].

Conduction Losses In A DC/AC converter. Bierhoff and Fuchus in [25], calculate conduction losses in an inverter using an analytical expressions of average and effective current values in each of the components. The total losses aggregates in the inverter are equal to six times the losses in a transistor and a diode.

Switching Losses in a DC/AC Converter. In [26], authors followed a simple approach based on experimentation. Considering the essential parameters for the transistor (maximum continuous voltage, maximum alternating current, the nominal current, the switching frequency and the time of ascent and descent) and those of the diode (Reverse recovery time, the load recovered). Thus, they define total losses in the inverter as the sum of the turn-on losses, turn-off losses, and losses related to reverse recovery.

4.4 *Losses in a Bidirectional DC/AC Single-Phase Converter*

A DC/AC single-phase converter can operate in two modes: the rectifier mode to inject power into the DC bus, and the inverter mode to inject power into the AC bus.

5 **Evaluation of Overall Hybrid System Buses Efficiency**

5.1 *Methodology*

Power device efficiency is defined as the ratio of its useful energy output to its total energy input. In our case, the HRES is built to supply both AC or DC loads and storage system in charge mode. Sometimes, it is allowed to inject energy excess to grid. In addition, loads will be supplied from grid or storage system (discharge mode). Otherwise, in a hybrid renewable energy system, storage device is prominent to improve the economics performance of the HRES, and to enable optimal load sharing among the sources. Note also that renewable sources may not provide energy simultaneously due to their intermittent nature. Consequently, the HRES efficiency evaluation depends on the AC loads or DC loads to supply and also on the availability of sources. For that, we will evaluate the HRES efficiency on the load side using individual source i.e. wind source, PV source, storage bank or grid. In addition, we assume that the efficiency is the same whatever the power flow direction via the

Table 1 DC coupling

	Direct consumption	
	DC loads	AC loads
Wind	$\eta_w^{dc} = \eta_{AC/DC} \cdot \eta_{ text{DC}/DC}$	$\eta_w^{ac} = \eta_{AC/DC} \cdot \eta_{DC/AC}$
PV	$\eta_p^{dc} = \eta_{DC/DC} \cdot \eta_{DC/DC}$	$\eta_p^{ac} = \eta_{DC/DC} \cdot \eta_{DC/AC}$
Grid	$\eta_g^{dc} = \eta_{AC/DC} \cdot \eta_{DC/DC}$	$\eta_g^{ac} = \eta_{AC/DC} \cdot \eta_{DC/AC}$

bidirectional converters. In following, we present the tables of equations relating ton DC coupling mode as an example to be applied to the others coupling modes.

Direct Consumption. Table 1 summarize some efficiency expressions when both AC and DC loads are supplied directly from power sources without storage system named direct consumption for DC coupling mode.

In this case, total efficiency can be evaluated by Eqs. (1–3):

$$\eta_{tot}^{dc} = \alpha_1 \eta_w^{dc} + \alpha_2 \eta_p^{dc} + \alpha_3 \eta_g^{dc} \tag{1}$$

$$\eta_{tot}^{ac} = \alpha_1 \eta_w^{ac} + \alpha_2 \eta_p^{ac} + \alpha_3 \eta_g^{ac} \tag{2}$$

$$\eta_{tot}^m = \alpha_1 \eta_w^m + \alpha_2 \eta_p^m + \alpha_3 \eta_g^m \tag{3}$$

where $\alpha_{i=1,2,3} = 1$ if the corresponding power source is on otherwise $\alpha_{i=1,2,3} = 0$. For example, if DC loads are supplied from wind and PV generators then $\alpha_1 = 1$, $\alpha_2 = 1$ and $\alpha_3 = 0$.

Deferred Consumption. Table 2 recapitulate expressions to evaluate the total bus efficiency when storage system is used to boost power sources to meet AC and/or DC loads, for DC coupling mode.

In the same way, we can calculate total bus efficiency by using the following Eqs. (4–6):

$$\eta_{tot}^{dc} = \beta_1 \eta_{w_b}^{dc} + \beta_2 \eta_{p_b}^{dc} + \beta_3 \eta_{g_b}^{dc} \tag{4}$$

$$\eta_{tot}^{ac} = \beta_1 \eta_{w_b}^{ac} + \beta_2 \eta_{p_b}^{ac} + \beta_3 \eta_{g_b}^{ac} \tag{5}$$

Table 2 DC coupling

	Deferred consumption (through battery)	
	DC loads	AC loads
Wind	$\eta_{w_b}^{dc} = \eta_{AC/DC} \cdot \eta_{DC/DC_Bat} \cdot \eta_{DC/DC}$	$\eta_{w_b}^{ac} = \eta_{AC/DC} \cdot \eta_{DC/DC_Bat} \cdot \eta_{DC/AC}$
PV	$\eta_{p_b}^{dc} = \eta_{DC/DC} \cdot \eta_{DC/DC_Bat} \cdot \eta_{DC/DC}$	$\eta_{p_b}^{ac} = \eta_{DC/DC} \cdot \eta_{DC/DC_Bat} \cdot \eta_{DC/AC}$
Grid	$\eta_{g_b}^{dc} = \eta_{AC/DC} \cdot \eta_{DC/DC_Bat} \cdot \eta_{DC/DC}$	$\eta_{g_b}^{ac} = \eta_{AC/DC} \cdot \eta_{DC/DC_Bat} \cdot \eta_{DC/AC}$

Table 3 Converters efficiencies

Efficiency	Power device	Value (%)
$\eta_{DC/DC}$	Basic BOOST DC/DC converter [17]	95.00
η_{DC/DC_bid}	Half bridge DC/AC converter [17]	95.00
η_{AC/DC_bid}	Bidirectional converter mode rectifier [17]	96.00
η_{DC/AC_bid}	Bidirectional converter mode inverter [17]	96.00
η_{AC/AC_wind}	Two converter blocks one AC/DC and one AC/DC	92.16
η_{AC/AC_Load}	AC/AC converter [27]	97.30
η_{DC/DC_Bat}	Storage battery	80

$$\eta_{tot}^m = \beta_1 \eta_{w_b}^m + \beta_2 \eta_{p_b}^m + \beta_3 \eta_{g_b}^m \quad (6)$$

where $\beta_{i=1,2,3} = 1$ if the corresponding power source is on otherwise $\beta_{i=1,2,3} = 0$. We notice:

$$\eta_{DC/DC_Bat} = \eta_{DC/DC_bid} \cdot \eta_{Bat} \cdot \eta_{DC/DC_bid} \quad (7)$$

$$\eta_{DC/AC_Bat} = \eta_{DC/AC_bid} \cdot \eta_{Bat} \cdot \eta_{DC/AC_bid} \quad (8)$$

Are respectively efficiencies through the storage cycle (battery and DC/DC bidirectional converter) and (battery and DC/AC bidirectional converter).

5.2 Case Study: Numerical Example

This application aims to calculate the bus numerical efficiency of each HRES configuration. Numerical values of converters efficiencies are taken from literature as shown in Table 3.

Referring to Table 4 values, the numerical result is depicted in Table 4.

6 Discussion

Through the numerical results obtained, it turns out that the overall conversion efficiency changes according to all parameters with different degrees (type of consumption, load, renewable energy and type of coupling).

In general, we note that the performance in direct mode is much higher than in deferred mode and this, because of the power lost by transiting through the cycle of the DC/DC converter and storage battery.

Table 4 Bus efficiency evaluation

		Direct consumption		Deferred consumption	
		DC load (%)	AC load (%)	DC load (%)	AC load (%)
DC BUS	Wind	91.20	92.16	65.85	66.54
	PV	90.25	91.20	65.16	65.85
	Grid	91.20	92.16	65.85	66.54
AC BUS	Wind	88.47	89.67	65.23	66.11
	PV	92.16	93.41	67.95	68.87
	Grid	96.00	97.30	70.78	71.74
Mixed BUS	Wind	84.05	89.67	60.68	59.67
	PV	90.25	88.74	65.16	64.07
	Grid	91.20	97.30	65.85	64.74

For the part of energy inherent in the production by the wind circuit, the efficiency is more interesting in DC coupling, whether for continuous or alternative loads. While for production through the photovoltaic generator, the coupling that gives the best conversion rate is AC coupling.

However, the best performance of the system is due to the combination of AC casting with power grid production, whether for continuous or alternative loads.

Through these results, it can be confirmed that choosing a specific architecture from the three configurations mentioned above (DC, AC or mixed) essentially amounts to mastering the sizing of the installed hybrid energy conversion system, and this through the determination of the parameters of the system, namely:

- Profiles of available input energy sources and the proportion of use each in the day.
- The share of live consumption compared to that of deferred consumption.
- The possibility of connecting to the electricity grid.
- The distribution of expenses by type of consumption (continuous or alternative).

7 Conclusion

In this work, we presented the different architectures of hybrid multi-source energy systems. Different types of power converters composing these systems have been described by analyzing the different equations for estimating the power losses found in the literature. A configuration of each coupling was chosen; we studied and calculated the overall conversion performance of each system through the unit yields of the power converters.

The current study results prove the important it is to consider power converter yields as a decisive factor in choosing one type of coupling or another.

It is obvious that this study needs to be continued, in order to develop a method of determining the optimal configuration to choose, taking into account the different parameters of the system. This would be achieved through the development of a decision-support algorithm that will act according to the input parameters studied in this article.

References

1. RENEWABLES 2019: global status report. www.ren21.net
2. Berringer K, Marvin J, Perruchoud P (1995) Semiconductor power losses in AC inverters. In: IAS '95. Conference Record of the 1995 IEEE Industry Applications Conference Thirtieth IAS Annual Meeting, Orlando, FL, USA, 1995, vol 1, pp 882–888. <https://doi.org/10.1109/IAS.1995.530391>
3. Zeb K et al (2018) A comprehensive review on inverter topologies and control strategies for grid connected photovoltaic system. *Renew Sustain Energy Rev* 94:1120–1141. <https://doi.org/10.1016/j.rser.2018.06.053>
4. Liu Q et al (2009) Solar and wind energy resources and prediction. *J Renew Sustain Energy* 1(4):043105. <https://doi.org/10.1063/1.3168403>
5. Wu TF, Chang CH, Lin LC, Yu GR, Chang YR (2013) DC-bus voltage control with a three-phase bidirectional inverter for dc distribution systems. *IEEE Trans. Power Electron.* 28(4):1890–1899. avr. 2013. <https://doi.org/10.1109/TPEL.2012.2206057>
6. Muselli M, Notton G, Poggi P, Louche A (2000) PV-hybrid power systems sizing incorporating battery storage: an analysis via simulation calculations. *Renew Energy* 20(1):1–7. [https://doi.org/10.1016/S0960-1481\(99\)00094-4](https://doi.org/10.1016/S0960-1481(99)00094-4)
7. Ashari M, Nayar CV (1999) An optimum dispatch strategy using sett points for a photovoltaic (PV)–diesel–battery hybrid power system. *Solar Energy* 66(1):1–9. [https://doi.org/10.1016/S0038-092X\(99\)00016-X](https://doi.org/10.1016/S0038-092X(99)00016-X)
8. Ahmed I, ElAmine SM, Saïd B, Youcef H (2017) Différentes Configurations du Système PV pour l'Alimentation Sans Interruption (ASI): Application au Relais GSM, p 10
9. Wichert B, Dymond M, Lawrance W, Friese T (2001) Development of a test facility for photovoltaic-diesel hybrid energy systems. *Renew Energy* 22(1–3):311–319. [https://doi.org/10.1016/S0960-1481\(00\)00024-0](https://doi.org/10.1016/S0960-1481(00)00024-0)
10. Elhadidy MA, Shaahid SM (1998) Feasibility of hybrid (WIND + SOLAR) power systems for DIIAHRAN, Saudi Arabia, p 7. [https://doi.org/10.1016/S0960-1481\(98\)00344-9](https://doi.org/10.1016/S0960-1481(98)00344-9)
11. Kaabeche A, Belhamel M, Ibtouen R, Moussa S (2006) Optimisation d'un système hybride (éolien – photovoltaïque) totalement autonome. *Revue des Energies Renouvelables* 9(3):199–209
12. Ekren O, Ekren BY (2008) Size optimization of a PV/wind hybrid energy conversion system with battery storage using response surface methodology. *Appl Energy* 85(11):1086–1101. <https://doi.org/10.1016/j.apenergy.2008.02.016>
13. Mar B (1999) Hybrid solar-wind domestic power generating system: a case study. *Renew Energy* 17:355–358. [https://doi.org/10.1016/S0960-1481\(98\)00123-2](https://doi.org/10.1016/S0960-1481(98)00123-2)
14. Pires VF, Silva JFA (2002) Teaching nonlinear modeling, simulation, and control of electronic power converters using MATLAB/SIMULINK. *IEEE Trans Educ* 45(3):253–261. <https://doi.org/10.1109/TE.2002.1024618>
15. Douangsyla S, Indarack P, Kanthee A, Kando M, Kittiratsatcha S, Kinnares V (2004) Modeling for PWM voltage source converter controlled power transfer. In: IEEE International Symposium on Communications and Information Technology, 2004. ISCIT 2004, Sapporo, Japan, vol 2, pp 875–878. <https://doi.org/10.1109/ISCIT.2004.1413844>

16. Zhou S, Rincon-Mora GA (2006) A high efficiency, soft switching DC-DC converter with adaptive current-ripple control for portable applications. *IEEE Trans Circuits Syst II* 53(4):319–323. <https://doi.org/10.1109/TCSII.2005.859572>
17. Wu H, Sechilariu M, Locment F (2017) Influence of dynamic efficiency in the DC microgrid power balance. *Energies* 10(10):1563. <https://doi.org/10.3390/en10101563>
18. Chen Z, Boroyevich D, Burgos R, Wang F (2009) Characterization and modeling of 1.2 kv, 20 A SiC MOSFETs. In: 2009 IEEE Energy Conversion Congress and Exposition, San Jose, CA, Sept 2009, pp 1480–1487. <https://doi.org/10.1109/ECCE.2009.5316106>
19. Biela J, Schweizer M, Waffler S, Kolar JW (2011) SiC versus Si—evaluation of potentials for performance improvement of inverter and DC–DC converter systems by SiC power semiconductors. *IEEE Trans Ind Electron* 58(7): 2872–2882. <https://doi.org/10.1109/TIE.2010.2072896>
20. Wintrich A, Nicolai U, Tursky W, Reimann T (2015) Application manual power semiconductors, 2nd revised edition. ISLE Verlag, Ilmenau
21. Forest F et al (2006) Use of opposition method in the test of high-power electronic converters. *IEEE Trans Ind Electron* 53(2):530–541. <https://doi.org/10.1109/TIE.2006.870711>
22. Lopez M, Morales D, Vannier J-C, Sadarnac D (2007) Influence of power converter losses evaluation in the sizing of a hybrid renewable energy system. In: 2007 International Conference on Clean Electrical Power, Capri, Italy, May 2007, pp 249–254. <https://doi.org/10.1109/ICCEP.2007.384218>
23. Nanakos AC, Tatakis EC, Papanikolaou NP (2012) A weighted-efficiency-oriented design methodology of flyback inverter for AC photovoltaic modules. *IEEE Trans Power Electron* 27(7):3221–3233. <https://doi.org/10.1109/TPEL.2011.2182211>
24. Valentini M, Raducu A, Sera D, Teodorescu R (2008) PV inverter test setup for European efficiency, static and dynamic MPPT efficiency evaluation. In: 2008 11th international conference on optimization of electrical and electronic equipment, Brasov, Romania, May 2008, pp 433–438. <https://doi.org/10.1109/OPTIM.2008.4602445>
25. Bierhoff MH, Fuchs FW (2004) Semiconductor losses in voltage source and current source IGBT converters based on analytical derivation. In: 35th Annual IEEE power electronics specialists conference, p 7
26. Casanellas F (1994) Losses in PWM inverters using IGBTs, p 5. *IEE Proc Electr Power Appl* 141(5). <https://doi.org/10.1049/ip-epa:19941349>
27. Andersen RL, Lazzarin TB, Barbi I (2013) A 1-kW step-up/step-down switched-capacitor AC–AC converter. *IEEE Trans Power Electron* 28(7):3329–3340. <https://doi.org/10.1109/TPEL.2012.2222674>

Estimation of Daily Direct Normal Solar Irradiation Using Machine-Learning Methods



Zineb Bounoua and Abdellah Mechaqrane

Abstract The sizing and simulation of all solar systems require the availability of reliable measurements of solar radiation at different time steps. Unfortunately, solar radiation measurements are not readily available for most worldwide locations. For this reason, it is desirable to develop accurate prediction models by developing relationships between available meteorological data and solar irradiation. Artificial Neural Networks (ANN) have been widely used for the estimation of different solar irradiation components. Recently, some machine learning methods have been reported and appear to be very promising. In this paper, we are interested in comparing the performance of ANN and three ensemble methods (Bagging, Boosting and Random Forests) in estimating the daily direct normal (DNI) solar irradiation from some commonly measured meteorological variables. Our study is performed using measurements data from five Moroccan cities: Oujda, Missour, Erfoud, Zagora, and Tan-Tan. The achieved results show that all developed models give good performances on training and validation datasets with a normalized Root Mean Squared Error (nRMSE) $< 20\%$.

Keywords Direct normal irradiation · MLP · Boosting · Bagging · Random forest

1 Introduction

After the energy crisis of 1973, researchers devoted an important part of their works to the development of alternative solutions to increase the independence of fossil fuels, while taking into account the environment protection. Of course, the use of solar energies is an obvious solution, which represents enormous advantages. After several difficulties, solar energy has gained a lot of interest in recent years. Indeed, several countries, including Morocco, have opted to diversify their energy mix by installing large photovoltaic or concentrated solar power plants, or both. However, and as it well known, solar energy is a fluctuating and intermittent renewable energy source.

Z. Bounoua (✉) · A. Mechaqrane
SIGER, Intelligent Systems, Georesources and Renewable Energies Laboratory, Faculty of Sciences and Techniques, Sidi Mohamed Ben Abdellah University, PO. Box 2202 Fez, Morocco
e-mail: zineb.bounoua@usmba.ac.ma

Indeed, its availability and its quantity depend on weather conditions and therefore exhibit a high degree of random variability over time. Therefore, the injection of energy produced from solar installations into an electrical grid creates problems in its management. To remedy to these problems, it is important to have, in advance, an idea about the amount of energy which will be produced in a given time horizon step. Depending on the solar conversion system, it is necessary to have a good knowledge of the global solar irradiation for photovoltaic and water heating systems, or of the direct normal solar irradiation for Concentrated Solar systems (CSP) or Concentrated Photovoltaic systems (CPV).

Solar component measurements (Global Horizontal solar Irradiation (GHI), Diffuse Horizontal solar Irradiation (DHI) and Direct Normal solar Irradiation (DNI)) are not always available in most regions of the world due to high equipment costs and maintenance problems. This strong demand for local and regional solar radiation and meteorological information databases prompted several researchers to develop different techniques for predicting solar radiation in a location using commonly measured meteorological variables.

According to the literature, Artificial Neural Networks (ANN) techniques have been widely employed for solar radiation prediction [1]. Their high performance and ability to solve complex non-linear problems by learning the relationship between inputs and outputs of systems were the main reasons for their wide use in different fields [2]. Mubiru [3] developed a prediction model using ANN to estimate the daily average monthly direct solar radiation for sites in Uganda. The results showed good agreement between the estimated and measured values of direct solar irradiation with a mean square error of 0.197 MJ/m².

Nowadays, several new machine-learning methods are increasingly used for solar radiation prediction. Hassan et al. [4] have explored the potential of tree-based ensemble methods (gradient boosting, bagging, and random forest (RF)) in estimating global, diffuse, and normal solar radiation components in daily and hourly time-scales. These models were tested on five sites in the MENA region and compared to multi-layer perceptron (MLP), support vector regression (SVR), and decision tree (DT) models, mentioning that the overcast-sky daily observations are eliminated before applying the machine-learning methods. Achieved results showed that ensemble models are more stable than decision trees and MLP and have close performances to the optimized SVR models, with significantly less computational costs.

It should be stressed that the majority of research works concern the GHI prediction. For the DNI component, the most existing models have been developed based on Weather Research and Forecasting methods [5], satellite methods [6], and image processing techniques [7].

The main objective of this work is to evaluate the ability of ensemble methods based on regression trees (Bagging, Boosting, and Random Forests) in estimating the daily direct normal solar irradiation (DNI). A comprehensive study aiming at assessing and comparing the performance of these new methods will play a crucial role in choosing the best method for estimating solar irradiation. First, each model is trained and tested using data from each city individually, as well, using another

database, which is constructed by aggregating data from the five cities (All cities). Such a comparison performed for different climates will lead to a more realistic and general conclusion about the models' suitability. To evaluate the effectiveness of these models, they were compared to the Multi-Layers Perceptron ANN (MLP-ANN) model. The accuracy of these models was assessed based on three major statistical indicators (R, nRMSE and nMAE). This work will help the researchers in evaluating the daily solar energy resource, which is essential to determine the performance of different solar energy systems and study their feasibility at any location with similar climatic condition.

2 Methodology

2.1 Multi-layer Perceptron Artificial Neural Network (MLP-ANN)

Inspired by biological neural networks, Artificial Neural Networks (ANN) represent the simplest models that have a great ability to solve complex nonlinear problems by deducing the relationship between inputs and outputs in several areas of prediction, optimization, and classification. In this study, we used a Multilayer Perceptron Neural Network model (MLP) applying the feed-forward backpropagation, and the Levenberg-Marquardt algorithm as an approximation function to reduce the error of non-linear functions. It consists of M inputs, one hidden layer with N tangent hyperbolic neurons, and a linear output neuron. Figure 1 shows the MLP-ANN architecture adopted in this study.

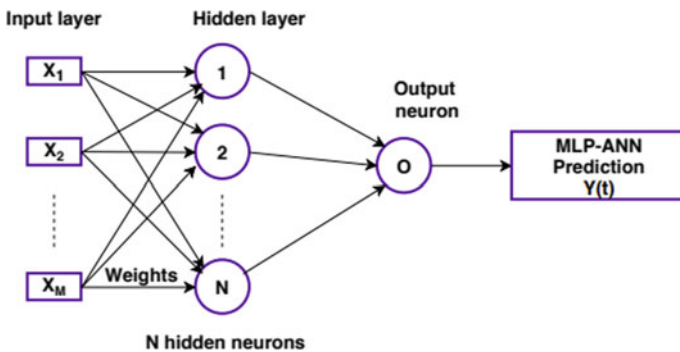


Fig. 1 MLP-ANN architecture

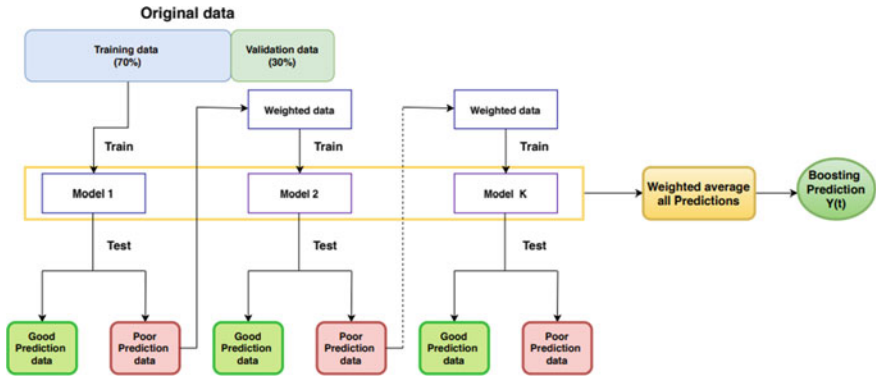


Fig. 2 Gradient boosting process diagram

2.2 Gradient Boosting

The most popular algorithm in the ensemble methods family is called Boosting and was introduced in 1996 by FREUND and SCHAPIRE [8]. The main characteristic of this algorithm is its ability to convert weak learners into strong learners by: (a) sequentially associating the outputs of individual weak learners during the training phase, and (b) by assigning, at each iteration, higher weights to poorly predicted samples.

The type of boosting algorithm chosen to solve our regression problem is Gradient Boosting. It is an algorithm, which creates the model by steps. Each model is obtained by optimizing the absolute differentiable loss function. For each weak learner added, a new model is created which gives a more accurate estimate of the output. The gradient boosting process diagram is presented in Fig. 2.

2.3 Bagging

Leo BREIMAN developed the bagging algorithm in 1996 [9]. This algorithm is based on two main steps; bootstrap and aggregation. Bagging adopts the bootstrap distribution to generate different base learners by applying bootstrap sampling. A sample that is taken from the original dataset with replacement is called a bootstrap sample, which provides the data subsets for training the base learner. When this process is repeated several times, several training samples can be obtained and from each sample, a base learner is trained using the base learning algorithm. For the regression problems, Bagging adopts a popular strategy to aggregate the base learner's outputs by calculating the average of the obtained estimations from each sample. This process is explained as a diagram in Fig. 3.

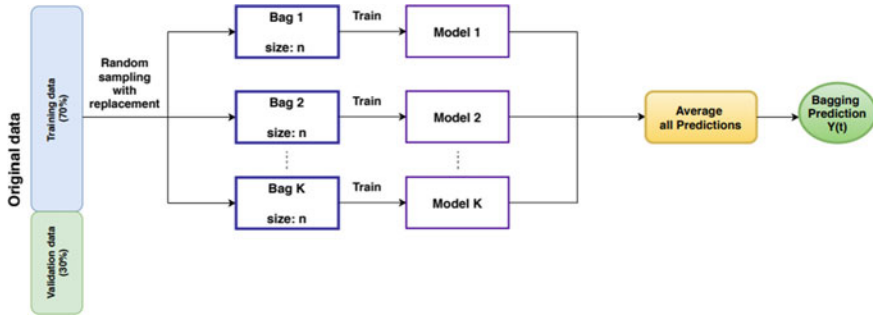


Fig. 3 Bagging process diagram

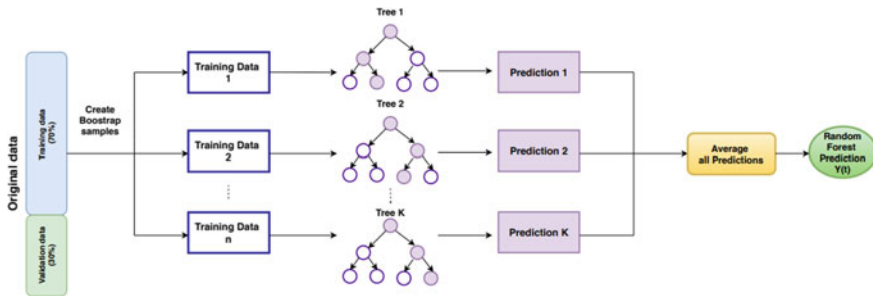


Fig. 4 Random forest process diagram

2.4 Random Forest

Random forests are part of the machine learning techniques proposed by Breiman, which combines several random trees constructed using the Bagging method [10]. This method represents the association of a number of predictors. A regression tree is developed for each sample with a random selection of input variables and an arbitrary selection of a subset of predictors. The generalization error tends towards a limit only if the number of trees initially selected in the forest is high. The final estimate of the set is obtained by calculating the average estimate of all developed trees. The process diagram of Random Forest is shown in Fig. 4.

2.5 Performance Evaluation

Trained models are evaluated using three statistical indicators, the coefficient of correlation (R), the normalised mean absolute error (nMAE), and the normalised root mean square error (nRMSE). Normalized MAE and RMSE are used to avoid the scale dependency. A low value of nRMSE indicates a very good prediction model.

$$R = \frac{\sum_{i=1}^n (y_{ei} - \bar{y}_e)(y_{mi} - \bar{y}_m)}{\sqrt{\sum_{i=1}^n (y_{ei} - \bar{y}_e)^2 \sum_{i=1}^n (y_{mi} - \bar{y}_m)^2}} \quad (1)$$

$$nMAE = \frac{\frac{1}{n} \sum_{i=1}^n |y_{ei} - y_{mi}|}{\bar{y}_m} \quad (2)$$

$$nRMSE = \frac{\sqrt{\frac{1}{n} \sum_{i=1}^n (y_{ei} - y_{mi})^2}}{\bar{y}_m} \quad (3)$$

With y_{mi} and y_{ei} are the i th measured value and the i th estimated value, respectively. \bar{y}_m and \bar{y}_e are the mean value of n measurements of y_{mi} ($\bar{y}_m = \frac{1}{n} \sum_{i=1}^n y_{mi}$) and the mean value of n estimations of y_{ei} ($\bar{y}_e = \frac{1}{n} \sum_{i=1}^n y_{ei}$), respectively.

3 Locations and Databases

In this work, daily solar and meteorological data are measured at five locations in Morocco as part of the enerMENA project. This project was initiated in 2010, by the Institute of Solar Research at the German Aerospace Center (DLR). The “thermal sensor” stations installed in Oujda, Missouri and Tan-Tan include a CHP1 pyrheliometer to measure DNI and two Kipp & Zonen CMP21 pyranometers to measure DHI and GHI. Whereas, the Erfoud and Zagora stations are equipped with a “Rotating Shadowband Irradiometer” (RSI), it is the least expensive technique for measuring the two solar components (GHI and DHI). These stations also contain temperature, relative humidity and pressure sensors, as well as an anemometer to measure the wind speed and direction at 10 m height. The measurement period is between 2013 and 2015 for Erfoud, Zagora and TanTan, between 2014 and 2015 for Missouri, and between 2011 and 2015 for Oujda. Table 1 shows the geographical coordinates of each station and the used instruments for measuring solar irradiation.

4 Results and Discussions

In this study, 70% of historic data is used for training phase and the network is adjusted according to its error. The remaining 30% of the data provides independent validation of network.

Building an efficient estimation model requires a good choice of relevant input variables with the most significant impact on the output variable fluctuations. For this, some possible combinations between the input parameters have been tested using an ANN-MLP model with a variable architecture, the structure of each trained model is

Table 1 Moroccan stations of the enerMENA network

Site	Latitude (°N)	Longitude (°W)	Altitude (m)	Measurement period	Station type	Measured solar components	Type of instruments	Model
OUJDA	34.650	1.900	617 m	18/08/2011 to 30/09/2015	TS	GHI DHI DNI	Pyranometer Pyranometer Pyrheliometer	Kipp & Zonen CMP21 Kipp & Zonen CMP21 Kipp & Zonen CHP1
MISSOUR	32.860	4.107	1107 m	01/01/2014 to 30/09/2015	TS	GHI DHI DNI	Pyranometer Pyranometer Pyrheliometer	Kipp & Zonen CMP21 Kipp & Zonen CMP21 Kipp & Zonen CHP1
ERFOUD	31.491	4.218	859 m	02/06/2013 to 30/09/2015	RSI	GHI DHI	Pyranometer Pyranometer	RSI PY67982
ZAGORA	30.272	5.852	783 m	03/06/2013 to 30/09/2015	RSI	GHI DHI	Pyranometer Pyranometer	RSI PY75722
TAN-TAN	28.498	11.322	75 m	01/06/2013 to 30/09/2015	TS	GHI DHI	Pyranometer Pyranometer Pyrheliometer	Kipp & Zonen CMP21 Kipp & Zonen CMP21 Kipp & Zonen CHP1

optimized using a different number of hidden neurons (from 1 to 20) and evaluated on five runs. The performed tests reveal that the best combination to estimate daily DNI is the same for all the five stations, and it is composed of the day of the year, daily normal top of atmosphere solar irradiation, daily mean air temperature and the daily clearness index (J_{an} , G_{toa_n} , T_{mean} , K_t), with 10 neurons in the hidden layer.

Table 2 presents the performance of daily DNI estimation models obtained by applying the three ensemble methods and the artificial neural network for each used database. The results corresponding to the best estimation model are shaded in gray.

Despite differences in climate and geographical positions between stations, it can be observed that the performances obtained by grouping the five stations data (Erfoud, Missouri, Oujda, Tan-Tan and Zagora) for all developed methods, vary between 94.79 and 95.44% for R-values and between 11.87 and 12.65% for nRMSE values. The results obtained at Erfoud progress from 94.96 (Boosting) to 95.30% (RF) for R-values and from 11.69 (Boosting) to 11.35% (RF) for nRMSE values. The four machine learning methods applied to Missouri gave results ranging between 95.97 and 96.25% for R-values and between 10.86 and 11.17% for nRMSE values. In Oujda, R-values vary between 96.46 and 96.76% and nRMSE values between 10.40 and 10.80%. The performance results of Zagora show a variation from 94.68 to 95.30% for the R-values, and from 10.60 to 11.25% for the nRMSE values. For Tan-Tan, R-values vary between 94.75 and 95.10% and nRMSE values between 12.64 and 13.03%.

According to [11], TanTan is characterized by frequent clouds and fogs, and a high relative humidity of 83% averaged all over the year. These conditions cause the formation of small droplets of water on the measuring instruments, resulting in the most of the time of errors in solar radiation measurements as long as the instruments are not cleaned. However, this station only experienced 84 cleaning events for the period between July 26, 2014 and June 1, 2015 [11]. Hence, the slightly weak performances obtained in TanTan compared to the other stations.

In general, the Random Forest model outperforms all the other three methods (ANN, Boosting and, Bagging) in the estimation of daily DNI for all used datasets. Figures 5 and 6 represent the training and validation scatter plots of the four developed machine-learning methods for each database. A good agreement between the estimated and the measured values for all databases can be noticed.

The obtained results prove that the tree ensemble methods (Boosting, Bagging and Random Forest) can compete the MLP-ANN to estimate daily direct normal solar irradiation. The performances of the database containing all cities with different climates are encouraging and to a certain extent general. From Fig. 7, which shows the validation results of randomly 100 days of DNI estimation for all cities using the four machine learning models, it can be noted that all developed models give good performances on validation datasets with a slight better performance of Random forest estimation that closely follows the measurement values against other models.

According to this study, it is possible to have an idea about the solar potential of new cities with the same climatic conditions with no DNI solar data measurements in order to design and analyse the performance of any concentrated solar system.

Table 2 Machine learning methods performance for daily DNI estimation in train and validation phases for each station and for all grouped stations

Stations	Model	Structure	Training			Validation		
			R (%)	nMAE (%)	nRMSE (%)	R (%)	nMAE (%)	nRMSE (%)
Erfoud	ANN	10 neurons	95.347	8.573	11.071	95.081	8.832	11.602
	Boosting	238 learners	95.638	8.454	10.729	94.962	9.233	11.695
	Bagging	71 learners	97.617	6.317	8.175	94.979	9.108	11.634
	RF	139 learners	97.560	9.874	8.290	95.307	8.785	11.357
Missour	ANN	10 neurons	96.828	7.755	10.377	96.168	8.473	10.909
	Boosting	254 learners	97.214	7.317	9.778	95.977	8.671	11.177
	Bagging	48 learners	98.417	5.559	7.575	96.112	8.467	11.018
	RF	137 learners	98.441	5.560	7.499	96.257	8.228	10.864
Oujda	ANN	10 neurons	97.386	6.656	9.091	96.655	7.672	10.476
	Boosting	257 learners	97.266	6.950	9.304	96.461	8.100	10.801
	Bagging	53 learners	98.619	4.895	6.764	96.692	7.870	10.499
	RF	165 learners	98.638	4.908	6.745	96.764	7.818	10.407
Tan-Tan	ANN	10 neurons	96.629	9.018	11.437	95.024	10.214	12.733
	Boosting	275 learners	96.797	8.744	11.210	94.751	10.272	13.034
	Bagging	35 learners	97.037	8.372	10.742	94.945	10.033	12.822
	RF	185 learners	97.452	7.738	9.954	95.109	9.828	12.648
Zagora	ANN	10 neurons	95.677	7.786	10.089	95.129	8.784	10.794
	Boosting	246 learners	96.708	6.792	8.821	94.682	8.989	11.254
	Bagging	42 learners	97.793	5.614	7.412	95.103	8.650	10.928

(continued)

Table 2 (continued)

Stations	Model	Structure	Training			Validation		
			R (%)	nMAE (%)	nRMSE (%)	R (%)	nMAE (%)	nRMSE (%)
	RF	138 learners	97.799	5.645	7.436	95.307	8.492	10.604
All cities	ANN	10 neurons	95.494	9.132	11.817	95.063	9.384	12.330
	Boosting	186 learners	95.614	9.130	11.662	94.793	9.670	12.654
	Bagging	63 learners	97.927	6.203	8.135	94.867	9.602	12.567
	RF	145 learners	98.025	6.092	7.960	95.440	9.046	11.877

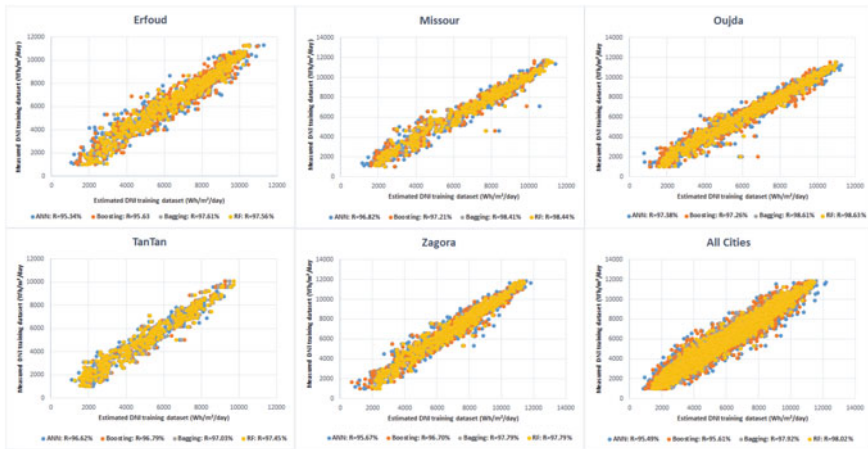


Fig. 5 Scatter plots of daily measured and estimated DNI using the four machine-learning models and the six training datasets

5 Conclusion

The objective of this work was to evaluate the potential of four machine-learning methods (Multilayer Perceptron Artificial Neural Network (MLP-ANN), Boosting, Bagging and Random Forest) in estimating the daily direct normal solar irradiation using measurement databases of five Moroccan stations (Erfoud, Missour, Oujda, Zagora and Tan-Tan). The achieved results show that all developed models give good performances on training and validation datasets (nRMSE < 20%).

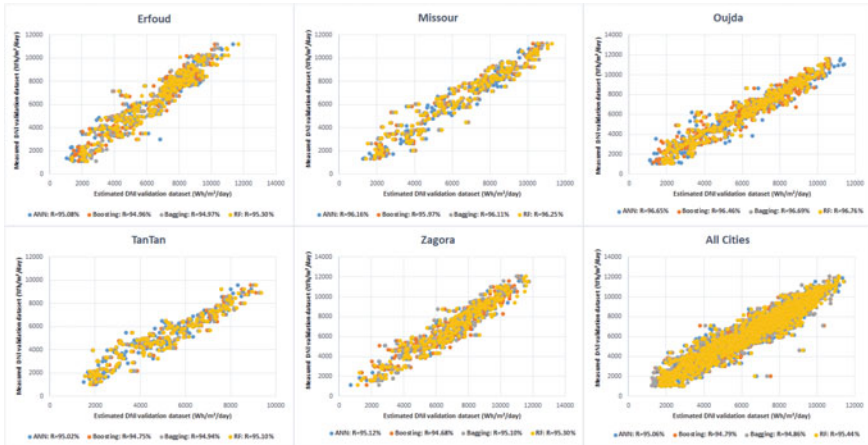


Fig. 6 Scatter plots of daily measured and estimated DNI using the four machine-learning models and the six validation datasets

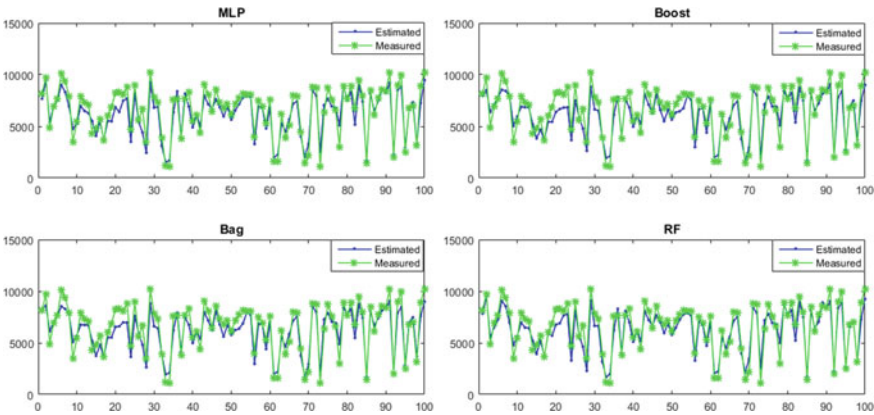


Fig. 7 Times series plot of measured and estimated daily DNI of a random selection of 100 days for all cities using the four machine learning models in the validation phase

The ensemble methods based on decisions trees (Bagging, Boosting, Random Forest) yielded a good performance and a high degree of stability. They are sufficiently efficient and give quite similar performance compared to MLP-ANN models. In addition, it was found that the Random Forest (RF) is the most efficient model for estimating daily DNI.

Finally, we can say that the ensemble methods based on decision trees can compete the Artificial Neural Networks models, which have been widely used in the domain of solar estimation and prediction. Therefore, it can be concluded that Bagging, Boosting and Random Forest are the future methods.

This work allowed to generate some reflections and to build solid ideas on prediction models. This will open up new horizons of research, and we anticipate to predict direct normal solar irradiation in different time horizons (hour, ½ hour, . . . , 10 min) by using the actually tested and eventually other machine learning methods.

Acknowledgements The authors would like to express their special gratitude to the German Aerospace Center (DLR) for their scientific support by making available to us the measurements of solar components and meteorological parameters used in this study.

References

1. Mohandes M, Rehman S, Halawani TO (1998) Estimation of global solar radiation using artificial neural networks. *Renew Energy* 14(1–4):179–184
2. Benganem M, Mellit A, Alamri SN (2009) ANN-based modelling and estimation of daily global solar radiation data: a case study. *Energy Convers Manage* 50(7):1644–1655
3. Mubiru J (2011) Using artificial neural networks to predict direct solar irradiation. *Adv Artif Neural Syst* (2011)
4. Hassan MA et al (2017) Exploring the potential of tree-based ensemble methods in solar radiation modeling. *Appl Energy* 203:897–916
5. Lara-Fanego V et al (2012) Evaluation of DNI forecast based on the WRF mesoscale atmospheric model for CPV applications. In: AIP conference proceedings, vol 1477, No. 1. American Institute of Physics
6. Polo J et al (2011) Solar radiation estimations over India using Meteosat satellite images. *Sol Energy* 85(9):2395–2406
7. Marquez R, Coimbra CFM (2013) Intra-hour DNI forecasting based on cloud tracking image analysis. *Solar Energy* 91:327–336
8. Marsland S (2015) *Machine learning: an algorithmic perspective*. CRC Press
9. Zhou Z-H (2012) *Ensemble methods: foundations and algorithms*. CRC press
10. Breiman L (2001) Random forests. *Mach Learn* 45(1):5–32
11. Schüler D et al (2016) The enerMENA meteorological network–solar radiation measurements in the MENA region. In: AIP conference proceedings, vol 1734, No. 1. AIP Publishing LLC

Greenhouse Design Selection in Moroccan Climatic Conditions



Laila Ouazzani Chahidi and Abdellah Mechaqrane

Abstract Greenhouse cultivation is one of the most productive agricultural techniques, by its product yield, its quality and its all-around year production. This technique makes it possible to create a suitable microclimate for plant growth. For that, a quantity of energy is required, which raises the production cost. To reduce the costs and the energy needs, numerous greenhouse shapes and different covering materials are available. The selection of the right greenhouse design can significantly decrease the energy needs during heating and cooling periods, therewith sparing a great part of operating cost. This work aims to analyze the impact of conventional and innovative shapes (even span, uneven span, single slope, mansard, modified IARI, quonset, modified quonset, gothic-arch, modified gothic-arch) and covering materials (glass, Low-density polyethylene film (LDPE), Bubbled polyethylene plastic (BPE) and Ethylene vinyl acetate film (EVA)) on the energy needs of the greenhouse, in the climatic conditions of Fez, Morocco. For this purpose, dynamic models of different greenhouse designs are created in EnergyPlus environment.

Keywords Greenhouse design · Thermal loads · Incident radiation

1 Introduction

Climate change has become a real dilemma which influences legitimately and by implication numerous parts of food security. Agriculture is one of the directly influenced sectors. Therefore, it ought to experience an adjustment to environmental changes. Greenhouse cultivation is one of the most suitable solutions; it is important for both, the crop protection and the off-season production, it also allows for rising the product quality and yield. Greenhouses can be considered as a refuge for the plants, in which, all their needs must be assured, i.e. lighting, CO₂ concentration,

L. Ouazzani Chahidi (✉) · A. Mechaqrane
SIGER, Intelligent Systems, Georesources and Renewable Energies Laboratory, Faculty of Sciences and Techniques of Fez, Sidi Mohamed Ben Abdellah University, PO. Box 2202, Fez, Morocco
e-mail: laila.ouazzanichahidi@usmba.ac.ma

humidity and temperature level depending on the time of the day, the season and the country's climate.

The greenhouse design is a key factor of the protected agriculture process, thus the shape and the covering materials must be carefully chosen, given their impact on the amount of solar irradiance captured and therefore the inside microclimate. The dynamic modeling is of great interest in analyzing greenhouse features thus, different models and tools have been presented in the literature [1–3]. In order to optimally chose the greenhouse design, a compromise must be found between its ability to take advantage of passive energy and its ability to withstand external stresses (e.g. wind speed).

Research has been for a long devoted to this target. To select the geometry that most opposes the impacts of the wind, Groener et al. [4] conducted several geometric tests on the software SOLIDWORKS Flow Simulation. Hoop designs are according to them, the best ones because they allow for mitigating the effects of wind loading, thus reducing the need for costly structural materials and simplify the on-site assembly process. From the energy optimization point of view, Gupta and Chandra [5] showed, under climate conditions of northern India, that a gothic arch shaped greenhouse requires less than 2.6 and 4.2% of heating compared to gable and quonset shapes, respectively. In the same country, Sethi [6] compared different greenhouse designs (even-span, uneven-span, vinery, modified arch and quonset) with the same dimensions. Their results show that the greenhouse shapes selection depends on the geographic characteristics of the site; during all year's months and all latitudes uneven-span greenhouse receives the maximum of solar radiation and quonset greenhouse receives the minimum. For other shapes and at 10°N, they receive more solar energy in winter and less in summer. While the opposite at 30 °N and at 50 °N latitudes. In the same target, the energy consumption of six most commonly used greenhouse shapes (even span, uneven span, vinery, single span, arch and quonset), with the same length, width and height, was evaluated under climatic conditions of Tabriz, Iran [7]. Their results show that an east–west oriented single span greenhouse with a north brick wall was the optimal design and that the north wall insulation allows for reducing 30% of energy used.

Greenhouse covering materials impact the photosynthesis and evapotranspiration processes. It must be optimally selected to protect the plants from the external weather conditions, and to control the exchanges between the outdoor and the indoor environment, while letting through the necessary solar irradiation for the photosynthesis process of the plant. The optical, the thermal and the mechanical properties of the greenhouse covering materials considerably affect its choice. Baxevanou et al. [8] created a 2D tunnel greenhouse model based on radiation transfer, in order to evaluate four covering materials (EVA, TPE, 3L, VPVC). The four materials were classified based on a comparison between the plant agronomic needs and the inside real parameters, namely visible spectrum irradiance, temperature and air velocity. In another study [9], an alternative covering material was evaluated, by comparing two identical greenhouses; glass house considered as the reference and a greenhouse covered by a polymer nanocomposite material. An extended review on different

covering materials used for improving the indoor environment have been presented by Rezaei et al. [10].

The aim of this study is to evaluate different greenhouse shapes with different covering materials, in order to select the most suitable design in term of thermal loads and the greenhouse floor incident solar radiation, in the climatic conditions of Fez, Morocco. For this purpose, dynamic energy models are created in EnergyPlus by combining nine greenhouse shapes (standard span, uneven span, single slope, mansard, modified IARI, quonset, modified quonset, gothic arch, modified gothic arch) and four covering materials (glass, LDPE, BPE, EVA).

2 Methodology

The greenhouse design can directly influence the interior microclimate and therefore the heating and cooling loads. The purpose of this study is to assess the impact of the design (i.e. the shape and the covering material) on the thermal loads (during both the heating and cooling periods) and the incident solar radiation on the greenhouse floor. The aim is to select the optimal one under the climatic conditions of Fez, Morocco. The weather data are provided from Meteonorm software.

Table 1 presents the principal geometrical and localization parameters of the studied greenhouses.

In this study, the modeling and simulation are carried out in EnergyPlus, the building dynamic energy simulator software. The calculation is based on the air heat balance of the greenhouse (considered as a single zone). The equations are solved by means of a third order backward approximation of the zone temperature derivative with a time step of six times per hour. The transparent surfaces of the greenhouse are considered as windows and the opaque ones are considered as external walls. The external wall heat balance takes into consideration the conduction in the wall, the internal and external shortwave radiation, the internal and external longwave radiation and the convective exchanges, as represented in Fig. 1.

The greenhouse external wall heat balance is calculated based on Eq. (1):

$$\dot{Q}''_{sol} + \dot{Q}''_{LwR} + \dot{Q}''_{conv,out} + \dot{Q}''_{sol} + \dot{Q}''_{sw} + \dot{Q}''_{LwX} + \dot{Q}''_{conv,in} + \dot{Q}''_{cond} = 0 \quad (1)$$

Table 1 Greenhouses localization and geometrical parameters

Greenhouses dimensions				Site localization			
Length	Width	Roof-top height	Orientation	City	Latitude	Longitude	Altitude
20 m	11 m	6 m	45° Relative north	Fez	33.93 °N	4.98 °W	579 m

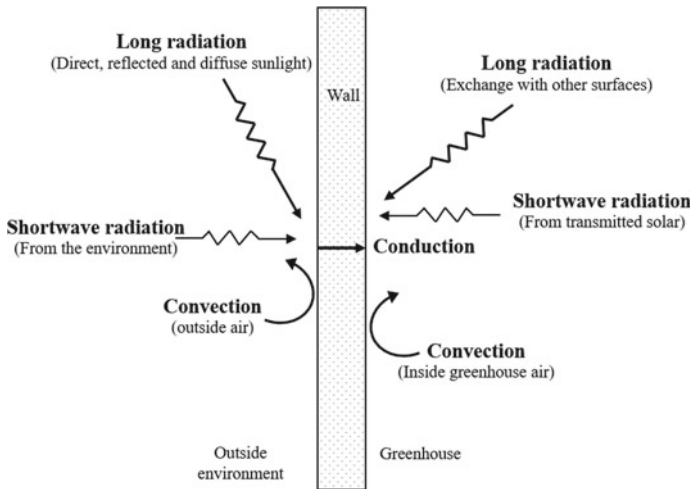


Fig. 1 Greenhouse external wall heat balance

where $\dot{Q}''_{\alpha sol}$ is the absorbed direct and diffuse solar (short wavelength) radiation heat flux; \dot{Q}''_{LwR} is the net long wavelength (thermal) radiation flux exchange with the air and surroundings; $\dot{Q}''_{conv,out}$ is the convective flux exchange with outside air; \dot{Q}''_{sol} is the transmitted solar radiation flux absorbed at surface; \dot{Q}''_{sw} is the internal short wave radiation flux to surface; \dot{Q}''_{LwX} is the net longwave radiant exchange flux between surfaces in the greenhouse; $\dot{Q}''_{conv,in}$ is the convective flux exchange with inside greenhouse air; \dot{Q}''_{cond} is the wall conduction flux.

2.1 Geometric Models

Nine different greenhouse shapes (as presented in Fig. 2: (1) even span, (2) uneven span, (3) single slop, (4) mansard roof, (5) modified IARI, (6) quonset, (7) modified quonset, (8) gothic-arch, (9) modified gothic-arch), with same length, width and roof top height, are studied. As a first step, the 3D geometric models were separately created by means of SketchUp graphical interface and OpenStudio Plugins, then implemented as inputs to EnergyPlus software where each greenhouse is considered as a single thermal zone. In the second step, the studied covering materials were integrated into the model.

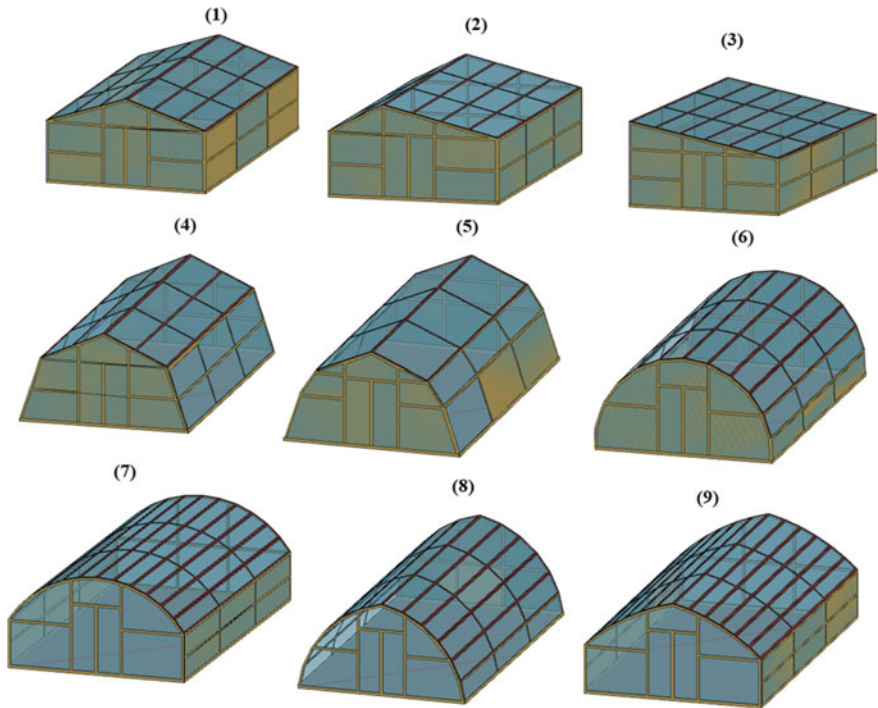


Fig. 2 Greenhouse studied shapes

2.2 Studied Covering Materials

After creating the geometric models, the covering material effect is tested by varying, each time and for each shape, the covering material then analyzing the variation of the mean annual floor incident solar radiation, and the mean annual thermal loads (during heating and cooling periods) of each studied case. Table 2 summarizes the physical proprieties of the studied materials. Low-density polyethylene film (LDPE) and glass are among the widely used greenhouse covering materials, that explains their choice in this study. Bubbled polyethylene plastic (BPE) is an improved type of Polyethylene film by the integration of air bubbles which rises its thermal resistance thus decreases

Table 2 Covering material proprieties [11]

Material	τ_{PAR} (%)	ρ_{PAR} (%)	α_{PAR} (%)	τ_{NIR} (%)	ρ_{NIR} (%)	α_{NIR} (%)	Q (%)
Glass	84	6	10	73	7	20	83
LDPE	83	8	9	87	8	5	83
BPE	63	14	23	68	14	18	63
EVA	89	8	3	89	7	4	89

Table 3 Plant and soil model parameters

Plant		Soil	
Height of the plant	1 m	Conductivity of dry soil	0.35 W/m K
Leaf area index	4	Density of dry soil	1100 kg/m ³
Minimum stomatal resistance	120 s/m	Specific heat of dry soil	

the heat exchanges between the greenhouse and the external environment. Ethylene vinyl acetate film (EVA) material is chosen by referring to a previous study [8], in which it was classified the first among three other ones, based on a comparison between plant needs and the inside real parameters (visible spectrum irradiance, temperature and air velocity).

2.3 Plant and Soil Model

The plant considered in this study is tomato. The plant and soil are modeled in EnergyPlus environment by considering them as the outer layer of the floor construction. Their impact on the overall heat balance is implemented based on the FASST model [12]. Table 3 summarizes the model essential parameters of the soil and plant used in this study.

3 Results and Discussion

In order to investigate the impact of the greenhouse design on its microclimate, simulation studies are conducted for nine shapes and four covering materials, by varying each time for each shape the material. The indoor temperature set point is fixed on a daily average of 21 °C. The analysis focus mainly on two variables; the minimum daily average floor incident solar radiation over a year and thermal loads during both the cooling and heating periods.

For the sake of clarity and avoiding a complex presentation of the results, only annual data are presented. The first part of the analysis is a comparison between the different studied shapes based on annual thermal loads during heating and cooling periods. In the second part, a comparison of the four covering materials regarding annual loads is carried out. And finally, an analysis of the minimum daily average floor incident solar radiation over a year in different combination (shape/material) is represented.

Figures 3 and 4 present the mean annual thermal loads of the studied designs during heating and cooling periods, respectively. Regarding shapes and as a general

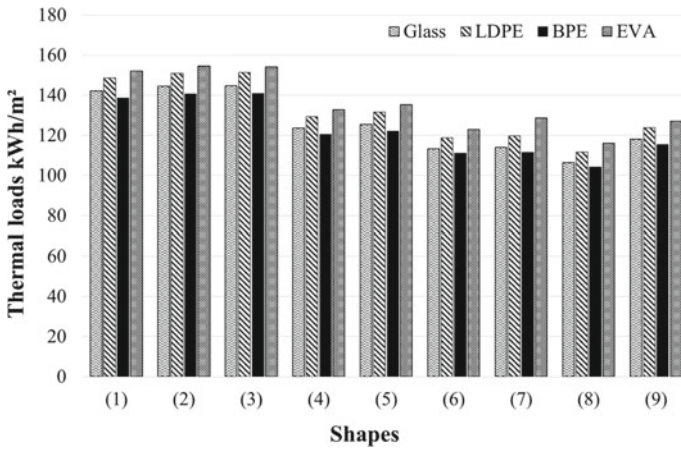


Fig. 3 Thermal loads during heating periods

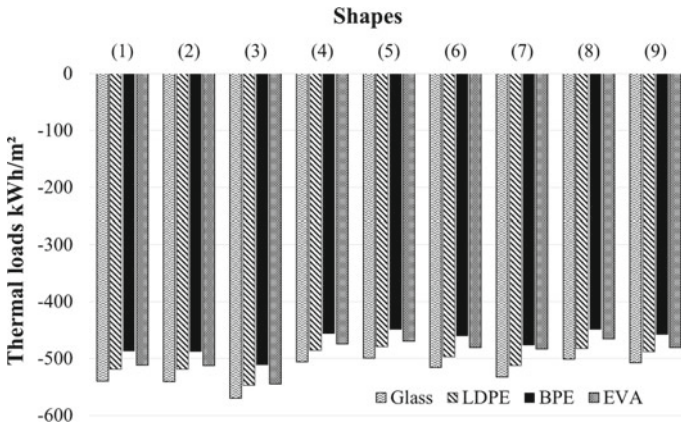


Fig. 4 Thermal loads during cooling periods

observation of the graphs, it can be remarked that the shape (8) is the optimal one, considering both heating and cooling thermal loads. The obtained results show that shapes (1), (2) and (3) have close thermal loads comparing to the others. Their thermal loads rise, regarding shapes, in the following order: (1), (2) then (3), which can be explained by the surface of the roof facing the south-east comparing one to another. Actually by an overall comparison, a maximal difference of about 2.6 kWh/m² annually during heating periods while a maximal difference of about 33 kWh/m² during cooling loads are recorded. The other five shapes i.e. (4), (5), (6), (7), and (9) have also close thermal loads with a maximal difference of about 12.7 kWh/m² during heating periods and of about 32.7 kWh/m² during cooling period.

The optimal shape (8) is compared to the two commonly used ones in protected agriculture; shapes (1) and (6). During heating period, the thermal loads of shape (8) are around 24% and 6% less than shapes (1) and (6), respectively. Regarding the cooling periods a relative reduction of around 8% and 3% is noticed comparing to shape (1) and (6), respectively. Note that these percentages are the average values of the ones obtained for the four materials.

For all shapes, the materials are inversely classified in the heating loads with respect to their classification in the cooling loads except for the BPE material which seems to be the best one in the two periods. During heating period EVA material generates more loads followed by LDPE material then glass and finally BPE material that generates less loads. For cooling period, glass is the one that generates more loads, followed by LDPE then EVA. The BPE material is still the best one. Having regard to shape (8), the heating loads are less by 10%, 7% and 2% when using BPE material comparing to EVA, LDPE and glass, respectively. The thermal loads in the cooling periods decrease by 10%, 7% and 4% comparing to glass, LDPE and EVA, respectively.

Figure 5 presents the minimum daily average floor incident solar radiation over a year for the studied shapes and covering materials. The amount of solar radiation that must reach the plants is a key factor when selecting the optimal design. It is one of the parameters having a direct and major influence on the plant growth process. In the present study, tomato plants are considered. Their minimum solar radiation needs recommended by [13] is 2.34 kWh/m² Day. The minimum daily average floor incident radiation over a year are investigated, and it can be remarked that most of the studied designs allow for reaching approximately the minimum value or greatly exceed it. Following the same approach as for the thermal loads comparison, and continuing ahead keeping the preliminary selected suitable combination (shape (8) with BPE material); this combination seems to be insufficient to let through the

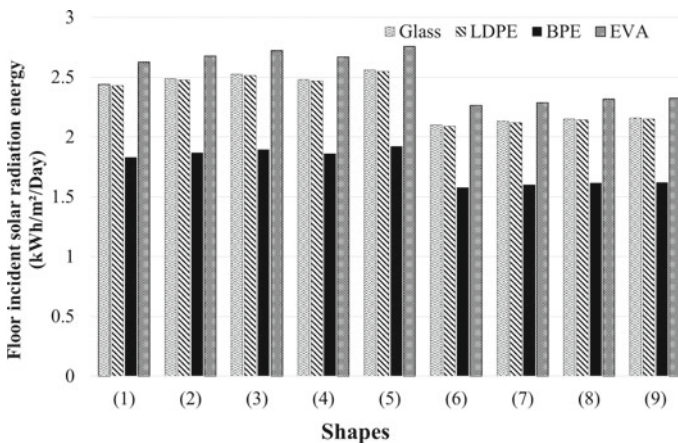


Fig. 5 Minimum daily average floor incident solar radiation over a year

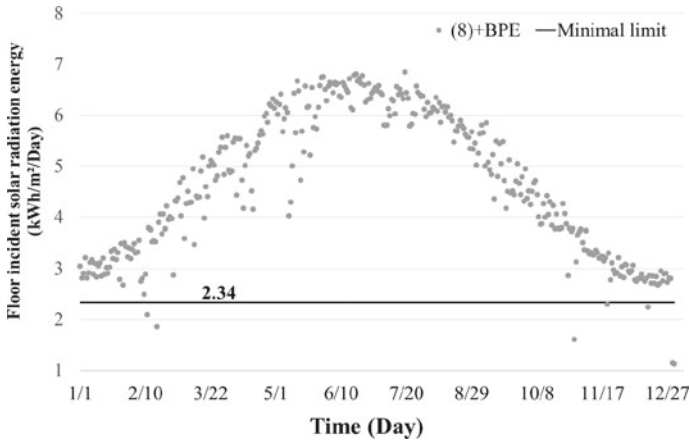


Fig. 6 Daily average floor incident solar radiation

minimum recommended solar radiations. Having a look on the daily average floor incident solar radiation of this design (Fig. 6), it can be mentioned that only on a few days during all the year, the values are under the minimal one. Therefore, this design is still the most optimal one and it is recommended to compensate the deficit of solar radiation by a lighting system. Moreover, the adoption of a design letting through the recommended quantity of solar radiation will undoubtedly lead to much more energy consumption than a lighting system operating for a few days during all the year. More studies can be carried out in this target.

In Fez climatic conditions, the combination of the shape (8) with the BPE material, with 45° relative north are the most suitable for tomato plants cultivation or others having approximately similar needs, but more detailed study are needed for more exhaustive evaluation.

4 Conclusion

In this work, different greenhouse shapes and covering materials are evaluated, for the purpose of selecting the most suitable design, in the climatic conditions of Fez, Morocco. A combination of nine greenhouse shapes (standard span, uneven span, single slope, mansard, modified IARI, quonset, modified quonset, gothic arch, modified gothic arch) and four covering materials (glass, Low-density polyethylene film LDPE, Bubbled polyethylene plastic BPE and Ethylene vinyl acetate film EVA) are investigated using EnergyPlus environment.

The research start comparing the studied shapes during both the heating and cooling periods. Then the covering materials are compared by fixing the shape. These comparisons are based on the annual thermal loads and the minimum daily average floor incident solar radiation over the year.

Based on the results, we can conclude that the design have a significant impact on thermal loads, thus the right choice can generate until 24% and 8% of energy saving during heating and cooling periods, respectively. Then the minimum daily average floor incident solar radiation over a year is investigated and compared to tomato plants' minimum solar radiation needs.

Finally, we can conclude that the combination of gothic arch shape and BPE material is a good compromise for tomatos greenhouse under the climatic conditions of Fez, Morocco, considering the minimal thermal loads all-around the year and the plant solar radiation needs.

References

1. Tavares C, Gonçalves A, Castro P, Loureiro D, Joyce A (2001) Modelling an agriculture production greenhouse. *Renew energy* 22(1):15–20. [https://doi.org/10.1016/S0960-1481\(00\)00030-6](https://doi.org/10.1016/S0960-1481(00)00030-6)
2. Mashonjowa E, Ronsse F, Milford JR, Pieters JG (May 2013) Modelling the thermal performance of a naturally ventilated greenhouse in Zimbabwe using a dynamic greenhouse climate model. *Sol. Energy* 91:381–393. <https://doi.org/10.1016/j.solener.2012.09.010>
3. Ouazzani Chahidi L, Fossa M, Priarone A, Mechaqrane A (Jan, 2021) Energy saving strategies in sustainable greenhouse cultivation in the mediterranean climate – A case study. *Appl Energy* 282:116156. <https://doi.org/10.1016/j.apenergy.2020.116156>
4. Groener B, Knopp N, Korgan K, Perry R, Romero J, Smith K et al (2015) Preliminary design of a low-cost greenhouse with open source control systems. *Procedia Eng*
5. Gupta MJ, Chandra P (2002) Effect of greenhouse design parameters on conservation of energy for greenhouse environmental control. *Energy* 27(8):777–794
6. Sethi VP (2009) On the selection of shape and orientation of a greenhouse: thermal modeling and experimental validation. *Sol Energy* 83(1):21–38
7. Ghasemi Mobtaker H, Ajabshirchi Y, Ranjbar SF, Matloobi M (2016) Solar energy conservation in greenhouse: thermal analysis and experimental validation. *Renew Energy* 96:509–519
8. Baxevanou C, Fidaros D, Bartzanas T, Kittas C (2018) Yearly numerical evaluation of greenhouse cover materials. *Comput Electron Agric* 149:54–70
9. Kavga A, Souliotis M, Koumoulos E, Fokaides PA, Charitidis CA (Jan, 2018) Environmental and nanomechanical testing of an alternative polymer nanocomposite greenhouse covering material. *Sol Energy* 159:1–9. <https://doi.org/10.1016/j.solener.2017.10.073>
10. Rezaei SD, Shannigrahi S, Ramakrishna S (2017) A review of conventional, advanced, and smart glazing technologies and materials for improving indoor environment. *Sol Energy Mater Sol Cells* 159:26–51
11. Kittas C, Bailie A (1998) Determination of the spectral properties of several greenhouse cover materials and evaluation of specific parameters related to plant response. *J Agric Eng Res* 71(2):193–202
12. Frankenstein S, Koenig G (2004) FASST vegetation models. *Cold Reg Res Eng Lab* 56
13. Baudoin W, Nono-Wondim R, Lutaladio N, Hodder A, Castilla N, Leonardi C, et al. (2013) Good Agricultural Practices for greenhouse vegetable crops: principles for mediterranean climate areas. FAO

Intelligent Architecture in Home Energy Management System for Smart Building, Moroccan Case Study



Mohammed Dhriyyef , Abdelmalek El Mehdi, and Mohammed Elhitmy

Abstract Managing energy in a building is an optimizing solution for smart homes. The user will be autonomous in managing his need in energy. It is an energy control and management that reacts to MPL (Maximum Power Limit), hybrid system Pv/Battery and temperature of heater. It manages the operation of appliances which are shiftable with respect to the tariffication of electricity, this minimizes the electricity bill. The proposed algorithm receives as input data, the tariffication profile, the power produced by the Pv, the Soc of batteries and the timing and sequencing of turning on the shiftable appliances. The turning on timing is fixed by the user's priorities. The batteries are charged by the Pv panels only during periods where the cost of electricity is high. It guaranties the thermal comfort at 24 °C and the free usage of all appliances when the hybrid system Pv/Battery is activated. In the contrary if there is a default in the hybrid system which does not respond to the energy requested, it flips the building's electricity supply to the public grid immediately. In this case the algorithm adjusts the temperature in the range 18–24 °C when the requested power is greater than the MPL and forbids the operation of shiftable appliances in periods where the cost of electricity is high. This will limit the power request to MPL and optimize the electricity bill. The study is realized according to the meteorological conditions of Oujda city and the tariffication of the Moroccan national office of electricity. The electric and thermal models of the building and the hybrid system Pv/Battery are implemented in Matlab/Simulink and the simulation results show that the cost is reduced to 16.41% if the building is uniquely supplied by the grid and to 55.22% for complete system.

M. Dhriyyef (✉) · A. El Mehdi
Smart ICT Laboratory, National School of Applied Sciences, Mohamed First University, Oujda,
Morocco
e-mail: m.dhriyyef@ump.ac.ma

A. El Mehdi
e-mail: a.elmehdi@ump.ac.ma

M. Elhitmy
Electromagnetism, Signal Processing and Renewable Energy Laboratory, Faculty of Science,
Mohammed First University, Oujda, Morocco
e-mail: mohammed.elhitmy1@gmail.com

Keywords Smart home · Smart grid · Demand response · Home energy management · Renewable energy source · Hybrid system

1 Introduction

The need for electric energy is increasing all the time worldwide. The residential sector presents an important part of the total energy consumption. The world aims to better consume the electricity, it means to better produce it, to economize its consumption and to preserve the environment. Research in smart building is the tendency which aims to reduce the energy consumption while maximizing the comfort of the inhabitants. The building aims to produce its energy demand through the renewable energy. It shifts its electricity consumption to periods where the cost is low. This shows that smart buildings contribute to programs where countries may control their electricity consumption [1]. It is a modification of the normal consumption, it consists of reducing or increasing the home appliances when there is a lack or an excess of power [2, 3]. Various algorithms were developed for implementing HEMS. Metaheuristic and developed algorithms are largely used for systems based on response to the demand. Metaheuristic GWO is used by Iqbal et al. [4] for optimizing the planification of home appliances and the power exchange between hybrid system and the grid. Authors in [5] make plans to home appliances and reduce the peak of the demand. HEMS of authors in [6] use the optimization of hybrid metaheuristic HEDE which reduces the cost and the peak of demand for a dynamic pricing. Authors in [7] have proposed a HEMS implemented in Raspberry Pi card capable of scheduling switchable appliances and optimizing the source selection with respect to the variable tariffication through a genetic algorithm GA. The system in [8] is controlled by an algorithm based on the Soc level which oblige the system to take decisions concerning the energy transfer from the Pv or the battery or the grid. Fuzzy logic technique is used by Soetedjo et al. [9] to modify the operation of the shiftable appliances and to control the energy flux of the Pv and the battery in order to minimize the cost.

In this work we propose a hybrid system based on Pv/Battery in order to reduce the supply by grid. An algorithm has been designed to manage and control the electricity consumption of a HEMS. It controls the shiftable home appliances, it limits the request power to MPL, it adjusts the indoor temperature, it looks for the appropriate source so that the building operates on Pv, grid or battery according to the electricity price.

In Sect. 2 we present the architecture of the smart building with the model of each of its components, in Sect. 3, the management algorithm is described. Section 4 studies three scenarios and the results obtained are interpreted. and we end with a conclusion.

2 Proposed Architecture of Smart Building

Figure 1 shows the proposed smart building. HEMS (Home Energy Management System) has two modes of simultaneous control and management. The power block is a local micro-grid system that contains the hybrid Pv/battery system and public grid. The control block controls the home appliances and gives the turning on timing of each appliance and sets the basic temperature desired by the user. The HEMS local controller determines the best operation electrically of the building while switching it between battery, Pv or grid. The aim is to optimize the electricity bill price during one day while taking into account the information about electricity price and the comfort of the user. The appliances which are non-shiftable are used freely by the users. The heating temperature of the building is controlled in an autonomous way with respect to the managing algorithm decision. HEMS decides to turn off the shiftable appliances in the peak hours. It looks for optimal combination for power supply of the building by controlling the switches between Pv, battery and grid. The decision is made with respect to the hour price, the Soc of the battery, the power requested and MPL.

Equation (1) shows the electricity cost function where EP is the hour electricity price and P_G is the power requested from the grid.

$$\text{Electricity Cost} = \sum_1^{24} (EP(t) \times P_G(t)) \tag{1}$$

It is then necessary to reduce the grid power by exploiting the hybrid Pv/battery system. The power requested from the grid P_G is:

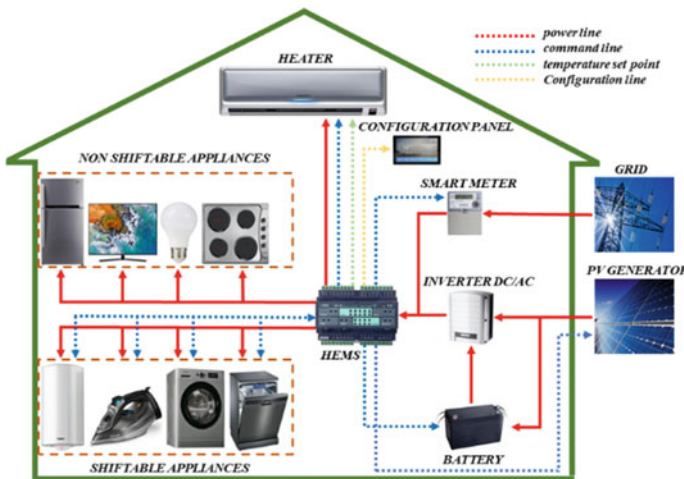


Fig. 1 Proposed architecture for smart building

$$P_G(t) = P_{home}(t) - P_{pv}(t) \pm P_{battery}(t) \tag{2}$$

where the $P_{home}(t)$ is the total power requested by the building, $P_{pv}(t)$ is the power produced by the Pv system and $P_{battery}(t)$ is the power of the battery.

The proposed HEMS limits the maximal power requested to flow from the grid to (3).

$$MPL \geq \sum P_{home}(t) \tag{3}$$

where MPL is the maximum power allowed to flow from the HEMS. The electricity hour price that we have adopted in this study is the Moroccan electricity tariffication for the winter period. The low hours start from 23 h until 18 h of the next day with a rate of the 1.24 dh/Kwh and the peak hours start from 18 to 23 h with a rate of 2.24 dh/Kwh.

2.1 Home Appliances

In this system, we suppose that there are two sets of home appliances, appliances which are controllable and which may operate at any interval of time and appliances where their operation may not be shifted to other times for ensuring the comfort of the users. The load profile for each appliance is summarized in Table 1. Each home appliance is modeled as an electric charge in Matlab/Simulink characterized by P is the active power, Q is the reactive power and $\cos(\varphi)$ is the power factor.

Table 1 Home appliances characteristics

Non shiftable appliances			Shiftable appliances		
Type	Power (W)	Run time (h)	Type	Power (W)	Run time (h)
Refrigerator	120	24	Aspirator	1500	0.5
Tv	70	5	Washing machine	Wash: 160 Heating: 1200 Spinning: 260	1
Freezer	100	24	Dishwasher	Wash: 160 Heating: 1200	0.75
Cooking	2000	2	Water-heater	1200	1
Oven	2500	0.5	Iron	1200	0.5
Lighting	20–40	0.5–8			
Pc	70	5			

Table 2 The thermal model parameters of the proposed smart building

R_{eq} (m ² k/w)	v (m ³)	ρ_0 kg/m ³	C_0 (J/kg k)	D (m ³ /h)
$8.54e^{-7}$	200	1.2250	1005.4	360

2.2 Thermal Model Configuration of the Building

According to the buildings thermal flux dynamic model and from [10, 11] the buildings indoor temperature is

$$\rho_0 c_0 v \frac{dT_{int}}{dt} = \frac{1}{R_{eq}} [T_{ex}(t) - T_{int}(t)] + Q_{heater} + q_i + q_s \quad (4)$$

where ρ_0 is the air density in kg/m³, c_0 is the air specific heat in J/kg K, v is the building's volume in m³, T_{int} is the indoor temperature in °C, T_{ex} is the outside temperature in °C, Q_{heater} is the thermal power produced by the heater in watt, q_i and q_s are the heat produced by the equipment, the users and lighting system, R_{eq} is the thermal resistance equivalent to the building envelope in m² K/w.

The thermal power produced by the heater is modeled by:

$$Q_{heater} = (T_{heater} - T_{int}) \times D \times C_0 \quad (5)$$

where D is the air blown in m³/h, C_0 is the air specific capacity.

The electric power of the heater is:

$$P_{electric-heater} = \frac{Q_{heater}}{COP} \quad (6)$$

where COP is the ratio of the evolution of thermal power to the electric demand supplied. In this work, we have considered COP to be 4. Table 2 gives the thermal model parameters of the proposed smart building with q_i and q_s are negligible.

2.3 Pv System

The output current I of a photovoltaic panel is [12]:

$$I = I_{Ph} - I_0 \left[\exp \left(\frac{V + R_S I}{N_S V_t} \right) - 1 \right] - \frac{(V + R_S I)}{R_{Sh}} \quad (7)$$

where I_{Ph} is the induced current by the sun, I_0 is the inverse saturation current, V is the output voltage, R_S is the series resistance, R_{Sh} is the shunt resistance, N_S is the series cell number, $V_t = \frac{AKT}{q}$ is the panel's thermodynamic voltage.

The installed power of the panels is conforming to the roof area to be covered by the panels. In this study we have considered 9 panels of 350 wp.

2.4 Battery System

The electric model of a battery contains a voltage source E_0 in series with an internal resistor R_B and a capacitor $\frac{Q_0}{K_B}$ [8]. The voltage across a battery is:

$$U_{BAT} = E_0 - K_B \frac{\int I_B dt}{Q_0} - R_B \cdot I_B \quad (8)$$

where discharge current is I_B in (A), Q_0 batterie's capacity in (Ah).

The state of the battery is measured by:

$$SOC(t) = SOC(t-1) - \int_{t-1}^t \frac{I_B}{Q_0} \quad \text{with } SOCmin < SOC < SOCmax \quad (9)$$

9 batteries are used with 140 ah of capacity each and the SOC limits considered in this study are $SOCmin = 20\%$ and $SOCmax = 90\%$.

3 Control and Management Algorithm Proposed

HEMS proposed operates according to the algorithm shown by its flowchart in Fig. 2. The proposed algorithm acts on the hybrid system in a way to minimize the usage of the grid. It controls the internal temperature; it takes the right to turn off the shiftable appliances in the peak hours and it limits the building's power demand to the Maximum Power Limit (MPL) by adjusting the heater temperature when the grid is taking on the building. The algorithm ensures that the battery is charging through the Pv only and guarantees that the battery's charge goes up to 70%, to make sure that it is entirely charged. It guarantees the discharge of battery during night and peak hours. When the hybrid system is not activated, the algorithm supplies the building directly by the grid.

The data that the algorithm receives as input are: the power produced by the Pv, the battery's Soc, the total power demanded by the building $Phome$, the desired temperature setpoint, electricity tariff, desired MPL, turn on timing of shiftable appliances programmed by the user.

If the hybrid system is activated, the algorithm checks the instantaneous electricity price. If the price is minimum, the algorithm considers three cases for the battery's Soc.

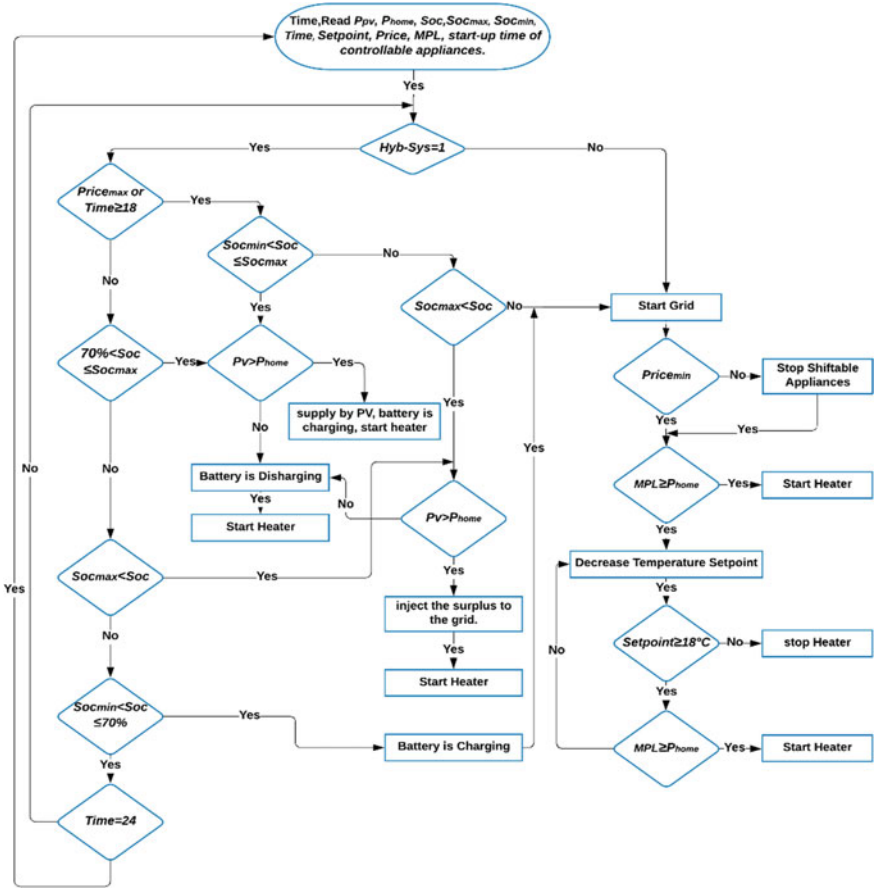


Fig. 2 Flowchart of the proposed algorithm

- If $70\% < Soc \leq Socmax$, the algorithm checks $Ppv > Phome$, if yes, the battery is charging, the heater is activated with the already determined setpoint, and the building is supplied by PV, if not, the battery discharges and the heater works with setpoint already determined.
- If $Socmax < Soc$, the algorithm looks at the Pv power, if Pv power is greater than the demand, the Pv supplies the building, it activates the heater and the excess power is injected to the grid. If not, the algorithm discharges the battery, it activates the heater with already determined setpoint.
- If $Socmin \leq Soc \leq 70\%$, the algorithm charges the battery and switches the building's power supply to the grid.

If the electricity price is maximum or $Time \geq 18$, the algorithm makes a test to see if $Socmin < Soc \leq Socmax$; if yes it discharges the battery and activates the heater, if not; it checks if $SOCmax < SOC$, if not, it supplies the building by the grid,

if yes it looks if $Ppv > P_{home}$, if yes it injects the excess power into the grid, if not it discharges the battery and activates the heater since there are power losses in the hybrid system.

For cases where the grid is activated, if the price is maximum, the algorithm disactivates the shiftable appliances. If the price is minimum, the algorithm measures MPL, if $MPL \geq P_{home}$ it activates the heater at desired setpoint, if not it reduces the temperature until $MPL \geq P_{home}$ while preserving temperature setpoint $\geq 18\text{ }^\circ\text{C}$. if temperature setpoint = $18\text{ }^\circ\text{C}$, even if $MPL < P_{home}$, the algorithm disactivates the heater.

4 Results and Discussion

In this study, the chosen MPL is 2600 W and the desired setpoint is $24\text{ }^\circ\text{C}$. So, the period of absence of the occupants according to their habit is in the range [9.5–12 h] and [14–18 h] so the desired time for starting the shiftable appliances is summarized in Table 3.

The discussion deals with three scenarios, to show the difference between each scenario regarding the electricity bill and to deduce the scenario which is the most optimized.

First scenario: In this case, the management of the building’s power supply is made without algorithm. This means that the building is electrically fed by the grid. The building’s inhabitants want to satisfy their comfort without paying attention to the electricity price and without appliance planification. The temperature setpoint is set at 24° . There have turned off the heater during their absence. Figure 3 shows (a) demand profile and (b) temperature profile.

The results show that there exists a lot of fluctuating points according to the demand in intervals: [7.11–7.8 h], [12–12.71 h], [18–18.51 h], [20–20.4 h] and [20.75–21.32 h], and [22–23 h] the demand may go up to 7820 W and the indoor temperature is preserved around $24\text{ }^\circ\text{C}$ Fig. 3(b). The heater works at its nominal power which is 2.5 kW. the electricity price may go up to 67DH (6.7 USD).

Second scenario: In this case, the Pv system is totally disconnected, MPL is 2600 W, the algorithm receives as input data, the operation timing of each shiftable appliances and the periods where the users are present in the building. The algorithm then takes the decision to shift the power supply of the building directly to the grid. Figure 4 shows: (a) demand profile and (b) temperatures profile for this scenario.

Table 3 Operating time of shiftable appliances

Aspirator	Wash. machine	Dishwasher	Water heater	Iron
[10.5–11 h]	[0–1 h]	[2–2.75 h], [13.25–14 h]	[6.5–7 h], [23–23.5 h]	[9.5–10 h]

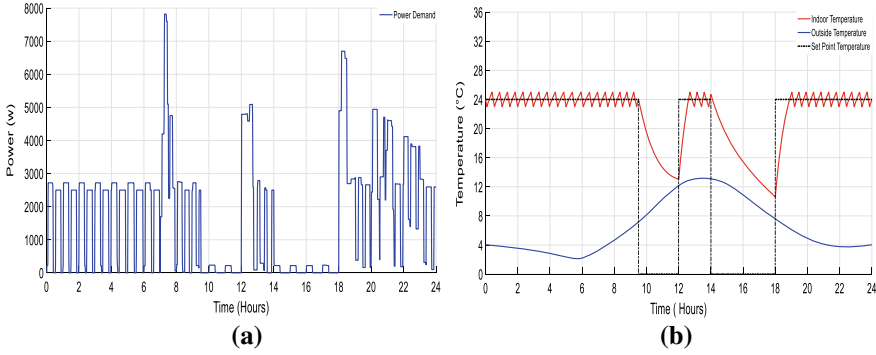


Fig. 3 (a) Demand power profile, (b) Temperature profile

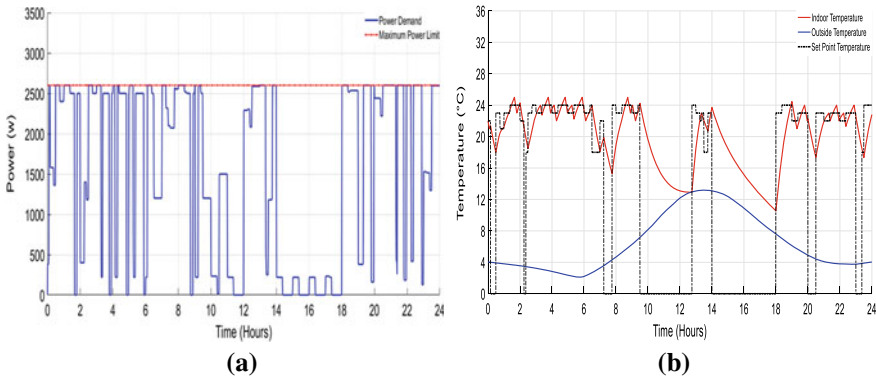


Fig. 4 (a) Demand power profile, (b) Temperature profile

Figure 4(a) shows that the algorithm limits the demand of the building to $MPL = 2600\text{ W}$. we also notice from Fig. 4(b) that the setpoint temperature is zero in periods [0.16–0.49 h], [2.25–2.37 h], [7.24–7.76 h], [12–12.75 h], [20–20.25 h] and [23–23.37 h] this means that $P_{home} > MPL$ even if the setpoint reaches $18\text{ }^\circ\text{C}$, this will oblige the HEMS to deactivate the heater. In the other periods, the algorithm varies the setpoint temperature between 18 and $24\text{ }^\circ\text{C}$, this is in accordance to the demand variation in order to let the peaks flattened and to limit the demand to MPL. It is to be noticed that in this scenario, the shiftable appliances are exploited during periods where the electricity price is minimum between [23–18 h], this is in accordance with the user choice. The electricity bill in this strategy is reduced to 56DH (5.6 USD).

Third scenario: the hybrid system is activated and $Soc = Soc_{min}$. Figure 5(a) shows the building’s demand profile.

It is to be noticed that the electricity price is minimum in the time interval [0–14.27 h] and that the power demand is limited to MPL. The algorithm has found the condition $Soc_{min} \leq Soc \leq 70\%$ and it has taken the decision to supply the building

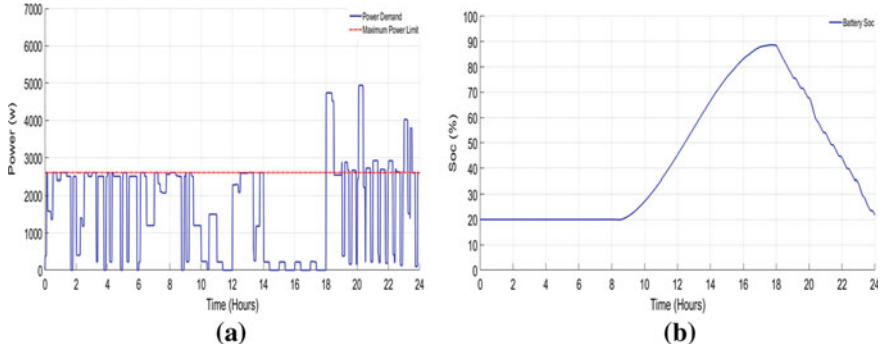


Fig. 5 (a) Demand power profile, (b) SOC variation of batteries

by the grid. It also adjusts the temperature setpoint to fix the power to MPL. It starts charging the battery once P_v is greater than zero. So, it is clear that in the interval [14.27–18 h] the demand did not exceed the MPL because the heater is turned off since the occupant is absent. We also notice that from the hour 14.8 h, the battery's Soc is becoming greater than 70%, the algorithm then satisfies the condition $70\% < Soc \leq Soc_{max}$, and since $P_v > P_{home}$, then the battery continues to charge and the demand is supplied by the Pv until 18 h. 18 h is the start of peak hours, the battery's Soc reaches almost the value of Soc_{max} , the algorithm takes the decision to discharge the battery and also even if the peak hours are ended at 23 h, the algorithm discharges the battery up to 24 h since it checked $Time \geq 18$ h. The heater's setpoint is 24 °C. The battery's Soc profile is shown in Fig. 5(b). Figure 5(a) shows that the peak points are in the intervals [18–18.51 h], [20–20.4 h], [23–23.51 h], this shows that the inhabitant's comfort is insured when it is the battery that supplies the building. Also, the building has avoided to be power supplied by the grid in the peak hours. Figure 6(a) shows the battery's power profile. It informs us that since the Pv panels starts to produce energy, $P_v > 0$, the battery begins charging in conformity with the

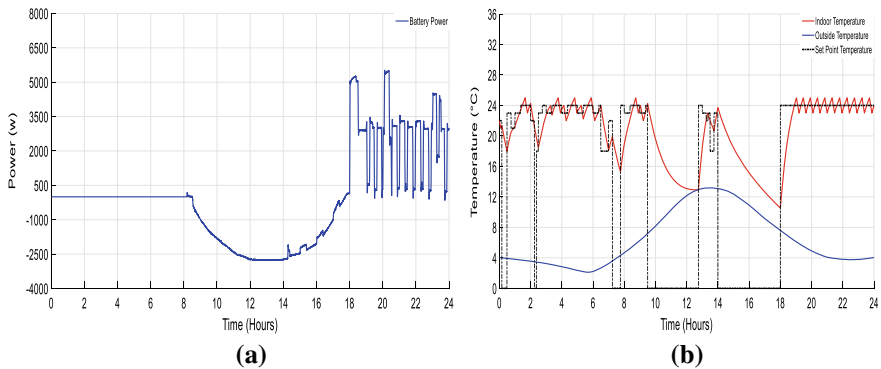


Fig. 6 (a) Batteries power profile, (b) Temperature profile

Pv power until Soc > 70%. From this instant on, the battery follows the profile of the difference between Pv and P_{home} . We have anyhow $P_v > P_{\text{home}}$ until 18 h. after 18 h until 24 h the power profile of the battery follows that of the power demand since the battery is discharging since the algorithm found the condition Pricemax or Time ≥ 18 h. and the Soc almost reaches Socmin up to 24 h Fig. 5(b).

In this scenario, using the complete system, shows that the algorithm has avoided the grid in peak hours. The thermal comfort has been guaranteed at 24 °C during the operation of the hybrid system and it is less affected during the use of the grid as shown in Fig. 6(b). Through this strategy, the algorithm has reduced the electricity bill up to 30DH (3 USD) compared to baseline scenario. The results of our study showed that the algorithm reduced the electricity bill by up to 55.22% when the hybrid system is used and by up to 16.41% when the building is supplied by the grid only.

5 Conclusion

In this study, we have proposed an architecture composed of a Pv/battery system and the grid together with an algorithm that controls and manages these components. The goal is to satisfy the power supply demand of a smart building. The algorithm has shown that it is able to avoid the grid in the peak hours. It exploits instead the Pv/battery hybrid system based on the battery's Soc level. It also limits the working of shiftable appliances in the peak hours. In case of supplying the building by the grid, the algorithm sets the power demand to MPL, in order to avoid the peaks and to adjust the heater setpoint to [18–24 °C]. The bi-hours tariffication of electricity in Morocco has been adopted. We have used the meteorological conditions of the city of Oujda for a day in winter. The complete system has been implemented in Matlab/Simulink. The simulation results show that the algorithm had considerably reduced the electricity bill up to 16.41% when the building is only supplied by the grid, and up to 55.22% when the hybrid system is exploited.

References

1. Stoll P et al (2014) Including dynamic CO₂ intensity with demand response. *Energy Policy* 65:490–500. <https://doi.org/10.1016/j.enpol.2013.10.044>
2. Beaudin M, Zareipour H (2015) Home energy management systems: a review of modelling and complexity. *Renew Sustain Energy Rev* 45:318–335. <https://doi.org/10.1016/j.rser.2015.01.046>
3. Faruqui A, Sergici S (2010) Household response to dynamic pricing of electricity: a survey of 15 experiments (2010)
4. Iqbal MM, Ali Sajjad I, Manan A, Waseem M, Ali A, Sohail A (2020) Towards an optimal residential home energy management in presence of PV generation, energy storage and home to grid energy exchange framework. In: 2020 3rd International Conference on Computing,

- Mathematics and Engineering Technologies. Idea to Innovation for Building the Knowledge Economy. iCoMET 2020. <https://doi.org/10.1109/iCoMET48670.2020.9073798>
5. Molla T et al (2019) Integrated energy optimization of smart home appliances with cost-effective energy management system. CSEE J Power Energy Syst 5(2):249–258. <https://doi.org/10.17775/cseejpes.2019.00340>
 6. Khan ZA, Zafar A, Javaid S, Aslam S, Rahim MH, Javaid N (2019) Hybrid meta-heuristic optimization based home energy management system in smart grid. J Ambient Intell Humaniz Comput 10:4837–4853. <https://doi.org/10.1007/s12652-018-01169-y>
 7. Kumar A, Singh R, Cai Y, Grijalva S (2020) Smart home energy management system with optimal source
 8. Dhriyyef M et al (2020) Management strategy of power exchange in a building between grid, photovoltaic and batteries. Springer Singapore. <https://doi.org/10.1007/978-981-15-6259-4>
 9. Soetedjo A, Nakhoda YI, Saleh C (2018) Simulation of fuzzy logic based energy management for the home with grid connected PV-battery system. In: 2nd International Conference on Smart Grid Smart Cities, ICSGSC 2018, pp 122–126. <https://doi.org/10.1109/ICSGSC.2018.8541271>
 10. Mendes N, Oliveira G, Araujo H (2001) Building thermal performance analysis by using Matlab/Simulink. In: Seventh International IBPSA Conference. Rio de Janeiro Brazil, pp 473–480
 11. Le K, Le K (2008) Gestion optimale des consommations d'énergie dans les bâtiments
 12. Chauhan A, Prakash S (2019) Considering various equivalent circuits for solar PV array modelling. In: 2nd International Conference on Energy, Power and Environment: Towards Smart Technology. ICEPE 2018, pp 1–6 (2019). <https://doi.org/10.1109/EPETSG.2018.8658741>

Evaluation of Adaptive Backstepping Control Applied to DFIG Wind System Used on the Real Wind Profile of the Dakhla-Morocco City



Mourad Yessef, Badre Bossoufi, Mohammed Taoussi, Ahmed Lagrioui, and Mohammed El Mahfoud

Abstract The conception of a control strategy of Doubly-Fed Induction Generator (DFIG) for providing a high quality of energy, without harmonic accumulations, to the electric network is a real challenge because of the no-linearity of the system and the variable wind speed. In this work, two commands based on two technics have been developed and then tested in order to control the system and the grid powers, respectively. Note that the main purpose of the control laws is to optimize the extraction of the wind energy in a real context and to push the DFIG working properly with the best performance in both static and dynamic modes. Therefore, the dynamic model turbine has been presented in this paper, also the FOC (Field Oriented Control) and the adaptive Backstepping commands are highlighted. Matlab/Simulink simulations analysis, with real parameters of the turbine and real wind profile of Dakhla-Morocco city, confirm the high accuracy of the adaptive Backstepping command, based on the Lyapunov stability technique, with a total harmonic distortion THD $\sim 0.16\%$.

Keywords Adaptive backstepping · DFIG · FOC · Wind turbines

1 Introduction

In the last decades, the demand of electrical energy is increased more and more. However, the major categories of energy for electricity generation are fossil fuels, petroleum and natural gas [1], high consumption of such categories of energy caused serious problems to our planet. Therefore, the renewable energy resources

M. Yessef (✉) · B. Bossoufi · M. El Mahfoud

Laboratory of Engineering, Modeling and Systems Analysis, SMBA University Fez, Fez, Morocco
e-mail: mourad.yessef@usmba.ac.ma

M. Taoussi

Laboratory of Technologies and Industrial Services, Higher School of Technology, SMBA University Fez, Fez, Morocco

A. Lagrioui

Department of Electrical and Computer Engineering, Higher National School of Arts and Trades, Moulay Ismail University Meknes, Meknes, Morocco

are revealed to be the suitable alternatives [2]. There are many kinds of renewable energy resources (e.g. biomass, hydropower, geothermal, wind and solar) [3]. Recently, The wind farms installation has been developed. Then, the wind energy becomes usual more and more in many countries with a power near 600 GW and target to be 1600 GW in 2030 [Word Wind Energy Association]. Thereby, due to their several advantages, the DFIG (Doubly-Fed Induction Generator) technology, with variable speed, is presented to be the serious way to develop turbine generators within other machines. The DFIG is characterized by its capacitance on a large domain of wind speeds and the optimal conversion of aero-dynamical power with low cost [4]. Figure 1 presents the general structure of this system.

The Kinetic power of the wind is transformed to mechanic power, by the turbine, and then delivered to the electrical machine by the gearbox in the transmission machine [5]. The DFIG stator is directly coupled to the electrical grid, in the same time, the rotor is connected by an electronic converter of power. Several algorithms and structures of control are then proposed to confident the stability, the performance and the robust of aero-generator such as PI (Proportional Integral) controllers and adaptive PI [6]. Other works focused on the other command types such as the scalar, the DPC and linearization controls [7]. Unfortunately, simulations with real wind and testing several commands on the same system in the same environment are lacking. In this work, the two commands (e.g. Adaptive Backstepping and Field-Oriented Control command) are used [7, 7]. Firstly, the turbine is modeled and the dynamical model (DFIG) is presented, then the modeling equations of the two strategies of commands are calculated. The results of simulations are given and compared with the available results.

Nomenclature

(continued)

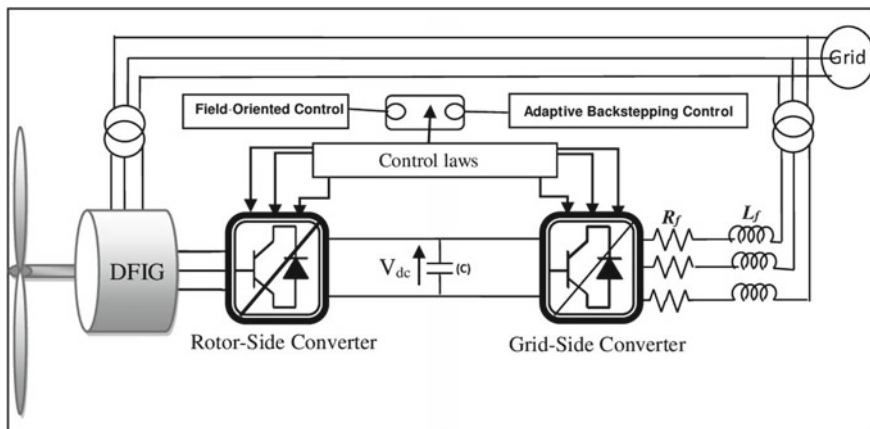


Fig. 1 Schematic of wind energy conversion system based on DFIG

(continued)

Nomenclature			
V_ω	Wind speed	Ω_{mec}	Angular velocity of the high speed shaft
C_p	Power coefficient	V_{sd}	Stator voltage components in PARK reference frame
P_m	The mechanical power captured from a wind turbine	V_{rd}	Rotor voltage components in PARK reference frame
β	Blade angle	K_p	Proportional gain of PI controller
λ	Tip speed ratio	A	Aerodynamic torque sensitivity to the mechanical speed
Q_s	Reactive power of the stator	R_s	Stator resistance
P_s	Active power of the stator	R_r	Rotor resistance
THD	Total harmonic distortion	J	Moment of inertia

2 Wind Turbine Model

The wind energy is catches by the wind turbine power system and converted into a torque or speed [7]:

$$\begin{cases} P_{Rotor} = P_{wind} \cdot C_p(\lambda, \beta) \\ P_{wind} = 0.5\rho Av^3 \\ T_{Rotor} = \frac{P_{Rotor}}{\Omega_t} \end{cases} \Rightarrow \begin{cases} P_{Rotor} = 0.5\rho \cdot A \cdot C_p(\lambda, \beta) \cdot v^3 \\ T_{Rotor} = \frac{1}{2\Omega_t} \cdot \rho \cdot S \cdot C_p(\lambda, \beta) \cdot v^3 \end{cases} \quad (1)$$

With

$$C_p(\lambda, \beta) = c_1 \cdot \left(\frac{c_2}{A} - c_3 \cdot \beta - c_4\right) \cdot e^{\left(\frac{-c_5}{A}\right)} + c_6 \cdot \lambda.$$

At the rotor of the turbine, the expression of the mechanical torque is:

$$\begin{cases} T_{mec} = J \frac{d\Omega_{mec}}{dt} \\ T_{mec} = T_g - T_{em} - f\Omega_{mec} \end{cases} \Rightarrow J \frac{d\Omega_{mec}}{dt} = T_g - T_{em} - f\Omega_{mec} \quad (2)$$

With the equations of the gearbox: $\begin{cases} \Omega_g = G \cdot \Omega_t \\ T_{Rotor} = G \cdot T_g \end{cases}$.

Table 1 The voltages and the currents equations

The equations of the stator in the reference (d, q)	The equations of the rotor in the reference (d, q)
$V_{sd} = R_s \cdot I_{sd} + \frac{d\varphi_{sd}}{dt} - \omega_s \cdot \varphi_{sq}$	$V_{rd} = R_r \cdot I_{rd} + \frac{d\varphi_{rd}}{dt} - \omega_r \cdot \varphi_{rq}$
$V_{sq} = R_s \cdot I_{sq} + \frac{d\varphi_{sq}}{dt} - \omega_s \cdot \varphi_{sd}$	$V_{rq} = R_r \cdot I_{rq} + \frac{d\varphi_{rq}}{dt} - \omega_r \cdot \varphi_{rd}$
$I_{sd} = \frac{1}{\sigma \cdot L_s} \cdot \varphi_{sd} - \frac{M_{sr}}{\sigma \cdot L_r} \cdot \varphi_{rd}$	$I_{rd} = \frac{1}{\sigma \cdot L_r} \cdot \varphi_{rd} - \frac{M_{sr}}{\sigma \cdot L_r \cdot L_s} \cdot \varphi_{sd}$
$I_{sq} = \frac{1}{\sigma \cdot L_s} \cdot \varphi_{sq} - \frac{M_{sr}}{\sigma \cdot L_s \cdot L_r} \cdot \varphi_{rd}$	$I_{rq} = \frac{1}{\sigma \cdot L_r} \cdot \varphi_{rq} - \frac{M_{sr}}{\sigma \cdot L_r \cdot L_s} \cdot \varphi_{sq}$

3 Dynamic Model of the DFIG Wind Energy System

The mechanical power transferred to electrical power by the Doubly-Fed Induction Generator [7]. In the reference (d, q), the electrical equations of the DFIG are given by Table 1:

The electromechanical torque, in the rotor, is modeled by the equation:

$$T_{em} = p(\varphi_{rd} \cdot \varphi_{sq} - \varphi_{rq} \cdot \varphi_{sd}) \quad (4)$$

With:

$$\begin{cases} \varphi_{sd} = L_s \cdot I_{sd} + M_{sr} \cdot I_{rd} \\ \varphi_{sq} = L_s \cdot I_{sq} + M_{sr} \cdot I_{rq} \\ \varphi_{rd} = L_r \cdot I_{rd} + M_{sr} \cdot I_{sd} \\ \varphi_{rq} = L_r \cdot I_{rq} + M_{sr} \cdot I_{sq} \end{cases}$$

4 Application of Control DFIG Strategy

To have a good behavior of the DFIG, it is recommended to adjust not only the amplitude, but also the frequency of the electrical grid.

4.1 DFIG Field-Oriented Control

Field Oriented Control (FOC) is the most widely used method in the industry. The objective of this command is to establish a simple model of DFIG which makes it

similar to a DC machine with separate excitation, where the inductive current controls the magnetic flux and the armature current controls the electromagnetic torque [9].

The equations which connect the rotor voltages and the active and reactive powers of the stator were calculated to control the rotor-side converter [10]:

$$\begin{cases} V_{rd} = R_r \cdot \left[-\frac{M_{sr}}{V_s^2 \cdot L_r} (V_{sd} \cdot P_s + V_{sq} \cdot Q_s) \right. \\ \left. + \frac{1}{\sigma} \left(\frac{1}{L_r} - \frac{M_{sr}^2}{L_r^2} \right) \varphi_r \right] + \frac{d\varphi_r}{dt} \\ V_{rq} = \frac{R_r}{V_s^2} (V_{sd} \cdot Q_s - V_{sq} \cdot P_s) + \omega_r \cdot \varphi_r \end{cases} \quad (5)$$

The grid voltages of the dynamic model of the grid-side converter, in the reference frame rotating, are as follows [9]:

$$\begin{cases} V_{gd} = \frac{2}{3V_g} \left(R_g \cdot Q_g + L_g \cdot \frac{dQ_g}{dt} - L_g \cdot \omega_s \cdot P_g \right) + V_{dinv} \\ V_{gq} = \frac{2}{3V_g} \left(R_g \cdot P_g + L_g \cdot \frac{dP_g}{dt} - L_g \cdot \omega_s \cdot Q_g \right) + V_{qinv} \end{cases} \quad (6)$$

With

$$\frac{dV_{dc}}{dt} = \left(\frac{V_{dc} \cdot I_{dc}}{C \cdot V_{dc}} \right) = \left(\frac{P_g - P_r}{C \cdot V_{dc}} \right).$$

The reactive power must be null ($Q_g = 0$) to guarantee a unity factor power at the grid side converter.

4.2 DFIG Adaptive Backstepping Control

The Backstepping command was developed by Kokotovic [10]. It doesn't require that the system be linear. The application of this command is done according to the system parameters [11]. If the parameters are known, we used the non-adaptive Backstepping command, otherwise we need an adaptation law, which determines the dynamics of estimation of the unknown parameters, and guarantees their convergence towards their respective values [12]. In this case we say that the used command is the adaptive Backstepping command. The adaptive version of Backstepping offers an iterative and systematic method which allows, for non-linear systems of any order, to recursively build the three essential parts to an adaptive command based on the Lyapunov function (Control law, Lyapunov function and Adaptation law) [8].

The control voltages V_{rq} and V_{rd} are calculated by the Lyapunov function [13]. These voltages control the speed and the powers. The expressions for the rotor side converter commands are given by the equations [14]:

$$\left\{ \begin{array}{l} V_{rd} = -\frac{1}{V_{sd}} \left(\frac{1}{M} \left(\begin{array}{l} -\left(\frac{2\sigma \cdot L_s \cdot L_r}{3}\right)(K_{p_s} \cdot e_{p_s} - \omega_s \cdot Q_s) \\ -\left(\frac{2}{3}(R_s \cdot L_r + R_r \cdot L_r)P_s \right. \\ \left. + (R_r + \omega_r \cdot L_r)(V_{sd} \cdot \varphi_{sd} + V_{sq} \cdot \varphi_{sq}) + L_r \cdot V_s^2 \right) \end{array} \right) \right) \\ V_{rq} = \frac{1}{V_{sd}} \left(\frac{1}{M} \left(\begin{array}{l} -\left(\frac{2\sigma \cdot L_s \cdot L_r}{3}\right)(K_{Q_s} \cdot e_{Q_s} - \omega_s \cdot P_s) \\ -\left(\frac{2}{3}(R_s \cdot L_r + R_r \cdot L_r)Q_s \right. \\ \left. + (R_r + \omega_r \cdot L_r)(V_{sd} \cdot \varphi_{sd} + V_{sq} \cdot \varphi_{sq}) \right) \end{array} \right) \right) \end{array} \right) \quad (7)$$

The control voltages V_{gq} and V_{gd} are calculated by the Lyapunov function [15]. These voltages control the DC bus voltage and the reactive power. The expressions of the commands on the grid side converter are given by the equations [13]:

$$\left\{ \begin{array}{l} V_{gd} = -\frac{2}{3} \left(\frac{L_f}{V_{sd}} \right) \left(K_{p_g} \cdot e_{p_g} + \left(\frac{R_f}{L_f} \right) P_g + \omega_s \cdot Q_g \right) \\ V_{gq} = \frac{2}{3} \left(\frac{L_f}{V_{sd}} \right) \left(K_{Q_g} \cdot e_{Q_g} + \left(\frac{R_f}{L_f} \right) Q_g + \omega_s \cdot P_g \right) \end{array} \right. \quad (8)$$

Equations (7) and (8) confirm the asymptotic stability of the origin in the equations of the DFIG system [16].

5 Simulation Results and Discussion

In order to analyze the performance and behavior of the studied system, in dynamic regime, it is necessary to test the DFIG by a real wind profile with variable speed (see Fig. 2). The chosen wind is that of the Dakhla region located in the south of Morocco. This choice of site was based on the studies by researcher Allouhi [4]. The parameters of the wind energy conversion system are presented in Tables 3 and 4.

Figure 3 illustrate the simulation results under the MATLAB/SIMULINK environment:

In this test, for the FOC command, we obtained appropriate dynamics for the reference active and reactive powers in order to test the decoupling of these powers in the case of variable speed wind operation (Fig. 2). The stator active power follows the mechanical power (reference power) with a dynamic error of 2.18%. Despite the variations of active power, it still remains negative confirming that the machine is supplying power to the grid. We observe, at startup, slight oscillations of high frequencies on the active and reactive powers, their amplitudes decrease when the reactive power become null. The DC bus voltage has fast dynamics with a response

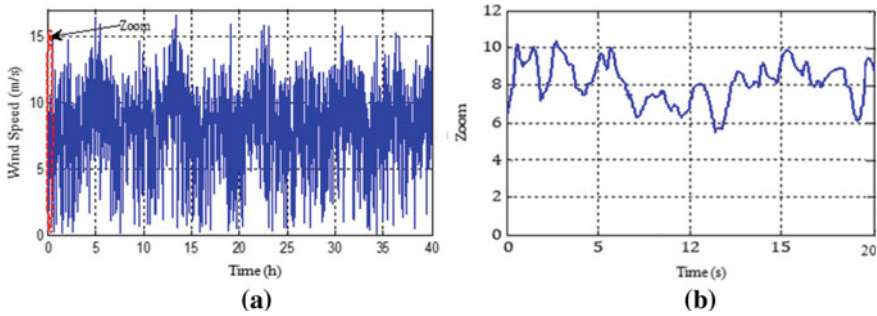


Fig. 2 Variable wind speed profile of Dakhla-Morocco city

time of $t_r(V_{dc}) = 800$ ms. This voltage is precise, because the static error is null when the steady state has been reached. This voltage V_{dc} reaches its reference value with an overshoot of $D(\%) = 3.34\%$. The stator currents varies according to the variation of the wind, which is logical since they are consequences of the power. They are sinusoidal with a frequency of 50 Hz, which is the frequency of the electrical grid.

On the other hand, we observe for the adaptive Backstepping command that the active power perfectly follows its reference value, generated by the MPPT strategy, with a dynamic error of $\epsilon_d = 1.05\%$. Reactive power always remains zero confirming operation with a unit power factor obtained after the end of its transient regime. Regarding the DC bus voltage, it is characterized by a fast and precise dynamic, it reaches its reference value at $t(V_{dc}) = 0.3$ s without overshoot with a small static error. The stator current varies according to the variation of the wind which confirms its proportional relationship with the power. Despite the variations of the wind, it remains sinusoidal with a frequency of 50 Hz. This current has less ripples compared to the FOC command.

After the results analyzing of each command separately, we do a comparative study in order to have a clear vision for the most suitable command strategie for our system giving its best performance. The comparison results are cited in Table 2.

In order to study the effect of the control on the quality of the energy supplied by the DFIG, a spectral analysis of the stator currents was carried out. Figure 4 shows respectively the current of the stator phase “ i_{sA} ” supplied by the DFIG and their harmonic spectrum.

These results confirmed the influence of the control on the quality of the supplied energy. The harmonic distortion rate (THD) is higher (THD $\sim 18.82\%$.) for the FOC command contrary to the adaptive Backstepping control which doesn't exceed 0.16% . This comparison, gave us a clear idea on the reduction of the harmonic rate of the powers and the currents injected by the DFIG in the electrical grid.

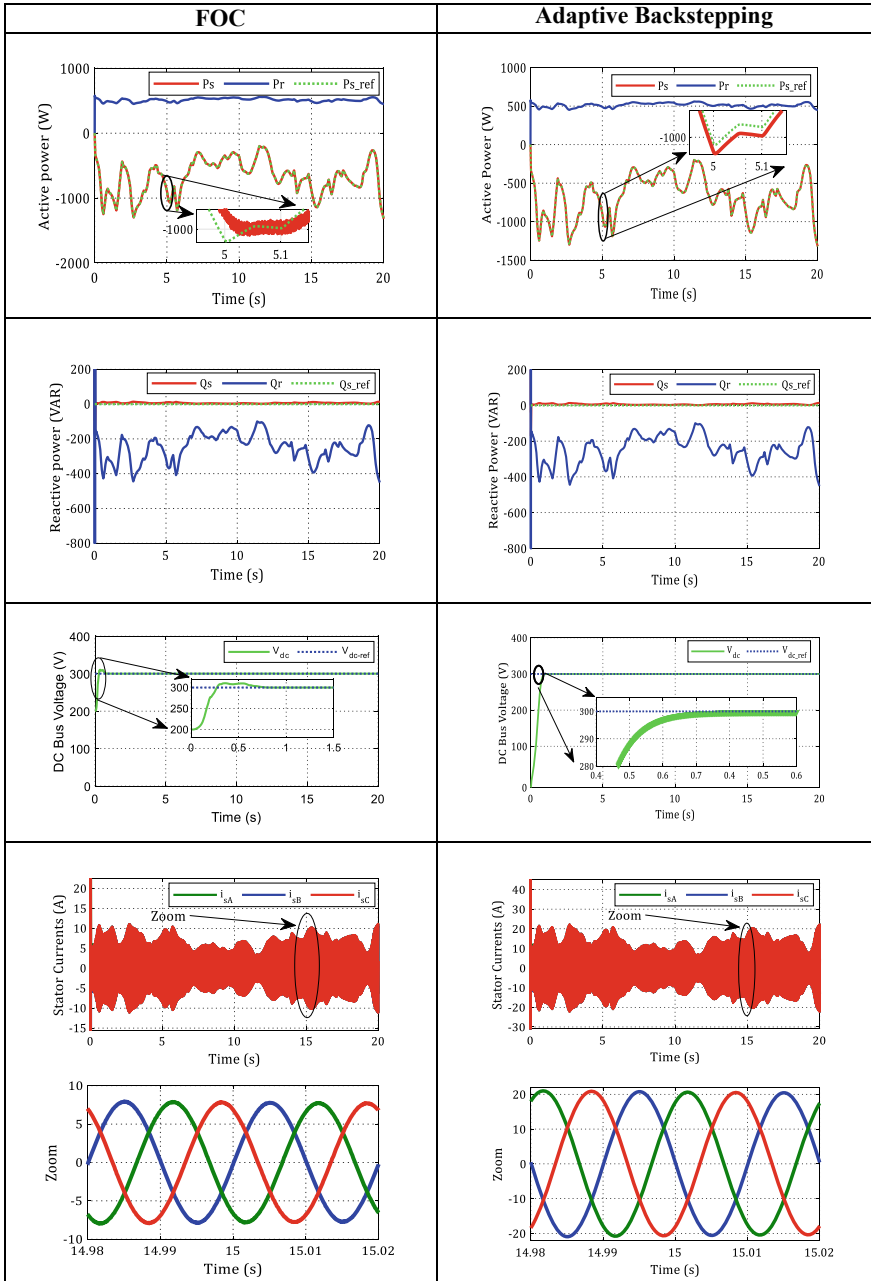


Fig. 3 Simulation results for FOC and adaptive Backstepping control

Table 2 Comparison between FOC and adaptive backstepping

		FOC	Adaptive backstepping	Improvement rate (%)
Error	Static	0.4%	0.067%	83.25
	Dynamic	2.18%	1.05%	51.83
Response time	Active power	260 ms	170 ms	34.61
	Reactive power	280 ms	50 ms	82.14
	DC bus	800 ms	510 ms	36.25
Overshoot	Active power	Null	Null	0
	Reactive power	Null	Null	0
	DC bus	3.34%	Null	99
Variation band	Active power	20 W	5 W	75
	Reactive power	20 VAR	5 VAR	75

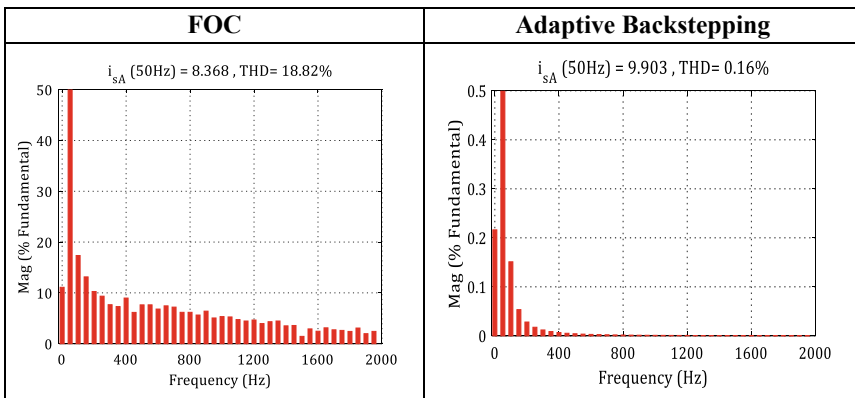


Fig. 4 THD for FOC and Adaptive Backstepping

6 Conclusion

In this work, we applied the Field-Oriented Control command and the adaptive Backstepping command to the DFIG. The simulation results have shown that the adaptive backstepping command gives a high dynamic performance in tracking reference in a scenario with a real wind profile and it also ensures optimal energy conversion. This command provides a concrete solution to the problems of robustness and dynamics encountered in the structure of the FOC command.

Table 3 The DFIG parameters

Name	Values
Nominal stator voltage	220/380 V
Nominal rotor voltage	12 V
Nominal current	3.64/6.31 A
Nominal power	$P_n = 1.5$ kW
Nominal frequency	$f_n = 50$ Hz
Nominal torque	$C_n = 10$ N m
Power factor	0.89
Number of pole pairs	$p = 2$
Nominal speed	1440 tr/min
Stator resistance	$R_s = 0.435$ Ω
Rotot resistance	$R_r = 0.816$ Ω
Stator inductance coefficient	$L_s = 0.071$ H
Rotor inductance coefficient	$L_r = 0,070$ H
Mutual inductance coefficient	$M = 0,069$ H
Friction coefficient	$f = 6.73 \times 10^{-3}$ kg m ²
Moment of inertia	$J = 0.3125$ N s/rad

Table 4 The wind turbine parameters

Name	Value
Nominal power	$P_n = 7.8$ kW
Density of air	$\rho = 1.225$
Blade angle	$\beta = 2^\circ$
Number of blades	3
Blade radius	$R = 3$ m
Gearbox ratio	$G = 10.38$
Conversion yield	$\eta = 1$
Moment of inertia	$J = 0.042$ kg m ²
Viscous friction coefficient	$f = 0.024$ N s/rad

Appendix

See Tables 3 and 4.

References

1. Jelavić M, Petrović V, Perić N (2018) Estimation based individual pitch control of wind turbine. *Automatika* 51:181–192

2. Allouhi A (2019) Energetic, exergetic, economic and environmental (4 E) assessment process of wind power generation. *J Clean Prod* 235:123–137
3. Laca Arantegui R (2015) Materials use in electricity generators in wind turbines estate-of-the-art and future specifications. *J Clean Prod* 87:275–283 (2015)
4. Allouhi A, Zamzoum O, Islam MR, Saidur R, Kousksou T, Jamil A, Derouich A (2017) Evaluation of wind energy potential in Morocco's coastal regions. *Renew Sustain Energy Rev* 72:311–324
5. De Luca E, Nardi C, Giuffrida LG, Krug M, Di Nucci MR (2020) Explaining factors leading to community acceptance of wind energy. *Results Expert Assess Energies* 13:2119
6. Ren Y, Li L, Brindley J, Jiang L (2016) Nonlinear PI control for variable pitch wind turbine. *Contr Eng Pract* 50:84–94
7. Bossoufi B, Karim M, Lagrioui A, Taoussi M, Derouich A (2014) Modeling and backstepping control of DFIG generators for wide-range variable-speed wind turbines. *J Electr Syst JES* 10(3):317–330
8. Bossoufi B, Karim M, Lagrioui A, Taoussi M, EL Hafyani ML (2014) Backstepping adaptive control of DFIG-generators for variable-speed wind turbines. *Int J Comput Technol* 12(7):3719–3733
9. Taoussi M, Karim M, Bossoufi B, Lagrioui A, El Mahfoud M (2014) The fuzzy control for rotor flux orientation of the doubly-fed asynchronous generator drive. *Int J Comput Technol* 13(08):4707–4722
10. Zamzoum O, El Mourabit Y, Errouha M, Derouich A, El Ghzizal A (2018) Power control of variable speed wind turbine based on doubly fed induction generator using indirect field-oriented control with fuzzy logic controllers for performance optimization. *Energy Sci Eng* 6:408–423
11. Taoussi M, Karim M, Bossoufi B, Hammoumi D, Lagrioui A (2015) Speed Backstepping control of the doubly-fed induction machine drive. *J Theor Appl Inf Technol* 74(2):189–199
12. El Mourabit Y, Derouich A, ElGhzizal A et al (2019) Implementation and validation of backstepping control for PMSG wind turbine using dSPACE controller board. *Energy Rep* 5:807–821
13. Bossoufi B, Karim M, Lagrioui A, Taoussi M, Derouich A (2015) Observer backstepping control of DFIG-Generators for wind turbines variable-speed: FPGA-based implementation. *Renew Energy* 81:903–917
14. Taoussi M, Karim M, Hammoumi D, Elbakkali C, Bossoufi B, El Ouanjli N (2017) Comparative study between backstepping adaptive and field-oriented control of the DFIG applied to wind turbines. *Processing IEEE Xplore*, 23 Oct 2017
15. Taoussi M, Karim M, Bossoufi B, Hammoumi D, El Bakkali C, Derouich A, El Ouanjli N (2017) Low-speed sensorless control for wind turbine system. *WSEAS Trans Syst Control* 12:405–417
16. Taoussi M, Karim M, Bossoufi B, Hammoumi D, Lagrioui A, Derouich A (2016) Speed variable adaptive backstepping control of the doubly-fed induction machine drive. *Int J Autom Control* 10(01):12–33

Comparative Study Between FOSMC and SMC Controllers for DFIG Under the Real Wind Profile of Asilah-Morocco City



Mohamed Amine Beniss, Hassan El Moussaoui, Tijani Lamhamdi, and Hassane El Markhi

Abstract This paper describes a comparative study between two advanced nonlinear controls strategies; the Sliding Mode Control (SMC) and the Fractional-Order Sliding Mode Control (FOSMC), in terms of both reactive and active powers to improve the quality of the energy injected into the distribution grid by the wind energy conversion system (WECS). This later is based on the doubly-fed induction generator (DFIG). The objective is to perform modeling and direct control of the (WECS). Firstly, the dynamic modeling of the different parts of the WECS is performed. Then, the second part of this work concentrates on the proposed nonlinear control laws that rely on FOSMC and SMC. Finally, the performance of those strategies has been simulated in the MATLAB/SIMULINK environment using two wind profiles. One of them is a real wind profile of Asilah-Morocco city to test the system robustness and dynamics as opposed to real conditions.

Keywords Doubly fed induction generator (DFIG) · Real wind profile · Fractional order calculus · Power ripples. sliding mode control (SMC)

1 Introduction

In recent years, the annual electrical energy demand has increased worldwide due to human needs in industrialization and also to get a better standard of living. For these reasons, the world is focused on the exploitation and development of clean and renewable energy sources [1]. Among them, wind energy, bio-fuel, solar energy, hydropower, etc. ... To satisfy this energy demand, many different wind turbines have been fabricated recently. The doubly-fed induction generators (DFIG) are one of the most popular (Fig. 1) and favorable kinds of wind generators in the market due to their variable speed operations, low systematic cost, and their remarkable advantages [2].

M. A. Beniss (✉) · H. El Moussaoui · T. Lamhamdi · H. El Markhi
Electrical Department, Laboratory of Intelligent Systems, Georesources and Renewable Energies,
Faculty of Sciences and Technologies, Sidi Mohamed Ben Abdellah University, Fez, Morocco
e-mail: mohamedamine.beniss@usmba.ac.ma

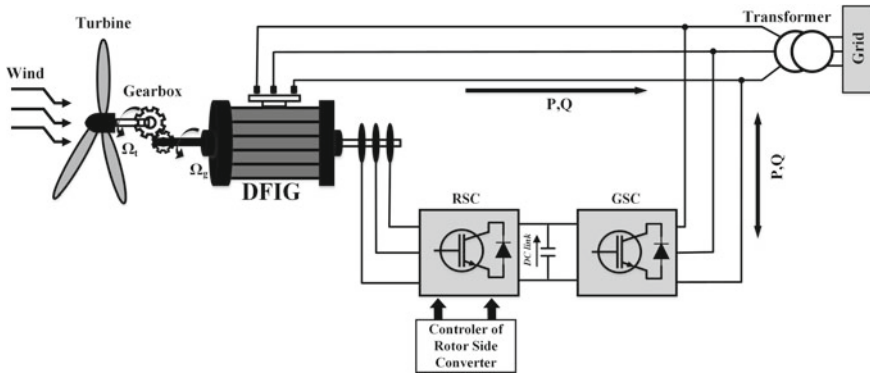


Fig. 1 Architecture of DFIG based WECS

Generally, the use of DFIG can adopt different types of control. So far, three strategies are used in controlling DFIG in the wind energy conversion system (WECS) [3]. Firstly, Field Oriented Control (FOC) which is based on classical (PI) controllers. Secondly, Direct Torque Control (DTC) that controls the stator flux. Finally, Direct Power Control (DPC) [4]. Today, few researches have shown great interest in applying the FOSMC strategy to the DFIG and have claimed its ability to replace the traditional control strategies (SMC). These later techniques are based on integer order calculus, which limit their performances [5]. Hence, the main purpose of this paper is to propose an enhanced sliding mode technique based on direct power control (FOSM-DPC) via a two-level NPC inverter in which principles of DPC, SMC are combined for higher operating performance, minimized ripples, improved the robustness and to confirm this claim by comparing the DFIG responses using both control strategies (SMC and FOSMC).

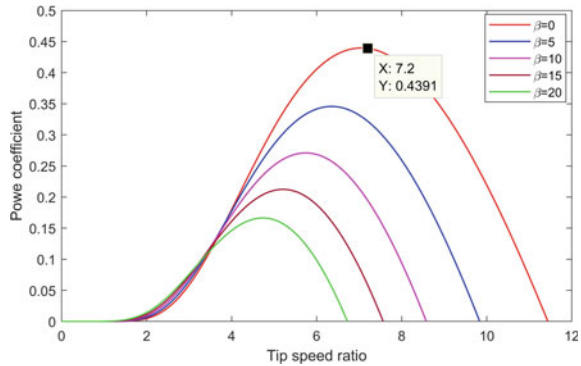
The remainder of this paper is structured in five sections: Sect. 2 is dedicated to the modeling of the wind energy conversion system, the MPPT command and the doubly-fed induction generator. Then, the principle of SMC and FOSMC based on the Lyapunov stability theory is briefly described in Sect. 3. We emphasize that only the rotor-side converter (RSG) control is considered in this work. The obtained simulation results under Matlab/Simulink are discussed in Sect. 4. Finally, a conclusion and future works of this article are summarized in Sect. 5.

2 Model of the Wind Energy Conversion System

2.1 Mathematical Model of the Wind Turbine

The aerodynamic power and the mechanical torque produced by the wind turbine can be written [6]:

Fig. 2 The power coefficient C_p versus λ and β



$$P_{mec} = \frac{1}{2} \cdot C_P(\lambda, \beta) \cdot \rho \cdot S \cdot V^3 \quad (1)$$

$$T_{mec} = \frac{P_{mec}}{\Omega_{tur}} \quad (2)$$

The power coefficient depending on the angle of the blades β and the tip-speed ratio (TSR) denoted by λ can be approximated as follows:

$$\begin{cases} C_P(\lambda, \beta) = 0.5872 \left(\frac{116}{\lambda_k} - (5 + 0.4\beta) \right) e^{-\frac{21}{\lambda_k}} + 0.0085\lambda \\ \frac{1}{\lambda_k} = \frac{1}{0.08\beta + \lambda} - \frac{0.035}{\beta^3 + 1} \end{cases} \quad (3)$$

$$\lambda = \frac{\Omega_t \cdot R}{V} \quad (4)$$

Figure 2 shows the power coefficient C_p as a function of the (TSR), for the adopted wind system, we have to set λ and β to their optimal values $\beta = 0^\circ$ and $\lambda = 7.2$ that correspond to the optimal power coefficient $C_{p-\max} = 0.4391$.

2.2 DFIG Modeling

The mathematical model of a DFIG is modeled in the synchronous d-q frame. The Park transformation can be described by the following equations:

- Voltages across the stator and rotor terminals [7]:

$$\begin{cases} V_{sd} = R_s \cdot i_{sd} + \frac{d\psi_{sd}}{dt} - \omega_s \cdot \psi_{sq} \\ V_{sq} = R_s \cdot i_{sq} + \frac{d\psi_{sq}}{dt} + \omega_s \cdot \psi_{sd} \\ V_{rd} = R_r \cdot i_{rd} + \frac{d\psi_{rd}}{dt} - \omega_r \cdot \psi_{rq} \\ V_{rq} = R_r \cdot i_{rq} + \frac{d\psi_{rq}}{dt} + \omega_r \cdot \psi_{rd} \end{cases} \quad (5)$$

The basic magnetic equations related to the flux expressions in the reference frame (d, q) are given as follows:

- Flux at the stator and rotor:

$$\begin{cases} \psi_{sd} = M i_{rd} + L_s i_{sd} \\ \psi_{sq} = M i_{rq} + L_s i_{sq} \\ \psi_{rd} = M i_{sd} + L_r i_{rd} \\ \psi_{rq} = M i_{sq} + L_r i_{rq} \end{cases} \quad (6)$$

- Pulsation equation:

$$\omega_r = \omega_s - P\Omega_g \quad (7)$$

The electromagnetic torque expression represents the link between electrical and mechanical parts of the DFIG. It can be obtained in terms of rotor currents and the stator flux [8]:

$$T_{em} = \frac{3}{2} p (I_{rq} \psi_{rd} - I_{rd} \psi_{rq}) \quad (8)$$

The mechanical equation of shaft turbine can be written as:

$$T_{mec} - T_{em} - f_v \Omega_{mec} = J \frac{d\Omega_{mec}}{dt} \quad (9)$$

where T_{mec} , f_v and J are respectively the mechanical torque applied to the generator, the viscous friction and the wind turbine inertia.

In order to complete the model, the stator active and reactive powers are expressed by [9]:

$$\begin{cases} P_s = V_{ds} I_{ds} + V_{qs} I_{qs} \\ Q_s = V_{qs} I_{ds} - V_{ds} I_{qs} \end{cases} \quad (10)$$

To control the electromagnetic torque and then the active, reactive power of the DFIG independently and ensure decoupling between them we have to apply the vector control, in this work, by choosing two phases direct and quadrature (d-q) linked to the rotating reference frame with the stator flux vector is oriented along with the d-axis, the expression of the flux becomes as follows[10]:

$$\begin{cases} \psi_{qs} = 0 \\ \psi_{ds} = \psi_s \end{cases} \quad (11)$$

For high and medium power machines, the resistance of the stator R_s can be neglected, and the stator voltages can be deduced as follows [11]:

$$\begin{cases} V_{sd} = 0 \\ V_{sq} = V_s = \omega_s \psi_s \end{cases} \quad (12)$$

By replacing the above equations into (5), the rotor voltage can be rewritten in terms of rotor currents:

$$\begin{cases} V_{dr} = R_r I_{dr} + \sigma L_r \frac{d}{dt} I_{dr} - \sigma L_r s \omega_s I_{qr} \\ V_{qr} = R_r I_{qr} + \sigma L_r \frac{d}{dt} I_{qr} - \sigma s \omega_s I_{dr} + s \frac{M V_s}{L_s} \end{cases} \quad (13)$$

With: $\sigma = 1 - (M^2 - L_r/L_s)$ and (S) is the slip of DFIG. $[I_{dr} \ I_{dr}]^T$ and $[V_{dr} \ V_{dr}]^T$ are the vectors output and input of the system, respectively.

Finally, the active and reactive powers dynamic and the electromagnetic torque of the generator can be rewritten in terms of rotor currents, the former expressions become:

$$\begin{cases} P_s = -\frac{M V_s}{L_s} I_{qr} \\ Q_s = \frac{V_s^2}{\omega_s L_s} - \frac{M V_s}{L_s} I_{dr} \\ T_{em} = -P \frac{M V_s}{\omega_s L_s} I_{qr} \end{cases} \quad (14)$$

In order to express the rotor currents in terms of stator reactive and active powers, we set $Q_s = 0$ to achieve a unity power factor. The relationship between stator reactive and active powers and the rotor currents should be estimated as follows.

$$\begin{cases} I_{qr-ref} = -\frac{L_s}{M V_s} P_{qr} \\ I_{dr-ref} = \frac{V_s}{\omega_s L_s} \end{cases} \quad (15)$$

The nonlinear state space model is given under the following form:

$$\dot{X}(t) = F(X) + GU(t) \quad (16)$$

where:

$$F(X) = \begin{pmatrix} -\frac{R_r}{\sigma L_r} I_{dr} + s\omega_s I_{qr} \\ -\frac{R_r}{\sigma L_r} I_{qr} - s\omega_s I_{dr} + s\frac{MV_s}{\sigma L_r L_s} \end{pmatrix} \text{ and } G = \begin{pmatrix} \frac{1}{\sigma L_r} & 0 \\ 0 & \frac{1}{\sigma L_r} \end{pmatrix} \quad (17)$$

3 Controller Synthesis

In this part, two types of controllers are presented, the Sliding Mode Control and Fractional-Order Sliding Mode Control (FOSMC) are applied to RSC converter.

3.1 Conventional Sliding Mode Controller Design

SMC theory has been widely used in controlling complex systems. Generally, the principle of this technique consists in bringing back the trajectory of the desired plant state to the sliding surface. The advantage of this technique is its simple implementation, good dynamic response, and robustness despite external disturbances and system uncertainties.

To determine the SMC law there are two fundamental steps: firstly, we need to find the sliding surface. Secondly, we developed control law. The general form of the integer order sliding surface is expressed as follows [10]:

$$S(x) = \left(\delta + \frac{d}{dt} \right)^{z-1} \cdot e(x) \quad (18)$$

where z is the order of the system, δ is a positive gain, and $e(x)$ represents the state variable error between the reference signal and the actual signal expressed as:

$$e = \begin{pmatrix} e_d \\ e_q \end{pmatrix} = \begin{pmatrix} I_{rd_ref} - I_{rd} \\ I_{rq_ref} - I_{rq} \end{pmatrix} \quad (19)$$

The integral sliding surface is expressed by:

$$S = \begin{pmatrix} S_d \\ S_q \end{pmatrix} = \begin{pmatrix} e_d + k_1 \int e_d \\ e_q + k_1 \int e_q \end{pmatrix} \quad (20)$$

where k_1 and is positive coefficients.

The time derivative of the sliding surface can be given as follows:

$$\dot{S} = \begin{pmatrix} \dot{S}_d \\ \dot{S}_q \end{pmatrix} = \begin{pmatrix} \dot{e}_d + k_1 \int e_d \\ \dot{e}_q + k_1 \int e_q \end{pmatrix} \quad (21)$$

Hence, the equivalent control signals of the SMC in the d-q reference frame is proposed as follow:

$$U = G^{-1}(-F(X) + \dot{X}_{ref} + \zeta_1 sign(S)) \tag{22}$$

where ζ_1 is the positive switching gain and $sign(S)$ denotes the sign function, given as:

$$sign(S) = \begin{cases} 1 & \text{if } S > 0 \\ 0 & \text{if } S = 0 \\ -1 & \text{if } S < 0 \end{cases} \tag{23}$$

but, to reduce the chattering phenomenon due to the use of the discontinuous control law we take the following expression of the sign function.

$$U = G^{-1}\left(-F(X) + \begin{pmatrix} I_{dr}^* \\ I_{qr}^* \end{pmatrix} + \zeta_1 sat(S)\right) \tag{24}$$

where: $\zeta_1 = \begin{pmatrix} \zeta_{11} & 0 \\ 0 & \zeta_{12} \end{pmatrix}$ with ζ_{11} and ζ_{12} are real positive coefficients.

where $sat(S)$ denotes the saturation function. It is defined as:

$$sat(S) = \begin{cases} \frac{S}{L} & \text{if } S < L \\ sig(s) & \text{if } S \geq L \end{cases} \tag{25}$$

To ensure the stability of the FOSMC during the reaching phase. We use the Lyapunov stability theory as shown in the Appendix A.

3.2 Fractional-Order Sliding Mode Control Design

The fractional calculus is the extended version of the integer order one. Many studies has confirmed that controllers based on fractional order operators are robust and accurate. This subsection deals with the design of FOSMC controller for the RSC of the DFIG.

Definition The Riemann–Liouville fractional operator (derivative and integration) of order α applied to a function f is defined as [5, 11]:

$${}_a D_t^\alpha f(t) = \frac{d^\alpha}{dt^\alpha} f(t) = \frac{1}{\Gamma(m - \alpha)} \frac{d^m}{dt^m} \int_a^t \frac{f(\tau)}{(t - \tau)^{\alpha - m + 1}} d\tau \tag{26}$$

$${}_a D_t^{-\alpha} f(t) = I^\alpha f(t) = \frac{1}{\Gamma(\alpha)} \int_a^t \frac{f(\tau)}{(t - \tau)^{1-\alpha}} d\tau \tag{27}$$

Here m is an integer that verify $m - 1 < \alpha < m$, and Γ represents the Gamma function.

To improve the sliding surface and reduce the chattering level in the sliding stage. We can replace the former sliding surface. The new sliding surface becomes as follows:

$$S = k_2 e + D^\alpha e \tag{28}$$

where S designates the sliding surface and k_2 is a positive real coefficient.

The proportional derivative fractional sliding surface can be rewritten as follows:

$$S = \begin{pmatrix} S_d \\ S_q \end{pmatrix} \tag{29}$$

where:

$$S = \begin{pmatrix} k_2 e_d + D^\alpha e_d \\ k_2 e_q + D^\alpha e_q \end{pmatrix} \tag{30}$$

Let us suppose that the DFIG is controlled by the following law:

$$U = G^{-1} \left(-F(X) + \dot{X}_{ref} + \frac{1}{k} (D^{\alpha+1} e + \zeta_2 \text{sign}(S)) \right) \tag{31}$$

Hence, the closed-loop state model of the DFIG is asymptotically stable, and the active and reactive powers track their reference values.

4 Results

In this section, we present the simulation results carried out under MATLAB/SIMULINK using the DFIG parameters summarized in Table 1.

In one hand, a comparative simulation study is conducted using both the SMC and FOSMC controllers under a step wind profile. Figs. 3, 4, 5 and 6 confirm the high performances of the FOSMC controller. It is clear that it tracks accurately the references of the active and reactive powers. In terms of quality, the FFT (Fast Fourier Transform) analysis demonstrates the superiority of the FOSMC over the SMC controller (Figs. 7 and 8). Table 2 resume the THD (Total Harmonic Distortion) values obtained during the first simulation test.

Table 1 DFIG parameters

Simulated DFIG parameters
Rated power—7.5 kW
Hub height—43.5 m
Moment of inertia—0.3125 kg m ²
$L_s = 0.084H, R_s = 0.455 \Omega, L_r = 0.081H, R_r = 0.62 \Omega, M = 0.078H, P = 2, f = 50 \text{ Hz}$

Fig. 3 Active power

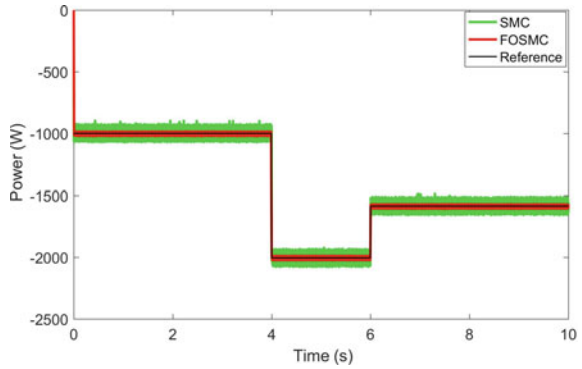


Fig. 4 Reactive power

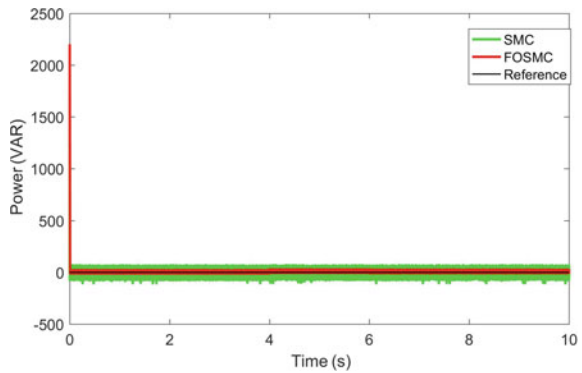


Fig. 5 Stator current FOSMC

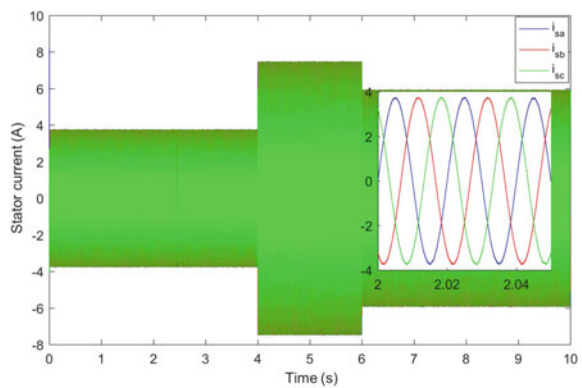


Fig. 6 Stator current SMC

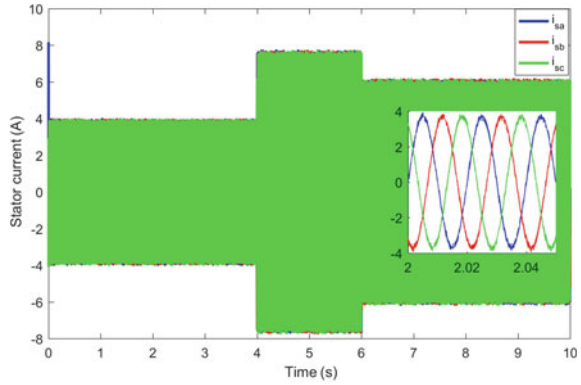


Fig. 7 Spectrum harmonic for FOSMC

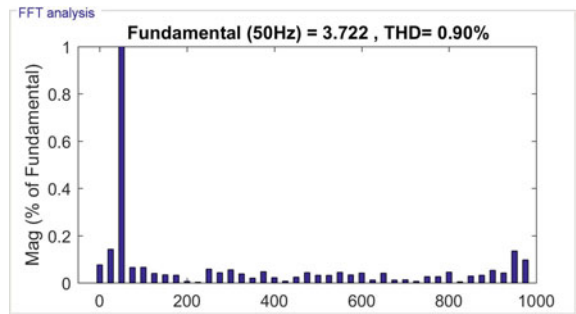


Fig. 8 Spectrum harmonic for SMC

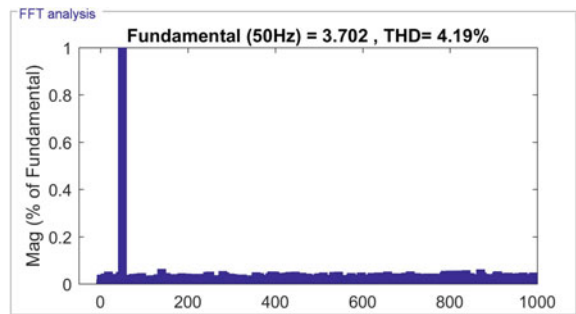


Table 2 THD comparison of two methods

	FOSMC	SMC
THD	0.90%	4.19%

In one hand, a comparative simulation study is conducted using both the SMC and FOSMC controllers under a step wind profile. Figures 3, 4, 5 and 6 confirm the highperformances of the FOSMC controller. It is clear that it tracks accurately

Fig. 9 Variable wind profile of the Asilah-Morocco city

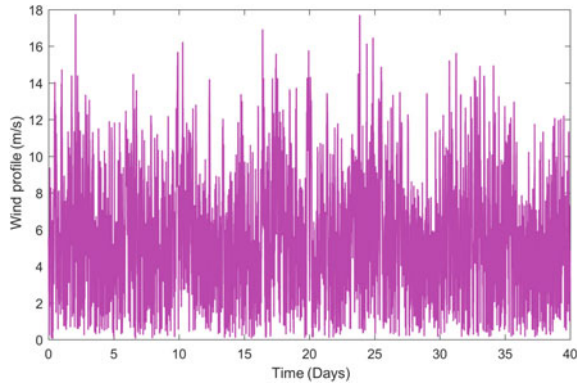
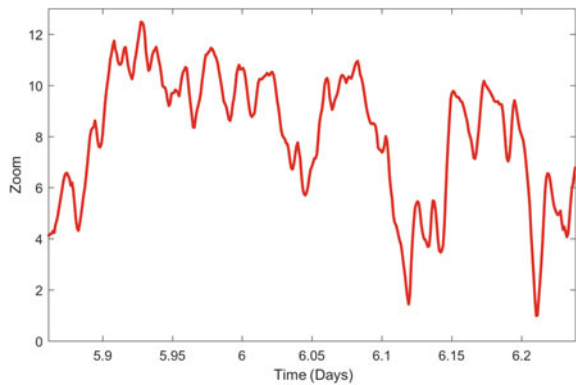


Fig. 10 Wind profile zoom city



the references of the active and reactive powers. In terms of quality, the FFT (Fast Fourier Transform) analysis demonstrates the superiority of the FOSMC over the SMC controller (Figs. 7 and 8). Table 2 resume the THD (Total Harmonic Distortion) values obtained during the first simulation test.

5 Conclusion

This paper aims to show the performances of both the conventional sliding mode controller and the fractional-order sliding mode one for a variable speed wind energy conversion system based on DFIG. First, the modeling of the system is established. Then, the design methodology of both controllers is given in detail. These two controllers are applied to the RSC converter.

Based on the results of this study we can draw these principal conclusions:

Fig. 11 Active power using the wind profile of Asilah City

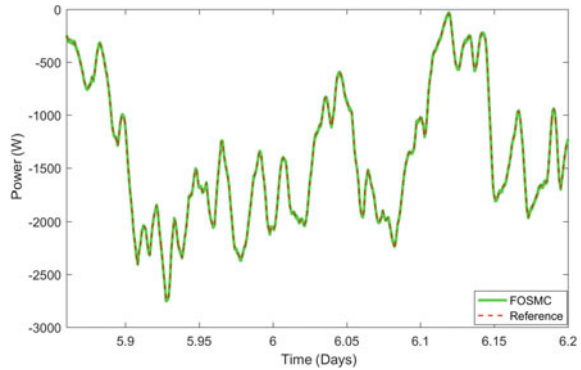
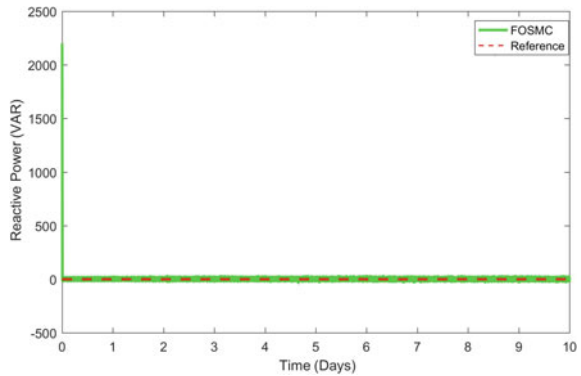


Fig. 12 Reactive power using the wind profile of Asilah City



- The power ripples are low and restrained in the two cases (with SMC or with FOSMC controls).
- All results confirms the advantages of the FOSMC controller over the SMC one in terms of rapidity and accuracy.
- The harmonic distortion rate has been reduced when using the FOSMC controller.

Our future works will address the experimental side of this study in order to demonstrate the effectiveness of the FOSMC controller in real applications.

References

1. Zamzoum O, El Mourabit Y, Errouha M, Derouich A, El Ghzizal A (2018) Power control of variable speed wind turbine based on doubly fed induction generator using indirect field-oriented control with fuzzy logic controllers for performance optimization. *Energy Sci Eng* 6(5):408–423
2. Benbouzid M, Beltran B, Amirat Y, Yao G, Han JG, Mangel H (2014) Second-order sliding mode control for DFIG-based wind turbines fault ride-through capability enhancement. *ISA*

Trans 53:827–833

3. Pande VN, Mate UM, Shailaja K (2013) Discrete sliding mode control strategy for direct real and reactive power regulation of wind driven DFIG. *Electr Power Syst Res* 100:73–81
4. Kiran KJ, Kanwarjit SS (2020) Real-time simulator-based hybrid controller of DFIG-WES during grid faults design and analysis. *Int J Electr Power Energy Syst* 116:762–773
5. Xiong L, Wang J, Mi X, Khan MW (2017) Fractional order sliding mode based direct power control of grid-connected DFIG. *IEEE Trans Power Syst* 33(3):3087–3096
6. Taoussi M, Karim M, Bossoufi B, Himmoumi D, Bakkali C, Derouich A, Ouanjli EN (2017) Low-speed sensorless control for wind turbine system. *WSEAS Trans Syst Control* 12:405–417
7. El Ouanjli N, Motahhir S, Derouich A, El Ghzizal A, Chebabhi A, Taoussi M (2019) Improved DTC strategy of doubly fed induction motor using fuzzy logic controller. *Energy Rep* 5:271–279. <https://doi.org/10.1016/j.egy.2019.02.001>
8. Ouanjli NE et al (2019) Direct torque control of doubly fed induction motor using three-level NPC inverter. *Protect Control Mod Power Syst* 4(3):196–204
9. Djeriri Y, Meroufel A, Massoum A (2014) Artificial neural network based direct torque control of doubly fed induction. *J Electr Eng JEE, Romania* 14(2):71–79. ISSN 1582-4594
10. Shehata EG (2015) Sliding mode direct power control of RSC for DFIGs driven by variable speed wind turbines. *Alexandria Eng J* 54(4):1067–1075
11. Ebrahimkhani S (2016) Robust fractional order sliding mode control of doubly-fed induction generator (DFIG)-based wind turbines. *ISA Trans* 63:343–354

Voltage and Power Control for a Grid Tied Single Phase Single Stage Transformer-Less Photovoltaic System Using Sliding Mode Control



Khalid Chigane and Mohammed Ouassaid

Abstract This study presents a Sliding mode control (SMC) strategy applied to a single-phase grid connected photovoltaic plant. The proposed controller is designed in such a way to control the DC voltage, active and reactive power smoothly, and with insensitivity to system parameter variations and external perturbations. The global asymptotic stability of the developed control laws is guaranteed employing Lyapunov stability theory. So as to verify the effectiveness of the proposed controller, a simulation based comparative study has been carried out under a change in solar irradiance and ambient temperature. The results demonstrate that the SMC provides better dynamic performance, great decoupling of active and reactive power, good reference tracking and improved power quality even when facing operating point variation comparing with the conventional linear controller.

Keywords Sliding mode control · Grid tied inverter · Voltage and power control

1 Introduction

The critical state of the planet's climate, the growth of energy demand, the exhaustion of fossil fuels and crises such as covid-19 pandemic, keep serves as a reminder of the necessity to change our power reliance policy and make clean and renewable energy sources a surviving requirement for the next generations.

Due to its interesting features of low cost, simplicity of implementation and direct conversion of sunlight to electricity, the Photovoltaic (PV) energy has increased to be one of the leading sources of green power used in the entire world. In fact, its popularity allowed it to have a total installed power capacity in excess of 635 GW

K. Chigane (✉) · M. Ouassaid
Engineering for Smart and Sustainable Systems Research Center (ESSSRC), Mohammadia
School of Engineers (EMI), Mohammed V University in Rabat, Rabat, Morocco
e-mail: khalidchigane@research.emi.ac.ma

M. Ouassaid
e-mail: ouassaid@emi.ac.ma

at the end of 2019 [1]. However, PV energy can be exploited using either non-autonomous (grid tied) or autonomous (stand-alone) systems even in a homogeneous configuration according to the needs [2]. Moreover, in the grid-connected topology, the PV power is fed to the network via a two conversion stages (DC-DC and DC-AC converters) or through one conversion stage using a Voltage Source Inverter (VSI) and with or without transformer respecting some injection criteria [3].

Unlike inverters with a high or low frequency transformer, transformer-less ones can benefit from reduced size, weight, and complexity with an additional 1–2% of efficiency and lower price. In fact, the drawbacks of galvanic insulation elimination can be processed in this topology using power electronics and diverse strategies of inverter control [3, 4].

So as to fulfill the grid requirements regarding power quality and safe operation of injection, various control techniques have been applied to the grid-connected VSI, for instance, Proportional Integral controller, Proportional Resonant control, Current Hysteresis control and Voltage Oriented control are studied and detailed in the literature. Despite the fact that they are characterized by simplicity of design and good reference tracking, these strategies of control suffer from sensitivity to the system parameter variation, notably for nonlinear systems [5, 6].

Furthermore, numbers of nonlinear and intelligent control methods have been adopted for the grid tied inverter such as Backstepping control [7, 8], Predictive Current control [9], Fuzzy Logic [10] and Artificial Neuron Network [11, 12]. Regardless of their complexity and computational burden, these control strategies try to enhance the power quality and ensure a better dynamic response in addition to the benefits of the conventional controllers [6, 13].

In this work, the sliding mode control is applied to a single-phase single-stage transformer-less grid-connected system for the voltage and current regulation. This variable structure control is typified mainly by its robustness against system parameter uncertainties and operation point variation even in the presence of external disturbances, which is suitable for this kind of nonlinear plants [14–16].

The rest of this paper is structured as follows. In Sect. 2, the mathematical modeling of the VSI connected to the electrical network was well developed. The Sliding mode control using the Lyapunov stability adopted for the studied system was handled in Sect. 3. Section 4 deals with the suggested control method achievement results and their related discussions and comparisons under climatic condition changes. Finally, some conclusions are mentioned in the final Section.

2 Mathematical Modeling of the Grid Connected VSI

As shown in Fig. 1, the transformer-less grid tied PV system considered in this study consists of a PV array, Pulse Width Modulation (PWM) inverter in full bridge structure and a grid filter. According to the Kirchoff's law, the dynamical model of the VSI and its DC-bus can be represented in the rotating synchronous reference frame (d, q) by:

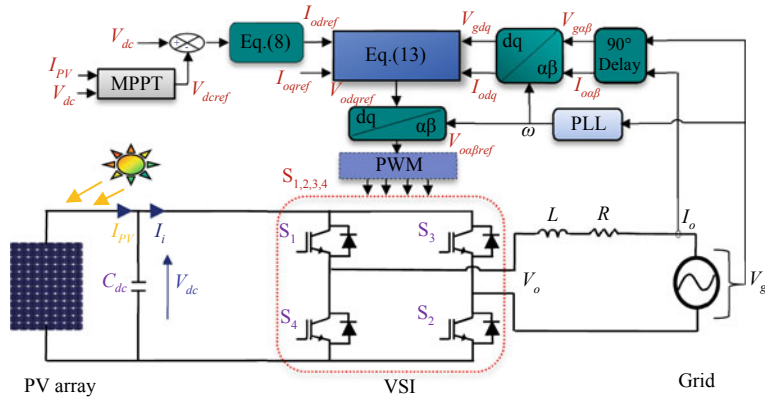


Fig. 1 Overall scheme of the studied system and its control

$$\begin{cases} \frac{dI_{od}}{dt} = \frac{1}{L} (\omega LI_{oq} - RI_{od} + V_{od} - V_{gd}) \\ \frac{dI_{oq}}{dt} = \frac{1}{L} (-\omega LI_{od} - RI_{oq} + V_{od} - V_{gq}) \\ \frac{dV_{dc}}{dt} = \frac{1}{C_{dc}} (I_{pv} - I_i) \end{cases} \quad (1)$$

where (V_{gd}, V_{gq}) , (I_{od}, I_{oq}) and (V_{od}, V_{oq}) are the grid voltage and the inverter outputs current and voltage components in the rotating reference frame, separately. The inductance L and its internal resistance R form the grid filter, V_{dc} and C_{dc} are the DC-bus voltage and its capacitor, respectively; I_{pv} and I_i are the output current of the PV array and the inverter input current, separately; ω is the angular frequency of the grid voltage provided by a Phase Locked Loop (PLL).

Therefrom and as $V_{gq} = 0$, the active and reactive powers at the point of common coupling can be determined by [16]:

$$P = \frac{1}{2} V_{gd} I_{od} \quad \text{and} \quad Q = -\frac{1}{2} V_{gd} I_{oq} \quad (2)$$

Obviously, the injected real and reactive power can be easily controlled using the output current components.

Based on the principle of energy conservation, while neglecting the losses through the inverter, and considering the external disturbances and the system uncertainties, the dynamic model (1) can be rewritten as follows:

$$\begin{cases} \frac{dI_{od}}{dt} = \frac{1}{L}(\omega LI_{oq} - RI_{od} + V_{od} - V_{gd}) + P_d \\ \frac{dI_{oq}}{dt} = \frac{1}{L}(-\omega LI_{od} - RI_{oq} + V_{od}) + P_q \\ \frac{dV_{dc}}{dt} = \frac{1}{C_{dc}}\left(I_{pv} - \frac{V_{gd}I_{od}}{2V_{dc}}\right) + P_{dc} \end{cases} \quad (3)$$

where P_d , P_q and P_{dc} describe the system uncertainties and external disturbances which their limits are assumed to be given, that are:

$$\begin{cases} |P_d| \leq \alpha_d \\ |P_q| \leq \alpha_q \\ |P_{dc}| \leq \alpha_{dc} \end{cases} \quad (4)$$

where α_d , α_q and α_{dc} are a positive constants and $|\cdot|$ is the operator of an absolute value.

3 VSI Control Using Sliding Mode Method

In short, the control system consists of two main loops which are the inner loop for current control and the outer loop for DC-bus voltage control. This last control loop aims at maintaining the inverter input voltage at the reference value and gives the reference direct current component, while the quadratic one is set to 0 in order to annul the reactive power consumption. Also, in a single-stage structure, the reference DC voltage can be given by a Maximum Power Point Tracker (MPPT) which is based, in this study, on the Perturb and Observe algorithm (P&O) for a maximum production of PV energy.

3.1 DC Side Control Design

So as to design the DC-bus voltage controller, we define the tracking error signal involving the desired variable $V_{dc\text{ref}}$:

$$e_{dc}(t) = V_{dc} - V_{dc\text{ref}} \quad (5)$$

The sliding surface is chosen as follows [15]:

$$S_{dc}(t) = e_{dc}(t) + \int_0^t K_{dc} e_{dc}(\tau) d\tau \quad (6)$$

where K_{dc} is a positive constant. Hence, the derivative of the sliding surface (6) using (3) is given as:

$$\frac{dS_{dc}}{dt} = \frac{1}{C_{dc}} \left(I_{pv} - \frac{V_{gd} I_{od}}{2V_{dc}} \right) + P_{dc} - \frac{dV_{dcref}}{dt} + K_{dc} e_{dc} \quad (7)$$

Considering the invariance condition and the nonlinear switching behavior around the sliding surface, the voltage controller can be designed as:

$$I_{odref} = \frac{2V_{dc} C_{dc}}{V_{gd}} \left[\frac{I_{pv}}{C_{dc}} - \frac{dV_{dcref}}{dt} + \alpha_{dc} \text{sgn}(S_{dc}) + K_{dc} e_{dc} \right] \quad (8)$$

$\text{Sgn}(\cdot)$ is the sign function, which is chosen in order to reduce the chattering phenomenon as [16]:

$$\text{Sgn}(S(t)) = S(t)/(|S(t)| + \varepsilon) \quad (9)$$

where ε is a small positive constant.

Theorem 1 *The asymptotic convergence of the DC-bus voltage V_{dc} to its reference V_{dcref} , is guaranteed when the dynamic sliding mode control law (8) is applied to the outer loop.*

Proof Considering the Lyapunov function defined as: $V_{dc} = 0.5(S_{dc})^2$.

By taking into account the assumption (4) and using (7, 8), the derivative of V_{dc} gives:

$$\begin{aligned} \dot{V}_{dc} &= S_{dc} \cdot \dot{S}_{dc} = S_{dc} \cdot \left[\frac{1}{C_{dc}} \left(I_{pv} - \frac{V_{gd} I_{odref}}{2V_{dc}} \right) + P_{dc} - \frac{dV_{dcref}}{dt} + K_{dc} e_{dc} \right] \\ &= -S_{dc} \cdot (\alpha_{dc} \text{sgn}(S_{dc}) - P_{dc}) \leq -(\alpha_{dc} - |P_{dc}|) |S_{dc}| \leq 0 \end{aligned} \quad (10)$$

According to the Lyapunov stability criteria, i.e. $\dot{S} \cdot S < 0$, the reaching condition of the sliding mode is achieved.

3.2 Grid Side Control Design:

In order to control the active and reactive powers, using Sliding mode control, the tracking error signals, including the reference variables I_{odref} and I_{oqref} are expressed as follows:

$$\begin{cases} e_d = I_{odref} - I_{od} \\ e_q = I_{oqref} - I_{oq} \end{cases} \quad (11)$$

Using the same sliding surface formula as before, the derivative of (11) using (3), can be written as:

$$\begin{cases} \frac{dS_d}{dt} = \frac{dI_{odref}}{dt} - \frac{1}{L}(\omega LI_{oq} - RI_{od} + V_{od} - V_{gd}) + P_d + K_d e_d \\ \frac{dS_q}{dt} = \frac{dI_{oqref}}{dt} - \frac{1}{L}(-\omega LI_{od} - RI_{oq} + V_{oq}) + P_q + K_q e_q \end{cases} \quad (12)$$

where K_d and K_q are a positive design constants. As done for the DC voltage controller, the control voltage laws, for the direct and quadratic current component tracking are expressed as follows:

$$\begin{cases} V_{odref} = V_{gd} + RI_{od} - L\omega I_{oq} + L\left(\alpha_d \text{sgn}(S_d) + K_d e_d + \frac{dI_{odref}}{dt}\right) \\ V_{oqref} = RI_{oq} + L\omega I_{od} + L\left(\alpha_q \text{sgn}(S_q) + K_q e_q + \frac{dI_{oqref}}{dt}\right) \end{cases} \quad (13)$$

Theorem 2 *The asymptotic convergence of the current components I_{od} and I_{oq} to their references I_{odref} and I_{oqref} , respectively, can be attained if the used control laws are given by (13).*

Proof: Considering the same Lyapunov function used previously ($V_{d,q} = 0.5(S_{d,q}^2)$), the differentiation for the two sliding surfaces based on (4, 12 and 13) can be written as follows:

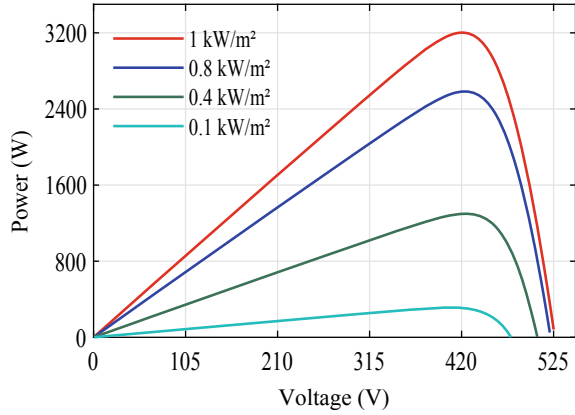
$$\begin{cases} \dot{V}_d = S_d \cdot \dot{S}_d = S_d \left[\frac{dI_{odref}}{dt} - \frac{1}{L}(\omega LI_{oq} - RI_{od} + V_{odref} - V_{gd}) + P_d + K_d e_d \right] \\ \qquad \qquad \qquad = -S_d \cdot (\alpha_d \text{sgn}(S_d) - P_d) \leq -(\alpha_d - |P_d|) |S_d| \leq 0 \\ \dot{V}_q = S_q \cdot \dot{S}_q = S_q \left[\frac{dI_{oqref}}{dt} - \frac{1}{L}(-\omega LI_{od} - RI_{oq} + V_{oqref}) + P_q + K_q e_q \right] \\ \qquad \qquad \qquad = -S_q \cdot (\alpha_q \text{sgn}(S_q) - P_q) \leq -(\alpha_q - |P_q|) |S_q| \leq 0 \end{cases} \quad (14)$$

Thus, the asymptotic convergence of the current components to their references is guaranteed. Therefore, the Sliding mode controller is globally asymptotically stable.

4 Results and Discussion

To evaluate the performance of the designed controller, a comparative simulation study has been performed between the conventional linear controller and the proposed SMC, by utilizing Matlab/Simulink software. Figure 2 shows the voltage power characteristic of the used PV array. In order to observe the system behavior in dynamic regime, the PV system receives a variable irradiance and temperature following the

Fig. 2 Used PV array voltage power characteristic at 25 °C



climatic conditions, as presented in Fig. 3. The system parameters are presented in Table 1.

A (*s*) and (*p*) subscripts are used in the figures showing the results, in order to distinguish the Sliding mode controller and the conventional PI controller, respectively. Figure 4 depicts the voltage and the current waveforms at the point of common coupling. It is clear that the injected current keeps its sinusoidal waveform even under

Fig. 3 Climatic variations applied to the system

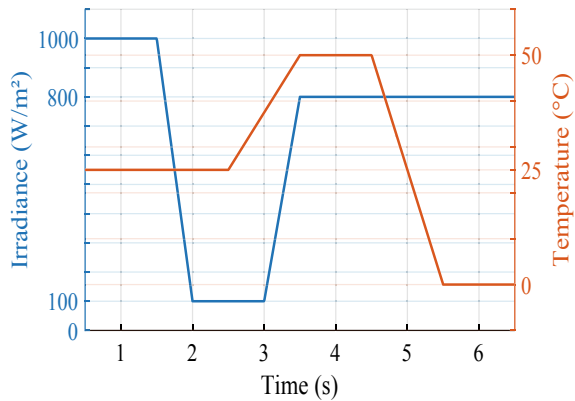


Table 1 Implementation parameters at STC

Parameters	Values	Parameters	Values
Nominal power of the PV array P	3.2 kW	Grid voltage (rms) V_g	220 V
Maximum power point voltage V_{dc}	420 V	Grid frequency f	50 Hz
DC-bus capacitance C_{dc}	3200 μ F	PWM switching frequency f_{swi}	10 kHz
Filter inductance L	30 mH	Tuning gains K_{dc}, K_d, K_q	25, 20, 50
Filter resistance R	2 m Ω	Switching gains $\alpha_{dc}, \alpha_d, \alpha_q$	8, 0.9, 2.3

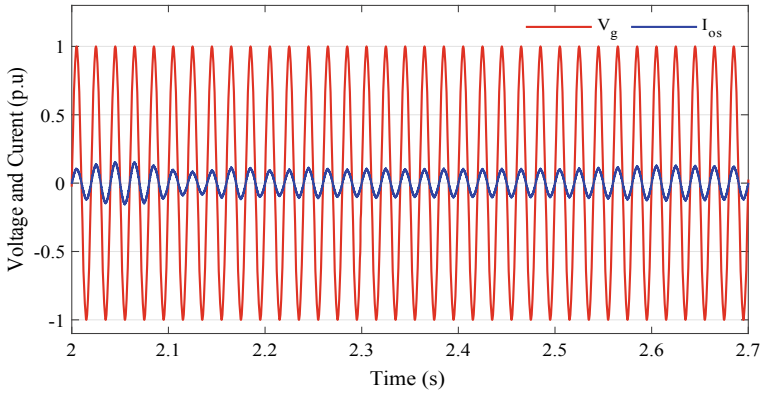


Fig. 4 Voltage and current at the point of common coupling using SMC

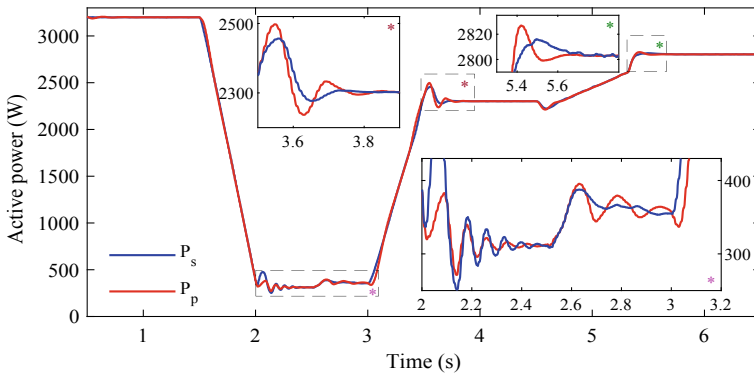


Fig. 5 Injected active power

low solar irradiance and it is in phase with the supply voltage. From Fig. 5, it can be noticed that the SMC presents a better dynamic performance in terms of error tracking and time response comparing with the PI controller, regarding the extracted active power injected into the grid. As it can be seen, also, in Fig. 6, SMC shows less disturbances around the reference value (0 Var), which proves that the power factor is unitary confirming the result shown in Fig. 4. In Fig. 7, it is shown that the DC-bus voltage tracks very well its reference given by the MPPT for both of the controllers in steady state, but during the transient regime, SMC presents lower dynamic error in comparison with the conventional PI controller.

In terms of harmonics, it can be easily observed from Figs. 8 and 9 that the proposed controller has the smallest values of injected current Total Harmonic Distortion (THD) during the applied weather scenario, and for different values of solar irradiance. Indeed, the SMC shows 3.49% of current THD compared to 3.59% given

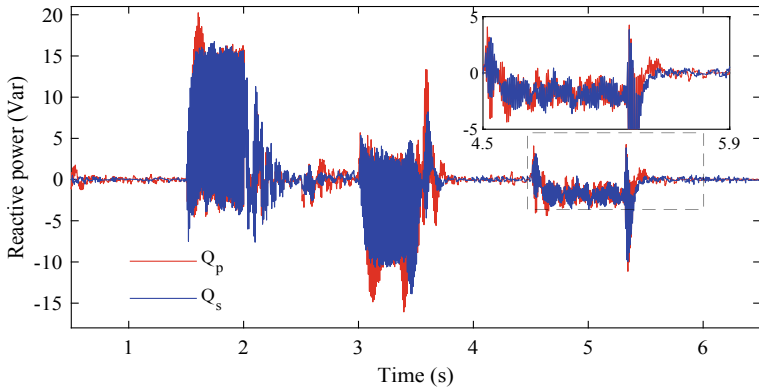


Fig. 6 Injected reactive power

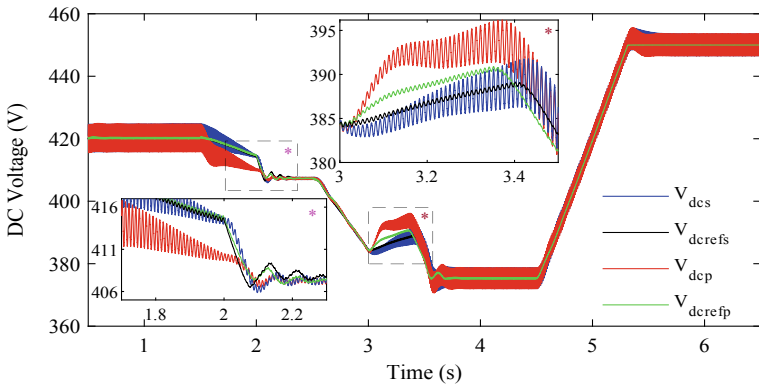


Fig. 7 DC-bus voltage

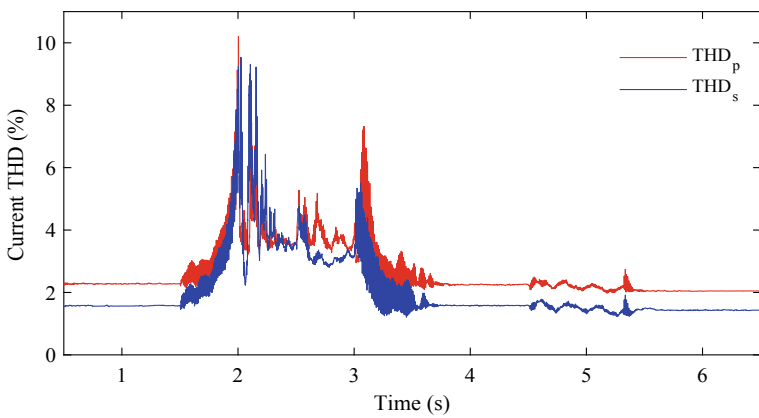


Fig. 8 Current THD during climatic condition variation

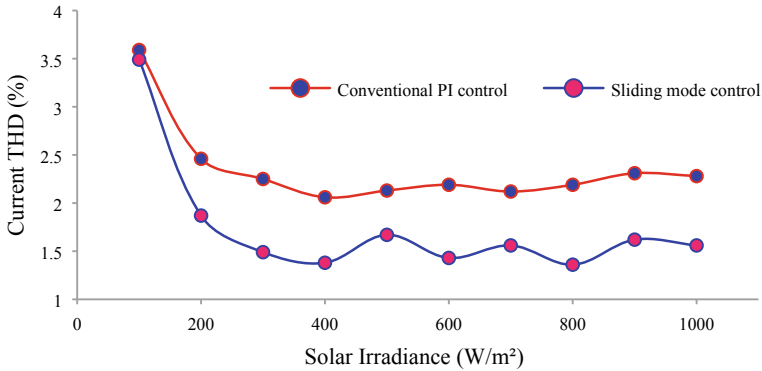


Fig. 9 Injected current THD for different solar irradiance

by the PI control for 100 W/m² of solar irradiance, which is lower than 5% imposed by the international standards [3].

5 Conclusion

In the present paper, a Sliding mode controller is designed for a transformer-less single stage single phase grid connected PV system. The key role of the proposed method is to overcome the sensitivity to the system operating point variation, when compared to the conventional controller. To this end, the mathematical modeling of the system DC and grid sides, has been developed taking into account perturbations and system uncertainties, which is concluded by the derivation of SM control laws using Lyapunov stability criteria.

The proposed SMC shows, through a comparative study, better dynamic performance and good reference tracking, especially in transient regime. Besides, the suggested controller enhances the power quality by reducing the injected current THD even under critical climatic conditions.

References

1. Jäger-Waldau A (2020) Snapshot of photovoltaics, Feb 2020. *Energies* 13(4):930
2. Goel S, Sharma R (2017) Performance evaluation of stand-alone, grid connected and hybrid renewable energy systems for rural application: A comparative review. *Renew Sustain Energy Rev* 78:1378–1389
3. Obi M, Bass R (2016) Trends and challenges of grid-connected photovoltaic systems: a review. *Renew Sustain Energy Rev* 58:1082–1094
4. Kerekes T, Teodorescu R, Rodríguez P, Vázquez G, Aldabas E (2011) A new high-efficiency single-phase transformerless PV inverter topology. *IEEE Trans Industr Electron* 58(1):184–191

5. Timbus A, Liserre M, Teodorescu R, Rodriguez P, Blaabjerg F (2009) Evaluation of current controllers for distributed power generation systems. *IEEE Trans Power Electron* 24(3):654–664
6. Monfared M, Golestan S (2012) Control strategies for single-phase grid integration of small-scale renewable energy sources: a review. *Renew Sustain Energy Rev* 16(7):4982–4993
7. Chigane K, Ouassaid M (2017) Enhancement of power quality for a transformerless single-phase grid-connected photovoltaic system using backstepping control approach. In: 3rd International conference on electrical and information technologies. IEEE, Rabat, Morocco
8. Kanti Roy T, Apel Mahmud M, Maung Than Oo A, Bansal R, Enamul Haque M (2018) Nonlinear adaptive backstepping controller design for three-phase grid-connected solar photovoltaic systems. *Electr Power Components Syst* 1–18
9. Chatterjee A, Mohanty K, Sagar Kommukuri V, Thakre K (2017) Design and experimental investigation of digital model predictive current controller for single phase grid integrated photovoltaic systems. *Renew Energy* 108:438–448
10. Hannana MA, Ghanib ZA, Mohameda A, Uddinc MN (2014) Real-time testing of a fuzzy logic controller based grid-connected photovoltaic inverter system. In: Industry Applications Society Annual Meeting (IAS). IEEE, Vancouver, BC, Canada
11. Chigane K, Ouassaid M (2018) Online control using ANN-PI controller for single stage transformerless grid Tied PV system. In: International symposium on advanced electrical and communication technologies (ISAECT). IEEE, Rabat, Morocco
12. Xingang F, Shuhui L (2015) Control of single-phase grid-connected converters with LCL filters using recurrent neural network and conventional control methods. *IEEE Trans Power Electron* 31(7):5354–5364
13. Kabalcı E (2020) Review on novel single-phase grid-connected solar inverters: circuits and control methods. *Solar Energy* 198:247–274
14. Chaoliang D, Xiangqian T, Weizhang S (2020) Sliding-mode control in dq-frame for a three-phase grid-connected inverter with LCL-filter. *J Franklin Institute*
15. Cortajarena JA, Barambones O, Alkorta P, Marcos JD (2017) Sliding mode control of grid-tied single-phase inverter in a photovoltaic MPPT application. *Sol Energy* 155:793–804
16. Chigane K, Ouassaid M (2017) Sliding mode control for a transformerless single-phase grid-connected photovoltaic system. In: 5th International renewable and sustainable energy conference (IRSEC). IEEE, Tangier, Morocco

Automatic Extraction of Photovoltaic Panels from UAV Imagery with Object-Based Image Analysis and Machine Learning



Imane Souffer, Mohamed Sghiouar, Imane Sebari, Yahya Zefri, Hicham Hajji, and Ghassane Aniba

Abstract We develop an automatic pipeline for photovoltaic panels extraction based on Object-Based Image Analysis (OBIA) and machine learning (ML). Automatic optimization of segmentation parameters, statistical and morphological feature engineering, and ML segment-based classification are the main building blocks of the proposed pipeline. Experimentation was conducted on a dataset comprising RGB and thermal orthomosaics generated from UAV data. An F-factor of 98.7% was scored with a recall rate above 98%. Obtained results were also compared to a developed solution under the software eCognition.

Keywords Photovoltaic · Panel · Extraction · UAV · OBIA · Image processing · Machine learning

1 Introduction

Renewable energy is emerging worldwide. Forecasting its development, actual green power capacity is expected to grow by about 50% in the horizon of 2024. Solar photovoltaic (PV) is one of the most promising technologies helping to move towards this goal. By the end of 2020, PV total generation capacity is predicted to surpass 800 GWp [1, 2]. PV installations require regular maintenance to guarantee panels optimal performance; the latter are permanently exposed to harsh environmental conditions making them subject to defects that diminish their lifespan [3]. Several techniques are used for panels inspection e.g. visual on field diagnosis, considered as the most traditional procedure; thermal infrared imagery via hand-held thermographs; and electrical-based techniques such as I-V characterization. Those techniques remain tedious and time-consuming for large-scale sites [4]. In this context, digital

I. Souffer · M. Sghiouar · I. Sebari (✉) · Y. Zefri · H. Hajji
Departement of Cartography and Photogrammetry, School of Geomatics and Surveying
Engineering (IAV Hassan II), 10101 Rabat, Morocco
e-mail: i.sebari@iav.ac.ma

G. Aniba
Mohammadia School of Engineers, Mohammed V University, 10090 Rabat, Morocco

image analysis shows up to be a promising alternative to automate inspection procedures; its efficiency has been proven particularly on large image datasets acquired by UAV [5]. The latter can deliver fast and cost-effective monitoring [6, 7]; it has been shown that their implementation can reduce the image acquisition time down to 5–8 min for a 1000 kWp site [8].

Although various works proposed workflows for automatic defects detection, they often conducted their studies on the whole image scene, which increases the processing time and false detections rate [9, 10]. Thus, for an accurate inspection, extracting panels and limiting the diagnosis on their surfaces show up to be essential steps in the process of defects detection. We develop in this work an automatic photovoltaic panels (PVP) extraction pipeline for UAV images, based on Object-Based Image Analysis (OBIA) and Machine Learning (ML). Its application on both RGB and thermal images yields fast and robust detection from various background scenes.

The paper is organized as follows: Sect. 2 presents related work to automatic PVP extraction from UAV images. Section 3 details the proposed methodology. In Sect. 4 we discuss the obtained results before concluding with future perspectives for the work's thematic.

2 Related Work

Several works tackled PVP extraction from UAV images. Zhang et al. [11] adopted an adaptive clustering algorithm based on k-means. After an automatic initialization of k values, the classification was performed using a four-dimensional vector comprising pixels RGB and texture values. However, the process scored a relatively high loss rate of 4.67%. Grimaccia et al. [12] proposed a color space transformation consisting in projecting the RGB orthomosaic on the HSV color space then applying a threshold to isolate PVP based on their color properties. However, the method is not fully automatic and requires manual intervention for the threshold determination.

Wang et al. [13] built a region-line primitive association framework (RLPAF) that models the topological relationship between two geographic primitives: a region primitive obtained from OBIA and a line primitive resulting from edge detection. Wang et al. [14] developed from the RLPAF a workflow to extract PVP where panels templates were automatically generated from geographic primitives. The matching was based on mutual fitting ratio and best-fitting template to recognize PVP. The technique performed a complete extraction but some irregularities remained and further contour adjustment was required. In addition, the process relied on a Supervised Segmentation Parameter Optimization (SSPO) that requires the user intervention.

Carletti et al. [15] used Canny edge detection and Hough transform to detect horizontal and vertical PVP lines, unwanted ones were filtered based on their angular coefficient before proceeding to final borders reconstruction. However, the method was applied only to thermal images. In the same framework, Deitsch et al. [16] established a thresholding method based on normalized image temperature variance.

However, the method was not experimented on enough data and also required manual intervention at multiple stages.

3 Methodology

Image objects are created then refined from the RGB image using a region-growing segmentation and an Unsupervised Segmentation Parameters Optimization (USPO). Various features are extracted object-wise to proceed either by a local training or an image-independent training for classification purposes. In the first, a portion of the image extracted segments is used to train a classifier; then the latter is applied on the whole image under test to extract PVP segments. In the second, the classifier knowledge is transferred from a training having been performed on other images. Afterwards, panels are extracted from the RGB and thermal image using the trained classifier. The algorithm performance is evaluated qualitatively, quantitatively then with respect to an OBIA workflow that we have parallelly developed under the software eCognition.

3.1 Proposed Approach

The extraction pipeline was developed using Python and R within the Grass GIS environment. Figure 1 depicts its key components.

Image Segmentation and Optimization. Before launching region-growing segmentation, an optimization procedure through USPO was applied; it consists of minimizing intra-objects variance and maximizing their homogeneity [17]. This was done by computing the normalized segment-weighted variance (WV) indicator and the Global Moran's I (MI). We chose the F-measure as an evaluation metric for the classification. The metric combines under and oversegmentation's precision and recall to compute the overall goodness (OG) [18]. The latter is calculated as follows:

$$OG_{F-function} = (1 + \alpha)^2 \frac{MI_{norm} \times WV_{norm}}{\alpha^2 \times MI_{norm} + WV_{norm}} \quad (1)$$

where α represents the relative weight between MI_{norm} and WV_{norm} . We adopted an $\alpha > 1$ in view of the individual panels object small dimensions.

The USPO was performed on the RGB, hue and intensity image layers. The optimal minsize and threshold values, required for running region-growing segmentation on Grass GIS, were automatically determined from the USPO approach.

Feature Extraction. After segmenting the RGB image, obtained segments were split into three sets: training, validation and test. Forty statistical and morphological

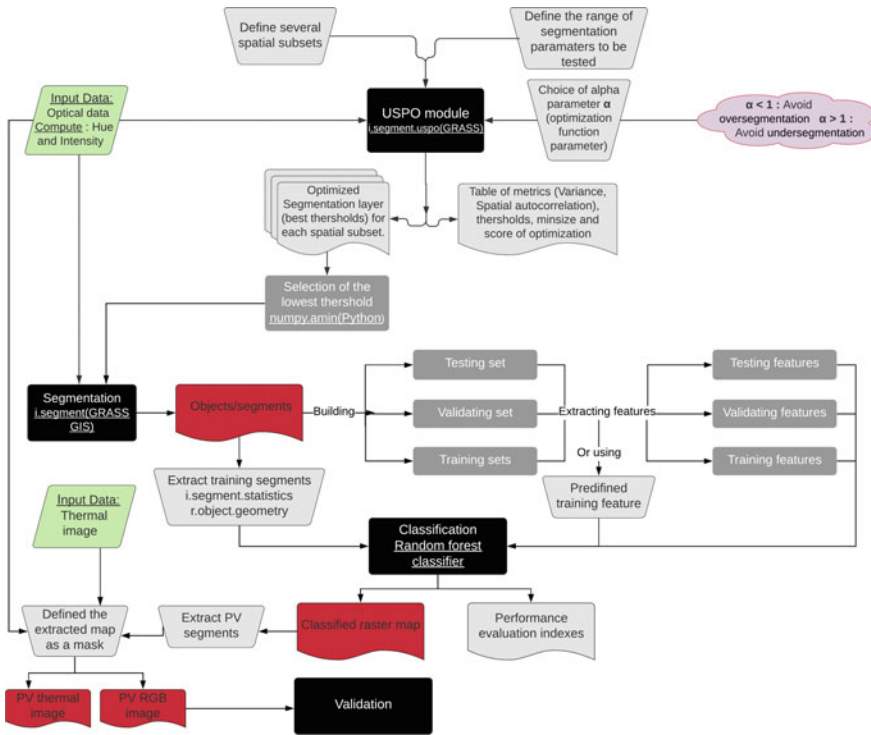


Fig. 1 The proposed extraction pipeline from RGB and thermal images

features (Table 1) were computed for each segment using “*i.segments.statistics*” and “*r.object.geometry*” modules [19].

Machine Learning Classification. Segments were labeled into three classes: “PVP”, “Non-PVP” and “Probable PVP” then fed to a Random Forests (RF) classifier. The latter’s performance was evaluated via a cross-validation procedure and using ground truth samples. Two training methods were tested: (1) A local training using images own training set; and (2) Using a global training set that doesn’t include the input image training segments. The resulting raster image was reclassified in the next step to keep only PVP objects. Finally, a mask was applied to remove non-PVP pixels from the original RGB ortho-image.

PV Extraction from Thermal Imagery. Several UAV models can embark RGB and thermal cameras at the same time. Image acquisition can be performed simultaneously and for each capture, an RGB plus its corresponding thermal image are saved. As a consequence, a panels mask having been extracted from a classified RGB orthomosaic can be utilized to extract panels from the thermal orthomosaic. If images were acquired separately, geo-referencing the obtained orthomosaics allows using the RGB mask for the same purpose.

Table 1 Segment-based computed features

Statistical features	Morphological features	Computation layers
Min	Area	Red
Max	Perimeter	Green
Sum	Compactness (with respect to a square)	Blue
Standard deviation	Compactness (with respect to a circle)	Hue
Variation coefficient	Fractal dimension calculated as follows: $2 * \log(\text{perimeter}) / \log(\text{area} + 0.001)$ (2)	

Quantitative Evaluation. For a quantitative evaluation, we measured the segmentation recall and precision then calculated the F-factor following the expressions below:

$$Recall = \frac{TP}{TP + FN} \quad (2)$$

$$Precision = \frac{TP}{TP + FP} \quad (3)$$

$$F\text{-Factor} = \frac{2 \times Recall \times Precision}{Recall + Precision} \quad (4)$$

3.2 PVP Extraction from RGB Imagery on eCognition

We compared the previous extraction pipeline with another one that we have developed under eCognition. The latter comprises three steps: (1) initial segmentation at a pixel level using a multi-resolution segmentation algorithm, (2) segments refining based on image objects characteristics, and (3) final objects classification through decision rules.

4 Experimental Implementation

Experiments were performed on UAV datasets then assessed quantitatively and qualitatively. We first present our experimental dataset and the obtained results.

4.1 Dataset

Table 2 presents the dataset underwent experimentation. IM5 and IM6 were generated from a flight where RGB and infrared thermal images were acquired simultaneously. Only complete panels were considered in the counting of PVP numbers.

4.2 Automatic Extraction

The established pipeline enabled automatic PVP extraction with an average accuracy of 99.1% and a 98.8% recall rate. Visual evaluation can be performed on Figs. 2 and

Table 2 Experimental dataset

Mission	Orthomosaic id	Image type	PVP number
Mission 1	IM1	RGB	956
	IM2		389
	IM3		816
	IM4		3404
Mission 2	IM5		4948
	IM6	Thermal	4948

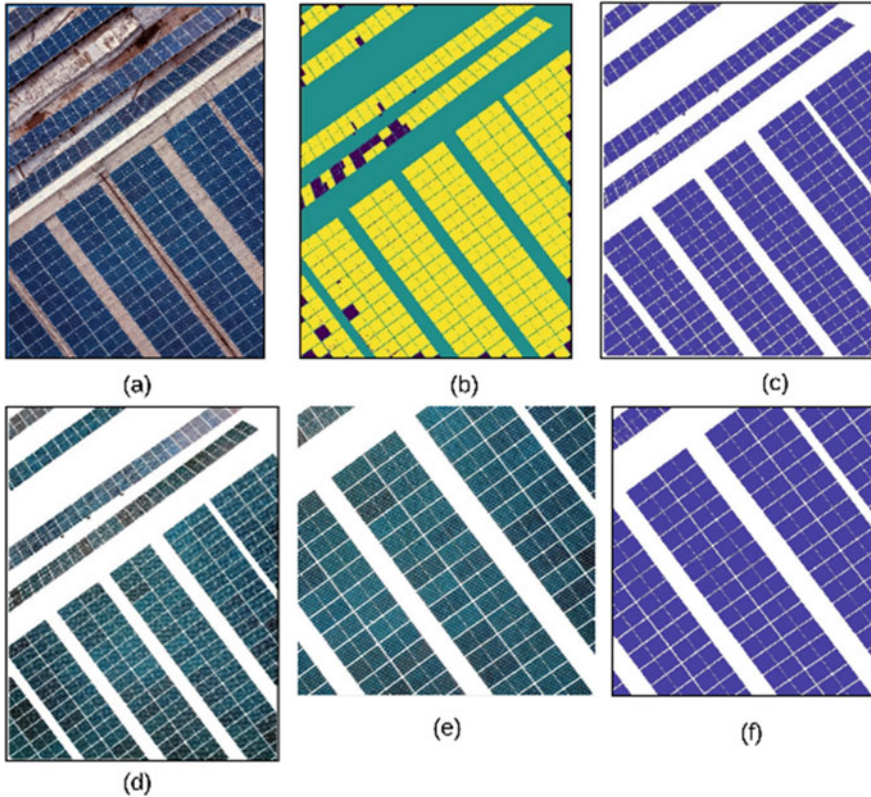


Fig. 2 Qualitative evaluation of the extraction quality. **a** The IM2 input orthomosaic; **b** classification results; **c** merged and recolored classes; **d** extracted RGB PVP; **e** extracted RGB panels (zoomed in); **f** PV class (zoomed in)

3. The USPO approach led to the creation of objects that match PVP surfaces; it also succeeded in creating smoothed edges conserving their geometry.

ML classification was evaluated through cross-validation where the RF classifier resamples 50 segments from the training, gives its prediction and generates a confusion matrix. The recall, precision and F-factor are presented in Table 4.

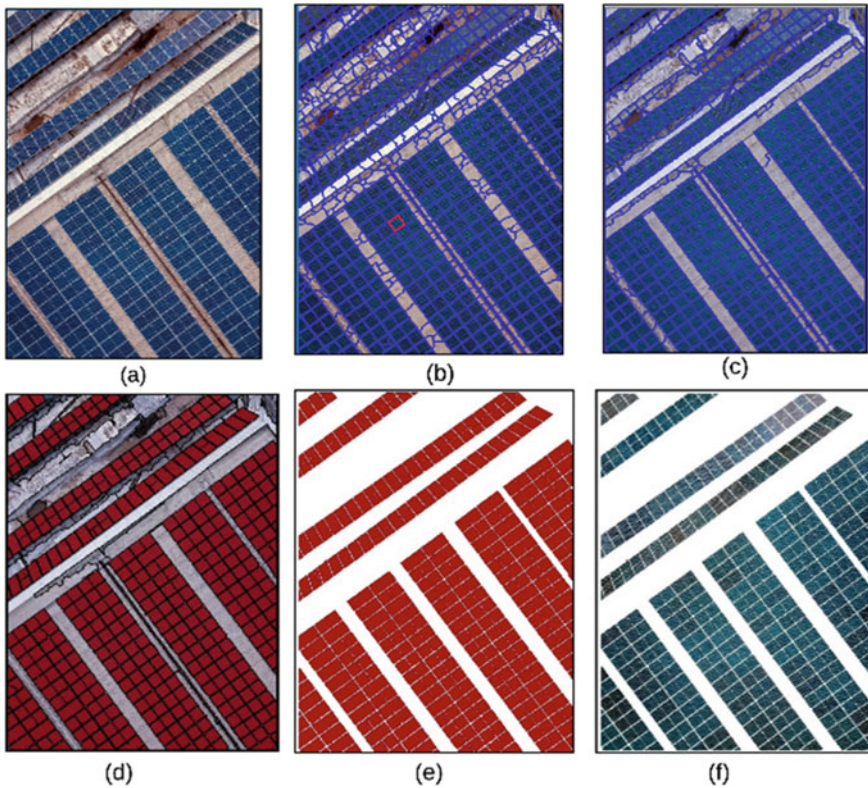


Fig. 3 RGB panels extraction based on the first approach under eCognition. **a** Original orthoimage. **b** Final multiresolution segmentation results. **c** Refined segments. **d** Classified segments: **e** Merging the two resulting classes. **f** Extracted RGB panels

Tables 3 and 4 show that local classification performs best; global classification also scores a high accuracy. This approach gathers PVP properties from other images in addition to the input one. It demonstrated that an uncorrelated image training set succeeded in reaching a complete extraction. Thus, using independent training for PVP classification remains more advantageous from a processing time point of view.

Table 3 RF accuracy rates

Orthomosaic id	Local approach (%)	Global approach (%)
IM1	97.9	97.1
IM2	94.8	97.8
IM3	98.3	97.1
IM4	96.5	96.9
IM5	98.5	97.2

Table 4 RF recall, precision and F-factor rates

Orthomosaicid	Local approach (%)			Global approach (%)		
	Recall	Precision	F-factor	Recall	Precision	F-factor
IM1	99.3	100	99.6	95.9	99.4	97.6
IM2	99.5	99.2	99.3	98.9	97.9	98.4
IM3	98.0	100.0	99.0	98	99.2	98.6
IM4	99.9	99.9	99.9	100	99.9	99.9
IM5	99.9	99.9	99.9	98.7	99	98.8

4.3 Comparison with eCognition

eCognition was able to extract PVP from heterogeneous orthomosaic scenes. However, the process quality depended on the supervision of conditioning thresholds. Figure 4 presents its classification steps applied on IM2.

Extracting PVP in eCognition was not seamless. Even if the Multiresolution segmentation algorithm creates iteratively smaller homogeneous objects from bigger

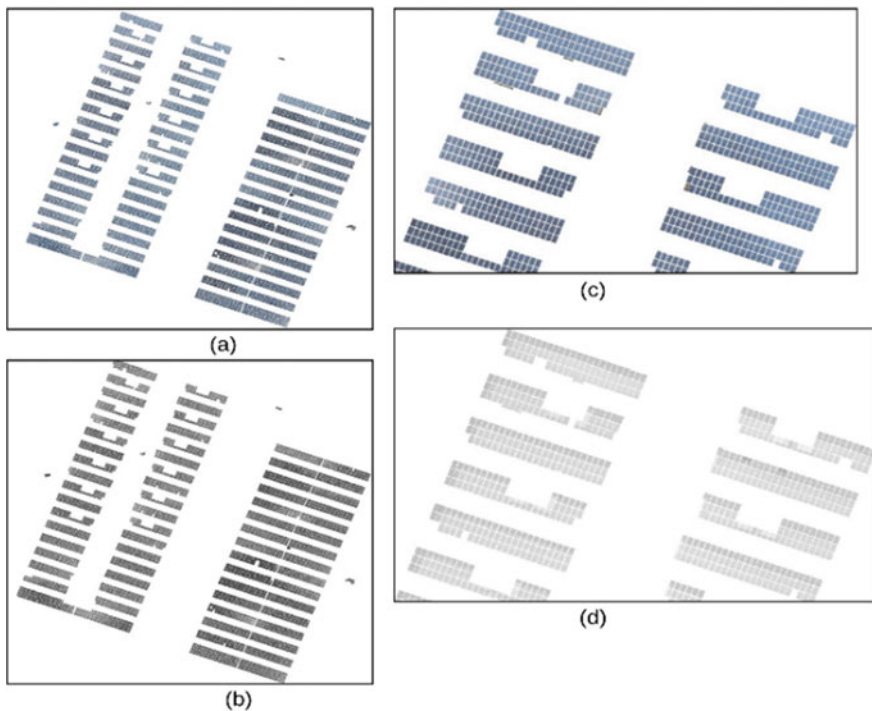


Fig. 4 Results of the eCognition classification applied on IM5. **a** Extracted RGB PVP; **b** extracted thermal PVP; **c** RGB extraction (zoomed in); **d** thermal extraction (zoomed in)

segments through shape and compactness factor weights [20], oversegmentation and undersegmentation errors persisted. They impacted the extracted edges and made the classification criteria not unified. Complete panels were all extracted successfully but incomplete ones were not. eCognition also took a longer time to perform the segmentation. On the other side, the USPO approach overcame those issues and yielded very good PVP objects. Even if it created larger amount of segments, it scored a higher PVP matching rate; in parallel, segments number did not overburden the processing steps.

The hue layer was an efficient discriminative parameter for the classification. Once included in calculating objects features, descriptors demonstrated high extraction accuracies. With adapting OBIA algorithms to PVP characteristics as proposed in Sect. 3, panels were extracted with an average precision rate equals to 99.7%, scored 99.7% for both the recall and the F-factor. On the other side eCognition process is supervised, time consuming, unique image-oriented and yields incomplete extraction.

5 Conclusion

We proposed in this work an automatic pipeline to extract robustly PVP from RGB and thermal images acquired by UAV, based on OBIA and ML. The process yielded high accuracy results where PVP borders were correctly extracted.

For future work, we recommend conducting in-depth tests within the OBIA-ML framework. We also suggest to experiment deep learning classifiers to test whether they will be able to enhance the obtained results. Collecting additional data to reinforce the classifiers generalization ability is also an important point to consider.

Acknowledgements The authors acknowledge the financial support from IRESEN: The Research Institute for Solar Energy and New Energies (Morocco) for the project SmartDrone4PV – Smart inspection of photovoltaic plants using aerial drone imaging.

References

1. Renewables, <https://www.iea.org/reports/renewables-2019>, last accessed 15/05/2020
2. Jäger-Waldau A (2019) A snapshot of photovoltaics. *Energies* 13:930. <https://doi.org/10.3390/en12050769>
3. Ferrara C, Philipp D (2012) Why do PV modules fail? *Energy Procedia* 15:379–387. <https://doi.org/10.1016/j.egypro.2012.02.046>
4. Balzategui J, Eciolaza L, Arana-Arexolaleiba N, Altube J, Aguerre J-P, Legarda-Ereño I, Apraiz A (2019) Semi-automatic quality inspection of solar cell based on convolutional neural networks. In: 2019 24th IEEE international conference on emerging technologies and factory automation (ETFA), Zaragoza, Spain, pp 529–535. <https://doi.org/10.1109/ETFA.2019.8869359>

5. Manoj Kumar N, Mahendran S, Jayaseelan V (2018) On the technologies empowering drones for intelligent monitoring of solar photovoltaic power plants. *Procedia Comput Sci* 133:585–593. <https://doi.org/10.1016/j.procs.2018.07.087>
6. Leva S, Aghaei M, Grimaccia F (2015) PV power plant inspection by UAS: Correlation between altitude and detection of defects on PV modules. In: 2015 IEEE 15th international conference on environment and electrical engineering, Rome, pp 1921–1926. <https://doi.org/10.1109/EEEIC.2015.7165466>
7. Zefri Y, ElKettani A, Sebari I, Ait Lamallam S (2018) Thermal infrared and visual inspection of photovoltaic installations by UAV photogrammetry-application case, Morocco, *Drones*, vol 2, p 41. <https://doi.org/10.3390/drones2040041>
8. Gallardo-Saavedra S, Hernández-Callejo L, Duque O (2018) Technological review of the instrumentation used in aerial thermographic inspection of photovoltaic plants. *Renew Sustain Energy Rev* 93:566–579. <https://doi.org/10.1016/j.rser.2018.05.027>
9. Lee DH, Park JH (2019) Developing inspection methodology of solar energy plants by thermal infrared sensor on board unmanned aerial vehicles. *Energies* 12:2928. <https://doi.org/10.3390/en12152928>
10. Tsanakas I, Ha L, Al Shakarchi F (2016) Advanced inspection of photovoltaic installations by aerial triangulation and terrestrial georeferencing of thermal/visual imagery. *Renew Energy* 102(PartA):224–233. <https://doi.org/10.1016/j.renene.2016.10.046>
11. Zhang D, Wu F, Li X, Luo X, Wang J, Yan W, Chen Z, Yang Q (2017) Aerial image analysis based on improved adaptive clustering for photovoltaic module inspection. In: International smart cities conference, ISC2 2017. <https://doi.org/10.1109/ISC2.2017.8090798>
12. Grimaccia F, Leva S, Niccolai A (2017) PV plant digital mapping for modules' defects detection by unmanned aerial vehicles. *IET Renew Power Gener* 11(10):1221–1228. <https://doi.org/10.1049/iet-rpg.2016.1041>
13. Wang M, Xing J, Wang J, Lü G (2017) Technical design and system implementation of region-line primitive association framework. *ISPRS J Photogramm Remote Sens* 130:202–216. <https://doi.org/10.1016/j.isprsjprs.2017.06.002>
14. Wang M, Cui Q, Sun Y, Wang Q (2018) Photovoltaic panel extraction from very high-resolution aerial imagery using region–line primitive association analysis and template matching. *ISPRS J Photogramm Remote Sens* 141. <https://doi.org/10.1016/j.isprsjprs.2018.04.010>
15. Carletti V, Greco A, Saggese A, Vento M (2019) An intelligent flying system for automatic detection of faults in photovoltaic plants. *J Amb Intell Humanized Comput*. <https://doi.org/10.1007/s12652-019-01212-6>
16. Deitsch S, Dalsass M, Winkler L, Wurzner T, Brabec C, Maier A, Gallwitz F (2016) Automatic detection and analysis of photovoltaic modules in aerial infrared imagery 1–9
17. Grippa T, Lennert M, Beaumont B, Vanhuyse S, Stephenne N, Wolff E (2017) An open-source semi-automated processing chain for urban object-based classification. *Remote Sens* 9:358. <https://doi.org/10.3390/rs9040358>
18. Grybas H, Melendy L, Congalton RG (2017) A comparison of unsupervised segmentation parameter optimization approaches using moderate- and high-resolution imagery. *GISci Remote Sens* 54(4):515–533. <https://doi.org/10.1080/15481603.2017.1287238>
19. GRASS GIS—Documentation. <https://grass.osgeo.org/documentation/>. Last Accessed 30/06/2020
20. eCognition Suite Documentation. <https://docs.ecognition.com/v9.5.0/Page%20collection/eCognition%20Suite%20Documentation.htm?tocpath=Documentation%20eCognition%20Suite%7C0>, Last Accessed 30/06/2020

Development of a Management Algorithm for a Compact Photovoltaic—Wind Turbine System



Yahya Lahlou, Abdelghani Hajji, and Mohammed Aggour

Abstract The exploitation of renewable energies despite their availability in domestic scale remains very insufficient. This is mainly due to three reasons. The first one is about the problem of intermittent power generation by solar and wind energy. The second problem is the high cost of traditional solar and wind installations. In addition, the third problem is the large space occupied by these systems. To help solve these problems and optimize the production of electricity and the space occupied, we proposed a compact system with flexible photovoltaic (PV) solar panels that automatically takes the shape of wind turbine blades named Savonius. This coupling ensures two modes of ecological production of green energy namely PV mode and wind turbine mode where these two technologies compensate to partially overcome the problem of intermittent and also save space. This is a new idea in the literature, unlike conventional hybrid systems which include wind turbines and PV solar panels separately. The proposed system is based on a management algorithm developed in MATLAB/Simulink and modeled with “Stateflow” which allows changing between the solar wind modes according of meteorological values.

Keywords PV mode · Wind turbine mode · Savonius · Compact system · Management algorithm · Stateflow · Autonomous system

1 Introduction

Today, it is necessary to choose alternative and renewable energy sources which contribute to the reduction of pollution of our planet, the exploitation of renewable energy technologies in particular solar and wind energy can be seen as a promising solution for producing clean electricity. Also, the growing demand for energy is considered one of the most critical problems of the twenty first century.

Y. Lahlou (✉) · M. Aggour
Ibn Tofail University of Kenitra, B.P. 133, 14000 Kenitra, Morocco
e-mail: yahya.lahlou@uit.ac.ma

A. Hajji
Mohammed V University of Rabat, Ibn Sina Avenue, B.P. 765, Agdal, Rabat, Morocco

Furthermore, the lack of exploitation of these two renewable energy sources when using these two intermittent solar PV and wind energy separately having unfavorable effects on the planet in the long term, thus a significant investment cost per compared to their energy yields still limited [1]. Photovoltaic panels generate electrical energy in a variable manner over time depending on availability of sunlight and the wind turbines generate variable electric energy depending of changes of wind speed [2]. These two energies sources have intermittences during the day, which requires the use of storage capacity to avoid power cuts during unfavorable conditions.

Wind and solar energy are the most studied by researchers in renewable energy. Among these recent studies exist in the literature, a hybrid PV-wind battery system which has been proposed on a laboratory scale for energy management with experimental results on the control system proposed by the authors [3]. A second study on a system composed of photovoltaic (PV) modules, wind turbines and biomass, so is mathematically modeled for energy management with the analysis of parameters such as installation and maintenance costs [4]. A third proposed study of energy management for a hybrid photovoltaic/wind system, designed for powering household loads where the authors tested and compared performance with two different strategies [5]. In another study, a hybrid model composed of a photovoltaic system, a wind turbine and a 6-kW battery were designed, modeled and executed using the MATLAB/Simulink program [6]. In the same context, a prototype of a dual-powered solar PV/wind system was proposed with analyzes simulations and experiments. Nature is intermittent but the wind and solar energy sources are often complementary [7]. In another research, the authors proposed to optimize the size of photovoltaic/wind systems with different combinations in low voltage residential distribution lines [8]. The installation of the hybrid system composed of a vertical axis wind turbine/photovoltaic solar panels have been explained in detail in Refs. [9, 10]. In addition, Ref. [11] also presents a hybrid system with an optimization of a 160 W street lamp. Another study on the integration of a vertical axis wind turbine, a photovoltaic panel, a battery and a microcontroller were carried out experimentally for a highway application [12]. And in addition, the design of a hybrid system contains a vertical axis wind turbine and a PV panel, so the data flows given are observed using the Arduino board presented in Ref. [13]. In order to overcome the problems of PV modules operating in high temperatures and at low wind energy in a hybrid system, different fans have been experimentally tested in Ref. [14]. Finally, a technical-economic analysis of a hybrid system proposed in regions far from city centers was carried out using HOMER software [15]. Thus, another technical-economic analysis was carried out for a hybrid system using the genetic algorithm [16].

The main objective of this work is the study of a proposed management algorithm for a compact 2 in 1 system which combines two renewable energy technologies, flexible PV with the vertical axis wind turbine Savonius. This proposed hybrid energy system partially solves the problem of intermittent energy and optimizes the space occupied. The management algorithm is developed in MATLAB/Simulink with “Stateflow” application which has made it possible to have state transition diagrams for an autonomous operation of the system with respect to climate change, the system

determines the production mode electric (Photovoltaic—wind) most profitable on a reduced surface compared to conventional hybrid systems.

2 Theoretical Study

2.1 Photovoltaic Systems

Photovoltaic solar energy (PV) is the main source of clean energy used in buildings that directly converts sunlight into electricity. These systems have a major limitation, compared to the output power which is directly dependent on sunlight, we can loss about 10–25% if no tracking system is used, because at the beginning and the end of the day the solar field will not be directly facing the sun’s rays [17]. Solar PV has specific advantages as an energy source: once installed, its operation generates no pollution and no emission of greenhouse gases, knowing that silicon is widely available in the earth’s crust [18].

The solar PV cell can be represented by a current source (I_g) in parallel with a diode, plus the internal resistance of the cell modeled by a shunt resistor (R_{sh}) in parallel and a connection resistance modeled by a series resistor (R_{sr}). The I_g current varies depending on the level of solar radiation to which the solar panel is exposed. The current passing through the diode (I_d) [2]. The equivalent circuit model of solar PV cell:

$$I = I_g - I_d - I_{sh} \tag{1}$$

where I_{sh} is the parallel branch current and I_d is the diode current. The current obtained from Eq. (1) is shown in Eq. (2).

$$I = I_g - I_0 \left[\exp\left(\frac{V + IR_{sr}}{nkT_c/q}\right) - 1 \right] - \left(\frac{V + IR_{sr}}{R_{sh}}\right) \tag{2}$$

I_g represents the solar radiation current in Eq. (3) and is a function of solar radiation at cell temperature:

$$I_g = I_{scR} \frac{G}{G_r} [1 + \alpha_T (T_c - T_{cR})] \tag{3}$$

The current I_0 is the saturation current in Eq. (4) and is called a function of the cell temperature:

$$I_0 = I_{0R} \left(\frac{T_c}{T_{cR}}\right) \exp\left(\frac{1}{T_{cR}} - \frac{1}{T_c}\right) \frac{qe_g}{n_k} \tag{4}$$

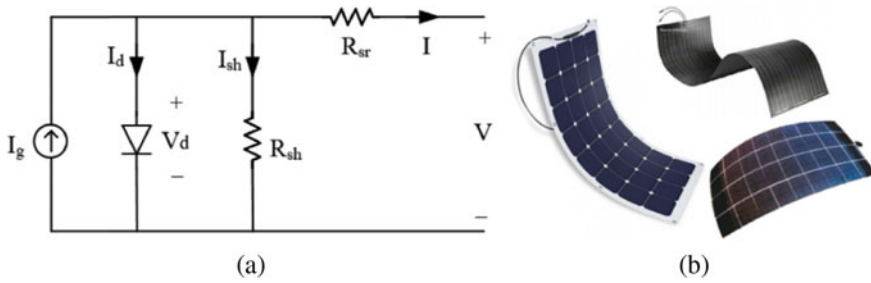


Fig. 1 a Solar PV cell equivalent circuit. b Flexible solar PV panel [2]

The flexible photovoltaic solar modules are very light and very thin (2–3 mm) compared to rigid modules [19]. They can be flexed from 30° to 248° [20, 21], allowing the module to be installed on curved surfaces and other uses. The average conversion efficiency of flexible modules varies from 15 to 25% [22–24]. High-efficiency solar modules are very useful when operating space is limited and large capacity PV systems must also be installed to satisfy a need (Fig. 1).

2.2 Savonius Wind Turbine

The wind turbines can produce electrical energy when this device capture the kinetic energy of the wind. Wind energy has become a major producer of electrical energy from renewable sources. Today, many countries in the world depend on this source to produce a part of their energy needs. Vertical axis wind turbines (VAWT) are classified according to their different in very low wind speed, reliability, etc.

The specific speed of wind turbine λ or Tip speed ratio (TSR) is defined as the ratio between the rotational speed of the rotor ωr and the actual wind speed ϑ by the following equation:

$$\lambda = \frac{\omega r}{\vartheta} = TSR \tag{5}$$

The aerodynamic efficiency of the turbine is expressed by the power coefficient C_p and the moment coefficient C_m , thus the torque applied along the surface of the rotor, these performance parameters of the Savonius turbine are estimated according of the TSR by the following two equations [25]:

- The power coefficient:

$$C_p = \frac{P_{turbine}}{P_{wind}} = \frac{T \omega}{\frac{1}{2} \rho A_S \vartheta^3} = TSR \cdot C_m \tag{6}$$

- The moment coefficient:

$$C_m = \frac{T}{\frac{1}{2} \rho A_S R \vartheta^2} \tag{7}$$

- ϑ : wind speed
- T: mechanical torque
- P_{turbine} : Mechanical power of the turbine
- A_S : surface encountered for the Savonius blades
- H: the height and $d = R/2$ the diameter (Fig. 2).

We note that typical Savonius turbines have a low power coefficient with typical maximum values around 0.15–0.25 [27, 28]. Commercial wind turbines currently have a power coefficient C_p of 0.35–0.45 [29] for large wind turbines with a horizontal axis.

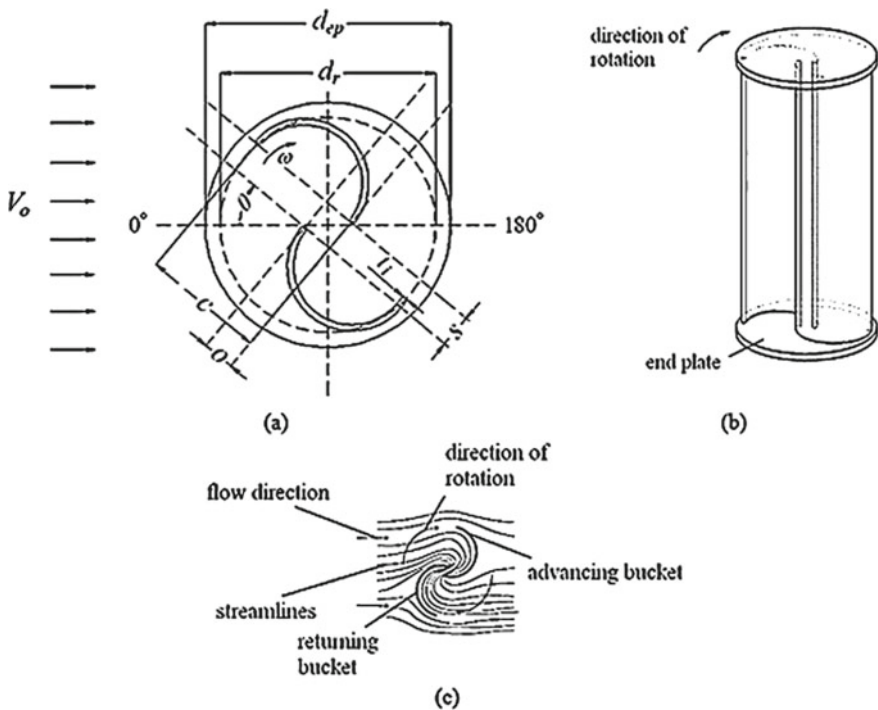


Fig. 2 Schematic representations of a Savonius rotor: **a** 2D representation; **b** 3D representation; **c** wind flow on the rotor [26]

3 Management Algorithm for the Compact System

3.1 Principle of the System Studies

Since traditional photovoltaic and wind systems occupy a large area and do not produce enough electric power due to intermittency, we suggest combining solar and wind power by creating a compact self-contained device that works intelligently to produce more and clean electricity and request just a small area. Figure 3 shows the general principle.

The studied system allows an ecological production of green energy over time, according to the input parameters of the sunshine and wind speed sensors, the compact system will choose and automatically transforms into two production modes: Photovoltaic (PV) mode or wind turbine (WT) mode, using a mechanism controlled by the embedded electronic and artificial intelligence. So, this system can improve electrical production and also reducing the space occupied compared to existing systems, see Fig. 4 which shows and describes a diagram of the system suggested in two modes.

The mechanism switch between PV and WT modes and can ensure PV mode when the system takes the tilted shape with flexible PV panel extension to collect maximum solar radiations. To switch to WT mode, the mechanism must first ensure a vertical shape for the system and then apply a curvature for the flexible PV panels to have the blades of the Savonius wind turbine and continue electricity production.

The system will be equipped at least with one battery mainly used for its self-operation and will also be useful for the continuity of the electrical supply when the transformation from one mode to another for a period of 10 seconds.

This system can keep a high efficiency due to the cleaning and cooling naturally of these photovoltaic blades during its rotary and its dynamic operation. The investment cost of this system is competitive since the majority of equipment are shared in between two modes photovoltaic—wind turbine, such that the two flexible solar modules have two roles when they are planar and inclined they will produce electricity in PV mode, and when these modules are bent and vertical they will produce

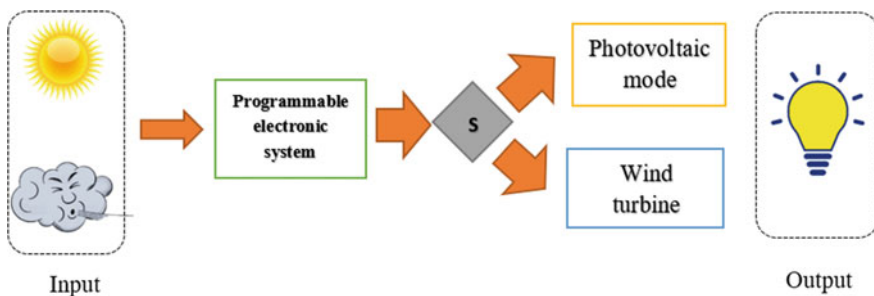


Fig. 3 Operating principle of the autonomous system in two modes

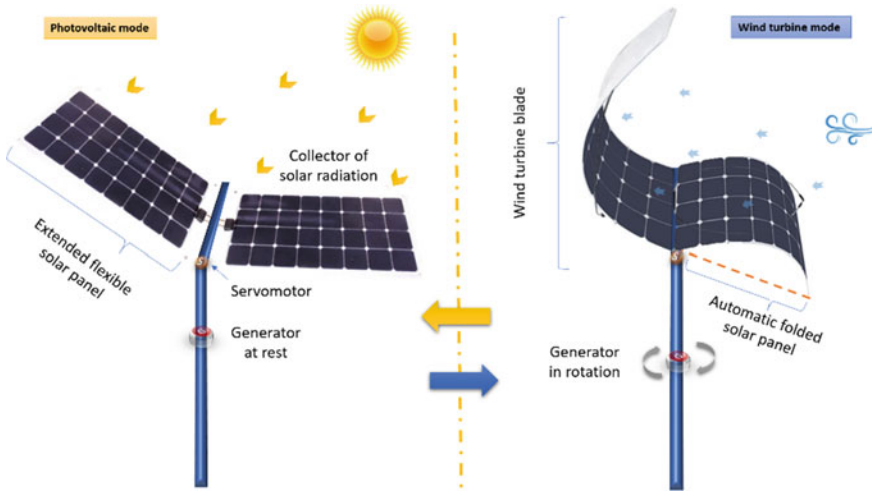


Fig. 4 The idea of the system studied in both photovoltaic and wind modes

electricity in wind turbine mode, also the support of the flexible modules is itself the mast of the wind turbine.

3.2 The Results of the Operating Algorithm

We proposed and modeled the operation of our compact system for one day by using the graphic language “Stateflow” in MATLAB/Simulink. It contains state transition diagrams, flow charts, state transition and truth tables [30]. That allows to trace the operating states of the system according to the solar radiation and the wind speed generated for 24 hours. During the day the system can pass from one mode to another depending on the metrological conditions. It goes into PV mode if the day is sunny or into Savonius wind mode if the day is rather windy. But in the night, the system will be always in Savonius wind turbine mode. When both wind and sun weather conditions are propitious, the system automatically chooses the mode that will produce the maximum power. The system can use the embedded electronic and artificial intelligence to ensure the autonomy of its operation and optimize electrical production (Figs. 5 and 6).

The algorithms depend on the variation of the input signals of solar radiation and wind speed that provide the behavior of our system, so the program checked the valid conditions to trace the states of the system according to the profile of the solar radiation and the wind speed assumed during four separate days in the year (see the results of simulation in Fig. 6).

Figure 6 presents the algorithm results with four different climatic condition inputs of solar radiation and wind speed selected for this study which allows to obtain

Fig. 5 Algorithm of different operating modes for the system studied

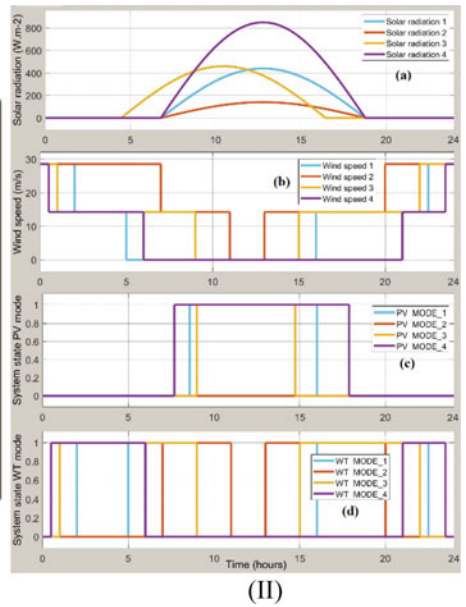
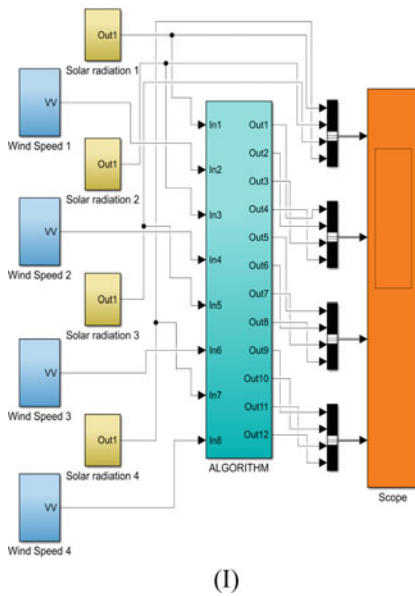
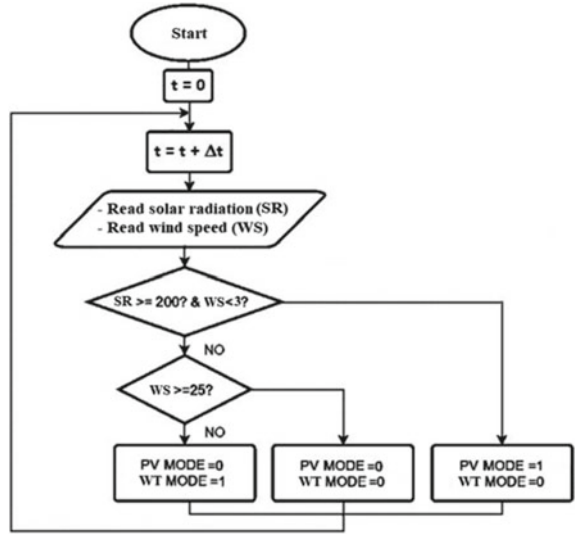


Fig. 6 I Representation of the algorithm realized in Simulink/MATLAB software. **II** Algorithm results of the study compact system in 24-h

four scenarios of system state for the PV or WT mode of our compact system. We represented the inputs climatic situations for the four days without fluctuations and mechanical constraints in order to simplify the algorithm results. Figure 6a, b show the daily evolution of global solar radiation and wind speed associated profile we have plotted for the four different days, in this case the day in purple color is clear with a low wind speed. The color blue and yellow present almost the same climatic conditions with slightly offset changes. The color orange shows a windy day with low solar radiation. While Fig. 6c, d show the states of PV and WT mode operating for different colors respectively. So, the behavior of the system studied at the beginning and at the end of the day is in rest mode because the wind speed exceeds the safety limit which is around 25 m/s. When the wind speed decreases to the nominal value, the system switches to wind turbine mode all night long. When the solar radiation reaches a considerable value of 200 W/m^2 or more and the wind speed becomes less than 5 m/s. The system goes into PV mode. When the solar radiation and the wind speed are at the same time very important in this case the priority mode is programmed to switch into wind turbine mode because this mode can produce more electricity. So, the interaction of the algorithm with the different inputs shows that the algorithm works well.

4 Conclusion

In this work we have suggested an operating algorithm which is one part among others of the global work for an innovative 2-in-1 ecological solution that contributes to protect the environment, optimize the space occupied and to maintain the high efficiency of these photovoltaic blades. The system uses a transformable mechanism, most of the equipment of this system are shared in the two photovoltaic—wind turbine modes power, so it enables two different technologies to be used with a competitive investment cost.

The algorithm developed has a major interest is to make our compact system self-functional with different situation. It makes it possible to determine the most consistent mode of production in different scenarios which will be chosen after analysis of the input climatic data. It describes the operating states as a function of the solar radiation and the wind speed generated during the 24 hours.

The realization of a prototype in pilot scale will be a good continuation of this work to demonstrate the operation of the compact system in PV and wind turbine modes according to the case adopted.

References

1. Ibrahim AMA, Noureldeen O (2018) Performance analysis of grid connected PV/wind hybrid power system during variations of environmental conditions and load. *Int J Renew Energy Res*

- (IJRER) 8(1):208–220
2. Demirdelen T, Ekinci F, Mert BD, Karasu İ, Tümay M (2020) Green touch for hydrogen production via alkaline electrolysis: the semi-flexible PV panels mounted wind turbine design, production and performance analysis. *Int J Hydrog Energy* 45(18):10680–10695. <https://doi.org/10.1016/j.ijhydene.2020.02.007>
 3. Merabet A, Tawfique Ahmed K, Ibrahim H, Beguenane R, Ghias AMYM (2017) Energy management and control system for laboratory scale microgrid based wind-PV-battery. *IEEE Trans Sustain Energy* 8(1):145–154. <https://doi.org/10.1109/TSTE.2016.2587828>
 4. Sichilalu S, Tazvinga H, Xia X (2016) Optimal control of a fuel cell/wind/PV/grid hybrid system with thermal heat pump load. *Sol Energy* 135:59–69. <https://doi.org/10.1016/j.solener.2016.05.028>
 5. Stroe D-I, Zaharof A, Iov F (2018) Power and energy management with battery storage for a hybrid residential PV-wind system—a case study for Denmark. *Energy Proc* 155:464–477. <https://doi.org/10.1016/j.egypro.2018.11.033>
 6. Chaib A, Achour D, Kesraoui M (2016) Control of a solar PV/wind hybrid energy system. *Energy Proc* 95:89–97. <https://doi.org/10.1016/j.egypro.2016.09.028>
 7. Wandhare RG, Agarwal V (2015) Novel integration of a PV-wind energy system with enhanced efficiency. *IEEE Trans Power Electron* 30(7):3638–3649. <https://doi.org/10.1109/TPEL.2014.2345766>
 8. Behraves V, Akbari Foroud A, Keypour R (2018) Optimal sizing methodology for photovoltaic and wind hybrid rooftop generation systems in residential low voltage distribution networks. *Sol Energy* 173:17–33. <https://doi.org/10.1016/j.solener.2018.07.054>
 9. Vignesh J, Christopher AS, Albert T, Pravin Tamil Selvan C, Sunil J (2020) Design and fabrication of vertical axis wind mill with solar system. *Mater Today Proc* 21:10–14 <https://doi.org/10.1016/j.matpr.2019.05.296>
 10. Prashanth BN, Pramod R, Kumar GBV (2018) Design and development of hybrid wind and solar energy system for power generation. *Mater Today Proc* 5(5, Part 2):11415–11422. <https://doi.org/10.1016/j.matpr.2018.02.109>
 11. Nyemba WR, Chinguwa S, Mushanguri I, Mbohwa C (2019) Optimization of the design and manufacture of a solar-wind hybrid street light. *Proc Manuf* 35:285–290. <https://doi.org/10.1016/j.promfg.2019.05.041>
 12. Bavchakar A, Chougale PKN, Belanekar SS, Rane SP, Sawant NB (2018) A hybrid model of vertical axis wind turbine-solar power generation for highway and domestic application. In: 2018 international conference on computation of power, energy, information and communication (ICCPEIC), Mar 2018, pp 135–139. <https://doi.org/10.1109/ICCPEIC.2018.8525152>
 13. Shyu L-S, Lee C-H, Lu K-Y, Horng C-T (2018) Independent wind-solar hybrid generation system for construction and verification in campus. In: 2018 1st international cognitive cities conference (IC3), Aug 2018, pp 174–178. <https://doi.org/10.1109/IC3.2018.00-34>
 14. Wang Y, Ni C, Shi Y, Huang Q, Hu Y, Cui Y (2018) Experimental study on a modified wind-solar hybrid system. *Trans Tianjin Univ* 24(1):59–65. <https://doi.org/10.1007/s12209-017-0105-7>
 15. Elsayed I, Nassar I, Mostafa F (2017) Optimization and economic evaluation of small scale hybrid solar/wind power for remote areas in Egypt. In: 2017 nineteenth international middle east power systems conference (MEPCON), Dec 2017, pp 25–30. <https://doi.org/10.1109/MEPCON.2017.8301158>
 16. Shadmand MB, Balog RS (2014) Multi-objective optimization and design of photovoltaic-wind hybrid system for community smart DC microgrid. *IEEE Trans Smart Grid* 5(5):2635–2643. <https://doi.org/10.1109/TSG.2014.2315043>
 17. Awasthi A et al (2020) Review on sun tracking technology in solar PV system. *Energy Rep* 6:392–405. <https://doi.org/10.1016/j.egypr.2020.02.004>
 18. Piano SL, Mayumi K (2017) Toward an integrated assessment of the performance of photovoltaic power stations for electricity generation. *Appl Energy* 186:167–174
 19. Gagliano A, Tina GM, Nocera F, Grasso AD, Aneli S (2019) Description and performance analysis of a flexible photovoltaic/thermal (PV/T) solar system. *Renew Energy* 137:144–156. <https://doi.org/10.1016/j.renene.2018.04.057>

20. 160-Watt 12 Volt flexible monocrystalline solar panel. Renogy United States. <https://store-fhncx.mybigcommerce.com/content/RNG-175DB-H/RNG-175DB-H-Datasheet.pdf>. Last accessed 03 July 2020
21. Duan X, Huang Z, Liu C, Yang J, Tan L, Chen Y (2019) A bendable nickel oxide interfacial layer via polydopamine crosslinking for flexible perovskite solar cells. *Chem Commun* 55(25):3666–3669. <https://doi.org/10.1039/C9CC00479C>
22. «Most efficient solar panels 2020—clean energy reviews». <https://www.cleanenergyreviews.info/blog/most-efficient-solar-panels>. Last accessed 3 Nov 2020
23. Wang C et al (2020) Efficiency improvement of flexible Sb_2Se_3 solar cells with non-toxic buffer layer via interface engineering. *Nano Energy* 71:104577. <https://doi.org/10.1016/j.nanoen.2020.104577>
24. Reinhard P et al (2012) Review of progress toward 20% efficiency flexible CIGS solar cells and manufacturing issues of solar modules. In: 2012 IEEE 38th photovoltaic specialists conference (PVSC), part 2, pp 1–9. <https://doi.org/10.1109/PVSC-Vol2.2012.6656789>
25. Meziane M, Essadiqi E, Faqir M, Ghanameh MF (2019) CFD study of unsteady flow through Savonius wind turbine clusters. *Int J Renew Energy Res (IJRER)* 9(2):657–666
26. Akwa JV, Vielmo HA, Petry AP (2012) A review on the performance of Savonius wind turbines. *Renew Sustain Energy Rev* 16(5):3054–3064. <https://doi.org/10.1016/j.rser.2012.02.056>
27. Ramar SK, Premkumar TM, Seralathan S, Hariram V (2018) Numerical analysis of different blade shapes of a Savonius style vertical axis wind turbine. *Int J Renew Energy Res (IJRER)* 8(3):1657–1666
28. Hariyanto R, Soeparman S, Widhiyanuriyawan D, Sasongko MN (2016) Experimental study on improvement the performance of Savonius Windmill with ventilated blade. *Int J Renew Energy Res (IJRER)* 6(4):1403–1409
29. Hariyanto R, Soeparman S, Widhiyanuriyawan D, Sasongko MN (2016) Analysis the vortex effect on the performance of Savonius windmill based on CFD simulation and video recording. *Int J Renew Energy Res IJRER* 6(3):1015–1021
30. Stateflow—model and simulate decision logic using state machines and flow charts © 1994–2020. The MathWorks, Inc. <https://www.mathworks.com/products/stateflow.html>. Last accessed 17 Mar 2020

Impact of Solar Gain on Energy Consumption and Thermal Comfort



Abdelghani Hajji, Yahya Lahlou, and Ahmed Abbou

Abstract Energy consumption in the residential and tertiary sectors is particularly high in developed countries. There is great potential for energy savings in these sectors. Among the techniques that reduce the energy consumption of a building in the winter, we have the orientation. Optimal exposure ensures thermal and visual comfort with a minimum of energy consumption. We will begin this work with a simulation that shows the effect of solar gain in winter on a room with four supposed orientations: South, East, West and North. Equations which show solar contribution as well as factors influencing it have been developed. Then, we will conduct an experimental comparison between two equivalent rooms with different orientations. For each room, we will measure the temperature, relative humidity and energy consumption of its heat pump. The obtained results show that a south orientation saves up to 8.5% of heating energy, ensures good natural lighting and reduces considerably the relative humidity in the room. Concerning the room facing north, we propose a practical solution which will contribute to the heat pump consumption reduction by exploiting the solar gain and improve natural lighting.

Keywords Thermal comfort · Solar gain · Bedroom · Orientation · Temperature and humidity sensor · Heat pump

1 Introduction

Buildings are responsible for about 25–40% of greenhouse gas emissions, which are the main determinant of climate change [1]. The energy consumption of a building can go up to 40% of the total energy consumption, especially in developed countries [2].

A. Hajji (✉) · A. Abbou
Mohammed V University of Rabat, EMI, Ibn Sina Avenue, B.P. 765, Agdal, Rabat, Morocco
e-mail: hajjiprepa15@gmail.com

Y. Lahlou
Faculty of Sciences, Ibn Tofail University of Kenitra, Kenitra, Morocco

This finding emphasizes the need to minimize the energy consumed to heat a building. In order to achieve this aim, several solutions are available such as the integration of renewable energies [3, 4], the envelope insulation [5, 6], the use of specific building materials [7, 8], the improvement of thermal inertia [7, 9], the optimization of the window sizes [3] and, why not, the building orientation.

The study by Vasaturo [1] shows that the building orientation has an impact on the energy demand for heating that varies between -5.2% and $+3.2\%$ [1].

Similarly, Destais [10] shows that North orientation of houses has an impact on their heating consumption, which increases between 7 and 8% [10].

In the same context, the results of Louafi [11] show that taking into account the orientation criterion allows the building to participate in a more efficient thermal and energy design [11]. This conclusion is confirmed thanks to the work of Merabtime [12].

Finally, Morel et al. [13] argue that solar gains can provide a significant portion of the heating needs in buildings from 10 to 50% [13].

Our study shows that a south-facing orientation saves up to 8.5% of heating energy, provides good natural lighting and considerably reduces the relative humidity in the building. This work is divided into three parts:

- Simulation part: we show that there is a very important difference for the total solar flux reaching a chamber according to its orientation. The solar flux simulation is done by Matlab/Simulink during 24 h in winter.
- Experimental part: a comparative experimental study is carried out between two chambers, showing the effect of solar gain on the energy consumed by the heat pump and the thermal comfort (temperature, relative humidity).
- Proposed solution: a solution is proposed for the underprivileged chamber in order to make both chambers equivalent in terms of solar gain.

2 Presentation of the Studied Building

The studied building is located in the town of Mehdia, in Morocco. It is 54 km away from Rabat, the capital city, and 2 km from the sea. The geographic position of our case study building is given by latitude 34.249241° and longitude -6.656567° [14].

Average annual temperatures range from 17°C (January) to 28°C (August). In winter, the minimum temperature can reach $T_{min} = 7^\circ\text{C}$, but in summer, temperatures are moderate and air conditioning is rarely used [15].

Both studied rooms are located in the building above (Fig. 1).

Table 1 gives the dimensions of both studied rooms.

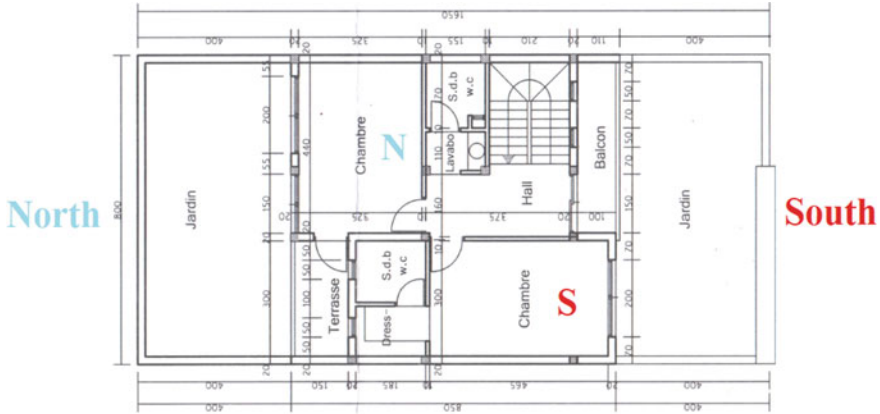


Fig. 1 First floor of the studied building. Original data from this study

Table 1 Room dimensions. Values determined from Fig. 1

Bedrooms	Room S	Room N
Area (m ²)	14.3	14.0
Height (m)	2.61	2.66
Volume (m ³)	37.3	37.2

3 Simulation of Solar Gain

3.1 Simulation

To calculate the solar illumination, we propose the following flowchart (Fig. 2).

The solar gain of a building depends on:

- the site where the building is located;
- its orientation;
- its receiving surfaces;
- the shading [16].

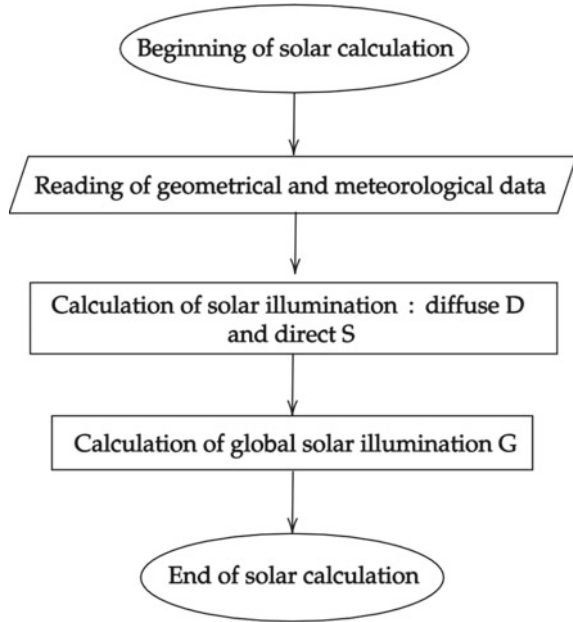
The total solar flux received by the room is given by the following equations [12]:

$$\dot{Q}_{tot} = \dot{Q}_{dir} + \dot{Q}_{dif} + \dot{Q}_{abs} \tag{1}$$

$$\begin{aligned} \dot{Q}_{tot} = & \alpha_{fe} \cdot A_{fe} \cdot G + \tau_{dir} \cdot A_v \cdot S + \tau_{dif} \cdot A_v \cdot D + \alpha_v \cdot A_v \cdot G + \alpha_{dir} \cdot \dot{Q}_{dir} \\ & + \frac{A_{ap}}{A_{tot} - A_{pv}} \cdot \dot{Q}_{dif} + \frac{A_{fi}}{A_{tot}} \left[\dot{Q}_{dif} + (1 - \alpha_{pl}) \cdot \dot{Q}_{dir} \right] \end{aligned} \tag{2}$$

\dot{Q}_{fe} Solar flux absorbed by the outside surface

Fig. 2 Calculation of solar illuminations S, D and G (Date December 17, 2019). Schema of this study



- \dot{Q}_{dir} Direct solar flux transmitted through the glass
- \dot{Q}_{dif} Diffuse solar flux transmitted by the glass
- \dot{Q}_{abs} Solar flux absorbed by the glass
- \dot{Q}_{pl} Solar flux reaching the floor
- \dot{Q}_{fi} The solar flux received by the interior faces
- τ_{dir} Transmission coefficient of direct solar flux
- τ_{dif} Transmission coefficient of diffus solar flux
- A_{fe} Face surface
- G Global solar illumination
- S Direct solar illumination
- D Diffus solar illumination
- A_v Glass surface
- α_v Glass absorption coefficient
- α_{fe} Absorption coefficient of the face.

On the other hand, the cumulative solar flux $C(t)$ is given by the following relation:

$$C(t_i) = C(t_{i-1}) + \dot{Q}_{tot}(t_i) \tag{3}$$

To make the simulation, we will take the room S and assume it in the four orientations (South, East, West and North) without shading.

In the same way as the washing machine, we modelled all electric charges and we obtained the following schema (Fig. 3).

Table 2 groups together the parameters used in the simulation.

Fig. 3 Room in the four situations. Diagram of this study

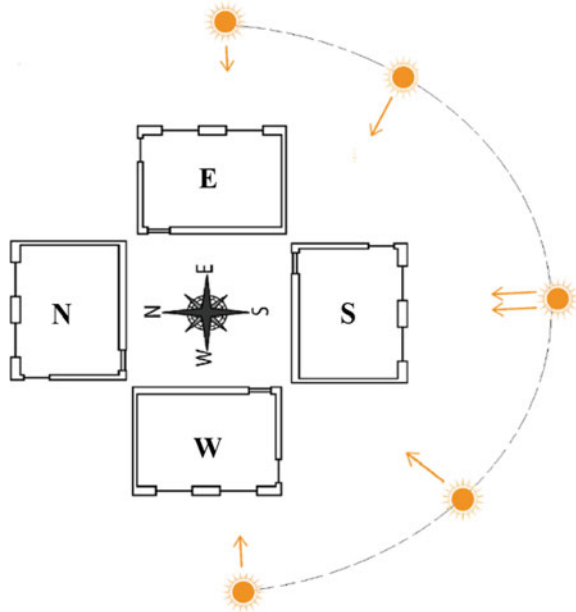


Table 2 Simulation parameters

Bedrooms	Room S	Room N
Absorption coefficient of the face α_{fe}	0.7	[16]
Surface of the face A_{fe} (m ²)	11.5	This study
Transmission coefficient of direct solar flux τ_{dir}	0.86	[12]
transmission coefficient of the diffuse solar flux τ_{dif}	0.77	[12]
Glass surface A_v (m ²)	3	This study
Glass absorption coefficient α_v	0.06	[12]
Floor absorption coefficient α_{pl}	0.7	[17]

3.2 Results and Discussion

When we use the above equations and the parameters of Table 2 then run a simulation on MATLAB /Simulink, we find the following results (Fig. 4).

According to the simulation results, the south orientation is very favored compared to the north in terms of solar gain. We note that the solar flux accumulated on the south face is 5 times greater than that in the north.

The east and west orientations are comparable in terms of solar gain and their solar gain curves are out of phase. It should be noted that only part of the cumulative solar flux will be restored overnight.

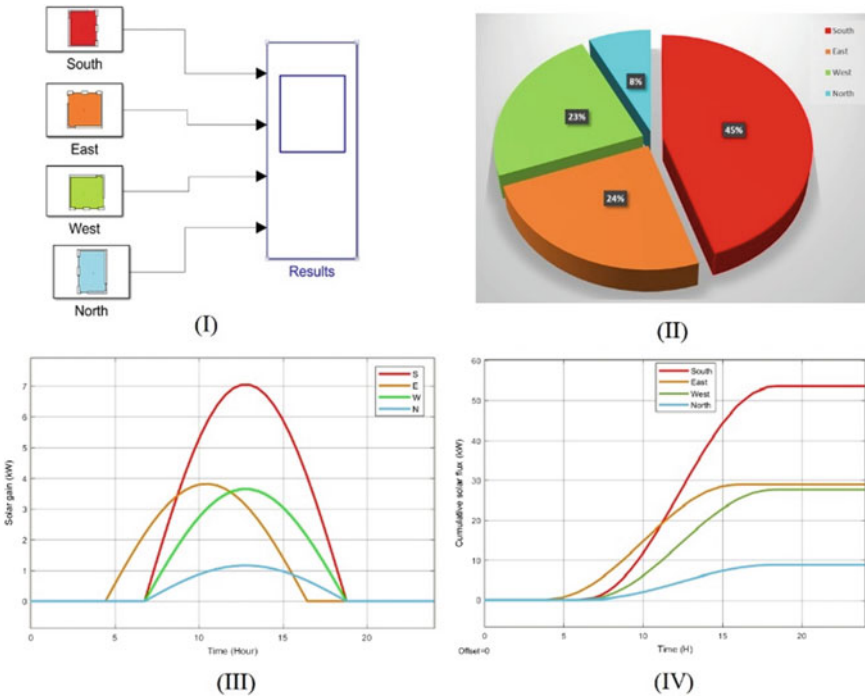


Fig. 4 I Simulation of solar gain in the studied room. II Comparison of the cumulative solar flux for the 4 orientations. III Evolution of solar gain for the 4 orientations for 24 h (17 Dec 2019) IV Evolution of the cumulative solar flux for the 4 orientations. Results of this study

We will confirm these simulation results using an experimental study. And we will show that solar gains reduce the energy requirements for heating in winter. These free contributions, which are favorable in winter, obviously become a charge in summer when using air conditioning.

4 Experimental Study

4.1 Equipment

The material used during this work is as follows:

- Two 9000 BTU heat pumps: both bedrooms are heated by heat pumps.
- Three DHT 22 sensors: measurement of temperature and relative humidity ($\pm 0.5\text{ }^\circ\text{C}$ and $\pm 5\%$).
- Arduino board: link with sensors and computer.
- Computer: data recording.

- Two Joule meters: measurement of the energy consumed by the heat pump (± 10 Wh).

4.2 Method

Date and time of the experience: December 17, 2019 at 7:00 p.m.

Duration of the experience: 90 min.

The initial conditions:

$$T_s = 17^\circ\text{C} \quad T_n = 15.6^\circ\text{C} \quad \text{and} \quad T_{out} = 15.1^\circ\text{C}$$

$$\Phi_s = 88\% \quad \Phi_n = 90\% \quad \text{and} \quad \Phi_{out} = 91\%$$

Hypotheses:

- Temperature is uniform in both rooms.
- Relative humidity is uniform in both rooms.
- The heat losses are the same for both rooms.

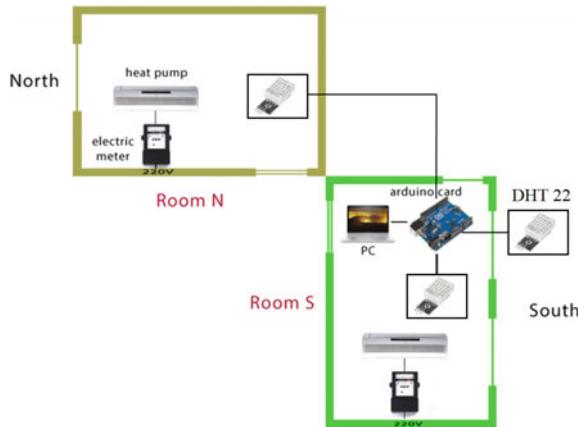
We carried out the following assembly (Fig. 5).

The measurements were recorded in the night of December 17, 2019, simultaneously in two separate rooms. They are of equivalent size but have different orientations. The first one is oriented to the south and the second one to the north.

The first DHT 22 sensor, capable of measuring ambient temperature and relative humidity, is placed in the middle of chamber S and a second one in the middle of chamber N. The third sensor will be placed outside, away from the wall.

The 3 sensors are connected via the Arduino board. Then the results are displayed on the computer.

Fig. 5 Experimental set-up of this study



According to the thermal building regulations in Morocco, the minimum comfort temperature in winter is 20 °C [18], but to have a clear difference between both rooms, we set both heat pumps at a temperature of 28 °C.

4.3 Results and Discussion

Figure 6a represents the ambient temperatures T_s and T_n of rooms S and N and the outside temperature.

Figure 6b represents the relative humidity Φ_s and Φ_n of rooms S and N and the external humidity Φ_{out} .

Figure 6c represents the consumed energies E_s and E_n of rooms S and N.

In the south-facing room (S), the initial temperature is slightly higher than in the north-facing one thanks to the solar gain during the day and the relative humidity is initially lower. In addition, we note that the temperature in room S quickly reaches the set temperature (28 °C) thanks to the solar gain and the low amount of humidity.

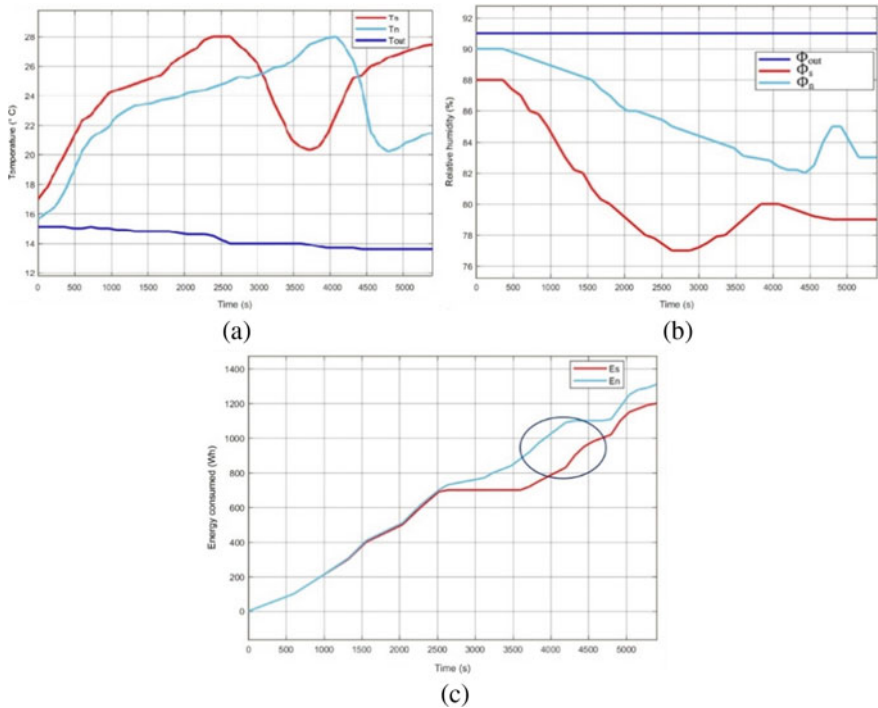


Fig. 6 a Temperatures evolution. b Relative humidity evolution. c Evolution of the energies consumed by the heat pumps



Fig. 7 North bedroom before and after opening the window. Photo of the ceiling of the studied room

The heat pump in room N arrives late at the set temperature (28 °C). That is why it uses more electrical energy. A south orientation is, therefore, very favored compared to a north one. It is confirmed that optimal exposure can reduce the heating bill by up to 8.5%! In addition, to optimize heating energy, south orientation improves natural lighting and reduces the need for artificial lighting.

5 Proposed Solution

To make the north-facing room balanced compared to the south room in terms of solar gain, we suggest the following solution: adding an opening window in the roof of the room oriented to the north (Fig. 7).

To make both rooms equivalent in terms of solar gain level, it is necessary that:

$$A = A_{\text{OPTIMAL}} \quad (4)$$

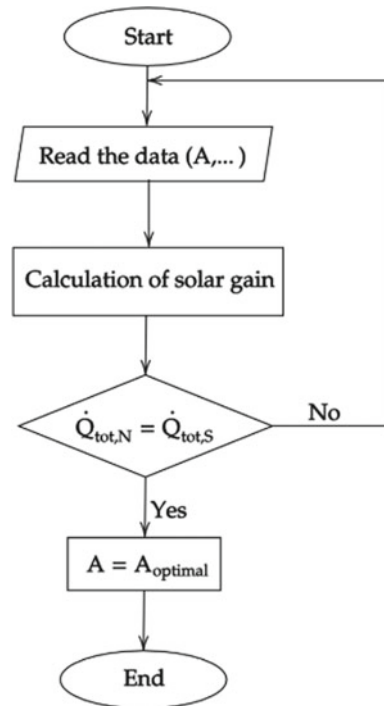
Here is the flowchart which allows to calculate the optimal size of the opening (Fig. 8).

The calculation of the solar gain is based on geometric data (A...) and solar data (G...). If the solar gain of chamber N coincides with that of chamber S, the program will display the optimal size of the window, otherwise it will start the calculation again.

6 Conclusion

The obtained experimental results show that a south orientation saves up to 8.5% of heating energy, ensures good natural lighting and reduces significantly the relative humidity in the room. The simulation results show that the solar flux accumulated

Fig. 8 Flowchart to calculate the optimal opening size. Algorithm proposed in this study



on the south face is 5 times greater than in the North. But only a part of this energy will be reused overnight.

The experimental and the simulation results are compatible with each other. Therefore, before building a house or buying an apartment, you have to take into account its orientation, the window sizes, the shading.... The living areas such as the living-room and the kitchen will preferably be situated in the south and the openings should also be oriented to the south with a design that facilitates passive solar collection in winter.

For the north-facing room (room N), we suggest to install a window on the roof which will allow to collect a free solar contribution so as to ensure thermal and visual comfort like in room S.

Perspectives

Thermal modeling of rooms N and S using Matlab/Simulink, and validation of the experimental results of this study.

References

1. Vasaturo R (2018) Impact of passive climate adaptation measures and building orientation on the energy demand of a detached lightweight semi-portable building. *Build Simul* 11(6):1163–1177
2. Pérez-Lombard L (2008) A review on buildings energy consumption information. *Energy Build* 40(3):394–398
3. Zainine MA (2016) Energetic and economic impact of using bioclimatic design technics. *Int J Renew Energy Res (IJRER)* 6(3):787–794
4. Chwieduk D (1996) Analysis of utilisation of renewable energies as heat sources for heat pumps in building sector in Poland. *Renew Energy* 9(1):720–723
5. Kim J, Moon JW (2009) Impact of insulation on building energy consumption. In: 11th international IBPSA conference, p 7
6. Simona P (2017) Increasing the energy efficiency of buildings by thermal insulation. *Energy Proc* 128:393–399
7. Reim R (2017) Correlation between energy efficiency in buildings and comfort of the users. *Energy Proc* 122:457–462
8. Benoudjafer I (2012) Etude comparative relative à l'efficacité énergétique de deux appartements situés à Béchar, Algérie. *Rev Energ Renouvelables* 1(12):1–12
9. Chahwane L (2011) Valorisation de l'inertie thermique pour la performance énergétique des bâtiments. Thèse Dr., no. Université de Grenoble, p 223
10. Destais G (2017) Variables explicatives de la consommation de chauffage dans l'habitat: les leçons de l'analyse d'une copropriété sur données journalières. *Dév Durable Territ Économ Géogr Polit Droit Soc* 8(2)
11. Louafi SB (2011) Impact de l'orientation sur le confort thermique interieur dans l'habitation collective. *Sci Technol Sci Terre* 33–40
12. Merabtime A (2012) Modélisation Bond graphs en vue de l'Efficacité Énergétique du Bâtiment. Ph.D. thesis. Université de Lorraine
13. Morel N, Gnansounou E (2008) Énergétique du Bâtiment. [studylibfr.com. https://studylibfr.com/doc/4042055/energetique-du-batiment](https://studylibfr.com/doc/4042055/energetique-du-batiment). Last accessed 17 Apr 2020
14. Google Maps (2020) <https://www.google.com/maps/@34.2505874,-6.6531225,15z>. Last accessed 17 Apr 2020
15. Mehdiya: Climat, Températureset Météo, <https://www.partir.com/Maroc/Mehdiya/2542768/quand-partir.html>. Last accessed 25 Apr 2020
16. Elamin M (2014) Contribution à l'évaluation énergétique des bâtiments au nord du Maroc: Cas de la ville de Tanger. Thèse. Université Abdelmalek Essaadi, Maroc
17. Vincet M (2018) Comportement thermique des matériaux, 2nd edn. Hachette, France
18. ADEREE (2014) Règlement thermique de Construction au Maroc (RTCM). Maroc. ISSN 0851-1217

A Model-Based Predictive Control Approach for Home Energy Management Systems. First Results



Antonio Ruano, Hamid Qassemi, Inoussa Habou Laouali, Manal Marzouq, Hakim El Fadili, and Saad Bennani Dosse

Abstract The use of renewable energies in buildings are a needed solution to decrease the overall energy consumption. In countries such as Portugal and Morocco, this is translated in the use of Photovoltaic systems, and, hopefully, Energy storage systems. This paper presents a simplified Model-Based Predictive Control (MBPC) approach for a Home Energy Management System of a residence in the region of Algarve, Portugal. Simulation results show that MBPC achieves considerable savings in the use of electricity obtained from the grid, as well as economic savings.

Keywords Home energy management systems · Model-based predictive control · Branch and bound algorithm · PV systems · Energy storage

1 Introduction

The building sector worldwide accounts for 40% of the total consumption [1]. Home energy management system (HEMS) and hybrid energy sources systems are the solution to reduce electricity bills [2]. To obtain further savings in electricity usage and economic costs, the control of energy flow between different electricity sources must be done efficiently. Recently, those systems started to use computational intelligence and machine learning techniques [3], as well as to establish an efficient communication between all appliances, which gives consumers and HEMS the ability to

A. Ruano · H. Qassemi (✉) · I. Habou Laouali
Faculty of Science and Technology, University of Algarve, 8005-294 Faro, Portugal
e-mail: hamid.qassemi@usmba.ac.ma

A. Ruano
IDMEC, Instituto Superior Técnico, Universidade de Lisboa, 1049-001 Lisboa, Portugal

H. Qassemi · M. Marzouq · H. E. Fadili
Laboratory of Computing and Interdisciplinary Physics (LIPI), Sidi Mohamed Ben Abdellah University, B.P. 5206, Bensouda, 30003, B.P. 2202, Route Immouzzar, 30003, Fez, Morocco

I. Habou Laouali · S. B. Dosse
Laboratory of Intelligent Systems, Geo-Resources and Renewable Energy (SIGER), Faculty of Sciences and Technologies, Sidi Mohamed Ben Abdellah University, Fez, Morocco

automatically control these appliances [4]. An efficient HEMS also allows to reduce the peak load, and to guarantee good home comfort [5].

One of the most important functions of smart grids is Demand Side Management (DSM) [6]. DSM techniques are used in the residential sector to shape the demand load, giving users the possibility to make decisions about managing and scheduling the energy flow between different power sources. These operations can be performed efficiently, automatically and adaptably. In [7], authors presented a survey on different hybrid microgrid architecture including optimization techniques, control strategy, simulation and results.

One of the most promising techniques for HEMS and occupant's comfort is Model Based Predictive Control (MBPC). MBPC is an optimization technique which has been applied in several different applications. For instance, in [8, 9] MBPC has been used for HVAC control, minimizing the energy spent while maintaining thermal comfort. The authors of [10] employed MBPC to implement different demand techniques.

This work employees MBPC, implemented with the Branch and Bound (BaB) algorithm, to control the flow of energy in a real household in the region of Algarve, in the south of Portugal.

The organization of the paper is as follows: Sect. 2 presents the description of our hybrid system. Energy obtained and injected to the grid are shown in Sect. 3. Section 4 describes the proposed power flow control strategy; Simulation results are presented in section V and conclusions and future works are given in Sect. 6.

2 System Description

As shown in Fig. 1, the HEMS system is composed of three energy sources: the main grid, the photovoltaic system (PV) and the storage system. The grid connection is bidirectional, which gives us the ability to inject excess energy to the grid.

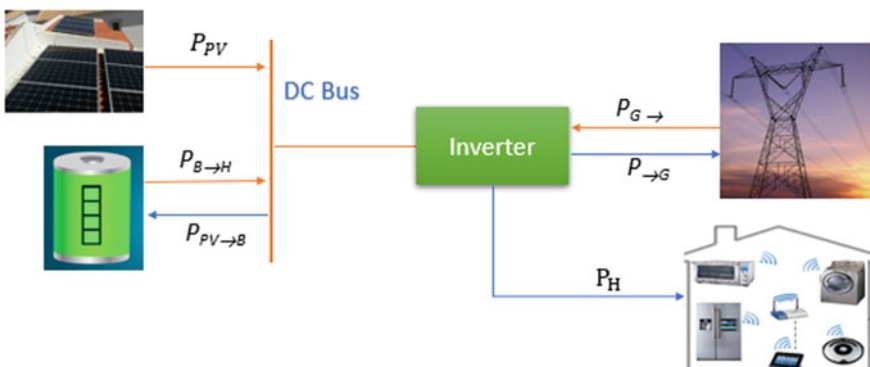


Fig. 1 Hybrid home power system

The power balance of our system is given by Eq. (1), where P_{PV} is the power product by PV system $P_{G \rightarrow}$ is the power supplied by grid, $P_{PV \rightarrow B}$ is the battery charging power, P_{BDisch} is the battery discharging power, P_H is home power demand and $P_{\rightarrow G}$ is the Power injected in the grid.

$$P_{pv} + P_{G \rightarrow} + P_{B \rightarrow H} - P_{PV \rightarrow B} - P_H - P_{\rightarrow G} = 0 \quad (1)$$

The case study that will be used is a detached house, with two floors, in the south of Algarve, Portugal. Different power, atmospheric and climate variables are measured every second.

The photovoltaic system considered consists of 20 PV panels, which should generate a maximum of 6 kW. The power produced by this PV system will be used in three ways:

- Satisfy the demand of the house
- Charge the battery
- Injected into the main grid.

The storage system is a battery box with a capacity of 12 kWh, where the maximum battery energy storage is 11.2 kWh. The inverter is a Kostal Plenticore Plus converter, which has a proprietary control system. In this work data measured by a Carlo Gavazzi electric meter (EM 340), namely the house total power consumption, will be used.

3 Consumed and Produced Energy

Using the data collected from inverter and the EM340, we calculated and analysed the energy obtained from the grid and injected to grid every day for 3 months of 2020: March, April, and May. Figure 2 shows those results. Please note that in some days these values are omitted, as no complete data was available, and that only on the 10th of March injection of energy to the grid was possible.

As it can be seen, while in March there was much more energy obtained than injected (mean values 10.3 vs. 4.6 kWh), in April these values are more similar (10 vs. 8.7) and in May the situation is reversed (5.6 vs. 13.6).

In terms of the economic cost, the situation is not the same thing. In Portugal, the EDP (Electricity from Portugal) energy seller has 5 different selling tariffs [11]: Simple, which is a flat rate, BiHourlyWeekly and BiHourlyDaily, which employ two different rates, and TriHourlyWeekly and TriHourlyDaily, which employ three different rates. The periods associated with these last 4 tariffs vary between the Daily and Weekly type, and between Winter and Summer periods.

The excess of energy, the one injected to the grid, is bought from EDP with 90% of OMIE (Operador de Mercado Ibérico Eléctrico) price [12]. Figure 3 illustrates the selling costs, according to each tariff, and the buying costs, where we are considering hourly prices.

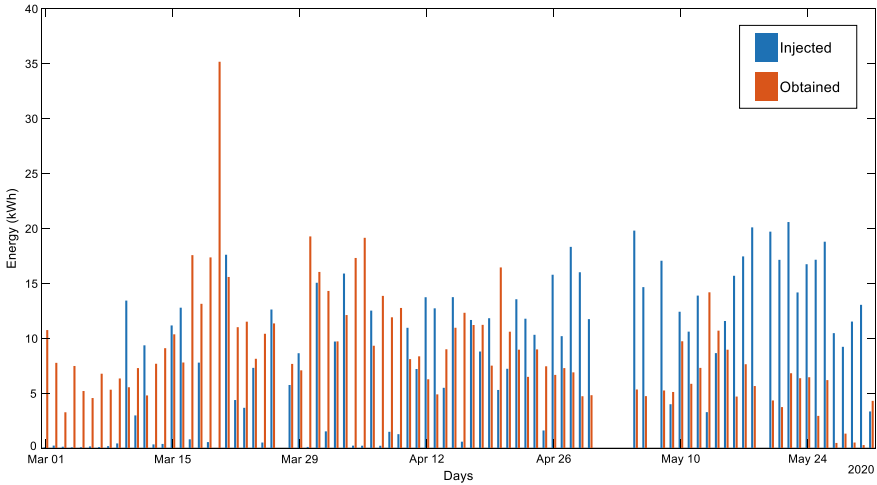


Fig. 2 Energy injected to grid and energy obtained from grid for 3 months

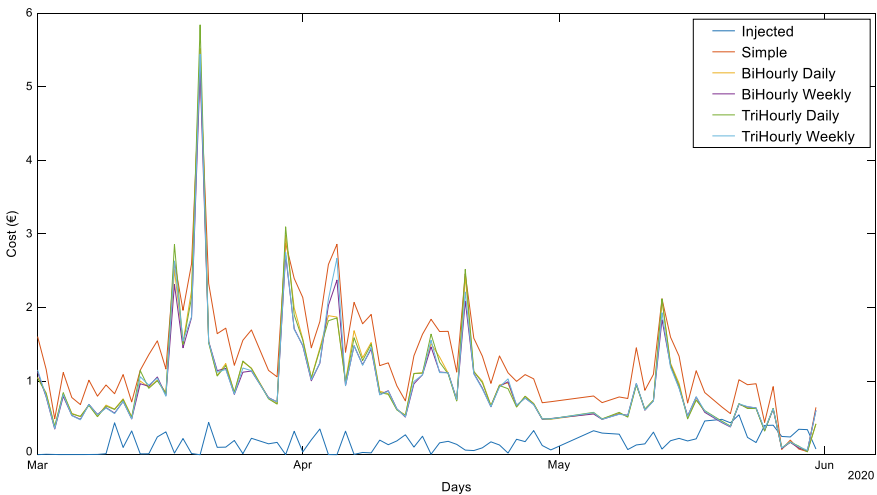


Fig. 3 Cost of energy sold (with different tariffs) and bought by EDP

4 Model-Based Predictive Control of the Inverter

The values shown in the last section are obtained with Plenticore’s control algorithm.

In this section, the aim is to see if it is possible to obtain better cost results using MBPC. For that, we shall use, in simulations, a simplified version of this control strategy. Some definitions are in order:

- P_{PV} : Power produced by PV system (kW)

- P_H : Home power consumption (kW)
- P_B : Battery power (kW)
- $P_{\rightarrow G}$ Power injected to the grid (kW)
- $P_{G \rightarrow}$ Power supplied from the grid (kW)
- $P_{PV \rightarrow H}$ Power delivered from PV to the House (kW)
- $P_{PV \rightarrow B}$ Power delivered from PV to the Battery (kW)
- $P_{PV \rightarrow G}$ Power delivered from PV to the Grid (kW)
- $P_{B \rightarrow H}$ Power delivered from the Battery to the House (kW)
- SOC: Battery state of charge
- $SOC_{Min/Max}$: Minimum and maximum battery state of charge
- $E_{B_{max}}$: Maximum Battery Energy Storage (kWh)
- $P_{B \rightarrow H_{max}}$ and $P_{PV \rightarrow B_{max}}$: present the maximum power delivered by battery to home and maximum power delivered by PV system to battery
- $P_{\rightarrow G_{max}}$: present maximum power injected to grid (kW)
- α and β : Selling and the buying tariffs respectively (€/kWh)
- $E_{\rightarrow G}$ and $E_{G \rightarrow}$: represent respectively the energy injected to the grid (kWh) and Energy obtained from the grid (kWh)
- $Cost_{E_{\rightarrow G}}$ and $Cost_{E_{G \rightarrow}}$: represent respectively the cost energy injected to the grid (kWh) and cost of energy obtained from the grid (kWh).

Our algorithm will control the charge/discharge states of the battery. Therefore, our control signals are $C_{\rightarrow B}$, $C_{B \rightarrow}$, which are binary variables indicating if the battery can be charging (1), or not (0), and if it can discharge energy (1) or not (0). The combination $C_{\rightarrow B} = C_{B \rightarrow} = 1$ is not allowed.

The MBPC problem can be formulated as:

$$\min_{C_{\rightarrow B}, C_{B \rightarrow}} J = \sum_{i=k+1}^{k+PH} J[i], \quad k \in [k_{start}, k_{end}]$$

s.t. restrictions (2)

where k is the index of the sample, belonging to the interval $[k_{start}, k_{end}]$, PH is the Prediction Horizon and $J[i]$ is our cost function at sample i . Here, as an economic cost function will be employed, it will be given as:

$$J[i] = \alpha[i]E_{G \rightarrow}[i] - \beta[i]E_{\rightarrow G}[i] \tag{3}$$

where $E_{G \rightarrow}[i] = P_{G \rightarrow}[i]T_s$, and $E_{\rightarrow G}[i] = P_{\rightarrow G}[i]T_s$, T_s being the sampling interval in hours.

The inequality restrictions are:

$$SOC_{min} \leq SOC[i] = \frac{E_B[i]}{E_{B_{MAX}}} \leq SOC_{Max} \tag{4}$$

$$P_{PV \rightarrow B}[i] \leq P_{PV \rightarrow B_{Max}} \tag{5}$$

$$P_{B \rightarrow}[i] \leq P_{B \rightarrow \text{Max}} \quad (6)$$

$$P_{B \rightarrow}[i] \leq \frac{E_B[i]}{T_s} \quad (7)$$

$$P_{\rightarrow G} \leq P_{\rightarrow G \text{MAX}} \quad (8)$$

$$P_{PV \rightarrow H}, P_{PV \rightarrow B}, P_{PV \rightarrow G}, P_{B \rightarrow H}, P_{B \rightarrow G}, P_{PV}, P_{\rightarrow G}, P_{G \rightarrow}, P_H \geq 0 \quad (9)$$

And the equality restrictions are:

$$P_{PV}[i] = P_{PV \rightarrow H}[i] + P_{PV \rightarrow B}[i]C_{B \rightarrow}[i] + P_{PV \rightarrow G}[i] \quad (10)$$

$$P_H[i] = P_{PV \rightarrow H}[i] + P_{B \rightarrow H}[i]C_{B \rightarrow}[i] + P_{G \rightarrow}[i] \quad (11)$$

$$P_{\rightarrow G}[i] = P_{PV \rightarrow G}[i] + P_{B \rightarrow G}[i] \quad (12)$$

$$P_{B \rightarrow G}[i] + P_{B \rightarrow H}[i] = P_{B \rightarrow}[i] \quad (13)$$

$$E_B[i+1] = \begin{cases} E_B[i] - P_{B \rightarrow}[i]T_s, & C_{B \rightarrow}[i] = 1 \\ E_B[i] + P_{PV \rightarrow B}[i]T_s, & C_{B \rightarrow}[i] = 1 \\ E_B[i], & C_{B \rightarrow}[i] = 0 \wedge C_{B \rightarrow}[i] = 0 \end{cases} \quad (14)$$

The solution of problem (2) is a sequence of control actions, where only the first is applied to the system. In the next instant, (2) is solved again, with new values, and the process goes on.

The solution of (2) is complicated, in general. However, as the decision variables are integer values, in this case, binary values, we can employ the Branch-and-Bound (BAB) algorithm, proposed in [13] and further discussed in [14]. This method implements a structured search over a tree structure, using bounds to restrict branching, thus preventing an exhaustive search to occur. For a detailed explanation of the BAB, the reader can consult [15]. Here, we shall just say that in BAB two bounds are employed: an upper bound on the total cost from instant $k+1$ to $k+PH$, and a lower bound on the cost from instant $k+i$ to $k+PH$.

The initial first bound is usually obtained as

$$J_{UB} = \sum_{i=k+1}^{k+PH} \min\{J(i)\} \Big|_{C_{B \rightarrow}[i-1], C_{B \rightarrow}[i-1] \in \{(0,0), (0,1), (1,0)\}} \quad (15)$$

i.e., the upper bound is obtained with the optimum cost values for every instant, within the control actions allowed. This upper bound is updated as we search the tree. If, when traversing the tree, the actual cost at that tree level is higher than the current upper bound, it means that this particular branch does not need to be searched.

The lower bound from instant $k + i$ to $k + PH$ assumes that the best we can do, at level i , is to inject all the energy produced by the PV and not needed for home consumption to the grid. This way,

$$J_{LB}(k + i) = T_s \sum_{j=k+i}^{k+PH} (P_{PV}[j] - P_H[i]), \quad T_s \text{ in hours} \quad (16)$$

If $\sum_{j=k+1}^{k+i-1} J[i] + J_{LB}(k + i) > J_{UB}$, i.e., the cost computed so far plus the estimated lower bound is greater than the current upper bound, than that particular branch does not need to be searched.

5 Simulation Results

The proposed MBPC is applied to two days of May 2020: the 13th which is considered to be a cloudy day and the 29th which was a sunny day. The atmospheric values for these two days are shown in Figs. 4 and 5.

In our simulations, we considered two scenarios. Both assumed a PH of 12 steps. As the sampling times considered were 5 (scenario 1) and 15 (scenario 2) minutes, this means that PH s of 1 and 4 h were employed. The restrictions used are shown in Table 1. We should also note that for MBPC calculations real values are used for the forecasted values, i.e., no forecasting model is employed.

The proposed MBPC strategy is implemented in MATLAB. Figures 7 and 8 shows, for 13th of May, the battery State of Charge (SOC) (left), the energy injected to the grid (middle) and the energy obtained from the grid (right), for the proprietary control, and the MBPC considering the two scenarios.

The actual power consumption in these two days are shown in Fig. 6.

As it can be seen, the proprietary system injects energy to the grid, while MBPC does not; because of that the battery SOC increases and a large quantity of energy that is bought from the grid, in the proprietary system, is not needed employing MBPC. The energy injected to the grid is 3.5 kWh and 0, considering the proprietary and the MBPC approach, while the energy obtained from the grid is 12 and 7.2 kWh (Figs. 7 and 8).

The figures for scenario 2 are identical to scenario 1, with the difference that the simulation ends at 20 h, instead of 23 h, due to the different PH s. The next figure shows the same variables, this time for the 29th May, considering scenario 1 (Fig. 9).

The evolution of variables is quite different from the 13th May. SOC now reaches 100%, for a significant period. The proprietary system starts injecting energy to the grid earlier than the MBPC, which has the nefarious effect of having to obtain energy

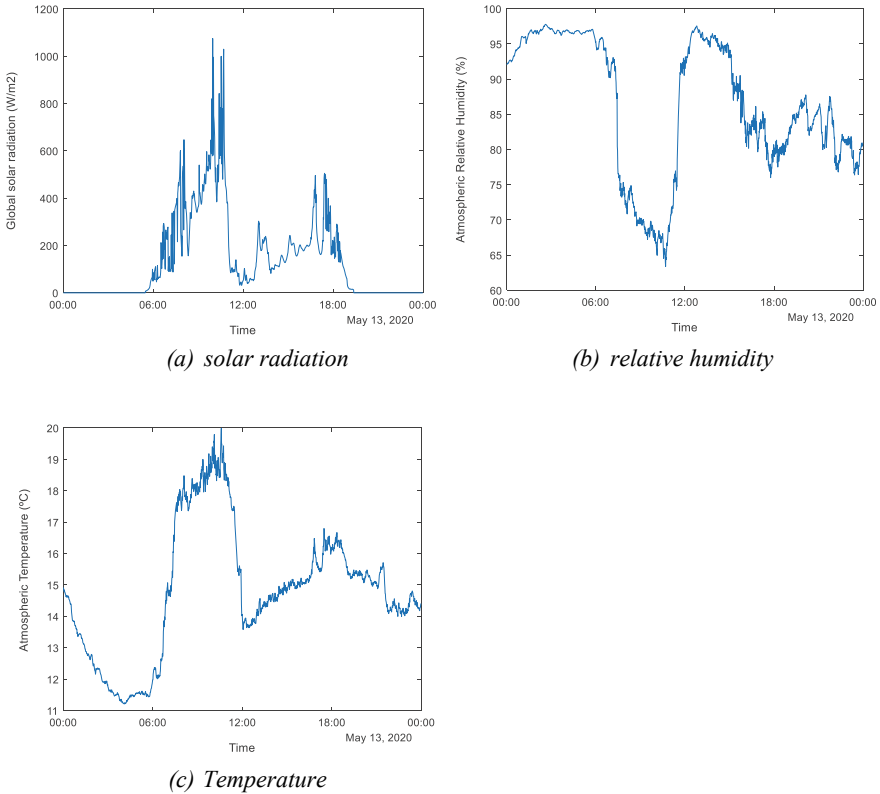


Fig. 4 Atmospheric values for the 13th of May 2020: **a** solar radiation, **b** relative humidity and **c** Temperature

from the grid, in the end of the day. As the figures for scenario 2 are equivalent to Fig. 7, they are not shown. The energy injected to the grid is 12.3 and 14.2 kWh, considering the proprietary and the MBPC approach, while the energy obtained from the grid is 0.4 kWh and 0.

In term of economic costs, we considered in our simulation the ‘Trihourly Daily’ tariff. Table 2 shows the energy cost sold to grid and bought from grid, during the 13th and 29th of May 2020.

As we can see, in the first day, the propriety control was translated into a net cost of 1.85 €, while with MBPC this cost was reduced to 0.75 €. Regarding the second day, there is a profit of 0.24 €, with the actual system, and an expected benefit of 0.33 €, with MBPC.

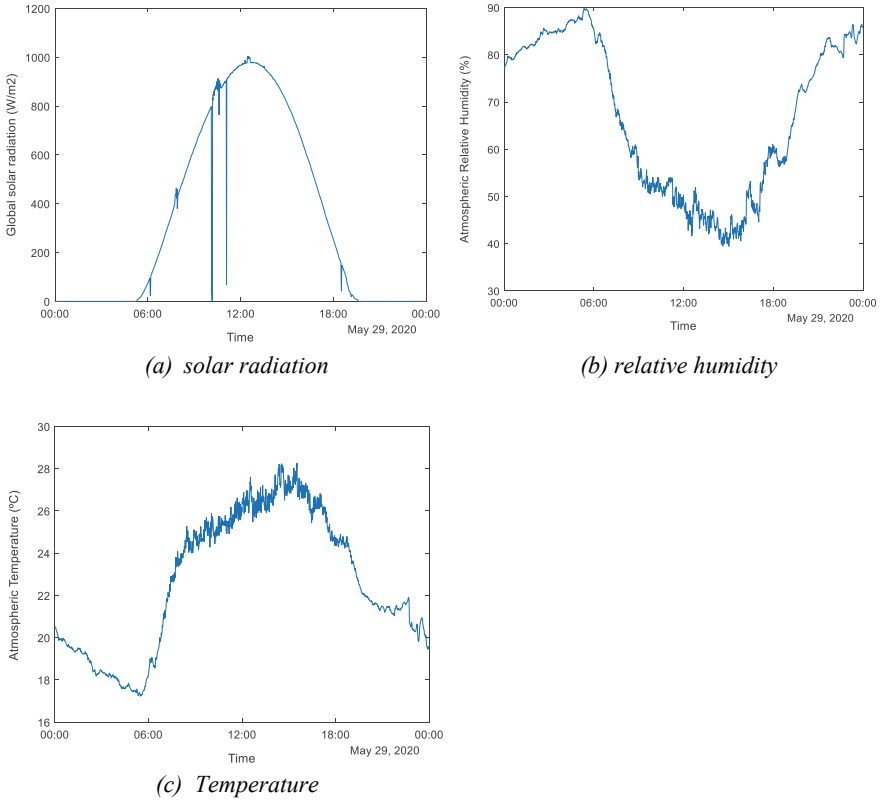


Fig. 5 Atmospheric values for the 29th of May 2020: **a** solar radiation, **b** relative humidity and **c** Temperature

Table 1 MBPC restrictions

SOC_{Min}	SOC_{Max}	$P_{BH_{max}}$	$P_{PV_{B_{max}}}$	$P_{G_{max}}$	$E_{B_{max}}$
5%	100%	5.5 kW	5.5 kW	5.5 kW	11.2 kWh

6 Conclusion and Future Work

Because of the high electricity consumption of the residential sector, hybrid systems are the ideal solution to reduce the electricity cost. This work shows that better results, whether in terms of energy or its economic costs are to be expected, if advanced control strategies are used for the flow control of energy between the different sources.

As mentioned before, this is a first approach, which must be improved.

First, a cost term related to the battery energy changes must be considered in (2).

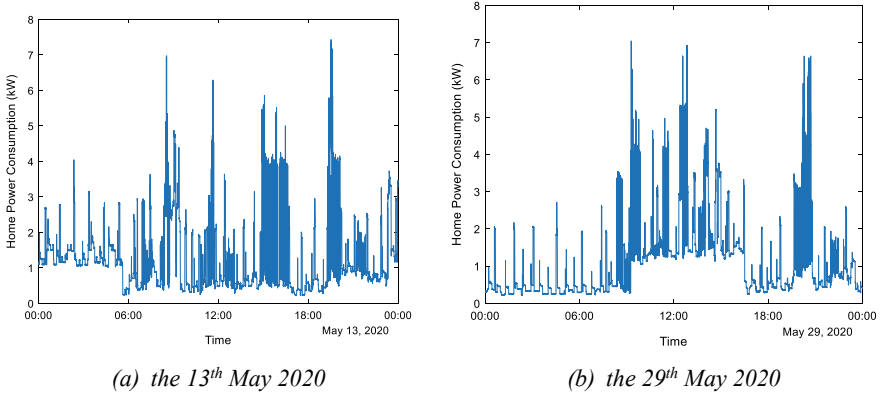


Fig. 6 Home power consumption: **a** for the 13th of May 2020 and **b** for the 29th of May 2020

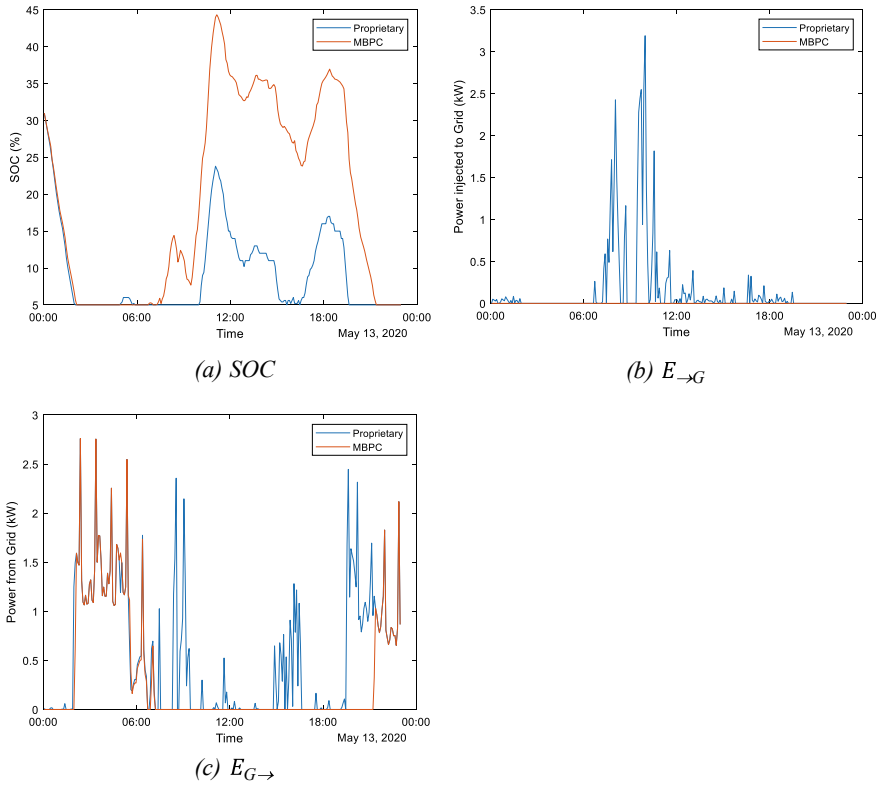


Fig. 7 **a** SOC, **b** $E_{\rightarrow G}$ and **c** $E_{G \rightarrow}$ for the 13th of May, considering scenario 1

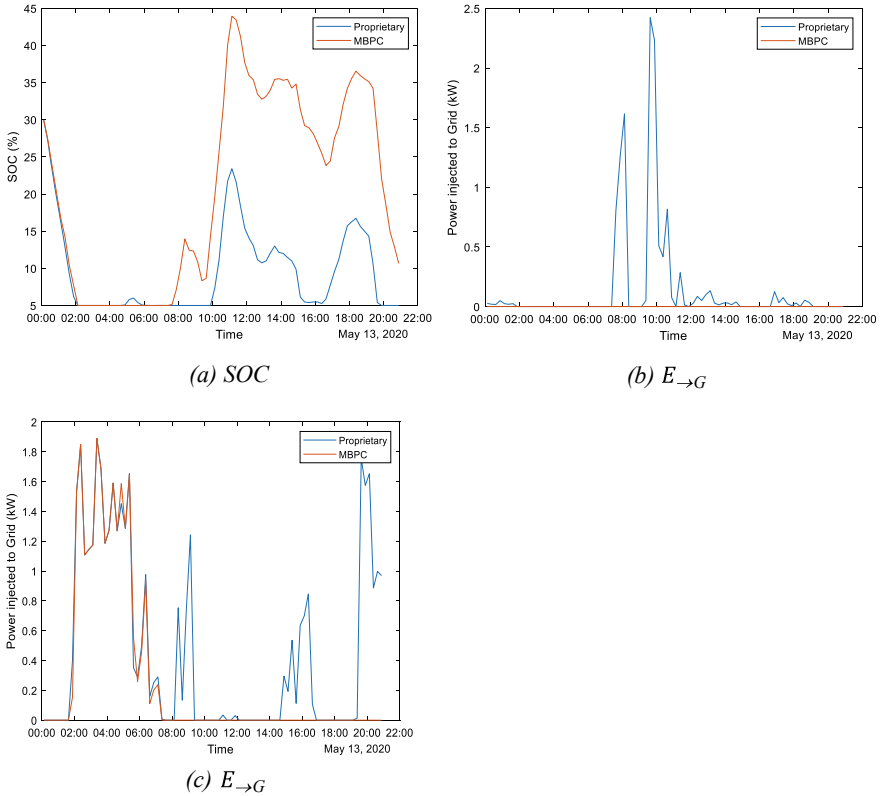


Fig. 8 SOC, $E_{G \to G}$ and $E_{G \to G}$ for the 13th of May, considering scenario 2

The fact that different Prediction Horizons gave similar results is strange and must be studied.

Real measured data was used in this first approach. This cannot be used in real-time, where a forecasting model, with approximation errors, must be employed.

Finally, an intelligent scheduling of schedulable appliances will allow additional demand mechanisms to be employed.

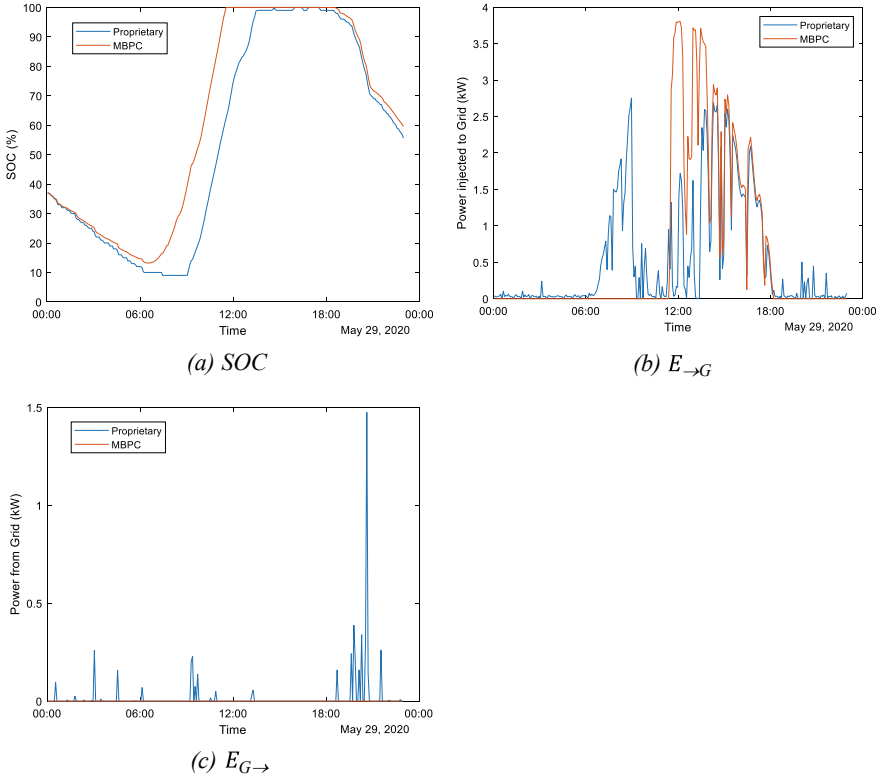


Fig. 9 SOC, $E_{\rightarrow G}$ and $E_{G \rightarrow}$ for the 29th of May, considering scenario 1

Table 2 Comparison of energy costs

		Sold to grid (€)	Bought from grid (€)
13/05	Proprietary	0.07	1.92
	Scenario 1	0	0.75
	Scenario 2	0	0.56
29/05	Proprietary	0.34	0.10
	Scenario 1	0.33	0
	Scenario 2	0.33	0

Acknowledgements The authors would like to acknowledge the support of Programa Operacional Portugal 2020 and Operational Program CRESC Algarve 2020 grant 01/SAICT/2018. Antonio Ruano also acknowledges the support of Fundação para a Ciência e Tecnologia grant UID/EMS/50022/2020, through IDMEC, under LAETA.

References

1. Energy SP, Heat G (2013) Transition to sustainable buildings strategies and opportunities to 2050
2. Vega AM, Santamaria F, Rivas E (2015) Modeling for home electric energy management: a review. *Renew Sustain Energy Rev* 52:948–959. <https://doi.org/10.1016/j.rser.2015.07.023>
3. Fallah S, Deo R, Shojafar M, Conti M, Shamshirband S (2018) Computational intelligence approaches for energy load forecasting in smart energy management grids: state of the art, future challenges, and research directions. *Energies*. 11:596. <https://doi.org/10.3390/en11030596>
4. Collotta M, Pau G (2015) A novel energy management approach for smart homes using blue-tooth low energy. *IEEE J Sel Areas Commun* 33:2988–2996. <https://doi.org/10.1109/JSAC.2015.2481203>
5. Shareef H, Ahmed MS, Mohamed A, Al Hassan E (2018) Review on home energy management system considering demand responses, smart technologies, and intelligent controllers. *IEEE Access* 6:24498–24509. <https://doi.org/10.1109/ACCESS.2018.2831917>
6. Logenthiran T, Srinivasan D, Shun TZ (2012) Demand side management in smart grid using heuristic optimization. *IEEE Trans Smart Grid* 3:1244–1252. <https://doi.org/10.1109/TSG.2012.2195686>
7. Shayeghi H, Shahryari E, Moradzadeh M, Siano P (2019) A survey on microgrid energy management considering flexible energy sources. *Energies* 12:2156. <https://doi.org/10.3390/en12112156>
8. Serale G, Fiorentini M, Capozzoli A, Bernardini D, Bemporad A (2018) Model predictive control (MPC) for enhancing building and HVAC system energy efficiency: problem formulation, applications and opportunities. *Energies* 11:631. <https://doi.org/10.3390/en11030631>
9. Ruano AE, Pesteh S, Silva S, Duarte H, Mestre G, Ferreira PM, Khosravani HR, Horta R (2016) The IMBPC HVAC system: a complete MBPC solution for existing HVAC systems. *Energy Build* 120:145–158. <https://doi.org/10.1016/j.enbuild.2016.03.043>
10. Godina R, Rodrigues E, Pouresmaeil E, Matias J, Catalão J (2018) Model predictive control home energy management and optimization strategy with demand response. *Appl Sci* 8:408. <https://doi.org/10.3390/app8030408>
11. <https://www.edp.pt/particulares/energia/tarifarios/>. Accessed on 01 June 2020
12. <https://www.omie.es/pt/market-results/daily/daily-market/daily-hourly-price>. Accessed on 01 June 2020
13. Sousa JM, Babuška R, Verbruggen HB (1997) Fuzzy predictive control applied to an air-conditioning system. *Control Eng Pract* 5:1395–1406. [https://doi.org/10.1016/S0967-0661\(97\)00136-6](https://doi.org/10.1016/S0967-0661(97)00136-6)
14. Morrison DR, Jacobson SH, Sauppe JJ, Sewell EC (2016) Branch-and-bound algorithms: a survey of recent advances in searching, branching, and pruning. *Discr Optim* 19:79–102. <https://doi.org/10.1016/j.disopt.2016.01.005>
15. Ferreira PM, Ruano AE (2008) Discrete model-based greenhouse environmental control using the branch & bound algorithm. *IFAC Proc* 41:2937–2943. <https://doi.org/10.3182/20080706-5-KR-1001.00494>

Comparative Study of Electricity Production by Photovoltaic Panels with Mirrors for Different Inclinations



Assia Benkaddour, Hanan Boulaich, and Elhassan Aroudam

Abstract This paper presents an analysis of a system consisting of a PV collector augmented with two reflectors to obtain more electrical energy. The model provides the possibility to predict the solar energy received by the panel in the day. To enhance the amount of solar radiation on the fixed photovoltaic Panel we daily changed the tilt angle of the two reflectors to get them in an optimal position which depends on the angle of elevation of the sun, the azimuth angle for typical days throughout the year. In this work, we calculated the electrical efficiency of the photovoltaic panel in two cases, without and with reflectors in the optimal position. The study is made on the site of Tetouan (longitude = -5° , latitude = 35.25°) for a daily variation (from sunset to sunrise) relatively for the days 21 March 21 Mai 21 June 21 September and 21 December, (the spring and autumn equinox and summer and winter solstices), days considered clear sky type.

Keywords Solar energy · Photovoltaic · Reflectors

1 Introduction

Nowadays, solar development projects are among the most frequent and seem to be the ideal solution for tomorrow's electricity production Because the world needs a safe, clean and economical source of energy to fill the energy gap such as solar energy, which can be either photovoltaic or thermal, Photovoltaic mirror systems seem to be well established as a means of converting solar energy into electrical energy.

Several experimental studies have been carried out in this direction, in particular, Farooqui [1] has optimized the angular orientation of two auxiliary mirrors of box-type solar cookers and confirms that with the optimized tilt, the cookers can be operated faithfully for at least 6 h per day without requiring solar tracking. Garg and Hrishikesan [2] who present an analysis of a system consisting of a flat-plate

A. Benkaddour (✉) · H. Boulaich · E. Aroudam
Physics Department, Modeling and Simulation of Mechanical Systems Team, Faculty of Sciences,
Abdelmalek Essaadi University, Tetouan, Morocco
e-mail: Benkaddourassia@gmail.com

collector supplemented by two reflectors. The model facilitates the prediction of the total energy absorbed by the collector. Baccoli [3] performed a numerical analysis of a reflector-enhanced solar collector by determining the optimal inclination of the two, and conclude that The amount of energy on the collector surface is significantly affected by the angular position of the collector and is slightly affected by the inclination of the reflector. Tanaka [4] also proposes a geometric model to calculate the solar radiation reflected from a lower reflector. Touafek et al. [5] concluded that the addition of reflectors increases the energy production of hybrid collector by the diminution of the reflected loss in the glass layer of cells. The theoretical study of the collector-reflector conducted by Taha and Eldighidy [6] indicates that the reflector can increase the solar energy absorbed by the collector by up to 13.1% for year-round operation with a single change of inclination angle. Santos et al. [7] the increase in total energy production of the PVT hybrid system can be achieved by using diffuse aluminum reflectors as amplifiers that will produce a uniform distribution of solar radiation reflected on the surface of the hybrid collector. Andrews et al. [8] experimentally tested the PV-booster system over a year. For the latitude of 44°N (Kingston, Canada), a specular reflector with a reflectance of 0.90 and a c-Si module, a gain of 45% of produced energy was estimated based on ISC measurements. Pavlovic and Kostic [9] have performed a geometrical optimisation of a flat plate solar collector with four adjacent reflector surfaces [10]. The author has analyze solar cells with flat mirror, convex mirror, concave mirror, and without reflector. Because the use of reflectors is an excellent way to maximum output with effective time.

2 Model Analysis

2.1 Description of the Studied System

To obtain more electrical energy, the reflectors have been mounted on the panel as illustrated in Fig. 1. To reach a higher solar radiation intensity, we determined the optimal position of the reflectors by numerical calculations to obtain a maximum concentration of the intensity of solar radiation, which gives the lowest optimal position of the reflector (5°) in December and the highest (38°) in June. In order to see the impact of the reflectors on the electrical efficiency of the photovoltaic panel, by numerical calculations, we determine the electrical efficiency in the two cases, without and with reflectors in the optimal position [11].

The system shown in Fig. 1 consists of three different parts: the PV panel, the upper reflector, and the lower reflector. The panel is tilted at 35° and faces south. The two reflectors are tilted concerning the horizontal plane by α_1 and vertical plane by α_2 at optimal inclinations calculated for each hour.

To estimate the intensity of solar radiation on the ground at a particular location the following relationship (7) is used [13]:

$$I = i_{oh} * 0.7^{(AM)*0.678} \tag{7}$$

where the extraterrestrial radiation intensity on a horizontal surface is:

$$i_{oh} = i_0 * \cos \theta_z \tag{8}$$

And the extraterrestrial intensity on a surface held perpendicular to the sun on a particular day of the year as:

$$i_0 = \left(i_{sc} * \left[1 + 0.0334 * \cos \left(\frac{2\pi(N - 1)}{365.25} \right) \right] \right) \tag{9}$$

where the solar constant is $I_{sc} = 1367 \text{ w/m}^2$.

To calculate the total solar radiation G on the inclined PV collector with β we applied the following model [14]:

$$G = G_{dir} + G_{dif} + G_{gr} + Gr1 + Gr2 \tag{10}$$

where

$$G_{dir} = G_{in} * \sin(\beta + h) \tag{11}$$

$$G_{dif} = G_d * \frac{1 + \cos \beta}{2} \tag{12}$$

$$G_{gr} = \rho_g * G_h * \frac{1 - \cos \beta}{2} \tag{13}$$

$$Gr1 = \rho_{al} * G_{in} * \sin \chi * \sin(h - \alpha 1) \Rightarrow \chi = \beta + 2 * \alpha 1 - h \tag{14}$$

$$Gr2 = \rho_{al} * G_{in} * \sin \tau * \sin(h + \alpha 2) \Rightarrow \tau = h + 2 * \alpha 2 - \beta \tag{15}$$

In the above expression, G_{dir} is the direct radiation on the collector, G_{dif} is the sky-diffuse radiation, G_{gr} is the reflected radiation from the ground, G_{r1} is the reflected radiation from bottom reflector which reached the collector surface with tilted angle $\alpha 1$, G_{r2} is the reflected radiation from the upper reflector which reached the collector surface with tilted angle $\alpha 2$. G_{in} , G_d and G_h are respectively the global solar incident radiation, the diffuse radiation and the global solar radiation on horizontal surface [14].

To see the impact of ambient temperature and irradiation on cell efficiency, we have calculated the cell temperature by the following equation:

$$T_c = T_m + (NOCT - 20) * \frac{G}{800} \tag{16}$$

where T_m is the ambient temperature and G the solar irradiance in W/m^2 .

The electrical efficiency of the panel η_e is calculated by relation [14]:

$$\eta_e = \frac{ImVm}{A0G} \tag{17}$$

The cell efficiency is calculated by the relation [15]:

$$\eta_c = \eta_{ref}[1 + \beta_{ref} * (T_c - T_m)] \tag{18}$$

2.3 Results and Discussion

Figure 2 shows the results of the variation of the solar radiation intensity G using the Eq. (10) on the surface of the PV collector, measured during May 4 at 12:00 noon as a function of the position of the reflectors, where α_1 and α_2 indicate the angle between the lower reflector and the horizontal plane and the angle between the upper reflector and the vertical plane respectively.

It can be deduced that the optimum reflector positions are at the angles of 10 and 37 for the upper and lower reflector respectively, for this position of the reflectors during the peak sun, the collector receives the maximum solar radiation ($1283 W/m^2$).

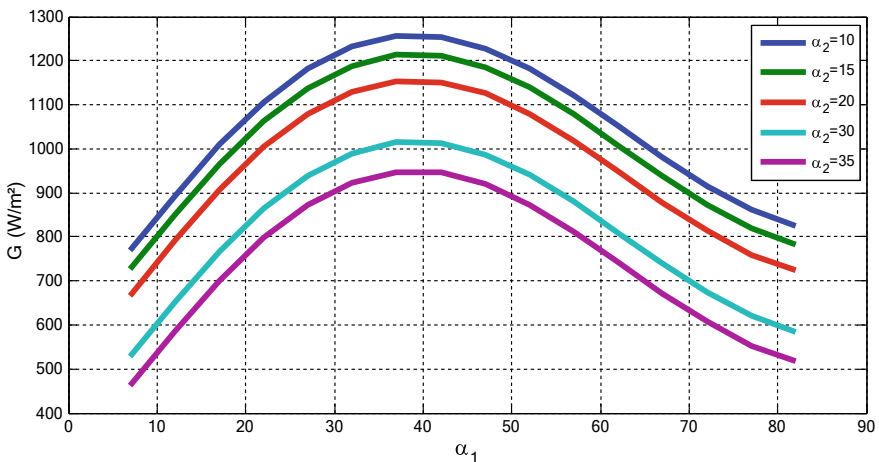


Fig. 2 The solar radiation G on the panel for different reflector inclinations

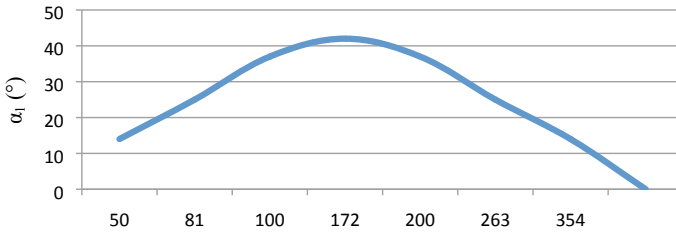


Fig. 3 Switching the optimum angles of the lower reflector in the sun peak

The numerical results for the optimal position of the lower reflector during peak sun [16] are shown in Fig. 3. It’s clear that, the maximum value of the optimal angle of the lower reflector (α_1) is 42° and is reached on June 21 while the minimum calculated value is 14° and is obtained on December 21, while for March 21 and September 21 its value reaches 28. The upper reflector (α_2) is 30° and is reached on December 21, as its minimum estimated value is 5° obtained on June 21, and 10° for March 21 and September 21.

The system performance is evaluated for a typical day in March, May, September and December, we have presented the total radiation falling on PV collectors tilted at a fixed orientation, $\beta = 35^\circ$, with and without reflectors. Then, a numerical modeling simulation was performed to show the effect of the reflector at optimal angles on the electrical performance of the collector.

To solve this system of equations we used a Fortran 90 program. The sensor parameters used in the calculation are shown in Table 1 and we arrived at the following results in Fig. 4. the graph shows a significant increase of the solar radiation received by the panel with the use of reflectors for all typical days, for December, we see that the values of solar radiation with and without reflectors approach each other after the solar peak.

Figure 5 shows the hourly variation in the electrical efficiency of the photovoltaic panel cell with temperature calculated by Eq. (18). It can be seen that the temperature

Table 1 Electrical data of the PV module

Module type	PWX500 mono crystalline
Power (w)	50
V_{mpp} (v)	17.5 vdc
I_{mpp} (A)	2.8
V_{OC} (v)	22.5 vdc
I_{sc} (A)	3.23
η_{ref} (%)	12
L (m)	0.9
W (m)	0.43
PV module area (m^2)	0.38

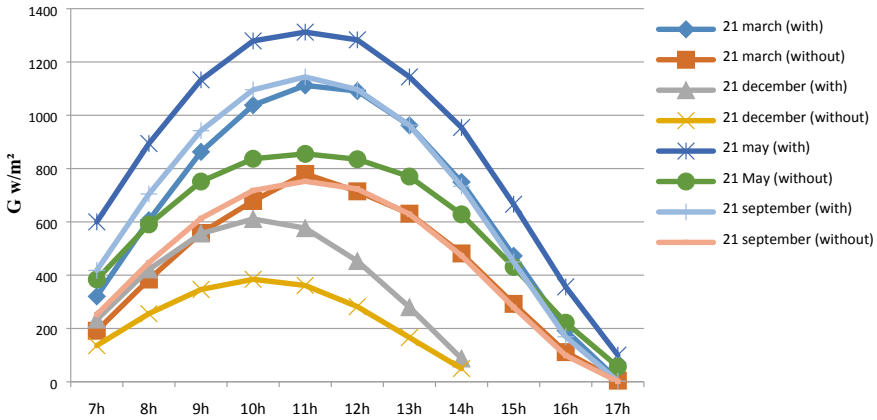


Fig. 4 A variation of solar intensity on the photovoltaic panel for typical days, without and with reflectors in optimal positions

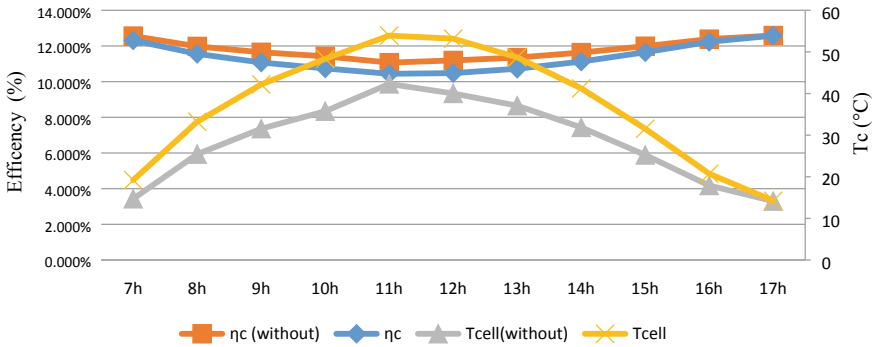


Fig. 5 The impact of cell temperature on efficiency of PV collector with and without reflectors

is higher with reflectors due to the increase in solar intensity. On the other hand, there is a decrease in the electrical efficiency of the cell with reflectors and the efficiency of the cell without a reflector is slightly higher.

Therefore, it can be deduced that the absorbed solar radiation has increased the temperature of the cells which reduces its efficiency.

From the Fig. 6 we can see the efficiency of PV (17) without Reflectors is lower than efficiency of PV collector with reflectors, the average daily PV efficiency values of without and with reflectors in optimal position are 12.77% and 14.12%, respectively.

The total generated electrical energy by PV collector with reflectors in optimal position 30.73 WH are higher than total generated electrical energy by PV collector without reflectors 20 Wh [14].

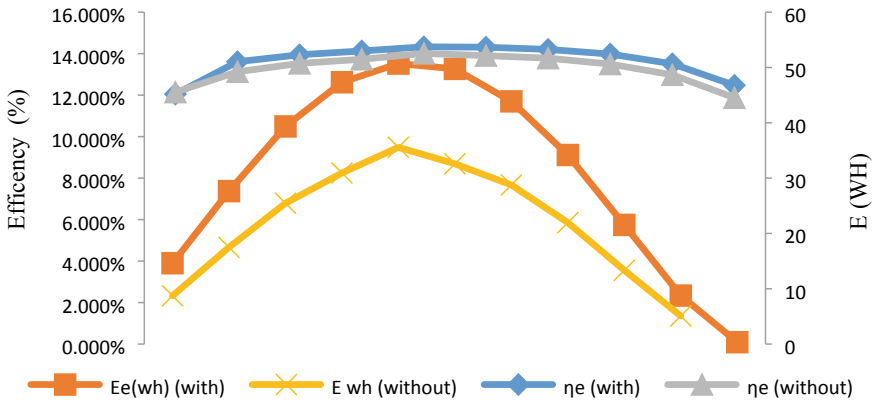


Fig. 6 The impact of reflectors on the electrical energy and electrical efficiency

3 Conclusion

In this document, a photovoltaic panel system with movable reflectors was considered. A change of the optimal angle of the reflectors during the day was analytically determined when the panel is fixed at $\beta = 35^\circ$ to obtain a maximum solar radiation.

The numerical results show that with the use of reflective mirrors more electrical energy is gained and the electrical efficiency of the panel is improved.

On the other hand we have found that the high temperature of the cells has a negative impact on their electrical efficiency, which decreases with increasing temperature.

References

1. Farooqui SZ (2015) Angular optimization of dual booster mirror solar cookers—tracking free experiments with three different aspect ratios. *Sol Energy* 114:337–348. <https://doi.org/10.1016/j.solener.2015.01.030>.(2015)
2. Garg HP, Hrishikesan DS (1988) Enhancement of solar energy on flat-plate collector by plane booster mirrors. *Sol Energy* 40(4):295–307. [https://doi.org/10.1016/0038-092X\(88\)90002-3](https://doi.org/10.1016/0038-092X(88)90002-3)
3. Baccoli R et al (2015) A mathematical model of a solar collector augmented by a flat plate above reflector: optimum inclination of collector and reflector. *Energy Proc* 81:205–214
4. Tanaka H (2011) Tilted wick solar still with flat plate bottom reflector. *Desalination* 273(2–3):405–413. <https://doi.org/10.1016/j.desal.2011.01.073>
5. Touafek K et al (2018) Integration of reflectors to improve energy production of hybrid PVT collectors. In: *Exergetic, energetic and environmental dimensions*. Elsevier, pp 533–549
6. Taha IS, Eldighidy SM (1980) Effect of off-south orientation on optimum conditions for maximum solar energy absorbed by flat plate collector augmented by plane reflector. *Sol Energy* 25(4):373–379. [https://doi.org/10.1016/0038-092X\(80\)90349-7](https://doi.org/10.1016/0038-092X(80)90349-7)
7. Tripanagnostopoulos Y, Nousia Th, Souliotis M, Yianoulis P (2002) Hybrid photovoltaic/thermal solar systems. *Sol Energy* 72(3):217–234. [https://doi.org/10.1016/S0038-092X\(01\)00096-2](https://doi.org/10.1016/S0038-092X(01)00096-2).(2002)

8. Andrews RW, Pollard A, Pearce JM (2013) Photovoltaic system performance enhancement with non-tracking planar concentrators: experimental results and BDRF based modelling. *IEEE*, pp 0229–0234
9. Pavlovic ZT, Kostic LT (2015) Variation of reflected radiation from all reflectors of a flat plate solar collector during a year. *Energy* 80:75–84
10. Siahaan Y, Siswono H (2019) Analysis the effect of reflector (flat mirror, convex mirror, and concave mirror) on solar panel. *IJPEDS* 10(2):943, juin 2019. <https://doi.org/10.11591/ijpeds.v10.i2.pp943-952>
11. Anand VP, Khan MM, Ameen E, Amuthan V, Pesala B (2014) Performance improvement of solar module system using flat plate reflectors. In: *IEEE 2014 International Conference on Advances in Electrical Engineering (ICAEE) - Vellore, India (2014.1.9-2014.1.11)*, pp. 1–4. <https://doi.org/10.1109/ICAEE.2014.6838547>
12. Pavlov M (2016) Numerical modelling of the coupling of thermal and photoelectric effects photovoltaic modules under low concentration. *Optics [physics.optics]*. Université Paris-Saclay
13. Farooqui SZ (2015) Angular optimization of dual booster mirror solar cookers—tracking free experiments with three different aspect ratios. *Sol Energy* 114:337–348
14. Kostić et al (2010) Optimal design of orientation of PV/T collector with reflectors. *Appl Energy* 87(10):3023–3029
15. Rauschenbach HS (1980) *Solar cell array design handbook*. Springer, Dordrecht
16. Belhadj M, Benouaz T (2016) Modeling of automatic reflectors for PV panel attached to commercial PV/T module 11(23):7
17. Steven C, Seitel (1975) Collector performance enhancement with flat reflectors. 17(5):291–295. [https://doi.org/10.1016/0038-092x\(75\)90046-8](https://doi.org/10.1016/0038-092x(75)90046-8)
18. Algifri AH, Al-Towaie HA (2001) Efficient orientation impacts of box-type solar cooker on the cooker performance. 70(2):165–170. [https://doi.org/10.1016/s0038-092x\(00\)00136-5](https://doi.org/10.1016/s0038-092x(00)00136-5)
19. Tabor H (1966) Mirror boosters for solar collectors. 10(3):111–118. [https://doi.org/10.1016/0038-092x\(66\)90025-9](https://doi.org/10.1016/0038-092x(66)90025-9)
20. Bari S (2000) Optimum slope angle and orientation of solar collectors for different periods of possible utilization. 41(8):855–860. [https://doi.org/10.1016/s0196-8904\(99\)00154-5](https://doi.org/10.1016/s0196-8904(99)00154-5)

A Non Linear Autoregressive Neural Network Model for Forecasting Appliance Power Consumption



Inoussa Habou Laouali, Hamid Qassemi, Manal Marzouq, Antonio Ruano, Saad Bennani Dosse, and Hakim El Fadili

Abstract Forecasting the electrical appliance power consumption is a necessary and important part of the management of electrical power system, in order to assess people's penchant for using electricity. Even though several studies are focused on forecasting building consumption, less attention is given to forecasting the use of single appliances. Indeed, some of the energy needs of consumers may be relatively delayed or anticipated to obtain a better consumption profile while maintaining consumer comfort. This paper focuses on forecasting appliance power consumption using a non-linear autoregressive (NAR) neural network model. The results obtained on the UK-DALE public dataset demonstrate that NAR models are suitable for forecasting of energy consumption with a good accuracy. The proposed model obtained the best Mean Absolute Errors, compared with the LSTM, Autoencoder, Combinatory optimization, FHMM, and Seq2point techniques.

Keywords Forecasting electric load · Artificial neural network · Energy consumption · Non linear autoregressive models

I. H. Laouali (✉) · S. B. Dosse

Intelligent Systems, Georesources and Renewable Energies Laboratory (SIGER),
Faculty of Sciences and Technology, Sidi Mohamed Ben Abdellah University,
B.P. 2202 Route Immouizzer, 30003 Fez, Morocco
e-mail: inoussa.haboulaouali@usmba.ac.ma

H. Qassemi · M. Marzouq · H. El Fadili

Computer Science and Interdisciplinary Physics Laboratory (LIPI), Sidi Mohamed
Ben Abdellah University, B.P. 5206 Bensouda, 30003 Fez, Morocco

I. H. Laouali · H. Qassemi · A. Ruano

Faculty of Science & Technology, University of Algarve, 8005-294 Faro, Portugal

A. Ruano

IDMEC, Instituto Superior Técnico, Universidade de Lisboa, Lisboa, Portugal

© Springer Nature Singapore Pte Ltd. 2022

S. Bennani et al. (eds.), *WITS 2020*, Lecture Notes in Electrical Engineering 745,
https://doi.org/10.1007/978-981-33-6893-4_69

1 Introduction

The largest consumer of electricity in the world is the building sector, for example, the US building's primary and electrical energy consumption is more than 40 and 76% respectively [1]. Indeed, reducing energy consumption is essential to meet national energy and environmental challenges and reduce costs for building users. According to the US department of energy (DOE), the possibilities for improving efficiency are colossal. By 2030, the energy consumption of buildings could be reduced by more than 20% by using technologies known to be profitable today, and by more than 35% if the research objectives are met [2].

The main goal of a Home Energy Management System (HEMS) is to manage efficiently the flow of electricity in the house so as to lower the price of the electric bill, while maintaining the comfort of its occupants [3]. Monitoring the electricity consumption of several devices is a first step of any HEMS and aims to perform (1) detailed energy detection, (2) provide information on the distribution of energy consumed, (3) profile energy-consuming devices to develop energy conservation strategies, like reprogramming consumption of high power devices during off-peak hours [3, 4].

In some cases, to minimize waste and improper use of energy, users must provide a lot of configuration information, this collection of information generally involving arduous measurement campaigns [5, 6]. Thus, forecasting electrical devices consumption is a necessary and an important part of managing the power system in order to forecast people's penchant for using electricity [7]. Indeed, forecasting consumer demand becomes very important as the non-urgent energy needs of users (washing machines, air conditioning or refrigeration) can be relatively postponed or anticipated to obtain a good adjustment of the production profile while maintaining consumer comfort and the level of service [7, 8]. Moreover, most of the work in the literature based on the forecasting of building consumption does not claim any attention to the individual consumption of each appliance.

In this paper, we propose a non-linear autoregressive neural network (NAR) model to predict the electrical consumption of the device in a house. Our objective is to provide a methodological framework for analyzing the historical data of the time series of device power consumption and to know if the forecasting of such energy consumption can be performed with this type of model. Moreover, we will assess the feasibility of the method using the UK-DALE public dataset and assess the model performance using various delays as well as different model configurations.

The rest of paper is organized as follows: Sect. 2 reviews related works on the prediction of electrical consumption in a house. Section 3 presents the proposed methodology and the description of the NAR model. It also describes the public dataset used, and the evaluation criteria employed. Section 4 shows the experimental results of the proposed model and conclusions are drawn in Sect. 5.

2 Related Work

Several works have been carried out in the literature to analyze, profile, classify and/or predict the electrical consumption in a house. This information can be used to plan energy-saving strategies, improve user behavior by helping them to change their habits in the use of household appliances, improve the overall grid performance and decrease the consumption of electricity [5]. Indeed, Ruiz et al. proposed in [9] a method based on non-linear autoregressive neural networks method to forecast energy consumption in public buildings. They compared the NAR model with the NARX model and demonstrated that, if no external data is available, energy consumption only can be used to obtain accurate forecasts. A method for building energy consumption using weighted SVRs was developed by Zhang et al. in [10]. Good results were obtained, their results showing that using half-hourly data a higher weight is given to nu-SVR, while, for daily data, a greater weight for epsilon SVR is applied. In [11], Fumo et al. presented a method based on linear regression analysis to forecast energy consumption in an individual family household. They claim that the future of residential energy prediction is going towards the development of single model for each house, due to the accessibility of smart meters data. Deb et al. [12] introduced a data-driven model to predict diurnal cooling load energy consumption for institutional buildings. They demonstrated that the artificial neural network is capable to predict the next day energy consumption based on 5 preceding days data with a suitable accuracy. In [13], Gul et Patidar focused on understanding the influence of occupancy of multi-purpose educational buildings in their energy consumption. Thus, they noted that detailed information on occupancy preference could help the management staff to rethink control policies for optimal energy management of the building. A technique based on short term load prediction in distribution systems using a neural network method was proposed by Ding et al. in [14]. They performed feature selection in models for electrical load prediction to enforce an optimal generalization capacity of the model. Motepe et al. presented a load prediction process for the distribution of power utilizing deep learning and hybrid AI algorithms [15]. They investigated the effect of the inclusion of loading cleaned data and weather variables on the load prediction performance of an hybrid AI method. In [16], Hong et al. developed a method for short-term residential load prediction based on deep learning. The results showed that both the devices load data and the proposed iterative ResBlocks can help to enhance the prediction performance. All of these above studies, however, are focused on forecasting the building consumption and no attention is paid to forecasting the use of a single appliance, thus preventing their applicability to appliance scheduling. Several works have focused on appliance disaggregation [17–22], Kelly et al. proposed a deep neural network for energy disaggregation [35]. They obtained good performances and showed a good capacity for generalization on unknown houses. A method based on sequence-to-point learning with CNN for energy disaggregation was developed by Zhang et al. in [24]. They showed that the CNN can inherently learn the features of the target devices, and their methods achieve state-of-the-art performance. Barbato et al.

focused on prediction the usage of household devices via power meter in [5]. They showed the effectiveness of their model in predicting device usage through experimental tests.

3 Methodology

A Non-linear autoregressive model (NAR) is a recurrent neural network model that can accept dynamic inputs [9]. Indeed, the choice of NAR can be explained by the fact that not only the power demand of electrical devices is a time series but also the classic recurrent network encounters some difficulties in the face of long-term dependence problems [25]. These difficulties have their origin in the problem of gradient descent [26]. According to Lin et al. in [27] the exponential decrease in the gradient means that the weights of the distant values do not change and, therefore, the network cannot be trained effectively. All internal recurrent networks suffer of this problem, which makes NARs models very adequate for use in forecasting and modeling time series [25].

The NAR model is used to forecast the values of a time series $y(t)$, using the d past values of the series $y(t)$. The NAR model has the following formula [9, 25]:

$$y(t) = F(y(t-1), y(t-2), \dots, y(t-d)) + e(t) \quad (1)$$

where the function $F(\cdot)$ is, in our case, a neural network. Therefore, the purpose is to train the model in order to approximate the unknown function by optimizing the network bias and weights. The term $e(t)$ represents the approximation error at time t . The d elements $y(t-1), y(t-2), \dots, y(t-d)$, are called feedback delays. The architecture used is a Multi-Layer Perceptron (MLP) composed of three layers: input layer, hidden layer(s) and output layer. The number of neurons per layer and hidden layers are utterly flexible and optimized via a trial and error procedure to obtain the network topology that could give the best performance.

In the intended application, the NAR is used to predict the appliance's power consumption. The inputs are the delayed versions of the consumption power, and the output the next value in the series $y(t)$. In order to find the best delays, we trained a model with a specific topology, varying the number of delays. As it will be explained later on, we shall use power series of four different appliances: kettle, Fridge, Dish-washer and Washing Machine. The RMSEs (Root Mean Square Error) that were obtained in the test set are shown in Table 1.

As it can be seen, there is not a specific delay that obtained the best values for all appliances. Using the average RMSE, the best value is obtained with 4 delays and the worst performance was obtained with 10 delays. We shall use 4 delays in the models from now on.

After the delays defined, the next step is to determine the number of hidden neurons and number of hidden layers to be used in the model.

Table 1 RMSE (W) with various delays

Delays	Kettle	Fridge	Dishwasher	Washing machine	Mean
2	78.16	24.97	49.95	38.97	48.01
4	78.51	24.92	34.70	38.96	44.27
6	78.71	27.08	46.06	39.08	47.73
8	78.68	24.97	47.83	38.07	47.38
10	82.19	25.42	61.60	38.72	51.98
12	79.45	25.01	52.07	38.12	48.66

Table 2 Statistical indicators obtained with various number of hidden layers and hidden neurons: RMSE (W) and MAE (W)

Topology		Kettle		Fridge		Dishwasher		Washing machine	
Number of hidden layer	Number of hidden neurons	RMSE	MAE	RMSE	MAE	RMSE	MAE	RMSE	MAE
1	2	92.36	50.23	25.26	4.67	46.75	5.91	38.53	3.46
1	4	78.96	10.8	25.75	6.89	34.51	2.52	38.84	2.74
1	6	78.63	5.9	24.95	1.62	56.22	7.77	39.47	2.88
1	8	78.51	5.15	24.92	1.70	34.70	2.59	38.96	3.18
1	10	78.54	6.31	24.92	1.63	56.85	7.84	38.91	3.59
1	12	80.67	20.22	24.97	1.82	33.24	1.53	39.34	3.24
2	2–4	119.46	9.81	46.06	38.24	57.65	8.01	51.69	5.78
2	3–6	79.64	10.47	25.31	5.00	61.87	8.54	38.61	4.21
2	6–10	78.77	7.29	25.24	3.55	56.39	8.11	39.78	2.98
2	8–3	81.23	5.52	25.22	4.37	55.46	7.44	48.93	5.50

Several tests were performed in order to determine the number of hidden layers and the number of hidden neurons in each layer. For that, the RMSE and the MAE (Mean Absolute Error) criteria. were used. For the training of the network we used the Levenberg-Marquardt algorithm as it is recognized to be the best method to train static neural networks [28]. Some results are presented in Table 2. Note that all the experimental results are obtained for the test dataset.

As before, there is not a single topology that obtains the best values for all cases. Using again the average values of the RMSE we can conclude that the best configuration contains 8 neurons in one hidden layer. The performance of this configuration in terms of RMSE are: 78.51 W, 24.92 W, 34.70 W, and 38.96 W respectively for Kettle, Fridge, Dishwasher, and Washing Machine.

3.1 Evaluation Criteria

To assess Artificial Neural Network forecasting performance, many prediction accuracy catalogs are proposed in the literature. We have selected among others the Root Mean Square Error (RMSE), and the Mean Absolute Error (MAE), which seem to be the most used metric in model assessment [16, 29–31].

$$RMSE = \sqrt{\frac{1}{N} \sum_1^N (y - p)^2} \quad (2)$$

$$MAE = \frac{\sum_1^N |y - p|}{N} \quad (3)$$

In (2) and (3) N is the number of patterns, y are the measured values and p the predicted values

3.2 Dataset

Since the work of Kolter et al. [32] and the deployment of the smart meter, several datasets containing data from house-hold electrical consumption as well as individual appliance consumption have been made available for the public [23, 33, 34].

We used the UK-DALE (United Kingdom-Domestic Appliance Level) data set, which regroups aggregated and disaggregated device data for five houses in London, England, over several years. Aggregate data represents the power demand of all devices in the house. The power data of each device was measured via smart sockets on single devices which measured their individual energy demands. The individual power of each appliance and the global aggregated power data are sampled every six seconds (0.1667 Hz). The labeled measurement data of each device are also available.

The dataset regroups the measurements of over 10 types of devices, however, we used four devices in all our experiments: Kettle, fridge, dishwasher, and washing machine which are popular appliances for evaluating energy disaggregation algorithms [23, 24, 35, 36]. We selected these devices because all exist in at least 2 houses in the dataset. This means that, for each device, we can train our model in at least 1 house and test on another house not seen during training. Moreover, these four devices consume a considerable proportion of energy and expose a range of various power features from the two-states on/off of the kettle to the complex characteristics of the washing machine.

4 Results

We trained our ANN-NAR model on house 5 (Train dataset) of the UK-DALE dataset and evaluated the testing performance on house 2. House 2 (Test dataset) contains data for several months between 17-02-2013 and 10-10-2013 and house 5 (Train dataset) contains data measurements from 29-06-2014 to 13-11-2014. The results in terms of the MAE criterion in comparison with some works mentioned on the state of the art are presented in Table 3. We point out that all the 5 methods used techniques to disaggregate the device data from the aggregate consumption data of the house prior to predict the device power consumption. Here we only used the historical data of each device to train our model. It should also be noted that the experiments were carried out over the entire period that constitutes the test dataset (house 2 data).

Table 3 shows that the developed model has surpassed all the 5 other state-of-the-art methods, in terms of the MAE criterion, for every appliance. FHMM and CO proposed by Batra et al. present the worst performance, followed by LSTM proposed by Kelly et al., for Kettle and Fridge. The Seq2point proposed by Zhang et al. outperforms LSTM, CO and FHMM on the four appliances but falls behind our NAR model, where the MAE was reduced by 33%, 92%, 90% and 75% for the Kettle, Fridge, Dishwasher and washing machine, respectively. The Autoencoder developed by Kelly et al. outperforms Seq2point for the kettle and dishwasher, but is still worse than our model, which obtains a reduction in MAE of 14% and 89% respectively.

To assess the performance of the proposed method, Figure 1 shows the measured power and the predicted power, for the 4 different appliances and for short periods. Notice, however, that the results shown in Table 3 are applicable to the whole test set.

Table 3 Mean absolute error (MAE) (W) performance for UK-DALE dataset on a house not seen during training. Best performances are shown in bold

Methods	MAE (W)			
	Kettle	Fridge	Dishwasher	Washing machine
LSTM (Kelly and Knottenbelt [35])	16	36	168	109
Autoencoder (Kelly and Knottenbelt [35])	6	26	24	18
CO (Batra et al. [36])	73	73	74	70
FHMM (Batra et al. [36])	98	67	110	107
Seq2point (Zhang et al. [24])	7.43	20.89	27.70	12.66
Our model (NAR this paper)	5.15	1.70	2.59	3.18

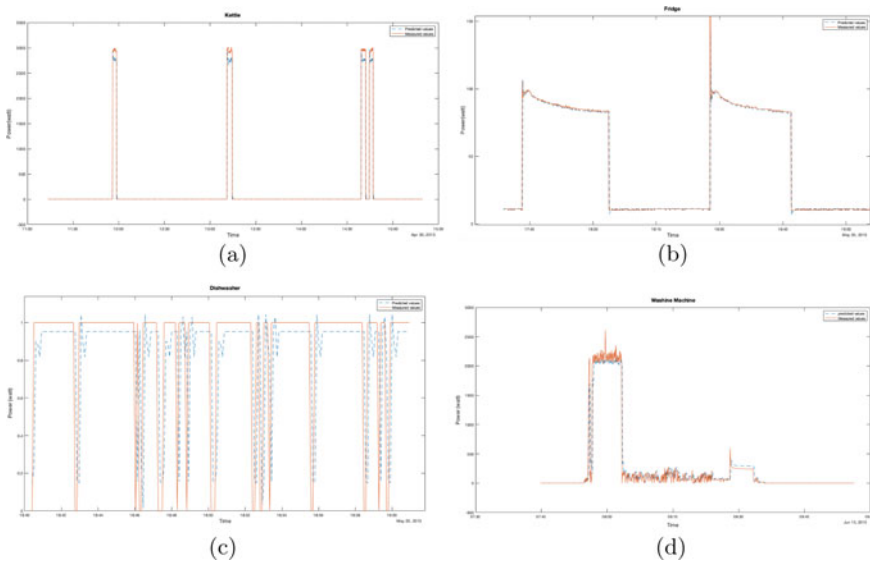


Fig. 1 Predicted versus measured appliance power consumption for **a** Kettle, **b** Fridge, **c** Dishwasher and **d** Washing machine

5 Conclusion

In this study, we proposed a non-linear autoregressive neural network model for forecasting appliance power consumption. We have considered four appliances that consume an important proportion of energy and exhibit different operation patterns, from two states to more complex pattern. We have tested the impact of hidden neurons and hidden layers, as well as number of delays on the performances of the model. It has also been shown that the model is highly efficient, obtaining better prediction performance than some state-of-the-art methods.

Our future research will focus on studying the effect of exogenous data on the forecasting method and how data other than power could be used to improve the accuracy of forecasting.

Acknowledgements The authors would like to acknowledge the support of Programa Operacional Portugal 2020 and Operational Program CRESC Algarve 2020 grant 01/SAICT/2018. Antonio Ruano also acknowledges the support of Fundação para a Ciência e Tecnologia grant UID/EMS/50022/2020, through IDMEC, under LAETA

References

1. US Department of Energy (DOE) (2015) An Assessment of energy technologies and research—Chapter 1. Enabling Mod Electr Power Syst Technol Rev September:99
2. US Department of Energy (DOE) (2015) An Assessment of energy technologies and research—Chapter 5. Enabling Mod Electr Power Syst Technol Rev
3. Ruano A, Hernandez A, Ureña J, Ruano M, Garcia J (2019) NILM techniques for intelligent home energy management and ambient assisted living: a review. *Energies* 12(11):1–29
4. Zoha A, Gluhak A, Imran MA, Rajasegarar S (2012) Non-intrusive load monitoring approaches for disaggregated energy sensing: a survey. *Sensors (Switzerland)* 12(12):16838–16866
5. Barbato A, Capone A, Rodolfi M, Tagliaferri D (2011) Forecasting the usage of household appliances through power meter sensors for demand management in the smart grid. In: 2011 IEEE international conference on smart grid communications, SmartGridComm 2011, pp 404–409
6. Huber P, Gerber M, Rumsch A, Paice A (2018) Prediction of domestic appliances usage based on electrical consumption. *Energy Inf 1(S1)*:
7. Abera FZ, Khedkar V (2020) Machine learning approach electric appliance consumption and peak demand forecasting of residential customers using smart meter data. *Wirel Pers Commun* 111(1):65–82
8. Hatami S, Pedram M (2010) Minimizing the electricity bill of cooperative users under a quasi-dynamic pricing model, pp 421–426
9. Ruiz L, Cuéllar M, Calvo-Flores M, Jiménez M (2016) An application of non-linear autoregressive neural networks to predict energy consumption in public buildings. *Energies* 9(9):684
10. Zhang F, Deb C, Lee SE, Yang J, Shah KW (2016) Time series forecasting for building energy consumption using weighted Support Vector Regression with differential evolution optimization technique. *Energy Build* 126:94–103
11. Fumo N, Rafe Biswas MA (2015) Regression analysis for prediction of residential energy consumption. *Renew Sustain Energy Rev* 47:332–343
12. Deb C, Eang LS, Yang J, Santamouris M (2016) Forecasting diurnal cooling energy load for institutional buildings using Artificial Neural Networks. *Energy Build*
13. Gul MS, Patidar S (2015) Understanding the energy consumption and occupancy of a multi-purpose academic building. *Energy Build*
14. Ding N, Benoit C, Foggia G, Besanger Y, Wurtz F (2016) Neural network-based model design for short-term load forecast in distribution systems. *IEEE Trans Power Syst*
15. Motepe S, Hasan AN, Stopforth R (2019) Improving load forecasting process for a power distribution network using hybrid AI and deep learning algorithms. *IEEE Access*
16. Hong Y, Zhou Y, Li Q, Xu W, Zheng X (2020) A deep learning method for short-term residential load forecasting in smart grid. *IEEE Access* 8:55785–55797
17. Jia Y, Wang H, Batra N, Whitehouse K (2019) A tree-structured neural network model for household energy breakdown. In: Web Conference 2019—Proceedings of World Wide Web Conference WWW 2019, pp. 2872–2878 (2019)
18. Welikala S, Thelasingha N, Akram M, Ekanayake PB, Godaliyadda RI, Ekanayake JB (2019) Implementation of a robust real-time non-intrusive load monitoring solution. *Appl Energy* 238:1519–1529
19. Devlin MA, Hayes BP (2019) Non-intrusive load monitoring and classification of activities of daily living using residential smart meter data. *IEEE Trans Consum Electron* 65(3):339–348
20. Çavdar IH, Faryad V (2019) New design of a supervised energy disaggregation model based on the deep neural network for a smart grid. *Energies* 12(7):
21. Fagiani M, Bonfigli R, Principi E, Squartini S, Mandolini L (2019) A non-intrusive load monitoring algorithm based on non-uniform sampling of power data and deep neural networks. *Energies* 12(7):
22. Machlev R, Belikov J, Beck Y, Levron Y (2019) MO-NILM: A multi-objective evolutionary algorithm for NILM classification. *Energy Build*

23. Kelly J, Knottenbelt W (2015) The UK-DALE dataset, domestic appliance-level electricity demand and whole-house demand from five UK homes. *Sci Data*
24. Zhang C, Zhong M, Wang Z, Goddard N, Sutton C (2018) Sequence-to-point learning with neural networks for non-intrusive load monitoring. In: 32nd AAAI conference on artificial intelligence. AAAI 2018:2604–2611
25. Ibrahim M, Jemei S, Wimmer G, Hissel D (2016) Nonlinear autoregressive neural network in an energy management strategy for battery/ultra-capacitor hybrid electrical vehicles. *Electr Power Syst Res*
26. Bengio Y, Simard P (1994) Frasconi P (1994) Learning long-term dependencies with gradient descent is difficult. *IEEE Trans Neural Networks*
27. Lin T, Horne BG, Giles CL (1998) How embedded memory in recurrent neural network architectures helps learning long-term temporal dependencies. *Neural Netw*
28. Ruano AEB, Jones DI, Fleming PJ (1991) A new formulation of the learning problem for a neural network controller. In: 30th IEEE conference on decision and control, pp 865–866
29. Gao X, Li X, Zhao B, Ji W, Jing X, He Y (2019) Short-term electricity load forecasting model based on EMD-GRU with feature selection. *Energies* 12(6):1–18
30. Chai T, Draxler RR (2014) Root mean square error (RMSE) or mean absolute error (MAE)?—Arguments against avoiding RMSE in the literature. *Geosci Model Dev*
31. Kim SH, Lee G, Kwon GY, Kim DI, Shin YJ (2018) Deep learning based on multi-decomposition for short-term load forecasting. *Energies*
32. Zico Kolter J, Johnson MJ (2011) REDD: a public data set for energy disaggregation research. In *Proceedings of the SustKDD workshop on data mining applications in sustainability*, San Diego, CA, USA, 21 Aug 2011
33. Anderson, K, Ocleanu A, Benitez D, Carlson D, Rowe A, Berges M (2012) BLUEED: a fully labeled public dataset for event-based non-intrusive load monitoring research. In: *Proceedings of the 2nd workshop on data mining applications in sustainability*, Beijing, China, 12 Aug 2012
34. Gao J, Giri S, Kara EC, Bergés M (2014) PLAID: A public dataset of high-resolution electrical appliance measurements for load identification research. In: *BuildSys 2014—Proceedings of the 1st ACM conference on embedded systems for energy-efficient buildings*
35. Kelly J, Knottenbelt W (2015) Neural NILM: Deep neural networks applied to energy disaggregation. In: *Proceedings of the 2nd ACM international conference on embedded systems for energy-efficient built environments*, Seoul, Korea, pp 55–64, 4–5 November 2015
36. Batra N, Kelly J, Parson O, Dutta H, Knottenbelt W, Rogers A, Singh A, Srivastava M (2014) NILMTK: an open source toolkit for non-intrusive load monitoring. In: *e-Energy 2014—Proceedings of the 5th ACM international conference on future energy systems*

Numerical Analysis of Bi-fluid PV/T Hybrid Collector Using the Finite Difference Method



Oussama El Manssouri, Bekkay Hajji, Antonio Gagliano,
and Giuseppe Marco Tina

Abstract The PV/T is called as a hybrid bi-fluid type solar collector when both fluids (water and air) are used as working fluids. This type of collector provide a wide range of thermal applications and several modes can be executed depending on energy needs and applications: air mode, water mode and simultaneous mode (air and water). This paper presents a numerical analysis of PV/T bi-fluid collector using the finite difference method. Energy balance equations were established for each layer and solved using the Gauss–Seidel iteration method. The performance of the PV/T hybrid is evaluated according to the operating mode of the fluid (independently and simultaneously). The simulation results are compared with literature (Modeling and performances assessments of PV/T bifluid hybrid collector: Three cooling modes operation case. <https://doi.org/10.1109/iceit48248.2020.9113233>, [10]), and indicate that when both fluids are used simultaneously, the overall electrical and thermal performance of the hybrid collector is considered satisfactory compared to the situation where two fluids operate independently.

Keywords PV/T collector · Bi-fluid · Performance analysis · Finite difference · Efficiency

Abbreviations

PV Photovoltaic
PV/T Photovoltaic/thermal

O. El Manssouri (✉) · B. Hajji
Renewable Energy, Embedded System and Data Processing Laboratory, National School of Applied Sciences, Mohamed First University, Oujda, Morocco
e-mail: elmanssouri.fso@gmail.com

A. Gagliano · G. M. Tina
DIEEI: Department of Electric, Electronic and Computer Engineering, University of Catania, Catania, Italy

Greek Symbols

δ	Thickness (m)
k	Thermal conductivity ($\text{Wm}^{-1} \text{A}^{-1}$)
η	Efficiency
τ	Transmittance
α	Absorptance
ε	Emissivity

Nomenclature

T	Temperature (K)
U	Overall heat loss coefficient ($\text{Wm}^2 \text{K}^{-1}$)
G	Solar irradiance (Wm^{-2})
Ac	Solar collector surface area (m^2)
h	Heat transfer coefficient ($\text{Wm}^{-2} \text{K}^{-1}$)

Subscripts

am	Ambient
sky	Sky
g	Glass
c	PV cell
ted	Tedlar
a	Air
w	Water
ins	Insulation
in	Input
ou	Output
f	Fluid
th	Thermal
elec	Electrical
end	Conduction
hf	Convection
hray	Radiation
$\eta_{f_{in}}$	Efficiency of fins

1 Introduction

Photovoltaic technology converts a small quantity of solar energy into electricity and the rest remains in the form of heat. This generated heat, not converted into energy, increases the temperature of the photovoltaic modules, which reduces their electrical efficiency [1]. Indeed, hybrid PV/T technology has been developed to effectively cool the photovoltaic module using air or water as a coolant [2]. Depending on the type of working fluid used, PV/T collectors can be classified into three families, namely: PV/T water collector, PV/T air collector, and PV/T bi-fluid (air/water) collector [3, 4].

Tripanagnostopoulos [5] et al. were the first to initiate research on the structure of the bi-fluid PV/T hybrid collector [5]. This type of hybrid collector offers more options, in which hot air or hot water can be utilized to supply the energy demand in different applications.

Assoa et al. [6] conducted a study on a PV/T solar collector which used water and air as operating fluids [6]. In their study, 2D steady state analyzes are developed. In addition, experimental indoor studies were carried out and the results were compared with the results of the simulation and found to be in good agreement.

Bakar et al. have developed a mathematical model based on finite difference method for studying the performance of the bi-fluid PV/T hybrid collector [7]. Su et al. [8] studied four PV/T hybrid system configurations with dual channels for different fluids [8]. The simulation numerical based an energy balance and the analysis of electrical and thermal performance was performed under operating conditions in China. They specified that the PV/T water-water collector is the best configuration which gives satisfactory results in electrical and thermal efficiency. In addition, a numerical method using finite difference methods based on a matrix resolution procedure has been proposed by Jarimi et al. [9] for the evaluation of the performance of bi-fluid PV/T hybrid collector [9]. This study was made for the independent and simultaneous operating mode with the experimental validation of numerical model.

In this work, a numerical analysis of bi-fluid PV/T hybrid collector using the finite difference method is developed and discussed. Then, the model is implemented in the MATLAB software and the equations of the energy balance of the PV/T bi-fluid are solved using the iterative method of Gauss–Seidel. Finally, the performance of the bi-fluid PV/T hybrid collector is evaluated when the two fluids worked independently and simultaneously.

2 Design PV/T

In this study, a simple PV/T bi-fluid hybrid collector is illustrated in Fig. 1. In the PV module consists of: a glass front cover, photovoltaic cells, a tedlar attached to a cooling unit, and thermal insulation. Thus, for the heating components consist of water in a copper tube in the form of a coil and a single-pass air channel with fins.

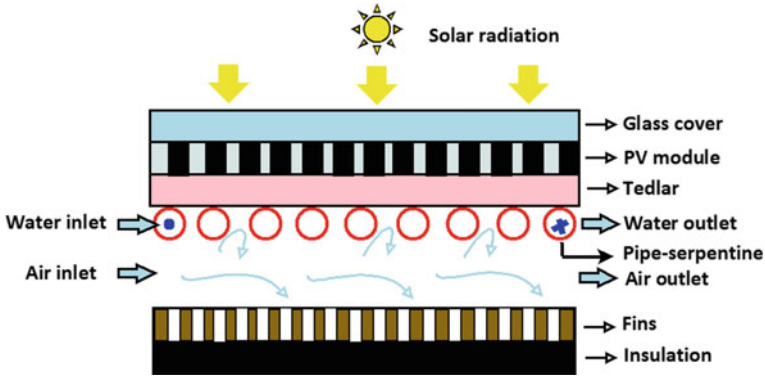


Fig. 1 The bi-fluid PV/T hybrid collector concept

In order to simplify this thermal model, some assumptions have been taken into consideration:

- The sky can be assimilated to a black.
- The proprieties physical of materials of collector are assumed to be constant.
- The effects due to the curvature of the serpentine copper tube are negligible [7].

2.1 Energy Balance Equations

A numerical study using the finite difference method is conducted to solve the system of partial differential Eqs. (2)–(7). The temporal derivatives have been replaced by:

$$\frac{dT}{dt} = \frac{T^t - T^{t-dt}}{\Delta t} \tag{1}$$

The equations are written considering the assumptions above:

For the PV Module

$$\begin{aligned} \rho_c \delta_c C_c \frac{T_c^t - T_c^{t-dt}}{dt} &= U_i \cdot (T_{sky} - T_c^t) \\ &\quad - h_{cnd-c-ted} \cdot (T_c^t - T_{ted}^t) + G \cdot \alpha_c \cdot F \cdot \tau_g \\ &\quad - G \cdot \eta \cdot \alpha_c \cdot \tau_g \cdot F \end{aligned} \tag{2}$$

For the Tedlar

$$\rho_{ted} \delta_{ted} C_{ted} \frac{T_{ted}^t - T_{ted}^{c-ted}}{dt} = h_{cnd-c-ted} \cdot (T_c^t - T_{ted}^t) - h_f \cdot (T_{ted}^t - T_a^t)$$

$$\begin{aligned}
& - h_f \cdot (T_{ted}^t - T_w^t) - h_{ray-ted-ins} \cdot (T_{ins}^t - T_{ted}^t) \\
& + \alpha_{ted} \cdot \tau_g \cdot (1-F) \cdot G
\end{aligned} \tag{3}$$

For the Air Flow

$$\begin{aligned}
\rho_a \delta_a C_a \frac{T_a^t - T_a^{t-dt}}{dt} &= h_f \cdot (T_{ted}^t - T_a^t) \\
& - 2 \cdot \dot{m}_a C_a \cdot (T_a^t - T_{a-in}^t) - h_f \cdot \eta_{fin} \cdot (T_a^t - T_{ins}^t)
\end{aligned} \tag{4}$$

For the Water Flow

$$\begin{aligned}
\rho_w \delta_w C_w \frac{T_w^t - T_w^{t-dt}}{dt} &= h_f \cdot (T_{ted}^t - T_w^t) \\
& - 2 \cdot \dot{m}_a C_a \cdot (T_w^t - T_{w-in}^t) - h_f \cdot (T_{ted}^t - T_w^t)
\end{aligned} \tag{5}$$

For the Fins

$$N_{fin} \left(- K_{fin} \cdot A_{fin} \frac{dT_{fin}}{dz} \right) = h_{cvfin,air} N_{fin} A_{c,fin} \cdot (T_{fin} - T_a) \tag{6}$$

For the Thermal Insulation

$$\begin{aligned}
\rho_{ins} \delta_{ins} C_{ins} \frac{T_{ins}^t - T_{ins}^{t-dt}}{dt} &= h_f \cdot \eta_{fin} \cdot (T_a^t - T_{ins}^t) \\
& - U_i \cdot (T_{ins}^t - T_{amb}) \\
& - h_{ray-ted-ins} \cdot (T_{ins}^t - T_{ted}^t)
\end{aligned} \tag{7}$$

The heat transfer coefficients of the PV/T hybrid collector are calculated according to the following [10, 11].

2.2 Performances Assessment of the Bi-Fluid PV/T Hybrid Collector

The overall thermal energy Q_{th} , generated by the PV/T hybrid collector is given by the summation of the thermal energy generated by both air and water as follows [7].

$$Q_{th} = \dot{m}_a C_a (T_{a-ou} - T_{a-in}) + \dot{m}_w C_w (T_{w-ou} - T_{w-in}) \tag{8}$$

The total thermal efficiency η_{th} of the PV/T hybrid collector can then be calculated as follows:

$$\eta_{th} = \frac{\dot{m}_a C_a (T_{a-ou} - T_{a-in}) + \dot{m}_w C_w (T_{w-ou} - T_{w-in})}{GA_c} \tag{9}$$

The electrical efficiency of the PV/T bi-fluid can be given in the form:

$$\eta_e = \eta_{ref}[1 - \beta_{ref}(T_c - T_{ref})] \tag{10}$$

2.3 Theoretical Solution Procedures

The PV/T bi-fluid hybrid system is modeled in this work using the finite difference method. Translate the temperature variations in the different layers considered as state variables. This iterative process continued until the calculated values converged, and the convergence value was set to 10^{-4} . After the replacement of the scheme in differential equations of the system, Eqs. (2)–(7) were algebraically solved and rearranged to matrix form, as shown below. The vector of temperatures of the various layers $\{T_i^t\}$ is calculated by solving the matrix equation $[M]\{T_i^t\} = \{S_i^t\}$, using the Gauss Seidel method. These temperatures were used as variable input parameters. The climatic data for solar radiation, ambient temperature, and inlet temperature of fluid are shown in Fig. 2.

$$\begin{pmatrix} M1 & -h_{cnd-c-ted} & 0 & 0 & 0 \\ -h_{cnd-c-ted} & M2 & -h_f & -h_f & 0 \\ 0 & -h_f & M3 & 0 & -h_f \cdot \eta_{fin} \\ 0 & -h_f & 0 & M4 & 0 \\ 0 & -h_{ray-ted-a} & -h_f \cdot \eta_{fin} & 0 & M5 \end{pmatrix} \begin{pmatrix} T_c^t \\ T_{ted}^t \\ T_a^t \\ T_w^t \\ T_{ins}^t \end{pmatrix} = \begin{pmatrix} S1 \\ S2 \\ S3 \\ S4 \\ S5 \end{pmatrix}$$

where

$$H_i = \frac{\rho_i \delta_i C_i}{dt} \text{ with } i \text{ is number of each layer}$$

$$M1 = H1 + U_i + h_{cnd} \quad S1 = H1 * T_c^{t-dt} + S_c + U_i \cdot T_{sky} \tag{11}$$

$$\begin{aligned} M2 &= H2 + h_{cnd} + h_{cnd} + h_{cnd} + h_{ray-ted-a} \\ S1 &= H1 * T_c^{t-dt} + S_c + U_i \cdot T_{sky} \end{aligned} \tag{12}$$

$$M3 = H3 + 2 \cdot \dot{m}_a C_a \quad S3 = H3 * T_a^{t-dt} + 2 \cdot \dot{m}_a C_a \cdot T_{a-in}^t \tag{13}$$

$$M4 = H4 + 2 \cdot \dot{m}_w C_w \quad S4 = H4 * T_w^{t-dt} + 2 \cdot \dot{m}_w C_w \cdot T_{w-in}^t \tag{14}$$

$$M5 = H5 + h_f \cdot \eta_{fin} + U_i \quad S5 = H5 * T_{iso}^{t-dt} + U_i \cdot T_{amb} \tag{15}$$

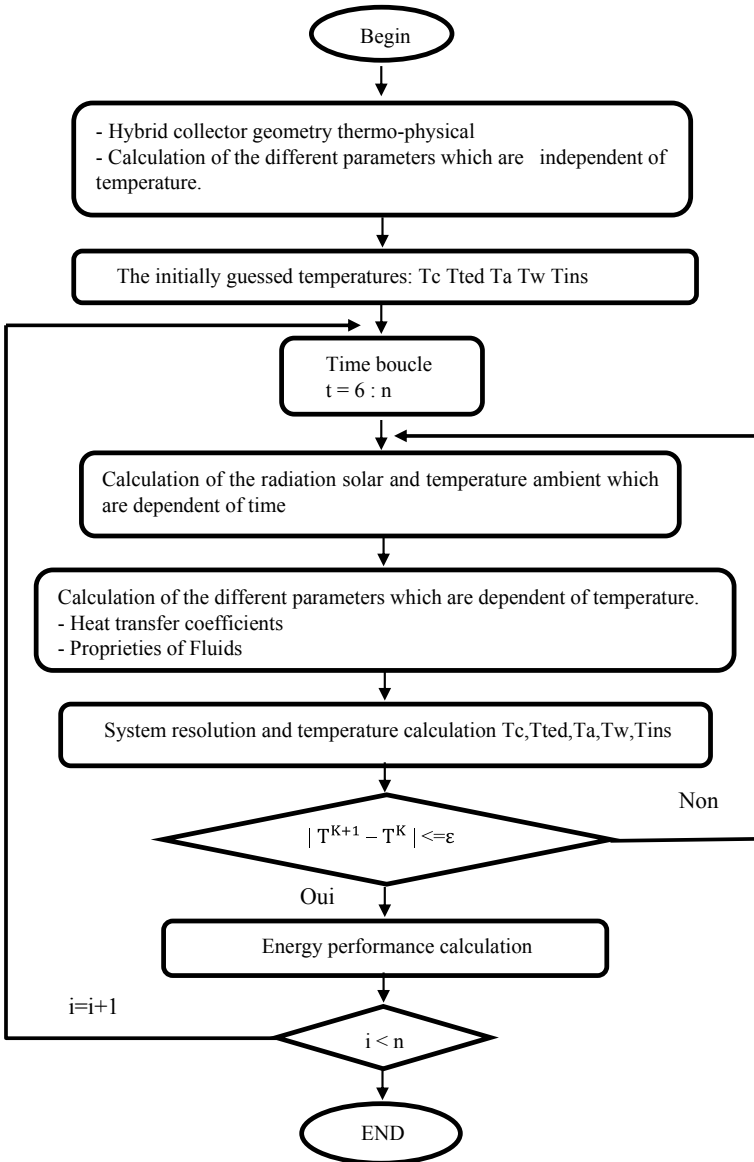


Fig. 2 Simplified flowchart for system simulation

3 Results and Discussion

In this part, the simulation results are achieved by considering the environmental-related conditions shown in Fig. 3.

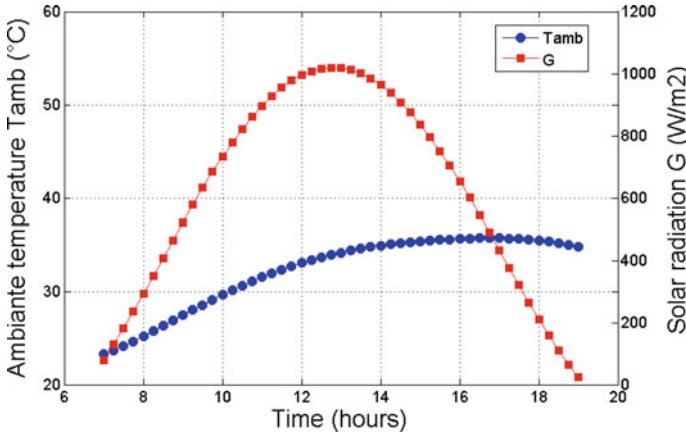


Fig. 3 Temporal variation of ambient temperature T_{amb} and solar irradiance G

The temperature profile of the hybrid collector PV/T is shown in Figs. 4 and 5. In Fig. 4, we observe the temperature evolution of three layers of PV/T namely layer of PV Cell, layer of Tedlar and layer of insulation. According to this figure, the highest temperature recorded is that of the layer of photovoltaic cells, which reaches a maximum of 58.96 during the peak of solar radiation (i.e. from 12:00 to 14:00).

In Fig. 5, the fluid outlet temperatures record minimum values of 30.99 °C and 29.51 °C respectively for air and water and this at 06:00 am with a solar radiation intensity of 150 W/m². In addition, the maximum fluid outlet temperatures are 46.88 °C and 44.20 °C respectively for air and water. These values were recorded around 13:30 with a solar radiation of 1000.39 W/m².

Figure 6 illustrates the trend of the temperature of PV Cell as well as the electrical efficiency of the PV/T collector.

Fig. 4 The evolution of PV/T bi-fluid temperature profiles

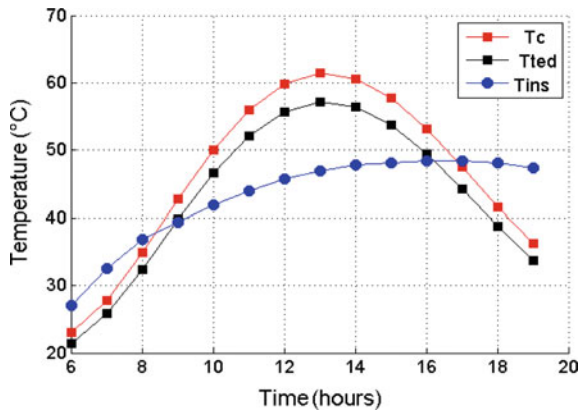


Fig. 5 The input and output temperatures of fluids

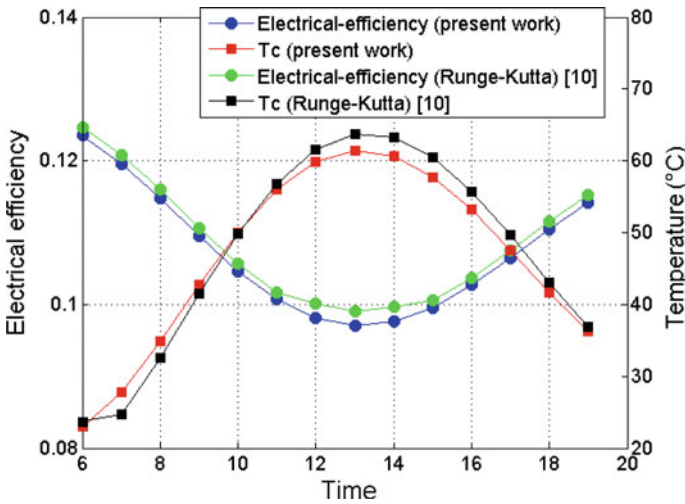
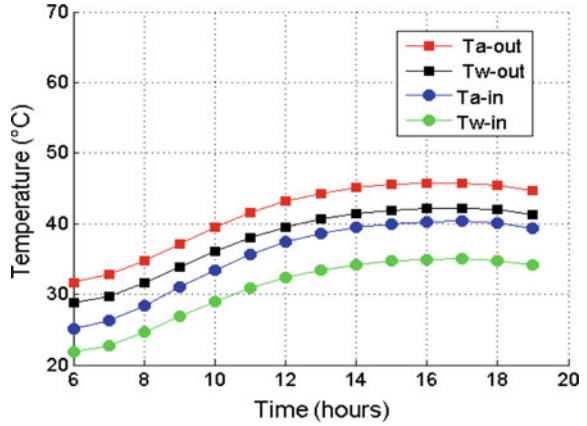


Fig. 6 Comparisons of the temperature of PV Cell and electrical efficiency with literature results [10]

As well known, the electrical efficiency is influenced by the increase in solar radiation as well as by the increase in the temperature of the PV cell. According to Fig. 6, the decrease in electrical efficiency with the increase in temperature of the PV module, from 6:00 to 13:00 to reach a minimum value from 12:00 to 14:00. After that, it is gradually increased with the reduction of the PV temperature.

It is observed that the simulated values are in accord with results in the literature [10]. For the profiles of Figs. 4 and 5 is not compared with [10] because it is not plotted in [10].

Fig. 7 Comparisons of PV/T thermal efficiency with literature results [10]

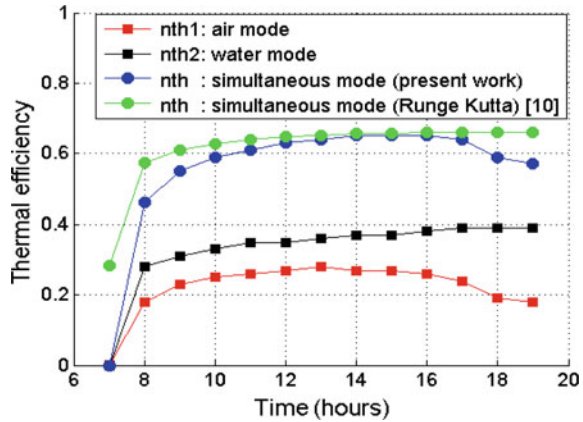


Figure 7 shows the trend of the thermal efficiency of the PV/T collector for running modes: water mode air mode, and simultaneous modes (air and water). The mass flow of air and water are fixed at 0.034 kg/s and 0.0066 kg/s respectively.

For the air mode, the evaluated thermal efficiency of the PV/T collector, noted (n_{th1}), achieves a maximum value of 24.17%. When the water mode is operated, the thermal efficiency, noted (n_{th2}) reaches a maximum value of 38.11%.

For the simultaneous mode, the total thermal efficiency of PV/T bi-fluid hybrid-collector is evaluated as the sum of the both thermal efficiencies (n_{th1} , air mode) and (n_{th2} , water mode) and reaches a maximum value of 62.8%.

The small difference in the first part between our method and method Runge–kutta [10] is due to the initial condition of fluids.

We conclude that the electrical and thermal performances of bi-fluid PV/T hybrid collector are better when both fluids operated simultaneously than in independent mode.

4 Conclusion

In this article, a numerical model based on the finite difference method was developed and implemented in MATLAB software using the iterative Gauss–Seidel method. This model allowed us to evaluate the performance of the PV/T bifluid hybrid collector for three running modes: water mode, air mode and simultaneous modes (air and water). The simulations results demonstrate that when two fluids are working simultaneously, the overall electrical and thermal performance of the hybrid collector is regarded as satisfactory compared to the situation where both fluids are operated independently.

The following conclusions are made:

- The maximum thermal efficiency increases to 62.82% while the electrical efficiency decreases to reach the value of 9.5% at the same time when the global radiation reaches its maximum of 1000 W/m².
- Better performance of thermal and electrical efficiency when air and water are exploited simultaneously.
- Comparison and validation of the results obtained with other method presented in the literature [10].
- The presented bi-fluid PV/T hybrid collector will allow the total exploitation of solar energy and it will be able to use in a range of potential applications and in various fields.

References

1. Fuentes M, Vivar M, Casa JD, Aguilera J (2018) An experimental comparison between commercial hybrid PV-T and simple PV systems intended for BIPV. *Renew Sustain Energy Rev* 93:110–120. <https://doi.org/10.1016/j.rser.2018.05.021>
2. El Manssouri O, El Fouas C, Hajji B, Rabhi A, Tina GM, Gagliano A (2019) Performance analysis of bi-fluid photovoltaic/thermal (PV/T) solar collector. <https://doi.org/10.1109/IRSE48032.2019.9078257>
3. Roonak D, Yavar K (2017) Design and fabrication of a bi-fluid type photovoltaic-thermal collector. *Energy*. <https://doi.org/10.1016/j.energy.2017.06.108>
4. Baljit SSS, Chan HY, Adidharma VA, Hamid SA, Fudholi A, Zaidi SH, Othman MY, Sopian K. Mathematical modelling of a dual-fluid concentrating photovoltaic-thermal (PVT) solar collector, *renew. Energy*. <https://doi.org/10.1016/j.renene.2017.08.001>
5. Tripanagnostopoulos Y (2007) Aspects and improvements of hybrid photovoltaic/thermal solar energy systems. *Sol Energy*. <https://doi.org/10.1016/j.solener.2007.04.002>
6. Assoa YB, Menezo C, Fraisse G, Yezou R, Brau J (2007) Study of a new concept of photovoltaic thermal hybrid collector, *Sol Energy* 81. 1132–1143
7. Abu Bakar MN, Othman M, Hj Din M, Manaf NA, Jarimi H (2014) Design concept and mathematical model of a bi-fluid photovoltaic/thermal (PV/T) solar collector. *Renew Energy* 67:153–164. <https://doi.org/10.1016/j.renene.2013.11.052>
8. Su D, Jia Y, Huang X, Alva G, Tang Y, Fang G (2016) Dynamic performance analysis of photovoltaic-thermal solar collector with dual channels for different fluids. *Energy Convers Manag* 120:13–24. <https://doi.org/10.1016/j.enconman.2016.04.095>
9. Jarimi H, Abu Bakar MN, Othman M, Din MH (2016) Bi-fluid photovoltaic/thermal (PV/T) solar collector: experimental validation of a 2-D theoretical model. *Renew Energy* 85:1052–1067 (2016). <https://doi.org/10.1016/j.renene.2015.07.014>
10. El Manssouri O, El Fouas C, Hajji B, Rabhi A, Tina GM, Gagliano A (2020). Modeling and performances assessments of PV/T bifluid hybrid collector: Three cooling modes operation case. <https://doi.org/10.1109/iceit48248.2020.9113233>
11. Incropera FP, DeWitt DP (2007) *Fundamentals of heat and mass transfer*, 6th edn. Wiley, Hoboken, New Jersey, NJ

Signal and Image Processing

A Novel Cryptosystem for Color Images Based on Chaotic Maps Using a Random Controller



Said Hraoui, Mounir Gouiouez, Faiq Gmira, Mohammed Berrada, Abdellatif Jarjar, and A. Oulidi Jarrar

Abstract A new encryption technique for multicolor images is outlined in this study. After vectorization of the clear image, an initialization value will be calculated. This value, allows changing only the first pixel. This pixel will start the encryption process. In parallel, in a first step, we will make a confusion by chaotic vectors entirely controlled by another chaotic vector. In a second step, three chaotic substitution matrices of size (256, 256) will be generated. The passage of each pixel through these matrices will also be controlled by another chaotic vector. Finally, a strong link will be set up between the new pixel state and the previous ones to set up better diffusion/confusion. This step increases the avalanche effect. Testing performed through our algorithm on standard images shows the durability of our system.

Keywords Image encryption · Dynamic encryption · Diffusion · Confusion · Substitution · S-box · Chaos

1 Introduction

The encryption of stored or exchanged images has become a primary necessity in many applications. This requirement was a motivation for the publication of several encryption algorithms [1–4]. Among which chaos-based encryption is no longer used. The mathematical properties of chaotic systems offer great flexibility of symmetric encryption systems. Generally, these algorithms obey to the conditions recommended

S. Hraoui (✉) · M. Berrada · A. O. Jarrar
LIASSE, ENSA, SMBA University, Fez, Morocco
e-mail: said.hraoui@usmba.ac.ma

F. Gmira
LMAEM, Faculty of Economics, UH2C, Casablanca, Morocco

A. Jarjar
School Moulay Rachid, Taza, Morocco

M. Gouiouez
PSCSL, FLDM, SMBA University, Fez, Morocco

by Shannon, namely confusion and diffusion [5]. However, in most of these algorithms, confusion and diffusion are implemented independently [6–9]. This approach presents a source of vulnerability, particularly by some known plaintext attacks [10]. To obtain better resistance to attack by known plaintext or chosen plaintext and to eliminate vulnerabilities, different schemes linking the characteristics of the plaintext image to the flow of diffusion and confusion keys have been developed [6–10]. In the encryption of color images, several algorithms use the three color channels separately. But most of these algorithms ignore the correlations between the R, G and B components, making them more vulnerable to differential attacks. However, these methods have several drawbacks which affect their robustness and of which we cite: (i) Low key space for mono-chaotic maps; (ii) Only one private key will be used in the entire encryption process. This results in an absence of the dynamics of encryption keys. In response to these disadvantages, we will propose in this article an approach based on dynamic confusion-diffusion controlled by a chaotic vector. In a preliminary step a clear image vectorization is prepared. Then, we build an initialization vector based on this matrix. This vector is used to change only the value of the first pixel. In fact, this vector generates a better confusion-diffusion within our encryption scheme and, consequently, a considerable increase in the sensitivity of the encryption algorithm to the plain-image. Then, we will carry out a confusion entirely controlled by a chaotic vector. In a second stage, three chaotic S-boxes of size (256, 256) will be generated. The passage of each pixel through these S-boxes will also be controlled by another chaotic vector. Finally, a chaining will be drawn from the encrypted block to the following clear block for a more accurate Diffusion. The next sections of the work sheds light on the details of our cryptosystem. In Section Four, a performance analysis of this new scheme will be closely explored.

2 Our Method: Encryption Process

This work outlines a new encryption method following Schanon's recommendations (Fig. 1). This chaos-based encryption scheme is fully controlled by chaotic vectors. Thus, Our algorithm is founded on:

1. Generation of chaotic encryption keys C_1 , C_2 and C_3 with coefficients in $\mathbb{Z}/256\mathbb{Z}$;
2. Construction of the control vectors with coefficients in $\mathbb{Z}/3\mathbb{Z}$;
3. Construction of three size S-boxes (256, 256) from the chaotic maps used;
4. Development of control vectors of the diffusion/confusion process;
5. Vectorization of the plain image;
6. Calculating the initialization value;
7. Realize a confusion by the three vectors C_1 , C_2 and C_3 control by the vectors constructed at the second step;
8. Carry out a diffusion/confusion through the 3-Sboxes controlled by a chaotic vector constructed in fourth step;
9. Read the encrypted image.

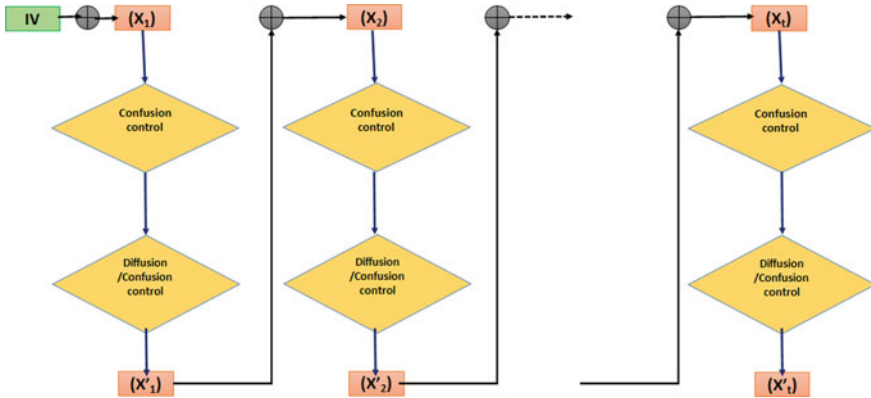


Fig. 1 The encryption process scheme

2.1 Step 1: Generation of Encryption Keys

This includes generating chaotic three vectors C_1 , C_2 and C_3 from two chaotic sequences most commonly used in encryption of images: the logistic map and the tent map.

(a) Logistic Map Construction

Due to its high sensitivity to initial conditions, chaos is largely utilized symmetric cryptography for the construction of cipher keys.

$$\begin{cases} u_0 \in]0.5, 1[, & \mu \in [3.75, 4]; \\ u_{n+1} = \mu \cdot u_n(1 - u_n) \end{cases} \quad (1)$$

These initial conditions guarantee the installation of chaos.

(b) Skew Tent Map Design

The tent suite is a real sequence structured from a step function of the first degree and given by Eq. (2):

$$\begin{cases} v_0 \in]0, 1[, & p \in]0.5, 1[; \\ v_{n+1} = \begin{cases} \frac{v_n}{p} & \text{if } 0 < v_n < p \\ \frac{1-v_n}{1-p} & \text{if } p \leq v_n < 1 \end{cases} \end{cases} \quad (2)$$

The vectors C_1 , C_2 , C_3 are generated by the following algorithm:

Algorithm 1 : Generation of three chaotic vector

```

1: for  $i = 1$  to  $3nm$  do
2:    $C_1(i) = \text{mod}(\text{Floor}(10^{10} * u(i)), 256)$ 
3:    $C_2(i) = \text{mod}(\text{Floor}(10^{11} * v(i)), 256)$ 
4:    $C_3(i) = \text{mod}(\text{Int}(10^{11} * (\sqrt{u(i)} + v(i))), 256)$ 
5: end for

```

The control vector (VC) will be developed by using the Algorithm 2:

Algorithm 2 : Generation of confusion process control vector

```

1: for  $i = 1$  to  $3nm$  do
2:    $VC(i) = \text{mod}(\text{Floor}(10^6 * u(i)), 3) + 1$ 
3: end for

```

(c) Construction of the Three S-Boxes

This stage consists in the construction of three S-Boxes of size (256, 256). To do this, we generate three chaotic vectors (VB), (WB), (TB) by the following algorithm:

Algorithm 3 : (VB), (WB), (TB) Generation

```

1: for  $i = 1$  to 256 do
2:    $VB(i) = \text{mod}(\text{Floor}(10^6 * u(i)), 251) + 4$ 
3:    $WB(i) = \text{mod}(\text{Floor}(10^6 * v(i)), 251) + 4$ 
4:    $TB(i) = \text{mod}(\text{Floor}(10^6 * \text{sup}(u(i), v(i))), 251) + 4$ 
5: end for

```

Sorting in ascending order the first 256 values of the vectors (VB), (WB) and (TB) thus generating respectively the permutations BV , BW and BT . The first line of the three S-boxes is given by Algorithm 4:

Algorithm 4 : Generation of the first line of the three S-BOXes

```

1: for  $i = 1$  to 256 do
2:    $SB1(i, 1) = BV(i)$ 
3:    $SB2(i, 1) = BW(i)$ 
4:    $SB3(i, 1) = BT(i)$ 
5: end for

```

Each line $i > 1$ is obtained by moving the line $i - 1$ by a step indicated by one of the chaotic vectors:

Algorithm 5 : Construction of the remaining lines of the three S-BOXes

```

1: for  $i = 2$  to 256 do
2:   for  $j = 1$  to 256 do
3:      $SB1(i, j) = SB1(i - 1, (j + VB(i)) \bmod 256)$ 
4:      $SB2(i, j) = SB2(i - 1, (j + WB(i)) \bmod 256)$ 
5:      $SB3(i, j) = SB3(i - 1, (j + TB(i)) \bmod 256)$ 
6:   end for
7: end for

```

2.2 Step 2: Vector Generation of Diffusion/Confusion Process Controls

The passage of the pixel x_j in one of the Sboxes is controlled by a chaotic vector (TC) defined by:

Algorithm 6 : Generation of Diffusion/Confusion process control vector

```

1: for  $i = 1$  to  $3nm$  do
2:    $TC(i) = \bmod(\text{Floor}(10^9 * (\frac{u(i)+2*v(i)}{3})), 3) + 1$ 
3: end for

```

2.3 Step 3: The Confusion Process

After extraction of the three color channels R, G and B and their vectorization into a vector $X (x_1, x_2, \dots, x_i, \dots, x_{3nm})$ and calculating the initialization value by the following algorithm:

Algorithm 7 : Generation of the initial value: IV

```

1: for  $i = 2$  to  $3.n.m$  do
2:    $IV = IV \oplus X(i)$ 
3: end for

```

This confusion process is defined according to the algorithm below:

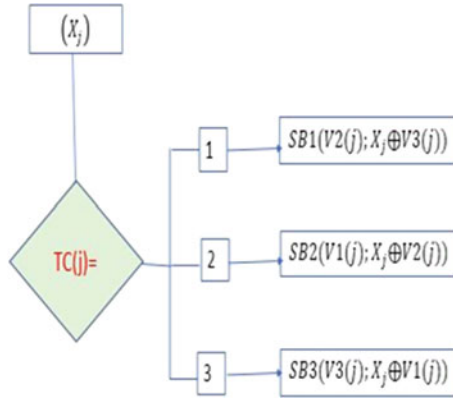


Fig. 2 The Diffusion/confusion process

Algorithm 8 : The confusion algorithm

```

1: for i = 1 to 3nm do
2:   if VC(i)=1 then X(i) = X(i) ⊕ C2(i);
3:   else
4:     if VC(i)=2 then X(i) = X(i) ⊕ C1(i);
5:     else
6:       if VC(i)=3 then X(i) = X(i) ⊕ C3(i);
7:     end for

```

2.4 Step 4: Diffusion/Confusion Process

The diffusion/confusion process is illustrated in Fig. 2:

3 Our Method: Decryption Process

Our algorithm is a symmetric encryption system, so decryption will start from the last block using the inverse operation while keeping the vector chaotic. Each row of the three S-Boxes used is a $\mathbb{Z}/256\mathbb{Z}$ arrangement; therefore, the inverse permutation matrix will be composed of the inverse permutation described in the following algorithm.

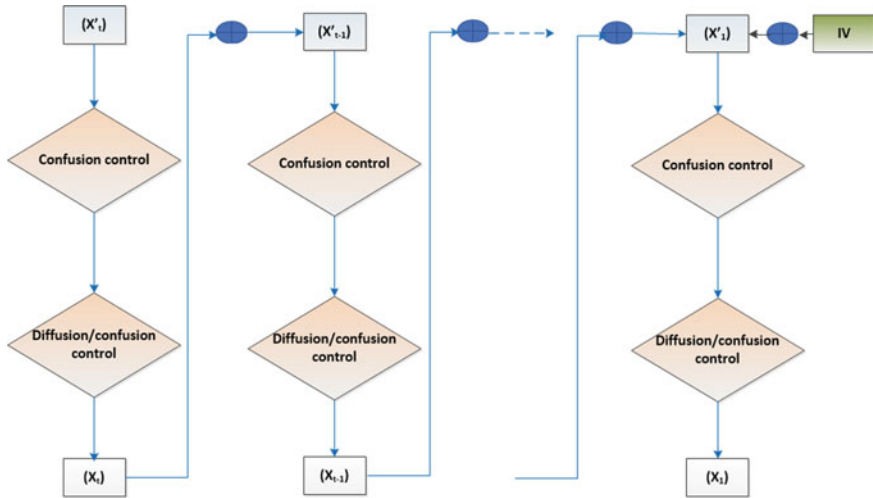


Fig. 3 The decryption process scheme

Algorithm 9 : Construction of the inverse substitution matrix (BS)

```

1: for i = 1 to 256 do
2:   for j = 1 to 256 do
3:     BS1(i, SB1(i, j)) = j
4:     BS2(i, SB2(i, j)) = j
5:     BS3(i, SB3(i, j)) = j
6:   end for
7: end for
    
```

This can be illustrated by Fig. 3.

4 Experimental Results and Performance Analysis

This part will be devoted to proving the performance of our system and studying its behaviour towards attacks. The images for testing are from the USC-SIPI Miscellaneous image database [11]. Thus, by applying our encryption scheme to the COVID19 image, we obtain the results of Fig. 4.

4.1 Histogram Analysis

The uniform distribution of the histogram of the encrypted image implies that the encrypted image does not provide any exploitable elements based on it, indicating

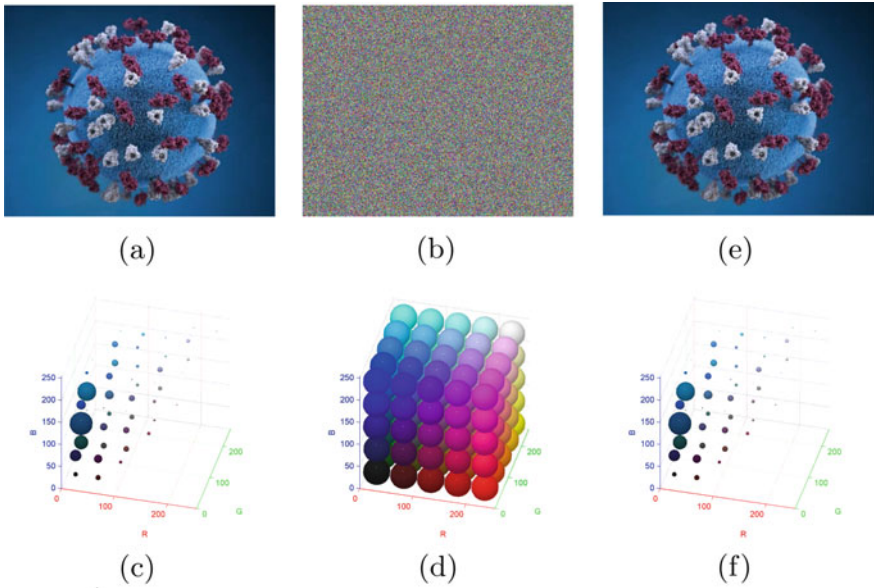


Fig. 4 **a** COVID19 original image **b** Encrypted image, **c** 3-D Histograms of COVID19, **d** 3-D Histograms of encrypted image, **e** Decrypted image, **f** 3-D Histograms of decrypted image

the unpredictability of our encryption algorithm. Figure 4 showing the original and encrypted images and their corresponding 3D histograms. The test image of size $441 \times 564 \times 3$ used is that of COVID19 virus. Through this encryption scheme, the COVID19 image is successfully encrypted. The results of the simulation obtained indicate that the proposed scheme has successfully passed the histogram test.

4.2 Correlation Analysis

A clear image always has a strong correlation between adjacent pixels. This is measured by the constant defined by:

$$r_{xy} = \frac{cov(x, y)}{\sqrt{V(x)}\sqrt{V(y)}} \tag{3}$$

The representative results of the correlation coefficients are well illustrated in Table 1. The comparison presented in Table 3 clearly shows that our approach outperforms well cited in the work [12, 13] encryption schemes. In addition, his performance has a close relationship with the size of the original image. We note that for images of small sizes, our crypto-system is equivalent to statistical perspective to the other methods. But as soon as the size becomes more and more, our approach provides better results.

Table 1 Correlation coefficient of adjacent pixels

Correlation		Image	Size	Original image			Encrypted image		
Algorithm	Vertical			Diagonal	Horizontal	Vertical	Diagonal	Horizontal	
[12]	House	256 × 256	0.8669	0.7321	0.7321	-0.0030	-0.0095	-0.0259	
	Lena	512 × 512	0.9341	0.9726	0.9191	-0.0048	-0.0112	-0.0045	
	Peppers	512 × 512	0.9756	0.9739	0.9575	-0.044	-0.0056	-0.0162	
	Airport	1024 × 1024	0.8153	0.8722	0.7386	-0.0275	-0.0154	-0.0187	
	Man	1024 × 1024	0.9415	0.9566	0.9072	-0.0155	-0.0276	-0.0157	
	Girl	256 × 256	0.878618	0.895442	0.834322	0.007395	-0.012370	0.005173	
	House	256 × 256	0.879324	0.932969	0.816038	0.003149	-0.006062	0.009519	
	Mandrill	512 × 512	0.449232	0.661067	0.533187	-0.015312	0.001732	0.009718	
	Lena	512 × 512	0.970850	0.954886	0.950905	-0.001587	-0.014706	0.002381	
	Pappers	512 × 512	0.974059	0.971855	0.949721	-0.014452	-0.010480	-0.004223	
[13]	Man	1024 × 1024	0.976925	0.986621	0.977167	-0.001694	-0.002491	-0.010536	
	Airport	1024 × 1024	0.908661	0.946783	0.899671	-0.000255	-0.005964	-0.007555	
	SanDiego	1024 × 1024	0.830043	0.863403	0.763782	-0.009713	0.000666	0.006865	
	Stockton	1024 × 1024	0.691237	0.721790	0.639152	0.002409	-0.008536	-0.009865	
	Washington, DC	2250 × 2250	0.900027	0.915863	0.874522	-0.009631	-0.001319	0.003053	
	Girl	256 × 256	0.972937	0.962201	0.948799	0.013098	0.003073	-0.004343	
	House	256 × 256	0.967086	0.935256	0.912852	-0.008841	0.000493	0.001834	
	Mandrill	512 × 512	0.866408	0.777247	0.766873	0.002571	0.005102	-0.002390	
	Lena	512 × 512	0.974186	0.981908	0.958263	-0.011147	0.003422	-0.004887	
	Pappers	512 × 512	0.957823	0.966377	0.946804	-0.004626	0.001041	-0.001922	
Ours algorithm	Man	1024 × 1024	0.977230	0.972628	0.955671	0.006001	-0.000608	-0.000049	
	Airport	1024 × 1024	0.920765	0.903059	0.862725	0.013244	0.005260	-0.002582	
	San Diego	1024 × 1024	0.869986	0.865715	0.765886	-0.011834	-0.005042	-0.003607	
	Stockton	1024 × 1024	0.788410	0.778147	0.731672	0.001338	0.003456	0.001449	
	Washington, DC	2250 × 2250	0.843071	0.808857	0.780803	0.005228	-0.000771	-0.000141	

4.3 Entropy Analysis

One of the parameters that measures the degree of randomness is entropy. Its formula is given by the equation below:

$$H(MC) = \frac{1}{t} \sum_{i=1}^t -p(i)\log_2 p(i) \tag{4}$$

The values in Table 2 are close to 8 “maximum values”, which proves that our system is safe from entropy attacks. In conclusion, our proposed algorithm, archive a high degree of confusion-diffusion. Therefore, any statistical attack of our encryption system is almost impossible. Also, the results obtained by the proposed scheme are generally better than those presented in [13].

Table 2 Entropy measurement results

Algorithm	Image	Size	Global entropy	
			Original image	Encrypted image
[13]	Girl	256 × 256	6.415479	7.999627
	House	256 × 256	6.400674	7.999225
	Mandrill	512 × 512	7.644440	7.999283
	Lena	512 × 512	7.271856	7.999282
	Pappers	512 × 512	7.297795	7.999246
	Man	1024 × 1024	7.523737	7.999823
	Airport	1024 × 1024	6.830330	7.999816
	San Diego	1024 × 1024	5.662656	7.999831
	Stockton	1024 × 1024	6.070791	7.999831
	Washington, DC	2250 × 2250	7.222260	7.999868
Ours algorithm	Girl	256 × 256	6.898139	7.999299
	House	256 × 256	7.068625	7.999148
	Mandrill	512 × 512	7.762436	7.999768
	Lena	512 × 512	7.750197	7.999765
	Pappers	512 × 512	7.669825	7.999753
	Man	1024 × 1024	7.523736	7.999939
	Airport	1024 × 1024	6.330101	7.999938
	San Diego	1024 × 1024	6.794728	7.999942
	Stockton	1024 × 1024	7.707984	7.999987
	Washington, DC	2250 × 2250	7.222260	7.999886
Covid19	441 × 564	7.437562	7.999750	

4.4 Differential Attack

The *NPCR* and *UACI* parameters, given by formulas (3) and (4), measure the effect on the encrypted image after the change of a single plain image pixel [14, 15]. The expected values of *NPCR* are 96% and 33.45% for the *UACI* [16].

$$NPCR = \frac{\sum_{i,j} D(i,j)}{M * N} * 100\% \tag{5}$$

$$UACI = \frac{1}{M * N} \frac{\sum_{i,j} | C_1(i,j) - C_2(i,j) |}{255} * 100\% \tag{6}$$

here $D(i, j)$ is a matrix defined by :

$$D(m, n) = \begin{cases} 1 & \text{if } C_1(i, j) = C_2(i, j), \\ 0 & \text{elsewhere} \end{cases}$$

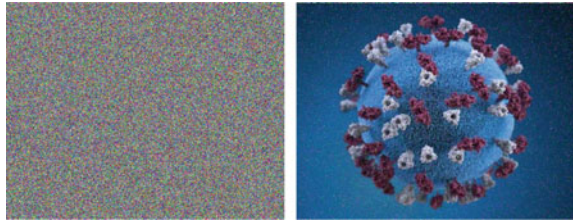
M and N are, respectively, the number of rows and columns of images. Table 3 shows, the values of *NPCR* and *UACI* for different images. The values obtained are of the order of 99.60% for the *NPCR* and the vicinity of 33.45 to the *UACI*. The theoretically estimated values for a best cryptosystem are 96% for the *NPCR* and 33.45% for the *UACI*, which justified robustness against differential attacks.

4.5 Noise Attack

We added 2% of salt and pepper noise to the encrypted image, then we decrypt the resulting image and study the encrypted image. The results of the simulations presented in Fig. 5, shows that we received the same image even if we apply noise attacks.

Table 3 Values of the NTCR and UACI for testing images

Image	Image size (Gray)	UACI (%)	NPCR (%)
Lena	512 × 512	33.4579	99.2149
Man	1024 × 1024	33.4407	99.6084
House	256 × 256	33.6727	99.3461
Covid19	441 × 564	33.757	99.7398

Fig. 5 Noise attack

5 Conclusion

Putting security first, our approach is a pixel level color image encryption system. The first step of this technique is entirely controlled by a chaotic vector to ensure pseudo-random confusion. The passage of a pixel in one of the three S-boxes constructed from the chaotic maps used which illustrate a strong improvement in the Vigenère matrix is also controlled by another chaotic decision vector. Finally, the chain established between the encrypted pixel and the clear pixel, considerably increases the impact of the avalanche effect and provides better protection against known attacks.

References

1. Mohamed J et al (2020) Further improvement of the HILL method applied in image encryption. In: 1st international conference on innovative research in applied science. Engineering and technology (IRASET). IEEE, p 2020
2. Hraoui S et al (2019) A new cryptosystem of color image using a dynamic-chaos hill cipher algorithm. *Proc Comput Sci* 148:399–408
3. Hraoui S et al (2018) A chaotic cryptosystem for color images using pixel-level and bit-level pseudo-random permutations. In: *The proceedings of the third international conference on smart city applications*. Springer, Cham
4. Farah MAB et al (2020) A new design of cryptosystem based on S-box and chaotic permutation. *Multimedia Tools Appl*, 1–22
5. Shannon CE (1949) Communication theory of secrecy systems. *Bell Syst Techn J* 28(4):656–715
6. Mollaefar M, Sharif A, Nazari M (2017) A novel encryption scheme for colored image based on high level chaotic maps. *Multimedia Tools Appl* 76(1):607–629
7. Zhang Y, Tang Y (2018) A plaintext-related image encryption algorithm based on chaos. *Multimedia Tools Appl* 77(6):6647–6669
8. Liu L, Chen Y, Ye R (2017) A plain image dependent image encryption scheme using half pixel level interchange permutation operation. *Int J Netw Secur Appl* 9:57–75
9. Ye G, Huang X (2017) An efficient symmetric image encryption algorithm based on an intertwining logistic map. *Neurocomputing* 251:45–53
10. Luo Y et al (2018) An efficient and self-adapting colour-image encryption algorithm based on chaos and interactions among multiple layers. *Multimedia Tools Appl* 77(20):26191–26217
11. University of Southern California, Signal and image processing institute. The USC-SIPI Image Database. Available at: <http://sipi.usc.edu/database/>
12. Belazi A, Abd El-Latif AA, Belghith S (2016) A novel image encryption scheme based on substitution-permutation network and chaos. *Sig Process* 128:155–170

13. Boriga R, Dăscălescu AC, Priescu I (2014) A new hyperchaotic map and its application in an image encryption scheme. *Sig Process Image Commun* 29(8):887–901
14. Kwok HS, Tang WKS (2007) A fast image encryption system based on chaotic maps with finite precision representation. *Chaos Solitons Fractals* 32(4):1518–1529
15. Peng J, Zhang D, Liao X (2009) A digital image encryption algorithm based on hyper-chaotic cellular neural network. *Fundam Inf* 90(3):269–282
16. Ghebleh M, Kanso A, Stevanović D (2018) A novel image encryption algorithm based on piecewise linear chaotic maps and least squares approximation. *Multimedia Tools Appl* 77(6):7305–7326

New Image Encryption Scheme Based on Dynamic Substitution and Hill Cipher



Younes Qobbi, Abdeltif Jarjar, Mohamed Essaid, and Abdelhamid Benazzi

Abstract In this work, we propose a new color image encryption technique. After transiting of the original image into a vector and decomposing it into blocks of three pixels, along with modifying of a seed block by an initialization vector computed from the plain image, a preliminary confusion will be handled by a substitution matrix developed under the control of the two chaotic maps used in the system. The achieved block will be injected in affine transformation provided by an invertible matrix accompanied by a dynamic translation vector to surmount the problem of null or uniform blocks. The encrypted block will be linked to the original block to set up diffusion and avalanche effect to protect the system from differential attacks. Simulations applied to on a large number of color images prove the robustness of the proposed approach against known attacks.

Keywords Chaotic maps · Affine transformation · Substitution

1 Introduction

In the last few years, and thanks to the immense development of communication and information technologies, the security of information exchanges through insecure networks has become a tangible problem. This is the rationale for developing effective systems to protect the transfer of confidential information. In particular the transmission of images raises a significant number of problems, such as confidentiality, and integrity [1]. Chao-based cryptography has asserted potential reliability and appropriateness for image encryption, where as traditional encryption systems (DES, IDEA, etc.) have become useless [2–4]. Currently, several crypto-systems

Y. Qobbi (✉) · A. Benazzi
HSTO, AMSPCS Laboratory, Mohamed First University, Oujda, Morocco
e-mail: qobbi.younes@ump.ac.ma

A. Jarjar
High School Moulay Rachid, Taza, Morocco

M. Essaid
LSI, Sidi Mohamed Ben Abdellah University, Taza, Morocco

are proposed, taking advantage of the interesting properties of chaotic systems, namely pseudo-random behavior, ergodicity and sensitivity to initial conditions [2, 5]. Fridrich is considered as the first author who introduced, in 1998, a chaos-based image encryption scheme in 1998 [4, 6]. Permutation and substitution are the main pillars of any encryption system. The permutation is a bijective transformation that allows to change the position of the pixels, substitution is a new technique which makes it possible to grasp confusion, one of the Shannon's main recommendations. Belazi and Khan [7] proposed an encryption algorithm based on permutation and substitution by S-boxes. In this work, the encryption is done over two phases: (a) The permutation phase of three image matrices using a chaotic cat map. (b) Then a substitution is applied to the three matrices permuted by three 16×16 S-boxes created using a logistic chaotic map. In this vein, Authors Nkandeu and Tiedeu [2] suggested a fast image encryption algorithm based on new chaotic map and technique dependent on the plain image. Such as a new chaotic map is used to generate two S-Boxes. The substitution is applied to the plain image by displacement and Boolean operator XOR. In another proposal [8], Sajjad T. Ali and Rashid Ali offer a three-step image encryption algorithm: In the first phase, the image pixels are swapped using a chaotic map. In the second phase a chaotic S-Box is used to replace the pixels, finally a Boolean operator XOR is used to mix a sequence of pseudo-random numbers with the pixels of the substituted image. Other algorithms [9] have adopted to improve the Hill cipher method (HC). This classic method is generally used for text encryption. It consists of choosing an encryption key in the form of an invertible 2×2 matrix. In the article [10], the authors HRAOUI and al proposed an improvement of the classical Hill algorithm, this improvement is due to the use of an invertible matrix of order three and of a vector of dynamic translation chaotic. The authors Essaid et al. [11] presented a new image encryption algorithm based on the improvement of several chaotic maps (logistics map, sine map and Chebyshev map) and also on the use of a new version of Hill cipher, which is deemed more secure. The authors of [12] proposed an improvement of HC called HC-PRE (Hill Cipher Modification based on Pseudo-Random Eigenvalues), this technique uses pseudo-random eigenvalues to generate dynamic key matrices. The authors of the article [13] recommended a modified HC algorithm that used a single-use key matrix to encrypt each block of plain text. In this algorithm, each block is encrypted using its own key. This unique key is calculated by multiplying the current key by a secret initial vector (IV). The multiplication operation is performed row by row. The authors of [14] arrived at a new technique for generating an auto-reversible matrix used in HC. Their main objective is to overcome the problem of using any key matrix, since the encrypted message cannot be decrypted if the matrix is not invertible. The authors claimed that the computational complexity can be reduced by avoiding the process of finding the inverse of the matrix at the time of decryption, as they use a self-reversible key matrix for encryption. The authors of [15] proposed an image scrambling algorithm derived from chaos theory and Vigenère cipher in which every pixel's grey level is encrypted with the Vigenère encryption mode.

Eliminating the diffusion, the classical encryption systems of Vigenère and Hill Cipher, which apply only the confusion, are always vulnerable to differential attacks.

Respecting the Shannon’s recommendations. Our method based on a combination of three basic encryption techniques namely, substitution, confusion and diffusion, in order to increase the complexity of our encryption system. The developed scheme is founded on two chaotic maps with excellent pseudo-random properties. The effectiveness of the proposed crypto-system has been validated by several experiments.

This paper is organized as follows: In the next section, the mechanism of encryption and decryption of image is described in details. In the 3rd section, the performance analyses and simulation are illustrated at length. Finally, conclusion of the present contribution is drawn in the 4th section.

2 Proposed Method

Based on chaos, our method is an enhanced of the HILL method and that the Vigenère. This method is articulated along five main axes.

2.1 Generating of Chaotic Sequences

Our technique is a symmetric encryption system of secret keys. Chaotic sequences are generated by two chaotic maps which are the most widely used in cryptography.

Logistics Map. It’s a float sequence generated and controlled by a second-degree polynomial. Defined by the following equation:

$$\{x_{n+1} = \mu_1 x_n(1 - x_n): \mu_1 \in [3.57, 4] \text{ and } x_0 \in [0.5, 1] \tag{1}$$

Tent Map. It is a very simple map to use in color image encryption. Defined by the following equation:

$$y_{n+1} = \begin{cases} \mu_2 y_n & \text{if } y_n < 0.5 \\ \mu_2(1 - y_n) & \text{Otherwise} \end{cases} : \mu_2 \in [0, 2] \text{ and } y_0 \in]0, 1] \tag{2}$$

These conditions ensure the chaotic behavior of two chaotic maps.

2.2 Preparation of Plain Image

Split the plain image of size (h, w) into the three vectors VR, VG and VB of size (1, t) such as t = h × w, which are concatenated to generate a vector Vc1 of size (1,

$3 \times t$), then a pixel's permutation is performed to decrease the correlation between adjacent pixels. This vector is divided into the blocks of three pixels.

Permutation vector V_p . The permutation vector V_p of proposed method is obtained by an ascending sort of the elements of the chaotic vector T of size $(1, 3 \times t)$ created by using the chaotic sequence of PRN (Pseudo-Random Numbers) which is generated by the tent map.

2.3 Encryption Settings

Generated of Substitution Table ST . In this part, we will present the technique for generating the substitution table ST of size $(256, 256)$. The first row of our substitution table is a permutation achieved through ascending a sort performed on the binary vector V_b , which is generated by the following algorithm.

```
For i=0 to 255
  Vb(i)=(int)(x(i)*1010)mod 2
Next i
```

The ascending sort performed on the elements of the V_b generate the initialization vector V_i .

The row of index k is obtained by a displacement of the previous row of step controlled by the rotation vector V_r . It is defined by the following algorithm:

```
For i=0 to 255
  Vr(i)=(int)((y(i)*106)mod 200)+10
Next i
```

Therefore, this substitution matrix represents an enhanced Vigenèr's table resulted by the following algorithm.

```
For j=0 to 255
  ST(0, j) = Vi(j)
Next j
For i =1 to 255
  For j =0 to 255
    ST(i, j) = ST((i - 1), (j + Vr(i))mod 256)
  Next j
Next i
```

Enhanced Hill Cipher (EHC). In this article we use the enhanced classic cipher Hill (ECH). This improvement use a full matrix of size $(3, 3)$ of the following form:

$$CH = \begin{pmatrix} a1 & a2 & a3 \\ b1 & b2 & b3 \\ c1 & c2 & c3 \end{pmatrix} \quad (3)$$

This matrix, used for image encryption, must be invertible in the ring $Z/256Z$. The invertible matrix used for image decryption.

Translation Vector Tv. After implementing the EHC (Enhanced Hill Cipher), a translation phase will be initiated by using the boolean operator XOR between the Vc2 vector and Tv vector. The translation vector is generated from two chaotic sequences of PRN (Pseudo-Random Numbers) created by iterating the logistics map and tent map for $(3 \times t)$ times by the following algorithm.

```

For i=0 to 3*t-1
    Tv(i)=(int)(max(x(i),y(i))*106) mod 256
Next i
    
```

2.4 Encryption Process

Once the plain image and the encryption settings are prepared, the image encryption process proposed by our method goes through the following steps.

Step (1): applying the permutation Vp on the plain image vector Vc1. This permutation is attained through the following algorithm.

```

For i=0 to 3*t-1
    Vc2(Vp(i))=Vc1(i)
Next i
    
```

Step (2): Improving the security of our encryption algorithm against differential attacks, the diffusion action starts from the beginning of the encryption system by using the setup vector Vs of size $(1, t)$, computed from the plain image, which allows to changing only the value of the first block of the vector Vc2. This action performed by adopting the following algorithm:

```

For i=0 to 2
    Vc2(i)=Vc2(i) ⊕ Vs(i)
Next i
    
```

Step (3): After the setup action, this block goes through a substitution phase by using the Substitution Table ST of size $(256, 256)$. The block substitution is carried out by using two vectors. The first is the translation vector Tv, which used to choose the substitution row from ST. The second is the plain image vector Vc2, which used to choose the substitution column from ST. The substitution is provided by the following algorithm:

```

For i=0 to t-1
    Vc1(3*i)=ST(Tv(3*i), Vc2(3*i))
    Vc1(3*i+1)=ST(Tv(3*i+1), Vc2(3*i+1))
    Vc1(3*i+2)=ST(Tv(3*i+2), Vc2(3*i+2))
Next i
    
```

Step (4): After the substitution phase, the result block will be encrypted by implementing the Enhanced Cipher Hill, using the complete invertible matrix CH. The equation below stimulates the abovementioned process:

$$\begin{pmatrix} Vc2(3*i) \\ Vc2(3*i + 1) \\ Vc2(3*i + 2) \end{pmatrix} = \begin{pmatrix} a1 & a2 & a3 \\ b1 & b2 & b3 \\ c1 & c2 & c3 \end{pmatrix} \times \begin{pmatrix} Vc1(3*i) \\ Vc1(3*i + 1) \\ Vc1(3*i + 2) \end{pmatrix} \tag{4}$$

Step (5): Increasing the complexity of our encryption system, a translation phase is performed by using the following algorithm:

```

For i=0 to t-1
    Vc2(3*i)=Vc2(3*i) ⊕ Tv(3*i)
    Vc2(3*i+1)=Vc2(3*i+1) ⊕ Tv(3*i+1)
    Vc2(3*i+2)=Vc2(3*i+2) ⊕ Tv(3*i+2)
Next i
    
```

The result of this phase gives an encrypted block of three pixels, which is attached to the next plain block. The diagram below (Fig. 1) represents the encryption process of the proposed method.

2.5 Decryption Process

The proposed method is based on symmetric encryption of keys (x_0, μ_1) and (y_0, μ_2) , afterwards, the decryption process uses the same encryption keys on condition to start with the last encryption phase.

Step (1): Split the cipher image into the blocks of three pixels.

Step (2): Using the vector (Tv) and the equation below for translation:

$$Vc1(i) = Vc1(i) \oplus Tv(i) \tag{5}$$

Step (3): Use the inverse matrix of CH.

Step (4): In this step we execute the reverse substitution by the following algorithm: The inverse substitution of Vc2(i) giving by the algorithm as below.

```

For j=0 to 255
    If (ST(Tv(i), j)=Vc2(i)
        Vc1(i)=j
        Break
    End
Next j
    
```

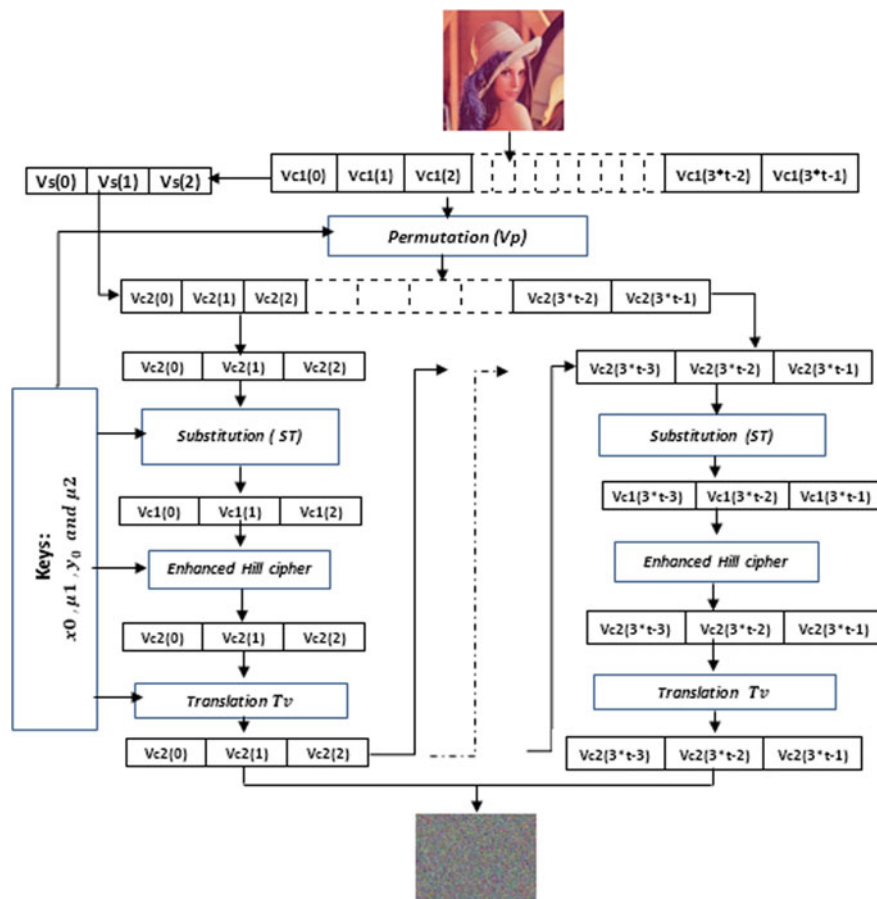



Fig. 1 Diagram of encryption process

Step (5): Inverse diffusing by using the following algorithm:

```

If (i>0)
    Vc1(3*i)=Vc1(3*i) ⊕ Vc1(3*(i -1))
    Vc1(3*i+1)=Vc1(3*i+1) ⊕ Vc1(3*(i -1)+1)
    Vc1(3*i+2)=Vc1(3*i+2) ⊕ Vc1(3*(i -1)+2)
Else
    Vc1(0)=Vc1(0) ⊕ Vs(0)
    Vc1(1)=Vc1(1) ⊕ Vs(1)
    Vc1(2)=Vc1(2) ⊕ Vs(2)
End
    
```

3 Experimental Results and Analysis

In order to prove the robustness of our proposed encryption algorithm. We present in this section several simulations: histogram analysis, Key sensitivity, correlation coefficients, entropy, NPCR and UACI. We choose several color plain images, Lena (256 × 256) Baboon (512 × 512) and ucid00622 (348 × 512). The plain images and its encrypted images are displayed in the following Fig. 2.

3.1 Correlation Analysis

$$Corr_{xy} = \frac{E((x - E(x))(y - E(y)))}{\sqrt{D(x) \times D(y)}} \tag{6}$$

$$E(x) = \frac{1}{N} \sum_1^N x_i \quad \text{and} \quad E(y) = \frac{1}{N} \sum_1^N y_i \tag{7}$$

$$D(x) = \frac{1}{N} \sum_1^N (x_i - E(x))^2 \quad \text{and} \quad D(y) = \frac{1}{N} \sum_1^N (y_i - E(y))^2 \tag{8}$$

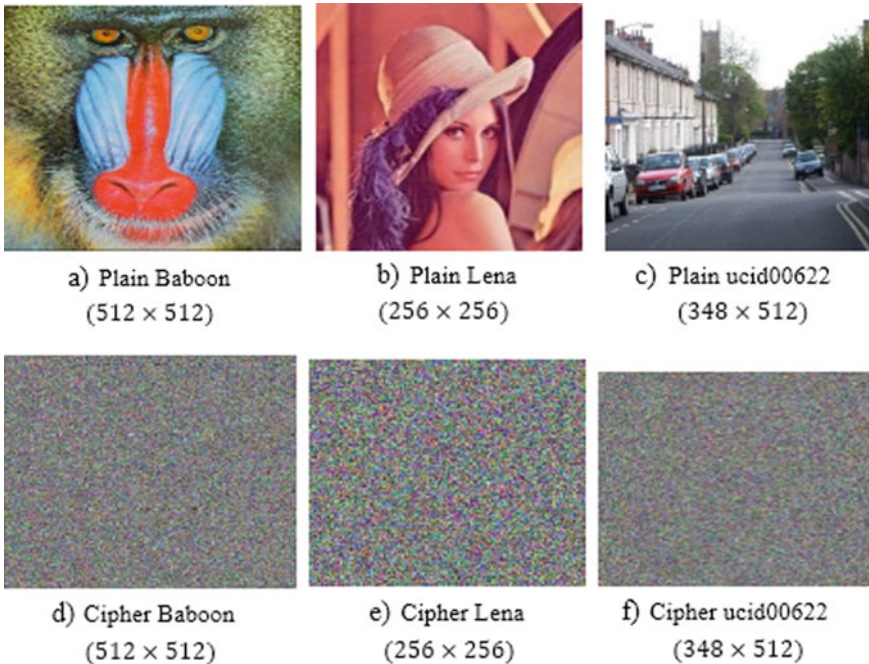


Fig. 2 Plain and ciphered images

Table 1 Correlation coefficients

	Horizontal	Vertical	Diagonal
Plain Lena (256 × 256)	0.9354	0.9576	0.8964
Cipher Lena (256 × 256)	-0.0072	0.0078	0.0039
Plain Peppers (512 × 512)	0.8397	0.7195	0.6985
Cipher Peppers (512 × 512)	-0.0064	-0.0062	-0.0049

Table 2 Information entropy results

Image	Proposed algorithm	Ref. [6]	Ref. [11]	Ref. [10]
Lena (512 × 512)	7.9998	7.9997	7.9998	7.9997
Baboon (512 × 512)	7.9998	7.9997	7.9997	-
Peppers (512 × 512)	7.9998	7.9997	7.9998	7.9995

where $E(x)$, $D(x)$ are the expectation and variance of variable x and $E(y)$, $D(y)$ are the expectation and variance of variable y .

The correlation of adjacent pixels from the plain images and the ciphered images of Lena (256 × 256) and Peppers (512 × 512) are shown in Table 1.

3.2 Entropy Analysis

The entropy of information is used to assess the uncertainty of a encrypted image’s information. It is defined by the following equation:

$$e(m) = - \sum_{i=1}^{255} \text{Pr}(m_i) \times \log \text{Pr}(m_i) \tag{9}$$

The maximum information entropy is about 8. The information entropy of our algorithm and some references are listed in Table 2.

3.3 Histogram Analysis

An image histogram is a graphical representation showing the number of pixels with the same intensity value. Intensity distribution of an encrypted image has the potential to be exploited in a statistical attack. The histograms of plain images and cipher-images are shown in the following Fig. 3.

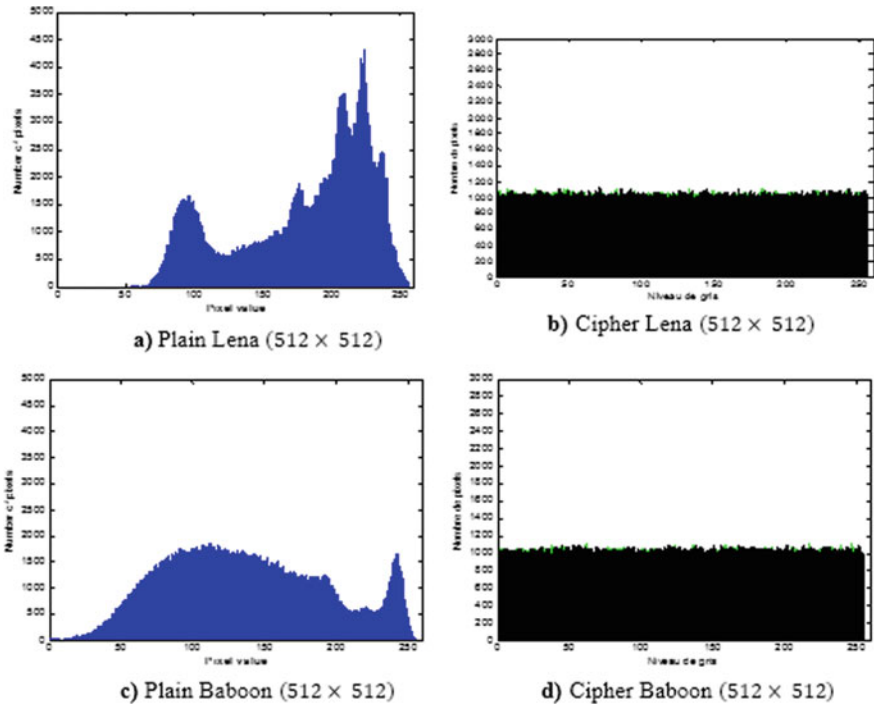


Fig. 3 Histogram analysis

3.4 Keys Analysis

In the proposed system, the key composed of two initial values x_0 and y_0 , and two control parameters μ_1 and μ_2 . Which are the floats represented in 32 bits. The key space size is much greater to 2^{104} . Then the key space is large to stay secure against the brute force attack [16].

3.5 Differential Analysis

Sometimes, attackers make a small modification in the plain image, and then apply the encryption algorithm to encrypt the original image and the changed image in order to observe how a tiny change in the plain image influence the encrypted image by comparing the two encrypted images. The sensitivity of a cryptosystem is evaluated through a Number of Pixels Change Rate (NPCR) and Unified Average Changing Intensity (UACI). Their definitions are presented as follows.

Table 3 Plaintext sensitivity analysis results

Plain image	Proposed scheme		Ref. [6]	
	NPCR	UACI	NPCR	UACI
Baboon	99.6189	33.4695	99.6090	33.457
Lena	99.6150	33.4277	99.6190	33.447
Peppers	99.6120	33.4650	99.6080	33.466

$$NPCR = \frac{\sum_1^w \sum_1^h D_{ij}}{w * h} \times 100\% \tag{10}$$

$$UACI = \frac{1}{w \times h} \frac{\sum_{ij} |IC1_{ij} - IC2_{ij}|}{255} \times 100\% \tag{11}$$

$$D_{ij} = \begin{cases} 1 & \text{if } IC1_{ij} \neq IC2_{ij} \\ 0 & \text{else} \end{cases} \tag{12}$$

The following Table 3 shows the measurement of NPCR and UACI between two cipher images of the Babon (512 × 512) Lena (512 × 512) and Peppers (512 × 512). When making a slight change in the plain image.

4 Conclusion

This work outlines a new color image encryption technique involving a substitution matrix that represents a deep refinement of Vigenère’s method combined to a Hill’s technique application on three pixels blocks, provided by an invertible matrix of arbitrary form. The new S-Box design technique can be easily modified and improved. The encryption method applied in the present paper brings strength to our algorithm. The simulation results and security analysis presented by a correlation coefficient close to zero and a flat histogram of the encrypted image ensure an entropy value close to 8, which have proved that the proposed image encryption scheme meets all the performance requirements of image encryption design criteria.

References

1. Machkour M, Saaidi A, Benmaati ML (2015) A novel image encryption algorithm based on the two-dimensional logistic map and the latin square image cipher. 3D Res 6(4):36
2. Nkandeu YPK, Tiedeu A (2019) An image encryption algorithm based on substitution technique and chaos mixing. Multimedia Tools Appl 78(8):10013–10034
3. Chen G, Mao Y, Chui CK (2004) A symmetric image encryption scheme based on 3D chaotic cat maps. Chaos Solitons Fractals 21(3):749–761

4. Fridrich J (1998) Symmetric ciphers based on two-dimensional chaotic maps. *Int J Bifurcat Chaos* 8(06):1259–1284
5. Jakimoski G, Kocarev L (2001) Chaos and cryptography: block encryption ciphers based on chaotic maps. *IEEE Trans Circ Syst I Fundam Theory Appl* 48(2):163–169
6. Fu C, Zhang GY, Zhu M, Chen Z, Lei WM (2018) A new chaos-based color image encryption scheme with an efficient substitution keystream generation strategy. *Secur Commun Netw*
7. Belazi A, Khan M, El-Latif AAA, Belghith S (2017) Efficient cryptosystem approaches: S-boxes and permutation–substitution-based encryption. *Nonlinear Dyn* 87(1):337–361
8. Ali TS, Ali R (2020) A new chaos-based color image encryption algorithm using permutation substitution and Boolean operation. In: *Multimedia tools and applications*. Springer, Berlin, pp 1–21
9. Hill LS (1929) Cryptography in an algebraic alphabet. *Am Math Mon* 36(6):306–312
10. Hraoui S, Gmira F, Abbou MF, Oulidi AJ, Jarjar A (2019) A new cryptosystem of color image using a dynamic-chaos hill cipher algorithm. *Proc Comput Sci* 148:399–408
11. Essaid M, Akharraz I, Saaidi A (2019) Image encryption scheme based on a new secure variant of Hill cipher and 1D chaotic maps. *J Inf Secur Appl* 47:173–187
12. Mahmoud A, Chefranov A (2014) Hill cipher modification based on pseudo-random eigenvalues. *Appl Math Inf Sci* 8(2):505
13. Ismail IA, Amin M, Diab H (2006) How to repair the Hill cipher. *J Zhejiang Univ Sci A* 7(12):2022–2030
14. Overbey J, Traves W, Wojdylo J (2005) On the keyspace of the Hill cipher. *Cryptologia* 29(1):59–72
15. Li S, Zhao Y (2011) Image scrambling based on chaos theory and Vigenère cipher. In: *2011 seventh international conference on computational intelligence and security*. IEEE, pp 555–558
16. François M, Grosjes T, Barchiesi D, Erra R (2012) A new image encryption scheme based on a chaotic function. *Sig Process Image Commun* 27(3):249–259

Touchless Palmprint Identification Based on Patch Cross Pattern Representation



Hakim Doghmane , Kamel Messaoudi, Mohamed Cherif Amara Korba, Zoheir Mentouri, and Hocine Bourouba

Abstract Over the last decade, palmprint recognition has been studied for many problems and applications. It has become one of the most well-known biometric recognition system. Its success is due to the rich features that can be extracted and exploited from the palmprint images captured by contact or contactless device. This paper presents a new representation based on textural structure of human palms for touchless palmprint identification. This representation method is called Patch Cross Pattern (PCP), which relies mainly on cross pattern encoder and the non-overlapping decomposition method. The feature vector is built using Cross Pattern (CP) encoder to capture the textural structure of palmprint image. Then, the non-overlapping decomposition on both directions is applied. Next, the feature vector representation of each palmprint image is constructed by concatenating all normalized histograms calculated at each patch. In addition, the reduced version of the PCP called R-PCP is obtained using whitened linear discriminant analysis. Finally, a K-nearest neighbor classifier is used for palmprint identification. The proposed system is successfully applied to IIT Delhi and CASIA touchless databases. Results show that, the proposed representation provides a significant performance improvement compared to the recent state-of-the-art in terms of accuracy.

Keywords Touchless palmprint · Texture descriptor · K-NN classifier

H. Doghmane (✉) · H. Bourouba
PI: MIS Laboratory, Université 8 Mai 1945 Guelma, Guelma, Algeria
e-mail: doghmane.hakim@univ-guelma.dz

K. Messaoudi · M. C. Amara Korba
Electrical Engineering Department, Mohamed Cherif Mssaadia University Souk-Ahras, Souk Ahras, Algeria

Z. Mentouri
Research Center in Industrial Technologies-CRTI, BP. 64, Chéraga, Algiers 16014, Algeria

1 Introduction

Today, biometric systems play an important role in our daily lives. They can be found in almost all areas, such as bank transaction, criminology, state security, etc. They are based on a person's physiological or behavioral traits to identify them. Different biometric systems have been suggested in the literature, such as iris [1], fingerprints [2] and hand signature [3]. The latter system is based on a study of the shape of the hand and the texture of the palm. It has many advantages over other biometric systems. Among them: (i) its capture device is less expensive than the iris recognition system, (ii) the characteristics of the hand are more numerous than those of fingerprints and can be extracted from low resolution images, and (iii) is well accepted by persons. Due to its importance in practical application fields, palmprint as a physiological biometric trait has received great attention in recent years. Based on 2D palmprint images, the palmprint can be represented using one of the following categories of approaches: line-based approaches, subspace-based approaches, coding-based approaches, local texture-based approaches and deep learning-based approaches.

Line-based approaches consist of extracting different structures from the palm of the hand such as principle lines, wrinkles, datum points, minutiae points, ridges and crease points [4].

Subspace-based approaches use another space to represent palmprint images by projecting them into a subspace providing a set of weights that represent the feature vector. This category of approaches includes Principal Component Analysis (PCA) [5], Linear Discriminant Analysis (LDA) [6] and Independent Component Analysis (ICA) [7]. However, subspace-based approaches are sensitive to palmprint translation, rotation and scaling.

Coding-based approaches typically involve the application of a set of filters to an image, the quantization of the magnitudes or phases of the filter responses, and the encoding of the results to compute a biometric template. Then, matching step based on the hamming distance is used to compare the resulting templates. There are a number of coding-based approaches such as double orientation coding [8], palm codes [9], Competitive Code [10], Ordinal Code [11] and Double Orientation Code [12].

Due to their high representational ability, local texture descriptors-based approaches have been used extensively in many applications of computer vision. Among them: Local Phase Quantization (LPQ) [13], Local Binary Pattern (LBP) [14], Binarized Statistical Image Feature (BSIF) [15] and Dual Cross Pattern (DCP) [16]. The reason for employing local texture descriptors for palmprint recognition is the possibility of treating the palmprint image as micro-patterns compositions that are properly characterized by such descriptors. BSIFs have shown to perform better than the other descriptors in face recognition, texture classification and other biometric traits.

In contrast to the approaches mentioned above, which are considered as algorithms for designing craft descriptors, deep learning-based approaches have, recently, been

used for palmprint classification. They allow joint learning of the feature representation while performing a prediction task (classification/regression). In this case, a Convolutional Neural Network (CNN), usually, is used to extract the features from palmprint images. Then, a trained classifier is employed to match the resulting palmprint templates. This category of approaches can be separated into two classes: (i) Approaches using pre-trained CNNs (transfer learning), (ii) approaches using CNNs trained on palmprint images. The approach presented in [17] belongs to class (i) which is based on a comparison among several pre-trained CNNs. Feature extraction from touchless palmprint images is performed using pre-trained AlexNet, VGG-16 and VGG-19 networks; subsequently, classification is performed using a support vector machine (SVM). The results show that the deeper network VGG-16 and VGG-19, obtain better results than those of AlexNet. Among the approaches of class (ii) is that presented in [18] which a CNN based on Alex model [19] and trained on palmprint images by optimizing a loss function describing the separation of the genuine and imposter distributions. The results demonstrate superior performance compared with recent coding-based approaches. Typically, deep learning-based approaches rely on large amounts of data to be able to efficiently learn the recognition task. Such data should provide good palmprint representation of different variations present in the training data.

This study interests on the 2D contactless palmprint identification, which is based on a new palmprint representation called Patch Cross Pattern (PCP). It is constructed by taking the following steps: (i) pretreatment step, (ii) local directional textural pattern extraction step, and (iii) non-overlapping spatial split step. The pretreatment step is performed on the raw palmprint images to reduce the effect of the illumination variation and noise by applying a median filter. Next, the Cross Pattern (CP) encoder is applied to extract local directional textural pattern. Then, the non-overlapping split step in both directions is carried out. Afterwards, the histograms obtained are normalized. After that, the global representation of the palmprint image is constructed by concatenating all the local features of each patch, thus providing Patch Cross Pattern (PCP) descriptor. Moreover, a reduced version of the PCP called R-PCP is calculated by using whitened linear discriminant analysis (WLDA). Finally, the obtained PCP (or R-PCP) feature is used for classification step. The remainder of this paper is structured as follows: Sect. 2 contains the methodology of the proposed representation. Then, Sect. 3 reports and analyzes the results of the palmprint identification experiments. Finally, Sect. 4 presents certain findings.

2 Proposed Touchless Palmprint Representation

A new supervised representation is proposed in this section, to overcome the challenges encountered when touchless palmprints are used for human identification. It explores spatially invariant texture patterns between different scales. Thus, this paper presents a new try to integrate the Cross Pattern coder with the non-overlapping spatial split method. A summary of the proposed representation is shown in Fig. 1.

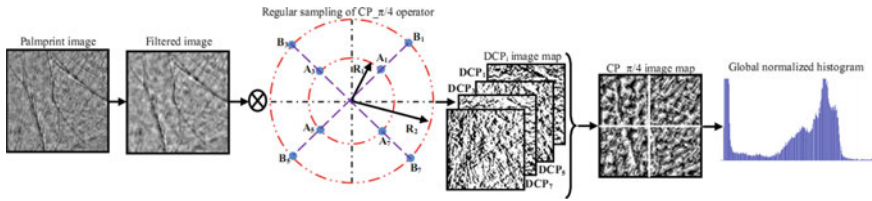


Fig. 1 Patch cross pattern (PCP) palmprint representation

2.1 Dual Cross Pattern (DCP)

Similar to the LBP descriptor the Dual Cross Pattern (DCP) as a hand-crafted descriptor based method is proposed by Ding et al. [20]. Its principle goal is to explore the richest scale and information directions for local sampling and pattern coding. The concept of local sampling of the DCP descriptor is depicted in Fig. 2. Sixteen points are sampled around the central pixel. For the inner circle of radius R_{in} , the points A_0 to A_7 are uniformly spaced, while for the outer circle of radius R_{ex} , the points B_0 to B_7 are also uniformly distributed [20].

For every one of the eight directions, a specific decimal number is assigned:

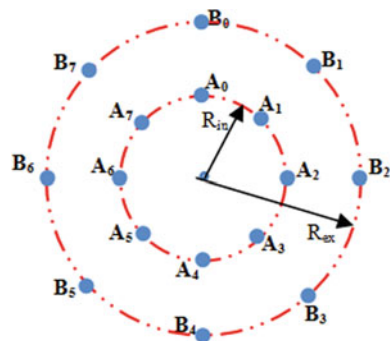
$$DCP_i = S(I_{A_i} - I_o).2^1 + S(I_{B_i} - I_{A_i}).2^0, 0 \leq i \leq 7 \tag{1}$$

where $S(x)$ is the sign function given by:

$$S(x) = \begin{cases} 1 & \text{If } x \geq 0 \\ 0 & \text{Otherwise} \end{cases} \tag{2}$$

Two subsets are constructed from the eight patterns DCP_0 – DCP_7 . The even subset is defined by $\{DCP_0, DCP_2, DCP_4, DCP_6\}$ and the odd subset is given by $\{DCP_1, DCP_3, DCP_5, DCP_7\}$. The two subsets mentioned earlier are referred to as cross encoders CP_0 and $CP_{\pi/4}$, respectively. Consequently, the codes generated by these

Fig. 2 Principle of DCP sampling



dual encoders at each pixel are expressed as follows:


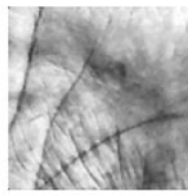
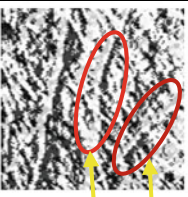
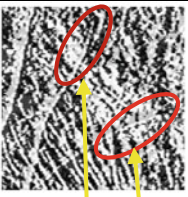
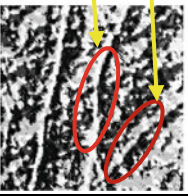
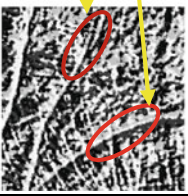
$$\begin{cases} CP_0 = \sum_{i=0}^3 DCP_{2i} \cdot 4^i \\ CP_{\pi/4} = \sum_{i=0}^3 DCP_{2i+1} \cdot 4^i \end{cases} \quad (3)$$

So, the DCP descriptor for a palmprint image is the concatenation of the two codes CP_0 and $CP_{\pi/4}$ [14].

$$DCP = \{CP_0, CP_{\pi/4}\} = \left\{ \sum_{i=0}^3 DCP_{2i} \cdot 4^i, \sum_{i=0}^3 DCP_{2i+1} \cdot 4^i \right\} \quad (4)$$

Table 1 shows an example of image maps and entropy values using $[R_{in} R_{ex}] = [1 \ 2]$ for even CP_0 and odd $CP_{\pi/4}$ encoders, where CP_0 captures the texture patterns in the horizontal and vertical directions while $CP_{\pi/4}$ captures the texture patterns in the diagonal direction.

Table 1 Entropy values of encoded plamprint images

	Touchless palmprint databases	
	CASIA	Delhi
ROI image		
CP_0 image map		
$CP_{\pi/4}$ image map		
Entropy(CP_0)	0.0035	0.0310
Entropy($CP_{\pi/4}$)	0.1233	0.2008

To assess our system, there are two criteria for choosing between CP_0 and $CP_{\pi/4}$ encoders: (i) subjective criteria (visual) and (ii) objective criteria (entropy). According to the first criteria, the results show that the map images of $CP_{\pi/4}$ contain more visible primitives (principle lines, wrinkles, etc.) of the palmprint than those of CP_0 (see Table 1).

To be more objective a second criteria, based on the image entropy is used. Computed for two palmprint image types, it shows higher values when using the $CP_{\pi/4}$ encoder. This confirms that this encoder allows getting map images with more information. Therefore, only the odd subset defined by cross encoders $CP_{\pi/4}$ is used in this work to evaluate the proposed approach.

3 Experimental Results and Discussions

The performance of the proposed method is demonstrated by conducting several experiments on touchless palmprint databases. This performance depends on three parameters which are: the decomposition level L , the radius R_{In} and R_{Ex} of the $CP_{\pi/4}$ encoder. Then, to find out the optimal radii $[R_{In}, R_{Ex}]$, for IIT Delhi and CASIA databases the error rates are computed with a changing radii pair as in Figs. 4 and 6 for an L level varying from 1 to 6. Using the obtained optimal values, the proposed method is compared, in the last experiments, to the existing ones by its application to the two mentioned databases.

The database information, the experimental setup and the results are presented in the sub-sections below. It is worth noting that in all tables, the highest Identification Rates (IR) appears in bold fonts.

3.1 IIT Delhi Database

In IIT Delhi touchless palmprint database, images were collected from 230 subjects using both hands (i.e., 460 distinct palms). Each person has at least five palmprint images for each hand. These images are acquired in severe variations of distortion, rotation, and translation. The Region of Interest (ROI) of palm images are publicly available. Consequently, there are 460 palm classes in the IIT Delhi database, each one with about five palmprint images.

Figure 3 shows some ROI examples of palmprint images from two different subjects. The three images in the first row (Fig. 3a) were captured from the first subject, whereas the images in the second row (Fig. 3b) were captured from the second subject.

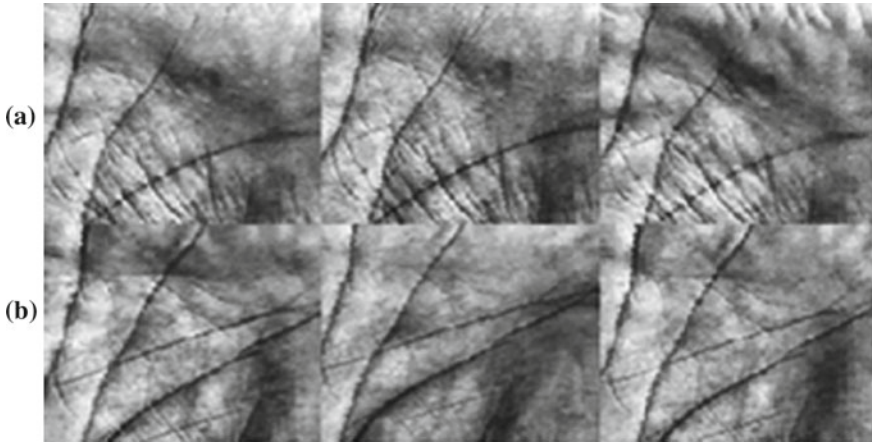


Fig. 3 Some palmprint images from IIT-Delhi database

During all experiments, the first three samples are selected as the training set and the remaining samples as the test set. Thus, we have 1380 (460×3) training samples and 920 (460×2) test samples.

Experiment #1

In the current part, we examine the most appropriate parameters of the proposed method. We study the effect of the non-overlapping decomposition level L , the interior radius R_{in} and exterior radius R_{ex} . All these parameters have an influence on the performance of the proposed method. In order, to find the optimal values of these parameters for PCP and R-PCP representations, we conducted experiments using different values of $[R_{in} R_{ex}]$ for L varies from 1 to 6.

As shown in Fig. 4a, the PCP representation allows a good performance (EIR = 1.74%) for a radii pair $[R_{in} R_{ex}]$ equal to [2 5] or [4 6] and an L parameter of 5. Moreover, with a fixed value of R_{in} , the EIR seems changing inversely to the radius R_{ex} . It decreases when this radius value increases. Yet, both parameters increase for an R_{in} changing to a higher value. As for the non-overlapping decomposition operation, it makes the EIR decreasing when its level (L) increases. Higher values of EIR are so obtained with no decomposition, and the highest error rate of 35.65% is reached with a radii pair of $[R_{in} R_{ex}] = [1 2]$ and a decomposition level $L = 1$.

On the other hand, Fig. 4b shows the performance obtained using the R-PCP representation. The system performance becomes more efficient (EIR = 0.22%) compared to the PCP representation. This is due to the use of the WLDA method,

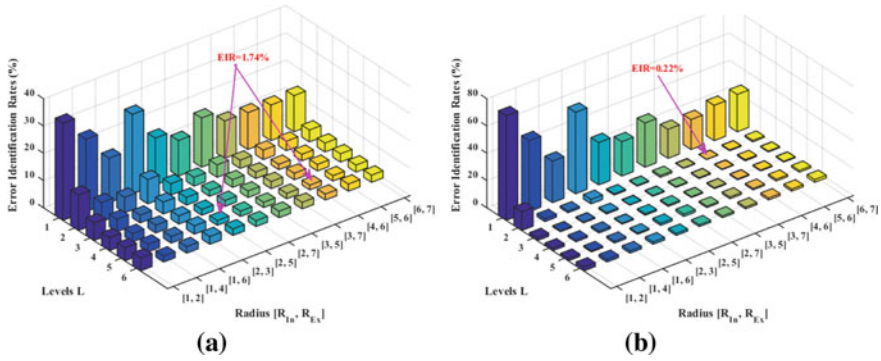


Fig. 4 Evaluation of the proposed approach on IIT-Delhi database. **a** PCP representation, **b** R-PCP representation

which makes the features more discriminating by maximizing inter-class and minimizing intra-class variations. Moreover, this improvement is achieved with two levels of decomposition instead of five levels in the case of PCP representation.

Experiment #2

To more demonstrate the effectiveness of the proposed approach, it has been compared to some previous works. As mentioned in Table 2, it achieves a highest identification rate, proving that the R-PCP representation method is much more efficient than the compared ones.

Table 2 Comparative results showing recognition rate of the proposed schemes and recently proposed methods on IIT Delhi database

Methods	Nbre classes	Protocol		Descriptors	IR(%)
		Train	Test		
[15]	460	First 3 images	Remaining samples	RPBSIFD	99.57
[21]	460			DGLSPH	99.57
[22]	460	Three images randomly selected		Texture Pattern + Principal lines shape	97.98
				Fractal (FDBC)	95.80
Proposed	460	First 03 images		PCP	98.48
				R-PCP	99.78

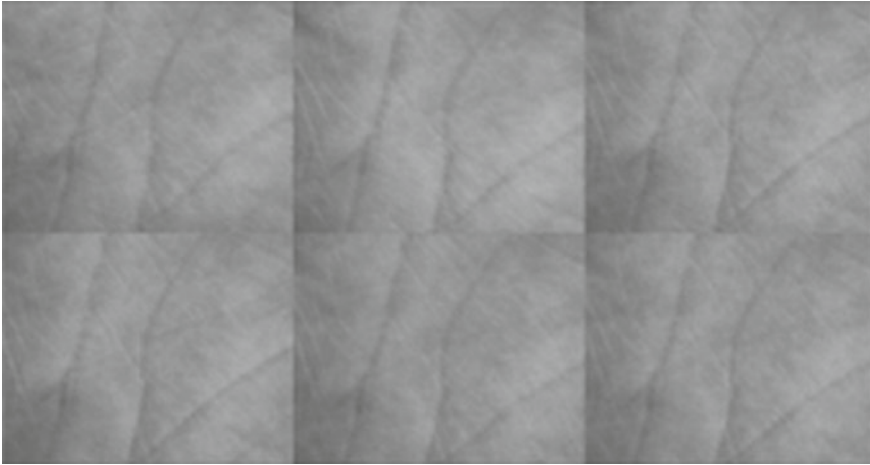


Fig. 5 Some palmprint images from CASIA database

3.2 CASIA Database

CASIA palmprint image database has been created by “China Academy of Sciences Institute of Automation (CASIA)” and gathered 5502 images from 312 subjects (i.e., 624 distinct palms). More than eight palmprint images are collected from the left and the right hands for each subject.

All images of this database are captured by a CMOS camera without any pegs. These images are 8-bit gray-level JPEG files. Examples of some images from the databases cited above are shown in Fig. 5.

Experiment #1

The illustration of Fig. 6a, shows that both EIR and R_{Ex} increase while R_{In} changes to a higher value. Whereas EIR varies inversely to the decomposition level L . So, with this PCP representation, the lowest error rate of 3.14% is obtained with a radii pair $[R_{In} R_{Ex}]$ equal to $[3 7]$ and an L level of 3. This error rate increases significantly when the decomposition operation is not used ($L = 1$); the highest error in this case reaches 20.23% with an optimal radii pair $[R_{In} R_{Ex}] = [1 2]$.

Figure 6b shows the performance obtained using the R-PCP representation. System performance becomes more efficient (EIR = 1.66%) compared to the PCP representation. Moreover, this improvement is achieved with $L = 4$ and $[R_{In} R_{Ex}] = [3 7]$.

Experiment #2

In this experiment, the proposed approach is compared to previous works, that have been applied to the CASIA palmprint database, taking into account the same protocol in comparison. The identification rates mentioned in Table 3 show that the R-PCP representation performs clearly better than the other compared methods, with the

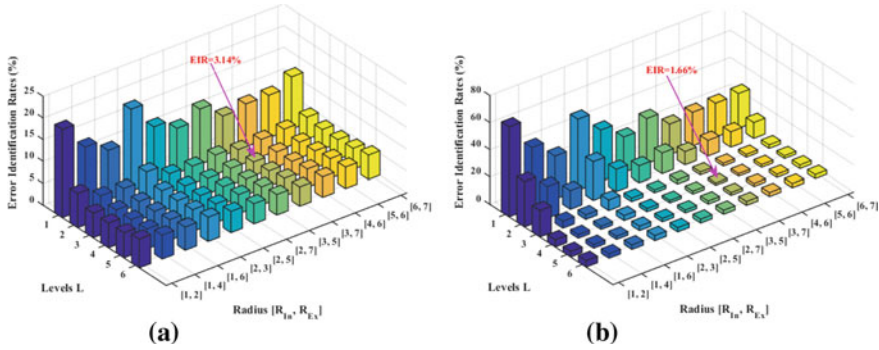


Fig. 6 Evaluation of the proposed approach on CASIA database. **a** PCP representation, **b** R-PCP representation

Table 3 Comparative results showing recognition rate of the proposed schemes and recently proposed methods on CASIA database

Methods	Nbre classes	Protocol		Descriptors	IR(%)
		Train	Test		
[15]	620	First four images	Remaining samples	RPBSIFD	99.34
[22]	310	First five images		Texture pattern	96.52
[23]	620			Principal lines	92.98
				Texture-Pattern	96.00
				Intra-modal	98.00
Proposed	620	First 03 images	PCP	96.86	
			R-PCP	98.34	

exception of the work presented in [15]. However, the dimensionality of the proposed representation before the reduction is 3.5 times smaller than that presented in [15]. This means significant time savings.

4 Conclusion

This paper deals with a new local textural structure representation based approach. The main objective of this work is to provide a representation of the touchless palmprint image, which should be as discriminating as possible, in order to minimize misclassifications. Thus, using only the odd encoder Cross Pattern $CP_{\pi/4}$ and the non-overlapping decomposition in both directions, a PCP and R-PCP representations are constructed to represent any palmprint image. Based on one of these representations, each palmprint image in the training and testing set is represented and then, used for palmprint identification.

References

1. Raghavendra R, Christoph B (2015) Robust scheme for iris presentation attack detection using multiscale binarized statistical image features. *IEEE Trans Inf Forensics Secur* 10(4):703–715
2. Maltoni D et al (2003) *Handbook of fingerprint recognition*, 1st edn. Springer, New York
3. Sanchez-Reillo R, Sanchez-Avila C, Gonzalez-Marcos A (2000) Biometric identification through hand geometry measurements. *IEEE Trans Pattern Anal Mach Intell* 22(10):1168–1171
4. Wu XQ, Zhang D, Wang KQ (2006) Palm line extraction and matching for personal authentication. *IEEE Trans Syst Man Cybern* 36(5):978–987
5. Lu G, Zhang D, Wang K (2003) Palmprint recognition using Eigenpalms features. *Pattern Recognit Lett* 24(9):1463–1467
6. Wu X, Zhang D, Wang K (2003) Fisher palms based palmprint recognition. *Pattern Recognit Lett* 24(15):2829–2838
7. Shang L et al (2006) Palmprint recognition using fastica algorithm and radial basis probabilistic neural network. *Neurocomputing* 69(13):1782–1786
8. Fei L et al (2016) Double-orientation code and nonlinear matching scheme for palmprint recognition. *Pattern Recognit* 49:89–101
9. Zhang D et al (2003) Online palmprint identification. *IEEE Trans Pattern Anal Mach Intell* 25(9):1041–1050
10. Kong AK, Zhang D (2004) Competitive coding scheme for palmprint verification. In: *Proceedings of the 17 th international conference on pattern recognition, ICPR 2004*. IEEE, vol 1, pp 520–523
11. Sun Z et al (2005) Ordinal palmprint representation for personal identification. In: *CVPR*, pp 279–284
12. Fei L et al (2016) Double-orientation code and non linear matching scheme for palmprint recognition. *Pattern Recognit* 49:89–101
13. Ojansivu V, Heikkila J (2008) Blur insensitive texture classification using local phase quantization. *Lect Notes Comput Sci* 5099:236–243
14. Guo X, Zhou W, Zhang Y (2017) Collaborative representation with HM-LBP features for palmprint recognition. *Mach Vision Appl* 28(34):283–291
15. Bendjoudi S, Bourouba H, Doghmane H et al (2019) Palmprint identification performance improvement via patch-based binarized statistical image features. *J Electron Imag* 28(5):053009
16. Mentouri Z, Doghmane H et al (2020) Surface flaw classification based on dual cross pattern. In: *International conference on communications, control systems and signal processing (CCSSP 2020)*, 16–17 March 2020, El Oued Algeria
17. Tarawneh AS, Chetverikov D, Hassanat AB (2018) Pilot comparative study of different Deep features for palmprint identification in low quality images. *CoRR* abs/1804.04602
18. Svoboda J, Masci J, Bronstein MM (2016) Palmprint recognition via discriminative index learning. In: *Proceedings of 2016 23rd international conference on pattern recognition (ICPR)*, December 2016, pp 4232–4237
19. Krizhevsky A, Sutskever I, Hinton GE (2012) ImageNet classification with deep convolutional neural networks. In: *Proceedings of 25th international conference on neural information processing systems (NIPS)*, pp 1097–1105
20. Ding C, Choi J, Tao D, Davis LS (2016) Multi-directional multi-level dual-cross patterns for robust face recognition. *IEEE Trans Pattern Anal Mach Intell* 38(3):518–531
21. Doghmane H, Bourouba H, Messaoudi K et al (2018) Palmprint recognition based on discriminant multiscale representation. *J Electron Imag* 27(5):053032
22. Mokni R, Drira H, Kherallah M (2017) Combining shape analysis and texture pattern for palmprint identification. *Multimed Tools Appl* 76:23981–24008
23. Hammami M, Jemaa SB, Ben-Abdallah H (2014) Selection of discriminative sub-regions for palmprint recognition. *Multimed Tools Appl* 68(3):1023–1050

Image Segmentation Approach Based on Hybridization Between K-Means and Mask R-CNN



Hanae Moussaoui, Mohamed Benslimane, and Nabil El Akkad

Abstract In this article, we will introduce a hybrid method based on the combination of two image segmentation techniques. The first method adopted is the k-means algorithm which is an unsupervised machine learning technique used to group data points, the second is the Mask R-CNN which is a neural network architecture which combines two sub-problems: object detection and semantic segmentation. The main objective of this study is to approve the segmentation of the image using k-means. The first step is to apply Mask R-CNN on our original image to detect the objects that are present in the image, then, we will apply k-means clustering to have better segmentation. For our approach we used a set of metrics to evaluate our proposed approach such as the mean square error (MSE); the peak signal to noise ratio (PSNR) and many other measures such as the difference between two images. These measurements have shown satisfactory results and a performance of the proposed method.

Keywords Segmentation · K-Means · Masque R-CNN · Instance segmentation

1 Introduction

Image processing is used in several areas of computer vision, in particular, image segmentation [1–4], 3D reconstruction [5, 6], camera self-calibration [7, 8] and cryptography [9, 10]. In this paper we have treated our proposed method in the field of image segmentation.

Image segmentation is the process that gives as the ability to separate a random image into parts, or objects that make up the image [11], which leads to separate the objects from the background. The idea of subdividing an image into its components parts or objects present in the image came from the need to analyze each of these

H. Moussaoui (✉) · N. El Akkad
LISA, Engineering, Systems and Applications Laboratory, ENSA of Fez, Sidi Mohamed Ben Abdellah University, Fez, Morocco
e-mail: hanae.moussaoui@usmba.ac.ma

M. Benslimane
LTI Laboratory, EST, Sidi Mohamed Ben Abdellah University, Fez, Morocco

components, or each of the objects present in the image, once they are identified or we have subdivided them. Thus, each of these constituents can be analyzed to extract certain information, which is used for high level machine learning applications. Segmentation is very useful in a lot of areas, like autonomous cars, where you want to identify for example which regions are occupied by a road, which regions are occupied by a car, vegetation, surveys or pedestrians. Another application is for biomedical purposes such as the identification of different types of cells, so this can be useful for identifying things like cancer cells. It can also be used for augmented reality purposes where you may want to overlay reflections in certain regions. We have two different approaches to image segmentation [11]:

- Approach based on discontinuity; when we are mainly interested in identifying isolated points, or identifying lines present in the image, or identifying edges;
- Similarity approach; here we are trying to group these pixels into an image, which are similar in some sense. The approaches under this similarity-based technique are:
 - Threshold operation;
 - The growth-based approach;
 - Splitting and merging of regions.

The segmentation of the instances goes a little further, it is still a classification based on pixels, but at the same time, we try to separate the instances from the objects.

In this article, we will be focusing on the segmentation process, by combining the unsupervised k-means method for clustering, which divides the image into clusters, these clusters can be defined manually by ourselves, or we can use one of the methods which choose the optimal value of k as the elbow method. The second stage of this work is the Mask R-CNN, with which we can generate an image with bounding boxes and also locate each pixel of the image. The hybrid method will be as follows, the k-means output image will be the input for the Mask R-CNN.

The advantage came from the fact that we wanted to have k-means segmentation, while keeping the objects of the image in advantage. During our test of the k-means algorithm, we found that using different values of k, the image loses a large amount of information as well as the objects appearing in the image. The advantage of this approach is that we can segment our image using different values of the parameter k while respecting the properties of the objects.

The rest of this paper is organized as follows; in the second part we will talk in detail about the proposed hybrid method. The third part will be devoted to experimentation, where the results obtained will be discussed. We will finish with a conclusion.

2 The Proposed Method

The idea came when we decided to apply k-mean clustering on the images and at the same time, try to make the objects visually clearer and detectable. The grouping of k-means on an image will not only tell us which pixels belong to which classes (value of k), it will also tell us what the average color of these classes is, so that we can simplify our image. In our situation, we choose the value k according to the image or the situation.

As shown in Fig. 1, we applied Mask R-CNN on an input image to detect the objects in that image using semantic segmentation, when we assign a class objects at each pixel of the image. Then, the output image will be the input of k-means clustering. The diagram of this method is shown below:

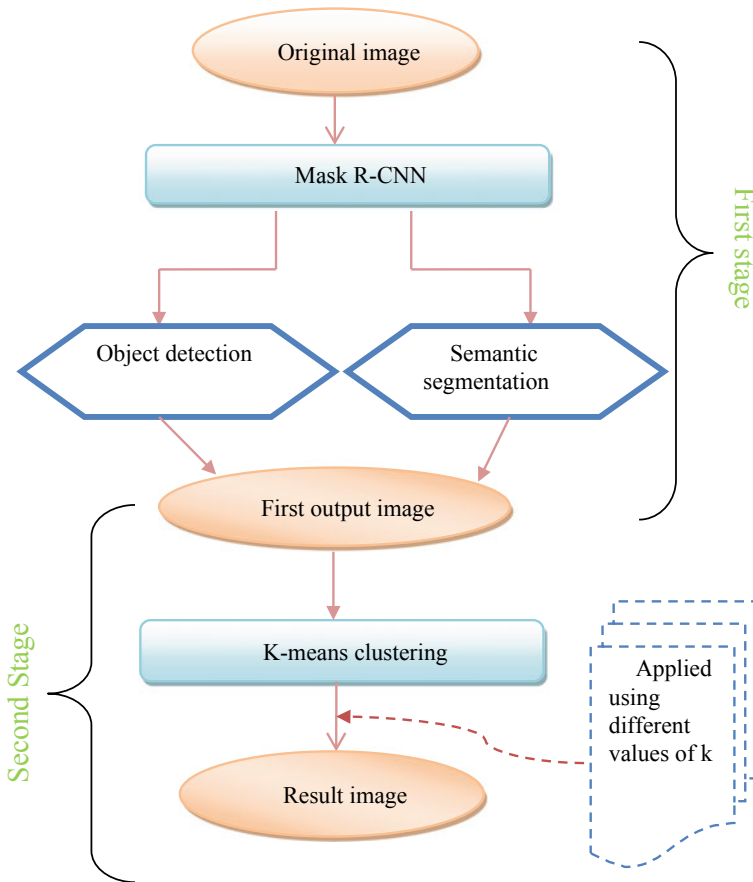


Fig. 1 The proposed approach

2.1 Mask R-CNN

Mask R-CNN is one of the famous techniques to implement instance segmentation, it essentially combines two architectures that already exist [3, 12]. The first is the Faster R-CNN. It comes when we have to identify and classify the object as well as find the bounding box for this object [13]. The second part is when we generate the detection mask using the FCN convolutional neural network. Figure 2 presents an overall architecture of the Mask R-CNN.

Mask R-CNN works in four steps [14]:

- Faster R-CNN uses ConvNET to extract feature cards from the image.
- These entity cards are then transmitted via a regional proposal network (RPN) and return the delimitation frameworks.
- Apply a layer of ROI Pooling on these candidate demarcation boxes to bring all the candidates to the same size.
- Finally, the proposals are passed through a fully connected layer to classify and output the object delimitation frames.

The output of the Mask RCNN loss function is as follows:

$$L_{\text{Mask - R-cnn}} = L_{\text{cls}} + L_{\text{box}} + L_{\text{mask}} \quad (1)$$

L_{cls} , L_{box} and L_{mask} respectively refer to the classified loss function, the prediction box loss function and the mask loss function.

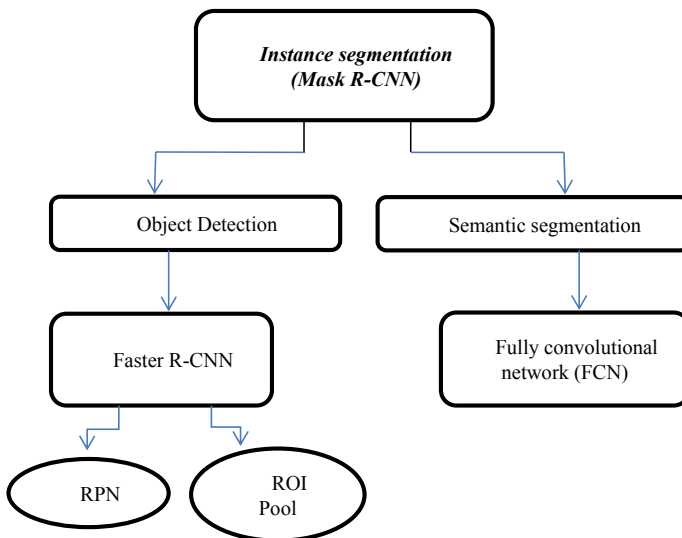


Fig. 2 Mask R-CNN architecture

L_{mask} is defined as the loss of mean binary cross entropy, including the k-th mask only if the region is associated with the ground truth class k

$$L_{\text{mask}} = \frac{-1}{m^2} \sum_{1 \leq i, j \leq m} [y_{ij} \log(\hat{y}_{ij}^k) + (1 - y_{ij}) \log(1 - \hat{y}_{ij}^k)] \quad (2)$$

where y_{ij} represents the label of a cell (i, j) in the real mask for the region of size $m \times m$; \hat{y}_{ij}^k is the predicted value of the same cell in the mask learned for the ground truth class k.

2.2 K-Means Clustering

K-means clustering is a clustering algorithm whose main objective is to group elements or similar data points in a cluster [2, 15, 16] where K represents the number of clusters or groups. The algorithm then runs iteratively to assign each data point to one of the k groups based on the functionality already provided. K-means clustering has a simple architecture like it's shown in Fig. 3.

To apply the K-Means method, the following steps must be followed:

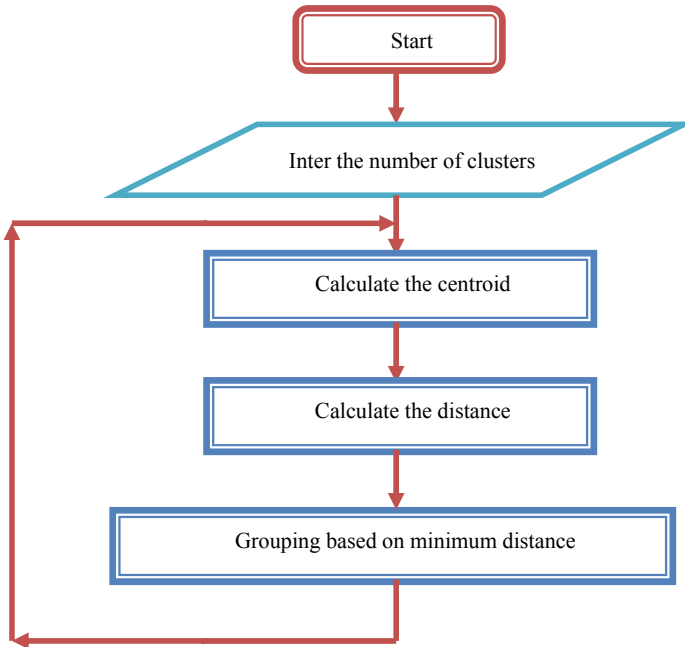


Fig. 3 K-means clustering architecture

Step 1 Select the number of clusters we want to identify in our data. This is the “k” in “k-means clustering”. The “Elbow” method is one of the very well known methods which are used to use the optimal value of the parameter K.

Step 2 Randomly select k separate data points.

Step 3 Measure the distance between the 1st point and the other initial clusters. This distance is calculated between the points of the same cluster and the centroid, and also between the centroids of the other groups. This is done using the following two formulas:

$$\text{Within clusters : } SSW(c, k) = \sum_{i=1}^n \|x_i - c_{p(i)}\|^2 \quad (3)$$

$$\text{Between clusters: } SSB(c, k) = \sum_{j=1}^k n_j \|c_j - \bar{x}\|^2 \quad (4)$$

Step 4 Allocate the 1st point to the nearest cluster.

Step 5 We do the same thing as we do all the points (we measure the distances, we assign the point to the nearest cluster).

The final formula of the k-means method is as follows:

$$J = \sum_{j=1}^k \sum_{i=1}^n \|x_i^{(j)} - c_j\|^2 \quad (5)$$

J	objective function
k	number of clusters
n	number de cases
x_i	case i
c_j	centroid of the cluster j
$\ x_i^{(j)} - c_j\ $	distance function.

3 Experimentation

In this experimentation part we will apply our approach on several random images to verify the performance of the proposed method. For this, we have tried a lot of algorithms dedicated to calculate the similarity between the input image or the original image and the images obtained by the k-means, mask rcnn and our approach (k-means + mask rcnn).

For our approach, the first step was to apply the Mask R-CNN on the original image, this will add to the input image the advantage of having a mask before going

into k-means. The mask applied during the Mask R-CNN phase will strengthen the pixels of the image, especially those of the objects present in the image; this comes back to the main objective of the Mask RCNN method of sorting objects apart from the background.

The second phase of this proposed approach is to apply the K-means method on the image obtained by the Mask R-CNN.

From the results obtained we see that our approach gives a favorable segmentation compared to the results of the k-means method alone. Our approach was applied to a set of images, and Table 1 represents some images and results of our experimentation.

For our study, we will use the mean square error (MSE) and the peak signal to noise ratio (PSNR) metrics to evaluate the proposed method

Peak Signal-to-Noise Ratio (PSNR) [11]: Peak signal-to-noise ratio, is a metric to compute the ratio between the maximum possible power of a signal and the power of corrupting noise that affects the fidelity of its representation. Because many signals have a very wide dynamic range, PSNR is usually expressed in terms of the logarithmic decibel scale.

$$PSNR = 10 \log \log_{10} \left(\frac{(L - 1)^2}{MSE} \right) = 20 \log_{10} \left(\frac{L - 1}{RMSE} \right) \tag{6}$$

Table 1 Table of the obtained results

















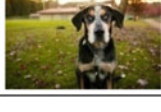

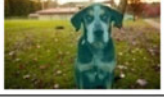

The original image	k-means	Mask R-CNN	The proposed method
			
			
			
			
			

Fig. 4 Similarity study table using the two similarity measures: MSE & PSNR

	MSE	PSNR
k-means	6.1625	19.82
Mask R-CNN	10.6780	17.85
Proposed method	3.8451	22.28

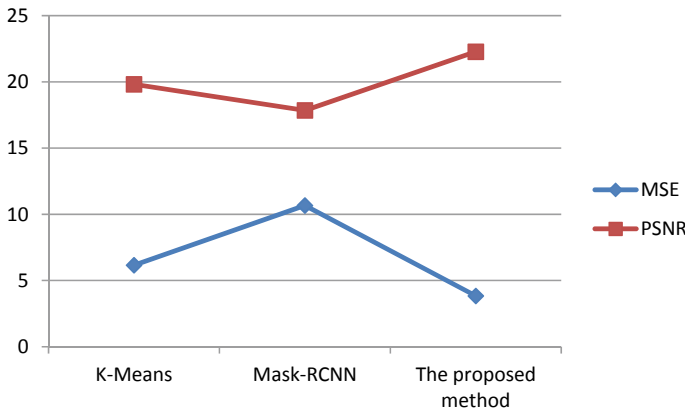


Fig. 5 MSE & PSNR similarity study graphic

L is the number of maximum possible intensity levels (minimum intensity level suppose to be 0) in an image.

The mean square error (MSE): indicates the average difference of the pixels over the entire image. A higher MSE indicates a greater difference between the original image and the processed image (Fig. 4).

$$MSE = \frac{1}{mn} \sum_{i=0}^{m-1} \sum_{j=0}^{n-1} [I(i, j) - k(i, j)]^2 \tag{7}$$

As the MSE increases, the images are less similar, unlike PSNR when the larger the value of PSNR, the more efficient is a corresponding compression or filter method (Fig. 5).

4 Conclusion

In this work we presented a hybrid approach between the k-means method which is an unsupervised approach for segmenting and partitioning an image into several

distinct regions containing each pixel with similar attributes, and the Mask R-CNN method which is used to detect all the objects present in an image by applying a mask which will advantage each object. Our method has been tested on several images and the results obtained show the effectiveness of this proposed hybridization approach.

References

1. Khrici L, Elakkad N, Satori H, Satori K (2019) Image Segmentation based on k-means and genetic algorithms. In: Proceedings of ESAI 19, embedded systems and artificial intelligence, pp 489–497 (2019)
2. Zheng X, Lei Q, Yao R, Gong Y, Yin Q (2018) Image segmentation based on adaptive K-means algorithm. EURASIP J Image Video Process. Article number: 68. <https://doi.org/10.1186/s13640-018-0309-3>
3. Zaitouna NM, Aqelb MJ (2015) Survey on image segmentation techniques. ScienceDirect. In: International conference on communication, management and information technology (ICCMIT 2015)
4. Ghosh S, Das N, Das I, Maulik U, Understanding deep learning techniques for image segmentation. ACM Comput Surv 52(4). <https://doi.org/10.1145/3329784>
5. El akkad N, El Hazzat S, Saaidi A, Satori K (2016) Reconstruction of 3D scenes by camera self-calibration and using genetic algorithms. 3D Res 6(7):1–17. <https://doi.org/10.1007/s13319-016-0082-y>
6. Merras M, Saaidi A, El Akkad N, Satori K (2016) Multi-view 3D reconstruction and modeling of the unknown 3D scenes using genetic algorithms. Soft Comput 22(19):6271–6289
7. El Akkad N, Merras M, Baataoui A, Saaidi A, Satori K (2017) Camera self-calibration having the varying parameters and based on homography of the plane at infinity. Multimed Tools Appl (77(11):14055–14075
8. El Akkad N, Merras M, Saaidi A, Satori K (2014) Camera self-calibration with varying intrinsic parameters by an unknown three-dimensional scene. Vis Comput 30(5):519–530
9. Es-sabry M, El akkad N, Merras M, Saaidi A, Satori K (2019) A novel color image encryption approach based on random numbers generation of two matrices and bit-shift operators. Soft Comput 24(5):3829–3848
10. Es-Sabry M, El Akkad N, Merras M, Saaidi A, Satori K (2018) A novel text encryption algorithm based on the two-square Cipher and Caesar Cipher. Commun Comput Inform Sci 872:78–88
11. Horé A, Ziou D (2010) Image quality metrics: PSNR vs. SSIM. In: 2010 20th international conference on pattern recognition, pp 2366–2369. <https://doi.org/10.1109/icpr.2010.579>
12. Singh Ch N (2019) Introduction to image segmentation with K-Means clustering. Towards Data Science
13. Nezamabadi H, Salwani A, Hatamlou A (2019) A combined approach for clustering based on K-means and gravitational search algorithms. Sci Direct Swarm Evolut Comput 6:47–52. <https://doi.org/10.1016/j.swevo.2012.02.003>
14. Shaodan L, Chen F, Zhide C (2019) A ship target location and mask generation algorithms base on mask RCNN. Int J Comput Intell Syst 12(2):1134–1143
15. Fahim AM, Salem AM, Torkey FA et al (2006) An efficient enhanced k-means clustering algorithm. J Zhejiang Univ Sci A 7:1626–1633
16. Peng Y, Liu X, Shen C, Huang H, Huang H, Zhao D, Cao H, Guo X (2019) An improved optical flow algorithm based on mask-R-CNN and K-means for velocity calculation. Appl Sci. <https://doi.org/10.3390/app9142808>
17. He K, Gkioxari G, Dollár P, Girshick R (2017) MaskR-CNN. In: IEEE international conference on computer vision (ICCV), pp 2980–2988, ID: 206771194. <https://doi.org/10.1109/iccv.2017.322corpus>

18. Aqil Burney SM, Humera T (2014) K-means cluster analysis for image segmentation. *Int J Comput Appl* 96(4):0975–8887
19. Ren S, He K, Girshick R, Sun J (2016) Faster R-CNN: towards real-time object detection with region proposal networks [arXiv:1506.01497v3\[cs.CV\]](https://arxiv.org/abs/1506.01497v3)
20. Wu X, Wen S, Xie Y (2019) Improvement of mask R-CNN object segmentation algorithm. *Intell Robot Appl* 582–591. https://doi.org/10.1007/978-3-030-27526-6_51
21. Abdulameer Aljanabi M, Hussain ZM, Lu SF (2018) An entropy-histogram approach for image similarity and face recognition. *Hindawi J. Article ID 9801308*. 18 pp. <https://doi.org/10.1155/2018/9801308>

Partial 3D Image Reconstruction by Cuboids Using Stable Computation of Hahn Polynomials



Mohamed Amine Tahiri, Hicham Karmouni, Ahmed Tahiri, Mhamed Sayyouri, and Hassan Qjidaa

Abstract In this paper, we will present a new method of partial reconstruction of the 3D image. The latter is based on the following two concepts: one is the stable discrete orthogonal Hahn polynomials (DOHPs), which significantly reduces numerical defects. The other is the 3D image cuboid representation (ICR) to accelerate the computation time of discrete orthogonal Hahn moments (DOHMs) and improve the quality of 3D image reconstruction. The results of the simulation confirm the ability of the 3D image reconstruction using the proposed process.

Keywords Numerical stability · 3D hahn moments · 3D image cuboid representation · 3D image reconstruction

1 Introduction

Research on 3D image reconstruction has always been a difficult challenge. The latter can be used for evaluating an object's 3D profile, as well as for defining a profile 3D coordinate at any given point. The reconstruction of 3D objects constitutes a

M. A. Tahiri · H. Karmouni (✉) · H. Qjidaa
CED-ST, STIC, Laboratory of Electronic Signals and Systems of Information LESSI, Dhar El Mahrez Faculty of Science, Sidi Mohamed Ben Abdellah-Fez University, Fez, Morocco
e-mail: hicham.karmouni@usmba.ac.ma

M. A. Tahiri
e-mail: mohamedamine.tahiri@usmba.ac.ma

H. Qjidaa
e-mail: qjidah@yahoo.fr

A. Tahiri
Laboratory of Computer Science and Interdisciplinary Physics LIPI Fez, Sidi Mohamed Ben Abdellah University, Fez, Morocco
e-mail: tahiri_amed@hotmail.com

M. Sayyouri
Laboratory of Engineering Sciences for Energy LabSIPE, National School of Applied Sciences of El Jadida, Chouaïb Doukkali University, PO Box 1166, 24004, EL Jadida Plateau, Morocco
e-mail: mhamed.sayyouri@usmba.ac.ma

scientific and technical challenge [1–4]. This problem led scientists to develop 3D image analysis and processing methods, including the theory of moments that will be the subject of study in this article. In theory, the moment approach is divided into three main categories: The non-orthogonal moments, such as geometric and complex moments [5, 6], the continuous orthogonal moments [7–13], and the discrete orthogonal moments (DOMs). We are going to focus mainly on DOMs such as the moments of Tchebichef [14, 15], Krawtchouk [14–17], Hahn [18], Charlier [19–21], and last but not least Meixner [21, 22], as these have concrete advantages over 3D image analysis. However, it has been noted that the computation of moments is a complex and costly task in terms of time. Therefore, several algorithms are implemented into the literature to reduce the cost of moment calculation; Most of the algorithms are either centered on the use of the image new representations [23–26], or the acceleration of time calculating values of polynomials [16–19, 22].

Motivated by the intention to solve these problems. In this post, we propose a new algorithm based on the integration of stable computation of Hahn polynomials (HPs) to ensure numerical stability, and the image cuboid representation (ICR) of 3D images, a set of cuboids of the same gray level, rather than voxels, shall decompose the 3D image in this representation, which guarantees the quality of the reconstruction of 3D images, which subsequently allows us to perform a partial reconstruction.

The remainder of the paper is organized as accordingly: in Sect. 2, we define the stable computation of HPs and 3D Hahn moments. In Sect. 3, we will present fast 3D discrete orthogonal Hahn moments by ICR. In Sect. 4, we will put forward a 3D image reconstruction via ICR by 3D stable Hahn moments, also in Sect. 5, we will present experimental results, and then in Sect. 6, we tackle the conclusion.

2 Stable Computation of Hahn Polynomials and 3D Hahn Moments

This section is divided into two sub-sections: the first is the stable computation of DOHPs when the moments order is high, and the second contains the discrete orthogonal Hahn moments.

2.1 Stable Computation of Hahn Polynomials

The n^{th} order DOHPs $h_n^{\varphi,\gamma}(x)$ is represented through using the following hypergeometric function [27]:

$$h_n^{\varphi,\gamma}(x) = \frac{(-1)^n(\gamma + 1)_n(N - n)_n}{n!} \times {}_3F_2(-n, -x, -n + 1 + \varphi + \gamma; \gamma + 1, 1 - N; 1) \tag{1}$$

We use the normalized form of DOHPs to avoid fluctuations in numerical computation:

$$\tilde{h}_n^{\varphi,\gamma}(x) = h_n^{\varphi,\gamma}(x) \sqrt{\frac{\omega_h(x)}{\rho_h(n)}} \tag{2}$$

with $\omega_h(x)$ is weight function and $\rho_h(n)$ is the squared Hahn norm defined as [27]:

$$\begin{aligned} \omega_h(x) &= \binom{\varphi+x}{x} \binom{\gamma+N-x}{N-x} \text{ and} \\ \rho_h(n) &= \frac{(-1)^n n!(n+\varphi+\gamma+1)_{N-1}(\gamma+1)_n}{N!(2n+\varphi+\gamma+1)(\gamma+1)_n(-N)_n} \end{aligned} \tag{3}$$

There is plenty of time to compute the Hahn polynomials coefficients (HPCs) in accordance with the weight Eq. (2), and its unstable values when the high order. In this spirit, the new HPs calculation algorithm is being implemented based on the x -direction integration, n -direction algorithm, and symmetrical properties. Below we will concentrate on both the theoretical calculation and the stable computation of HPCs algorithm.

a. Recurrence relation with respect to the order n

The recurrence relations in n -direction [27]:

$$\begin{aligned} \tilde{h}_n^{\varphi,\gamma}(x) &= A \sqrt{\frac{\rho_h(n-1)}{\rho_h(n)}} \tilde{h}_{n-1}^{\varphi,\gamma}(x) - B \sqrt{\frac{\rho_h(n-2)}{\rho_h(n)}} \tilde{h}_{n-2}^{\varphi,\gamma}(x) \\ n, x &= 0, 1, 2, \dots, N-1 \end{aligned} \tag{4}$$

The initial values for the below recurrence are (Table 1):

$$\tilde{h}_0^{\varphi,\gamma}(x) = \sqrt{\frac{\omega_h(x)}{\rho_h(0)}} \text{ and } \tilde{h}_1^{\varphi,\gamma}(x)$$

Table 1 Factors A, B, C, and D of DOHPs

$A = x - \frac{\varphi - \gamma + 2N - 2}{4} + \frac{(\varphi^2 - \gamma^2)(\gamma + \varphi + 2N)}{4(\varphi + \gamma + 2n - 2)(\varphi + \gamma + 2n)}$
$B = (-1) \times \frac{(\varphi+n-1)(\gamma+n-1)}{(\varphi+n+2n-2)} \times \frac{(\varphi+\gamma+N+n-1)(N-n+1)}{(\varphi+\gamma+2n-1)}$
$C = \frac{2(x-1)(N+\varphi-x+1)+(\gamma+1)(N-1)-(\varphi+\gamma+2)(x-1)-n(\varphi+\gamma+n+1)}{(x-1)(N+\varphi-x+1)+(\gamma+1)(N-1)-(\varphi+\gamma+2)(x-1)}$
$D = \frac{(x-1)(N+\varphi-x+1)}{(x-1)(N+\varphi-x+1)+(\gamma+1)(N-1)-(\varphi+\gamma+2)(x-1)}$

$$= [(\gamma + 1)(1 - N) + (\varphi + \gamma + 2)x] \times \sqrt{\frac{\omega_h(x)}{\rho_h(1)}} \tag{5}$$

b. Recurrence relation with respect to the variable x

The recurrence relations in x -direction [27]:

$$\begin{aligned} \tilde{h}_n^{\varphi,\gamma}(x) &= C \sqrt{\frac{\omega_h(x)}{\omega_h(x-1)}} \tilde{h}_n^{\varphi,\gamma}(x-1) - D \sqrt{\frac{\omega_h(x)}{\omega_h(x-2)}} \tilde{h}_n^{\varphi,\gamma}(x-2) \\ n, x &= 0, 1, 2, \dots, N-1 \end{aligned} \tag{6}$$

The initial values for the below recurrence are:

$$\begin{aligned} \tilde{h}_n^{\varphi,\gamma}(0) &= (-1)^n \frac{(\gamma + 1)_n (N - 1)_n}{\Gamma(n + 1)} \times \sqrt{\frac{\omega_h(0)}{\rho_h(n)}} \\ \text{and } \tilde{h}_n^{\varphi,\gamma}(1) &= \frac{n(n + \varphi + \gamma + 1) + 1}{(\gamma + 1)(1 - N)} \sqrt{\frac{\omega_h(1)}{\omega_h(0)}} \tilde{h}_n^{\varphi,\gamma}(0) \end{aligned} \tag{7}$$

After introducing the theoretical calculations, we will focus in the following on the algorithms for the stable computation of DOHPs, but we must remember the HPCs is available in a 2D assemblage with the parameters $n \in [0, N - 1]$ and $x \in [0, N - 1]$, where n and x refer respectively to the polynomial order and signal time index. The proposed algorithm is a programming approximation as follows:

Algorithm 1: The stable data processing of HPCs

Step 1: Compute the coefficients of stable HPs using Eqs. (6) and (7) in the specific intervals defined by $n \in [0, \frac{N}{2} - 1]$; $x \in [0, \frac{N}{2} - 1]$ where x and n incrementing by 1

Step 2: At predetermined intervals, $n \in [\frac{N}{2}, N - 1]$; $x \in [X, \frac{N}{2} - 1]$ we calculate the coefficients of stable HPs using Eq. (4), where x and n are increased by 1 (it should be noted that the $X = 0.5N - \sqrt{(0.5N)^2 - (0.5n)^2}$ is location of parameter x)

Step 3: In the specific intervals $n \in [\frac{N}{2}, N - 1]$; $x \in [X - 1, X - 12]$, using Eq. (6) we are calculating the stable coefficients of HPs. where n incrementing by 1, x decrementing by 1 and $X = 0.5N + \sqrt{(0.5N)^2 - (0.5n)^2}$

Step 4: Compute the stable coefficients of HPs where $n = 0, 1, 2, \dots, N - 1$ and $x = \frac{N}{2}, \frac{N}{2} + 1, \dots, N - 1$ using the property defined by symmetry condition:

$$\tilde{h}_n^{\varphi,\gamma}(N - x - 1) = (-1)^n \tilde{h}_n^{\gamma,\varphi}(x)$$

To assess for efficiency for great order of the new algorithm we study them using a number of 3D plots as shown in Fig. 1. We will remember that to preserve the symmetry property of our polynomial, we are going to handle the case of $\varphi = \gamma$; after analyzing the results we can conclude that the new algorithm maintains the

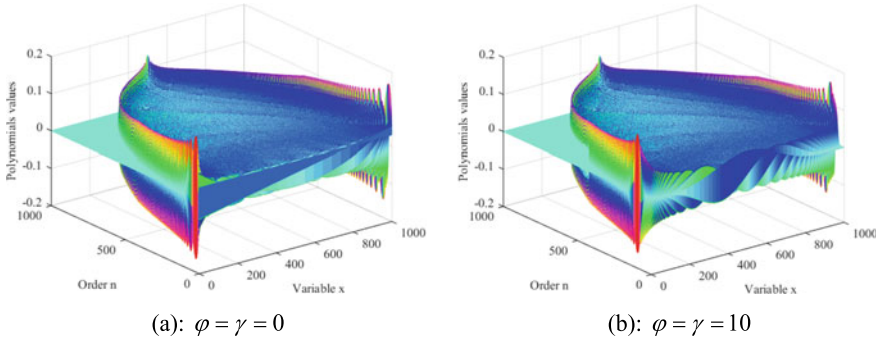


Fig. 1 Computation of HPCs values for $N = 1000$, and up to the order 1000

numerical stability up to the maximum order $N = 1000$ for the following cases $\varphi = \gamma = 0$ as shown in Fig. 1a and $\varphi = \gamma = 10$ as shown in Fig. 1b.

2.2 3D Discrete Orthogonal Hahn Moments

Theoretically, for the 3D image $f(x, y, z)$ with a size of $N \times M \times K$ samples and order $(n + m + k)$ th, the 3D Hahn moments Π_{nmk} can be defined as [26]:

$$\Pi_{nmk} = \sum_{x=0}^{N-1} \sum_{y=0}^{M-1} \sum_{z=0}^{K-1} \tilde{h}_n^{\varphi,\gamma}(x) \tilde{h}_m^{\varphi,\gamma}(y) \tilde{h}_k^{\varphi,\gamma}(z) f(x, y, z) \tag{8}$$

In theory, to reconstruct the 3D image, the inverse transformations of the 3D Hahn moments can be applied as follows [26]:

$$\hat{f}(x, y, z) = \sum_{n=0}^{N-1} \sum_{m=0}^{M-1} \sum_{k=0}^{K-1} \tilde{h}_n^{\varphi,\gamma}(x) \tilde{h}_m^{\varphi,\gamma}(y) \tilde{h}_k^{\varphi,\gamma}(z) \Pi_{nmk} \tag{9}$$

The direct calculation by means of the Eq. (8) of the 3D Hahn moments Π_{nmk} results in an extremely high calculation time. The following section presents an approach, for the fast calculation of 3D Hahn moments Π_{nmk} by the 3D image cuboid representation (ICR).

3 Fast 3D Discrete Orthogonal Hahn Moments

In this section, we present a new way of calculating the Hahn moment, based on the stable HPs, which we talked about in the previous part on the one hand; and the ICR on the other hand.

We shall prioritize submitting the ICR, in this representation; we no longer need to describe the voxels with zero intensity for the 3D images. However, it should be emphasized that the intensity is between 0 and 255 in gray images, whereas zero intensity cuboids are neglected. With this methodology, we will have few elements to treat [26]. We assume the volume can be expressed by a discrete function $f(x, y, z)$, in which the intensity f_i represents each voxel of coordinates (x, y, z) as shown in Fig. 2.

We wish to implement an algorithm for 3D cuboid image representation as described in the following:

Algorithm 2: Algorithm of image cuboid representation

Step 1: Divides the image $f(x, y, z)$ into k matrix of size $N \times M$, in order to find object level intervals for each intensity value that exists in line y to finish this step compare intervals and blocks that have the same intensity line $y - 1$

Step 2: The beginning of a new block: If there is no block of the same intensity in the interval. The end of the block is in the line y , when a block exceeds the same intensity interval

Step 3: The blocks in matrix k_{z-1} are compared with the same intensity

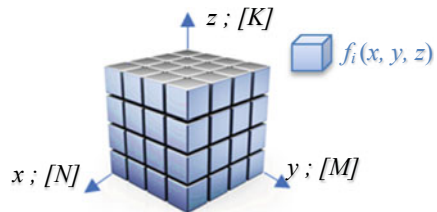
Step 4: In the output, we have L cuboid in production defined by its intensity f_i and its position $(x_1, x_2, y_1, y_2, z_1, z_2)$

After we have presented this algorithm, below we present a new method, in which the 3D DOHMs is calculated from the 3D image cuboid representation, furthermore the stable HPs.

However, the 3D image intensity i th, takes 0 to 255 values. The mathematical expression for a 3D image $f(x, y, z)$ containing L cuboids is written as follows:

$$f(x, y, z) = \sum_{i=1}^{255} f_i(x, y, z) \text{ with } f_i(x, y, z) = cub_j^{f_i} \tag{10}$$

Fig. 2 3D Image Cuboid representation



where $Cub_j^{f_i}$ is the cuboid j of intensity f_i , $j = 1, \dots, L_i$ is the j th cuboid of intensity f_i . Whereas $L = \sum_{i=1}^{255} L_i$, L_i the number of cuboid for each intensity f_i .

The 3D DOHMs can therefore be defined as:

$$\Pi_{nmk} = \sum_{i=1}^{255} \sum_{j=1}^{L_i} \Pi_{nmk}^{Cub_j^{f_i}} \tag{11}$$

whereas $\Pi_{nmk}^{Cub_j^{f_i}}$ is the $(n + m + k)$ th order of the 3D discrete orthogonal Hahn moments of intensity f_i for each cuboid:

$$\Pi_{nmk}^{Cub_j^{f_i}} = \sum_{x=x_{1,Cub_j^{f_i}}}^{x_{2,Cub_j^{f_i}}} \sum_{y=y_{1,Cub_j^{f_i}}}^{y_{2,Cub_j^{f_i}}} \sum_{z=z_{1,Cub_j^{f_i}}}^{z_{2,Cub_j^{f_i}}} \tilde{h}_n^{\varphi,\gamma}(x) \tilde{h}_m^{\varphi,\gamma}(y) \tilde{h}_k^{\varphi,\gamma}(z) f_i(x, y, z) \tag{12}$$

4 3D Image Reconstruction via DOHMs

The capabilities for the 3D image reconstruction are determined by stable DOHMs, this reconstruction takes place using two methods: a global reconstruction of the image as well as the partial reconstruction of the image. In the following, we focus on the partial image reconstruction, in order to stay within the specified target of this article.

In theory, an original 3D image function $f(x, y, z)$ of size $[N \times M \times K]$ can be represented from infinite series of 3D moments [25].

$$\hat{f}(x, y, z) = \sum_{i=1}^{255} \sum_{j=1}^{L_i} f^{Cub_j^{f_i}}(x, y, z) \tag{13}$$

where $f^{Cub_j^{f_i}}(x, y, z)$ is the partial reconstruction of the 3D DOHPs for each cuboid, can be rewritten as:

$$f^{Cub_j^{f_i}}(x, y, z) = \sum_{n=0}^{N-1} \sum_{m=0}^{M-1} \sum_{k=0}^{K-1} \Pi_{nmk}^{Cub_j^{f_i}} \tilde{h}_n^{\varphi,\gamma}(x) \tilde{h}_m^{\varphi,\gamma}(y) \tilde{h}_k^{\varphi,\gamma}(z) \tag{14}$$

where $\begin{cases} x_{1,Cub_j^{f_i}} \leq x \leq x_{2,Cub_j^{f_i}} \\ y_{1,Cub_j^{f_i}} \leq y \leq y_{2,Cub_j^{f_i}} \\ z_{1,Cub_j^{f_i}} \leq z \leq z_{2,Cub_j^{f_i}} \end{cases}$.

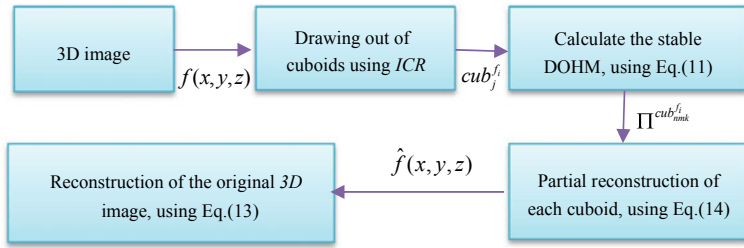


Fig. 3 Diagram for 3D image reconstruction via ICR

It is important to note that the cuboid is determined by the coordinates $(x_1, x_2; y_1, y_2; z_1, z_2)$, with $f^{Cub_j^f}(x, y, z)$ is the partial reconstruction for each cuboid. For further clarification, the Fig. 3 shows the flow chart for calculating the stable Hahn moments and its inverse by the new algorithm; firstly, we begin to break the 3D image to extract the cuboids. We used afterwards the extracted cuboids to calculate the 3D stable Hahn moments. Then we reconstruct every cuboid by calculating every cuboid using the 3D stable Hahn’s moments. Finally, we collect the cuboid to find the reconstruction of the 3D image.

5 Experimental Results

This section presents the findings of experiments to test the theoretical structure of the previous sections. In order to achieve the objective of this section, a process is envisaged for track screening: the Mean Square Error (MSE) used to measure the error of reconstruction between the original image and the restoration image, MSE given by this equation [25] in the case of 3D image:

$$MSE = \frac{1}{N \times M \times K} \sum_{x=0}^{N-1} \sum_{y=0}^{M-1} \sum_{z=0}^{K-1} \left(f(x, y, z) - \hat{f}(x, y, z) \right)^2 \quad (15)$$

In order to perform this simulation taking the case of $\varphi = \gamma$, it is noteworthy that in the McGill 3D shape benchmark database [28], we choose two 3D images, the first called the “Human,” and the second one called the “Dog”.

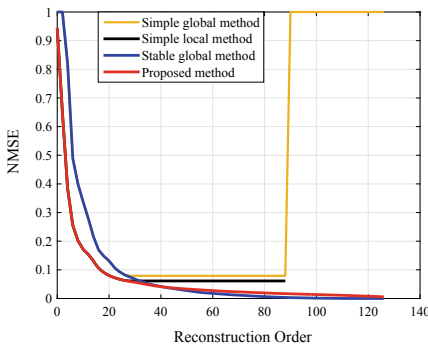
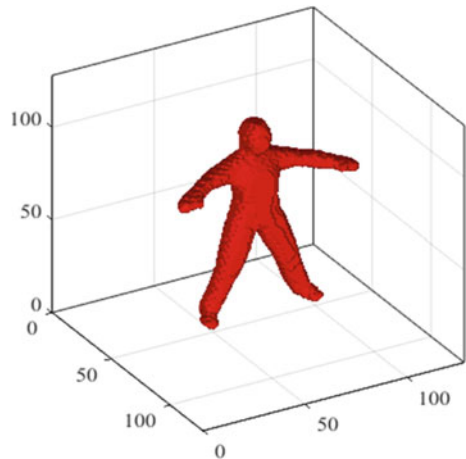
Regarding the first part of this section, we will compare the reconstruction capacity of the proposed method with three methods, the first called simple global method by the global method in Eq. (9) using the recurrence relation with respect to the variable x Eq. (6), the second is simple locale method by the local method in Eq. (13) using the recurrence relation with respect to the variable x Eq. (6), the third named stable global method by the global method in Eq. (9) using the algorithm 1.

In this respect, we compare the four methods using MSE of the 3D image “Human” Fig. 4 for the case $\varphi = \gamma = 0$ as pointed out in Fig. 5a and $\varphi = \gamma = 10$ as in Fig. 5b.

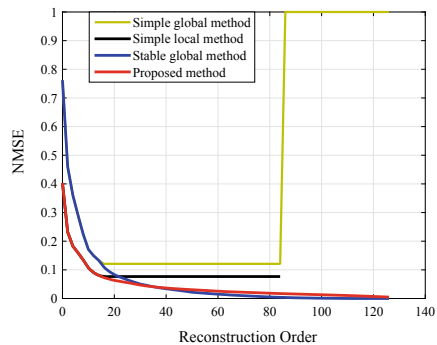
The MSE of 3D image for $\varphi = \gamma = 0$ as demonstrated in Fig. 5a indicates some similar features of the stable global methods and our proposed method. These methods begin with a significant Squared Error: 1 for stable global methods and 0.95 for the proposed method, however, they contracted to 0.08 at a moment order of 40, in addition to that, we can notice that if φ and γ are higher as shown in Fig. 5b, the initial MSE value is lowered relative to the other method. From this simulation, we can conclude that the two simple method does not maintain stability. Commonly, the proposed algorithm can perfectly reconstruct the 3D image for all order moments considered in this experiment.

We will continue our experimental results, in what follows we compare the proposed method with another base called the 3D moments of Krawtchouk, using

Fig. 4 3D image “Human” with size $128 \times 128 \times 128$



(a): $\varphi = \gamma = 0$

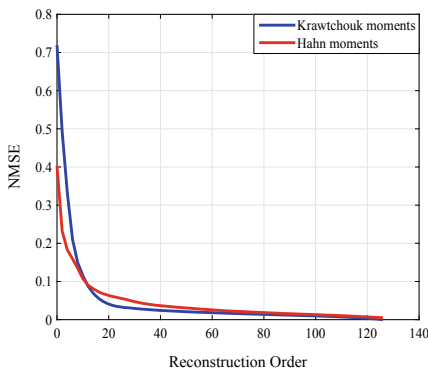
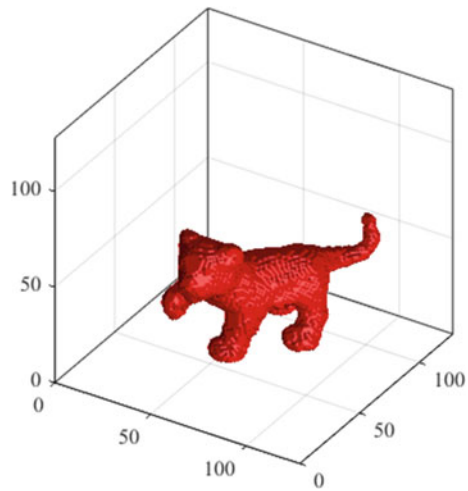


(b): $\varphi = \gamma = 10$

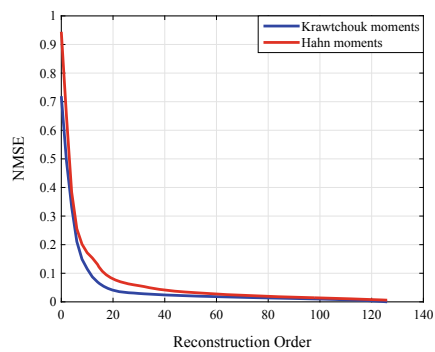
Fig. 5 MSE for the 3D images “Human”

MSE of the 3D image “Dog” Fig. 6 for the case $\varphi = \gamma = 0$ as can be seen in Fig. 7a, and $\varphi = \gamma = 10$ as shown in Fig. 7b. Figure 7 shows the average reconstruction errors based on MSE values, using the proposed method based on the Hahn moments compared to the same method with a Krawtchouk base (3D Krawtchouk moments), by increasing maximum moments order from 0 to 128. With regard to the case $\varphi = \gamma = 0$, the proposed method starts with an MSE value equivalent to 0.4, while the other method starts with 0.73, as seen in Fig. 7a. As for the next case wherein $\varphi = \gamma = 10$, the proposed method begins with a large MSE value compared to the other method, as illustrated in Fig. 7b, then the readings soon go back down to maintain stability, starting from moments order 60 to the maximum moments order

Fig. 6 3D image “Dog” with size $128 \times 128 \times 128$



(a) $\varphi = \gamma = 0$



(b) $\varphi = \gamma = 10$

Fig. 7 MSE for the 3D images “Dog”

128. To conclude, the parameters of the HPs affect the consistency of the recovered image, therefore, if the φ , γ increase, the quality of the output image improves.

6 Conclusion

We presented in this paper a new method to reconstruct a 3D image, which is based on two concepts. Firstly, the stable HPs, which significantly reduce numerical defects, secondly, the 3D image cuboid representation. This representation decomposes the 3D image into a group of cuboids that allows us to do a partial reconstruction; several experiments to show the performance of the proposed method have been performed on several 3D images selected from the “McGill” reference image database. The results show that our method in terms of 3D image reconstruction exceeds the other algorithms. In the future, we plan to apply this method for the classification of 3D images using the other discrete orthogonal polynomials.

References

1. Shen J, Meng S, Ye M, Yang W, Liu Z (2020) 3D image reconstruction using an ECT sensor with a single layer of electrodes. *Meas Sci Technol* 31(8):085106
2. Shalaby A, Elmogy M, Elfetouh AA (2019) 3D image reconstruction from different image formats using marching cubes technique. *Int J Comput Vis Robot* 9(3):293–309
3. Liu X, Li Y, Liu J, Zhang Q, Luo Y (2019) 3D image reconstruction of spinning cone-shaped target. *J Eng* 2019(20):6461–6465
4. Al-Shayea QK, Al-Ani MS (2016) An efficient approach to 3d image reconstruction. *Int J Comput Sci Netw Secur (IJCSNS)* 16(8):35
5. Bedratyuk L (2020) 2D geometric moment invariants from the point of view of the classical invariant theory. *J Math Imag Vis* 1–14
6. Suk T, Flusser J, Boldyž J (2015) 3D rotation invariants by complex moments. *Pattern Recogn* 48(11):3516–3526
7. Hosny HKM, Khalid AM, Mohamed ER (2020) Efficient compression of volumetric medical images using Legendre moments and differential evolution. *Soft Comput* 24(1):409–427
8. Elaziz MA, Hosny KM, Selim IM (2019) Galaxies image classification using artificial bee colony based on orthogonal Gegenbauer moments. *Soft Comput* 23(19):9573–9583
9. Wu G, Xu L (2019) Shape description and recognition by implicit Chebyshev moments. *Pattern Recogn Lett* 128:137–145
10. Hosny KM, Elaziz MA (2019) Face recognition using exact Gaussian-Hermit moments. In: *Recent advances in computer vision*. Springer, Cham, pp 169–187
11. Zhao Z, Kuang X, Zhu Y, Liang Y, Xuan Y (2020) Combined kernel for fast GPU computation of Zernike moments. *J Real-time Image Proces*
12. Bolourchi P, Moradi M, Demirel H, Uysal S (2020) Ensembles of classifiers for improved SAR image recognition using pseudo Zernike moments. *J Defense Model Simulat* 17(2):205–211
13. He B, Cui J, Peng Y, Yang T (2020) Image analysis by fast improved radial harmonic-Fourier moments algorithm. *Int J Imag Syst Technol*
14. Karmouni H, Jahid T, El affar I, Sayyouri M, Hmimid A, Qjidaa H, Rezzouk A (2017) Image analysis using separable Krawtchouk-Tchebichef’s moments. In: *International conference on*

- advanced technologies for signal & image processing (Atsip'2017), May 22–24 2017, Fez, Morocco
15. Sayyouri M, Hmimid A, Karmouni H, Qjidaa H, Rezzouk A (2015) Image classification using separable invariant moments of Krawtchouk-Tchebichef. In: 12th international conference of computer systems and applications (AICCSA), 17–20 November 2015 Marrakech, Morocco. doi: 10.1109/AICCSA.2015.7507142
 16. Jahid T, Karmouni H, Hmimid A, Sayyouri M, Qjidaa H (2017) Image moments and reconstruction by Krawtchouk via Clenshaw's recurrence formula. In: 3rd international conference on electrical and information technologies (ICEIT) November 15–18 2017, Rabat, Morocco
 17. Karmouni H, Jahid T, Lakhili Z, Hmimid A, Sayyouri M, Qjidaa H, Rezzouk A (2017) Image reconstruction by Krawtchouk Moments via digital filter. In: International conference on intelligent systems and computer vision, ISCV'2017, April 17-18-19-20 2017, Fez, Morocco
 18. Karmouni H, Jahid T, Sayyouri M, Hmimid A, El affar A, Qjidaa H (2018) Image analysis by Hahn moments and a digital filter. In: Ezziyyani M (eds) Advanced intelligent systems for sustainable development (AI2SD'2018). AI2SD 2018. Advances in Intelligent Systems and Computing, vol 915. Springer, Cham
 19. Karmouni H, Jahid T, Sayyouri M et al (2019) Fast 3D image reconstruction by cuboids and 3D Charlier's moments. *J Real-Time Image Process* 1–17
 20. Hmimid A, Sayyouri M, Qjidaa H (2014) Image classification using novel set of Charlier moment invariants. *WSEAS Trans Signal Process* 10(1):156–167
 21. Hmimid A, Sayyouri M, Qjidaa H (2018) Image classification using separable invariant moments of Charlier-Meixner and support vector machine. *Multimed Tools Appl* 1–25
 22. Jahid T, Hmimid A, Karmouni H, Sayyouri M, Qjidaa H, Rezzouk A (2017) Image analysis by Meixner moments and a digital filter. *Multimed Tools Appl* 1–21
 23. Spiliotis IM, Karampasis ND, Boutalis YS (2020) Fast computation of Hahn moments on gray images using block representation. *J Electron Imaging* 29(1):013020
 24. Spiliotis IM, Bekakos MP, Boutalis YS (2020) Parallel implementation of the image block representation using OpenMP. *J Parallel Distrib Comput* 137:134–147
 25. Karmouni H, Jahid T, Sayyouri M, Hmimid A, Qjidaa H (2019) Fast reconstruction of 3D images using Charlier discrete orthogonal moments. *Circuits Syst Signal Process* 38(8):3715–3742. <https://doi.org/10.1007/s00034-019-01025-0>
 26. Jahid T, Karmouni H, Sayyouri M, Hmimid A, Qjidaa H (2019) Fast algorithm of 3D discrete image orthogonal moments computation based on 3D cuboid. *J Math Imaging Vis* 61(4):534–554
 27. Zhu H, Liu M, Shu H, Zhang H, Luo L (2010) General form for obtaining discrete orthogonal moments. *IET Image Proc* 4(5):335–352
 28. Siddiqi K, Zhang J, Macrini D, Shokoufandeh A, Bouix S, Dickinson S (2008) Retrieving articulated 3-D models using medial surfaces. *Mach Vis Appl* 19:261–275

Analysis of Online Spiral for the Early Detection of Parkinson Diseases



Yassir Elghzizal, Ghizlane Khaissidi, Mostafa Mrabti, Aouraghe Ibtissame, and Ammour Alae

Abstract Parkinson's disease (PD) is a neurodegenerative disorder that affects a person's movement. As the early diagnosis of the disease is crucial, the main aim of this work is to implement an online analysis system of patients' handwriting, through computer vision and signal processing techniques, using the database collected in the neurology department of the University Hospital Center Hassan II in Fez. For this, we studied the handwriting tests on a WACOM graphic tablet to retrieve the spatiotemporal data (position, pressure and angles of inclination), for each point ($P(n)$) of the trajectory. The features vector was obtained basing on five types of features: (a) Kinematic features related to the dynamics of spiral design, (b) Mechanical based on the pressure exerted on the writing surface, (c) Inclination angles, (d) Spatial interrelation feature and (e) Pen-Up. The used classification and clustering algorithms are respectively the Hoeffding tree and the FarthestFirst clusters. We observed coherence between the classification results and the clustering ones, thus the results being encouraging and promising with a recognition rate of 98.36%

Keywords Parkinson disease · Online handwriting · Graphic tablet · Signal processing · Computer vision · Classification · Clustering

Y. Elghzizal (✉) · G. Khaissidi · M. Mrabti · A. Ibtissame · A. Alae
Laboratory LIPI ENS, USMBA, Fez, Morocco
e-mail: elghzizalyassir@gmail.com

G. Khaissidi
e-mail: ghizlane.derkaoui1@hotmail.com

M. Mrabti
e-mail: mostafa.mrabti@yahoo.fr

A. Ibtissame
e-mail: aouraghe.ibtissame@gmail.com

A. Alae
e-mail: alae.am19@gmail.com

1 Introduction

Parkinson's disease is a disorder of the central nervous system (brain) characterized by the destruction of specific neurons: the dopamine neurons of the black substance of the brain. These neurons are involved in movement control, which gradually leads to movement abnormalities such as tremors or difficulty in achieving movements, rigidity, slow and difficult movements (Akinesia), stiffness of the whole body, as well as people with the disease gradually suffer from changes in their ability to speak and write [1].

The first clear medical description was written in 1817 by James Parkinson [2]. In the mid-1800s James Martin CHARCOT played a particularly important role in refining and expanding this first description and in disseminating information about Parkinson's disease. He separated Parkinson's disease from other disorders characterized by tremors [3]. To date, the causes of the disease remain unknown, and the available treatments do not improve the quality of life of the patients nor the stopping the progression of the disease.

In recent years, several studies have attempted to exploit the rapid emergence of technologies to facilitate the diagnosis of Parkinson's disease. Especially methods based on handwriting analysis, since patients with Parkinson's disease have difficulties during writing [4]. Two approaches are proposed in the literature on this context:

Offline Where the manuscript is scanned and processed as an image. Then, in the phase of automatic PD recognition, pattern recognition techniques were used. Pereira et al. [5], have applied the Optimum-Path Forest (OPF) classification. Pan et al. [6] have studied the effectiveness of the three methods; support vector machines (SVM), neural networks such as Multi-LayerPerceptron and RBF to evaluate the occurrence of tremor for the PD patients. Ma et al. [7] presented a computerized approach based on "optimization of particle swarms" and "ranking of the nearest neighbors" to facilitate PD diagnosis, with an accuracy of 97.47%. It is worth noting that these techniques used on the above-mentioned data set [7]. Despite the remarkable results reported, 74% of the database includes patients with PD, which can distort the results. By combining known and supervised classification techniques, such as OPF, SVM and NB, Yassir et al. [8] obtained promising results, reaching 98.36% on the database (NewHandPD) [8].

Online Due to the emergence of advanced new technologies, we are led to proceed to the acquisition of some online features of the handwriting signals, instead of working with spatial characteristics. The digitizing tablet gives us the possibility to add, to x and y coordinate, information about time, pressure sensitivity and angles of the pen inclination in order to quantify the writing movements of the patients in a temporal, dynamic and kinematic way [9]. In [10, 11], the authors show that kinematic features are of great interest in the analysis of PD dysgraphia. Drotar et al. [12] have shown that empirical mode decomposition (EMD) can achieve a classification accuracy of up to 89%. Then, Kotsavasiloglou et al. achieved an average accuracy of 91%

using features describing speed variability, deviation from the horizontal plane, and trajectory entropy [13].

In this paper, we use the digital outputs of the handwritten spiral tests to diagnose PD and assess a patient's writing ability. Our results and an in-depth review of the literature allowed us to prove the effectiveness of the proposed features, such as:

- Power = $P * V * \cos(\Phi)$,
- Work = $P * D * \cos(\Phi)$,

which combine features based on pressure (P), velocity (V) and altitude angle (Φ) on the one hand, and pressure, displacement (D) and altitude angle on the other hand.

- Spatial interrelation features: describe the geometry of the shape, it should be noted that the study of the geometry of the patient's handwritten has been applied for the first time in the online diagnosis of PD.

During the recognition phase, we assess the performance of the proposed descriptor using the "Hoeffdingtree (VFDT)" classifier, and then compare the classification results with the clustering ones using "Farthestfirst clusters". The results are very promising compared to other related works.

2 Materials and Methods

2.1 Data Acquisition

The handwriting database was collected using a Wacom Intuos Pro creative pen tablet with a sampling rate of 125 Hz. Using the "Paper Edition" technology, where the drawing paper on which patients take their handwritten tests, the tablet converts each of its pencil strokes into digital format.

These online digital trajectory data were the main information for building our database with this graphic tablet, the collected information are:

- $(X_n(t), Y_n(t))$, represent the abscissa and ordinate respectively,
- $P_n(t)$: The tablet is able to detect 2048 sensitivity levels to pressure,
- Detection of the natural pen inclination angle,
- The coordinates when the pen is in the air (up to 5 cm above the tablet).

2.2 Handwriting Tests

We have developed a new data base mentioned in [14] consisting of images from handwritten examinations (offline) and digital data (online) from 61 individuals, including 9 with Parkinson's disease (patient group) and the rest in good health

Fig. 1 Sample of the handwritten examination acquisition sheet

(control group). Furthermore, the age of all individuals is in the range [15, 85]. This database was acquired within the neurology department of the Hassan II University Hospital Centre in Fez.

The writing exam essentially consists of filling out a form to accomplish certain tasks, which we have presented to the patients as we go along. Our study consists of 3 exercises. The first exercise consists in copying given texts in Arabic and French. The second exercise consists of writing a free text in Arabic and French, followed by a series of four letters “I”. The rest of the drawing exercises consist of drawing circles, a spiral and back and forth between two tiles. Figure 1 shows the proposed handwritten form template.

In this work, we are interested only by the spiral tests.

2.3 Features Extraction and Analysis

From the numerical values (T, X, Y, P, Θ and Φ) of the manuscript signal of the people included in the study, we try to extract as much information as possible from the signal, by creating new parameters, which purpose is to describe the patient’s behavior during writing. In this section, we present the list of the extracted features classified into 5 categories:

Kinematic Features

The kinematic characteristics are dependent on the dynamics of the spiral design [12]; displacement, velocity, acceleration, jerk, number of changes of velocity (NCV), number of changes of acceleration (NCA), and Normalized Velocity Variability NVV where: $NVV = 1/T|MV| * \sum |V_{i+1} - V_{i-1}|$ (1)

The smoothest movements correspond to the lowest values of NVV (Constant Speed)

Mechanical features

They are based on the pressure exerted on the tablet screen [12]: P(t), d(P(t)), Energy, work, and so on.

Inclination angles

The tablet gives us two angles: Azimuth angle between the pen and the vertical plane on the pad ($\Theta(n)$), and altitude angle between the pen and the tablet screen ($\Phi(n)$), $d(\Theta(n))$ and $d(\Phi(n))$.

Spatial interrelation feature

Spatial interrelation feature describe the contour or a region of the curve shape. Usually, the representation is made by using their geometrical characteristics: curvature, length, area, distance, orientation and location... In this work, we are only interested in: Tangent deviation; Curvature total error; Beam angle statistics and Mean relative Tremor (MRT).

Tangent deviation.

For each point on the drawing path of the spiral, the tangent of the sampling point is:

$$AG(i) = \arctan[r(i) * \{ \Theta_i - \Theta_{i-1} \} / \{ r_i - r_{i-1} \}] \tag{2}$$

And the tangent of the Template spiral is always equal to $\pi/2$.

The deviation tangent will be calculated as the difference between $AG(i)$ and $\pi/2$ to quantify the writing deterioration of the patients [8]:

$$TD = 1/n \sum \sqrt{AG^2(i) - (\pi/2)^2} \tag{3}$$

Curvature total error.

The curvature total error is the difference between Curvature radius and the radius on template spiral [8]:

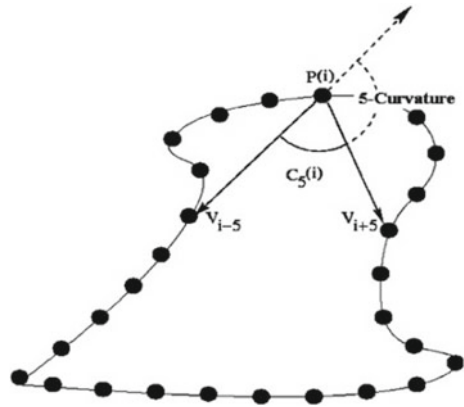
$$CTE = (1/n) * \sum \sqrt{(\rho_i^2 - r_{ST}^i)^2} \tag{4}$$

where r_{ST}^i is the radius on template spiral and ρ_i is the Curvature radius of the ith sampling point:

$$E[C^m(i)] = \sum_{k=1}^{(\frac{N}{2})-1} [C_k^m(i) * P_k(C_k(i))] \quad m = 1, 2, 3, \dots \tag{5}$$

Beam angle statistics.

Fig. 2 Beam angle at the neighboring system 5



For the *i*th sampling point P(*i*), the beam angle in the neighboring system of order *k*, is then calculated as follows as:

$$C_k(i) = (\Theta_{vi + k} - \Theta_{vi - k})$$

Where $\Theta_{vi + k} = \arctan((y_{i+k} - y_i)/(x_{i+k} - x_i))$.

And $\Theta_{vi - k} = \arctan((y_{i-k} - y_i)/(x_{i-k} - x_i))$.

For each sample point P(*i*), the angle C_k(*i*) can be considered as a random variable and P(C_k(*i*)) as the associated probability density function, for which the moment of C_k(*i*) is defined as follows:

$$E[C^m(i)] = \sum_{k=1}^{(\frac{N}{2})-1} [C_k^m(i) * P_k(C_k(i))] \quad m = 1, 2, 3, \dots \quad (6)$$

The Beam Angle Statistics Descriptor (BAS) [15] uses all the statistical information extracted from the beams of individual points to form an overall view related to the shape of the path. It tries to give us discriminating characteristics at each boundary point regarding all other points already calculated. Finally, each point of curvature will be presented by a vector of the beam angles moments:

$$\Gamma(i) = [E[C_1(i)], E[C_2(i)], \dots]$$

Mean relative Tremor (MRT).

The MRT presents quantitative evaluation to determine the “amount of tremor”, it is the average difference between the displacement of a sample (D_i) and its previous neighbors:

$$\text{MRT} = [1/(n - d)] * \sum_{i=d}^n |D^i - D^{i-d+1}| \quad (7)$$

where D_i is the displacement of a sample: $D_i = \sqrt{(x_{i+1} - x_{i-1})^2 + (y_{i+1} - y_{i-1})^2}$ $1 < i < n - 1$

n is the number of sampling points, and d is the displacement step used.

Pen-Up

These types of values specifically describe the aspect of in-air writing movements: in-air/on the pad normalized ratio, time in-air, number of Pen-Up and Pen-Down...

2.4 Features Selection

All the previously mentioned features were assembled to create a vector of 74 components which were evaluated according to their quality and informative content. To estimate the quality of the 74 extracted features, the ReliefF selection algorithm is implemented [16]. It gives a relevance score to each element. Then, we rank the features according to their individual relevance by a ranking method. The idea behind is to choose the first few relevant ones to be used for classification and rejecting the rest using the ANOVA Test.

The one-way analysis of variance (ANOVA) method is a filtering algorithm that evaluates the variance of the components by the distance between classes. The component can be considered as a discriminating characteristic if the calculated Fisher value F is greater than 2. Furthermore, the degree of discrimination of the characteristics can be assessed by the p -value, if p -value is greater than 0.05, the F -value will be considered statistically significant. Finally, after the application of the ANOVA, 54 optimal parameters have been selected to discriminate between these classes.

2.5 Classification and Clustering Algorithms

A comparison of a classification and clustering algorithm was carried out to distinguish between the two classes. The clustering method was the FarthestFirst clusters [17], and the classification method was the Hoeffding tree (VFDT) [18]. The accuracy of the Hoeffding tree method was established by 10-Fold Cross Validation.

FarthestFirst clusters

The farthest-first traversal k -center [17] selects k points as cluster centers. The first center is chosen randomly, the second center is carefully chosen in such a way that it is the point farthest from the first center. The other centers were identified carefully

by choosing the farthest point from the set of centers already selected, and similarly adding the remaining points until the convergence of the system. The implementation of this method does not require a lot of relocation and tuning so can speed up the clustering process considerably

Hoeffding tree (VFDT) classifier

The Very Fast Decision Tree (VFDT) is a decision tree induction classifier, in the training phase it is capable of learning accurate models at high speed from more complex data streams and dynamic design. For each new test example, the VFDT is able to quickly generate a decision tree updated with the learning one.

To determine the number of examples needed for each decision, the VFDT uses a statistical result known as Hoeffding limits, which is why it is called: A Hoeffding tree (VFDT) classifier. Hoeffding’s bound can prove that its result is almost identical, asymptotically, to that of a non-incremental classifier, by applying to the large number of examples [18].

3 Experimental Results

The first step in the experimentations is ranking the extracted features according to their “relevance score”. Then, The ANOVA attempts to identify which components of the features set are the most discriminating between classes (Fig. 3).

To construct the final set of features, the component was excluded if its p-value is less than 0.05 and its F-value is less than two. Otherwise, the component is kept in the features vector. Finally, we obtained 54 significant components instead of the 74 extracted components. Tables 1 and 2 present the results for the FarthestFirst clusters and the Hoeffding tree classifier (VFDT) considered respectively. The parameters of the two algorithms were set experimentally.

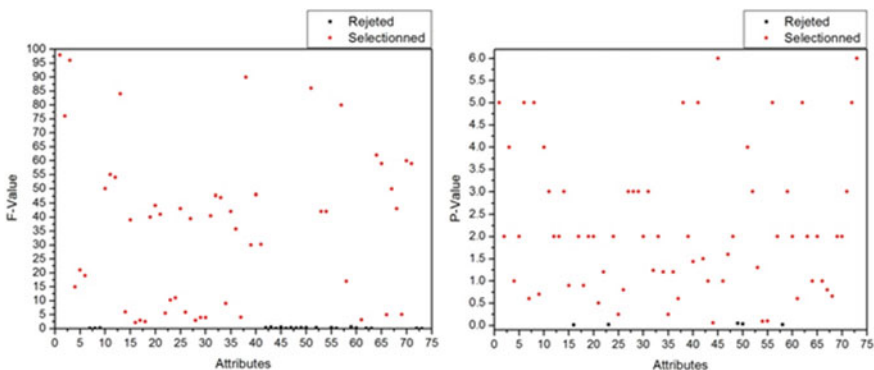


Fig. 3 The statistical F-values and p-values of the two classes

Table 1 Distribution of participants after the application of farthest first clusters

Group	Feature vector	Number of components	Clusters
PD = 9	ReliefF	74	ClassI: 18
HC = 52			ClassII: 43
PD = 9	ReliefF + ANOVA	54	ClassI: 10
HC = 52			ClassII: 51

Table 2 Classification results of Hoeffding tree classifier (VFDT)

Classifier	Feature vector	Number of components	Correct classification (%)
Hoeffding tree	ReliefF	74	95.08
Classifier (VFDT)	ReliefF + ANOVA	54	98.36

The application of the ANOVA filtering, as shown in the experimental results, was beneficial because it minimizes the number of components, by eliminating non-significant components that may deviate the clustering or classification process. This reduces the number of characteristics without significant loss of information decreasing thus the calculation time.

The clustering results were similar with the classification ones, especially after the addition of the ANOVA feature selection algorithm. We obtained a very high recognition rate of 98.36%. To judge the performance of a considered Hoeffding tree classifier (VFDT), we calculated four measures: Recall, Accuracy, F-Score and Precision (Table 3).

Some people have poorly designed the spiral of the examination, this may explain the Recall = 100% scores of the patient group and Recall = 98.36% of the healthy group. We can observe that our descriptor made the error at the control group level. The confusion matrix presented in Table 4 gives us a clearer vision on the classification of our database.

Table 3 Experimental classification results with ANOVA

Hoeffding tree classifier (VFDT)		
Accuracy		98.36%
Patient	F-Score	94.7%
	Precision	90%
	Recall	100%
Healthy	F-Score	99%
	Precision	100%
	Recall	98.4%

Table 4 Confusion matrix of the Hoeffding tree classifier (VFDT) with ANOVA

		Prediction		
		Patient	Healthy	
Observation	Patient	9	0	9
	Healthy	1	51	52
		10	51	

As already mentioned, we found coherence between the classification results and the clustering results (Tables 1 and 4), 51 healthy people and 10 patients as simulation results occurred from 52 healthy people and 9 patients.

4 Conclusion

This paper presents the intelligent part of an automatic classification system for patients with PD based on computer vision. This system is able to diagnose PD using online handwriting information, such as kinematic, pressure, Inclination, in-air and spatial features that describe a region of the contours of the drawn spiral with respect to their pixels. The used classification and clustering algorithms are Hoeffding tree and FarthestFirst clusters respectively.

The quality of the obtained results (98.36% accuracy rate) encouraged us to think about improving the performance of our system, so, we aim to apply the proposed method to all the tasks of the writing exam (texts, series of character “l”, circles,...), to create and analyze a complete descriptor that perfectly describes patient handwriting. In addition, we plan to develop our dataset to contain more patients from others cities.

References

1. Burke RE (2010) Evaluation of the Braak staging scheme for Parkinson’s disease: Introduction to a panel presentation. *Mov Disord* 25(1)
2. Parkinson J (2002) An essay on the shaking palsy. *J Neuropsychiatr Clin Neurosci* 14(2):1817
3. Waraich M, Shah S (2018) The life and work of Jean-Martin Charcot (1825–1893): ‘The Napoleon of Neuroses’. *J Intensive Care Soc* 19(1):48–49
4. McLennan J, Nakano K, Tyler H, Schwab R (1972) Micrographia in Parkinson’s disease. *J Neurol Sci* 141–152
5. Pereira JC, Schelp AO, Montagnoli AN, Gatto AR, Spadotto AA, De Carvalho LR (2006) Residual signal auto-correlation to evaluate speech in Parkinson’s disease patients. *Arq Neuropsiquiatr* 64(4):912–915
6. Pan S, Iplikci S, Warwick K, Aziz TZ (2012) Parkinson’s disease tremor classification— a comparison between support vector machines and neural networks. *Expert Syst Appl* 39(12):10764–10771

7. Ma C, Ouyang J, Chen HL, Zhao XH (2014) An efficient diagnosis system for Parkinson's disease using kernel-based extreme learning machine with subtractive clustering features weighting approach. *Comput Math Methods Med*
8. Yassir E, Ghizlane K, Mostafa M, Driss C (2019) Towards an automatic and early detection of Parkinson's disease: modeling of a polar coordinates system based on spiral tests. In: *AIP conference proceedings*, vol 2074
9. Letanneux A, Danna J, Velay JL, Viallet F, Pinto S (2014) From micrographia to Parkinson's disease dysgraphia. *Mov Disord* 29(12):1467–1475
10. Heremans E, Nackaerts E, Broeder S, Vervoort G, Swinnen SP, Nieuwboer A (2016) Handwriting impairments in people with Parkinson's disease and freezing of gait. *Neurorehabil Neural Repair* 30(10):911–919
11. Taleb C, Khachab M, Mokbel C, Likforman-Sulem L (2017) Feature selection for an improved Parkinson's disease identification based on handwriting. In: *1st international workshop on Arabic script analysis and recognition (ASAR)*, pp 52–56
12. Drotár P, Mekyska J, Rektorová I, Masarová L, Smékal Z, Faundez-Zanuy M (2015) Decision support framework for Parkinson's disease based on novel handwriting markers. *IEEE Trans Neural Syst Rehabil Eng* 23(3):508–516
13. Kotsavasiloglou C, Kostikis N, Hristu-Varsakelis D, Arnaoutoglou M (2017) Machine learning-based classification of simple drawing movements in Parkinson's disease. *Biomed Signal Process Control* 31:174–180
14. Ibtissame A et al (2017) Automatic analysis of on-line handwriting for the early detection of neurodegenerative pathologies
15. Arica N, Yarman Vural FT (2003) BAS: a perceptual shape descriptor based on the beam angle statistics. *Pattern Recognit Lett* 24(9–10):1627–1639
16. Demšar J, Zupan B (2009) From experimental machine learning to interactive data mining. *Qual Reliab Eng Int* 38(2):162–315
17. Doshi RH, Bhadka HB, Mehta R (2013) Development of pattern knowledge discovery framework using clustering data mining algorithm. *Int J Comput Eng Technol* 4(3):101–112
18. Hulten G, Spencer L, Domingos P (2001) Mining time-changing data streams. In: *Proceedings of seventh ACM SIGKDD International Conference Knowledge discovery and data mining*, pp 97–106

Learning Hand-Crafted Palm-Features for a High-Performance Biometric Systems



Amel Bouchemha, Abdallah Meraoumia, Lakhdar Laimeche,
and Lotfi Houam

Abstract The extraction of distinctive image features is the most important step in pattern recognition systems due to their direct impact on learning the machine commonly used in these types of systems. In this paper, we propose a handcraft feature learning, which based on local distinctive image descriptors, for multispectral palmprint representation and recognition. In the training phase, a projection matrix (hash functions) and a codebook are obtained using the Pixel Difference Vectors (PDVs) of non-overlapping sub-blocks, in order to use it as prior knowledge in the feature extraction step. For the test phase, the extracted PDVs are encoded into binary codes using the projection matrix, then pooled as a histogram feature using the codebook. The experimental results carried out on the CASIA database show that the proposed framework achieves better performances compared to the state-of-the-art methods, in particular the handcrafted ones.

Keywords Feature extraction · Handcrafted features · Encoded features · Biometrics · Multispectral palmprint · Data fusion

A. Bouchemha (✉)

Department of Electrical Engineering, University of Larbi Tebessi, 12002 Tebessa, Algeria

e-mail: amel.bouchemha@univ-tebessa.dz

A. Meraoumia · L. Laimeche · L. Houam

Laboratory of Mathematics, Informatics and Systems (LAMIS), University of Larbi Tebessi, 12002 Tebessa, Algeria

e-mail: ameraoumia@univ-tebessa.dz

L. Laimeche

e-mail: lakhdar.laimeche@univ-tebessa.dz

L. Houam

e-mail: lotfi.houam@univ-tebessa.dz

© Springer Nature Singapore Pte Ltd. 2022

S. Bennani et al. (eds.), *WITS 2020*, Lecture Notes in Electrical Engineering 745,

https://doi.org/10.1007/978-981-33-6893-4_77

1 Introduction

The increasing demand to develop a biometric system with low-error rates have prompted researchers to use multispectral imaging to overcome the limits of visible light technologies. The effectiveness of multispectral imaging lies in the ability to provide additional information that cannot be provided by visible light. As a consequence, palmprint recognition under this technology is a dynamic field due to the perceived effectiveness of this modality which makes it widely used. Recently, the multispectral representation of the palmprint image has given particular attention due to its serious and crucial impact on the performances of the biometric system. The palmprint modality is the central area of the hand palm that contains numerous wrinkles and creases so that it can be used to extract many unique and rich features, which qualifies it to be effectively used for human identification and therefore its use in physical/logical access control systems in several highly secure applications.

In any biometric recognition system, the feature extraction step is one of the most important steps in the system flowchart due to its significant and direct impact on system accuracy. Based on the feature types that can be extracted from the biometric modality (lines, texture or shape), several feature extraction methods have been proposed. As one of the powerful texture analysis methods, the local features representation of the biometric modality shows an efficient performance to extract the distinctive texture characteristics. In the biometric literature, various local features are proposed for image representation, such as the gray-scale/multispectral palmprint recognition and face identification. Generally, these methods describe each pixel's neighborhood by a binary code which is obtained by convolving the image with a set of linear filters and then binarizing their responses.

Specifically, the Local Binary Pattern (LBP) [1], Local Phase Quantization (LPQ) and Basic Image Features (BIF), with their variants, are the most adopted methods widely used in pattern recognition systems. As examples, in [2], the authors propose an efficient multi-resolution approach based rotation invariant LBP and as classification rule, they use non-parametric discrimination based on log-likelihood. The authors, in [3], use the histogram of Binarized Statistical Image Features (BSIF) codes of images processed by Gabor filters with different wavelengths and orientations. Likewise, the authors, in [4] decompose the palmprint image using the shiftable Complex Directional Filter Bank (CDFB), in which the coefficients of CDFB subbands are exploited by the uniform LBP. In recent years, very discriminative and computationally efficient local texture descriptors based on LBPs have been proposed. With this in mind, Hassner et al. [5] propose a new variety of LBP, called Three-Patch LBP (TP-LBP) and Four-Patch LBP (FP-LBP), to labeled faces in the Wild image set. Also, in their work, Bouchemha et al. [6] attempted to extract critical information from multispectral palmprint images using dynamic and statistic features based on ridgelet transform and the parameters of the Gray-Level Co-occurrence Matrix (GLCM). Finally, it should be noted that several methods combine these features to increase the performance of multispectral/hyperspectral palmprint recognition systems.

All the image representation methods described above, which are commonly known as handcraft methods, attempt to improve the extracted image's feature, in particular those based on texture, but unfortunately, they have reached their limits, especially for large databases that contain highly correlated interclass. In order to overcome the limitation of the handcrafted methods, the researchers tried to provide these methods with prior knowledge, generally related to the application context, in order to increase their performance. Basically, prior knowledge of the handcrafted method can be obtained by the learning principle. To this end, many efforts have been made and are fortunately yielded to an effective method called Compact Binary Descriptor (CBD) [7]. In this method, the learning of local features uses the key-point detection and acts directly on the features by learning a transformation of the handcrafted descriptors towards a new space in which the discriminating power of the best features and the matching accuracy are improved.

In this paper, a hand-craft image feature learning method, based on LBP, is applied to multispectral palmprint representation and recognition to increase the performance of the biometric system. In our scheme, the CBD-based feature extraction method is used in conjunction with an SVM classifier to design a biometric system with high accuracy.

The remainder of the paper is organized as follows: Sect. 2 presents the methods used for the image feature extraction step. In this section, handcrafted and learned-handcrafted methods are briefly discussed. In Sect. 3, the experimental results are given and discussed. Finally, Sect. 4 concludes the paper and presents future work.

2 Image Feature Extraction

Feature extraction is the process of transforming the image's raw pixel values into more meaningful and useful information that can be used in a machine vision application [8]. For this reason, these processes have been carefully designed by specialists (Hand-craft) using their knowledge and expertise. Generally, these techniques are applied to the image without prior knowledge of its content. Thus, to improve their performance, these techniques were provided with prior knowledge of their context through automatic learning (Learned Hand-craft). In recent years, with the advent of deep learning, the neural networks themselves automatically do the work of the expert in the convolutional layers.

2.1 Handcrafted Image Feature

The image contains many features that can be used to analyze such a scene. The type of feature used varies depending on the intended application. For example, in an image containing a scene composed of different patterns, several methods must be used to extract each pattern separately [9]. Therefore, it is necessary to know the scene

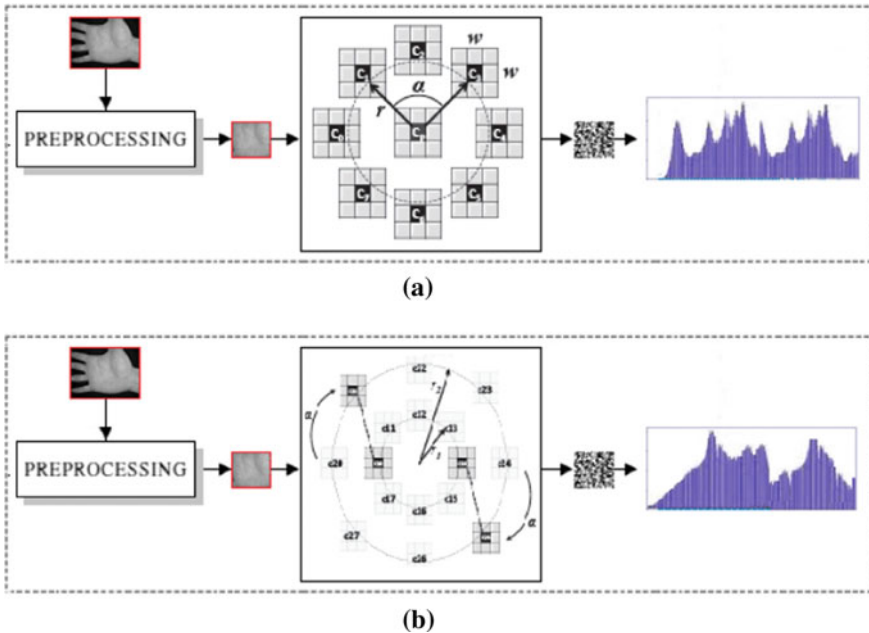


Fig. 1 Handcrafted palmprint feature extraction techniques. **a** Three-Patch LBP Codes Feature (TP-LBP), and **b** Four-Patch LBP Codes Feature (FP-LBP)

type to effectively choose the appropriate method. Therefore, as these techniques require expertise, the obtained features are considered handcrafted. Certainly, due to the effectiveness of the LBP in PR systems, many researchers have attempted to improve this technique, resulting in many variants of LBP, in which TP-LBP and FP-LBP are two effective extensions of LBP.

Three-Patch LBP Codes Feature In the TP-LBP method (see Fig. 1a), the code for each image’s pixel is obtained by comparing the two patches with the central patch of size $w \times w$ around the pixel. The code assigned of each pixel is of S bits. The following equation gives the expression of TP-LBP [5]:

$$TP-LBP_{r,S,w,\alpha}(p) = \sum_i^S f(D_S)2^i \tag{1}$$

$$D_S = d(C_i, C_p) - d(C_{i+\alpha \bmod S}, C_p) \tag{2}$$

where C_p is the central patch, C_i and $C_{i+\alpha \bmod S}$ are two patches along the ring of radius r , $d(\bullet, \bullet)$ the distance between two patches and f is defined as $f(x) = 1$ if $x > \tau$, otherwise 0. The value of τ is set slightly greater than zero.

Four-Patch LBP Codes Feature In the FP-LBP (see Fig. 1b), two rings of r_1 and r_2 are considered and centered on the pixel. The FP-LBP code is obtained by compared two center symmetric patches in the inner ring with two center symmetric patches in the outer ring positioned α patches away along the circle [5]:

$$\text{FP-LBP}_{r_1, r_2, S, w, \alpha}(p) = \sum_i^{S/2} f(D_S)2^i \quad (3)$$

$$D_S = d(C_{1,i}, C_{2,i+\alpha \bmod S}) - d(C_{1,i+S/2}, C_{2,i+S/2+\alpha \bmod S}) \quad (4)$$

In both methods, the resulting response is then divided into non-overlapping regions and a histogram is computed for each region. Histograms are normalized to unit-rank and concatenated into a single vector to represent the characteristics of the entire image.

2.2 Learned Handcrafted Image Feature

The CBD method [7] can be considered as a learned extension of LBP. This method is learned directly and once on the raw pixel of the image at the beginning. This method has two stages (feature learning and feature extraction) and can be briefly summarized as follows:

In the feature learning phase (see Fig. 2a), for each pixel, the Pixel Difference Vector (PDV), obtained by measuring the difference between the pixel central and his neighbors in a predefined $w \times w$ -sized window, is calculated. All the vectors obtained were used to train the CBD method. Then, a projection matrix (W), which aims to learn K hash functions, is calculated. This matrix is used later to quantify each PDV vector into a binary vector. To calculate the matrix W , an optimization criterion is used. Finally, to reduce the number of binary vectors found for each image, a codebook is used. This codebook is obtained from all binary vectors (obtained by the projection of all PDVs) using the unsupervised k -means clustering algorithm.

In the feature extraction phase (see Fig. 2b), after having formulated all the PDV vectors of the image, their binary correspondences are obtained thanks to the projection matrix W . Then, each binary vector is replaced by the closest vector coordinate in the codebook. Finally, using the different coordinates, a histogram is formed to represent the entire image. Practically, to find discriminating feature vectors, the raw image is analyzed under several regions (each region is used as an image) and all the histograms are concatenated to form the feature vector of the entire image.

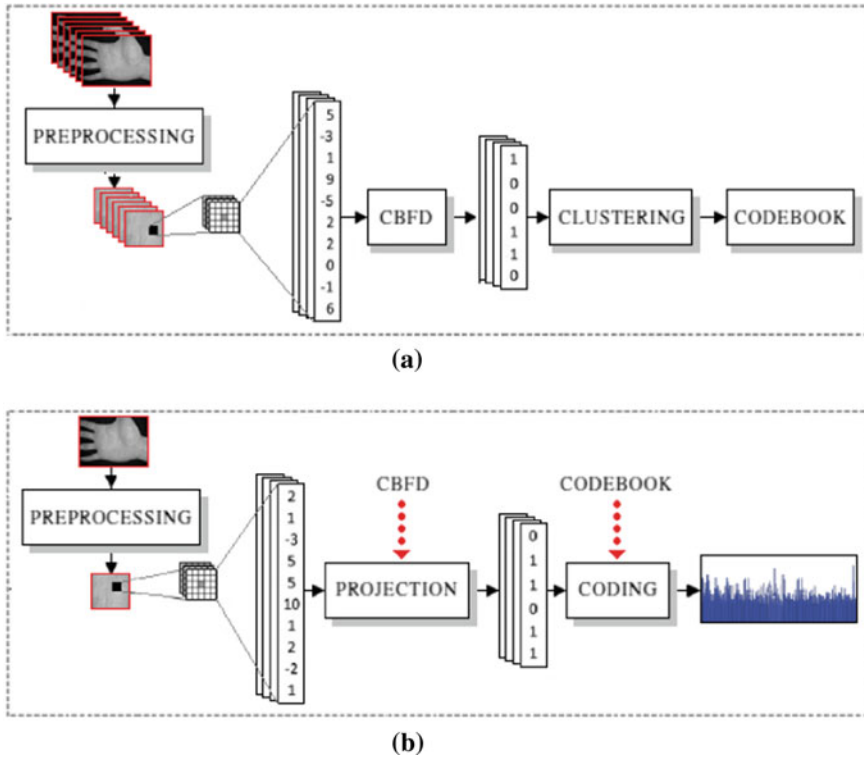


Fig. 2 Learned handcrafted palmprint feature based on compact binary descriptors. **a** Feature learning phase, and **b** feature extraction phase

3 Experimental Results

In our work, we use the CASIA multispectral palmprint database [10] which contains hand images acquired using a contact-free sensor at a low resolution in six different spectral bands (460, 630, 700, 850, 940 nm and WHT (White Light)). In this section, we highlight the performance and the robustness of the proposed binary learning feature approach for multispectral palmprint identification. In our experimental test, we divide the dataset into two galleries in which = 33% (400 images) are randomly selected for enrolment and the other = 67% (800 images) are reserved for the various tests (identification). During the identification test, 40,400 results were obtained using all the images in the test gallery, assigning 800 scores to genuine experiences and the remaining 39,600 to impostor experiences. It should also be noted that the set of experimental results is divided into two parts: the first part is the main process of selecting the best parameters for the learned hand-craft feature extraction technique (number of regions in each image, pixel’s neighborhood size and codebook size), while the second part is devoted to testing the proposed biometric identification

system in the two modes of identification: *open-set* and *closed-set* identification mode.

To improve the performance of the CBD-based multispectral palmprint identification system, we have tested two important parameters, which are the size of the pixel neighborhood (R) and the projection matrix length (BIN) in order to adapt the CDF method to the database used. In our tests, the values of the parameters listed above are changed each time then the Equal Error Rate (EER) is calculated. The results of the tests obtained for the three spectral bands are illustrated in Table 1. Thus, from this table, we can clearly see that the two CBD parameters can give good results in all spectral bands. The highest EER does not exceed 1000% and this is when using 850 nm spectral band (EER = 0.994% at a threshold, T_o , equal to 0.6538). It should be noted that in all these tests, we also modify the number of regions within the image (from 1 to 16) and the codebook size (from 25 to 500 with a step of 25) and the results obtained show that 9 regions with a 100-sized codebook are sufficient to allow better performance.

The aim of the second series of experiments is to assess the performance of the system when using a handcrafted feature extraction method instead of handcrafted methods. To this end, we compare the performance of the CBD method (using the optimal parameters previously selected) with two promising LBP variants (TP-LBP and FP-LBP) and the results, for the three spectral bands in the open-set identification mode, are presented in Fig. 3a–c. From these figures, it clear that the system works perfectly using the learned hand-crafted feature extraction method. Indeed, An EER of 0.994% ($T_o = 0.6538$), 0.409% ($T_o = 0.6998$) and 0.250% ($T_o = 0.7260$) can be obtained, using the CBD method, when using the spectral band of 850 nm, 940 nm and *WHITE*, respectively. In general, an improvement of about 77.78% and 84.62% was achieved when using the CBD method instead of TP-LBP and FP-LBP, respectively. We also examined the closed-set identification mode by applying the optimal CBD parameters obtained previously, then calculated the Rank-One Recognition (ROR) and Rank of Perfect Recognition (RPR) values. We limit the test only for the *WHITE* spectral band. Thus, Fig. 3d, which shows the Cumulative Match Curves (CMC), compares the three feature extraction methods. It is also clear that the CBD method always works better in our system with a ROR of 97,000% (RPR = 72) instead of a ROR of 98,500% (RPR = 93) and 98,625% (RPR = 44) for TP-LBP and FP -LBP, respectively. Finally, for more details, Table 2 gives the ROR and the RPR of all the spectral bands.

Finally, a comparison between the three spectral bands, when using the CBD based feature extraction method, in the two identification modes, is plotted in Fig. 4a (open-set identification mode) and in Fig. 4b (closed-set identification mode). From these figures, the performance of the biometric system is improved by using the *WHITE* spectral band for the two identification modes (EER = 0.250% to $T_o = 0.7260$). Thus, improvements of approximately 38.87 and 74.85% can be obtained when the *WHITE* is used as a biometric modality. The experimental results obtained in this paper, using a multispectral palmprint database of 100 persons, clearly demonstrate the effectiveness of the learning principle in the feature extraction task, which allows these types of systems suitable for several high-security applications.

Table 1 Selection of CBD parameters under the three spectral bands

Bands	Window = 15 × 15 (R = 7)						Window = 19 × 19 (R = 9)					
	BIN = 19		BIN = 23		BIN = 25		BIN = 19		BIN = 23		BIN = 25	
	T_o	EER	T_o	EER	T_o	EER	T_o	EER	T_o	EER	T_o	EER
850nm	0.6140	1.298	0.6577	1.196	0.6844	1.018	0.6194	1.307	0.6168	1.375	0.6538	0.994
940nm	0.7047	0.485	0.6651	0.678	0.6740	0.750	0.6592	0.500	0.6998	0.409	0.6530	0.625
WHITE	0.7118	1.157	0.6980	0.875	0.7260	0.250	0.6884	1.000	0.7356	0.921	0.711	0.875

Table 2 Performance comparisons of the CBD method

Methods	Open-set identification						Closed-set identification					
	850 nm		940 nm		WHITE		850 nm		940 nm		WHITE	
	T_o	EER	T_o	EER	T_o	EER	ROR	RPR	ROR	RPR	ROR	RPR
FP-LBP	0.2569	6.798	0.2962	4.750	0.2451	1.625	71.505	92	81.124	89	93.500	65
TP-LBP	0.2653	3.250	0.2475	2.936	0.2058	1.125	86.875	90	87.375	85	94.875	69
CBD	0.6538	0.994	0.6998	0.409	0.7260	0.250	97.000	72	98.500	93	98.625	44

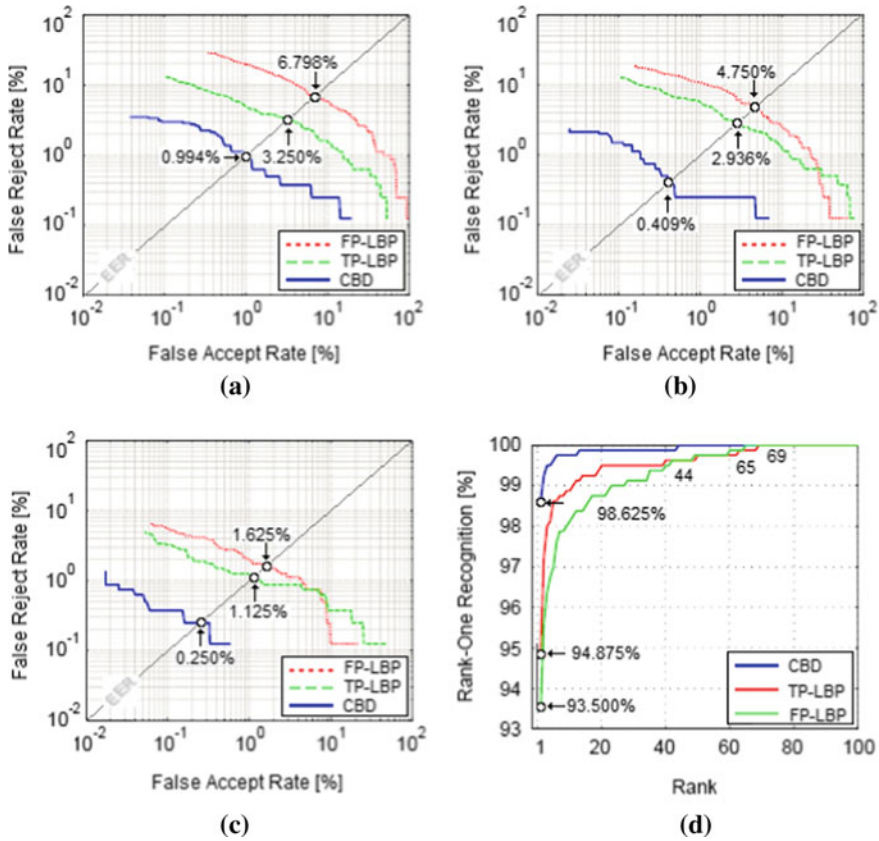


Fig. 3 Open-set/closed-set biometric identification system performance. **a** Open-set identification performance under 850 nm, **b** open-set identification performance under 940 nm, **c** open-set identification performance under WHITE, and **d** closed-set identification performance under WHITE

4 Conclusion

Feature extraction is an important task in the pattern recognition applications due to the large amount of different existing features in signal (especially in image) and his multiple areas of applications. Due this necessity, a well considerable effort has been made by the researchers in this direction, resulting in many cases an excellent enough classification results. Today, learning techniques are widely used in many applications to provide an effective pattern recognition system. The main objective of this study is to show the performance of the learned handcrafted feature extraction method by developing a multispectral palmprint identification system. The obtained experimental results, using several palmprint spectral bands, show the interest of

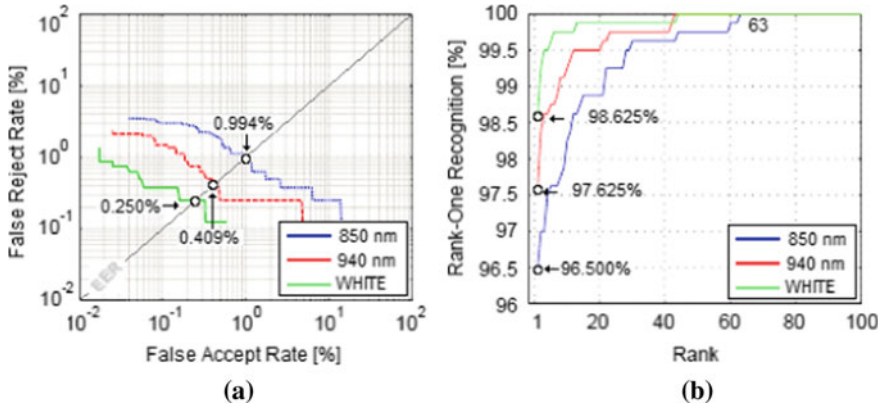


Fig. 4 Open-set/closed-set biometric system performance comparison. **a** Open-set biometric identification system and **b** closed-set biometric identification system

the learning principle to improve the biometric system accuracy. Recent advances in deep learning have shown that learning hierarchical features in deep networks can generally achieve better performance. For this, we plan in our future work to exploit more hierarchical features under the deep learning to further improve recognition performance.

Acknowledgements The authors are grateful to the anonymous referees for their valuable and helpful comments. This research has been carried out within the PRFU project (Grant: A01L08UN12012 0180001) of the Department of Electrical Engineering, University of Laarbi Tebessi, Tebessa. The authors thank the staff of LAMIS laboratory for helpful comments and suggestions.

References

1. Yang B, Chen S (2013) A comparative study on local binary pattern (LBP) based face recognition: LBP histogram versus LBP image. *Neurocomputing* 120(23):365–379
2. Ojala T, Pietikäinen M, Mäenpää T (2002) Multiresolution gray-scale and rotation invariant texture classification with local binary patterns. *IEEE Trans Pattern Anal Mach Intell* 24(7):971–987
3. Younesi A, Amirani MC (2017) Gabor filter and texture based features for palmprint recognition. *Proc Comput Sci* 108(C):2488–2495
4. Mu M, Ruan Q, Guo S (2011) Shift and gray scale invariant features for palmprint identification using complex directional wavelet and local binary pattern. *Neurocomputing* 74:3351–3360
5. Wolf L, Hassner T, Taigman Y (2008) Descriptor based methods in the wild. *ECCV workshop on faces in real life images: detection, alignment, and recognition*
6. Bouchemha A, Doghmane N, Nait-Hamoud MC, Ali AN (2015) Multispectral palmprint recognition methodology based on multiscale representation. *J Electron Imag* 24(4):043005
7. Lu J, Liang VE, Zhou X, Zhou J (2015) Learning compact binary face descriptor for face recognition. *IEEE Trans Pattern Anal Mach Intell (T-PAMI)* 37(10):2041–2056
8. Nanni L, Ghidoni S, Brahmam S (2017) Handcrafted vs. non-handcrafted features for computer vision classification. *Pattern Recogn* 71:158–172

9. Ahonen T, Hadid A, Pietikainen M (2006) Face description with local binary patterns: application to face recognition. *IEEE Trans Pattern Anal Mach Intell* 28(12):2037–2041
10. CASIA multispectral palmprint database. Available at <http://biometrics.idealtest.org/>

CNN-Based Obstacle Avoidance Using RGB-Depth Image Fusion



Chaymae El Mechal, Najiba El Amrani El Idrissi, and Mostefa Mesbah

Abstract In the last few years, deep learning has attracted wide interest and achieved great success in many computer vision related applications, such as image classification, object detection, object tracking, pose estimation and action recognition. One specific application that can greatly benefit from the recent advance of deep learning is robot vision-based obstacle avoidance. Vision-based obstacle avoidance systems are mostly based on classification algorithms. Most of these algorithms use either color images or depth images as the main source of information. In this paper, the aim is to investigate whether using information extracted from both types of images simultaneously would give better performance than using each one separately. To do this, we chose the convolutional neural network (CNN) as the classifier and HSV-based method to achieve the fusion. We tested this approach using two widely used pre-trained CNN architectures, namely Resnet-50 and GoogLeNet using a dataset locally collected. The results indicate that the image fusion-based classification algorithm achieve a higher accuracy (91.3%) than the one based on depth images (80.4%) but lower than the one based on color images (93.7%). These results can be partly explained by the fact that the used classifiers were pre-trained using color image datasets.

Keywords Robot vision · Obstacle avoidance · Image fusion · Deep learning · Convolutional neural network

C. E. Mechal (✉) · N. E. A. El Idrissi
Faculty of Sciences and Technology of Fez, University Sidi Mohamed Ben Abdellah, B.P. 2202,
Road of Imouzzar, Fez, Morocco
e-mail: chaymae.elmechal@usmba.ac.ma

N. E. A. El Idrissi
e-mail: najiba.elamrani@usmba.ac.ma

M. Mesbah
Sultan Qaboos University, Al Khoudh, Muscat 123, Muscat, Oman
e-mail: m.mesbah@squ.edu.om

1 Introduction

In recent years, sensors have become economically affordable and commonplace. But even with the cost of good quality sensors going down, autonomous real-time navigation and obstacle avoidance performances have not significantly increased. This was until high performance learning algorithms, such as deep learning, and computationally efficient platforms were introduced. With this in place, real-time processing of large amount of information obtained from different sensors became achievable.

Vision-based obstacle avoidance is one of the areas that can significantly benefit from the introduction of deep learning algorithms [1, 2]. Vision-based obstacle avoidance systems are mostly built around classification algorithms. Most of the existing algorithms use either color images or depth images as the source of information. Few image fusion algorithms, however, have been proposed in the context of CNN-based image classification [3–6].

To investigate whether using image fusion algorithms would give better performance than algorithms using only RGB or depth images, we choose to perform this information fusion at the level of HSV image representation. To benefit from the transfer learning provided by deep learning, we chose two widely used CNN-based classifiers, namely Resnet-50 and GoogLeNet [2]. The classifiers have been fine-tuned by replacing the final layers of the networks and training them using data locally acquired. This data was acquired using image sensors attached to a TurtleBot mobile robot. The classification process is made up of the following steps: (1) acquire color and depth images from a camera and a depth sensor imbedded in Kinect, (2) map the color image from RGB to HSV representation, (3) replace the channel V with a normalized version of the depth image to get an HSD representation and finally, (4) use the HSD image as an input to the CNN. As a variation of this approach, an extra step that performs the inverse mapping from HSD to RGB prior to using CNN was introduced. The new modified RGB image is known as the RGBD image. A CNN is then used to classify the HSV and the RGBD images into one of 5 classes characterized by angle information obtained from an inertial measurement unit (IMU) attached to the TurtleBot.

A generic CNN architecture consists of several basic building blocks, called layers (Fig. 1). A brief description each layer is given below [2].

- (1) Convolution layer: This layer consists of a set of 2D learnable filters that act on the input images, through convolution operations, followed by a bias addition and a nonlinear activation function, to generate feature maps (output images). Its main task is to detect local features in the input images and map them to the feature maps. The mathematical expression of the overall operation is given by:

$$y_{ijk} = f((W_i * X)_{jk} + b_i) \tag{1}$$

where, y_{ijk} denotes the pixel value at coordinate (j, k) of the i th output feature map. W_i denotes the i th convolution kernel, X is the input image and b_i is the

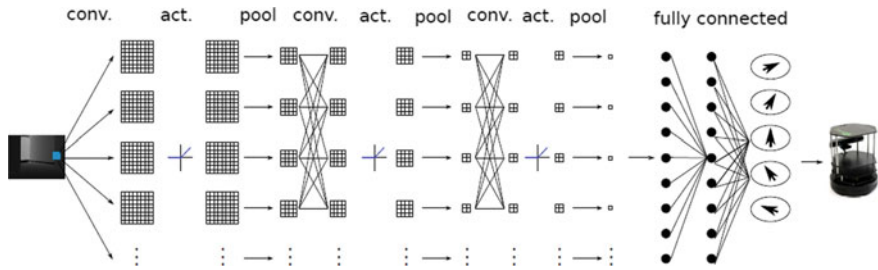


Fig. 1 An example of a CNN architecture [7]

i th element of the bias vector associated with the i th convolution kernel (filter). The function f is a nonlinear activation function such as the ReLU.

ReLU has been widely used in deep learning as it has been shown to be much faster than the other conventional activation functions and does not suffer from the vanishing gradient problem. ReLU is mathematically defined as:

$$f(x) = \max(x, 0) \tag{2}$$

- (2) Pooling operation: The main task of the pooling (or subsampling) operation is to reduce the size of the output. This leads to a reduction of the number of the network parameters and, hence, an increase of the speed of the learning process. The most commonly used pooling techniques are the max pooling and the average pooling.
- (3) Fully connected layer: A stack of above-mentioned convolution and pooling layers act as an automatic feature extractor. Once the features are extracted, they are fed to one or more fully connected layers followed by a softmax function layer for classification.

Two pre-trained CNNs were used for classification, namely GoogLeNet and ResNet-50. One of the distinguishing characteristics of GoogLeNet, introduced by Google in 2015, is the use of a basic building block called the inception module. This 2-layer module was introduced to performs the following tasks: (1) multiple convolutions using filters of different sizes, (2) pooling, and (3) concatenation of the multiple-scale features. GoogLeNet uses 22 layers and 5 pooling layers as shown in Table 1. More detailed information can be found in [2].

Microsoft introduced a CNN architecture called the Residual Network (ResNet) in 2015. ResNet-50 is a newer version of the ResNet and can classify images into 1000 categories of objects. An interesting property of the ResNet architecture is the identity skip connections in the residual blocks. This is used to propagate information over layers allowing deeper networks to be built. Skip connection helps the network to understand global features and to enhance the detection of smaller objects in the image [8].

Table 1 The details of the Resnet-50 and GoogLeNet

GoogLeNet	Resnet-50
<i>cnv</i> : 7×7 (64), stride 2 <i>maxpool</i> : 3×3 , stride 2	<i>cnv</i> : 7×7 (64), stride 2 <i>maxpool</i> : 3×3 , stride 2
$3 \times \{cnv3 \times 3(64)cnv3 \times 3(64)\}$	$3 \times \{cnv1 \times 1(64)cnv3 \times 3(64)cnv&1 \times 1(256)\}$
$4 \times \{cnv3 \times 3(128)cnv3 \times 3(128)\}$	$4 \times \{cnv1 \times 1(128)cnv3 \times 3(128)cnv&1 \times 1(512)\}$
$6 \times \{cnv3 \times 3(256)cnv3 \times 3(256)\}$	$6 \times \{cnv1 \times 1(256)cnv3 \times 3(256)cnv&1 \times 1(1024)\}$
$3 \times \{cnv3 \times 3(512)cnv3 \times 3(512)\}$	$3 \times \{cnv1 \times 1(512)cnv3 \times 3(512)cnv&1 \times 1(2048)\}$
$3 \times \{cnv1 \times 1(512)cnv3 \times 3(512)cnv&1 \times 1(2048)\}$	<i>avgpool</i> <i>cnv1</i> $\times 1(1000)$ <i>softmaxloss</i>
<i>avgpool</i> <i>cnv1</i> $\times 1(1000)$ <i>softmaxloss</i>	

2 Data Acquisition and Pre-processing

This section describes how the data (RGB images, depth images, and IMU output) used in this project was generated. More details information can be found in [7]. This data was collected using the Microsoft motion sensing device Kinect [9] attached to the TurtleBot 2 Personal Robot [10] running the Robot Operating System (ROS) [11]. Kinect features an RGB camera, a depth sensor and microphone array. The depth sensor includes an infrared laser emitter and an infrared camera. The data was recorded while TurtleBot was navigating different environments with obstacles and was controlled by a joystick. The ROS, running on the controller unit, interacts with the different hardware component of the robot. The imaging system generates RGB & D images at a resolution of 640×480 pixels.

After data collection, the images were manually filtered to remove duplicated and blanks copies. The remaining images were separated into 5 categories (classes) based on their associated IMU reading and the control generated by the joystick. These categories are: 1—“go-straightforward”, 2—“turning-half-left”, 3—“turning-full-left”, 4—“turning-half-right”, and 5—“turning-full-right”. These correspond to the following readings from the IMU ($-10^\circ \leq \theta \leq 10^\circ$) (Table 2):

Table 2 Class definition based on IMU reading

Angle (°)	Class
$\theta \geq 10^\circ$	5
$1^\circ \leq \theta < 10^\circ$	4
$-1^\circ \leq \theta \leq 1^\circ$	1
$-10^\circ < \theta \leq -1^\circ$	2
$\theta \leq -10^\circ$	3

3 Feature Fusion Methods

As discussed above, the information fusion took place in an RGB alternative representation, namely HSV (Hue, Saturation, Value or Brightness). This approach was originally proposed in [12] in the context of semantic labelling. It involves the following steps:

Step 1 (RGB to HSV Mapping): This represents a linear transformation from the RGB representation to the HSV representation. The transformation is essentially a conversion from a rectangular coordinate system to a cylindrical coordinate system for 2-D image and 3-D array comprising three channels (H, S, V).

Step 2 (HSV to HSD Mapping): For transforming the images from HSV to HSD, we kept the channels Hue and Saturation and replaced V channel by depth image D. We normalized the depth values to [0, 1] to be consistent with H and S [13].

Step 3 (HSD to RGBD): RGBD is obtained by using the inverse of the transform operation used in step 1.

Exemplary of the different image formats used in the present study are shown in Fig. 2.

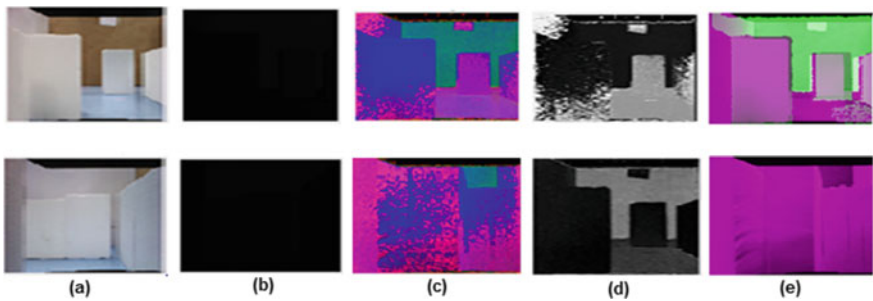


Fig. 2 a RGB, b Depth, c HSV, d HSD and e RGBD

4 Results and Discussion

As mentioned above, the classifications of the different format images were performed using two pre-trained CNN algorithms, namely Resnet-50 and GoogLeNet, within MATLAB. The distribution of the images used in training and testing the CNN-based classifiers is shown in Table 3.

To assess the performance of the classification process, we generate the four confusion matrices associated with RGB, Depth, HSD, and RGBD images (see Tables 4, 5, 6 and 7). The confusion matrix is a specific table layout used to summarize the performance of a classification algorithm. From this matrix, a number of performance measures can be extracted. These performances include sensitivity, specificity, positive predictive value, negative predictive value, and accuracy [14]. In this paper, we

Table 3 The distribution of training and testing images per class

	1	2	3	4	5	Total
Training	520	360	316	416	368	1980
Testing	130	90	79	104	92	495
Total	650	450	395	520	460	2475

Table 4 Confusion matrix for RGB: ResNet-50

		Target classes					
		1	2	3	4	5	
Output classes	1	(130) 26%	(1) 0.2%	(6) 1.2%	(0) 0%	(1) 0.2%	94.2–5.8%
	2	(0) 0%	(89) 17.9%	(1) 0.2%	(2) 0.4%	(0) 0%	96.7–3.3%
	3	(0) 0%	(0) 0%	(64) 12.8%	(4) 0.8%	(3) 0.6%	90.1–9.9%
	4	(0) 0%	(0) 0%	(6) 1.2%	(95) 19%	(2) 0.4%	92.2–7.8%
	5	(0) 0%	(0) 0%	(2) 0.4%	(3) 0.6%	(86) 17.2%	94.5–5.5%
%		100–0%	98.9–1.1%	81–19%	91.3–8.7%	93.5–6.5%	93.7–6.3%

Table 5 Confusion matrix for Depth: ResNet-50

		Target classes					
		1	2	3	4	5	
Output classes	1	(98) 19.6%	(0) 0%	(10) 2%	(0) 0%	(0) 0%	90.7–9.3%
	2	(13) 2.6%	(73) 14.6%	(5) 1%	(8) 1.6%	(4) 0.8%	70.9–29.1%
	3	(6) 1.2%	(14) 3%	(51) 10.4%	(1) 0.2%	(3) 0.6%	68–32%
	4	(9) 1.8%	(1) 0.2%	(11) 2.2%	(91) 18.2%	(0) 0%	81.3–18.7%
	5	(4) 0.8%	(2) 0.4%	(2) 0.4%	(4) 0.9%	(85) 17%	87.6–12.4%
%		75.4–24.6%	81.1–18.9%	64.6–35.4%	87.5–12.5%	92.4–7.6%	80.4–19.6%

Table 6 Confusion matrix for HSD: ResNet-50

		Target Classes					
		1	2	3	4	5	
Output classes	1	(100) 20%	(7) 1.4%	(6) 1.2%	(0) 0%	(0) 0%	88.5–11.5%
	2	(10) 2%	(70) 14%	(9) 3.6%	(5) 1.1%	(2) 0.4%	72.9–27.1%
	3	(6) 1.2%	(4) 0.9%	(57) 11.4%	(0) 0%	(1) 0.2%	83.8–16.2%
	4	(5) 1%	(6) 1.2%	(0) 0%	(91) 18.2%	(5) 1%	85–15%
	5	(9) 1.8%	(3) 0.6%	(7) 1.4%	(8) 1.6%	(84) 16.8%	75.7–24.3%
%		76.9–23.1%	77.8–22.2%	72.2–26.8%	87.5–12.5%	91.3–8.7%	81.2–88.8%

Table 7 Confusion matrix for RGBD: ResNet-50

		Target classes					
		1	2	3	4	5	
Output classes	1	(130) 26%	(0) 0%	(5) 1%	(0) 0%	(0) 0%	96.3–3.7%
	2	(0) 0%	(83) 16.7%	(3) 0.7%	(2) 0.4%	(4) 0.8%	90.2–9.8%
	3	(0) 0%	(3) 0.6%	(67) 13.5%	(5) 1%	(0) 0%	89.3–10.7%
	4	(0) 0%	(3) 0.6%	(3) 0.6%	(87) 17.4%	(3) 0.6%	90.6–9.4%
	5	(0) 0%	(1) 0.2%	(1) 0.2%	(10) 2%	(85) 17.1%	91.3–8.7%
%		100–0%	92.2–7.8%	84.8–15.2%	83.7–16.3%	92.4–7.6%	91.3–8.7%

only show the results obtained using ResNet50 as GoogLeNet results showed similar trends.

In the Tables 4, 5, 6 and 7, the diagonal cells show the number of the images correctly classified by the classifier (and their percentages relative to the total number of test images (495)). For example, in Table 4, 130 RGB images (26% of all RGB images used for testing) were correctly classified as ‘go-straightforward’ or class 1. Based on Table 3, this represents 100% of the images in class 1. This latter result is shown in the first cell of the bottom row.

The off-diagonal cells show the number misclassified images (and their percentages relative to 495). Using, once again the Table 1 is used as an example, cells 2 and 3 of the first row, show that none of the images (0%) of class 2 were classified as belonging to class 1 and 6 images (1.2%) of class 3 were classified as belonging to class 1.

The last row shows the percentages of correctly classified images per class. For example, cell 2 indicates that 98.9% (89 out of 90) of the images belonging to class 2 were correctly classified and 1.1% (1 out of 90) of the images of this class were incorrectly classified.

The last column reports the ratios of the number images “correctly” classified as belonging to specific classes over the “total” number of images assigned by the classifier to these classes. For example, in Table 4, the number of correctly images

correctly classified as belonging to class 1 are 130. The total number of images that were assigned to class 1, however, is 138 (130 + 1+6 + 0+1). This gives a ratio of 94.20% (130/138).

A metric that is widely used to when assessing the performance of classifiers is the accuracy. Accuracy is defined as the total number of correctly classified images over the total number of images. Using the above confusion matrices, the accuracy is obtained by:

$$ACC = \frac{\text{sum of diagonal elements}}{\text{total number of images}}$$

For example, in Table 4, the accuracy is given by:

$$ACC = \frac{130 + 89 + 64 + 95 + 86}{495} \approx 93.7\%$$

This value appears in the last cell of the confusion matrix.

The accuracy rate is altered according to the result of Tables 4, 5, 6 and 7, (RGB 93.7%, RGBD 91.3%, HSD 81.2% and Depth 80.4%). One logical explanation of the obtained results is that the two pre-trained networks were pre-trained using RGB images from ImageNet [15].

The results also show that RGB and RGBD based classifications obtained the best results (100% accuracy) for class 1. RGB, however, outperformed RGBD for all other classes except class 3 (81% vs. 84.8%). Depth and HSD performed relatively poorly especially for first 3 classes.

The classification results depend on a number of factors such as the total number of images used in training and testing, the number of the images per class, the type of images, the type and complexity of the classifier and the environments where the experiments take place. This latter factor includes the nature of the obstacles, their positions, and the illumination. Another important factor that affects the classification performance is the class labelling. In this paper, the labeling has been performed by the person conducting the experiment.

5 Conclusion

The paper presented a comparative analysis of CNN-based classification using different types of images, namely RGB, Depth, HSD, and RGBD. The images were locally obtained using RGB and Depth sensors attached to a TurtleBot 2 Personal Robot. The classifications have been performed using pre-trained GoogleNet and ResNet-50. The aim was to classify the images in 5 classes indicating the actions to be taken by the robot to avoid colliding with obstacles. The results obtained show that classification using RGBD (fusion of RGB and Depth) images performed better

than those using HSD or Depth images (larger than 10% in term of the overall accuracy) but slightly lower than the classification using RGB (lower by 2.3%). A logical explanation of the superiority of the RGB-based classification is the fact that the CNN classifiers have been trained using RGB images. The work done in this project can act as a basis for further improvements to increase accuracy and adaptability of obstacle detection in diverse environments.

Acknowledgements The authors would thank the Department of Electrical and Computer Engineering of Sultan Qaboos University for hosting the first author during the work on the project that let to this paper.

References

1. Cornacchia M, Kakillioglu B, Zheng Y, Velipasalar S (2018) Deep learning-based obstacle detection and classification with portable uncalibrated patterned light. *IEEE Sens J* 18(20):8416–8425
2. Khan S, Rahmani H, Shah SAA, Bennamoun M (2018) A guide to convolutional neural networks for computer vision. Morgan & Claypool Publishers, San Rafael
3. Pujar K, Chickerur S, Patil MS (2017) Combining RGB and depth images for indoor scene classification using deep learning. In: IEEE international conference on computational intelligence and computing research, Coimbatore, India
4. Eitel A, Springenberg JT, Spinello L, Riedmiller M, Burgard W (2015) Multimodal deep learning for robust RGB-D object recognition. In: IEEE/RSJ international conference on intelligent robots and systems, Hamburg, Germany
5. Zeng H, Yang B, Wang X, Liu J, Fu D (2019) RGB-D object recognition using multi-modal deep neural network and DS evidence theory. *Sensors* 19:529. <https://doi.org/10.3390/s19030529>
6. Ophoff T, Van Beeck K, Goedemé T (2019) Exploring RGB + Depth fusion for real-time object detection. *Sensors* 19:866. <https://doi.org/10.3390/s19040866>
7. Al Jabri K (2018) Vision-based mobile robot obstacle-avoidance using deep learning algorithm, MSc Thesis, Department of Electrical and Computer Engineering, Sultan Qaboos University
8. He K, Zhang X, Ren S, Sun J (2015) Deep residual learning for image recognition. [arXiv:1512.03385v1\[cs.CV\]](https://arxiv.org/abs/1512.03385v1) 10 Dec 2015
9. Charreyron S, Jackson S, Miranda-Moreno L (2013) Toward a flexible system for pedestrian data collection with a microsoft Kinect motion-sensing device. *Transp Res Record J Transp Res Board* 2339(1):80–89
10. Koubaa A, Sriti M-F, Javed Y, Alajlan MM, Qureshi B, Qureshi B, Mahmoud A (2016) Turtlebot at office: a service-oriented software architecture for personal assistant robots using ROS. In: International conference on autonomous robot systems and competitions (ICARSC)
11. Ademovic A (2016) An introduction to robot operating system: the ultimate robot application framework. Developers
12. Iwaszczuk D, Koppanyi Z, Gard N, Zha B, Toth C, Yilmaz A (2018) Semantic labeling of structural elements in buildings by fusing RGB and depth images in an encoder-decoder CNN framework. *Int Arch Photogramm Remote Sens Spat Inf Sci* 42(1):225–232
13. Iwaszczuk D, Koppanyi Z, Gard NA, Zha B, Toth C, Yilmaz A (2018) Semantic labeling of structural elements in buildings by fusing RGB and depth images in an encoder-decoder CNN framework. In: The International Archives of the Photogrammetry, Remote Sensing and Spatial Information Sciences, vol XLII-1
14. Powers DMW (2011) Evaluation: from precision, recall and F-measure to ROC, informedness, markedness & correlation. *J Mach Learn Technol* 2(1):37–63

15. Yang K, Qinami K, Fei-Fei L, Deng J, Russakovsky O (2019) Towards fairer datasets: filtering and balancing the distribution of the people subtree in the ImageNet hierarchy. IMAGNET, 17 Sept 2019

Arabic Handwriting Word Recognition Based on Convolutional Recurrent Neural Network



Manal Boualam, Youssef Elfakir, Ghizlane Khaissidi, and Mostafa Mrabti

Abstract The success of any words-characters recognition system depends on board parameters such as the language (Arabic, Latin, Indi ...), the document type (writing or typing), based or free-segmentation, pretreatment, features extraction and classification approaches. Within these fields, Building a robust and viable recognition system for Arabic handwritten has always been a challenging task since a long time. In this study, we propose an end-to-end system based on deep Convolutional Recurrent Neural Network CNN/RNN; we trained our system on IFN/ENIT extended database in order to improve our results.

Keywords Arabic handwriting recognition · Convolutional neural network · Recurrent neural network · IFN/ENIT database

1 Introduction

Optical Character recognition OCR system for Arabic used to solve several problems in different areas: analyze humans sentiment [1, 2], writer identification [3]. Disease detection such as Parkinson's [4], speech recognition [5], etc.

Usually, the process of word recognition achieved through four steps: preprocessing, segmentation, features extraction and classification. In this model, each step input depends on the output of the previous one (pipeline), which could increase the error rate. In the recent studies, researchers used deep learning in order to realize

M. Boualam (✉) · Y. Elfakir · G. Khaissidi · M. Mrabti
Laboratory of Information and Interdisciplinary Physics, ENS, University Sidi Mohamed Ben Abdellah, Fes, Morocco
e-mail: Boualam.manal@gmail.com

Y. Elfakir
e-mail: Elfakir.youssef11@gmail.com

G. Khaissidi
e-mail: Ghizlane.derkaoui1@hotmail.com

M. Mrabti
e-mail: Mostafa.mrabti@yahoo.fr

the system. Which is a free-segmented model starts by preprocessing then features extraction and classification. Our proposed model inspired by [6] constructed of Convolutional Neural Network (CNN) layers, Recurrent Neural Network (RNN) layers and Connectionist Temporal Classification (CTC) layer.

Elbashir [7] proposed a Convolutional neural network (CNN) model for off-line Arabic handwritten, they used Sudan University of Science and Technology dataset (SUST ALT), the model accuracy is 93.5%. In [8] Najib Tagougui et al. built a hybrid model NN/HMM for Arabic handwritten recognition (AHR), they trained the segments on a multi-layer perceptron Neural Network (MLPNNs) to extract characters probabilities. A Hidden Markov Model (HMM) used to decode the outputs of the first system, the evaluation of their model done on ADAB database; it achieved 96.4%.

Younis [9] used a deep neural network to build an Arabic handwritten recognition system, they started by a Batch Normalization to improve the speed and the accuracy of their system, the accuracy is 94.8% on AIA9k [10] dataset and 97.6% on AHDC dataset. El-Sawy et al. [11] model a deep learning architecture based on CNN to recognize Arabic Handwritten characters, with two convolutional layers and two pooling layers, they created their own dataset in order to train and test the proposed system, the dataset is composed of 16,800 character with 94.9% of accuracy.

Sahlol et al. [12] proposed a novel method for Arabic characters recognition, starting with a new preprocessing step based on noise removal and different kind of features, then they trained the system on CENPRMI database [13] to feed a neural network, it gives an accuracy = 88%. Abdalkafor et al. [14] used the same database to build their system based on novel features extraction techniques and MLP NN, the system accuracy reached up to 94.75%.

In [15] Mohammed Ali Mudhsh et al. presented an Alphanumeric VGGNet for Arabic character recognition, their system is developed by thirteen convolutional layers, three fully connected layers and two max-pooling layers, the system shows a high performance with an accuracy equal to 99.66% after training it on ADBBase [16] database and 97.32% for HACDB Dataset [17]. In [18] Ahmed El-Sawy et al. provided a deep learning technique for Arabic Digits Recognition, five CNN layers trained on MADBase with 88% of accuracy.

Few researchers focused on Arabic word/text recognition. In [19, 20] Mohamed Elleuch et al. integrated two classifiers: Convolutional Neural Network (CNN) and Support Vector Machine (SVM) in order to recognize Arabic words Handwritten, the training and testing is done on IFN/ENIT [21] and HACDB [22] databases, their model compared to other Optical Character Recognition systems (OCR) gives better results. Shi et al. [6] developed a novel End-to-End Convolutional Recurrent Neural Network (CRNN) for scene Text recognition; their system handles the variation of length and height of words in scenes, the experiments is evaluated on the IIIT-5 K [23], Street View Text [24] and ICDAR [25] datasets it shows a competitive performance. Alaa Alsaeedi et al. [26] adopted their system to use it in smartphones; they used a CNN for characters recognition and transparent neural Network (TNN) for printed words recognition, the recognition rate of their system is 98%.

Or, text recognition in video is a very interesting topic for OCR community, Yousfi et al. [27] improved Bidirectional Long Short-Term Memory-Connectionist Temporal Classification (BLSTM-CTC) segmentation-free model for Arabic video text recognition based on a joint learning of Maximum entropy and RNN models, they judged that their model outperform the classical BLSTM-CTC model by 36%. In [28] Ali Mohcine et al. proposed a model, which convert an Arabic line into characters, and then feed into a neural network, their model achieved an accuracy up to 83%.

This paper arranged as follow: Sect. 2 describes the existing OCR systems based on neural networks with a brief discussion, Sect. 3 presents the proposed approach, used techniques and results discussion. The paper ends with conclusion and perspectives for future work.

2 Material and Methods

2.1 Database

As input of our model, we used 946 name of Tunisian town/village written by more than 1000 writers. The original database is composed of 32,492 handwritten name, to improve the performance/ability and prevent over fitting of our model a large dataset is crucial, we used Keras deep learning neural network to fit our model using image data augmentation via the ImageDataGenerator, by applying domain-specific techniques to base images in order to create transformed versions of images. The main challenge is the selection of techniques used for data expand to not lose information or generate damaged/unreadable images.

In our model, we used a simple and powerful library for data preparation, the library provides class that define the configuration for image data preparation and augmentation, instead of choose specific arguments for each image, the function fits different arguments to model then randomly transform the original image to generate the desired augmented images. In our model, we used a rotation up to 2° , width and height shift up to 2 and shearing up to 4, in order to generate 15 examples for each image in IFN/ENIT database, as result we fit 487,350 training sample and (~3,876,648 characters) to our CNN-RNN model (Fig. 1).

2.2 Methodology

The main purpose of this work is to propose a robust approach for Arabic word recognition; the model achieved in four steps: preprocessing in order to normalize the input data, five CNN layers to extract relevant features from image, and then two RNN layers for sequence modeling, at the end CTC layer for transcription (Fig. 2).



Fig. 1 Image augmentation using image data generator from Keras library of Tensorflow, **a** original image, **b** fifteen randomly generated images: rotation up to 2° , width and hight shift up to 2, shearing up to 4

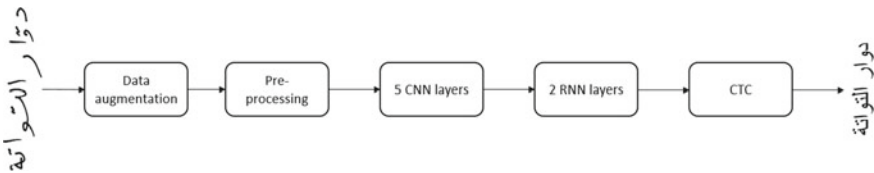


Fig. 2 Overview of the end-to-end proposed model

The proposed model gave significant results for Latin language in different research [6].

Preprocessing. The first fundamental step in an OCR model is preprocessing, the aim is to improve the quality of image data to suppress unwilling distortions or enhances in order to get better results. Even if IFN/ENIT images are already extracted and binarized, we used preprocessing to resize images to 128×32 without distortion by copying it to a white target image of same size, and convert our text corpus into UTF-8 to be readable.

CNN Model. A convolutional Neural Network (CNN) used in different fields (image processing, audio processing, etc.), it is the method of loosely simulate the neural human brain network, it define features in the image in two parts: the *convolution layers* that extract features from input images, *Fully connected layers* that used data from the previous part to generate output. In the training step, two importing processes

are involved: *forward propagation* process the input data and generate the output, *Backward Propagation* calculate error and update parameters (weight and bias). The CNN that we created contain five layers to identify multiple features, each layer composed of three operations: filter Kernel of size 5×5 in the first two layers and 3×3 in the last three layers. Then, all negative outputs of the previous layer converted into zero by RELU function (1), in this step the image shape is not transform. The last layer “Pooling” reduce the image dimensionality in order to run the algorithm at a decent speed, the pooling technique used in our model is max-pooling (2×2 squares).

$$\{F(x) = \max(0, x)\} \quad (1)$$

RNN Model. RNN is a very powerful neural network, it captures sequential information present in the input data, the output at each step depends on the current word and the previous one, since it is equipped with a mechanism of recurrent feedback that have a memory which captures information about the calculations done previously. RNN suffers from vanishing and exploiting gradient problem (with a large number of time steps), this problem was explored in depth by [29, 30]. In [31] S. Hochreiter and J. Schmidhuber designed LSTMs to avoid the previous problem:

$$h_t = f(W_{xh}x_t + W_{hh}x_{t-1} + b_h) \quad (2)$$

$$y_t = W_{hy}h_t + b_y \quad (3)$$

where x : input sequence given as input, h : sequence of hidden vectors computed by hidden NN, y : output vector. W the matrices weight, b the bias vectors and f the activation function it could be Sigmoid or tanh function. Long Short-Term Memory (LSTM) have access to past but not to future, for this reason, a Bidirectional RNN is used; it feeds the learning algorithm with the original data from beginning to the end, and once from end to beginning using a forward recurrent component and a backward recurrent component. Our model composed of two RNN layer to propagate relevant information through a sequence that contain 256 features per time-step.

CTC function. The Connectionist Temporal Classification [32] CTC loss layer provide end-to-end training and free-segmentation transcription, it takes as input the output matrix of the last RNN layer and the ground truth text (GT), then computes the loss value and infer/decode the matrix to get the text represented in the image. The loss calculation done by summing up all scores of all possible alignments of GT text. Alternatively, decoding done in two steps: First takes the most likely character per time-step and calculates the best path. Second, removes duplicate characters and blanks from path to represent the recognized text.

Hybrid CNN-RNN model. CNN-RNN hybrid model proved excellent results in different fields such as visual description [33], video emotion recognition [33], etc. In our model as described in Fig. 2, we performed feature extraction using CNN,

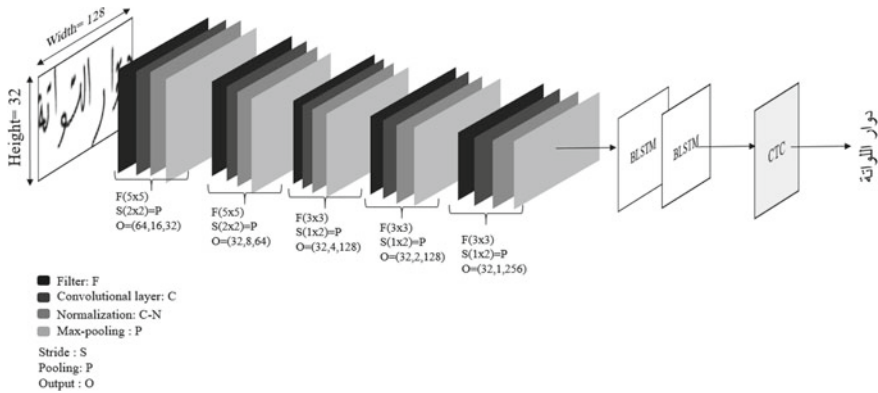


Fig. 3 Proposed end-to-end hybrid architecture based on CNN-RNN-CTC

which acts like encoder, then generate a language model and provide sequence-using RNN, which acts like decoder. Otherwise, the RNN is language based model use the output features of CNN layers and translate it into natural language sentence. Our end-to-end hybrid CNN-RNN model generally used to map static spatial inputs (images) to sequence outputs (text), the proposed model can perform classification of image and text inputs by taking advantages of CNN and RNN (Fig. 3). Our model classify the word containing in the provided image, and recognize it character per character. This allow the model to recognize words even if they are not present in the database (if they are well classified).

3 Results and Discussion

To construct our model we used python language, which have lot of advantages comparing to other languages such as MATLAB widely used for machine learning, C, etc.: it is free and open source, interpreted language so it is ported in different operating systems, it is easier for programing, it contains a wide choice of libraries for learning machine, etc. In [34] Colliau Taylor et al. presented a comparative study between Matlab, Python and R. We implemented our model using TensorFlow [35] library. In the proposed approach, we used 25,000 sample/epoch; 50 sample/batch, the model proved a high performances comparing to similar models using the same dataset IFN/ENIT. Our database split to training and testing images, we wanted to prove that the size of training and testing database affects the results, we used different scales of inputs for training and testing respectively (95–5%, 80–20%, 70–30%), we notice that the results of training dataset between (80–95%) gave the best results with minimal difference. We trained our network until our character error rate (CER) on the development set did not improve for at least 8 epochs, the results are shown in Table 1.

Table 1 CNN-RNN-CTC CER results for different training and testing dataset sizes

Train-test size	CER (%)	WER (%)
95–5%	2.07	91.49
80–20%	2.10	91.79
70–30%	3.03	88.49

Table 2 Performance comparisons with other methods

References	Techniques	CER (%)
Elleuch et al. [19]	SVM + CNN	7.05
Yan et al. [36]	LSTM	6.91
Awni et al. [37]	CNN	6.63
Maalej [38]	Maxout into MDLSTM	10.11
Present work	CNN + RNN + CTC	2.1

To evaluate our system we used character error rate (CER) and word error rate (WER), which represent the number of correct detected words from testing data set, we obtained significant results compared to previous studies using same database (IFN/ENIT). The resulting WER, CER respectively were above 91.79 and 2.10% (Table 2).

4 Conclusion and Future Work

We have presented an offline Arabic end-to-end hybrid recognition system; based on convolutional neural network and recurrent neural network specially bidirectional LSTM method and connectionist temporal classification CTC, we used image data augmentation in order to increase training images.

For perspectives, to improve our model we will focus on training-test data improvement (data preparation), as it is the first source of recognition errors, by eliminating damaged images, and improve the quality of training dataset. The next step will be improving the CNN-RNN by adding more layers, we will try to increase image size to use complex text lines/paragraphs, focusing on two main issues: touching and overlapping.

References

1. Al-Kabi MN, Al-Ayyoub M, Wahsheh HA, Alsmadi I (2016) A prototype for a standard Arabic sentiment analysis corpus. *Int Arab J Inf Technol* 13(1A):163–170
2. Alayba AM, Palade V, England M, Iqbal R (2017) Arabic language sentiment analysis on health services. <https://arxiv.org/abs/1702.03197>

3. Akram B (2018) Clonal selection classification algorithm applied to Arabic writer identification. In: 8th international conference on off-line handwriting based writer identification. <https://doi.org/10.1145/3200842.3208087>
4. Ibtissame A, Ammour A, Khaissidi G, Belahsen F, Mrabti M, Aboulem G (2020) A novel approach combining temporal and spectral features of Arabic online handwriting for Parkinson's disease prediction. *J Neurosci Methods*. <https://doi.org/10.1016/j.jneumeth.2020.108727>
5. El Choubassi MM, El Houry HE, Alagha CEJ, Skaf JA, Al-Alaoui MA (2003) Arabic speech recognition using recurrent neural networks. In: Proceedings of the 3rd IEEE international symposium on signal processing and information technology, pp 543–547. <https://doi.org/10.1109/ISSPIT.2003.1341178>
6. Shi B, Bai X, Yao C (2016) An end-to-end trainable neural network for image-based sequence recognition and its application to scene text recognition. *IEEE Trans Pattern Anal Mach Intell* 39:2298–2304. <https://doi.org/10.1109/TPAMI.2016.2646371>
7. Elbashir MK, Mustafa ME (2018) Convolutional neural network model for Arabic handwritten characters recognition. *Int J Adv Res Comput Commun Eng* 7(11). <https://doi.org/10.17148/IJARCE.2018.7111>
8. Tagougui N, Boubaker H, Kherallah M, Alimi AM (2014) A hybrid NN/HMM modeling technique for online Arabic handwriting recognition. *CoRR (Online)* <https://arxiv.org/abs/1401.0486>
9. Younis KS (2017) Arabic handwritten character recognition based on deep convolutional neural networks. *Jordanian J Comput Inf Technol* 3(3). <https://doi.org/10.5455/jjcit.71-1498142206>
10. Toriki M et al (2014) Window-based descriptors for Arabic handwritten alphabet recognition: a comparative study on a novel dataset. arXiv preprint [arXiv:1411.3519](https://arxiv.org/abs/1411.3519)
11. El-Sawy A, Loey M, EL-Bakry H (2017) Arabic handwritten characters recognition using convolutional neural network. *WSEAS Trans Comput Res* 5:11–19
12. Sahlol A, Suen C (2013) A novel method for the recognition of isolated handwritten Arabic characters. Technical report. Cornell University
13. Alamri H, Sadri J, Suen CY, Nobile N (2008) A novel comprehensive database for arabic off-line handwriting recognition. In: 11th international conference on frontiers in handwriting recognition 2008. Montreal
14. Abdalkafor AS, Sadeq A (2016) Arabic offline handwritten isolated character recognition system using neural network. *Int J Bus ICT* 2:41–50
15. Mudhsh M, Almodfer R (2017) Arabic handwritten alphanumeric character recognition using very deep neural network. *Information* 8(3):105. <https://doi.org/10.3390/info8030105>
16. Abdelazeem S, El-Sherif E (2017) The Arabic handwritten digits databases ADBase & MADBase. Available online: <https://datacenter.aucegypt.edu/shazeem/>. Accessed on 24 Aug 2017
17. Lawgali A, Angelova M, Bouridane A (2013) HACDB: handwritten Arabic characters database for automatic character recognition. In: 4th European workshop on visual information processing (EUVIP), pp 255–259. <https://doi.org/10.4108/eai.18-7-2019.2287842>
18. El-Sawy A, EL-Bakry H, Loey M (2016) CNN for handwritten Arabic digits recognition based on LeNet-5. In: Proceedings of the international conference on advanced intelligent systems and informatics 2016, pp 566–575. <https://doi.org/10.1007/978-3-319-48308-5>
19. Elleuch M, Maalej R, Kherallah M (2016) A new design based-SVM of the CNN classifier architecture with dropout for offline Arabic handwritten recognition. *Proc Comput Sci* 80:1712–1723. <https://doi.org/10.1016/j.procs.2016.05.512>
20. Elleuch M, Tagougui N, Kherallah M (2016) A novel architecture of CNN based on SVM classifier for recognizing Arabic handwritten script. *Int J Intell Syst Technol Appl* 15(4):323–340. <https://doi.org/10.1504/IJISTA.2016.10000779>
21. Yin F, Wang QF, Zhang XY, Liu CL (2013) ICDAR Chinese handwriting recognition competition. In: 2013 12th ICDAR on document analysis and recognition
22. Lawgali A, Angelova M, Bouridane A (2013) HACDB: handwritten Arabic characters database for automatic character recognition. In: 2013 4th European workshop on visual information processing (EUVIP), pp 255–259. <https://doi.org/10.4108/eai.18-7-2019.2287842>

23. Mishra A, Alahari K, Jawahar CV (2012) Scene text recognition using higher order language priors. *BMVC*. <https://doi.org/10.5244/C.26.127>
24. Wang K, Babenko B, Belongie S (2011) End-to-end scene text recognition. In: *ICCV*, 2011. <https://doi.org/10.1109/ICCV.2011.6126402>
25. Lucas SM, Panaretos A, Sosa L, Tang A, Wong S, Young R, Ashida K, Nagai H, Okamoto M, Yamamoto H, Miyao H, Zhu J, Ou W, Wolf C, Jolion J (2003) ICDAR 2003 robust reading competitions: entries, results, and future directions. *IJDAR*. <https://doi.org/10.1109/ICDAR.2003.1227749>
26. Alsaeedi A, Al Mutawa H, Natheer S, Al Subhi W, Snoussi S, Omri K (2018) Arabic words recognition using CNN and TNN on a smartphone. In: *IEEE 2nd international workshop on Arabic and derived script analysis and recognition*, pp 57–61. <https://doi.org/10.1109/ASAR.2018.8480267>
27. Yousfi B (2016) Contribution of recurrent connectionist language models in improving lstm-based Arabic text recognition in videos. *Pattern Recogn*. <https://doi.org/10.1016/j.patcog.2016.11.011>
28. Mohsin A (2020) Developing an Arabic handwritten recognition system by means of artificial neural network. *J Eng Appl Sci*. <https://doi.org/10.36478/jeasci.2020.1.3>
29. Schäfer AM, Udluft S, Zimmermann HG (2006) Learning long term dependencies with recurrent neural networks. In: *Proceedings of the 16th international conference on artificial neural networks (ICANN 2006)*, vol 4131. https://doi.org/10.1007/11840817_8
30. Bengio Y, Simard PY, Frasconi P (1994) Learning long-term dependencies with gradient descent is difficult. *IEEE Trans Neural Networks* 5(2):157–166. <https://doi.org/10.1109/72.279181>
31. Hochreiter S, Schmidhuber J (1997) Long short-term memory. *Neural Comput* 9(8):1735–1780. <https://doi.org/10.1162/neco.1997.9.8.1735>
32. Graves A, Fernández S, Gomez F, Schmidhuber J (2006) Connectionist temporal classification: labelling unsegmented sequence data with recurrent neural networks. In: *Proceedings of the 23rd international conference on machine learning*, vols 12, 13, 16 and 20. *ACM*, pp 369–376. <https://doi.org/10.1145/1143844.1143891>
33. Schuster M, Paliwal K (1997) Bidirectional recurrent neural networks. *IEEE Trans Signal Process* 45:2673–2681
34. Taylor C, Rogers G, Hughes Z, Ceyhun O, MatLab vs. Python vs. R (2017) Business faculty publications. 51. https://scholar.valpo.edu/cba_fac_pub/51
35. Abadi M, Agarwal A (2016) TensorFlow: large-scale machine learning on heterogeneous distributed systems. *arXiv:1603.04467v2*
36. Yan R, Peng L, Xiao S, Johnson MT, Wang S (2019) Dynamic temporal residual network for sequence modeling. *Int J Doc Anal Recogn (IJDAR)*. <https://doi.org/10.1007/s10032-019-00328-x>
37. Awni M, Khalil MI, Abbas HM (2019) Deep-learning ensemble for offline Arabic handwritten words recognition. In: *2019 14th international conference on computer engineering and systems (ICCES)*. <https://doi.org/10.1109/icc48960.2019.9068184>
38. Maalej R, Kherallah M (2019) Maxout into MDLSTM for offline Arabic handwriting recognition. In: Gedeon T, Wong K, Lee M (eds) *Neural information processing. ICONIP 2019. Lecture notes in computer science*. Cham. https://doi.org/10.1007/978-3-030-36718-3_45

Tuning Image Descriptors and Classifiers: The Case of Emotion Recognition



Latifa Greche , Abdelhak Taamouch, Mohamed Akil, and Najia Es-Sbai

Abstract In general, the recognition involves several steps as follows: data acquisition, pre-processing, segmentation, feature extraction and classification. Automatic facial expression recognition has become a crucial technology in the computer vision field and its applications including identification and security, Medicine and Monitoring. The facial expression recognition system requires an algorithmic pipeline that involves two main blocks: feature extraction and classification. A large experimental session must lead to the adequate algorithmic pipeline, notably for identifying the best methods for feature extraction and classification to achieve robust facial expression recognition with high accuracy. Thus, it is essential to analyse data using multiple methods of feature extraction and classification. In this paper, we propose an approach to automate the analysis of data by repeating tests made to tune and compare feature extraction and classification methods. We evaluate our proposed data analysis approach using video sequences with fundamental emotion states: neutral expression, disgust, fear, happiness, sadness, anger and surprise. To transform the face images into vectors of features, we use shape, texture, and contour descriptors. This enables storing images in a table of vectors. Each table related to every descriptor is analysed with Five classifiers have been used, which are support vector machine, linear discriminant analysis, k-nearest neighbors, naïve Bayes, and binary tree classifiers. The techniques 10-fold and Leave-One-Out Cross-validations and the grid search have been used to tune the hyperparameters methods and compare them, computing the average recognition rate F-measure as evaluation metric. Experimentation on ChonKanade Image database (CK+) show that the proposed data analysis approach can find out the optimal combination to separate the data classes and identify the expression with a an F-score of 96.44%.

Keywords Data analysis · Facial expression recognition · Features extraction · Classification

L. Greche (✉) · A. Taamouch · N. Es-Sbai
Laboratoire SIGER, FST, USMBA, Fès, Morocco
e-mail: latifa.greche@usmba.ac.ma

M. Akil
LIGM, A3SI, ESIEE Paris, CNRS, Université Gustave Eiffel, Marne-la-Vallée 77454, France

1 Introduction

In computer vision, feature extraction resolves the problem of transforming the image into a compact set of features, thereby it improves data storage and processing. Feature extraction is a step in image processing that involves a classification step [1]. The reason is that the notion of the vector of features, extracted from images, is the practical mean of representing data for classification problem. Using this notion, data can be stored in a table where the rows represent the examples, and the columns represent the features extracted from the image. Each feature results from a quantitative measure also called attribute, e.g. computing histograms after dividing the image into cells.

Recent advances in the fields of feature extraction and classification help designing recognition systems capable of detecting faces and recognizing the expression of each face, which couldn't be done in the past. The recognition process in computer vision is based on two crucial steps: feature extraction and classification. The challenges that arise when building such recognition systems [2] relate to the choice of the feature extraction technique that helps discriminating the object from the rest of the image and the classification technique that allows identifying the class to which the object belongs. Image databases are provided by psychologists in the format of video sequence recordings [3] and images [4] of a set of participants showing different classes of emotional expression, such as expressions of joy, surprise, fear, anger, sadness, disgust and the neutral face. Therefore, image analysis requires detecting the face first, then describing the variation of intensity at the contours in order to give a compact representation of the expression. This, helps preparing data and training the classifier so it can separate between the expression classes and identify the expression in images that don't belong to the training data.

Considering the challenges mentioned in the above paragraphs and as part of building an emotion recognition system for video sequences, in this paper we propose an algorithm to analyse images using variety of descriptors and classifiers. After detecting the face on the image, we extract the vector of features that helps to describe the appearance of the face. We use shape, contour, and texture descriptors in order to test their reliability and compare them. Using those descriptors, we describe and transform all the images into a table containing vectors of features assigned to their label. Indeed, without analysing the training data using variety of classification algorithms, it is difficult to know whether the class of expressions can be separable and to determine which classifier can be generalized best on data. To overcome this challenge, it is imperative to analyse the data structure using as many classification algorithms as possible. Since image descriptors and classifiers have parameters and hyperparameters that require adjustment to an optimal value, we want to try many values of them making it possible to research the combination of values which gives the best F-score. However, we cannot search for these parameters manually. The algorithm we propose in this paper allows us to automate the process of searching the optimal values for parameters and hyperparameters. The next section explains our

approach to analyse images. Section 2 describes our experimental results. Section 3 discusses related work, and Sect. 4 concludes and presents the perspectives of this work.

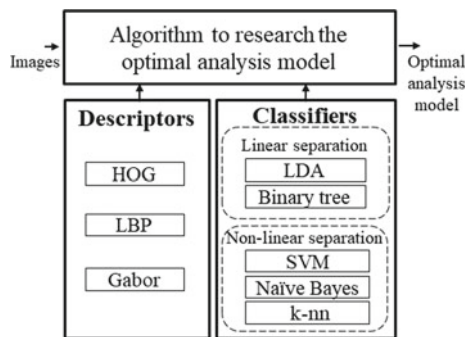
2 The Proposed Approach to Automate the Image Analysis

Designing and implementing a facial expression recognition system needs extracting a vector of features from the image, storing vectors extracted from a set of images in a table, and then training the classifier to recognize the expression in real world. However, determining the adequate feature extraction and classification methods requires analysing images using variety of image descriptors and classifiers. In Fig. 1 we present our approach to analyse images on two main stages. The first stage automates the selection of the optimal values of parameters and hyperparameters that tune each combination descriptor-classifier formed during data analysis. In the rest of the paper, we refer to each combination of descriptor-classifier as “analysis model”. The second stage operates to compare all the analysis models and select the optimal one. So, we can choose the model that gives high F-score in a minimal processing time. In the next subsections we detail the steps of feature extraction, classification, and the algorithm we use to tune the analysis models.

2.1 Feature Extraction Stage

We use two categories of image descriptors. In the first category, the image descriptor operates in the spatial domain where the face analysis is realized by measuring image gradients and histograms using the pixels intensity. The image processing is done by dividing the image into a small rectangular cells, for example, 8×8 pixels. Then, calculating histograms of oriented gradients in each cell. By combining the histograms extracted from each cell we use reconstruct the overall appearance of

Fig. 1 An overview diagram showing the main components of the proposed approach to auto analyse training data



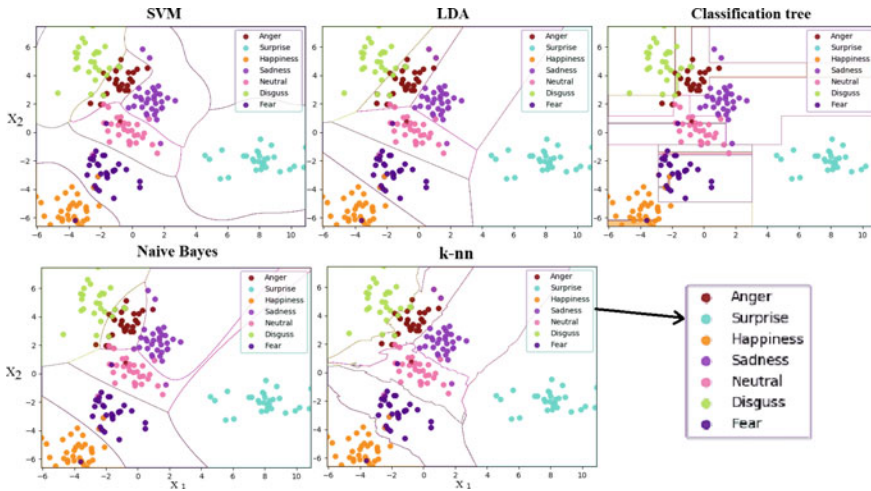


Fig. 2 Two dimensional representation of the training data. Each point in the scatter diagrams refers to an example inside the training data, the color indicate the label of the example. Every scatter diagram represents the linear or non-linear decision boundaries of classification techniques used in experimentation

the face which describes the orientation of the contours and removes any other detail existing in the original image. This technique is called Histogram of Oriented Gradient descriptor (HOG) [5]. We also use a texture descriptor like the local binary pattern (LBP) descriptor [6]. This helps comparing the grey intensity value of the central pixel in a region of 3×3 pixels with the intensity value of neighbours. Indeed, if the region includes pixels with close intensity values, the contrast converges to zero. On the contrary, if the difference in grey level between the neighbours is high, the contrast increases. The extraction of such property enables describing the change of intensity in the contours of the face and this by calculating distribution of LBPs in the image cells. In addition to the previous descriptors, a description expressing the spatial frequency proves to be interesting. It is used to extract the contour at different orientations in the spectral domain. The use of 2D Gabor wavelet technique [7] allows to filter the image contours having the same orientation. The choice of using such descriptors is motivated by various factors. In addition to the ability to extract the contour orientations and represent them as a vector of features, these descriptors are tolerant in certain image transformations, like rotation, translation and image scale.

2.2 Classification Stage

In this stage our choice is motivated by the fact that the classification methods must be supervised, since our data contain labeled examples. To know if facial

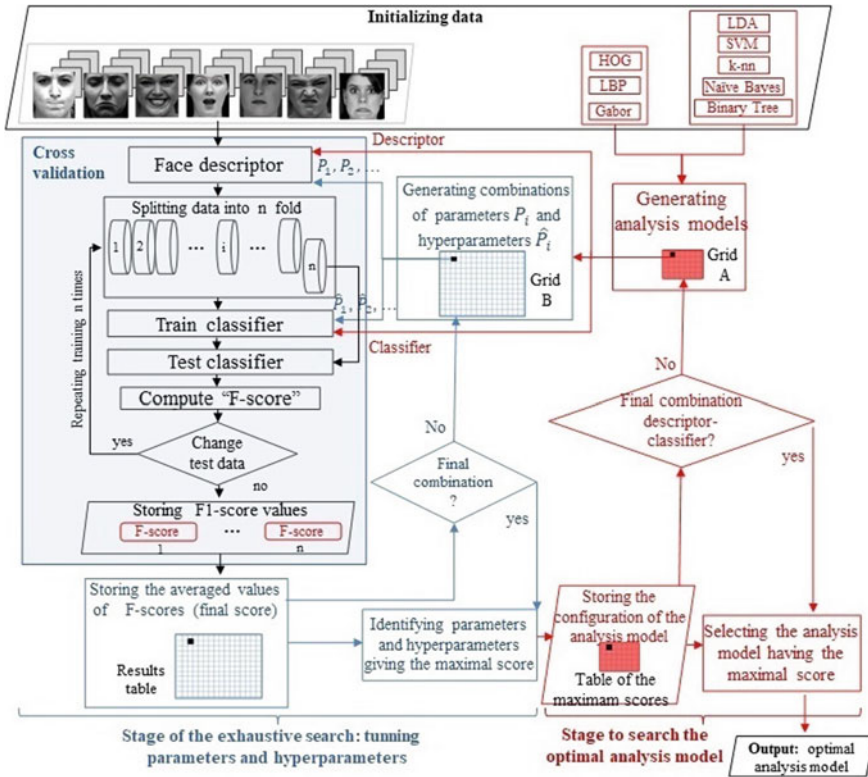


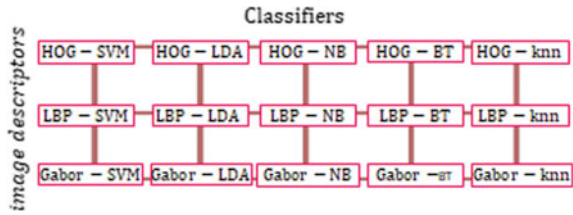
Fig. 3 Flowchart of the proposed algorithm to automate the analysis of images. The algorithm takes as input the labelled images and the pre-selected descriptors and classifiers. Then, generates and tunes the analysis models to find out the model with the highest F-score, after cross validating the each analysis model

expression classes are separable, in Fig. 2 we visualize the relationship between two data attributes X_1 and X_2 . In this figure we test linear decision boundary using: linear discriminant analysis [8] and binary tree [9], as well as non-linear decision boundary, like SVM [10], k-nn [11], and naive Bayes [12]. Given the values of data attributes, each classifier uses its own mathematical formulas to calculate the parameters of the lines representing the decision boundaries.

2.3 The Proposed Algorithm to Search the Optimal Analysis Model

The flowchart in Fig. 3 represents the sequence of operations and decisions made during the analysis of images, which are organized mainly in two stages. The first stage,

Fig. 4 Generation of the grid A containing the analysis models. Each analysis model is a combination descriptor-classifier which we can call “grid node”, as well. BT is the Binary Tree



represented in blue color, operates to find the optimal parameters and hyperparameters for each analysis model. The second stage, represented in red color, searches the analysis model that gives maximum F-score and a minimum classification time. In the following paragraphs we address in detail the algorithm steps.

2.3.1 Initialising Inputs

First, we import the following inputs: the labelled images, descriptors and classifiers. Then, the algorithm initializes the variables that need adjustment, such as the parameters P_i of the image descriptors, the hyperparameters \hat{P}_i of classifiers and the values $[v_1, v_2, \dots, v_k]$ to test for each P_i and \hat{P}_i .

2.3.2 Generating the Analysis Models

The algorithm combines each descriptor with a classifier, as shown in Fig. 4. In this figure, we have three descriptors and five classification methods, which gives a total of fifteen analysis models useful to analyze our images. The analysis models represent the grid nodes in Fig. 4, using a loop we tune the analysis models sequentially when sweeping nodes in the grid we call grid A.

2.3.3 Tuning Parameters and Hyperparameters

We start by generating combinations of parameters and hyperparameters values for one analysis model. The combinations are organized in the nodes of a grid we call grid B. In Fig. 5 we give an example of grid B which is constructed from two parameters and one hyperparameter. For each combination, a cross-validation and a test are carried out. In this case there are $3 \times 3 \times 3 = 27$ combinations to test and compare.

After generating the combinations of parameters and hyperparameters values corresponding to the current analysis models, we execute a loop that sweeps each node in grid B, see Fig. 3. For each iteration the algorithm sets the parameters values of the descriptor and the hyperparameters values of classifiers, performs a cross-validation and stores the scores obtained after testing the analysis model. In the top left of Fig. 3, we can see the training set including seven classes of the universal expressions. The

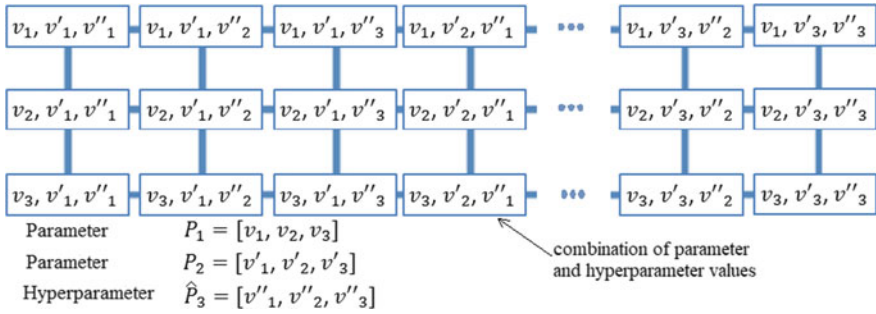


Fig. 5 Example of grid B including combinations of values of two parameters (P_1, P_2) and one hyperparameter P_3 . Here we give to each P_i 3 different values v_i . but in reality P_i have more than 3 values. We call each combination in the grid “node”

training data is collected from CK+ database [3], which is acquired for facial expression analysis. The reason we use CK+ database is: the diversity of samples within the same classes in terms of gender, as well as ethnicity and age; the necessity to compare the performance of our results to the results found in literature. After extracting the vector of features from all the images, we store the vectors in a table to prepare data to the classification step. Data are partitioned into n folds. We set the number of folds to ten folds. The classifier being trained and tested when applying 10-fold cross-validation, the F-scores, are recorded and then averaged to measure the final score for the current model. This score is then saved in result table shown in the left bottom of Fig. 3. The table has a size similar to the size of grid B. This allows to save the scores computed when repeating the training for all the combinations in grid B. The recording of scores stops when all the combinations in the grid B are tested. Once all the combinations in the grid B are tested and the values of F-score are stored, we can see what score is assigned to each combination. As a result, we can compare all the scores recorded during the research process to find out the combination of the parameters and hyperparameters values that produce the best score.

2.3.4 Searching the Optimal Analysis Model

Once the tuning of parameters and hyperparameters is finished for a given analysis model. In this stage, a loop helps repeating the tuning for all the analysis models generated in the grid A, see Fig. 4. For each iteration, an analysis model is selected and adjusted in a fixed order from the left of the grid A to the right and from the top to the bottom. The best configuration of the analysis model as well as the final score associated with it are selected and recorded in Table 1, which we mark in Fig. 3 as “table of maximum scores” having the same size as the grid A. We can finally compare the scores and determine the output of the algorithm that returns the best analysis model in the grid A and this by identifying the highest score among the maximum scores in Table 1. We notice from this table that the model analysis composed of

Table 1 The maximum scores obtained from each analysis model after the configuration of descriptors and classifiers applying 10-fold cross-validation and leave-one-out cross-validation

	Mesure des scores par validation croisée					
	10-plis			Leave-one-out		
	HOG	LBP	Gabor	HOG	LBP	Gabor
k-nn	85.78	62.67	81.78	74.50	52.90	71.02
LDA	96.44	82.67	92.89	93.02	78.77	–
Binary tree	73.33	53.33	63.11	70.01	55.06	56.24
Naïf Bayes	92.00	80.50	89.78	82.14	62.88	77.54
SVM	89.27	79.17	82.79	92.55	77.13	90.62

HOG descriptor and LDA classifier gives the highest F-scores (highlighted in bold in Table 1) with an average of 96.44 and 93.02% when splitting data with 10-fold and LOO cross-validation.

Regarding image descriptors, we note from Table 1 that HOG descriptor is more efficient than LBP descriptor and Gabor descriptor regardless the classifier they are associated with. In fact, even HOG and Gabor descriptors reach high scores, greater than 90%, when associated with the LDA classifier, the Gabor descriptor consumes more time and extracts more information on the images. For this reason and in addition to the important number of calculations of the Leave-one-out cross-validation technique, the image analysis algorithm was not able to complete the learning of the LDA classifier when the image contour is described by Gabor features. For this, the score is missing in Table 1. As the tuning has been made using 10-fold and LOO methods, that enables to observe how pre-selected methods behave with different splits of data. 10-fold method has been widely used in many previous studies for its applicability to handle medium data size (thousands of images). However, LOO Cross-validation has been used in few studies related to facial expression analysis because it is computationally expensive in terms of time. LOO Cross-validation technique is more stable than 10-fold technique when no change is made to the database like removing or adding samples inside the database [13]. On the other hand, when observing the lines of Table 1 and comparing the scores of the classifiers we find that the LDA classifier outperforms SVM, Naïve Bayes, k-nn, and Binary Tree classifiers, with a rate of 96.44%.

3 Discussion and Comparison with Previous Work

In addition to the average recognition rates, the proposed algorithm compares the time of feature extraction and classification. Indeed, the computational time of descriptors and classifiers has been measured considering an average of 100 frames using Intel core i7 processors, CPU @ 2.20GHz 2.2GHz, and RAM of 16.0 Go. Analysis

shows that the resulting optimal combination achieves good F-score with low costs in comparison to the state-of-the art. The average F-score are 96.44% and 93.02% respectively, using 10-fold and LOO cross-validation. The recognition time is equal to 18 ms, with 2.6 ms for feature extraction time and 15.4 ms for classification time using one face image. Realizing the extensive analysis by means of the proposed approach we found that LDA classifiers together with the HOG descriptor gives the appropriate pipeline that enables real-world face expression recognition. Indeed, the implementation of the pipeline, which we detail in our previous work [14], using video sequences, showed that the recognition of the face expression is achievable, even if more than one face are in the scene. It is worthwhile to explore data over a large number of classifiers. As a preliminary study toward building systems of recognition, automating data analysis when using a set of descriptors and classifiers can provide strong basis to build any system of recognition. In literature, few researchers go through the process of analyzing face images before proposing their approaches. Khadija Lekdioui et al. [15] used some image descriptors like HOG and LBP and their combinations to analyze the training data. To evaluate the performance of recognition, the descriptors and their combinations were tuned manually using SVM classifier. The authors reached the highest f-score at 96.06% using images of CK+ database. Pierluigi Cargani et al. [16] proposed an in-depth study of the HOG application in conjunction with the SVM classifier. The authors pointed out that finding the optimal parameters of HOG can effectively helps in describing the shape of facial expression. For that they carried out an experimental session by exploiting an algorithmic pipeline to seek the optimal parameters of the HOG descriptor. Associating HOG descriptor to an SVM classifier the authors obtained an F-score equal to 94% with a preprocessing time of 43.38 ms.

4 Conclusion

This paper proposes an algorithm to automate the image analysis procedure. By auto analysing images with various image descriptors and linear and non-linear classifiers, we was able to identify that the model HOG-LDA gives the highest F-score 96.44% with a recognition time of 18 ms.

The implementation of the algorithm that auto analyse images has shown us the points to improve in the proposed algorithm. We propose the following improvement. Indeed, tuning and evaluating analysis models is a parallel operational process: it does not require any intercommunication, because the tasks are executed independently on the same set of data. Two particular processes of this nature are the parameter sweeping and testing. When sweeping the combinations of parameters and hyperparameters values, the analysis model is executed several times on the same data set followed by an evaluation on a validation set. In cross-validation, the training and the test of the analysis model is repeated on different subsets of data. In this case, we can to scale machine learning using parallel computing with the aim of being able to reduce the analysis time which is quite high.

References

1. Zubiolo A (2015) Extraction de caractéristiques et apprentissage statistique pour l'imagerie biomédicale cellulaire et tissulaire. Ph.D. thesis. Nice
2. Goyal SJ, Upadhyay AK, Jadon RS, Goyal R (2018) Real-life facial expression recognition systems: a review. In: Smart computing and informatics. Springer, pp 311–331
3. Lucey P, Cohn JF, Kanade T, Saragih J, Ambadar Z, Matthews I (2010) The extended cohn-kanade dataset (CK+): a complete dataset for action unit and emotion-specified expression. In: 2010 IEEE computer society conference on computer vision and pattern recognition workshops (CVPRW). IEEE pp 94–101
4. Gao W, Cao B, Shan S, Chen X, Zhou D, Zhang X, Zhao D (2007) The CAS-PEAL large-scale Chinese face database and baseline evaluations. IEEE Trans Syst Man Cybernet Part A Syst Hum 38(1):149–161
5. Dalal N, Triggs B (2005) Histograms of oriented gradients for human detection. In: International conference on computer vision and pattern recognition (CVPR'05), vol 1. IEEE Computer Society, pp 886–893
6. Huang D, Shan C, Ardabilian M, Wang Y, Chen L (2011) Local binary patterns and its application to facial image analysis: a survey. IEEE Trans Syst Man Cybernet Part C Appl Rev 41(6):765–781
7. Cruz A, Bhanu B, Thakoor NS (2013) Facial emotion recognition with anisotropic inhibited Gabor energy histograms. In: 2013 IEEE international conference on image processing, pp 4215–4219
8. Ghassabeh YA, Rudzicz F, Moghaddam HA (2015) Fast incremental LDA feature extraction. Pattern Recogn 48(6):1999–2012
9. Brandmaier AM, von Oertzen T, McArdle JJ, Lindenberger U (2013) Structural equation model trees. Psychol Methods 18(1):71
10. Van den Burg GJJ, Groenen PJF (2016) Gensvm: a generalized multiclass support vector machine. J Mach Learn Res 17(1):7964–8005
11. Almalawi AM, Fahad A, Tari Z, Cheema MA, Khalil I (2015) k nnwvc: an efficient k -nearest neighbors approach based on various-widths clustering. IEEE Trans Knowl Data Eng 28(1):68–81
12. Jiang L, Zhang L, Liangjun Y, Wang D (2019) Class-specific attribute weighted naive Bayes. Pattern Recogn 88:321–330
13. Fawcett T (2004) Roc graphs: notes and practical considerations for researchers. Mach Learn 31(1):1–38
14. Greche L, Akil M, Kachouri R, Es-Sbai N (2019) A new pipeline for the recognition of universal expressions of multiple faces in a video sequence. J Real Time Image Process, 1–14
15. Lekdioui K, Messoussi R, Ruichek Y, Chaabi Y, Touahni R (2017) Facial decomposition for expression recognition using texture/shape descriptors and SVM classifier. Sig Process Image Commun 58:300–312
16. Carcagni P, Del Coco M, Leo M, Distanto C (2015) Facial expression recognition and histograms of oriented gradients: a comprehensive study. SpringerPlus 4(1):645

Prediction Potential Analysis of Arabic Diacritics and Punctuation Marks in Online Handwriting: A New Marker for Parkinson's Disease



Alae Ammour, Ibtissame Aouraghe, Ghizlane Khaissidi, Mostafa Mrabti, Ghita Aboulem, and Faouzi Belahsen

Abstract Parkinson's disease (PD) is a progressive movement disorder characterized by tremors at rest, bradykinesia, and stiffness. The alteration of handwriting (HW) faculties is one of the earliest motor symptoms in PD patients. This characteristic can be exploited to develop an automatic aid system for early detection of this pathologie. This article aims to assess the importance of diacritics and punctuation marks (DPM) in the PD patients and healthy controls (HCs) discrimination problem, by comparing the classification results obtained from three components: text carrying DPM, text without DPM, as well as only DPM. This work includes the Arabic manuscripts of 31 PD patients and 31 HCs. Furthermore, kinematic, mechanic, and inclination features were calculated for each component. Then, Adaboost models have been constructed on different feature sets, as well as on reduced sets formed in incremental manner using mRMR ranked-feature selection method. From the obtained results, it was concluded that the separating power of HW features in the classification problem of PD patients and HCs is present in all components of the Arabic text, but in varying degrees of importance. Despite the simple graphical nature of DPM, they are carrying of relevant diagnostic information, and effectively contributing to the improvement of PD detection performance. The highest accuracy of 93.54% was achieved for this component.

A. Ammour (✉) · I. Aouraghe · G. Khaissidi · M. Mrabti
Laboratory LIPI ENS, USMBA, Fez, Morocco
e-mail: alae.am19@gmail.com

I. Aouraghe
e-mail: aouraghe.ibtissame@gmail.com

G. Khaissidi
e-mail: ghizlane.derkaoui1@hotmail.com

M. Mrabti
e-mail: mostafa.mrabti@yahoo.fr

G. Aboulem · F. Belahsen
Laboratory ERMSC, FMPF, CHU Hassan II Fez, Fez, Morocco
e-mail: aboulemghita@gmail.com

F. Belahsen
e-mail: belahsenfaouzi@gmail.com

Keywords Parkinson's disease · Arabic online handwriting · Online segmentation · Clustering · mRMR feature selection · Adaboost model

1 Introduction

Parkinson's Disease (PD) is a progressive, age-related disorder that is mainly characterized by irreversible destruction of dopaminergic substantia nigra neurons that are involved in body movement control [1]. To date, the detection of PD is essentially based on the clinical observation of the patient, by looking for the parkinsonian triad include tremors at rest, stiffness and slowness of movement. This medical diagnosis may be supported by tools such as imaging (e.g. magnetic resonance imaging) [2]. However, it is difficult to establish PD diagnosis at an early stage because all the predominately symptoms of this disease arise for unknown reasons and appear only after the degeneration of 60–80% of neurons [1]. This creates a critical necessity for the development of a new approaches adopted for the early detection of this disease.

Handwriting (HW) is the graphic result of perceptual-motor and cognitive processes [3]. The act of writing involves the use of a series of cognitive and motor attributes which change according to the form or figure developed. It is this aspect that, increasingly, has attracted the attention of health experts and data scientists, the focus being on what HW can bring as information in the diagnosis of certain pathologies such as PD [4], Alzheimer's disease [5], and schizophrenia [6]. Previous studies focused on PD have shown that the motor disorders caused by this pathology could lead to a partial or complete impairment of HW capacities. Parkinson's dysgraphia [7] appears several years before the clinical diagnosis of the disease, and commonly manifested by a micrographia, a slowing down of the HW speed and acceleration, as well as blockages and interruptions of the HW rhythm (freezing and festination) [8–11]. Recently, machine-learning researchers investigate the effectiveness of HW analysis as a tool to develop mathematical prediction models for PD diagnosis and monitoring.

In this regard, Drotar et al. conducted a series of experiments on the PaHaW dataset which includes the HW tasks of 37 PD patients and 38 HCs. In Ref. [12], the authors concluded that classification performance can be considerably improved considering in-air features which provide better results than on-surface features. These findings were improved in Ref. [13], by considering, in addition to classic kinematic HW features, a novel feature category based on entropy, energy, and empirical mode decomposition of the HW signals. In Ref. [14], the authors introduced features based on the pressure signals captured by the tablet during writing. They have shown that pressure features can be used, in addition to the kinematic ones, in the development of classification models with a high accuracy. In Ref. [15], the authors improved the classification performance obtained on PaHaW dataset by combining classic kinematic features to new velocity-based features by applying the sigma-lognormal model, the Maxwell–Boltzmann distribution, and the Discrete Fourier Transform to the HW signal velocity. Nowadays, researchers are trying to distinguish between the

severity levels of PD, based on HW features. A classification study was conducted by Impedovo et al. [16] always on the PaHaW dataset with the purpose of assessing the impact of the disease stages on the classification results. They concluded that prediction accuracy considerably drops when including PD patients with earlier and mild degree of disease severity, compared to the entire dataset which includes more patients in a severe stage.

From another angle, the performance of the envisaged diagnostic system could also depend on the graphic characteristics of the considered writing system. The present paper aims to assess the contribution of certain Arabic HW text elements that are diacritics and punctuation marks, in the classification process of 32 PD patients and 32 HCs. Therefore, three components will be analyzed: text with diacritic and punctuation marks, text without diacritic and punctuation marks, as well as diacritic and punctuation marks. The extraction of these elementary graphic units from the text is carried out by applying an online segmentation technique based on the pressure signal captured by the tablet, combined with the unsupervised classification algorithm k-medoids. This evaluation was performed considering kinematic, mechanic and inclination features. The obtained classification results following the application of the mRMR selection method combined with adaptive boosting (Adaboost) model, have highlighted the important role of the small strokes, which particularly correspond to the diacritic and punctuation marks, in improving the prediction results.

This work is original in the fact that it uses Arabic manuscripts to develop an aid system for the early diagnosis of PD. Moreover, this work was conducted on an Arabic HW dataset that our research team has collected within the neurology department of the CHU of Fez, by developing an entire acquisition protocol [17]. In fact, on the one hand, there is no similar studies on the Arabic language in the literature and, on the other hand, the Arabic graphic system has several graphic characteristics, different from those of Latin and, more generally, from other languages, that have been exploited to model HW impairments in PD patients and improve consequently the detection performance. The rest of the paper is organized as follows: Sect. 2, is devoted to data acquisition and methods. Section 3 presents the adopted selection and classification approach. Section 4 is about experiment results and discussion. Eventually, last section concludes the study.

2 Data Acquisition and Methods

2.1 Participants

A total of 62 right-handed participants volunteered to take part in this study including 31 PD patients and 31 HCs matched according to age and intellectual level. Data collection was carried out at the neurology department of the CHU of Fez according to the inclusion and exclusion criteria detailed in [17]. The acquisition protocol and the used equipment are described in [18, 19]. Mean standard deviation (std) of age,

Table 1 Demographic and clinical characteristics of PD patients and HCs population

Cognitive profile	Age		MMSE		DR		UPDRS	
	Mean	STD	Mean	STD	Mean	STD	Mean	STD
PD patients	57.2	9.49	29.02	0.93	7.45	3.71	10	6.41
HCs	54.28	8.21	30	0	–	–	–	–

disease’s duration (DR), MMSE score [20], UPDRS score [21], are represented in Table 1.

2.2 Handwriting Task

The analysis presented in this article concerns the first exercise of the protocol described in the [17] which consists in copying, in an indefinite period of time, an imposed Arabic text that is composed of 6 lines, 3 of which are vocalized. This text, extracted from a popular Arabic tale “Joha”, was chosen for its grammatical and syntactic simplicity which is appropriate for all intellectual levels. It contains graphic elements of different natures namely: cursive letters, short and long vowels, diacritical signs, punctuation marks, specific to the Arabic writing system [18, 19].

2.3 Diacritics and Punctuation Marks Extraction

The present work aims to analyze the HW dynamics related to the production of the Arabic text in the presence and absence of diacritical signs and punctuation marks, while assessing the contribution of each component in the classification process of PD patients and HCs. Diacritical marks (also diacritics or short vowels) are small graphic units, usually having simpler forms than letters and long vowels, which are used in Arabic text to change the sound-values of the letters to which they are added. Punctuation marks are also elements of a simple graphic nature that are employed in the text to remove ambiguity in the meaning of sentences. The evaluation of the discriminating power of HW features by adding or removing these simple graphic elements will allow, on the one hand, to study the impact of the graphic complexity on the discrimination of PD patients and HCs and, on the other hand, to determine the graphic nature of the most suitable elements to reveal PD. Therefore, three components are considered in this work namely: text with diacritic and punctuation marks (TWDP), text without diacritic and punctuation marks (TNDP), and the small strokes including diacritics and punctuation marks (DPM).

The extraction of DPM from the text is carried out in two stages: A segmentation stage which consists in dividing the digitized text trajectory into reduced elements (stroke) based on the instantaneous pressure values provided by the tablet. Indeed,

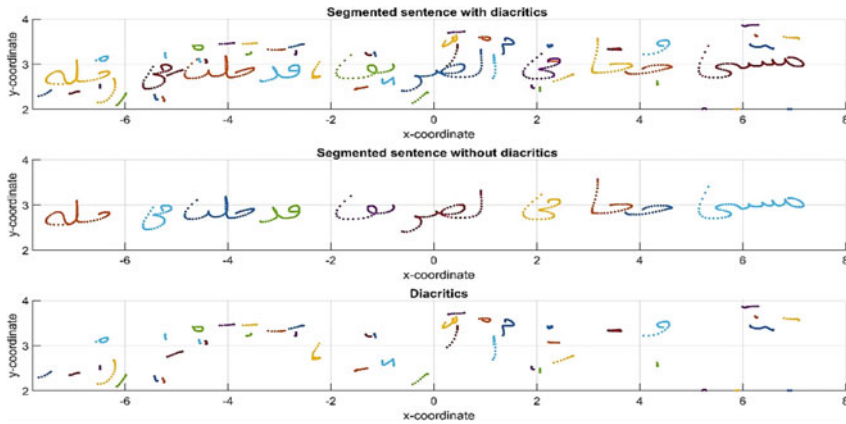


Fig. 1 Text sentence before and after diacritics extraction

by traversing all the trajectory points, the recording of a new stroke starts when the segmentation algorithm crosses a non-null pressure value and ends when this pressure becomes zero. Each extracted stroke is consisting of the trajectory's subset of points which are associated with the corresponding spatiotemporal parameters given by the tablet. The second step consists in generating three groups of strokes by applying the k-medoids clustering method on the vector of stroke lengths. The group containing the small strokes corresponds to that of the diacritical and punctuation marks. The Fig. 1 shows a segmented text sentence before and after the extraction of diacritics, as well as the extracted diacritics. Every extracted stroke is represented by a different color.

2.4 Feature Extraction

Three different feature sets have been extracted from the HW signals associated with each studied text component (TWDP, TNDP, DPM) namely: **features based on kinematic analysis (KF)**, **mechanical features based on pressure (MF)**, and **features based on inclination (IF)**. For a given feature, the local values have been computed at each point [n] of the stroke trajectories related to the corresponding component. A detailed overview of these computed feature is given in [18]. Thus, six statistical measures include **average, standard deviation, minimum, maximum, skewness, kurtosis** have been applied on the generated local feature vectors. Hence, the HW signal for a given person is represented by 72-dimensional features.

3 Selection and Classification

3.1 Classification Method

The classification approach adopted in this study is based on Boosting. This method which seeks to improve the accuracy of a given learning algorithm by linearly combining results from so-called “weak” classifiers in order to build a “strong” one. AdaBoost (Adaptive Boosting) [22, 23] is an iterative algorithm that creates a linear combination an number T weak classifiers in the form:

$$H(x) = \text{sign} \left(\sum_{t=1}^T \alpha_t h_t(x) \right) \tag{1}$$

where h_t represents a weak classifier and α_t its weight. One of the main ideas of this algorithm is to give instances that are difficult to classify a high weight, so as to cause the algorithm to focus on them. Each classifier is assigned a coefficient proportional to the weighted error which quantifies its contribution to the final prediction. An important point of AdaBoost is to choose a weak classifier. This choice constitutes one of the parameters of this algorithm. The base estimator used in this paper is decision trees classifier. In addition, it is also necessary to determine the optimal number of weak classifiers N_{est} which will provide the best classification accuracy. This hyperparameter will be chosen in a value range from 1 to 50 according to the strategy detailed in the following section.

3.2 Selection Approach

Minimum redundancy-maximum relevance (mRMR) [24] is a filter-based feature selection method that has been applied in this study in order to find the optimal HW feature subset that improves the performance of the Adaboost model and reduce its complexity. The best scores returned by this method correspond to the features having the most correlation with the target class and the least correlation between themselves. Based on the Spearman’s correlation coefficient, the relevance (Rel) and redundancy (Red) of a given feature i are defined as:

$$\text{Rel}(i) = |\text{Spe_corr}(F_i, R)| \tag{2}$$

$$\text{Red}(i) = \frac{1}{|N|} \sum_{i,j \in N} \text{Spe_corr}(F_i, F_j) \tag{3}$$

where: $\text{Spe_corr}(F_i, R)$ is the Spearman’s correlation coefficient between the vector of the i th parameter and the response vector R . $\text{Spe_corr}(F_i, F_j)$ is the

Spearman's correlation coefficient between the vector of the i th and j th parameter. N and $|N|$ represent, respectively, the group of features and its size.

The mRMR algorithm ranks the features through the forward addition scheme. The calculation of the features scores is done iteratively by seeking at each iteration the feature which maximizes the following quantity:

$$\xi(\text{Rel}, \text{Red}) = \alpha \times \text{Rel} + \beta \times \text{Red} \text{ where } \alpha, \beta \in [0, 1] \quad (4)$$

The classification performance for the Adaboost model were obtained by proceeding with a double optimization. The latter consists in finding a reduced combination of the most important features, and then identifying for each feature subset the optimal hyperparameter $Nest$ which maximizes the prediction accuracy. For this purpose, the features are ranked first in decreasing order according to their mRMR scores. Then, a sequence of the candidate feature subsets denoted P_k where $1 \leq k \leq 72$ are formed by affecting to the first subset P_1 the feature having the highest mRMR score, then, by adding to each subset P_k the highest mRMR score feature which is not contained in the previous generated subset i.e., P_{k-1} . In the following step, Adaboost model is trained on all these subsets in incremental manner, and it is optimized by using an exhaustive search strategy which assess, at each training stage, the prediction accuracy for the range of $Nest$ values specified above. Consequently, the optimal Adaboost model is defined by the feature subset and the value of $Nest$ that led to the best performances. It should be noted that, following a series of experiences, the best classification results were obtained for $\alpha = 0.7$ and $\beta = 0.3$.

3.3 Evaluation and Validation

The selection of the best model, as well as the estimation of classification performance of the models built by the Adaboost algorithm are performed using a stratified nested 5-fold cross validation (CV) strategy with an inner loop CV nested in an outer CV. The inner loop is used to tune the hyperparameter $Nest$, while the outer loop is used for error estimation. Thus, our dataset including 31PD patients and 31HCs is first splitted into 5 random outers splits. The data from 4 outer splits are further divided into 5 inner splits. The resulting model with the optimal hyperparameter that is trained on the inner splits, is tested on the held-out outer split. This operation is done 5 times so that all outer splits are once considered as a testing set. The performances of the generated prediction models are evaluated via four statistical measures including accuracy (Acc), sensitivity (Sen), specificity (Spec), F-Score.

4 Experiment Results and Discussion

In this section, the adopted classification process was conducted on the three components: TWPD, TNPD, DPM. In each case, the prediction models were trained on {**KF**}, {**MF**}, {**IF**} separately, in order to assess, in the comparison, the predictive power contained in each feature category. The training of Adaboost models was also performed on the combination of the three feature categories {**KF + MF + IF**} before and after the application of the selection strategy detailed in the previous section. This allowed to observe the possible improvement of the classification performance by injecting a reduced number of the most relevant and least redundant features. The classification results associated with each component are shown in Tables 2, 3 and 4. NF is the number of features used for the Adaboost classifier training.

From the experimental results, it is clear that KF category contains a high predictive power compared to the other categories, and this for all the studied components. Indeed, the performance achieved from training Adaboost models on the MF and IF

Table 2 Classification of PD patients versus HCs using TWDP

Feature set	NF	Nest	Acc	Sen	Spec	F-score
KF	36	5	80.65	91.67	73.68	78.57
MF	12	3	64.52	72.73	60	59.26
IF	24	1	77.42	70	90.91	80
KF + MF + IF	72	10	74.19	78.57	70.59	73.33
mRMR KF + MF + IF	6	4	87.10	87.50	86.67	87.55

Table 3 Classification of PD patients versus HCs using TNPD

Feature set	NF	Nest	Acc	Sen	Spec	F-score
KF	36	6	80.65	85.71	76.47	80
MF	12	1	74.19	76.92	72.22	71.43
IF	24	6	77.42	77.52	76.47	75.86
KF + MF + IF	72	5	80.65	91.67	73.68	78.57
mRMR KF + MF + IF	8	3	90.32	87.50	93.14	91.43

Table 4 Classification of PD patients versus HCs using DPM

Feature set	NF	Nest	Acc	Sen	Spec	F-score
KF	36	6	77.42	90.91	70	74.07
MF	12	1	64.42	76.32	61.78	62.75
IF	24	1	61.29	57.89	66.67	64.71
KF + MF + IF	72	9	87.10	83.33	92.31	88.24
mRMR KF + MF + IF	10	14	93.54	93.75	93.33	93.75

features is not equally important. Moreover, the combination of KF, MF, and IF has resulted in a remarkable performance improvement only in the case of DPM. For this component, the constructed model based on this combination has revealed an accuracy of 87.10% for an optimal value of Nest = 9 (Table 4). Furthermore, the highest prediction performance was achieved in particular by considering reduced subsets of the most optimal features among the combination {KF + MF + IF}, which were constructed based on the proposed selection strategy. It should be noted that the improvement in performance of Adaboost model is due to the fact that the sequential injection of the mRMR ranked-features successfully eliminate the most redundant and least relevant features from the starting sets. The increase in classification accuracy before and after selection was remarkable for all the components. Besides, the highest accuracy of 93.54% was achieved for the DPM component with sensitivity of 93.75% and specificity of 93.33% for 10 features and Nest = 14 (Table 4). It was also observed that the accuracy increased between TNDP and TWDP. The accuracy has reached 90.32% for TWDP (Table 2) and only 87.10% for TNDP (Table 3). This shows that an Arabic text with DPM contains greater predictive power than a text without these graphic elements.

These results were also confirmed by the Receiver Operating Characteristic (ROC) curves (Fig. 2) and area under the curve (AUC) measures. These were used to assess the detection performance of the optimal Adaboost models obtained from the three studied components before and after the application of the mRMR selection strategy on the combination {KF + MF + IF}. It can be observed, that the insertion of DMP in the Arabic text led to a considerable improve in classification performance represented by an increase in AUC between TNDP and TWDP. The AUC measures were also increased following the application of the mRMR-based selection strategy, which supports the results discussed previously.

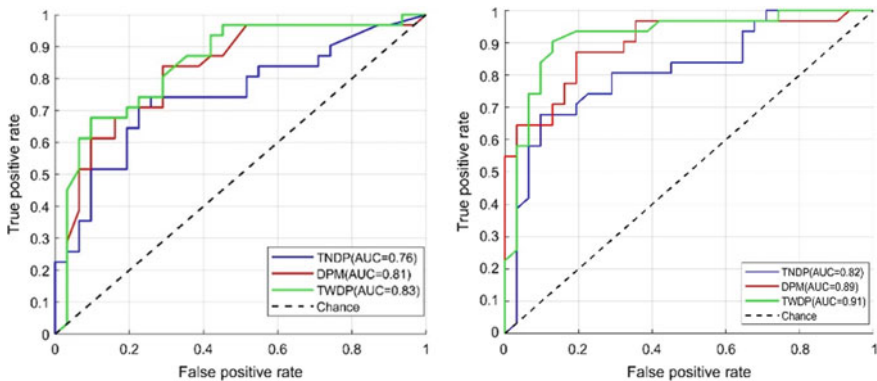


Fig. 2 ROC curves for PD patients versus HCs classification trained on the combination {KF + MF + IF}: before the application of mRMR selection strategy (left), after the application of mRMR selection strategy (right)

5 Conclusion

This study is a contribution to the development of an aid system for the early diagnosis of Parkinson's disease based on the automatic processing of online Arabic HW. The starting idea was to assess the predictive power contained in an Arabic text by adding or removing diacritics and punctuation marks, as well as quantifying the impact of these elementary graphical units in the Parkinson's patients and healthy controls discrimination problem. The training of the prediction models was carried out by considering three features categories namely: kinematic, mechanic, and inclination. Moreover, to improve PD detection accuracy, mRMR feature selection method was combined with Adaboost model while performing a double optimization to select the best prediction model for each considered case.

The proposed system has highlighted, through a series of experiments, the important role of diacritics and punctuation marks in the adopted classification process. These simple-form graphic units in Arabic language constitute an important source of relevant discriminant information, which contributes effectively to the improvement of classification performance. Accuracy has reached a maximum of 93.54% by considering only these elements.

Future work will focus on extending this reasoning to the French HW text (6th task of our protocol) in order to identify the graphic elements in French writing system that could lead to the best PD detection performance, while relying on deep learning strategies.

References

1. Cheng HC, Ulane CM, Burke RE (2010) Clinical progression in Parkinson disease and the neurobiology of axons. *Ann Neurol* 67(6):715–725
2. Hou JGG, Lai EC (2007) Non-motor symptoms of Parkinson's disease. *Int J Gerontol* 1(2):53–64
3. Tseng MH, Cermak SA (1993) The influence of ergonomic factors and perceptual—motor abilities on handwriting performance. *Am J Occup Ther* 47(10):919–926
4. Rosenblum S, Samuel M, Zlotnik S, Erikh I, Schlesinger I (2013) Handwriting as an objective tool Parkinson's disease diagnosis. Springer, Berlin, Heidelberg
5. Impedovo D, Pirlo G, Barbuzzi D, Balestrucci A, Impedovo S (2014) Handwritten processing for pre diagnosis of Alzheimer disease. In: *Proceedings of BIOSTEC 2014, SCITEPRESS, Portugal*, pp 193–199
6. Crespoi Y, Ibañez A, Soriano MF, Iglesias S, Aznarte JI (2019) Handwriting movements for assessment of motor symptoms in schizophrenia spectrum disorders and bipolar disorder. *PLoS ONE* 14(3):e0213657
7. Letanneux A, Danna J, Velay J-L, Viallet F, Pinto S (2014) From micrographia to Parkinson's disease dysgraphia. *Mov Disord* 29(12):1467–1475
8. Lang AE, Lozano AE (1998) Parkinson's disease. *New England J Med* 339(15):1044–1053
9. Gemmert A, Teulings HL, Contreras-Vidal JL, Stelmach GE (1999) Parkinsons disease and the control of size and speed in handwriting. *Neuropsychologia* 37(6):685–694
10. Ponsen MM, Daffertshofer A, Wolters EC, Beek PJ, Berendse HW (2008) Impairment of complex upper limb motor function in denovo Parkinson's disease. *Parkinsonism Related Disord* 14(3):199–204

11. Broderick MP, Van Gemmert AWA, Shill HA (2009) Hypometria and bradykinesia during drawing movements in individuals with Parkinson disease. *Exp Brain Res* 197(3):223–233
12. Drotár P, Mekyska J, Rektorová I, Masarová L, Smékal Z, Faundez-Zanuy M (2013) A new modality for quantitative evaluation of Parkinson's disease: in-air movement. In: Proceedings of the 13th IEEE international conference on bioinformatics and bioengineering, Chania, Greece, 10–13 November 2013, pp 1–4
13. Drotár P, Mekyska J, Smékal Z, Rektorová I, Masarová L, Faundez-Zanuy M (2015) Contribution of different handwriting modalities to differential diagnosis of Parkinson's disease. In Proceedings of the IEEE international symposium on medical measurements and applications (MeMeA) proceedings, Torino, Italy, 7–9 May 2015, pp 344–348
14. Drotár P, Mekyska J, Rektorová I, Masarová L, Smékal Z, Faundez-Zanuy M (2016) Evaluation of handwriting kinematics and pressure for differential diagnosis of Parkinson's disease. *Artif Intell Med* 67:39–46
15. Impedovo D (2019) Velocity-based signal features for the assessment of Parkinsonian handwriting. *IEEE Signal Process Lett* 26:632–636
16. Impedovo D, Pirlo G, Vessio G (2018) Dynamic handwriting analysis for supporting earlier Parkinson's disease diagnosis. *Information* 9:247
17. Aouraghe I, Ammour A, Aboulem G, Khaissidi G, Mrabti M, Belahsen F, El-Yacoubi MA, Garcia-Salicetti S (2017) Analyse automatique de l'écriture manuscrite en ligne pour la détection précoce des pathologies neurodégénératives. *Open Sci Internet des objets*, ISTE 17(2):1–8
18. Ammour A, Aouraghe I, Khaissidi G, Mrabti M, Aboulem G, Belahsen F (2020) A new semi-supervised approach for characterizing the Arabic on-line handwriting of Parkinson's disease patients. *Comput Methods Programs Biomed* 183
19. Aouraghe I, Alae A, Ghizlane K, Mrabti M, Aboulem G, Faouzi B (2020) A novel approach combining temporal and spectral features of Arabic online handwriting for Parkinson's disease prediction. *J Neurosci Methods* 108727
20. Movement Disorder Society Task Force on Rating Scales for Parkinson's Disease (2003) The unified Parkinson disease rating scale (UPDRS): status and recommendations. *Mov Disord* 18(7):738–750
21. Rakuša M, Granda G, Kogoj A, Mlakar J, Vodušek DB (2006) Mini-Mental State Examination: Standardization and validation for the elderly Slovenian population. *Eur J Neurol* 13(2):141–145
22. Tang X, Ou Z, Su T, Zhao P (2005) Cascade adaboost classifiers with stage features optimization for cellular phone embedded face detection system. In: International conference on natural computation. Springer, Berlin, pp 688–697
23. Prabhakar S, Rajaguru H (2018) Adaboost classifier with dimensionality reduction techniques for epilepsy classification from eeg. In: Precision medicine powered by pHealth and connected health. Springer, Berlin, pp 185–189
24. Ding C, Peng H (2005) Minimum redundancy feature selection from microarray gene expression data. *J Bioinform Comput Biol* 3(2):185–205
25. Rios-Urrego C, Vásquez-Correa J, Vargas-Bonilla J, Nöth E, Lopera F, Orozco-Arroyave J (2019) Analysis and evaluation of handwriting in patients with Parkinson's disease using kinematic, geometrical, and non-linear features. *Comput Methods Programs Biomed* 173:43–52
26. Werner P, Rosenblum S, Bar-On G, Heinik J, Korczyn A (2006) Handwriting process variables discriminating Mild Alzheimer's disease and mild cognitive impairment. *J Gerontol Psychol Sci* 61b(4):228–236

Telecom

Development of an Ultra Wide Band Hybrid Coupler with Adjustable Phase Shifter for 5G Applications



Abdellatif Slimani, Saad Bennani Dosse, Ali El Alami, Mohammed Jorio, Abdelhafid Belmajdoub, Mohamed Amzi, Sudipta Das, and Ghir Elmahjouby

Abstract The goal of this paper is to design and develop of an ultra-wideband (UWB) hybrid coupler with a variable phase shift (90° – 180° and vice versa) which operates around the resonant frequency of 3.8 GHz required for 5G applications. The design approach is based on the microstrip waveguide technique with localized lumped elements to control the phase shift between outputs ports. The proposed coupler is planar etched onto a Rogers RT substrate with an overall size of $50 \times 42 \times 1.6 \text{ mm}^3$ and dielectric constant $\epsilon_r = 2.2$. The performance of the coupler can be seen from its important characteristics: Adaptation, Coupling, Isolation and Phase shifter.

Keywords Hybrid coupler · Ultra-wideband · Phase shift · Isolation · Coupling

1 Introduction

The first frequencies that will be used by 5G expected from 2020, will be those under 6 GHz, between 3.4 and 3.8 GHz. This band is close to that of 4G at 2.6 GHz, and of 3G at 2.1 GHz. These different standards will thus share a various number of devices such as antennas, transmission lines, amplifier, etc., which will require having frequency selective directional couplers with high performance [1, 2].

A. Slimani (✉) · S. B. Dosse · M. Jorio · A. Belmajdoub · M. Amzi
Intelligent Systems, Georesources and Renewable Energies Laboratory (SIGER), University of Sidi Mohamed Ben Abdellah, Fez, Morocco
e-mail: slimani.abdellatif.ma@gmail.com

A. E. Alami
Renewable Energies, Information Processing and Transmission Laboratory, Moulay Ismail University, Errachidia, Morocco

S. Das
Department of Electronics and Communication Engineering, IMPS College of Engineering and Technology, Jadupur, WB, India

S. Elmahjouby
MIET Laboratory, FST Settati, Hassan 1st University, Settati, Morocco

Hybrid (Directional) couplers are the single integral components employed in several microwave integrated circuits, that can be used such as power dividers, combiners and frequency duplexers. These bidirectional structures can give equal power split between the two output (coupled and through ports) with a well-defined phase shift difference, while the fourth port is strictly isolated. In the literature, there are two popular hybrid couplers, the first, where the phase difference between the two output signals is 90° and a power split of 3 dB, while the second, the phase shift between the two output signals is 180° and also a power split of 3 dB [3–5].

In this work, our objective is to develop a single hybrid coupler that can be control both phase shifts at the same time with approximately 3 dB attenuation. The choice of phase shift difference (90° or 180°) depends totally on the user.

The range (3.5–4.5 GHz) and resonant (3.8 GHz) frequency selected in this work are chosen carefully to satisfy UWB 5th generation applications.

It is defined that UWB technology is a radio modulation technique that is based on the transmission of very short pulses with very low energy level. From FCC commission rules, each microwave component, has at least a bandwidth of 500 MHz in the range frequency of 3.1–10.6 GHz, it can be used in UWB communication systems [6–8].

In this paper, we propose a planar microstrip hybrid coupler with localized lumped elements to control the phase shift between all output ports. The parameters structure of the proposed coupler are optimized to have a high performance in terms of adaptation, coupling, isolation and phase shifter. The simulation tool used in this work is Ansoft's High Frequency Structure Simulator (HFSS) and to compare the various parameters, CST tool is used.

This paper is divided into two principal parts. In Sect. 2, the methods and design techniques are presented, while the simulation discussion results is done in Sect. 3.

2 Methods and Materials

2.1 Conventional Couplers

The conventional Hybrid Couplers found in the literature with four designated ports are shown in Figs. 1 and 2. The first one is a coupler with 90° phase shift difference, while the second is a 180° phase shifter coupler. To understand the coupler's functioning, port 1 (Σ -port) and port 2 (Δ -port) are considered as input ports, port 3 and port 4 are output ports, while Z_0 is the input impedance.

An excitation of port (1) leads to signals having the same amplitude and phase shift between the output (3) and (4), while the input port (2) is isolated. The distance between output (3) and (4) that controls the phase shift in the coupler outputs. If the distance is $\lambda/4$, the phase shift is 90° , while $\lambda/2$ leads to 180° [9–16].

According to [17, 18], scattering matrix of these couplers is defined as Eq. (1).

Fig. 1 90° conventional hybrid coupler

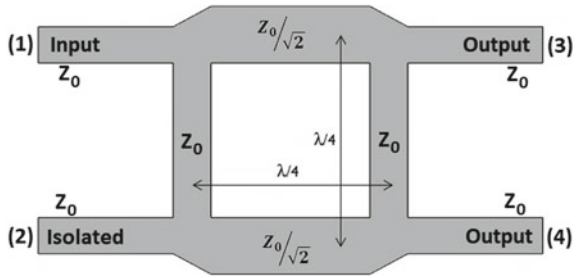
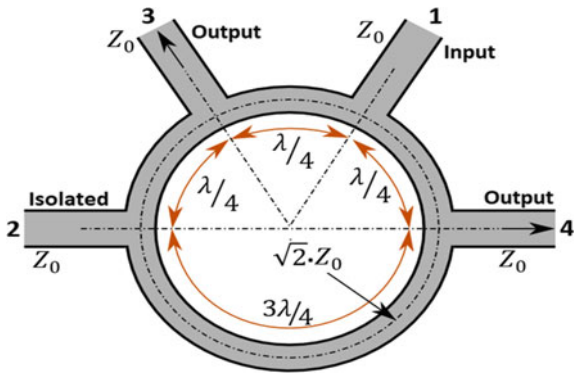


Fig. 2 180° conventional hybrid coupler



$$[S] = \begin{bmatrix} S_{11} & S_{12} & S_{13} & S_{14} \\ S_{21} & S_{22} & S_{23} & S_{24} \\ S_{31} & S_{32} & S_{33} & S_{34} \\ S_{41} & S_{42} & S_{43} & S_{44} \end{bmatrix} \tag{1}$$

S_{ij} values in Eq. 1, represent the theoretical ideal results in couplers, and through these parameters, we can know and evaluate the performance of the couplers. Equation (2) represents a coupler with adapted input ports.

$$[S] = \begin{bmatrix} 0 & \beta e^{j\theta} & \alpha & 1 \\ \beta e^{j\theta} & 0 & 1 & \alpha \\ j & 1 & 0 & \beta e^{j\phi} \\ 1 & j & \beta e^{j\phi} & 0 \end{bmatrix} \tag{2}$$

With,

- $S_{13} = S_{24} = \alpha$, $S_{12} = \beta e^{j\theta}$ and $S_{34} = \beta e^{j\phi}$.
- $\alpha^2 + \beta^2 = 1$
- θ and ϕ are phase constants to be determined

2.2 Proposed UWB Hybrid-Coupler

The proposed coupler is built on Roger RT Duroid with a thickness h_{sub} of 1.6 mm and a dielectric constant ϵ_r of 2.2. The dimensions of the prototype (Figs. 3 and 4) are $50 \times 42 \text{ mm}^2$. Our proposed coupler is composed of five ports, two for input, the first one (1) is for excitation and the second (2) is isolated, the last three for output, the (3) is for through transmission, the (4) is for coupled transmission of 90° phase shift, while the (5) port is for coupled transmission of 180° phase shift. In the top view we have two localized lumped elements (diodes), to play the switch role, and

Fig. 3 Proposed UWB hybrid coupler for 90° and 180° phase shift

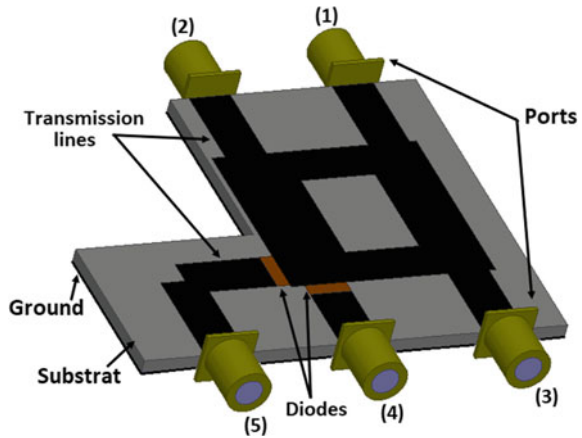
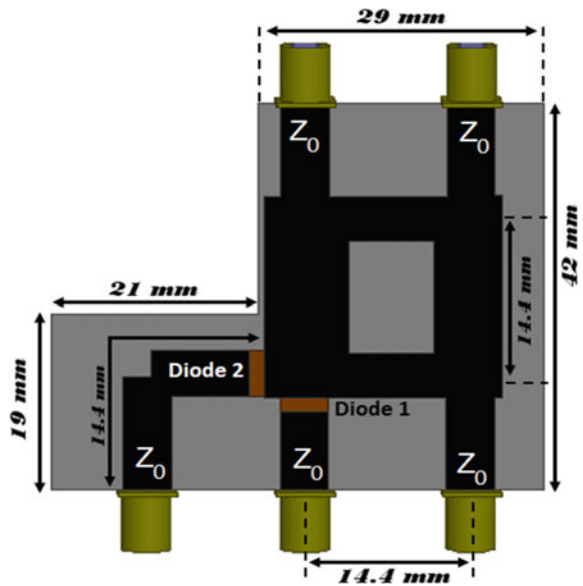


Fig. 4 Dimensions characteristics of the proposed UWB hybrid coupler



therefore, to allow the current passage or not, to the two output ports 4 and 5. To put the diode in the active case (ON), it is represented by an internal resistance and capacity of very low values, whereas, for the OFF case, the value of the resistance and the capacity must be very high.

3 Results and Discussion

The four most important parameters of a hybrid coupler are the S -parameters, phase shift, isolation and coupling, which will be considered in this section. For that, we will present these parameters in two parts, in the first where the diode 1 is turned on, while the second is turned off, and vice versa, to show really the phase shift variation between the two cases from 90° to 180° and inversely. As can be seen in Figs. 5 and 6, the S -parameters results in HFSS and CST simulators successively, where the first

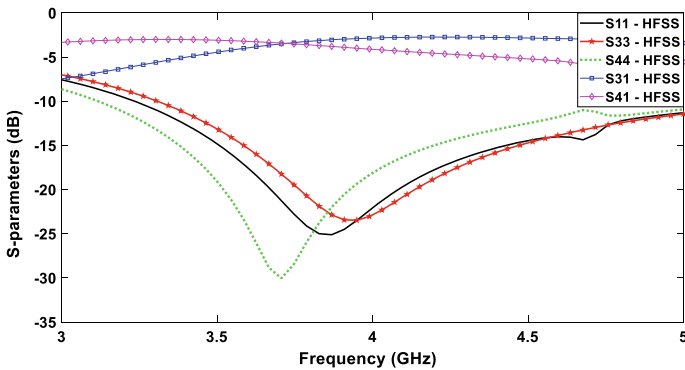


Fig. 5 HFSS S-parameters (diode 1 ON, diode 2 OFF)

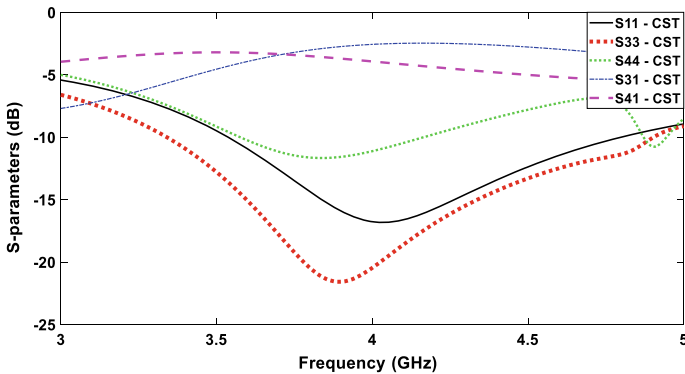


Fig. 6 CST S-parameters (diode 1 ON, diode 2 OFF)

diode is activated. We can observe that S11, S33 and S44 are well adapted in ports 1, 3 and 4, where the returns loss are lower than -10 dB, and the transmissions level between input port 1 and output ports 3 (S31) and 4 (S41) are approximately around -3 dB in the range frequency 3.5–4.5 GHz. As can be seen in Fig. 7, S31 and S41 are ninety degrees out of phase shift in all range frequency. As can be seen in Figs. 8 and 9, the *S*-parameters results in HFSS and CST simulators successively, where the second diode is activated while the first is turned off.

As can be seen that S11, S33 and S44 are lower than -10 dB, and the transmissions level (S31) and (S41) are approximately around -3 dB in the desired range frequency.

Also, as can be seen in Fig. 10, S31 and S41 are about 180° out of phase shift in the desired range frequency, which justifies the passage of the phase from 90° to 180° , when we active the second diode and the first is turned off.

The results shown in Fig. 11 are loss, isolation and coupling factors when the first diode is activated (90° phase shift), whereas in Fig. 12 the results are for 180° phase shift, where the second diode is activated. (H: HFSS & C: CST)

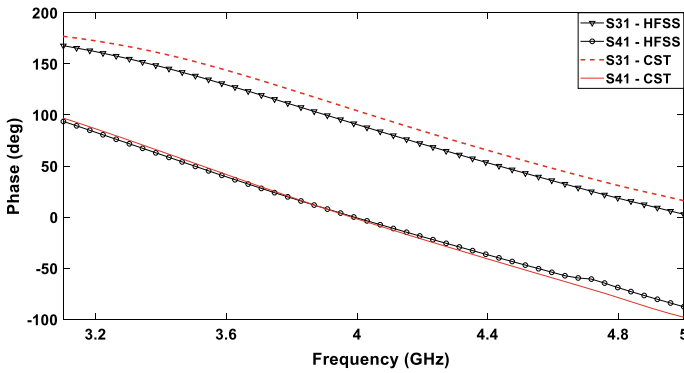


Fig. 7 Phase shift 90° (diode 1 ON, diode 2 OFF)

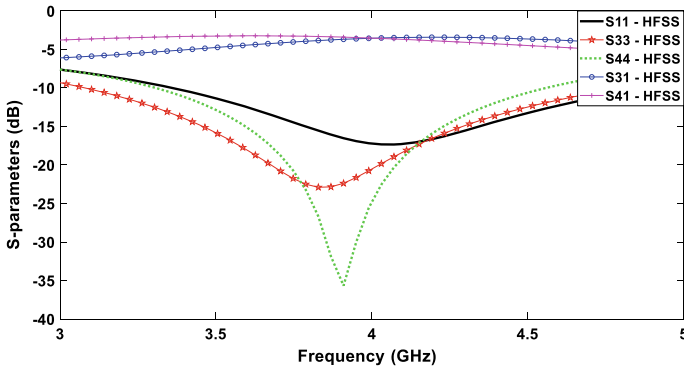


Fig. 8 HFSS S-parameters (diode 2 ON, diode 1 OFF)

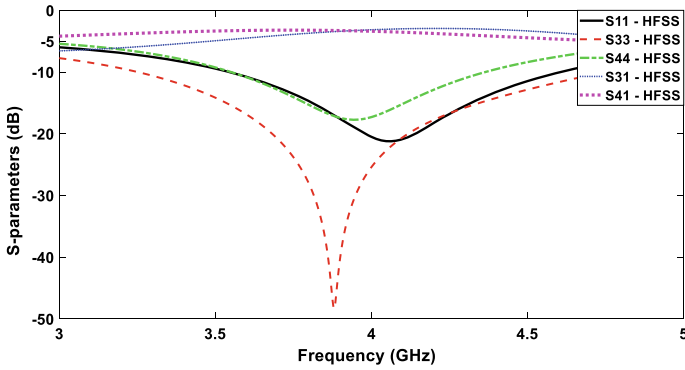


Fig. 9 CST S-parameters (diode 2 ON, diode 1 OFF)

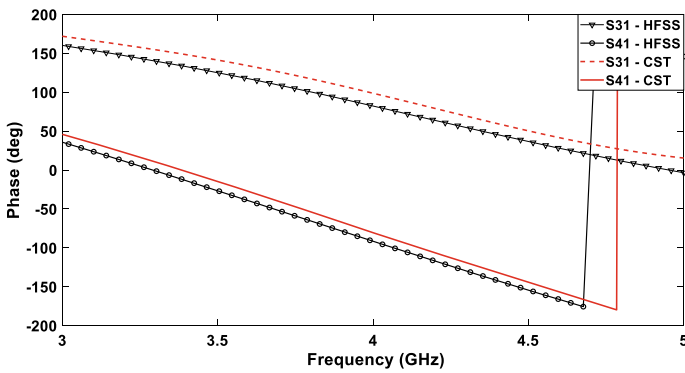


Fig. 10 Phase shift 180° (diode 2 ON, diode 1 OFF)

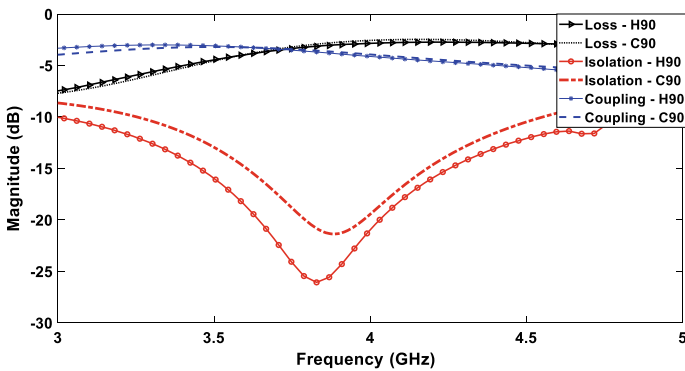


Fig. 11 Comparison loss, isolation and coupling factors (diode 1 ON, diode 2 OFF)

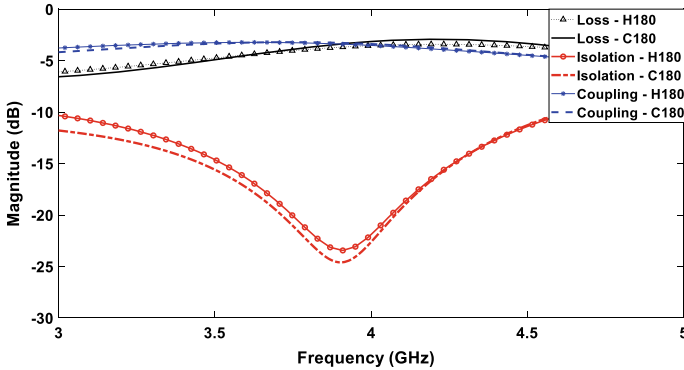


Fig. 12 Loss, isolation and coupling factors (diode 2 ON, diode 1 OFF)

For both cases, we can observe that the isolation is lower than -10 dB in the full frequency range of 3.5–4.5 GHz, also the loss and the coupling factors are around -3 dB.

4 Conclusion

The design and development of an UWB (3.5–4.5 GHz) hybrid coupler for 5G (3.8 GHz) applications with adjustable phase shift (90° – 180°) has been presented.

This work establishes a new technique based on diodes to change the phase shift between output ports, which is justified by the good simulation results displayed in terms of phase shift, loss, coupling and isolation factors. The developed coupler shows excellent phase shift of 90° and 180° depending on the case of the diodes (activated or deactivated), loss and coupling factors of about -3 dB, and isolation factor better than -20 dB over in full frequency band.

The design of this hybrid coupler is very robust and easier in fabrication. It can be utilized in many UWB 5G applications like radars and satellites employment.

References

1. 5G System Principles (2019) Nokia IEEE
2. 5G Spectrum (2017) Public policy position. Huawei Technologies Co., Ltd.
3. IEEE (2004) RF directional couplers and 3 dB hybrids overview. IEEE
4. Smolskiy SM, Belov LA, Kochemasov VN (2012) Handbook of RF, microwave, and millimeter-wave components, 1 edn. Artech House
5. Dunsmore JP (2012) Handbook of microwave component measurements: with advanced VNA techniques. Wiley, Hoboken
6. First Report and Order (2002) Revision of Part 15 of the Commission’s rules regarding ultra-wideband transmission systems FCC, FCC 02–48

7. Siriwongpairat WP, Liu KJR (2008) Ultra-wideband communication systems. Wiley, Hoboken
8. Welborn M, Siwiak K (2002) Ultra-wideband tutorial. IEEE P802.15 working group for wireless personal area networks (WPANs), 8 March 2002
9. Yoon HJ, Min BW (2017) Two section wideband 90° hybrid coupler using parallel-coupled three-line. *IEEE Microw Wirel Compon Lett* 27(6):548–550
10. Ding K, Kishk A (2017) Wideband hybrid coupler with electrically switchable phase-difference performance. *IEEE Microw Wirel Compon Lett* 27(11):992–994
11. Hagag MF, Zhang R, Peroulis D (2019) High-performance tunable narrowband SIW cavity-based quadrature hybrid coupler. *IEEE Microw Wirel Compon Lett* 29(1):41–43
12. Niu Z, Zhang B, Ji D, Yang Y, Liu Y, Feng Y, Fan Y, Chen Z, Chen X, Li D (2019) A Novel 3-dB waveguide hybrid coupler for terahertz operation. *IEEE Microw Wirel Compon Lett* 29(4):273–275
13. Fernandez MD, Ballesteros JA, Belenguer A (2015) Design of a hybrid directional coupler in empty substrate integrated waveguide (ESIW). *IEEE Microw Wirel Compon Lett* 25(12):796–798
14. Lomakin K, Klein L, Ringel L, Ringel J, Sippel M, Helmreich K, Gold G (2019) 3D printed e-band hybrid coupler. *IEEE Microw Wirel Compon Lett* 29(9):580–582
15. Ahn HR, Tentzeris MM (2019) Comments on: a universal approach for designing an unequal branch-line coupler with arbitrary phase differences and input/output impedances. *IEEE Trans Compon Packag Manuf Technol* 9(6):1208–1209
16. Li A, Luk KM (2019) Millimeter-wave dual linearly polarized endfire antenna fed by 180° hybrid coupler. *IEEE Antennas Wirel Propag Lett* 18(7):1390–1394
17. Mohammadi P, Rezavni M (2017) Design of compact branch-line hybrid coupler with adjustable outputs. In: 3rd national conference on avionics, Tehran
18. Cormier G (2012) *Diviseurs de puissance et coupleurs*. Université de Moncton, Hiver

WiMAX Throughput Maximization for MIMO-OFDM Systems via Cross-Layer Design



Hadj Zerrouki and Salima Azzaz-Rahmani

Abstract WiMAX system is based on the IEEE 802.16-2005 specification and provides wireless broadband to fixed and mobile users. It adopts MIMO technology to produce a high system capacity and spectral efficiency. By coupling a robust and efficient OFDM technique with MIMO antenna diversity systems, we offer a very compelling high-speed data downlink solution for future wireless communications systems. IEEE802.16e WiMAX system proposes an adaptive digital modulation and coding schemes according to the wireless link quality. In this work, we present a Cross-Layer approach based on the adaptive Modulation and Coding Scheme (MCS) mechanism which incorporates Network layer adaptive code with the PHY layer feedback information. Results show that this design achieves better performance of the WiMAX achievable throughput and transmission efficiency than adaptive modulation and coding used only with ARQ retransmissions through STBC and SM schemes.

Keywords WiMAX · MIMO · Cross-layer design · OFDM · SM · STBC · Adaptive MCS · PER · FEC

1 Introduction

Worldwide interoperability for Microwave Access (WiMAX) standard is based on the IEEE 802.16d [1] standard developed in June 2004. Mobile WiMAX, based originally on 802.16e-2005 [2], is the enhancement that was made to the standard on mobility support. The potential of Multiple-Input-Multiple-Output (MIMO) technology systems combined with Orthogonal Frequency Division Multiplexing (OFDM) provides a promising solution to improve the robustness of wireless data transmission. MIMO-OFDM spectral efficiency has configured these technologies as

H. Zerrouki (✉)

Department of Telecoms, Faculty of Technology, University of Tlemcen, Tlemcen, Algeria
e-mail: zerrouki.hadj@gmail.com

S. Azzaz-Rahmani

Department of Telecoms, Faculty of Electrical Engineering, University of Sidi Bel Abbès, Sidi Bel Abbès, Algeria

a perfect candidate for numerous wireless communications systems in development [3, 4].

Space Time Block Code (STBC) [5] is a technique used to get higher resistance to interference by transmitting multiple copies of a data stream across a number of antennas, and the same modulation and coding scheme can be used at a poor SNR situation. However, Spatial Multiplexing (SM) is used to enable the transmission of multiple streams of data in different antennas simultaneously to achieve higher throughput [6]. In order to make a decision which modulation and coding scheme to be selected in the communication system during transmission, many link adaptation algorithms are designed to improve the performance of wireless communications systems. In a typical modulation rate adaptation, a dynamic variation of the modulation and coding schemes (MCSs) under various link conditions is possible [7].

In the WiMAX system, different MCSs and messages formats are specified for the standard to deliver wireless broadband service. On the other hand, the procedure on how and which MCS must be used under different link conditions are not specified. For enhancing the performance of the WiMAX systems, many research and development activities are working to evaluate different link adaptation algorithms. In this paper, we propose a cross-layer based adaptive modulation and coding scheme (MCS) algorithm, which incorporates Network (IP) layer adaptive code with the PHY layer wireless information to maximize considerably the downlink throughput.

In cross-layer approach [8–13], most of these approaches consider that a high layer adaptive Forward Error Correction (FEC) mechanism acquires the low layer feedback information that aims to enhance greatly the channel reliability, which improves the network throughput. This powerful approach can be applied both to Uplink (UL) and Downlink (DL) traffic flows. For the purposes of our analysis, we focused on the DL flows.

In [14] the authors propose an approach based on improvement adaptive Modulation and Coding scheme for Cross layer approach, with small modifications in the existing adaptive MCS. Authors in [15] describe the recent advancements for enhanced spectral efficiency (SE) using adaptive modulation and coding (AMC) MIMO-OFDM in WiMAX (IEEE 802.16d) System. Cross-layer solution of AMC for multicast system based on the combination of PHY layer link implementation and Network coding can reduce largely the Frame Loss Ratio (FLR) [16].

2 Proposed Cross-Layer Architecture

The disadvantage to guarantee the transmission reliability of WiMAX system by applying an Automatic Repeat Request (ARQ) mechanism at the MAC layer, impacts negatively on the end-to-end latencies and may reduce the network throughput. To provide maximum reliability of data transmission within an acceptable latency, we

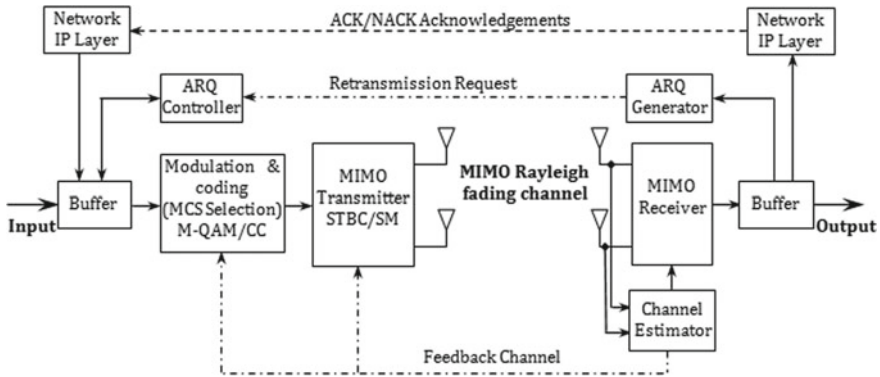


Fig. 1 Proposed cross-layer architecture for MIMO-WiMAX system

propose to avoid retransmission by ARQ mechanism [1, 2] and get channel state feedback information from positive ACKnowledgement (ACK) or Negative ACKnowledgement (NACK) messages. Our proposed architecture based on the Cross-Layer approach for the MIMO (STBC/SM)-WiMAX system is shown in Fig. 1.

3 Problem Formulation

The system throughput performance enhancement is attained by applying a Network layer adaptive FEC mechanism that allows correcting errors according to the monitoring of Packet Error Rate (PER) and the instant SNR at the Base Station (BS) and Mobile Station (MS) sides. Our proposal is based on a new decision mechanism that implements a dynamic mapping function which allows the base station to choose the MCS that offers the best throughput, by taking into consideration the current SNR and the instantaneous PER. The optimal MCS corresponding to the best throughput is then dynamically selected. Our proposal makes it possible to delay the recourses to a lower MCS when signal degrades and offers an enhanced throughput.

In order to identify an efficient FEC adaptation and dynamically adjust to channel losses, we dynamically update a mapping algorithm distinct for the current communication situation of the mobile station. The PER_{SNR}^i when a given MCS_i is chosen for a current SNR value defined as:

$$PER_{SNR}^i = f(MCS, SNR) \tag{1}$$

We presume that the mobile stations supervise the PER and are informed of the current SNR (SNR_{cur}) which are either sent periodically by the base station or obtain from the SNR supervised by mobile station. For the Downlink flows, SNR_{cur} can be acquired from the Channel Quality Indicator (CQI) field. To cancel oscillations, a periodic smoothing of the SNR variations with an exponential moving average

(EMA) as:

$$SNR = ((1 - k) \times SNR) + (k \times SNR_{cur}) \text{ where } k \in [0; 1] \quad (2)$$

The current PER_{cur} can be periodically achieved by examining the ACK/NACK feedback information. Similarly to SNR procedure, PER_{SNR}^i corresponding to the estimated SNR and the current MCS_i is also smoothed and periodically estimated as:

$$PER_{SNR}^i = (a \times PER_{cur}) + ((1 - a) \times PER_{SNR}^i) \text{ where } a \in [0; 1] \quad (3)$$

By this way, the base station can create a dynamic database that contains the PER_{SNR}^i corresponding to a given MCS_i for a given SNR interval. This database allows the base station to estimate the system throughput if it uses a higher or lower MCS.

4 Decision Algorithm of Adaptive MCS

Our proposal goal is to decide the optimal combination of the Network layer FEC and the default AMC. This combination results from the searching to use the higher MCS while maximizing the MIMO-WiMAX system throughput and spectral efficiency (SE). The downlink current system throughput successfully received by the mobile stations is given by:

$$TH_{cur} = R_{cur} \times (1 - PER_{cur}) \quad (4)$$

where R_{cur} denote the current downlink transmission rate. We can also denote R_{low} the downlink transmission rate if the base station uses the next lower MCS and R_{high} if the base station uses the next higher MCS. In order to successfully make an efficient MCS decision, our algorithm compares the resulting current throughput TH_{cur} to the obtained throughput if the mobile station uses the next lower or higher MCS. From the dynamic WiMAX system database, we can obtain the corresponding PER_{SNR}^i ($i = low$ or $i = high$) for the current SNR_{cur} , then the downlink throughput becomes TH_i when the mobile station take advantage of the neighbors adaptive MCS:

$$TH_i = R_i \times (1 - PER_{SNR}^i) \text{ with } i = high \text{ or } i = low \quad (5)$$

WiMAX base station should evaluate periodically the value of TH_{cur} to TH_{low} and TH_{high} . The optimal MCS which can achieve the maximum data throughput is chosen and informed as possible to the mobile station by sending a downlink messages comprise the burst which indicates the MCS used in the communication channel.

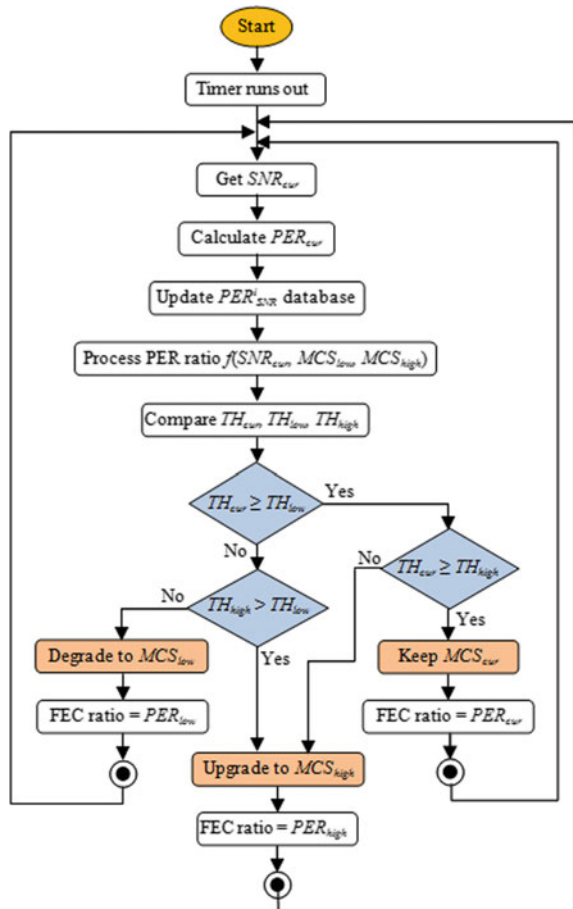
WiMAX system allows for seven different combinations of modulation order and coding rates which are briefly summarized in Table 1. The decision algorithm of

Table 1 Modulation schemes and coding rates

MCS mode	Modulation order	Overall coding rate
MCS1	BPSK	1/2
MCS2	QPSK	1/2
MCS3	QPSK	3/4
MCS4	16QAM	1/2
MCS5	16QAM	3/4
MCS6	64QAM	2/3
MCS7	64QAM	3/4

adaptive MCS of our proposal is described in Fig. 2. Our decision algorithm permits selecting an optimal MCS for maximizing data throughput for the mobile station.

Fig. 2 Proposed cross-layer decision algorithm of adaptive MCS



The proposal solution can competently increase transmission efficiency in the total coverage of the considered WiMAX base station and improving the robustness of data transmission in the context of MIMO-OFDM technology that provides a promising solution by exploiting spatial diversity.

Our proposed mechanism aims to retard the MCS degradation decision while guaranteeing the requested quality of service (QoS) and the reliability of transmission. Indeed, our proposal not only guarantees the best data throughput at the considered mobile station, but also keeps the used time slots for other connected mobile stations in the same WiMAX base station cell. As a result, this solution improves the network overall data throughput.

Our proposed decision algorithm allows mobile stations to benefit from a higher MCS at the same time as guarantee their transmission reliability. Based on the simulation results that our Cross-Layer-based approach offers, we will then show a greater useful data throughput, compared to the classical adaptive MCS mechanism, which is based on the discontinued and abrupt change of MCS.

5 Simulation Results

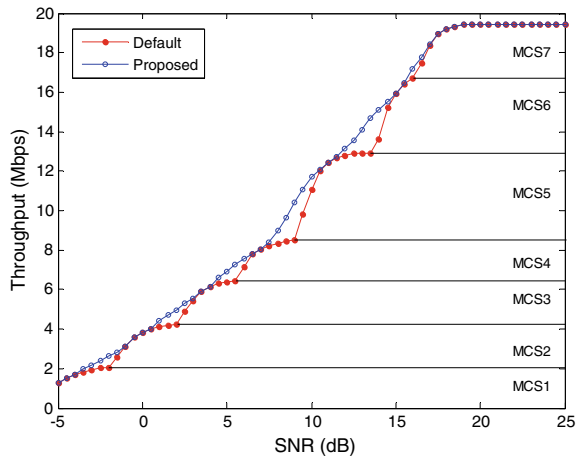
This section presents the simulation results obtained by applying our proposal then compared to the classical adaptive MCS. The simulations are made for a MIMO-OFDM system in both 2×2 STBC and 2×2 SM configurations. We assume that all available downlink subframes and base station data subcarriers are assigned to a single mobile station. The parameter values for different simulations are given in Table 2. We assume also that the WiMAX mobile station is in movement and is approaching the base station. As a consequence of this mobility scenario, the supervised SNR at the receiver side (MS) varies from -5 to 35 dB (covering all MCSs).

Figure 3 shows Throughput versus SNR curves of 2×2 STBC-OFDM system for default and proposed adaptive MCS mechanisms. The default mechanism is based only on a static correspondence table according to the SNR parameter, whereas our proposed mechanism is based on the cross-layer concept, which takes into account

Table 2 Simulation parameters

Parameter	Value	Parameter	Value
Carrier frequency (GHz)	3.5	Cyclic prefix or guard time (Tg/Tu)	1/4
Channel Bandwidth (MHz)	5	Over-sampling rate (Fs/BP)	28/25
FFT Size (NFFT)	512	Subcarriers Spacing (KHz)	10.94
Number of active subcarriers (Nu)	360	Useful symbol time (μ s)	91.4
Number of pilot subcarriers	60	OFDM symbol duration (μ s)	102.86
Number of guard subcarriers (zero)	92	Number of OFDM symbols (in 5 ms)	48

Fig. 3 Throughput of 2×2 STBC system versus SNR for both adaptive MCS mechanisms

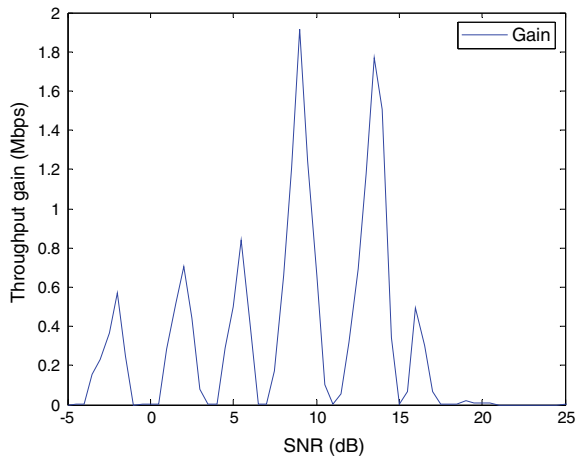


not only the SNR, but also the instant PER corresponding to the dynamic variations of the channel state.

Results show clearly that our approach makes it possible to avoid the sudden discrete reduction of throughput, caused by a sudden adaptive MCS change, and select the MCS that offers the best throughput. According to our proposal, the optimal MCS is then dynamically selected, with a “continuous” behavior that offers a higher throughput. At SNR = 9 dB, WiMAX system uses default MCS: 16QAM-1/2 ($1/2 \times \log_2(16) = 2$ bits/symbol). Our proposed mechanism allows the mobile station to exploit a higher MCS: 16QAM-3/4 ($3/4 \times \log_2(16) = 3$ bits/symbol) with a FEC rate of 25%.

Throughput gain of our proposal compared to the default adaptive MCS method is shown in Fig. 4. In fact, for SNR of -2, 2, 5.5, 9, 13.5 and 16 dB, our proposed

Fig. 4 Throughput gain of 2×2 STBC system versus SNR



mechanism offers useful throughput gain peaks respectively of 0.57, 0.7, 0.84, 1.92, 1.77 and 0.49 Mbps compared to the default AMC mechanism.

In Fig. 5, we show the performance of the 2×2 SM adaptive MCS techniques. The simulation results show that our proposed mechanism always to offer a higher throughput compared to the default AMC method. In fact, for the transition from a MCS to another of higher order, our proposed mechanism offers a throughput gain with a continuous behavior compared to the default behavior in staircase (resulting from the use of the consultation table based only on the SNR).

We can see in Fig. 6, a quite consistent gain of our approach, when the system changes the MCS according to the SNR variation. It can be seen that the implemented cross-layer algorithm performance is better compared to the traditional AMC technique, due to an efficient adaptation policy that dynamically adjusts and updates

Fig. 5 Throughput of 2×2 SM system versus SNR for both adaptive MCS mechanisms

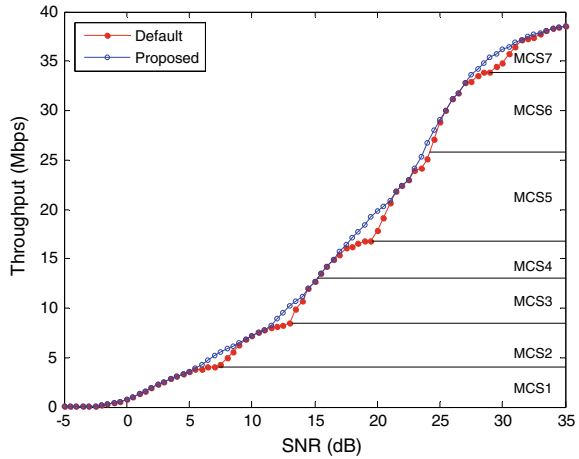


Fig. 6 Throughput gain of 2×2 SM system versus SNR

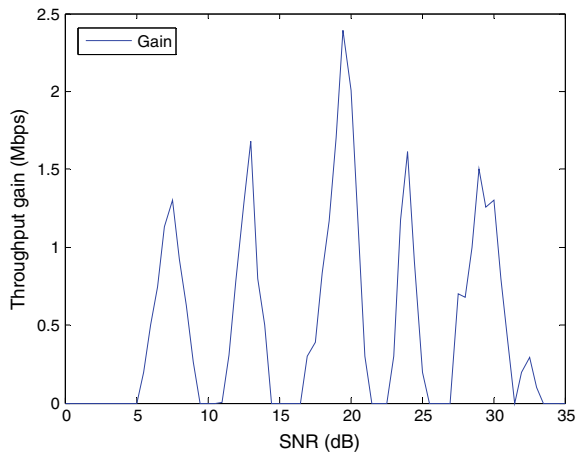
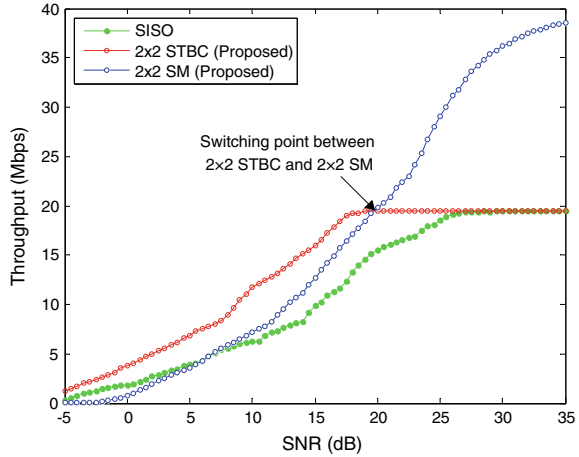


Fig. 7 WiMAX systems throughput (switching point between 2×2 STBC and 2×2 SM)



an identification function defined for the current condition of MIMO channel. As a result, for SNR values of 7.5, 13, 19.5, 24 and 29 dB, the maximum throughput gains obtained are respectively 1.3, 1.6, 2.39, 1.61 and 1.5 Mbps.

The maximum throughput gain value is obtained for SNR of 19.5 dB, where WiMAX system uses a default MCS4: 16-QAM-1/2, which offers a throughput of 16.82 Mbps. Our proposal allows the mobile station to use MCS5: 16-QAM-3/4 that offers a throughput of 19.21 Mbps, with a gain of 2.39 Mbps.

Figure 7 shows throughput curves of 2×2 STBC and 2×2 SM using proposed Cross-Layer based adaptive MCS technique. Clearly, the two MIMO schemes outperform SISO (Single-input single-output) system. However, for a low SNR channel (<6 dB), SISO performs better than 2×2 SM. In this case, the performance of STBC would overlap SISO. STBC produces the best performance for the low and medium SNR values, because of its robustness in bad channel conditions. In opposition, at high SNR values; the increase in throughput makes the SM system the best choice [5]. WiMAX MIMO system supports an Adaptive MIMO Switch (AMS) to select the optimal MIMO (SM or STBC) system. Figure 7 clearly shows that the system switches from 2×2 STBC to 2×2 SM after 19.9 dB. This cross-over point value increases for the higher order spatial correlation.

Simulation results show that our proposed algorithm outperforms the default method and offers a higher system throughput; which is due to the implementation of a mechanism based on the cross-layer concept in Network layer. As a result, our proposal does not cause modification of WiMAX standard, but minimally requires a simple crossing point between MAC and IP layers for the dynamic supervision of PER database according to a suitable adaptive MCS and a given SNR interval.

6 Conclusion

In this paper, we have proposed and explored a new mechanism for adaptive MCS based on the cross-layer concept, which relies on an adaptive code in a moderately high layer (Network layer or IP layer) and PHY layer information, such as SNR and PER to significantly maximize the data throughput and spectral efficiency of WiMAX wireless system. The proposed dynamic mechanism is optimized to the different MIMO channel conditions. Such a procedure also results in a good improvement of the system throughput, greater than that seen in a default mechanism driven by a sudden change in adaptive MCS technique. Indeed, instead of reducing the modulation and coding transmission rate immediately when the signal is degraded, we recommend to the mobile station to maintain its high transmission rate and strengthen its transmission reliability by redundancy packets to assign a better FEC in the Network layer. The theoretical suggestion and numerical simulation results presented in this paper show a considerable improvement in data throughput and transmission efficiency accessible to WiMAX mobile station.

References

1. IEEE 802.16-2004 (2004) IEEE standard for local and metropolitan area networks Part 16: air interface for fixed broadband wireless access systems. Technical Report, IEEE
2. IEEE 802.16e-2005 (2006) IEEE standard for local and metropolitan area networks, part 16. Air interface for fixed and mobile broadband wireless access systems. IEEE Press
3. Kowal M, Zieliński RJ, Chaczko Z (2014) The study of the OFDM and MIMO-OFDM networks compatibility—measurements and simulations. In: *Advanced methods and applications in computational intelligence*, vol 6. Springer, Heidelberg
4. Doğan H (2016) On detection in MIMO-OFDM systems over highly mobile wireless channels. *Wireless Pers Commun* 86(2):683–704
5. Kumar V, Ram Singla C (2014) Space-time block code analysis for MIMO-OFDM system. *Space* 100(2):1–7
6. Cuan-Cortes JV et al (2014) MIMO channel capacity using antenna selection and water pouring. *Eurasip J Wirel Commun Netw* 01–11
7. Zerrouki H, Feham M (2010) High throughput of WiMAX MIMO-OFDM including adaptive modulation and coding. *IJCSIS* 7(1):86–90
8. Lin X, Shroff NB, Srikant R (2006) A tutorial on cross-layer optimization in wireless networks. *IEEE J Selected Areas Commun* 24(8):1452–1463
9. Kim J, Kim KA, Jeong JS, Kang CG (2014) Cross-layer design of adaptive modulation and coding for multicast system with random network coding. *EURASIP J Wirel Commun Netw*
10. El-Mayet R, El-Badawy H, Elramly S (2013) Novel optimized cross-layer design with maximum weighted capacity based resource allocation for AMC/HARQ wireless networks. *Wirel Eng Technol* 4(2):77–86
11. Let GS, Bala GJ (2014) A review of cross-layer design in dynamic spectrum access for cognitive radio networks. *J CIT* 22:21–29
12. Dai C-Q, Rao Y, Jiang L, Chen Q-B, Huang Q (2012) Cross-layer design of combining HARQ with adaptive modulation and coding for Nakagami-m fading channels. *J Commun Acad Publ* 7(6):458–463

13. Karyotis V, Stai E, Papavassiliou S (2016) A component-based cross-layer framework for software defined wireless networks. In: 8th IFIP international conference on NTMS, November 2016
14. Shanthi KG, Manikandan A (2019) An improved adaptive modulation and coding for cross layer design in wireless networks. *Wirel Pers Commun* 108(2):1009–1020
15. Barreto FTR, Patni SY, Unnikrishnan S (2010) Enhanced spectral efficiency using AMC MIMO-OFDM in WiMAX (802.16d) system. ICWET' 2010—TCET, Mumbai, India
16. Kim J, Kim KA, Jeong JS et al (2014) Cross-layer design of adaptive modulation and coding for multicast system with random network coding. *J Wirel Commun Netw* 4

Equivalent Circuit Modelling of a Cantor Multifractal Slots Antenna



Fatima Ez-Zaki , Hassan Belhrach, and Abdelilah Ghammaz

Abstract The paper aims to study the effect of Cantor multifractal introducing in the radiating element of the reference antenna, then to propose an equivalent circuit model of the investigated antenna by means of two approaches. The First approach is based on the Vector fitting approximation of simulated data. In the second approach, the antenna input impedance is described by means of the first Foster canonical form. To ensure the validity of the suggested equivalent circuit model the results of the used methods are compared.

Keywords Multiband fractal antenna · Equivalent circuit model · Vector fitting · Foster approximation

1 Introduction

Next generation systems need to be small, compact, and operate over multiple standards, so then they requires for more compact, small size and multiband antennas. As a matter of fact various wideband and multiband antennas have been investigated.

In antenna design, there are some theoretical parts must be followed, indeed antennas are represented by means of equivalent circuit models because of their theoretical interest and practical importance. Then so, to use a component in the best conditions, reliable and efficient models are required. Especially concerning the EMC aspects, it is necessary to design models taking into account all the parasitic

F. Ez-Zaki (✉) · H. Belhrach · A. Ghammaz
Electrical Systems and Telecommunication Laboratory, Faculty of Science and Technology,
UCAM, Marrakech, Morocco
e-mail: ftimaezzaki@gmail.com

H. Belhrach
e-mail: h.belhrach@gmail.com

A. Ghammaz
e-mail: aghammaz@yahoo.fr

H. Belhrach
Royal School of Aeronautics, Marrakesh 40150, Morocco

elements such as parasitic capacitance, leakage inductance and magnetic coupling [1, 2]. To do this, several approaches are treated in the literature; the most recognized being a method based on impedance measurements, admittance, or S parameters associated with a fitting algorithm by iterative approximation of rational functions. It consists of curve fitting of the measurement data and post-processing of the fitting results to generate the equivalent circuit [1]. Another widely used procedure based on Foster's canonical forms technique where resistive elements are introduced to model metal, dielectric, and radiation losses [3]. First Foster form is used to model the "electric antenna" and the second Foster form is used to describe the "magnetic antenna". There are other methods such as modelling each part of the separate antenna according to the models studied in antenna theory for patches, and considering the slots as a dipole. The problem recognized in this method is that it is usable for simple structures, but it becomes more and more complex for complex structures such as fractal antennas [4].

Significant researches on the antenna equivalent circuit modelling have been aroused in many works in the literature. In [5] a dual band Planer Inverted-F Antenna (PIFA) measured frequency response is approximated to a rational function using a vector fitting technique and the given poles are used to extract the electrical circuit parameters. Gerald R. De Jean and al [6] proposed a methodology of resistance invariability of 2 non-physical circuits derived based the rational functions approximation by vector fitting which is used to model antenna designs with equivalent circuits of lower order. SCHOLZ and al [7] investigated a reduced network topology of inductive coupled RFID antenna systems equivalent circuit models, the lumped elements parameters are extracted through the approach of partial element equivalent circuit (PEEC). In [8] RIPIN and al derived an equivalent circuit model of the UHF miniature double E-shaped meander line printed monopole antenna by representing each section of the antenna by the depending inductance and capacitance circuit values on the structure dimensions. SAYIDMARIE and al [9] modelled a dual-band crescent-shape monopole antennas for WLAN applications by an RLC equivalent circuit. The used procedure in [10] overcomes the problems of physical manufacturing of the equivalent circuit and the starting values estimation of the based algorithm to compute a rectangular and E-shaped Microstrip antenna equivalent models. Das et al. [11, 12] have investigated T and π slots loaded multi frequency microstrip antennas to reduce the size of the antenna with increased frequency ratio and multi-frequency operation.

SPICE compatible equivalent circuit using a vector fitting technique is used in the first approach. Whereas, the second approach is based on canonical Foster forms using the simulated scattering parameters of the antenna. This paper is arranged as following. Section 2 discusses the effect of introducing a Cantor multi-fractal slots on the antenna patch. Section 3 describes two approaches to model the antenna by an equivalent circuit model, the results are analysis. Conclusions are listed in Sect. 4.

2 Antenna Configuration and Simulation Results

The antenna proposed in [11] was taken as a basic antenna in this work. The antenna was investigated using CST software to match the 50Ω feed line. More details on reference antenna design and results are given in [11]. In order to improve the antenna behavior a Cantor multifractal slots are introduced in the antenna radiating element as depicted in Fig. 1. To explore the effect of the Cantor multifractal slots on the antenna features, a slight parametric study is conducted. Figure 2 illustrates the investigated antenna S11. It can be seen that the antenna resonates at 5 frequencies with a significant bandwidth. Whereas, Figs. 3 and 4 illustrate the antenna results in term of VSWR and gain in (dBi). It can be clearly seen that the antenna resonates at 5 frequencies with a significant bandwidth, $VSWR < 2$, and a good gain which indicates a good impedance matching behavior

Table 1 gives a brief summarize of antenna results. It can be note that the introduced multifractal slots in the antenna patch helped well to achieve a wide bandwidth which is very important to increase the data rate transmitting.

The suggested antenna cover C-band, X-band, and Ku-band. It can be used for various wireless applications such LTE, WiMAX, WLAN/WIFI/5G, radar, satellite applications.

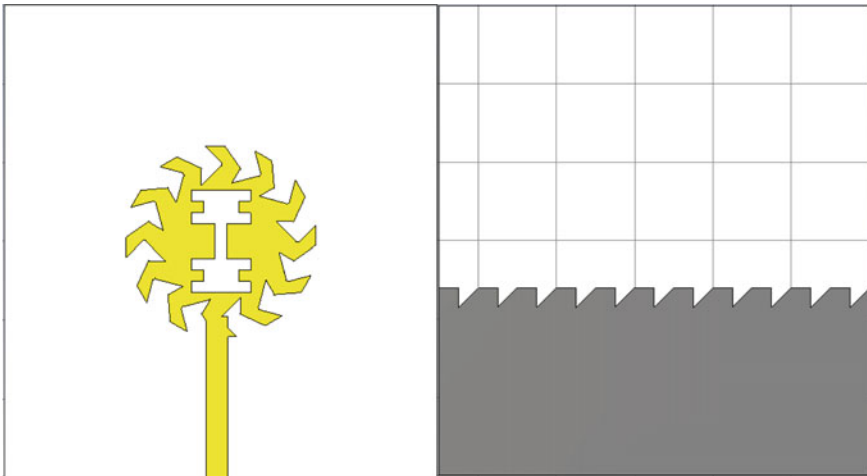


Fig. 1 Proposed antenna configuration

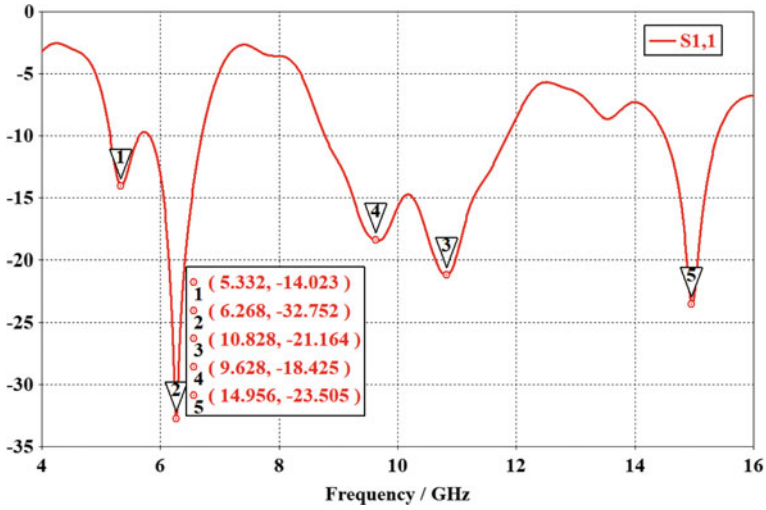


Fig. 2 Proposed antenna reflexion coefficient (S11)(dB)

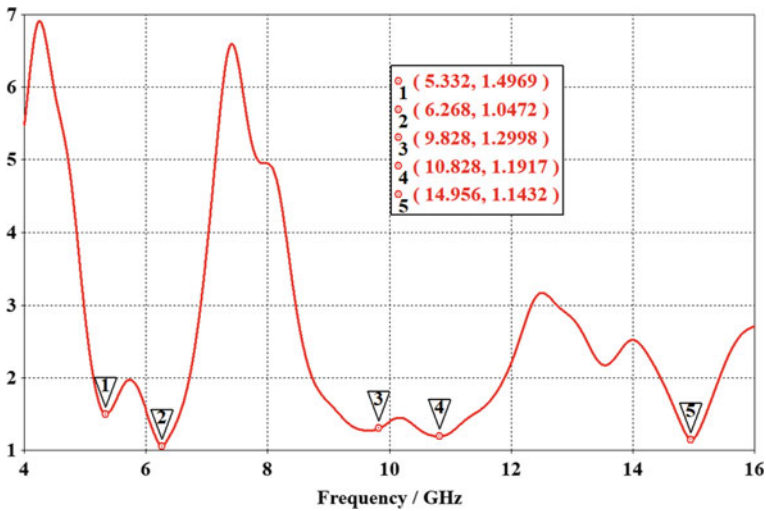


Fig. 3 Proposed antenna VSWR

3 Equivalent Circuit Results and Discussions

A theoretical study was performed by considering an equivalent circuit of the antenna obtained using two approaches. The equivalent circuits modelling derivation and the achieved results are discussed in the following subsections.

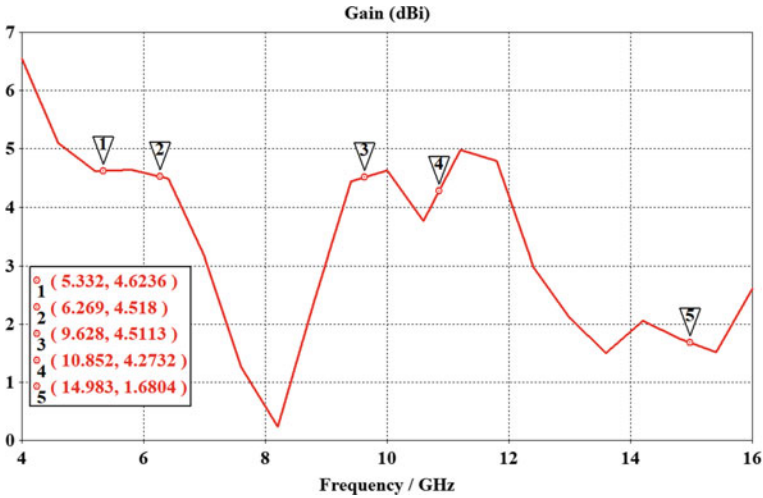


Fig. 4 Proposed antenna gain (dBi)

Table 1 Proposed antenna results

Resonant frequency (GHz)	S11 (dB)	VSWR	Bandwidth (MHz)	Gain (dBi)
5.332	-14.023	1.497	498.4	4.623
6.269	-32.689	1.047	888.5	4.518
9.628	-18.425	1.299	3063.1	4.511
10.852	-21.125	1.192		4.273
14.983	-23.397	1.143	884	1.68

3.1 Model Based on Rational Approximation Approach (Vector Fitting)

The approach aims to fit the simulated antenna input admittance using the Vector Fitting method. Recently the rational function approximation based on vector fitting technique is widely and efficiently used to achieve the equivalent circuit model of antennas.

The fitting of a transfer function can be expressed as Eq. (1).

$$Y(s) = d + j\omega e + \sum_{k=1}^N \frac{r_k}{(j\omega - p_k)} \tag{1}$$

where $\omega = 2\pi f$, f is the operating frequency. The terms r_k and p_k are the residues and the poles respectively, which can be real or complex conjugate pairs. The terms d

and e are real terms. The employing of this approach to obtain the antenna equivalent model is studied in [1, 2] and other references.

The antenna simulated admittance data is fitted using an approximation order of $N = 26$ which gives two real poles one with a negative residues and 13 complex pairs. The synthesised equivalent circuit is given in Fig. 5 with the computed lumped elements values. Figure 6 illustrates the equivalent circuit frequency results compared to the simulated antenna results. It is clearly observed that the obtained equivalent circuit gives a good results which are in very good matching with simulated ones.

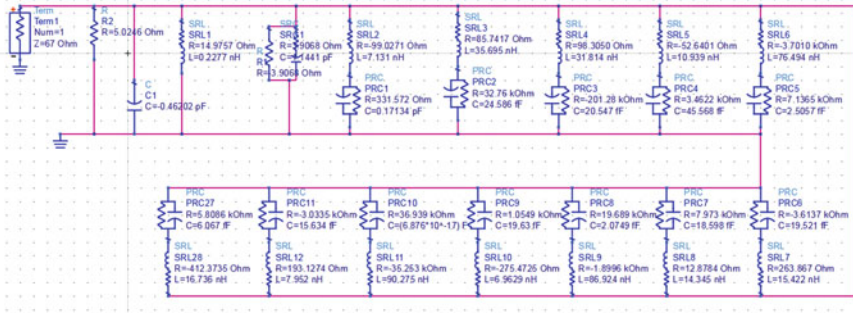


Fig. 5 ADS equivalent circuit model based on VF approximation

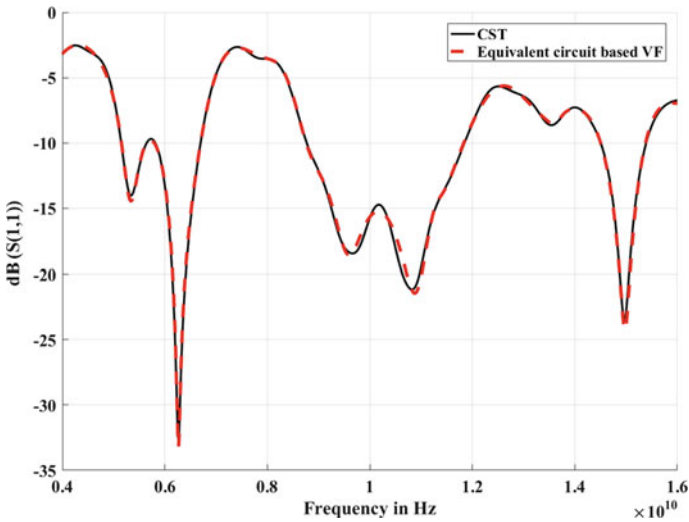


Fig. 6 S11 results of simulated antenna and equivalent circuit model based VF approximation

3.2 Model Based Reflection Coefficient Approach

The simulated antenna impedance curve shows 7 points with a local maxima in real part and an imaginary part around to zero as depicted in Fig. 7, each one can be represented by a parallel RLC circuit. So then the investigated antenna can be modelled by 7 parallel RLC cells those are connected in series. The started values of the lumped elements (Ri, Li, Ci, LO, and C0) are extracted from the impedance curve and tuned in ADS to achieve a very closer and similar response to the CST response by using the procedure described in [3]. This approach lead to suggest the equivalent circuit described in Fig. 8 as well as the tuned values of the lumped elements of each RLC circuit. Figure 9 depicts the suggested equivalent circuit frequency response compared to the CST frequency response. It can be note clearly that the both responses are in good agreement at the resonant frequencies with a slight sifting in others.

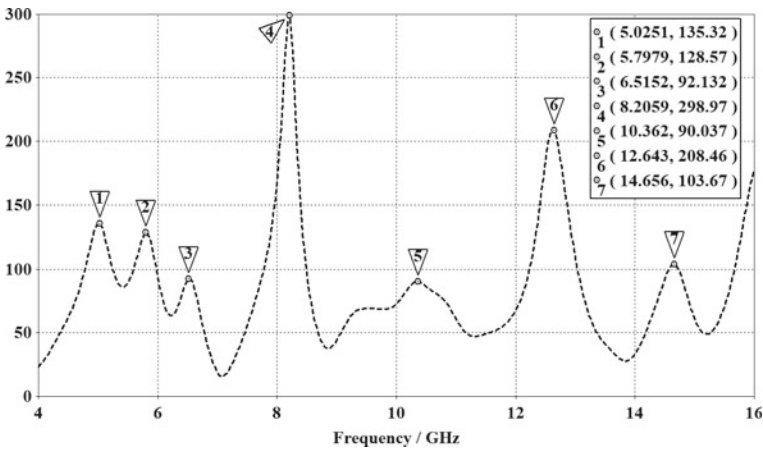


Fig. 7 Antenna simulated input impedance

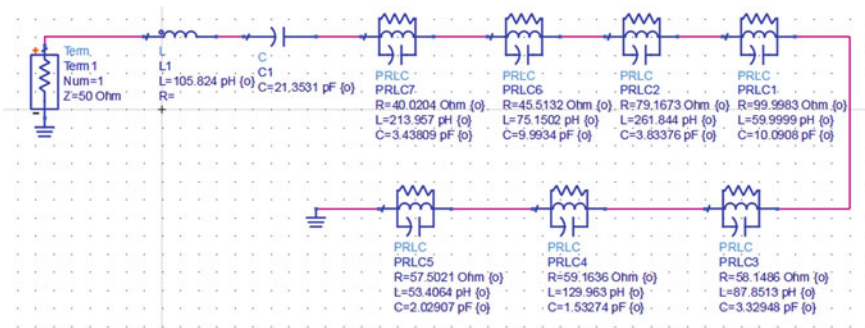


Fig. 8 ADS equivalent circuit model based on Foster approximation

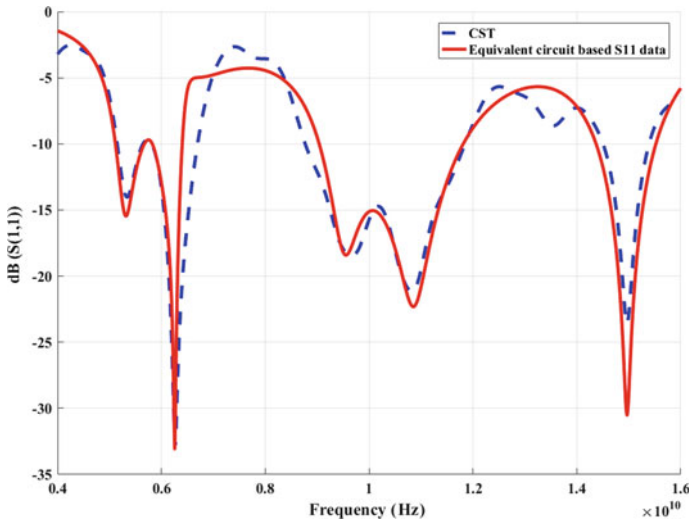


Fig. 9 Simulated antenna and equivalent circuit model based Foster approximation S11

4 Conclusion

The effect of inserted a Cantor multi fractal slots in the reference antenna radiating patch is shown, then the modelling of the investigated antenna has been demonstrated. Indeed electrical models are applied to represent the antenna input impedance using two approaches. The first approach is based on the vector fitting technique to compute a SPICE-compatible equivalent circuit of the antenna using ADS software. In the second approach, the antenna input impedance is described by means of six parallel RLC-circuits connected in series and derived either from the simulation reflection coefficient of the antenna. The suggested equivalent circuit models using the above approaches show a good agreement with CST simulation.

References

1. Antonini Giulio (2003) SPICE equivalent circuits of frequency-domain responses. *IEEE Trans Electromagn Compat* 45(3):502–512
2. Tan W (2012) Modeling and design of passive planar components for EMI filters. Thèse de doctorat
3. Caratelli D, Cicchetti R, Bit-Babik G et al (2007) Circuit model and near-field behavior of a novel patch antenna for WWLAN applications. *Microw Opt Technol Lett* 49(1):97–100
4. Yeung LK, Wu K-L (2011) Generalized partial element equivalent circuit (PEEC) modeling with radiation effect. *IEEE Trans Microw Theor Tech* 59(10):2377–2384
5. Yousaf J, Jung H, Kim K et al (2016) Design, analysis, and equivalent circuit modeling of dual band PIFA using a stub for performance enhancement. *J Electromagn Eng Sci* 16(3):169–181

6. Dejean GR, Tentzeris MM (2007) The application of lumped element equivalent circuits approach to the design of single-port microstrip antennas. *IEEE Trans Antennas Propag* 55(9):2468–2472
7. Scholz P, Ackermann W, Weiland T et al (2010) Antenna modeling for inductive RFID applications using the partial element equivalent circuit method. *IEEE Trans Magn* 46(8):2967–2970
8. Ripin N, Sulaiman AA, Rashid NEA (2018) An equivalent circuit model of miniature double e-shaped meander line printed monopole antenna. *J Telecommun Electron Comput Eng (JTEC)* 10(2–5):59–63
9. Sayidmarie KH, Yahya LS (2014) Modeling of dual-band crescent-shape monopole antenna for WLAN applications. *Int J Electromagn Appl* 4(2):31–39
10. Ansarizadeh M, Ghorbani A, Abd-Alhameed RA (2008) An approach to equivalent circuit modeling of rectangular microstrip antennas. *Progr Electromagn Res* 8:77–86
11. Das S et al (2015) Modified π -shaped slot loaded multifrequency microstrip antenna. *Progr Electromagn Res B* 64(1):103–117
12. Das S et al (2014) Design and analysis of a novel open ended T-shaped slot loaded compact multifrequency microstrip patch antenna. *Microw Opt Technol Lett* 56(2):316–322
13. Fatima E-Z, Ghammaz A, Belahrach H (2018) Multiband fractal antenna for wireless applications. In: 2018 6th international conference on wireless networks and mobile communications (WINCOM). IEEE. pp 1–6

A Novel Two-Branch Dual-Band Rectifier for 2.45 GHz 5.8 GHz RFID Systems



Sara El Mattar, Abdennaceur Baghdad, and Abdelhakim Ballouk

Abstract In this paper, we present a novel design of high-efficiency, dual-band and two-branch rectifier for wireless energy harvesting in the 2.45 and 5.8 GHz frequency bands. The rectifier is based on a two conversion circuit; a dual-band voltage doubler for the first branch and a single-diode rectifier for the higher frequency band in order to further enhance in 5.8 GHz the efficiency of the resulting circuit. The rectifier achieves a maximum conversion efficiency of 59.683% for the primary band at 1dBm of incident power, while it reaches in the second band (5.8 GHz) at 3 dBm an efficiency of 51.521%. These results allowed the resulting rectifier to be the most efficient at these frequencies and in particular for the low incident powers compared to other reported designs with the same radio frequency conditions.

Keywords RF energy harvesting · Rectifier · Dual band · ISM band

1 Introduction

Thanks to the current evolution of wireless systems and microelectronics, new contactless identification technologies have emerged: RFID (for Radio-Frequency IDentification). The development of these technologies is initiated by scientific discoveries for great flexibility, making the exchange of information much faster and more efficient. Unlike conventional communication systems, most of these new technologies are powered remotely using Wireless power transmission (WPT) technique, to guarantee the energy autonomy of these devices and their independence from the power outlet [1].

This technique, therefore, makes it possible to transmit microwave energy via the antenna of the transmitter, with a view to recovering it and converting it into a continuous signal at the receiver, and this technique is discovered in 1964 by Brown [2]. The receiver of this system, called rectenna, is composed of an antenna and a

S. El Mattar (✉) · A. Baghdad · A. Ballouk
Laboratory of Electronics, Energy, Automatics and Data Processing (EEA & TI), Department of Electrical Engineering, Hassan II University, FstMohammedia-Casablanca, Mohammedia, Morocco
e-mail: saraelmattar@gmail.com

rectification circuit. Therefore, numerous research has been directed towards rectenna in recent years. The work of this paper concerns the study of the rectification circuit.

With the increasing use of wireless communication systems that radiate in the ISM (Industry, Science, and Medical) bands a large number of mobile devices with Wi-Fi transceivers can act as radiofrequency(RF) sources to power the RFID tags [3]. Thus, certain rectifiers have been proposed and optimized in previous publications for these frequency bands.

The authors in [4] present a rectifier operating at 2.45 GHz band with a maximum conversion efficiency achieved of 76%, particularly for incident powers of 20 dBm (100 mW). A rectenna unit with a conversion efficiency of 82% and operating at 5.8 GHz was designed in [5] by exploiting 50 mW (≈ 16.98 dBm) as incident power. The authors in [6] present a dual-band rectifier with maximum efficiencies 66.8 and 51.5% for the primary band and second band respectively at 10 dBm input power. Similarly, in [7] a rectenna for the two bands (2.45/5.8 GHz) was presented operating with an incident power of above 16 dBm for having higher conversion efficiency than 80%.

Incident power levels used by the mentioned works; 20 dBm [4], 16 dBm [5, 7] and 10 dBm [6] does not seem reasonable as a power level collected from the air. Whereas the possible power levels of the ambient RF energy for these frequency bands are low due to the current standards, which organize maximum radiation level of the access points for these communications they are of the order of nW to μ W per cm^2 .

The other observed limitation of dual-band rectifiers is the degradation of their efficiency for the 5.8 GHz frequency and this is due to the losses of the diodes used at the higher frequency and even losses linked to the substrate.

In this paper, we propose a three-diode rectifier circuit with a two-branch impedance matching unit, the first branch will be a dual-band rectifier using voltage doubler topology, and the second branch linked to a serial mono-band rectifier to improve the rectifier efficiency resulting in the frequency 5.8 GHz.

2 Design and Analysis of the Rectifier Circuit

A conventional rectifier circuit includes an impedance matching network followed by an RF-DC conversion circuit with a non-linear characteristic. This circuit generally contains one or more Schottky diodes, a DC output filter, and a resistive load, which models the consumption of the powered system.

The general configuration of the rectifier is illustrated in Fig. 1.

Our proposed work uses two rectification circuits; the first is a voltage doubler circuit for the two operating frequencies (2.45 and 5.8 GHz) and the second is a classic simple one-diode rectification circuit for 5.8 GHz.

As illustrated in Fig. 2 both rectifiers form two separate branches, then each branch has its appropriate impedance matching circuit due to their non-linearity and taking

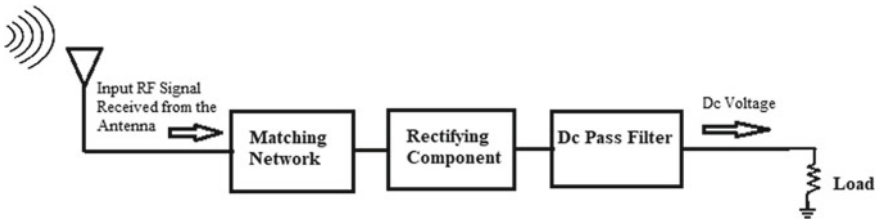


Fig. 1 A block diagram of a rectifier circuit

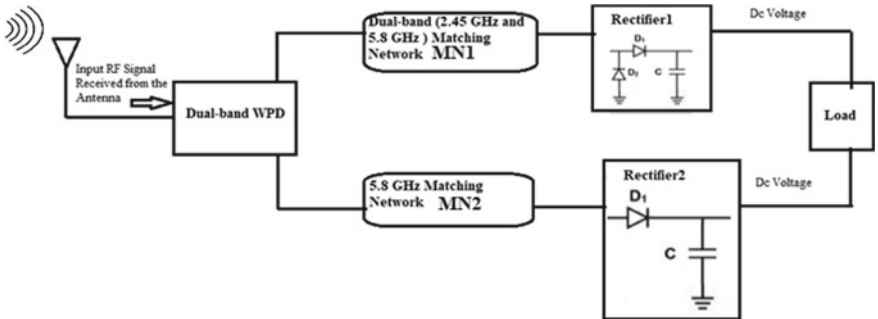


Fig. 2 Configuration of the two-branch rectifier circuit

into account the low power levels considered, the frequency, and the load resistance value used.

We used to divide the power on the two branches a double band Wilkinson Power divider (WPD) its role is to split the received power by the antenna into two equal signals.

After the presentation of all the units of our rectifier. We will then exploit the power of ADS (Advanced Design System) software to design the circuit by simulation. The initial design parameters of WPD and MN1 are calculated in Matlabemploying the equations mentioned in [8, 9] respectively. Subsequently, the result parameters were optimized using the ADS optimization tool for a more efficient final rectifier.

Concerning MN2; it is based on Stub matching which is also designed and optimized with ADS to provide a good adaptation to the second branch for the frequency 5.8 GHz. The Rogers RT/Duroid 5880 substrate with the low dissipation factor (0.0004), a relative permittivity of 2.2 and a thickness of 1.575 mm was selected for the designed circuit.

The diode in general is an important element for rectifying RF energy, the selection of the most appropriate and the effective one is a crucial step. The SMS7630 is the chosen diode for our rectifier because its characteristics make it the best one for low incident power [10]. For the simulation in ADS, we used the SPICE model of SMS7630.

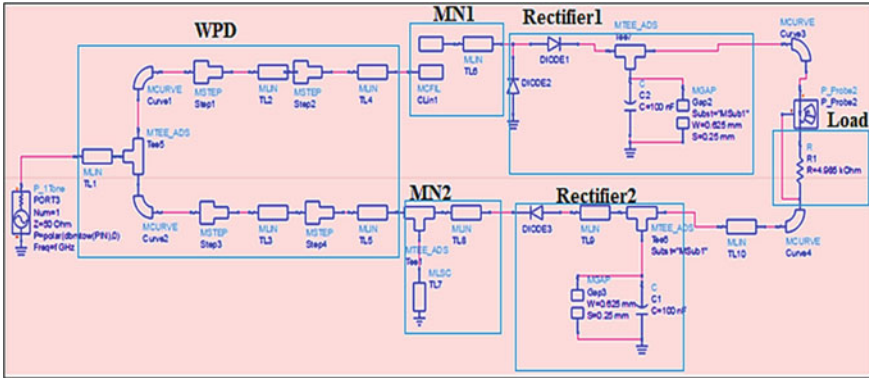


Fig. 3 ADS resulting dual-band rectifier circuit

Table 1 Optimized design dimensions

Parameter	Value (mm)
TL1, TL4 and TL5	W = 2.402415, L = 6.61535
TL2 and TL3	W = 3.3113695, L = 8.985906
TL6	W = 0.944584, L = 21.28736
TL7	W = 5.4082999, L = 16.747424
TL8	W = 5.4082999, L = 6.6192969
TL9	W = 2.7907048, L = 2.75
TL10	W = 1.3, L = 14.6375
Curve1 and Curve2	W = 3.2447504, Radius = 6.7548976
Curve3 and Curve4	W = 1.2012075, Radius = 4.898624224
CLin1	W = 1.118325, L = 15.079484

For conversion circuit topologies in this work, we have chosen to use a voltage doubler for the dual-band Rectifier1 due to the better energy management capacities given by this topology, in addition, it provides high power conversion efficiency (PCE) and it is the most used for double band circuits [11, 12]. While the Rectifier2 has the serial topology of the diode, with the objective of maximizing the DC output in terms of RF-DC conversion efficiency for the higher frequency (5.8 GHz).

The proposed rectifier schematic diagram in ADS is illustrated in Fig. 3 and its design parameters are presented in the following Table 1.

3 Results and Discussions

The proposed rectifier simulation is done using harmonic balance and S-parameters analysis of ADS software.

Figure 4a presents the return loss S11 variation. These results show that our proposed rectifier is well adapted with a return loss magnitude of -10.239 dB for 2.45 GHz and -12.813 dB at 5.8 GHz.

We used to judge the resulting rectifier performances from its conversion efficiency in terms of input power. The used formula for efficiency calculation is:

$$efficiency = 100 \cdot \frac{P_{DC}}{P_{RF}} \tag{1}$$

P_{DC} : the recovered continuous power and P_{RF} : the rectifier input power.

The illustrated results in Fig. 4b show that conversion efficiency reaches a maximum of 59.683% for 2.45 GHz at 1 dBm and achieved 51.521% at 3 dBm for 5.8 GHz. Based on the comparison in Table 2 the proposed rectifier has the high maximum efficiencies obtained at low input Rf power levels for both frequencies. Furthermore, it is shown that our approach by adding a rectifier branch for 5.8 GHz made it possible to improve the efficiency at this frequency and what allowed to maximizing it.

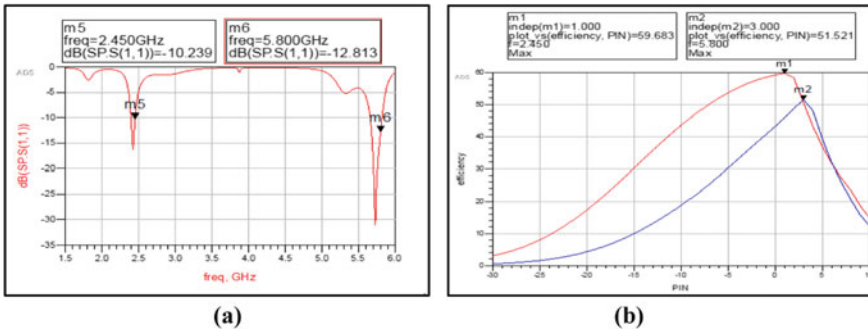


Fig. 4 Simulationresult: **a** S11 Parameter of the rectifier circuit, **b** efficiencies based on input power

Table 2 Comparison between previously designed dual-band rectifiers and our rectifier

References	Bands (GHz)	Maximum efficiency (%) at PIN
[6]	2.45	66.8 at 10 dBm
	5.8	51.5 at 10 dBm
[7]	2.45	84.4 at ≈ 16 dBm
	5.8	82.7 at ≈ 16 dBm
[13]	2.45	57.1 at 0 dBm
	5.85	39.2 at 1 dBm
This work	2.45	59.683 at 1 dBm
	5.8	51.521 at 3 dBm

4 Conclusion

This article presents a new conception of a dual-frequency rectifier for low input RF power. We have adopted an approach of adding a second monoband rectifier to the double band rectifier in order to improve the efficiency at the upper frequency of 5.8 GHz. The resulting two-branch rectifier reached a maximum efficiency of 59.683% for 2.45 GHz at 1 dBm and achieved a 51.521% at 3 dBm for 5.8 GHz. Compared to other double-band rectifiers operating at the same frequencies, this rectifier has maximum RF/Dc conversion efficiencies especially for a low incident power range, which makes it a very good rectifier for realistic applications.

References

1. Harb A (2011) Energy harvesting: state-of-the-art. *Renew Energy* 36:2641–2654
2. Brown WC (1984) The history of power transmission by radio waves. *IEEE Trans Microw Theory Tech* 32:1230–1242
3. Piñuela M, Mitcheson PD, Lucyszyn S (2013) Ambient RF energy harvesting in urban and semi-urban environments. *IEEE Trans Microw Theory Tech* 61:2715–2726
4. Zulkifli FY, Leza YM, Basari, Rahardjo ET (2015) Design of rectifier for rectenna application. In: 2015 Asia-Pacific microwave conference (APMC). pp 1–3
5. Mc Spadden JO, Fan L, Chang K (1998) Design and experiments of a high-conversion-efficiency 5.8-GHz rectenna. *IEEE Trans Microw Theor Tech* 46:2053–2060. <https://doi.org/10.1109/22.739282>
6. Wang D, Negra R (2013) Design of a dual-band rectifier for wireless power transmission. In: 2013 IEEE wireless power transfer (WPT). pp 127–130
7. Suh Y-H, Chang K (2002) A high-efficiency dual-frequency rectenna for 2.45- and 5.8-GHz wireless power transmission. *IEEE Trans Microw Theor Tech* 50:1784–1789. <https://doi.org/10.1109/TMTT.2002.800430>
8. Wu Y, Liu Y, Li S, Yu C (2012) New coupled-line dual-band dc-block transformer for arbitrary complex frequency-dependent load impedance. *Microw Opt Technol Lett* 54:139–142. <https://doi.org/10.1002/mop.26480>
9. Dib N, Khodier M (2008) Design and optimization of multi-band Wilkinson power divider. *Int J RF Microw Comput Aided Eng* 18:14–20 (Co-sponsored by the Center for Advanced Manufacturing and Packaging of Microwave, Optical, and Digital Electronics (CAMPmode) at the University of Colorado at Boulder)
10. Liu D-S, Li F-B, Zou X-C, Liu Y, Hui X-M, Tao X-F (2011) New analysis and design of a RF rectifier for RFID and implantable devices. *Sensors* 11:6494–6508
11. Mousa Ali E, Yahaya NZ, Nallagownden P, Zakariya MA (2017) A novel rectifying circuit for microwave power harvesting system. *Int J RF and Microw Comput-Aided Eng* 27:e21083
12. Kim P, Chaudhary G, Jeong Y (2013) A dual-band RF energy harvesting using frequency limited dual-band impedance matching. *Progr Electromagn Res* 141:443–461
13. ur Rehman M, Ahmad W, Khan WT (2017) Highly efficient dual band 2.45/5.85 GHz rectifier for RF energy harvesting applications in ISM band. In: 2017 IEEE Asia Pacific microwave conference (APMC). pp 150–153

A Survey of NOMA for 5G: Implementation Schemes and Energy Efficiency



Jamal Mestoui and Mohammed El Ghzaoui

Abstract The 5th generation (5G) Network technology must meet various stringent necessities such as high spectral efficiency, low energy consumption and immense connectivity. Current wireless communication system uses radio resources to transmit data with Orthogonal Multiple Access (OMA). But, as the number of user's growths, OMA-based technique might not meet user requirements. That why, NOMA has been introduced to fulfil the challenges of 5G network. This article provides a comparison between NOMA and OMA systems. The main NOMA strategies are debated by dividing them into two classes, namely, the power domain and the NOMA code domain. In addition, benefits and limitations are discussed.

Keywords 5G · OMA · NOMA · Network capacity

1 Introduction

The Internet of Things (IoT) has experienced rapid development in recent years. This development creates difficult necessities for 5th generation (5G) network. Each year several new devices and an increased intelligence are introduced in the market. About 8.4 billion personal mobile devices and 3.9 billion M2M connections will be connected in 2022. To meet those requirements data rate will increase seven-fold between 2017 and 2022 [1].

The generations of wireless networks implemented so far have employed orthogonal multiple access techniques (OMA) namely, Time Division Multiple Access (TDMA), Frequency Division Multiple Access (FDMA) or Orthogonal Frequency Division Multiple Access (OFDMA). The MA techniques mentioned above, tolerate only one single user to be connected in a time/frequency resource frame. On the other hand, Code Division Multiple Access (CDMA) allows several users to share the same RB using the application of different spreading sequences unique and specific to each user to distinguish them.

J. Mestoui (✉) · M. El Ghzaoui
Intelligent Systems Networks and Telecommunications Team, Image Laboratory, EST-Meknes,
Moulay Ismail University, Meknes, Morocco
e-mail: mestoui@hotmail.com

However, none of these techniques can meet the high demands of future wireless communication systems. Solutions are proposed on the one hand, to increase energy efficiency by exploiting reduced PAPR waveforms [2–5] and on the other hand to exploit the unoccupied frequency bands such as terahertz bands [6]. Currently, Non-orthogonal Multiple Access (NOMA) is a candidate technical family to meet the challenges of 5G. The basic concept of NOMA is to allow more users to be connected than the number of users of orthogonal resources of frequency, time or of code available.

NOMA techniques may be separated into two main classes: NOMA which uses different power levels [7–9] and NOMA which uses codes to distinguish users. Figure 1 shows different NOMA techniques.

The rest of this article is organized as follows; Sect. 2 is reserved for the capacity comparison in related works. In Sect. 3 and considering the large number of NOMA solutions we focus in this article on the presentation of two dominant schemes namely NOMA of the power domain and the only case of a system that uses a spreading code in frequency domain called MC-CDMA. The advantages and limitations of NOMA are briefly mentioned in Sect. 4. Section 5 concludes this work.

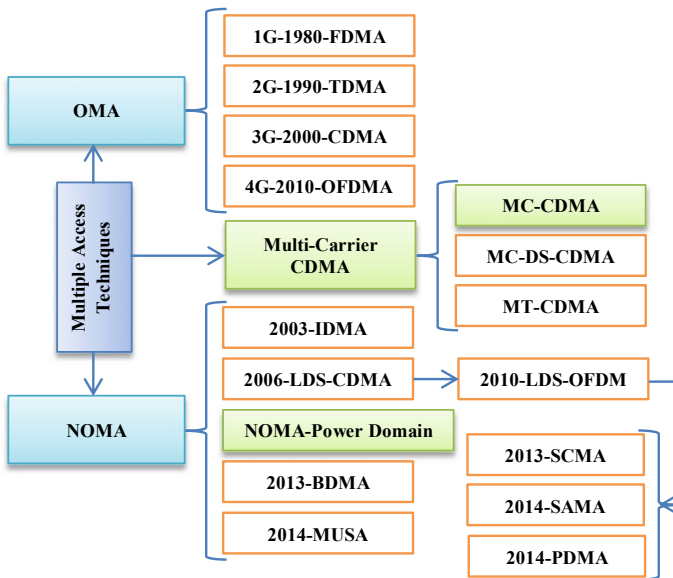


Fig. 1 Multiple access technologies

2 Capacity Comparison in Related Works

In this section, the basic principles of OMA and NOMA are compared under various parameters. Next, the advantages of NOMA compared to OMA are presented.

In the case of conventional OMA schemes, the maximum number of users that can be allowed is restricted by the number of orthogonal channels (time/frequency) available. This limit becomes strict when enormous connectivity is requested for 5G. The main advantage of NOMA is to serve more users than orthogonal (time/frequency) resources, using power or code resource allocation. Note that canceling interference between users increases the complexity at the receiver level.

An effective strategy for increasing the capacity of the system is to use the Multi-users Detection (MUD) which exploits the information of the spreading code and synchronization information. NOMA scheme is based on the usage of superposition coding (SC) at the transmitter side and successive interference cancellation method (SIC) at the receiver level.

The SC method allow NOMA to be proficient of encoding a message for a user associated with harsh channel environments at a lower rate and also place over the signal of a user having better channel conditions on it. SIC is observed as a hopeful IC technique in wireless communication system. The principle of SIC is to first detect the strongest signal, which is therefore the signal least contaminated by interference and which must subsequently be removed from the compound signal. The same practice is followed by the second strongest symbol. When all signals except one have been perceived, the feeblest user receives their information without any interference. The SIC has better performances for NOMA of the power domain taking in the case where the users sell different power levels [10].

In the following, a comparison between OMA and NOMA in terms of the access capacity of two types of channels, Additive Gaussian White Noise (AWGN) and fading channels are presented. Note that these results are applicable to both the NOMAs techniques mentioned above. Equation (1) describes the capacity of the MA system in the uplink in presence of an AWGN channel allowing K users to be connected [11].

$$\sum_{i=1}^K R_i \leq W \log \left(1 + \frac{\sum_{i=1}^K P_i}{N_0 W} \right) \quad (1)$$

where P_i is power at the transmitter, W is the bandwidth, and N_0 is the power spectral density of AWGN channel. Based reference [12], Figs. 2 and 3 of [13], present a channel capacity comparison of OMA and NOMA.

From Fig. 2, the uplink of NOMA can cover the capacity region, while OMA is generally suboptimal, excluding the point where the equity of the flow is not maintained especially when the difference of power received from both users is high. These results in the case of two users might be generalized to the scenario where the number of users connected to the network is greater than two [14].

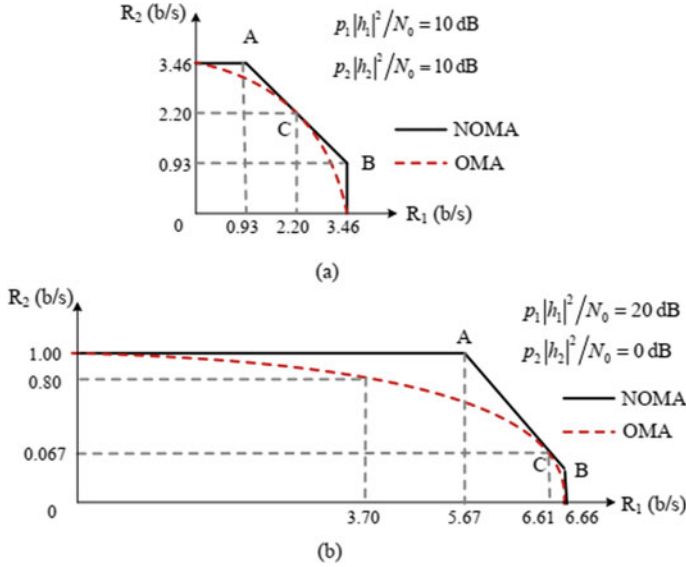
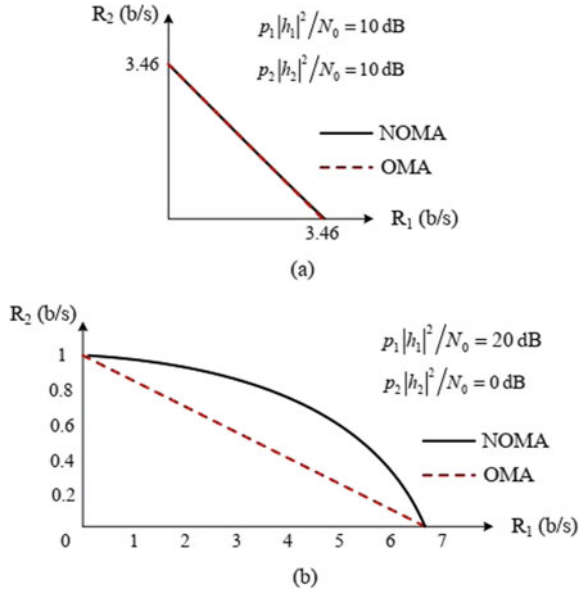


Fig. 2 Comparison between capacity of uplink-OMA and uplink-NOMA in presence of AWGN channel: **a** for the case of Symmetric channel; **b** for Asymmetric channel [13]

Fig. 3 Comparison between capacity of downlink-OMA and downlink NOMA in presence of AWGN channel: **a** for the case of Symmetric channel; **b** for Asymmetric channel [13]



When the downlink is considered, the limit of the capacity region can be determined by:

$$R_k \leq W \log \left(1 + \frac{P_k |h_k|^2}{N_0 W + \left(\sum_{j=k+1}^K P_j \right) |h_k|^2} \right) \quad (2)$$

Using overlay coding at the transmitter and SIC at each receiver allows NOMA to reach optimal points [12]. Figure 3 shows that the limit of NOMA is generally beyond that of OMA in the case where the channels are asymmetrical.

When the channels are fading, the sum capacity in the uplink can be described as

$$C_{sum} = E \left[\log \left(1 + \frac{\sum_{k=1}^K |h_k|^2 P_{ave}}{N_0} \right) \right] \quad (3)$$

According to [12], uplink-OMA is severely sub-optimal, while uplink-NOMA relying on MUD is optimal in the case where all users have the same average power P_{ave} . It is demonstrated in [15] that MIMO-NOMA exceeds MIMO-OMA in terms of data rate.

The allocation of non-orthogonal resources in NOMA gives the latter the capacity to increase the number of users who can simultaneously exploit the channel. NOMA therefore supports massive connectivity, at the cost of complex hardware and software implementation.

3 Systems Models of NOMA

In this section, we will present the basic implementations and characteristics of the two main NOMA schemes namely power domain NOMA and code domain NOMA.

3.1 NOMA Power Domain

In general, power-domain NOMA uses signals superimposition principle for frequency domain as well as for time domain with different power levels. For interference cancellation at receivers, SIC technique is exploited. The implementation principles (SC technique at transmitter side and SIC technique at receiver side) are illustrated in Fig. 4a.

In case of NOMA for downlink, the BS employs SC method, as shown in Fig. 4b. In literature, we find many contributions have studied the performance of downlink transmission NOMA [14, 16]. In [14] Saito et al. propose, a two user NOMA downlink transmission with SIC receivers. This scheme is generalized in [16] for NOMA

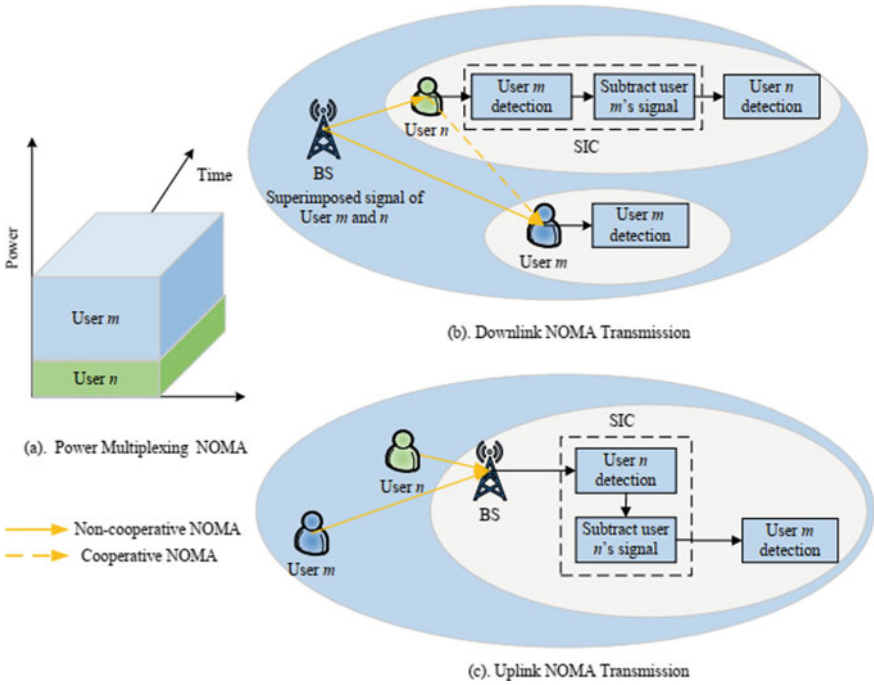


Fig. 4 NOMA transmission principles

transmission scheme. From these studies it was confirmed that NOMA outperform OMA system in terms of outage probability. Moreover, the energy consumption problem in downlink NOMA systems is treated in [17] by Zhang et al. It was approved that NOMA is more suitable than OMA when energy efficiency is required.

The second type of NOMA transmission is shown in Fig. 4c. In this case, the BS uses SIC operation to detect all the signals. Note that for the uplink NOMA and downlink NOMA, the SIC operations and interference experienced are also slightly different. As shown in Fig. 4b, the SIC technique is carried out on the strong user in downlink to cancel interference on the weak user's, i.e. the signal of User n is not affected by the interference from User m , which is achieved by first detecting the stronger signal of User m , re-modulating it and then subtracting it from the received signal. On the contrary for uplink-NOMA, SIC operation is used at the BS level to receive the strong signal of user n first by considering user m signal as interference (Fig. 4c). After that, the recovered signal is re-modulated and the interference generated by User n is subtracted to receive User m .

In [18], Benjebbour et al. discuss the real-world considerations for power-domain NOMA. Also, a combination between NOMA with MIMO to achieve enhancement of its spectral efficiency is discussed in [7, 19]. In other words, it is approved that the MIMO-NOMA is superior to MIMO-OMA in terms of channel capacity.

3.2 Code Domain NOMA

The second category of NOMA approaches is known as the NOMA code domain [20]. This technique is generally used to deal with interference caused by the lack of resources (time/frequency).

In case of CDMA, a user transmits permanently throughout the band using a spread spectrum technique. Each user is therefore assigned a specific code for the duration of the call. Unlike FDMA and TDMA where the capacity in number of users is restricted respectively by the frequency and time resources, the number of users is fixed by the properties of the spreading codes used. The CDMA therefore constitutes an alternative to the FDMA and TDMA making it possible to increase the capacity of the systems [21].

Code Division Multiple Access (CDMA) was used for the first time in 1993. Then and exploiting the simplicity of the fast Fourier transformation and the high spectral efficiency guaranteed by the spacing of the subcarriers, three schemes which combine the CDMA and OFDM techniques have been proposed, namely Multicarrier DS-CDMA (MC-DS-CDMA), MultiCarrier CDMA (MC-CDMA), and Multi-tone CDMA (MT-CDMA). DaSilva and ESSousa proposed MC-DS-CDMA in [22]. In [23], Vandendorpe described MT-CDMA. Also, MC-CDMA was proposed by Yee et al. [24], Fazel and Papke [25], and Chouly et al. [26].

As in the MC-DS-CDMA, MT-CDMA uses a spreading code in the time domain after the conversion of the serial data in parallel, so that each subcarrier can satisfy the condition of orthogonality before spreading operation [23]. The most important difference is that the MT-CDMA technique uses spreading codes longer than the number of subcarriers, compared to a normal DS-CDMA technique which uses a single carrier. In general MT-CDMA allows more users than DS-CDMA.

The only case of a multi-carrier CDMA system that uses a frequency domain spreading code at the transmitter is called MC-CDMA [24, 26]. In the case of the downlink of a synchronous mobile radio communication, it is advisable to use the Hadamard Walsh codes as an optimal orthogonal set. When the Walsh-Hadamard codes are chosen, it is possible to carry out the spreading function and the Fourier transform in a single operation thus making it possible to reduce the complexity of the MC-CDMA transmitters [27, 28].

Figure 5a, b present the MC-CDMA signal at the transmitter and its power spectrum with $N = 4$ and the processing gain or Length of code sequence $G_{MC} = L_{CS} = 4$, respectively.

The transmitted signal of the u -th user can be expressed by

$$T S_{MC}^u(t) = \sum_{-\infty}^{+\infty} \sum_{k=0}^{N-1} d^u(i) C S_k^u . \Pi(t) e^{2\pi i (f_0 + k \Delta f) t} \tag{4}$$

where $\Delta f = 1/T_s$ is space between two adjusted subcarrier, and $\Pi(t)$ is a filter defined by

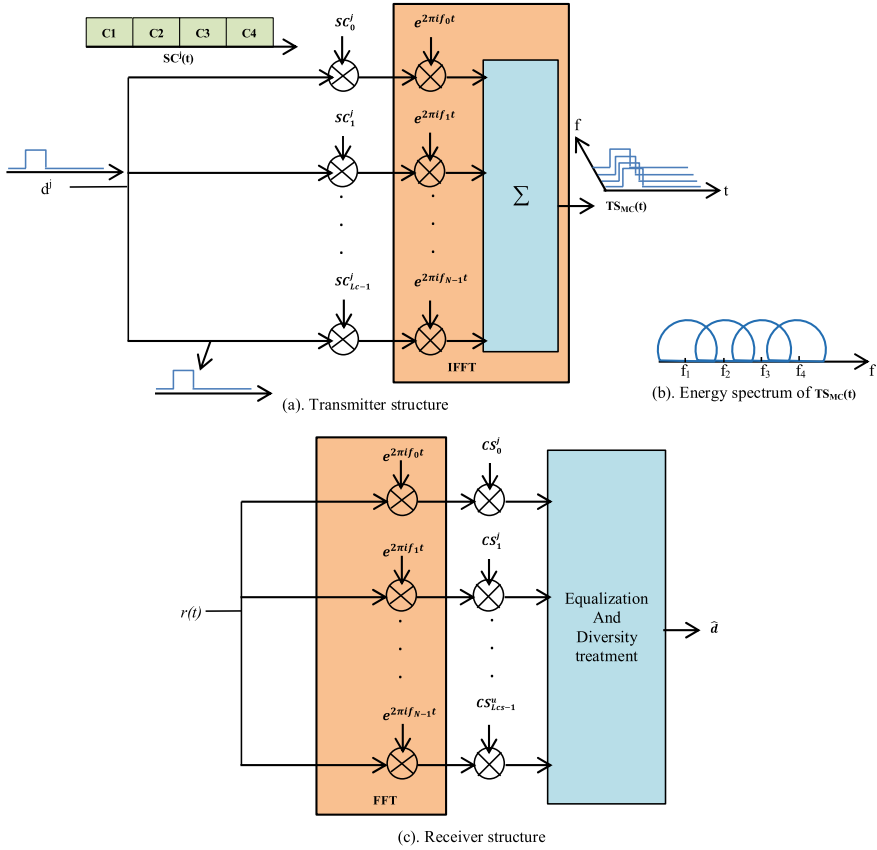


Fig. 5 MC-CDMA system model. **a** Transmitter structure. **b** Energy spectrum of TSMC(t). **c** Receiver structure

$$\Pi(t) = \begin{cases} 1 & 0 \leq t < T_c \\ 0 & \text{otherwise} \end{cases} \tag{5}$$

Figure 5c presents the MC-CDMA receiver of the u -th user. In this diagram, where multiple access processing is dissociated from diversity and channel equalization processing, the users are separated in the frequency domain since the spreading and multiple access codes are applied in this domain.

The decision variable in MC-CDMA at the receiver can be expressed by:

$$\hat{d}^u = \sum_{k=0}^{N-1} g_k^u r_k \tag{6}$$

$$r_k = \sum_{u=0}^{N_u-1} h_k^u S C_k^u d^u + n_k \quad (7)$$

where r_k is the received signal in baseband and n_k is the complex additive Gaussian noise at the k -th subcarrier, h_k^u is the complex envelope of the k -th subcarrier for the u -th user ($u = 0, 1, \dots, N_u$).

4 Advantages and Limitations of NOMA

In general, the ability to support multiple users using the same time and frequency resources which results in good spectral efficiency by reducing interference via SIC is the main reason why NOMA techniques are recommended in 5G systems.. In addition, we can mention several other advantages that allow NOMA to dominate OMA, such as: (a)—The possibility of having massive connectivity in the case of millimeter wave (mmWave) communications while simultaneously providing a very large number of users. (b)—Lower latency, because a user does not have to go through a pre-programmed time interval to transmit his information. (c)—Maintaining user equity and diversified quality of service through flexible power control between strong and weak users or through the use of spreading codes [29]. For example, when more power is allocated to a weak user, it is possible to have a higher cell edge rate. Additionally, NOMA is also functional in communications via millimeter wave (mmWave) as proven in [30] and visible light as shown in [31].

NOMA has many advantages, but it also suffers from a number of limitations, such as: (1)—5G wireless communication systems are heterogeneous, when BS covers a large number of users, interference become severe and the management of the different power levels becomes difficult. (2)—The information processing algorithms become complex as the number of users increases and the allocation of low complexity resources becomes necessary for performance optimization. (3)—In NOMA of the power domain, each user has to decode the information of all other users before decoding their own information, which leads to additional receiver complexity and power consumption compared to OMA. (4)—If an error occurs in SIC at the level of a user, the reception of information from other users will probably be carried out in an erroneous manner which imposes the minimization of the number of users to reduce the effect of error propagation. (5)—To benefit from the advantages of multiplexing in the power domain, a considerable channel gain difference between strong and weak users is necessary. This is difficult to maintain as the number of users increases.

Finally, massive MIMO and mmWave, are two important technologies to integrate with NOMA in 5G systems. In addition, transmission security for NOMA is of interest in future wireless communication systems.

5 Conclusion

NOMA strategies allow multiple users to operate at the same time in the same frequency band and the same time slots. This is possible either by different power levels or by different codes which make it possible to distinguish the users from one another. This work presents the basic principles, advantages and implementation schemes of the NOMA power domain and the NOMA code domain. The spread spectrum and multi-carrier modulation techniques have many advantages, such as the confidentiality of the transmitted information, the low power consumption and its multiple access capacity by code distribution. For multicarrier-CDMA modulations, we note the excellent spectral efficiency and the great ability to limit the ISI.

Based on what we mentioned in Sect. 4, the major problem with massive communications is real-time transmission over very limited frequency bands which have stringent requirements in 5G communication systems. These problems could be remedied in different ways. Our next work focuses on the proposal of a new variant of the MC-CDMA system through which we aim, on the one hand to increase the capacity of the system with low levels of interference and on the other hand, to minimize the power consumption for mobile devices powered primarily by batteries.

References

1. White Paper (2019) Cisco visual networking index: global mobile data traffic forecast update, 2017–2022. Cisco Public
2. Mestoui J, EL Ghzaoui M, Fattah M, Hmamou A, Foshi J (2019) Performance analysis of CE-OFDM-CPM Modulation using MIMO system over wireless channels. *J Ambient Intell Humaniz Comput*. <https://doi.org/10.1007/s12652-019-01628-0>
3. Mestoui J, El Ghzaoui M, El Yassini K (2020) BER performance of CE-OFDM system: over AWGN channel and frequency-selective channel using MMSE equalization. In: *Embedded Systems and Artificial Intelligence. Advances in Intelligent Systems and Computing*, vol 1076, pp 61–73. ESAI 2019, Fez, Morocco, 2, 3 May 2019
4. Mestoui J, Ghzaoui ME, Hmamou A, Foshi J (2019) BER performance improvement in CE-OFDM-CPM system using equalization techniques over frequency-selective channel. *Proced Comput Sci* 151:1016–1021
5. Belkaid J, Benbassou A, EL Ghzaoui M (2013) PAPR reduction in CE-OFDM system for numerical transmission via PLC channel. *Int J Commun Antenna Propag* 3:267–272
6. El Ghzaoui M, Das S (2020) Data transmission with terahertz communication systems. In: *Emerging trends in terahertz solid-state physics and devices*, pp 121–141. Springer, Singapore
7. Zeng M, Yadav A, Dobre OA, Tsiropoulos GI, Vincent Poor H (2017) Capacity comparison between MIMO-NOMA and MIMO-OMA with multiple users in a cluster. *IEEE J Sel Areas Commun* 35(10):2413–2424
8. Ding Z, Dai L, Poor HV (2016) MIMO-NOMA design for small packet transmission in the internet of things. *IEEE Access* 4:1393–1405
9. Choi J (2016) On the power allocation for a practical multiuser superposition scheme in NOMA systems. *IEEE Commun Lett* 20(3):483–441
10. Patel P, Holtzman J (1994) Analysis of a simple successive interference cancellation scheme in a DS/CDMA system. *IEEE J Sel Areas Commun* 12(5):796–807
11. Cover TM, Thomas JA (2006) *Elements of information theory*. Wiley, Hoboken

12. Tse D, Viswanath P (2005) *Fundamentals of wireless communication*. Cambridge University Press, Cambridge
13. Higuchi K, Benjebbour A (2015) Non-orthogonal multiple access (NOMA) with successive interference cancellation for future radio access. *IEICE Trans Commun E98-B(3)*:403–414
14. Saito Y, Kishiyama Y, Benjebbour A, Nakamura T, Li A, Higuchi K (2013) Non-orthogonal multiple access (NOMA) for cellular future radio access. In: *IEEE Proceedings of vehicular technology conference (VTC)*, Dresden, Germany, pp 1–5
15. Liu Y, Pan G, Zhang H, Song M (2016) On the capacity comparison between MIMO-NOMA and MIMO-OMA. *IEEE Access* 4:2123–2129
16. Ding Z, Yang Z, Fan P, Poor HV (2014) On the performance of non-orthogonal multiple access in 5G systems with randomly deployed users. *IEEE Signal Process Lett* 21(12):1501–1505
17. Zhang Y, Wang H-M, Zheng T-X, Yang Q (2017) Energy-efficient transmission design in non-orthogonal multiple access. *IEEE Trans Veh Technol* 66(3):2852–2857
18. Benjebbour A, Saito Y, Kishiyama Y, Li A, Harada A, Nakamura T (2013) Concept and practical considerations of non-orthogonal multiple access (NOMA) for future radio access. In: *Proceedings of IEEE intelligent signal processing and communications systems (IEEE ISPACS'13)*, pp 770–774
19. Zeng M, Yadav A, Dobre OA, Tsiropoulos GI, Vincent Poor H (2017) On the sum rate of MIMO-NOMA and MIMO-OMA systems. *IEEE Wirel Commun Lett* 6(4):534–537
20. Dai L, Wang B, Yuan Y et al (2015) Non-orthogonal multiple access for 5G: solutions, challenges, opportunities, and future research trends. *IEEE Commun Mag* 53(9):74–81
21. Glisic S, Vucetic B (1997) *Spread spectrum CDMA systems for wireless communications*. Artech House, ISBN 0-89006-858-5
22. Da Silva VM, Sousa ES (1993) *Proc IEEE ICUPC'93*, pp 995–999, Ottawa, Canada
23. Vandendorpe L (1993) *Proceedings of IEEE first symposium of communications and vehicular technology in the Benelux*, pp 4.1-1–4.1.8, Delft, The Netherlands
24. Yee N, Linnartz J-P, Fettweis G (1993) *Proceedings of IEEE PIMRC'93*, pp 109–113, Yokohama, Japan
25. Fazel K, Papke L (1993) *Proceedings of IEEE PIMRC'93*, pp 468–472, Yokohama, Japan
26. Chouly A, Brajal A, Jourdan S (1993) *Proceedings of IEEE GLOBECOM'93*, pp 1723–1728, Houston, USA
27. Bogucka H (1999) Effective implementation of OFDM-CDMA base station transmitter using joint FHT and IFFT. In: *IEEE signal processing workshop on signal processing advances in wireless communications*, pp 162165
28. Bogucka H (1999) Application of the new joint complex Hadamard inverse Fourier transform in a OFDM-CDMA wireless communication system. In: *IEEE vehicular technology conference*, vol 5, pp 2929–2933
29. Wei Z, Yuan J, Ng DWK, Elkashlan M, Ding Z (2016) A survey of downlink non-orthogonal multiple access for 5G wireless communication networks. *ZTE Commun* 14(4):17–25
30. Ding Z, Fan P, Poor HV (2017) Random beamforming in millimeter-wave NOMA networks. *IEEE Access* 99:1–1
31. Marshoud H, Kapinas VM, Karagiannidis GK, Muhaidat S (2016) Non-orthogonal multiple access for visible light communications. *IEEE Photon Technol Lett* 28(1):51–54

A Modified E-Shaped Compact Printed Antenna for 28 GHz 5G Applications



Yousra Ghazaoui, Ali El Alami, Sudipta Das, and Mohammed El Ghzaoui

Abstract A single band printed antenna with a modified E-shaped structure is proposed for 5G applications at 28 GHz band. The suggested antenna has been constructed on a $5.5 \times 4.35 \text{ mm}^2$ FR-4 substrate ($\epsilon_r = 4.4$ and $h = 1.6 \text{ mm}$) through slot loading technique. The incorporation of rectangular and tiny square shaped slots has improved the resonance and radiation characteristics of the designed antenna. The wide operating bandwidth of the suggested antenna covers 25.99–29.88 GHz frequency spectrum to support 28 GHz 5G applications. The presented antenna depicts low mismatch loss and thus better impedance matching offering a reflection coefficient of about -40.88 dB at 28 GHz. The proposed antenna offers desired radiation patterns (E and H planes) with a peak gain of about 5.64 dBi at 28 GHz. Furthermore, an extensive analysis of VSWR, input impedance, and surface current distribution are also presented to explain the working functionality of the suggested antenna. The proposed structure is a preferable choice for 28 GHz 5G applications due to its compact size and high performance parameters and it covers the bandwidth requirements of 5G applications at 28 GHz.

Keywords Printed antenna · Wideband · 5G applications

Y. Ghazaoui (✉) · M. El Ghzaoui

Intelligent Systems Networks and Telecommunications Team, IMAGE Laboratory, EST-UMI, Meknes, Morocco

e-mail: y.ghazaoui@gmail.com

M. El Ghzaoui

e-mail: elghzaoui.mohammed@gmail.com

A. El Alami

Faculty of Sciences and Technics, Renewable Energies, Information Processing and Transmission Laboratory, Moulay Ismail University, Errachidia, Morocco

e-mail: a.elalami1984@gmail.com

S. Das

Department of Electronics and Communication Engineering, IMPS College of Engineering and Technology, Malda, India

e-mail: sudipta.das1985@gmail.com

© Springer Nature Singapore Pte Ltd. 2022

S. Bennani et al. (eds.), *WITS 2020*, Lecture Notes in Electrical Engineering 745, https://doi.org/10.1007/978-981-33-6893-4_87

961

1 Introduction

The continuous expansion of wireless systems demands technological advancement in antenna design techniques. The design and implementation of printed antenna technology have become very popular in recent decades due to its various benefits such as minimum manufacturing cost, miniaturized dimension, and light weight. The printed antennas can be designed carefully to acquire compactness [1–4], high gain [5], multiband [6, 7], wideband [8], and ultra-wideband [9, 10] operation to support different popular wireless communication applications such as PCS, Bluetooth, RFID, WLAN, HiPERLAN, Wi-MAX, IMT, UMTS, and 4G LTE systems. However, based on most of the forecasts, the fifth-generation (5G) wireless communication system with high speed data rate and wider bandwidth will be considered as the most promising next generation wireless technology. The frequency bands in the sub-6 GHz and millimeter wave (mmW) range such as 28/38/60/70 have been considered as the potential spectrum for 5G systems. However, the spectrum at 28 GHz has given priority for 5G uses because of the negligible atmospheric absorption rate and less free space path loss at this frequency band. Accordingly, the antenna being one of the key components in 5G systems, there will be revolutionary changes in the design requirements of printed antenna technology to obtain wide bandwidth, high gain, and directional radiation patterns to support 5G applications at mmW radio spectrum. Recently, the researchers have proposed several antenna designs [11–21] for 28 GHz 5G applications. The antenna design configurations include DGS [11, 12], U-slot patch array [13], Grid array antenna [14], antipodal tapered slot antenna [15], EBG ground plane [16], dual polarized array [17], quarter wave transformer feed [18], inset feed 2×2 array [19], inset feed rectangular patch [20], and FSS [21].

In this article, an extremely small printed antenna (ESPA) is designed using FR-4 substrate having physical dimensions of $4.35 \times 5.5 \text{ mm}^2 \times 1.6 \text{ mm}^2$ for 28 GHz 5G applications is proposed. The proposed compact modified E-shaped printed antenna has been designed by incorporating slots on the radiating patch to offer good impedance matching, wide bandwidth, standard gain, and desired radiation patterns for the intended application.

2 Design of the Proposed Antenna

2.1 Structural Evolution of the Proposed Antenna

Figure 1a demonstrates the geometry of the microstrip line fed conventional element antenna. The designed antenna structure is constructed on a 1.6 mm thick FR-4 having ϵ_r of 4.4 and a compact area of only $4.35 \times 5.5 \text{ mm}^2$. The overall size of the radiating patch is only $1.8 \times 2.5 \text{ mm}^2$. To improve the characteristic parameters of the basic element antenna and to achieve the resonant frequency at around 28 GHz for

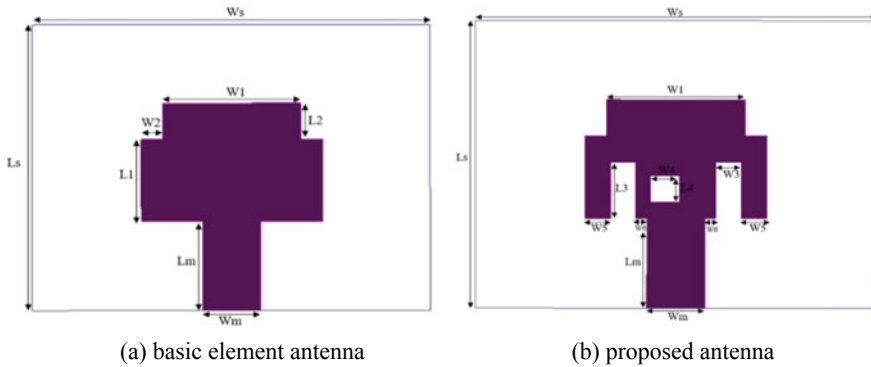


Fig. 1 Geometric evolution of the proposed antenna

Table 1 Optimal geometric parameters of the designed antenna

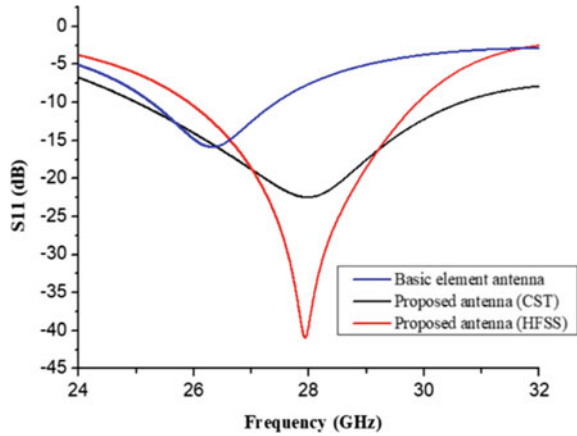
Parameters	Value (mm)	Parameters	Value (mm)
L_s	4.35	L_2	0.55
W_s	5.5	W_3	0.35
L_m	1.35	L_3	0.85
W_m	0.8	W_4	0.4
W_1	1.9	L_4	0.4
L_1	1.25	W_5	0.35
W_2	0.3	W_6	0.15

the intended 5G applications, two identical rectangular slots (L_3, W_3) and a square-shaped slot (L_4, W_4) have been incorporated on the radiating patch as presented in Fig. 1b. The concluding parameters of the suggested structure are listed in Table 1.

2.2 Results and Discussion

The simulation results of the basic and the proposed antennas are analyzed by HFSS software. Besides, in order to verify the reliability of our results, we use CST software as a simulator for microscript antenna. The comparison between the simulated S_{11} parameters of the basic and the proposed antennas is shown in Fig. 2. It is noted from this figure that, single element does not cover the 28 GHz band with a return los of about -15.88 dB at 26.32 GHz. However, the prposed antenna cover the required spectrum of the 28 GHz 5G applications either in with CST as wel as with HFSS. Moreover, due to the modified geometry, the proposed antenna shows improved S_{11} of about -40.88 dB at 28 GHz with a wide impedance bandwidth (IBW) of about 3890 MHz (25.99–29.88 GHz) in the cas of HFSS while the bandwidth obtainet by CST is oft about 5.65 GHz (25–30.65 GHz) with a return loss of 22.49 dB. A

Fig. 2 S_{11} parameters versus frequency



clear observation indicates that the proposed antenna offers much better impedance matching offering excellent S_{11} parameter, and operating bandwidth relative to the basic antenna to support the intended 5G application band. As a result, we can notice that S_{11} was verified by the two simulators which are based on two different methods. We recorded a slight difference between the results of CST and HFSS in terms of reflection coefficient and impedance bandwidth for this antenna. This slight difference can be explained by the trade-off between return loss and bandwidth, also the discretization used by HFSS and CST has a major impact on the performance of an antenna. The simulated parameters such as voltage standing wave ratio (VSWR), input impedance, gain, and radiation patterns, at 28 GHz are presented in Figs. 3, 4, 5, and 6, respectively. As displayed in Fig. 3, the VSWR reaches a value of 1.01 at 28 GHz. The VSWR values are observed within 2:1 throughout the operating band, which signifies good adaptation characteristics of the designed

Fig. 3 Simulated VSWR

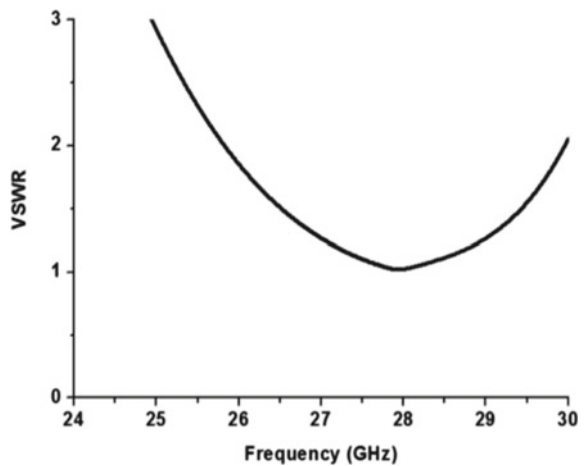


Fig. 4 Simulated input impedance

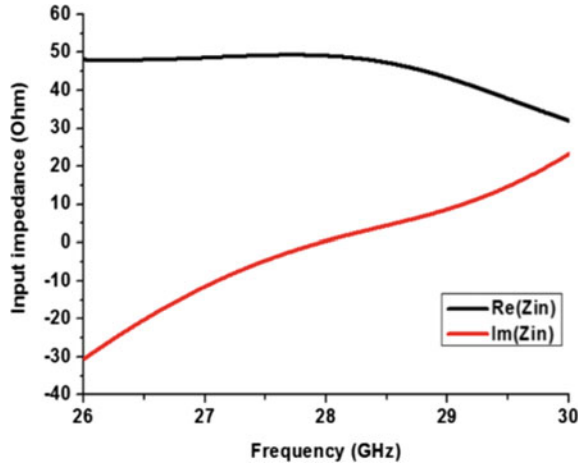
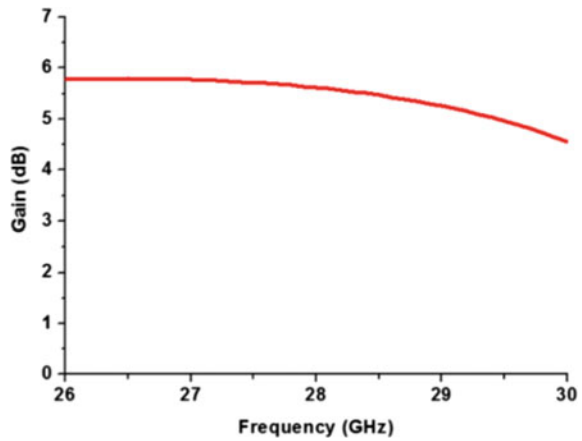


Fig. 5 Simulated gain versus frequency



antenna. The variations of the input impedance are shown in Fig. 4. The real part of the impedance is noted as 49.10Ω at the resonance frequency 28 GHz which indicates excellent matching. This result also indicates that the designed antenna is well adapted. It is noticed from Fig. 5 that the peak gain of the proposed antenna reaches 5.64 dB at 28 GHz which ensures the proper functioning of the suggested antenna. As noticed from Fig. 6, directional E-plane and nearly omni-directional H-plane radiation patterns are observed at 28 GHz. The H-plane radiation pattern resembles slightly distorted ‘O’ shaped and this may be a result of the higher density of the originated surface current that mainly circulates and concentrates around the slot for the resonant frequency 28 GHz. The surface current distribution of the proposed antenna at 28 GHz has been analyzed and presented in Fig. 7. The partial distribution of the surface current is observed near the edge of the feed line but the higher concentration

Fig. 6 Simulated E and H planes radiation patterns at 28 GHz

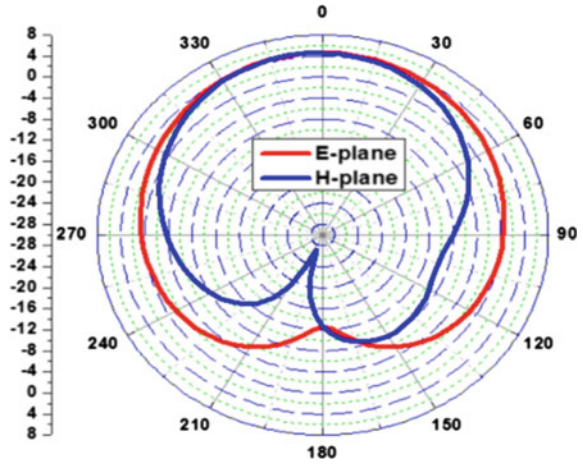
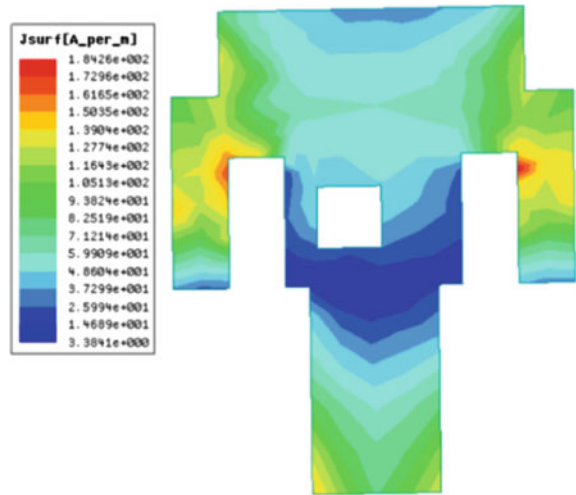


Fig. 7 Surface current distributions at 28 GHz



of the surface current is mainly visualized along the edges of the incorporated rectangular slots on the radiating patch. So, the circulating dense surface currents along the edges of the slots create extra resonances which merge with the resonance of the basic patch and this may create wide resonance envelope to offer wide operating bandwidth at a reference level of $S_{11} \leq -10$ dB.

Table 2 Comparison with other 5G antennas in the literature

Reference works	MPAs structure	Antenna size (mm ²)	ϵ_r	Frequency (GHz)	Bandwidth (GHz)
[11]	DGS	5×5.26	2.2	28	2.1
[12]	DGS	5×5	2.94	28	1.44
[13]	2×2 U-slot array	41.3×46	2.2	28.3	3.35
[14]	Grid array antenna	15×15	2.2	28	2.2
[15]	tapered slot	25×30	2.2	28.5	1.42
[16]	EBG ground plane	20×20	2.2	28	2.5
[17]	Dual polarized array	11.6×11.6	4.2	28.5	2.0
[19]	Inset feed 2×2 array	20.37×26.51	2.9	28	0.4
[20]	Inset feed patch	6.285×7.235	2.2	28	0.847
[21]	Single layer FSS	10.2×27.8	3.38	28	3.0
This Work	Modified E-shaped	4.35×5.5	4.4	28	3.89

3 Performance Comparison with Other Reference Works

A comparative analysis of the proposed antenna with some previously reported single band antennas for 28 GHz 5G applications is summarized in Table 2. It is evident from the table that the proposed antenna has an attractive compact size, implies a different design approaches, and provides much better bandwidth compared to other reported antenna structures for 28 GHz 5G applications.

4 Conclusion

A novel modified E-shaped printed antenna is proposed for 28 GHz future 5G applications. An optimization between antenna size reduction and wide bandwidth is maintained in this designed model. The proposed antenna resonates at 28 GHz with -10 dB impedance bandwidth of about 3.89 GHz (25.99–29.88 GHz) which covers the allocated spectrum for desired 5G application. So, the extremely small size, wide bandwidth, good gain, low VSWR, and satisfactory radiation pattern confirm the applicability of the presented antenna for next generation 5G communications at 28 GHz millimeter-wave band. The performance of the proposed antenna was compared in HFSS and CST in terms of S11. It has been verified that the proposed antenna performance better for 5G band because it covers bandwidth requirements of 5G applications at 28 GHz with high gain and good radiation pattern.

References

1. Das S, Sarkar PP, Chowdhury SK (2013) Investigations on miniaturized multifrequency microstrip patch antennas for wireless communication applications. *J Electromagn Waves Appl* 27(9):1145–1162
2. Das S, Sarkar PP, Chowdhury SK (2014) Design and analysis of a compact monitor-shaped multifrequency microstrip patch antenna. *J Electromagn Waves Appl* 28(7):827–837
3. Das S, Sarkar PP, Chowdhury SK (2015) Modified π -shaped slot loaded multifrequency microstrip antenna. *Progr Electromagn Res B* 64(1):103–117
4. Das S, Sarkar PP, Chowdhury SK (2014) Design and analysis of a novel open ended T-shaped slot loaded compact multifrequency microstrip patch antenna. *Microwave Opt Technol Lett* 56(2):316–322
5. El Alami A, Das S, Madhav BTP, Bennani SD (2019) Design, optimization and realization of high gain RFID array antenna 4×1 for detection system of objects in motion. *J Instrum* 14(5):P05002
6. Das S, Sarkar PP, Chowdhury SK (2014) Design and analysis of a compact triple band slotted microstrip antenna with modified ground plane for wireless communication applications. *Progr Electromagn Res B* 60(1):215–225
7. Salamin MA, Das S, Zugari A (2018) Design and realization of low profile dual-wideband monopole antenna incorporating a novel ohm (Ω) shaped DMS and semi-circular DGS for wireless applications. *AEU—Int J Electron Commun* 97:45–53
8. Boutejdar A, Salamin MA, Challal M, Das S, El Hani S, Bennani SD, Sarkar PP (2018). A compact wideband monopole antenna using single open loop resonator for wireless communication applications. *Telkomnika (Telecommun Comput Electron Control)* 16(5):2023–2031
9. Salamin MA, Ali WAE, Das S, Zugari A (2019) Design and investigation of a multi-functional antenna with variable wideband/notched UWB behavior for WLAN/X-band/UWB and Ku-band applications. *AEU—Int J Electron Commun* 111:152895
10. Lakrit S, Das S, Ghosh S, Madhav BTP (2020) Compact UWB flexible elliptical CPW-fed antenna with triple notch bands for wireless communications. *Int J RF Microw Comput-Aided Eng* e22201. doi: <https://doi.org/10.1002/mmce.22201>
11. Prachi VG, Vijay S (2020) A novel design of compact 28 GHz printed wideband antenna for 5G applications. *Int J Innov Technol Expl Eng* 9(3):3696–3700
12. Awan WA, Zaidi A, Baghdad A (2019) Patch antenna with improved performance using DGS for 28 GHz applications. In: *International conference on wireless technologies, embedded and intelligent systems (WITS)*. pp 1–4
13. Yoon N, Seo C (2017) A 28-GHz wideband 2×2 U-slot patch array antenna. *J Electromagn Eng Sci* 17(3):133–137
14. Chen Z, Zhang Y (2013) FR4 PCB grid array antenna for millimeter-wave 5G mobile communications. In: *IEEE MTT-S international microwave workshop series*
15. Ashraf MA, Haraz OM, Alshebeili S (2015) Compact size enhanced gain switched beam conformal antipodal tapered slot antenna system for 5G MIMO wireless communication. In: *IEEE 11th international conference on wireless and mobile computing, networking and communications (WiMob)*, pp 613–618
16. Haraz OM, Elboushi A, Alshebeili SA, Sebak A (2014) Dense dielectric patch array antenna with improved radiation characteristics using EBG ground structure and dielectric superstrate for future 5G cellular networks. *IEEE Access* 2:909–913
17. Du JK, So K, Ra Y, Jung SY, Kim J, Kim SY, Woo S, Kim HT, Ho YC, Paik W (2017) Dual-polarized patch array antenna package for 5G communication systems. In: *11th European conference on antennas and propagation (EUCAP)*, pp 3493–3496
18. Cusicuna DNA, Cusicuna JLA, Arenas MC (2018) High gain 4×4 rectangular patch antenna array at 28 GHz for future 5G applications. In: *IEEE international conference on electronics, electrical engineering and computing*, pp 1–4
19. Johari S, Jalil MA, Ibrahim SI, Mohammad MN, Hassan N (2018) 28 GHz microstrip patch antennas for future 5G. *J Eng Sci Res* 2(4):01–06

20. Darboe O, Konditi DBO, Manene F (2019) A 28 GHz rectangular microstrip patch antenna for 5G applications. *Int J Eng Res Technol* 12(6):854–857
21. Mantash M, Kesavan A, Denidni TA (2018) Beam-tilting endfire antenna using a single-layer FSS for 5G communication networks. *IEEE Antennas Wirel Propag Lett* 17(1):29–33

Design of Microstrip Sierpinski Carpet Antenna Using a Circular Pattern with Improved Performance



Abdelhakim Moutaouakil, Younes Jabrane, Abdelati Reha,
and Abdelaziz Koumina

Abstract In this work, we present the two first iterations design of the Sierpinski carpet fractal antenna by using a circular pattern. The proposed antenna is printed on FR4 substrate with a dielectric constant of 4.4. At the second iteration, the studied antenna has a multiband behavior with four resonant frequencies: 3.92, 4.89, 6.61 and 7.22 GHz with a good impedance matching. The simulated results performed by CADFEKO a Method of Moments (MoM) based Solver and measurement using Vector Network Analyzer (VNA) Anritsu MS2026C are in good agreement.

Keywords Sierpinski carpet · Circular pattern · Multiband · Antenna

1 Introduction

For the wireless communication system, an antenna is one of the most critical components. A good design of the antenna can thus improve overall system performance. As the demand increases day by day to multi-band antennas, Thus, a major issue in multi-band communications concerns small or very small terminal dimensions, intended for short radio ranges and in association with sensors or networks for information transfer in a domestic, multimedia or professional context [1–3]. Low consumption, ease of integration, and above all cost are essential aspects that are not very compatible with performance, these antennas also have wide applications in long range of wireless systems.

A. Moutaouakil (✉) · Y. Jabrane
Modelisation of Complex Systems Laboratory (LMSC), Cadi Ayyad University, Marrakech,
Morocco
e-mail: moutaouakilabdo@gmail.com

A. Reha
Laboratory of Innovation in Management and Engineering for the Enterprise, ISGA, Marrakech,
Morocco

A. Koumina
Nanostructures Physics Laboratory, ENS, Cadi Ayyad University, Marrakech, Morocco

Fractal Antennas Elements are currently beneficial to antenna designers and researchers. By applying fractals to antenna elements. The concept of fractal geometry was introduced for the first time by Mandelbrot in [4].

In this paper, we propose a new microstrip Sierpinski carpet antenna using a circular pattern.

2 The Antenna Geometry

Applying fractal theory for antenna design is a clever method of improving antenna performance thanks to the property of self-similarity that characterizes fractal geometries [5–7]. As shown in Fig. 1, the studied antenna is a microstrip patch antenna designed with the modification of the traditional fractal structure of Sierpinski Carpet by replacing the rectangular slots with circular ones.

To excite the patch. Here, the feed is applied through a microstrip inset feed.

The table below gives the corresponding values of design parameters [8, 9] (Table 1).

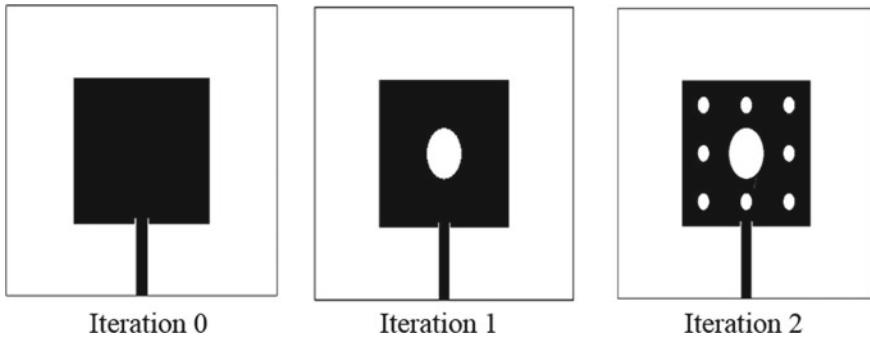


Fig. 1 Iteration steps to get Carpet geometry

Table 1 Design parameters and corresponding values

Design parameters	Value (mm)
Length of substrate	56.02
Width of substrate	72.44
Length of patch	28.01
Width of patch	36.22
Thickness of the substrate	1.6
Width of supply line	2.8
Length of inset point	1

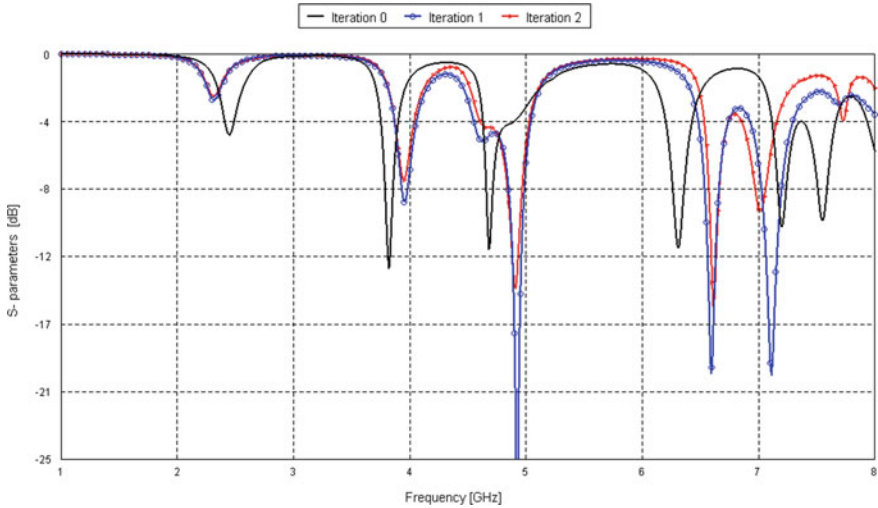


Fig. 2 Simulated reflection coefficient (S11) versus frequencies for tree first iterations

3 Simulation Results Using FEKO Suite 5.5

The following figures represent a comparison of the reflection coefficient versus frequencies for different iteration numbers (Fig. 2).

It is worth noting from the simulation that the resonance frequencies become lower when the iteration number increases. Also, for the higher frequencies, the bandwidth becomes larger.

Figure 3 shows the 3D gain pattern of the Simulated antenna for the resonance frequencies for each iteration.

According to the simulations, we see that the gains for all the resonance frequencies increase from one iteration to another, for example, for the first frequency F1 at iteration 0 we have the same gain 6.4 dB and for the second iteration it is 6.9 dB, for the third frequency the gain go from -1.8 dB to 11 dB at iteration 2, and for the fourth frequency F4, the gain equals 10.2 dB at iteration 0 and 11.4 dB at iteration 2.

4 Experimental Results

The antenna is than fabricated and tested using Vector Network Analyzer (VNA Master, Anritsu MS2026C) to validate the simulated results in the band [1–5 GHz]. We confirm with measurements that resonance frequencies become lower when the iteration number increases. Also, for the higher frequencies, the bandwidth becomes bigger (Fig. 4).

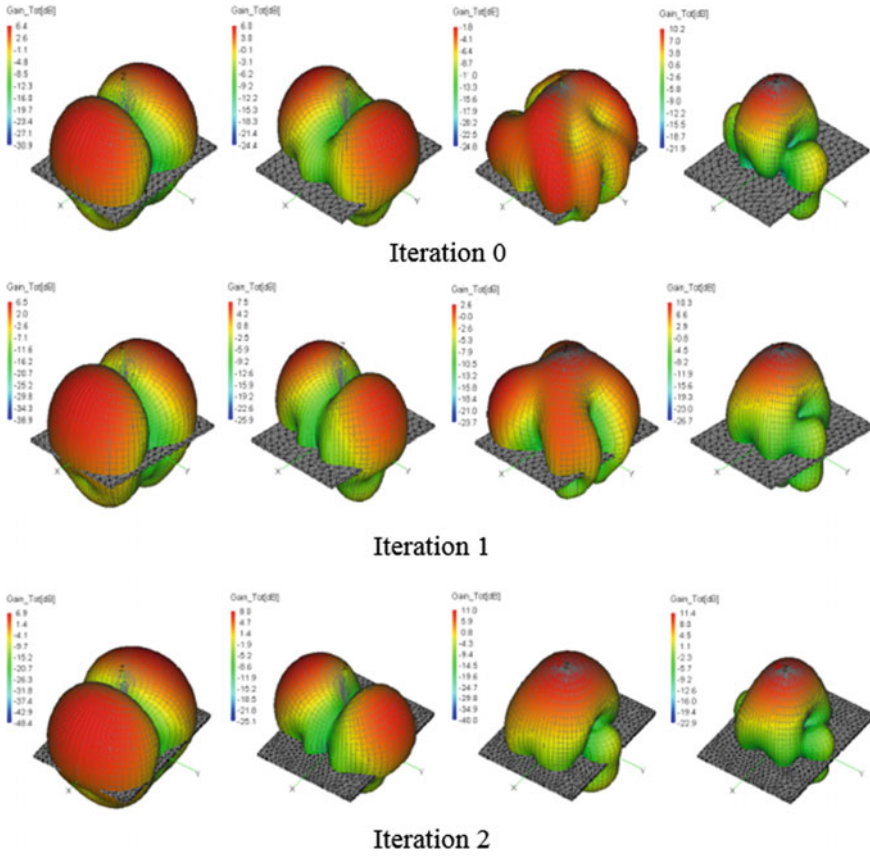


Fig. 3 3D Gain pattern of the simulated antenna

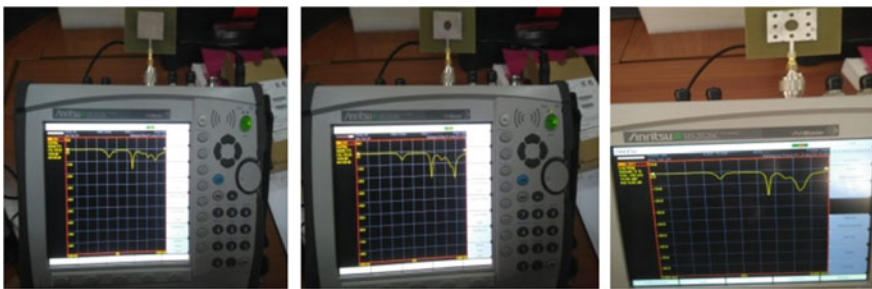


Fig. 4 S11 Measurement by VNA for the tree antennas

Table 2 Comparative results of existing antennas and our antenna

References	Dimensions of antenna (mm ³)	Resonance frequency (GHz)	Gain in dB	Applications
[10]	36 × 36 × 1	6.05/8.55	5.29/6.34	Satellite communication
[11]	37 × 62.6 × 1.59	5.59/6.4/7.84	−6/−3.1/−9	Wideband
[12]	37.25 × 27.99 × 1.59	5.3/7.4/14.6	−15.8/−26.3/−26.5	Wi-Max
Ourwork	72.44 × 56.02 × 1.6	3.92/4.89/6.61/7.22	6.9/8.0/11/11.4	Multi-band

The following table represents a comparison between the performances of the antennas found in indexed works and our antenna, we note that our work has an improvement in performances Compared to existing works (Table 2).

5 Conclusions

In this paper, the setup of slots on the patch antenna using the Sierpinski Carpet Fractal structure allows the miniaturization of the antenna since the resonant frequency becomes smaller when increasing the number of iteration and the gain becomes higher. The simulated results performed by CADFEKO a MoM based Solver and measurement using Vector Network Analyzer (VNA) Anritsu MS2026C are in good agreement. The proposed antenna will be a good solution for many wireless telecommunications systems and especially for the embedded systems where easy integration, miniaturization, multi-band and broadband are the essential requirements.

References

1. Reha A, El Amri A, Benhammouch O, Oulad Said A, El Ouadih A, Bouchouirbat M (2016) CPW-fed slotted CANTOR Set fractal antenna for WiMAX and WLAN applications. *Int J Microw Wireless Technol* 1–7
2. Jayasinghe J, Andújar A, Anguera J (2019) On the properties of Sierpinski gasket fractal microstrip antennas. *Microw Opt Technol Lett* 61:772–776
3. Moutaouakil A, Jabrane Y, Reha A, Koumina A (2019) Effect study of a ring on the performances of a patch antenna. In: 2019 international conference of computer science and renewable energies (ICCSRE), Agadir, Morocco, pp 1–3
4. Mandelbrot BB (1983) *The fractal geometry of nature*. San Francisco, pp 152–180
5. Constantine Balanis A (1997) *Antenna theory analysis and design*. Wiley Sons Inc.
6. Chen WL, Wang GM (2008) Small size edge-fed Sierpinski carpet microstrip patch antenna. *PIERS C* 3

7. Gupta S, Kshirsagar P, Mukherjee B (2018) Sierpinski fractal inspired inverted pyramidal DRA for wide band applications. *Electromagnetic* 38(2):103–112
8. Moutaouakil A, Jabrane Y, Reha A, Koumina MA (2020) Design and simulation of a fractal multiband antenna printed on a circular patch. *Int J Adv Sci Technol* 29(06):5290–5296
9. Boutejdar A, Halim BI (2019) Design and manufacturing of a dual patch ring antenna using parasitic ring resonators and partial ground plane for multiband applications. In: 2019 IEEE international symposium on phased array systems and technology
10. Jena MR, Mangaraj BB, Pathak R (2014) A novel Sierpinski Carpet fractal antenna with improved performances. *Am J Electr Electron Eng* 2(3):62–66
11. Mohanamurali R, Shanmuganatham T (2012) Sierpinski Carpet fractal antenna for multiband applications. *Int J Comput Appl* 39(14)
12. Namdeo P, Agrawal N, Yadav P, Vishwakarma R, Chaitanya G (2015) Design and analysis of Sierpinski Carpet fractal antenna. *Int J Innov Res Electr Electron Instrum Control Eng* 3(5)

Load Condition for Minimum Backscattering Antennas



Zaed S. A. Abdulwali  and Majeed A. S. Alkanhal 

Abstract The scattered fields of antennas can be decomposed into two terms; one depends only on the structure of the antenna while the other depends on the antenna radiation parameters and the loading conditions. This decomposition is used to investigate the antenna radar cross section (RCS) behavior with variable loadings. Then, a general analytical load condition for zero or minimum bistatic radar cross section is derived. The derived formula is used to obtain the regions of feasible passive loads for zero backscattering for three different antenna structures. The backscattering levels of these antennas are examined to validate this formula. The results demonstrate the validity of the procedure with almost zero backscattering for all structures with evident RCS reduction factors.

Keywords Electromagnetic scattering · Radar cross section · Antenna scattering · Zero scattering · Scattering pattern · RCS reduction

1 Introduction

Electromagnetic scattering from antennas fascinated investigators especially those concerned with radar cross section reduction. In general, objects scatter electromagnetic fields as a result of currents induced on them due to the incident fields. The antenna is a special scatterer that its scattering can be decomposed into two terms [1–4]. One is independent of antenna loading and called the structural term while the other depends on the antenna feed loading and called the antenna mode scattering. Therefore, the antenna mode can be reformed by different loading to interfere with the field from the structural part to produce the desired scattering control [5].

Basically, there are two methods to reduce antenna RCS without using material techniques or changing incident field direction [6]. They are, either, using suitable

Z. S. A. Abdulwali (✉) · M. A. S. Alkanhal
King Saud University, Riyadh 11421, Saudi Arabia
e-mail: zabdulwali@ksu.edu.sa

M. A. S. Alkanhal
e-mail: majeed@ksu.edu.sa

loading modifications [5, 7] or using structural modifications as adding parasitic elements or reflectors [8, 9]. This paper explores the first method that uses suitable mismatching loads to control the antenna scattered fields. Studies related to special antenna structures to predict their scattered fields as a function of the load impedance and also to find a suitable load for radar cross section (RCS) minimization are presented in [5, 7, 10]. For example, [5, 7], obtained a minimum back scattering from thin cylindrical antennas using central impedance loadings while [11] used double loadings. In [10], a method to control the scattering from thin and thick cylindrical and planar structures was presented. Other efforts rely on optimization algorithms as in [12, 13], where a genetic algorithm (GA) is used to find the optimum load that would control and eliminate the backscattering of wire antennas with and without reflectors. However, this method needs to run the heuristic algorithm in stacks of iterations to get high accuracy results.

In this paper, the general scattered field decomposition formula is analyzed and accurately examined. Then, a general loading condition for zero or minimum bistatic RCS for arbitrary antenna structures is derived and validated. The zero-backscattering load feasible regions of three different antennas are acquired and demonstrated. The minimum scattering and the RCS reduction level for all the studied structures are compared to the RCS of the antennas when they are terminated by open-circuit and conjugate matched loadings.

2 Formulation and Validation of Antenna Scattering

The electromagnetic (EM) field scattered by an antenna as a function of the load impedance is given by the following expression at an arbitrary direction aspect [4]:

$$\mathbf{E}_s = \mathbf{E}_s^{sc} - \frac{I_{sc}Z_L}{Z_A + Z_L} \mathbf{E}_r^{1A} \tag{1}$$

where \mathbf{E}_s is the total scattered field at the desired aspect, \mathbf{E}_s^{sc} is the short circuit antenna scattered field (when $Z_L = 0$), Z_A is the input impedance of the antenna, Z_L is the load impedance, I_{sc} is the short circuit current through the antenna feed points, and \mathbf{E}_r^{1A} is the radiated field at the transmitting regime with unit input current excitation. The antenna radar cross section (RCS, σ) at the selected direction can be found using the above formula by substituting \mathbf{E}_s in the below shown equation:

$$\sigma = \lim_{r \rightarrow \infty} 4\pi r^2 \left| \frac{\mathbf{E}_s}{\mathbf{E}_i} \right|^2 \tag{2}$$

where r is the distance at which the scattered fields are measured and \mathbf{E}_i is the incident field on the antenna structure. By substituting (1) into (2), the antenna RCS can be predicted as

$$\sigma = \left| \frac{2r\sqrt{\pi}E_s^{sc}}{E_i} - (1 - \Gamma_A)\frac{2r\sqrt{\pi}I_{sc}E_r^{1A}}{2E_i} \right|^2, \text{ where } \Gamma_A = \frac{Z_A - Z_L}{Z_A + Z_L} \quad (3)$$

Γ_A is the antenna current reflection coefficient which is similar to the formula given in [3] if a unit current through the antenna in the transmit regime is assumed. Formula (3) is applied on a dipole of length 0.4718λ ($\lambda = 105.98 \text{ cm}$) and wire-diameter of 1 mm as depicted in Fig. 1. The incident field is a normal incident linearly polarized plane wave co-polarized with the dipole axis. The dipole forward scattered RCS as a function of load resistance is shown in Fig. 2. Results of Formula (3) almost match the results obtained from a full wave simulator and, hence, it is suitable for predicting the RCS for any loading impedance. Also, it can be investigated to find

Fig. 1 Dipole structure with a wire-diameter of 1 mm

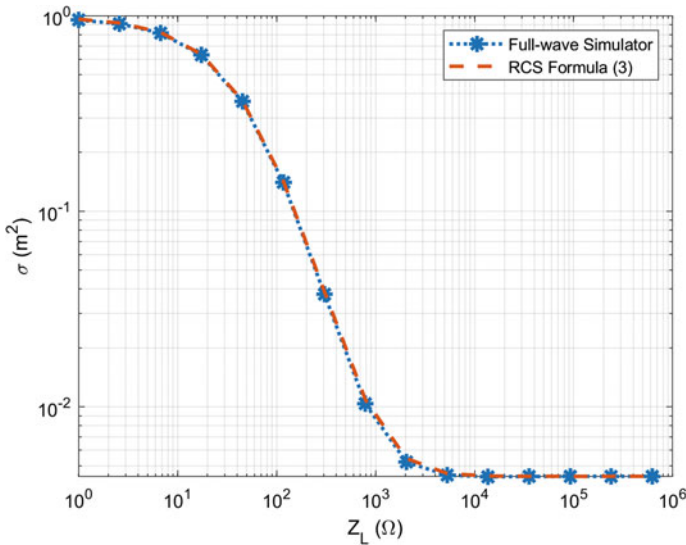
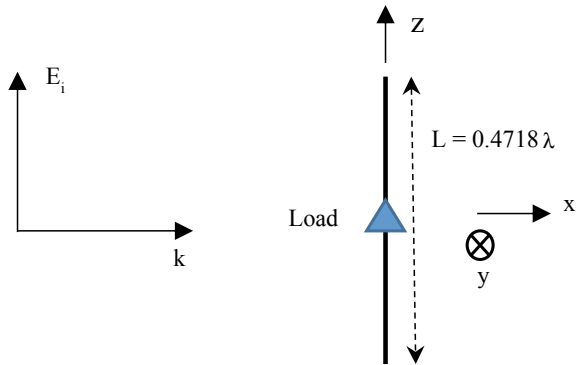


Fig. 2 Accuracy of the RCS formula with load variation

the condition for minimum RCS (MRCS) or zero RCS (ZRCS) as it is presented in the next section.

3 Load Condition for Minimum Radar Cross Section

Equation (3) can be used to find the conditions of the current reflection coefficient and, consequently, to find the load impedance that can make the RCS minimum or zero at a specific direction and frequency. Alternatively, the MRCS/ZRCS loading condition can be derived by starting with Eq. (3) and solving for zero RCS at a specific direction to get the following value

$$Z_{Lzero} = \frac{Z_A E_s^{sc}}{I_{sc} E_r^{1A} - E_s^{sc}} \quad (4)$$

In the above load condition, Z_{Lzero} is the load that satisfies zero scattering RCS at the direction chosen for the values of E_r^{1A} and E_s^{sc} .

4 Application to Antenna Structures

In this section three antenna structures are studied for minimum RCS (MRCS). Utilizing a full wave simulator, the short circuit scattered field and all the required variables of input impedance and unloaded short circuit current are applied into (4) to find the load that fulfils ZRCS for these antennas. Then, all the feasible aspects where the radar cross section can be set to zero using only passive loads are computed and plotted at these aspect regions. Finally, the backward aspect is chosen to be investigated with the zero scattering loading condition and validated using a full wave simulator. Results of the RCS of the antenna with common termination loads (i.e. open circuit (OC), short circuit (SC), and conjugate matched (CM) loads) at the same direction are presented as well. However, if backward directed RCS cannot be set to zero by passive loading, reactive loading is applied to further reduce the RCS.

To quantify the RCS reduction, a RCS reduction factor (μ) is defined as the ratio of the reduced RCS to the RCS with conjugate matched loading for the same antenna structure at the same studied direction aspect. The reduction factor is

$$\mu = 10 \log \frac{\sigma}{\sigma_{cm}} \quad (5)$$

where σ_{cm} is the RCS of the antenna when terminated with the conjugate matched load. EM field scattering depends on the current induced on the antenna structure which is maximum when the antenna is short circuited and it is minimum when the antenna is open circuited, for simple isolated resonant structures. However, if the

structure is more complex with parasite elements and/or reflectors, the scattering may decrease or increase in some directions due to the destructive or constructive interference of scattering from different elements. The comparisons in the shown graphs involve the zero/minimum scattering case with those of OC, SC and CM terminated scattering antennas at two orthogonal planes.

4.1 Scattering from Dipole Antennas

The structure of the cylindrical copper dipole is shown in Fig. 1 with length of 0.4718λ resonating at 283.07 MHz. The feasible aspect region that can be set to zero RCS (ZRCS) for this antenna is derived from Formula (4) and it shows that for dipole antenna, the feasible ZRCS regions are at aspects ($\theta = \{0^\circ, 180^\circ\}$, $\phi = \{90^\circ, 270^\circ\}$). The best feasible passive loading for minimum backward scattering ($\theta = 90^\circ$, $\phi = 180^\circ$) has $Z_{Lzero} = +j1120.0624 \Omega$. After applying this reactive load, the scattering pattern of the dipole antenna is reformed. The comparison of the ZRCS pattern using the reactive loading with that of OC, SC, and CM loading antennas is shown in Fig. 3. It is clear that zero RCS is almost achieved at the backscattering aspect ($\theta = 90^\circ$, $\phi = 180^\circ$).

The dipole antenna belongs to the minimum scattering antennas (MSA) that are almost invisible when they are open-circuit terminated [14]. Scattering from an open circuited dipole is noticeable as compared to its scattering if terminated with the MRCS/ZRCS load. The RCS minimization factor difference between the two cases is calculated with (5) and shown in Table 1.

4.2 Scattering from Three-Element Yagi Antennas

The second studied structure is a three elements Yagi with $L_1 = 0.4198 \lambda$ ($\lambda = 108.85$ cm), $L_2 = 0.4739 \lambda$, $L_3 = 0.4577 \lambda$, $D_1 = 0.1168 \lambda$, $D_2 = 0.1899 \lambda$ and wire-diameter = 1 mm as shown in Fig. 4. This antenna is resonant at frequency of 275.6 MHz and the feasible ZRCS aspect region that can be set to zero scattering by passive loading is plotted in Fig. 5. It is clear that a Yagi structure has a passive load for the backward aspect scattering (i.e. $\theta = 90^\circ$, $\phi = 180^\circ$) which is $Z_{Lzero} = 16.248 + j 4.767 \Omega$. After applying this load, the comparison of scattering at ZRCS loading and OC, SC and CM loadings is plotted in Fig. 6. The zero RCS is practically achieved at backward aspect ($\theta = 90^\circ$, $\phi = 180^\circ$). The minimization level is calculated for the ZRCS load and at unloaded OC antenna using (5) as in Table 2. The RCS attains a minimized value of about -45 dB compared with a conjugate matched antenna and about -55 dB compared with an unloaded OC antenna.

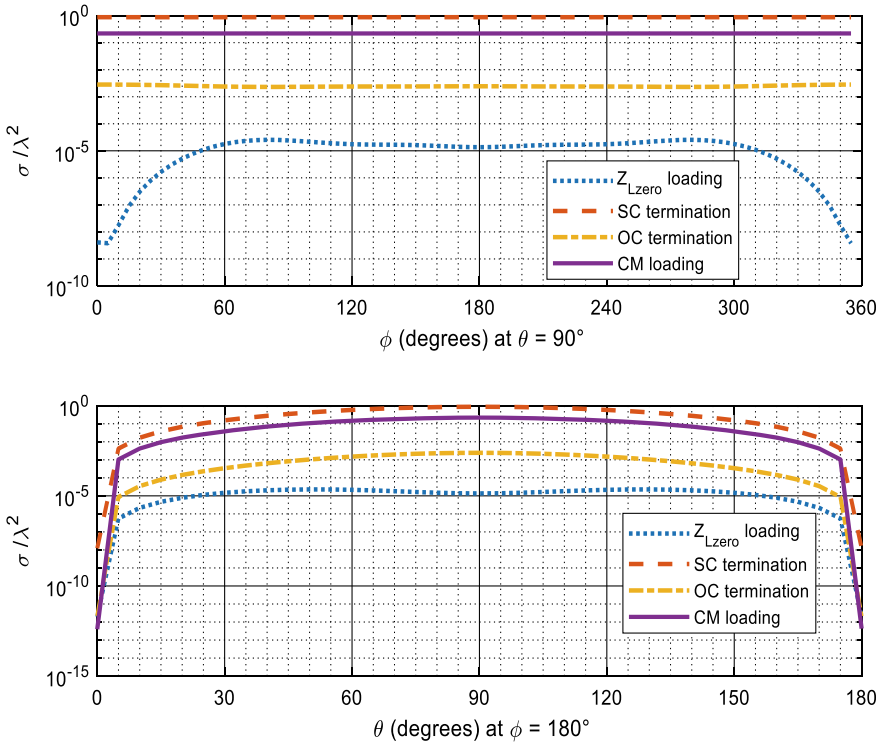
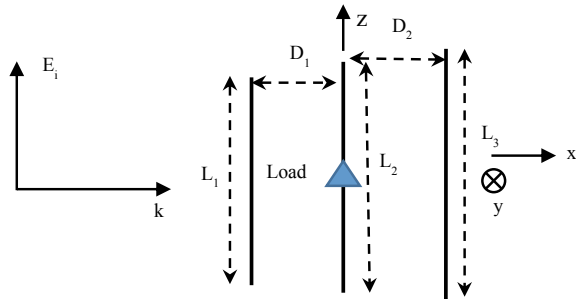


Fig. 3 The dipole RCS patterns at two planes ($\theta = 90^\circ$ plane and $\phi = 180^\circ$ plane) with different load terminations

Table 1 Minimization factor of the dipole at ZRCS and OC loadings

Loading	Applied loading for ($\theta = 90^\circ, \phi = 180^\circ$) aspect (Ω)	Resultant RCS (m^2)	μ (dB)
Equation (4)	$+j 1120.0624$	$12.497E-10$	-82.934
OC termination	Unloaded (open terminal)	$27.356E-4$	-19.532

Fig. 4 Three element Yagi with $L_1 = 0.4198 \lambda, L_2 = 0.4739 \lambda, L_3 = 0.4577 \lambda, D_1 = 0.1168 \lambda, D_2 = 0.1899 \lambda$ and wire-diameter = 1 mm



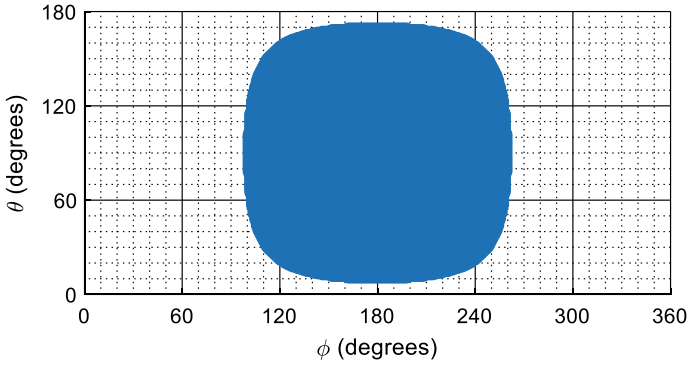


Fig. 5 The three-element Yagi feasible ZRCS region using passive loading

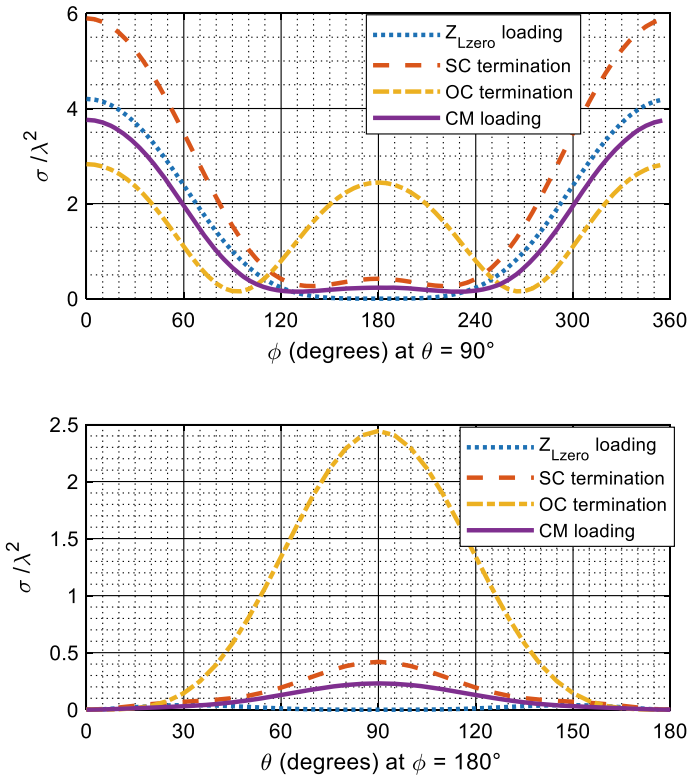
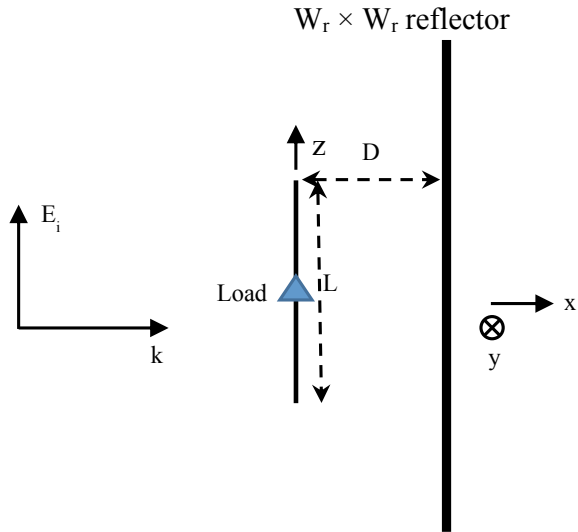


Fig. 6 The Yagi RCS patterns at two planes ($\theta = 90^\circ$ plane and $\phi = 180^\circ$ plane) with different load terminations

Table 2 Minimization factor of the Yagi for ZRCS and OC loadings

Loading	Applied loading for ($\theta = 90^\circ, \phi = 180^\circ$) aspect (Ω)	Resultant RCS (m^2)	μ (dB)
Equation (4)	$16.248 + j 4.767$	$8.3879E-6$	-45.134
OC termination	Unloaded (open terminal)	2.895	10.2465

Fig. 7 Structure of the ground backed dipole with $L = 0.4523 \lambda$ and wire-diameter = 1 mm, $D = 0.2262 \lambda$ with a plane square reflector of width, $W_r = 0.9046 \lambda$ and thickness of 2 mm



4.3 Scattering from Ground Backed Dipole Antennas

The last studied case is for a ground backed dipole illustrated in Fig. 7, which is a cylindrical copper dipole with total length $L = 0.4523 \lambda$ ($\lambda = 110.54$ cm), and diameter 1 mm backed at a distance of 0.2262λ by a $0.9046 \lambda \times 0.9046 \lambda$ perfectly conducting plane reflector with thickness of 2 mm. This antenna is operated at a resonant frequency of 271.4 MHz. The feasible aspect regions that satisfy ZRCS with passive loading is illustrated in Fig. 8. A full wave simulator is used to compute the back-scattering RCS ($\theta = 90^\circ, \phi = 180^\circ$) of this structure with CM and OC loadings and at the derived ZRCS loading of $Z_{Lzero} = 7.023 + j34.129 \Omega$. The backscattering RCS at CM loading is $\sigma = 2.783 m^2$ and after applying the derived minimizing load σ approaches zero as shown in Fig. 9. The comparison between RCS minimization factor for this antenna structure at the ZRCS loading and at OC termination at this aspect direction is given in the Table 3. Almost zero scattering is achieved with a reduction level of -23 dB referred to CM antenna RCS. The OC terminated antenna has positive (μ) which means that its scattering is greater than the CM loaded antenna reference. This is attributed to the weak destructive interactions between the dipole scattering and the ground plate scattering in the desired direction.

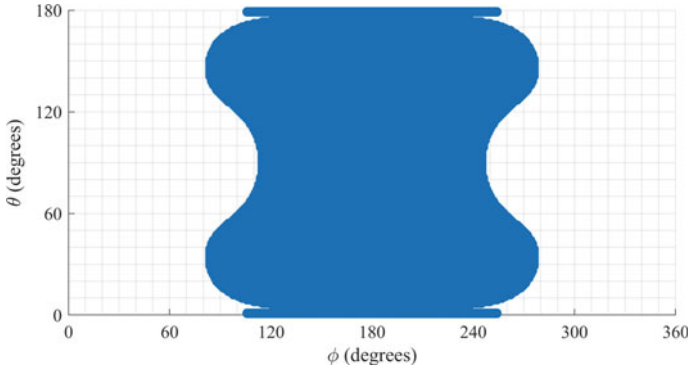


Fig. 8 The ground backed dipole feasible ZRCS region using passive loading

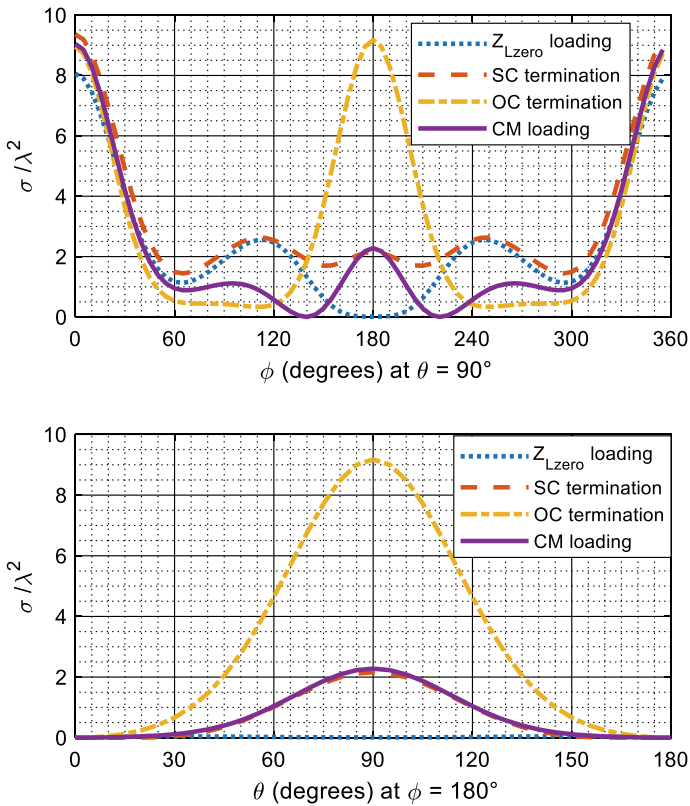


Fig. 9 The ground backed dipole RCS pattern at two planes ($\theta = 90^\circ$ plane and $\phi = 180^\circ$ plane) with different load terminations

Table 3 Minimization factor of the ground backed dipole for ZRCS and OC loadings

Loading	Applied loading for ($\theta = 90^\circ$, $\phi = 180^\circ$) aspect (Ω)	Resultant RCS (m^2)	μ (dB)
Equation (4)	$7.023 + j34.129$	$13.426E-3$	-23.1655
OC termination	Unloaded (open terminal)	11.213	6.052

5 Conclusions

This research exploits the antenna scattering model that decomposes the total scattered fields of an antenna at the desired aspect into two components. The first component is the structural scattered field from the short circuited antenna while the second component is a term proportional to the antenna radiated fields at the transmitting mode weighted by an impedance ratio. Based on that model, this paper derived a load condition that realizes zero or minimum scattering antennas at the desired direction. The derived load condition is applied to three different antenna structures to investigate their RCS behavior with loading impedances and particularly with the ZRCS loading values. This study focused on computing the zero backscattering feasible load regions and then characterized the RCS reduction by a reduction factor defined as the ratio of the reduced RCS to the RCS with conjugate matched loading for the same antenna structure at the same studied aspect. The derived load condition succeeded to attain zero/minimum radar cross section in all studied antenna structures using only passive loadings. The backscattering reduction factor of all antenna cases with the derived loadings is substantially superior than that of open-circuited or arbitrary loaded antennas.

References

1. King R (1944) The receiving antenna. Proc IRE 32:18–34. <https://doi.org/10.1109/JRPROC.1944.232736>
2. Harrington RF (1964) Theory of loaded scatterers. Proc Inst Electr Eng 111:617. <https://doi.org/10.1049/piee.1964.0111>
3. Hansen RC (1989) Relationships between antennas as scatterers and as radiators. Proc IEEE 77:659–662. <https://doi.org/10.1109/5.32056>
4. Collin RE (2003) Limitations of the Thevenin and Norton equivalent circuits for a receiving antenna. IEEE Antennas Propag Mag 45:119–124. <https://doi.org/10.1109/MAP.2003.1241318>
5. Chen KM, Liepa V (1964) The minimization of the back scattering of a cylinder by central loading. IEEE Trans Antennas Propag AP-12, 576–582. <https://doi.org/10.1109/TAP.1964.1138280>
6. Zainud-Deen SH, Malhat HAEA, Shabayek NA (2020) Reconfigurable RCS reduction from curved structures using plasma based FSS. Plasmonics 15:341–350. <https://doi.org/10.1007/s11468-019-01048-y>
7. Braga Filho OM, De Faro Orlando AJ, Migliano ACC (2003) Reduction of the radar cross section of a moderate cylindrical structure using central impedance loading. SBMO/IEEE MTT-S Int Microw Optoelectron Conf Proc 461–465. <https://doi.org/10.1109/imoc.2003.1244904>

8. Kwon DH, Pozar DM (2009) Optimal characteristics of an arbitrary receive antenna. *IEEE Trans Antennas Propag* 57:3720–3727. <https://doi.org/10.1109/TAP.2009.2025975>
9. Huang H, Shen Z, Omar AA (2017) 3-D absorptive frequency selective reflector for antenna radar cross section reduction. *IEEE Trans Antennas Propag* 65:5908–5917. <https://doi.org/10.1109/TAP.2017.2751670>
10. Schindler JK, Mack RB, Blacksmith P (1965) The control of electromagnetic scattering by impedance loading. *Proc IEEE* 53:993–1004. <https://doi.org/10.1109/PROC.1965.4079>
11. Chen KM (1965) Minimization of backscattering of a cylinder by double loading. *IEEE Trans Antennas Propag* 13:262–270. <https://doi.org/10.1109/TAP.1965.1138415>
12. Zainud-Deen SH, El-Shanawany EH, Awadalla KH, Sharshar HA (2005) Elimination of backscattering from scatterer using genetic algorithm. In: National radio science conference, NRSC, proceedings. IEEE Press, Cairo, Egypt, pp 105–114
13. Issamil MN, Hashish EA, Sabry W (2006) Control of scattered field pattern from a straight conducting wire utilizing the equivalent TEM mode theory of radiation and genetic algorithm. In: National radio science conference, NRSC, Proceedings. IEEE Press, Menoufiya, Egypt
14. Kurss H (1965) Minimum-scattering antennas. *IEEE Trans Antennas Propag* 13:671–675. <https://doi.org/10.1109/TAP.1965.1138529>

LTE-M Evolution Towards Massive MTC: Performance Evaluation for 5G mMTC



Adil Abou El Hassan , Abdelmalek El Mehdi , and Mohammed Saber 

Abstract Since emerging fifth generation (5G) wireless network is expected to significantly revolutionize the field of communication, its standardization and design should regard the Internet of Things (IoT) among the main orientations. Long Term Evolution-Machine Type Communication (LTE-MTC/LTE-M) is among the emerging technologies that are promising candidates for 5G wireless network, enabling massive deployment of devices for massive Machine-Type Communication (mMTC). This paper describes LTE-M evolution in recent 3rd Generation Partnership Project (3GPP) releases. A complete evaluation of LTE-M performance against 5G massive MTC requirements is presented. The results analysis of this evaluation show that these requirements can be met but under certain conditions regarding the configuration and deployment of the system. The enhancements provided by the recent 3GPP releases are also discussed.

Keywords Performance evaluation · IoT · 5G · LTE-M · mMTC · 3GPP.

1 Introduction

Internet of Things (IoT) is seen as a driving force behind recent improvements in wireless communication technologies such as third Generation Partnership Project (3GPP) Long Term Evolution (LTE) and 5G New Radio (NR) to meet the expected requirements of various massive Machine-Type Communication (mMTC) applications. The mMTC introduces a new communication era where billions of devices,

A. Abou El Hassan (✉) · A. El Mehdi · M. Saber
SmartICT Lab, National School of Applied Sciences, Mohammed First University, Oujda,
Morocco

e-mail: a.abouelhassan@ump.ac.ma

A. El Mehdi

e-mail: a.elmehdi@ump.ac.ma

M. Saber

e-mail: m.saber@ump.ac.ma

such as remote indoor or outdoor sensors, will need to communicate with each other while connected to the cloud-based system.

It should be recalled that the purpose of the 5G system design is to cover three categories of use cases: enhanced Mobile Broadband (eMBB), massive Machine-Type Communication (mMTC), as well as ultra Reliable Low Latency Communication (uRLLC) which is designed to support critical Machine-Type Communication (cMTC) [1].

The benefit of 5G system is the flexibility of its structure, which allows the use of a common integrated system to cover many use cases, by using a new concept which is network slicing based on SDN (Software-Defined Networking) and NFV (Network Function Virtualization) technologies [2].

LTE-M or LTE-MTC, is low power wide area (LPWA) technology introduced by 3GPP in Release 13 (Rel-13) specification [3]. It supports IoT through lower device complexity with performance appropriate for low and middle-end IoT applications, while allowing the reuse of the LTE installed system.

The 3GPP Rel-13 core specifications for LTE-M were finalized in June 2016 [4]. However, further work on improving LTE-M is ongoing as part of 3GPP. Rel-14 and Rel-15 enhancements were completed respectively in June 2017 and June 2018 [4], while Rel-16 enhancements are underway and scheduled for completion in 2020 [1].

The aim of this paper is to prove that LTE-M technology complements 5G NR by supporting the mMTC deployment. In Sect. 2, an overview of LTE-M is given. In Sect. 3, a complete evaluation of LTE-M performance against 5G mMTC requirements for coverage, throughput, latency, battery lifetime and connection density is presented. According to the results of this evaluation, it is shown that these requirements can be met but under certain conditions regarding the system configuration and its deployment. The enhancements provided by the recent 3GPP releases are also discussed. Finally, Sect. 4 concludes the paper.

2 LTE-M Overview

The overall time structure of the LTE-M frame is identical to that of the LTE frame where one physical resource block (PRB) spans 12 subcarriers, which corresponds to 180 kHz with subcarrier spacing of 15 kHz. LTE-M reuses an identical numerology as LTE, orthogonal frequency division multiple access (OFDMA) is used in downlink while single-carrier FDMA (SC-FDMA) is used in uplink, with subcarrier spacing of 15 kHz in both uplink and downlink [3]. The LTE-M transmissions are limited to a narrowband size 6 PRBs corresponding 1.4 MHz including guard bands. As the LTE system has a bandwidth from 1.4 to 20 MHz, a number of non-overlapping narrowbands can be used if the LTE bandwidth exceeds 1.4 MHz [4]. Up to Rel-14, LTE-M device uses QPSK and 16-QAM modulation schemes with a single antenna for downlink and uplink. Whereas support for 64-QAM in downlink has been introduced in Rel-15 [4].

Two device categories are defined by LTE-M: Cat-M1 and Cat-M2 corresponding to device categories introduced in Rel-13 and Rel-14 respectively. Cat-M1 has only an maximum channel bandwidth 1.4 MHz compared 5 MHz for Cat-M2 [4]. The Cat-M1 is designed for IoT applications that does not require high throughput, such as utilities metering applications, while Cat-M2 can be used to support multimedia IoT applications requiring a relatively high throughput, such as voice over LTE (VoLTE) and User Equipment (UE) positioning [4].

Two coverage enhancement (CE) modes have been standardized in Rel-13: CE mode A, which supports data transmissions with a maximum of 32 repetitions, and CE mode B, which supports a maximum of 2048 repetitions. All LTE-M devices must support CE mode A, however support of CE mode B is optional feature [4].

The following channels and signals are reused by LTE-M in downlink (DL): Physical Downlink Shared Channel (PDSCH), Physical Broadcast Channel (PBCH), Primary Synchronization Signal (PSS), Secondary Synchronization Signal (SSS), Positioning Reference Signal (PRS) and Cell-specific Reference Signal (CRS). MTC Physical Downlink Control Channel (MPDCCH) is the new control channel which has the role of carrying downlink control information (DCI) for uplink, downlink and paging scheduling [3, 4].

Whereas for uplink (UL), the following signals and channels are reused: Demodulation Reference Signal (DMRS), Sounding Reference Signal (SRS), Physical Uplink Shared Channel (PUSCH), Physical Random Access Channel (PRACH) and Physical Uplink Control Channel (PUCCH) which conveys Uplink Control Information (UCI) [3, 4].

For cell access, the UE uses the PSS/SSS signals to synchronize with the evolved Node B (eNB), and PBCH which carries the Master Information Block (MIB) containing new LTE-M specific information. After decoding the MIB and then the new System Information Block for reduced bandwidth UEs (SIB1-BR) carried by PDSCH, the UE initiates the random access (RA) procedure using PRACH and waits for the scheduling uplink grant on MPDCCH [3]. Once the RA procedure has been successfully completed, the reception or transmission of data by the UE can be performed using the PDSCH or PUSCH channels respectively [3].

3 Performance Evaluation and Results Analysis

In this section, a complete evaluation of LTE-M performance is presented against the five 5G mMTC requirements defined by 3GPP in Rel-15 [5]. The evaluated performances corresponding to these requirements are the following: maximum coupling loss (MCL) that define the level of coverage that a system can support, throughput, latency, battery lifetime and connection density.

3.1 Coverage

The MCL depends on the the maximum transmitter power (P_{TX}), the required signal-to-interference-and-noise ratio (SINR), the receiver noise figure (NF) and the signal bandwidth (BW) as follows:

$$MCL = P_{TX} - (SINR + NF + 10 \log_{10}(k.T.BW)) \tag{1}$$

where k is Boltzmann’s constant (1.38×10^{-23} J/K) and T is the ambient temperature of 290K. For thermal noise assumed as white noise with spectral density N_0 at the specified bandwidth BW , the MCL can also be defined with another formula deduced from formula (1) which will be used in coverage calculation:

$$MCL = P_{TX} - (SINR + NF + N_0 + 10 \log_{10}(BW)) \tag{2}$$

N_0 is the thermal noise density which is a constant equal -174 dBm/Hz.

Based on simulation assumptions according to [6] and using (2) to calculate MCL, Table 1 illustrates the LTE-M channels coverage to achieve the MCL of 164 dB which corresponds to 5G mMTC coverage requirement to be supported by low-cost and ultra-low complexity IoT devices [5]. The required acquisition time, transport block size (TBS) and block error rate (BLER) associated with each channel to achieve the targeted MCL of 164dB are also shown in Table 1. From the table, it is seen that in order to achieve the MCL of 164 dB at the adequate BLER, the technique of time repetitions of the simulated channels must be used. However, in order to achieve the MCL of 164 dB, PUSCH requires the longest acquisition time which makes it the limiting channel in terms of coverage performance.

Table 1 Downlink and uplink coverage of LTE-M

Simulation assumptions	Downlink physical channel			Uplink physical channel		
	PBCH	MPDCCH	PDSCH	PRACH	PUSCH	PUCCH
TBS (Bits)	24	18	328	–	712	1
Aquisition time (ms)	800	256	768	64	1536	64
BLER (%)	10	1	2	1	2	1
Max transmit power (dBm)	46	46	46	23	23	23
Transmit power/carrier (dBm)	39.2	36.8	36.8	23	23	23
Noise figure NF (dB)	7	7	7	5	5	5
Channel bandwidth (kHz)	945	1080	1080	1048.75	30	180
Required SINR (dB)	-17.5	-20.8	-20.5	-32.9	-16.8	-26
MCL (dB)	163.95	164.27	163.97	164.7	164	165.45

3.2 Throughput

The downlink and uplink throughputs are obtained according to the PDSCH and PUSCH transmission time intervals issued from PDSCH and PUSCH scheduling cycles respectively and the acquisition times shown in Table 1.

Figure 1 depicts PDSCH scheduling cycle according to [6], where the MPDCCH user-specific search space is configured with a maximum repetition factor R_{max} of 256 and a relative starting subframe periodicity G of 1.5.

Given a 2% PDSCH BLER, TBS of 328 bits and overhead (OH) of 5 bytes corresponding to radio protocol stack, a MAC-layer throughput (THP) in downlink of 245 bps is obtained with the following formula:

$$THP = \frac{(1 - BLER)(TBS - OH)}{MPDCCH \text{ Period}} \tag{3}$$

Regarding the uplink throughput calculation, Fig. 2 illustrates the PUSCH scheduling cycle according to [6] which ensures a MAC-layer THP in uplink of 343 bps from (3) with a 2% PUSCH BLER, TBS of 712 bits and overhead OH of 5 bytes.

As part of 3GPP Rel-15, 5G mMTC requires that the throughput supported at the MCL of 164 dB must be at least 160 bps [5]. As can be seen, the 5G mMTC target for throughput is achieved in both downlink and uplink. Noteworthy is that the BLER targets associated with each channel shown in Table 1 mandate the required acquisition times. Therefore by choosing an operation with PDSCH and PUSCH BLER levels higher than 2% and the use of the new Cat-M2 device supporting a larger TBS of 6968 bits and 4008 bits in uplink and downlink respectively, in addition to the configuration of Hybrid Automatic Repeat reQuest-Acknowledgment (HARQ-ACK) bundling [4], should further improve throughput levels.

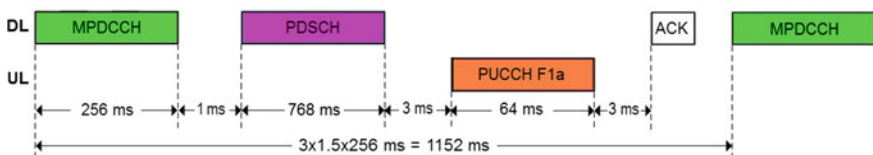


Fig. 1 PDSCH scheduling cycle ($R_{max}=256$; $G=1.5$) at the MCL

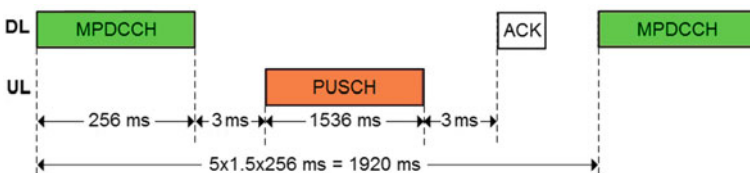


Fig. 2 PUSCH scheduling cycle ($R_{max} = 256$; $G = 1.5$) at the MCL

3.3 Latency

The latency should be evaluated in two cases: the first case is to use the Radio Resource Control (RRC) Resume procedure depicted in Fig. 3, while the second case consists in use of new Early Data Transmission (EDT) procedure introduced in 3GPP Rel-15 and depicted in Fig. 4. When the device has small data to transmit and it is in RRC-Idle mode, it can transmit its data without switching to RRC-Connected mode by using the EDT procedure. The latency evaluation is based on the radio related assumptions according to [6], and using the data and signaling flows corresponding at RRC Resume and EDT procedures.

The packet sizes used and latency evaluation at the MCL of 164 dB are shown in Table 2 [6].

By use of the RRC Resume procedure we obtain a latency of 7.7s while the EDT procedure allows us to obtain a latency of only 5s. What we can conclude is that

Fig. 3 LTE-M RRC resume procedure

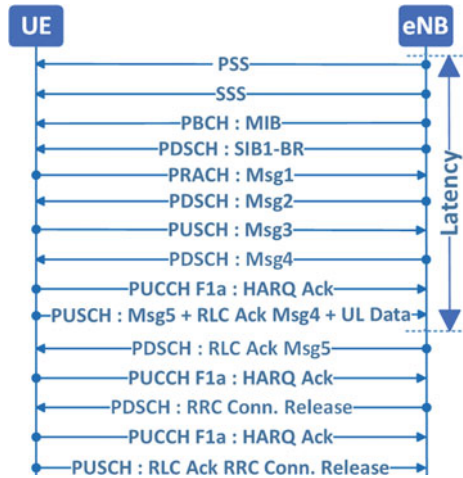


Fig. 4 LTE-M EDT procedure

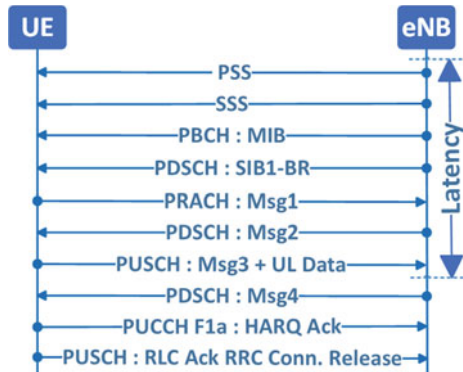


Table 2 Packet sizes and evaluation results of LTE-M latency

RRC resume procedure		EDT procedure	
Random access response: Msg2	7 bytes	Random access response: Msg2	7 bytes
RRC conn. resume request: Msg3	7 bytes	RRC conn. resume request: Msg3 + UL report	11 + 105 bytes
RRC conn. resume: Msg4	19 bytes	RRC conn. release: Msg4	25 bytes
RRC conn. resume complete: Msg5 + RLC Ack Msg4 + UL report	22 + 200 bytes		
RRC conn. Release	18 bytes		
Latency	7.7 s	Latency	5 s

5G mMTC target of 10s latency at the MCL of 164 dB defined in 3GPP Rel-15 [5] is achieved, for both RRC Resume and EDT procedures. However, the best latency obtained of 5 s using EDT procedure is mainly due to the multiplexing of the user data on PUSCH channel with the Msg3 as shown in Fig. 4.

3.4 Battery Life

The RRC resume procedure is used in battery life evaluation instead of the EDT procedure since EDT procedure does not supports uplink TBS of size larger than 1000 bits. Battery life is evaluated for a device of 23 dBm power class with an 5 Wh battery providing better coverage and reduced power consumption than 20 dBm power class. Whereas the eNB transmitting power is 46 dBm with use of 2 antennas for transmission and 2 antennas for reception according to [7]. Furthermore, the packet flow used to evaluate LTE-M battery life is the same as shown in Fig. 3, while the assumed traffic model according to Rel-14 scenario and device power consumption levels are given in Table 3 according to [7].

Noteworthy that 5G mMTC requires battery life beyond 10 years at the MCL of 164 dB, using infrequent small packet transmissions and supposing an energy storage capacity of 5 Wh [5]. Under the assumptions used in battery life evaluation according to [7], a battery life is estimated at 8.8 years and does not fulfills the 5G mMTC target. In order to significantly increase battery life, the uplink throughput should be improved by the increase of the number of base station receiving antennas, thereby reducing UE transmission time. Therefore if the number of base station receiving antennas is 4 instead of only 2 according to [6], a battery life is estimated at 11.9 years which fulfills the 5G mMTC target.

Table 3 Assumptions for LTE-M battery life evaluation.

<i>Message format</i>	
UL report	200 bytes
DL application acknowledgment	20 bytes
Report periodicity	Once every 24h
<i>Device power consumption</i>	
Transmission	500 mW
Reception	80 mW
Idle-light sleep	3 mW
Idle-deep sleep	0.015 mW

3.5 Connection Density

The 5G mMTC requirement on connection density which is also part of the International Mobile Telecommunication requirements for 2020 and beyond (IMT-2020), requires the support of one million devices per square kilometer in four different urban macro scenarios. These four scenarios are based on two channel models (UMA A) and (UMA B) and two distances of 500 and 1732 m between adjacent cell sites denoted by ISD (inter-site distance) [8].

Based on the non-full buffer system level simulation for evaluating connection density according to [9], Fig. 5 shows the latency required at 99% reliability to deliver 32 bytes payload as a function of the connection requests intensity (CRI) to be supported, corresponding to the number of connection requests per second, cell and PRB. Noteworthy is the latency in Fig. 5 is defined as the delay between the cell access initiated by the device and the successful receipt of UL data by the eNB.

Knowing that each UE must submit a connection request to the system periodically, we can determine the connection density to be supported (CDS) per cell area using the following formula:

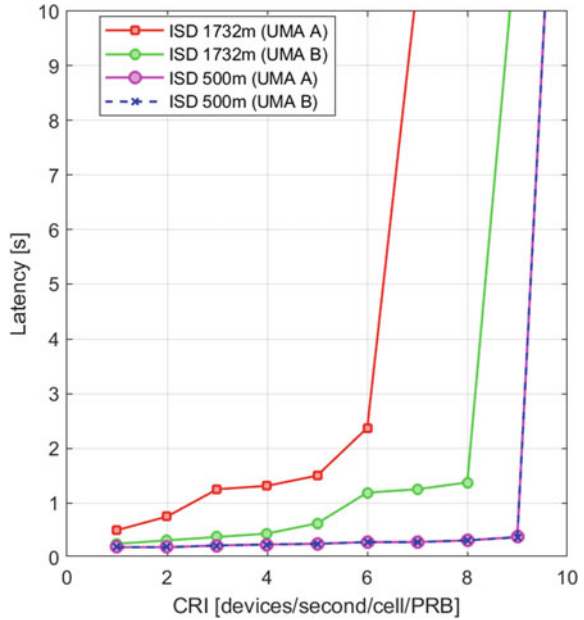
$$CDS = \frac{CRI \cdot RP}{A} \tag{4}$$

where RP is periodicity of connection requests given in seconds and cell area A is calculated by the following formula:

$$A = ISD^2 \cdot \sqrt{3} / 6$$

To evaluate the connection density per narrowband and square kilometer depicted in Fig. 6 and corresponding to the overall number of devices that successfully transfer a payload of 32 bytes accumulated over two hours with the required latency, the CDS

Fig. 5 Intensity of connection requests in relation to latency



values are obtained from (4) using the CRI values of Fig. 5, a periodicity of connection requests of two hours and a scaling of a factor 6 corresponding to narrowband (NB) of 6 PRBs.

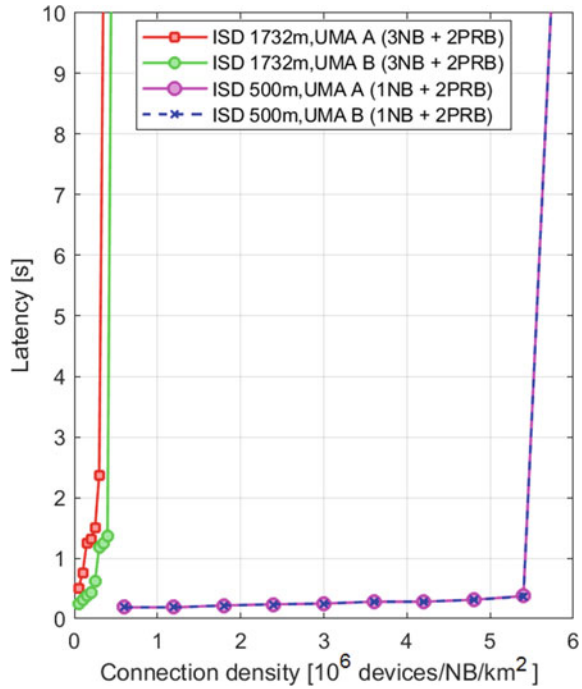
As shown in Fig. 6, in 500m ISD scenario a single narrowband can support up to 5.68 million devices within the 10-s latency limit, by addition of 2 further PRBs with a configuration at the bandwidth limits of LTE system to transmit PUCCH. For the 1732m ISD and (UMA B) scenario, cell size is a 12 times larger which explains a LTE-M carrier can only support 445 000 devices which corresponds to a connection density 12 times lower than that supported for the 500m ISD scenario with a maximum latency of 10s.

Also, to further improve connection density, sub-PRB resource allocation for uplink that has been introduced in 3GPP Rel-15 can be used.

4 Conclusion

To conclude, this paper shows that the five targets of 5G mMTC are achieved by LTE-M. However, the results of the evaluations show that the performances are achieved except under certain conditions regarding system configuration and deployment, such as the number of repetitions configured for channels transmission, the number of antennas used by the base station and the density of base stations. In addition, 3GPP Rel-15 offers the possibility to introduce 5G NR in carriers where LTE-M devices

Fig. 6 Connection density in relation to latency



are in service, without compromising the quality of services offered by massive IoT applications. Thus it can be concluded that LTE-M is promising technology of the 5G system for massive IoT.

References

1. Ghosh A, Maeder A, Baker M, Chandramouli D (2019) 5G evolution: a view on 5G cellular technology beyond 3GPP release 15. *IEEE Access* 7:127639–127651. <https://doi.org/10.1109/ACCESS.2019.2939938>
2. Barakabitze AA, Ahmad A, Mijumbi R, Hines A (2020) 5G network slicing using SDN and NFV: a survey of taxonomy, architectures and future challenges. *Comput Netw* 167:106984. <https://doi.org/10.1016/j.comnet.2019.106984>
3. Rico-Alvarino A, Vajapeyam M, Xu H, Wang X, Blankenship Y, Bergman J, Tirronen T, Yavuz E (2016) An overview of 3GPP enhancements on machine to machine communications. *IEEE Commun Mag* 54(6):14–21. <https://doi.org/10.1109/MCOM.2016.7497761>
4. Ratasuk R, Mangalvedhe N, Bhatoolaul D, Ghosh A (2017) LTE-M evolution towards 5G massive MTC. In: 2017 IEEE Globecom workshops (GC Wkshps), pp 1–6. <https://doi.org/10.1109/GLOCOMW.2017.8269112>
5. 3GPP (2018) TR 38.913, 5G: study on scenarios and requirements for next generation access technologies Release 15, version 15.0.0. Technical report. ETSI. https://www.etsi.org/deliver/etsi_tr/138900_138999/138913/15.00.00_60/tr_138913v150000p.pdf

6. Ericsson (2019) R1-1907398, IMT-2020 self evaluation: mMTC coverage, data rate, latency & battery life. Technical report. 3GPP TSG-RAN WG1 meeting #97. <https://portal.3gpp.org/ngppapp/CreateTDoc.aspx?mode=view&contributionUid=R1-1907398>
7. Ericsson (2017) R1-1706161, early data transmission for MTC. Technical report. 3GPP TSG RAN1 meeting #88bis. <https://portal.3gpp.org/ngppapp/CreateTDoc.aspx?mode=view&contributionUid=R1-1706161>
8. ITU-R (2017) ITU-R M.2412-0, guidelines for evaluation of radio interface technologies for IMT-2020. Technical report. International Telecommunication Union (ITU), Oct 2017. https://www.itu.int/dms_pub/itu-r/opb/rep/R-REP-M.2412-2017-PDF-E.pdf
9. Ericsson (2019) R1-1907399, IMT-2020 self evaluation: mMTC non-full buffer connection density for LTE-MTC and NB-IoT. Technical report, 3GPP TSG-RAN WG1 meeting #97, May 2019. <https://portal.3gpp.org/ngppapp/CreateTDoc.aspx?mode=view&contributionUid=R1-1907399>

Communication Optimization Approach for S-Band LEO CubeSat Link Budget



Mohammed Amine El Moukalafe and Khalid Minaoui

Abstract CubeSats has evolved a lot since their first appearance in 1999. Indeed, we see that small satellites have emerged in several areas that were exclusive to large satellites. However, this miniaturization is costly in term of size and energy which are crucial for high data rate communication systems. Hence, the need to optimize communication link parameters for energy efficiency. Previous works on link budget analysis adjust modulation and coding schemes on worst cases in order to guarantee a robust communication link between CubeSats and Grounds Stations. Thus, penalizing the data rate. In our work we start by establishing a classic link budget on S-band transceivers, then we study the impact of communication conditions improvement on data rate using Variable Coding and Modulation (VCM) approach. Our results have demonstrated a notable performance gain from applying VCM technique to a Low Earth Orbit (LEO) CubeSat link budget.

Keywords Cubesat · Nano-satellite · Transceivers · Link budget · Data rate · Variable coding and modulation

1 Introduction

Nano-satellites, also called CubeSats, are small artificial satellites that are built of multiples of 10 cm^3 cubic units. This technology appeared 20 years ago and mainly attracted researchers interest due to their low cost manufacturing compared to conventional satellites. Nano-satellites were firstly used by California Polytechnic State University and Stanford University in the United States in 1999. Later, space companies also started using them for their advantages [1]. Nano-satellites can be sent with large satellites when launched into orbit, which allows universities around the world to conduct scientific experiment at low cost. Lately nano-satellites are dedicated either to observe and measure terrestrial environment or to test new technologies in space. Nowadays, more than 2500 CubeSats are currently in use or under devel-

M. A. El Moukalafe (✉) · K. Minaoui
Faculté des Sciences de Rabat, Université Mohammed V, Rabat, Morocco
e-mail: elmoukalafe.medamine@gmail.com

© Springer Nature Singapore Pte Ltd. 2022
S. Bennani et al. (eds.), *WITS 2020*, Lecture Notes in Electrical Engineering 745,
https://doi.org/10.1007/978-981-33-6893-4_91

1001

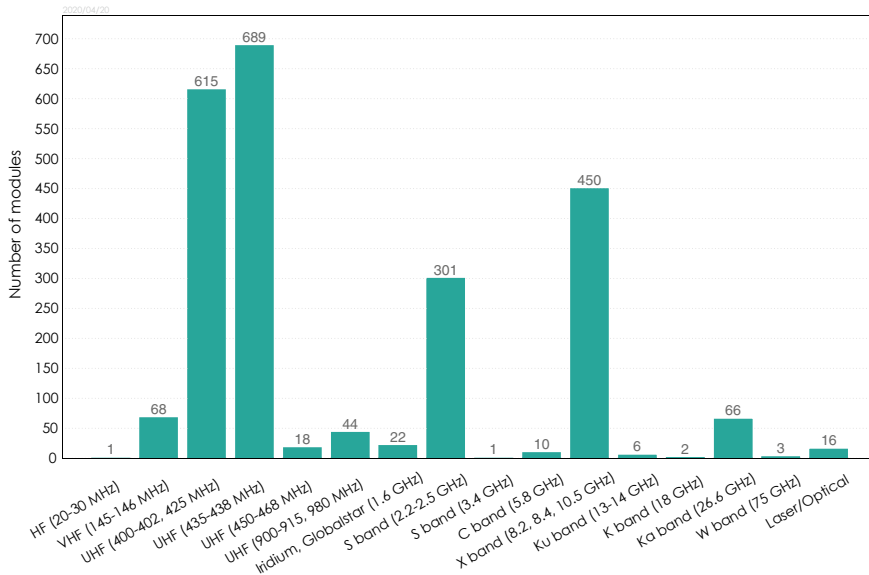


Fig. 1 Frequencies and bands used in CubeSat missions [2]

opment [2]. The emergence of such small satellites is due to the miniaturization of embedded systems empowered by Commercial Off-The-Shelf (COTS) products. COTS components present a lot of advantages in space like flight heritage, simplicity in communication with On-Board Computers (using I2C protocol) and the support of AX.25 protocol, widely used by the amateur radio community. Regarding the ascension of CubeSats, scientists are now focusing on improving the quality of on-board components. One of the main challenges is boosting the performance of communication systems, thus to allow the use of high resolution imaging for Earth observation, to put CubeSats in high Earth orbits, and to open up the opportunity for small satellites to participate in deep space missions [3, 4]. Such functionalities were atypical for small satellites few years ago. In order to set the appropriate frequency band for CubeSat’s communication sub-system, we must first refer to the International Telecommunication Union (ITU) that is responsible for coordinating the shared global use of the radio spectrum. Figure 1 shows that the most used frequencies for CubeSats are the Ultra High Frequency (UHF) bands. In the last years, we see particular interest for high frequencies (especially X and Ka bands) as it allows high data rate capabilities. Therefore, using such frequencies increases the global cost of CubeSats missions. One solution is to try to take advantage from lower frequencies using adequate modulation and coding methods. In this paper, UHF band is used for Remote Control (RC) and TeleMetry (TM) link seeing the low need of data rate, while S band is intended for exchanging large data with the CubeSat.

Previous work on link budget are based on worst case parameters in order to guarantee a reliable communication link [5, 6]. Such approach put safety in first

position because it prevents losing communication with the satellite. However, this approach overlooks the favorable cases, thus, penalizing the data rate. In this paper we start by an introduction in Sect. 1. Section 2 presents the fundamentals of link budget calculation in order to understand the parameters that can be improved. Section 3 presents findings of our paper and the application of Variable Coding and Modulation method to optimize data rate. In Sect. 4, we present limitations and future work and then we conclude our paper.

2 Methodology

In order to study complex communication systems, we need to build mathematical models of transceivers, antennas and radio wave propagation, especially if we want to focus on key aspects that influence the quality of the link. Also, a radio link simulation will be implemented in AGI STK software for more detailed calculations. We start from geometric background so that distances and angles can be comprehensive to model the motion of the CubeSat. Then, we include different types of communication losses so we can use all these parameters in the link budget. The calculation of the distance between the CubeSat and the Ground Station, also called Slant range s in Fig. 2, is essential in order to establish the first influencing parameter of our radio communication system. Indeed, by increasing the distance between the transmitter and the receiver, we end up with large path losses. We calculate the Slant range s by using the Law of cosines. Therefore, it becomes easier to determine the dependence between the slant range s , the altitude of the CubeSat h and the ground antenna elevation El in Eq. (1), where R_E is Earth radius.

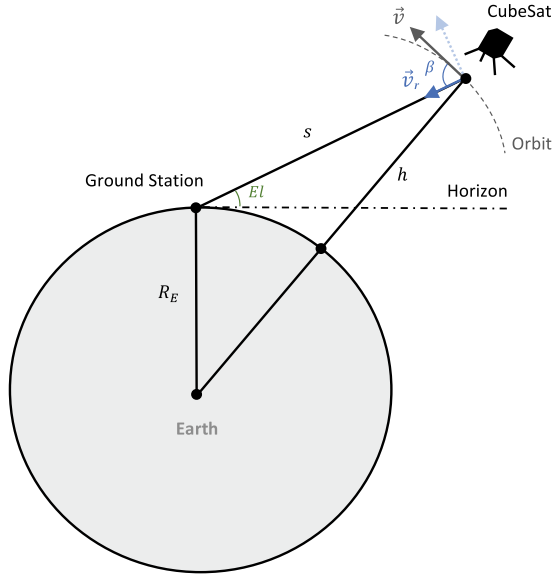
$$s = R_E \cdot \left[\sqrt{\left(\frac{R_E + h}{R_E}\right)^2 - \cos(El)^2} - \sin(El) \right] \tag{1}$$

Also, the high velocity of Low Earth Orbit (LEO) satellites (about 7.58 km/s in our application) leads to a significant Doppler shift Δf , which is a deviation of the received signal frequency f from the emitted signal frequency f_0 (or carrier frequency). It is estimated at approximatively ± 50 KHz for S-band LEO satellites using Eq. (2), where v_r is the velocity of the CubeSat transmitter relative to the Ground receiver and c is the light speed.

$$\Delta f = f - f_0 = \frac{v_r}{c} \cdot f_0 \tag{2}$$

We can calculate the radial component v_r using Eq. (3), where v is the CubeSat velocity (We assume here that the Earth is a uniform spherical body), μ_E is the Earth standard gravitational parameter and β is the angle between the CubeSat velocity vector and the direction to the ground station.

Fig. 2 CubeSat motion and geometry with respect to Earth Ground Station



$$v_r = v \cdot \cos(\beta) = \left(\sqrt{\frac{\mu_E}{R_E + h}} \right) \cdot \left(\frac{R_E}{R_E + h} \cdot \cos(El) \right) \tag{3}$$

Therefore, by setting, in Eq. (4), the CubeSat altitude h at 560 km (LEO), the carrier frequency f_0 at 2250 MHz (S-Band) and the Ground Station antenna minimum elevation El_{min} at 5° (this mask represents the value of the antenna elevation in all azimuth directions, in order to start and to stop CubeSat access in each pass), we end up with a maximum Doppler deviation $|\Delta f_{max}|$ of approximately 105 kHz. In this study, we use GOMspace trancivers with Doppler Shift Compensation (DSC) technology adapted to such deviation values [7]. Consequently, we don't include DSC methods in our study.

$$\Delta f = \left(\frac{R_E \cdot (\mu_E)^{1/2} \cdot f_0}{c \cdot (R_E + h)^{3/2}} \right) \cdot \cos(El) \tag{4}$$

Figure 3 shows a simplified radio communication system where the principal components are illustrated. First, a transmitter uses electrical power to form radio waves, which could include feed losses. These radio waves are communicated to the transmitted antenna that drives energy in different directions according to its gain pattern. The radiated radio waves propagates through space, which includes propagation loss like atmospheric effects. On the other side, a receiver detects the radio waves delivered by its antenna. We include in our study free space loss L_{fs} calculated in Eq. (5), atmospheric loss detailed in IUT-R P.676 and IUT-R P.618 recommendations (L_{atm} and L_{rain}), signal polarization loss L_{pol} and pointing losses ($L_{pointingSAT}$ and $L_{pointingGS}$) included in Eqs. (6) and (8). In most cases, the choice of a circular polarization is recommended for space systems given the high attenuation of linear polarizations

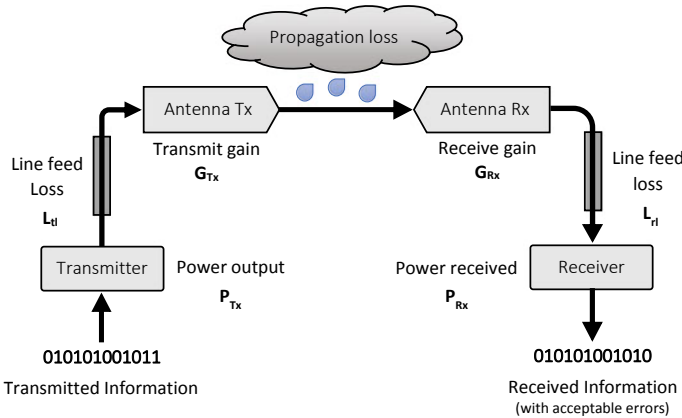


Fig. 3 A block diagram of radio communication system

by the atmosphere [8]. It is also important to note that Ground Station antennas must compensate the few energy on board the CubeSats. Thus, by using high gain ground antennas, their beamwidths become very small. Therefore, small pointing errors can lead to large losses. For this reason, we must have an efficient satellite tracking method on the Ground Station using accurate orbit restitution.

$$L_{fs(dB)} = 10 \log_{10} \left(\frac{4\pi s}{\lambda} \right)^2 = 32.45 + 20 \log_{10} s_{km} + 20 \log_{10} (f_{MHz}) \quad (5)$$

$$L_{tot(dB)} = L_{pointingSAT} + L_{pol} + L_{fs} + L_{atm} + L_{rain} \quad (6)$$

In Transmitter side, impedance matching is important in order to maximize the power transfer to the antenna. Indeed, the output impedance of the radio transmitter has to be equal to the antenna input impedance so that signal reflection to the source will be close to zero. If not, impedance mismatch results in standing waves along the transmission line. This is measured by Voltage Standing Wave Ratio (VSWR) where AC voltages irregularities along the transmission line are estimated. In this study we assume that the mismatch loss is equal to 0.12 dB (VSWR equal to 1.4), which is equivalent of saying that 97.2% of the power is effectively transmitted to the antenna [9].

The overall power output of the transmitter, or the Effective Isotropic Radiated Power (EIRP), is calculated in Eq. (7).

$$EIRP_{(dBW)} = P_{Tx} - L_{tl} + G_{Tx} \quad (7)$$

On the other side, the power received at the input of the Low Noise Amplifier (LNA) is calculated in Eq. (8).

$$P_{Rx(dBW)} = EIRP + G_{Rx} - L_{Tot} - L_{pointingGS} - L_{rl} \quad (8)$$

It is important to consider the effective Noise temperature of the receiver because it's a limiting factor on the information that can be transmitted over a radio communication link. Noise is often characterized as having a uniform power density, where the noise spectral density No relates to the receiver temperature T via Boltzmann's constant k . We can therefore calculate the Signal-to-Noise Power Density C/No in Eq. (9).

$$C/No_{(dBHz)} = P_{Rx} - 10 \log_{10}(k \cdot T) \quad (9)$$

Finally, the modulation and Forward Error Correction (FEC) schemes will determine the levels that the system must meet in order to reach the Bit-Error-rate (BER) performance via $Eb/No_{Threshold}$ in Eq. (10), where R is data rate. In this study, we consider a specified BER of 10^{-5} .

$$Margin_{(dB)} = C/No - 10 \log_{10}(R) - Eb/No_{Threshold} \quad (10)$$

After examining 5 S-band solutions, we choose, for our high data application, the NanoCom SR2000 CubeSat transceiver with the ANT2000-DUP-215 S-band patch antenna from GOMspace because they can reach high data rates (up to 2 Mbps) in full duplex. On the other hand, we use the NanoCom GS2000 Ground Station transceiver matched with the NanoCom AS2000 parabolic antenna. Also, for RC and TM links, we choose GOMspace UHF transceivers [7].

We first established a classic link budget using Eqs. (6)–(10) implemented in AMSAT IARU Excel Link Model [9] and AGI STK software. We have also introduced 3 scenarios in order to understand the behavior of the radio link by varying different condition parameters. The main difference between these scenarios is detailed in Table 1 where a color code is assigned to each case. In adverse case (red) we use the worst conditions in order to consider any side effects in our communication link. The main purpose of such approach is to assure an uninterrupted radio communication. However, these conditions are mostly overestimated. For example, we consider here 0.5 dB of rain effects loss and an attenuation of 3 dB on CubeSat and Ground Station antennas pointing (i.e. half of power is effectively radiated) [10]; In nominal case (blue) we consider moderate conditions, however, overestimating CubeSat and Ground Station pointing antennas errors and atmospheric losses; In favorable case (green) we take into consideration only atmospheric and free space losses. Such approach is very important to understand the impact of good radio conditions in link margin.

Then, we study the influence of CubeSat altitude h and Ground Station minimum elevation El_{min} in order to increase link margin. Finally, we introduce Variable Coding and Modulation (VCM) method which increases data rate by dynamically changing the modulation scheme and forward error correction. The advantage of VCM method is that high-order modulations are used when link conditions are favorable, in order to maximize the data transfer. While, in poor link conditions, robust modulation and FEC are used to increase the link margin. VCM techniques are efficient when

Table 1 Summarized link budget for S-band CubeSat Downlink

Link budget (S-band Downlink)	Nominal	Adverse	Favorable
CubeSat			
Transmitter power output (dBW)	2.0	2.0	2.0
Antenna gain (dBi)	8.0	8.0	8.0
Voltage standing wave ratio	1.40	1.40	1.40
Total transmission losses (dB)	1.3	1.3	1.3
Effective isotropic radiated power (dBW)	8.8	8.8	8.8
Downlink path			
Frequency (MHz)	2250.0	2250.0	2250.0
Minimum elevation (deg)	5.0	5.0	5.0
CubeSat height above surface (Km)	560.0	560.0	560.0
Slant range (Km)	2230.9	2230.9	2230.9
Free space loss (dB)	166.5	166.5	166.5
CubeSat antenna pointing bias (deg)	15.0	32.5	0.0
CubeSat antenna pointing loss (dB)	1.0	3.0	0.0
Polarization losses (dB)	1.0	2.0	0.06
Atmospheric and rain losses (dB)	1.5	2.5	1.0
Total link loss (dB)	170.0	174.5	167.5
Ground station			
Isotropic signal level at ground station (dBW)	-161.2	-165.7	-158.8
Ground station antenna pointing bias (deg)	2.2	3.8	0.0
Antenna pointing loss (dB)	1.0	3.0	0.0
Antenna gain (dBi)	26.0	26.0	26.0
Total reception line losses (dB)	1.6	1.6	1.6
Effective noise temperature (K)	697.0	767.0	628.0
System link margin			
Signal-to-noise power density C/No (dBHz)	62.3	55.4	66.2
System desired data rate (Kbps)	500	500	500
Command system Eb/No (dB)	5.3	-1.6	9.2
Demodulation method selected	QPSK		
Forward error correction coding used	Cv(R = 1/2, K = 7)+ RS(255, 223)		
System specified bit-error-rate	10 ⁻⁵	10 ⁻⁵	10 ⁻⁵
Demodulator implementation loss (dB)	0.5	1.0	0.0
Eb/No threshold (dB)	6.5	7.0	6.0
Link margin (dB)	-1.2	-8.6	3.2

the radio link can be predicted with accurate modeling. This method has proved its efficiency in NASA’s experimental link SCaN Testbed on the International Space Station (ISS) [11]. In order to improve the VCM performance, a hysteresis algorithm is implemented to prevent the VCM method from rapid transitions. We have chosen 6 dB for Up Threshold and 3 dB for Down Threshold, hence, the On-board transceiver will wait for additional margin before changing states, keeping link margin around 3–6 dB, which is recommended for LEO CubeSat’s communication systems. In this study, we only focus on varying data rate because the NanoCom SR2000 transceiver uses only Quadrature Phase Shift Keying (QPSK) modulation scheme.

3 Results and Discussions

S-band Downlink link margin estimated in STK software (Fig. 4), shows that results are much closer to the favorable case calculated on AMSAT IARU Link Model. This is justified firstly because STK does not take into consideration antennas pointing errors. Secondly, we oversized some losses in Adverse and Nominal link budget in order to be sure that the link is functional. We also notice that link margin on S-band Downlink is tighter than S-band Uplink because the power on board the CubeSat and embedded antenna size remains limited. Therefore, in order to increase the link margin in S-band Downlink, we tried to variate the CubeSat altitude h and the minimum ground antenna elevation El_{min} as we see in Table 2. Firstly, we notice a gain of only 1.9 dB by decreasing the CubeSat altitude by 160 km. This solution is not interesting because the choice of CubeSat’s orbit remains on Launch opportunities. Also, decreasing CubeSat altitude leads to less lifespan [12]. Secondly, by increasing the minimum elevation by 15° , we notice a gain of almost 4.6 dB. This choice is

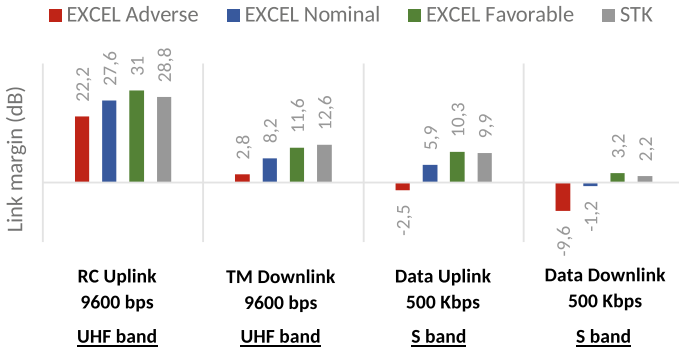


Fig. 4 Comparative link margin results for LEO CubeSat

Table 2 Link margin for S-band CubeSat Downlink for different cases

	500 kbps			1 Mbps		
	Adverse (dB)	Nominal (dB)	Favorable (dB)	Adverse (dB)	Nominal (dB)	Favorable (dB)
$h = 560 \text{ km}$ $El_{min} = 5^\circ$	-9.6	-1.2	3.2	-12.6	-4.2	0.2
$h = 400 \text{ km}$ $El_{min} = 5^\circ$	-7.7	0.7	5.1	-10.7	-2.3	2.1
$h = 560 \text{ km}$ $El_{min} = 20^\circ$	-5.0	3.4	7.8	-8.0	0.4	4.8
$h = 400 \text{ km}$ $El_{min} = 20^\circ$	-2.5	5.9	10.3	-5.5	2.9	7.3

actually time costly. Indeed, by using 20° as minimum elevation, we will only have 2 (or 3 depending on Ground Station location) short CubeSat passes (or visibilities) per day (about 4 min each pass) instead of 4 longer passes per day (between 7 and 10 min for each pass). In this study, the Ground Station is located in Rabat (Morocco), this limits our CubeSat visibilities to only 2 per day when using 20° of minimum elevation. Finally, doubling the communication data rate leads to decrease the overall link margin by 3 dB.

By using the VCM method, we manage to adapt data rate according to the link margin, which is improved for high elevations. We apply it on a 24 h scenario on STK. We see in Fig. 5 that we manage to reach a speed of 1.5 Mbps instead of 500 kbps while keeping link margin between approximately 2.5–6 dB in daily visibilities (data rate step used is 500 Kbps according to the NanoCom GS2000 Ground transceiver). Therefore, the VCM approach allowed us to get more downloadable data from the CubeSat, keeping a minimum elevation of 5° , compared to a conventional link budget. Indeed, by changing dynamically data rate depending on Ground Station elevation, we increase data that can be downloaded from the CubeSat by 116 MB per day (Table 3).

To do this calculation, we apply a data coding efficiency of 87 % using Viterbi Convolutional code Cv ($R = 1/2, K = 7$) and Reed Solomon code R.S. (255, 223) [7].

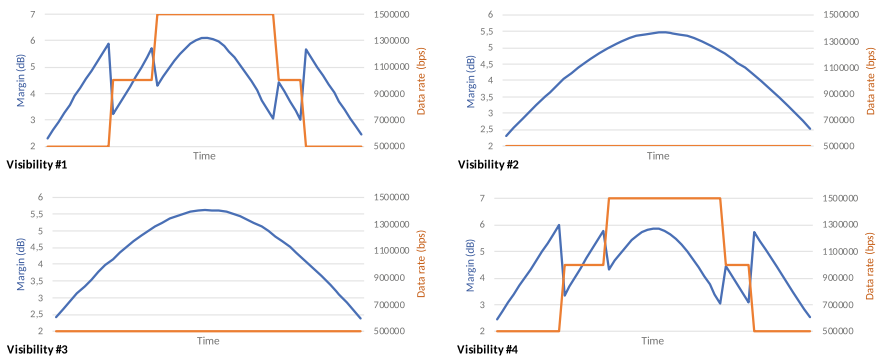


Fig. 5 The impact of VCM method on data rate and link margin

Table 3 Comparative results using VCM method on S-band CubeSat Downlink

	Classic	Classic	VCM
	$El_{min} = 20^\circ$	$El_{min} = 5^\circ$	$El_{min} = 5^\circ$
Data rate	1 Mbps	500 kbps	Variable
Number of passes per day	2	4	4
Total passes duration per day (s)	534	1991	1991
Maximum data downloaded per day (MB)	58	108	224

4 Conclusion and Further Research

This paper begins by a classic link budget on S-Band downlink between a LEO CubeSat and a Ground Station located in Rabat (Morocco) for 3 different cases in order to apprehend the impact of communication conditions on link margin. Then, we apply VCM technique, which consists of varying data rate depending on the position of the CubeSat in its orbit. Our results have proven the outstanding performance gain on the amount of data that can be downloaded from the CubeSat. Thus improving the communication channel performance for optimized use of bandwidth. There are other more advanced approaches, notably the Adaptive Coding and Modulation (ACM) method [13], which instead of being based on propagation losses prediction, it uses real-time values of the Signal-to-Noise (SNR) measured on the receiver side. This method is more accurate but requires establishing an additional low data rate communication channel, in order to send to the CubeSat the link quality measured on ground. This feedback helps choosing the appropriate communication parameters. However, to examine in depth this approach, we should do the experiment using real space conditions. Next, we will try to apply Neural Network algorithms in order to optimize the choice of modulation and coding by including other parameters instead of focusing only on free space losses variation. We will also try to implement an Automatic Modulation Recognition in the Ground Station to detect the type of modulation chosen by the CubeSat. This approach will allow an automatic synchronization without having to create a dedicated channel.

Acknowledgements This paper was supported by the project “ADN” of Mohammed V University in Rabat.

References

1. Sweeting MN (2018) Modern small satellites-changing the economics of space. *Proc IEEE* 106:343–361. <https://doi.org/10.1109/JPROC.2018.2806218>
2. Nanosats Database (2020) <https://www.nanosats.eu>. Last accessed 12 June 2020
3. Chahat N, Hodges RE, Sauder J, Thomson M, Peral E, Rahmat-Samii Y (2016) CubeSat deployable Ka-band mesh reflector antenna development for earth science missions. *IEEE Trans Antennas Propag* 64:2083–2093. <https://doi.org/10.1109/TAP.2016.2546306>
4. Hodges RE, Chahat NE, Hoppe DJ, Vacchione JD (2016) The Mars Cube One deployable high gain antenna. In: 2016 IEEE international symposium on antennas and propagation (APSURSI). IEEE, Fajardo, PR, USA, pp 1533–1534. <https://doi.org/10.1109/APS.2016.7696473>
5. Acharya R (2017) Satellite link performance. In: *Satellite signal propagation, impairments and mitigation*. Elsevier, pp 279–300. <https://doi.org/10.1016/B978-0-12-809732-8.00009-0>
6. Latachi I, Karim M, Hanafi A, Rachidi T, Khalayoun A, Assem N, Dahbi S, Zouggar S (2017) Link budget analysis for a LEO CubeSat communication subsystem. In: 2017 international conference on advanced technologies for signal and image processing (ATSIP). IEEE, Fez, Morocco, pp 1-6. <https://doi.org/10.1109/ATSIP.2017.8075571>
7. GOMspace Homepage. <https://gomspace.com/>. Last accessed 12 June 2020
8. Pahl J (2016) Fundamental concepts. In: *Interference analysis*. Wiley, Chichester, pp 43–143. <https://doi.org/10.1002/9781119065296.ch3>

9. AMSAT Homepage. <https://www.amsat.org/>. Last accessed 12 June 2020
10. Pahl J (2016) Propagation models. In: Interference analysis. Wiley, Chichester, pp 144–216. <https://doi.org/10.1002/9781119065296.ch4>
11. Downey JA, Mortensen DJ, Evans MA, Tollis NS (2016) Variable coding and modulation experiment using NASA's space communication and navigation Testbed, vol 36
12. Chen X, Yao W, Harkness P (2017) Pocketcube deorbit times: susceptibility to the solar cycle. In: 2017 IEEE aerospace conference. IEEE, Big Sky, MT, USA, pp 1–12. <https://doi.org/10.1109/AERO.2017.7943625>
13. Downey JA, Mortensen DJ, Evans MA, Briones JC, Tollis N (2016) Adaptive coding and modulation experiment with NASA's space communication and navigation testbed, vol 11

Ground Penetrating Radar Data Acquisition to Detect Imbalances and Underground Pipes



Tahar Bachiri, Gamil Alsharahi, Abdellatif Khamlichi, Mohammed Bezzazi, and Ahmed Faize

Abstract Past research shows that the Ground Penetrating Radar (GPR) can be an effective and efficient way to map buried pipeline systems. This paper presents a GPR data analysis technique, which is first generated by applying the Finite Differences Time Domain (FDTD) method to estimate the thickness of the subsurface layers and characterize the piping systems buried in the underground. In practical investigations, the GPR unit with a 400 MHz antenna was used to detect imbalances and underground pipes. The GPR profiles provided details on the shapes and nature of the target in the underground. These profiles can, therefore, detect water pipes, utility systems up to a depth than 2 m.

Keywords FDTD method · Ground penetrating radar (GPR) · GPR profiles · Underground pipes

T. Bachiri (✉)

Civil Engineering from Faculty of Sciences and Technology, University Abdelmalek Essaadi, 91001 Tangier, Morocco
e-mail: tbachiri@uae.ac.ma

G. Alsharahi · A. Faize

Department of Physics, Faculty Polydisiplinarily Nador, Mohammed First University, Oujda, Morocco
e-mail: alsharahigamil@gmail.com

A. Faize

e-mail: ahmedfaize6@hotmail.com

A. Khamlichi

Department STIC, National School of Applied Sciences, University Abdelmalek Essaadi, 93030 Tetouan, Morocco
e-mail: khamlichi7@yahoo.es

M. Bezzazi

Department of Mechanical and Civil Engineering, Faculty of Sciences and Technology, University Abdelmalek Essaadi, 91001 Tangier, Morocco
e-mail: bezzazi@hotmail.com

1 Introduction

Today, the underground space, especially in the big cities, is becoming increasingly congested by various networks such as drinking water pipes, telecommunication pipes, gas pipes, liquid sewerage pipes. Spatial information on these underground networks forms the basis of any utility management system. The location of the buried pipe network in the old cities is often unknown. This problem imposes many difficulties when reconstruction takes place in the older parts of a city. Due to the lack of information on the development of underground pipes, for example, civil construction projects can easily damage a hidden pipe and stop the supply of gas or drinking water. It is noted that the operation of underground pipe networks has become a crucial aspect in the field of underground urban engineering [1].

There are several non-destructive methods of detection, such as acoustic detection, electromagnetic induction and GPR [2], which locate underground targets such as buried cables and pipes and monitor water leaks [3–7]. The GPR method is used in many areas of civil engineering and has advantages, including its speed of application, low cost, security, anti-interference, and lack of destruction [8, 9].

This technological tool makes it possible to process all A-scan and B-scan or 2D image waveforms (radargram) by applying a color palette to the reflection intensity values of the recorded electromagnetic waves or amplitudes. In cases, a grayscale color palette is applied, which assigns the black color to the minimum values of electromagnetic wave reflection intensity (minimum amplitude) and the white color at the maximum reflection intensity values of the electromagnetic waves (maximum amplitude). The intermediate values are converted to gray colors of different tone. These B-scans are XZ graphical representations of the reflected electromagnetic waves detected.

2 Principles of Applications GPR in Civil Engineering

GPR has become a more widely used technological tool in the field of civil engineering, particularly its application in the detection of buried pipes. The choice of antennas and the frequency adapted to the situation studied, is fundamental [10, 11]. Most commercially available GPR antennas are bow-tie dipole antennas, with a central frequency f_c generally exceeding 400 MHz. Antennas can be divided into types: horn antennas (or aperture) and dipole antennas (or elements). Each antenna has its characteristics and transmit (Tx) and receive (Rx) capability. Also, the low-frequency antennas are physically much larger and transmit a pulse with great penetration into the inspected medium, however, they produce a result with a low resolution of the target under the surface. Civil engineering work involves the measurement of far-field with frequencies often in the frequency range from 400 MHz to 4 GHz, according to this equation:

$$\lambda = \frac{v}{f_c} = \frac{c}{f_c \sqrt{\epsilon_r'}} \quad (1)$$

where λ is the wavelength of the GPR, f_c is the central frequency of the antenna, v is the speed of displacement of the electromagnetic wave in the medium, c is the speed of displacement of the electromagnetic wave in free space, this constant is 0.3 m/ns and ϵ_r' is the real part of the host material of the complex permittivity. Among the antennas widely used when studying the basic characteristics of an antenna is a short dipole. The antenna diameter and width are minimal compared to the λ length of the radiated wave, so that the excitation current of the antenna is especially uniform along its length. The distance to the far-field boundary can be estimated as follows [12–14]:

$$R_{FF} = \frac{2L_A^2}{\lambda} + \lambda \quad (2)$$

where L_A is a characteristic antenna length and a value of R_{FF} of less than 3λ is also taken as an overall minimum. Spatial resolution calculation, for a GPR system, is always conditioned by many factors such as frequency, antenna properties, host medium properties and beam angle. The shape of the radiation has a significant influence on the footprint of the GPR beam. The footprint is often calculated as the first Fresnel area (FFA) in the field. The following equation is used for its performance and estimation efficiency [15, 16]:

$$A = \sqrt{\left(\frac{v^2}{16f_c^2} + \frac{vz}{2f_c} \right)} \quad (3)$$

where A is the radius de FFA.

La résolution horizontale R_h de chaque antenne, en fonction d'une distance de 30 cm entre la surface du réflecteur et l'antenne, et la résolution vertical R_v peuvent être estimées comme suit. The horizontal resolution R_h for each antenna based on a distance of 30 cm between the reflector surface and the antenna and the vertical resolution R_v can be estimated as follows [7, 17–19]

$$\left. \begin{aligned} R_h &= 2 \left(\frac{\lambda^2}{4} + d\lambda \right)^{\frac{1}{2}} \\ R_v &= \frac{1,39.v.\Delta t}{2} \end{aligned} \right\} \quad (4)$$

where d is the vertical distance between the antenna and the reflector surface and Δt is the effective duration of the GPR pulse.

The depth resolution is defined as the minimum distance between two layers so that the latter appears distinct during GPR surveys. The data recorded by the GPR (pulse radar) is based on the sending of an electromagnetic pulse through an antenna on the surface, then the recording of reflected electromagnetic waves from the internal

interfaces, where there is a contrast in dielectric properties. Since the bidirectional travel time measured between Tx and Rx is half the time (t_i).

Therefore, the thickness of the third layer can be estimated by the following equation:

$$z_i = \frac{ct_i}{2\sqrt{\epsilon_r, i}} \tag{5}$$

Where z_i is the thickness of the i^{th} layer, t_i is the electromagnetic wave travel time through the i^{th} layer.

In order to validate the concept against the GPR techniques for the material distortion of buried pipes, a numerical simulation was carried out using the GprmaxV2.0 software in the Matlab environment.

3 Methodology

The free software GprMax in the Matlab environment [20] was used in the numerical simulation to solve Maxwell equations in the time domain which is based on the FDTD method [21]. This software is simple and robust in electromagnetic modeling and makes it possible to distinguish different sizes of buried targets with various depths in different mediums, such as free space, water, sand, clay, concrete. GprMax input file that includes all the information to run a model requires information about materials, geometry, antenna, and other features to perform the simulation. A 2D model is chosen to perform B-scan perpendicular on pipes of different types such as cast iron, plastic, and concrete. Each pipe has a diameter of 100 mm and is buried inhomogeneous concrete-covered soil at a depth of 20.4 cm. The model geometry is illustrated in Fig. 1.

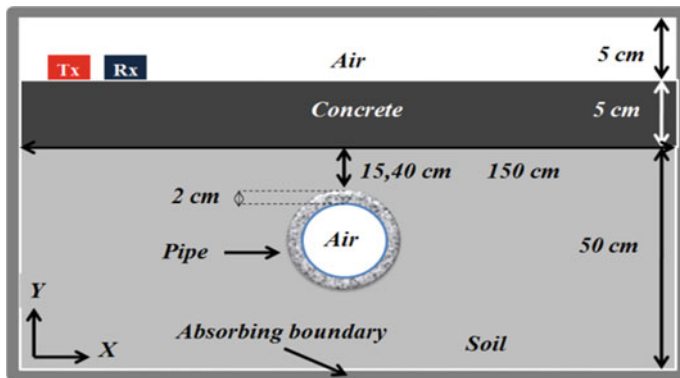


Fig. 1 Model geometry of pipe in soil recovered with concrete

Table 1 GPR model description

		Permeability μ_r	Permittivity ϵ'_r	Conductivity σ (S/m)
Medium	Concrete	1	6	10^{-3}
	Soil	1	9	10^{-3}
Materials of pipe	Concrete with air	1	6	10^{-3}
	Plastic with air	1	3	10^{-4}
	Void with water	1	81	5×10^{-4}
	Metal with air	Perfect conductor		
Geomtry models		domain: 1.30 0.6		
		dx_dy: 0.005 0.005 m		
		Time_window: 12.0e-9 s		
Antenna (Tx/Rx)		Scanning: Axis X		
		Offset (Tx/Rx): 13 cm		
		Source type: Ricker		
		Frequency: 400 MHz		

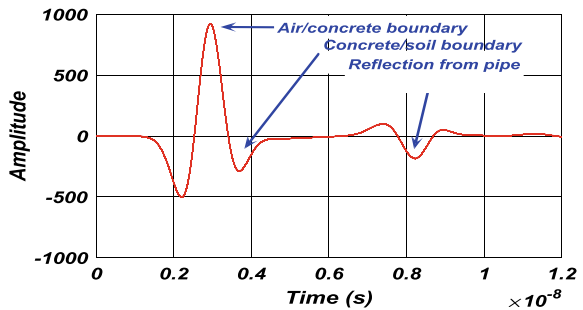
Table 1 lists the description of the GPR model with the antenna parameters and medium geometry.

4 Results and Discussion

4.1 Numerical Simulations

The simulated GPR data was performed by placing the GPR on the target and moving the coil along an X-axis and perpendicular to the pipe. Figure 2 shows the A-scan measurements of the tube center position, while Fig. 3 shows the parabolic signatures that appear on the GPR radargram.

Fig. 2 A-scan for detecting an empty pipe



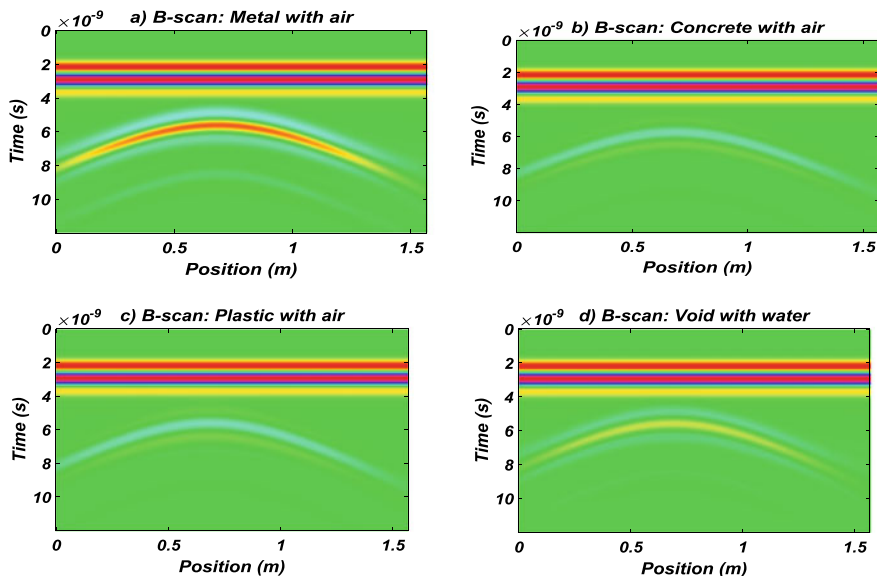


Fig. 3 Model and GPR images with different materials of pipe constructed at same color scale: **a** air-filled metal pipe, **b** air-filled concrete pipe, **c** air-filled plastic pipe, **d** water-filled vacuum

Based on Fig. 2, the distances from the GPR antenna to the air/concrete interface, to the concrete/soil interface and the upper generator interface of the pipe, can be estimated using the differential travel times of the antenna at these interfaces. The thickness of the concrete layer and the depth of burial of the pipe can be determined respectively by multiplying the speed of the electromagnetic wave in the concrete and the ground and the differential travel times of the electromagnetic wave between the interfaces sus-indicated. Using the example in Fig. 2, the travel time between the two air/concrete and concrete/ground interfaces is 0.785 ns and the travel time between the concrete/ground interfaces and the top pipe generator is 2.97 ns. Using Eq. (5), we can estimate the thickness of the concrete layer is 4.807 cm with a 3.86% error percentage and that the depth of the pipe is 19.657 cm with a 3.64% error percentage.

The B-scans of the numerical simulations are shown in Fig. 3. These results illustrate the distinction between pipes that are made up of different materials in a medium that includes two layers of concrete ($\epsilon'_r = 6$) and soil ($\epsilon'_r = 9$). These simulations show good resolution while simultaneously solving the location of the pipes with good precision. Based on the resolution properties, it may be suggested that GPR with a central frequency of 400 MHz is suitable for providing indirect information on the nature of buried pipe materials.

The most significant feature observed is when the nature of the pipe materials changes, the intensity of the hyperbole function also changes. For example, the B-scan simulating a metal pipe (a) has clear contrasts with other acquisitions (b–d), because the difference in dielectric constant between steel and ground is the greater of

the three conditions, and the reflection of the electromagnetic wave is stronger. In the B-scans (b, c) of the empty pipes, there is a double reflection of the electromagnetic wave, because the second reflected curve comes from the lower edge of the pipe. Since water strongly absorbs the electromagnetic wave, only one electromagnetic wave curve can be seen in the B-scan (d) relating to an empty opening filled with water. Note that all these B-scans are done on the same color scale. Similar results were obtained in [22–25].

It can be argued that B-scan observations are unavoidable due to the high contrast between the host medium and the permittivity of pipe materials. To mount this, we note the decrease in the intensity of hyperbolic reflections is always present with low permittivity pipe materials. The ability to obtain acceptable resolution B-scans with a 400 MHz GPR that is capable of clearly distinguishing the nature of pipe materials, is possible in conventional GPR surveys as prescribed in this paper.

4.2 Practical Application

GPR profiles using 400 MHz antennas were acquired at the site. First, the acquisition of GPR data was performed on known targets, to allow the calibration of GPR equipment. We then carried out on-site GPR profiles to cover the entire zone to be examined. GPR processing was done by the Radan software, using standard steps such as zero-time correction and the application of a band-pass filter. The physical parameters that are taken as a function of medium moisture are relative dielectric permittivity ($\epsilon_r = 9$) and electrical conductivity ($\sigma = 0.001$ s/m). Among the many GPR profiles that have been acquired in the site, we present in this paper only the most representative ones. In addition to the GPR profiles, we did a full scan of the area with the VIVAX VLOC Pro2 brand radio detector, which allows us to detect buried arrays at quite significant depths compared to the GPR up to 5 m or more when using the detector in active mode. On the different profiles we observe:

On the GPR image below (Fig. 4) we see the presence of reinforcements in the concrete with a rather high reinforcement density. There is also heterogeneity of the subsoil, in the form of a clear hyperbolic reflection of low amplitude, which is located at the position up to 4.40 m and a depth bounded between 0.60 m and 1.40 m because this does not repeat on the other profiles. A view of the perpendicular profiles made in this area, confirms the presence of an object in the basement.

The existence of a reinforced concrete slab prevents penetration of the reflected GPR signal back to the surface. This signal can be reflected again and re-enters the basement, causing a reverberation signal, masking information from deeper depths.

Hyperbolic reflections are observed in Fig. 5 corresponding to five pipes, which are placed next to each other, used to transport stormwater. These pipes are confirmed at the same depth of 2.20 m from the top pipe generator.

In Fig. 6 the measurement was carried out on a full drinking water pipe located on the subsurface; it can be seen that the rate of propagation of electromagnetic waves decreases due to high relative permittivity ($\epsilon'_r = 81$). The delay of the reflected

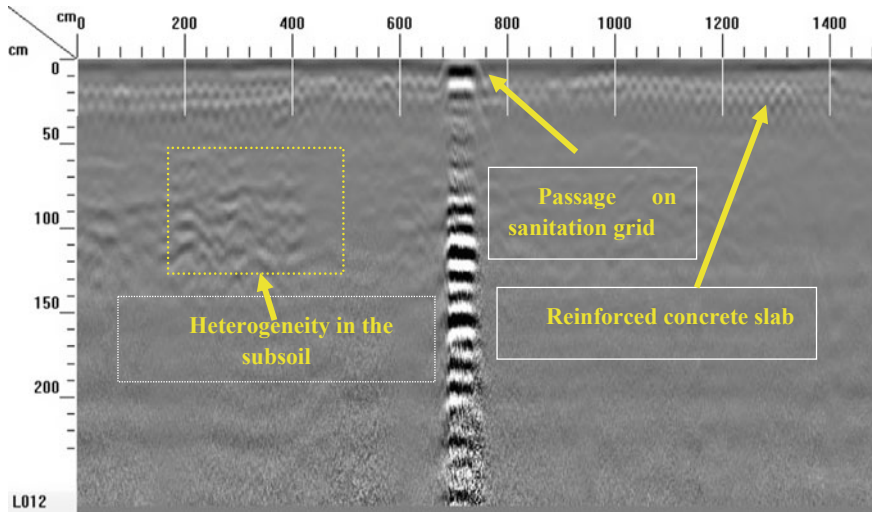


Fig. 4 GPR profile showing reinforced concrete slab and subsoil heterogeneity

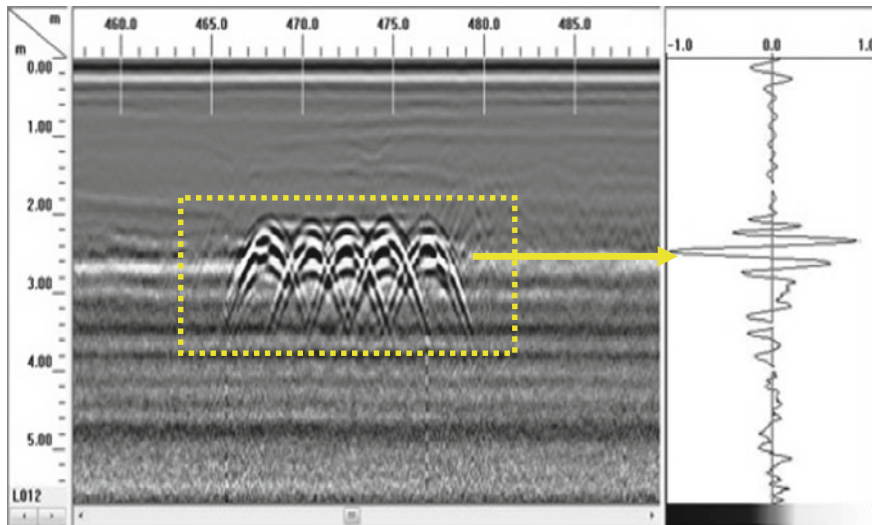


Fig. 5 GPR profile shows five metal pipes that are located at the same depth

wave which is recorded by the receiving antenna generates, at different times, the hyperboles corresponding to the reflections of electromagnetic waves.

In Fig. 7a, we see two sewer pipes clogged by waste. These two pipes are confirmed from a depth of 2 m and are approximately 0.50 m above each other. In the profile associated to Fig. 7b, clear hyperbolic forms are observed, it is a single pipe that

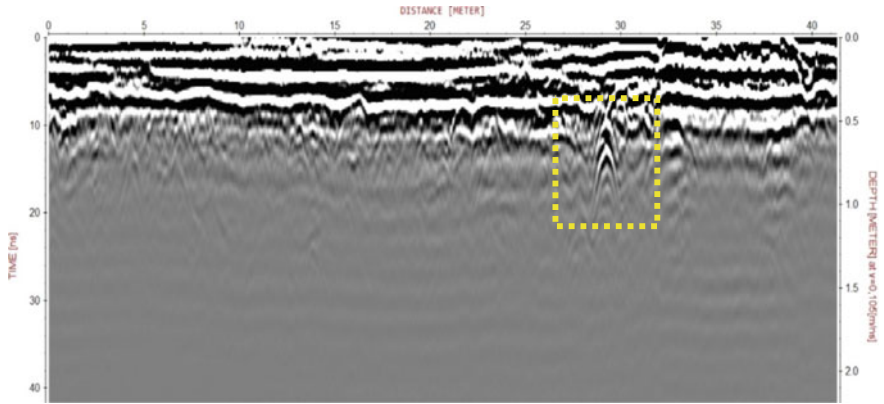


Fig. 6 GPR profile shows a water-filled pipe on the subsurface

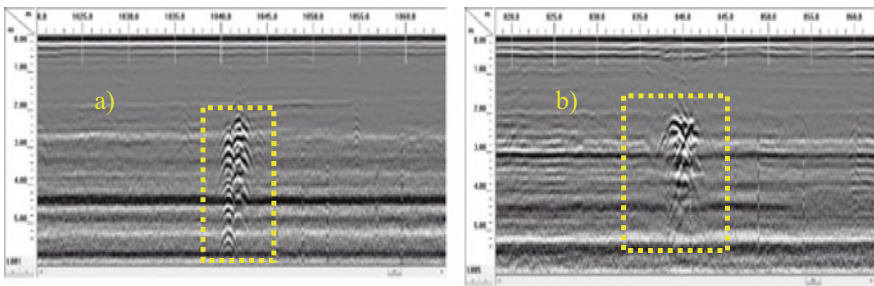


Fig. 7 a, b Radargrams of the profiles detecting sewer pipes

shows an imbalance. This pipe can be broken and filled with alluvial and clay-silty sediments. The hyperboles were obtained with a peak of 2.10 m.

This study shows that the GPR method is an important step before starting civil works, because it provides the precise location of utilities in the underground, as well as an estimate of their depths. Based on these results, interventions to remedy anomalies accurately, safely and without risk of dangerous accidents. The information improves and updates public service placement plans and serves as a basis for urban planning. This paper complements the work already published in [7].

5 Conclusions

This paper has been carried out to develop the use of GPR techniques in the field of civil engineering, in particular the assessment of the condition and defects of pipeline networks. The numerical simulation can provide a solid database of data from the underground, which allows a concrete validation of the principle for the use of the

GPR technique with a 400 MHz antenna (Tx) that is suitable for this type of survey evaluation.

In practical investigations, despite the presence of a reinforced concrete slab, which could have attenuated the GPR signal, we were able to detect an anomaly that is related to a heterogeneity of the ground. The GPR profiles provided details on the shapes and nature of the target in the basement. These profiles can, therefore, detect water pipes, utility systems in the basement up to a depth of than 2 m.

References

1. Costello SB, Chapman DN, Rogers CDF, Metje N (2007) Underground asset location and condition assessment technologies. *Tunnel Underground Space Technol* 22(5–6):524–542
2. Daniels DJ (2004) *Ground penetrating radar*, 2nd edn. Institution of Electrical Engineers, London
3. Zeng X, McMechan GA (1997) GPR characterization of buried tanks and pipes. *Geophysics* 62(3):797–806
4. Pettinelli E, Di Matteo A, Mattei E, Crocco L, Soldovieri F, Redman JD, Annan AP (2009) GPR response from buried pipes: Measurement on field site and tomographic reconstructions. *IEEE Trans Geosci Remote Sens* 47(8):2639–2645
5. Ristić A, Bugarinović Ž, Govedarica M, Pajewski L, Derobert X (2017) Verification of algorithm for point extraction from hyperbolic reflections in GPR data. In: 2017 9th international workshop on advanced ground penetrating radar (IWAGPR). IEEE, pp 1–5
6. Ghorbel O, Ayadi A, Ayadi R, Aseeri M, Abid M (2019) Combined methods based outlier detection for water pipeline in wireless sensor networks. In: *International conference on advanced information networking and applications*. Springer, Cham, pp 214–224
7. Bachiri T, Alsharahi G, Khamlichi A, Bezzazi M, Faize A (2020) GPR application in civil engineering to search and detect underground Networks. *Int J Emerg Trends Eng Res* 8(5). <https://www.warse.org/IJETER/static/pdf/file/ijeter59852020.pdf>
8. Benedetto A, Pajewski L (2015) Civil engineering applications of ground penetrating radar. *Trans Civ Environ Eng*
9. Faize A, Alsharahi G (2020) Preliminary study of roots by georadar system. In: *Embedded systems and artificial intelligence*. Springer, Singapore, pp 173–182
10. Bachiri T, Khamlichi A, Bezzazi M (2018) Detection of rebar corrosion in bridge deck by using GPR. In: *MATEC web of conferences*, vol 191. EDP Sciences, p 00009
11. Tosti F, Ferrante C (2019) Using ground penetrating radar methods to investigate reinforced concrete structures. *Surv Geophys* 2019:1–46
12. Yaghjian A (1986) An overview of near-field antenna measurements. *IEEE Trans Antennas Propag* 34(1):30–45
13. Millard SG, Shaari A, Bungey JH (2002) Field pattern characteristics of GPR antennas. *NDT & E Int* 35(7):473–482
14. Van der Wielen A, Courard L, Nguyen F (2012) Detection of thin layers into concrete with static and CMP measurements. In: 2012 14th international conference on ground penetrating radar (GPR). IEEE, pp 530–535
15. Pérez-Gracia V, González-Drigo R, Di Capua D (2008) Horizontal resolution in a non-destructive shallow GPR survey: an experimental evaluation. *NDT E Int* 41(8):611–620
16. Luo TX, Lai WW (2020) GPR pattern recognition of shallow subsurface air voids. *Tunnel Underground Space Technol* 99:103355
17. Jol HM (2009) *Ground penetrating radar: theory and applications*. Elsevier Sciences
18. Pérez-Gracia V, Di Capua D, González-Drigo R, Pujades L (2009) Laboratory characterization of a GPR antenna for high-resolution testing: radiation pattern and vertical resolution. *NDT & E Int* 42(4):336–344

19. Prego FJ, Solla M, Puente I, Arias P (2017) Efficient GPR data acquisition to detect underground pipes. *NDT & E Int* 91:22–31
20. Giannopoulos A (2005) Modelling ground penetrating radar by GprMax. *Constr Build Mater* 19(10):755–762
21. Kunz KS, Luebbers RJ (1993) *The finite difference time domain method for electromagnetics*. CRC Press
22. Alsharahi G, Faize A, Maftei C, Bayjja M, Louzazni M, Driouach A, Khamlichi A (2019) Analysis and modeling of GPR signals to detect cavities: case studies in Morocco. *J Electromagnet Eng Sci* 19(3):177–187
23. Prego FJ, Solla M, Puente I, Arias P (2017) Efficient GPR data acquisition to detect underground pipes. *NDT E Int* 91:22–31
24. Alsharahi G, Faize A, Louzazni M, Mostapha AMM, Bayjja M, Driouach A (2019) Detection of cavities and fragile areas by numerical methods and GPR application. *J Appl Geophys* 164:225–236
25. Alsharahi G, Mint Mohamed Mostapha A (2016) Modelling and simulation resolution of ground penetrating radar antennas. *J Electromagnet Eng Sci*

Nash Equilibrium Based Pilot Decontamination for Multi-cell Massive MIMO Systems



Abdelfettah Belhabib , Mohamed Boulouird , and Moha M'Rabet Hassani

Abstract Due to the limitation imposed by the scarcity of pilot resources, Massive multi-input multi-output (M^{MIMO}) technology suffers from the problem of pilot contamination (PC), which is due to the reuse of the same pilot sequences for the users of the adjacent cells. To deal with this constraint, this paper proposes a new decontaminating strategy, which is based on the Nash Equilibrium theory. Specifically, by exploiting the large-scale fading coefficients, the users are assigned with the available pilot sequences under the constraint to fulfill a good/fairness signal-to-interference-plus-noise ratio (SINR) to the users of the overall cells. Because, even though the users of the same cell are optimally assigned with the pilot sequences, the achieved SINR in some adjacent cells can be degraded, which is unfair; consequently, the proposed strategy assigns the available pilots to the users to reach an acceptable SINR for the users of the overall cells; in other words, to guarantee a high and similar quality of service for the users of all cells. Simulation results prove the effectiveness of our proposal on boosting the per-cell achievable rate.

Keywords Pilot contamination · Massive MIMO · Multi-cellular systems · Pilot assignment · Nash equilibrium · 5G wireless communications

A. Belhabib · M. M. Hassani
Instrumentation, Signals and Physical Systems (I2SP) Group,
Faculty of Sciences Semlalia, Cadi Ayyad University, Marrakesh, Morocco
e-mail: abdelfettah.belhabib@edu.uca.ac.ma

M. M. Hassani
e-mail: hassani@ucam.ac.ma

M. Boulouird (✉)
Smart Systems and Applications (SSA) Group, National School of Applied Sciences of
Marrakesh (ENSA-M), Cadi Ayyad University, Marrakesh, Morocco
e-mail: m.boulouird@uca.ac.ma

1 Introduction

To control the dramatically increased demand for higher throughput and good quality-of-service(QoS) for several users, M^{MIMO} has been proposed [1] to reach that goal. This technology proposes to increase the number of antennas at the base station (BS) side, which can allow BSs to benefit from an increasing number of degrees of freedom, which enables the BSs to serve several users; therefore, the spectral efficiency can be significantly boosted [2]. Unfortunately, the main M^{MIMO} subject to a constraint known as pilot contamination (PC), which limits the expected performances of M^{MIMO} in multi-cellular systems [3].

Due to the large benefits of M^{MIMO} , much attention has been carried out to solve the problem of PC that limits this promising technology. In [4], cells are clustered and the same set of pilots is reused within cells that belong to the same cluster, while orthogonal pilots are allocated to different clusters; therefore, the PC problem is reduced by exploiting the graph coloring theory. Regarding the problem of pilot scarcity, the same set of pilot sequences is reused across different cells. [5] proposes an adaptive pilot clustering strategy, which is based on exploiting such coalitions between BSs to allow them to benefit from extra pilots and to address the constraint of PC. Based on the graph coloring theory, the strength of interference upon users of different cells had been investigated in the work of [6, 7], which aims to reduce the problem of PC upon users that employ the same training sequences. That through assigning the same pilot sequence to users that would generate the smallest impact of interference upon these users. To enhance the QoS for users, [8] proposes soft pilot reuse (SPR) based multi-block diagonalization precoding (SPRMBDP) strategy, which considers that the problem of PC upon users is not similar. Accordingly, users who are close to the BSs enjoy a good QoS compared to edge users. Consequently, [8] allocates orthogonal pilots to edge users while center users are obliged to reuse the same set of pilots in all cells. Therefore, the edge users' QoS is enhanced by precoding their corresponding signals through a specific subspace. However, [8] requires extra pilot sequences. In [9] a game theory-based decontaminating strategy had been exploited to ensure the fairness between users of different cells. However, this strategy assumes having perfect channel state information (CSI) at all BSs. Under orthogonal frequency division duplex (OFDM) multicarrier modulation, [10] shown that the problem of interference caused by the adjacent bands can be mitigated through either increasing the number of antennas BSs or through an oversampling rate. The OFDM was consolidated with the Alamouti code in the work of [11]. It was shown in [12], that a large number of antennas is not always beneficial, specifically in the case of a MIMO system that operates at a bandwidth of several Gigahertz under OFDM modulation technique. The problem of hardware impairment was analyzed in [13], therefore, it proposes a new system model that takes into account different problems that relate to the hardware impairments, which helps to accurately analyzing the M^{MIMO} systems based OFDM technique. The quantized M^{MIMO} was studied in the work of [14], where a new detection and estimation algorithms were investigated under the OFDM.

The Nash equilibrium theory is defined as a justiciary theory that aims to allow a set of players to benefits from similar performances. This theory is frequently applied for the cases where a set of players compete with each other to achieve a goal [15]. Inspiring from this theory, players here are the users of each cell and they compete with each other to achieve a good SINR within all cells based on the reuse of the same set of pilots. Specifically, the set of pilots is limited and users of each cell should reuse the same set of pilots, which leads to generating a mutual degradable effect between users that employ the same pilots. However, even the degradable impact is mutual, the strength of PC upon users that employ the same pilots is not similar. Accordingly, the achieved SINR in a cell may be too bad compared to the adjacent cells. In other words, users that employ the same pilots can benefit from large/different performances, which is unfair. Hence, the contributions of the present paper are as follows:

- The proposed decontaminating based Nash Equilibrium strategy aims to enhance the QoS of the users of all cells even they reuse the same set of pilot sequences.
- Our proposed strategy aims to guarantee good performances for the users of all cells instead of the conventional scheme where each cell is selfish and tries to increase its achieved performances even at the cost of degrading the performances of adjacent cells.
- Simulation results of our proposed strategy outperform those of the SPRMBDP [8].

To the best of our knowledge, no prior research works analyzing our proposed decontaminating strategy in Multi-cell M^{MIMO} under Time Division Duplex (TDD) protocol, which is inspired in the Nash Equilibrium theory.

Notation

$(.)^T$ denotes the transpose, $(.)^\dagger$ is the transpose conjugate (i.e. Hermitian), and $\mathbb{E}(\cdot)$ is the expectation, while $(\cdot) = \emptyset$ refers to an empty group. $\delta_{k',k}$ denotes the Dirac function.

Organization

The remaining of this paper is as follows: In Sect. 2, the system model adopted herein is presented; Sect. 3 provides a short description of the specific phases of communication between users and BSs under TDD protocol. The proposed strategy is investigated in Sect. 4; simulation results are presented in Sect. 5. Finally, a conclusion of the present paper is given in Sect. 6.

2 System Model

We consider a multi-cellular M^{MIMO} system of L hexagonal cells, and K single antenna users wandering in each cell, which is centered with a BS of M antennas (e.g. see Fig. 1). The channel vector linking a user k of cell i to a BS of j th cell is denoted $g_{j,i,k} \in \mathbb{C}^{M \times 1}$ can be expressed as:

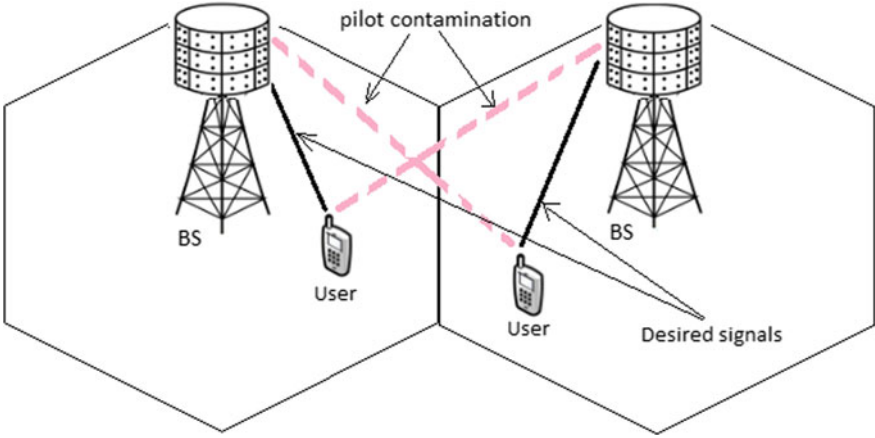


Fig. 1 Illustration of M^{MIMO} system of $L = 2$ and $K = 1$.

$$g_{j,i,k} = h_{j,i,k} \sqrt{\beta_{j,i,k}} \quad (1)$$

The small-scale fading vectors $h_{j,i,k} \in \mathbb{C}^{M \times 1}$ are considered to be statistically independent between the K users and they follow a complex Gaussian distribution of zero-mean vector and a covariance matrix \mathbb{I}_M i.e. $h_{j,i,k} \sim \text{CN}(0, \mathbb{I}_M)$. The large-scale fading coefficients $\beta_{j,i,k}$ account for the path loss and shadow fading, and it can be expressed as:

$$\beta_{j,i,k} = \frac{z_{j,i,k}}{(r_{j,i,k}/R)^\alpha} \quad (2)$$

where $z_{j,i,k}$ is the log-normal shadow fading that follows a Gaussian distribution of zero-mean having a standard deviation σ_{shadow} . $r_{j,i,k}$ denotes the distance between the k th user of the i th cell to the BS of j th cell, while R and α denote respectively, the cell radius and the decay exponent.

3 Communication Schemes

Due to the property of reciprocity that characterizes the TDD protocol, there is no need for training on the downlink phase [2]. Consequently, the number of pilot sequences required for channel training will depend only on the number of active users instead of being depending on the number of antennas BS [2], moreover the problem of the no-reciprocal transceivers that faces the TDD can be fixed through calibration [16] and it was validated through experiments [17]. Hence, during this paper, we adopt a TDD protocol where the communication between the pair user-BS is divided into frames [18, 19]. Channels within each frame of length T_c (i.e. coher-

ence time interval) are considered static. Each frame can be split into four specific phases. To describe these phases, let us focus on a user k of cell j communicating with its BS of the j th cell. Therefore, the four phases are.

3.1 Uplink Pilots

During τ samples, users uplink their pilot sequences. Hence, when the k th user of each cell uplink its pilot sequences, the received pilot signal $y_{j,k} \in \mathbb{C}^{M \times \tau}$ at the BS of the j th cell can be expressed as:

$$y_{j,k} = \sqrt{\rho_p} \sum_{i=1}^L g_{j,i,k} \phi_k + n_j = \sqrt{\rho_p} g_{j,j,k} \phi_k + \sum_{i \neq j, i=1}^L g_{j,i,k} \phi_k + n_j \quad (3)$$

where ρ_p is the transmitted power during the uplink of pilot sequences, while $\phi_k = [\phi_k^{[1]}, \phi_k^{[2]}, \dots, \phi_k^{[\tau]}] \in \mathbb{C}^{1 \times \tau}$ is the pilot sequences of the considered user k and $n_j \in \mathbb{C}^{M \times \tau}$ is an Additive White Gaussian Noise (AWGN) at the antennas of BSs.

3.2 Channel Estimation

BSs exploit the received pilot signals [i.e. see (3)] to estimate the users' channels. These channels are then used by BSs to construct detectors and precoders respectively for data detection and data precoding. Hence, based on the least square estimator [8] where BSs correlate the received pilot signals with the local pilots. The estimated channel (of the considered user k th user) at the BS of the j th cell is:

$$\hat{g}_{j,j,k} = \frac{y_{j,k} \phi_k^\dagger}{\sqrt{\rho_p}} = g_{j,j,k} + \sum_{i \neq j, i=1}^L g_{j,i,k} + \frac{n_j \phi_k^\dagger}{\sqrt{\rho_p}} \quad (4)$$

Here, we exploit the orthogonality condition (i.e. $\phi_k \phi_{k'}^\dagger = \delta_{k',k}$ where $k \neq k'$) for the channel estimation (CE). As can be seen in (4), the BS of the j th cell estimates not only the desired channel [i.e. first component of (4)] but also the undesired channels [i.e. second component of (4)]. Consequently, the estimated channels at BSs are inaccurate. Unfortunately, these estimated channels are exploited to construct detectors and precoders respectively for data detection and data precoding [8]. Notice that the PC problem means that the desired channels are contaminated by the undesired channels.

3.3 Data Detection

Users uplink their data symbols. Therefore, the uplink SINR of the considered user (i.e. k of j th cell to its BS) can be expressed as [8]:

$$SINR_{j,k}^u \xrightarrow{M \rightarrow \infty} \frac{\beta_{j,j,k}^2}{\sum_{i \neq j, i=1}^L \beta_{j,i,k}^2} \quad (5)$$

Therefore, the average uplink achievable rate can be expressed as:

$$C_{j,k}^u = (1 - \mu) \mathbb{E}\{\log 2(1 + SINR_{j,k}^u)\} \quad (6)$$

where $0 < \mu = \frac{\tau}{T_c} < 1$ denotes a parameter that accounts for the loss of spectral efficiency caused by the payload pilots during the training phase.

3.4 Downlink Data

BSs use the constructed precoders to focus data symbols toward users. Hence, the SINR-in the downlink of the considered user (i.e. k of j th cell to its BS) can be expressed as [8]:

$$SINR_{j,k}^d \xrightarrow{M \rightarrow \infty} \frac{\beta_{j,j,k}^2}{\sum_{i \neq j, i=1}^L \beta_{i,j,k}^2} \quad (7)$$

Therefore, the downlink achievable rate can be expressed as:

$$C_{j,k}^d = (1 - \mu) \mathbb{E}\{\log 2(1 + SINR_{j,k}^d)\} \quad (8)$$

It is well seen from (5) and (7) that, the users' SINR is saturated for a large number of antennas at BSs which limit the expected performances of M^{MIMO} . This is the degradable impact of PC.

4 The Proposed Strategy

Even though the users' SINR is optimized within different cells. It may be found that the achieved total SINR (TSINR) of a cell is lower than the other cells, or possibly lower than the TSINR that can be obtained in the random pilot assignment strategy. Thus, the fairness between users of different cells is not respected. Hence, some cells can benefit from good performances at the expense of adjacent cells. Therefore, it is necessary to compare the obtained TSINR in each cell with the

threshold $TSINR_{threshold}$, which is considered to be the lower bound of TSINR in all cells. In other words, the TSINR in each cell should be higher or at least equal to $TSINR_{threshold}$. Accordingly, while the TSINR of a cell is lower to that threshold, extra pilots are allocated to users of the considered cell and these pilots are again optimally assigned to users and so on until the TSINR of the considered cell becomes larger/equal to $TSINR_{threshold}$. This strategy allows users of all cells to benefit from good performances. The proposed strategy is provided in Algorithm 1, which can be explained in details as follows.

To compute the TSINR in each cell based on the random pilot assignment strategy, users of all cells are simultaneously assigned with the same set of pilots Φ (Step 3). Hence, the SINR of each user in each cell is computed based on (5). Therefore, the TSINR in each cell is computed based on (4). Now, the lower bound is computed through (5), which expresses the average TSINR per cell obtained by adopting the random pilot assignment strategy. In step 6, users are optimally assigned with pilots

Algorithm 1 Proposed Strategy

1: Input: System parameters $K, L, S, \mu, \beta_{j,k}/\{j = 1, \dots, L : k = 1, 2, \dots, K\}$.

2: Output:

3: Simultaneously, users within cells are randomly assigned with the same set of pilot sequences $\Phi = [\phi_1^T, \phi_2^T, \dots, \phi_K^T]^T \in \mathbb{C}^{K \times \tau}$.

4: Compute the TSINR in each cell as follows:

$$TSINR_j = \sum_{k=1}^K SINR_{j,k}^u / j = 1, 2, \dots, L \tag{9}$$

5: The threshold is computed as follows:

$$TSINR_{threshold} = \frac{\sum_{j=1}^L TSINR_j}{L} \tag{10}$$

6: Users of all cells are optimally assigned with pilot sequences as follows:

$$p_{j,k}^{opt} = \arg \max_{p_{j,k} \in \Phi} SINR_{j,k} \tag{11}$$

7: the optimized TSINR in each cells is then computed based on (4). Therefore, cells having TSINR lower than $TSINR_{threshold}$ are selected as follows:

- for $j = 1 : L$
- while $TSINR_j < TSINR_{threshold}$ do
- $\omega \leftarrow$ "cell j "
- end while
- end for

8: A new pilot (ϕ^+) is added to Φ as follows:

$$\Phi = \Phi \cup \phi^+ \tag{12}$$

9: "the Step 6" is repeated with the new Φ for the selected cells in step 7, and so on until $w = \emptyset$.

10: end

based on (6). However, even the TSINR is optimized in all cells, it may be found a cell, which has a TSINR lower than the threshold $TSINR_{threshold}$. Accordingly, those cells are selected and stored in ω (step 7 \rightarrow step 8). Therefore, the selected cells are again back to restart from step 6 with the new set of pilots Φ , this process is repeated until ω becomes empty. Even though the fulfilled TSINR within a cell still bellow $TSINR_{threshold}$, algorithm. (1) is forced to stop under the constraint of the limited pilot resources.

5 Simulation Results

In this section, we present the simulation results of our proposed strategy, where a Monte Carlo simulation is employed to evaluate the performance of our proposed strategy compared to both: the optimal case where there is no PC, and to the well-known strategy of [8] which is called SPRMBDP. Hence, we adopt a Multi-cell M^{MIMO} system, which is described in Sect. 2, the adopted parameters are summarized in Table 1.

In Fig. 2, we plot the average of the uplink achievable rate (AUAR) against the number of antennas BS (M), it is well seen that the Nash Equilibrium strategy (NES) performs better than the SPRMBP by about 10bps/Hz for $M = 32$, and the gap is smoothly increased to reach about 16bps/Hz for $M = 256$. Moreover, the gap between the optimal case and our proposed strategy is about two times smaller than the gap between the SPRMBDP and the optimal case.

Figure 3 depicts the average of the downlink achievable rate(ADAR) against M . As can be seen, the NES outperforms the SPRMBDP by about 20bps/Hz however the value of M . Moreover, the NES is close to the optimal case by about 3bps/Hz for $M = 32$ and by about 10bps/Hz for $M = 256$.

Table 1 System settings

Number of cells	$L = 7$
Number of antennas BS	$32 \leq M \leq 256$
Number of users per cell	$K = 10$
Number of pilots S	$K < S \ll LK$
Cell radius	$R = 500$ m
Inner radius	$r = 30$ m
Log normal shadow fading	$\sigma_{shadow} = 8$ dB
Transmit power from users ρ_p, ρ_u	10 dBm
Transmit power to the users ρ_d	12 dBm
Path loss exponent	$\alpha = 3$
Pilot overhead parameter μ	$0 < \mu < 1$, fixed $\mu = 0.1$

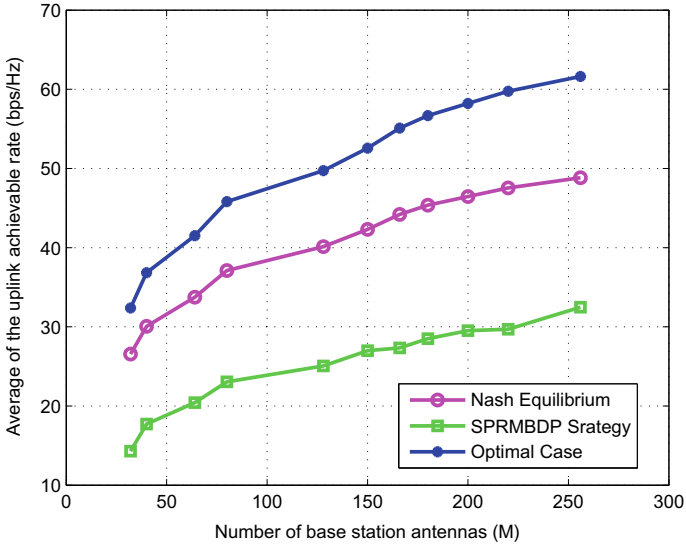


Fig. 2 Average of the uplink AAR against the number of antennas BSs, $S = 12$.

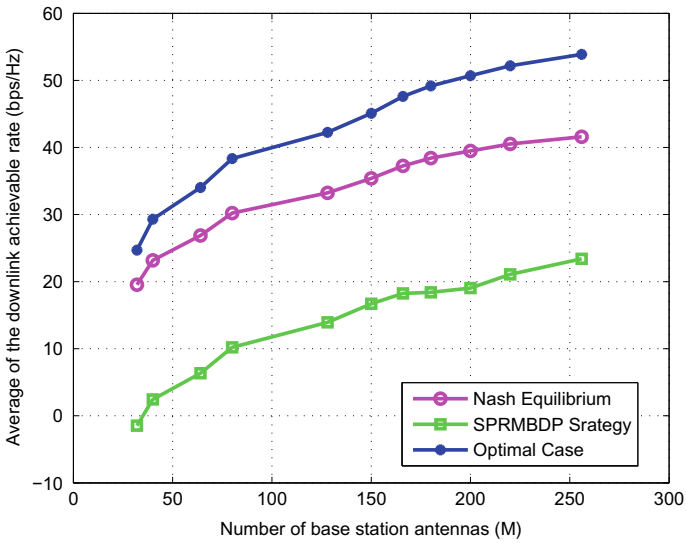


Fig. 3 Average of the downlink AAR against the number of antennas BSs, $S = 12$.

6 Conclusion

This paper provides a new mitigating strategy for the problem of pilot contamination in M^{MIMO} systems. Since the users that employ the same pilot sequences are subject to severe, but not the same, degradable impact of the PC problem, the users of the adjacent cells, fulfill a largely different SINRs. Specifically, the impact of PC upon the users that reuse the same pilots is not similar. Consequently, it can be found that the users of a cell reach a very low SINR compared to those achieved by the users of the adjacent cells. Hence, to ensure such fairness between the users of the adjacent cells, under the constraint of limited pilot resources, our proposal strategy stands on the Nash Equilibrium theory, which aims to ensure a balance of the achieved SINR per each cell, where the assignment of the pilots is controlled by the fulfilled SINR; specifically, orthogonal pilots are allocated to the users of low SINR, whereas the same pilots are reused for the rest users. Simulation results show the effectiveness of the proposed strategy on enhancing the per-cell achievable rate, in future work, we propose the consolidation of our strategy with the power control algorithm; or finding the equilibrium by employing the metaheuristic optimization algorithms such as the ant system algorithm.

References

1. Thomas L (2010) Marzetta: noncooperative cellular wireless with unlimited numbers of base station antennas. *IEEE Trans Wirel Commun* 9(11):3590–3600
2. Rusek F, Persson D, Lau BK, Larsson EG, Marzetta TL, Edfors O, Tufvesson F (2013) Scaling up MIMO: opportunities and challenges with very large arrays. *IEEE Sig Process Mag* 30(1):40–60
3. Boulouird M, Riadi A, Hassani MM (2017) Pilot contamination in multi-cell massive-MIMO systems in 5G wireless communications. In: 2017 International conference on electrical and information technologies (ICEIT), pp 1–4. <https://doi.org/10.1109/EITech.2017.8255299>
4. Shaalan IE, Khattaby AA, Dessouki AS (2019) A new joint TSPA/WGC pilot contamination reduction strategy based on exact graph coloring grouping algorithm. *IEEE Access* 7:150552–150564
5. Mochaourab R, Bjornson E, Bengtsson M (2016) Adaptive pilot clustering in heterogeneous massive MIMO networks. *IEEE Trans Wirel Commun* 15(8):5555–5568
6. Zhu X, Dai L, Wang Z, Wang X (2017) Weighted-graph-coloring-based pilot decontamination for multicell massive MIMO systems. *IEEE Trans Veh Technol* 66(3):2829–2834
7. Zhu X, Dai L, Wang Z (2015) Graph coloring based pilot allocation to mitigate pilot contamination for multi-cell massive MIMO systems. *IEEE Commun Lett* 19(10):1842–1845
8. Zhu X et al (2016) Soft pilot reuse and multicell block diagonalization precoding for massive MIMO systems. *IEEE Trans Veh Technol* 65(5):3285–3298
9. Ahmadi H, Farhang A, Marchetti N, MacKenzie A (2016) A game theoretic approach for pilot contamination avoidance in massive MIMO. *IEEE Wirel Commun Lett* 5(1):12–15
10. Ucuncu AB, Bjornson E, Johansson H, Yilmaz AO, Larsson EG (2020) Performance analysis of quantized uplink massive MIMO-OFDM with oversampling under adjacent channel interference. *IEEE Trans Commun* 68(2):871–886
11. Reyouchi E-MAR, Ghomid K, Ameziane K, El Mrabet O (2014) The powerful Alamouti code in MIMO-OFDM improvement for the next generation of terrestrial television broadcasting systems. *Int J Eng Sci (IJET)* 14(1):33–42

12. Borgmann M, Bölcskei H (2005) On the capacity of noncoherent wideband MIMO-OFDM systems. In: IEEE international symposium on information theory, pp 651–655
13. Jacobsson S, Gustavsson U, Durisi G, Studer C (2018) Massive MU-MIMO-OFDM uplink with hardware impairments: modeling and analysis. In: Proceedings of the 52nd Asilomar conference on signals, systems and computers, pp 1829–1835
14. Studer C, Durisi G (2016) Quantized massive MU-MIMO-OFDM uplink. *IEEE Trans Commun* 64(6):2387–2399
15. MacKenzie AB, DaSilva LA (2006) Game theory for wireless engineers. In: Synthesis lectures on communications, pp 1–86
16. Elijah O, Leow CY, Rahman TA, Nunoo S, Iliya SZ (2016) A comprehensive survey of pilot contamination in massive MIMO-5G system. *IEEE Commun Surv Tutor* 18(2):905–923
17. Guillaud M, Slock DTM, Knopp R (2005) A practical method for wireless channel reciprocity exploitation through relative calibration. In: Proceedings of the eighth international symposium on signal processing and its applications. Sydney, Australia, pp 403–406
18. Jose J, Ashikhmin A, Marzetta TL, Vishwanath S (2011) Pilot contamination and precoding in multi-cell TDD systems. *IEEE Trans Wirel Commun* 10(8):2640–2651
19. Belhabib A, Boulouird M, Hassani MM (2019) The impact of using additional pilots on the performance of massive MIMO systems. In: 2019 international conference on signal, control and communication (SCC). Hammamet, Tunisia, pp 87–92. <https://doi.org/10.1109/SCC47175.2019.9116177>

Channel Estimation for Massive MIMO TDD Systems and Pilot Contamination with Uniformly Distributed Users



Jamal Amadid , Mohamed Boulouird , and Moha M'Rabet Hassani

Abstract This work introduces a straightforward and applicable channel estimator for Rayleigh Fading Channels (RFC) in Multi-Cell (M-C) Multi-User (M-U) Massive MIMO (m-MIMO), Time Division Duplex (TDD) systems with Pilot Contamination (P-C). The traditional Least Square (LS) channel estimator undergoes considerable performance degradation whereas the Ideal Minimum Mean Square Error (I-MMSE) presents a much better performance in comparison with the LS estimator. Nonetheless, in many studies, the I-MMSE estimator depends on a supposition unjustified, which is prior knowledge of channel statistics. The Maximum Likelihood (ML)-based estimator solves those problems of both current estimators and furnishes Channel Estimation (C-E) performance approaching that of the I-MMSE estimator.

Keywords Massive MIMO · Channel estimation · Pilot contamination · Maximum likelihood · 5G wireless communications

1 Introduction

M-MIMO is a new technology for telecommunications networks of the future, that is based on using hundreds of antennas at each BS and can furnish an enormous number of users at the likewise Time-Frequency. M-MIMO systems were initially based on the point-to-point MIMO wherein two devices connected and using multiple antennas per device. After that, M-C m-MIMO systems are presented [1]. For M-C

J. Amadid · M. M. Hassani

Instrumentation, Signals and Physical Systems (I2SP) Group, Faculty of Sciences Semailia, Cadi Ayyad University, Marrakesh, Morocco
e-mail: jamal.amadid@edu.uca.ac.ma

M. M. Hassani

e-mail: hassani@ucam.ac.ma

M. Boulouird (✉)

Smart Systems and Applications (SSA) Group, National School of Applied Sciences of Marrakesh (ENSA-M), Cadi Ayyad University, Marrakesh, Morocco
e-mail: m.boulouird@uca.ac.ma

© Springer Nature Singapore Pte Ltd. 2022

S. Bennani et al. (eds.), *WITS 2020*, Lecture Notes in Electrical Engineering 745,
https://doi.org/10.1007/978-981-33-6893-4_94

1037

m-MIMO networks, an enormous number of single-antenna users are furnish by a BS fitted with multiple antennas. For a M-C system [2], the number of pilots used is limited by the coherence block therefore, when we use a significant number of pilots we increase the part designated for the transmission of Pilot Sequences (P-S). Therefore, the part designated for the data becomes smaller. To prevent this problem, the P-S used in each cell have to be used in another cell which is namely frequency-reuse, which leads to giving P-C. For C-E, Frequency Reuse (F-R) induces Inter-Cell Interference (ICI) in M-C m-MIMO systems and is known as P-C [2]. Channel State Information (CSI) plays a key role in M-C m-MIMO systems because it is delicate to obtaining high system performance. For m-MIMO, TDD is considered to be a better method for obtaining CSI in M-C m-MIMO systems in comparison with Frequency Division Duplex (FDD), because TDD needs C-E alone in the Uplink (UL) and the Downlink (DL) is identical to the transpose of the UL, meaning that the estimated channel is applicable in both UL and DL [3–5]. BSs typically estimate channels based on LS method [3] or I-MMSE method [6–8]. Besides, in the large majority of study, inter-cell and intra-cell Large-Scale Fading Coefficients (LSFC) are believed to well know when applying the I-MMSE method [4, 8, 9].

Our work presents a straightforward and convenient channel estimator for M-C M-U m-MIMO systems with P-C, the use of this estimator which relies on ML-based estimator is to overtake the issues of both current estimators namely I-MMSE and LS. The I-MMSE estimator requires knowledge of channel statistics while the LS channel estimator does not have the necessity for any prior information about channel but presents the lowest performance in comparison with others.

Notation: In this work, $(.)^H$, $\|.\|^2$, \mathbb{I}_K , $B(. , .)$, $\mathbb{E}\{.\}$ stand for the transpose-conjugate, norm, identity matrix, beta function, and expectation, respectively. $p \sim CN(0, Q)$ means p has a pdf of the zero-mean complex Gaussian vector with covariance matrix, $Q \sim N(0, \sigma^2)$ denotes a Gaussian pdf wherein zero presents the mean and σ^2 presents the variance.

1.1 Organization

This work is split into four parts, in Sect. 2, we describe the system model adopted for this work. Discussed and evaluated the channel estimators and drived the expressions of the Mean Square Error (MSE) for each estimator in Sect. 3. Section 4 presents numerical results to display the effectiveness of our method. For Sect. 5, a conclusion and subsequent work are presented.

2 System Model

This part purposeful to describe the system model wherein a M-C M-U m-MIMO system is considered with L cells wherein every cell be composed of a central BS equipped with M antennas and K users uniformly distributed (Fig. 1).

We suppose that RFC existing in this work are independent across antennas and users. \mathbf{h}_{ilm} represents the complex gain of the channel from the k -th user in the l -th cell to the m -th BS antenna in the i -th cell.

$$\mathbf{h}_{ilm} = \sqrt{\beta_{ilk}} \mathbf{g}_{ilm} \tag{1}$$

where β_{ilk} represents the LSFC which includes both Path Loss (PL) and shadowing (SD). We suppose the same LSFC value for all M BS antennas, and \mathbf{g}_{ilm} is the Small-Scale Fading Coefficient (SSFC) with $CN(0, 1)$ distribution.

The overall channel matrix is express by $\mathbf{H}_{il} \in \mathbb{C}^{M \times K}$ wherein the k -th column represented par $\mathbf{h}_{ilk} = [h_{ilk1}, \dots, h_{ilkM}]^T$ is the gains of the channels from user k in cell l to BS i . During our study, we assume that the LSFC $\{\beta_{ilk}\}$ is deterministic.

2.1 UL Training

Before that the BSs estimate the channels of its users, all users should transmit the τ pilot symbols. The frequencies used by each cell are repeated on the remains cells.

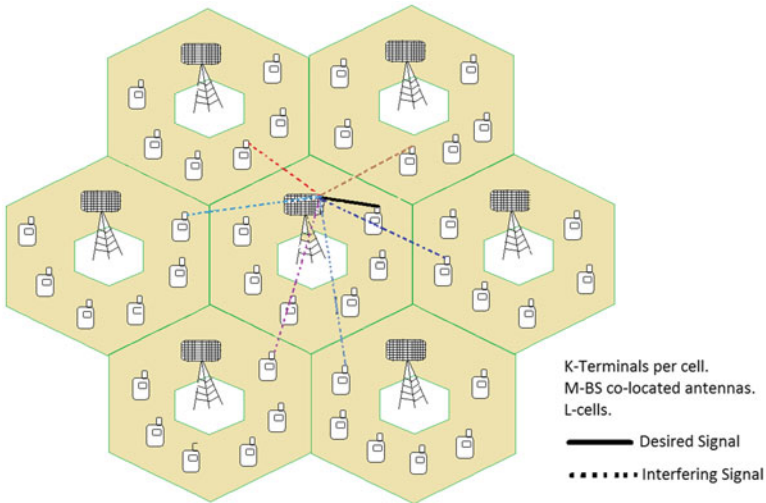


Fig. 1 System model

Which means that all cells have used the same group of frequency. Therefore, the F-R is 1, and we considered that all users in various cells transmit their pilot synchronously. $\Phi^H (K \times \tau)$ represents the matrix of pilot signals of K users, which has as property $\Phi^H \Phi = \tau \mathbb{I}_K, (K \leq \tau)$. The signal Y_i received at i -th BS is determined by

$$Y_i = \sum_{l=1}^L \sqrt{\mu} \mathbf{H}_{il} \Phi^H + W_i \tag{2}$$

where μ represents UL power or Transmit Signal to Noise Ratio (TSNR) and W_i represent $M \times \tau$ noise matrix which is follows $CN(0, 1)$. Therefore Eq. (2) can be written as

$$Y_i = \sqrt{\mu} \mathbf{H}_{ii} \Phi^H + \underbrace{\sqrt{\mu} \sum_{l=1, l \neq i}^L \mathbf{H}_{il} \Phi^H}_{\text{Inter-Cell interference}} + W_i \tag{3}$$

3 Channel Estimation Methods

3.1 LS Channel Estimator

As described in [10–12], the estimation of the channel vector \mathbf{h}_{ilk} using LS estimator is determined by

$$\hat{\mathbf{h}}_{ik}^{LS} = \Delta_{ik} = \frac{1}{\sqrt{\mu\tau}} Y_i \phi_k = \underbrace{\mathbf{h}_{ik}}_{\text{Desired}} + \underbrace{\sum_{l=1, l \neq i}^L \mathbf{h}_{ilk}}_{\text{Inter-Cell interference}} + \underbrace{\frac{W_i \phi_k}{\sqrt{\mu\tau}}}_{\text{Noise}} \tag{4}$$

where Δ_{ik} follows a $CN(0_M, \lambda_{ik} \mathbb{I}_M)$ distribution where the 2nd statistics of Δ_{ik} can be written as

$$\lambda_{ik} = \sum_{l=1}^L \beta_{ilk} + \frac{1}{\mu\tau} \tag{5}$$

Therefore the LS channel estimates is given in [10], which can be expressed as

$$\hat{\mathbf{h}}_{ik}^{LS} = \Delta_{ik} \tag{6}$$

The MSE of each antenna is determined by

$$\rho_{ik}^{LS} = \frac{1}{M} \mathbb{E} \left\{ [(\hat{\mathbf{h}}_{ik}^{LS} - \mathbf{h}_{ik})(\hat{\mathbf{h}}_{ik}^{LS} - \mathbf{h}_{ik})^H] \right\} = \lambda_{ik} - \beta_{ik} \tag{7}$$

According to the literature, LS estimator presents less performance than the I-MMSE estimator which means that LS presents MSE larger than the I-MMSE. Nevertheless, LS doesn't have the necessity for any information about the channel, but I-MMSE needs knowledge of channel statistics.

3.2 I-MMSE Channel Estimator

I-MMSE estimator adopts in a great number of m-MIMO works [4, 7]. Those works suppose absolutely knowledge of channel statistics (LSFC and SSFC). This supposition may not be acceptable for implementation. The I-MMSE channel estimate can be expressed as

$$\hat{\mathbf{h}}_{ik}^{I-MMSE} = \frac{\beta_{iik}}{\lambda_{ik}} \Delta_{ik} \tag{8}$$

wherein $\hat{\mathbf{h}}_{ik}^{I-MMSE}$ follows a $CN(0_M, \frac{\beta_{iik}^2}{\lambda_{ik}} \mathbb{I}_M)$. The MSE expression for I-MMSE channel estimate is written as

$$Q_{ik}^{I-MMSE} = \frac{1}{M} \mathbb{E}[\|\hat{\mathbf{h}}_{ik}^{I-MMSE} - \mathbf{h}_{ik}\|^2] = \beta_{iik} \left(1 - \frac{\beta_{iik}}{\lambda_{ik}}\right) \tag{9}$$

3.3 ML-Based Channel Estimator

In this section, we present and discuss the ML-based technique to estimate the variable λ_{ik} . Applying the ML technique to $f(\Delta_{ik}; \lambda_{ik})$ which follows a $CN(0_M, \lambda_{ik} \mathbb{I}_M)$, as a result

$$\hat{\lambda}_{ik} = \frac{\|\Delta_{ik}\|^2}{M} \tag{10}$$

This property $\mathbb{E}[\hat{\lambda}_{ik}] = \lambda_{ik}$ indicates that the ML-based estimator is unbiased and $var[\hat{\lambda}_{ik}] = \lambda_{ik}^2/M$. The high performance of this estimator is obtained by applying The Cramér-Rao bound, which is described in [10].

$$var(\hat{\lambda}_{ik}) \geq \frac{\lambda_{ik}^2}{M} \tag{11}$$

The Minimum Variance (MV) Unbiased Estimator (UE) is an estimator that possesses a smaller variance than all other UE existed in the literature [10]. This straightforward and efficient estimator is derived based on the consideration that the I-MMSE estimator does not have to know the individual LSFC, β_{iik} , as offered in the extant literature.

Replacing λ_{ik} with $\hat{\lambda}_{ik}$ in (8) gives the ML-based estimator, which is determined by

$$\hat{\mathbf{h}}_{ik}^{ML} = M \beta_{iik} \frac{\Delta_{ik}}{\|\Delta_{ik}\|^2} \tag{12}$$

Taking into account the Number of BS Antennas (NBSA) M , the ML-based estimation is quite close to that of the ideal I-MMSE. The average of the $\hat{\mathbf{h}}_{ik}^{ML}$ is expressed by $\mathbb{E}[\hat{\mathbf{h}}_{ik}^{ML}] = 0_M$ and the variance is defined by

$$\text{Var}[\hat{\mathbf{h}}_{ik}^{ML}] = \mathbb{E}[\hat{\mathbf{h}}_{ik}^{ML}(\hat{\mathbf{h}}_{ik}^{ML})^H] = \left(\frac{M^2}{M-1} \frac{\beta_{iik}^2}{\lambda_{ik}} \right) \mathbf{I}_M \tag{13}$$

We can remark that when the NBSA M tends to infinity, we obtain the following expression

$$\text{Var}[\hat{\mathbf{h}}_{ik}^{ML}] \rightarrow \frac{\beta_{iik}^2}{\lambda_{ik}}$$

The MSE for ML-based channel estimates can be defined as

$$\mathcal{Q}_{ik}^{ML} = \frac{1}{M} \mathbb{E}[\|\hat{\mathbf{h}}_{ik}^{ML} - \mathbf{h}_{iik}\|^2] \approx \beta_{iik} \left[1 - \frac{(M-2)\beta_{iik}}{(M-1)\lambda_{ik}} \right] \tag{14}$$

\mathcal{Q}_{ik}^{ML} presents the MSE approximate for each BS antenna.

The paragraph below presents a Closed-Form (C-F) for MSE which performs like the MSE expression above [13].

$$\mathcal{Q}_{ik}^{prop(C-F)} = \frac{M}{M-1} \frac{\beta_{iik}^2}{\xi_{ik}} + \beta_{iik} - 2\beta_{iik}\theta_{ik} \tag{15}$$

wherein

$$\theta_{ik} = \int_0^1 \int_{-1}^1 \frac{K_{ik}^2(1-t) + K_{ik}\sqrt{t(1-t)}}{K_{ik}^2(1-t) + 2K_{ik}w\sqrt{t(1-t)} + t} f_T(t) f_W(w) dw dt \tag{16}$$

with $K_{ik} = \sqrt{\frac{\beta_{iik}}{\xi_{ik} - \beta_{iik}}}$ and $f_T(t)$ and $f_W(w)$ are defined by

$$f_T(t) = \frac{\Gamma(2M)}{(\Gamma(M))^2} (t(t-1))^{M-1}, \quad 0 < t < 1 \tag{17}$$

$$f_W(w) = \frac{M}{\pi} B(1/2, M) ((1-w^2))^{M-1/2}, \quad |w| < 1 \tag{18}$$

$$Q_{ik}^{prop(C-F)} - Q_{ik}^{prop(approx)} = 2\beta_{ik} \left\{ \frac{\beta_{ik}}{\xi_{ik}} - \theta_{ik} \right\} \tag{19}$$

where θ_{ik} is given in [13].

When both μ and $M \rightarrow \infty$, $\theta_{ik} \rightarrow \frac{\beta_{ik}}{\lambda_{ik}}$ therefore $Q_{ik}^{prop(C-F)} - Q_{ik}^{prop(approx)} \rightarrow 0$. In this equation below, we have calculated the square Euclidean distance between the I-MMSE and ML-based estimators which is defined as follows

$$\frac{1}{M} \mathbb{E}[||\hat{\mathbf{h}}_{ik}^{ML} - \mathbf{h}_{ik}^{I-MMSE} ||^2] = \frac{1}{M-1} \frac{\beta_{ik}^2}{\lambda_{ik}} \tag{20}$$

The demonstration of Eq. (20) is existing in [14].

4 Numerical Results and Discussion

In this section, we simulate and analyze the performance of the ML-based estimator in comparison with that of I-MMSE and LS estimators.

A typical M-C M-U constitution as exposed in the Fig. 1 with $L = 7$ hexagonal cells (1 cell ringed by 6 cells), $K = 10$ users in each cell uses $\tau = K$ pilot symbols, and F-R is 1. We consider one type of setup for β_{ilk} , wherein the LSFC are dependent on the distance between the users and the BS. The users in each cell are uniformly allocated between two radii $r_0 = 100$ m and $r_1 = 1000$ m successively, according to the following model

$$\beta_{ilk} = \alpha / \left(\frac{r_{ilk}}{r_0} \right)^\nu \tag{21}$$

wherein $\nu = 3.8$ (For all results except when ν is variable as depicted in Fig. 5), $10\log_{10}(\alpha) \sim N(0, \sigma_{shadow,dB}^2)$ wherein $\sigma_{shadow,dB} = 8$ and r_{ilk} represents the distance between the k -th user in l -th cell to the i -th BS. We have introduced the radius $r_0 = 100$ m in our study, to take a look over the effect of the users which are not near from the BS, since when the users are near from the BS, it presents a higher β_{ilk} , in this case, the BS can easily neglect the interfering signals (Higher values for the desired user in comparison with interference users). While our work treats C-E with consideration of P-C.

All simulation results in this section are taken through the LSFC given in Eq. (21) which model (PL and SD) a real propagation setup. A multitude of works treat this case but they consider that the LSFC values as constant.

Figure 2 shows the MSE in dependence of SNR underneath random LSFC β_{ilk} with $M = 40$. Our results are achieved by the average of MSE up 10,000 realizations of β_{ilk} . The simulation result shown that the performance analytical and simulated of each estimator are the same. wherein the LS estimator presents the inferior performance in comparison with other estimators while the I-MMSE estimator presents better performance. Moreover, when M increases the ML-based estimator

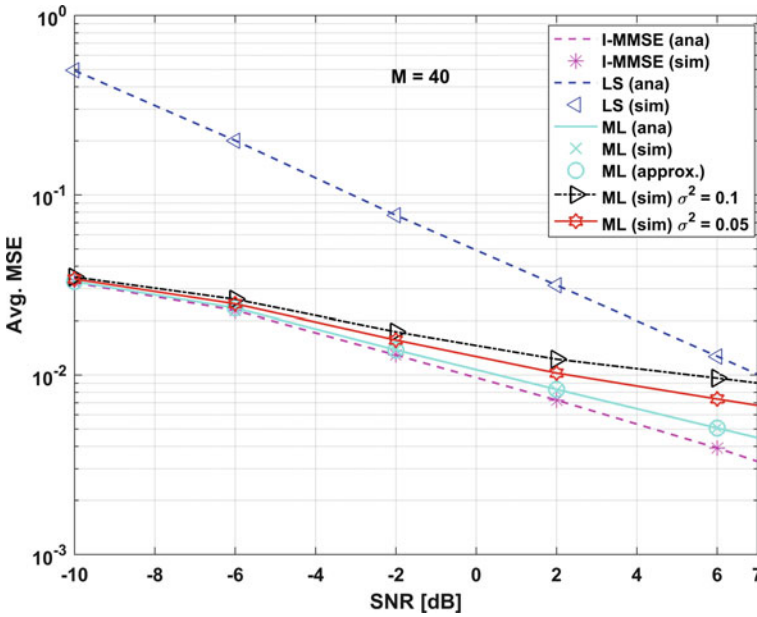


Fig. 2 Avg. MSE versus SNR

approaching the I-MMSE estimator. We have also study and shown the effect of the sensitivity on the performance of ML-based estimator with make use of an estimate $\beta_{iik} = \beta_{iik}(1 + N(0, \sigma^2))$, for different values of σ^2 . According to Fig. 2, For $\sigma^2 = 0.1$ the performance deteriorates, while for $\sigma^2 = 0.05$ we obtain less deteriorate than the first case.

Figure 3 shows the MSE in dependence of M which presents the NBSA. The power allocated for transmission is $\mu = 10dB$ and the LSFC are generated through Eq. (21). The MSE performance of LS and I-MMSE channel estimates is constant which means that these estimators are independent of M, while the ML-based estimator is nearing the I-MMSE estimator as M grows.

From the Eq. (15), which presents a C-F MSE expression is has a practical issue, which is reflected in the fact that when M is great than 85, the *Gamma Function* $\Gamma(2M)$ grows to arrive unlimited values which are biggest than the most workable values introduced with IEEE precision which equal $1.7977e + 308$ [14]. Besides, the result exposed in Fig. (3), is obtained using the approximated MSE which does not show de same issue as the C-F, which means that the approximated MSE may be utilized for all NBSA M values.

Figure 4 shows the MSE in dependence of SNR for the ML-based and I-MMSE estimators under various NBSA M. As reported by Eq.(20) and from the Fig. 4, we remark that for small SNR values the distance between ML-based and I-MMSE estimators is small whereas when the SNR increases a limit value is obtained, and this limit value depends on the NBSA M, this is justified by Eq. (20).

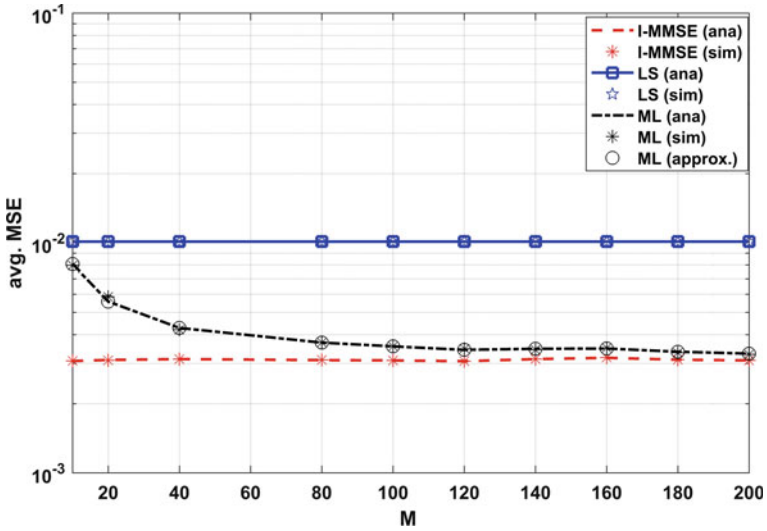


Fig. 3 Avg. MSE versus NBSA, M

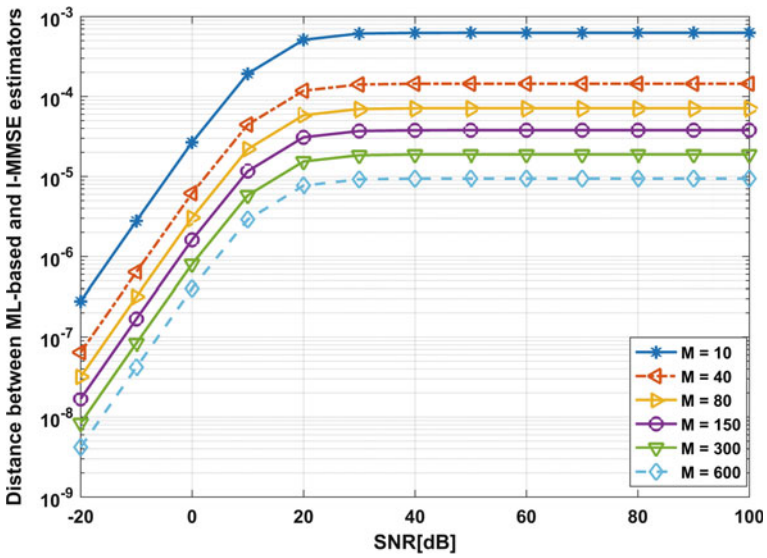


Fig. 4 The distance among ML-based and I-MMSE estimators versus SNR

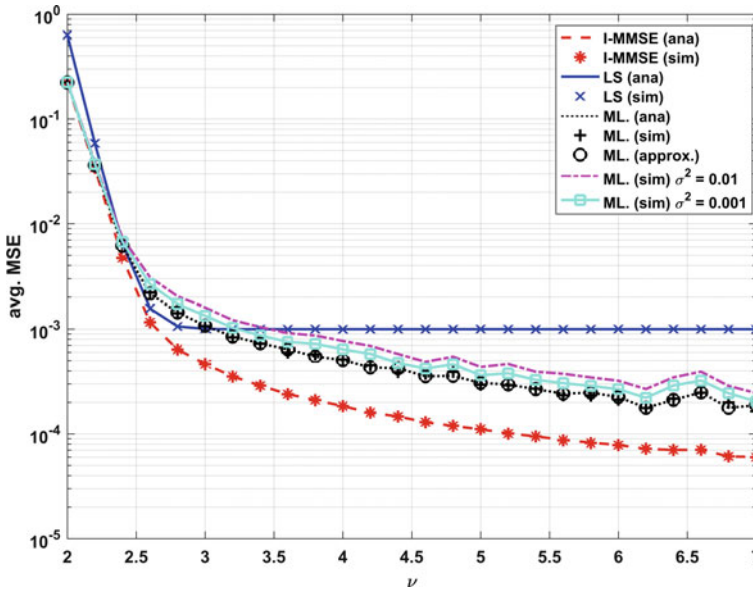


Fig. 5 Avg. MSE versus PL exponent

Figure 5 shows the Average of the MSE in dependence of PL exponent ν which represents the rate at which the signal puissance decreases with distance. As depicted Fig. 5, for $\nu \in [2, 2.8]$ all estimators behavior is almost the same, whereas when ν is greater than 2.8, LS estimator presents the worse performance, while the ML-based estimator is keeping close to I-MMSE, the I-MMSE presents a better performance in comparison of other estimators. We have also study and shown the effect of the sensitivity on the performance of ML-based estimator with make use of an estimate $\beta_{iik} = \beta_{iik}(1 + N(0, \sigma^2))$, for different values of σ^2 . According to Fig. 2, For $\sigma^2 = 0.01$ the performance deteriorates, while for $\sigma^2 = 0.001$ we obtain less deteriorate than the first case.

5 Conclusion

In this study, we have presented a straightforward channel estimator for M-MIMO T-DD systems with P-C. The unrealistic property produced by the I-MMSE estimator, which is manifesting in the required foreknowledge of LSFC, which is solving by using the ML-based estimator, in which the expression of interference plus noise power is replaced in the I-MMSE estimator using the ML estimator. Besides, by increasing M the ML-based estimator provides MSE results that approximate those of the I-MMSE estimator without the need foreknowledge of channel and noise and interference statistics. Furthermore, an approximate analytical MSE expression for

an ML-based estimator is given. We leave the use of a hybrid method based on an ML estimator for combat the unrealistic property produced by the I-MMSE estimator as future work.

References

1. Lu L, Li GY, Swindlehurst AL, Ashikhmin A, Zhang R (2014) An overview of massive MIMO: benefits and challenges. *IEEE J Sel Top Sig Process* 8(5):742–758
2. Marzetta TL (2010) Noncooperative cellular wireless with unlimited numbers of base station antennas. *IEEE Trans Wirel Commun* 9(11):3590–3600
3. Elijah O, Leow CY, Rahman TA, Nunoo S, Iliya SZ (2016) A comprehensive survey of pilot contamination in massive MIMO 5G system. *IEEE Commun Surv Tutor* 18(2):905–923
4. Jose J, Ashikhmin A, Marzetta TL, Vishwanath S (2011) Pilot contamination and precoding in multi-cell TDD systems. *IEEE Trans Wirel Commun* 10(8):2640–2651
5. Bjornson E, Larsson EG, Marzetta TL (2016) Massive MIMO: ten myths and one critical question. *IEEE Commun Mag* 54(2):114–123
6. Hoydis J, ten Brink S, Debbah M (2013) Massive MIMO in the UL/DL of cellular networks: how many antennas do we need? *IEEE J Sel Areas Commun* 31(2):160–171
7. Ngo HQ, Larsson EG, Marzetta TL (2013) The multicell multiuser MIMO uplink with very large antenna arrays and a finite-dimensional channel. *IEEE Trans Commun* 61(6):2350–2361
8. Shariati N, Bjornson E, Bengtsson M, Debb M (2014) Low-complexity polynomial channel estimation in large-scale MIMO with arbitrary statistics. *IEEE J Sel Top Sig Process* 8(5):815–830
9. Mawatwal K, Sen D, Roy R (2017) A semi-blind channel estimation algorithm for massive MIMO systems. *IEEE Wirel Commun Lett* 6(1):70–73
10. Kay SM (1993) *Fundamentals of statistical signal processing: estimation theory*, vol 1. Pearson Education, New York
11. Rao CR (1973) *Linear statistical inference and its applications*, 2nd edn. Wiley, New York
12. Fisher RA (1922) On the mathematical foundations of theoretical statistics. *Phil Trans R Soc A* 222:309–368
13. Khansefid A, Minn H (2015) On channel estimation for massive MIMO with pilot contamination. *IEEE Commun Lett* 19(9):1660–1663
14. de Figueiredo Felipe AP et al (2018) Channel estimation for massive MIMO TDD systems assuming pilot contamination and flat fading. *EURASIP J Wirel Commun Netw* 1:1–10

Mapping the Geothermal Potential of the Jbel Saghro Massif by Airborne Magnetism (Anti-Atlas, Morocco)



Miftah Abdelhalim and El Azzab Driss

Abstract The main objective of this research is to use the aeromagnetic data covering the Jbel Saghro Massif (Southern Morocco) to study the transition zone between magnetized and non-magnetized rocks by estimating the curie isotherm depth, to calculate the thermal flux in mW m^{-2} . The processing and filtering of magnetic data has given the possibility to trace the lateral limits of hidden and magnetic geological sources, the latter have directions ENE–WSW, NNW–SSE, W–E and NW–SE inherited by the geodynamic evolution of the study area. Using the local wave number method, a curie depth isobaths map was generated, showing varying values from 6.9 to 25.9 km. The regional geothermal gradient map shows values between 22 and 85 $^{\circ}\text{C km}^{-1}$. The calculation of the thermal flux reveals several geothermal provinces ($>190 \text{ mW m}^{-2}$) with a total area of about 1500 km^2 associated with inliers of Precambrian age.

Keywords Aeromagnetism · Curie depth · Thermal flux

1 Introduction

Geothermal energy is the exploitation of heat stored in the subsoil. The use of geothermal resources is subdivided into two main families: electricity generation and heat production. The interest given to these resources lies in the importance and multitude of their use, particularly indirect use (domestic heating, cattle and sheep rearing, greenhouse crops, soil heating, aquaculture) as well as in the production of clean and secure source electricity.

M. Abdelhalim (✉)

Hassan First University of Settat, Faculty of Sciences and Technology, Research Team of Geology of the Mining and Energetics Resources, BP577 Settat, Morocco
e-mail: a.miftah@uhp.ac.ma

E. A. Driss

Sidi Mohamed Ben Abdellah University, Faculty of Science and Technology, SIGER Laboratory, BP30050 Fez, Morocco
e-mail: driss.elazzab@usmba.ac.ma

© Springer Nature Singapore Pte Ltd. 2022

S. Bennani et al. (eds.), *WITS 2020*, Lecture Notes in Electrical Engineering 745,
https://doi.org/10.1007/978-981-33-6893-4_95

1049

In Morocco, regional mapping trials were conducted by Rimi et al. [1] for the Rif, [2] for Eastern Morocco, and by Boukdir [3] for the Tadla Basin. Zarhloule [4] produced a first geothermal gradient map of Morocco in gradient zoning, based on the mean gradient calculation of all temperatures in each borehole. However, one difficulty in this procedure is that the temperature gradient is by definition related to the depth and nature of the rock.

Regional thermal gradient mapping also has the disadvantage of having very limited resolution, the mapping of regional variations in the thermal gradient should take into account that the gradient may vary laterally in the case of granite or salt collapse or intrusion structures [5]. To remedy these problems, in the present study, we have adopted a new methodology based on indirect investigation methods by airborne geomagnetism by measuring the intensity of the Earth's magnetic field associated with subtle variations in the magnetic susceptibility of the subsoil. This method has been widely used in several cases worldwide [6, 7].

However, no studies in Morocco were applied, this is how our work aimed at the application of airborne geophysics for the estimation of the curie point depth (km) and thermal flux (mW m^{-2}) in the Jbel Saghro Massif. The immediate goal is to explore new sources of clean energy.

2 Geological Context

The patterns of geological formation outcropping in the study area are generally associated with high increases in temperature and pressure in-depth, and can generate significant geothermal reservoirs. Rocks, unlike metals, lose their heat very slowly, they are poor thermal conductors (or relatively effective insulators). They therefore, stop internal energy transfers and thus allow a form of heat storage inside the globe.

Geologically (Fig. 1), the Jbel Saghro Massif is located among the Bou-Azzer inlier in the S–W and the Ougnat in the N–E and it is structurally oriented E–W. The Paleoproterozoic basement of the region is formed by amphibolite and gneiss betwixt Sekoura and Ouarzazate and in the West of Imiter by granite. The lower Neoproterozoic is composed by volcano-sedimentary terrains forming the central part of inliers, the latter being intersected by plutonic rocks. The middle Neoproterozoic is marked by gabbros, quartzic diorites, diorites, and andesite. The terminal Neoproterozoic which overcomes in major discordance with the Paleoproterozoic basement. The outcropping of the latter in the form of inliers in most of the study area may indicate a shallow curie isotherm depth.

3 Materials and Methods

In crustal rocks, the magnetic minerals hotter than their curie temperature exhibit random magnetic moments and their vector sum is statistically zero. Hence, they lose

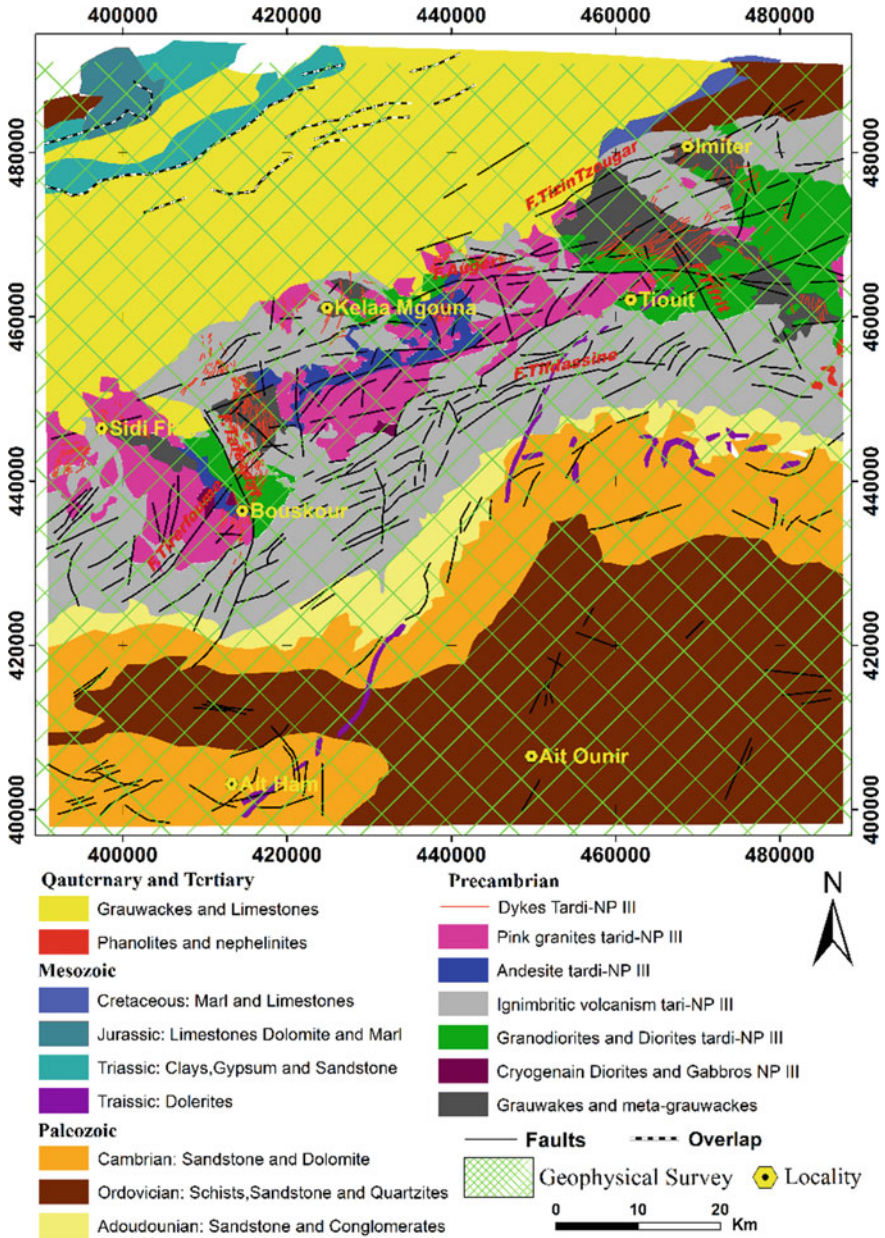


Fig. 1 Geological map of the Jbel Saghro Massif (modified after [8])

their ability to generate detectable magnetic anomalies. These demagnetized rocks confirm the existence of a very hot rock mass in-depth at which magnetic minerals lose their ferromagnetism, and which can be exploited for the use of geothermal energy. The Curie temperature isotherm therefore corresponds to the basal limit of magnetic anomalies and can be calculated from the measurements of the total magnetic field made on the Earth's surface.

In the present study, the magnetic method was applied to deduce the variations in rocks magnetizations in the Jbel Saghro Massif (Southern Morocco), which corresponds to an area of about 10,300 km². The total magnetic field maps at 1/100,000, acquired in 1981 at a flying altitude of 2600 m and a spacing of 1000 m between the flight lines were used (Fig. 1). Various manipulations and transformations have been made to these data in order to make them easy to interpret and to extract as much information as possible:

3.1 Reduction to the Pole (RP)

This treatment aims to transform bipolar anomalies into unipolar anomalies. It transforms the observed anomaly into the one that would have been obtained if the magnetization and the local magnetic field were both vertical. This transformation, therefore consists of eliminating the distortions induced by the magnetic inclination and allows to place exactly the magnetic anomalies observed at the plumb of the structures likely to generate them [9].

3.2 Source Parameter Imaging (SPI)

Due to the lack of measurements of precise magnetic properties of susceptibility and magnetization, which covers all geological facies in the study area. It was not easy to model or reverse the magnetic data. The local wavenumber method described as SPI (Source Parameter Imaging) was first introduced by Thurston and Smith [10]. The principle of this technique is based on the complex attributes obtained from the amplitude and local phase of the analytical signal to estimate the depths of the magnetic sources and their locations in the horizontal plane. Local wave number parameters are used to determine the limits of magnetic sources and calculate their depths.

3.3 Heat Flow Estimation

The Curie depth estimated by the SPI method can be converted into thermal flux by the application of Fourier's law, determined by the following formula:

$$q = \lambda \frac{dT}{dz} \quad (1)$$

Where q is the heat flow (W m^{-2}) and λ is the coefficient of thermal conductivity ($\text{W m}^{-1} \text{ }^\circ\text{C}^{-1}$). In this equation, it is assumed that the direction of the temperature variation is vertical and the temperature gradient dT/dz ($^\circ\text{C km}^{-1}$) is constant.

According to Tanaka et al. [11], the Curie temperature (θ) can be obtained from the Curie point depth (Z_c) and the thermal gradient dT/dZ using the following equation:

$$\theta = \left[\frac{dT}{dz} \right] Z_c \quad (2)$$

In Eqs. 1 and 2, a relationship can be determined between the Curie point depth (Z_c) and the heat flow (q) as:

$$q = \lambda \left[\frac{\theta}{Z_c} \right] \quad (3)$$

Tanaka et al. [11] showed that any given depth to a thermal isotherm is inversely proportional to heat flow, where q is the heat flow. This equation implies that regions of high heat flow are associated with shallower isotherms, whereas regions of lower heat flow are associated with deeper isotherms.

4 Results and Discussion

4.1 Magnetic Source Boundary Mapping

The database from the total magnetic field allowed us to make the map of the residual magnetic field. The latter was reduced to the pole ($I = 40.4^\circ$, $D = -2.5^\circ$). The application of the RP method at the level of the study area allowed us to make a global map (Fig. 2) in which the positive lobe moved Northward at the depend of the negative lobe in order to position anomalies at the aplomb of the causative sources.

The analysis of this map (Fig. 2) allows the possibility of raising the main magnetic anomalies of different intensities, of variable size and shape, isolated or interfered, showing preferential directions, which are generally ENE–WSW, NNW–SSE, W–E, and NW–SE which are in good correlation with the global tectonic evolution of the study area. Generally, positive anomalies of high intensities and long wavelengths are associated with magnetic structures linked to the Paleoproterozoic basement. The negative ones are linked to structures with low magnetization generally situated in the Paleozoic cover [12].

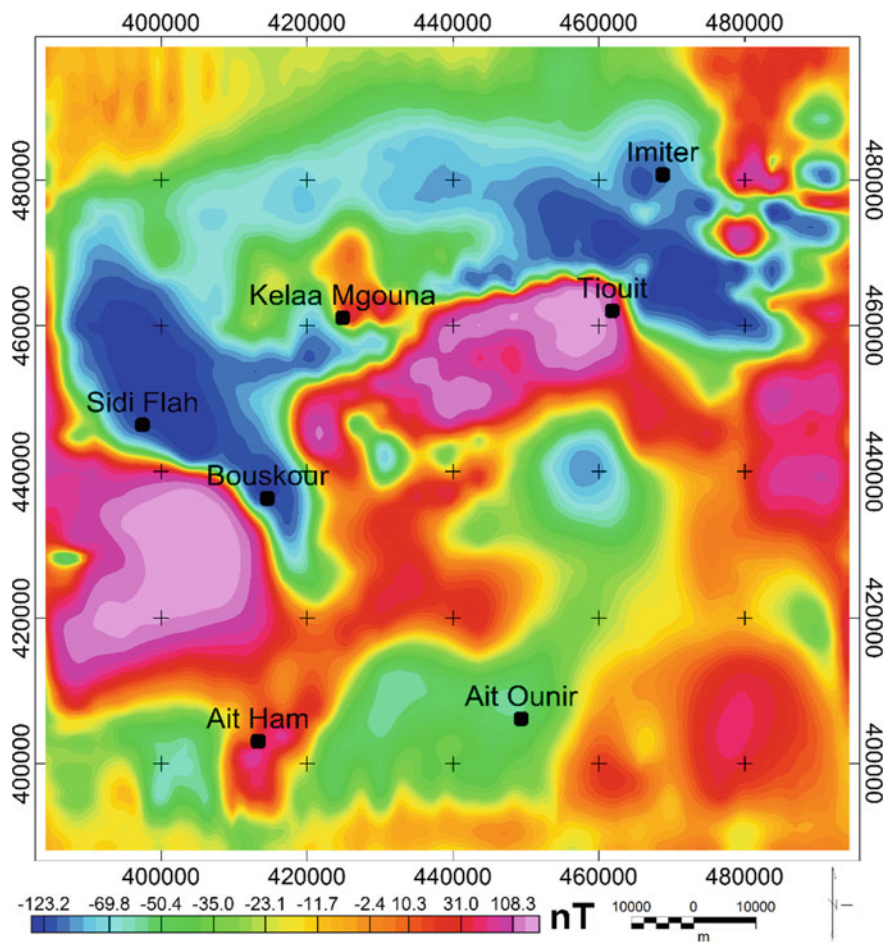


Fig. 2 Map of magnetic field reduced to the pole of the Jbel Saghro massif

4.2 Depths of Magnetic Sources

The SPI application on the magnetic field reduced to the pole allowed to draw the isobaths map of curie point, the depths obtained vary from 6.9 to 25.9 km, with an average value of 10.5 km (Fig. 3).

The entire area generally shows isolated and punctual fluctuations in curie depth ($Z_c < 10$ km), which strongly correlate with the outcrops of the upper Proterozoic age inliers of the Jbel Saghro Massif (Figs. 1 and 3), which are formed of granodiorites, granites, diorites, andesite, rhyolites. The work of [13] has shown that these inliers are essentially composed of volcano-clastic and volcanic series that can produce magnetic anomalies of high intensities [14], and they are bordered by late- to post-tectonic granitic intrusions. Thus, these late-tectonic granitic rocks can be considered

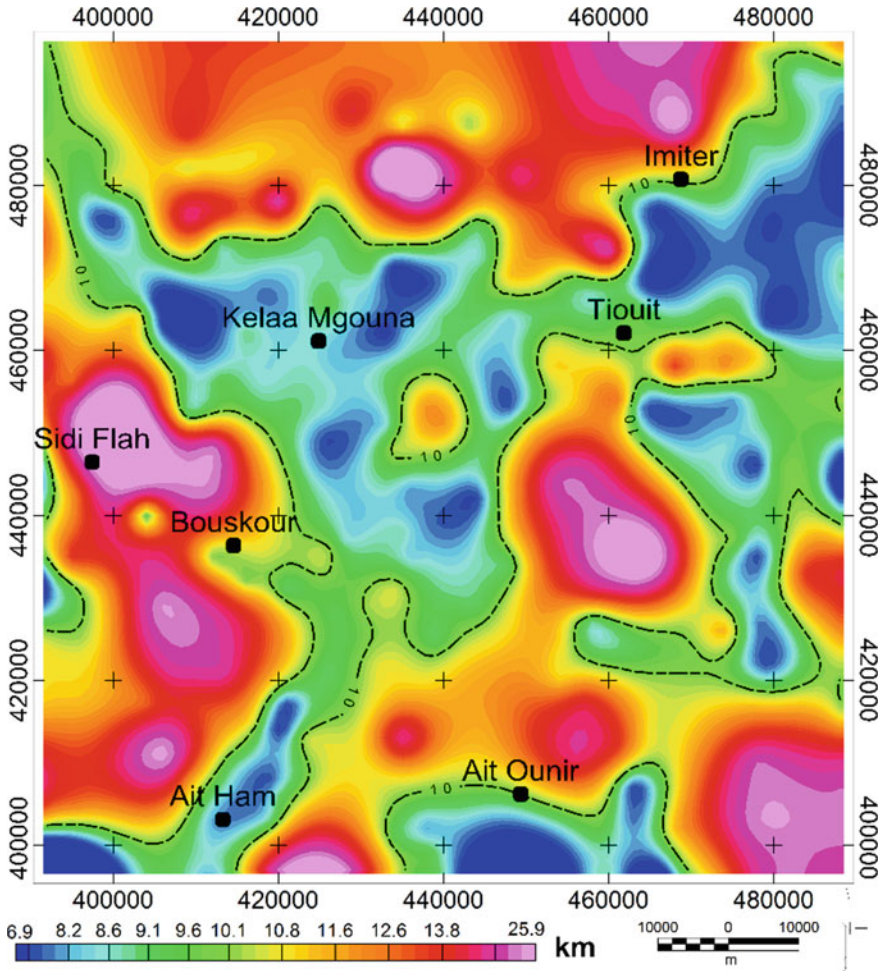


Fig. 3 Map of the curie point depths obtained by the SPI method

as forming a large intrusive batholite, which outcrops discontinuously in the Jbel Saghro massif.

On the other hand, regional isobaths of low fluctuation ($Z_c > 10$ km) is observed in all the study area (Figs. 1 and 3), in which the intrusions of the large batholite outcrop. This arrangement can be explained by the geodynamic evolution of the Anti-Atlas during the Paleozoic, according to the work of [15] it is a stable platform affected subsequently by a rifting phenomenon in the Cambrian and epi-orogenic movements.

4.3 Geothermal Potential of the Jbel Saghro Massif

In order to remedy the problem that the geothermal gradient can vary laterally, and therefore an average gradient may not represent the thermal state of the formations due to the contrasts in thermal conductivity and the circulation of fluid which could even reverse the temperature gradient (Fig. 4). Using magnetic data, we established a geothermal gradient variation map of the study area. A curie temperature of 580 °C was used, representing the average temperature at which the magnetic minerals lose their magnetizations.

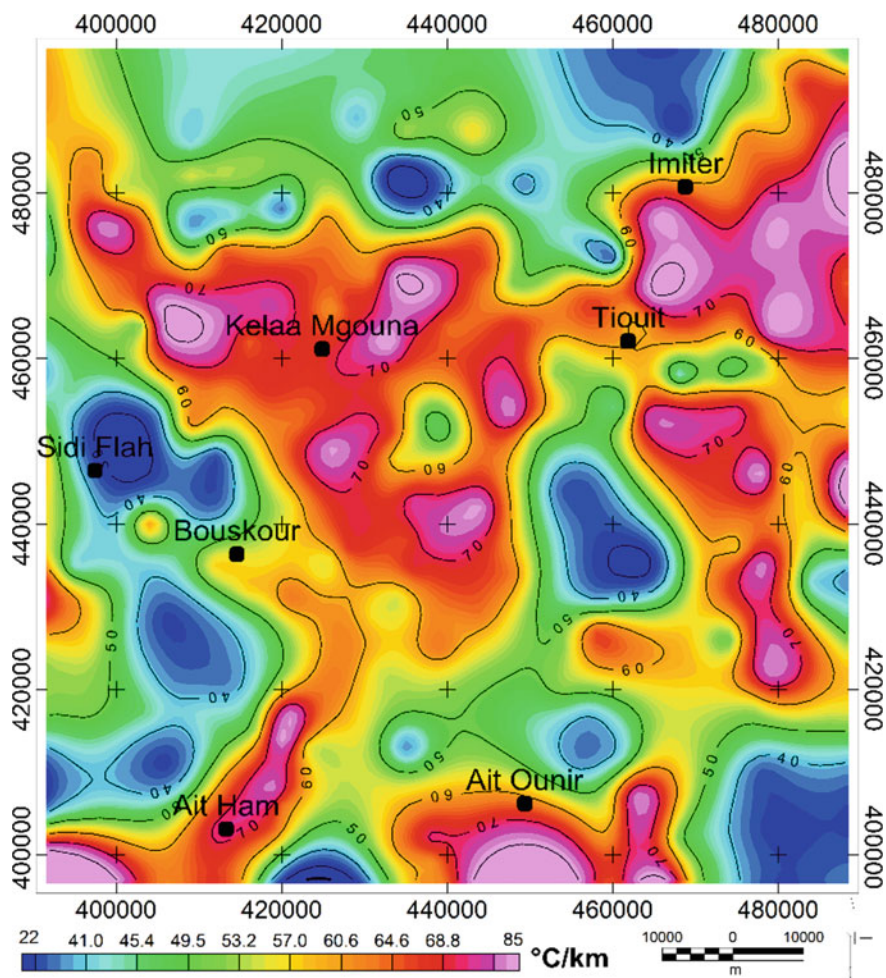


Fig. 4 Map of the geothermal gradient of the of the Jbel Saghro massif

The resulting map shows (Fig. 4) a gradient varying from 22 to 85 °C km⁻¹ and an average of 58 °C km⁻¹. The high values correlate with the Precambrian basement located in the center of the study area represented by high gradient metamorphic rocks, intruded by the injection of several granitic plutons. An average value of 28 °C km⁻¹ was found, which is very close to the results obtained by field measurements [4]. these results show the effectiveness of the approach we used in terms of sampling density (1 station per km²) which allow good coverage of the study area, thus allowing better lateral delineation of the geothermal gradient.

In order to map the potential geothermal zones, we established a heat flux map. Because of the significant heterogeneity of geological formations, it was difficult to adopt a single thermal conductivity value. To remedy this problem, we used the values of the work of [16], which show that magmatic rocks have an average value of 2.5 W m⁻¹ °C⁻¹, and those sedimentary of the order of 3.14 W m⁻¹ °C⁻¹. For reasons of simplicity, we have chosen the average value of 2.82 W m⁻¹ °C⁻¹.

The Examination of the thermal flux map (Fig. 5) shows variant values from 63 to 240 mW m⁻² and an average value of 160 mW m⁻². These values compared to those measured in the field by [5], which found an average value of 40 mW m⁻², can be interpreted by the investigation depths of the boreholes used (<500 m) since the temperature increases proportionally with the depth. From a geothermal potential point of view, the Jbel Saghro Massif could indicate very promising areas with a thermal flux (>190 mW m⁻²) at the level of Kelaa Mgouna, Imiter, at the SSE of Tiouit, Ait Ounir and Ait Ham. Their extending are 506, 465, 225, 204 and 124 km², respectively. These can be considered as geothermal provinces of great value, which deserve to be explored further.

5 Conclusions

The use of airborne magnetism has shown the effectiveness of indirect methods in the rapid and precise discrimination of geothermal deposits. The results obtained are compatible with those measured in the field. The Jbel Saghro massif with a thermal flux reaching 240 mW m⁻² may provide in the future a geothermal province essential for Morocco's economic development.

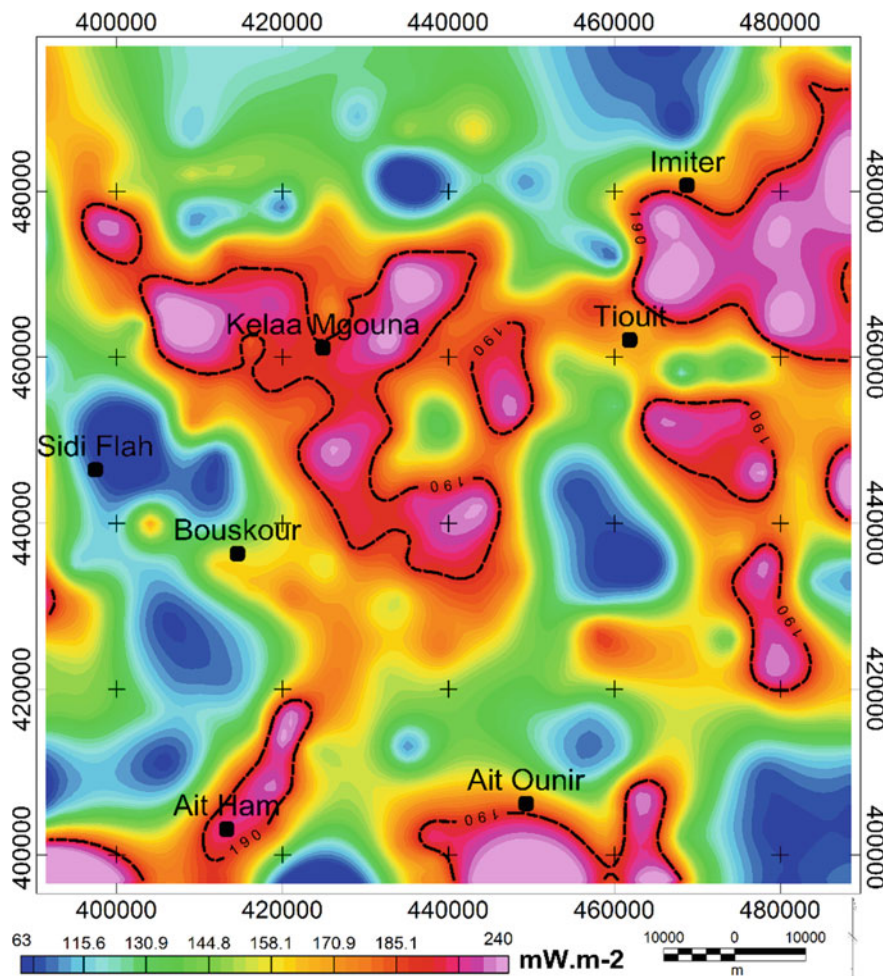


Fig. 5 Heat flux map calculated from magnetic data. The black line shows the areas greater than 190 mW m^{-2}

References

1. Rimi A, Chalouan A, Bahi L (1998) Heat flow in the westernmost part of the Alpine Mediterranean system (the Rif, Morocco). *Tectonophysics* 285:135–146
2. Lahrach A (1994) Potentialités hydrogéothermiques du Maroc oriental. Université de Sfax, Tunisie, Doctorat de spécialité
3. Boukdir A (1994) Contribution à l'étude géothermique du bassin du Tadla, Plateau des phosphates et Tassaout aval. Application au réservoir calcaire du Turonien (Crétacé). D.E.S. Université Cadi Ayad, Fac. Sci. Marrakech, Maroc
4. Zarhloule Y (2004) Le gradient géothermique profond du Maroc : détermination et cartographie. *Bulletin De l'Institut Scientifique, Rabat, Section Sciences De La Terre* 26:11–25

5. Rimi A (1990) Geothermal gradient and heat flow trends in Morocco. *Geothermics* 19(5):443–454
6. Trifonova P, Zhelev Z, Petrova T, Bojadgieva K (2009) Curie point depths of Bulgarian territory inferred from geomagnetic observations and its correlation with regional thermal structure and seismicity. *Tectonophysics* 473(3–4):362–374
7. Selim EI, Aboud E (2014) Application of spectral analysis technique on ground magnetic data to calculate the Curie depth point of the eastern shore of the Gulf of Suez, Egypt. *Arab J Geosci* 7(5):1749–1762
8. Hindermeyer J, Gauthier H, Destombes J, Choubert G (1977) Carte géologique au 1/200 000, Jebel Saghro Dadès (Haut Atlas central, sillon Sud-Atlasique et Anti-Atlas oriental). Notes et Mémoires Service Géologique du Maroc, pp 161
9. Baranov V (1957) A new method for interpretation of aeromagnetic maps pseudo-gravimetric anomalies. *Geophysics* 22:359–383
10. Thurston JB, Smith RS (1997) Automatic conversion of magnetic data to depth, dip, and susceptibility contrast using the SPI (TM) method. *Geophysics* 62(3):807–813
11. Tanaka A, Okubo Y, Matsubayashi O (1999) Curie point depth based on spectrum analysis of the magnetic anomaly data in East and Southeast Asia. *Tectonophysics* 306(3–4):461–470
12. Miftah A, El Azzab D, Attou A, Manar A (2017) Contribution of the geomagnetism to the region of the massif Jbel Saghro geology, Eastern Anti-Atlas, Morocco. *Arab J Geosci* 10(21):460
13. Saquaque A (1992) Un exemple de suture-arc: le Précambrien de l' Anti-Atlas centre-oriental. Thèse Doctorat Es-Sciences. 348 p; U.C.A. Marrakech
14. El Azzab D, El Wartiti M (1998) Mise en place de la chaîne volcanique du moyen Atlas (Maroc): Traitement des données aéromagnétiques. The middle Atlas volcanic orogeny setting (Morocco): aeromagnetic data analysis. *Pangea* 29:45–51
15. Michard A (1976) Elément de géologie marocaine. Notes et Mémoires Service Géologique du Maroc 252:408
16. Stacey FD (1977) *Physics of the earth*, 2nd edn. Wiley, New York

A Compact Flexible UWB Antenna for Biomedical Applications: Especially for Breast Cancer Detection



Nirmine Hammouch, Hassan Ammor, and Mohamed Himdi

Abstract Worldwide, cancer remains a scary topic that cause many deaths in recent years such as breast cancer, which affects many women in many ways. UWB antennas play an important role in early detection. The design of UWB antennas for biomedical applications presents a promising challenge and requires more research to improve health care system. This paper proposes an UWB antenna printed on a flexible substrate with thickness of 0.254 mm and relative permittivity $\epsilon_r = 2.2$, operating in the range of 3.64–12.11 GHz. For its realization, we applied some techniques of miniaturization to improve some antenna characteristics. In addition, the effects of the curvature and the biological tissues on the return loss and radiation pattern were investigated.

Keywords Antenna · UWB · Breast cancer

1 Introduction

Currently, Radar based microwave imaging (MWI) technology is the golden method for biomedical detection developed over the recent few years [1–3]. This technology offers a good accord between spatial resolution and depth of penetration using the high and low frequencies. Microwave imaging techniques give better results with the advantages of non-ionizing electromagnetic radiation, comfortable, and soft sensing technique [4, 5]. The electromagnetic wave is transmitted via transmitter antenna and is received back via receiver antenna. Therefore, UWB antennas are the most

N. Hammouch (✉) · H. Ammor

Research Team in Smart Communications, Engineering for Smart and Sustainable Systems
Research Center, EMI, Mohammed V University in Rabat, Rabat, Morocco
e-mail: hammouchnirmine1@gmail.com

H. Ammor

e-mail: ammor@emi.ac.ma

M. Himdi

Institute of Electronics and Telecommunications of Rennes, University of Rennes I, UMR 6164,
Rennes 35042, France
e-mail: Mohamed.himdi@univ-rennes1.fr

© Springer Nature Singapore Pte Ltd. 2022

S. Bennani et al. (eds.), *WITS 2020*, Lecture Notes in Electrical Engineering 745,
https://doi.org/10.1007/978-981-33-6893-4_96

1061

important element of a system radar, they allow to reduce cluttered data to create highly localized images [5–8]. This technology uses a very wide frequency band in the range from 3.1 to 10.6 GHz according to the Federal Communications Commissions (FCC) standard [4, 8, 9]. Antennas are components requires a special study. Many research teams being interested in many methods to improve their performances, they must be adapted to most recent applications [10, 11]. The development of printed antenna presents several challenges including the miniaturization of the radiating structure and integrate them in a small volume while trying to keep their properties specially the radiation efficiency and bandwidth [12, 13].

Over the last few years, microwave-imaging techniques give better results with many advantages including non-ionizing, comfortable, and high accuracy of detection malignant tissues [6, 14]. This technique is still better than the old screening methods such as mammography, which generates a wide range of limitations such as ionizing radiation, lower spatial resolution, false positive and false negative results [7, 8, 15].

This paper is focused on the development and miniaturization of a flexible UWB antenna. An UWB microstrip patch antenna was described and fabricated. The antenna has a wide bandwidth with frequency band from 3.8 to 12.11 GHz. The effects of various parameters on the bandwidth and radiation characteristics were discussed. All the improvements we have made to this antenna, allow it be used on different curved surfaces of the breast while maintaining all its performances. A 3D breast model is modelled to describe the part of the effect of biological tissues on antenna performances.

2 Antenna Design

The antenna configuration used for this study is illustrated in Fig. 1. The antenna structure is printed on a 21 mm × 14 mm ROGERS RT-5880 substrate with a dielectric constant of 2.2 and a loss tangent of 0.0009. Where the shape of the slot and the partial ground plane are an important factor in increasing bandwidth and minimizing the size of the proposed antenna. The final dimensions of the antenna designs are summarized in Table 1 (Figs. 1, 2 and 3).

The ground plane is one of the main elements that can influence the performance of the antenna. It is observed that the resonance frequency is affected. In addition, the bandwidth variation inevitably depends on the size of the ground plane and the insertion of different slots inside the patch. The reflection coefficient of the final antenna gives us a better result than that of the previous antenna, which can be obtained by optimizing their dimensions.

With the selected design, the return loss of the proposed antenna is shown in Fig. 5. In the operating frequency range of 3.8–12.11 GHz, a good agreement is obtained between two simulations and measurement results. A slight difference at the level of the resonance frequencies, but at the level of the bandwidths, the results are very

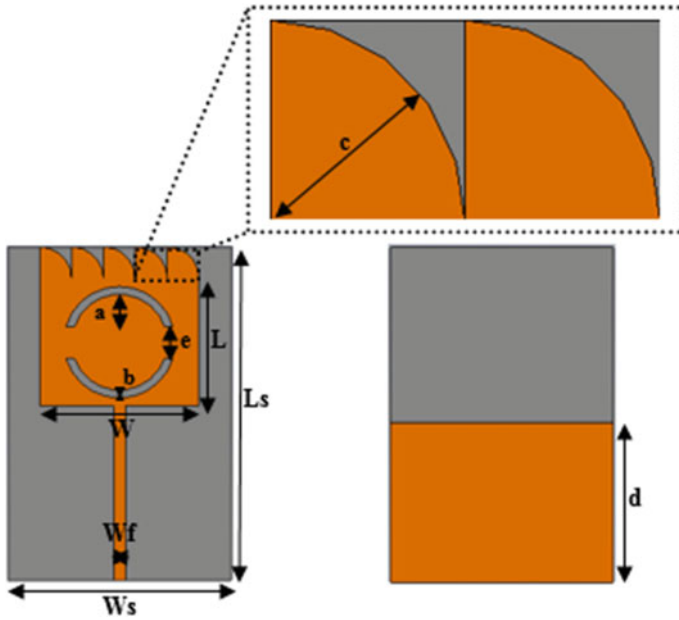


Fig. 1 Structure of the proposed antenna: **a** top layer, **b** bottom layer

Table 1 Antenna dimensions in mm

Parameters	Ws	Ls	W	L	Wf	t	a	b	c	d	e
Value (mm)	14	21	10	8	0.73	0.254	3	0.5	2	10	2

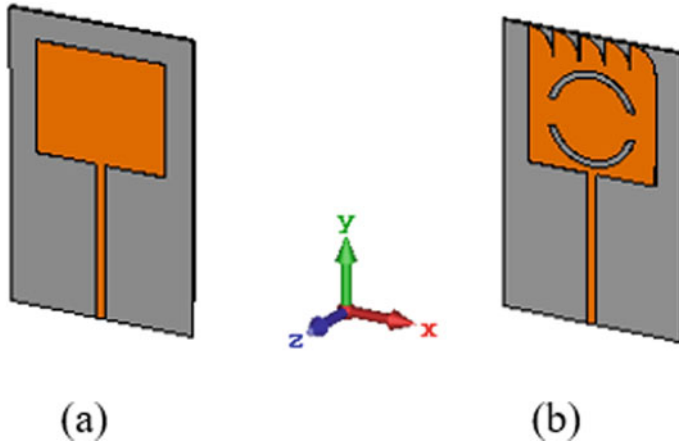


Fig. 2 **a, b** Design evolution of the proposed antenna

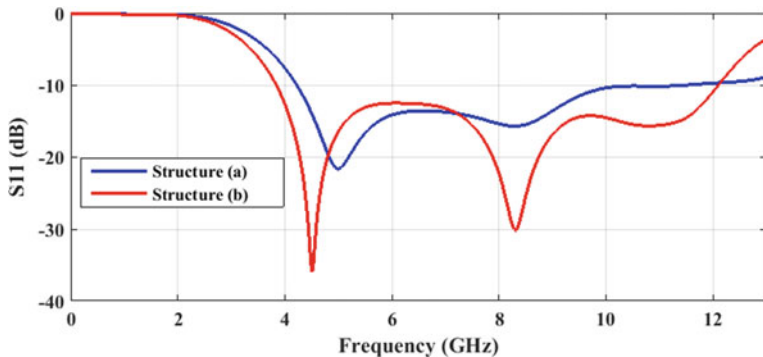


Fig. 3 Simulated S₁₁ of the antenna for different structures

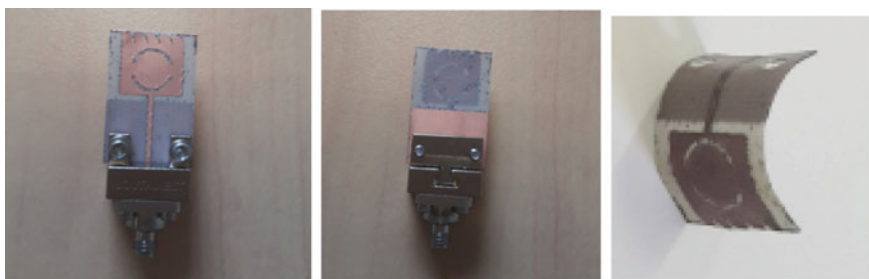


Fig. 4 The fabricated prototype UWB antenna

close, even a good impedance matching that varies around 50 Ω over the bandwidth (Figs. 5, 6 and 7).

The radiation patterns in the two principal planes (E-plane and H-plane) were simulated. It can be seen that over the most of frequencies the radiation power is

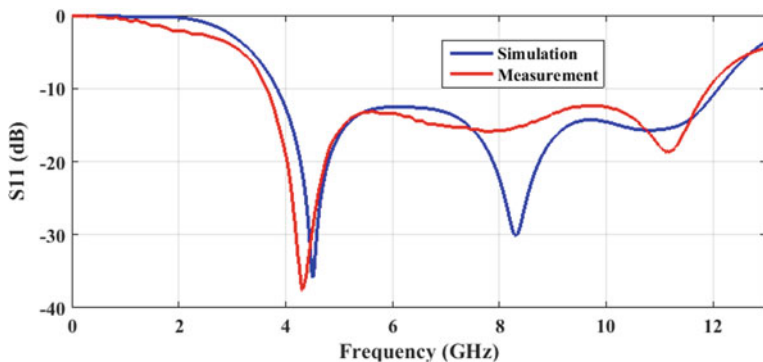


Fig. 5 Return loss of the proposed antenna

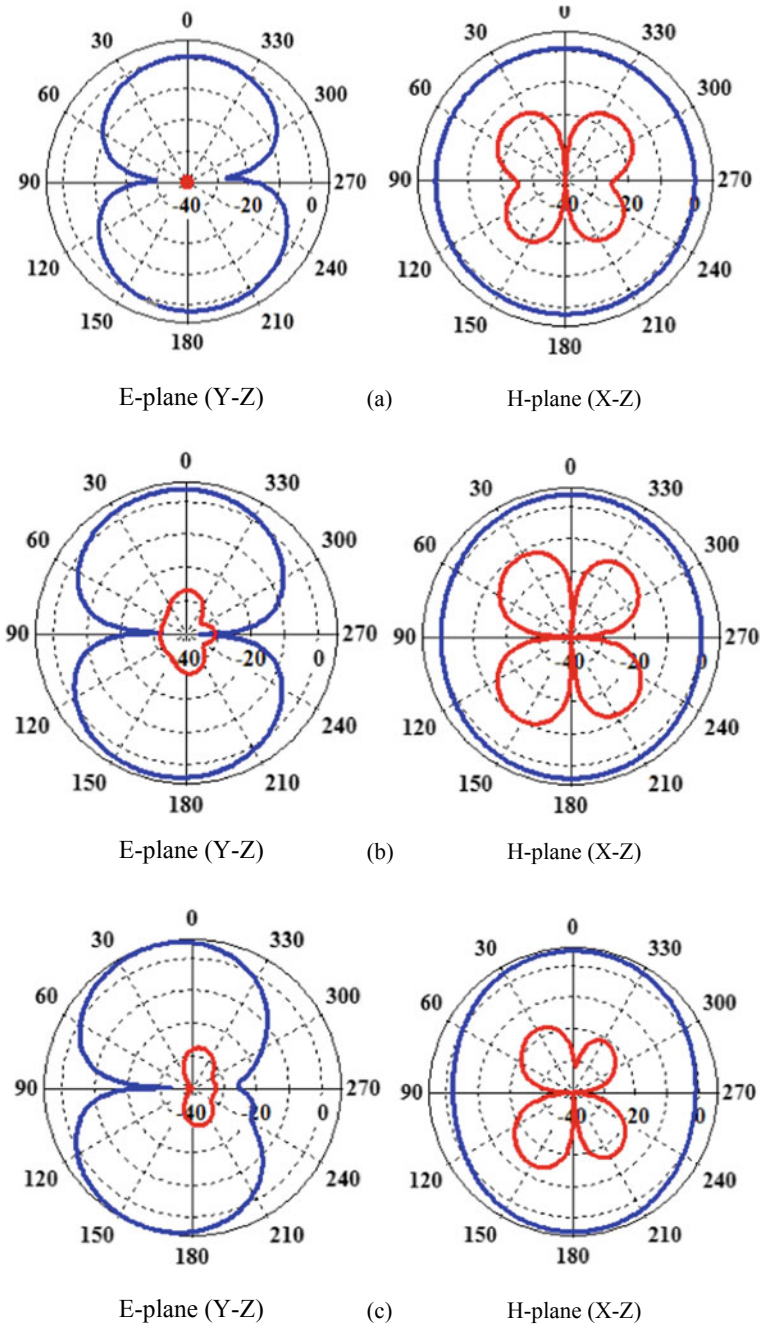


Fig. 6 Radiation pattern 2D in E-plane (co-polarization and cross-polarization) and H-plane (co-polarization and cross-polarization) at **a** 5.5 GHz, **b** 10.5 GHz and **c** 12 GHz. Blue line co-polarization, Red line cross polarization

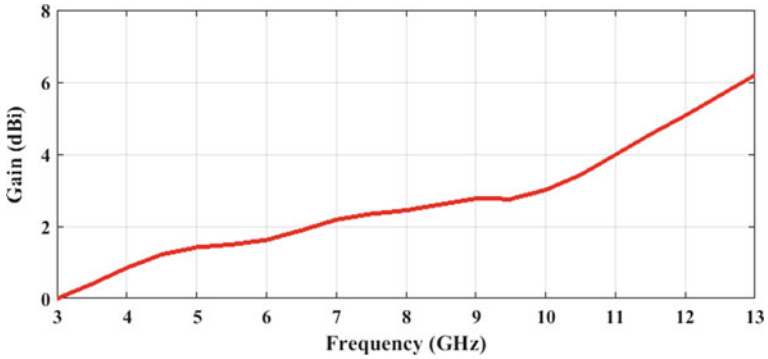


Fig. 7 Maximum gain of the proposed antenna

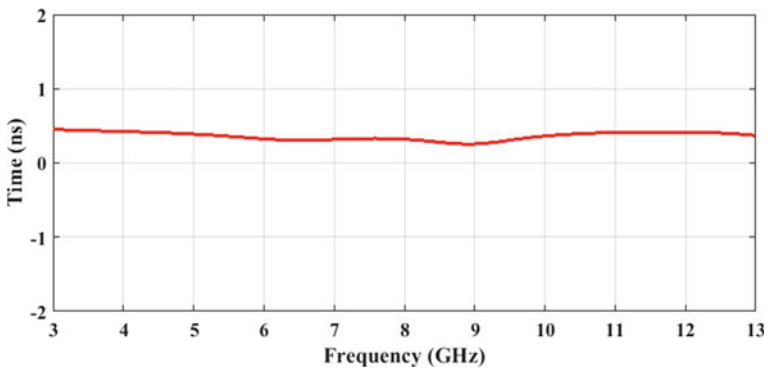


Fig. 8 Group delay of the proposed antenna

omni-directional in plane H and nearly bidirectional in E plane. The antenna achieved simulated gains of 1.5 dBi at 5.5 GHz, 3.42 dBi at 10.5 GHz and 5.07 dBi at 12 GHz, respectively.

Figures 8 and 9 illustrate the group delay characteristics of the proposed antenna for two modes: face-to-face and side-to-side. The group delay of the two antennas at 50 mm is almost smooth over the whole UWB band frequencies.

3 Bended Antenna

The antenna is meant to be placed in contact with breast. The difficulty is to take into account the impact of the environment and the human body on its performance. Some deformations of the structure influence the levels of adaptation, a variation of the bandwidth and the radiation patterns. This step is intended to study the influence

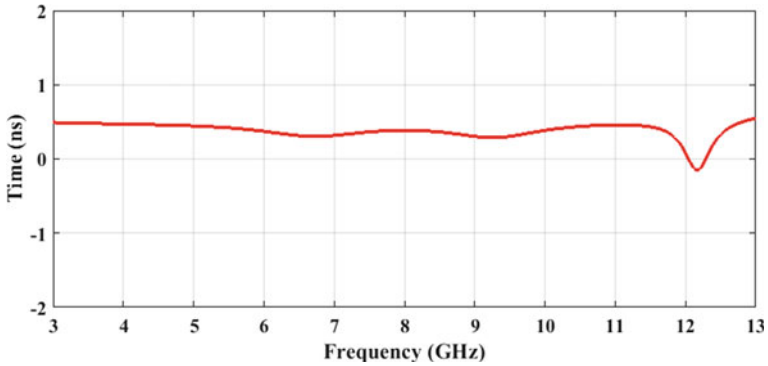


Fig. 9 Group delay of the proposed antenna

of various bending that can affect the antenna characteristics. There are four focused bending conditions of 0, 10, 20, 30 and 40 mm, as summarized in Table 2 (Fig. 10).

Figure 11 shows the reflection coefficients of flat and curved antenna. As it can be observed, even with the small bandwidth change, the reflection coefficients are almost similar. In addition, in all curved cases the adaptation at -10 dB is greater than 500 MHz. Therefore, we can conclude that the curvature does not affect much the adaptation of the antenna once it is placed in contact with breast. It has good stability over the entire frequency band (Figs. 11, 12, 13 and Table 3).

Table 2 Antenna characteristics for different cases of curvature

Radius of curvature (mm)	0 (Flat)	10	20	30	40
Bandwidth (GHz) (< -10 dB)	3.8–12.11	3.6–11.92	3.6–11.94	3.62–11.83	3.61–11.77
Gain (dBi)	5.07	5.2	5.18	5.25	5.37

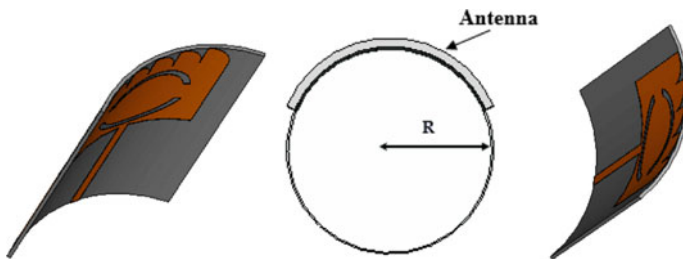


Fig. 10 Structure of the curved antenna

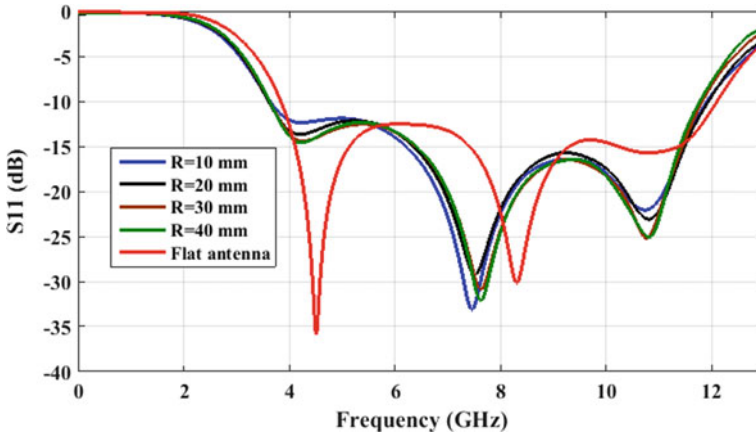


Fig. 11 Simulated S_{11} of the antenna for different cases

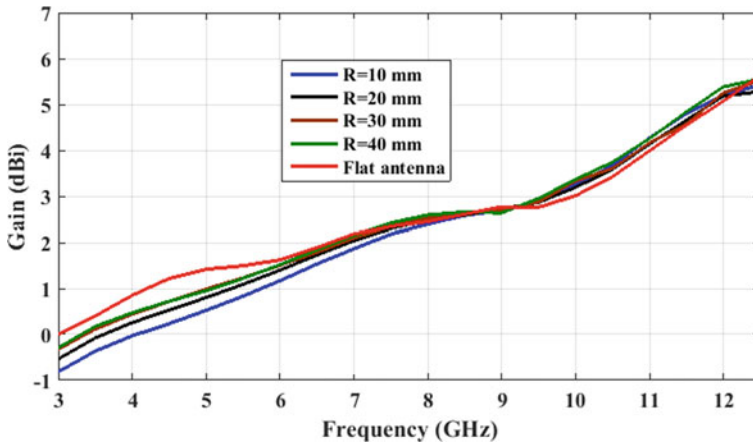


Fig. 12 Maximum gain of the proposed antenna for different cases

4 Effect of Biological Tissues on Antenna Performances

It is certainly true that some deformations of the structure influence the performance of the antenna, but the presence of biological tissues is one of the most important factor that can disrupt all its electromagnetic properties. A 3D hemispherical breast structure is modelled which contains several tissues. Their dielectric properties are approximate to those of real breast tissues. We choose three types of tissues: Skin, Fat and Fibroglandular based on very specific parameters like relative permittivity, conductivity and tissue density, all these parameters have been calculated based on Eq. 1 [19, 20].

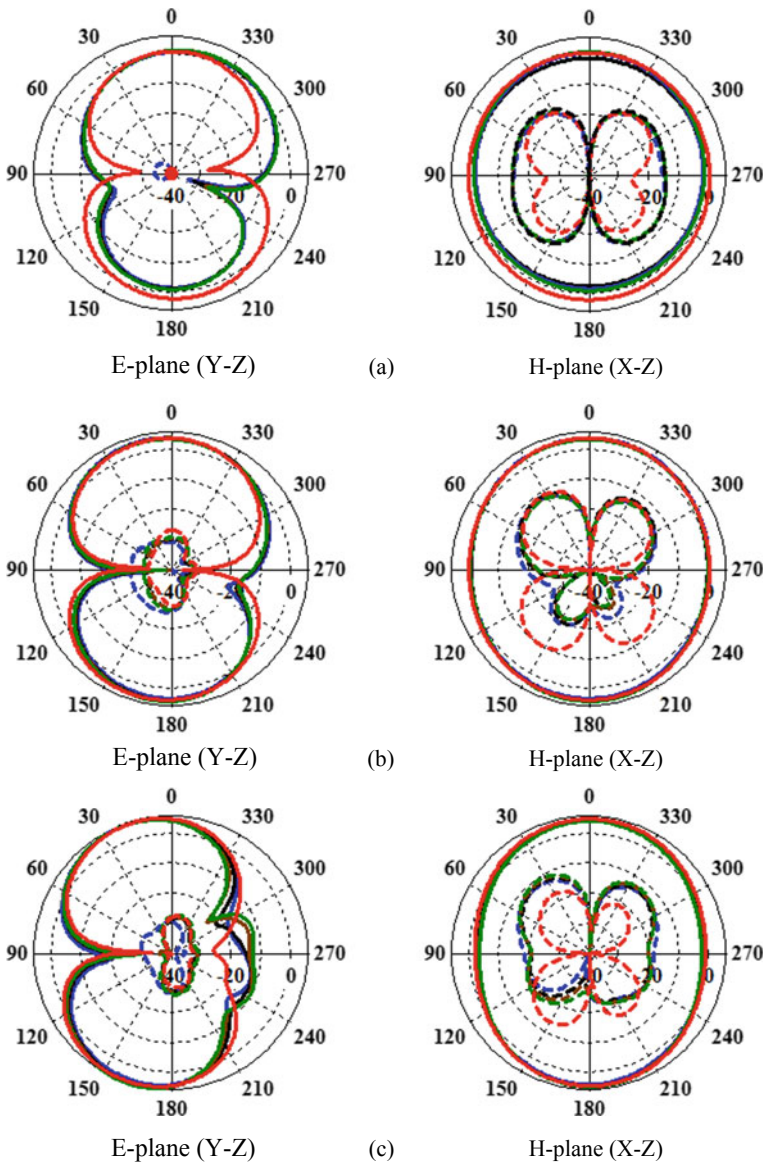


Fig. 13 Radiation pattern 2D in E-plane (co-polarization and cross-polarization) and H-plane (co-polarization and cross-polarization) at **a** 5.5 GHz, **b** 10.5 GHz and **c** 12 GHz. Blue line R = 10 mm, Black line R = 20 mm, Brown line R = 30 mm, Green line R = 40 mm, Red line Flat antenna. Solid line: co-polarization, Dashed line: cross polarization

Table 3 Comparison of previous flexible antennas with the proposed antenna

Antenna	Substrate ϵ_r	Antenna area (mm)	Bandwidth (GHz) (< -10 dB)	Thickness (mm)	Gain (dBi)
[16]	2.9	40 × 22	2.6–10.6	0.018	4
[17]	3.4	36 × 47.5	5.5–11.7	0.05	3.40
[18]	2.9	75 × 18	4.9–9.6	0.018	1.26
Proposed antenna	2.2	21 × 14	3.64–11.92	0.254	5.5

$$\epsilon_\omega = \epsilon_\infty + \frac{\epsilon_s - \epsilon_\infty}{1 + (j\omega\tau)^{1-\alpha}} + \frac{\sigma}{j\omega\epsilon_0} \tag{1}$$

where, ϵ_∞ is the relative permittivity, ϵ_s is the static relative permittivity, α is the exponent parameter, ω is the angular frequency, τ is the time constant, σ is the static conductivity and ϵ_0 is the permittivity of free space.

In our case, the antenna is intended to be used in an environment that is close to the breast. Figure 15 shows that the antenna is not too affected by the breast tissues. From these simulation results, it is clear that the antenna is more sensitive to the tissues. The radiation patterns are compared in free space and on the phantom. It can be observed that the radiation is more strongly impacted by the presence of tissues, due to a strong absorption in the phantom.

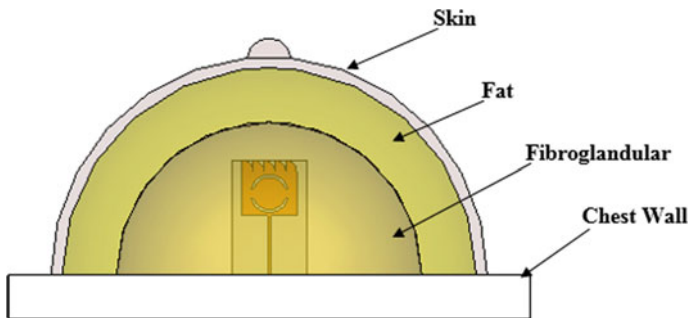


Fig. 14 The 3D breast structure

Table 4 Parameters of breast tissues at 5 GHz

Tissues type	Relative permittivity (ϵ_r)	Conductivity (σ)	Tissue density (ρ)
Skin	35.8	3.06	1109
Fat	4.65	0.35	911
Fibroglandular	53.3	3.66	1041

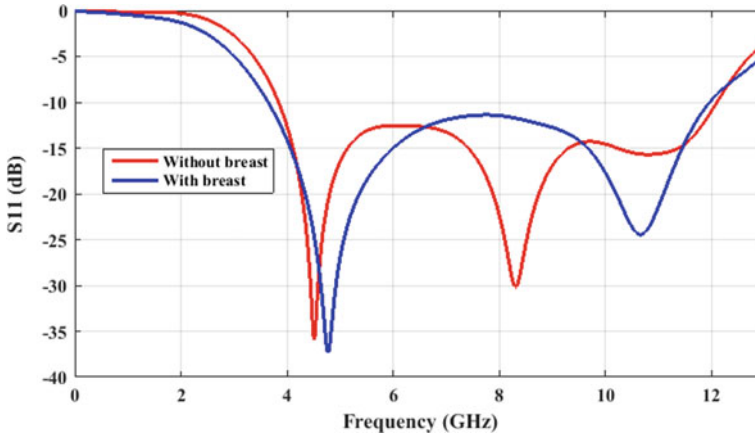


Fig. 15 Return loss of the proposed antenna (with phantom and without phantom)

5 Conclusion

In this paper, a flexible UWB antenna has been designed, simulated and fabricated successfully. An optimization of different parameters that affect the characteristics of the antenna makes it possible to obtain a reduced antenna with better performances. The effects of the curvature on the return loss and radiation pattern were investigated. The results showed that the bandwidth was not affected by the curvature of the antenna, which make it be placed in contact with any breast size. A 3D phantom of breast is implemented to validate the antenna performances in the presence of biological tissues. The proposed antenna operates on wide band frequency range (3.64–12.11 GHz) that supports biomedical applications, especially for breast cancer detection.

References

1. Chandra R, Zhou H, Balasingham I, Narayanan RM (2015) On the opportunities and challenges in microwave medical sensing and imaging. *IEEE Trans Biomed Eng* 62(7):1667–1682
2. Colgan TJ, Hagness SC, Van Veen BD (2015) A 3-D level set method for microwave breast imaging. *IEEE Trans Biomed Eng* 62(10):2526–2534
3. Nezirovic A, Yarovoy AG, Lighthart LP (2010) Signal processing for improved detection of trapped victims using UWB radar. *IEEE Trans Geosci Remote Sens* 48(4):2005–2014
4. Mohammed BJ, Abbosh AM, Ireland D, Bialkowski ME (2012) Compact wideband antenna immersed in optimum coupling liquid for microwave imaging of brain stroke. *Prog Electromagnet Res C* 27:27–39
5. Klemm M, Leendertz JA, Gibbins D, Craddock IJ, Preece A, Benjamin R (2010) Microwave radar-based differential breast cancer imaging: imaging in homogeneous breast phantoms and low contrast scenarios. *IEEE Trans Antennas Propag* 58(7):2337–2344

6. O'Halloran M, Glavin M, Jones E (2010) Rotating antenna microwave imaging system for breast cancer detection. *Prog Electromagnet Res* 107:203–217
7. Klemm M, Craddock IJ, Leendertz JA, Preece A, Benjamin R (2009) Radar-based breast cancer detection using a hemispherical antenna array—experimental results. *IEEE Trans Antennas Propag* 57(6):1692–1704
8. Wang Y, Zhu F, Gao S (2015) Design and implementation of connected antenna array for ultra-wideband applications. *Prog Electromagnet Res C* 58:79–87
9. Bah MH, Hong J, Jamro DA (2015) Ground slotted monopole antenna design for microwave breast cancer detection based on time reversal MUSIC. *Prog Electromagnet Res C* 59:117–126
10. Zhang C-X, Zhuang Y-Q, Zhang X-K, Hu L (2014) An UWB microstrip antenna array with novel corporate-fed structure. *Prog Electromagnet Res C* 52:7–12
11. Al-Sehemi A, Al-Ghamdi A, Dishovsky N, Atanasova G, Atanasov N (2017) A flexible planar antenna on multilayer rubber composite for wearable devices. *Prog Electromagnet Res C* 75:31–42
12. Bahrami H, Mirbozorgi SA, Ameli R, Rusch LA, Gosselin B (2016) Flexible, polarization-diverse UWB antennas for implantable neural recording systems. *IEEE Trans Biomed Circ Syst* 10(1):38–48
13. Raad HK, Al-Rizzo HM, Abbosh AI, Hammoodi AI (2016) Compact dual band polyimide based antenna for wearable and flexible telemedicine devices. *Prog Electromagnet Res C* 63:153–161
14. Fear EC (2005) Microwave imaging of the breast. *Technol Cancer Res Treatment* 4(1)
15. Hady Bah M, Hong JS, Ali Jamro D (2016) UWB patch antenna and a breast mimicking phantom are designed and implemented for microwave breast cancer detection using time reversal MUSIC. *Microw Opt Technol Lett* 58(3)
16. Zahran SR, Abdalla MA, Gaafar A (2017) Time domain analysis for foldable thin UWB monopole antenna. *Int J Electron Commun*
17. Lukacs P, Pietrikova A, Potencki J, Tomaszewski G (2015) UWB antenna based on nanoparticles of silver on polyimide substrate. In: 2015 38th international spring seminar on electronics technology (ISSE), Eger, pp 408–413
18. Zahran SR, Abdalla MA (2015) Novel flexible antenna for UWB applications. In: 2015 IEEE international symposium on antennas and propagation and USNC/URSI National Radio Science Meeting, Vancouver, BC, pp 147–148
19. Gabriel C, Gabriely S, Corthout E (1996) The dielectric properties of biological tissues: I. Literature survey. *Phys Med Biol* 41:2231–2249
20. Zastrow E, Hagness SC, Veen BD (2010) 3D computational study of non-invasive patient-specific microwave hyperthermia treatment of breast cancer. *Phys Med Biol* 55:3611–3629

A Low Profile Frequency Reconfigurable Antenna for mmWave Applications



Wahaj Abbas Awan , Niamat Hussain , Adnan Ghaffar ,
SyedaIffat Naqvi , Abir Zaidi , Musa Hussain, and Xue Jun Li 

Abstract A compact frequency reconfigurable printed antenna for millimeter-wave applications is presented in this paper. This design is obtained by the merging of a half-arc and a right-angled triangle patch extracted from a rectangular radiator. The design approach is based on the use of two S-PIN diodes to obtain frequency reconfigurability. The antenna exhibits seven reconfigurable bands while showing good performances in terms of return loss, bandwidth and gain. The proposed antenna is well suited for future fifth-generation (5G) networks because of its notable features of small overall size ($7.5 \times 5 \times 0.762 \text{ mm}^3$), wide bandwidth, and frequency reconfigurability.

Keywords Compact antenna · Frequency reconfigurable · 5G · mm-wave

W. A. Awan (✉)

Department of Integrated IT Engineering, Seoul National University of Science and Technology, Seoul, South Korea

e-mail: wahajabbasawan@ieee.org

N. Hussain

Department of Computer and Communication Engineering, Chungbuk National University, Cheongju, South Korea

A. Ghaffar · X. J. Li

Department of Electrical and Electronic Engineering, Auckland University of Technology, Auckland, New Zealand

S. Naqvi

Telecommunication Engineering Department, University of Engineering and Technology Taxila, Taxila, Punjab, Pakistan

A. Zaidi

Laboratory EEA and TI, Faculty of Science and Techniques (FSTM) Mohammedia, Hassan II University, Casablanca, Morocco

M. Hussain

Department of Electrical Engineering, Bahria University, Islamabad, Pakistan

1 Introduction

An exponential increase in mobile traffic, yielded by cell phones and all other types of connected devices, has exacerbated spectrum congestion for commercial mobile radio services, particularly in some mid-range frequency bands ranging from 11 to 23 GHz [1]. This spectrum congestion issue has impeded existing wireless communication technologies from meeting the ever-increasing end-user requirements, particularly for applications demanding an increased data throughput of the order of Gbps [2]. This problem has sparked political and economic claims to maintain competition in mobile broadband services. Therefore, commercial companies and government organizations devoted a substantial amount of effort to come up with alternative solutions and strategies to mitigate spectrum scarcity, among which we can cite exploring unused portions of the spectrum such as the millimeter wave spectrum also referred to as the extremely high-frequency band (EHF) ranging from 30 to 300 GHz [3]. These wavelengths ranging from 10 to 1 mm are nowadays used in highly advanced technologies, allowing the transmission and reception of multimedia data in no time with higher bandwidth for data transfer rates [4, 5].

Moreover, millimeter waves are considered to be a fundamental pillar for the elaboration of the fifth-generation (5G) of mobile technology which is expected to play a major role in the mobile communication field. Because of the enormous features of this technology, it will be adopted by many economic sectors and industries [6, 7]. The 5G is expected to afford a huge base to connect the ever-increasing number of devices to the Web, while still upgrading end-user experience in many applications requiring higher data throughput along with very feeble delays through the network [8]. However, millimeter wave is subjected to some serious problems such as its limited coverage, its vulnerability to the atmosphere and for being highly sensitive to interference. Thereby, designing performing antennas for future handheld devices at this range of frequency presents a real challenge for antenna engineers [9, 10]. Moreover, to reap the maximum benefits from this new portion of the spectrum, antennas capable to perform multi-tasking with good radiation characteristics are urgently required [11, 12]. In this context, multiband and reconfigurable antennas have drawn more attention for their ability to switch between different frequency bands. Thus, a single reconfigurable antenna can replace the multiple number of antennas operating at a given frequency [13–17].

In this regard, reconfigurable antennas are considered to be a great development in the field of telecommunications and wireless networks, due to their versatility, their ability to obtain strong performances with a small-sized antenna at a reduced cost. Reconfigurable antennas are also attractive for being capable to adjust dynamically, multiple antenna parameters, including frequency, radiation pattern, polarization or else by providing a compound reconfiguration, that consists of adjusting simultaneously several antenna parameters. The reconfigurability in its most types is achieved through an inner mechanism that is implemented inside the antenna structure. Several active elements are used such as PIN switches [18, 19], MEMS [20], optical switches

[21], varactors [22], FET transistors [23], etc. It stimulates the intentional redistribution of the RF currents over the antenna structure and generates reversible alterations of its properties, therefore, strong antenna performance can be achieved for changing applications and operational frequency. Among the ultimate proper candidates to achieve reconfigurability when the frequency is increased up to the millimeter-wave band. The microstrip patch antennas are highly used for their advantageous characteristics of having a lightweight, small size, low-cost, robust design, and ease of manufacturing which facilitates their mass production [24].

Several papers have discussed reconfigurable antennas, particularly the frequency reconfigurable antennas, for their promising ability to provide a diversity of the operating resonant frequency. The works presented in [18, 19] discuss respectively a “Y” shaped and an “F” shaped patch antennas dedicated to the 5G millimeter-wave applications. Frequency reconfigurability in these works is achieved respectively, using a single and two PIN diodes implemented in the radiating elements. Good performance has been reported in terms of all radiation characteristics, however, only three frequency bands are achieved by the first and two frequencies for the second antenna, which is insufficient for most mobile radio services. In [24–26], millimeter-wave coplanar waveguide fed patch antennas for 5G applications are presented. The reconfiguration in these works is achieved by varying the value of two resistors connected between stubs and the radiating element of each antenna, which disturbs the current distribution, hence provide frequency reconfiguration. The antennas presented in these papers are found to be able to operate in a wide range of frequencies. The antenna presented in [24] is capable to operate at nine frequencies, while the work presented in [25] operates at six frequencies, while five frequencies are achieved in the work presented in [26]. However, the resistors implemented in these antennas have introduced a significant amount of losses that have affected the return loss of these antennas.

After judicious investigations of the research papers presented in the open literature, it may be concluded that a millimeter-wave reconfigurable antenna, capable to operate at numerous frequencies of the 5G technology, while still maintaining good performance in terms of return loss, bandwidth and all radiation characteristics is still a challenge. In the proposed design, a simple, yet novel frequency reconfigurable patch antenna, characterized by a compact size, has been studied and analyzed. The antenna performance is investigated in terms of reflection coefficient, radiation pattern, gain, and bandwidth. Afterward, the proposed antenna in this paper will be subjected to a comparison between related works for the same frequency and application. The rest of paper is organized as: In Sect. 2, the antenna design and configuration are discussed. Section 3 gives detail of simulated results and Section 4 concludes the paper.

2 Antenna Design and Methodology

Figure 1a–c illustrate the geometrical view of the presented antenna. The radiating element of the proposed frequency reconfigurable multi-band antenna is composed of two different shapes. A half-arc and a right-angled triangle, made using copper with a standard cladding thickness of 0.0035 mm. The substrate used in the presented design, with dimensions of (7.5 mm × 5 mm) is chosen to be ROGERS 6002, with a dielectric permittivity (ϵ_r) = 2.94 and a loss tangent (δ) = 0.0012.

2.1 Antenna Designing

The copper ground plane used covers approximately 26.5% of the substrate surface (2 mm × 5 mm). Its dimensions are chosen for the proper impedance matching. The steps used to design the frequency reconfigurable antenna are shown in Fig. 2. In first step, a conventional monopole antenna was designed where central frequency (f_c) of the rectangular monopole radiator can be estimated by following equations, provided by [12]

$$f_c = \frac{c}{\sqrt{\epsilon_{eff}} \lambda_g} \quad (1)$$

here

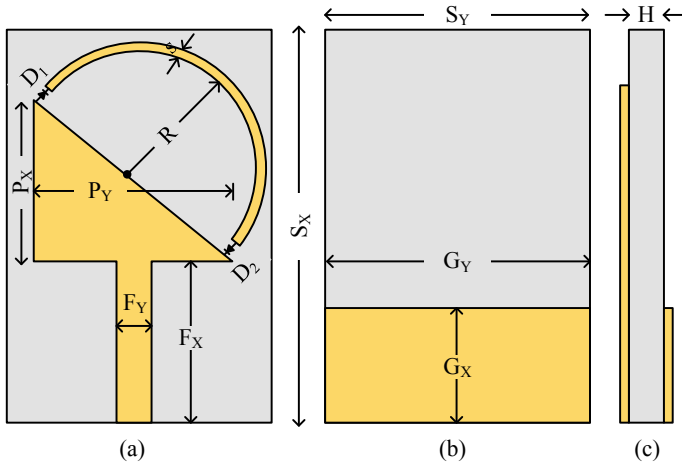


Fig. 1 Geometry of the proposed reconfigurable 5G antenna, **a** top view, **b** bottom view, **c** side view. $S_x = 7.5$ mm; $S_y = 5$ mm; $G_y = 5$ mm; $G_x = 2$ mm; $F_x = 2.6$ mm; $F_y = 0.8$ mm; $P_x = 3.5$ mm; $P_y = 3.5$ mm; $H = 0.762$ mm; $R_1 = 2.6$ mm

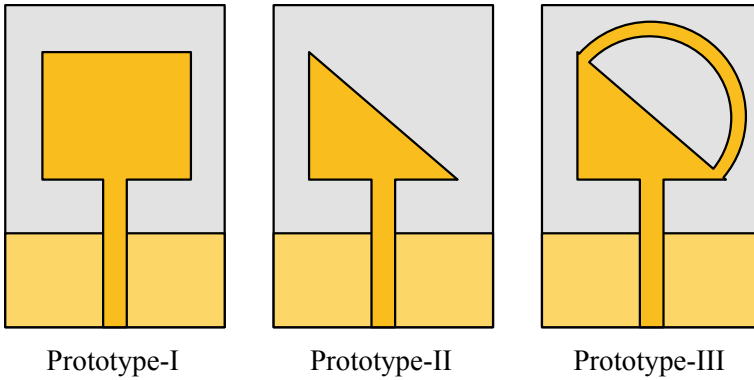


Fig. 2 Various steps involved in the evaluation of proposed work

λ_g is the guided wavelength at the central frequency
 c is the speed of light $\approx 3 \times 10^8 \text{ ms}^{-1}$.
 ϵ_{eff} is the effective dielectric constant which is given by

$$\epsilon_{\text{eff}} \approx \frac{\epsilon_r + 1}{2} + \frac{\epsilon_r - 1}{2} \left(1 + 12 \left(\frac{S_Y}{H} \right) \right)^{-0.5} \tag{2}$$

here

ϵ_r is the dielectric constant of the substrate
 S_Y is the width of the monopole
 H is the thickness of the substrate.

On the other hand, the length of the monopole (P_X) can be estimated by using the following relation:

$$P_X = \frac{c}{4f_C \sqrt{\epsilon_{\text{eff}}}} \tag{3}$$

The resultant antenna shows dual-band behavior where fundamental harmonic commonly known as first resonance was observed around 20 GHz while the first harmonic is observed around 32.5 GHz having respective impedance bandwidth of 4.1 GHz (17.5–21.6 GHz) and 3.8 GHz (31.4–35.2 GHz), as depicted in Fig. 3.

Truncated patch structures were well known for their wideband behavior, a detailed discussion was done in [3, 13]. The upper edge of the rectangular monopole is truncated by using an equilateral triangle having a side length of P_X . It can be observed from Fig. 3 after truncation the impedance bandwidth at both resonances widen along with the shift in frequency toward the upper side is observed. In the last step a semicircular stub having internal radius R_I and thickness S was introduced

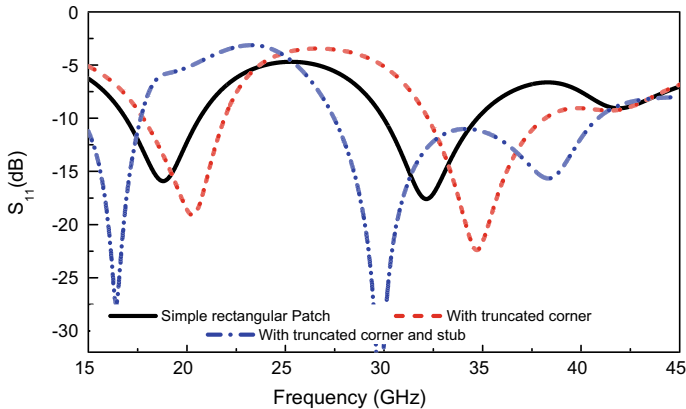


Fig. 3 S_{11} of the various prototypes used in evolution of the proposed 5G antenna

along with the truncated structure, the insertion of this stud results in the introduction of additional reactive load which significantly improve impedance matching thus widen the impedance bandwidth. The resultant antenna exhibits impedance bandwidth of 6.1 GHz (13.7–19.8 GHz) and 13.4 GHz (27.4–41.8 GHz) with two resonances at 17 GHz and 30 GHz, respectively.

Finally, in order to achieve frequency reconfigurability, we incorporated two PIN switches (D1 and D2) in the radiating element as shown in Fig. 1, so that we can toggle between different frequencies using a single antenna. The equivalent model of AlGaAs-Flip-Chip-PIN (PIN) diode having a maximum operating frequency of 50 GHz [27] was used in simulations. The diodes are inserted in such a way that the proposed antenna operates in 3 different modes, first mode when both diodes are in off state representing case 00, while in the other two modes the diodes form pair of cases 01 and 10. On the other hand, case 11 is not possible due to an inverted combination of diodes, in fact when both radiator and stub are either 0 V or 1.5 V the diodes are in the off state.

3 Antenna Characterization

The simulations of the proposed work are done using Electromagnetic solver, Higher Frequency Structural Simulator (HFSS). The equivalent model of AlGaAs-Flip-Chip-PIN (PIN) diode having a maximum operating frequency of 50 GHz was constructed by using a lumped element. The diode in such a way that for On-state it acts as a series combination of $0.5nH$ inductor with 4.2Ω resistor and for Off-state it behaves like a series combination of $0.5nH$ inductor with the parallel combination of $20fF$ capacitor and $3K\Omega$ resistor.

Figure 3 presents the resultant return loss of the different switching states of the diodes. It can observe that the case-00 provides a dual-band antenna having resonances at 19.67 and 35.39 GHz with a respective impedance bandwidth of 4.23 and 8.61 GHz. For case-01, the antenna resonates at 3 different frequencies of 17.21, 25.8, and 35.75 GHz with obtained bandwidths of 1.66 GHz, 2.13 GHz, and 5.6 GHz, respectively. Numerically calculated results for the last case-10 depicts that antenna exhibits dual bands at 20.49 and 32.53 GHz having respective bandwidths of 4.04 and 4.85 GHz (Fig. 4).

Figure 5 presents the radiation pattern of the proposed antenna for case-00 at the resonating frequencies of 19.7 and 32.4 GHz. The antenna exhibits a broad side radiation pattern along with gain values of 6.98 and 7.96 dB at the resonating frequencies of 19.7 GHz and 32.4 GHz, respectively. Figure 6 presents the radiation

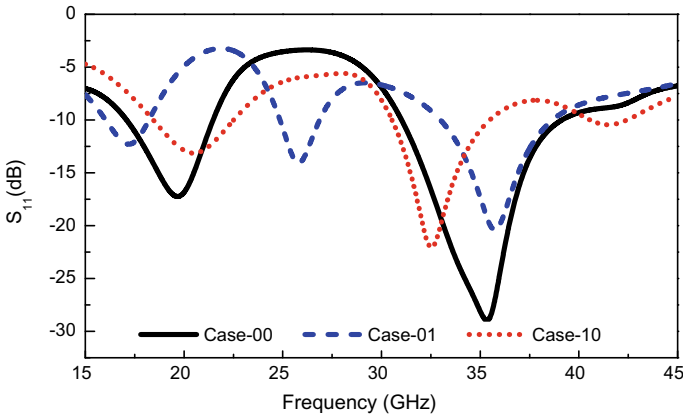


Fig. 4 S_{11} for various switching state of diodes

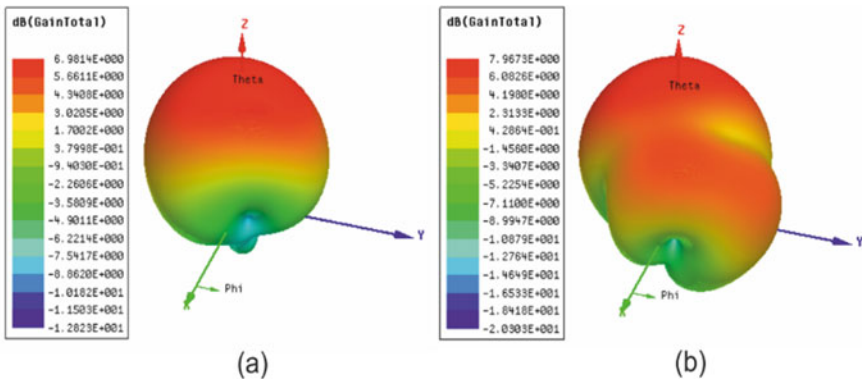


Fig. 5. 3D gain plots for case-00 a 19.7 GHz, b 32.4 GHz

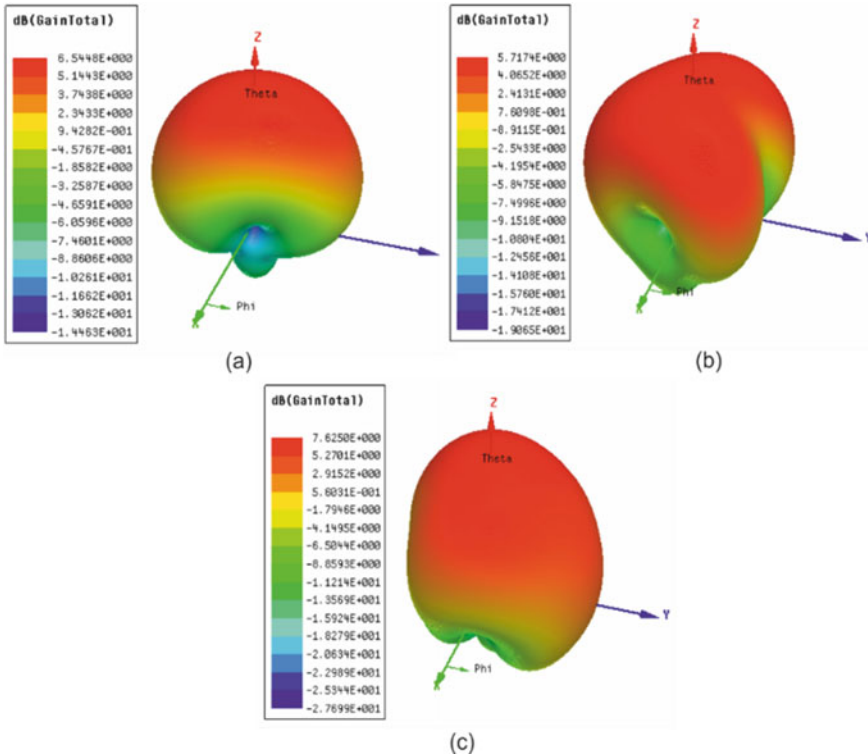


Fig. 6. 3D gain plots for case-01 **a** 17.2 GHz, **b** 25.8 GHz, **c** 35.75 GHz

pattern for case-01, the exhibits three passbands at 17.25, 25.8 and 35.75 GHz with respective gain values of 6.54, 5.71 and 7.62 dB with broadside radiation pattern.

Figure 7 presents the radiation pattern of the last case-10, it could be observed that the antenna still exhibits broadside radiation pattern with gain values of 7.26 and 9.28 dB at the respective resonating values of 20.5 and 32.55 GHz. The calculated efficiency of the proposed antenna varies between 74 and 82% for all passbands.

Table 1 presents a comparison between the proposed antenna performances with some related works dedicated for 5G applications in the millimeter-wave range. After analyzing results reported in this table, we can clearly deduce that our presented antenna presents a compact size compared to works [18, 24–26], while the work [19] presents better results in terms of compactness, however, our proposed antenna surpass their performance in terms of the number of provided frequencies by reconfiguration, return loss and gain.

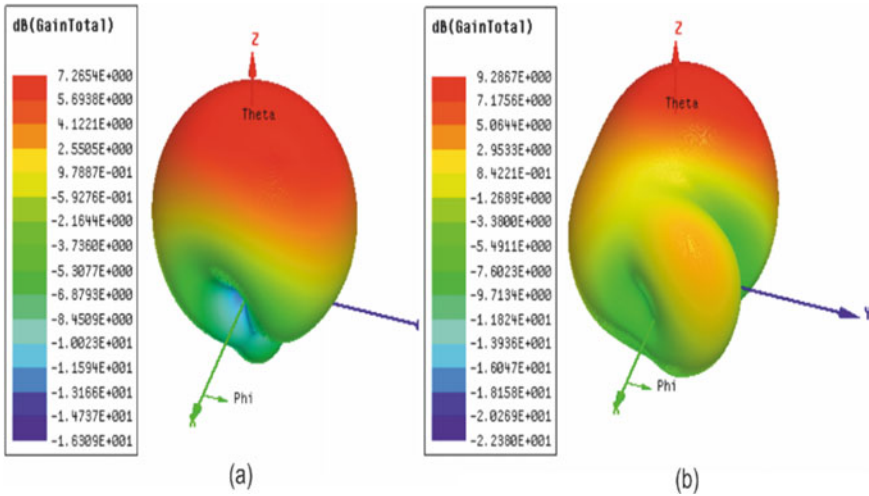


Fig. 7. 3D gain plots of case 3 a 20.5 GHz, b 32.55 GHz

Table 1 Comparison of proposed antenna with state-of-the-art-work

References	Dimensions (mm ²)	Provider frequencies (GHz)	Return loss (dB)	Gain (dBi)
[18]	49	25 and 50	-21.6 and -17.18	6.68 and 8.14
[19]	20	31.4, 45.5, and 49.84	-22.97, -28.2, and -45.27	4.97, 6.73, and 7.8
[24]	80	35.85, 36.18, 36.79, 39.19, 47.85, 51.87, and 53.34	-27.7, -19.7, -14.5, -11.79, -14.3, -14.24, and -50.71	3, 2.57, 2.4, 2.3, 4, 3.19, and 3.66
[25]	144	24.55, and 25.28, 25.87, 26.3, 26.74, and 26.88	-11.89, -21.45, -40.34, -24.1, -19.8, and -19.45	<2, <2.5, 2.7, 3.7, 3.7, and 4.2
[26]	144	26, 27, 28 and 29	-20, -23, -21, and -18	3.4, 3.5, 3.7, 3.6
This work	37.5	17.2, 19.7, 20.5, 25.8, 32.55, 32.4, and 35.75	-12.6, -17.8, -12.07, -14.3, -22, -30.4, and -20.40	6.54, 6.98, 7.26, 5.71, 7.96, 9.28, and 7.6

4 Conclusion

A planar frequency reconfigurable antenna using two S-PIN diodes for 5G millimeter-wave applications is presented. The antenna consists of a triangular patch and a semicircular half-arc connected/disconnect through diodes. These different states of the diodes are used to reconfigure the frequency band based on system requirements.

The antenna offers a compact size with seven reconfigurable bands having desirable performances in terms of return loss, bandwidth, and stable gain characteristics.

References

1. Zaidi A, Baghdad A, Ballouk A, Badri A (2018) High gain microstrip patch antenna, with PBG substrate and PBG cover, for millimeter wave applications. In: 4th international conference on optimization and applications (ICOA). IEEE, pp 1–6
2. Bong HU, Jeong M, Hussain N, Rhee SY, Gil SK, Kim N (2019) Design of an UWB antenna with two slits for 5G/WLAN-notched bands. *Microw Opt Technol Lett* 61(5):1295–1300
3. Hussain N, Jeong MJ, Park J, Kim N (2019) A Broadband circularly polarized fabry-perot resonant antenna using a single-layered PRS for 5G MIMO applications. *IEEE Access* 7:42897–42907
4. Naqvi A, Lim S (2018) Review of recent phased arrays for millimeter-wave wireless communication. *Sensors* 18(10):3194
5. Zaidi A, Baghdad A, Ballouk A, Badri A (2018) Performance enhancement of an inset fed circular microstrip patch antenna using periodic defected ground structure and EBG superstrates for applications in the millimeter wave band. *Int J Commun Antenna Propag IRECAP* 8(2):116–122
6. Awan WA, Zaidi A, Baghdad A (2019) Super wide band miniaturized patch antenna design for 5G communications. In: International conference on wireless technologies, embedded and intelligent systems (WITS). IEEE, pp 1–2
7. Awan WA, Zaidi A, Hussain N, Baghdad A (2019) Compact size Y-shaped broadband antenna for E-Band applications. In: International conference on wireless technologies, embedded and intelligent systems (WITS). IEEE, pp 1–3
8. Awan WA (2018) Very small form factor with ultra wide band rectangular patch antenna for 5G applications. In: International conference on computing, mathematics and engineering technologies (iCoMET). IEEE, pp 1–4
9. Naqvi SI et al (2019) An integrated antenna system for 4G and millimeter-wave 5G future handheld devices. *IEEE Access* 7:116555–116566
10. Jeong MJ, Hussain N, Park JW, Park SG, Rhee SY, Kim N (2019) Millimeter-wave microstrip patch antenna using vertically coupled split ring metaplate for gain enhancement. *Microw Opt Technol Lett* 61(10):2360–2365
11. Awan WA, Hussain N, Le TT (2019) Ultra-thin flexible fractal antenna for 2.45 GHz application with wideband harmonic rejection. *AEU-Int J Electron Commun* 110:152851
12. Awan WA, Zaidi A, Hussain N, Iqbal A, Baghdad A (2019) Stub loaded, low profile UWB antenna with independently controllable notch-bands. *Microw Opt Technol Lett* 61(11):2447–2454
13. Hussain N, Jeong M, Park J, Rhee S, Kim P, Kim N (2019) A compact size 2.9–23.5 GHz microstrip patch antenna with WLAN band-rejection. *Microw Opt Technol Lett* 61(5):1307–1313
14. Naqvi SI, Khan A, Azam MA, Amin Y, Loo J, Tenhunen H (2019) A planar flexible quad-band antenna for WLAN/WiMAX/LTE applications. In: 2nd international conference on computing, mathematics and engineering technologies (iCoMET). IEEE, pp 1–5
15. Awan WA, Ghaffar A, Hussain N, Li XJ (2019) CPW-fed dual-band antenna for 2.45/5.8GHz applications. In: 8th Asia-Pacific conference on antennas and propagation, Incheon, Korea, IEEE, pp 1–2
16. Naqvi AH, Lim S (2018) Design of polarization reconfigurable antenna using liquid metal. In: International symposium on antennas and propagation (ISAP). IEEE, pp 1–2
17. Ghaffar A, Li XJ, Seet BC (2017) Dual frequency band and polarization reconfigurable antenna for mobile devices. In: 17th international conference on communication technology (ICCT). IEEE, pp 696–700

18. Awan WA, Zaidi A, Hussain N, Khalid S, Baghdad A (2019) Frequency reconfigurable patch antenna for millimeter wave applications. In: 2nd international conference on computing, mathematics and engineering technologies (iCoMET). IEEE, pp 1–5
19. Awan WA, Zaidi A, Hussain N, Khalid S, Baghdad A (2018) Characterization of dual band MIMO antenna for 25 GHz and 50 GHz applications. In: International conference on computing, electronic and electrical engineering (ICE Cube). IEEE, pp 1–4
20. Wright MD, Baron W, Miller J, Tuss J, Zeppettella D, Ali A (2018) MEMS reconfigurable broadband patch antenna for conformal applications. *IEEE Trans Antennas Propag* 66(6):2770–2778
21. Webb GW, Vernon W, Sanchez MS, Rose SC, Angello S (1999) Optically controlled millimeter wave antenna. In: International topical meeting on microwave photonics. MWP'99. Technical Digest (Cat. No. 99EX301). IEEE, pp 275–278
22. Ding Z, Jin R, Geng J, Zhu W, Liang X (2019) Varactor loaded pattern reconfigurable patch antenna with shorting pins. *IEEE Trans Antennas Propag*
23. Yang XJ, Lin GC, Chen C, Kong FL (2014) Frequency reconfigurable antenna for wireless communications using GaAs FET switch. *IEEE Antennas Wirel Propag Lett* 14:807–810
24. Zaidi A, Baghdad A, Awan WA, Ballouk A, Badri A (2019) CPW fed wide to dual band frequency reconfigurable antenna for 5G applications. In: International conference on wireless technologies, embedded and intelligent systems (WITS). IEEE, pp 1–3
25. Jilani SF, Abbas SM, Esselle KP, Alomainy A (2015) Millimeter-wave frequency reconfigurable T-shaped antenna for 5G networks. In: 11th international conference on wireless and mobile computing, networking and communications (WiMob). IEEE, pp 100–102
26. Shereen MK, Khattak MI, Shafi M, Saleem N (2018) Slotted Y-shaped millimeter wave reconfigurable antenna for 5G applications. In: International conference on computing, mathematics and engineering technologies (iCoMET). IEEE, pp 1–5
27. 'MACOM'. www.macom.com. Accessed Apr 2019

On-Demand Frequency Reconfigurable Flexible Antenna for 5Gsub-6-GHz and ISM Band Applications



Musa Hussain , Syed Naheel Raza Rizvi , Wahaj Abbas Awan ,
Niamat Husain , Halima, and Ahsan Hameed

Abstract This paper presents the design and characterization of on-demand frequency reconfigurable antenna for 5Gsub-6-GHz and ISM-band applications. The antenna comprises of compact overall size having dimensions of $0.23\lambda_0 \times 0.2\lambda_0 \times 0.002\lambda_0$. The octagonal patch was loaded with stub to enhance bandwidth along with improvement in return loss, afterword a slot and diode was utilized to achieve frequency reconfigurability. The numerical analysis of the proposed antenna was done using Higher Frequency Structural Simulator (HFSS). Furthermore, to demonstrate the potential of the proposed work it is compared with state of the art works for similar applications.

Keywords Compact size · Flexible antenna · Frequency reconfigurability · 5Gsub-6-GHz · ISM band

M. Hussain

Department of Electrical Engineering, Bahria University, Islamabad, Pakistan

S. N. R. Rizvi

Department of Electronics Engineering, University of Engineering and Technology Taxila, Taxila, Punjab, Pakistan

W. A. Awan (✉)

Department of Integrated IT Engineering, Seoul National University of Science and Technology, Seoul, Republic of Korea

e-mail: wahajabbasawan@ieee.org

N. Husain

Department of Computer and Communication Engineering, Chungbuk National University, Cheongju, Republic of Korea

Halima

Department of Telecommunication Engineering, Baluchistan University of Information Technology, Engineering and Management Sciences, Quetta, Pakistan

A. Hameed

Research Institute of Microwave and Millimeter-Wave Studies, National University of Science and Technology, Islamabad, Pakistan

1 Introduction

Due to the rapid inclusion of wireless communication and RFID systems in devices, the requirement of antennas with a specific characteristic like high directivity, broad-band, and frequency reconfiguration has exponentially increased for high data rates transfer [1]. The process of antenna design incorporates size miniaturization and physical considerations due to a trend of compactness in wireless systems [2]. Besides, a drift towards the swift development of flexible electronics is expected due to its characteristics which are not achievable in rigid devices [3]. Hence, flexible antennas have an edge on rigid antennas due to its easy integration with flexible electronic devices [4].

Antennas operating at a single wideband spectrum are limited in terms of its diversity of applications since band spectrums have faced congestion in recent times, mainly due to a wave of increase in radio communication devices [5]. This closeness in band spectrum can cause unnecessary interference in radio signals which may cause the loss of valuable information. One important eradicating entity for this unnecessary interference is the property of frequency reconfiguration by varying the electrical properties of switching elements like PIN-diodes, RF MEMS, optical switches etc. integrated within the antenna [6]. Monopole antennas were comparatively performing better for frequency reconfigurability applications as compared to other types of the antenna [7].

Each band spectrum has its own valuable and unwanted characteristics. For example, 5G bands (microwave and mm-wave) are quite robust in data transmission but mm-wave 5G bands get distorted from atmospheric conditions and obstacles [8]. ISM band, as its name suggests, is useful for industrial, scientific, medical and telecommunication applications. S-band designated by IEEE intersections 2 conventional frequency bands, namely Ultra High Frequency and Super High-Frequency bands, typically between 2 and 4 GHz band of operation. This band finds its applications in low-power wireless communication applications like Bluetooth and Wi-Fi [9]. Table 1 presents the various bands along with their operational region and center frequencies.

Thus researchers and academia have done a tremendous job to design high-performance antenna for the aforementioned applications. In [10], although the presented antenna had the advantages of flexibility along with frequency reconfigurability but the presented antenna had setbacks of large size and complex structure. The

Table 1 Operational bands for presented antenna

Frequency band	Frequency range (GHz)	Central frequency (GHz)
5Gsub-6-GHz	<6	3.5
ISM	2.4–2.5	2.45
S (IEEE)	2–4	3.2
WiMAX	3.5–3.8	3.5

Table 2 Comparison of proposed work with similar state of the art works

References.	Dimensions (m \times m) ($\lambda_0 \times \lambda_0$)	Operating frequency (GHz)	Gain (dBi)	Flexibility	Reconfigurable
[10]	89 \times 83 0.70 \times 0.65	WBAN (2.4–2.5 GHz), WIMAX (2.35–2.52 GHz and (3.28–3.38 GHz)	6.4 dB (with AMC)	Yes	Yes
[11]	20 \times 17.2 0.173 \times 0.149	2.6–4.2 GHz (continuous due to varactors)	Not provided	Yes	Yes
[12]	40 \times 40 0.314 \times 0.314	2.35–3.43 GHz	4.3 dBi	No	Yes
[13]	10.5 \times 14 0.109 \times 0.145	3.1–10.6, 3.46–5.96, 3.28–6.26 and 9.04–9.526 GHz	Not provided	No	Yes
[14]	150 \times 150 0.8 \times 0.8	1.6–2.4 GHz	7.50 dB	No	Yes
This work	30 \times 25 0.25 \times 0.195	2.33–2.54, 2.75–3.87, and 3.51–4.21 GHz	2.9 dBi	Yes	Yes

antenna proposed in [11] has a compact size and covers the bands of ISM and 5G-sub-6 GHz but the physical structure was very complex along with limited bandwidth. In [12–14], although good results were demonstrated in terms of operating frequencies along with the advantage of reconfigurability characteristic but the substrate was not flexible thus antennas could not be integrated with wearables. By having a detailed investigation of literature it can be deduced that the already presented works lack a mixture of frequency reconfiguration, flexibility, simple geometrical configuration and relatively small in size. A summary of existing literature work is tabulated in the Table 2. Thus to overcome the aforementioned challenges a compact flexible frequency reconfigurable was presented in this paper. The return Sect. 2 presents the antenna designing while results were illustrated in Sect. 3 accompanied by the conclusion in Sect. 4.

2 Antenna Design

A physically small, flexible, frequency reconfigurable and relatively simply designed antenna is presented covering 4 band spectrums. The frequency reconfigurability was achieved by etching slot and then activate or deactivate slot by means of diode

embedded within the propagating element. The proposed design of the antenna is given in Fig. 1. The radiator has a shape like an octagon and truncated stub was loaded at the bottom of the octagonal radiator, as depicted in Fig. 1. Co-Planner Waveguide (CPW) feeding technique was used to design antenna where the gap between virtual grounds and the metallic strip of CPW feedlines are designed on the basis of impedance matching of 50 Ohms. The antenna had an overall size of $30 \text{ mm} \times 25 \text{ mm}$ which correspond to $0.23\lambda_0 \times 0.2\lambda_0 \times 0.002\lambda_0$. The substrate material was ROGERS RT-5880 having a thickness of 0.254 mm, the relative permittivity of 2.2 and Loss tangent of 0.0009 [15]. Higher Frequency Structural Simulator (HFSS) an infinite element method based electromagnetic solver was utilized to perform numerical analysis of the proposed work.

Fig. 1 Geometrical configuration of proposed flexible antenna

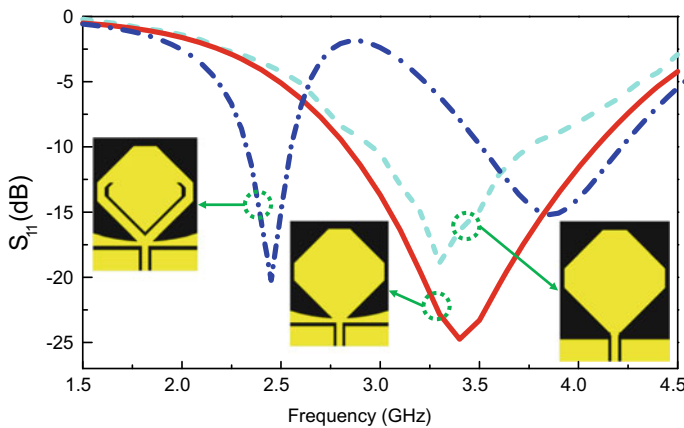
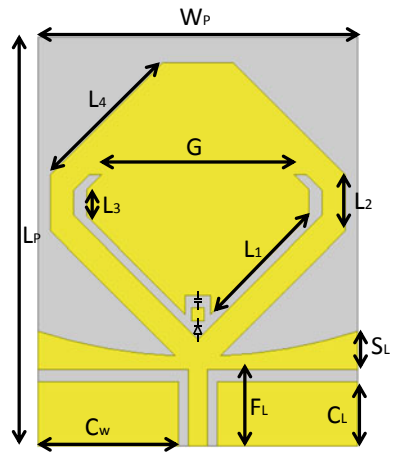


Fig. 2 Comparison of return losses of antenna design at different stages

Figure 2 presents the various steps involve in antenna designing and their corresponding s-parameters. In the first step, a square patch was designed to resonate at 3.5 GHz, the length and width of the patch can be calculated by using the equations provided in [16]. To improve the bandwidth and impedance matching corners were truncated as well. The resultant antenna shows an impedance bandwidth of 700 MHz ranging from 3.05 to 3.75 GHz. Afterword, a stub was inserted at the bottom of the radiator to improve the bandwidth of the basic octagonal-shaped radiator [17] presents a detailed study on the effect of stubs insertion at various part of the radiator. The resultant antenna after lording of stub exhibits an impedance bandwidth of 1210 MHz ranging 2.99–4.12 GHz, as depicted in Fig. 2. Finally, to achieve frequency reconfigurability, a slot was etched from radius were total effective length was estimated by using the equation provided in [16]. The resultant antenna starts resonating at 2.45 GHz and 3.85 GHz with < -10 dB bandwidth of 220 MHz ranging 2.33–2.55 GHz and 600 MHz (3.51–4.21 GHz). In final step a diode was inserted in the middle of the slot in such a way when the diode is in Off-state the slot becomes active while for On-state of diode the slot becomes inactive. The optimized parameters of the proposed antenna are as follow: $L_p= 30$ mm; $W_p= 25$ mm; $C_L= 5$ mm; $C_W= 11$ mm, $F_L= 6$ mm; $S_L= 3$ mm; $G = 15$ mm; $L_1= 10.9$ mm; $L_2= 2$ mm, $L_3= 2$ mm; $L_4= 12.5$ mm.

3 Results and Discussions

Various performance parameters of the antenna were investigated in this section to show the potential of the proposed work. Figure 3 presents the scattering parameters of the proposed antenna. It could be observed when the antenna was in ON-state the

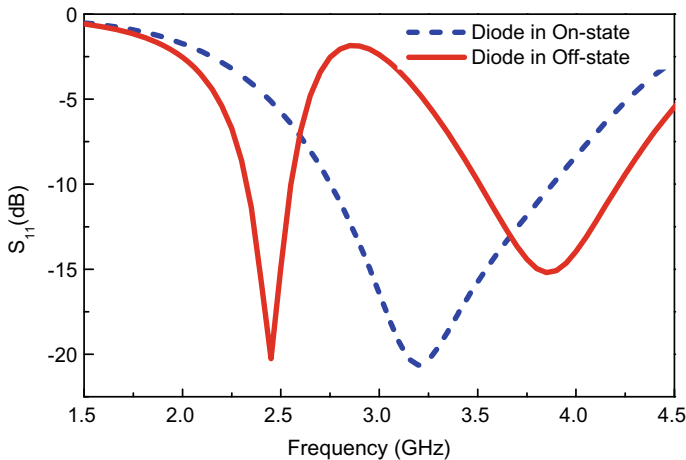


Fig. 3 Return loss of proposed reconfigurable antenna for ON/OFF state of the diode

antenna exhibits a wide impedance bandwidth of 1.12 GHz (2.75–3.87 GHz). On the other hand, when the diode is in Off-state the antenna exhibits two distinguished bands of 2.45 GHz having impedance bandwidth of 220 MHz (2.33–2.55 GHz) and 600 MHz (3.51–4.21 GHz) with respect to $|S_{11}| < -10$ dB, respectively.

Conformability, being one of the key requirements for the flexible devices, therefore the presented flexible antenna was bent along a cylinder having a radius (R) of 25 mm. Figure 4 illustrates the return loss graphs of the proposed antenna under bent condition. It can be observed from Fig. 4 that antenna exhibits wideband from 2.7 to 3.95 GHz when the diode was in On-state while dual-band ranging 2.3–2.6 GHz and 3.44–4.29 GHz where observed for diode Off-state. The results were in good agreement with those of unbent conditions, thus states the stability of the antenna under bending condition.

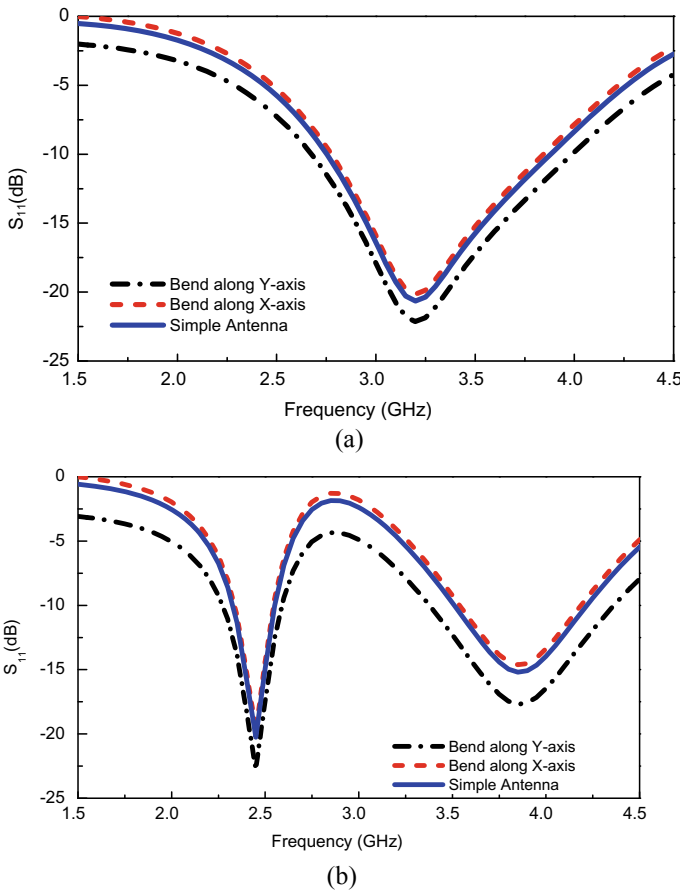


Fig. 4 Comparison of return losses of antenna design at under bend condition **a** diode On-state, **b** diode Off-state

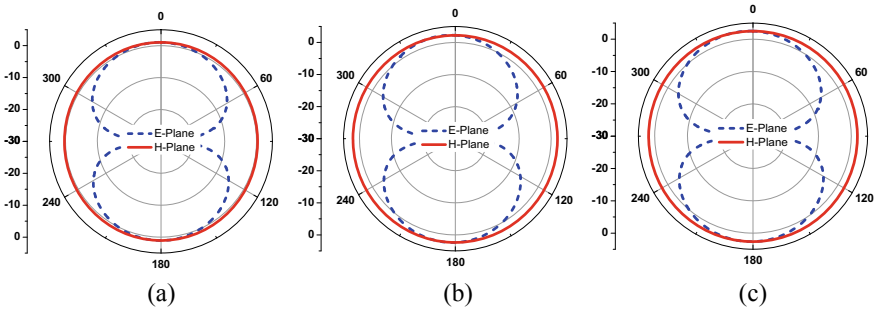


Fig. 5 Radiation patterns of proposed antenna at **a** 2.4 GHz, **b** 3.2 GHz for diode Off-state, **c** 3.8 GHz for diode On-state

Figure 5 illustrate the radiation pattern of the proposed antenna at different operating frequencies in E-plane ($\phi = 0^\circ$) and H-plane ($\phi = 90^\circ$). The antenna has omnidirectional radiation pattern in E-plane while bi-directional at H-plane at 2.45 and 3.85 GHz, when the diode is in Off-state, a similar pattern is observed for 3.2 GHz, when the diode is in On-state, as depicted in Fig. 5. The numerically calculated gain and efficiency at resonating frequency of 2.45 GHz were 1.8 dBi and 84%, respectively. For 3.85 GHz the reported gain was 2.9 dBi and efficiency was 91%. On the other hand, for resonating frequency of 3.2 GHz the gain and efficiency were reported to be 2.78 dBi and 92%, respectively.

4 Conclusion

A compact flexible frequency reconfigurable antenna was presented in this paper. Truncating radiator and insertion of the slot was utilized to achieve wideband and low return loss at the resonating frequency. Afterward, a slot and diode were utilized to achieve on-demand wideband to dual-band frequency reconfigurability. The antenna exhibits good performance in both unbent and conformal scenarios. Moreover, presented work over-performed other related works in terms of compact size, flexibility, frequency reconfigurability, a moderate gain and simple geometrical structure. Thus the presented work becomes a potential candidate for both rigid and flexible devices operating in ISM band (2.45 GHz), WiMAX band (3.5 GHz), 5Gsub-6-GHz band (3.5 GHz) and S-band (2–4 GHz).

References

1. Hussain N, Azimov U, Jeong M, Rhee S, Lee SW, Kim N (2020) A high-gain microstrip patch antenna using multiple dielectric superstrates for WLAN applications. *Appl Comput*

- Electromagnet Soc J 35(2)
2. Awan WA, Hussain N, Naqvi SA, Iqbal A, Striker R, Mitra D, Braaten BD (2020) A miniaturized wideband and multi-band on-demand reconfigurable antenna for compact and portable devices. *AEU-Int J Electron Commun* 153:266
 3. Awan WA, Hussain N, Ghaffar A, Zaidi A, Li XJ (2020) A compact flexible antennas for ISM and 5G Sub-6-GHz band application. In: 24th international ITG workshop on smart antennas, VDE, pp 1–3
 4. Ghaffar A, Li XJ, Hussain N, Awan WA (2020) Flexible frequency and radiation pattern reconfigurable antenna for multi-band applications. In: 4th Australian microwave symposium (AMS). IEEE, pp 1–2
 5. Abbas A, Hussain N, Jeong MJ, Park J, Shin KS, Kim T, Kim N (2020) A rectangular notch-band UWB antenna with controllable notched bandwidth and centre frequency. *Sensors* 20(3):777
 6. Naqvi AH, Lim S (2018) Microfluidically polarization-switchable metasurfaced antenna. *IEEE Antennas Wirel Propag Lett* 17(12):2255–2259
 7. Zaidi A, Baghdad A, Awan WA, Ballouk A, Badri A (2019) CPW fed wide to dual band frequency reconfigurable antenna for 5G applications. In: International conference on wireless technologies, embedded and intelligent systems (WITS). IEEE, pp 1–3
 8. Hussain N, Jeong MJ, Park J, Kim N (2019) A broadband circularly polarized Fabry-Perot resonant antenna using a single-layered PRS for 5G MIMO applications. *IEEE Access* 7:42897–42907
 9. Awan WA, Hussain N, Le TT (2019) Ultra-thin flexible fractal antenna for 2.45 GHz application with wideband harmonic rejection. *AEU-Int J Electron Commun* 110:152851
 10. Saeed SM, Balanis CA, Birtcher CR (2016) Inkjet-printed flexible reconfigurable antenna for conformal WLAN/WiMAX wireless devices. *IEEE Antennas Wirel Propag Lett* 15:1979–1982
 11. Zhang K, Zhang J, Zhang S, Cao Z, He Y (2019) A frequency reconfigurable microstrip patch antenna based on liquid metal and PDMS. In: 11th international conference on wireless communications and signal processing (WCSP). IEEE, pp 1–5
 12. Boukarkar A, Lin XQ, Jiang Y, Yang XF (2018) A compact frequency-reconfigurable 36-states patch antenna for wireless applications. *IEEE Antennas Wirel Propag Lett* 17(7):1349–1353
 13. Devi GA, Aarthi J, Bhargav P, Pandeewari R, Reddy MA, Daniel RS (2019) UWB frequency reconfigurable patch antenna for cognitive radio applications. In: International conference on antenna innovations and modern technologies for ground, aircraft and satellite applications (iAIM). IEEE, pp 1–4
 14. Dhanade YB, Choukiker YK (2017) Frequency and polarization reconfigurable antenna for wireless communication. In: International conference of electronics, communication and aerospace technology (ICECA), vol 1. IEEE, pp 287–290
 15. 'Rogers Corporation', www.rogerscorp.com. Accessed May 2020
 16. Awan WA, Zaidi A, Hussain N, Iqbal A, Baghdad A (2019) Stub loaded, low profile UWB antenna with independently controllable notch-bands. *Microw Opt Technol Lett* 61(11):2447–2454
 17. Zaidi A, Awan WA, Hussain N, Baghdad A (2020) A wide and tri-band flexible antennas with independently controllable notch bands for Sub-6-GHz communication system. *Radio Eng* 29(1)

Dual-Band BPF Based on a Single Dual-Mode Stepped-Impedance Resonator for 4G Systems



Mohamed Amzi, Jamal Zbitou, and Saad Bennani Dosse

Abstract A dual-band bandpass filter (BPF) based on a dual-mode stepped-impedance resonator (SIR) operating at 1.8/2.6 GHz is proposed. It is shown that the dual-band BPF has a smaller area ($12.6 \times 15 \text{ mm}^2$), lower Insertion loss ($<0.5 \text{ dB}$) and good return loss ($>15 \text{ dB}$) at both passbands. In addition, two transmission zeros are created by the input and output tapping to enhance the rejection band ($>30 \text{ dB}$). The simulations are carried out using Ansoft's HFSS and CST-MS software.

Keywords Multi-band filter · Bandpass filter · Stepped-impedance resonator · Transmission zero

1 Introduction

The majority of wireless communication systems simultaneously support multiple standards that operate at different frequency bands, requiring the development of multi-band filters for separating these bands. A multi-band filter is a filter (with one input and one output) that can serve two or more bands, and several different approaches are used to their design [1]. One of the most used approaches is based on multimode resonators where each passband is associated with one mode. Multi-mode resonators represent good candidates for miniature multiband filters, since they support several resonant modes [1]. The main types of multi-mode resonators are: resonators with perturbation that have two-dimensional symmetry. This type supports propagation of two degenerative modes that have the same resonant frequency but orthogonal field distributions, this idea was employed in [2–4]. The second type is based on Stub-Loaded Resonators (SLR) [5–7]. Another technique is called the multi-mode Stepped-Impedance Resonators (SIR), which can provide resonances at

M. Amzi (✉) · S. B. Dosse
SMBA University, Fez, Morocco
e-mail: amzi.mohamed@yahoo.com

J. Zbitou
Hassan I University, Settat, Morocco

non-harmonically related frequencies and offers significantly more design freedom in passband control compared to the two previous techniques [8–11].

However, small size, high performance, lower cost, and especially independent control of passbands are required to design multi-band filters.

In this work, a dual-band bandpass filter with compact size, low insertion loss, and high rejection band is proposed. The filter is based on a single dual-mode SIR with an I/O port that consists of a feeding line (50Ω) and a parallel coupling arm, to simultaneously resonate at $f_1 = 1.8 \text{ GHz}$ and $f_2 = 2.6 \text{ GHz}$. A wide rejection band is obtained using tapped input/output lines. The proposed filter is formed on RT/Duroid 5880 substrate. The dielectric constant is 2.2 and the loss tangent is 0.0009, the thickness is 0.127 mm with $35 \mu\text{m}$ thick copper conductor layer. The simulations are carried out using Ansoft’s HFSS and CST-MS software.

2 Dual-Mode SIR Characteristics

SIR structures allow the design of filters with good performance and compact size. Multi-mode SIR supports two modes that are formed by the fundamental and higher-order mode whose resonant frequencies are not harmonically related, Fig. 1. It consists of two different characteristic impedances and are constructed by cascading

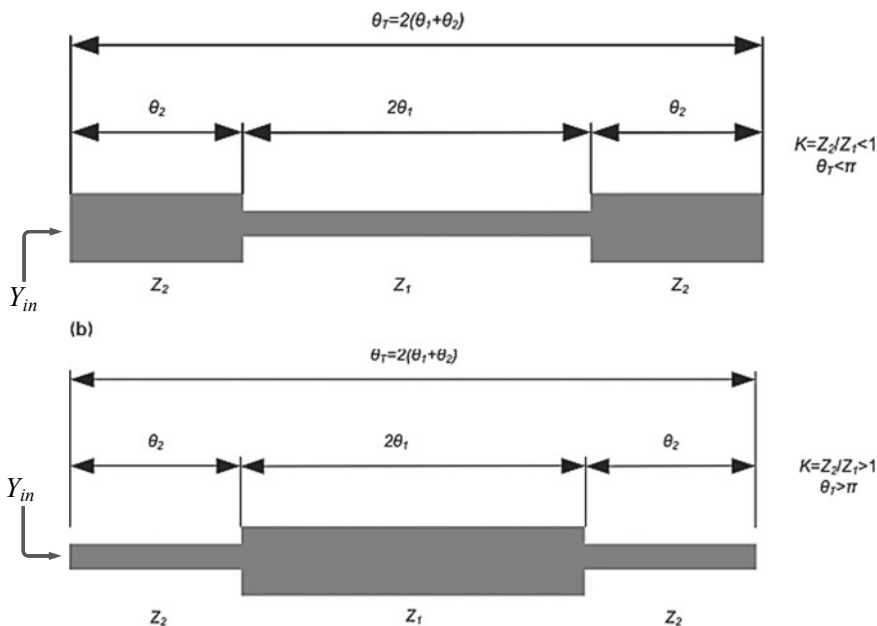


Fig. 1 The configuration of stepped-impedance resonator (SIR)

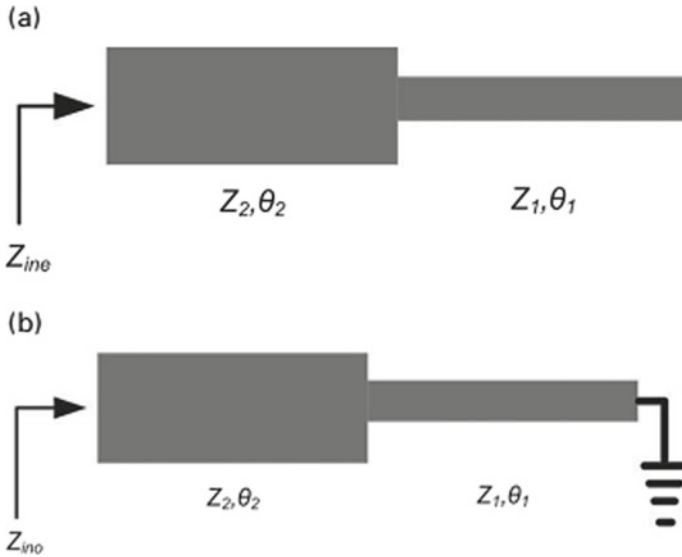


Fig. 2 SIR equivalent circuit for: **a** even mode, **b** odd mode

a long-length ($2\theta_1$) section in the center connected with the two short-length (θ_2) sections in the two sides [1].

One of the key features of an SIR is that its resonant frequencies can be tuned by adjusting its structural parameters, such as the impedance ratio of the high-Z and low-Z segments.

SIR can be analyzed, due to its symmetry, using even- and odd-mode analysis [1]. The equivalent circuits even and odd are shown in Fig. 2.

The input admittance (Y_{in}) at the left end, looking into the right side, can be derived in the following way:

$$Y_{in} = jY_2 \frac{2(K \tan \theta_1 + \tan \theta_2)(K - \tan \theta_1 \tan \theta_2)}{K(1 - \tan^2 \theta_1)(1 - \tan^2 \theta_2) - 2(1 + K^2) \tan \theta_1 \tan \theta_2} \tag{1}$$

where $K = Z_2/Z_1$ is the impedance ratio, and $Y_2 = 1/Z_2$.

The resonant condition at the resonances leads to:

$$Y_{in} = 0 \tag{2}$$

From these equations:

$$\begin{aligned} K - \tan \theta_1 \tan \theta_2 &= 0 \quad (\text{odd - mode frequencies}) \\ K \tan \theta_1 + \tan \theta_2 &= 0 \quad (\text{even - mode frequencies}) \end{aligned} \tag{3}$$

In order to analyze the ratio of fundamental (f_1) and higher-order modes resonances (f_2, f_3, f_4, \dots), we can analyze two cases:

In the case of $\theta_2 = 2\theta_1 = \theta$, we have:

$$\theta(f_1) = \tan^{-1}\left(\sqrt{\frac{K}{2+K}}\right); \theta(f_2) = \tan^{-1}\left(\sqrt{\frac{2+K}{K}}\right); \theta(f_3) = \frac{\pi}{2} \quad (4)$$

Thus,

$$\frac{f_2}{f_1} = \frac{\tan^{-1}\left(\sqrt{\frac{2+K}{K}}\right)}{\tan^{-1}\left(\sqrt{\frac{K}{2+K}}\right)}; \frac{f_3}{f_1} = \frac{\pi}{\tan^{-1}\left(\sqrt{\frac{K}{2+K}}\right)} \quad (5)$$

Figure 3a shows the two normalized frequencies, f_2/f_1 and f_3/f_1 , versus the ratio K . As K decreases from unity ($K < 1$, i.e. $Z_2 < Z_1$), both second resonant frequency (f_2) and third resonant frequency (f_3) depart from the first resonance (f_1), thus widening the upper stopband, which can be used to design single-mode SIR bandpass filters [1]. On the other hand, as K increases from unity, the second-order resonance drops off towards the first one much faster than the third one. Consequently, the first two frequencies could occur in proximity to each other as K increases.

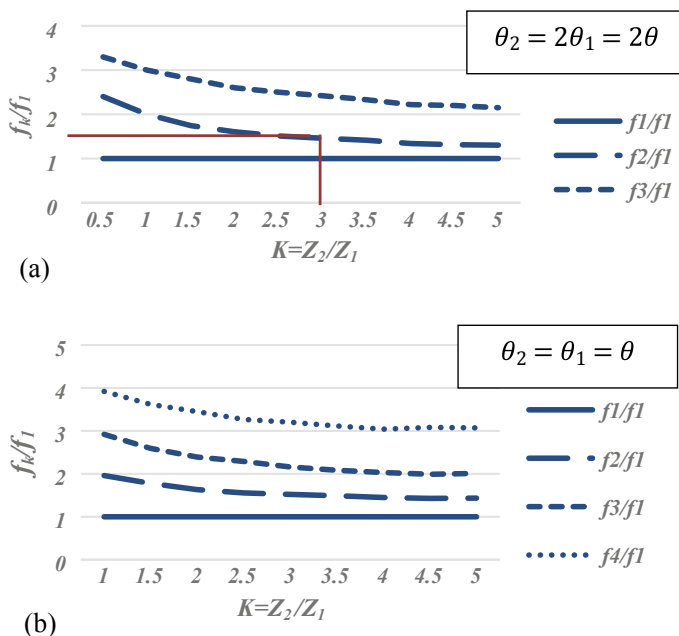


Fig. 3 Normalized resonant frequencies versus K of a multiple mode SIR. **a** Two-mode resonator with $\theta_2 = 2\theta_1$, **b** three-mode resonator with $\theta_2 = \theta_1$

In the case of $\theta_2 = \theta_1 = \theta$, we obtain from previous equations:

$$\theta(f_1) = \tan^{-1}(\sqrt{K}); \theta(f_2) = \frac{\pi}{2}; \theta(f_3) = \pi - \tan^{-1}(\sqrt{K}); \theta(f_4) = \pi \quad (6)$$

Therefore,

$$\frac{f_2}{f_1} = \frac{\pi}{2 \tan^{-1}(\sqrt{K})}; \frac{f_3}{f_1} = \frac{\pi}{\tan^{-1}(\sqrt{K})} - 1; \frac{f_4}{f_1} = \frac{\pi}{\tan^{-1}(\sqrt{K})} \quad (7)$$

Figure 3b depicts the three normalized frequencies, $f_2/f_1, f_3/f_1$ and f_4/f_1 . Similar to those in the previous case, the first three resonant frequencies become very close to each other as K increases, while the fourth one is still distinct from them. Compared with the last case in Fig. 3a, one additional resonant mode (f_4) is moved down.

3 The Proposed Dual-Band BPF Design

The objective of this work is to design a dual-band BPF operating at 1.8 and 2.6 GHz, with the fractional bandwidths 5% and 4%, respectively. Figure 4 shows the layout of the proposed BPF, it consists of one single dual-mode SIR with an I/O port that consists of a feeding line (50Ω) and a parallel coupling arm.

In the filter design procedure, the SIR is firstly characterized to simultaneously resonate at $f_1 = 1.8$ GHz and $f_2 = 2.6$ GHz. The frequencies f_3 and f_4 are considered to be spurious frequencies that should be as far away from the passbands as possible. It shown from Fig. 3. that the resonator with $\theta_2 = 2\theta_1$ is the proper choice for this design since, the first two resonant frequencies (f_1 et f_2) become very close to each other as K increases, while the third and fourth one are still distinct

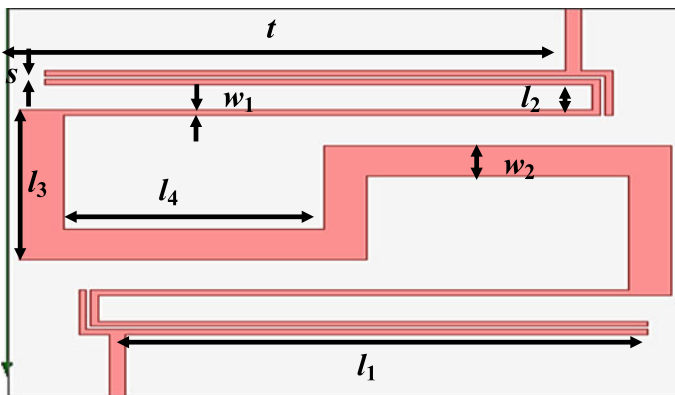


Fig. 4 The layout of the proposed dual-band BPF, where: $w_1 = 0.17, w_2 = 0.97, l_1 = 12, l_2 = 0.83, l_3 = 4.87, l_4 = 5.83, s = 0.11$, all dimensions are in mm

from them. Thus, a wide stopband can be obtained. Considering that $f_2/f_1 = 2.6/1.8 = 1.44$, this value corresponds to $K = 3$, Fig. 3a, with $Z_1 = 25\Omega$ and $Z_2 = 75\Omega$. The electrical length θ can be explicitly determined as 37.8° [from Eq. (3)].

Next, the position of the tapped I/O lines ($t = 12.45$ mm, green line) with a $50\ \Omega$ line is well designed to enhance the rejection band (the third mode is suppressed) by using the full-wave electromagnetic (EM) simulation, Fig. 5. As we can see, the tap position is varied along the coupling arm and the position of TZs is varied.

The dual-band BPF is designed on the substrate of RT/Duroid 5880, with dielectric constant 2.2, loss tangent 0.0009, thickness 0.127 mm, and $35\ \mu\text{m}$ thick copper conductor layer, and excited by a $50\ \Omega$ microstrip line with 0.36 mm width. The simulations are carried out using Ansoft's HFSS and CST-MS software.

Figure 6 shows the simulated frequency response of the proposed dual-band BPF filter. It's seen that the proposed filter has good performances. The insertion loss (S_{21}) and the return loss (S_{11}) are about $-0.31\ \text{dB}$, $-18.9\ \text{dB}$ at 1.8 GHz, and $-$

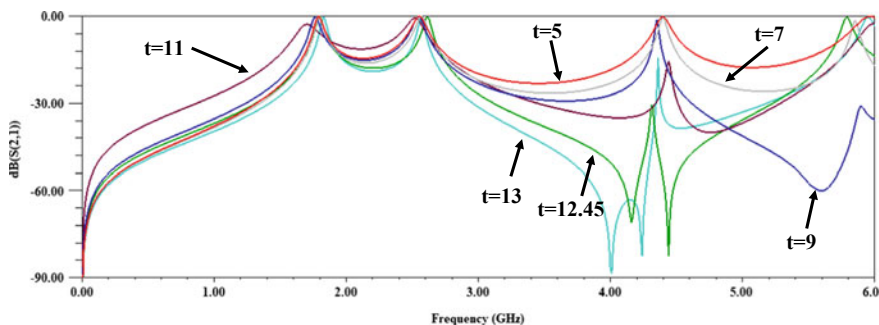


Fig. 5 Simulated frequency response under different values of t (mm)

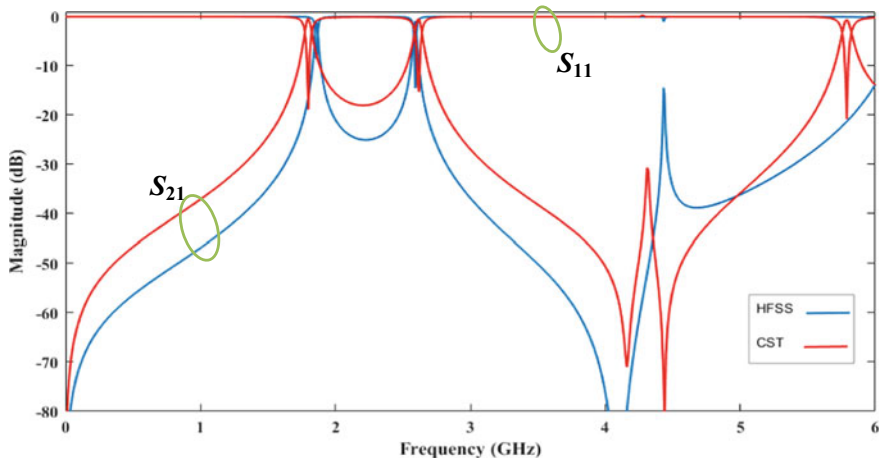


Fig. 6 Simulated result of the proposed dual-band BPF

0.49 dB, -15.3 dB at 2.62 GHz (with HFSS). In addition, two transmission zeros are created by the input and output tapping to enhance the rejection band.

4 Conclusion

The proposed design achieves high performance, better return loss, and insertion loss less than -0.4 dB are realized with a high level rejection band more than 30 dB at lower (DC-1.3 GHz) and upper (3.1–5.2 GHz) stopbands. It is shown that the design of a dual-band BPF based on one single dual-mode SIR makes it very small in term of size (12.6×15 mm²), which is suitable for multi-band communication systems.

References

1. Crnojevic-Bengin V (2015) *Advances in multi-band microstrip filters*, 1st edn. Cambridge University Press, United Kingdom
2. Youngje S (2020) A novel dual-mode dual-band bandpass filter based on a single ring resonator. *J Electromagnet Eng Sci* 20(2):91–95
3. Tang MC, Shi T, Chen S (2016) Dual-band bandpass filter based on a single triple-mode ring resonator. *IEEE Microw Electron Lett* 52(9):722–724
4. Xu LJ, Zhang G, Tang YM, Bo YM (2015) Compact dual-mode dual-band bandpass filter with wide stopband for WLAN applications. *Electron Lett* 51(17):1372–1374
5. Jiang W, Shen W, Wang T, Huang YM, Peng Y, Wang G (2016) Compact dual-band filter using open/short stub loaded stepped impedance resonators (OSLSIRs/SSLSIRs). *IEEE Microw Wireless Compon Lett* 26(9):672–674
6. Wu X, Wan F, Ge J (2016) Stub-loaded theory and its application to balanced dual-band bandpass filter design. *IEEE Microwave Wireless Comp Lett* 26(4):231–233
7. Khani S, Mousavi SMH, Danaie M, Rezaei P (2018) Tunable compact microstrip dualband bandpass filter with tapered resonators. *Microw Opt Technol Lett* 60:1256–1261
8. Deng K, Chen Z, Hu G, Feng W (2018) Dual-band bandpass filters with multiple transmission zeros using $\lambda/4$ stepped-impedance resonators. *Int J RF Microw Comput Aided Eng*
9. Sung G (2018) Compact dual-band bandpass filter using U-shaped stepped-impedance resonators with parallel coupled structures. *J Electromagn Eng Sci* 18(2):73–77
10. Gómez-García R, Yang L, Muñoz-Ferreras JM, Psychogiou D (2019) Selectivity-enhancement technique for stepped-impedance-resonator dual-passband filters. *IEEE Microw Wireless Compon Lett* 29(7):453–455
11. Luo C, Wei B, Wang X et al (2020) Wideband and wide stopband superconducting bandpass filter using asymmetric stepped-impedance resonators connected to open stub. *Int J RF Microw Comput Aided Eng*

High Gain Cascaded GaAs-pHEMT Broadband Planar Low Noise Amplifier for WiMAX-802.16b Applications



Moustapha El Bakkali, Naima Amar Touhami, and Taj-Eddin Elhamadi

Abstract Low noise amplifiers are essential structures in telecommunications systems. The problem of LNAs in planar technology is the difficulty of having a flat gain with a low noise figure in a wide bandwidth. In this work, we focus on the design of a broadband low noise amplifier for WiMAX-802.16d applications using GaAs-pHEMT ATF-35176 of Avago technologies. The three-stage cascade configuration mounted on an FR-4 substrate is used and provides a high gain, with an average value of 34.3 dB and a low noise figure of 0.95 ± 0.1 dB with a power consumption of 417 mW. The total die size is 9.5×2 cm².

Keywords Low noise amplifier · GaAs-pHEMT · Noise figure NF · Cascade

1 Introduction

Wireless broadband technologies are mainly developed to make all kinds of digital sources available to a large part of the world's population at any time [1, 2]. WiMAX is a broadband wireless network based on the IEEE 802.16 standard, which guarantees compatibility and interoperability between broadband wireless access equipment and which meet specific compliance criteria defined by the WiMAX forum [3, 4]. The 802.16b standard offers the appropriate solution to increase the amount of spectrum that can be used in the range 5–6 GHz with service quality guarantees [5, 6].

Low noise amplifiers or LNAs are active low signal devices used to amplify the RF signal and minimize the noise received by an antenna or generated by the passive or active elements constituting this system. In the literature, several works are carried out in this context. Narrowband LNAs have become classic [7–10], they are made in different technologies (Gallium arsenide “GaAs”, Gallium Nitride “GaN”, Complementary Metal Oxide Semiconductor “CMOS”, ...) and architectures [11, 12].

M. El Bakkali (✉) · N. A. Touhami · T.-E. Elhamadi
Informations System and Telecommunication Laboratory, Faculty of Science, Abdelmalek Essaadi University, BP.2121, M'Hannech II, 93030 Tetuan, Morocco
e-mail: moustapha.elbakkali@etu.uae.ac.ma

Technological progress has become an obsession of universities and industrial companies, resulting in the development of a large number of broadband low-noise amplifier architectures [13–15].

In this paper, an improvement of the gain S_{21} of a low noise amplifier using the cascade architecture is presented. The GaAs pseudomorphic High electron mobility transistor (pHEMT) ATF-35176 transistor of Avago technology is chosen which is characterized by a low noise figure and a significant gain.

This work will be presented in three parts. The first part will present the proposed structure, the study of the bias circuit, stability, types of noise that can infect the amplifier and the linearity. The second part will deal with simulation results, interpretations and a comparison. Finally, a summary of this work will be presented in the last part.

2 Design Methodology

2.1 LNA Structure

The proposed block diagram of the low noise amplifier is shown in Fig. 1. It consists of a chain of amplifiers connected one after the other. Its principle is to reduce the noise to the minimum possible and to amplify the signal received by a receiving antenna which picks up a very low power from the other of -20dBm .

The first stage is adapted to minimize the noise; hence the input adaptation circuit reduces the noise figure NF expression of Eq. (1) to NF_{\min} , by putting the equality of reflection coefficient of the source Γ_s with the optimal reflection coefficient Γ_{opt} ($\Gamma_s = \Gamma_{\text{opt}^*}$). The output matching circuit transmits the maximum power to the load.

$$NF = F_{\min} + \frac{2R_n}{Z_0} \frac{|\Gamma_s - \Gamma_{\text{opt}}|^2}{|1 + \Gamma_{\text{opt}}|^2 (1 - |\Gamma_s|^2)} \tag{1}$$

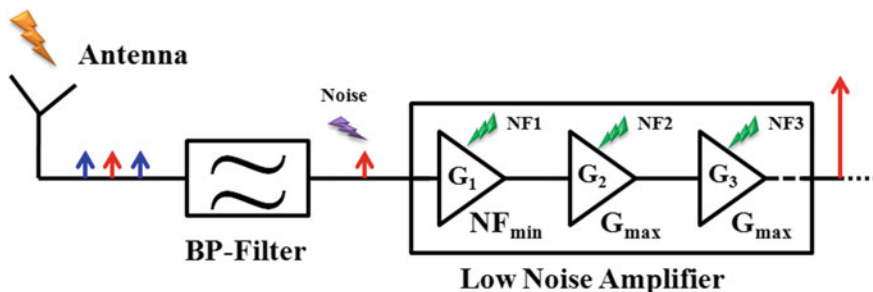


Fig. 1 Position of low noise amplifier LNA in the receptor chain

Γ_{opt} : The optimal reflection coefficient allows a minimum noise figure equal to NF_{min}

R_n : The equivalent noise resistance of the transistor

Z_0 : The characteristic impedance.

$$\text{NF} = \text{NF}_1 + \frac{\text{NF}_2 - 1}{G_1} + \frac{\text{NF}_3 - 1}{G_1 G_2} + \frac{\text{NF}_4 - 1}{G_1 G_2 G_3} + \dots \quad (2)$$

According to Eq. (2) was always the interest to first place in the chain an amplifier which has very low noise and high gain. This gain masks the noise provided by subsequent stages.

The noise of the second and third stages does not have great influence if the G_2 and G_3 gains are significant. In this case, it is recommended to adapt the two last stages of LNA to have a maximum gain without taking into account the effect of its noises (NF_2 and NF_3).

According to Eq. (3), the first stage gain cannot reach its maximum value because of the difference in values between Γ_{opt} and S_{11} . The output is already adapted, so the $1/(1-|S_{11}|^2)$ term tends towards zero.

$$G_u = \frac{1}{1 - |S_{11}|^2} |S_{21}|^2 \frac{1}{1 - |S_{22}|^2} \quad (3)$$

The maximum gain G_{max} of the amplifier depends on reverse transfer gain and stability factor K .

$$G_{\text{max}} = \frac{|S_{21}|}{|S_{12}|} \left(K - \sqrt{K^2 - 1} \right) \quad (4)$$

2.2 Bias Network

The bias circuit in the form of Tee is designed in Advanced Design System software (ADS). The role of Tee of polarization is to guarantee the good functioning of the transistor. It consists of three ports, port P1 is used to transmit the radio frequency RF signal, port P3 is used to inject the DC component and port P3 receives the RF + DC signal.

The high impedance $\lambda/4$ stubs play the role of an inductor while the radial-stub of the electrical length 90° has a condensing behaviour.

According to Fig. 2, the circuit has a better adaptation to the central frequency of 5.5 GHz. The isolation S_{13} is perfect between ports P1 and P3 with the total transmission of the signal S_{12} from port P1 to port P2. Parameter S_{33} tends to zero, which means that the RF signal is fully reflected at port P3.

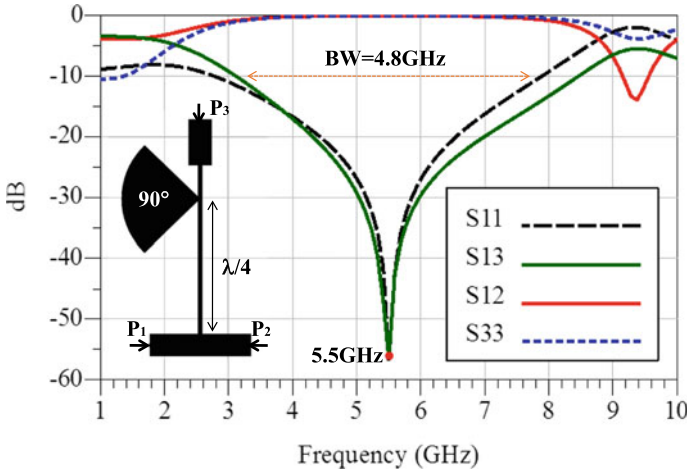


Fig. 2 Bias circuit and its scattering parameters behaviour

2.3 Stability

The main cause of an amplifier’s malfunction is the presence of oscillations. They are all the more difficult to detect as they often appear outside the frequency band considered, the useful band. Each stage should be made unconditionally stable for all frequencies.

The stability of LNA is satisfied if the stability factor K is greater than 1 and the parameter B is positive.

$$K = \frac{1 - |S_{11}|^2 - |S_{22}|^2 + |\Delta|^2}{2 - |S_{12} \cdot S_{21}|} > 1 \tag{5}$$

$$B = 1 - |S_{11}|^2 - |S_{22}|^2 + |\Delta|^2 > 0 \tag{6}$$

where: $\Delta = S_{11} \cdot S_{22} - S_{12} \cdot S_{21}$.

Sometimes these two conditions are not checked, several techniques in the literature are available. The use of the series or parallel resistor at the transistor output is the most recommended to ensure the stability of the amplifier. If the resistance value is large enough, a capacitor in parallel is added with this dipole to avoid decreasing the gain under the joule effect.

2.4 Noise Source

Noise is a random or deterministic signal providing no information and which disturbs the transmission of the useful signal. In each electrical circuit, we can identify three internal sources: Thermal noise, Shot Noise, and Flicker Noise $1/f$.

2.5 Compression Point P_{1dB}

The low noise amplifier is an active element operating in the small-signal regime, neglecting the harmonics. The output signal of an ideal amplifier which is not subject to any distortion is written in the form:

$$P_{out} = a_1 \cdot P_{in} \quad (7)$$

As the input signal P_{in} increases, the output signal moves away from the ideal case due to the appearance of the phenomenon of gain compression.

In the real case, the output signal expression P_{out} becomes:

$$P_{out} = a_1 \cdot P_{in} + \frac{3}{4} a_3 \cdot P_{in}^3 \quad (8)$$

As the input signal P_{in} increases, the output signal moves away from the ideal case due to the appearance of the phenomenon of gain compression.

2.6 Third Intercept Point $IP3$

In the case of a “two-tone” signal at frequencies f_1 and f_2 , harmonics and intermodulation terms are obtained at the frequency $m \cdot f_1 \pm n \cdot f_2$ ($m, n \in N^2$).

The existence of intermodulation terms (IM) is problematic in terms of the difficulty of removing these spectra by filtering when they are close to the fundamentals of f_1 and f_2 .

Third-order Intermodulation IM3 is characterized by third-order intercept point $IP3$. $IP3$ is the point at which the amplitudes of the fundamental and IM3 are equal. The fundamental growth is proportional to the input signal power and that of IM3 is proportional to the cube of the input signal.

3 Result and Discussion

The layout of the proposed structure of broadband planar low noise amplifier is presented in Fig. 3. Broadband LNA is mounted on an FR-4 substrate, of thickness $H = 0.8$ mm, of relative permeability $\epsilon_r = 4.6$ and of loss tangent $\text{tang}\delta = 0.0026$.

The transistor chosen is of GaAs-pHEMT technology and the ATF35176 type. From a transistor datasheet given by the ATF foundry, the transistor is characterized by a minimum noise figure at drain-source voltage $V_{ds} = 1.5$ V and gate-source voltage $V_{gs} = -0.1$ V.

So the first stage is polarized with these voltages. The second and third stages are polarized and adapted with open-circuit stubs at the input and the output to have a maximum gain. The optimal values of $V_{ds\text{opt}}$ and $V_{gs\text{opt}}$ of these two last stages are successive -0.1 V and 3.2 V. To ensure the stability of each stage of the low noise amplifier over the entire study band which is between 5 and 6 GHz, a resistor R_s of model `sr_ims_RC_I_0603` is added in series to the drain output. Figure 4 shows the variation of stability as a function of the LNA frequency. For a resistor R_s of 5.1Ω , the value of stability factor K is greater than unity and the parameter B is positive which shows that LNA is unconditionally stable. The Advanced Design System ADS simulator Smith Chart tool is used to find the initial electrical values of LNA input/output matching circuits. These values are also converted to physical values and optimized using the FR-4 substrate. Table 1 gives the dimensions of the adaptation circuits.

Figure 5, shows the variation of the input S_{11} , output S_{22} and optimal Γ_{opt} coefficients according to the frequency. This result shows that the broadband LNA is adapted to the input and the output ($S_{11} < -10$ dB and $S_{22} < -10$ dB), i.e. there is a total transmission of the power towards the load. The coefficient Γ_{opt} is also less than -10 dB between 5 and 6 GHz.

According to Fig. 6, the gain S_{21} is very high with an average value of 34.3 dB and ripple of 3.2 dB. The maximum gain found of LNA is 37.5 dB at 5 GHz and its minimum value is 31.1 dB at 6 GHz. The input network of the amplifier circuit adapts LNA to have a minimum noise figure NF. The minimum noise found of LNA

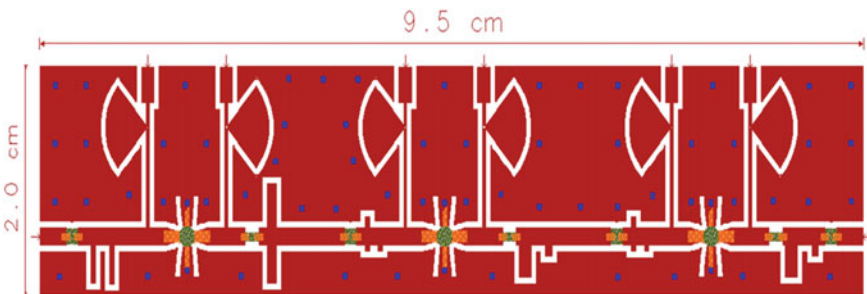


Fig. 3 The layout of broadband cascaded Low Noise Amplifier ($9.5 \times 2 \text{ cm}^2$)

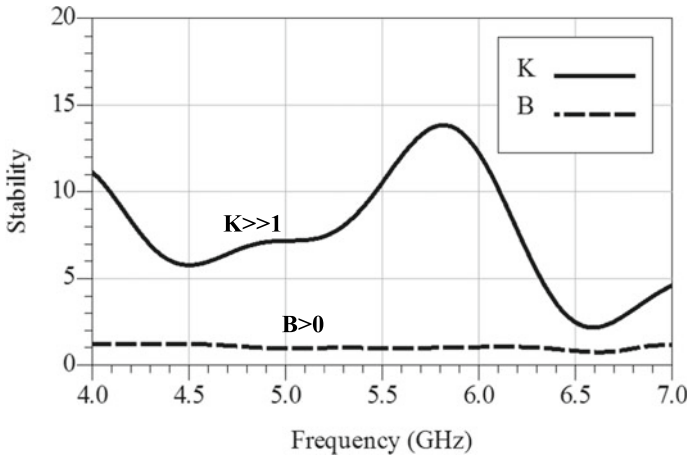


Fig. 4 Broadband LNA stability with a series resistor ($R_s = 5.1\Omega$)

Table 1 Dimensions of the adaptation circuits

Stage	Input matching network (mm)				Output matching network (mm)			
	Stub 1 (W&L)		Stub 2 (W&L)		Stub 3 (W&L)		Stub 4 (W&L)	
1	0.51	3.32	0.51	3.39	1.05	3.26	1.05	3.8
2 and 3	Stub 6 (W&L)		Stub 7 & 8 (W&L)		Stub 9 (W&L)		Stub 10 (W&L)	
	0.5	1	0.5	0.5	1.36	2.77	0.72	0.94

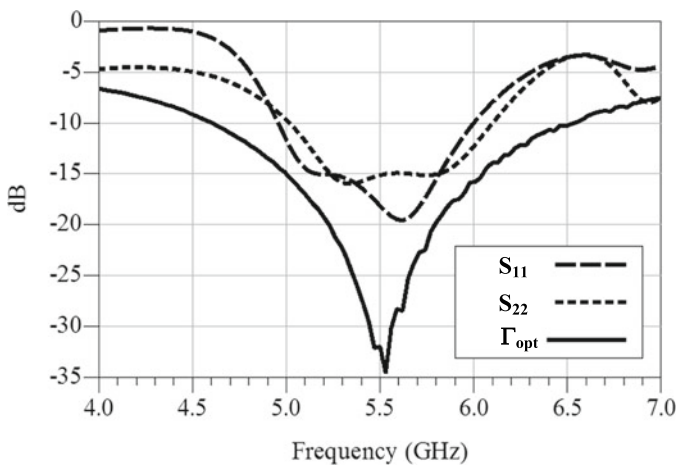


Fig. 5 Adaptation results of broadband planar low noise amplifier

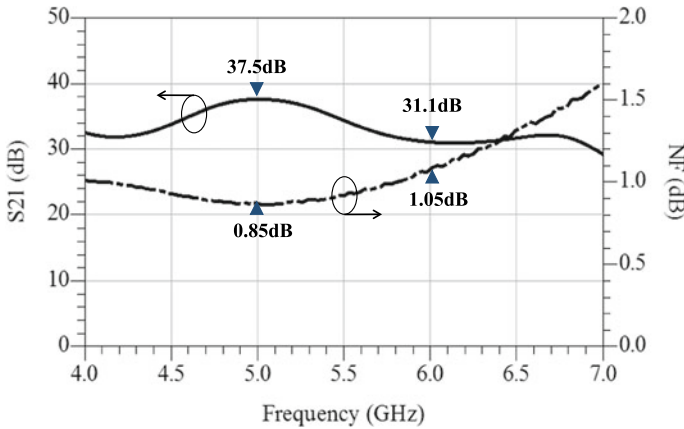


Fig. 6 Gain S_{21} and noise figure NF of broadband planar low noise amplifier

is 0.85 at 5 GHz and its maximum value is 1.05 dB at 6 GHz. The amplifier designed is, therefore, a good candidate in terms of power and low noise figure.

The 1 dB compression point is the operating point of the amplifier for which the small-signal gain is reduced by 1 dB compared to an ideal perfectly linear amplifier. IP3 is the point at which the amplitudes of the fundamentals and IM3 are equal. This point is of great importance in the design of low noise amplifiers. The 1 dB compression point of LNA is -16 dBm and third-order input intercepts point IIP3 for two close frequency of 5.5 ± 0.001 GHz is -7.75 dBm which shows that the amplifier has high linearity as illustrated in Fig. 7.

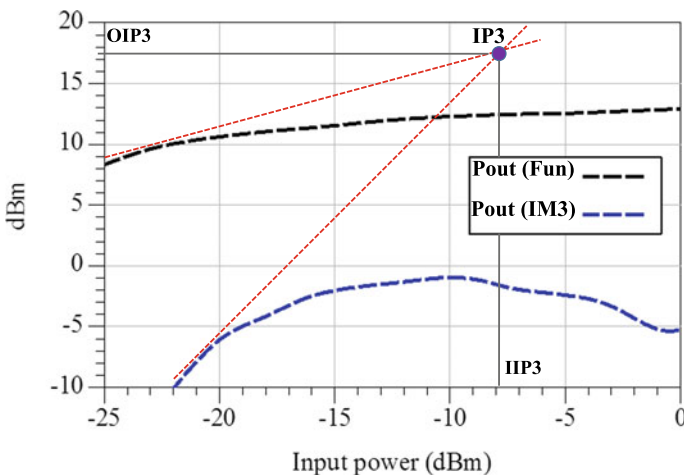


Fig. 7 Interception point representation

Table 2 Dimensions of the adaptation circuits

	[16]	[17]	This work
Year	2020	2020	2020
Tech	MOSFET	CMOS	GaAs- pHEMT
BW(GHz)	5–5.7	5–5.8	5–6
S ₁₁ (dB)	<–10.2	<–11	<–10
S ₂₂ (dB)	<–10.5	NA	<–10
Γ _{opt} (dB)	NA	NA	<–10
S ₂₁ (dB)	16.77 ± 0.77	16.4 ± 0.4	34.3 ± 3.2
NF (dB)	2.12 ± 0.37	1.75 ± 0.25	0.95 ± 0.1
P1dB (dBm)	NA	NA	–16
IIP3 (dBm)	NA	–4.1	–7.75
P _{dc} (mW)	2.3	7.4	417
Chip size	0.77 × 1.09 mm ²	NA	9.5 × 2 cm ²

Table 2 presents a comparison of broadband planar LNA designed with other recently published works.

The amplifier designed presents a very high gain and very low noise compared to work [16, 17].

4 Conclusion

In this work, a high gain cascaded GaAs-pHEMT broadband low noise amplifier is presented. This amplifier is designed in planar technology with three stages. The role of the first stage is to minimize the NF noise figure; the second and third are used to maximize the gain. Stability is improved with an R_s resistor connected in series with the drain electrode. Broadband adaptation is performed using open-circuit stubs. The results show that the amplifier designed has an average gain of 34.3 dB and very low noise figure of 0.95 dB on the frequency band between 5 and 6 GHz. This band is reserved for WiMAX 802.16b applications.

References

1. Kuran MS, Tugcu T (2007) A survey on emerging broadband wireless access technologies. *Comput Netw* 51(11):3013–3046
2. Ahmadi S (2016) Wireless broadband standards and technologies. In: Academic Press library in mobile and wireless communications. Academic Press, pp 559–619
3. Matange G, Ritesh G (2019) Performance evaluation of fixed WiMAX IEEE 802.16 d and mobile WiMAX IEEE 802.16 e System. In: Proceedings of recent advances in interdisciplinary

- trends in engineering and applications (RAITEA)
4. Barbeau M (2005) WiMax/802.16 threat analysis. In: Proceedings of the 1st ACM international workshop on quality of service and security in wireless and mobile networks
 5. Bogdanoski M, Latkoski P, Risteski A et al (2008) IEEE 802.16 security issues: a survey
 6. Vaughan N, Steven J (2004) Achieving wireless broadband with WiMax. *Computer* 6:10–13
 7. Elbakkali M, Amartouhami N, Elftouh, H (2019) Design of 5.2 GHz low noise amplifier for wireless LAN. *Procedia Manuf* 32:739–744
 8. El Bakkali M, Touhami NA, El Hamadi T (2019) Design at 2.4 GHz low noise amplifier for wifi-application. In: 2019 international conference on wireless technologies, embedded and intelligent systems (WITS). IEEE, pp 1–5
 9. Reddy MR, Sharma NSM, Sekhar PC (2018) A 2.4 GHz low noise amplifier design at 130 nm CMOS technology using common gate topology for WiFi/WiMAX application. *Int J Eng Technol* 7(13):69–73
 10. Cao L, Liu R, Zhang Y (2017) A 5.8 GHz digitally controlled CMOS receiver with a wide dynamic range for Chinese ETC system. *IEEE Trans Circ Syst II: Exp Briefs* 65(6):754–758
 11. Chen C, Wang Y (2017) A 2.4/5.2/5.8 GHz triple-band common-gate cascode CMOS low-noise amplifier. *Circ. Syst Signal Process* 36(9):3477–3490
 12. Qadir MW, Memon MHM, Adeel F (2018) Multigain cascode technique for low power BLE ISM band 2.4 GHz differential inductive source degeneration based LNA. In: 2018 IEEE MTT-S international wireless symposium (IWS). IEEE, pp 1–4
 13. Kahar NH, Ibrahim AB, Kob CGC et al (2020) Low noise amplifier (LNA) of 5–6 GHz using various architecture for LTE: a review. *Int J Adv Res Eng Innov* 2(2):11–19
 14. Kim B, Gao W (2016) X-band robust current-shared GaN low noise amplifier for receiver applications. In: IEEE compound semiconductor integrated circuit symposium (CSICS), pp 1–4
 15. Jarndal AH, Bassal AM (2019) A broadband hybrid GaN cascode low noise amplifier for WiMax applications. *Int J RF Microwave Comput Aided Eng* 29(10):e21456
 16. Yu-xiang U (2020) A Novel 5–5.7 GHz low-power LNA using low-power techniques. *DESTech Trans Eng Technol Res*, no acaai
 17. Kim DM, Im DG (2020) A 5–5.8 GHz Sub-2 dB NF CMOS low noise amplifier with bandwidth extension and noise optimization techniques. *J Integr Circ Syst* 6(2)

Application of Electrical Resistivity Soundings to Identify Unstable Areas, “Tghat-Oued Fez” District as a Case Study (Fez—Morocco)



Jabrane Oussama, El Azzab Driss, El Mansouri Bouabid,
and Charroud Mohammed

Abstract Measurements of 72 vertical electrical soundings (VES) using a Wenner-Schlumberger electrode array configuration were conducted on “Tghat-Oued Fez” district of Fez city. The purpose of this study is to identify voids inside basement, to prevent collapse and landslides in urban areas. The natural parameters acting to accelerate the phenomenon are mainly the tectonic activity, topography, and lithology. The studied area is close to the major active south rifain fault, marked by a steep slope and heterogeneous lithology, which is composed of a glaciais surface, marls, and conglomerate deposits. We suspect the presence of weak zones inside the marls layer because of cracks and fissures which sometimes appear even on the surface and the surrounding building’s wall. This is due to the presence of gypsum which left many voids and cavities due to dissolution. Thirteen iso-resistivity maps resulting from VES measurements were created. The electrical survey has accurately detected and located high resistivity anomalies inside the conductive marly formation between 7 and 15 m depth. The survey results suggest that VES is a viable geophysical tool to explore electrical anomalous linked to medium vulnerable to lands movement.

Keywords Vertical electrical sounding · Cavity detection · Wenner-Schlumberger · Resistivity

J. Oussama (✉) · E. A. Driss
Faculty of Science and Technology, Siger Laboratory, Sidi Mohamed Ben Abdellah University,
BP2202 Fez, Morocco
e-mail: oussama.jabrane@usmba.ac.ma

E. A. Driss
e-mail: driss.elazzab@usmba.ac.ma

E. M. Bouabid · C. Mohammed
Faculty of Science, LGRN Laboratory, Ibn Toufail University, Kenitra1400, BP133 Kenitra,
Morocco
e-mail: bouabid.elmansouri@uit.ac.ma

C. Mohammed
e-mail: mohammed.charroud@usmba.ac.ma

1 Introduction

During the last four decades, the urban area of Fez continues to develop locally on more or less unstable grounds, in particular its northern limit. These are linked to rapid population growth coupled with various natural factors such as the tectonic regime, morphology, bedrock lithology, and entropic action. All these parameters generate an imbalance unfortunately leading to tragic events. As the statistics show, most of the disorders of these large buildings can be due to foundation soils incompatible with the type of construction. Other types of disastrous disorders inducing heavy losses in infrastructures requiring more expenses are related to the lithological nature of the subsoil, in particular to the volumetric modifications of the clay soils (shrink-swell capacity) or to landslides on the slopes, affecting buildings, roads and structures in particular in the Oued-Fez sector.

Considering its exceptional panoramic view, the Tghat-Oued Fez districts are in great demand for new construction. In this context, the main purpose is to prospect and identify possible cavities and voids. A geophysical survey campaign was carried using VES method, aim to highlighting anomalies and identify the most vulnerable sectors to risks (land subsidence, collapse, landslide, etc.), linked to the behavior of the underlying materials, in this zone, subject to strong urbanization.

2 Geology of the Study Area

2.1 Overview

The Geology of the region, the geomorphological nature, as well as the anthropic actions, combined with climatic conditions and sometimes with tectonic and seismic activities make this area, a region at high risk of potentially very destructive collapse.

The study area is located on the southeastern side of Jbel Tghat. Its geological nature surveyed on the surface and the location of the sounding points are shown in (Figs. 1 and 2). From a structural point of view, it is located in a compressive context with high tectonic, morphological, and significant sedimentary activity. Indeed, the Tghat structure (Fig. 1) is an elongated East–West direction relief, south of the frontal limit of the “pre-rifain complex”. It is a massif with a Jurassic formation heart and Miocene coverage. Its 873 m above sea level, makes it strongly straightened and dominating more than 400 m of Fez plain.

Saïis plain has evolved from a foreland basin before the Miocene to a continental endorheic basin in the Pliocene and then to an inclined plateau in the Quaternary [1–3]. This development has enabled a variety of deposits depending on different environments.

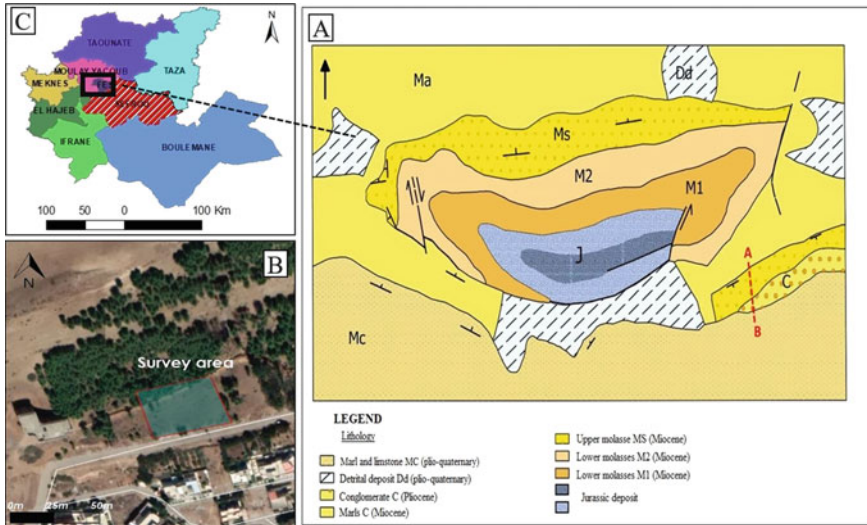


Fig. 1 a Tghat massif geological map, based on the geological map of Fez with the location of the AB geological section. b Satellite image (taken by Google earth) showing the survey area. c Fez-Meknes region

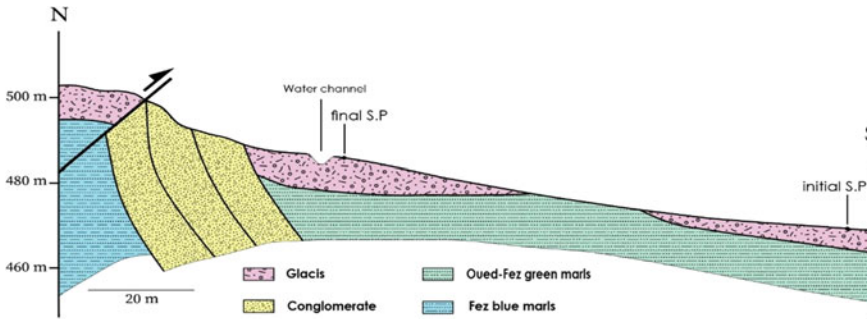


Fig. 2 N-S oriented geological section of the study area showing the layout of the outcrops in the study area

2.2 Lithostratigraphy

The study area, is composed of Mio-plio-quaternary materials (Figs. 2 and 3). There are three well-defined formations:

Glacis surface: are mainly distributed on the southern side of Tghat, with smaller thicknesses in our study area. The thickness varies depending on the location between 0.5 and 5 m, this layer is predominantly made up of rounded elements which come from the erosion of the overlying pudding drowned in a greenish to whitish marly matrix.

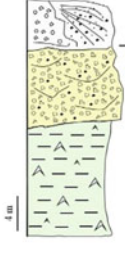
Lithostratigraphic column	Facies	Age / deposit environment
	Glacis, Slope deposits	Quaternary Continental deposits environment
	polygenic polymetric Conglomerates	Late Pliocene Continental fluvial deposits environment
	Green marls with gypsum concretions	Late Pliocene lacustrine deposits environment

Fig. 3 Lithostratigraphic column showing the 3 sets described in the study area

Marlstone formation these are the greenish to whitish marls of the Oued-Fez, which contain concreted gypsum, reflecting a lacustrine environment with intense evaporation; this formation is described in previous work [1–5]. It is a fairly homogeneous and compact unit in depth. However, these marls are sensitive to water, constituting a swelling and slippery formation towards the south, the marl outcrops have generally gentle slopes but in some places can be locally steeper (between 10° and 15°).

Conglomerate formation. are terrigenous detrital deposits, it is a pudding of mostly rounded elements, the elements of which vary from a few millimeters to 30 cm, its a polygenic conglomerate of probably Liassic and Miocene origin.

2.3 Study Area

The study area is located on a parcel north of the urban limit of Fez city. It covers 2000 m². The choice of this site was guided by the fact that it presents a great panoramic interest, therefore susceptible to new urban development, besides we were able to identify on the close building walls as well as on the surface, cracks, soil collapse and sometimes landslides. However, the geological formations nature is not sufficient enough to allow us to have an idea about the spatial organization of these cracks and voids. Doubts remain about the presence of new cracked construction probably due to the behavior of the underlying layers. We try to resolve this problem by the adequacy of combining geological field-work with geophysical techniques of investigation.

3 Methodology

Geophysical prospecting methods have proved a very useful tool for determining the location and size of cavities below the surface [6–10].

The VES investigations were performed by using The Syscal Pro manufactured by IRIS Instruments using Wenner-Schlumberger (W-S) configuration [11]. This method involves the supply of direct current (I) into the ground through a pair of current electrodes and the measurement of the resulting potential (ΔV) through another pair of electrodes called potential electrodes (Fig. 4).

The calculation of the apparent resistivity was performed using the resolution of the laplacian electrical potential equation in spherical coordinates:

$$\nabla^2 V = \frac{d^2 V}{dr^2} + \frac{2}{r} \frac{dV}{dr} = 0 \quad (1)$$

According to Ohm’s low in hemispherical medium, the resolution of Eq. (1) gives the apparent resistivity formula ρ_a , in the case of W-S configuration, as follow:

$$\rho_a = \frac{\Delta V}{I} \times \pi n(n + 1)a \quad (2)$$

3.1 Field Investigations

VES is essential to give a judicious interpretation of the results as well as a real depth to the model, in order to characterize the different geological formations and the detection of possible voids. The VESs were deployed as a set of 9 equidistant

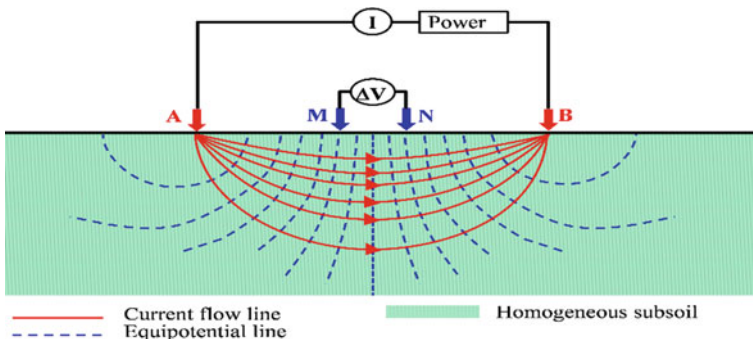


Fig. 4 Wenner-Schlumberger array ($MN = a$; $AM = n \times a$) and distribution of electric field underneath in homogeneous medium

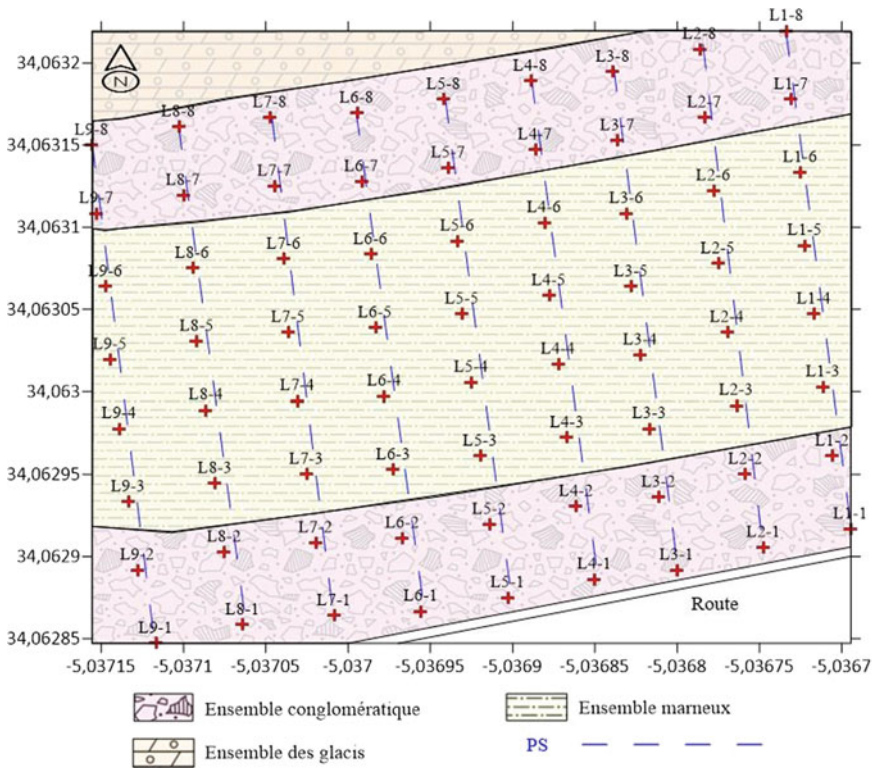


Fig. 5 Location map of VES survey points with the geological distribution of the surface layers in the investigation site

profiles (Fig. 5) each consisting of 13 AB spacings, between 4 and 160 m to reach depths of 20 m, making sure that we have crossed the marls.

This potential method giving access to the electrical resistivity of different layers. It is well suited to differentiate the 3 formation sets, given the enormous contrast of resistivities as evidenced by the first tests.

The first sub-surface level corresponds to the glacis deposits, with variable resistivity (10–132 Ω m) and thickness between 0.5 and 4 m.

A second level matches to the marly deposits, the relatively low average resistivities obtained, correspond well to a homogeneous facies of variable resistivity (3.8–12 Ω m).

The underlying resistance level in the study area corresponds to the conglomerate level at depths of more than 17 m with a resistivity between (110–640 Ω m).

4 Results and Discussion

The iso-resistivity maps were generated from the 72 executed VESs using the minimum curvature method [12]. Each map shows the resistivity behavior in horizontal surface for each AB length corresponding to 0.125 times depth in the case of S-W configuration. The resulting maps help monitor the evolution of resistivities in three directions. They make it possible to have an idea about the sedimentary facies distribution and the presence of possible fissures and voids inside those layers.

For small AB spacings (4 and 8 m), the lateral variations in apparent resistivity mainly represent variations in the composition of the surface materials. In our case, the more resistive areas on the surface are associated with the compaction of the subsurface sediments and the presence of slope deposits attributed to the glacia formation. The less resistive zones begin to appear at a depth of 1.5 m, associated with the sectors where the marl is the main outcropping material. The lateral variations in resistivity can be explained by lateral variations in the formations nature, especially small AB spacings.

The slope material horizon is complex, by its varied composition and the resulting differences in resistivity. It is partly because of this complexity that the measured apparent resistivity does not give the same distribution for this layer.

This surface distribution is justified by the fact that the slope is more or less significant over the entire northern and southern part of the study area, the lowest resistivity values are obtained at the spots where the slope is low.

At a depth of almost 2.5 m (Fig. 6a), we can distinguish the presence of a homogeneous layer, associated with the conductive marl formation which dominates the subsoil. In the southern part, we noted low resistivity values (between 12 and 16 Ω m), before passing to a purely marly environment, which can probably be attributed to a glacia-marl passage which evokes rather a soil compression linked to the slope and proximity to the road.

With AB spacing between 40 and 60 m (Fig. 6), on a rather flat topography in the region, led to believe that the surface of the marly layer was also flat, the distribution of apparent resistivity highlights a homogeneous subsoil, the relatively low resistivities obtained on these iso-resistivity maps, correspond well to the facies rich in marl which contain many gypsum concretions. At this depth, the rock is soft, means it is more vulnerable to alteration, gypsum goes into solution or easily erodes and forms voids, pipes, and cracks.

Marls are easily detected on the iso-resistivity maps, on the one hand, because of its low resistivity and on the other hand because of its generally large thickness (15 m on average).

The lowest resistivities are obtained in-depth where the thickness of the marl deposits are larger. In cases where the apparent resistivity of the last layer is less than 13 Ω m, it can be assumed that the top of the conglomerate horizon is not reached yet since it generally has a resistivity higher than 20 Ω m. Furthermore, the marly layer includes high resistivity anomalous zones higher than the rest of the region (Figs. 6b–d and 7e), It is likely associated with the presence of cracking or

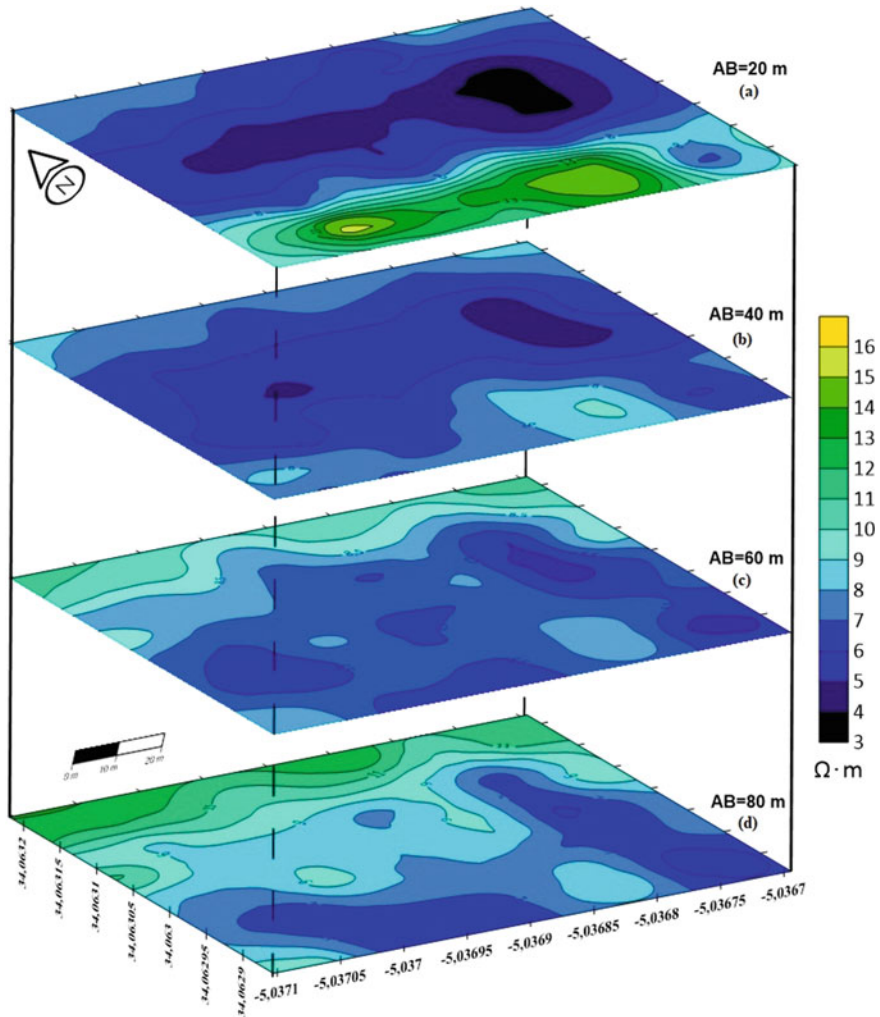


Fig. 6 Iso-apparent resistivity maps for AB = 20, AB = 40, AB = 60, AB = 80

alteration. Less pronounced, which can be attributed to natural fissures and zones of weakness within the soil.

The iso-resistivity map with AB spacing between 60 and 120 m reflects another anomaly that is added to confirm our opinion. It is obvious that resistivity values in the central part better defined on (Fig. 7e) are higher than side parts. These may correspond to a possible cavity inside the marly conductive layer.

Analyzing the results of the real data on the iso-resistivity maps with AB spacing between 80 and 160 m (Figs. 6d and 7e, f, j, h), with a depth of investigation between 10 and 20 m, we can notice a cloud of significant apparent resistivities within the

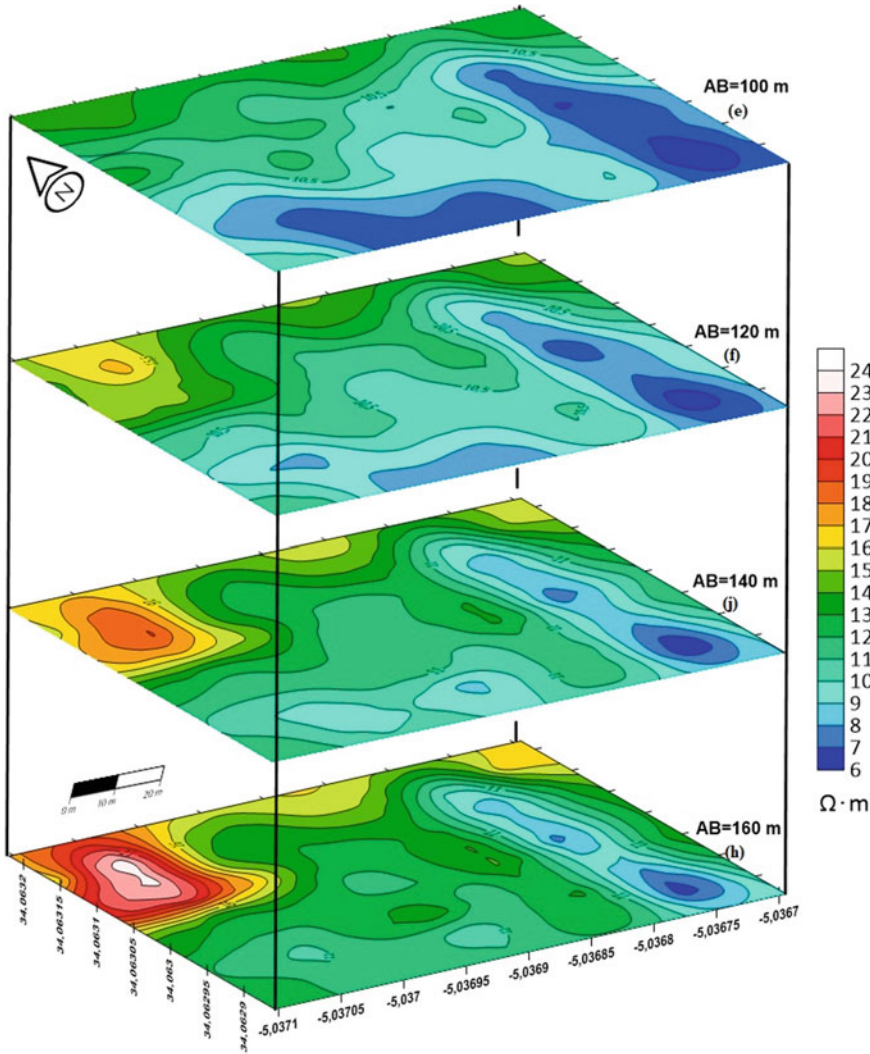


Fig. 7 Iso-apparent resistivity maps for AB = 100, AB = 120, AB = 140, AB = 160

longitude values -5.03685 and -5.0368 elongated south-north. In this case, the layer with conductive materials showed resistive anomalies, a vertical structure is identified, this discontinuity seems probable to indicate a possible cavity of significant size, which extends in-depth, there has moreover several cracks and fissures which sometimes appear even on the surface in this sector. This zone can be interpreted as a cavity filled with loose sediments and can be considered as the main reason for the subsidence of the middle zone of the parcel.

The last iso-resistivity maps (Fig. 7j, h), reflects the lateral variation over a horizontal plane at a depth of about 20 m. It indicates the beginning of the conglomeratic formation, the presence of these facies in the northwest part of the parcel, illustrated with a large thickness that extends deeply. The northwest part of our study area shows massive deposits of conglomerate, those formations are verticalized due to the pre-rifain compressional tectonic regime, oriented to the south in Tghat mountain. The presence of this layer at this depth especially in the northern part comes to confirm the results obtained by geological mapping.

5 Conclusion

The study has demonstrated that the non-destructive investigation method of electrical soundings allows on the one hand to locate the 3 horizons and to estimate their thickness. The geological units are distinguished from one another by their signature of highly contrasted electrical resistivity. However, we note a significant spatial variability within some of these units, marls is certainly the element most recognizable by electrical measurements. Interpretation of Wenner-Schlumberger configuration resistivity data revealed the presence of high resistivity anomalous zones that have been attributed to possible fissures or small cavities.

In this work we identify weakness zones (areas with potential risk evidenced by cracks and voids in-depth). Consideration must be given to this phenomenon in the urban planning process and development. In our case, it requires other additional complete VES surveys at the south limit of the urban area of Tghat mountain, to define the necessary preventive measures.

References

1. Charroud M, Cherai B, Benabdelhadi M, Charroud A, El Moutaouakkil N, Falguères C, Lahrach A (2006) Sedimentary evolution of a fore-chain Sais basin during plio-quadrenary and modalities of tectonic inversion (Sais basin, Morocco). *Geophys Res Abst, Eur Geosci Union* 8:10039
2. Charroud M, Cherai B, Babault J, Benabdelhadi M (2007) Quaternary neotectonic elevation of the Sais basin between the Rifian and Atlasic belts. Sedimentary dynamics and geomorphologic impact. (Sais Fez, Morocco). Poster. The third workshop of the ILP task force on sedimentary basins, in the frame of MAPG intervention conversion on conference and exhibition. Marrakech (Morocco), 28–31 Oct 2007
3. Cherai B, Charroud M, Lahrach A, Babault J (2008) Influence de la tectonique compressive et des mouvements verticaux d'origine mantellique sur l'évolution quaternaire du Saïs entre le Rif et le Moyen Atlas. *Actes RQM4, Oujda*, pp 171–181
4. Ahmamou M (1987) Etude sédimentologique des calcaires lacustres (plioquaternaire) du bassin de Fès-Meknès (Maroc). Thèse de 3^e cycle, Univer. Aixmarseille III, 178 p
5. Taltasse P (1953) Recherches géologiques et hydrogéologiques dans le bassin lacustre de Fès-Meknès. *Notes et Mémoires du Service Géologique, Maroc* 115:152

6. Beres M, Luetscher M, Olivier R (2001) Integration of ground-penetrating radar and microgravimetric methods to map shallow caves. *J Appl Geophys* 46:249–262
7. McGrath RJ, Styles P, Thomas E, Neale S (2002) Integrated high-resolution geophysical investigations as potential tools for water resource investigations in karst terrain. *Environ Geol* 42:552–557
8. Militzer H, Rosler R, Losch W (1979) Theoretical and experimental investigations for cavity research with geoelectrical resistivity methods. *Geophys Prospect* 27:640–652
9. Smith DL (1986) Application of the pole–dipole resistivity technique to the detection of solution cavities beneath highways. *Geophysics* 51:833–837
10. Thierry P, Debeblia N, Bitri A (2005) Geophysical and geological characterization of karst hazards in urban environments: application to Orléans (France). *Bull Eng Geol Environ* 64:139–150
11. Pazdirek O, Blaha V (1996) Examples of resistivity imaging using ME-100 resistivity field acquisition system. In: EAGE 58th conference and technical exhibition extended abstracts, Amsterdam
12. Smith WHF, Wessel P (1990) Griding with continuous curvature splines in tension, *Geophysics* 55(3):293–305

A New Compact 1.0 GHz LPF Using Double Hi-Lo-Resonators and Cross Defected Ground Structure for Radar Applications



A. Boutejdar, H. Bishoy, and Saad Bennani Dosse

Abstract In this work, a novel miniaturized microstrip low pass filter using a double Hi-Lo and cross defected ground structure resonators is presented. The Hi-Lo resonator is placed on the top layer of the structure while the two identical cross DGS resonators are etched in the ground plane. Each DGS shape consists of two cross heads, which are connected with a channel slot. The both DGS resonators are electromagnetically coupled. The proposed filter has been designed simulated, optimized and manufactured. The filter topology is simulated using HFSS simulator and measured using Agilent Field Fox NA, N9918A VNA. The both results of the proposed LPF shown a sharp roll-off (ξ) of 84 dB/GHz and exhibit a very low insertion loss in the pass band of 0.4 dB from DC to 0.9 GHz and it achieves a wide rejection bandwidth with overall 20 dB attenuation from 1.2 GHz up to 3.2 GHz. The compact low pass structure occupies an area of $(0.37\lambda_g \times 0.37\lambda_g)$ where $\lambda_g = 94$ mm is the waveguide length at the cut-off frequency 1 GHz. The carried-out results confirm the effectiveness of the proposed method.

Keywords L-band-LPF · Hi-Lo-resonator · Cross-DGS

1 Introduction

Rapid progression of modern wireless communication systems leads to increasingly stringent specifications that put a tough challenge to RF engineers. The requirements of low cost, compact, integrable design are necessary. In order to meet these requirements, much effort has been made to develop a variety of compact lowpass filters [1]. Currently, the wireless communication and radar systems require L-band operating

A. Boutejdar (✉)

German Research Foundation (DFG), Bonn, Germany

e-mail: boutejdar69@gmail.com

H. Bishoy

Communication and Electronics, University of Ottawa, Ottawa, Canada

S. B. Dosse

SIGER Laboratory, USMBA, Fez, Morocco

© Springer Nature Singapore Pte Ltd. 2022

S. Bennani et al. (eds.), *WITS 2020*, Lecture Notes in Electrical Engineering 745,
https://doi.org/10.1007/978-981-33-6893-4_102

1123

transceivers. Low band and very low band filters are in demand for these wireless systems. Beside the previous features, high performance, ease of fabrication and simplicity are desired proprieties for these topologies. To find a solution for these problems, Electrophotonic bandgap structures (EBG) [2], defected ground structure (DGS) [3] and defected microstrip structure (DMS) [4] techniques can play an important role. In the last years, DGS technique has received much attention because of their use in radar, satellite, microwave areas and mobile communication systems. Such systems often demand devices and electric topologies with very small dimensions, which occupied small areas. The DGS shapes are the dominant technique which can guarantee a size reduction and a suppression of harmonics and spurious suppression without an additional device. The DGS can take several forms and geometries and can be applied to various kinds of components such as low-pass- band stop- and band-pass filters as well as RF couplers [5], filtenna [6] and power divider [7]. DGS topologies, which were evolved from EBG structures, are achieved by etching arbitrary surface in the metallic ground plane. This gap disturbs the current distribution in the ground and leads to an increasing of the effective inductance and capacitance of the microstrip line. Because of this disturbance, the DGS can presents as several lumped circuits. The easiest is the cohesion of the narrow gap and vast surface, which presents an equivalent LC circuit [8]. Often microwave low pass filters are realized by series connected high-low stepped impedance lines [9]. Other researchers have been used fractal method, SIW-technique [10], microstripopen-loop ring resonators [11], tapered- or bowtie resonators [12]. Disadvantages of previous methods have been showing in big losses, which appear along the pass band and leads to a creating of the undesired harmonics along the reject band. In order to diminish the insertion loss in pass band and to suppress the periodic harmonic in stop band, the DGS technique is used. To achieve successfully this aim, several DGS topologies, as yagi-, meander-, dumbbell-DGS-shapes [13].

In this work, a new concept of a sharp roll-off L-band low pass using slow wave effect, which sprang up from cross DGS resonators and Hi-Lo technique is presented. The structure is composed of electromagnetically coupled Hi-Lo- and cross-DGS resonators. This combination shows an acceptable rejection level and a nearly lossless pass band. The proposed filter is simulated, optimized and fabricated. The simulation and measurement results are presented.

2 Characteristics of the Cross-DGS Resonator

The new used DGS shape consists of two cross-heads connected to each other through a thin slot channel, as shown in Fig. 1. The heads occupier a vast part of the substrate, while the slot channel presents only a small gap thus a narrow aperture between the both heads. The thin slot presents a capacitor. Basing on the scattering results of the cross DGS (see Fig. 3), it can easily to deduce that the DGS-shape is a parallel resonator and the heads represent the inductances (see Fig. 2). All the dimensions of the proposed cross DGS slot are depicted in Fig. 8b.

Fig. 1 The 3D views of the cross-slot

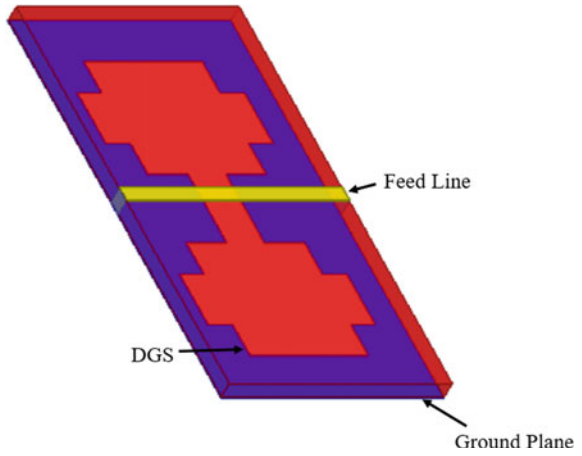


Fig. 2 Equivalent circuits of one-pole LPF

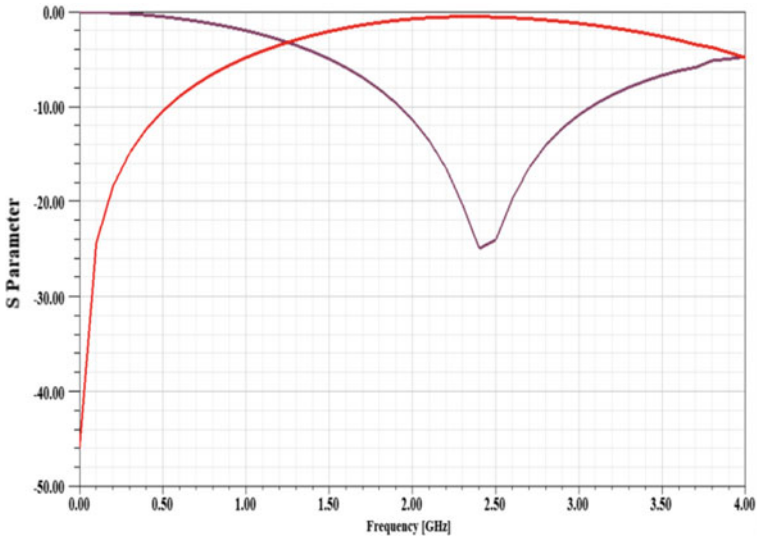
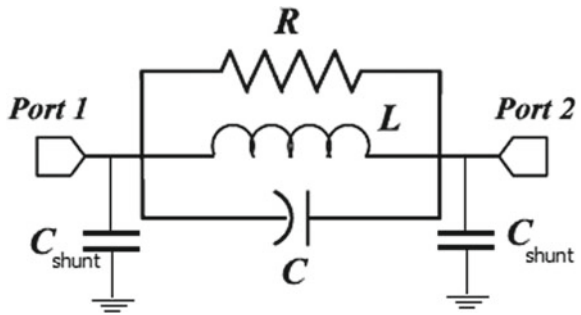


Fig. 3 The S-scattering results of the cross-DGS topology

The extracted information from the scattering results exhibit that this DGS topology corresponds to a parallel resonator placed between two 50Ω ports and composed of capacitance, inductance and resistance (see Fig. 2). The parallel capacitances C_{shunt} , placed between the 50Ω feed line and the metallic ground, presents the effect caused of the fringing field around the DGS element. Figure 2 shows a quasi-lossless equivalent circuit based on a Tchebysheff's π -lumped-element model.

In order to calculate the values of the lumped-elements using in the approach one pole circuit, the prototype element value of the one-pole Butterworth response. The prototype element value is given by various references [13–16]. The L and C values of the DGS resonator can be computed using the attenuation pole location (f_0) from simulated scattering (Fig. 3) and the following equations:

$$jX_{LC} = \frac{j\omega L \left(\frac{1}{j\omega C} \right)}{j\omega L + \frac{1}{j\omega C}} = \frac{j\omega L}{1 - \omega^2 LC} \quad (1)$$

$$L = \frac{g_1 Z_0}{\omega_c} \Rightarrow \omega L = X_L = g_1 Z_0 \frac{\omega}{\omega_c} = g_1 Z_0 \omega' \quad (2)$$

where ω_0 , ω' , Z_0 , $g_1 = 2$ are the resonant frequency, normalized angular frequency, the scaled characteristic impedance and prototype value of the Butterworth-type low-pass filter respectively. Because until $\omega = \omega_c$ the behavior of the one pole filter remains inductance and the capacitance can be negligible. In this case the matching of two previous reactances can be used, with help the below equations, to define the parallel capacitance and the inductance of the equivalent DGS-circuit

$$X_{LC}|_{\omega=\omega_c} = X_L|_{\omega'=1} \quad (3)$$

$$L = \left[\frac{250}{C(\pi f_0)^2} \right] nH, \quad C = \frac{5f_c}{\pi Z_0 [f_0^2 - f_c^2]} pF \quad (4)$$

As is mentioned before, the scattering results of the DGS provides the both values of cut-off frequency f_c and resonance frequency f_0 . In order to follow the influence of the DGS dimensions on the filter results, an investigation has been carried out. The aim of this simulations research is to win enough data, which can be used to improve the features of the proposed filter. Two variations of the dimensions are carried out.

1. The variation of the cross head.
2. The variation of the channel slot.

The Fig. 5a shows the scattering results of the DGS element while the length (h) of the cross-head undergoes three variations. All dimensions remain constant, while the length-parameter h varies from 1 to 5 mm (see Fig. 4a), this leads to decreasing of the resonance frequency from 3 to 2 GHz. The cut-off frequencies move along narrow frequency range from 1.1 to 0.8 GHz. For the second simulation (Fig. 5b),

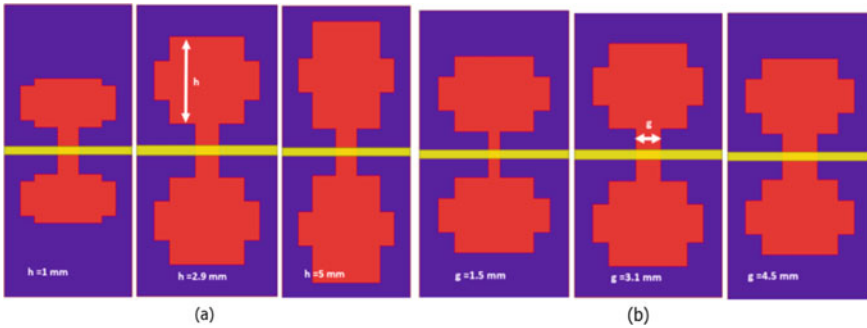


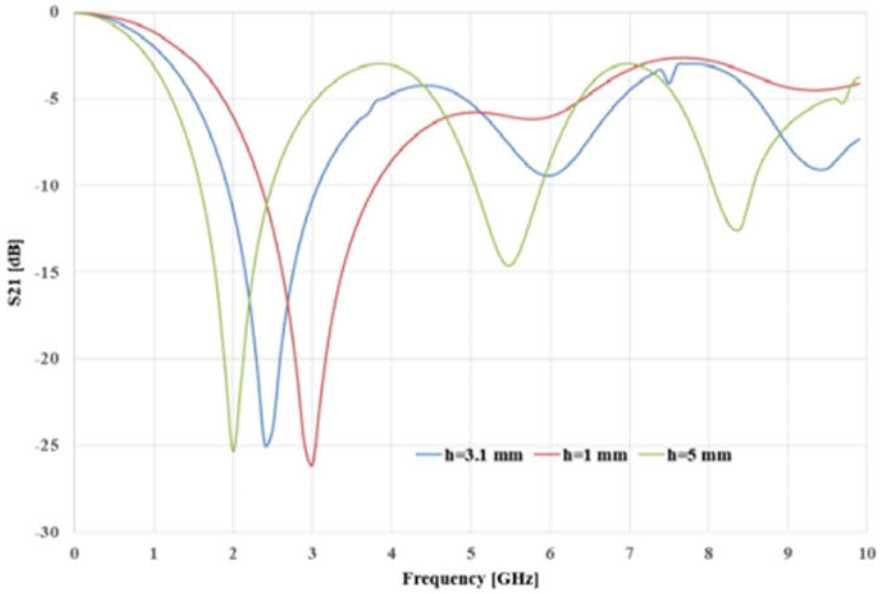
Fig. 4 The cross DGS with several dimensions: **a** length-variation of DGS-head (h). **b** Variation of width-variation of channel slot (g) of DGS

all parameters keep constant while only the parameter g width of the gap (channel) undergoes a modification from 1.5 to 4.5 mm (see Fig. 4b).

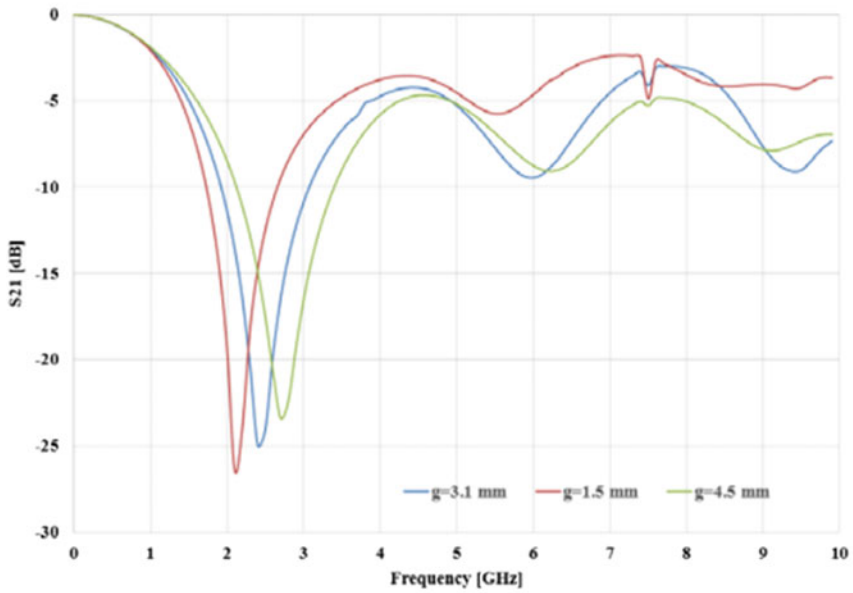
It can observe that the resonance frequency increase along a narrow frequency range in comparison with the previous experiment, from 2.1 to 2.8 GHz (see Fig. 5), while the cut-off frequency does not undergo any modifications. It can conclude that if a reconfigurable filter with only variation of the resonance frequency is required, then the advantageous solution will be, to integrate a varactor across the slot channel (g).

3 Design and Simulation of the Cross L-band Low Pass Filter

In order to test the performance of this proposed topology, a compact L-band filter has been designed optimized and simulated. As Fig. 6a, b show the LPF structure consists of two parallel layers. Double Hi-Lo resonators are placed on the top layer. Two identical cross DGS resonators are etched in the metallic ground plane. The both resonators are one the one hand electromagnetically coupled each other, on the other hand are electric coupled with the Hi-Lo resonators. The both extremes of Hi-Lo resonators are connected through the input and output via a microstrip feed line. The feed line has a width of 1.9 mm and 50Ω as impedance. The used of patch capacitors of Hi-Lo minimize the loss in the pass band while the cross DGS shape improve the stop band and thus a minimizing of the filter topology. Figure 7a presents the 3D view of the suggested filter. The design and its simulation results are carried out using HFSS software. The structure is designed on Rogers duroid 6010 substrate with dielectric constant of 10.2, a thickness of 1.27 mm and a dielectric loss tangent (δ) = 0.0023. As the Fig. 7b demonstrates, the investigated cross 1 GHz LPF shows a cut of frequency and first attenuation poles at 1 GHz and 2.5 GHz respectively and shows a rejection level better than 20 dB from 1.2 to 3.2 GHz. The insertion loss



(a)



(b)

Fig. 5 a Simulated S_{21} -parameters with variation of dimension 'h', b simulated S_{21} -parameters with variation of dimension 'g'

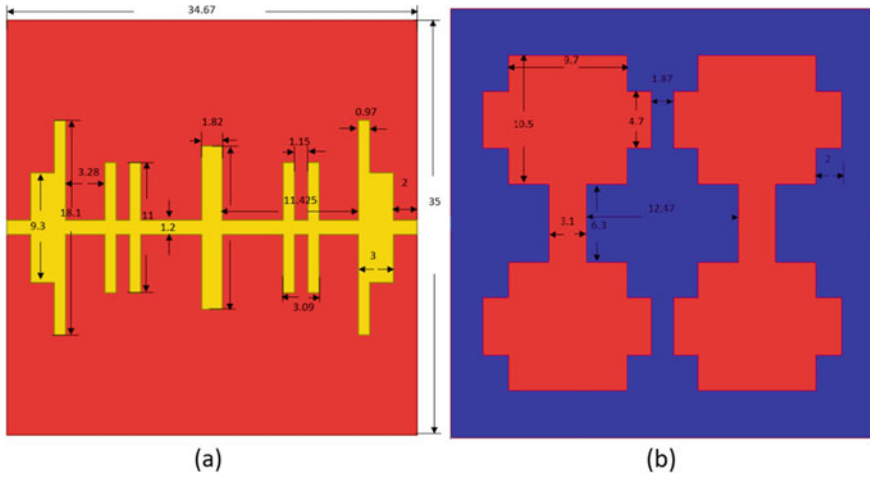


Fig. 6 The proposed cross-DGS low pass filter and its dimensions: **a** Front view, **b** back view

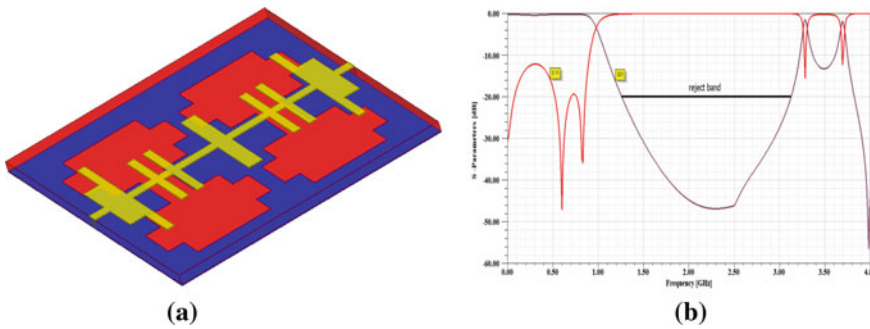


Fig. 7 **a** The 3D view of the proposed cross-DGS LPF, **b** the simulation of S-scattering results of cross-DGS LPF

in the pass band remained less than 0.30 dB along from DC to 0.9 GHz. The sharp roll-off rate (ξ) between 3 and 20 dB is equal 84 dB/GHz. All simulation results were carried out using HFSS software and are presented in Fig. 7b. The dimensions of the filter are calculated using Chebyshev-Richard-Kourod-Kourod-Transformation. The whole area of this filter is less than (35 mm \times 35 mm). All dimensions are depicted in Fig. 6.

4 EM Field Distribution Along on the Hi-Lo Resonators

The goal of this short chapter is to observe the behavior of electromagnetic field distribution along the topology and to discuss the relationship, which connects the

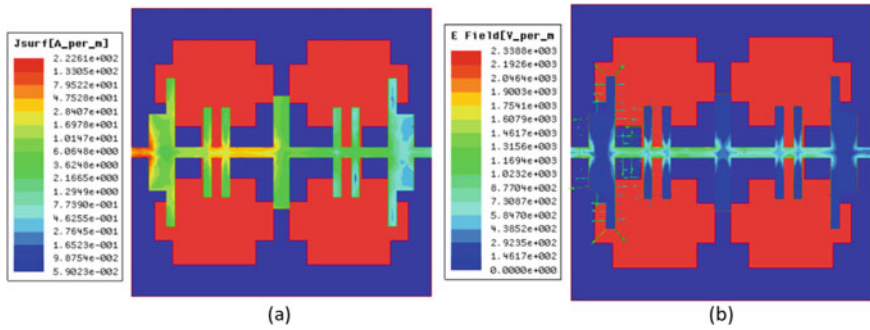


Fig. 8 Field distribution along of the improved LPF: **a** pass-band at 0.2 GHz and **b** stop-band at 2.5 GHz

modification of the field and the variation of the current at the surface of the both layers, briefly to understand the working of the equivalent circuit. The investigation of the field features will be focused on two different frequencies. As the Fig. 8 shows, around of 0.5 GHz, the current travels from input to output. The magnetic energy is more concentrated near of the thin microstrip lines and it's disperses around the extreme patch of Hi-Lo resonator, which means that the full magnetic energy is transmitted through the 50Ω feedline-Hi-Lo-DGS resonators.

The transmission power between the both ports is magnetic. The small arms of the Hi-Lo represent inductances and the pass band behaviors (see Fig. 8a). At frequency equal 2.5 GHz, the whole power is stocks on the edge between the input and the patch capacitor. The magnetic and electric energies have the equal amount but with different, thus the whole energy disappears. This demonstrates that the structure is in the stopband state (resonance behavior). This behavior indicated that the structure is in the stopband state, as shown in Fig. 8b. Basing on this won data, it can be concluded that the Hi-Lo structure consists of resonators constructed of inductance and capacitance. This EM-approach helps in understanding the physical principle and the behavior of the equivalent circuit of Hi-Lo filter.

5 Fabrication and Measurement

To prove the effectiveness of the cross DGS and Hi-Lo resonator, the 1 GHz L-band low pass filter is simulated and tested on a of $(0.37\lambda_g \times 0.37\lambda_g)$ substrate, where $\lambda_g = 94$ mm. Agilent Field Fox NA, N9918A network analyzer is used to measure the S-parameters of the proposed LPF. Figures 9 and 10a illustrate the photograph of the fabricated filter. As the Fig. 10b shows, it can be seen that the scattering S_{21} is less than 0.30 dB from DC to 0.9 GHz and the stop band is improved, and the spurious frequencies from 1.2 GHz up to 3.2 GHz are suppressed with a rejection level of -20 dB. The filter provides a very sharp transition band, which has been leading

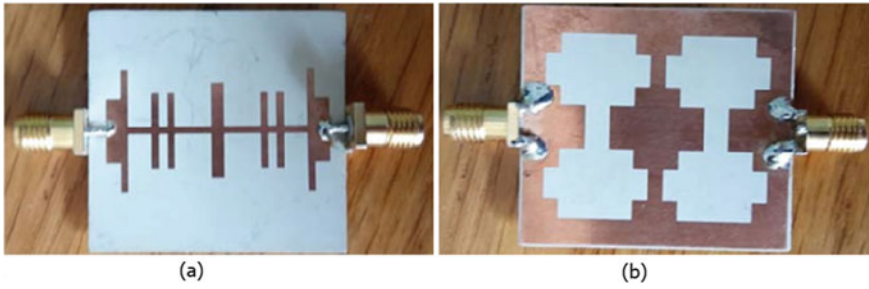


Fig. 9 Photograph of the fabricated cross-DGS-LPF: **a** top view, **b** bottom view

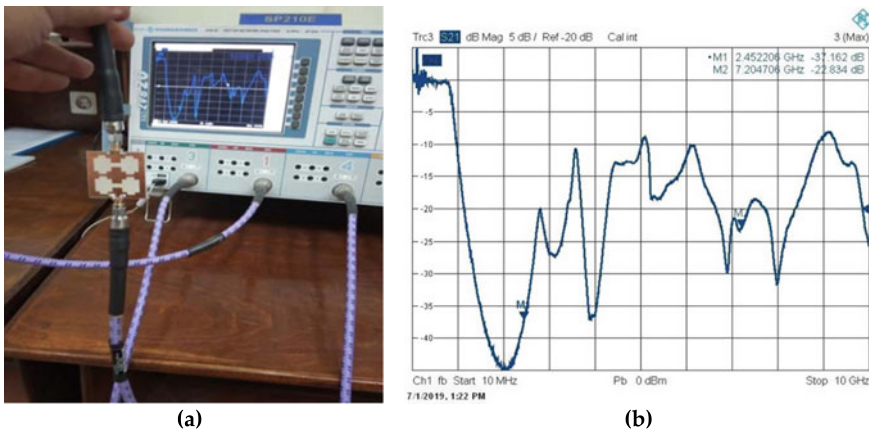


Fig. 10 **a** The measurement results of the proposed cross LPF using VNA, **b** the measurement results of the proposed cross-DGS LPF

to appearance of a transmission zero close to the stop-band edge at 2.5 GHz. The slight incurred ripple along pass band (0–0.4 GHz) can be attributed one hand to unexpected tolerance errors in fabrication and manual welding inaccuracies and on the other, to an imperfect calibration. Due to its features, such filter structures will be widely used in radar and microwave applications.

$$\lambda_g = \frac{\lambda}{\sqrt{\epsilon_{r,eff}}} = 0.54 \left(\frac{c}{f_0} \right) \tag{5}$$

$$\xi(\text{selectivity}) = \frac{\alpha_{\min} - \alpha_{\max}}{f_0 - f_c} \text{ (dB/GHz)} \tag{6}$$

where, ξ is the filter selectivity, α_{\max} is the 3 dB attenuation point, α_{\min} is the attenuation at f_0 , $f_s = f_0$ (attenuation pole) and $f_c = 3$ dB cut-off frequency.

Table 1 Comparison of proposed work with previous works

References	Cut off (GHz)	S-B (GHz) Over -20 (dB)	Pass band I-L (dB)	Size (mm ²)	Roll-off rate (ξ) (dB/GHz)
[8]	3.7	4.2–11.3	0.20	30 × 20	17
[13]	3.0	3.5–11.5	0.30	20 × 20	34
[14]	2.0	2.5–5.50	0.40	60 × 15	4.25
[15]	4.8	6.0–12.5	0.30	30 × 20	14.16
[16]	2.8	4.0–10.0	0.20	60 × 45	14.16
Proposedwork	1.0	1.2–3.20	0.30	35 × 34	84

6 Comparison

Table 1 shows the comparison of the proposed L-band filter topology with previous published similar works having the similar features and is suitable for radar applications. The proposed filter consists of simple quarter-wave length DGS resonators, which are electromagnetically coupled with microstrip Hi-Lo resonator with the aim to achieve a high compactness- and sharpness factors. This Hi-Lo-DGS-Combination is the first time simultaneously applied in the proposed structure which gives valuable results. Table 1 shows that the proposed filter has simple geometry, easy design and better sharpness factor moreover its compactness factor is higher than other structures relatively with their cutoff frequencies.

7 Conclusions

In this paper, a new concept of a compact L-band low pass filter with a very sharp transition band using cross DGS resonator and Hi-Lo technique is presented. A low loss in passband is reached because of three compensated capacitors, which are distributed along the top layer. The etched neighbor DGS resonators in the ground plane lead, through its slow wave effect, to an increasing of sharpness factor and thus a high compactness factor is achieved. The 1 GHz-low pass filter has been designed and simulated on a Rogers duroid 6010 substrate with a relative dielectric constant of $\epsilon_r = 10.2$, a thickness of $h = 1.27$ mm and loss tangent $\tan \delta = 0.0023$. The investigated low pass filter has a low insertion loss less 0.4 along the pass band, a sharpness factor higher as 80 dB/GHz and a rejection level of better than 20 dB until 2 GHz. The overall size of the filter topology is less as (35 mm × 35 mm). The simulation and measurements results are presented. Such filter structures with similar features have applications in the L-Band, namely, radars, GPS, telecommunication system and aircraft surveillance.

References

1. Boutejdar A, Bennani SD (2017) Design high-frequency filters with cross DGS circuit elements. *Microwave RF* 3(1):37–41
2. Kim M, Kam DG (2014) A wideband and compact EBG structure with a circular defected ground structure. *IEEE Trans Compon Packag Manuf Technol* 4:496–503
3. Kim M, Koo K, Hwang C, Shim Y, Kim J (2012) A compact and wideband electromagnetic bandgap structure using a defected ground structure for power/ground noise suppression in multilayer packages and PCBs. *IEEE Trans Electromagn Compat* 54:689–695
4. Boutejdar A, Challal M, El Hani S (2019) Design and manufacturing of a novel compact 2.4 GHz LPF using a DGS-DMS combination and quasi octagonal resonators for radar and GPS applications. *Prog Electromagnet Res* 90:15–28
5. Lee S, Lee Y (2010) A design method for microstrip directional couplers loaded with shunt inductors for directivity enhancement. *IEEE Trans Microw Theory Tech* 58(4):994–1002
6. Alhegazi A, Zakaria Z, Shairi NA, Ahmed S, Sutikno T (2017) UWB filtenna with electronically reconfigurable band notch using defected microstrip structure. *Indo J Electr Eng Comput Sci* 8(2):302–307
7. Cheng KKM, Law C (2008) A novel approach to the design and implementation of dual-band power divider. *IEEE Trans Microw Theory Tech* 56(2):487–492
8. Boutejdar A (2017) Design of compact reconfigurable broadband band-stop filter based on a low-pass filter using half circle DGS resonator and multi-layer technique. *Prog Electromagnet Res* 71:91–100
9. Lung HH, Kai C (2003) Compact elliptic-function low-pass filters using microstrip stepped-impedance hairpin resonators. *IEEE Trans Microw Theory Tech* 51:193–199
10. Weiping L, Xin C, Zongxi T (2017) Design of a SIW bandpass filter using defected ground structure with CSRRs. *Active Passive Electron Compon* 1–6
11. Boutejdar A, Bennani SD (2017) Design and optimization of the cascaded band-stop filters using vertically coupled open-loop ring resonators. In: *International conference on wireless technologies, embedded and intelligent systems (WITS)*, pp 1–7
12. Fu Z, Lum KM, Koh WT (2012) Novel bow-tie bandpass filter design using multiple radial stubs. In: *PIERS proceedings*, pp 1484–1487
13. Boutejdar A, Challal M, El Hani S (2018) Design of a new broad stop band (BSB) lowpass filter using compensated capacitor and II-H-II DGS resonator for radar applications. *Prog Electromagnet Res* 73:91–100
14. Lu K, Wang G-M, Wang Y-W, Yin X (2011) An improved design of Hi-Lo microstrip LPF using uniplanar double spiral resonant cells. *Prog Electromagnet Res Lett* 23:89–98
15. Boutejdar A, Omar A (2010) New low-pass filter design by using compensated microstrip capacitor and coupled meander defected ground structure (DGS). *Recent patents on electrical and electronic engineering (formerly recent patents on electrical engineering)* vol 3, issue 1, pp 30–34
16. Ahn D, Park JS, Kim CS, Kim J, Qian Y, Itoh T (2001) A design of the low-pass filter using the novel microstrip defected ground structure. *IEEE Trans Microw Theory Tech* 49:86–93

Author Index

A

Abbou, Adil Ben, 515
Abbou, Ahmed, 723
Abbou, Rachid Ben, 515
Abdelhalim, Miftah, 1049
Abdulwali, Zaed S. A., 977
Abou El Hassan, Adil, 989
Aboulem, Ghita, 897
Abounaima, Mohammed Chaouki, 25
Agalit, Mohamed Amine, 507
Aggour, Mohammed, 711
Aghoutane, Badraddine, 15, 241, 247
Ahaitouf, Abdelaziz, 389
Ahaitouf, Ali, 353, 389, 457
Aharchi, Moncef, 365
Aissaoui, Karima, 65
Aitoumeri, Abdelhamid, 341
Akil, Mohamed, 887
Alae, Ammour, 843
Alami, Ali El, 911
Alami, Mustapha, 341
Alaoui, Chakib, 297, 411
Ali, Kartit, 257
Al-Jedaani, Abdulrhman Wassil, 101
Alkanhal, Majeed A. S., 977
Allouhi, Amine, 583, 595
Alqarni, Mohammed, 101
Alsharahi, Gamil, 1013
Alshdadi, Abdulrahman A., 101
Amadid, Jamal, 1037
Amane, Meryem, 65
Amara Korba, Mohamed Cherif, 809
Ammor, Hassan, 1061
Ammour, Alae, 897
Amraqui, Samir, 575
Amzi, Mohamed, 911, 1093
Aniba, Ghassane, 699

Aouraghe, Ibtissame, 897
Aroudam, Elhassan, 749
Awan, Wahaj Abbas, 1073, 1085
Ayadi, Nabil, 445
Azeroual, Mohamed, 607
Aziz, Wajid, 101
Azzaz-Rahmani, Salima, 921

B

Bachiri, Tahar, 1013
Badri, Abdelmajid, 483
Baghdad, Abdennaceur, 943
Bakdid, Amar, 125, 145
Ballouk, Abdelhakim, 943
Bamou, Abdelouahed, 15
Barbosa Castro, Neider Duan, 553
Baya, Maryem, 49
Bazi, Kaoutar, 527
Belahrach, Hassan, 933
Belahsen, Faouzi, 897
Belhabib, Abdelfettah, 1025
Belkasmi, Mohammed G., 223
Belmajdoub, Abdelhafid, 911
Benabdelouahab, Farid, 541
Benazzi, Abdelhamid, 797
Beniss, Mohamed Amine, 673
Benjelloun, Sarah, 189, 201
Benkaddour, Assia, 749
Bennouna, Khadija, 179
Ben Sassi, Hicham, 297
Benslimane, Mohamed, 113, 821
Berbia, Hassan, 135
Berrada, Mohammed, 65, 285, 783
Berraho, Mohamed, 49
Berrahou, Aissam, 135
Berrajaa, Achraf, 411

Berrich, Jamal, 223
 Bezzazi, Mohammed, 1013
 Bikrat, Youssef, 321
 Bishoy, H., 1123
 Borraez, Alejandra Santos, 469
 Bossoufi, Badre, 661
 Bouabid, El Mansouri, 1111
 Boualam, Manal, 877
 Bouamrane, Omar, 615
 Bouchemha, Amel, 855
 Bouchentouf, Toumi, 223
 Bougroun, Zineb, 211
 Boujoudar, Younes, 607
 Boulaich, Hanan, 749
 Boulouird, Mohamed, 1025, 1037
 Bounoua, Zineb, 627
 Bourouba, Hocine, 809
 Boushaba, Abdelali, 515
 Boushaki, Abdessamad El, 201
 Boutejdar, A., 1123
 Bouyahyaoui, Abdelmalik, 341
 Bustos, Catalina Ríos, 469

C

Castro, Phillip Meziath, 469
 Chaatouf, Dounia, 575
 Chadli, Hajar, 321
 Chadli, Sara, 321
 Chakir, El Mostapha, 507
 Cheddadi, Fatima, 419
 Cheddadi, Youssef, 419
 Chigane, Khalid, 687
 Chougrad, Hiba, 179, 201

D

Damoiseaux, Jean Luc, 3
 Das, Sudipta, 911, 961
 Derouiche, Imane, 125, 145
 Dhriyyef, Mohammed, 649
 Doghmane, Hakim, 809
 Dosse, Saad Bennani, 333, 735, 759, 911,
 1093, 1123
 Driss, El Azzab, 1049, 1111

E

El Aissi, Mohamed El Mehdi, 189, 201
 El Akkad, Nabil, 821
 El Alami, Ali, 961
 Elalami, Jamila, 377
 Elalami, Noureddine, 377
 El Alaoui, Mustapha, 309

EL Baghdadi, Salah-Eddine, 135
 El Bakkali, Moustapha, 265, 1101
 El Boushaki, Abdessamad, 179
 El Fadili, Hakim, 495, 759
 El Ftouh, H., 265
 El Ghzaoui, Mohammed, 949, 961
 El Haj Ben Ali, Safae, 179
 El Hajjami, Lhoussain, 285
 El Hanouti, Imad, 495
 El Idrissi, Najiba El Amrani, 867
 El Khachine, Houda, 541
 El khadiri, Karim, 309
 El Khattabi, Mohammed Zakariae, 89
 EL Madani, Hakima, 49
 El Mahfoud, Mohammed, 661
 EL Makhfi, Noureddine, 25
 El Manssouri, Oussama, 769
 El Markhi, Hassane, 607, 673
 El Marzouki, Nisrine, 189
 El Mattar, Sara, 943
 EL Mazouri, Fatima Zahra, 25
 El Mehdi, Abdelmalek, 649, 989
 El Moukalafe, Mohammed Amine, 1001
 El Moussaoui, Hassan, 607, 673
 Elfakir, Youssef, 877
 Elfarissi, Ihame, 211
 Elghzizal, Yassir, 843
 Elhaj Ben Ali, Safae, 201
 Elhamadi, Taj-Eddin, 1101
 Elhitmy, Mohammed, 649
 Elkihel, Ali, 125, 145
 Elkihel, Yosra, 125, 145
 Elmahjoubi, Sghir, 911
 Elmajidi, Azeddine, 377
 Elmazoudi, Elhoussine, 377
 EL Ouadghiri, Moulay Driss, 15
 Errahimi, Fatima, 297, 419
 Essahlaoui, Ali, 241
 Essaid, Mohamed, 797
 Es-Sbai, Najia, 297, 419, 887
 Ez-Zaki, Fatima, 933

F

Fadili, Hakim El, 735
 Faize, Ahmed, 1013
 Fakir, Amine, 321

G

Gadi, Taoufiq, 167
 Gagliano, Antonio, 769
 Galadi, Abdelghafour, 445

Ghaffar, Adnan, 1073
 Ghammaz, Abdelilah, 933
 Ghazaoui, Youssa, 961
 Gmira, Faiq, 783
 Gouiouez, Mounir, 783
 Greche, Latifa, 887
 Gziri, Hassan, 125, 145

H

Habou Laouali, Inoussa, 735
 Habous, Amine, 77
 Hajji, Abdelghani, 711, 723
 Hajji, Bekkay, 431, 445, 769
 Hajji, Hicham, 699
 Hali, Aissa, 565
 Halima, 1085
 Hameed, Ahsan, 1085
 Hammouch, Nirmine, 1061
 Hanafi, Ahmed, 273
 Hassani, Abdelhadi Eloudrhiri, 483
 Hassani, Hamid, 353, 457
 Hassani, Moha M'Rabet, 1025, 1037
 Hernández Martin, Jhon Alexander, 553
 Himdi, Mohamed, 1061
 Houam, Lotfi, 855
 Hraoui, Said, 495, 783
 Husain, Niamat, 1085
 Hussain, Musa, 1073, 1085
 Hussain, Niamat, 1073

I

Ibriz, Abdelali, 113
 Ibtissame, Aouraghe, 843
 Iguernaissi, Rabah, 3

J

Jabrane, Younes, 971
 Jalti, Fakhreddine, 431
 Jamil, Abdelmajid, 583, 595
 Jarjar, Abdellatif, 495, 783
 Jarjar, Abdeltif, 797
 Jarrar, Oulidi A., 783
 Jedidi, Youssef, 89, 113
 Jorio, Mohammed, 911

K

Kaddari, Zakaria, 223
 Karim, Mohammed, 273
 Karmouni, Hicham, 831
 Karrouchi, Mohammed, 57

Kartit, Ali, 233
 Kassmi, Kamal, 57
 Kbir, M'hamed Ait, 365
 Khachouch, Mohamed Karim, 189
 Khaissidi, Ghizlane, 843, 877, 897
 Khalili, Tajeddine, 615
 Khamlichi, Abdellatif, 1013
 Khamlichi, Youness Idrissi, 179, 507
 Khlifé, Yamina, 565
 Korchi, Ayoub, 189
 Koumina, Abdelaziz, 971

L

Lachgar, Mohamed, 233
 Lagrioui, Ahmed, 661
 Lahlou, Yahya, 711, 723
 Lahmadi, Youssef, 89
 Lahrech, Khadija, 583, 595
 Laimeche, Lakhdar, 855
 Lakhri, Younes, 189, 201, 241
 Lale, Ahmet, 445
 Lamhamdi, Tijani, 607, 673
 Lamrini, Loubna, 25
 Laouali, Inoussa Habou, 759
 Latachi, Ibtissam, 273
 Launay, Jerome, 445
 Lberni, Abdelaziz, 389
 Li, Xue Jun, 1073
 Loukili, Yassine, 201

M

Maaroufi, Mohammed, 401
 Madani, Mohammed Amine, 65
 Madjarov, Ivan, 3
 Mansouri, Anass, 333, 353, 457
 Mansouri, Khalifa, 615
 Marktani, Malika Alami, 389
 Martin, Jhon Hernández, 469
 Marzouq, Manal, 735, 759
 Masmoudi, Nouri, 389
 Mbarki, Abderrahim, 431
 Mechal, Chaymae El, 867
 Mechaqrane, Abdellah, 627, 639
 Mellah, Youssef, 223
 Mellouli, El Mehdi, 285
 Mentouri, Zoheir, 809
 Meraoumia, Abdallah, 855
 Merrouchi, Mohamed, 167
 Mesbah, Abderrahim, 135
 Mesbah, Meryem, 157
 Mesbah, Mostefa, 867

Messaoudi, Abdelhafid, 57
 Messaoudi, Kamel, 809
 Mestoui, Jamal, 949
 Mezrhab, Ahmed, 575
 Minaoui, Khalid, 1001
 Mohamed, Lachgar, 257
 Mohammed, Charroud, 1111
 Moumen, Aniss, 241
 Moumeni, Loubna, 211
 Moumkine, Noureddine, 37
 Moussaoui, Hanae, 821
 Moutaouakil, Abdelhakim, 971
 Mrabti, Mostafa, 843, 877, 897
 Mustapha, Aatila, 257

N

Nadeem, Malik Sajjad Ahmed, 101
 Nafis, Fouad, 247
 Naim, Soufiane, 37
 Naqvi, Syedalfat, 1073
 Nasri, Ismail, 57
 Nassereddine, Bouchaib, 527
 Nfaoui, El Habib, 77
 Nkengue, Marc Junior Pierre, 3

O

Ortiz, Fran Pérez, 469
 Ouahabi, Mohamed Hatim, 541
 Ouassaid, Mohammed, 401, 687
 Ouazzani Chahidi, Laïla, 639
 Oubrich, Lhoussaine, 401
 Oughdir, Lahcen, 89
 Oussama, Jabrane, 1111
 Ouzarf, Mohamed, 25

Q

Qassemi, Hamid, 735, 759
 Qjidaa, Hassan, 309, 831
 Qobbi, Younes, 797

R

Rachidi, Tajjeeddine, 273
 Rahhali, Mounia, 89, 113
 Raihani, Abdelhadi, 615
 Raillani, Benyounes, 575
 Raouhi, El Mehdi, 233
 Reha, Abdelati, 971
 Rizvi, Syed Naheel Raza, 1085
 Ruano, Antonio, 735, 759
 Ruichek, Yassine, 333

S

Saber, Mohammed, 211, 321, 989
 Sáenz Blanco, Fabiola, 553
 Sabri, My Abdelouahed, 157
 Sadiqui, Ali, 507
 Sahel, Aïcha, 483
 Saïkouk, Hajar, 411
 Salhi, Mourad, 575
 Sallem, Amin, 389
 Sayyouri, Mhamed, 831
 Schlindwein, Fernando S., 101
 Sebari, Imane, 699
 Sejai, Mohamed, 333
 Sghiouar, Mohamed, 699
 Skittou, Mustapha, 167
 Slimani, Abdellatif, 911
 Slimani, Ilham, 211
 Smiri, Safae, 515
 Snoussi, Hajar, 57
 Souffer, Imane, 699
 Soufiane, Ezzaim, 135

T

Taamouch, Abdelhak, 887
 Tahani, Abdelwahed, 321
 Tahiri, Ahmed, 309, 831
 Tahiri, Mohamed Amine, 831
 Talibi Alaoui, Mohammed, 25
 Taoussi, Mohammed, 661
 Tapias Forero, Evy Fernanda, 553
 Temple-Boyer, Pierre, 445
 Tina, Giuseppe Marco, 769
 Tmimi, Mehdi, 113
 Touhami, Naima Amar, 265, 1101
 Tyass, Ilham, 615

W

Wailoo, Mike P., 101

Y

Yahyaouy, Ali, 157, 247
 Yazghich, Ikrame, 49
 Yessef, Mourad, 661

Z

Zahi, Azeddine, 515
 Zaidi, Abir, 1073
 Zakriti, A., 265
 Zbitou, Jamal, 1093
 Zefri, Yahya, 699

Zerrouki, Hadj, [921](#)
Zhar, Rania, [583](#), [595](#)

Zouaq, Karim, [341](#)